

Nonequilibrium Processes in Partially Ionized Gases

NATO ASI Series

Advanced Science Institutes Series

A series presenting the results of activities sponsored by the NATO Science Committee, which aims at the dissemination of advanced scientific and technological knowledge, with a view to strengthening links between scientific communities.

The series is published by an international board of publishers in conjunction with the NATO Scientific Affairs Division

A	Life Sciences	Plenum Publishing Corporation
B	Physics	New York and London
C	Mathematical and Physical Sciences	Kluwer Academic Publishers Dordrecht, Boston, and London
D	Behavioral and Social Sciences	
E	Applied Sciences	
F	Computer and Systems Sciences	Springer-Verlag
G	Ecological Sciences	Berlin, Heidelberg, New York, London,
H	Cell Biology	Paris, and Tokyo

Recent Volumes in this Series

Volume 214—Science and Engineering of One- and Zero-Dimensional Semiconductors
edited by Steven P. Beaumont and Clivia M. Sotomayor Torres

Volume 215—Soil Colloids and their Associations in Aggregates
edited by Marcel F. De Boodt, Michael H. B. Hayes,
and Adrien Herbillon

Volume 216A—The Nuclear Equation of State, Part A:
Discovery of Nuclear Shock Waves and the EOS
edited by Walter Greiner and Horst Stöcker

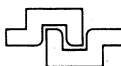
Volume 216B—The Nuclear Equation of State, Part B:
QCD and the Formation of the Quark-Gluon Plasma
edited by Walter Greiner and Horst Stöcker

Volume 217—Solid State Microbatteries
edited by James R. Akridge and Minko Balkanski

Volume 218—Applications of Statistical and Field Theory
Methods to Condensed Matter
edited by Dionys Baeriswyl, Alan R. Bishop, and José Carmelo

Volume 219—Physics and Applications of Pseudosparks
edited by Martin A. Gundersen and Gerhard Schaefer

Volume 220—Nonequilibrium Processes in Partially Ionized Gases
edited by Mario Capitelli and J. Norman Bardsley



Nonequilibrium Processes in Partially Ionized Gases

Edited by

Mario Capitelli

Department of Chemistry and
Centro di Studio per la Chimica dei Plasmi del CNR
University of Bari
Bari, Italy

and

J. Norman Bardsley

Lawrence Livermore National Laboratory
Livermore, California

Plenum Press

New York and London

Published in cooperation with NATO Scientific Affairs Division

Proceedings of a NATO Advanced Study Institute on
Nonequilibrium Processes in Partially Ionized Gases,
held June 4-17, 1989,
in Acquafrredda di Maratea, Italy

Library of Congress Cataloging-in-Publication Data

NATO Advanced Study Institute on Nonequilibrium Processes in Partially Ionized Gases (1989 : Acquafrredda di Maratea, Italy)
Nonequilibrium processes in partially ionized gases / edited by Mario Capitelli and J. Norman Bardsley.
p. cm. -- (NATO ASI series. B, Physics ; v. 220)
"Proceedings of a NATO Advanced Study Institute on Nonequilibrium Processes in Partially Ionized Gases, held June 4-17, 1989, in Acquafrredda di Maratea, Italy"--T.p. verso.
"Published in cooperation with NATO Scientific Affairs Division."
Includes bibliographical references and index.
ISBN 0-306-43586-1
1. Nonequilibrium plasmas--Congresses. 2. Collisions (Nuclear physics)--Congresses. I. Capitelli, M. II. Bardsley, J. Norman. III. North Atlantic Treaty Organization. Scientific Affairs Division. IV. Title. V. Series: NATO ASI series. Series B, Physics ; v. 220.
QC718.5.E66N38 1989
530.4'4--dc20

90-7487
CIP

© 1990 Plenum Press, New York
A Division of Plenum Publishing Corporation
233 Spring Street, New York, N.Y. 10013

All rights reserved

No part of this book may be reproduced, stored in a retrieval system, or transmitted in any form or by any means, electronic, mechanical, photocopying, microfilming, recording, or otherwise, without written permission from the Publisher

PREFACE

The NATO Advanced Research Institute on Nonequilibrium Processes in Partially Ionized Gases was held at Acquafrredda di Maratea during 4-17 June 1989.

The Institute considered the interconnections between scattering and transport theories and modeling of nonequilibrium systems generated by electrical discharges, emphasizing the importance of microscopic processes in affecting the bulk properties of plasmas.

The book tries to reproduce these lines. In particular several contributions describe scattering cross sections involving electrons interacting with atoms and molecules in both ground and excited states (from theoretical and experimental point of view), of energy transfer processes as well as reactive ones involving excited molecules colliding with atoms and molecules as well as with metallic surfaces. Other contributions deal with the basis of transport theories (Boltzmann and Monte Carlo methods) for describing the bulk properties of non equilibrium plasmas as well as with the modeling of complicated systems emphasizing in particular the strong coupling between the Boltzmann equation and excited state kinetics. Finally the book contains several contributions describing applications in different fields such as Excimer Lasers, Negative Ion Production, RF Discharges, Plasma Chemistry, Atmospheric Processes and Physics of Lamps.

The Organizing Committee gratefully acknowledges the generous financial support provided by the NATO Science Committee as well as by Azienda Autonoma di Soggiorno e Turismo of Maratea, by University of Bari, by C.N.R. (Centro di Studio per la Chimica dei Plasmi and Comitato per la Chimica), by ENEA, by Lawrence Livermore Laboratory and by US Army Research Office.

The editors wish to thank all the contributors for their co-operation in submitting the final version of their manuscripts on time.

M. Capitelli
J.N. Bardsley

CONTENTS

INVITED PAPERS

THEORY OF ELECTRON COLLISIONS IN PARTIALLY IONIZED GASES.....	1
J.N. Bardsley	
ELECTRON COLLISIONS WITH MOLECULES.....	19
H. Ehrhardt	
ELECTRON TRANSPORT IN PARTIALLY IONIZED GASES.....	33
L.C. Pitchford	
NON EQUILIBRIUM PLASMA KINETICS.....	45
M. Capitelli and C. Gorse	
MODELING HIGH PRESSURE ELECTRIC DISCHARGES: APPLICATIONS TO EXCIMER LASERS.....	63
M.J. Kushner	
ENERGY TRANSFER IN ATOM/MOLECULE COLLISIONS WITH MOLECULES AND SURFACES.....	91
G.D. Billing	
REACTIVITY CALCULATIONS FOR ELEMENTARY ATOM-DIATOM PROCESSES AND APPLICATIONS TO NON-EQUILIBRIUM SYSTEMS.....	105
A. Laganà	
EXCIMER LASERS: STATUS AND PERSPECTIVES.....	129
S. Bollanti and T. Letardi	
FUNDAMENTAL PROPERTIES OF RF GLOW DISCHARGES: AN APPROACH BASED ON SELF-CONSISTENT NUMERICAL MODELS.....	155
J.P. Boeuf and Ph. Belenguer	
THEORY OF HIGH-FREQUENCY DISCHARGES.....	187
C.M. Ferreira	

VOLUME PRODUCTION OF HYDROGEN NEGATIVE IONS.....	213
M. Bacal	
LASER DIAGNOSTICS OF A HYDROGEN DISCHARGE.....	227
H.J. Hopman	
HYDROGEN-SURFACE INTERACTIONS.....	241
H.J. Hopman	
PLASMA ASSISTED THIN FILM PRODUCTION WC, a-C:H and DIAMOND FILMS.....	251
H. Ehrhardt	
ELECTRIC DISCHARGE LAMPS.....	261
L.C. Pitchford	

CONTRIBUTED PAPERS

INELASTIC SCATTERING OF ELECTRONS FROM H ₂ MOLECULE AND FIRST-BORN APPROXIMATION: ROLE OF CORRELATION.....	269
G.P. Arrighini, C. Guidotti and N. Durante	
ELECTRON-MOLECULE COLLISION CROSS SECTIONS FOR ETCHING GASES.....	283
K.H. Becker	
ELECTRON COLLISIONS IN GAS SWITCHES.....	291
L.G. Christophorou	
THEORY OF e ⁻ -DIATOM SCATTERING AT LOW ENERGIES.....	311
E. Ficocelli Varracchio and U.T. Lamanna	
A PARAMETER-FREE THEORETICAL MODEL FOR LOW-ENERGY ELECTRON SCATTERING FROM POLYATOMIC MOLECULES.....	323
F.A. Gianturco and S. Scialla	
ELECTRON COLLISION CROSS-SECTIONS DETERMINED FROM BEAM AND SWARM DATA BY BOLTZMANN ANALYSIS.....	333
M. Hayashi	
ELECTRON COLLISION CROSS SECTIONS INVOLVING EXCITED STATES.....	341
W.M. Huo	
ELECTRON COLLISION CROSS SECTIONS INVOLVING EXCITED STATES.....	349
E.J. Mansky	
NEW THEORETICAL APPROACHES FOR STUDYING ELECTRON COLLISIONS WITH SMALL MOLECULES.....	357
T.N. Rescigno	
ION-NEUTRAL REACTIONS.....	365
R. Johnsen	

ENERGY POOLING COLLISIONS: A STEP TOWARDS IONIZATION.....	373
S. Gozzini, C. Gabbanini and L. Moi	
POTENTIAL ENERGY CURVES OF OPEN SHELL SYSTEMS (EXCIMERS)	
FROM MOLECULAR BEAM SCATTERING.....	383
V. Aquilanti, R. Candori, D. Cappelletti and F. Pirani	
MOLECULAR BEAM MEASUREMENTS OF IONIZATION CROSS SECTIONS RELEVANT TO THERMAL PLASMAS AND EXCIMER LASER SYSTEMS.....	393
S. Bianco, B. Brunetti, M. Gonzalez and F. Vecchiocattivi	
THE SILENT DISCHARGE AND ITS APPLICATION TO OZONE AND EXCIMER FORMATION.....	401
B. Eliasson and U. Kogelschatz	
NON EQUILIBRIUM EXCIMER LASER KINETICS.....	411
C. Gorse	
STUDY OF A PHOTOSWITCHED DISCHARGE FOR EXCIMER LASER.....	425
V. Puech, S. Mizzi and B. Lacour	
A SELF-CONSISTENT MONTE CARLO MODELING OF RF NON-EQUILIBRIUM PLASMA.....	433
A. Date, K. Kitamori and H. Tagashira	
CHARGED PARTICLES DYNAMICS IN ELECTROPOSITIVE GLOW DISCHARGES PROBED BY OPTICAL DIAGNOSTICS.....	441
J. Derouard, H. Debontride, M.P. Alberta and N. Sadeghi	
PROBLEMS IN THE EXPERIMENTAL DETERMINATION OF ELECTRON ENERGY DISTRIBUTION FUNCTION IN RF DISCHARGES.....	451
G. Dilecce, M. Capitelli, S. De Benedictis and C. Gorse	
SPECTROSCOPIC DIAGNOSTICS IN THE CATHODE FALL AND NEGATIVE GLOW OF A NITROGEN GLOW DISCHARGE.....	459
J. Jolly	
ELECTRON KINETICS IN RF DISCHARGES.....	467
T. Makabe	
A RADIOFREQUENCY TRAP FOR TESTS ON PRODUCTION AND EXCITATION OF IONS.....	479
G. Brautti, A. Boggia, A. Rainò, V. Stagno, V. Variale and V. Valentino	
GAS-PHASE AND GAS-SURFACE INTERACTIONS OF VIBRATIONALLY EXCITED HYDROGEN MOLECULES.....	485
M. Cacciatore	

TRANSLATIONAL ENERGY DISTRIBUTION FUNCTIONS OF H AND H ⁺ IN H ₂ VOLUME DISCHARGES.....	499
M. Capitelli, R. Celiberto and M. Cacciatore	
NUMERICAL SIMULATION ON TANDEM NEGATIVE ION SOURCE.....	505
O. Fukumasa and S. Ohashi	
ATOMIC AND MOLECULAR SURFACE AND VOLUME PROCESSES IN THE ANALYSIS OF NEGATIVE HYDROGEN DISCHARGES.....	517
J.R. Hiskes and A.M. Karo	
INTERPRETATION AND ANALYSIS OF THE H ₂ VIBRATIONAL DISTRIBUTION IN A HYDROGEN DISCHARGE.....	525
J.R. Hiskes and A.M. Karo	
ELECTRON ENERGY DISTRIBUTION FUNCTIONS IN MAGNETIC MULTIPOLE PLASMAS.....	533
M.B. Hopkins	
EFFECTS DUE TO NEGATIVE IONS AND PARTICLES IN PLASMAS.....	541
A. Garscadden	
ELECTRON AND VIBRATIONAL KINETICS IN MOLECULAR DISCHARGES.....	551
J. Loureiro	
LASER DIAGNOSTIC OF RADIO-FREQUENCY OXYGEN PLASMA.....	561
A. Sasso, M. Inguscio, G.M. Tino and L.R. Zink	
SPECTROSCOPY AND KINETICS OF AN OXYGEN GLOW DISCHARGE.....	571
M. Touzeau, G. Gousset, J. Jolly, D. Pagnon, M. Vialle, C.M. Ferreira, J. Loureiro, M. Pinheiro and P.A. Sà	
SIMULATION WORK IN NOBLE GAS RADIATION DETECTORS.....	581
C.A.N. Conde and T.H.V.T. Dias	
A DESCRIPTION OF THE NON-EQUILIBRIUM BEHAVIOR OF ELECTRONS IN MATTER: MACRO-KINETICS.....	589
E.E. Kunhardt	
THERMALIZATION AND TRANSPORT OF SPUTTERED PARTICLES IN GLOW DISCHARGES.....	601
K.T. Waldeer, H.M. Urbassek, A. Gras-Martí and J. A. Vallés-Abarca	
THE FREE ELECTRON LASER: A SIMPLE QUANTUM PICTURE.....	607
R. Caloi, G. Dattoli, M. Richetta and A. Torre	
ELECTRON AND PHOTON COLLISIONS IN STRONG LASER FIELDS.....	617
R. Daniele, G. Messina, F. Morales and G. Ferrante	

RESONANT PHOTOPUMPING OF LITHIUMLIKE IONS IN LASER-PRODUCED PLASMAS.....	641
Y.T. Lee	
IONIZATION AND DEIONIZATION OF ELECTRON BEAM DISTURBED AIR.....	651
A.W. Ali	
RE-ENTRY PROBLEMS.....	659
C. Bruno and L. Guarino	
DIAGNOSTICS OF ATOMIC SPECIES NEAR THE ELECTRODES OF A FLUORESCENT LAMP.....	669
A.K. Bhattacharya	
EXCITED STATE DIAGNOSTICS IN HIGH PRESSURE ARC LAMPS.....	677
D. Karabourniotis	
PARTICIPANTS.....	685
INDEX.....	693

THEORY OF ELECTRON COLLISIONS IN PARTIALLY IONIZED GASES

J. N. Bardsley

Lawrence Livermore National Laboratory
P.O. Box 808, L-296
Livermore, California 94550

1. Introduction

The emphasis in this Institute will be on plasmas created from molecular gases. This is appropriate, since most stable gases are made up of molecules. The additional degrees of freedom provided by the nuclear motion greatly increase the variety of collision processes and the loss of spherical symmetry makes collision theory much more difficult.¹⁻⁴ Only recently have the available computational facilities been adequate to permit reliable quantitative calculations to be made. In the lectures and subsequent seminars many of these calculations will be discussed. We will also review some of the approximation techniques and theoretical models that are useful in the interpretation of experimental results.

Although most singly-ionized molecules are stable against dissociation further ionization almost always leads to fragmentation. Thus in the study of molecular gases at high temperature one must also understand collision processes involving atomic ions. Since the Coulomb repulsion hinders the close approach of two positive ions, the most important collisions are those between electrons and ions. For highly charged ions experiments are more difficult but theory becomes easier since independent-particle models become more accurate. Thus Hartree-Fock or Dirac-Fock calculations may be adequate for electron structure determinations and distorted-wave methods may suffice in the calculation of collision cross-sections.

The starting point for most theoretical studies of electron-molecule collisions is the Born-Oppenheimer approximation. Because of their larger mass, the nuclei usually move much more slowly than the electrons. One

can therefore learn much from the study of electron scattering by molecules with fixed nuclei, especially if one repeats the calculation for several values of the inter-nuclear separations. One must take special care if the electron motion is anomalously slow, for example near thresholds, and when the time of interaction of the electron with the molecule is lengthened through strong long-range forces or the formation of resonant states.

2. Ab Initio Theories of Electron-Molecule Collisions With Fixed Nuclei

For collisions of low-energy electrons with small molecules, one can now perform calculations with wave functions that both have the correct asymptotic form and are sufficiently flexible to describe the electron correlation at short distances. The different character of short-range and long-range interactions is exploited in the R-matrix method^{5,6} through the separation of configuration space into two regions. When an electron is far from the nucleus, say with $r > a$, exchange is neglected and its wave function is expanded in spherical harmonics about a single center. In this region it is essential that the dominant long-range interaction, such as the dipole potential or polarization force, is treated well through the inclusion of the appropriate excitation channels or the introduction of effective potentials.

The radius a which defines the border between the two regions must therefore be chosen so that all of the molecular orbitals that are required to describe each of the states that can be excited during the collision are negligibly small for $r > a$.

In the inner region with all $r_i < a$, one would like to make maximal use of the extensive software that has been developed by quantum chemists for the study of molecular bound states. Thus one expands the wave functions in terms of atomic orbitals $x_i(\vec{r})$, which are either Slater functions, which consist of exponentials multiplied by polynomials in r and spherical harmonics, or Gaussian functions multiplied by polynomials in cartesian coordinates. If these orbitals are indeed small for $r > a$, all integrals involving these functions over the internal region can be extended to infinity and evaluated by standard techniques.

Following Gillan et al.,⁵ the wave function describing the $(N + 1)$ -electron system in the internal region, with fixed inter-nuclear separation R , is written

$$c_k = \mathcal{A} \sum_{ij} \bar{\phi}_i(x_1, \dots x_n, \sigma_{n+1}) \eta_j(\vec{r}_{N+1}) \alpha_{ijk} + \sum_i \rho_i(x_1, \dots x_{N+1}) \beta_{ik} \quad (1)$$

Here we have written a single symbol $x_i \equiv (\vec{r}_i, \sigma_i)$ to represent the spatial and spin coordinates of each electron. In the first term the $\bar{\phi}_i$ are constructed by coupling the electronic target eigenstates (describing the initial, final or other open states) or pseudostates (describing temporary distortion effects such as polarization) to the spin function of the extra electron to form spin eigenstates. The one-electron functions η_j may be linear combinations of the atomic orbitals x_i . However, to provide wave functions that do not vanish at the boundary these orbitals are supplemented by numerically-generated functions

$$\eta_j(\vec{r}) = \frac{1}{r} u_j(r) Y_{\ell m}(\hat{r}) \quad (2)$$

in which the origin of coordinates is assumed to be the centre of mass of the molecule. The radial functions $u_j(r)$ should not vanish at the boundary, and are usually defined as the solutions of a one-electron Schrödinger equation with a suitable effective potential and are made orthogonal to the atomic orbitals x_i .

The second term in Eq. (1) describes short-range correlation effects and the ρ_i are constructed as linear combinations of anti-symmetrized products of the atomic orbitals x_i with the appropriate symmetry properties.

The first major step in an R-matrix calculation is to diagonalize an operator $H_{N+1} + L_{N+1}$ in the internal region, so that

$$\langle \psi_k | H_{N+1} + L_{N+1} | \psi_k \rangle = \epsilon_k \delta_{kk}, \quad (3)$$

Here H_{N+1} is electronic part of the $(N+1)$ -electron Hamiltonian and L_{N+1} is a surface projection or Bloch operator introduced to ensure that the total operator is Hermitian in the interior region. It is defined in Eq. (3) of Ref. 5.

The resulting eigenstates ψ_k are now used as expansion functions for the scattering wave functions Ψ corresponding to the energy E . Since

$$(H_{N+1} + L_{N+1} - E) \Psi = L_{N+1} \Psi \quad (4)$$

we can write

$$| \Psi \rangle = \sum_k \frac{|\psi_k\rangle \langle \psi_k| L_{N+1}| \Psi \rangle}{\epsilon_k - E} \quad (5)$$

In order to connect with the external region we need to know the behavior

of $|\psi\rangle$ on the boundary. Let us define the reduced radial functions F_i corresponding to the scattering states by

$$F_i(r) = \langle \bar{\phi}_i Y_{\ell_i m_i} | \Psi \rangle \quad (6)$$

and the surface amplitudes for the eigenstates ψ_k by

$$w_{ik} = \langle \bar{\phi}_i Y_{\ell_i m_i} | \psi_k \rangle_{r=a} \quad . \quad (7)$$

We can now derive a relationship between the values of $F_i(r)$ and their derivatives on the boundary

$$F_i(a) = \sum_j R_{ij}(E) a \left(\frac{dF_j}{dr} \right)_{r=a} \quad (8)$$

where

$$R_{ij}(E) = \frac{1}{2a} \sum_k \frac{w_{ik} w_{jk}}{\epsilon_k - E} \quad (9)$$

This latter quantity is called the R-matrix and it provides the boundary condition that must be imposed on the solution of the Schrödinger equation in the external region.

One advantage of the R-matrix approach is that the problem of short-term correlations is solved once, through the computation of the parameters ϵ_k and w_{ik} , and does not have to be repeated for different values of the scattering energy. A second advantage is found when long-lived resonant states are formed, since the intermediate resonant state will usually be well described by one of the eigenstates ψ_k , and the resonant form of the scattering cross sections arises naturally from the form of the R-matrix.

Since exchange can be neglected in the external region, the radial functions $F_i(r)$ can be obtained by solving a set of coupled differential equations of the form

$$\left[\frac{d^2}{dr^2} - \frac{\ell_i(\ell_i + 1)}{r^2} + k_i^2 \right] F_i(r) = 2 \sum_{ij} V_{ij}(r) F_j(r) \quad (10)$$

The direct potentials $V_{ij}(r)$ can be expressed as multipole expansions in inverse powers of r . These equations must be solved for each energy E , and fitted to the asymptotic form

$$F_{ij} \approx \sin(k_i r - \frac{1}{2} \ell_i \pi) \delta_{ij} + \cos(k_i r - \frac{1}{2} \ell_i \pi) K_{ij} \quad (11)$$

in the open channels. The scattering cross sections can then be derived from the K-matrix, either directly or through the T-matrix

$$T = 2i K / (1 - iK)$$

A similar strategy is used in the linear-algebraic method,⁷ but the wave function in the inner region is calculated in a different manner. Exchange is treated through a separable approximation and Green's functions are introduced to transform the coupled differential equations for the radial wave function of scattered electron into integral equations. Expressing the integrals in these equations as quadratures results in a set of linear algebraic equations for the values of the wave functions at the quadrature points.

The development of more traditional variational techniques has been retarded by the appearance of anomalous singularities in the scattering matrices. These singularities can be avoided through the use of the Schwinger variational principle,^{7,8} which is based on the integral equation approach, or by applying the Kohn variational approach to the complex T-matrix instead of the real K-matrix.⁹ The Schwinger method requires the evaluation of matrix elements of the Green's function, but does not require that the trial wave function satisfies the correct boundary condition. It can therefore be applied with a basis set constructed entirely from square-integrable functions. On the other hand the complex Kohn technique only involves matrix elements of the Hamiltonian, but does require that the trial wave functions possess the correct asymptotic form appropriate to the scattering process under consideration with a trial value for the scattering T-matrix. The Kohn procedure then produces a stationary expression for the actual T-matrix in terms of the trial value. Recent progress using each of these variational techniques is described in papers by Huo and by Rescigno in this volume.

These methods are all computationally intensive and are most successful when the number of open excitation channels is small. The number of closed channels that are included explicitly must also be limited. The effects of closed channels are often described through correlation terms or optical potentials. The use of complex optical potentials to represent excluded open channels has not yet been thoroughly tested in electron-molecule collisions.

At higher energies special techniques can be used. Some, such as the plane-wave or distorted-wave born approximation,¹⁰ use perturbation theory. Others, such as the eikonal approximations^{11,12} and the Gryzinski method,¹³ use analogies with ray optics and classical scattering theory, respectively.

3. Allowance For Nuclear Motion

When the duration of a collision is short in comparison to the rotational period, cross sections for rotational excitation can be inferred from calculations made with fixed nuclei. At very low energies, and for molecules with large dipole moments, the situation is more complex, as is clear from the review by Shimamura² and from the article by Ficocelli Varrachio and Lamanna in this volume.

For collisions which are short in comparison to the vibrational period, cross sections for vibrational excitation or dissociative excitation can be obtained through the adiabatic nuclei approximation, by computing the K-matrix for the appropriate electronic transition at several values of the inter-nuclear separation and calculating its matrix element between the initial and final vibrational wave functions. Extensions of this approach, such as the hybrid method and the energy-modified adiabatic approximation are summarized in the article by Buckley, Burke and Noble in Ref. 2, which provides a comprehensive review of the theory of electron-molecule scattering. When resonances occur the collision time may exceed the vibrational period, and the Born-Oppenheimer approximation must be applied to the composite negative-ion system. Resonant scattering theories, recently reviewed by Herzenberg,^{2,4} provide the basis for the understanding of dissociative attachment and recombination and their predictions will be examined in the sessions on H⁻ formation.

In resonant scattering theory, the total wave function describing both the electronic and nuclear motion is written in the form

$$\Psi = \Phi_0(x_1, \dots x_{N+1}, R) \zeta_v(R) + \sum_n \psi_n(x_1, \dots x_{N+1}, R) \xi_n(R) \quad (12)$$

Here Φ_0 is an anti-symmetrized electronic wave function which describes a plane wave incident upon the target molecule in its initial electronic state and $\zeta_v(R)$ is the nuclear wave function describing the initial vibrational and rotational motion of the neutral molecule. The second term describes the formation and decay of the intermediate resonant states of the negative ion and is almost always truncated to a single term. The electronic wave function are approximate eigenfunctions of the electronic Hamiltonian

$$[H_{el} - W_n(R)] \psi_n = 0 \quad (13)$$

satisfying the outgoing boundary conditions appropriate to decaying states. The eigenvalues $W_n(R)$ are complex

$$W_n(R) = E_n(R) - \frac{i}{2} \Gamma_n(R) \quad (14)$$

and the imaginary part $\Gamma_n(R)$ indicates the rate of decay of the resonant state through electron emission. The corresponding nuclear wave function then satisfies the equation

$$[-\frac{1}{2M} \nabla_R^2 + W_n(R) - E] \xi_n(R) = v(R) \zeta_v(R) \quad (15)$$

where $v(R)$ is an entry amplitude which controls the probability of formation of the resonance at the nuclear separation R . Note that the effective nuclear potential is now complex.

If we introduce the Green's function $G(R, R')$ of the operator on the LHS of Eq. (15), then

$$\xi_n(R) = \int_0^\infty dR' G(R, R') v(R') \zeta_v(R') \quad (16)$$

To determine the vibrational excitation cross section we need to know the probability that the resonant state decays leaving the target molecule in the vibrational state v' . If the formation and decay of the resonance involve the same electronic process, the amplitude for vibrational excitation takes the form

$$f_{v'v} = \iint dR dR' \zeta_{v'}(R) v(R) G(R, R') v(R') \zeta_v(R') \quad (17)$$

The version of resonant scattering theory described above is appropriate when the formation and decay of the resonant state can be decoupled from the nuclear motion. This is not valid for very low energy collisions since the energy available to the emitted electron depends strongly on the vibrational level of the residual molecule. The effective potential then becomes non-local and the rate of decay is sensitive to the number of open vibrational channels.

Many resonant states of negative molecular ions become stable as the nuclear separation is increased. In such a case the process of dissociative attachment



can occur. The cross section for this process is proportional to the asymptotic value of the amplitude squared of the nuclear function, $|\xi_n(R)|^2$. Although this is usually obtained from the numerical solution of Eq. (15), a semi-classical solution leads to a formula for the dissociative attachment cross section with a simple physical interpretation. We write

$$\sigma_{DA}(E) = \sigma_{cap}(R_o) S(R_o, R_s) \quad (19)$$

$\sigma_{cap}(R_o)$ is the cross section for electron capture, which occurs near the separation R_o at which the difference in the electronic energies of the resonant negative ion state and the initial state of the neutral molecule is equal to the energy ϵ of the incident electron. The second factor $S(R_o, R_s)$, called the survival factor, describes the probability the resonant state lives long enough for the nuclei to separate from the capture point R_o to the stabilization point R_s at which the two electronic energy curves cross as shown in Fig. 1. The survival probability is given by

$$S(R_o, R_s) = \int_{R_o}^{R_s} \frac{\Gamma(R) dR}{\sqrt{2(E - E_n(R))/\mu}} \quad (20)$$

where μ is the reduced mass of the nuclei.

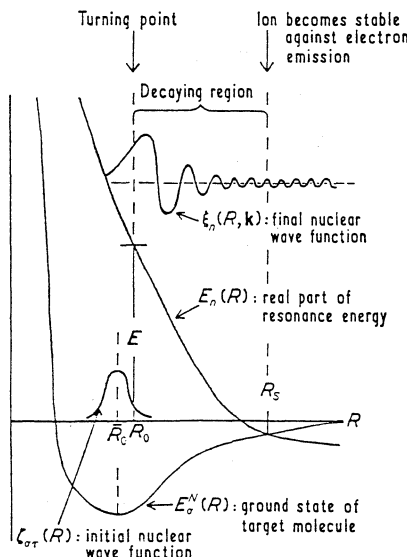


Figure 1 Potential energy curves and nuclear wave functions in dissociative attachment. The final wave function is schematic only.

Two features of dissociative attachment cross sections can be immediately understood on the basis of this expression. For reactions involving short-lived resonances the survival factor can be very small. In such cases one expects strong isotope effects, since a larger reduced mass results in a lower speed of dissociation and an even smaller survival probability. On the other hand if the stabilization separation R_s greatly exceeds the equilibrium separation R_e , the cross section can be enhanced

by many orders of magnitude if the molecule is initially in an excited vibrational state. This is because capture can occur with R_o closer to R_s , resulting in a large increase in the survival factor. The peak in the cross section often moves to lower energy as the vibrational quantum number increases, so that the increase in the rate of attachment at low temperatures is even more dramatic.

4. The Formation of Resonant States

The simplest type of resonant states are the shape resonances. These can occur when the effective potential experienced by the electron is attractive at short range and repulsive at long range, providing a potential barrier which can support quasi-bound states. The formation and decay of these states involves quantum tunnelling through the barrier. In atomic and molecular physics the repulsive potential usually arises from the centrifugal term and so these resonances almost always correspond to non-zero angular momentum. In electron scattering the centrifugal barriers can be penetrated easily and the shape resonances usually have very short lifetimes. In electron-molecule collisions, even though angular momentum is not conserved, states often have no s-wave component because their parity is odd or the coefficient of angular momentum about a symmetry axis is non-zero.

The most well-known examples of shape resonances are the $^2\Sigma_u^-$ ground state of H_2^- (predominantly p-wave) and the $^2\Pi_g^-$ ground state of N_2^- (d-wave). The former resonance is so short-lived that there has been considerable debate concerning its qualifications as a quasi-bound state, but resonant scattering theory does provide a semi-quantitative understanding of many low energy e- H_2 collision processes.

Resonances can also be formed when an electron loses energy through temporary excitation of the target molecule and falls into a bound molecular orbital. Decay then requires a further redistribution of energy. These are often called Feshbach resonances and exist in two varieties, depending on whether the energy is transferred to electronic excitation or nuclear excitation. Since the formation of nuclear-excited Feshbach resonances involves the transfer of energy from electronic to nuclear motion, the use of a non-local resonance theory is essential.

When the local width approximation is valid the energy $E_n(R)$ and width $\Gamma_n(R)$ of each resonance can be calculated by imposing outgoing boundary conditions and computing the eigenvalues of the electronic Hamiltonian, as in Eqs. (13) and (14), or by using R-matrix theory to search for poles

of the S-matrix. Alternatively one can fit the energy dependence of phase shifts or collision cross sections to the form expected in the neighborhood of a resonance. For example, near an isolated resonance in elastic scattering below the threshold for electronic excitation the phase shift rises rapidly. The eigenphase sums computed by Huo et al., using the Schwinger variational method and by Hazi, using a Stieltjes imaging technique, for $e\text{-N}_2$ scattering at various values of the nuclear separation are shown in Fig. 2. It is clear that the width of the resonance and the electron energy at which it occurs both decrease with increasing R.

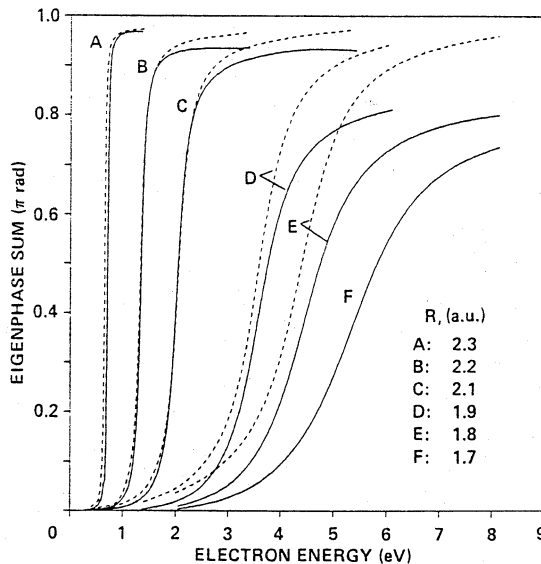


Figure 2 Eigenphase sums calculated for the $^2\Pi_g$ channel in $e\text{-N}_2$ scattering; — Schwinger variational method from Ref. 8,
- - - Stieltjes imaging calculations from Ref. 46.

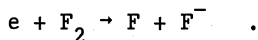
5. Scattering Near Thresholds

The behaviour of inelastic scattering cross sections near thresholds is of special interest to both experimenters and theorists. The slow motion of the electron after excitation enhances correlation and polarization effects and leads to the breakdown of the adiabatic-nuclei approximation. Narrow structures are often found challenging the resolution of experimenters and the interpretative skills of theorists. In applications to electron scattering processes with threshold energies that exceed the electron temperature, or average electron energy in non-

equilibrium situations, the excitation rate is often controlled by collisions at energies just above the threshold.

Molecules containing halogen atoms are of special interest in this respect, since the atomic negative ions have large positive electron affinities, but the molecular negative ions are often unstable at small inter-nuclear separations.

For molecules such as H_2 and F_2 in which the ground state of the negative ion has an outer electron orbital with non-zero angular momentum, one expects that as R is reduced the stable negative ion becomes a shape resonance. Although this picture is sufficient to explain the qualitative feature of $e-H_2^-$ collisions it fails to explain the very sharp peak seen near zero energy for the exothermic dissociative attachment reaction



This peak was observed by Chantry¹⁴ and confirmed by Chutjian and Alajajian.¹⁵

For exothermic processes the cross section near zero energy is proportional to $k^{2\ell-1}$, where k is the wave numbers and ℓ is the quantum number of the lowest partial wave that participates in the process. Thus the s-wave contribution to exothermic cross sections always diverges at zero energy, and we should always expect a zero-energy peak. The size of this feature depends on the strength of the s-wave component. For attachment of thermal electrons ($E \approx 40$ meV) to HI, this component is strong and the cross section¹⁶ is $\sim 2 \times 10^{-14} \text{ cm}^2$. For F_2^- the s-wave component is weaker and the cross section¹⁵ is $\sim 1.5 \times 10^{-15} \text{ cm}^2$. Even this is surprising since the electronic symmetries of the lowest three resonant states of F_2^- are $^2\Sigma_u^-$, $^2\Pi_g$ and $^2\Pi_u$, none of which have s-wave components. Within the Born-Oppenheimer picture, the capture of zero energy electrons must lead to a $^2\Sigma_g^-$ state of the negative ion, and there are no low-energy states of this symmetry, the first one being the third excited state. Through the breakdown of the Born-Oppenheimer separation, and the transfer of angular momentum from the nuclei to the electrons, one could form the first excited $^2\Pi_g$ state of F_2^- . Calculations of the cross section for such capture would be worthwhile.

Experimental study of vibrational excitation in the hydrogen halides has also stimulated much theoretical debate. Prominent peaks have been observed in electron scattering by HF and HCl^- , as described in Ehrhardt's contribution to this volume. The HCl^- negative ion is stable for large values of R , but is unstable at the equilibrium separation of HCl . On the other hand in HF^- the dipole moment is strong enough that the long-range dipole interaction alone can support bound states. The most plausible

explanation of the narrow structures in the vibrational excitation cross section for HF is that they are associated with nuclear-excited Feshbach resonance. Recent R-matrix calculations by Morgan et al.¹⁷ suggest that this interpretation may also be valid for HC₂. The alternative explanation in terms of virtual states seems to be losing favor.

The theory of electron-molecule collisions near threshold has recently been reviewed by Morrison.¹⁸ That excellent article provides an overview of the theoretical methods and shows many comparisons between theory and experiment.

6. Electron Scattering by H₂ and D₂

To provide an example of the status of current theoretical and experimental knowledge of electron-molecule collisions, let us examine the simplest molecule H₂. In principle, the most stringent experimental tests of low energy scattering cross sections come from measurements of transport data, such as drift velocities and diffusion coefficients, which can be obtained with uncertainties of less than 1%. Buckman and Phelps¹⁹ have derived a set of cross sections which is consistent with the transport data and includes most of the significant energy loss processes.

In the energy range below 2 eV the transport properties are determined by the cross sections for momentum transfer, rotational excitation and vibrational excitation. The theory of these processes, as reviewed by Morrison et al.,²⁰ is well developed and is in good agreement with the results obtained by beam experiments. However, the cross sections between 1 and 2 eV differ significantly from those deduced from the transport data. Although one could argue that the derivation of cross sections from such data is not unique, when more than one collision process lead to significant energy loss, it is clear that the calculated collision cross sections would produce drift velocities and diffusion coefficients which are inconsistent with the measurements. Penetrante and Bardsley have carried out Monte Carlo simulations to check that this discrepancy does not arise from approximations used in the solution of the Boltzmann equation.

Between 1 eV and 5 eV vibrational excitation is dominated by the ² Σ_u^- shape resonance of H₂⁻. This resonance is very broad near the equilibrium separation of 1.4 a₀, but the width decreases with increasing R and the negative ion is stable for R > 3 a₀. The cross sections for the excitations of the levels v = 1 - 2 show a broad peak with no prominent structure, but many narrow peaks are seen in the cross sections for v = 3

- 6, as predicted by Mundel et al.²¹ and observed by Allan²² (see Fig. 3). As more energy is transferred to the vibrational motion less is available to the escaping electron. Tunnelling through the centrifugal potential barrier is then more difficult and the effective resonance width is reduced. This effect is well explained by the non-local resonance theory.²³

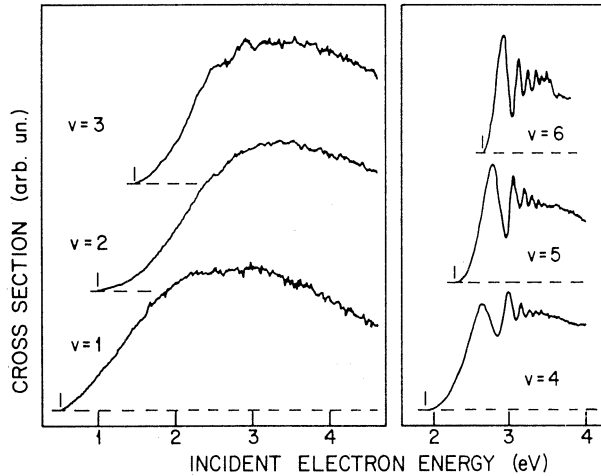


Figure 3 Vibrational excitation cross sections in H_2 measured by Allan (Ref. 22).

The lowest electronic excitation in H_2 is that of the repulsive $b\ 3\Sigma_u^-$ state which immediately dissociates to give two ground state H atoms. Although the detection of ground state dissociation fragments is difficult, this molecular state is sufficiently far removed from all others that the cross section can be measured by observing the energy loss of the scattered electron. Recent calculations,²⁴⁻²⁶ performed with the nuclei fixed at the equilibrium separation, using the R-matrix, Schwinger variational and linear algebraic approach, give results which agree well with the beam measurements, but are almost twice those recommended by Buckman and Phelps. More recently, Rescigno and Schneider²⁷ have applied the complex Kohn method to study the R-dependence of the excitation cross section and have derived cross sections for several different initial vibrational states ($v = 0 - 9$) for electron energies above 12 eV. The cross sections increase slightly as v rises. Extension of these results to lower energies would be very valuable, but this would require a more careful treatment of nuclear motion than was used in Ref. 23. Significant lowering of the apparent threshold for dissociation is expected as v increases and the thermal dissociation rate for temperatures less than 5 eV should increase dramatically as v is raised.

Since the Buckman-Phelps data set provides total energy loss rates which are consistent with measurements of diffusion coefficients, it seems likely that an upward revision of the $b^3\Sigma_u$ excitation cross section should be accompanied by a downward revision of other cross sections. Prime candidates would be the excitation of the states $B^1\Sigma_u$ and $C^1\Pi_u$ which lead to the emission of the Lyman and Werner bands. Optical measurements by Shemansky et al.,²⁸ which rely on a high-energy normalization to Born approximation values, suggest a decrease of ~ 30% in the Buckman-Phelps values. However, the Schwinger calculations by Gibson et al.²⁹ lead to only a 10% reduction.

Excitation of the B and C states is usually followed by radiative decay to the ground electronic state of H_2^- . The residual molecule is often left in a high vibrational level. Hiskes³⁰ has pointed out that this indirect mechanism for vibrational excitation can be much more efficient than the direct electron-impact excitation.

Dissociative attachment to H_2^- is an important mechanism for H^- , both in stellar atmospheres and in many laboratory plasmas. The threshold behavior of the attachment cross section is also controlled by the $^2\Sigma_u$ shape resonance. When this state is formed with $R \approx 1.4 a_0$ through collisions with ground state molecules it almost always decays by electron emission and the attachment cross section is very small ($< 10^{-21} \text{ cm}^2$). With highly excited molecules capture can occur near the stabilization point and the cross section rises by several orders of magnitude. This sensitivity to initial vibrational state is even stronger in D_2 , and is illustrated in Fig. 4.

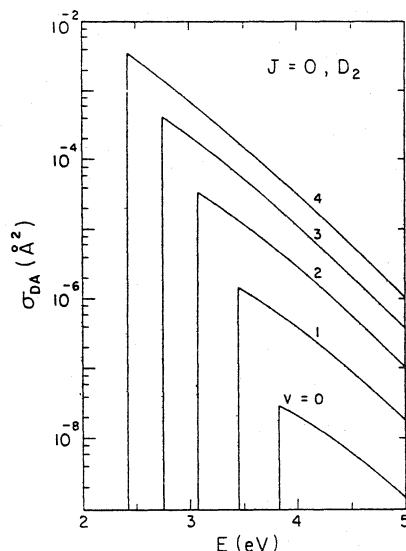
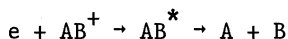


Figure 4 Dissociative-attachment cross sections for various rotationless vibrational states of D_2 .

Evidence for large increases in the threshold cross sections for attachment to H_2 and D_2 as v is raised was seen in the observations by Allan and Wong.³¹ These experiments were analyzed by Wadehra and Bardsley³² in terms of resonant scattering theory with a local width and by Mundel et al.³³ using a non-local theory.

7. Electron-Ion Scattering

Perhaps the most interesting process in electron scattering by molecular ions is dissociative recombination



Although this process is analogous to dissociative attachment the number of intermediate states AB^* that can play a role is much larger and the process is further complicated by the formation of vibrationally or rotationally excited levels of high Rydberg states. Even for H_2^+ there is significant disagreement between the calculations that have been reported.³⁴⁻³⁶ The dependence of the recombination rate on vibrational state is again of interest, since the merged beam data of Hus et al.³⁷ suggest that the rates are comparatively small for ions in the ground vibrational state.

Further experimental and theoretical work is also required to determine the branching ratios for the formation of the various possible final states. Even in $e-H_2^+$ collisions the distribution over the (nl) levels in the dissociating H atoms is not known. There is particular interest in the atmospheric ions³⁸⁻⁴⁰ N_2^+ , NO^+ and O_2^+ , and in the polyatomic ions⁴¹⁻⁴⁵ which are observed in inter-stellar gas clouds.

Although doubly charged molecular ions have been observed in the laboratory, they are extremely fragile and high-temperature plasmas are dominated by atomic ions. Elastic collisions of electrons with multiply-charged ions are extremely large, indeed they are infinite for isolated ions. This leads to efficient transfer of momentum from electrons to the ions and even to significant transfer of energy. For inelastic collisions involving highly excited ions, independent electron models of the target ions often lead to accurate cross sections, but the contributions of inner-shell excitation or ionization must not be neglected.

8. Conclusions

Computational techniques have been developed so far that calculations of low-energy electron collisions with small diatomic molecules can be calculated accurately in the Born-Oppenheimer approximation. Further work is needed to extend these techniques to situations with many open channels, and to polyatomic molecules. Considerable progress has been made in the treatment of nuclear effects, but several puzzles remain concerning the threshold behavior of vibrational excitation and dissociative attachment.

Acknowledgment

Work performed under the auspices of the U.S. Department of Energy by the Lawrence Livermore National Laboratory under contract number W-7405-ENG-48.

REFERENCES

1. L. G. Christophorou (ed.), *Electron-Molecule Interactions and Their Applications* (Academic; Orlando) 1984 (2 Vols.).
2. I. Shimamura and K. Takayanagi (eds.), *Electron-Molecule Collisions* (Plenum, New York) 1984.
3. L. C. Pitchford, B. V. McKoy, A. Chutjian and S. Trajmar (eds.) *Swarm Studies and Inelastic Electron-Molecule Collisions* (Springer Verlag, New York) 1987.
4. P. G. Burke and J. B. West (eds.) *Electron-Molecule Scattering and Photoionization* (Plenum, New York) 1988.
5. C. J. Gillan, O. Nagy, P. G. Burke, L. A. Morgan and C. J. Noble, *J. Phys. B* 20, 4585 (1987).
6. L. A. Morgan and P. G. Burke, *J. Phys. B* 21, 2091 (1988).
7. M. A. Lima, T. L. Gibson, K. Takatsuka and V. McKoy, *Phys. Rev. A* 30, 1741 (1984).
8. W. M. Huo, T. L. Gibson, M. A. Lima and V. McKoy, *Phys. Rev. A* 36, 1632 (1987).
9. B. I. Schneider and T. N. Rescigno, *Phys. Rev. A* 37, 3749 (1988).
10. R. W. Zurales and R. R. Lucchese, *Phys. Rev. A* 37, 1176 (1988).
11. R. Bijker and R. D. Amado, *Phys. Rev. A* 37, 1425 (1988).

12. A. Mengoni and T. Shirai, J. Phys. B 21, L567 (1988).
13. M. Cacciatore and M. Capitelli, Chem. Phys. 55, 67 (1981); R. Celiberto, M. Cacciatore and M. Capitelli, to be published.
14. P. J. Chantry, in Applied Atomic Collision Physics, eds. H. S. W. Massey, E. W. McDaniel and B. Bederson (Academic, New York, 1982), Vol. 3, p. 56.
15. A. Chutjian and S. H. Alajajian, Phys. Rev. A 35, 4512 (1987).
16. S. H. Alajajian and A. Chutjian, Phys. Rev. A 37, 3680 (1988).
17. L. A. Morgan, P. G. Burke and C. J. Gillan, submitted to J. Phys. B (1989).
18. M. A. Morrison, Adv. Atom. Mol. Phys. 24, 51 (1988).
19. S. J. Buckman and A. V. Phelps, J. Chem. Phys. 82, 4999 (1985).
20. M. A. Morrison, R. W. Crompton, B. D. Saha and Z. L. Petrovic, Aust. J. Phys. 40, 239 (1987).
21. C. Mundel, M. Berman and W. Domcke, Phys. Rev. A 32, 181 (1985).
22. M. Allan, J. Phys. B18, L451 (1985); Int. J. Quant. Chem. 31, 161 (1987).
23. W. Domcke and L. S. Cederbaum, J. Phys. B 13, 2829 (1980).
24. K. L. Baluja, C. J. Noble and J. Tennyson, J. Phys. B 18, L851 (1985).
25. M. A. Lima, T. L. Gibson, C. C. Lin and V. McKoy, J. Phys. B 18, L865 (1985).
26. B. I. Schneider and L. A. Collins, J. Phys. B 18, L857 (1985).
27. T. N. Rescigno and B. I. Schneider, J. Phys. B 21, L691 (1988).
28. D. E. Shemansky, J. M. Ajello and D. T. Hall, Astrophys. J. 296, 765 (1985).
29. T. L. Gibson, M. A. P. Lima, V. McKoy and W. M. Huo, Phys. Rev. A 35, 2473 (1987).
30. J. R. Hiskes, J. Appl. Phys. 9, 4592 (1980); Comm. At. Mol. Phys. 19, 59 (1987); J. R. Hiskes, A. M. Karo, M. Bacal, A. M. Bruneteau and W. G. Graham, J. Appl. Phys. 53, 3469 (1982).
31. M. Allan and S. F. Wong, Phys. Rev. Lett. 41, 1791 (1978).
32. J. M. Wadehra and J. N. Bardsley, Phys. Rev. Lett. 41, 1795 (1978); J. N. Bardsley and J. M. Wadehra, Phys. Rev. A 20, 1398 (1978).
33. C. Mundel, M. Berman and W. Domcke, Phys. Rev. A 32, 181 (1985).
34. A. Giusti-Suzor, J. N. Bardsley and C. Derkits, Phys. Rev. A 28, 682 (1983).
35. A. P. Hickman, J. Phys. B 20, 2091 (1987).
36. K. Nakashima, H. Takagi and H. Nakamura, J. Chem. Phys. 86, 726 (1987).

37. H. Hus, F. Youssif, C. Noren, A. Sen and J. B. A. Mitchell, Phys. Rev. Lett. 60, 1006 (1988); H. Hus, F. Youssif, A. Sen and J. B. A. Mitchell, Phys. Rev. A 38, 658 (1988).
38. J. L. Queffelec, B. R. Rowe, M. Morlais, J. C. Gomet and F. Vallee, Planet. Space Sci. 33, 263 (1985).
39. J. N. Bardsley, Planet. Space Sci. 31, 667 (1983).
40. S. L. Guberman, Planet. Space Sci. 36, 47 (1988).
41. D. R. Bates, Planet. Space Sci. 37, in press (1989).
42. S. Green and E. Herbst, Astrophys. J. 229, 121 (1979).
43. H. H. Michels and R. H. Hobbs, Astrophys. J. Lett. 286, L27 (1984).
44. F. Vallee, B. R. Rowe, J. C. Gomet, J. L. Queffelec and M. Morlais, Chem. Phys. Lett. 124, 317 (1986); B. R. Rowe, F. Vallee, J. L. Queffelec, J. C. Gomet and M. Morlais, J. Chem. Phys. 88, 845 (1987).
45. N. G. Adams, C. R. Herd and D. Smith, J. Chem. Phys. 91, 963 (1989).
46. A. U. Hazi, in Electron-Atom and Electron-Molecule Collisions, ed. J. Hinze (Plenum, New York, 1983), p. 103.

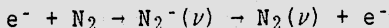
ELECTRON COLLISIONS WITH MOLECULES

H. Ehrhardt

Physikalisches Institut der Universität Kaiserslautern
Erwin-Schrödinger-Str. 46
6750 Kaiserslautern, Federal Republic of Germany

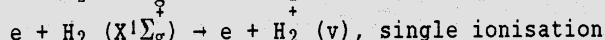
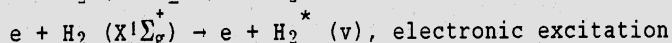
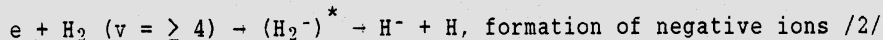
INTRODUCTION

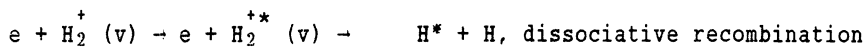
In most gas discharges which are used for ion sources, for laser media, in plasma chemistry and for the generation of thin films, the average electron energy ranges from a few eV up to some 10-30 eV. The energy distribution is not quite a Maxwellian distribution, often it has an extended high energy tail and it may have some deviations due to individual collision processes with very large cross sections. This is for example the case in the earth lower ionosphere because of the process



i.e. the formation of short living negative ion states of the nitrogen molecules, which decay by autoionisation but the molecules remain excited in high vibrational states. Since the majority of the electrons have energies of only a few eV, vibrational and rotational excitations by electrons are of great importance. On the other hand, most electronic excitation and ionisation processes need impact energies of more than 10 eV, i.e. their thresholds are already in the range of the exponentially decreasing intensity of the electron distributions. This means that it is necessary to know both, the electron energy distributions and the cross sections close to the relevant thresholds.

In the case of low energy gas discharges only electron impact processes are relevant, by which outer shell electrons of the molecule are involved. This means that rotational and vibrational excitations due to direct and resonance interactions, outer shell electron excitation and single ionisation are most prominent processes. For complex molecules the list of possible reactions and cross sections would be rather long. Only for the case of molecular hydrogen the experimental and theoretical data of the involved processes are rather complete /1/.





have rather large cross sections and therefore play an important role in hydrogen discharges.

EXPERIMENTAL METHODS FOR CROSS SECTION MEASUREMENTS

Several experimental methods exist for special measurements. Total cross sections can be measured very sensitively with trochoidal spectrometers developed by Stamatovic and Schulz /3/ and time-of-flight spectrometers brought to great perfection by Ferch et al /4/. Bederson et al /5/ have used the beam recoil method, i.e. the deflection of a molecular beam induced by the momentum transfer from the colliding electron to the target particle for low energy elastic collisions and for rotational excitations of highly polar alkali halogen molecules.

By far the most flexible electron impact spectrometer has been developed during the time between 1960 and 1967. Most important was the development of small 127° electrostatic analysers by Marmet and Kervin /6/ and the 180° analysers by Simpson and Kuyatt and Simpson /7/. A modern version of such a spectrometer is shown in Figure 1. It is used in the laboratory of the author.

The electrons are produced by thermal emission from a heated tungsten or iridium cathode and are focussed to the entrance slit of the first tandem energy selector. This tandem system has in principle the same energy resolution as a single system, but it reduces the background due to stray electrons. The second system reduces the stray intensity in the wings of a spectral line on the high and low energy side so that small signals close to large peaks can be measured. The two cylindrical selectors in Figure 1 are electrically separated by a small lens system L. This lens can be used to shift the transmission curves of the two selectors slightly with respect to each other so that the overall resolution is electrically tunable from outside the vacuum chamber. The exit lens system of the gun is quite open in order to reduce electron impact contaminations on its metal surfaces. The shape of the electron beam is visualised by multichannel plates followed by a phosphor (not shown in the figure) and its intensity is measured by a Faraday cup.

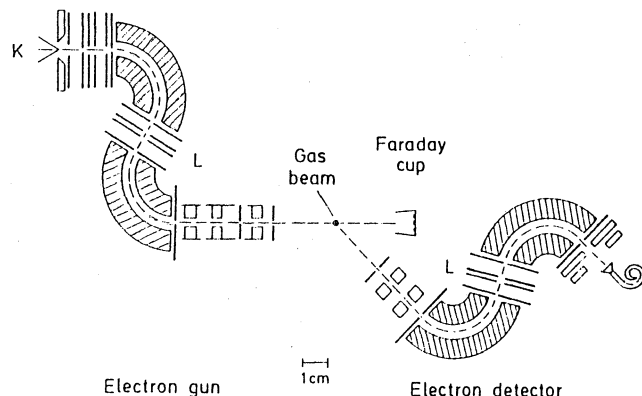


Figure 1. Schematic representation of a double tandem electron impact spectrometer with rotatable electron detector in the angular range from 0° to 150° . The energy resolution can be tuned electrically from outside the vacuum chamber.

The electron detector is built and operated similar as the electron gun. It can be rotated from 0° to 150° with respect to the primary electron beam. For operation in forward direction the Faraday cup is pushed away by the detector system.

The gas beam is produced by a single channel tube of 10 mm length and 0.5 mm diameter. The target gas pressure just above the tube is about 10^{-3} mbar.

All systems, the gun, the detector and the gas inlet tube are heated during operation up to 250° C in order to reduce adsorption of molecules and consequently potential disturbances on the metal surfaces. The residual magnetic field in the region of the gun and detector is less than 1 mG and the residual electric field in the scattering area is less than 1 mV if surface charging is not considered.

The operational data of such a spectrometer are as follows: Energy of the electron beam tunable from 0.05 eV to several 100 eV, energy inhomogeneity about 10 meV FWHM for all four selectors together, primary current ca. 10^{-10} A or higher depending on the desired energy resolution of the gun system. Several experimental groups use now the double monochromators and -analysers, often with 180° electrostatic energy selectors.

Of course, the so called classical electron impact spectrometer is quite versatile. Threshold energies of many processes can be measured, cross sections which are optically forbidden, angular dependencies which give information on the symmetry of a short living negative ion state or on the partial waves which are involved in the scattering and therefore one obtains information on the type of process which is occurring, i.e. whether it is resonant or a direct process proceeding mainly via the dipole or quadrupole moment or the long or/and short range polarizability of the molecule.

Many attempts have been made in the last years to improve such spectrometers, but keeping their versatility. One major improvement is the production of photoelectrons by lasers or synchrotron radiation as a substitute for the thermoionic cathode and the complicated gun system which introduces the major troubles in spectrometers. Thermally produced electrons have an energy distribution which normally is about 300 meV wide, which means that if one wants an energy inhomogeneity of only one meV, one has to eliminate about 99 % of all electrons and use only about 1 % in order to form a decent electron beam. Of course the 99 % electrons produce space charge and surface contaminations in the whole gun system. Therefore it is reasonable to produce only electrons which are already monochromatic and the classical gun system is reduced to an electron optical system which forms a well collimated electron beam of those photoelectrons.

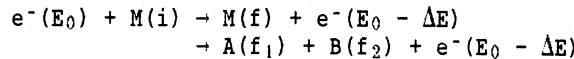
Such attempts have been made by several groups. Kennerly et al /8/ have photoionized metastable barium atoms (1D_2) with 3.8 eV photons from a He-Cd ultraviolet laser and obtained electrons with kinetic energy of 17 meV, an energy inhomogeneity of 5 meV and an electron beam current of about 10^{-12} A.

More intensity was obtained by Field et al /9/ by producing very slow electrons using synchrotron radiation for the photoionisation of argon. The photo-electrons have been shaped to a beam with kinetic energy ranging from 0.1 to 0.3 eV and directed to a supersonic beam of molecular oxygen. The authors measured the energy dependence of the vibrational

excitation of the molecule. They were able to measure fine structure splitting and saw effects of rotational excitations on the width of the O_2^- -resonance peak. The final energy resolution was 5.5 meV.

Another rather new development is the introduction of position sensitive detectors in electron spectrometers which was achieved first by Comer et al /10/. Such a device reduces the time for measurements of energy loss spectra by a factor up to 1000, which means that one obtains a much higher reproducibility and therefore reliability of the data and an enormous increase in sensitivity. These authors were able to obtain a lowest overall energy spread of 10 to 25 meV in the range of impact energies from about 1.5 eV to some 100 eV. Energy loss measurements have been performed using N_2 , CO , CO_2 , HCl and other molecules.

Occasionally the expressions "state-to-state" or "state specific" cross sections are used for the reaction



it would be the most detailed information if one could prepare an atom or molecule in a specific state with a set of quantum numbers i and if one could find out how many particles after the collisions are in a specific final state f or, in the case of a break-up channel, how many particles A and B are produced with quantum numbers f_1 and f_2 . The scattered electron carries the information about the process energy, the momentum transfer and the spin.

Of course, we are still far away from such ideal conditions. Nevertheless, during the last few years the technical feasibilities to prepare the initial state have increased quite rapidly, especially by the use of lasers, super sonic beams and by sputtering. The following list contains the most important technical means, the particles which can be prepared and the particle fluxes which can be obtained in the scattering center.

1. Gaseous matter or easy to evaporate target material,
particles in the electronic ground state,
particle flux ca. 10^{16} p/s
2. Super sonic beams,
low rotational and vibrational excitations, dimers and clusters,
particle flux ca. 10^8 - 10^{12} p/s
3. Gas discharge, microwave and radio frequency sources,
long living metastable particles, atoms like H , O , N , Cl , and radicals
particle flux 10^8 - 10^{15} p/s
4. Sputtering (mostly with argon ions on solid surfaces),
atoms, dimers and clusters, which cannot be produced by evaporation,
particle flux 10^8 - 10^{13} p/s
5. Lasers, single and multiphoton excitation,
particles in well defined rotational, vibrational and electronic states,
Rydberg states, fine and hyperfine states,
particle flux $\leq 10^{14}$ p/s
6. Polarized atoms 10^{14} p/s

This is of course a very coarse list with rough orders of magni-

tudes. A more detailed information would be beyond the scope of this article.

The final states can be identified by:

- energy loss of the scattered electron, its scattering angle and spin state
- detection of emitted photons and its polarization
- detection of metastable particles on a metal surface
- detection of ions in a mass spectrometer
- laser induced fluorescence
- photoionisation with laser, spin state of the photo-electron with a Mott detector
- cluster identification by scattering with neutral helium, photoionisation or electron impact.

From the two lists one can see the future trends in experimental electron collision physics. Nearly each method of the first list can be combined with any method of the second list. Of course, we are still far away from a perfect preparation and a perfect identification in any collision process.

TYPES OF COLLISION PROCESSES AND EXPERIMENTAL RESULTS

1. Rotational Excitation of Molecules by Electron Impact

Pure rotational excitation of molecules by low energy electrons (0.1-10 eV) can have cross sections which differ by approximately five orders of magnitude depending on the interaction mechanism between the electron and the molecule. For a molecule with weak polarizability and a weak permanent quadrupole moment like N₂ /11,12/, rotational excitation cross sections are in the order of 10⁻¹⁸ cm², whereas for the same molecule the rotational excitation via a shape resonance may have cross sections of ca. 10⁻¹⁶ cm². Molecules with strong dipole moments have rotational excitation cross sections in the order of 10⁻¹³ cm² /13,17/. In the last six years the laboratory of the author has therefore made a systematic study of rotational excitations by low energy electron impact with consideration of the different interaction molecules.

This has been done by selecting molecules with different permanent multipole configurations and by energy loss measurements with an electron spectrometer at different scattering energies and angles. The angular dependence of the scattered electrons gives information on the interaction mechanism.

On the other hand, the energy resolution even of the best electron spectrometer is still too low to separate state-to-state transitions except for H₂, HD and D₂ /18,19,20/. Therefore, the only measurable quantity with information on the cross sections of rotational transitions is the line width and line shape of the "elastic" scattering peak. The spectrometer must of course have a good energy resolution ($\Delta E \approx 10-20$ meV) and must be very stable in order to measure the wings of a line quite accurately. Experimentally one can see (see Figure 2), that the lines are always broader (up to 4 times) than the line width measured using helium, neon or argon. With rare gases the apparatus profile (true elastic scattering) is obtained. The line shape contains information on the relative transitions $\Delta J = 0,1,2,\dots$ and whether the electron transfers energy to the molecule (energy loss) or rotational energy is transferred from the molecule to the free electron (energy gain).

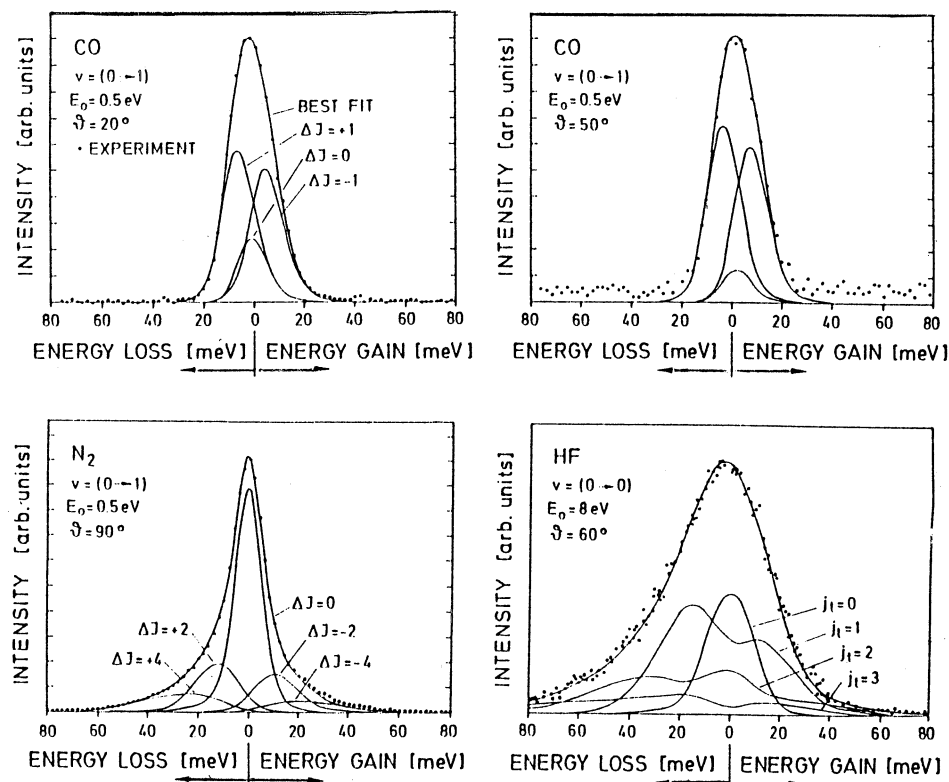


Figure 2. Rotational excitation of CO, N_2 and HF using the branch fitting and the high-J-approximation or the Shimamura formula. The true line width of the apparatus is measured using neon and argon (see $\Delta J = 0$ and $j_l = 0$ curves) and is always considerably smaller than the measured line shape (dots). The measured lines are unsymmetric, since the energy transfer from the electron to the molecule (energy loss) is preferred with respect to the energy transfer from the molecule to the scattered electron (energy gain).

The evaluation of line shapes in terms of rotational cross sections can proceed via one of the two methods:

- i) The branch construction method, which depends on the high-J-approximation /21/.
- ii) A cross section formula for transitions of a spherical top or a linear rotator molecule by Shimamura /22/.

A rather large number of representative molecules have been measured during the last years using the line shape analysis giving electron impact rotational excitation cross sections, which otherwise cannot be obtained. In this paper only a rather short overview can be given. For more details the reader should see the original publications (see Table). For all experiments, the impact energies range from 0.1 eV to about 10 eV and only such rotational and vibrational transitions have been measured which start and end in the molecular ground state.

In most molecules there are energy ranges in which transitions occur via a shape resonance, and other energy ranges in which non-resonant, i.e. direct interactions between the colliding electron and the molecule leads to rotational transitions. Therefore it is possible to quote integrated (with respect to scattering angles) rotational cross sections for

different interactions (see Table). From the table can be concluded, that the most important mechanisms for rotational excitations in the molecular ground states are shape resonances, strong permanent dipole moments and the polarizabilities of the molecules by the colliding electrons.

2. High Energy Impact Rotational Excitation

The physics of the rotational excitation of molecules by high energy electrons is in principle not different from the mechanisms at low impact energies. A torque is needed to transfer angular momentum from the impinging electron to the molecule. This torque results from the interaction of the electron with the permanent dipole or quadrupole moment of the molecule or with the induced multipole moment due to the polarisation of the molecular electron cloud by the incoming electron. An incoming beam of electrons contains (at higher energies) several partial waves, i.e. waves with higher angular momentum, and these momenta can be transferred to the molecule. For distant collisions, i.e. in forward direction the First Born Approximation and the selection rules according to the interaction mechanisms are valid. In this case only small ΔJ -values (mostly $\Delta J = 0, \pm 1, \pm 2$ and ± 3) are expected.

For close collisions an increase of large angle scattering is expected and accordingly the First Born Approximation and the corresponding selection rules will break down. One also can assume that higher angular

Table 1.

Integrated Rotational Cross Sections						
Mol.	transition via direct interactions			transitions via shape-resonances		Ref.
	main interaction	ΔJ	σ 10^{-16} cm^2			
H ₂	weak quadrupole polarizability	0, ± 2	≈ 0.1	0, ± 2	0.8	18, 19, 20, 23
N ₂	weak quadrupole polarizability	0, ± 2	0.015	0, $\pm 2, \pm 4$	2.8	11, 12, 24
CO	weak dipole	0, ± 1	0.17	0, $\pm 1, \dots \pm 4$	1	12, 25
H ₂ O	strong dipole	0, ± 1	2.5	0, ± 1	> 0.3	12
HCl	strong dipole	0, $\pm 1, \pm 2$	≈ 1	0, $\pm 1, \pm 2$	≈ 1	28, 29
CH ₄	octupole polarizability	0, $\pm 3, \pm 4$	0.06	0, $\pm 1, \dots \pm 4$	≈ 1	24, 26
CO ₂	strong quadrupole	0, $\pm 2, \pm 4$	≈ 0.1	0, $\pm 2, \dots$	0.6	27
HF	strong dipole	0, $\pm 1, \pm 2$	≈ 1	no shape resonance visible		28

momentum quanta are transferred. Unfortunately there is only one experimental paper published /30/ for impact energies as high as 100 eV and scattering angles between 10° and 135° . The pure rotational excitation of H₂ was measured mostly for J = 1 → 3. It was found that for large scattering angles rotational excitation can even exceed the pure elastic scattering.

3. Rotational Rainbow Scattering

Recently, the large angle scattering with rotational excitation was measured by Ziegler et al /31/. The idea was to measure state-to-state rotational transitions of Na₂ molecules for collisions, by which the electrons are preferentially scattered into the backward direction. The impact energy of the electron was chosen to be 150 eV, 225 eV and 300 eV, so that short living negative ion states do not contribute to rotational excitation within the electronic ground state. Differential cross sections for scattering angles in the range from $90^{\circ} \leq \theta \leq 180^{\circ}$ have been measured. The results have been surprising, since very large rotational excitations with ΔJ-values up to 28 have been found.

The explanation of the results can be made using classical arguments. The internuclear distance of the Na₂-molecule is quite large ($r_e = 0.3079$ nm) and larger than the de Broglie wave length of the colliding electrons. For backward scattering of the electrons the angular momentum transferred to the molecule is $\Delta J = k r_e \cdot \sin \gamma$, where k is the wave vector of the incoming electron and γ the angle between k and the molecular axis. The maximum value of $\Delta J = k r_e$ occurs for $\gamma = 90^{\circ}$ and $\theta_e = 180^{\circ}$. Since the molecular positions $\gamma = 90^{\circ} + \delta$ and $\gamma = 90^{\circ} - \delta$ produce each an reflected wave with the same angular momentum transfer, the two waves interfere leading to supernumerary rotational rainbows. For $\gamma = 90^{\circ}$ these two orientations coincide giving rise to the main rainbow. These experimental results are in good agreement with classical and quantum mechanical calculations /32/.

If we generalize these results for high energy electron impact rotational excitation of molecules, we come to the following conclusions:

- i) For very large angle scattering of the electrons, $120^{\circ} \leq \theta_e \leq 180^{\circ}$, very large ΔJ-values are to be expected depending on the size of the molecule in comparison to the de Broglie wave length. The scattering can be understood semi-classically.
- ii) For intermediate angle scattering $60^{\circ} \leq \theta_e \leq 120^{\circ}$, the colliding electrons penetrate deeply into the electronic cloud of the molecule. Rather large ΔJ-values are to be expected, possibly $6 \leq \Delta J \leq 10$, depending on the short range polarizability of the molecule.
- iii) For small angle scattering the First Born Approximation is valid and therefore small ΔJ-values are to be expected.
- iv) The cross sections for rotational excitations are connected to the elastic cross sections.

VIBRATIONAL EXCITATION OF MOLECULES BY ELECTRON IMPACT

During the last 25 years numerous experiments applying the crossed beam technique have been made to measure the vibrational excitation of molecules in their electronic ground states /33/. Most of these experiments were connected to the search for new shape resonances, the determination of their energy positions, symmetries, life times, dissociative

attachment channels and the population of vibrational states in the molecular ground states after the autoionisation of the resonance.

On the other hand, vibrationally excited molecules are produced not only by shape resonances, but also through virtual states, and by non-resonant interactions between the colliding electron and the molecule. Different interactions may be dominant for the vibrational excitation in the same molecule, but in different energy ranges. The following molecules have been measured:

Small dipole moment	CO
Large dipole moment	HCl, HF, H ₂ O
Weak quadrupole moment	N ₂ , H ₂
Weak polarisability	N ₂ , CH ₄ (only octupole)
Strong polarisability	CO ₂

In certain ranges of the impact energy all these molecules form shape resonances.

The different interaction mechanisms can produce vibrationally excited molecules in low energy electron collisions with rather high cross sections. This can be seen easily from Figure 3 /34/. It shows a

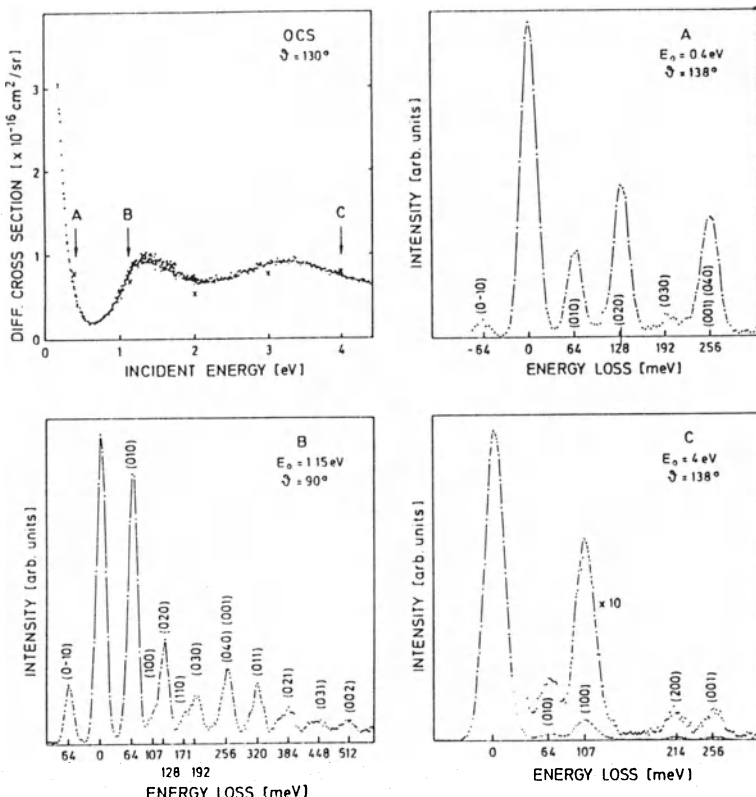


Figure 3. Energy dependence of the elastic scattering cross section of OCS at a scattering angle of 130° . A low energy peak and two shape resonances (1.3 eV and 3.4 eV) are visible. The arrows and capital letters indicate the energy positions, in which the energy loss spectra of the figures A), B) and C) have been measured. This is an example of mode selective excitation of vibrations due to different interaction mechanisms.

strong rise of the differential cross section below 0.5 eV incident energy of the electrons colliding with OCS molecules. This rise and its angular dependence is in agreement with a First Born calculation, in which the permanent dipole moment of the molecule was inserted. In this energy region vibrational excitation mostly of the bending modes (0,n,0) is observed, although its angular dependence is not very well reproduced by the Born calculation.

We therefore conclude, that this rise is partly due to a virtual state, which is observable especially in the inelastic channels. A virtual state in molecules was first observed by Rohr and Linder /35/ in the electron scattering from HCl.

In Figure 3 the rise is followed by two maxima at 1.4 eV and 3.5 eV. These maxima are explained by shape resonances. Between the virtual state and the two shape resonances are energy areas, in which non-resonant interactions for vibrational excitations play a role. The three figures 3 A, B, C show that the vibrational excitation is quite different depending on the impact energy of the electrons. In the virtual state we mostly find excitation of the bending mode, in the lower shape resonance between 1 and 2 eV the bending and the asymmetric stretch mode is dominant, whereas in the high energy shape resonance (3 to 4 eV) the symmetric stretch mode is quite strongly excited.

Such mode selective vibrational excitations have been observed in all molecules with more than two atoms. H_2H_2 , CO_2 , CS_2 are examples /36,37/. Infrared active modes are excited quite effectively by the interaction of the colliding electron with the dipole moment of the molecule. Many partial waves are involved in the excitation of such a mode, which is evident from the increase of the cross section in forward direction. The Born Dipole Approximation describes the cross sections quite well at all impact energies and scattering angles from 0° to 30° , at higher angles the Born Dipole Approximation gives too low cross sections. Vibrational excitation cross sections induced by quadrupole or octupole interaction are very small, e.g. in the order of 10^{-18} cm^2 . Test molecules have been H_2 and N_2 /38/ outside the region of a shape resonance. These finding, however, may be affected by the vibrational excitation through the polarizability. The contributions to vibrational excitation via polarization of the molecule can be quite large. In a molecule with large long range polarizability like CS_2 /34/, the integrated cross section may be as large as 10^{-16} cm^2 . In general, the cross sections for the excitation of one or two vibrational quanta are in the order of 10^{-18} to 10^{-16} cm^2 close to the thresholds. The effect of the short range polarizability is well detectable in backward scattering and has been observed for the case of CO, $v = 0 \rightarrow 1$ below the shape resonance at 0.5 eV collisions energy /39/. The effect of the polarizability is tested best for the excitation of Raman active vibrational modes.

Shape resonances are very effective in exciting vibrations. The integrated cross sections are mostly in the order of 10^{-16} cm^2 . In some molecules quite large numbers of $\Delta\nu$ have been observed, in H_2 up to $\Delta\nu \approx 20$, of course with smaller cross sections /40/. As already mentioned, in polyatomic molecules the shape resonances act often only on selected vibrational modes, namely on those, where the symmetry is in accordance with the symmetry of the resonance. In this way mode selective vibrational excitation can be achieved quite easily.

The dissociative attachment /41,2/ process is closely connected with the existence of a shape resonance in the region of the electronic ground state of the molecule and it is a very effective mechanism for the formation of negative ions.

ELECTRONIC EXCITATION OF MOLECULES

Electronic excitation of stable and gaseous molecules is experimentally rather well known and also well documented in data collections /42/. In spite of that, only very few high resolution measurements /43/ exist in the energy range from threshold to a few eV above. In this threshold region strong variations of the cross sections exist due to the so called threshold laws and the super imposed structures from different types of short living negative ion states such as Feshbach resonances, virtual states and shape resonances. The situation is qualitatively the same as for atomic targets (see Fig. 4), but quantitatively one expects quite different structures which depend on the symmetry of the excited state.

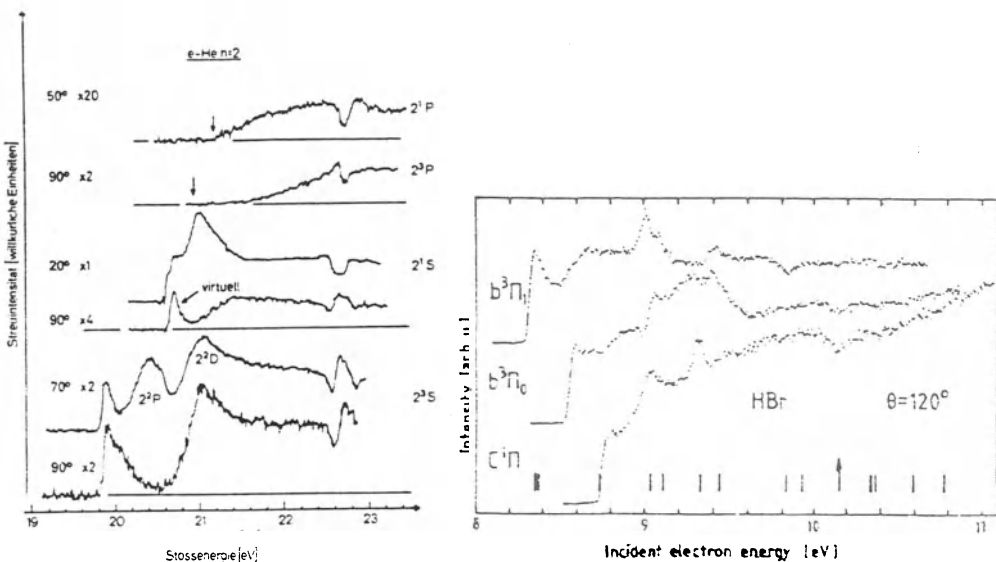


Figure 4. Resonance states close to thresholds of electronically excited HBr (from 43a) and Helium (from 43b). These resonance states cause large intensity variations in a range of 1 to 2 eV above the threshold.

Another phenomenon is the cascading of electronically (and simultaneously vibrationally) excited molecules into lower states including the molecular ground state. This results in highly vibrationally excited neutral molecules and fragments. Broad vibrational population distributions are the consequences /44,45/ ($\nu \leq 20$) and it is well known that such vibrationally hot molecules and radicals are chemically very reactive. Figure 5 gives an example of the cascading of H₂ Feshbach resonances into lower lying electronic states of the molecule.

It is also known that the vibrational excitation is often mode selective (only certain modes of a triatomic or polyatomic molecule can be vibrationally excited depending on the symmetry of the electronic state). This fact might also be of importance for chemical reactions in the plasma.

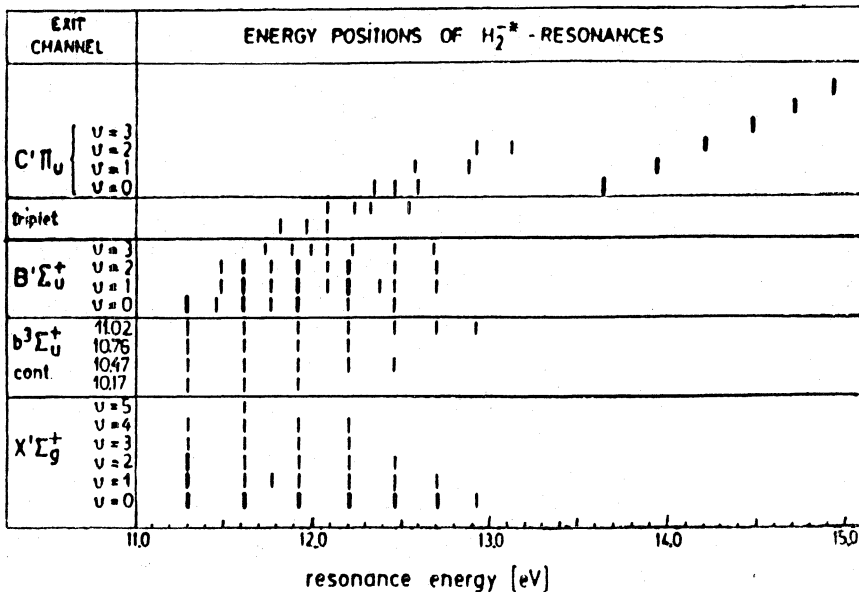


Figure 5. Energy positions of H_2^{-*} -resonances and the decay of these states into the different final states (exit channels). Broad marks indicate strong vibrational excitations of the exit channel.

ELECTRON IMPACT IONISATION OF MOLECULES

In principle this type of process is very complex /46,47/, since also multistep processes such as innershell excitation followed by auto-ionisation can play an important role, especially for heavy particles and unfilled d and f-shells.

In such a case the innershell processes can have cross sections which are several times larger than the single ionisation of outer shell electrons and therefore the tabulated single step (direct) ionisation cross sections of Lotz /48/ may be quite incorrect.

For molecules consisting of light atoms only outer shell single ionisation is of importance. The cross sections are rather well known from the measurements of the produced ions and ionic fragments. Many relative data on ion intensities are tabulated in data collections of mass spectrometry. But little is known concerning the nature and the vibrational excitation of neutral fragments which are produced in the collisions.

Differential cross section measurements $d\delta/dE$, $d^2\delta/d\Omega dE$ and $d^3\delta/d\Omega_1 d\Omega_2 dE$ provide detailed information on the electron energy distributions after the collisions, on the energy and angular distributions and on the dynamics of the collision process /47/. Electron energy distributions for different impact energies and for outer shell single ionisation of helium and molecular hydrogen have been published /49,50,51/.

REFERENCES

- /1/ R.K. Janev et al, "Elementary Processes in Hydrogen-Helium Plasmas", Springer Verlag Berlin, Heidelberg, New York 1987
/2/ J.M. Wadehra and J.N. Bardsley, Phys. Rev. Lett. 41, 1795 (1978)
/3/ A. Stamatovic and G.J. Schulz, Rev. Sci. Instr. 41, 423 (1970)
/4/ J. Ferch, B. Granitza, C. Masche and W. Raith, J. Phys. B 18, 967 (1985)
/5/ B. Jaduszliwer, G.F. Shen, J.L. Cai and B. Bederson, Phys. Rev. A 31, 1157 (1985)
/6/ P. Marmet and L. Kervin, Can. J. Phys. 38, 787 (1960)
/7/ J.A. Simpson, Rev. Sci. Instr. 35, 1698 (1964)
C.E. Kyatt and J.A. Simpson, Rev. Sci. Instr. 38, 103 (1967)
/8/ R.E. Kennerly, R.J. van Brunt and A.C. Gallager, Phys. Rev. A 23, 2430 (1981)
/9/ D. Field, G. Mrotzek, D.W. Knight, S. Lunt and J.P. Ziesel, Proc. of the XV. International Conference on the Physics of Electronic and Atomic Collisions (ICPEAC), Bristol 1987, p. 266
/10/ P.J. Hicks, S. Daviel, B. Wallbank and J. Comer, J. Phys. E 13, 713 (1980)
T.A. York and J. Comer, J. Phys. B 16, 3627 (1983)
T.A. York and J. Comer, J. Phys. B. 17, 2563 (1984)
/11/ S.F. Wong and L. Dubé, Phys. Rev. A 17, 570 (1978)
/12/ K. Jung, Th. Antoni, R. Müller, K.-H. Kochem and H. Ehrhardt, J. Phys. B 15, 3535 (1982)
/13/ R.C. Slater, M.G. Fickes, G.W. Becker and R.C. Stern, J. Chem. Phys. 60, 4697 (1974)
/14/ R.C. Slater, M.G. Fickes, W.G. Becker and R.C. Stern, J. Chem. Phys. 61, 2290 (1974)
/15/ M.R.H. Rudge, S. Trajmar and W. Williams, Phys. Rev. A 13, 2074 (1976)
/16/ L. Vuskovic, S.K. Srivastava and S. Trajmar, J. Phys. B 11, 1643 (1978)
/17/ B. Jaduszliwer, A. Tino, P. Weiss and B. Bederson, Phys. Rev. Lett. 18, 1644 (1983)
/18/ H. Ehrhardt and F. Linder, Phys. Rev. Lett. 21, 419 (1968)
/19/ F. Linder and H. Schmidt, Zeitschr. f. Naturforschung 26a, 1603 (1971)
/20/ E.S. Chang and S.F. Wong, Phys. Rev. Lett. 38, 1327 (1977)
/21/ F.H. Read, J. Phys. B 5, 255 (1972)
/22/ J. Shimamura, Chem. Phys. Lett. 73, 328 (1980)
/23/ K. Jung, K.-M. Scheuerlein, W. Sohn, K.-H. Kochem and H. Ehrhardt, J. Phys. B. 20, L327 (1987)
/24/ H. Tanaka, Symp. on Electron-Molecule Collisions, p. 31, Tokyo, 1979
/25/ E.S. Chang, Th. Antoni, K. Jung and H. Ehrhardt, Phys. Rev. A 30, 2086 (1984)
/26/ R. Müller, K. Jung, K.-H. Kochem, W. Sohn and H. Ehrhardt, J. Phys. B 18, 3971 (1985)
/27/ Th. Antoni, K. Jung and H. Ehrhardt, and E.S. Chang, J. Phys. B 19, 1377 (1986)
/28/ G. Knoth, M. Rädle, K. Jung and H. Ehrhardt, to be published
/29/ G. Knoth, M. Rädle, H. Ehrhardt and K. Jung, Europhys. Lett. 4, 805 (1987)
/30/ S.K. Srivastava, R.I. Hall, S. Trajmar and A. Chutjian, Phys. Rev. A 12
/31/ G. Ziegler, M. Rädle, O. Pütz, K. Jung, H. Ehrhardt and K. Bergmann, Phys. Rev. Lett. 58, 2642 (1987)
/32/ H.-J. Korsch, H. Kutz and H.D. Meyer, J. Phys. B 20, L433 (1987)
/33/ G.J. Schulz, Phys. Rev. 125, 229 (1962)

- /34/ W. Sohn, K.-H. Kochem, K.-M. Scheuerlein, K. Jung and H. Ehrhardt, J. Phys. B 20, 3217 (1987)
- /35/ K. Rohr and F. Linder, J. Phys. B 9, 2521 (1976)
- /36/ K.-H. Kochem, W. Sohn, K. Jung, H. Ehrhardt and E.S. Chang, J. Phys. B 18, 1253 (1985)
- /37/ K.-H. Kochem, W. Sohn, N. Hebel, K. Jung and H. Ehrhardt, J. Phys. B 18, 4455 (1985)
- /38/ W. Sohn, K.-H. Kochem, K.-M. Scheuerlein, K. Jung and H. Ehrhardt, J. Phys. B 19, 4017 (1986)
- /39/ W. Sohn, K.-H. Kochem, K. Jung, H. Ehrhardt and E.S. Chang, J. Phys. B 18, 2049 (1985)
- /40/ M. Allan, J. Phys. B 18, L451 (1985)
M. Allan, J. Phys. B 18, 4511 (1985)
- /41/ R. Azria, Y. LeCoat, D. Simon and M. Tronc, J. Phys. B 13, 1909 (1980)
- /42/ Atomic Data for controlled Fusion Research, Oak Ridge Nat. Lab. Report Nr. ORNL-5206, Vol. I and II (1977)
Atomic and Molecular Data for Fusion, UKAEA Reports, Culham Lab., Abingdon, England, 1982.
Several Data Collections have also been published by the Institute of Plasma Physics, Nagoya, Japan.
See also G. Csanak, D.C. Cartwright, S.K. Srivastava and S. Trajmar, in "Electron-Molecule Interactions and Their Applications", Vol. 1 and 2, Academic NY 1984
- /43a/ D.Cubrić, J. Jureta and S. Cvejanović, III. European Conference on Atomic and Molecular Physics, Bordeaux, April 1989
- /43b/ H. Ehrhardt, L. Langhans, F. Linder, Z. Phys. 214, 179 (1968)
- /44/ J.R. Hiskes and A.M. Karo, Appl. Phys. Lett. 54 (1989)
- /45/ A. Weingartshofer, H. Ehrhardt, V. Hermann and F. Linder, Phys. Rev. A 2, 294 (1970)
- /46/ T.D. Märk, "Ionisation of Molecules by Electron Impact" in L.G. Christophorou (ed.) "Electron-Molecule Interactions and Their Applications", Vol. 1, Academic, NY (1984) and
T.D. Märk and G.H. Dunn (eds.) "Electron Impact Ionisation", Springer Verlag, Wien 1985
- /47/ H. Ehrhardt, K. Jung, G. Knoth and P. Schlemmer, Z. Phys. D - Atoms, Molecules and Clusters 1, 3 (1986)
- /48/ W. Lotz, Z. Phys. 232, 101 (1970) and references given in this article
- /49/ N. Oda, Radiat. Res. 64, 80 (1975)
- /50/ R. Müller-Fiedler, K. Jung, H. Ehrhardt, J. Phys. B 19, 1211 (1986)
- /51/ T.W. Shyn, W.W. Sharp, Y.K. Kim, Phys. Rev. A 24, 79 (1981)

ELECTRON TRANSPORT IN PARTIALLY IONIZED GASES

L.C. Pitchford

Centre de Physique Atomique de Toulouse
CNRS Laboratoire Associeé URA N° 277
31062 Toulouse, Cedex, France

INTRODUCTION

A partially ionized gas consists of free electrons, positive (and perhaps negative) ions and neutral particles. In this article we are interested in the behavior of partially ionized gases in electromagnetic fields. The electron and ions are accelerated or decelerated in the fields present, and during their trajectories they collide with the background particles, losing energy and momentum to the neutral gas. Because the electrons are so much lighter than the ions, it is the electrons which are thus primarily responsible for the conductivity of the gas. For the same reason, it is through the agent of the electrons that electrical energy is deposited into the gas in the form of gas heating or excitation. A knowledge of the electron component is therefore fundamental to a description of phenomena in partially ionized gases. The aim of this article is to present a brief description of the electron component of partially ionized gases in terms of electron transport, excitation and ionization rate coefficients. Transport coefficients, such as electron drift velocity or mobility and the diffusion coefficients, describe the response of the electrons on the average to the combined influences of the fields and the collisions, while excitation and ionization rate coefficients describe the flow of energy from the electrons to the neutral gas.

There is an enormous variety in the phenomena in partially ionized gases, and only the most general descriptions apply to all cases. In the discussion below, we will begin by considering the relatively simple situation of "hydrodynamic" electron transport¹, that is, electron transport in a weakly ionized gas subjected to a uniform electric field in space and time and far removed from any boundaries. This corresponds in practice to the classical drift regime² where except for a small region near the electrodes, the energy gained by the electrons between collisions is balanced by the energy lost in collisions on the average and the transport and rate coefficients are correspondingly independent of space and time. Electrons collide predominately with the neutral particles, and electron-electron or electron-ion collisions can be neglected.

In this regime and for low to moderate field strengths, the transport and rate coefficients can be parameterized by E/N , the ratio of the electric field to the gas density, and the composition of the

gas. Growth (or decay) of the electron number density due to electron impact ionization or attachment are included in this hydrodynamic description, and the growth are exponential because the ionization rate is a constant independent of space and time. A large body of experimental and computational data exist in this regime,^{3,4} and the data are referred to as "electron swarm" data, in analogy with a drifting, spreading swarm of bees. If the electric field is space or time dependent, but only slowly changing, the transport and rate coefficients can still be parameterized by the local value of the field, $E(r,t)/N$. Although the hydrodynamic description is restrictive, there is a wide range of electron transport phenomena and many applications which are well described by these concepts.

A description of electron transport based on coefficients which are functions of E/N is of wide, but not universal validity. The particular circumstances which are not well-described by E/N dependent parameters are electron transport 1) near physical boundaries (near electrodes), 2) in rapidly varying fields in time (high frequency excitation) or space (in the cathode fall region of a glow discharge), and 3) in the presence of sources (for example, an electron-beam). Electron transport phenomena under these conditions can depart significantly from hydrodynamic electron transport, as will be discussed in the latter sections of this article.

The concept of an electron velocity distribution function⁵, evdf, is central to the description of electron transport in gases in all cases. The evdf, $f(\mathbf{r}, \mathbf{v}, t)$, is the probability of finding an electron in an element of velocity space from \mathbf{v} to $\mathbf{v} + d\mathbf{v}$ and in an element of configuration space \mathbf{r} to $\mathbf{r} + d\mathbf{r}$ at a time t . The evdf contains all the information about the electron component of the weakly ionized gas, and the electron impact ionization and excitation rate coefficients and transport coefficients are just various averages over the evdf. Under certain conditions and in extremely careful experiments, the distribution of electron energies may be measured. In most cases of interest, however, it is necessary to calculate the evdf taking into account the complex changes in the electron velocities in collisions with the heavy particles and with each other, the electron energy gain (or loss) in any fields which are present, and the creation of new electrons in ionization events or their loss in attaching collisions. The Boltzmann equation is an integral-differential equation in three velocity coordinates, three spatial coordinates and in time which describes the interplay of the various collisional phenomena and any electromagnetic fields present⁵, and the solution of the Boltzmann equation is the evdf.

There are a number of techniques which have been developed over the years and a vast literature describing methods for solving the Boltzmann equation to obtain the electron velocity distribution function. (See, for example, references 6-9.) Under certain idealized conditions, analytical forms for the electron energy distribution function (eedf) can be found; e.g. Druyvesteynian or Maxwellian. For realistic cases it is necessary to develop numerical solution techniques, and these techniques all rely on certain approximations and assumptions which are valid in different regimes. Some of these are discussed below.

Monte Carlo simulations of electron transport in gases provide the same information as do solutions of the Boltzmann equation; i.e., electron transport and rate coefficients and the electron velocity distribution function^{10,11}. In principle, the simulation results are as accurate as the physical description of the electron motion and interaction with the background gas included in the simulation. Monte Carlo simulations obviate the need for introducing boundary conditions

or numerical approximations which are required in Boltzmann solutions. On the other hand, the difficulty in interpreting Monte Carlo simulations is in distinguishing small physical effects from statistical fluctuations.

The more recent simulation algorithms^{11,12} make use of several features which enhance the statistical accuracy and reduce the computational time. These include the null collision technique¹³, sampling before collisions¹⁴, and artificial attachment or ionization¹⁵. Detailed comparisons between the numerical solutions of the Boltzmann equation and the simulation results have been performed^{16,17}, and such comparisons have served to validate (or invalidate) the various assumptions and approximations which are necessary in the numerical solution of the Boltzmann equation. An example of a recent calculation will be presented below.

In most cases of technological interest it is the averages over the distribution function such as the electron drift velocity, diffusion coefficient, ionization or excitation rate coefficients, that are the desired results of the calculation. Boltzmann solutions or simulation results contain far more information than is used or required. An alternative to descriptions of electron behavior based on the evdf is the velocity moment description which is based on approximate solutions of the first three velocity moments¹⁸ of the Boltzmann equation, the electron continuity equation and equations for the momentum and energy balance. These equations form the basis of many of the models of discharge devices some of which are described in elsewhere in this proceedings.

GENERAL FORMULATION

The Boltzmann equation for electrons under the influence of an electric field and interacting with a weakly ionized gas can be written⁵

$$\frac{\partial F(\mathbf{r}, \mathbf{v}, t)}{N \partial t} + \mathbf{v} \cdot \frac{\partial F(\mathbf{r}, \mathbf{v}, t)}{N \partial \mathbf{r}} + \frac{\mathbf{a}}{N} \cdot \frac{\partial F(\mathbf{r}, \mathbf{v}, t)}{\partial \mathbf{v}} = C[F(\mathbf{r}, \mathbf{v}, t)] \quad (1)$$

where $F(\mathbf{r}, \mathbf{v}, t)$ is the evdf in a six dimensional phase space, $\mathbf{a} = -e\mathbf{E}/m$ is the acceleration due to the applied field, e and m are the electron charge and mass, respectively, and C is the collision operator to be defined below. This equation describes the time rate of change of the evdf in terms of a flux in configuration space, a flux in velocity space, and the effect of collisions on the electron energy and momentum, and the evdf is related to the electron number density, $n_e(\mathbf{r}, t)$, by the relation,

$$\int F(\mathbf{r}, \mathbf{v}, t) d\mathbf{v} = n_e(\mathbf{r}, t) \quad (2)$$

Factors of N , the neutral density, are explicitly included here to illustrate the scaling; i.e., the space and time parameters always enter in products with the density.

Even before considering the details of the collision operator, it is clear that some assumptions must be made in order to make practical the solution of eq. 1. Fortunately, there few experimental situations that demand the detail of a complete solution of $F(\mathbf{r}, \mathbf{v}, t)$. For a wide range of conditions, the "hydrodynamic" approximation provides an accurate description of the space-time evolution of the electron swarm^{1,19}. The hydrodynamic approximation is valid when the electrons have lost memory of their initial conditions and if the fields are uniform in space and time. These conditions are typical of the drift regime mentioned above

in which after a short relaxation distance near the cathode, the evdf and therefore all average electron properties are independent of space and time. That is, there is a local balance between the electron energy gained in the field and lost in collisions on the average. Following Kumar, et al¹, the space and time dependence in the evdf can be expressed in terms of the electron number density and its gradients,

$$F(\mathbf{r}, \mathbf{v}, t) = f(\mathbf{v}) n_e(\mathbf{r}, t) - \frac{g_r(\mathbf{v})}{N} \frac{\partial n_e(\mathbf{r}, t)}{\partial r} - \frac{g_z(\mathbf{v})}{N} \frac{\partial n_e(\mathbf{r}, t)}{\partial z} + \dots \quad (3)$$

We have followed the notation of reference 20. Integration over all velocities yields the continuity equation for electrons,

$$\begin{aligned} \frac{\partial n_e(\mathbf{r}, t)}{\partial Nt} &= \frac{V_R}{N} n_e(\mathbf{r}, t) - w \frac{\partial n_e(\mathbf{r}, t)}{\partial Nz} + \\ &D_L N \frac{\partial^2 n_e(\mathbf{r}, t)}{\partial Nz^2} + D_T N \frac{1}{r} \frac{\partial}{\partial Nr} (r \frac{\partial}{\partial Nr} n_e(\mathbf{r}, t)) \end{aligned} \quad (4)$$

The coefficients are the reaction rate coefficient, the drift velocity, the longitudinal diffusion and the transverse diffusion coefficients. These depend only on E/N and the gas composition, and their explicit relations to the distributions, $f(\mathbf{v})$, $g_r(\mathbf{v})$ and $g_z(\mathbf{v})$ are well described by Kumar, et al. With some algebra, equations defining $f(\mathbf{v})$, $g_r(\mathbf{v})$ and $g_z(\mathbf{v})$ can be derived, and the first one is,

$$- \frac{eE}{Nm} \cdot \frac{df(\mathbf{v})}{dv} = C[f(\mathbf{v})] - \frac{V_R}{N} f(\mathbf{v}) \quad (5)$$

Solution techniques developed for this form can also be applied with straight-forward extensions to the equations defining the g's.

There has been considerable discussion in the literature as to the relation between the coefficient in eq. 4 and those measured experimentally²¹. An alternative formulation in the hydrodynamic regime to the density gradient expansion which is useful in steady-state^{20,21} (SS) and where the growth of current is exponential is expressed as,

$$F(\mathbf{r}, \mathbf{v}) = e^{\alpha z} f_{SS}(\mathbf{v}). \quad (6)$$

This is equivalent to eq. 3 under steady-state, hydrodynamic conditions, and it is often easier to use. The equation defining f_{SS} is,

$$- \frac{eE}{Nm} \cdot \frac{df_{SS}(\mathbf{v})}{dv} = C[f_{SS}(\mathbf{v})] - v_z \frac{\alpha}{N} f_{SS}(\mathbf{v}) \quad (7)$$

The same solution techniques developed for eq. 6 can be applied equally well here.

By far the most common solution technique for eqs. 5 and 7 is an expansion of the angular dependence of the velocity in Legendre polynomials²²⁻²⁴, and it is often assumed that the first two terms are adequate,

$$f(\mathbf{v}) = \sum_{j=0} f_j(v) P_j(\cos\theta) \approx f_0(v) + f_1(v) \cos\theta. \quad (8)$$

The two-term form can be manipulated to result in a second order differential equation for f_0 which is,

$$-\left(\frac{eE}{mN}\right)^2 \frac{1}{3} v^{-2} \frac{d}{dv} \left(\frac{df_0}{v_m dv} \right) = C(f_0), \quad (9)$$

where v_m is the momentum transfer collision frequency.

The Legendre expansion is a physically reasonable choice of a basis set since rapid convergence is expected in the region of low fields where, because of the frequent elastic (direction randomizing) collisions, the small amount of energy gained between collisions in falling through the field is rapidly converted to thermal energy. Thus the evdf is isotropic to first order, and the corrections for the angular dependence are small. In addition, the transport and rate coefficients depend only on the isotropic or on the first anisotropy ($\cos\theta$ dependence) of the evdf. Thus, it is primarily important to develop a computational technique which describes well the isotropic and $\cos\theta$ parts of the evdf rather than the full evdf, and these are the first two terms in the Legendre series. Because the coupling to the higher order components is not too severe, the Legendre expansion technique has proven useful even for high E/N^2 .

The collision operator in the equations above describes exchange of energy and momentum between the electrons and the neutral particles due to elastic, inelastic, superelastic, ionizing and attaching collisions. Because of the small ratio of the electron to the neutral mass, elastic collisions result primarily in a randomization of the electron velocities and very little energy is lost by the electrons. Inelastic collisions are those in which electrons lose a discrete amount of energy in exciting internal levels of atoms or molecules, and because of these discrete energy losses, the inelastic terms in the collision operator are non-local in energy. When there is an appreciable population of heavy particles in excited states, superelastic collisions may also become important; that is, collisions in which electrons can gain discrete amounts of energy in collisions with the excited states of the heavy particles, leaving the heavy particles with no internal excitation. This subject is described in other articles in this proceedings. Ionizing collisions result in the production of secondary electrons which enter the distribution with an energy distribution which depends on the energy of the primary electron. These are also described by terms in the collision operator. Rather than show these terms explicitly, the reader is referred to references 5,20,24 and 25 which describe them in detail.

There have been numerous studies of the various techniques for solution of the Boltzmann equation^{9,17,26} and the evaluation of the various assumptions^{20,25-28}. Extremely accurate and efficient solution techniques are available now for electron transport in the hydrodynamic regime. Advances have been made recently in the development of techniques for time²⁹ or space dependent^{9,17} situations in which the growth of electron density or current is not necessarily exponential.

MONTE CARLO SIMULATIONS

Monte Carlo simulations have long been used to study the motion of electrons in weakly ionized gases under the influence of an electromagnetic field^{10,11}. In a Monte Carlo simulation, the system is

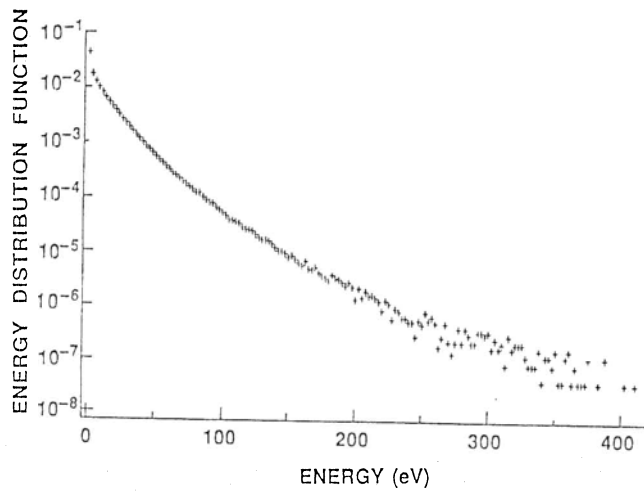


Fig. 1. Electron energy distribution function in nitrogen at 1500 Td calculated from a Monte Carlo simulation and corresponding to the simulation parameters of Table 1. (From ref. 15)

modeled exactly as in the experiment - electrons are released from the cathode or some given position, and their individual trajectories are followed in space and time. The effect of collisions is simulated by updating the velocity of the electrons after each collision. The collision time and the particular kind of collision which results at a collision event are determined by random sampling from the appropriate probability distributions³⁰.

Random sampling of a discrete probability distribution can be illustrated by considering, for example, X_1, \dots, X_k which are k independent and mutually exclusive events with probabilities p_1, \dots, p_k , where $p_1 + \dots + p_k = 1$. The event X_i is determined to have occurred when a random number, R , $0 \leq R \leq 1$, is such that

$$p_1 + \dots + p_{i-1} \leq R \leq p_1 + \dots + p_i.$$

The events, X_i , can be, for example, collision processes and the p 's normalized collision probabilities. The same idea applies to random sampling of a continuous probability distribution such as the probability distribution of free flight times.

Monte Carlo simulations are inherently computationally intensive because it is necessary to follow many electrons for many collisions. The total number of simulated collisions often exceeds 10^6 in order to reduce the statistical fluctuations in quantities such as the ionization rate coefficient. Therefore, it has been important to develop algorithms that streamline the calculations as much as possible. An example of a recent calculation¹⁵ of the eedf using Monte Carlo techniques is shown Fig. 1, and Table 1 lists the corresponding simulation parameters. The important features of this simulation were the use of the null collision method for calculations of the free flight time¹³, sampling electron properties at collision events¹⁴, and artificial attachment for rescaling the number density¹⁵. Null collisions are the result of a fictitious scattering channel with a collision frequency chosen to make the total collision frequency (an arbitrary) constant. Electrons exit null collision events with their

momentum and energy unchanged, and there is no net effect of these collisions. Their inclusion, however, results in an analytical expression for the free flight time in terms of the constant collision frequency and a random number,

$$t_c - t_0 = \frac{1}{v_T} \log \frac{1}{1-R} \quad (10)$$

where $t_c - t_0$ is the free flight time, and v_T is the total (constant) collision frequency. Sampling electron properties at collision events rather than at specified times or positions simplifies the bookkeeping and speeds the simulation since the electrons must be stopped at collision events in any case. Artificial attachment is another fictitious scattering channel which has no net effect on the eedf, but which provides a means of avoiding the exponential build-up of number of electrons which must be simulated when electron impact ionization is important. The analogous process, artificial ionization gets around the problem of having to start simulations with a huge number of electrons when attachment is important in order to have a finite electron density at the end of the simulation.

Unlike the Boltzmann equation where analytical solutions are available for testing the numerical methods for certain simplifying conditions, it is very difficult to assess the accuracy of Monte Carlo simulations because the effect of small errors can be confused with statistical uncertainties. It is thus especially important to make any and all internal self-consistency checks, such as a check of the energy balance, etc.

Table 1. Simulation parameters and transport coefficients at 1500 Td in N₂ as reported in ref.15.

Neutral density	10^{17} cm^{-3}
Artificial attachment rate coefficient	$2.31 \cdot 10^{-8} \text{ cm}^3/\text{sec}$
Ionization rate coefficient	$2.35 \cdot 10^{-8} \text{ cm}^3/\text{sec}$
Avg. energy	22.7 eV
Drift velocity	$8.95 \cdot 10^7 \text{ cm/sec}$
Total number of:	
Real and null collisions	$1.25 \cdot 10^6$
Real collisions	$8.15 \cdot 10^5$
Ionizing collisions	$7.35 \cdot 10^4$
Run time (IBM3081)	15.5 minutes

VELOCITY MOMENTS OF THE BOLTZMANN EQUATION

The kinetic Boltzmann equation describing the evolution of the electron velocity distribution in phase space is especially complicated to solve when the hydrodynamic approximation can no longer be reliably invoked. In any case, it is not usually the evdf which is the desired end point of a calculation, but rather its various moments. An

alternative approach is then to solve directly for the moments of the Boltzmann equation. From the Boltzmann equation,

$$\frac{\partial F(\mathbf{r}, \mathbf{v}, t)}{N \partial t} + \mathbf{v} \cdot \frac{\partial F(\mathbf{r}, \mathbf{v}, t)}{N \partial \mathbf{r}} + \frac{\mathbf{a}}{N} \cdot \frac{\partial F(\mathbf{r}, \mathbf{v}, t)}{\partial \mathbf{v}} = C[F(\mathbf{r}, \mathbf{v}, t)]$$

the first three moment equations are the electron continuity, the momentum balance and the energy balance,

$$\frac{\partial}{N \partial t} \int F d\mathbf{v} = \frac{\partial n_e}{\partial N t} = \frac{v_R}{N} n_e - \frac{\partial n_e \langle \mathbf{v} \rangle}{N \partial \mathbf{r}} \quad (11)$$

$$\frac{\partial}{N \partial t} \int \mathbf{v} F d\mathbf{v} = \frac{\partial n_e \langle \mathbf{v} \rangle}{\partial N t} = \frac{v_m}{N} n_e \langle \mathbf{v} \rangle - \frac{eE}{mN} n_e - \frac{\partial n_e \langle \mathbf{v} \mathbf{v} \rangle}{N \partial \mathbf{r}} \quad (12)$$

$$\frac{\partial}{N \partial t} \int \epsilon F d\mathbf{v} = \frac{\partial n_e \langle \epsilon \rangle}{\partial N t} = \frac{v_u}{N} n_e \langle \epsilon \rangle - \frac{eE}{mN} n_e \langle \mathbf{v} \rangle - \frac{\partial n_e \langle \mathbf{v} \epsilon \rangle}{N \partial \mathbf{r}} . \quad (13)$$

where the brackets denote average quantities, ϵ is the electron energy, and the \mathbf{v} 's appearing in first terms on the RHS's of the equations are the reaction (attachment or ionization) frequency, the momentum exchange frequency and the energy exchange frequency, respectively. These terms result from integrals over the collision operator weighted by 1, \mathbf{v} or ϵ and the replacement of an average of a product by a product of averages, i.e.; $\langle v_u \epsilon \rangle$ is approximated by $v_u \langle \epsilon \rangle$. The \mathbf{v} 's are coupled to higher order moments through their dependence on the distribution function which can be expanded in terms of its moments. Some truncation scheme is therefore necessary to handle the \mathbf{v} 's as well as the terms involving spatial derivatives in order to limit the number of moment equations which must be considered. Note that these equations are valid independently of how rapidly E/N changes in space or time.

For most applications, we are interested in the solution of the electron continuity equation (eq.11) which in turn depends on the electron flux or momentum balance (eq.12). The average electron velocity from the steady-state momentum balance equation contains a convective term which depends on the electric field and a diffusive term which depends on the gradient of the electron density. If the coefficients of these terms and the reaction frequency are known functions of E/N, then the continuity equation can be solved independently of the higher order moments. There are many practical cases, however, where the evdf and the corresponding transport and rate coefficients cannot be simply parameterized by E/N either because of the presence of physical boundaries or sources of electrons or because E/N is changing so rapidly in space or time that the evdf cannot follow its instantaneous, local value.

When the coefficients are unknown functions of E/N or if they can no longer be described by the local field, $E(r,t)/N$, some approximation to the distribution function is needed to effect a truncation of the moment series. Many different approximations have been used, for example, one³¹⁻³³ or two^{34,35} temperature distributions; displaced spherical shells where the displacement is related to the drift velocity and the radius of the shell to the random energy³⁶; single-beam

distributions where the distribution is monoenergetic and in the field direction³⁷; multibeam distributions where each secondary electron created in ionization is described by a single-beam distribution³⁷⁻³⁹; and combinations such as a local field description of the bulk electrons and a single-beam for the high energy tail⁴⁰, etc. In all of these parameterizations, the edf is expressed as a function of the average velocity or average energy or both, thus reducing the problem to the solution of two or three coupled partial differential equations.

The approximation of a one-temperature, Maxwellian eedf sometimes goes by the name of momentum transfer theory, and has been used extensively in many areas of transport theory. Recently Bayle, et al³² have applied it to the calculation of glow discharge development, and Yee et al made use of this approximation in their calculation of microwave propagation in the atmosphere³³. Because the eedf's most often encountered in applications involving electron transport are far from Maxwellian, this description is approximate at best. The high energy tail which often determines the ionization rate is controlled by different physical processes than is the bulk which determines, for example, the drift velocity. In a series of calculations related to models of low pressure positive column discharges, Vriens and his colleagues have made extensive use of the two-electron-group or two temperature description of the edf where one temperature describes the bulk and another describes the tail, the dividing point being the threshold energy of the first inelastic channel^{34,35}. Comparisons with Boltzmann calculations have shown that this description is quite reasonable for positive column discharges in Cs-Ar, for example.

Recently it has been shown that when the electric field changes abruptly in time⁴¹⁻⁴², undershoots or overshoots in the transient drift velocity appear which have analogues to those in electron transport in semiconductors. Such behavior is shown in Fig. 2 where the average electron energy, the excitation rate coefficient and the drift velocity are shown for a model atom which is described by an elastic cross section which is a constant equal to $6 \cdot 10^{-16} \text{ cm}^2$ and one inelastic process whose cross section rises linearly with energy above a threshold of .2 eV and with a slope of $10^{-15} \text{ cm}^2/\text{eV}$. The overshoot in the drift velocity is related to the transient decoupling of the momentum and energy; that is, the momentum responds faster to changes in the field than does the average energy. The one or two temperature descriptions of the eedf are insufficient to describe this behavior because those descriptions assume that the momentum is a function of the electron energy at all times. Using his displaced spherical shell model of the evdf, Ingold was able to accurately predict the undershoots and overshoots for simple test cases⁴³. The same displaced spherical shell model applied to the calculation of the Paschen curve in argon yields reasonable results near the minimum and to the left, but it fails to predict the right hand side³⁶. Ingold suggests that this is because it is the few high energy tail electrons which are responsible for the behavior of the left hand side of the Paschen curve, and these are not included in the model.

At very high E/N and in the region near the cathode where the evdf is highly peaked in the forward direction, single-beam models have been used successfully to predict the ionization rates³⁷. The evdf in these models is monoenergetic and forward directed, and the energy can be determined either from the energy balance or from the momentum balance since the velocity and the energy are related. These two equations, however, do not yield the same energy since the frequency for momentum exchange is very different from the frequency for energy exchange. Calculations based on the energy balance equation yield ionization rates

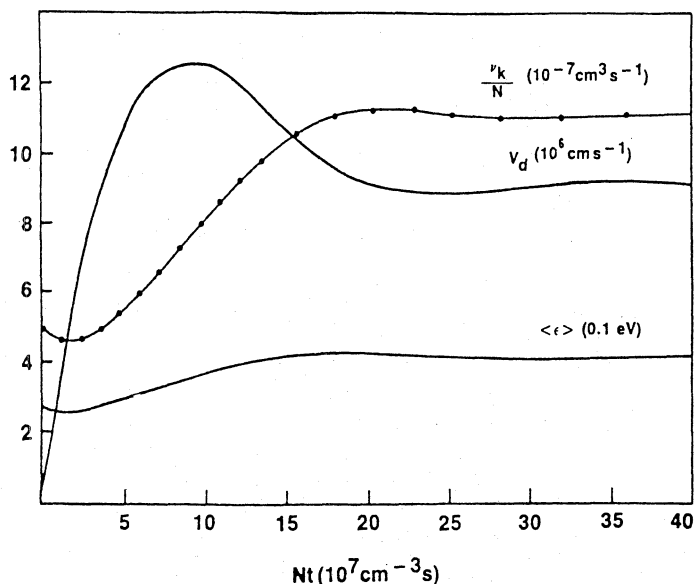


Fig. 2. Average energy, drift velocity and excitation rate coefficient as functions of N_t , the product of the neutral density and time, for a model atom as described in the text at 24 Td.

which are closer to experiment at high E/N than the results using the momentum balance to determine the beam energy.

Multibeam models have been described which differ from the single-beam models in the way ionization is treated^{38,39}. In the multibeam models, each new electron born in ionization events is assumed to follow the history of its parent, and the trajectory of the original parent is described by single beam momentum and/or energy equations. Multibeam models are close in spirit to Monte Carlo simulations except that collisions are treated as a continuous friction rather than a stochastic force, and much of the 'simulation' can be done analytically. Comparisons with Monte Carlo simulations at high E/N where the assumptions are reasonable yields excellent agreement for the transient as well as steady-state results. These models also provide a simple, intuitive picture of electron transport at high E/N where any individual electron can gain energy without limit in the field. Because secondary electrons are born at or near zero energy and in proportion to the number of electrons, the ensemble is always dominated by the newest and most numerous secondary electrons. The runaway component does not contribute significantly to averages over the eedf.

Recently, Boeuf has combined elements of these various descriptions in his self-consistent models of the cathode fall⁴⁰. Thus, the bulk electrons are described by the local field model and the high energy tail is described by a single-beam, energy balance model. This two-group approach has successfully described the ionization source term in the low field region at the end of the cathode fall. Comparisons with source terms calculated from Monte Carlo simulations for a given field configuration in the cathode fall show that the single-beam energy balance description of the high energy tail plus a local field description of the bulk distribution yields a source term which is qualitatively correct, but which extends further into the low field region (the negative glow) than does the Monte Carlo source term.

CONCLUDING COMMENTS

The hydrodynamic description of electron transport in weakly ionized gases is a highly developed theory which is valid for uniform (or almost uniform) fields in space and time and when the electron swarm has lost memory of its initial conditions. In these cases, the transport and rate coefficients defining the properties of the electron swarm interacting with the gas and under the influence of an electric field are well parameterized by E/N. Considerable effort has been devoted to the development of very accurate numerical solutions of the Boltzmann equation and efficient Monte Carlo simulations in the hydrodynamic regime. The presence of electron absorbing, emitting or reflecting boundaries disrupts the local electron energy balance as do external sources of volume ionization produced, for example, by a laser or an electron beam. The local electron energy balance is also perturbed if the electric field varies rapidly in space and time such as in the cathode fall of a discharge or for high frequency excitation. Under these conditions there is no general parameterization, but the velocity moment approach, judiciously applied, can often provide a good qualitative description of the electron behavior.

REFERENCES

1. K. Kumar, H.R. Skallerud and R.E. Robson, *Aust. J. Phys.*, 33:343 (1980).
2. L.G.H. Huxley and R.W. Crompton, "The Diffusion and Drift of Electrons in Gases", John Wiley & Sons, Inc., New York, 1974.
3. J. Dutton, *J. Phys. Chem. Ref. Data*, 4:577 (1975).
4. J.W. Gallagher, E.C. Beaty, J. Dutton and L.C. Pitchford, *J. Phys. Chem. Ref. Data*, 12:109 (1983).
5. W.P. Allis, *in: "Handbuch der Physik"*, S. Flugge, ed., Springer, Berlin (1956).
6. L.C. Pitchford, S.V. O'Neil and J.R. Rumble, Jr., *Phys. Rev.A*, 23:294 (1981).
7. R. Winkler, G.L. Braglia, A. Hess and J. Wilhelm, *Beitr. Plasmaphys.*, 24:657 (1984).
8. S.L. Lin, R.E. Robson and E.A. Mason, *J. Chem. Phys.*, 71:3483 (1979).
9. P. Segur, M. Yousfi, J.P. Boeuf, E. Marode, A.J. Davies, and C.J. Evans, *in: "Electrical Breakdown and Discharges in Gases"*, E.E. Kunhardt and L.L. Luessen, eds. Plenum, New York, (1983).
10. T. Itoh and T. Musha, *J. Phys. Soc. Jpn.*, 15:1675 (1960).
11. J.P. Boeuf and E. Marode, *J. Phys. D*, 15:2069 (1982).
12. T.J. Moratz, L.C. Pitchford, and J.N. Bardsley, *J. Appl. Phys.*, 61:2146 (1987).
13. H.R. Skallerud, *J. Phys. D*, 1:1567 (1968).
14. L. Friedland, *Phys. Fluids*, 20:1461 (1977).
15. Y.M. Li, L.C. Pitchford, and T.A. Moratz, to appear in *Appl. Phys. Lett.* (1989).
16. G.L. Braglia, L. Romano and M. Diligenti, *Lett. Nuovo Cim.*, 35:193 (1982).
17. P. Segur, M. Yousfi, M.H. Kadri and M.C. Bordage, *Transport Theory and Stat. Phys.*, 15:705 (1986).
18. I.P. Shkarofsky, T.W. Johnston and M.P. Bachynski, "The Particle Kinetics of Plasmas", Addison-Wesley, Reading, (1966).
19. K. Kumar, *Phys. Repts.*, 112:319 (1984).
20. A.V. Phelps and L.C. Pitchford, *Phys. Rev.A*, 31:2932 (1985).
21. H. Tagashira, Y. Sakai and S. Sakamoto, *J. Phys.D*, 10:1051 (1977).
22. L.S. Frost and A.V. Phelps, *Phys. Rev.*, 127:1621 (1962).

23. W.L. Morgan, JILA Information Center Report No. 19, unpublished, (1979).
24. T. Holstein, Phys. Rev., 70:367 (1946).
25. S. Yoshida, A.V. Phelps and L.C. Pitchford, Phys. Rev.A, 27:2858 (1983).
26. R.E. Robson and K.F. Ness, Phys. Rev.A, 33:2068 (1986).
27. Y. Tzeng and E.E. Kunhardt, Phys. Rev.A, 34:2148 (1986).
28. E.E. Kunhardt and Y. Tzeng, Phys. Rev.A, 34:2158 (1986).
29. P.J. Drallos and J.M. Wadehra, J. Appl. Phys., 63:5601 (1988).
30. E.D. Cashwell and C.J. Everett, "A Practical Manual on the Monte Carlo Method for Random Walk Problems", Pergamon Press, Inc., New York, (1959).
31. E.A. Mason and E.W. McDaniel, "Transport Properties of Ions in Gases", John Wiley & Sons, Inc., New York, (1988).
32. P. Bayle, J. Vacquie and M. Bayle, Phys. Rev.A, 34:360 (1986).
33. J.H. Yee, R.A. Alvarez, D.J. mayhall, D.P. Byrne, and J. DeGroot, Phys. Fluids, 29:1238 (1986).
34. L. Vriens, R.A.J. Keijser, and F.A.S. Ligthart, J. Appl. Phys., 49:3807 (1978).
35. W.L. Morgan and L. Vriens, J. Appl. Phys., 51:5300 (1980).
36. J.H. Ingold, in: "Gaseous Electronics, Electrical Discharges", M.N. Hirsch and H.J. Oskam, eds., Academic, New York, (1978).
37. A.V. Phelps, B.M. Jelenkovic and L.C. Pitchford, Phys. Rev.A , 36:5327 (1987).
38. K.G. Muller, Z. Phys., 169:432 (1962).
39. L. Friedland, J. Phys. D, 7:2246 (1974).
40. J.P. Boeuf and P. Segur, in: "Interactions Plasmas Froide Matériaux", C. Lejeune, ed., Les Editions de Physique, Les Ulis, France, (1987).
41. L.C. Pitchford, Technical Report No. AFWAL-TR-85-2016 (1985).
42. A.G. Ponomarenko, V.N. Tishchenko, and V.A. Shveigert, Sov. J. Plasma Phys., 11:288 (1985).
43. J.H. Ingold and L.C. Pitchford, Bull. Am. Phys. Soc., 30:143 (1985).

NON EQUILIBRIUM PLASMA KINETICS

M. Capitelli and C. Gorse

Centro di Studio per la Chimica dei Plasmi del CNR
Dipartimento di Chimica, Università di Bari
Trav. 200 Re David, 4 - 70126 Bari, Italy

Non equilibrium plasma kinetics play an important role in understanding chemical reactions occurring under plasma conditions. The heart of the problem involves the characterization of the electron component through the Boltzman equation and of the heavy particle components through a generalized master equation approach^{1,2}. For a long time the two kinetics have been decoupled, the lower decoupling being represented by a Maxwell distribution function for characterizing the electron energy distribution function (EDF). This approach, however, tends to be cancelled, despite the strong resistance of a part of the scientific community. Many years ago we have presented the first attempts to couple EDF and kinetics of heavy particles, in particular we have shown the strong coupling between EDF and the vibrational content of the molecules³. Nowadays this coupling is practically considered in all the calculations, as can be appreciated by looking at the specialized literature^{4,5}.

In these last years, however, it has been realized that not only the vibrational states of the molecule but also the electronic ones can strongly affect EDF and related properties in molecular plasmas⁶⁻⁸.

Moreover the action of vibrational and electronic states can not be decoupled. In fact the kinetics of the population densities of vibrational and electronic excited states is coupled through the so called V-E processes, which transform vibrational into electronic energy (and viceversa). Moreover the influence of superelastic electronic collisions (SEC) tends to disappear in the presence of large concentrations of vibrational excited states⁸.

A realistic description of non equilibrium plasma kinetics therefore requires a selfconsistent solution of Boltzmann equation with 1) the vibrational master equation 2) the electronic master equation 3) the plasma chemistry. This approach will be discussed in the following for different plasma conditions.

1. Method of calculation and results

Figure 1 shows in a schematic form the model utilized for understanding

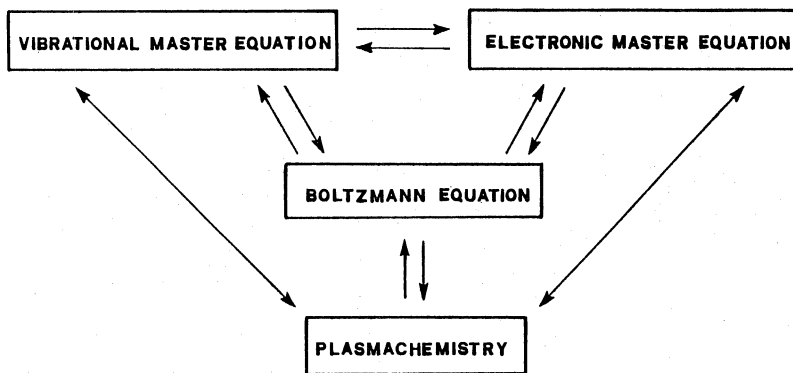


Fig.1 Schematic model showing the interconnections between BE, VK, EK and PK

non equilibrium plasma kinetics. The key of the model is the solution of the Boltzmann equation (BE) for EDF which strongly affects, being at the same time strongly affected, the vibrational kinetics (VK), the electronic kinetics (EK) and the plasma chemistry (PK).

All these kinetics are deeply connected so that only a selfconsistent solution of the different kinetics (BE, VK, EK, PK) can give us a correct description of non equilibrium plasma kinetics. Of course the general scheme is good to be seen but difficult to be applied, so that many approximations must be introduced during the solution. Details of these approximations can be found in our previous papers. Here we want to show some examples of the application of the general scheme for different plasma conditions. In particular we report the behaviour of N_2 in discharge and post discharge conditions^{9,10}, of H_2 in multipole magnetic plasmas^{11,12} and of different systems in rf plasmas¹³⁻¹⁵. The three examples, though particular, can generalize many situations occurring in non equilibrium plasma kinetics.

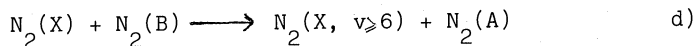
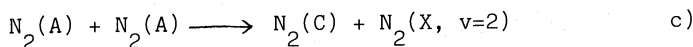
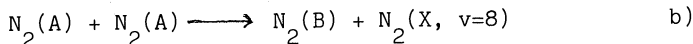
1a. DC discharge and post discharge conditions

As a first example we want to show results recently obtained by solving the selfconsistent problem for N_2 flowing in a discharge characterized by given reduced electric field E/N , electron density (n_e) and gas temperature (T_g) values. These assumptions are indeed approximations, because a "true" selfconsistent problem should also solve appropriate equations for E/N , n_e and T_g . Before examining the results we want to remind that the most important couplings between VK, EK, and EDF come from the superelastic vibrational (SVC) and electronic (SEC) collisions^{9,10}. In particular SVC affect EDF in the bulk energy region, while SEC, which in the present case involve the collision of low energy electrons with the A,B,C ($A = A^3 \Sigma_u^+$, $B = B^3 \Pi_g$, $C = C^3 \Pi_u$) states of N_2



drain electrons from the low energy part of EDF to the high energy one. Other couplings interest VK and EK kinetics which are linked in the

present study also through bimolecular reactions of the type (see refs. 9-10 for details)



The initial conditions ($t=0$) necessary to start the integration of coupled kinetics are as follows

- 1) all the molecules concentrated in the ground vibroelectronic state of the molecule (cold gas approximation)
- 2) EDF corresponding to the selected E/N value in the cold gas approximation.

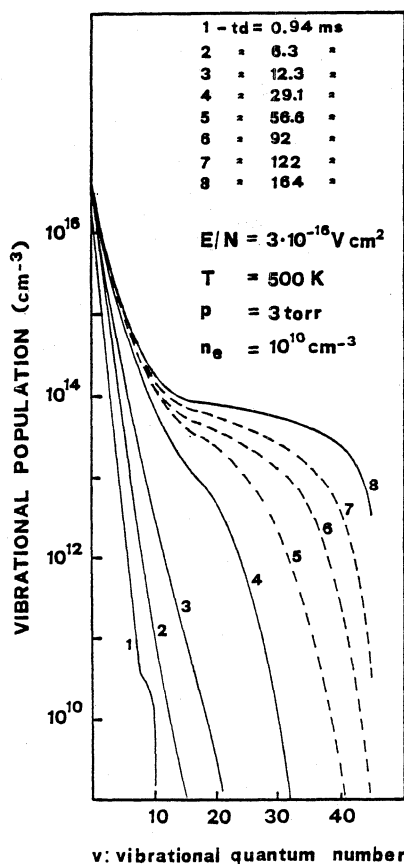


Fig. 2 Temporal evolution of N_2 vibrational distribution under discharge conditions (t_d :residence time in the discharge)

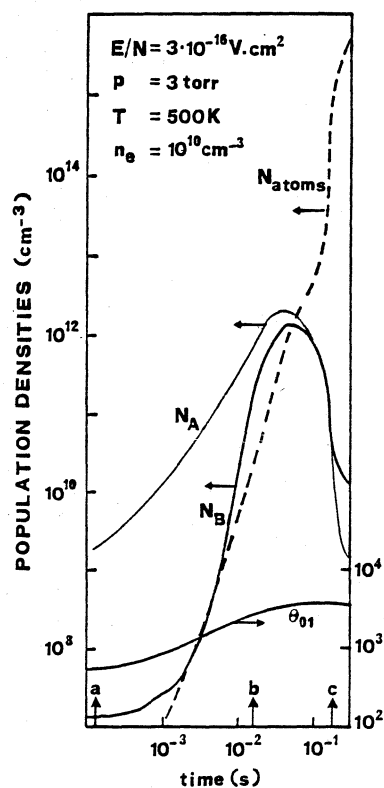


Fig. 3 Temporal evolution of $A^3\Sigma_u^+$, $B^3\Pi_g$ electronic states and N atoms population densities as well as of 0-1 vibrational temperature (θ_{01}) under discharge conditions

After starting the different kinetics, the increased concentrations of vibrational and electronic states of N_2 begin to affect EDF.

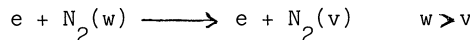
Keeping in mind these simple ideas, we can examine characteristic results obtained by the different kinetics. In particular figs. 2-4 show respectively the temporal growth

a) of the vibrational distribution (N_v) (fig. 2)

b) of the concentrations of electronic states (A, B, C) as well as of the atom density and of the 0-1 vibrational temperature (θ_{01}) of N_2 (fig.3)

c) of the electron energy distribution function (fig. 4a,b).

Inspection of figure 2 shows that the vibrational distribution of N_2 becomes more and more non-Boltzmann as the residence time in the discharge increases. The non-Boltzmann character of N_v is due to the onset of V-V (vibration-vibration) energy exchange processes which are able to redistribute the vibrational quanta, introduced by e-V (electron-vibration) energy exchanges, over the whole vibrational manifold of N_2^{16} . As a result the vibrational distribution of N_2 is characterized by a long plateau, which can affect the dissociation and ionization kinetics of N_2^{17} . Moreover superelastic vibrational collisions



affect EDF in the electron energy range $2 < \epsilon < 10$ eV as can be appreciated by looking at the temporal evolution of EDF reported in fig.4. We can

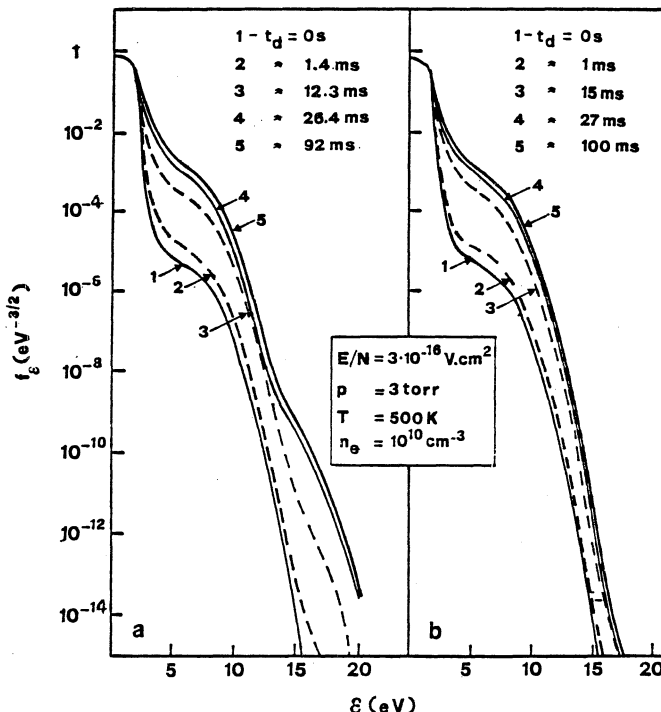


Fig. 4 a-b Temporal evolution of electron energy distribution function of pure N_2 under discharge conditions
a) calculations with SEC and SVC b) only SVC

infact note that EDF strongly increases in time following the corresponding increase of non equilibrium vibrational distribution of N_2 . On the other hand the tail of EDF ($\varepsilon > 10$ eV) grows in time as a result of superelastic vibrational and electronic collisions. The action of superelastic electronic collisions can be better appreciated by comparing the temporal evolution of EDF obtained by inserting (fig. 4a) and by neglecting (fig. 4b) SEC.

The most important point which can be derived from figs. 2-4 is that the concentration of the different species strongly depends on the residence time in the discharge. This point is of particular importance when we want to follow the relaxation of the different quantities in the post-discharge regime (i.e. for $E/N = 0$). The residence time in the discharge in fact prepares different situations for the post discharge regime. Roughly speaking we can consider three general situations. The first one, characterized by short residence times, is able to populate only the electronic states of the molecule. The second situation is characterized by residence times sufficient to populate both vibrational and electronic states, while the third one (very long residence times) is able to create a non equilibrium vibrational distribution strongly exceeding the population of electronic states.

The three situations have been numerically studied in a recent paper¹⁰.

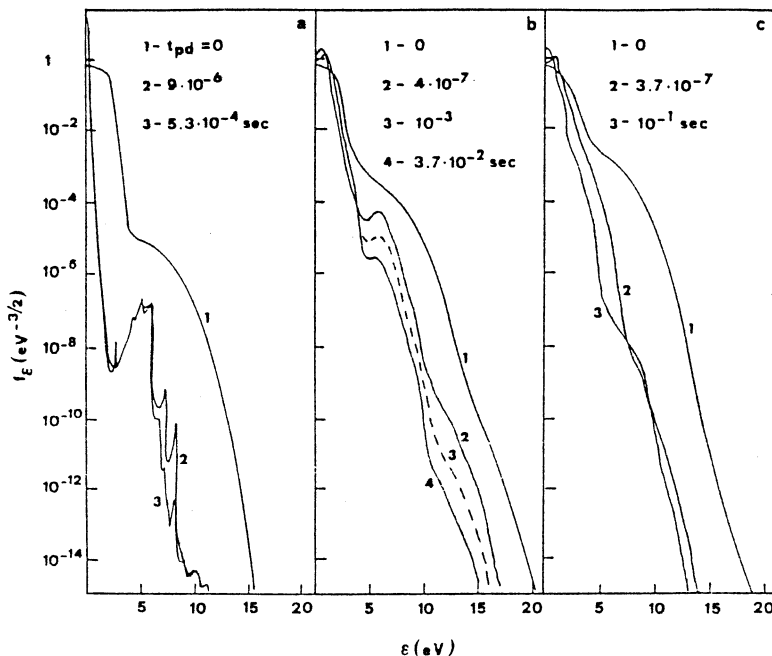


Fig. 5 a-c Temporal evolution of electron energy distribution function in the post discharge regime (a, b, c differ from the selection of intial conditions see arrows in fig. 3)(t_{pd} : residence time in the postdischarge regime)

Figures 5a-c in particular report the relaxation of EDF, which strongly depends on the way of preparing the non equilibrium vibrational and electronic populations in the discharge (i.e. on the residence time in the discharge regime). In particular a well structured EDF can be observed when only the electronic states are populated (fig. 5a), while

at very long residence times (fig. 5c) only SVC act in affecting EDF. At the moderate residence times (fig. 5b) both SVC and SEC act in shaping EDF.

Unfortunately a selfconsistent approach to the experimental determination of the different theoretical quantities does not exist, so that only a qualitative comparison between theoretical and experimental N , N^* and EDF can be done. Here is sufficient to say that our calculated N distributions satisfactory reproduce the experimental values recently obtained by Massabieaux et al. by CARS spectroscopy¹⁸. Moreover, the experimental relaxation of CO pumped by vibrationally excited N_2^v in the post-discharge regime has been recently interpreted by using the present approach¹⁹. Similar arguments apply to the relaxation of EDF in He- N_2 post-discharge which has been discussed in ref. 20.

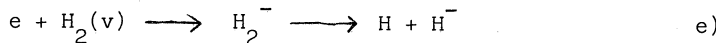
Before ending this section we want to discuss the accuracy of the reported distributions, which of course depend on the corresponding accuracy of the input data utilized in the model. In this context we want to remind that a) V-V (vibration-vibration) and V-T (vibration-translation) energy exchange rates are those calculated by Billing et al. several years ago²¹ b) e-V (electron-vibration) rates have been calculated by using the cross-sections of ref. 22 c) electron inelastic cross sections (including dissociation and ionization) involving vibrationally excited N_2^{17} molecules have been calculated by using Gryzinski' method¹⁷ d) V-T rates involving N atoms have been considered equal to the corresponding $N_2(v)-N_2$ rates e) deactivation of vibrationally excited nitrogen molecules on the wall of the container has been neglected.

These points represent to our opinion the most important weakness of our model.

It is well known infact that V-V and V-T rates strongly depend on the N_2-N_2 interaction potential, which has been recently improved²³. On the other hand e-V rates involving vibrationally excited N_2 molecules recently calculated by Huo²⁴ present a trend which is different from that one reported in ref. 16. The use of Gryzinski' method is open to criticism, even though the results for $N_2(v=0)$ transitions are in satisfactory agreement with existing experimental and theoretical values (see ref. 17). Points d) and e) can only be justified by the lack of experimental and theoretical values even though a certain effort is being made for better understanding these cross sections^{23,25}. All these remarks should emphasize the qualitative nature of our results, which however represent an important guideline for future improvements.

2. Multipole magnetic H_2 plasmas

Non equilibrium kinetics occurring in this kind of plasma is of particular interest because of their wide use for producing beams of negative ions (H^-). The accepted mechanism for the production of H^- is the dissociative attachment from vibrationally excited H_2 molecules



Optimization of these sources requires the knowledge of the vibrational distribution of H_2 in the ground state as well as the EDF in this kind of

plasmas. These simple statements however require an enormous theoretical effort since numerous microscopic processes determine the non equilibrium vibrational kinetics of H_2 (see table 1). Once more the general scheme

Table 1 List of microscopic processes inserted in the kinetics

e-V	$e + H_2(v) \rightarrow e + H_2(w)$
E-V*	$e + H_2(v=0) \rightarrow e + H_2(B^1\Sigma_u^+, C^1\Pi_u) \rightarrow e + H_2(v') + h\nu$
V-V	$H_2(v) + H_2(w) \rightarrow H_2(v-1) + H_2(w+1)$
V-T	$H_2(v) + H_2 \rightarrow H_2(v-1) + H_2$
V-T	$H_2(v) + H \rightarrow H_2(w) + H$
e-D*	$e + H_2(v) \rightarrow e + H_2^* \rightarrow e + 2H$
e-D*	$e + H_2(v) \rightarrow e + H_2^* \rightarrow e + H + H^*$
e-I*	$e + H_2(v) \rightarrow e + H_2^+ + e$
e-da	$e + H_2(v) \rightarrow H + H^+$
e-E*	$e + H_2(v) \rightarrow e + H_2^*$
wall	$H_2(v) \rightarrow H_2(w)$
wall	$H + H \rightarrow H_2(v)$
wall	$H_2^+ + (e)_{\text{sup}} \rightarrow H_2(v)$

reported in fig. 1 has been utilized to obtain the temporal evolution of EDF, N_v , N_H^+ , N_H^- . In this case the kinetics of electronically excited states of both H_2^* and H^* has been neglected, representing a further step toward the complete understanding of this kind of plasmas.

Figures 6-8 report the temporal evolution of the different quantities. To understand these results, we want to remind that EDF in multipole magnetic plasmas are formed by a flux of electrons emitted by a filament and accelerated by the applied field. Then the emitted electrons (approximately at 50 eV) are degraded toward thermalization. On the other hand vibrationally excited H_2 molecules are formed not only through e-V processes i.e.



but also through E-V ones i.e.



i.e. by electron excitation over the singlet states of H_2 and subsequent radiative transitions over the vibrational levels of electronic ground state.

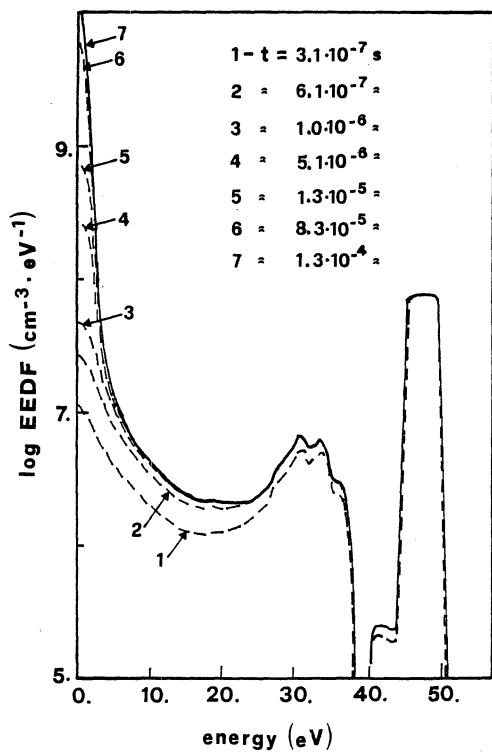


Fig. 6 Temporal evolution of electron energy distribution function in multipole magnetic plasma (volume: 8.81; loss surface: 831 cm^2 ; pressure: 2 mtorr; filament current: 5A; plasma potential: 1.96V; applied voltage: 50V)

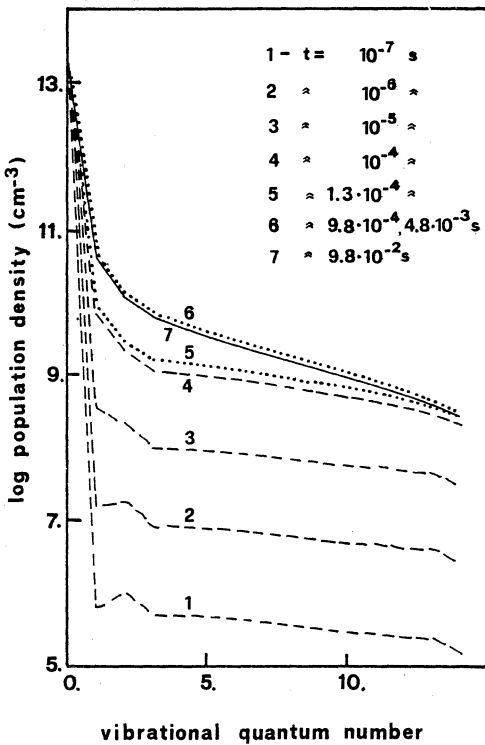


Fig. 7 Temporal evolution of vibrational distribution function of H_2 in multipole magnetic plasmas (same conditions as in fig. 6)

Keeping in mind these points we can follow the evolution of EDF, N_v , N_H and N_{H^-} reported in the relevant figures.

Note that the times necessary to EDF to reach quasistationary conditions are orders of magnitude shorter than the corresponding times necessary to the other quantities to reach quasistationary values. It is also worth noting that the reported EDF strongly differs from EDF in glow discharge. Apparently the vibrational distribution of H_2 closely follows that one reported in N_v . However the plateaux present in H_2 are a consequence of E-V processes (i.e. process g), while those in N_2 are a direct consequence of V-V (vibration-vibration) energy transfer processes¹⁶.

Finally we want to point out that the role of SVC in affecting (average energy), T_e (electron temperature) and n_e (electron density) values is less important than the corresponding one in glow discharge situations (see ref. 12). In particular the neglection of SVC underestimates the values of $\bar{\epsilon}$ and T_e , overestimating at the same time the value of electron density.

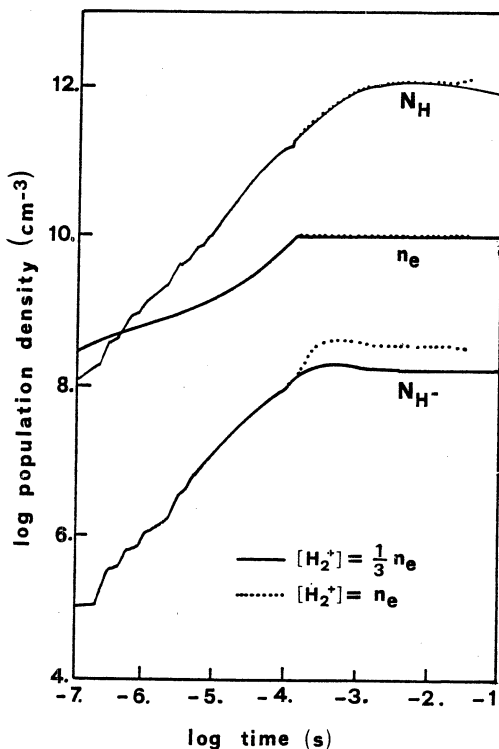


Fig. 8 Temporal evolution of electron density n_e , atom density N_H and ion density N_{H^-} in multipole magnetic plasmas (same conditions as in fig. 6)

As for the comparison of the present results with the experimental values, we have in general found a satisfactory agreement between theory and experiments concerning the vibrational temperature of H_2 ($v=1$) as well as the values of T_e , n_e and N_{H^-}/n_e (see refs. 11,12,26,27).

Let us now examine the accuracy of the reported results with respect to

the choice of input data. First we note that electronic and ionization cross sections involving vibrationally excited molecules have been calculated by the Gryzinski' method²⁸. Very recently Rescigno and Schneider²⁹ reported a very accurate calculation of excitation cross section of H_2 to the repulsive state $b^3\Sigma_u^+$ for different initial H_2 vibrational levels. A comparison between these values and our calculated semiclassical values³⁰ (see fig. 9) for different vibrational levels shows a satisfactory agreement i.e. Gryzinski' cross sections can be considered accurate within a factor 2. Similar arguments apply to the other electronic transitions as well as to E-V cross sections, which have been recently recalculated by our group³⁰. In this last case we have found that our E-V cross sections are approximately a factor 2 less than the values obtained by Hiskes³¹ some years ago. The same accuracy can be expected on the dissociative attachment cross sections involving $H_2(v)$.

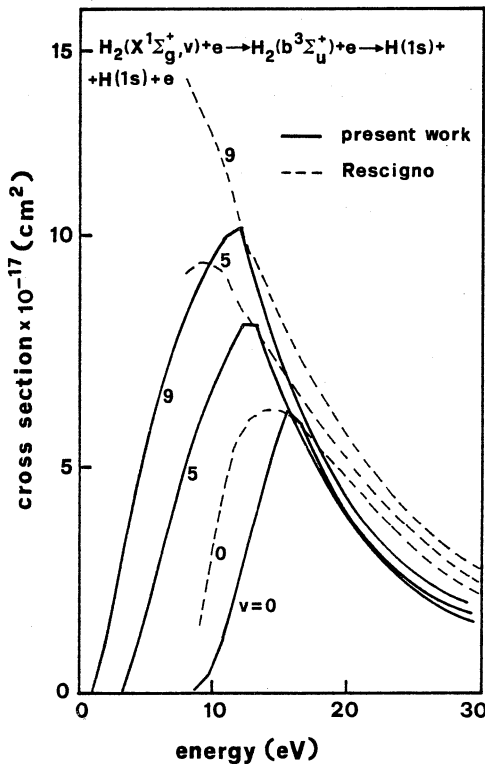


Fig. 9 A comparison between theoretical cross sections for the excitation of first triplet of H_2 at different initial vibrational quantum numbers

The validity of Bardsley and Vadehra³² cross sections utilized in the present calculations, infact resists to the accurate quantum mechanical method developed by Mundel et al.³³.

The situation for V-T ($H_2(v)-H_2$) and V-V rates is rather encouraging due to the large computational effort performed by Cacciatore et al.³⁴ and by Laganà³⁵. Note that the results present in figure 8 contain Laganà cross sections for $H-H_2(v)$, while we plan to insert in our model Cacciatore et al. rates in the next future.

The situation is rather complicated for the deactivating rates of $H_2(v)$

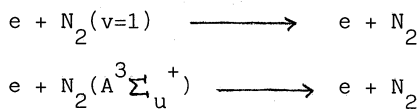
on metallic surfaces. Two independent calculations do exist. The first one, made by Karo and Hiskes ³⁶ shows a strong deactivation of $H_2(v)$ ³⁷ on iron surfaces. The second calculation, performed by Cacciatore et al. ³⁸, shows little deactivation of $H_2(v)$ ³⁹ on copper surfaces. Observations made by different groups about the formation of highly vibrationally excited molecules during atomic recombination on metallic surfaces seem to contradict Hiskes and Karo results, being in better agreement with Cacciatore et al. calculations. Additional calculations on the relaxation of $H_2(v)$ on metallic surfaces urge to shed light on the problem.

An other important mechanism for producing $H_2(v)$ is the recombination of H_2^+ / H_3^+ ³⁹ on metallic surfaces as pointed out by Hiskes and Karo. Improvement of cross sections as well as a better description of positive ion kinetics seems necessary to correctly insert this mechanism in the overall kinetics. This last point can be appreciated by looking at fig. 8, where the concentrations of H^- and electrons have been calculated by making different hypotheses on the concentration of H_2^+ in the discharge. This last species does influence the overall kinetics through the recombination on the metallic walls yielding $H_2(v)$. We can note that in particular the concentration of H^- depends on that one of H_2^+ i.e. it increases with increasing $[H_2^+]$.

In conclusion we can say that large progress has been done in modeling H_2 discharges since the first attempts made by our group in this direction ²⁸. Probably now is time to finalize the efforts toward D_2 discharges.

3. Radiofrequency discharges

As a third example we want to show the influence of superelastic collisions in affecting EDF in radiofrequency discharges, a problem which has been widely discussed in the last few years for several systems. Here we show the effect of second kind collisions



in affecting EDF and related properties of N_2 rf bulk plasmas. The method of calculation consists in solving the time dependent Boltzmann equation in the presence of a rf field of the form

$$E/p_o = (E_o/p_o) \cos \omega t$$

and in the presence of given concentrations of $N_2(v=1)$ and $N_2(A^3\Sigma_u^+)$ states ¹³. This last assumption does imply quasistationary concentrations of excited states during the alteration of the rf field.

Figure 10a reports the behaviour of EDF at different reduced times t' ($t' = \omega t / 2\pi$), at fixed frequency (ω / p_o) and fixed amplitude (E_o / p_o) values, in the cold gas approximation (i.e. with the concentration of excited states put equal to zero), while figs. 10b-d report the behaviour of EDF in the presence of different concentrations of excited states.

Inspection of the results shows the importance of second kind collisions in affecting EDF. In particular SVC tend to fill the hole of EDF in the

energy range 4–8 eV, while SEC tend to form structures in the high energy tail of EDF. These effects are similar to those observed in DC and post discharge conditions, even though we want to remind that at the considered frequency $\omega/p_0 = \pi \cdot 10^7 \text{ sec}^{-1} \text{ torr}^{-1}$ neither the quasistationary

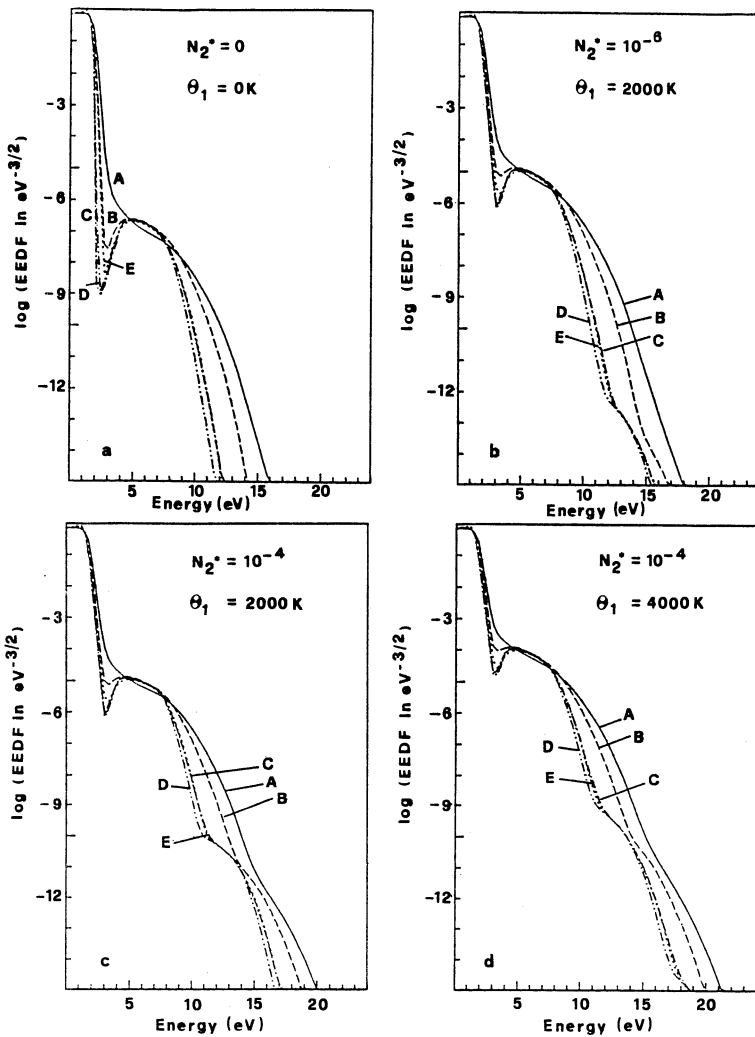


Fig. 10 a-d Temporal evolution of EDFs for different population of excited states ($N_2^* = N_2(A^3\Sigma_u^+)$; θ_1 : vibrational temperature), (the different curves refer to various reduced times $t' = \omega t / 2\pi$, (A:t'=0, 0.5; B:t'=0.16; C:t'=0.25; D:t'=0.29, E:t'=0.34), ($\omega/p_0 = \pi \cdot 10^7 \text{ s}^{-1} \text{ torr}^{-1}$; $E_0/p_0 = 9.9 \text{ V cm}^{-1} \text{ torr}^{-1}$)

approximation nor the effective field approximation holds for EDF (see figure 12 of ref. 13). Let us now consider the influence of SVC and SEC on the ionization collision frequency of $N_2(\nu_i)$ (see fig. 11). Inspection of this figure, which reports the temporal evolution of ν_i for different concentrations of excited states, shows that the presence of SVC and SEC strongly alters the ionization frequency specially in the temporal region

close to the zero passage of the electric field (remind that $t' = 0$ means $E = E_0$, $t' = 0.25$ means $E = 0$ and so on). It is worth noting that the increase of $N_2^*(A \Sigma^+)$ concentration strongly decreases the modulation of the ionization frequency, having minor consequences on the delay of this rate with respect to the applied field.

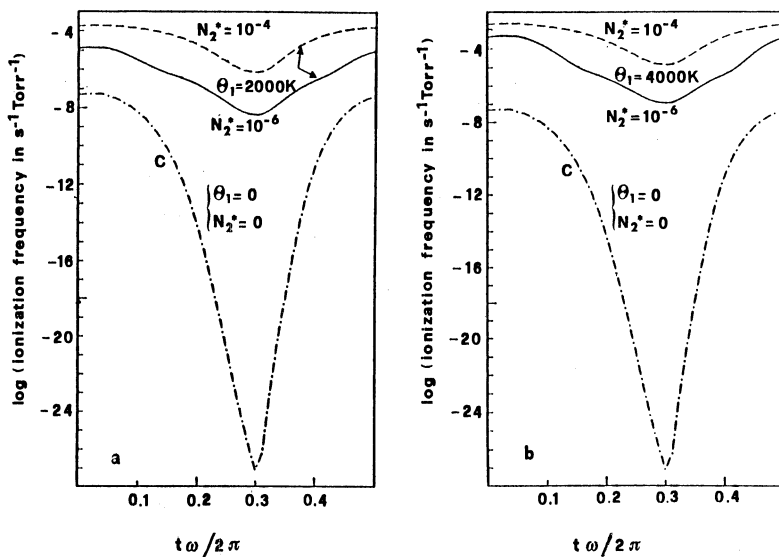


Fig. 11 a-b Temporal evolution of the ionization frequency of N_2 versus t' for different concentrations of excited states ($\omega/p_0 = \pi 10^7 \text{ s}^{-1} \text{ torr}^{-1}$, $E_0/p_0 = 9.9 \text{ V cm}^{-1} \text{ torr}^{-1}$)

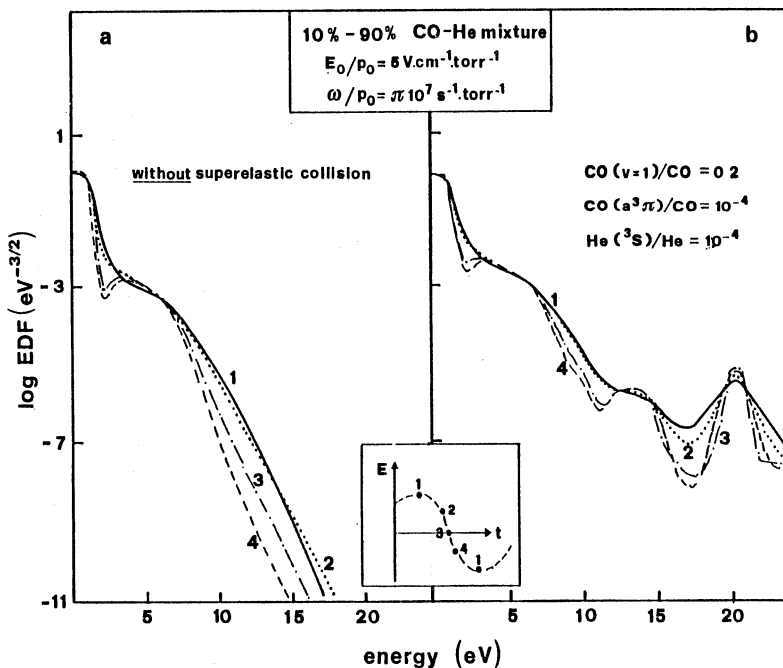


Fig. 12 a-b Temporal evolution of EDF in a 10%-90% CO-He mixture calculated without (a) and with (b) superelastic collisions

As a further example figures 12a-b show EDF for a CO-He (0.1:0.9) mixture ($E_0/p_0 = 5 \text{ V cm}^{-1}$, $\omega/p_0 = \pi 10^8 \text{ s}^{-1}$ torr $^{-1}$) calculated with and without superelastic collisions. We see that the presence of the metastable He(S^3) state strongly affects the temporal evolution of EDF in this mixture (see ref. 14 for details).

The behaviour reported for N $_2^{40}$ and He-CO has been also found in other systems, thereby indicating the importance of excited states in affecting EDF in rf plasmas. Of course the next step is to couple the EDF with the kinetics of excited states as done in DC and post-discharges conditions.

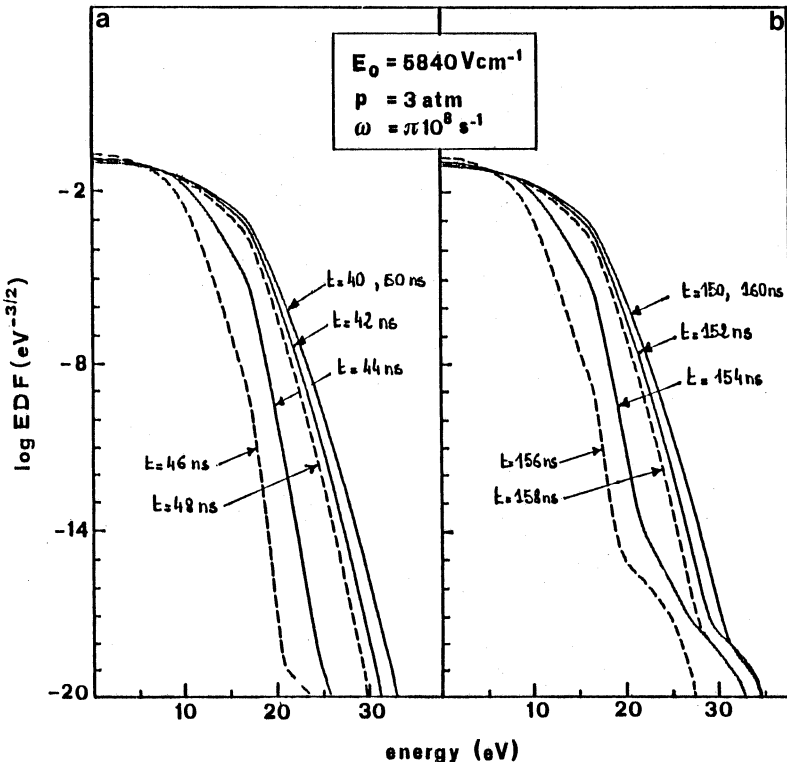


Fig. 13 a-b Self-consistent temporal evolution of EDF in rf Ne-Xe-HCl mixture for two half cycles

This coupling has been recently realized in the case of an excimer Ne-Xe-HCl (0.95:0.044:0.0066) mixture¹⁵. In this case infact the time dependent Boltzmann equation has been solved selfconsistently with the complex chemical kinetics occurring in the rf discharge. Figure 13 a,b shows the temporal evolution of EDF during two complete rf cycles, one in the early stage of the discharge, the other one after 100 ns. Comparison of the results shows that superelastic electronic collisions coming from metastable Xe and Ne atoms tend to destroy the symmetry of the tail of EDF passing from a cycle to an other one as a result of the increased concentration of excited states. This last point can be better understood by looking at figure 14 where we have reported the temporal evolution of selected species in the active excimer medium during the two reported cycles. Once again we can note that some species present an oscillatory

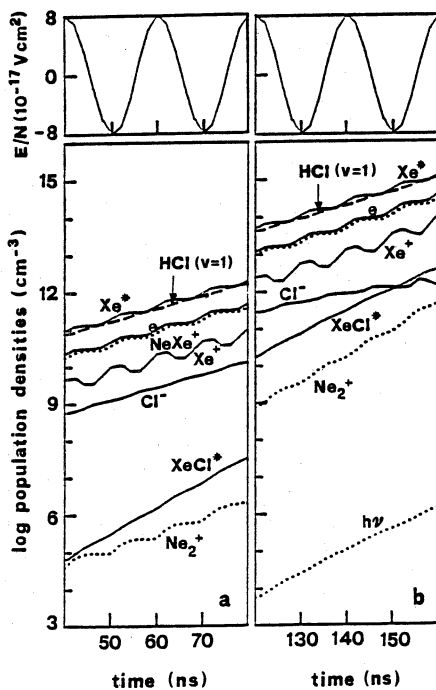


Fig. 14 a-b Temporal evolution of selected species in a rf Ne-Xe-HCl mixture for two cycles at the early (a) and late (b) times

behaviour due to the sinusoidal behaviour of the electric field. Finally to better understand the role of superelastic collisions in affecting EDF we have reported in Fig. 15 different EDF corresponding to different passages of electric field to the zero values. We can note that the

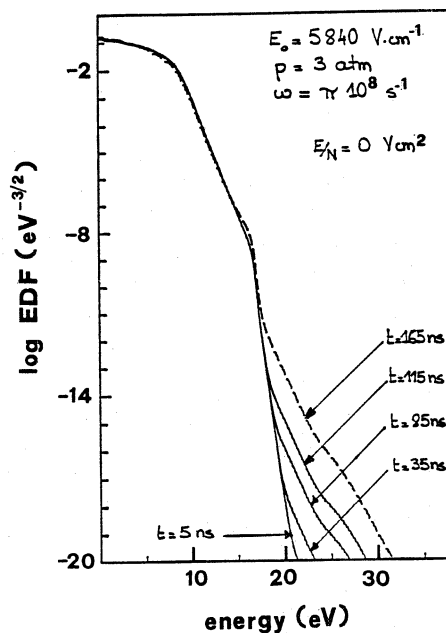


Fig. 15 The behaviour of EDF in a rf Ne-Xe-HCl mixture during the different zero passage of the electric field

increased concentration of excited states during the temporal evolution of rf discharge affects more and more the tail of EDF.

Concluding remarks

We have presented different examples of the influence of excited states on the modeling of different kinds of plasmas. We believe that our microscopic approach can open new perspectives in the understanding of plasma kinetics. Of course our approach can be improved either by improving the input data (electronic and heavy particle collision cross sections) or by introducing new processes in the macroscopic treatments of the kinetics. In particular the role of the walls in producing and destroying excited states should be seriously taken into account, this point being particularly important for the H₂ kinetics discussed in section 3.

As for the results presented in rf discharges, we want to point out that our model considers only the behaviour of EDF in the bulk plasma, completely neglecting sheath problems. These problems however can be very important in rf plasmas as shown by Belenguer and Boeuf⁴¹ so that future efforts in the modeling of rf discharges should take into account both our results as well as those discussed in ref.41.

In conclusion we can say that plasma modeling progressed very much in these last years due to the cooperative efforts made by researchers coming from different areas.

Acknowledgments

This work has been partially supported by the CNR under the "Progetto Finalizzato Sistemi Informatici e Calcolo Parallelo, sottoprogetto Calcolo Scientifico per Grandi Sistemi"

REFERENCES

- /1/ M. Capitelli and E. Molinari, Top. Curr. Chem. 90:59 (1980)
- /2/ "Non-Equilibrium Vibrational Kinetics" Ed. M. Capitelli, Top. Curr. Phys. 39 (1986) Springer-verlag
- /3/ M. Capitelli, Pure and Appl. Chem. 52:1721 (1981)
- /4/ J.P. Boeuf and E.E. Kunhardt, J. Appl. Phys. 60:915 (1986)
- /5/ J. Loureiro and C.M. Ferreira, J. Phys. D: Appl. Phys. 19:17 (1986)
- /6/ A.P. Ershov and A.A. Kuzovnikov, Proceedings of VII ESCAMPIG Bari, (1984) p. 230
- /7/ C. Gorse, J. Bretagne and M. Capitelli, Phys. Lett. A 126:277 (1988)
- /8/ C. Gorse, F. Paniccia, J. Bretagne and M. Capitelli, J. Appl. Phys 59:731 (1986); 59:4004 (1986)
- /9/ C. Gorse and M. Capitelli, J. Appl. Phys. 60:4072 (1987)
- /10/ C. Gorse, M. Cacciatore, M. Capitelli, S. De Benedictis and G. Dilecce, Chem. Phys. 119:63 (1988)
- /11/ C. Gorse, M. Cacciatore, M. Capitelli, R. Celiberto and P. Cives, Proc. of International Symposium on Plasma Chemistry (Pugnochiuso 1989)
- /12/ C. Gorse, M. Capitelli, M. Bacal, J. Bretagne and A. Laganà, Chem. Phys. 117:177 (1987)

- /13/ M. Capitelli, R. Celiberto, C. Gorse, R. Winkler and J. Wilhelm J. Phys. D: Appl. Phys. 21:691 (1988)
- /14/ M. Capitelli, R. Celiberto, C. Gorse, R. Winkler and J. Wilhelm, J. Appl. Phys. 62:4398 (1977)
- /15/ C. Gorse and M. Capitelli, 41st Annual Gaseous Electronics Conference (GEC 1988) Minneapolis paper 11-3 page 84
- /16/ M. Capitelli, M. Dillonardo and C. Gorse, Chem. Phys. 56:29 (1981)
- /17/ M. Cacciatore, M. Capitelli and C. Gorse, Chem. Phys. 66:141 (1982)
- /18/ B. Massabieaux, J. Gousset, M. Lefebvre and M. Pealat, J. Phys. (Paris) 48:1939 (1987)
- /19/ S. De Benedictis, M. Capitelli, F. Cramarossa and C. Gorse, Chem. Phys. 111:361 (1987)
- /20/ G. Dilecce, M. Capitelli, S. De Benedictis and C. Gorse, Proc. of International Plasma Chemistry Symposium (Tokyo 1987)
- /21/ M. Capitelli, C. Gorse and G.D. Billing, Chem. Phys. 52:299 (1980)
- /22/ N. Chandra and A. Temkin, Phys. Rev. A13:188 (1976)
- /23/ G.D. Billing, Private Communication
- /24/ W. Huo, this volume
- /25/ A. Laganà, C. Ciccarelli, J. Phys. Chem., 92:932 (1988)
- /26/ C. Gorse, J. Bretagne, M. Bacal and M. Capitelli, Chem. Phys. 93:1 (1985)
- /27/ M. Bacal, this volume
- /28/ M. Cacciatore, M. Capitelli and M. Dillonardo, Chem. Phys. 34:193 (1978); M. Cacciatore and M. Capitelli, Chem. Phys. 55:67 (1981); M. Cacciatore, M. Capitelli and C. Gorse, J. Phys. D: Appl. Phys. 13:575 (1980)
- /29/ T.N. Rescigno and B.I. Schneider, UCRL-99210 (to be published on J. Phys. B)
- /30/ R. Celiberto et al., (to be published)
- /31/ J.R. Hiskes, J. Appl. Phys. 51:4592 (1980)
- /32/ J.N. Bardsley and J.M. Wadehra, Phys. Rev. A20:1398 (1979)
- /33/ C. Mundel, M. Berman and W. Domcke, Phys. Rev. A 32:181 (1985)
- /34/ M. Cacciatore, M. Capitelli and G.D. Billing, Chem. Phys. Lett. 157:305 (1989)
- /35/ A. Laganà, this volume
- /36/ A.M. Karo, J.R. Hiskes and R.J. Hardy J. Vac. Sci. Technol. A3:1229 (1985)
- /37/ M. Cacciatore, M. Capitelli and G.D. Billing, Surface Science 217:391 (1989)
- /38/ R.I. Hall, I. Cadez, M. Landau, F. Pichou and C. Schermann, Phys. Rev. Lett. 60:337 (1988); P.J. Eenshuistra, J.H.M. Bonnie, J. Los and H.J. Hopmann, Phys. Rev. Lett. 60:341 (1988); D.C. Robie, L.E. Jusinski, W.K. Bischel and W. Huo to be published (1989)
- /39/ J.R. Hiskes and A.M. Karo, this volume
- /40/ M. Capitelli, C. Gorse, R. Winkler and J. Wilhelm, Plasma Chem. Plasma Process. 8:175 (1988); 8:399 (1988)
- /41/ P. Belenguer and J.P. Boeuf, this volume

MODELING HIGH PRESSURE ELECTRIC DISCHARGES:

APPLICATIONS TO EXCIMER LASERS

Mark J. Kushner

University of Illinois
Department of Electrical and Computer Engineering
Gaseous Electronics Laboratory
607 E. Healey
Champaign, Illinois 61820
USA

ABSTRACT

Low temperature plasmas as used in electric discharge devices are often transient and not uniform. As a result the properties of these plasmas are not in equilibrium with the local electric field. The modeling of the devices using such plasmas is therefore problematic. In this chapter the modeling of electric discharges will be discussed with respect to methods which may be employed to describe their nonequilibrium nature, and to address their multidimensional nature. Applications to high pressure excimer lasers are discussed.

I. Introduction

Low temperature partially ionized plasmas are in the realm of "eV physics" as described by J. Waymouth.¹ "eV physics" refers to phenomena for which technologically relevant applications have been, and are now being, developed, and whose energy range is sub-nuclear (≤ 100 's keV). This range of energy includes fusion plasmas since their energies of interest are only 10's keV. The applications of fusion plasmas, though, are still being developed. Therefore "eV physics", at least with respect to plasmas, refers to what are classically described as "electric discharges". These are devices which are currently being used, or being developed, for commercial technology. The plasmas utilized in these devices typically have the following characteristics:

Ionization Fraction $10^{-6} - 10^{-1}$

Average Electron Energy $0.1 \text{ eV} - 20 \text{ eV}$

These characteristics are obtained with values of pressure, voltage, frequency, repetition rate, current density, and power deposition which span a fairly impressive parameter space (see Fig. 1). The ranges of operating conditions for commercially available electric discharge devices

span more than 10^7 Torr in pressure (10^{-4} Torr for magnetically assisted plasma processing reactors² to 10^4 Torr for excimer lasers³) and 10^{10} W-cm⁻³ in power deposition (10^{-3} W-cm⁻³ for plasma deposition reactors⁴ to 10^7 W-cm⁻³ for spark gap switches⁵). The parameter space for the frequency of excitation spans from single pulses and CW for lamps and lasers, to 10^9 s⁻¹ for electron cyclotron resonance (ECR) devices.⁶ The applied voltage for these devices span 10's V to 10's keV.

Another fairly large parameter space in which these devices operate is that which describes the complexity of their plasma chemistry in terms of neutral and ionic species, excited states, electron impact processes, and heavy particle reactions. Our degree of understanding of their operation also spans a fairly large parameter space. For example, it is ironic that the species list in the argon ion discharge laser contains only electrons, argon, argon excited species and argon ions, yet there is no predictive model for its performance. At the other extreme, gas mixtures for excimer lasers usually contain at least three feedstock species, (e.g., Ar/Kr/F₂) and generate as many as 30 additional species (e.g., Kr₂F, ArKr⁺) during excitation. More than 200 electron impact and heavy particle reactions have been identified in the plasma. In spite of this complexity, the performance of excimer lasers has been successfully described by models.⁷

In principal, one may construct a computational representation for an electric discharge device by "simply" solving the time and spatially dependent Boltzmann's equation for every species in the discharge, and couple those calculations to solutions of Maxwell's equations. This approach, though, becomes nearly intractable for even a single species. This computational representation would best be called a simulation. A simulation is a representation in which all of the processes and interaction potentials are known, and one simply integrates the equations of motion of the system. Given the complexity of gas discharge devices and the large parameter space in which they operate, it is clear that these devices cannot be directly simulated. They must instead be modeled. A model is a computational representation of a physical device in which certain simplifications have been made in order to make the problem tractable. The simplifications may take the form of using a lumped excited state to represent an entire manifold of states; or using time averaged quantities. The practice of modeling involves choosing and applying computational techniques and modeling approximations which are applicable to individual devices, and which retain the pertinent physics.

Of particular interest to modeling electric discharge devices is resolving time and spatially dependent phenomena. There are few devices beyond a simple positive column discharge which can be well represented by time and spatially averaged models. As new computers and computational techniques become available one is motivated to use those resources to model transient and multidimensional phenomena observed in gas discharge devices. In the spirit of modeling, as opposed to simulation, we must choose appropriate methods and make reasonable approximations to construct those representations.

In this chapter, we will discuss methods whereby transient and multidimensional phenomena in high pressure gas discharges as used in excimer lasers may be modeled. We will begin by briefly reviewing the physics of excimer lasers and low pressure plasma switches as a prelude to the discussion of modeling techniques.

II. A Brief Overview of High Pressure Gas Discharge Excimer Lasers

In this section, we will briefly review the physics of high pressure

discharges as pertains to selecting and developing models for their performance. Our model system will be excimer lasers, which operate at many atmospheres of pressure and 100's $\text{kW}\cdot\text{cm}^{-3}$ of power deposition.

Electric discharge excimer lasers provide highly efficient sources of pulsed coherent ultra-violet (UV) radiation.³ The term "excimer" has now come to refer to a class of excited molecules which are bound in their excited states, and repulsive or weakly bound ($D_0 \leq kT_g$) in their ground states. Laser transitions typically occur between the lowest excited states of these molecules and their ground states. These molecules thereby constitute nearly ideal laser media. Since their ground states are unstable inversions are readily obtained by pumping the upper level. Transitions to the ground state then dissociate the molecule. The fact that their ground states are not stable, though, means that excimer species cannot be feedstock gases and must be generated "real time" in the plasma. Excimer lasers are therefore accurately described as "plasma chemical" lasers.

A variety of excimer molecules have demonstrated laser action. The most successful in terms of efficiency, laser energy, and technological development are the rare gas halogen (RgH) excimers. Those RgH lasers most intensively developed are listed in Table I. The excited RgH excimer results from the ion pair consisting of the rare gas (Rg) positive ion, and the halogen (H) negative ion. (See Fig. 2). These excimer lasers typically operate between the bound B state of the ion pair and the repulsive (or weakly bound) X state. The B-X transitions have wavelengths ranging from 192 nm for ArF(B-X) to 351 nm for XeF(B-X). Visible wavelengths can be obtained by operating on the lower gain (C-A) transitions of the XeCl and XeF molecules.

Table I. Important RgH Lasers

RgH	Wavelength (nm)
ArF	192
KrF	248
XeCl	308
XeF	351

Electric discharge RgH excimer lasers are both research devices and are commercially available. A schematic of a typical discharge laser appears in Fig. 3.^{8,9,10} The electrode separation is a few to 10 cm with lengths of 10's cm to > 1 m. The gas pressure is 1-4 atm (see below). The discharge circuit consists of a pulse forming line

(PFL) with electrical lengths of 10's - 100's ns. The charging voltage of the PFL is 1-4 kv/cm-atm resulting in power deposition of 100's $\text{kW}\cdot\text{cm}^{-3}$ to a many $\text{MW}\cdot\text{cm}^{-3}$. The voltage is switched onto the laser head using a thyratron or low inductance rail-gap switch, causing breakdown and sustaining a discharge current of 100's $\text{A}\cdot\text{cm}^{-2}$. The impedance of the discharge is typically 0.1-0.5 Ω -meter based on a square aperture. Variants of the discharge circuit use saturable magnetic inductors¹¹ to aid in switching, or a separate "spiker" circuit to breakdown the gas,¹² thereby allowing better impedance matching between the PFL and the laser head. It is mandatory that the discharge volume be uniformly preionized to 10^7 - 10^8 cm^{-3} prior to applying high voltage. Preionization is accomplished using UV spark arrays,¹³ x-rays,^{14,15} and corona bars.¹⁶

Commercial excimer lasers are currently available delivering a few joules of pulse energy at repetition rates of 100's Hz, yielding as much as 500 W.¹⁷ The discharge apertures on these devices are a few cm, wallplug efficiencies are a few percent, and the laser pulse lengths are usually ≤ 30 ns. Higher pulse energies ($\leq 66 \text{ J}$),^{18,19} larger apertures ($\leq 20 \text{ cm}$),¹⁹ higher efficiencies ($\leq 4\%$),¹¹ and longer pulse lengths ($\leq 1.5 \mu\text{s}$)¹³ have been obtained with XeCl laboratory lasers, though not all on a single device.

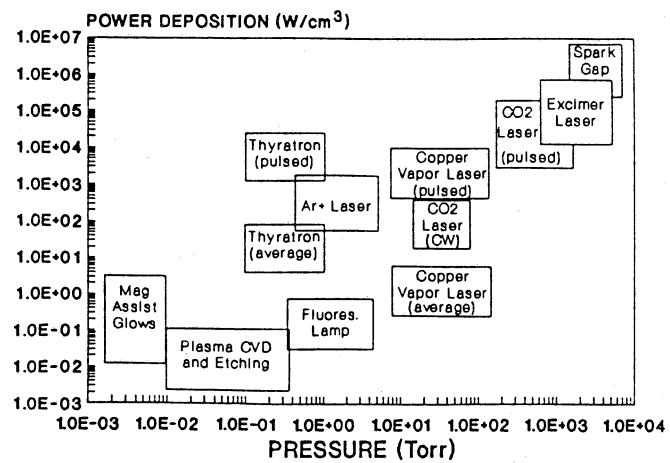


Fig. 1. Gas pressure-power deposition parameter space for various gas discharge devices.

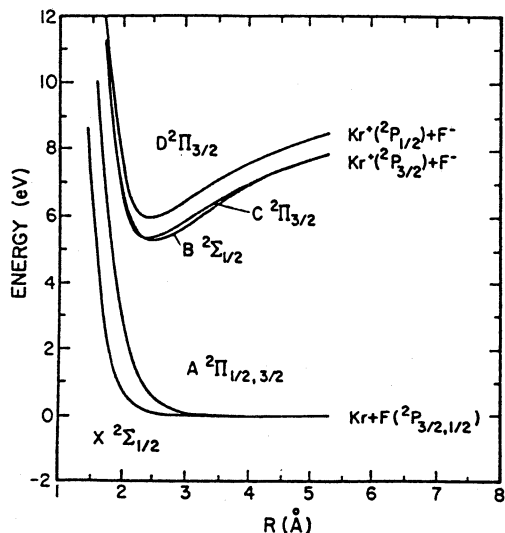


Fig. 2. Potential energy diagram for KrF (from Ref. 3).

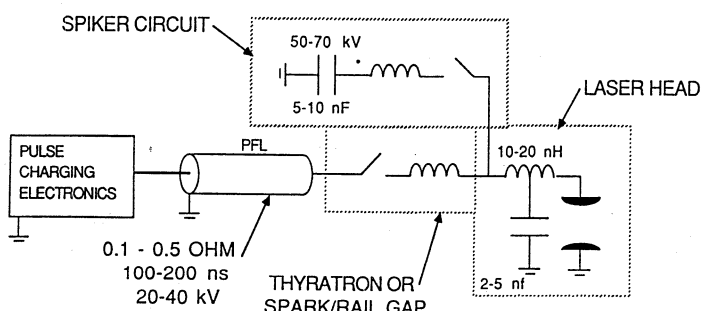
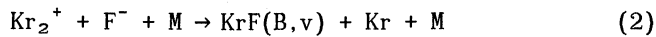
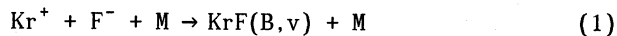
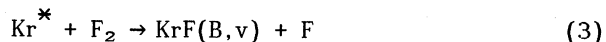


Fig. 3. Schematic of an electric discharge excimer laser showing Pulse Forming Line (PFL) and spiker circuit.

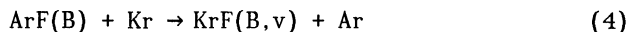
Excited states of the RgH exciplex are typically generated via an ion-ion neutralization process constituting the ion channel, or a harpooning reaction constituting the neutral channel. For purposes of discussion, we will use the KrF laser in Ar/Kr/F₂ and He/Kr/F₂ mixtures as a model system. The processes discussed for KrF are directly analogous to other RgH systems. For example, the KrF(B) molecule is formed through the ion channel by^{20,21}



where M is a stabilizing third body. The neutral channel consists dominantly of harpooning reactions, exemplified by²²

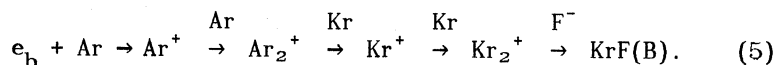


where Kr* represents Kr in an excited state. As argon is often used in the gas mixture for a KrF, additional excitation reactions such as



are possible, where the ArF exciplex was previously formed by reactions analogous to those shown above. These formation reactions are exothermic by a few to many eV, resulting in KrF(B,v) being formed high in the vibrational manifold. Lasing, though, occurs out of KrF(B,v=0). Therefore, collisional relaxation of the vibrational manifold must occur before lasing.²³

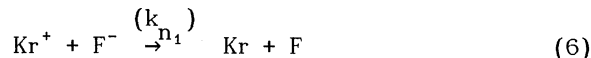
The formation efficiency (power channeled to the upper laser level compared to power deposited in the plasma) of KrF excimer lasers may be as high as 40%. This high efficiency results from the fact that with the exception of the repulsive A states of the F₂ molecule (which has a small mole fraction anyway) the upper laser level is energetically the lowest excited electronic state in the system. Therefore power deposited in the plasma will naturally channel by excitation transfer down to the upper laser level (see Fig. 4).²⁴ For example, suppose an Ar⁺ is produced by an electron impact collision. Dimerization rapidly follows, after which charge transfer produces Kr⁺. This reaction is followed by an ion-ion neutralization which produces the upper laser level;



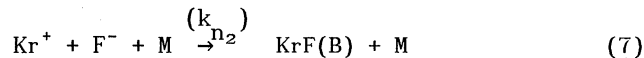
Gas mixtures for excimer lasers are usually tertiary containing a

lower atomic weight noble gas in addition to the rare gas and halogen for the excimer molecule. For example, in discharge excited KrF lasers a typical gas mixture is He/Kr/F₂ = 99.5/0.5/0.05. Although binary gas mixtures (eg., Kr/F₂) have been investigated, optimum performance is usually obtained with a tertiary mixture. The tertiary mixture is necessary due to the large momentum transfer cross section of the Rg which forms the exciplex. The cross sections for electron impact momentum transfer, σ_m , for Ar, Kr, and Xe exceed 10 Å² for energies in the range of 5-10 eV.²⁵ These values of σ_m would require excessively high operating and breakdown voltages for large aperture discharges (> a few cm). Therefore, the average σ_m of the mixture must be reduced by diluting with either He or Ne, both of which have lower momentum transfer cross sections compared to the heavier rare gases. In practice, avalanche discharge excimer lasers (pulse lengths \lesssim 20-30 ns) tend to use He as a buffer gas. Long pulse (\geq many 10's ns) discharge excimer lasers tend to use Ne as a buffer gas since its lower momentum transfer cross section at energies \leq 10 eV is advantageous.

The requirement that excimer lasers must operate at pressures exceeding an atmosphere results from the fact that the formation of the upper laser level through the ion channel requires a three body reaction in order for its rate to be competitive with other excitation or quenching processes. For example, the rate constant for ion-ion neutralization resulting in atomic products,



is $k_{n_1} \approx 10^{-7} - 10^{-6}$ cm³s⁻¹.²⁶ The ion-ion neutralization reaction resulting in formation of the exciplex dimer is a three body reaction,^{20,21}



In order for the exciplex forming reaction to effectively compete with the neutralization reaction, the density of the third body must be $[\text{M}] \gg k_{n_1}/k_{n_2}$. Although there is a complicated dependence of k_{n_2} on $[\text{M}]$, over the range of 0-3 atm, $k_{n_2} [\text{M}=\text{Ar}] \approx 3 \times 10^{-6}$ cm³s⁻¹atm⁻¹.²⁰ Therefore, the total gas pressure must exceed an atmosphere in order for the reaction which forms the exciplex to dominate.

Due to the efficiency with which deposited power is channeled to the upper laser level, the characteristics of laser operation are largely a function of local power deposition. Therefore the manner and uniformity of power deposition is often the greatest concern in constructing the device and optimizing laser performance.^{10,27-30} The uniformity of power deposition is largely determined by the distribution of the preionization density. Since near its optimum value laser efficiency is relatively insensitive to small changes in other parameters such as gas mixtures, power deposition is the only remaining parameter that may be optimized and which characterizes the laser. For example, in discharge excimer lasers, discharge instabilities limit power deposition and constrain laser performance as opposed to a limiting aspect of the kinetics. Therefore

modeling of transient and multidimensional phenomena in excimer lasers must emphasize issues pertaining to power deposition.

From past experience and simple scaling laws, one would recommend that excimer lasers be operated at low power deposition to enhance their discharge stability. The short radiative lifetime of the upper laser level, though, sets stringent requirements on pump rate and gas pressure. For example, the radiative lifetime of the upper laser level of RGH B-X excimers ranges from 6 ns for KrF to 15 ns for XeF.³ When also considering quenching processes, the total lifetime, τ_t , of the B state is 0.5 - 0.75 that of the radiative value. The short lifetimes of these molecules sets a requirement on the rate of pumping of the medium. For example, for power deposition P (W-cm⁻³) and formation efficiency, η_f , the unsaturated density of the upper laser level is $N_u = \eta_f P \tau_t / h\nu$, where $h\nu$ is the laser photon energy. To obtain a specific small signal gain, g_0 (cm⁻¹), the power deposition must be

$$P \approx \frac{g_0 h\nu}{\sigma_e \eta_f \tau_t} \quad (8)$$

where σ_e is the optical stimulated emission cross section. Since the excimer transition is essentially bound-free, the optical emission cross section tends to be small compared to that for atomic bound-bound transitions. For example, the optical stimulated emission cross section for KrF is 2.6×10^{-16} cm².³ Therefore with a formation efficiency of 25%, and total lifetime of 5 ns, the power deposition in a KrF laser must be 250 kW-cm⁻³ to obtain a small signal gain of 0.1 cm⁻¹. With this rate of power deposition the system must be operated pulsed. This requirement is dictated by the pulsed power electrical circuitry and gas heating. The rate of gas heating for this power deposition is 5×10^8 K-atm/s. Therefore to prevent excessive heating (less than 100's K) the laser must be operated with short pulses ($< 1 \mu s$) and with gas pressures exceeding 1 atm.

The fact that high power deposition is required sets further limits on the gas pressure. Power deposition in an electric discharge is given by $P = j_d E_s$, where j_d is the discharge current density and E_s is the self sustaining electric field. The self sustaining electric field is determined almost entirely by the gas mixture. It is that value where

$$\sum_j f_j k_{I_j} = \sum_j f_j k_{a_j} \quad (9)$$

where f_j is the mole fraction of component j, k_{I_j} is its ionization rate coefficient, and k_{a_j} is its attachment rate coefficient. For typical lasers $E_s/N \approx 2-5$ Td (1 Td = 1×10^{-17} V-cm²),^{9,11} or $E_s/p \approx 0.4-1.0$ kV/cm-atm. The current density is $j_d = E_s n_e e^2 / (m_e v_m)$ and in typical gas mixtures $v_m = 2 \times 10^{12} \cdot p(\text{atm}) \text{ s}^{-1}$. These values result in $j_d \approx 3.5 \times 10^3 \cdot E_s (\text{kV/cm-atm}) \cdot p(\text{atm}) \cdot f \text{ kA-cm}^{-2}$ where f is the fractional ionization. Power deposition in an excimer laser discharge is therefore

$$P(\text{kW}\cdot\text{cm}^{-3}) \approx 3.5 \times 10^6 \cdot E_s^2 (\text{kv/cm}\cdot\text{atm}) \cdot p^2 (\text{atm}) \cdot f. \quad (10)$$

Since discharges lasers typically operate with fractional ionization of 10^{-5} , to obtain power depositions of 100's $\text{kW}\cdot\text{cm}^{-3}$ the gas pressure must be at least a few atmospheres.

III. Useful Approximations in Modeling High Pressure, Low Temperature Plasma Devices

Modeling kinetic processes in plasma devices from first principals requires solution of Boltzmann's equation, or the transport equation equivalents, for each species in the plasma. When considering spatial and temporal phenomena, the complexity of this approach rapidly exceeds the rate of return on the investment in development and computer resources. The time and spatial scales of interest, though, may allow that approximations to these fundamental equations can be made while still retaining the essential physics. This is particularly true with excimer lasers where gas pressures are high ($> 1 \text{ atm}$), pulse lengths are short ($\leq 1 \mu\text{s}$), and spatial scales are usually large ($\geq 1 \text{ cm}$). The fact that laser performance is dominated by the specifics of power deposition enable implementation of some of these approximations. Under these conditions, the local field approximation and stationary kinetics approximations may be made. In this section, we will review useful approximations which may be employed in modeling gas discharges while retaining the pertinent physics.

A. The Local Field Approximation

Obtaining the correct form of the electron energy distribution (EED), $f(\epsilon)$, is essential in obtaining accurate values of electron impact rate coefficients, k_i (cm^3s^{-1}). The coefficient for process i is obtained from

$$k_i = \int_0^\infty \sigma_i(\epsilon) \left(\frac{2\epsilon}{m_e}\right)^{1/2} f(\epsilon) \epsilon^{1/2} d\epsilon \quad (11)$$

where σ_i is the electron impact cross section for that process and $f(\epsilon)$ has units $\text{eV}^{-3/2}$. The electron distribution function is obtained from solution of Boltzmann's equation for electrons

$$\frac{\partial f}{\partial t} = - \vec{v} \cdot \nabla_x f + \frac{e\vec{E}}{m_e} \cdot \nabla_v f + \left(\frac{\partial f}{\partial t} \right)_c, \quad (12)$$

where \vec{v} is the electron velocity and \vec{E} is the local electric field. The terms on the right side represent the changes in $f(\epsilon)$ due to the divergence of f in coordinate space, the divergence in velocity space, and collisions. Methods whereby Boltzmann's equation is solved to obtain $f(\epsilon)$ are the subject of many previous works.³¹ Obtaining a spatially and time dependent solution to Boltzmann's equation using these methods may be computationally too intensive to be included in plasma kinetics models of electric discharge devices. We therefore seek methods whereby the calculation can be simplified.

If we assume that the density of collision partners appearing in the collision integral is uniform and time invariant, the time and spatial dependence of $f(\epsilon, \vec{r}, t)$ is determined solely by the time and spatial dependence of $\vec{E}(\vec{r}, t)$. Let us define $v_E(s^{-1})$ as the smaller of the frequency at which electrons relax in energy or momentum to their values which are in equilibrium with a time invariant local electric field, and λ (cm) as the drift distance over which electrons come into equilibrium. If

$$v_E \gg \frac{1}{E} \frac{dE}{dt}, \text{ and } 1/\lambda \gg \frac{1}{E} \frac{dE}{dx} \quad (13)$$

then $f(\epsilon, \vec{r}, t)$ depends only on the local instantaneous value of the electric field, since $f(\epsilon)$ comes into equilibrium with E at a rate which is fast compared to either the time or spatial frequency of E . In this case, one can characterize the local electron distribution by the instantaneous and local value of the electric field. This approximation is known as the Local Field Approximation (LFA). Using the LFA, Boltzmann's equation simplifies to

$$-\frac{e\vec{E}}{m_e} \cdot \nabla_v f = (\frac{\partial f}{\partial t})_c. \quad (14)$$

The energy relaxation time, $\Delta t_E = 1/v_E$, and energy relaxation distance for electrons in argon and N_2 are shown in Fig. 5. These values were obtained by imposing a step function in E/N on a thermal electron distribution and observing the time required for the distribution to come into equilibrium with the new field. The energy relaxation distance is approximated by

$\Delta t_E \cdot \bar{v}_d$, where \bar{v}_d is the average drift velocity during the transient. For high pressure discharges ($p \gtrsim 1$ atm) and typical E/N ($2-20 \times 10^{-17}$ v-cm 2), $10^{-10} \lesssim \Delta t_E \lesssim 10^{-8}$ and $1 \mu\text{m} \lesssim \lambda \lesssim 20 \mu\text{m}$. Therefore the LFA is valid for most spatial scales of interest, and for voltage rise times $\gtrsim 10$ ns.

The appropriate application of the LFA greatly simplifies construction of time and spatially dependent models of gas discharge devices. To construct such models, one need only parameterize Boltzmann's equation as a function of E/N and other pertinent parameters (e.g., gas mixture, ionization fraction) and record the resulting rate constants and transport coefficients in a look-up table. During execution of the model, rate constants are obtained from the table by interpolating the entries based on the instantaneous values of E/N and other parametric variables.

B. Approximations Relating to Heavy Particle Transport

Local variations in the total gas number density impacts the electron and heavy particle kinetics most dramatically through changes in the local E/N . Electron impact rate coefficients for processes which have a threshold energy (e.g., electronic excitation and ionization) are sensitive functions of E/N , and often change by orders of magnitude for fractional changes in E/N (see Fig. 6).

Just as Boltzmann's equation governs the energy and spatial distribution of electrons, Boltzmann's equation is also valid for gas

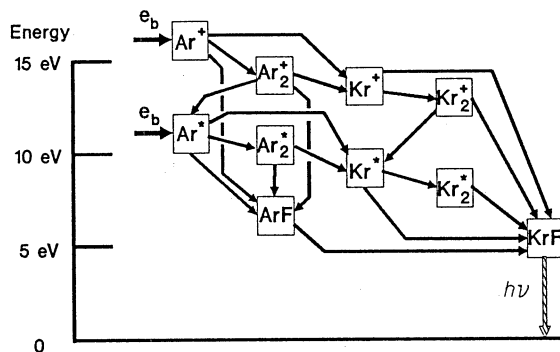


Fig. 4
Energy flow leading to excitation of $\text{KrF}(\text{B})$ in an $\text{Ar}/\text{Kr}/\text{F}_2$ mixture.

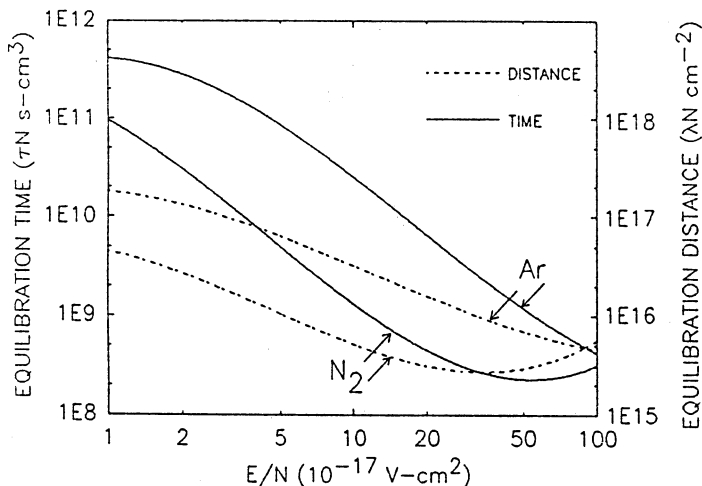


Fig. 5. Equilibration time and distance (normalized by gas density $N \text{ cm}^{-3}$) required for the electron energy distribution to come into equilibrium with the applied electric field.

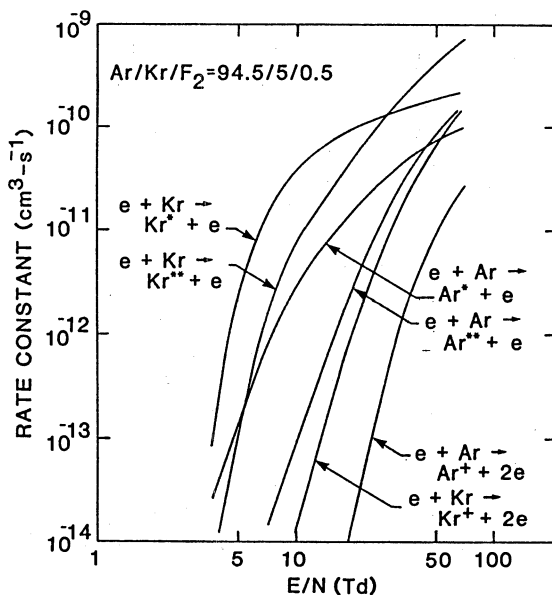


Fig. 6
Electron impact rate constants for excitation and ionization of ground state species in an $\text{Ar}/\text{Kr}/\text{F}_2$ mixture.

atoms and molecules. Since, however, the details of the velocity distribution for atoms is not particularly important for our purposes the local density of heavy particles which "appears" in E/N are well represented by continuity, momentum, and energy conservation equations.³² For our purposes, these equations may be approximated as

$$\frac{\partial N}{\partial t} = -\nabla \cdot \vec{v}N + \nabla \cdot D\nabla N \quad (15)$$

$$\frac{\partial(\rho\vec{v})}{\partial t} = -\nabla p - \nabla \cdot \vec{v}(\rho\vec{v}) - \vec{u}\vec{v} \quad (16)$$

$$\frac{\partial(c_v kT_g)}{\partial t} = \vec{j} \cdot \vec{E} - \nabla \cdot \vec{v}(c_v kT_g) + \nabla \cdot \kappa \nabla T_g - \sum_i f_i \Delta H_i N \quad (17)$$

where N is the total gas number density, \vec{v} is the convective velocity, D is the gas diffusion coefficient, ρ is total gas mass density, p is the thermodynamic pressure, and u is an effective viscous damping term. c_v is the specific heat of the gas mixture, $j \cdot E$ is the local joule heating, κ is the thermal conductivity, f_i is the mole fraction of species i , and ΔH_i is the heat of formation of that species. In writing Eqs. 16 and 17, we have assumed that there is no slippage between species so that all heavy particles have the same convective velocity, and that the local thermal conductivity is high so that all neutral species may be described by the same temperature. We have also assumed that there are no shear viscous forces so that the viscosity is isotropic. With little loss of generality we can assume ideal gas behavior and write $p = NkT_g$ (T_g is the gas temperature), $c_v = \frac{1}{\gamma - 1} \cdot Nk$ and $\gamma = \frac{f + 2}{f}$ where f is the number of degrees of freedom, so that $c_v kT_g = \frac{f}{2} NkT_g$. Also For purposes of discussion, we will assume a monoatomic gas having $f = 3$.³³

It is instructive to examine the time scale for which changes in gas density may occur because it is over this time scale that one must account for changes in E/N and its impact on $f(\epsilon)$ and electron impact rate coefficients. For purposes of examining these time scales we will simplify the energy equation to

$$\frac{\partial T_g}{\partial t} \approx \frac{1}{(3/2)Nk} \left(jE - \frac{\kappa T_g}{\ell^2} \right) \quad (18)$$

where ℓ is the characteristic distance for variation in power deposition. It is this difference in power deposition which generates the pressure gradient which drives the convective velocity. Using transport coefficients for argon ($\kappa \approx 0.02 \text{ J}/(\text{cm-s-K})$)³⁴ the time rate of change in gas temperature is

$$\frac{\partial T_g}{\partial t} (\text{K-s}^{-1}) \approx 2000 \frac{P (\text{W-cm}^{-3})}{p (\text{atm})} - \frac{40}{\ell^2 (\text{cm})} \cdot T_g (\text{K}) \quad (19)$$

where P if the specific power deposition and p is the total gas pressure. The first term is for joule heating and the second term is for thermal conduction. We see that thermal conduction in pulsed plasmas is unimportant for power deposition in excess of 10^3 W-cm^{-3} -atm if the

spatial variation in power deposition is $\gtrsim 1$ cm. In the analysis of excimer lasers, where $P > 10^3$ kW \cdot cm $^{-3}$, $p = 1\text{--}4$ atm and the pumping duration is 100's ns to a few μ s, thermal conduction may be ignored for $\ell \gtrsim 1$ cm. For these conditions the gas temperature will not come into equilibration with conduction and the gas temperature will monotonically increase during the pulse. In plasma etching reactors where $P \approx 10^{-3}$ - 10^{-2} W \cdot cm $^{-3}$, $p \approx 10^{-3}$ atm, and residence times are 10^{-2} - 1 s, the term for thermal conductivity is commensurate with that for joule heating. Heat transfer out of the medium by conduction must therefore be included in the analysis.

To examine the necessity to include gas motion in the analysis, we first limit ourselves to pulsed devices with high power deposition. For these conditions the convective velocity and gas densities can be approximated as

$$v(\text{cm}\cdot\text{s}^{-1}) \approx \frac{NkT}{\rho\ell} \cdot \Delta t \approx \frac{0.004 \Delta t^2 (\mu\text{s}^2)}{\ell(\text{cm})} \cdot \frac{P (\text{W}\cdot\text{cm}^{-3})}{p (\text{atm})} \quad (20)$$

$$\left| \frac{1}{N} \frac{\partial N}{\partial t} \right| \approx \frac{v}{\ell} + \frac{D}{\ell^2} \quad (21)$$

where we have used values for Ar. For typical excimer lasers, ($P \approx 200$ kW \cdot cm $^{-3}$, $p = 4$ atm, $\ell \gtrsim 1$ cm), the convective velocity is less than $1\text{--}3$ m \cdot s $^{-1}$ at the end of a 1 μ s pulse, and therefore can be ignored during the pulse length. For pulse lengths in excess of many μ s, or for spatial scales considerably less than 1 cm, the convective motion of the gas must be considered. Ignoring the convective velocity, the continuity equation for heavy particles reduces to the diffusion term

$$\left| \frac{1}{N} \frac{\partial N}{\partial t} \right| (\text{s}^{-1}) \approx \frac{D}{\ell^2} \approx \frac{0.18}{\ell^2 (\text{cm}) \cdot p(\text{atm})}. \quad (22)$$

where for argon, $D \approx 0.18$ cm $^2\text{-s}^{-1}\text{-atm}$.³⁴ During the pulse lengths of typical excimer lasers, diffusion may also be ignored provided that $p \gtrsim 0.1$ atm and $\ell \gtrsim$ mm's.

It appears, then, that for high pressure ($p > 100$'s Torr) pulsed discharges having pulse lengths less than a few μ s and having power deposition uniform on scale lengths of $\gtrsim 1\text{--}10$ mm the gas remains motionless during the discharge. With this approximation, the gas phase chemical kinetics may be considered on only a local basis with no convective or diffusional coupling to adjacent plasma segments. (Coupling does, though, occur indirectly through photon transport and the electric field.). This is an extremely important approximation because all spatially dependent phenomena then result strictly from differences in local power deposition. We call these conditions the Stationary Kinetics Approximation (SKA).

In high pressure, pulsed lasers departures from the SKA approximation occur dominantly because the spatial scale, ℓ , is significantly less than 1 cm. This condition may result from non-uniformities in preionization density, in E/N caused by imperfections in the electrodes, or by instabilities in the plasma-cathode fall boundary. Some of these issues will be discussed below. In low pressure quasi-cw discharges, the gas

temperature may come into equilibrium with the power deposition by the balance between joule heating and thermal conduction. Therefore the local gas density is well represented by ideal gas considerations. Although convective velocities may be ignored under these conditions differences in local power deposition may lead to gradients in the densities of excited states for which diffusion must be considered.

C. Local Power Deposition: Gas Discharges as Circuit Elements

In cases where the local field approximation (LFA) and stationary kinetics approximation (SKA) may be used, the modeling of transient and multidimensional phenomena in gas discharges greatly simplifies. By using these approximations, one may build a multidimension model by constructing obtrusively "independent" sets of coupled rate equations (ordinary differential equations) for the species of interest, one set for each computational mesh point, and integrate them simultaneously in time. Each mesh point, though, is not actually independent of its neighbor. Their dependence results from the response of their local electric fields to the conductivity of their neighbor as required by current continuity. This dependence is given by

$$\nabla \cdot \vec{j} = \nabla \cdot \sigma \vec{E} = - \frac{\partial \rho}{\partial t} \quad (23)$$

where j is the current density, σ is the local plasma conductivity, E is the electric field, and ρ is the local charge density

To illustrate this dependence, consider a cylindrical electric discharge having radius r and length L , assume that $L \gg r$ so that the discharge may be approximated as being 1-dimensional as shown in Fig. 7a. Conceptually, the discharge is sustained by a simple electrical circuit, consisting of a voltage source V_0 , ballast resistor R_b , and series inductance L . The dimension of interest is parallel to the applied electric field. To represent the discharge, we partition it into n segments, each having length ℓ_i . The electrical resistance of each segment is then $R_i = \sigma_i \ell_i / A_i$, where σ_i and A_i are the plasma conductivity and cross sectional area of the segment. In this 1-dimensional construction, the discharge may be represented as a resistive element in the discharge circuit. This element consists of an array of resistors in series, whose total resistance is $R_d = \sum_{i=1}^n R_i$. The dc current through the circuit is then $I = V_0 / (R_b + R_d)$. The local current density in each segment is then $j_i = I / A_i$, and the local electric field in each plasma segment is $E_i = j_i / \sigma_i$ or in the dc case $E_i = R_i V_0 / (\ell_i (R_b + R_d))$. These values simply result from a 1-dimensional solution of Eq. 23 where $\partial \rho / \partial t = 0$. Given these values of the electric field, one then obtains the pertinent electron impact rate coefficients by applying the LFA, and then obtains local species densities by integrating their local rate equations.

An analogous process can be used to represent the discharge in the dimension perpendicular to the electric field (see Fig. 7b). We again simply consider the discharge to be a resistive element in the electrical circuit. In this case, though, the discharge element consists of an array

of parallel resistors, each in turn consisting of a segment of plasma with length ℓ_i and cross sectional area A_i as before. The resistance of the

discharge is now $R_d = 1/(\sum_{i=1}^n 1/R_i)$. In this case though, the voltage drop across each segment is the same, which in the dc case is $V_d = R_d/(R_b + R_d)$. The local electric field in each segment for use in the LFA is then $E_i = V_d/\ell_i$.

These simple 1-dimensional representations of discharge devices are very useful for illuminating the basics of discharge stability when the LFA and SKA are valid. We will discuss some of these stability issues below. The resistor analogy for these discharge devices are, in fact, exact representations of their behavior when quasi-neutrality (i.e., $\frac{\partial \rho}{\partial t} = 0$) holds and when skin depth effects are not important. One would like to extend this simple method of resolving dimensional phenomena in discharge devices to more than 1 dimension. The methodology of viewing each segment of the plasma as having a well defined conductivity and local electric field is still valid. The discrete resistor analogy, though, breaks down due to there being ill-defined current paths in a multi-dimensional array of discrete resistors. Under these conditions, one must revert to a direct solution of Eq. 23 to obtain the electric potential and, by differentiation, the local electric field. Invoking quasi-neutrality, one must then solve a modified Laplaces Equation³⁵

$$\nabla \cdot \vec{j} = \nabla \cdot \sigma \vec{E} = - \nabla \cdot \sigma \nabla \phi = 0, \quad (24)$$

$$\nabla^2 \phi = \frac{\nabla \sigma \cdot \nabla \phi}{\sigma} \quad (25)$$

This equation may be solved using a variety of methods. For rectilinear or cylindrical meshes, the method of successive-over-relaxation (SOR) is particular useful.³⁶

The purpose of the discussion above is to motivate the reader to view discharges for which the LFA and SKA apply as devices whose local properties depend on local power deposition and total energy loading. At the same time the magnitude of local power deposition may depend on the local value of conductivity as compared to the rest of the discharge volume. Excimer lasers are particularly good candidates for the "resistor" analogy since for pulse lengths less than many microseconds and scale lengths $>$ mm's, the LFA and SKA are excellent approximations.

D. Departures from the Resistor Analogy

The resistor analogy entails solving of Eq. 23 while invoking charge neutrality ($\dot{\rho} = 0$) to obtain the local electric field. The validity of the resistor analogy and the LFA do not depend on the other being valid. In high pressure discharges, it is most often the resistor analogy which breaks down while the LFA remains valid. Departures from the resistor analogy are most often caused by introduction of space charge ($\dot{\rho} = 0$) when using an injected e-beam, or when skin depth effects are important.

The skin depth is the characteristic distance over which the electric field penetrates into a conductor during a transient.³⁷ The time and spatially dependent electric field for the conditions of interest (i.e., $\nabla \cdot \vec{E} = 0$, $\frac{\partial(\epsilon_0 E)}{\partial t} \ll \sigma E$) may be obtained from solving the a diffusion-like equation

$$\frac{\partial(\sigma E)}{\partial t} = - \frac{1}{\mu_0} \nabla^2 E \quad (26)$$

For penetration of a sinusoidal electric field into a plane conductor, the skin depth, or characteristic penetration distance, is $\delta = 1/(\pi v \sigma \mu_0)^{1/2}$, where v is the oscillation frequency (s^{-1}) and μ_0 is the magnetic permeability. Highly conductive plasmas have short penetration distances. The conductivity of excimer lasers may be approximated by $4000 \cdot f$ ($\Omega^{-1} \text{cm}^{-1}$), where f is the fractional ionization, and the equivalent frequency for a rapidly rising current pulse is $v \approx 5 \times 10^6$. This yields a skin depth of $\delta = 0.04/f^{1/2}$ cm. For typical fractional ionizations ($f \approx 10^{-6} - 10^{-5}$), $\delta \approx 20$ cm. Therefore, the resistor analogy is invalid for excimer laser discharges which have characteristic dimensions of greater than 10's of cm¹⁷ and skin depth effects are observed in excimer lasers of those dimensions.¹⁹ Under these conditions Eq. 23 may not be used to obtain the electric field and the electric field from must be obtained from Eq. 26, or its equivalent.

E. Departures from the Local Field Approximation

When the Local Field Approximation is not valid, then the electron energy distribution, and hence electron transport coefficients, cannot be characterized by the instantaneous local electric field. The failure of the LFA may result from non-equilibrium in either the space or time domain, or both. For example, in the cathode fall of a quasi-cw discharge, non-equilibrium results from fact that the mean free path for energy equilibration is larger than the distance over which the electric field changes. Steady state conditions may be obtained without there being local equilibration with the electric field.

Departures from the LFA require that the non-equilibrium nature of the electron distribution function in space or time must be considered in calculating the electron impact rate coefficients. Although in principal one may directly solve the multidimensional, time dependent Boltzmann's equation this approach is impractical. As a result, there are currently few methods whereby a time and spatially dependent electron impact rate coefficients may be obtained which account for the non-equilibrium nature of the electron energy distribution. Use of Monte Carlo particle simulations is one such method. In using this method, the Monte Carlo simulation is typically used to generate electron impact rate coefficients which are used in the continuity equation for electrons and heavy particles. This method is best described as a particle-continuum hybrid.³⁸ By its nature, the coupling between the two methods is complex and time consuming. One is therefore motivated to find methods whereby the non-equilibrium nature can be directly included in the model in the same manner as the LFA.

One such method is to characterize electron impact rate coefficients

by the local average electron energy, $\bar{\epsilon}$, instead of the local E/N, and allow $\bar{\epsilon}$ to be dependent on electron transport. This is accomplished by using an electron energy equation which accounts for local electron heating and energy dissipation, while including contributions to the local electron energy due to electron transport.³⁹ The transport term consists principally of directed drift velocities. For example, ignoring diffusion, $\bar{\epsilon}$ may be represented by

$$\frac{\partial(n_e \bar{\epsilon})}{\partial t} = \sigma_e E^2 - \sum_i \Delta\epsilon_i n_e k_i(\bar{\epsilon}) N - \nabla \cdot (\vec{v}_d n_e \bar{\epsilon} - \frac{2}{3} \kappa v T_e) \quad (27)$$

where the electron temperature is defined as $\bar{\epsilon} = \frac{3}{2} k T_e$, n_e is the local electron density, σ_e is the electron conductivity, and $\Delta\epsilon_i$ is the energy loss due to collisions with heavy particles having rate constant k_i , which in turn depends on the local average electron energy. The transport terms include contributions from convection with drift velocity $\vec{v}_d = \mu_e \vec{E}$, and conduction having thermal conductivity κ . Including only the first two terms of Eq. 27 are equivalent to the LFA. The addition of the transport terms result in $\bar{\epsilon}$ not necessarily being a function of only the local value of E/N.

One then must specify the $k_i(\bar{\epsilon})$ which requires a direct relationship between $\bar{\epsilon}$ and the electron energy distribution. From a practical standpoint, this is usually accomplished by parameterizing the k_i as a function of E/N, in the same manner as for the LFA, while recording $\bar{\epsilon}(E/N)$. The independent variable for k_i in the model, usually E/N, is then replaced by $\bar{\epsilon}$. This practice is valid providing there is a unique relationship between E/N and $\bar{\epsilon}$, which is not the case in many Ramsauer gases.

IV. Modeling Spatial Phenomenon in High Pressure Gas Discharge Excimer Lasers

In this section we will discuss the origin of spatial phenomenon in high pressure gas discharges using excimer lasers as an example. The discussion considers two cases; large scale nonuniformities (mm's to cm) when the Stationary Kinetics Approximation is valid, and small scale nonuniformities (\ll mm's) when the SKA is not valid.

A. Operating Point Instability in Excimer Lasers

Under quasi-steady state conditions, the local self sustaining electric field in a discharge laser is determined by a balance between ionization and electron loss. The electron loss is by diffusion, recombination, or attachment. In most electric discharge excimer lasers, electron loss is dominated by attachment and ionization is dominated by electron impact of ground state species. (With high power loading

multistep ionization from excited states will also make a significant contribution. For purposes of discussion we will ignore those processes.) For these conditions, the quasi-steady state local operating point of the discharge, that is the local value of E/N at which the discharge is self sustaining, is obtained from solution of Eq. 9. The operating point of the discharge is therefore at the intersection of the mole fraction weighted values of the ionization and attachment coefficients, \bar{k}_I and \bar{k}_a in Fig. 8.

The mole fraction weighted rate coefficients for ionization and attachment are functions of halogen density, excited state density, and electron density in addition to being functions of E/N. Therefore the operating point in a discharge may vary as a function of position as these parameters vary as a function of position. The operating point instability (OPI) occurs when the operating point of the discharge is different as a function of position while the discharge cannot operate at all of those points simultaneously.

The OPI is most important when discharge conditions vary transversely to the applied field and the device can be well represented by a network of parallel resistors. When the SKA is valid and the electrodes are plane parallel, the E/N is the same for each plasma segment. If, for example, the halogen density varies as a function of position then it is not possible to be at the operating point of every spatial position in the discharge simultaneously. Since the operating point E/N will be highest where the halogen density is largest then there will be an ionization excess at locations where the halogen density is lower. That occurs when $\bar{k}_I(E/N) > k_a(E/N) \cdot f$. The electron density thereby increases in those plasma segments. If the halogen donor is consumed by the attachment process (e.g., $e + F_2 \rightarrow F^- + F$) and not replenished during the discharge pulse, then the rate of burnup of the halogen also increases, leading to a higher electron density, and further burnup. The process is unstable and will eventually lead to arcing. (See Fig. 8.)

If we assume that the initial halogen fraction, and electric field are uniform, then the onset of an OPI must result from non-uniform halogen burnup. For these conditions, non-uniform halogen burnup can only result from non-uniform preionization. The local fractional loss of the halogen donor is, to first order, given by

$$\Delta f(x, t) = \int_0^t n_e(x, t') k_a(x, t') dt' \\ = n_{eo}(x) \cdot N \cdot \int_0^t \left[\int_0^{t'} k_I(x, t'') dt'' \right] k_a(x, t') \cdot dt' \quad (28)$$

where $n_{eo}(x)$ is the preionization electron density. Therefore, non-uniformities in the preionization density lead to differences in the local halogen density, which eventually leads to the OPI. The "imprint" of the preionization density may result in arcing many 100's ns after breakdown.⁴⁰

The OPI results from non-uniformities in the direction transverse to the electric field. The discharge is stable against the OPI in directions parallel to the electric field. Again, invoking the resistor analogy, the voltage drop across each individual plasma segment may be different and is determined only by the requirements of current continuity. If halogen burnup is for some reason larger in one particular segment, then the

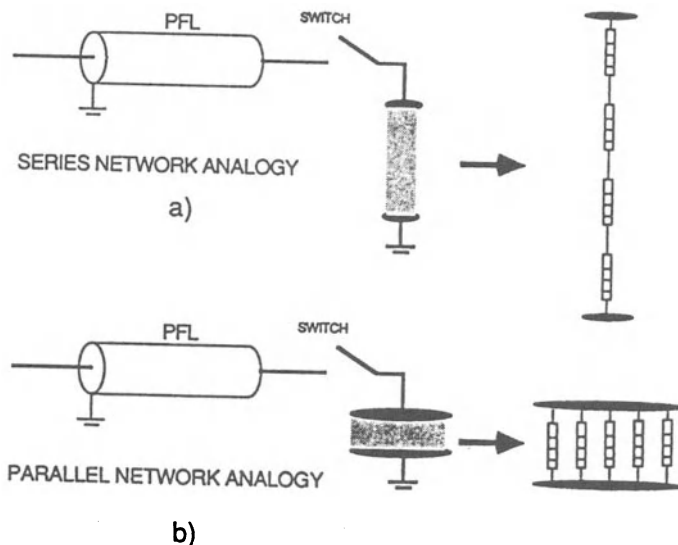


Fig. 7. Schematics showing resistor analogy for gas discharges used to resolve spatial phenomena. a) Series analogy for longitudinal effects; b) Parallel analogy for transverse effects.

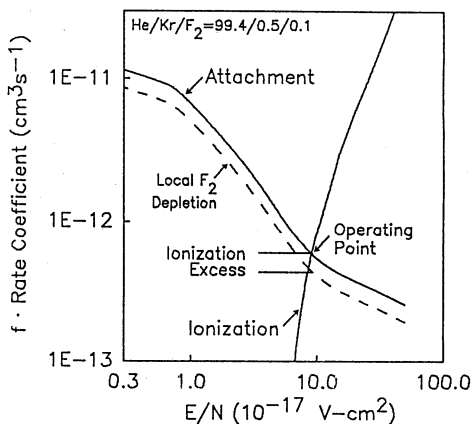


Fig. 8

Mole fraction weighted electron electron impact rate coefficients for ionization and attachment in a He/Kr/F₂ mixture. The operating point is at the intersection. An ionization excess results from F₂ depletion.

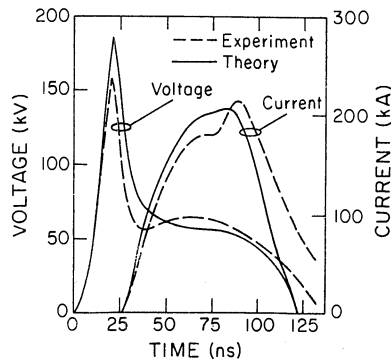


Fig. 9

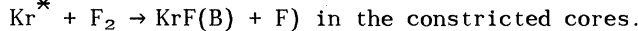
Theoretical and experimental (Ref. 9) current and voltage waveforms of a large aperture KrF(B → X) laser.

conductivity increases and E/N decreases until the new operating point is reached.

To demonstrate the effect of the OPI on the performance of a high pressure device, an electric discharge KrF(B-X) laser has been modeled. This model includes rate equations for the heavy particle and electron collisions, and includes models for the external electrical circuitry and laser extraction. The model is a time dependent, two dimensional representation using the LFA and SKA and is based on these models described in Refs. 11, 35, 40 and 41. The local electric field is obtained by solving the modified Poisson equation, Eq. 24, as described in Section III.C. The experimental conditions for this demonstration are those of Watanabe and Endoh.⁹ The device uses a He/Kr/F₂ = 99.47/0.44/0.09 gas mixture at 4.5 atm. The discharge active volume is 7 x 7 x 80 cm³. An intrinsic laser energy efficiency of 1.2% was obtained with an output energy of 10 J. A comparison of experimental and theoretical waveforms are show in Fig. 9. The predicted laser efficiency is 1.4%.

The OPI results from a non-uniformity in electric field, preionization electron density or gas mixture which results in preferential halogen burnup. The most common source is non-uniformities in preionization electron density. To demonstrate this effect, we have varied the preionization density profile in the discharge KrF laser, as shown in Fig. 10. The spatial dimension in the figure is parallel to the electrodes and perpendicular to the optical axis. Power deposition as a function of time and position between the electrodes is shown in Fig. 11 for these initial conditions. In all cases, power deposition at the leading edge of the discharge pulse is fairly uniform as a function of position and no worse than in the ratio of the preionization density. At these early times, the F₂ has not been significantly depleted so that all spatial locations have the same E/N operating point. As F₂ begins to become depleted, more rapidly near the axis where the preionization density is the highest, the stable operating point at those locations decreases to a value smaller than the average E/N thereby creating an ionization excess. An electron avalanche is then initiated, resulting in more rapid depletion of F₂, and causing constriction of the discharge.

The electron and F₂ density as a function of position at 150 ns for the conditions of Fig. 11 are shown in Fig. 12. Even though the local F₂ depletion and power deposition are strong functions of position, the total power deposition in the discharge is nearly the same for these cases, as shown in Fig. 13a. The constrictions resulting from non-uniform power deposition, on these spatial scales, are therefore not accurately described as arcs. The total laser power, though, is a sensitive function of the spatial distribution of power distribution, as shown in Fig. 13b. The more constricted cases result in lower total laser power. The decrease in laser power is due to a higher rate of electron collision quenching of KrF(B) and a reduction in the efficiency of the harpooning reaction (i.e.,



B. Small Spatial Scale Non-Uniformities

The validity of the Stationary Kinetics Approximation (SKA) in modeling high pressure pulsed gas discharges depends upon the spatial scale of any non-uniformity in electric field, preionization electron density, or gas mole fractions; and the duration of the discharge pulse.

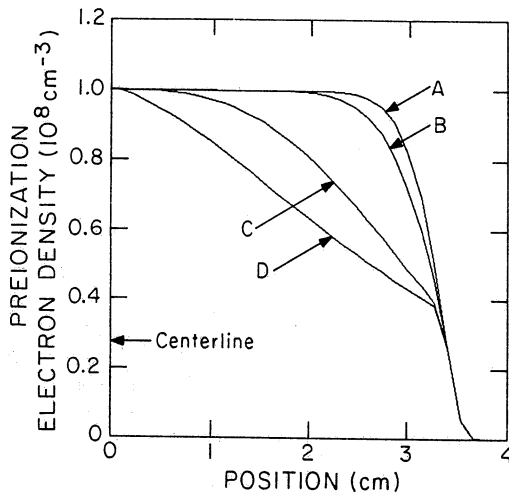


Fig. 10

Preionization electron density profiles for our parametric study. The discharge is symmetric across the center line. The dimension shown is parallel to the electrodes and perpendicular to the optical axis.

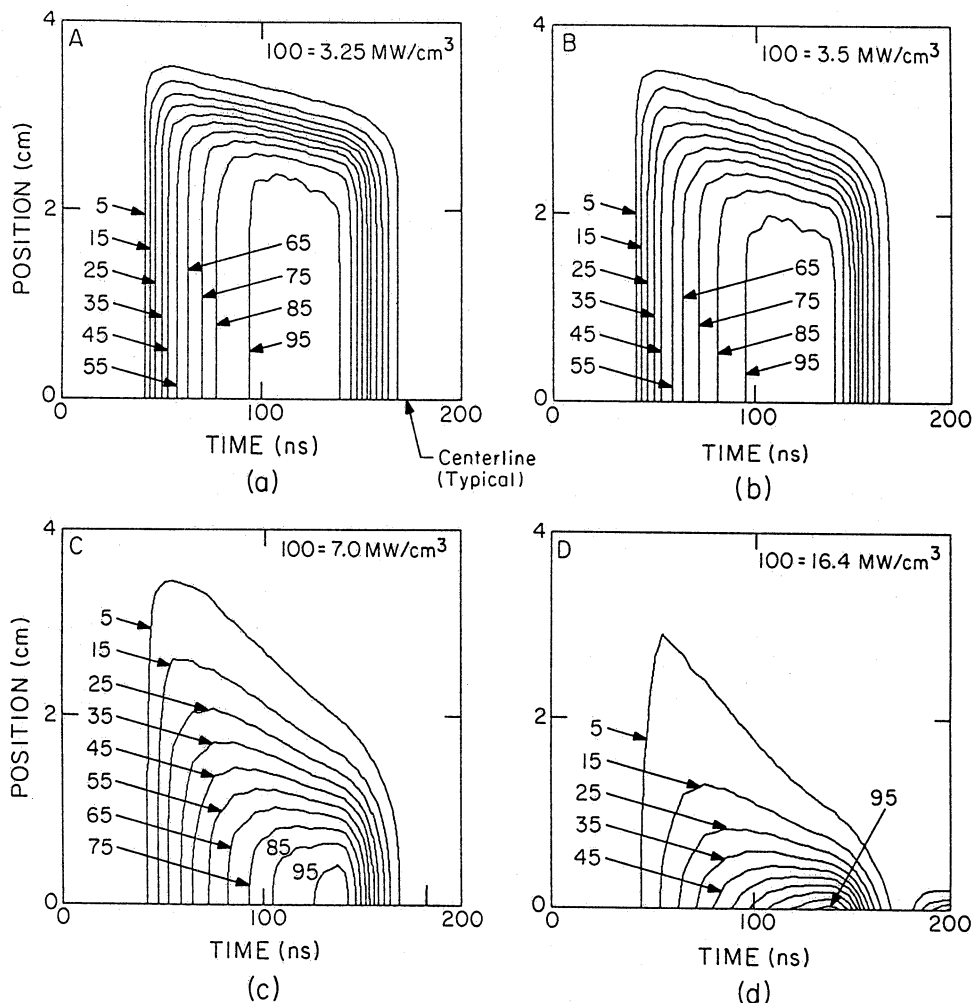


Fig. 11. Power deposition as a function of position and time for the preionization electron density profiles (identified by A-D) shown in Fig. 10.

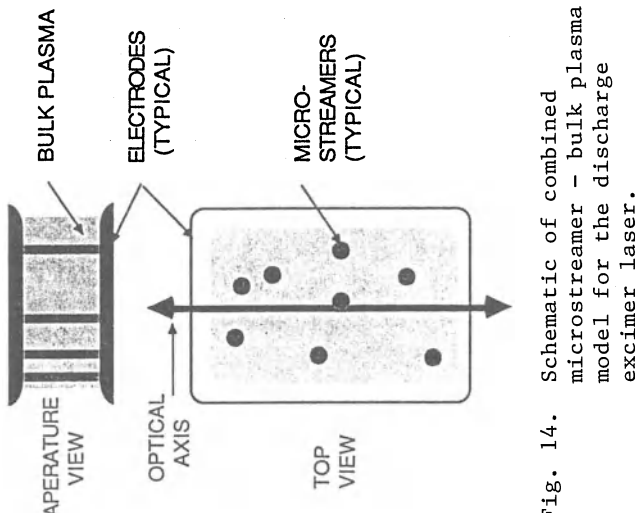


Fig. 14. Schematic of combined microstreamer - bulk plasma model for the discharge excimer laser.

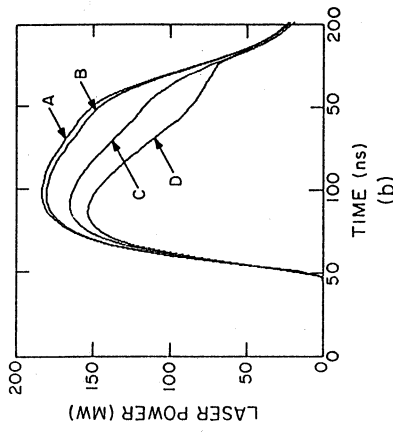
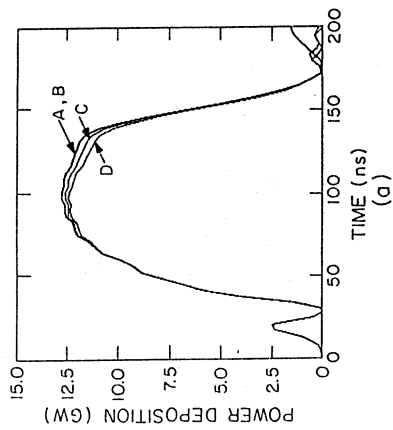


Fig. 13. Total a) power deposition and b) laser power vs time for the preionization profiles (labeled A-D) shown in Fig. 10.

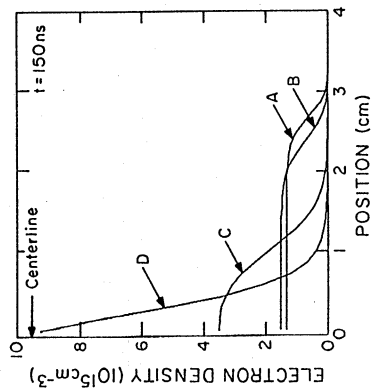
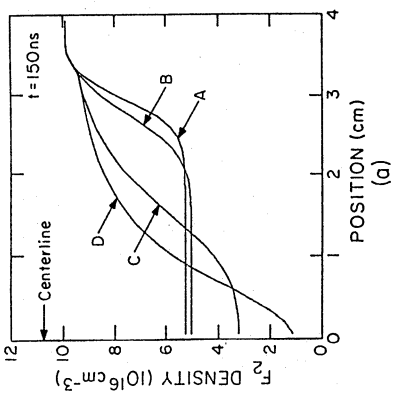


Fig. 12. Density of a) F_2 and b) electrons at $t = 150$ ns vs position for the preionization profiles (labeled A-D) shown in Fig. 10.

These parameters determine whether significant convection will occur, which would lead to changes in E/N which in turn could result in instabilities. In this section, we will investigate this spatial scale by modeling streamer formation in electric discharge excimer lasers.

To maximize the efficiency of an electric discharge excimer laser one must uniformly excite the gas by operating with both uniform electric fields and uniform preionization density. Even if uniform, the preionization density must exceed a minimum value to prevent formation of microscopic streamers. Levatter and Lin modeled the early stages of development of a high pressure preionized pulsed gas discharge.⁴² They hypothesized that each individual preionization electron forms the seed of a micro-streamer. As avalanche proceeds the head of the streamer expands by diffusion. If during the formative stage of the discharge (that is, during avalanche) the transverse diffusion of the head of each streamer overlaps its neighboring streamers, then the discharge will develop as a uniform glow. If, however, the heads of the micro-streamers do not overlap, the discharge will be filamentary with power primarily deposited in small channels. This method of power deposition is obviously not optimum for laser applications. For typical excimer laser discharges Levatter and Lin estimated that uniform discharges can only be obtained if the initial preionization electron density, n_{eo} , is

$$n_{eo} (\text{cm}^{-3}) > \frac{5 \times 10^6}{t_0^{2/3} (\text{ns})} p^{3/2} (\text{atm}) \quad (29)$$

where t_0 is the voltage rise time (ns) and p is the gas pressure (atm). For typical discharges ($t_0 = 10$'s of ns, $p = 2\text{-}4$ atm) one must have $n_{eo} \gg 2 \times 10^6 \text{ cm}^{-3}$, which is easily obtained with corona and x-ray preionization.^{14,15}

Given that excimer laser discharges may be uniformly initiated by having greater than a minimum preionization density, which is easily obtained, the observation that these discharges terminate in arcs and streamers must be explained otherwise. Recent observations of the structure of XeCl excimer laser discharges by Taylor have shed considerable light on this topic.²⁷ Taylor took framing camera photographs of the discharge simultaneously to recording laser intensity, voltage, and current waveforms. He found that the discharge was initially a uniform glow, but that during the discharge streamers appeared to originate from each electrode and slowly propagate towards the center of the discharge, "consuming" the glow as they went. Eventually, the streamers bridged the inter-electrode gap at which time laser oscillation ceased, however the discharge impedance did not significantly collapse as one would expect during arcing. This latter behavior indicated that power was still being deposited in the discharge, albeit in an array of small arcs or streamers in a fashion not conducive to sustaining laser oscillation.

Given that the streamers begin near the electrodes, one would assume that their origin lies with a non-uniformity associated with the electrode surface or cathode/anode sheaths. The non-uniformity then perturbs the delicate balance between electron ionization and attachment, thereby setting off a local OPI. This interpretation qualitatively agrees with the theories of Coutts and Webb⁴³, and Coutts,⁴⁴ who hypothesized that the termination of laser oscillation in XeCl lasers results from what they call a "halogen depletion instability" (HDI), which is analogous to an

OPI. The HDI is a consequence of there being local perturbations in the electron or halogen density which cause a decrease in the local halogen density due to excessive burnup. The spatial scale over which the HDI occurs is unspecified but is described as being filamentary.

To investigate these issues, Osborne and Hutchinson measured the homogeneity of an XeCl excimer laser discharge by passing a dye laser beam through the discharge and observing its diffraction pattern.⁴⁵ They found that the probe beam experienced considerable scattering coincident with the termination of the laser output pulse but while volume averaged spontaneous emission continued. The fact that streamers could not be identified in framing camera photographs of the medium lead to the conclusion that the discharge had collapsed into a dense framework of filaments.

The spatial scale of the streamers or filaments is particularly important with respect to the validity of the SKA. As implied by Eq. 21, if the spatial scale of the non-uniformity is sufficiently large or pulse length small enough, then convective gas motion is not important during the pulse. The SKA is then valid, and the gas density, N, remains a constant. In this case, the filaments or streamers described above can only grow as a result of local depletion of the halogen, which shifts the OPI to lower E/N. If, however, the spatial scale of the non-uniformity is small enough or pulse long enough then convective motion will occur and the SKA is not valid. In that case, rarification of the channel of the filament or streamer will occur (i.e., N decreases) in addition to depletion of the halogen. An OPI is doubly reinforced by a decrease in the stable E/N and an increase in the local E/N. To investigate the effects of small scale nonuniformities, the model described in Section IV. A was modified in the following fashion.

The discharge volume was modeled as being a homogeneous with a random distribution of cylindrical sub-volumes in which perturbations in preionization or halogen density, precursors to streamers, occur. We assumed that the perturbation, and hence streamers, bridged the entire gap between anode and cathode (see Fig. 14). Within each sub-volume, we solved the local rate equations for each individual species and the transport equations as given by Eqs. 15-17. For n randomly distributed streamers, the resistance of the discharge was then given by

$$R_D = \left[\frac{\sigma_b(Lw - \pi r_{\max}^2)}{d} + \frac{n}{d} \int_0^{r_{\max}} \sigma(r) 2\pi r dr \right]^{-1} \quad (30)$$

where the electrode separation, length, and width are d, L, and w, $\sigma(r)$ is the local conductivity in the sub-volume containing the streamer, σ_b is the conductivity in the bulk plasma, and r_{\max} is the maximum extent of the streamer subvolume. Due to the random distribution of streamers and their poor optical quality, we assume that laser oscillation occurs only in the bulk plasma. For the examples which follow, we again used the experimental conditions of Watanabe and Endoh⁹ as a base case except that we lengthened the PFL to 100 ns.

To demonstrate the importance of spatial scale of small scale non-uniformities, we chose the case where the preionization electron density was non-uniform. We specified a preionization electron density of the form

$$n_{eo}(r) = n_{eb} \cdot (1 + \alpha \cdot \exp(-(r/r_u)^2)) \quad (31)$$

where n_{eb} is the preionization density in the bulk plasma, α is the magnitude of the inhomogeneity, and r_u is its spatial extent.

The gas, electron and F_2 densities, and gas temperature in the vicinity of the streamer at 100 ns into the discharge pulse are shown in Fig. 15. The spatial coordinate has been normalized by r_u and the magnitude of the inhomogeneity in preionization density is $\alpha = 0.05$. There has been only nominal gas motion for $r_u > 60 \mu\text{m}$ whereas significant rarification has begun in the channel of the streamer for $r_u < 6 \mu\text{m}$. The rarification of F_2 is more severe than that of the total gas density due to burnup resulting from both dissociative electron attachment and direct dissociation by electron impact. The combined effects of rarification and depletion of F_2 result in a decrease in the local operating point and a strong ionization excess in the core of the streamers having small r_u .

Even at this early time during the discharge pulse, there is nearly an order of magnitude increase in the electron density and power deposition in the cores. The higher power deposition in the core of the streamers with small r_u cause a substantial increase in the local gas temperature.

It is this increase in gas temperature, and small scale of the inhomogeneity, which set up the pressure gradient driving the radial convection. The rarification of the core of streamers having small r_u is clearly unstable due to the decrease in their operating point below that of the average E/N of the discharge. The result is "micro-arcing" and generating a "blast", or rarification wave, from the core, as shown in Fig. 16. The small oscillations in radius of the core result, in part, from oscillations in the current.

Given that one has a micro-inhomogeneity that is sufficiently small to set up convection, a micro-arc will also occur regardless of the magnitude of the inhomogeneity. The magnitude of the inhomogeneity determines only the time required to initiate the arc. For this system the time is that required to completely deplete the F_2 in the core. This effect is shown in Fig. 17 where the gas density in the vicinity of the micro-streamer at 210 ns after breakdown is shown for inhomogeneities of $\alpha = 0.02, 0.05$ and 0.1 . The streamer channels are quite similar, differing only in their time evolution.

The effect of micro-streamers on the performance of the discharge depends, of course, on the current carried by the streamers relative to the bulk homogeneous plasma. The streamers appear as parallel resistors to the bulk plasma and divide current accordingly. In this respect, our measure of streamer density will be number/(electrode area). The effect that streamers have on laser performance is two fold. First, power is dissipated in the streamers which is not used in excitation of the laser medium. Second, the optical homogeneity of the gas is spoiled by the lensing action of the density variations caused by the streamers. These effects are shown in Fig. 18 where the laser power and fractional discharge power dissipated in the streamers are plotted for the conditions of Fig. 22. The streamer density is approximately 1.8 cm^{-2} . Negligible power is dissipated in the streamers until their cores rarify and F_2 is depleted. At this time, their expansion is rapid and current is quickly

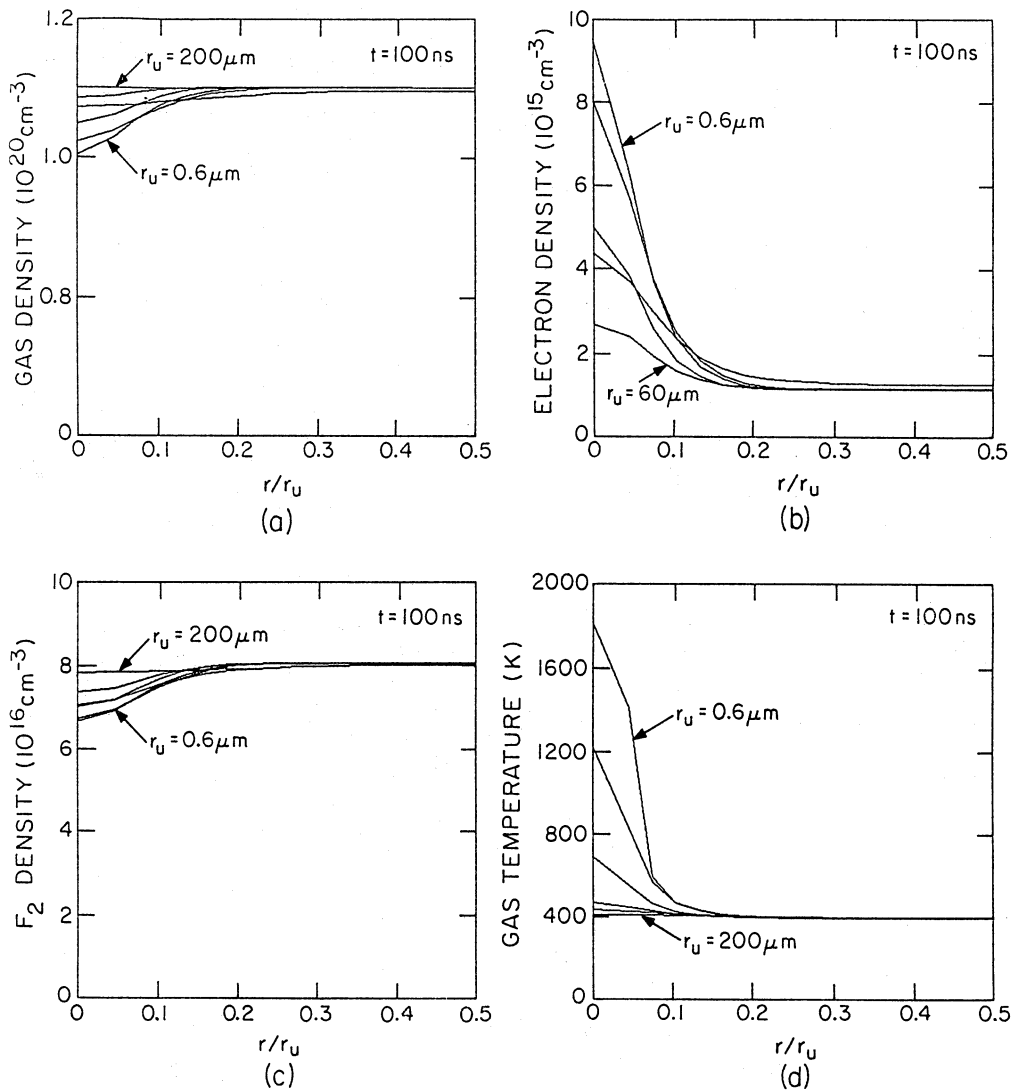


Fig. 15. Discharge parameters in the vicinity of a microstreamer as a function of radius at $t = 100$ ns: a) gas density, b) electron density, c) F_2 density and d) gas temperature. The radius is normalized by the spatial scale of the nonuniformity in pre-ionization electron density, r_u ($0.6, 2, 6, 20, 60, 200 \mu\text{m}$).

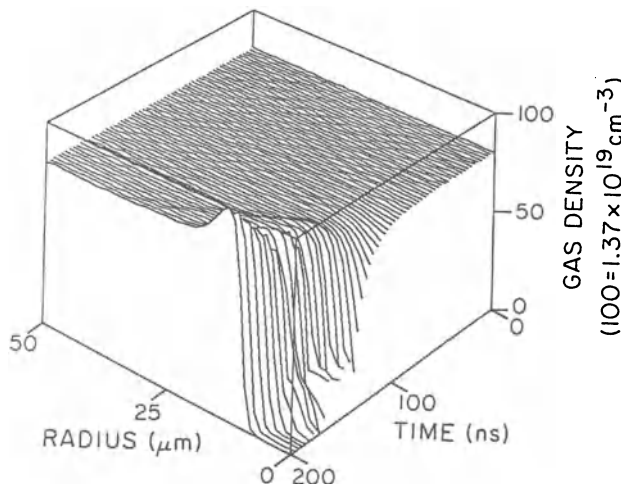


Fig. 16.

Gas density as a function of radius and time in the vicinity of a microstreamer showing transition to an arc.

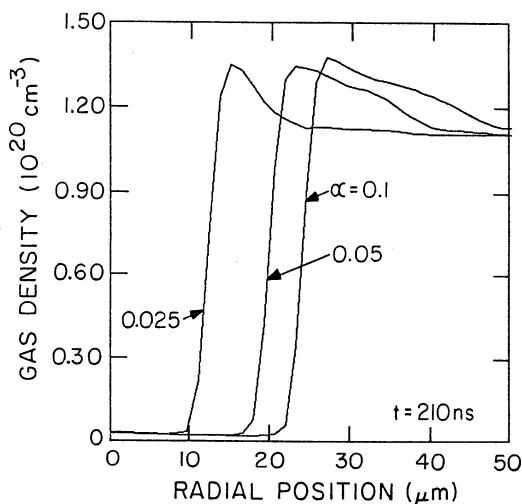


Fig. 17

Gas density as a function of radius at $t = 210$ ns for differing degrees of non-uniformity, α , in the preionization electron density.

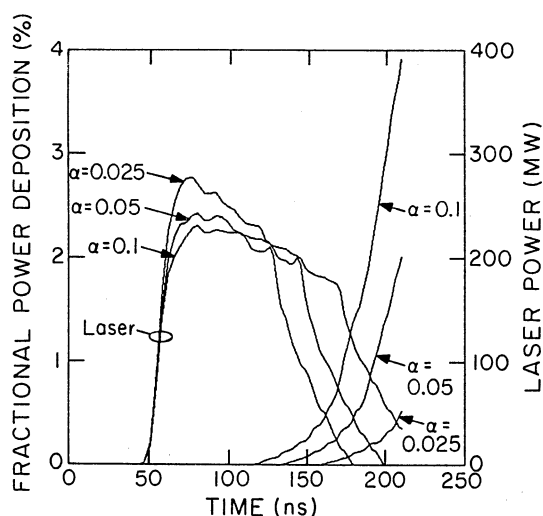


Fig. 18

Fraction of discharge power dissipated in microstreamers (1.8 cm^{-2}), and laser power as a function of time for differing degrees of non-uniformity, α , in the preionization electron density.

channeled through them. For our conditions, this occurs at 150-200 ns. The optical homogeneity of the laser, though, has been significantly spoiled prior to the time at which power is channeled into the streamer. Total laser power decreases, and eventually quenches, for this reason.

V. Concluding Remarks

In spite of the fact that the Local Field Approximation may be valid for specifying electron impact rate coefficients in high pressure pulsed electric discharge devices, such as excimer lasers, nonequilibrium phenomena may still occur. These nonequilibrium effects are due to changes in the self sustaining local value of E/N resulting from time and spatially dependent changes in species mole fractions. These effects are ultimately a result of some nonuniformity in discharge parameters such as electrode profiles or preionization electron density. The spatial extent of that nonuniformity is the measure of whether additional nonequilibrium effects, such as gas motion, must be considered.

VI. Acknowledgements

This work was supported by Sandia National Laboratories, Los Alamos National Laboratory, and the National Science Foundation (ECS88-15781, CBT88-03170)

References

1. J. Waymouth, Physics Today (Letters), March 1989
2. T. E. Wicker and T. D. Mantei, J. Appl. Phys. 57, 1638 (1985)
3. Ch. A. Brau, in "Excimer Lasers", edited by Ch. K. Rhodes (Springer, Berlin, 1979), pp. 87-134.
4. J. W. Coburn and H. F. Winters, J. Vac. Sci. Tech. 16, 391 (1979)
5. J. R. Woodworth, C. A. Frost and T. A. Green, J. Appl. Phys. 53, 1 4734 (1982)
6. M. Matsuoka and K. Ono, Appl. Phys. Lett. 54, 1645 (1989)
7. F. Kannari, M. Obara and T. Fujioka, J. Appl. Phys. 57, 4309 (1985)
8. R. S. Taylor and K. E. Leopold, J. Appl. Phys. 65, 22 (1989)
9. S. Watanabe and A. Endoh, Appl. Phys. Lett. 41, 799 (1982)
10. G. J. Hirst, V. Rivano and C. E. Webb, J. Appl. Phys. 61, 2438 (1987)
11. C. H. Fisher, M. J. Kushner, T. E. DeHart, J. P. McDaniel, R. A. Petr and J. J. Ewing, Appl. Phys. Lett. 48, 1574 (1986)
12. W. H. Long, M. J. Plummer and E. A. Stappaers, Appl. Phys. Lett. 43, 1576 (1983)
13. R. S. Taylor and K. Leopold, Appl. Phys. Lett. 47, 81 (1985)
14. K. Midorikawa, M. Obara and T. Fujioka, IEEE J. Quant. Elect. QE-20, 198 (1984)
15. M. R. Osborne, J. Appl. Phys. 63, 32 (1988)
16. T. S. Fahlen, IEEE J. Quant. Elect. QE-15, 311 (1979)
17. Product announcement from XMR Inc. (Santa Clara, CA) at Conference on Lasers and Electro-Optics (Baltimore, MD, 1989).
18. T. Hasama, K. Miyazaki, K. Yamada and T. Sato, IEEE J. Quant. Elect. QE-25, 113 (1989)

19. L. G. Champagne, A. J. Dudas and N. W. Harris, *J. Appl. Phys.* 62, 1576 (1987)
20. W. L. Morgan, J. N. Bardsley, J. Kin and B. L. Whitten, *Phys. Rev. A* 26, 1696 (1982)
21. M. R. Flannery and T. P. Yang, *Chem. Phys. Lett.* 56, 143 (1978)
22. J. E. Velazco, J. H. Koltz and D. W. Setser, *J. Chem. Phys.* 65, 3468 (1976)
23. A. Kvaran, M. J. Shaw and J. P. Simons, *Appl. Phys. B* 46, 95 (1988)
24. W. J. Witteman and B. M. H. H. Kleikamp, *J. Appl. Phys.* 55, 1299 (1984)
25. M. Hayashi, "Recommended Values of Transport Cross Sections", Report. No. IPPJ-AM-19, Nagoya Institute of Technology, 1981
26. R. E. Olsen, J. R. Peterson and J. Moseley, *J. Chem. Phys.* 53, 3391 (1970)
27. R. S. Taylor, *Appl. Phys. B* 41, 1 (1986)
28. S. Suminda, K. Kunitomo, M. Kaburagi, M. Obara and T. Fujioka, *J. Appl. Phys.* 52, 2682 (1981)
29. S. Watanabe, A. J. Alcock, K. E. Leopold and R. S. Taylor, *Appl. Phys. Lett.* 38, 3 (1981)
30. A. B. Treshchalov and V. E. Peet, *IEEE J. Quant. Elect.* QE-24, 169 (1988)
31. A. V. Phelps and L. C. Pitchford, *Phys. Rev. A* 31, 2932 (1985); and references therein.
32. D. Hershey, "Transport Analysis" (Plenum, London, 1973), Ch. 3.
33. P. A. Thompson, "Compressible Fluid Dynamics" (McGraw, New York, 1972), Ch. 2
34. A. C. Jenkins and G. A. Cook, in "Argon, Helium and the Rare Gases", edited by G. A. Cook (Interscience, New York, 1961), Ch. 7
35. M. J. Kushner and A. L. Pindroh, *J. Appl. Phys.* 60, 904 (1986)
36. W. F. Ames, "Numerical Methods for Partial Differential Equations, 2nd Ed." (Academic, New York, 1977), pp. 114-135
37. M. J. Kushner and B. E. Warner, *J. Appl. Phys.* 54, 2970 (1983)
38. K. H. Schoenbach, H. Chen and G. Schaefer, to be published in *J. Appl. Phys.*, 1989
39. D. B. Graves and K. F. Jensen, *Trans. Plasma Science* PS-14, 78 (1986)
40. M. J. Kushner, A. L. Pindroh, C. H. Fisher, T. A. Znotins and J. J. Ewing, *J. Appl. Phys.* 57, 2406 (1985)
41. M. J. Kushner, *J. Appl. Phys.* 62, 101 (1987)
42. J. I. Levatter and S.-C. Lin, *J. Appl. Phys.* 51, 210 (1980)
43. J. Coutts and C. E. Webb, *J. Appl. Phys.* 59, 704 (1986)
44. J. Coutts, *J. Phys. D* 21, 255 (1988)
45. M. R. Osborne and M. H. R. Hutchinson, *J. Appl. Phys.* 59, 711 (1986)

ENERGY TRANSFER IN ATOM/MOLECULE COLLISIONS WITH MOLECULES AND SURFACES

Gert Due Billing

H.C. Ørsted Institute
University of Copenhagen
Copenhagen 2100 Ø, Denmark

Energy transfer in molecule-molecule or molecule-surface collisions are described theoretically by a number of recently formulated mainly semi-classical models in which a part of the dynamics is described by classical mechanics. Results obtained with these methods have been used for comparison with experimental data and for kinetic modelling of bulk systems.

INTRODUCTION

The theoretical modelling of chemical kinetics requires detailed information upon the underlying dynamics. This information is becoming available in the form of cross sections or rates for the elementary chemical processes. By a fruitful interplay between experiment and theory has it been possible during the last decades to obtain more and more reliable values for the state resolved rates. Thus the predictive ability of these kinetic models has greatly improved.

Although dynamical calculations have been made feasible through the developments of new methods and the availability of high speed computers it is still a rather elaborate undertaking to compute the full set of rates even for diatomic molecule-molecule energy transfer. It is therefore often necessary to introduce fitting or scaling procedures in order to diminish the number of dynamical calculations which have to be carried out. Another complicating aspect arises due to the lack of detailed information on the intermolecular potentials especially in the short and intermediate range region. Therefore one often has to apply semiempirical potential energy surfaces and to adjust potential parameters so as to obtain

agreement with experimental information on e.g. relaxation rates, transport and molecular beam data. Once the intermolecular potential has been adjusted in this manner it can be used to calculate quantities as e.g. multiquantum transition rates or rates for transitions among excited states - information which is not yet directly available experimentally.

Although multiquantum vibrational transitions are not very important near the vibrational ground state it has been known for many years that they cannot be neglected in highly excited molecules. Thus the kinetic coupling matrix increases significantly near the dissociation limit of the molecules.

Although the situation as far as information on state to state rates in diatomic molecules is concerned is well investigated the situation is less satisfactory for polyatomic and especially for molecule/polyatomic collisions much more work is needed. The most complex situations occur for small tri or tetra atomic molecules in which large amplitude soft motions, anharmonic couplings, Fermi resonances and Coriolis couplings are aspects which need to be considered. Also organic molecules contain motions as e.g. torsional motion which are easily excited in the collision and therefore have to be treated within a full coupling description. As soon as the molecules become much larger it is possible to incorporate approximations for large rigid parts of the molecule. An approximation which often offers a sufficiently accurate description of the energy transfer to these parts invoke a linearly and quadratically forced harmonic oscillator model for the normal modes. Thus the various motions may be separated and for large enough molecules we may e.g. neglect the rotational motion altogether. In this limit the internal excitation of the molecule resembles that of solid, i.e. the main excitation is of the soft (low frequency) vibrations (phonons). However for a solid the periodicity of the lattice gives rise to another phenomena namely collective mode excitation. Such collective modes are e.g. surface waves, electron bands, plasmons etc. which have to be treated by methods different from those used in molecular systems.

As far as surface processes or surface reactions on metals are concerned the most important influence of the solid has to do with the possibility of acting as an electron donor, i.e. to donate an electron into an antibonding orbital of the

molecule thereby weakening the bond and lowering the dissociation energy. This makes it easier for the molecule to dissociate at the surface. However, for heavy molecules this is to some extent counteracted by the transfer of some of the available energy to the surface phonons. But for light molecules as hydrogen the mass difference between the molecule and the surface atoms is so large that the excitation process is very inefficient and therefore hydrogen dissociates easily at many metal surfaces. Excitation of the metal electrons is another process which can be induced by the incoming atom/molecules. However, this process is usually of secondary importance although recent investigations have shown that it does influence the finer details of the scattering picture. The dynamics of the incoming molecule is governed by the molecule surface and the intramolecular potentials. Especially the dependence of the potential with the surface distance is important. Due to the complexity of this many electron problem the construction and calculation of ab initio surfaces is only in its infancy. Thus one has to rely upon semiempirical models where the parameters are adjusted so as to be in agreement with experimental information on binding energies, sites and frequencies. When doing so the lower adiabatic surface is found and when trajectories are run on this surface it is implicitly assumed that the nonadiabatic transition from the neutral molecule-solid potential curve to the ion-solid potential curve is unity near a point where the electron affinity of the molecule exceeds the work function of the metal. The proper dynamical treatment would then be to treat the molecule surface collision as a two potential energy surface problem and include the nonadiabatic transitions explicitly in the statistical averaging over the collision parameters.

In order to deal with the variety of phenomena mentioned above a number of theoretical models and theories have been developed. Results obtained with these methods will be discussed below.

ATOM-DIATOM AND DIATOM-DIATOM COLLISIONS

Although energy transfer in atom-diatom collisions constitutes the simplest possible problem an exact quantum mechanical treatment of this problem cannot be carried out

Table 1. Important aspects in atom-diatom and diatom-diatom energy transfer

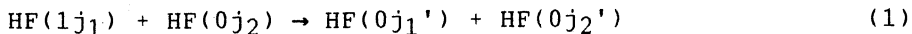
-
- Rotational/vibrational energy conversion.
 - Centrifugal stretch terms.
 - Multiquantum vibrational transitions.
 - Inverse temperature behaviour of rates.
 - Importance of long-range forces.
 - Vib-Vib and Rot-Rot energy transfer.
 - Effect of initial state.

except at very low collision energies. The reason being that the number of energetically allowed states grows rapidly with stitutes the simplest possible problem an exact quantum mechanical treatment of this problem cannot be carried out except energy and the number of coupled differential equations which can be integrated numerically is soon exceeded. However, a number of reliable approximate quantum mechanical methods and semiclassical methods have been developed over the last decades^{1,2}. These methods are sufficiently accurate for a detailed description of the important aspects of energy transfer processes, for testing sensitivity to changes in the intermolecular potential and molecular parameters.

The table 1 gives a list of the important aspects which should be considered in atom-diatom and diatom-diatom collisions. The collision induced conversion of vibrational to rotational energy is known from molecules, with small moments of inertia, in vibrational excited states at low kinetic energies. This mechanism in which vib/rot transitions $v_j \rightarrow v'j'$ where for H_2 $v_j=10$ and $v'j' = (06 \text{ or } 04)$ dominate yields a large isotop effect in the relaxation rates at low temperatures. Thus the vibrational relaxation rate for ${}^4He-nH_2$ is $1.7 \cdot 10^{-19} \text{ cm}^3/\text{sec}$ and for ${}^4He-nD_2$ $1.6 \cdot 10^{-20} \text{ cm}^3/\text{sec}$ at 50 K³.

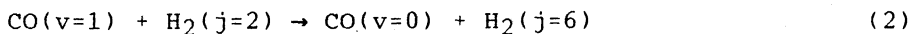
The vibrational to rotational energy conversion at low energies populates higher j-levels preferably and therefore creates an inversion which could be used to initiate a laser operating on the rotational levels of a molecule as HF. Extensive calculations on the HF-HF system have shown that such an inverted distribution can be obtained on the rotational

levels and that the cross sections for the processes:



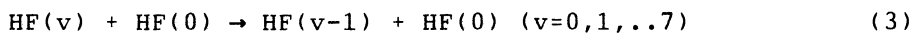
peak at $j_1' \sim j_2' \sim 4-5$ if $(j_1j_2) = (00), (20), (11)$ or (02) . However, for $j_1=j_2=3$ a much broader distribution with $j_1' + j_2'$ between 5 and 16 is obtained⁴. Extensive tables of rates or cross sections for the process(1) is, however, not available. If one of the molecules has a small and the other a large moment of inertia as in the $\text{H}_2^+ + \text{CO}$ system the transfer of H_2 rotational to vibrational energy of CO has been reported.⁵.

The transition



has an energy mismatch of only 83.3 cm^{-1} . Hence it may be induced by long range forces as e.g. the dipole-hexadecapole interaction term. The inclusion of long range forces may lead to an "inverse" temperature dependence, i.e. an increase in the rate constant with decreasing temperature. The effect increases with the strength of the potential and decreases with the energy mismatch. Thus the phenomena is especially significant for heteronuclear diatom-diatom collisions where vibration-vibration (VV) energy exchange less than a few hundred wavenumbers can be supported by the dipole-dipole interaction. The effect of long range forces can lead to a dramatic increase in the cross section as e.g. known from resonance rotational energy transfer processes in $\text{HF} + \text{HF}$ collisions^{4,6} where the cross section is as large as $4-500 \text{ \AA}^2$ at kinetic energies around $0.05 - 0.1 \text{ eV}$.

Of special significance is the attractive van der Waals forces which at low enough energies and impact parameters can support the formation of sticky complexes. This can lead to an inverse temperature dependence even for vibration-translation (VT) transitions with large energy mismatch. Thus for the processes:



the V-T rates increase with a factor of two from values of 10^{-12} to 10^{-10} cm³/sec when the temperature is decreased from 1000 K to 300 K. The life time for most of the sticky collision complexes varies from 5-10 ps. However, at $E_{\text{kin}} = 200$ cm⁻¹ about one third of the trajectories have much longer life times⁷. The van der Waals well for this system is as large as 350 K but in certain geometries the interaction is much larger due to large dipole-dipole forces⁸. But even in atom-diatom systems with wells of the order 1-2 meV an inverse temperature dependence is encountered for kinetic energies below 0.01 eV⁹.

Rotational/vibrational coupling within the diatomic molecule can be induced by the centrifugal term:

$$-j^2 m^{-1} \bar{r}^{-3} (r - \bar{r}) \quad (4)$$

where j is the rotational angular momentum, m the reduced mass, r the internuclear distance and \bar{r} its equilibrium value. This term may be significant and if so, it implies a breakdown of the rigid rotor approximation¹⁰. For a system as He + CO the inclusion of this coupling term increases the cross sections with 10-20% at a kinetic energy of 50 meV¹⁰. for molecules with smaller moments of inertia the effect is much bigger. Thus for the He-H₂ system the vib/rot cross sections increase due to this term by a factor of two at $E_{\text{kin}} \sim 0.3$ eV³.

As important as the sensitivity to the potential energy surface is the effect of the initial state of the molecule.

For V-V processes as:



the energy mismatch (assuming a Morse oscillator) is:

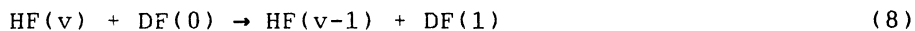
$$\Delta E = 2 \hbar \omega_e x_e^{(v'+1-v)} \quad (6)$$

Since the probability for the process (5) is sensitive to the energy mismatch the rates are expected to show a maximum at $v \sim v'+1$ when plotted (for a fixed v') as a function of v .

Simple theories based upon long range forces and a first order quantum treatment of the "transition" yield a gaussian like expression for the rate as a function of v . However, the calculated rates are not symmetric around $v' + 1$ but slightly asymmetric with the larger rates at $v > v'$ ¹¹. Although the energy mismatch often is the most important parameter which influences the cross section there are cases where the largest ΔE yield the largest rate or cross section. This happens when some interference between the force inducing the VV transition and the frequency factor in the integral

$$\int dt \text{ force } \exp(i\Delta Et/\hbar) \quad (7)$$

is either constructive or destructive as a function of the initial vibrational state. This has been observed for the VV transitions¹²



where $v=4, 5$ or 6 .

Although the increase in transition matrix element and decrease in energy mismatch should favour the $60 \rightarrow 51$ transition we find that $k_{40 \rightarrow 31}$ and $k_{50 \rightarrow 41} > k_{60 \rightarrow 51}$ at 300 K. The reason is as mentioned found in a subtle interplay between the "VV force" $\partial^2 V / \partial r_1 \partial r_2$ and the frequency term $\exp(i\omega t)$ in the forcing integral (7)¹².

Other cases where the energy mismatch is not the only important quantity are encountered for transitions induced by long range forces where selection rules in the matrix elements favour certain transitions. This is known from e.g. ion-molecule collisions (see below).

Very often the effect of multiquantum vibrational transitions are neglected in kinetic modelling. The reason being that most scaling theories are based upon simple first order models for the collision and multiquantum transitions are either neglected or seriously underestimated¹³. Only recently has it become possible to calculate the rates by reliable methods¹³. Calculations with these methods have shown that both multiquantum VV and VT processes can be significant -

especially in the energy range where the molecules are in vibrationally excited states¹⁴.

POLYATOMIC MOLECULES

In polyatomic molecules a number of new energy relaxation pathways open up. Thus both intra and intermolecular energy transfer play a role. The former can be induced through anharmonic or Coriolis coupling. For small polyatomic molecules it is difficult to give any rules of thumb as far as the preferred pathways are concerned. Since the situation is also not one where statistical concepts appear to be of any use, we are faced with a very heavy computational and/or experimental problem if state resolved energy relaxation in polyatomics has to be considered. In the semiclassical model which has been developed over the last decade the problem is reduced by treating some of the degree's of freedom (typically translation and rotation) classically. Thus only the vibrational motion is quantized².

Table 2. Coupling scheme among H₂O vibrational levels.

v ₁ v ₂ v ₃	000	010	020	100	001	030	110	011
000	-	(a)VT	(a)	a,VT	VT	(a)	(VT)	(VT)
010	-	-	(a)VT	VV	Co,VV	(a)	VV	VT
020	-	-	-	a		a,VT	VV	VV
100	-	-	-	-	Co,VV		(a)VT	
001	-	-	-	-	-			Co(a)VT
030	-	-	-	-	-	-	-	a
110	-	-	-	-	-	-	-	VV

a: anharmonic coupling

(a): small anharmonic coupling

VT: vibration/translational-rotation coupling

(VT): small VT coupling

VV: vibration-vibration coupling

Co: Coriolis coupling.

The quantum mechanical part of the problem is treated in the following manner: The part of the hamiltonian including up to quadratic terms in the normal mode coordinates and momenta the "harmonic oscillator" (HO) part is treated within a quantum operator approach whereas the remaining anharmonic part is included using a state expansion technique².

Table 2 shows the coupling scheme for H₂O colliding with an inert gas atom. We see that almost all levels are coupled even to first order. Since the equations have to be solved to infinite order, one can only investigate the importance of specific coupling terms by omitting them in the hamiltonian and compare the results with calculating where the terms are included. Such an investigation has been carried out for He + H₂O and N₂ + CO₂¹⁵. Some of the results obtained in ref. 15 have been reported in table 3. We see that except for the excitation of the bending mode and the VV transition between the asymmetric stretch of CO₂ and N₂ vibrational mode the harmonic oscillator description fails. Especially the small probabilities are sensitive to the anharmonic perturbations. As the kinetic energy of the collision increases the HO description becomes more accurate! Similarly if the polyatomic molecule becomes larger the energy transfer problem also simplifies. The reason being firstly that the heavy polyatom is not appreciably rotational excited, and hence Coriolis coupling is unimportant, secondly the density of soft vibrational modes increases and the energy transfer to these modes are often well described by the HO-model. Thus energy transfer in atom or ion molecule collisions with CF₄, SF₆ etc. can be treated accurately by the simplest possible model in which each of the normal modes is forced independently and as linearly forced oscillators¹⁶. The soft vibrational modes can take up an appreciable amount of the kinetic energy¹⁶, and for atom-polyatom collisions governed by short range forces the energy to these modes is dominating. However, if long range forces are important as e.g. in ion-molecule collisions, the forward scattering is governed by the normal mode derivative of the ion-multipole interaction. Thus, although molecules as CH₄, SF₆ etc. do not have permanent dipole or quadrupole moments the transition dipole for modes v₃ and v₄ are

Table 3. Average probabilities for collision induced
vibrational transitions in He-H₂O (upper panel)
and N₂-CO₂ (lower panel)

Transition	U = 0.2 $\hat{\epsilon}$			
000→010 ^{b)}	0.10	0.078	0.076	0.077
000→020	3.2(-4) ^{c)}	1.9(-4)	1.5(-4)	1.7(-4)
000→100	2.4(-8)	5.0(-7)	2.1(-6)	2.1(-6)
000→001	2.8(-8)	2.4(-7)	7.8(-7)	2.0(-6)
010→020	0.20	0.18	0.17	0.17
010→100	1.2(-4)	1.3(-3)	1.3(-3)	1.3(-3)
Approximation	HO + cubic + quartic + Coriolis ^{d)}			
	U=2000 cm ⁻¹		U=8000 cm ⁻¹	
0000→0100 ^{e)}	3.9(-6)	3.7(-6)	3.3(-3)	3.3(-3)
0000→1000	1.1(-10)	2.8(-10)	1.5(-3)	1.8(-3)
0000→1100	6.0(-15)	2.3(-10)	1.2(-5)	1.4(-5)
1000→0200	3.5(-8)	2.8(-3)	5.0(-4)	4.2(-3)
0010→1100	1.1(-15)	1.1(-6)	3.5(-8)	9.5(-6)
0010→1000	6.4(-12)	3.0(-8)	1.7(-7)	1.7(-6)
0010→0100	1.5(-12)	6.2(-10)	5.3(-9)	4.2(-8)
0010→0001	1.4(-4)	1.4(-4)	7.1(-5)	7.1(-5)
Approximation	HO	anharmonic	HO	anharmonic

a) U = E_{kin} + E_{rot}

b) quantum numbers for H₂O

c) means 3.2 . 10⁻⁴

d) cubic, quartic anharmonic and Coriolis coupling included successively

e) v₁v₂v₃v quantum numbers for CO₂ and N₂(v)

non-zero, and hence the energy transfer to these modes dominates even at scattering angles as large as $\theta = 100^\circ$.

Organic molecules contain motions which are of different nature than those mentioned above. They are motions which change character as the energy is increased. Such a motion is e.g. the torsional motion which at low energies can be approximated by a harmonic motion but at higher energies turn into a rotational like motion along the C-C bond. In ref. 17 it was shown that the classical treatment of this degree of freedom for small values of the kinetic energy is questionable. This is due to the non proper treatment of the zeropoint vibrational energy in classical mechanics.

For large molecules as proteins the mode corresponding to the lowest frequency becomes a highly delocalized surface like

wave travelling along the helix¹⁸. The calculations reported in ref. 18 showed an excitation pattern which was very site dependent.

MOLECULE SURFACE SCATTERING

Atom/molecule-surface scattering also shows strong dependence upon the corrugation of the surface. Thus the energy accommodation, the energy transfer to the surface phonons divided by the incident kinetic energy, plotted as a function of the scattering angle θ to the surface normal show characteristic energy loss loops¹⁹. These loops come about when the atom hits various sites on a unit cell area thereby probing the corrugation. However, when the residence time at the surface becomes larger, the scattering becomes less regular i.e. the scattering angle more random.

The interaction between a molecule and a metal surface has several important features. The metal acts as an electron donor and an electron or part of an electron is donated into an antibonding orbital of the molecule. Thereby is the bond-length increased and dissociation energy lowered. Thus the probability for dissociation at the surface is increased as compared to the gas phase one. This simple mechanism accounts for the catalytic effect of many metals. Part of the effect may, however, be compensated by the possibility of exciting collective surface modes as phonons and electron-hole pairs. Thereby the incoming molecule loses part of its energy. For heavy molecules as N₂ or CO the energy transfer to the phonons may amount to 10-30%. For light molecules as H₂ only 1-2% of the kinetic energy is transferred due to the smaller mass. Excitation of electron hole pairs has turned out to be a process which can effect the finer details of the scattering pictures as e.g. angle resolved energy accommodation.

In principle the electron-transfer makes the molecule-surface collision a two potential problem. Usually the dynamical calculations are carried out on the lower adiabatic surface. Thus the probability for transition from the neutral molecule-surface interaction potential to the ion-surface

potential is set to unity on the way in and for the reverse process on the way out. For light molecules it is furthermore necessary to estimate the tunnelling probability through a barrier separating the precursor state and the chemisorbed surface bound molecular state. We have in table 4 listed the important features for molecule-surface scattering in the order of decreasing importance. The order is of course system dependent and based upon experience obtained for a relatively small number of systems for which reliable potential energy surfaces are available. However, often models which do neglect many of the dynamical features in table 4 are proposed. Thus any agreement obtained with experimental data can only come about because these aspects somehow are taken into account by the use of an effective potential - a potential which may not have much to do with the true potential surface. Neglecting for instance phonon excitation may place the activation barrier much too high, when it is adjusted to experimental data. Thus one should be careful not to overlook a dynamical process by the use of experimentally adjusted surfaces. The agreement with experiment obtained in this manner will always be fortuitous and system dependent. But in this respect the gas-surface scattering is not different from any other dynamical gas phase problem.

Table 4. Important aspects in atom/molecule surface scattering

Molecule-surface interaction potential.

Phonon excitation.

Effect of initial state or kinetic energy of the molecule.

Approach angle or aiming point.

Surface corrugation.

Tunnelling.

Electron-hole pair excitation.

Surface temperature.

Non-adiabatic effects.

REFERENCES

1. See e.g. Atom-Molecule Collision Theory, Ed. by R. B. Bernstein, Plenum Press, New York 1979.
2. G. D. Billing, Comp. Phys. Rep. 1:237 (1984).
3. M. M. Audibert, R. Vilaseca, J. Lukasik and J. Ducuing, Chem. Phys. Lett. 37:408 (1976); J. Lukasik and J. Ducuing, J. Chem. Phys. 60:331 (1974); G. D. Billing, Chem. Phys. 30:387 (1978).
4. G. D. Billing, J. Chem. Phys. 84:2593 (1986); Chem. Phys. 112:95 (1987).
5. A. J. Andrews and C. J. S. M. Simpson, Chem. Phys. Lett. 36:271 (1975); 565 (1976). L. L. Poulsen and G. D. Billing, Chem. Phys. 73:313 (1982) ibid 89: 219 (1984).
6. P. F. Vohralik and R. E. Miller, J. Chem. Phys. 83:1609 (1985).
7. G. D. Billing and L. L. Poulsen, J. Chem. Phys. 68:5128 (1978).
8. D. R. Yarkony, S. V. O'neil, H. F. Schaefer, C. P. Baskin and C. F. Bender, J. Chem. Phys. 60:885 (1974); L. L. Poulsen, G. D. Billing and J. I. Steinfeld, J. Chem. Phys. 68:5121 (1978).
9. R. J. Price, D. C. Clary and G. D. Billing, Chem. Phys. Lett. 101: 296 (1983).
10. G. D. Billing, Chem. Phys. 107:39 (1986).
11. M. Cacciatore and G. D. Billing, Chem. Phys. 58:395 (1981).
12. L. L. Poulsen and G. D. Billing, Chem. Phys. 36:271 (1979).
13. G. D. Billing, Non equilibrium Vibrational Kinetics, Ed. M. Capitelli, Springer Verlag Berlin 1986, vol. 39 pp. 85.
14. G. D. Billing and M. Cacciatore, Chem. Phys. Lett. 94:218 (1983).
15. G. D. Billing, Chem. Phys. 67:35 (1982); ibid. 76: 315 (1983).
16. T. Ellenbrock and J.P. Toennies, Chem. Phys. 71:309 (1982); G. D. Billing, Chem. Phys. 79:179 (1983).
17. G. D. Billing, Chem. Phys. 104:19 (1986).
18. G. D. Billing, Chem. Phys. 127:107 (1988).

19. U. Gerlach-Meyer, E. Hulpke and H.D. Meyer, Chem. Phys.
36:327 (1979); G. D. Billing, Chem. Phys. 74:143
(1983).

REACTIVITY CALCULATIONS FOR ELEMENTARY ATOM-DIATOM PROCESSES AND APPLICATIONS TO NON-EQUILIBRIUM SYSTEMS

Antonio Laganà

Dipartimento di Chimica
Università di Perugia
Perugia, Italy

ABSTRACT

In this chapter quantum and quasiclassical theoretical approaches to the calculation of atom-diatom reactive cross sections and rate constants are outlined. Calculations performed using fast parallel and vector computer programs based on high level quantum and quasiclassical three dimensional approaches have allowed an extended numerical investigation of elementary chemical reactions useful for the rationalization of the dynamics and the kinetics of non-equilibrium gaseous chemical systems. As an application, some processes relevant to the modeling of H^- sources and $XeCl$ laser systems.

INTRODUCTION

The theoretical study of non-equilibrium gas phase systems has made great progress in recent years.¹ For theorists of elementary chemical processes such a study is a great challenge. In fact, the rationalization of typical non equilibrium gas phase systems implies the calculation of detailed rate constants of several elementary processes in a range of reaction conditions so extended to make difficult a detailed experimental investigation. As a consequence, accurate and fast theoretical calculations of reactive properties for extended intervals of translational and internal energy values are a necessary complement to the experimental information.

In this chapter, our attention will be focussed on atom diatom reactions. In fact, in spite of their simpleness, these systems are important constituents of several non-equilibrium processes of practical interest (see for example refs. 2 and 3). The chapter is organized as follows: In section (2) outlines of theoretical methods concerning the calculation of reactive properties of atom-diatom systems are given. Vibrational excitation and deexcitation effects associated with elementary atom-diatom processes and their applications to non-equilibrium systems of interest for the technology of ion sources and lasers are illustrated in section (3).

THEORETICAL APPROACHES

Atomic and molecular collisions of conservative systems are described by the stationary Schrödinger equation

$$H(\mathbf{w}, \mathbf{W})Z(\mathbf{w}, \mathbf{W}) = EZ(\mathbf{w}, \mathbf{W}) \quad (1)$$

where \mathbf{w} and \mathbf{W} are electronic and nuclear coordinates respectively. For computational purposes the total many body Hamiltonian can be partitioned as:

$$H(\mathbf{w}, \mathbf{W}) = H_e(\mathbf{w}; \mathbf{W}) + T_N(\mathbf{W}) = H_e(\mathbf{w}; \mathbf{W}) + \sum_I \left(-\frac{\hbar^2}{2M_I} \nabla_{\mathbf{W}_I}^2 \right) \quad (2)$$

where the $H_e(\mathbf{w}, \mathbf{W})$ term collects electronic and fixed nuclei contributions to the Hamiltonian

$$\begin{aligned} H_e(\mathbf{w}; \mathbf{W}) &= T_e(\mathbf{w}) + V_{ee}(\mathbf{w}) + V_{eN}(\mathbf{w}, \mathbf{W}) + V_{NN}(\mathbf{W}) \\ &= \sum_i \left(-\frac{\hbar^2}{2m_i} \nabla_{\mathbf{w}_i}^2 \right) + \sum_{i>j} \frac{1}{|\mathbf{w}_i - \mathbf{w}_j|} - \sum_{iI} \frac{z_I}{|\mathbf{w}_i - \mathbf{W}_I|} + \sum_{I>J} \frac{z_I z_J}{|\mathbf{W}_I - \mathbf{W}_J|} \end{aligned} \quad (3)$$

and spin-orbit and mass polarization terms have been neglected. The separation of $H_e(\mathbf{w}; \mathbf{W})$ is motivated by the fact that nuclear masses (M_I) are three orders of magnitude heavier than electronic masses (m_i) and, as a consequence, related terms in the Hamiltonian (see equation (2)) are damped by very small coefficients. To solve equation (1) the wavefunction $Z(\mathbf{w}, \mathbf{W})$ is usually expanded in terms of products of nuclear ($\Xi(\mathbf{W})$) and electronic ($\Phi(\mathbf{w}; \mathbf{W})$) functions

$$Z(\mathbf{w}, \mathbf{W}) = \sum_K \Xi_K(\mathbf{W}) \Phi_K(\mathbf{w}; \mathbf{W}) \quad (4)$$

In (4) the Φ functions are the eigensolutions of the equation

$$H_e(\mathbf{w}; \mathbf{W}) \Phi_K(\mathbf{w}; \mathbf{W}) = V_K(\mathbf{W}) \Phi_K(\mathbf{w}; \mathbf{W}) \quad (5)$$

By inserting expansion (4) into equation (1) one obtains a set of decoupled nuclear equations of the type

$$H_N(\mathbf{W}) \Xi(\mathbf{W}) = [T_N(\mathbf{W}) + V_K(\mathbf{W})] \Xi(\mathbf{W}) = E \Xi(\mathbf{W}) \quad (6)$$

provided that the overall contribution of terms containing $\langle \Phi \nabla_{\mathbf{w}} \Phi \rangle$ and $\langle \Phi \nabla_{\mathbf{w}}^2 \Phi \rangle$ integrals is negligible (Born Oppenheimer approximation).⁴ In equations (6) $V(\mathbf{W})$ (whenever possible the index k has been dropped for aim of simplicity) is usually given as a suitable functional fitted to the calculated potential energy values.⁵ In this approach the solution of the dynamical problem is, in general, determined in two steps. The first step consists of determining $V(\mathbf{W})$ values for a number of nuclear geometries large enough to describe the processes of interest. These values are calculated using *ab initio* techniques.⁶ The second step is devoted to the integration of equation (6) to calculate the nuclear dynamics.

Two radically different theoretical methods can be adopted for determining molecular dynamics. One is the quasiclassical method. In this approach the nuclear motion is described in terms of the classical formulation of the Hamiltonian (H_N^C)

$$H_N^C = \sum_I \frac{P_I^2(\mathbf{W})}{2M_I} + V(\mathbf{W}) \quad (7)$$

(where P_I is the momentum of the I nucleus). The classical problem of the N mass point particles is solved by integrating numerically equations relating time derivatives of position and momenta to partial derivatives of the Hamiltonian. Proper constraints simulating the discrete nature of quantum eigenstates are then imposed at both initial and final steps of the integration process.

The other method is the quantum one. Such a method solves equation (6) by expanding the nuclear wavefunction Ξ in terms of products of propagating and bound functions. After averaging over the coordinates describing the bound motions, a set of coupled differential equations in the propagation coordinate is obtained. The dimension of this set has to be large enough to ensure the convergency of calculated reactive properties. The coupled differential equations are integrated from the origin of the propagation coordinate to a value large enough to consider the atom-diatom interaction negligible (asymptotic value). The comparison of the value of the wavefunction calculated at the asymptote with the unperturbed solution leads to the evaluation of the detailed scattering matrix from which all reactive and non-reactive scattering and kinetic quantities can be evaluated.

The quasiclassical treatment

To solve the classical equations of the nuclear motion the center of mass of the three atoms O is usually taken as the origin of the coordinates

$$m_A \mathbf{W}_A + m_B \mathbf{W}_B + m_C \mathbf{W}_C = 0 \quad (8)$$

so as to profit from the fact that the motion of the center of mass for a conservative system is a constant. This implies that the nuclear Hamiltonian of an atom diatom system can be expressed in terms of quantities of two particles only (say A and C).

Classical trajectories

Among the different classical mechanics formulations of the equations of the motion of mass point particles, we have adopted the popular Hamilton canonical treatment which leads to the equations⁷

$$\begin{aligned} \frac{dW_{Ik}}{dt} &= \frac{\partial H_N^C}{\partial P_{Ik}} \\ \frac{dP_{Ik}}{dt} &= -\frac{\partial H_N^C}{\partial W_{Ik}} \end{aligned} \quad (9)$$

where I is either A or C and k indicates any of the three cartesian axes. By numerically integrating these six pairs of Hamilton equations one can determine positions and momenta of the various atoms at each time point of the integration grid. The curve connecting calculated position values is the trajectory followed by the system during its evolution. Usually the conservation of the total energy and total angular momentum are not incorporated into the equations of the motion to further reduce their number. Therefore, the constance of these quantities can be used as an *a posteriori* check of the accuracy of the numerical integration.

The 12 starting values of the W_{Ik} and P_{Ik} variables are determined from static and dynamical properties of reactants in their initial arrangement. To this purpose the z and y axes are chosen to lie on the plane formed by the three atoms (see the upper panel of figure 1). The atom A is located on the negative side of the z axis at a distance S from the center of mass of the BC diatom (O') sufficiently large to neglect the atom diatom-interaction. The angle θ gives the orientation of the diatom with respect to the z axis, r_c is the distance of the diatom center of mass from the C atom (as an alternative, the phase angle η of the oscillator can be used). In the chosen reference frame the initial values S° , θ° and η° of S , θ and η fully determine the \mathbf{W}_I vectors. Initial values of momenta are derived from atom-diatom relative velocity $\mathbf{v}_{A,BC}$ as well as from the characteristics of diatomic rotation and vibration. Relative atom-diatom velocity is fully determined by the initial collision energy (E_{tr}), the value e° of the angle ϵ that $\mathbf{v}_{A,BC}$ forms with the z axis (as shown by the central panel of figure 1 the impact parameter b , defined as the distance of O' from $\mathbf{v}_{A,BC}$, may also be used) and the initial value β° of the angle β formed by the projection of $\mathbf{v}_{A,BC}$ onto the xy plane and the y axis. The other values to be provided as initial parameters are the diatom rotational (E_j) and vibrational (E_v) energies and the initial value ϕ° of the angle ϕ formed by the rotational angular momentum of the diatom and the z axis (see the lower panel of figure 1). Usually, internal energies are expressed in terms of eigenvalues v (for vibration) and j (for rotation). As a result, a classical trajectory is fully determined by the following set of initial values: S , θ° , η° , E_{tr} , b , β° , ϕ° , v and j .

After integrating a trajectory (*i.e.* when at least one atom-diatom distance has become again larger than S) the procedure adopted for calculating initial values has to be inverted for recovering product properties from the final value of coordinates and momenta. In this way, the type of formed product, its scattering direction and how energy is partitioned between translation and internal modes can be determined. Internal energies are usually expressed in terms of action angle variables and related classical numbers v'_c and j'_c (for vibration and rotation respectively).

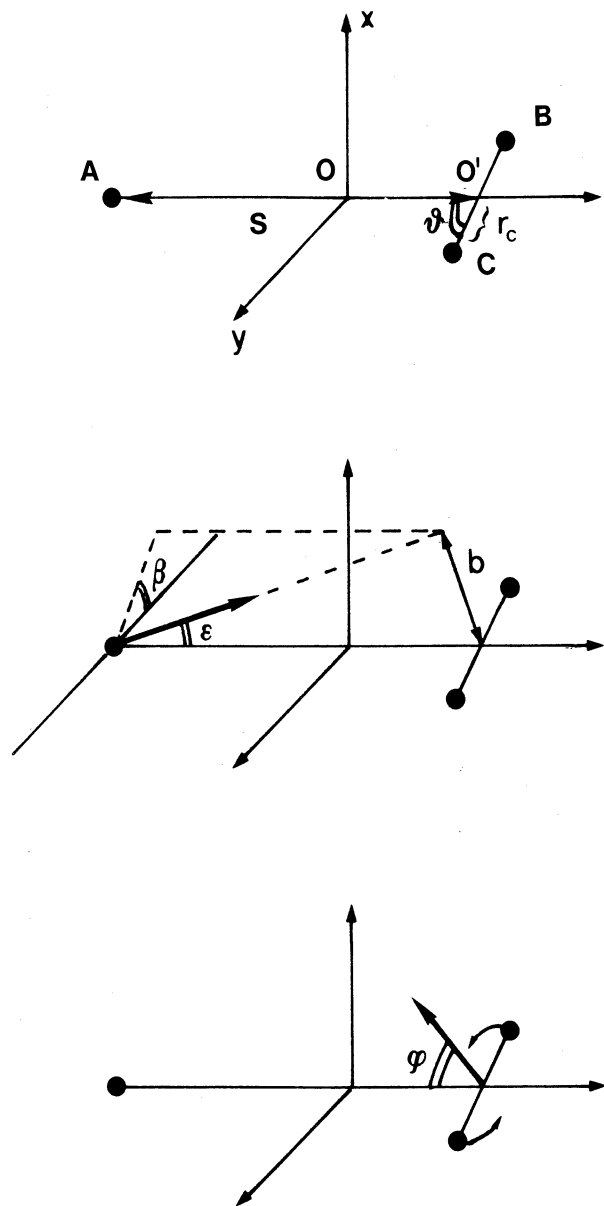


Figure 1. A schematic representation of quantities defining the initial conditions of the reactant atom diatom arrangement. Upper panel: quantities defining initial position vectors; Central panel: quantities defining the initial velocity vector; Lower panel: quantities defining the diatom rotational angular momentum.

Quasiclassical quantities

In a quasiclassical calculation collision properties are estimated by running a finite batch of trajectories. To this purpose initial conditions are chosen to simulate a real situation. Therefore, once that S has been taken sufficiently large and the initial collision, rotational and vibrational energies have been fixed, the remaining five initial conditions are selected randomly from a specified ensemble (Monte Carlo method⁸)

$$P_{vj,v'j'}(E_{tr}) = N^{-1} \int_0^{b_{max}} db^2 \int_0^\pi d\beta^o \int_{-1}^1 d\cos\theta^o \int_0^{2\pi} d\eta^o \int_0^{2\pi} d\phi^o f_{vj,v'j'}(b, \beta^o, \theta^o, \eta^o, \phi^o) \quad (10)$$

where N is the number of trajectories integrated starting with internal energy corresponding to that of the state vj . This function is a boolean function that is unity when the integer value of $j'_c + 1/2$ and $v'_c + 1/2$ obtained from the trajectory calculation are respectively equal to j' and v' . To perform the integral over a unit cube the following changes of variable are usually performed

$$\begin{aligned} \xi_1 &= b/b_{max} \\ \xi_2 &= \beta^o/\pi \\ \xi_3 &= (1 - \cos\theta^o)/2 \\ \xi_4 &= \phi^o/(2\pi) \\ \xi_5 &= \eta^o/(2\pi) \end{aligned} \quad (11)$$

where b_{max} is a value of the impact parameter large enough to ensure that no collision with $b > b_{max}$ leads to a reactive outcome. The value of b_{max} is usually determined by running trajectories on a grid of b values and examining the variation of the number of reactive trajectories as a function of b . The value of the detailed reactive cross section is then determined by using the formula

$$S_R^{vj,v'j'}(E_{tr}) = \pi b_{max}^2 P_{vj,v'j'}(E_{tr}) \quad (12)$$

Quite recently the detail of experimental measurements has led to the determination of properties of oriented and aligned target molecules.⁹ In this case, ϵ^o , β^o and θ^o are linked by a relationship.

More frequently, however, experimental quantities are less detailed than the state to state differential cross section and therefore a further averaging is required. In many gas kinetics studies, for example, what is actually needed is the temperature (T) dependent reactive rate constant which can be calculated using the following expression

$$k_{v,v'}(T) = \left(\frac{2}{kT}\right)^{3/2} \frac{e^{-E_v/kT}}{(\pi\mu_{A,BC})^{1/2} Q_{VR}(T)} \sum_{j=0}^{\infty} (2j+1) e^{-E_j/kT} \int_0^{\infty} dE_{tr} E_{tr} e^{-E_{tr}/kT} S_R^{vj,v'}(E_{tr}) \quad (13)$$

where k is Boltzmann's constant, $\mu_{A,BC}$ is the A, BC reduced mass, $S_R^{vj,v'}(E_{tr})$ is the degeneracy averaged detailed reaction cross section summed over final AB rotational states and $Q_{VR}(T)$ is the BC vib-rotational partition function.

The quantum approach

In a quantum approach, the reactive probability can be calculated by integrating equation (6) has using exact means. As already mentioned, this can be done by expanding the wavefunction Ξ in a suitable set of propagation and bound functions once that an appropriate reference frame and coordinate system have been adopted.

The Jacobi coordinates

The most obvious choice for formulating quantum scattering equations are the Jacobi coordinates. These coordinates are defined as

$$\mathbf{X}_\tau = \mathbf{W}_\tau - \frac{M_{\tau+1}\mathbf{W}_{\tau+1} + M_{\tau+2}\mathbf{W}_{\tau+2}}{M_{\tau+1} + M_{\tau+2}}$$

$$\mathbf{x}_\tau = \mathbf{W}_{\tau+1} + \mathbf{W}_{\tau+2} \quad (14)$$

being τ the label of the atom considered as isolated. For scattering calculations these physical coordinates are usually mass scaled

$$\mathbf{R}_\tau = d_\tau \mathbf{X}_\tau$$

$$\mathbf{r}_\tau = d_\tau^{-1} \mathbf{x}_\tau \quad (15)$$

where

$$d_\tau = \left[\frac{M_\tau}{\mu} \left(1 - \frac{M_\tau}{M} \right) \right]^{1/2} \quad (16)$$

and

$$M = M_A + M_B + M_C \quad (17)$$

$$\mu = \left[\frac{M_A M_B M_C}{M} \right]^{1/2} \quad (18)$$

An expansion of Ξ in terms of functions of Jacobi coordinates of the reactant arrangement is always appropriate for non reactive processes. On the contrary, for reactive processes the chemical system evolves in a way that at a given value of the reaction coordinate a switch from reactant to product arrangement coordinates has to be made. The transformation between different sets of mass scaled Jacobi coordinates are kinematic rotations

$$\begin{pmatrix} \mathbf{R}_\zeta \\ \mathbf{r}_\zeta \end{pmatrix} = \mathbf{T}(\chi_{\zeta,\tau}) \begin{pmatrix} \mathbf{R}_\tau \\ \mathbf{r}_\tau \end{pmatrix} \quad (19)$$

where \mathbf{T} is the rotation matrix

$$\mathbf{T}(\chi_{\zeta,\tau}) = \begin{pmatrix} \cos \chi_{\zeta,\tau} \mathbf{1} & \sin \chi_{\zeta,\tau} \mathbf{1} \\ -\sin \chi_{\zeta,\tau} \mathbf{1} & \cos \chi_{\zeta,\tau} \mathbf{1} \end{pmatrix} \quad (20)$$

and $\mathbf{1}$ is the 3×3 unit matrix. Being the Jacobi coordinates symmetric the kinematic angles are defined as

$$\cos \chi_{\tau+1,\tau} = -\frac{\mu}{d_\tau d_{\tau+1} M_{\tau+2}}$$

$$\sin \chi_{\tau+1,\tau} = -\frac{1}{d_\tau d_{\tau+1}} \quad (21)$$

The remaining values of the kinematic angles can be obtained from the following additional relationships

$$\chi_{\tau,\tau} = 0$$

$$\chi_{\tau,\zeta} = -\chi_{\zeta,\tau} \quad (22)$$

The scattering equations

Using mass scaled Jacobi coordinates the Hamiltonian of an atom-diatom system reads as

$$H_N = -\frac{\hbar^2}{2\mu} (\nabla_{R_\tau}^2 + \nabla_{r_\tau}^2) + V(R_\tau, r_\tau, \theta_\tau) \quad (23)$$

where θ_τ is the angle formed by the R_τ and r_τ .

To solve scattering equations the usual nuclear wavefunction having the form of an incident plane wave and of a set of outgoing scattered waves is expanded in a Space Fixed (SF) formalism:

$$\Xi(R_\tau, r_\tau, \theta_\tau) = \frac{2\pi}{k_i^{1/2}} \sum_{JMl_i} i^{l_i+1} C(j_i l_i J; m_i, M - m_i, M) Y_{l_i, M-m_i}^*(\hat{k}_i) \Psi^{JM\tau_i v_i j_i l_i} \quad (24)$$

where i is a composite index indicating initial state labels, C is the Clebsch-Gordan coefficient, J and M are the total angular momentum and its projection, k_i is the initial wavenumber (k_i^2 is $2\mu(E - E_{v_i j_i})/\hbar^2$, $E_{v_i j_i}$ is the initial vibrotational energy and k_f the analogue of k_i for the final state $v_f j_f$).

The wavefunction Ψ of equation (24) can be expanded as

$$\begin{aligned} \Psi^{JM\tau_i v_i j_i l_i} = & \sum_{\tau_f v_f j_f l_f} \frac{1}{R_{\tau_f} r_{\tau_f}} G_{\tau_f v_f j_f l_f}^{J\tau_i v_i j_i l_i}(R_{\tau_f}) F_{v_f j_f l_f}(r_{\tau_f}) \sum_{m_f} C(j_f l_f J; m_f, M - m_f, M) \\ & Y_{j_f, m_f}(\hat{r}_{\tau_f}) Y_{l_f, M-m_f}(\hat{R}_{\tau_f}) \end{aligned} \quad (25)$$

The radial functions G satisfy the usual boundary conditions

$$G_{\tau_f v_f j_f l_f}^{J\tau_i v_i j_i l_i} \sim \frac{1}{k_f^{1/2}} [\delta_{\tau_f \tau_i} \delta_{v_f v_i} \delta_{j_f j_i} \delta_{l_f l_i} e^{-i(k_f R_{\tau_f} - \frac{\pi}{2} l_f)} - S_{\tau_f v_f j_f l_f, \tau_i v_i j_i l_i}^J e^{i(k_f R_{\tau_f} - \frac{\pi}{2} l_f)}] \quad (26)$$

where S^J is the scattering matrix from which the differential cross section $\sigma_R^{\tau_i v_i j_i l_i, \tau_f v_f j_f l_f}$

$$\sigma_R^{\tau_i v_i j_i m_i, \tau_f v_f j_f m_f}(k_i, k_f, \hat{k}_i, \hat{R}_f) = \left| \frac{2\pi}{k_i} \sum_{JMl_i l_f} i^{l_i-l_f+1} A_i A_f T_{\tau_f v_f j_f l_f, \tau_i v_i j_i l_i}^J \right|^2 \quad (27)$$

where

$$T_{\tau_f v_f j_f l_f, \tau_i v_i j_i l_i}^J = \delta_{\tau_f \tau_i} \delta_{v_f v_i} \delta_{j_f j_i} \delta_{l_f l_i} - S_{\tau_f v_f j_f l_f, \tau_i v_i j_i l_i}^J \quad (28)$$

and

$$\begin{aligned} A_i &= C(j_i l_i J; m_i, M - m_i, M) Y_{l_i, M-m_i}^*(\hat{k}_i) \\ A_f &= C(j_f l_f J; m_f, M - m_f, M) Y_{l_f, M-m_f}(\hat{R}_{\tau_f}) \end{aligned}$$

is obtained. By averaging over m_j and integrating over all outgoing angles (θ_f and ϕ_f) one obtains the integral cross section

$$S_R^{v_i j_i v' j'}(E) = \frac{1}{2j+1} \sum_{m_i m_f} \int_{-1}^1 d\cos\theta_f \int_0^{2\pi} d\phi_f \sigma_R^{\tau_i v_i j_i m_i, \tau_f v_f j_f m_f}(k_i, k_f, \hat{k}_i, \hat{R}_f) \quad (29)$$

At intermediate and short distances the Body Frame (BF) formalism is often more conveniently used. In a BF frame the nuclear Hamiltonian reads in mass scaled Jacobi coordinates

$$H_N = -\frac{\hbar^2}{2\mu} \left(\frac{1}{R_\tau} \frac{\partial^2}{\partial R_\tau^2} R_\tau + \frac{1}{r_\tau} \frac{\partial^2}{\partial r_\tau^2} r_\tau - \frac{\mathbf{L}_\tau^2}{R_\tau^2} - \frac{\mathbf{J}_\tau^2}{r_\tau^2} \right) + V(R_\tau, r_\tau, \theta_\tau) - E \quad (30)$$

where \mathbf{J}_τ are the rotational and \mathbf{L}_τ the orbital angular momentum operators respectively (by introducing the total angular momentum conservation \mathbf{L}_τ can be eliminated). The transformation between SF and BF coordinate frames is an ordinary spatial rotation

$$\begin{pmatrix} \mathbf{R}_\tau^{BF} \\ \mathbf{r}_\tau^{BF} \end{pmatrix} = \mathbf{R}_{BF, SF} \begin{pmatrix} \mathbf{R}_\tau^{SF} \\ \mathbf{r}_\tau^{SF} \end{pmatrix} \quad (31)$$

where the matrix $\mathbf{R}_{BF,SF}$ has the form

$$\mathbf{R}_{BF,SF} = \begin{pmatrix} \mathbf{R} & \mathbf{0} \\ \mathbf{0} & \mathbf{R} \end{pmatrix} \quad (32)$$

being the matrix \mathbf{R} defined as

$$\begin{pmatrix} \cos \alpha \cos \beta \cos \gamma - \sin \alpha \sin \gamma & \sin \alpha \cos \beta \cos \gamma + \cos \alpha \sin \gamma & -\sin \beta \cos \gamma \\ -\cos \alpha \cos \beta \sin \gamma - \sin \alpha \cos \gamma & -\sin \alpha \cos \beta \sin \gamma + \cos \alpha \cos \gamma & \sin \beta \sin \gamma \\ \cos \alpha \sin \beta & \sin \alpha \sin \beta & \cos \beta \end{pmatrix} \quad (33)$$

(α , β and γ are the three Euler angles of the $SF \rightarrow BF$ transformation).

Transformation between SF and BF radial wavefunctions are well known.¹⁰ Sometimes, to avoid confusion between different BF axes mixed functions with SF initial and BF final labels are used.¹¹ In these cases the Ψ function is expressed as

$$\Psi^{JM\tau_i v_i j_i l_i} = \sum_{\tau_f v_f j_f \Lambda_f} \frac{1}{R_{\tau_f} r_{\tau_f}} G_{\tau_f v_f j_f \Lambda_f}^{J\tau_i v_i j_i l_i}(R_{\tau_f}) F_{v_f j_f}(r_{\tau_f}) \hat{P}_{j_f \Lambda_f}(\theta_f) \hat{D}_{\Lambda_f M}^J(\alpha_f, \beta_f, \gamma_f) \quad (34)$$

where

$$G_{\tau_f v_f j_f \Lambda_f}^{J\tau_i v_i j_i l_i}(R_{\tau_f}) = \sum_{l_f} \left(\frac{2l_f + 1}{2J + 1} \right)^{1/2} C(j_f l_f J; \Lambda_f 0 \Lambda_f) G_{\tau_f v_f j_f l_f}^{J\tau_i v_i j_i l_i}(R_{\tau_f}) \quad (35)$$

Two mathematical dimension approximations

To integrate the scattering equations formulated using Jacobi coordinates one has to define somewhere in the strong interaction region a separating surface at which perform a kinematic rotation of the Jacobi coordinates and a matching of the propagated solutions. This is a difficult problem for a generic $A + BC$ system because no symmetry argument can be invoked to define a separating surface having the same characteristics on both reactant and product sides. Therefore, one is left with the problem either of choosing a different set of coordinates allowing a simultaneous representation of all arrangement channels (such as hyperspherical coordinates; see next section) or of introducing approximations. The latter approach is followed when a reduction of the dimensionality of the problem is made by forcing appropriate physical constraints onto the system dynamics. This means, for two mathematical dimension approaches, a collapse of the matching surface into a line.

A popular two mathematical dimension method is the Infinite Order Sudden (IOS) approximation. In the IOS formalism the application of both the energy sudden and the centrifugal sudden decoupling schemes¹² reduces the scattering equations to a set of fixed angle of collision (θ_τ) two mathematical dimension differential equations. In the Body Fixed formulation these equations read as:

$$\left[-\frac{\hbar^2}{2\mu} \left(\frac{1}{R_\tau} \frac{\partial^2}{\partial R_\tau^2} R_\tau + \frac{1}{r_\tau} \frac{\partial^2}{\partial r_\tau^2} r_\tau - \frac{A_\tau}{R_\tau^2} - \frac{B_\tau}{r_\tau^2} \right) + V(R_\tau, r_\tau; \theta_\tau) - E \right] \Xi(R_\tau, r_\tau; \theta_\tau) = 0 \quad (36)$$

where $A_\tau = l_\tau(l_\tau + 1)$ and $B_\tau = j_\tau(j_\tau + 1)$ being l_τ and j_τ the orbital and rotational quantum numbers of the arrangement τ .

For each value of θ_τ the (R_τ, r_τ) plane is divided into two regions by a straight line originating at $R_\tau = r_\tau = 0$ and following the ridge in the region where the two channels separate. Such a choice makes unique the correspondence between θ_α (reactants') and θ_β (products') and ensures a correct matching between reactant and product channels. To integrate equations (36) the two channels are segmented into many small sectors. Inside each sector i , the global wavefunction $\Xi(R_\tau, r_\tau; \theta_\tau)$ is expanded as the sum of NV products of two terms: A propagation $\psi_{irv}(R_\tau; \theta_\tau)$ and a bound $\phi_{irv}(r_\tau; R_\tau^i, \theta_\tau)$ local functions. The value of NV is chosen large enough to include for any sector all open plus a few (lower) closed channels. The vibrational functions $\phi_{irv}(r_\tau; R_\tau^i, \theta_\tau)$ are calculated at the sector midpoint value (R_τ^i) of the propagation coordinate R_τ . To this purpose the one dimensional bound state problem

$$\left[-\frac{\hbar^2}{2\mu} \frac{\partial^2}{\partial r_\tau^2} + V(r_\tau; R_\tau^i, \theta_\tau) - E_{\tau v}^i \right] \phi_{\tau v}^i(r_\tau; R_\tau^i, \theta_\tau) = 0 \quad (37)$$

is solved using a numerical technique.¹³

At each value of θ_τ equations (36) are solved by premultiplying both their lhs and rhs terms by $\phi_{\tau v'}^*(r_\tau; R_\tau^i)$ and averaging over r_τ . In this way one obtains a set of fixed energy coupled differential equations of the type

$$\left[\frac{d^2}{dR_\tau^2} - D_\tau^i \right] \psi_{\tau v}(R_\tau; \theta_\tau) = 0 \quad (38)$$

where D_τ^i is the coupling matrix. To obtain a smooth evolution from the reactant to the product arrangement situation in the short range part of each channel use is made of circular coordinates u_τ and w_τ . In fact, the bound circular coordinates of the two half-channels (w_α and w_β) coincide at the intermediate line apart from an origin shift. The introduction of the circular coordinates has little effect on the complexity of the calculation. Its impact on the computational procedure is mainly relevant to the construction of the D matrix elements. Finally, equations (38) are integrated from the origin to reactant and product asymptotes. A matching of the solutions is imposed at the separatrix while at the asymptotes the appropriate boundary conditions¹⁴ are imposed. In this way the detailed IOS fixed θ_i S matrix elements ($S_{v l, v'}(\theta_i, E)$) for the reactive process can be derived. From these values the vibrational state (v) to state (v') reactive cross section ($S_R^{v, v'}(E)$) can be calculated using the relationship

$$S_R^{v, v'}(E) = \frac{\pi}{k_{v j}^2} \sum_l (2l+1) \int_{-1}^1 |S_{v l, v'}(\theta_i, E)|^2 d \cos \theta \quad (39)$$

by assuming, as usual, $j = 0$.

Another popular two mathematical dimension approach is based on the formalism of the Rotating Linear Model (RLM) and its Bending Corrected (BCRLM) version.¹⁵ In the BCRLM approach the equations to be integrated are

$$\left[-\frac{\hbar^2}{2\mu} \left(\frac{1}{\eta^2} \frac{\partial^2}{\partial u^2} + \frac{1}{\eta} \frac{\partial}{\partial \nu} \eta \frac{\partial}{\partial \nu} - \frac{l(l+1)+1}{\rho^2} \right) + V(\gamma_\alpha = 180^\circ; u, \nu) - E^{BC} \right] \Phi(u, \nu) = 0 \quad (40)$$

where u and ν are natural coordinates, $\rho = (R_\alpha^2 + r_\alpha^2)^{1/2}$, $\eta = 1 + \nu \sigma(u)$ (σ is the inverse radius of the local curvature) and E^{BC} is the total energy subtracted of the amount lodged in the (adiabatically evolving) bending motion.¹⁵ Once performed in the usual way a partial wave expansion, the resulting coupled differential equations have the same form of equations (38) provided that E^{BC} is estimated at each step of the integration. After performing the propagation of the solution from the central line to large R_λ values, using the same computational machinery of the IOS program, detailed BCRLM S matrix elements ($S_{v l, v'}$) of the reactive process can be derived by applying the appropriate asymptotic conditions.¹⁵ The reactive cross section $S_R^{v, v'}(E)$ can then be obtained using the relationship

$$S_R^{v, v'}(E) = \frac{\pi}{k_v^2} \sum_l (2l+1) |S_{v l, v'}(E)|^2 \quad (41)$$

Finally the detailed reactive rate constants $k_{v v'}(T)$ can be calculated from the following equation

$$k_{v v'}(T) = N \left[\frac{8}{k_B^3 T^3 \pi \mu} \right]^{\frac{1}{2}} \int_0^\infty S_R^{v, v'}(E_{tr}) e^{-E_{tr}/k_B T} dE_{tr} \quad (42)$$

where N is Avogadro's number.

A particularly simple two mathematical dimension approach is the collinear one which can be derived either from the IOS method by setting $l = j = \cos \theta_r = 0$ or from the BCRLM method by setting the bending and rotaional energy equal to zero.

Hyperspherical coordinates

Several authors have worked out scattering equations using hyperspherical coordinates to avoid the problem of defining a matching surface in the strong interaction region.¹⁶ The first hyperspherical calculations ever reported for a generic three different atom system¹⁷ are based on hyperspherical coordinates derived as polar representations of Adiabatically adjusting Principal axes of inertia (AP) coordinates Q and q ¹¹. The AP coordinates result from the kinematic rotation of R_r and r_r which maximizes Q (and minimizes q) and force them to lie along the principal axes of inertia. These hyperspherical (APH) coordinates, which are defined as

$$\begin{aligned}\rho^2 &= Q^2 + q^2 \\ \theta &= \frac{\pi}{2} - 2 \arctan q/Q\end{aligned}\quad (43)$$

provide with the other angle χ_r a suitable set of internal coordinates for formulating scattering equations. APH coordinates are related to Jacobi coordinates by simple relationships.¹¹

In APH coordinates the Hamiltonian reads as

$$H_N = T_\rho + T_h + T_r + T_c + V(\rho, \theta, \chi_i) \quad (44)$$

where

$$T_\rho = -\frac{\hbar^2}{2\mu\rho^5} \frac{\partial}{\partial\rho} \rho^5 \frac{\partial}{\partial\rho} \quad (45)$$

$$T_h = -\frac{\hbar^2}{2\mu\rho^5} \left(\frac{4}{\sin 2\theta} \frac{\partial}{\partial\theta} \sin 2\theta \frac{\partial}{\partial\theta} + \frac{1}{\sin^2\theta} \frac{\partial^2}{\partial\chi_i^2} \right) \quad (46)$$

$$T_r = AJ_x^2 + BJ_y^2 + CJ_z^2 \quad (47)$$

$$T_c = \frac{i\hbar \cos\theta}{\mu\rho^2 \sin 2\theta} J_y \frac{\partial}{\partial\chi_i} \quad (48)$$

being

$$\begin{aligned}A(\rho, \theta) &= \frac{1}{\mu\rho^2(1 + \sin\theta)} \\ B(\rho, \theta) &= \frac{1}{2\mu\rho^2 \sin^2\theta} \\ C(\rho, \theta) &= \frac{1}{\mu\rho^2(1 - \sin\theta)}\end{aligned}\quad (49)$$

Such an Hamiltonian, although more complex than the one written in Jacobi coordinates, is simpler than those obtained when using other curvilinear coordinates. To solve the Schrödinger equation the ρ interval is segmented into a large number of small sectors starting from the origin. Within each sector i the APH wavefunction Ψ is expanded as

$$\Psi^{JMpn} = 4 \sum_{t\Lambda} \rho^{-5/2} \psi_{t\Lambda}^{Jpn}(\rho) \phi_{t\Lambda}^{Jp}(\theta, \chi_i; \rho^i) \hat{D}_{\Lambda M}^{Jp}(\alpha_Q, \beta_Q, \gamma_Q) \quad (50)$$

where $\hat{D}_{\Lambda M}^{Jp}(\alpha_Q, \beta_Q, \gamma_Q)$ are the normalized Wigner functions

$$\hat{D}_{\Lambda M}^{Jp}(\alpha_Q, \beta_Q, \gamma_Q) = \left[\frac{2J+1}{16\pi^2(1 + \delta_{\Lambda 0})} \right]^{1/2} [D_{\Lambda M}^J(\alpha_Q, \beta_Q, \gamma_Q) + (-1)^{J+\Lambda+p} D_{\Lambda M}^J(\alpha_Q, \beta_Q, \gamma_Q)] \quad (51)$$

In expansion (50) the ψ s are functions of the reaction coordinate ρ while functions ϕ are chosen to satisfy the two dimensional differential equation

$$\left[-\frac{\hbar^2}{2\mu(\rho^i)^2} \left(\frac{4}{\sin 2\theta} \frac{\partial}{\partial \theta} \sin 2\theta \frac{\partial}{\partial \theta} + \frac{1}{\sin^2 \theta} \frac{\partial^2}{\partial \chi_i^2} \right) + \frac{A+B}{2} \hbar^2 J(J+1) + \frac{15\hbar^2}{8\mu(\rho^i)^2} \right. \\ \left. + \frac{2C-A-B}{2} \hbar^2 \Lambda^2 + V(\rho^i, \theta, \chi_i) + E_{t\Lambda}^{Jp}(\rho^i) \right] \phi_{t\Lambda}^{Jp}(\theta, \chi_i; \rho^i) = 0 \quad (52)$$

By inserting such an expansion into the scattering equations one obtains the following set of coupled differential equations in ρ

$$\left[\frac{\partial^2}{\partial \rho^2} + \frac{2\mu E}{\hbar^2} \right] \psi_{t\Lambda}^{Jpn}(\rho) = \frac{2\mu}{\hbar^2} \sum_{t'\Lambda'} < \phi_{t\Lambda}^{Jp} \hat{D}_{\Lambda M}^{Jp} | H_i | \phi_{t'\Lambda'}^{Jp} \hat{D}_{\Lambda' M'}^{Jp} > \psi_{t'\Lambda'}^{Jpn}(\rho) \quad (53)$$

where

$$H_i = T_h + T_r + T_c + \frac{15\hbar^2}{8\mu\rho^2} + V(\rho, \theta, \chi_i) \quad (54)$$

At reasonable large ρ values it is more practical to reformulate the scattering equations in terms of Jacobi coordinates. In Jacobi coordinates, in fact, the different reaction channels are well separated and coupling between different surface functions goes to zero at shorter distances. To simplify the procedure, the transformation from APH to Jacobi coordinates is performed in two steps. In a first step a conversion from symmetric to asymmetric hyperspherical coordinate (of the appropriate arrangement) formalism is performed. In the second step the solution is mapped into related Jacobian coordinates.

CALCULATION OF NON-EQUILIBRIUM EFFECTS

In principle, theoretical approaches outlined in the previous section can be implemented on any mainframe. However, when extended calculations of scattering quantities for an atom-diatom reactive system are needed, modern supercomputers having vector and parallel features need to be used to greatly reduce the necessary computing time.¹⁸ The large saving of computer time obtained because of the restructuring has eased massive calculations of non-equilibrium effects for some prototype atom-diatom systems. On the theoretical side these calculations allow to gain insights into relationships tieing reactants' and products' energy distributions to the main features of the potential energy surface. To this purpose, collision properties are calculated for extended ranges of collision and internal energy as well as for quite different energy partitionings between vibrational, rotational and translational motions of the system. From the same calculations it is possible to estimate how a variation of the reactant energy partitioning can influence product properties (final population of vibrational and rotational states, branching ratios, energy and angular distributions, alignment and orientation properties, ...).

The feasibility of massive calculations leads also to practical advantages such as the possibility of understanding the outcome of several gas phase experiments and of estimating quantities difficult to measure. This is particularly useful when modeling chemical plasmas for some modern technological applications. In the following we shall discuss the case of some elementary processes of interest for the design of H^- sources and $XeCl$ lasers.

The $H + H_2$ system

It is well known that the production of H^- ions in magnetic multicusp H_2 discharges occurs through a dissociative attachment of electrons onto vibrationally excited hydrogen molecules.² Therefore, when modeling such a source competition from processes deexciting vibrationally excited hydrogen molecules has to be considered. Deexcitation of vibrationally excited hydrogen molecules can occur by collision with electrons, hydrogen atoms, hydrogen molecules and walls.

Being our attention focussed on atom diatom processes, we shall discuss in some detail only the $H + H_2$ reaction and its isotopic variants. The hydrogen atom hydrogen molecule system has been in the past investigated using a variety of theoretical

methods.¹⁹ Converged close coupling three dimensional calculations have been performed up to total energy of 0.7 eV. The main goal of these calculations was however the investigation of low energy reactivity to provide a benchmark for approximate treatments. Exact methods, in fact, are unviable at the energies at which vibrational excitations and deexcitations occur in a H^- source because of their large memory and computing time demand. For this reason, our calculations were performed by making use of 3D quasiclassical and reduced dimensionality quantum computational procedures implemented on supercomputers (the Cray XMP and 48 at Cineca)

Collinear calculations

As is well known $H + H_2$ is an ideal system for quantum calculations because of the large spacing of its vibrational states and the full nuclear and electronic symmetry. A first investigation was performed using the collinear quantum method. The potential energy surface used for the calculations (LSTH) was the one fitted by Truhlar and Horowitz²⁰ to the *ab initio* points of Liu and Siegbahn.²¹ Preliminary results were reported in ref. 22 by plotting the detailed collinear probabilities as a function of the collision energy. Here, we report in the left panels of figure (2) some collinear reactive rate constants ($v=1, 4$ and 7) of the $H + H_2$ reaction by plotting their logarithm as a function of the product vibrational number v' .

Obviously, collinear rate constants have not the proper dimensionality the right to compare with the experiment. Their plots, therefore, can be only used for a qualitative discussion of the vibrational excitation and deexcitation properties of the $H + H_2$ system. As apparent from the figure, at low temperature (lower panel) the most efficient reactive process is the adiabatic conservation of the reactant vibrational number while the efficiency of excitation and deexcitation processes decreases with the vibrational jump Δ ($\Delta = v' - v$).

At the lowest temperature (300 K) the value of the rate constant decreases slowly with v' for deexcitation processes while it sharply falls to zero for excitation processes. By increasing the temperature (central and upper panels show results for $T=1000$ K and 4000 K respectively) collisions leading to a conservation of the reactant vibrational number are still the most efficient processes. However, when the temperature increases, the efficiency of excitation processes increases dramatically. Such a behaviour seems to suggest that there may be a temperature at which excitation effects balance deexcitation effects. Such a conclusion, however, by no means can be considered as definitive (see next sections) because of the severe dynamical constraints built-in into the collinear model that channels internal energy exclusively into vibrations acting along the same direction as translation.

In the right panels of figure (2) are reported corresponding non-reactive collinear rate constants calculated at the same temperatures of reactive results. The collinearity constraint makes a comparison of these results with the experiment even less appropriate than for the reactive case. In fact, while the collinearity of the minimum energy path to reaction makes collinear calculations realistic for reactive events, there is no reason for excluding non reactive processes occurring with the three atoms aligned. Nonetheless, collinear results may still be taken as a rough approximation to non reactive three dimensional rate constants by introducing a steric factor. As a matter of facts, the behaviour of non-reactive collinear rate constants is similar to that of reactive ones. The similarity of the two results is so high to suggest the possibility of interpolating them by means of a unified model functional parametrically dependent on initial and final vibrational numbers. The figure suggests also that in both cases a suitable parametrization can be obtained in terms of Δ .

Approximate three-dimensional calculations

To obtain a more accurate estimate of the rate constant values we repeated the calculations using techniques including the approximate treatment of the system rotations. To this purpose we have performed BCRLM and quasiclassical calculations at the same temperatures used for collinear calculations. The BCRLM calculations were performed by assuming the translational motion to be thermalized at a given temperature T (no correction for the thermalization of the reactants' rotations was included).

Preliminary estimates of the BCRLM rate constants have already been reported

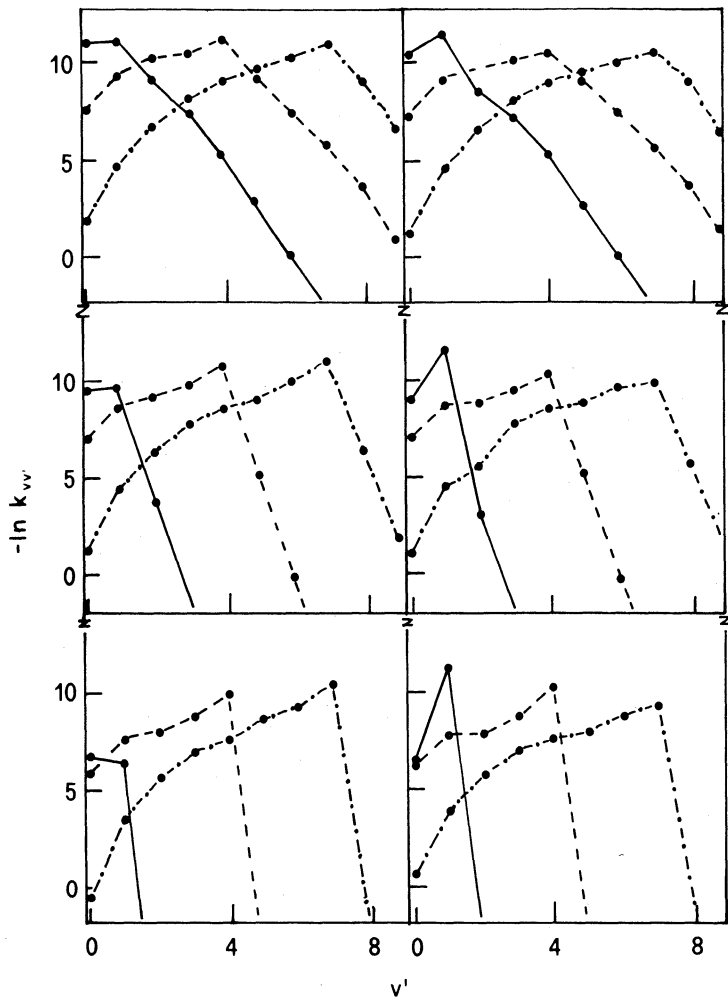


Figure 2. Logarithm of reactive (left panels) and non-reactive (right panels) quantum collinear vibrational state (v) to state (v') rate constants (in $\text{cm molecule}^{-1}\text{s}^{-1}$) of the reaction $H + H_2$ plotted as a function of v' for $v = 1$ (solid line), $v = 4$ (dashed line) and $v = 7$ (dashed-dotted line) at $T=300\text{ K}$ (lower panels), 1000 K (central panels) and 4000 K (upper panels). Calculated values are indicated by solid circles. Connecting lines have been drawn for aim of clarity.

in refs. 22-24. Here we show in figure (3) detailed BCRLM rate constants for $v=1, 4$ and 7 reporting as for the collinear case reactive results in the left panels and non reactive ones in the right panels. Features of the non-reactive rate constant plots are similar to those of collinear calculations. The most efficient process (largely more efficient than all others when compared with collinear results) are elastic collisions. Rate constants decrease smoothly for deexcitation processes (more smoothly than for collinear results) while those for excitation processes still drop dramatically when v' increases. As in the collinear case the BCRLM rate constant cannot be considered for comparison with the experiment because dynamical constraints introduced by the model can be too severe for simulating non reactive collisions. For the reactive case deviations from collinear results are evident when comparing the values of deexcitation processes. In fact, the rate constant for deexcitation to next lower states is so high that there is little difference with the value of the rate constant for processes conserving the vibrational number. This is likely to be due to the inclusion in the model (although only partial) of the deviation from collinearity.

As already mentioned, at high energies only a quasiclassical procedure is viable to deal with the full dimensionality of the problem and the coupling of different types of motion. For this reason, we ran on the same surface quasiclassical calculations for the $H + H_2$ system with v ranging from 1 to 9. To obtain a significant number of reactive trajectories the b parameter was limited to 2 \AA and batches of 4000 trajectories were used. For highly excited reactants this b_{max} value can lead to an error of 20% in the calculated rate constant. Features of the BCRLM results which are confirmed by quasiclassical calculations are the exceptional efficiency of processes conserving the initial vibrational number (though in a quasiclassical approach the absolute value of the elastic quasiclassical rate constant is meaningless) and the sharp decrease of excitation rate constants with v' .

In agreement with BCRLM results, quasiclassical deexcitation rate constants vary quite smoothly when plotted versus v' . This further proves that an appropriate inclusion of the system rotations (in addition to vibration) makes quite efficient large Δ deexcitations. As a result, the possibility of obtaining a compensation between deexcitation and excitation effects when increasing the temperature is quite remote.

An important feature of quasiclassical results is the fact that rate constants for non reactive processes are not distorted by the imposition of arbitrary dynamical constraints invoked to facilitate the calculation of the reactive events. Therefore, the fact that non reactive deexcitation rate constants are smaller than reactive ones confirms that reaction is the most effective way for deexciting vibrationally excited H_2 molecules.

Isotope and temperature effects

A first important question on how the variation of the system parameters alters the dynamical outcome of the $H + H_2$ reaction has been investigated by studying the isotopic variants of the $H + H_2$ reaction. To this purpose quasiclassical calculations have been performed for the $D + D_2$ reaction at $v=2, 8$ and 14 (these states are approximately isoenergetic with $v=1, 5$ and 9 of the $H + H_2$ system). Results of these calculations performed at $T=500 \text{ K}$ are shown in the left panels of figure (5) where values calculated for the hydrogen atom hydrogen molecules system are also plotted. As shown in the figure values calculated for the two systems are almost identical once that a scaling for the different reduced mass is performed.

Another question important for practical applications is how the system behaviour changes when the collisional temperature (T_{tr}) differs from the rotational temperature (T_{rot}). For this reason we performed quasiclassical calculations by cooling the rotational temperature down to 500 K while keeping T_{tr} at its highest value (4000 K). Results are reported in figure (6) by plotting the rate constant values of $H + H_2$ for reactive excitation to the next (higher) v value as a function of v' .

As shown in the figure where values calculated at $T_{tr} = T_{rot}=4000 \text{ K}$ and $T_{tr} = T_{rot}=500 \text{ K}$ for the $H + H_2$ system are also reported for comparison, an increase of the collisional temperature is far more effective than an increase in rotational temperature. In particular, the effect of increasing the translational temperature while keeping the rotational temperature cold leads to rate constants similar to that of processes occurring at $T_{tr} = T_{rot}=4000 \text{ K}$. The similarity between the two curves indicates that, in gen-

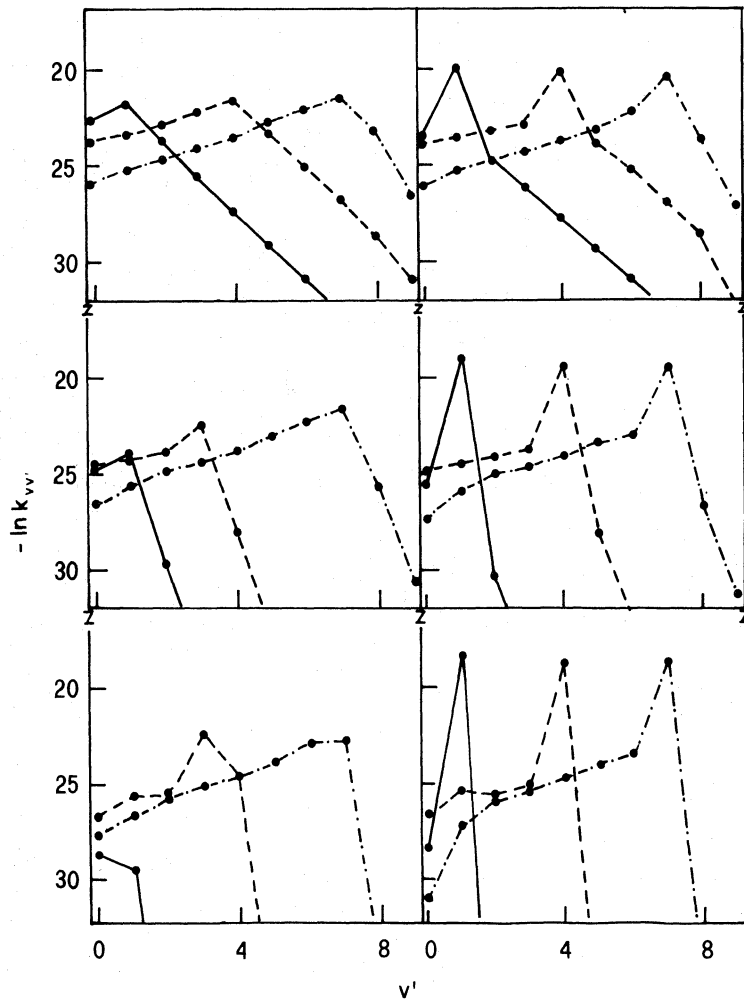


Figure 3. As in figure (2) for BCRLM quantum rate constants (in $\text{cm}^3 \text{molecule}^{-1} \text{s}^{-1}$)

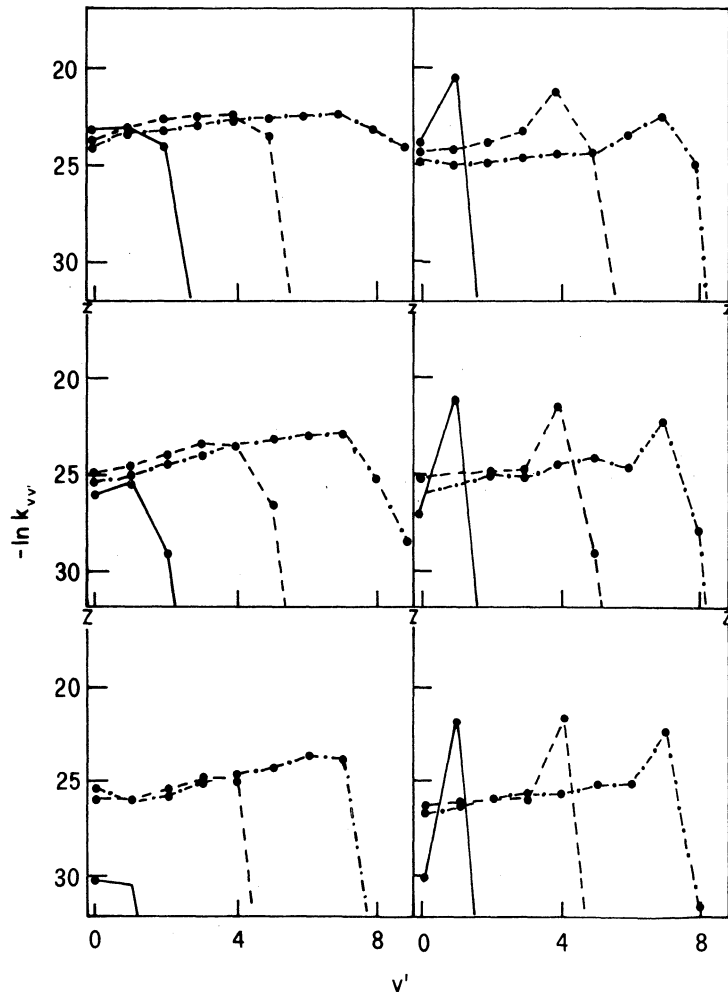


Figure 4. As in figure (2) for 3D quasiclassical rate constants (in $\text{cm}^3\text{molecule}^{-1}\text{s}^{-1}$)

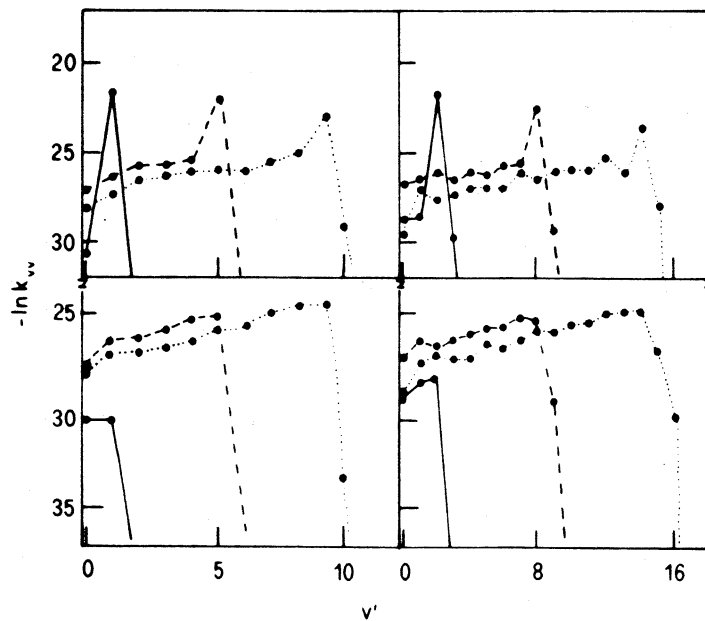


Figure 5. Logarithm of non-reactive (upper panels) and reactive (lower panels) quasi-classical vibrational state (v) to state (v') rate constants (in $\text{cm}^3 \text{molecule}^{-1} \text{s}^{-1}$) of the reactions $H + H_2$ (left panels) and $D + D_2$ (right panels) at $T=500$ K plotted as a function of v' . For the H reaction $v = 1$ (solid line), $v = 5$ (dashed line) and $v = 9$ (dotted line) have been considered. For the D reaction $v = 2$ (solid line), $v = 8$ (dashed line) and $v = 14$ (dotted line) have been considered. Calculated values are indicated by solid circles. Connecting lines have been drawn for aim of clarity.

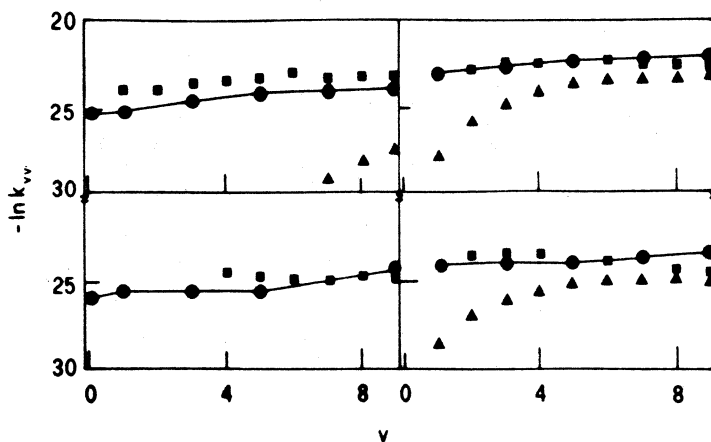


Figure 6. Logarithm of reactive (upper panels) and non-reactive (lower panels) quasi-classical rate constants (in $\text{cm}^3 \text{molecule}^{-1} \text{s}^{-1}$) for excitation to the next higher (left panels) and deexcitation to the next lower (right panels) vibrational state of the $H + H_2$ reaction plotted as a function of v . Values calculated at $T_{tr}=4000$ K and $T_{rot}=500$ K (solid line) are compared with those obtained at $T_{tr} = T_{rot}=500$ K (triangles) and $T_{tr} = T_{rot}=4000$ K (squares). Connecting lines have been drawn for aim of clarity.

eral, an increase of the translational temperature is the main responsible for a higher efficiency of excitation and deexcitation for both reactive and non-reactive processes.

The reaction of HCl with H and Cl

The $XeCl$ laser system is made of a mixture of Ne , Xe and HCl at a pressure of 4 atmospheres.³ The overall mechanism of a $XeCl$ laser is rather complex but it is now well understood that the key step is the formation of the excimer ($XeCl^*$). The vibrationally excited excimer can be obtained either when Xe^+ recombines in a three body collision with Cl^- or when Xe^* harpoons the Cl atom out of a molecule containing it. This means that the efficiency of the production of XCl molecule (where X can be an atomic or molecular species) in a suitable internal energy condition is crucial for the optimization of an excimer laser. The Cl^- ion, in fact, is usually produced by a dissociative electron attachment to a molecule containing Cl . The HCl molecule is used as a source of Cl atoms to minimize the absorption of laser frequencies.³ The electron attachment is more efficient when the HCl molecule is vibrationally excited. Vibrational deexcitation of the HCl molecule by collisions with H and Cl atoms formed during the complex kinetics of the rare gas HCl mixture are therefore competing processes.

Collinear calculations for the $H + HCl$ and $H + ClH$ reactions

As for the $H + H_2$ reaction a preliminary investigation was carried out using the collinear quantum method. The potential energy surface used for the calculations is the DIM PES of Last and Baer.²⁵ A first question to answer to is whether the reaction occurs through abstraction ($H + HCl \rightarrow H_2 + Cl$) or exchange ($H + ClH \rightarrow HCl + H$) and which of them is the most efficient process in vibrationally deexciting HCl .

Experimental data available for the $D + HCl$ reaction indicate a large difference between the values of the rate constants for the abstraction and exchange processes. The characteristics of the stationary points of the PES (the minimum energy path is collinear for both processes) suggest that an assessment of what is the most effective deexcitation process can be performed using a collinear quantum approach. These calculations have been performed as for $H + H_2$ on a Cray XMP. Values of total energy were scanned in step of 0.02 eV up to a maximum value of 1.7 eV (this means that the first five vibrational states have been considered). From calculated probabilities collinear rate constants were estimated. Preliminary indications on the effect of vibrationally exciting reactants were reported in ref. 26. In figure (7) reactive and non reactive rate constants for reagents in the first excited vibrational state are reported. The upper panel shows results for the reaction $H + HCl \rightarrow H_2 + Cl$ while results for the reaction $H + ClH \rightarrow HCl + H$ are reported in the lower panel. As shown by the figure rate constants for processes conserving the initial value of the vibrational number are largely more efficient than deexcitation processes although of different nature (non reactive in the first case, reactive in the second). The less efficient process seems to be the formation of H_2 .

The approximate 3D calculations

More accurate calculations have been performed using both the IOS and quasiclassical trajectory techniques on an IBM 3090 at CNUCE and CNUSC. The IOS calculations have been carried out at low energies (so as to include mainly the $v=0$ case only) for values of the angle of approach ranging from 180° to 90° . Some of the calculated fixed angle probabilities are plotted in the upper panel of figure (8) as a function of the collision energy. The corresponding reactive cross section is plotted in the lower panel. As expected, the increase of the reaction cross section with energy depends not only from the rise of the fixed angle reaction probability with energy but also from the opening of the reactive cone. The threshold to reaction can be located slightly below 2 kcal/mol while the cross section shows a kind of plateau starting from E_{tr} around 6 kcal/mol. Around this energy excitation to the first excited state begins to be appreciable.

To obtain accurate estimates of deexcitation effects due also to non reactive processes we have also carried out quasiclassical 3D calculations. For these calculations the

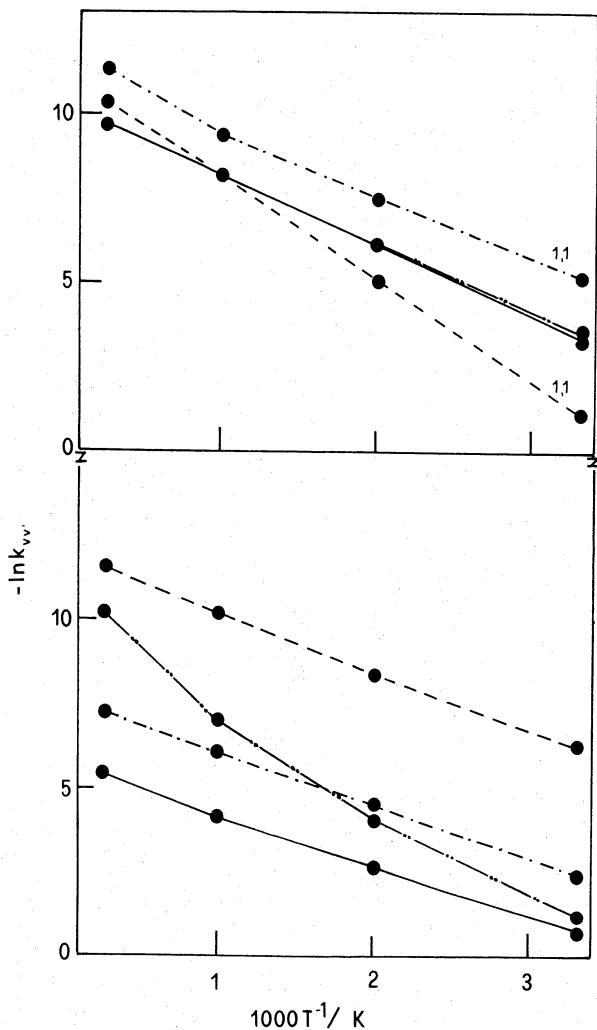


Figure 7. Logarithm of non-reactive ($v = 1, v' = 1$ dashed-dotted lines and $v = 1, v' = 0$ solid lines) and reactive ($v = 1, v' = 1$ dashed lines and $v = 1, v' = 0$ dashed-double-dotted lines) collinear quantum rate constants (in $\text{cm}^3 \text{molecule}^{-1} \text{s}^{-1}$) of the $H + HCl$ (upper panel) and $H + ClH$ (lower panel) reactions plotted as a function of the inverse temperature. Calculated values are indicated by solid circles. Connecting lines have been drawn for aim of clarity.

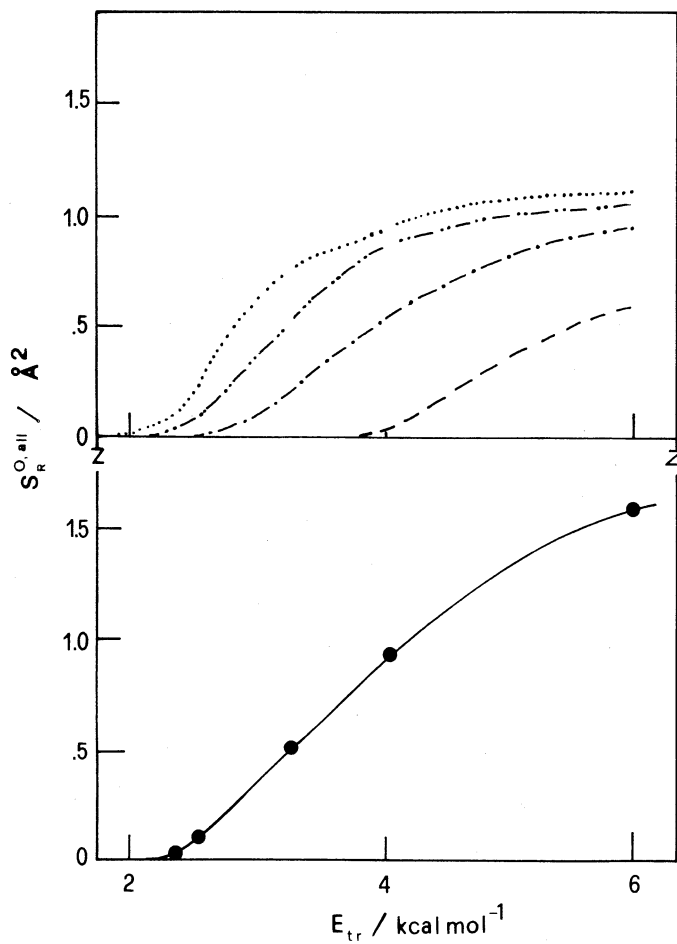


Figure 8. IOS reactive cross section (lower panel) of the $D + HCl(v = 0) \rightarrow DCl + H$ reaction and its fixed angle components (upper panel) plotted as a function of the collision energy. Calculated values are indicated by solid circles. Connecting lines have been drawn for aim of clarity.

temperature was set at T=500 K and the ground and first excited reactant vibrational states were considered. Quasiclassical calculations confirm that the conservation of the initial vibrational number is definitely the most efficient process (the usual caution has to be taken in considering the elastic non-reactive rate constant). Excitation processes are largely less efficient. The situation for $v = 1$ is about the same.

The $Cl + HCl$ reaction

The last process we have considered is the reaction of a chlorine atom with HCl . The potential energy surface used for the calculation is the LEPS functional of ref. 27 whose parameters have been optimized to reproduce some kinetic experimental isotope effects. Again calculations have been performed at T=500 K while the initial vibrational number was varied from zero to 10. Plots of rate constants calculated for $v = 2, 5$ and 8 are shown in figure (9) as a function of the final vibrational number for reactive (upper panel) and non-reactive (lower panel) processes. These plots confirm findings discussed for the $H + H_2$ reaction. Their shape differs almost negligibly when v changes confirming that a modeling of the rate constants can be obtained using simple functionals. Another important finding confirmed by these calculations is that deexcitation is much more efficient for reactive processes than for non-reactive ones.

CONCLUSIONS

The large amount of cpu time saved when calculating rate constants using computational procedures based on the approximate dynamical treatment of the atom diatom dynamics and restructured to run on supercomputers, has been reinvested for widening the range of investigated initial conditions. This has made possible to extend the theoretical investigation enough to allow the calculation of quantities of interest for the modeling of some non-equilibrium complex systems, to complement experimental data and attempt a parametrization of the efficiency of intervening elementary processes.

As test cases, the reactions of the H and Cl atoms with hydrogen and hydrogen chloride molecules have been considered. In both cases, results obtained from usual approximate methods agree in suggesting a large effectiveness of deexcitation processes although some of these calculations may overemphasize structures in rate constant plots because based on models preventing an efficient redistribution of internal energy among all possible degrees of freedom. Another important conclusion that can be drawn from the calculations is that reactive processes are far more efficient than non-reactive ones in favouring a redistribution of the internal energy among all (preferably lower) product vibrational states.

A suggestion that appears to be supported by our calculations is that electron dissociative attachments are favoured by low temperature because of the reduced rate of deexcitation from high vibrational states. Another suggestion obtainable from the wealth of results produced by our calculations is the lower efficiency of rotational temperature (in comparison with the collisional one) in favouring vibrational deexcitation for the systems discussed in this chapter. A final indication is that it is possible to incorporate excitation and deexcitation mechanisms into rule-based deciding procedures typical of some expert systems.²⁸

ACKNOWLEDGMENTS

Calculations have been performed at IBM ECSEC (Roma, Italy), CNUCE (Pisa, Italy), CNUSC (Montpellier, France) and CINECA (Casalecchio di Reno, Italy). Partial financial support from CNR (Italy) and the Italian Ministry of Education is acknowledged.

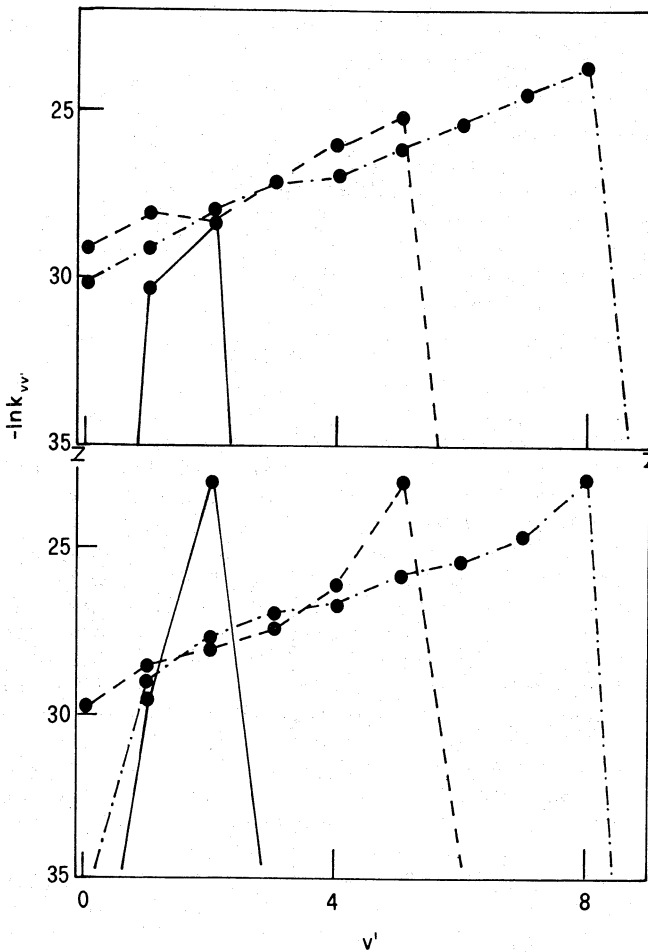


Figure 9. Logarithm of reactive (upper panel) and non-reactive (lower panel) quasi-classical rate constants (in $\text{cm}^3 \text{molecule}^{-1} \text{s}^{-1}$) of the $\text{Cl} + \text{HCl} \rightarrow \text{HCl} + \text{Cl}$ reaction plotted as a function of v' for $v = 2$ (solid line), $v = 5$ (dashed line) and $v = 8$ (dashed-dotted line) at $T=500$ K. Calculated values are indicated by solid circles. Connecting lines have been drawn for aim of clarity.

References

1. Topics in Current Physics, *Nonequilibrium Vibrational Kinetics*, M. Capitelli ed., Springer, Berlin (1986).
2. C. Gorse, M. Capitelli, M. Bacal, J. Bretagne, and A. Laganà Chem. Phys. 117:177(1987).
3. S. Bollanti, *Laser a XeCl con scarica autosostenuta: caratterizzazione sperimentale e confronto con simulazioni numeriche*, Tesi di Laurea, Università la Sapienza, Roma (1986).
4. M. Born, and J.R. Oppenheimer, Zur Quantentheorie der Moleküle, Ann. der Phys. 84:457-484(1927); A. Messiah, Quantum Mechanics, Vol. II, Chap. 18, John Wiley, New York (1962).
5. N. Sathyamurthy, Comp. Phys. Reports, 3:1(1985).
6. C.W. Bauschlicher, Jr, S.R. Langhoff, and P.R. Taylor, *Recent advances in electronic structure theory and their influence on the accuracy of ab initio potential energy surfaces*, in: *Supercomputer Algorithms for Reactivity, Dynamics and Kinetics of Small Molecules*, A. Laganà ed., Kluwer, Dordrecht (1989); N.C. Handy, *Modern electronic structure calculations: the accurate prediction of spectroscopic band origins*, ibid.; K. Morokuma, K. Yamashita, and S. Yabushita, *Potential energy surfaces of several elementary chemical reactions*, ibid.; T.H. Dunning, Jr, L.B. Harding, and E. Kraka, *Calculation and characterization of potential energy surfaces for chemical reactions*, ibid.; S.P. Walch, and C. McMichael Rohlfing, *Computed potential energy surfaces for chemical reactions*, ibid..
7. J.B. Marion, *Classical Dynamics of particles and systems*, Academic Press, New York (1965).
8. E. Clementi, J. Phys. Chem. 89:4426(1985).
9. R.B. Bernstein, D.R. Herschbach, and R.D. Levine, J.Phys.Chem, 91:5365(1987); J.P. Simons, ibid. 91:5378(1987).
10. R.B. Walker, and J.C. Light, Phys. Chem, 7:84(1975).
11. R.T Pack, and G.A. Parker, J. Chem. Phys. 87,3888(1987)
12. S.I. Drodzov, Zh. Exp. Theor. Fiz. 28:2734(1955) (English translation Sov. Phys. JETP 1:591(1955); D. Chase, Phys. Rev. 104:838(1956). R.T. Pack, J. Chem. Phys. 60:653(1974); P.M. McGuire and D.J. Kouri, J. Chem. Phys. 60:2488(1974); D.J. Kouri in: *Atom Molecule Collision Theory: A Guide for the Experimentalist*, R.B. Bernstein ed., Plenum, New York (1979); D.J. Kouri and D.E. Fitz, J. Phys. Chem. 86:2224(1982).
13. J.W. Cooley, Math. Comput. 15:363(1961).
14. D.C. Clary and G. Drolshagen, J. Chem. Phys. 76:5027(1982); D.C. Clary, Chem. Phys. 81:379(1983); M. Baer, E. Garcia, A. Laganà, O. Gervasi, Chem. Phys. Letters (in press)
15. R.B. Walker and E.F. Hayes, J. Phys. Chem. 88:1194(1984); E.F. Hayes and R.B. Walker, J. Phys. Chem. 88:3318(1984).
16. M. Mishra, J. Linderberg and Y. Ohrn, Chem. Phys. Letters 111:439(1984); A. Kuppermann, P.G. Hypes, J. Chem. Phys. 84:5962(1986); J. Linderberg, Int. J. Quantum Chemistry, S19:467(1986); P.G. Hypes, A. Kuppermann, Chem. Phys. Letters 133:1(1987); J. Linderberg and B. Vessal, Int. J.

- Quantum Chemistry, 31:65(1987); G.A. Parker, R.T Pack, B.J. Archer, R.B. Walker, Chem. Phys. Letters 137:564(1987); J.M. Launay, B. Lepetit, Chem. Phys. Letters 144:346(1988).
17. A. Laganà, R.T Pack and G.A. Parker, Faraday Discuss. Chem. Soc. 84:409(1987); G.A. Parker, R.T Pack, A. Laganà, B.J. Archer, J.D. Kress and Zlatko Baćic *Exact Quantum Results for Reactive Scattering Using Hyperspherical (APH) Coordinates*, in: *Supercomputer Algorithms for Reactivity, Dynamics and Kinetics of Small Molecules*, A. Laganà ed., Kluwer, Dordrecht (1989).
 18. R.A. Bair, and T.H. Dunning, Jr., J. Comput. Chem., 5:471(1984); H.J.C. Berendsen, W.F. van Gunsteren, and J.P.M. Postma, *Molecular Dynamics on the Cray, Cyber and DAP*, in: *High-Speed Computation*, J.S. Kowalik ed., Springer, Berlin (1984); L.C. Bernard, and F.J. Helton, Comput. Phys. Comm. 25:73(1982); F.B. Brown, W.R. Martin, and D.A. Calahan, Trans. Amer. Nucl. Soc. 39:755(1981).
 19. D.G. Truhlar and R.E. Wyatt, Ann. Rev. Phys. Chem. 27:1(1976); G.C. Schatz, *Overview of Reactive Scattering* in: *Potential energy Surfaces and Dynamics Calculations* D.G. Truhlar ed., Plenum, New York (1981); V. Aquilanti and A. Laganà, in ref.1; G.C. Schatz, *Recent Quantum Scattering Calculations on the H + H₂ Reaction and its isotopic Counterparts* in: *Theory of Chemical Reaction Dynamics* D.C. Clary ed., Reidel, Dordrecht (1986).
 20. D.G. Truhlar and C.J. Horowitz, J. Chem. Phys. 68:2466(1978); 71:1514(E) (1979)
 21. B. Liu, J. Chem. Phys. 58:1925(1973); B. Liu, and P. Siegbahn, J. Chem. Phys. 68:2457(1978).
 22. A. Laganà, Gazz. Chim. Ital. 116:143(1986).
 23. L. Ciccarelli and A. Laganà, J. Phys. Chem. 92:932(1988).
 24. A. Laganà Int. J. Chemical Kinetics 18:1009(1986).
 25. I. Last and M. Baer, Chem. Phys. Letters 73:514(1980); J. Chem. Phys. 75:288(1980).
 26. V. Aquilanti, S. Cavalli, G. Grossi and A. Laganà, Hyperfine Interactions 17/19:739(1984).
 27. J.N.L. Connor, W. Jakubetz, J. Manz and J.C. Whitehead, J. Chem. Phys. 72:6209(1980).
 28. A. Laganà and S. Rivoira, *An artificial Intelligence Approach to modeling of Gas Phase Processes* in: *Artificial Intelligence in Numerical and Symbolic Simulation* A. Pavè ed. (in press).

EXCIMER LASERS: STATUS AND PERSPECTIVES

S. Bollanti and T. Letardi

ENEA, Dip. TIB, U.S. Fisica Applicata, CRE Frascati
C.P. 65 - 00044 - Frascati, Rome, Italy

ABSTRACT

In this paper a status of the art on the excimer lasers is reported. After some general remarks, attention is fixed on rare gas halide lasers (RGH), in particular on the self-sustained discharge pumped ones. Problems related to a stable discharge development are considered and related technological requirements are deduced. Considerations on the propagation of light beams in inverted media show the best way to exploit the active volume. Moreover, a brief review of excimer lasers with unconventional characteristics is done and finally few examples of experimental techniques to measure relevant laser parameters are reported.

1. INTRODUCTION

With the term "Excimer Laser" we intend to refer to lasers which use, as active medium, diatomic molecules which are bound only in the excited electronic states and unbound, or only weakly bound, in the ground state (Excited dimers).

These molecules decay emitting one photon with energy of few eV, that is with wavelength ranging between visible and VUV.

The first experimental evidence of laser emission from excimer system has been done on 1970 by Basov et al.¹ The availability of efficient laser sources emitting in the UV was regarded as an extremely interesting event because it disclosed new experimental possibilities: indeed, UV radiation is absorbed more efficiently by most part of materials, metals and non metals, even by those materials (gold, silver..) which are highly reflecting to the IR radiation.

The lower wavelength reflects in lower diffraction limited divergence angle, i.e. possibility of smaller minimum beam radius, which scales as λ , and higher power density in the focal region, which scale as λ^{-2} .

Moreover, the photon energy is high enough to excite in a single step electronic transitions, i.e. laser sources at this wavelength are very interesting for photochemical reactions.

Later on, the observed photoablative mechanism of materials,² strictly connected with the photochemical ability of breaking chemical bonds, opened the possibility of removing organic materials by means of a direct, non thermal process,

reducing the temperature increase in the non ablated material to extremely low values.

The applications in the years following the operation of excimer lasers confirmed these possibilities, and the list can now be completed with the mention of very sophisticated laser systems which are used for efficient x-ray sources, for pumping x-ray lasers and, last but not least, as driver for inertial confinement fusion.

Such a large spectrum of applications has been possible also for the flexibility of this laser source, with respect to peak power, average power, pulse timewidth, etc., as it will be described in the following.

2. DESCRIPTION

A classification of excimer lasers can be done based on the different active media employed. The first excimer lasers developed were the rare gas dimers ones (Xe_2^* [$\lambda = 172 \text{ nm}$], Ar_2^* [$\lambda = 126 \text{ nm}$], Kr_2^* [$\lambda = 146 \text{ nm}$]), all emitting in the ultraviolet spectral region, with the laser transitions taking place between excited Rydberg states and unbound ground states;^{1,3} typically they reach energies of the order of 1 J.

Also mercury halides, like HgCl , HgBr and HgI , present excimer characteristics, with laser transitions between an excited bound state and a weakly bound ground state. They emit in the visible region of the spectrum, respectively at $\lambda = 557.6 \text{ nm}$, $\lambda = 501.8 \text{ nm}$ and $\lambda = 441.2 \text{ nm}$, and then can be efficient sources for the blue-green light.⁴ There are many other classes of excimer lasers and for a detailed description see reference.⁵

Nowadays the most studied and promising excimer sources are the rare gas halides ones (RGH), whose schematic potential energy curves are shown in Fig. 1. The interaction between the rare gas M ($ns^2 np^6$) and the halogen X ($ms^2 mp^5$) in their ground state is of covalent character and gives rise to two molecular states, different from each other for the orientation of the p orbital of X lacking in one electron with respect to the molecular axis. In fact when the X's p orbital without one electron is along the molecular axis, the repulsion is lower than when it is orthogonal and so a rather flat (little bound in the case of XeCl and XeF) ground state ${}^2\Sigma$ and a repulsive ${}^2\Pi$ state will result(*).

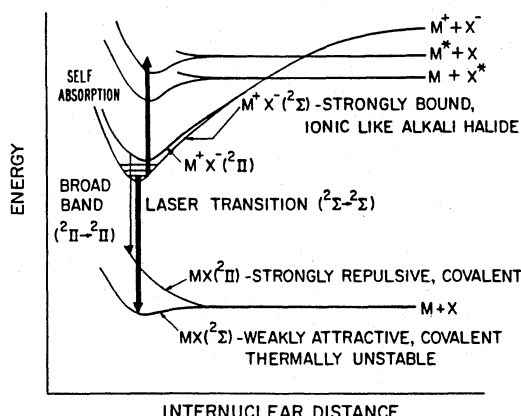


Fig.1. Schematic potential energy diagram illustrating the electronic structure of the rare gas monohalides.

(*) The spin-orbit coupling interaction is not taken into account.

The first two excited states correlate with M^+ and X^- and are strongly bound as a result of the Coulomb interaction between the positive, ionized rare gas and the negative, electron attached halogen. As in the ground state configuration, here also there are a $^2\Sigma$ and a $^2\Pi$ states, with the first one the more bound; the binding energy ranges from 1 eV to several eV, going from the heavier to the lighter species. The main electronic transition goes from the excited state $^2\Sigma$ to the ground state $^2\Sigma$ and, observing the fluorescence spectrum at very low pressure, it is possible to distinguish several lines corresponding to transition from different upper vibrational states to the ground state, lines that disappear at high pressures because of collisional quenching (Fig. 2).⁶ In the case of XeCl^* , owing to the little bond in

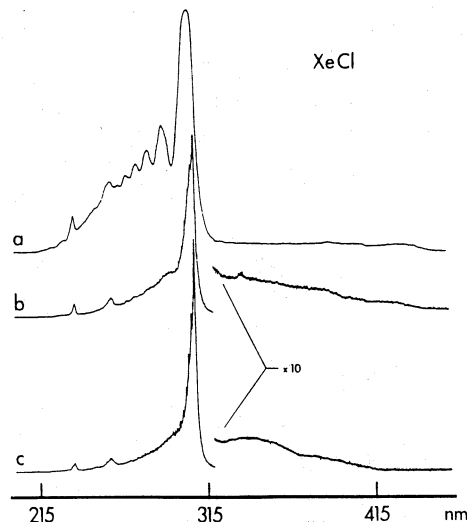


Fig.2. Spontaneous emission spectra of XeCl^* at different pressures (without buffer gas): (a) 1.7 Torr; (b) 6 Torr; (c) 26 Torr [6].

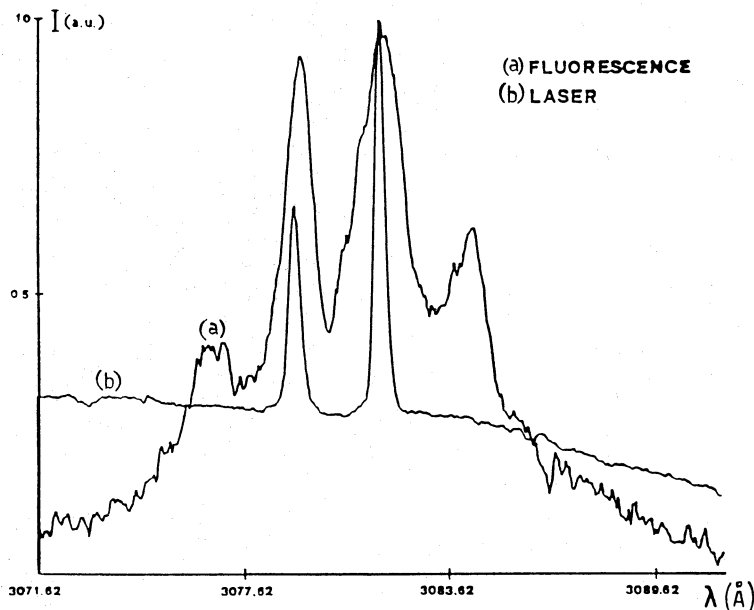


Fig.3. Spontaneous (a) and stimulated (b) emission spectra from a XeCl^* laser ($\text{Ne}/\text{Xe}/\text{HCl}$ mixture) [7].

Table 1. Radiative lifetimes and emission wavelengths on $^2\Sigma$ - $^2\Sigma$ transition of RGH molecules (all the references in [5]).

RGH	τ [ns]	λ [nm]
NeF	2.6	108
ArF	4.2	193
ArCl	--	175
KrF	9.0	248
KrCl	--	222
KrBr	--	206
XeF	16	351
XeCl	11	308
XeBr	17	282
XeI	12	253

the ground state, with a high resolution spectral measurement it is possible to observe transitions from the $v = 0$ vibrational state in the upper level to four ones of the lower level, as reported in Fig. 3.7 Here also the laser emission is shown, that, as the fluorescence intensity of the two central lines is comparable, takes place on two different transitions.

In Table 1 radiative lifetimes and emission wavelengths are reported for several RGH molecules.

3. PUMPING SCHEMES FOR RGH LASERS

The pumping process allows the transfer of energy, usually stored in a capacitor bank, to the active medium. To do this, electrostatic energy is transformed in a suitable form of energy which can be coupled efficiently to the gas contained in the cell.

The systems used as pumping processes are: electron beam, proton beam, particles from nuclear reactions, radio frequency, self-sustained electric discharge.

Usually, at each pumping process different characteristics of the laser source correspond, so that one can say that the choice between the different pumping source, at the end, will be dictated by the specific application.

In the electron beam pumping^{8,9} an electron beam, generated by a suitable accelerator, enters the gas region through a thin, low Z window. The thickness will depend on the compromise between the requirement of withstanding the gas pressure (some bars) and the requirement of minimizing the electron energy losses in crossing the window. Materials as mylar, aluminum, titanium with thickness between 5 and 50 μm are normally used.

The power density dissipated in the gas by the electron beam P_d can be expressed as a function of electron current density J and specific energy loss in the gas dE/dx (eV/cm)

$$P_d = J \frac{dE}{dx} \quad (1)$$

As an example, for 500 keV electrons propagating in Ar at 3 bar is $dE/dx = 8 \text{ keV/cm}$, so that for $J=1 \text{ kA/cm}^2$ pumping densities up to 8 MW/cm^3 can be achieved.

The lower limit of the electron energy is determined by the losses in the entrance window at a level $> 200 \text{ keV}$, while a maximum energy of few MeV is permitted if an efficient coupling of the energy to the gas is required. The main advantages of this technique are the possibility of easily scaling to systems with large volumes (i.e. with large energy/pulse), and the possibility of achieving high pumping density, i.e. high peak power pulses, so that it is generally used in inertial confinement fusion drivers,¹⁰ while their use in small laboratories or as commercial systems is not convenient for complexity, radiation problems, and limited lifetime of some components (input window) which require continuous technical assistance.

In the devices which use radio frequency (RF) power as pumping source the arrangement which has been tried very successfully¹¹ consists of an RF source, an impedance matching circuit and two electrodes, between which a small insulator tube containing the gas is put. The gas is preionized, and then the RF pulse is applied to the electrodes producing a diffuse discharge in the gas.

Interesting results have been obtained using glass or ceramic tubes with diameters $< 1 \text{ mm}$, and length around 30 cm. The RF frequency is typically around 1 GHz, and the pumping power is about 10 kW/cm^3 .

The advantages of this technique are:

- electroless discharge, so that all the gas eventually could be contained in a long life, sealed chamber
- high repetition rate, up to 100 kHz, because the gas is quickly cooled by means of diffusion to the walls
- long pulses, up to hundreds of nanoseconds.

These characteristics approach a quasi-c.w. working operation.

The disadvantages are:

- low efficiency
- small active volume
- low energy/pulse.

Best results obtained up to now are:

- energy per pulse $> 1 \mu\text{J}$
- repetition rate $> 10 \text{ kHz}$
- pulse length $> 300 \text{ ns}$
- average power $> \text{mW}$.

These performances are interesting for sources used in material processing.

Proton pumping^{12,13} is quite similar to e-beam pumping, in that it uses the energy lost by fast particles moving in the gas. It differs from e-beam pumping because, due to the higher dE/dx , it could realize higher pumping power density. Anyway, the technology is more severe: proton beam sources are more difficult than e-beam ones, the entrance window for proton beams must be extremely thin (few microns); few successful results have been reported, with low efficiency and low performances.

Nuclear pumping¹⁴ is another kind of particle beam pumping: it uses the fission fragments as energetic particles. The interest in this technique lies on the fact that high energy density can be stored in a fissionable material: up to $\approx 10^{11}$

J/cm², it is 10⁹ times the energy density in electrostatic capacitors. Some results have been obtained with low efficiency.

In the self-sustained discharge excitation¹⁵ the laser chamber consists of two conveniently shaped electrodes between which is put the gas to be excited. Typically, few torrs of the reacting species (Xe or Kr, with F₂ or HCl) are mixed with some bars of a noble gas (usually Ne); a pulsed ionizing radiation (U.V., X-ray, electrons) creates a suitable electron density, so that when a charged capacitor is connected to the electrodes an electric discharge can develop in the conducting gas. The laser chamber can take different shapes, depending also in the specific preionization source to be used.

In the case of preionization by means of u.v.light the radiation is created by means of sparks (see Fig. 4) near the discharge region.

In the case of X-rays (Fig. 5), the source consists of an external diode in which an electron emitting cathode is put near a high voltage (50 kV-100 kV) anode. The bremsstrahlung produced X-rays enter the laser chamber through a thin, low Z material window (usually, 0.5 mm Al window is a satisfactory solution).

In every case, the pulse of the ionizing radiation must be short enough in time. Indeed, the quality of the discharge depends not on the total number N_e of electrons produced per cm³, but on the maximum preionization density n_e which is lower than N_e due to electron attaching species in the gas, which limit the lifetime of free electrons. Indeed, if we indicate with n_e(t) the electron density at time t, with τ the lifetime of free electrons, with R the production rate of electrons, constant in a time interval T, we can easily see that the preionization density at the end of the pulse T is

$$n_e(T) = \tau R [1 - e^{(-T/\tau)}] \quad (2)$$

and the total number of electrons produced (per cm³) is

$$N_e = RT \quad (3)$$

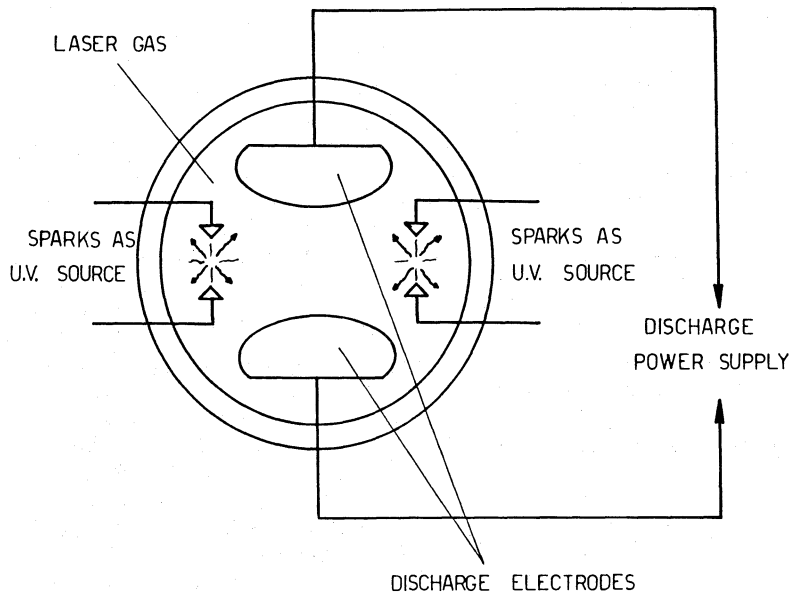


Fig.4. Laser pumped by self-sustained discharge with u.v. preionization.

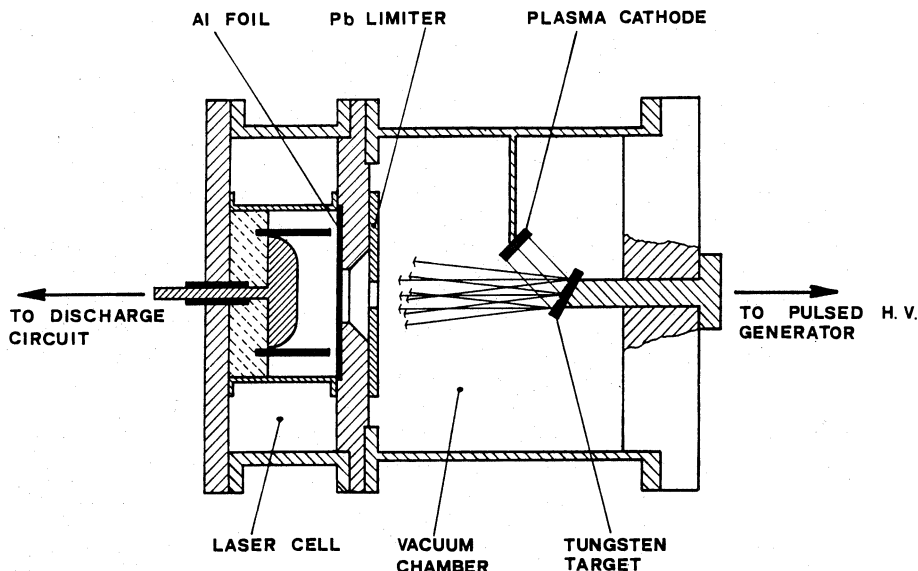


Fig.5. Laser pumped by self-sustained discharge with x-ray preionization.

so that the ratio between maximum number density $n_e(T)$ and the total number of produced electrons N_e is

$$\frac{n_e(T)}{N_e} = \frac{\tau}{T} [1 - e^{(-T/\tau)}] \quad (4)$$

Only if $T \ll \tau$ is $n_e(T) \approx N_e$.

Being $\tau \approx 100$ ns, at the normally used concentration of HCl or F₂, this would be the order of magnitude of the pulsedwidth of the preionization pulse.

From the electrical point of view, the circuit can be represented as in Fig. 6 a) and b).

In both cases, only most relevant parameters for the discharge are reported. A capacitor (C or C₁) is charged at a high voltage V_0 , and then connected to the laser head directly by means of a switch S (case a) or after the transfer of energy to a second capacitor bank (case b).

In every case, the final system consists of an RLC discharge circuit, in which we have indicated only the main parameters: the resistance of the discharge R_d (omitting all the parasitic resistances), the total inductance of the discharge circuit L, and the energy storage capacitor C.

The normal operating characteristics impose severe constraints on the maximum permitted values of the parasitic inductance L. Indeed, the discharge resistance usually ranges between 0.1 Ω and 1 Ω, while capacitors of many tens of nanofarad (up to hundreds of nanofarad) must be used to store the energy at the voltage suitable for the discharge. In these conditions, usually an oscillating discharge develops, because practically always it is

$$\frac{4}{R^2} \frac{L}{C} > 1 \quad (5)$$

Moreover, the period T of the oscillating discharge current, given by

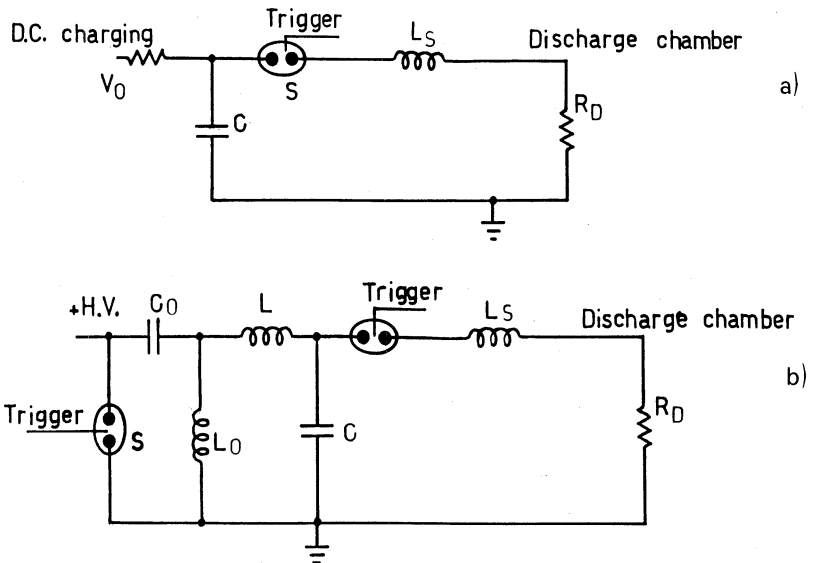


Fig.6. Schematic diagram of the discharge pumping circuit: (a) D.C. charging circuit; (b) resonantly charging circuit.

$$\frac{1}{T} = \frac{1}{2\pi} \sqrt{\frac{1}{LC} - \frac{R^2}{4L^2}} \quad (6)$$

defines the useful pumping period and must be as short as possible because the discharge is stable only for times shorter than a microsecond. This condition can be expressed by means of the fraction of energy delivered to the gas in the first half period $T/2$, that is (see Flora, ENEA Internal Report)

$$\delta_d = 1 - e^{-T/\tau} \quad (7)$$

where $\tau = 2L/R$ so that L must satisfy the condition

$$R \gg \sqrt{\frac{L}{C}} \quad (8)$$

if efficient utilization of the stored energy is required.

Typical behaviours of the discharge current and voltage are shown in Fig. 7.

As it has been previously mentioned, only uniform (diffuse) discharges are useful for laser action. When the discharge collapses in arcs the laser emission terminates.

On short time scale, a bad development of the discharge can be related with an inadequate level of preionization, that is initial electron number density, also in connection with the risetime of the subsequent discharge voltage, if it is applied after the end of the preionization. For each working condition there is a minimum preionization electron density required, whose estimation can be done following this line: suppose that each electron created by the preionization under the applied

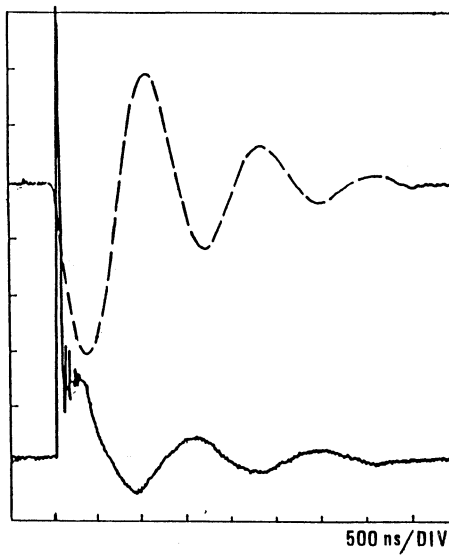


Fig.7. Time resolved discharge voltage (solid line) and current (dashed line). 8.8 kV/div for voltage, 40 kA/div for current.

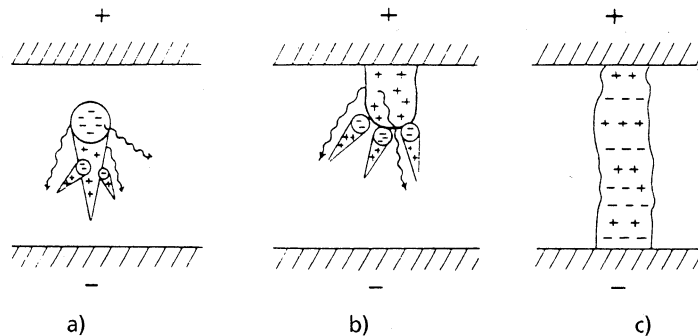


Fig.8. Schematic diagrams showing (a) streamer development around a single primary electron avalanche after its space-charge field has grown beyond a certain critical value; (b) continuous backward propagation of the cathode-directed plasma streamer after the arrival of the primary avalanche head at the anode; (c) complete bridging of the electrode gap by the plasma streamer [16].

electric field develops an electron avalanche, whose negative head is growing more and more, leaving behind itself positive ions. Consequently, also the corresponding space charge field will be stronger and stronger, until it will become comparable with the applied electric field, finally causing the formation of a streamer through the discharge gap, as shown in Fig. 8. On the other hand, all these avalanches can give a glow discharge only when their heads will superimpose each other, in such a way to uniform the charge distribution and to reduce the gradients of the space charge field. A condition to be met after these preliminary remarks is that when the space charge field becomes comparable with the external field, the avalanche heads must be superimposed each other. This sets an upper limit to the initial distance of the preionization electrons, that is on their density.¹⁶

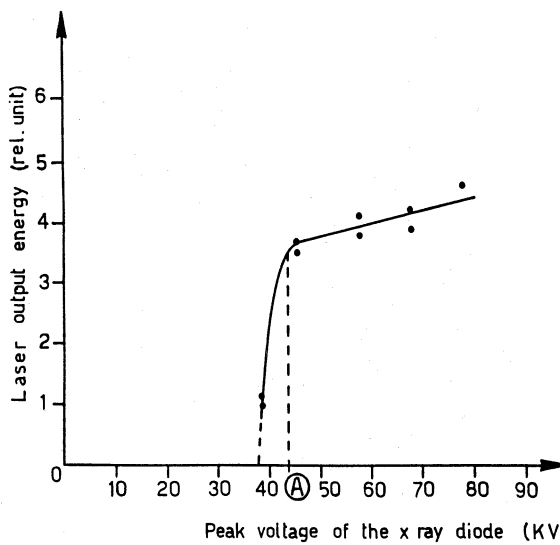


Fig.9. Laser output energy vs preionization intensity.
XeCl* laser mixture pressure: 3 atm; discharge capacitance: 0.48 μ F; charging voltage: 50 kV.

In addition to this requirement, if the high voltage is applied to the laser cell after the end of the preionization pulse, the drift of the electrons away from the cathode in the pre-breakdown phase has to be taken into account. For a good discharge the voltage risetime must be short enough to not allow to the electron depleted region near the cathode to become larger (in the electric field direction) than the electron avalanche head at the critical point (i.e. space charge field = external field). This requirement adds to the previous one, giving voltage risetimes of the order of tens of nanoseconds and preionization electron number densities of $\approx 10^5 \div 10^6 \text{ cm}^{-3}$.¹⁷

If we plot the laser output energy vs the preionization density in a practical device we get a result as depicted in Fig. 9. It is clear that above point A the laser output depends very weakly on the preionization density, and a useful working point can be set at a value of 3-4 times the preionization density of upper knee.

4. CHARACTERISTICS OF THE ACTIVE MEDIUM

The mechanisms through which the RGH excited molecules and the laser radiation are formed and extinguished during a discharge are very complex. Big kinetic codes have been developed with the aim of reproducing the laser working characteristics, taking into account many kinds of reactions, the electron energy distribution function and the coupling of the discharge region with the external circuit,¹⁸ following the general scheme reported in Fig. 10.

Related to the big effort around kinetic codes there is the spur of understanding the processes which generate instabilities in the discharge on long timescale, its collapse in arcs and premature termination of the laser action due to the reduction of the discharge volume.¹⁹ One possible explanation of this fact deals with local depletion of the halogen donor: suppose that there are little disomogeneities in the electron spatial distribution; where the electron density is higher, due to the attachment process the number of halogen molecules will decrease; in turn, in this region the electron losses by attachment will be lower and the electrons will grow at an higher rate than in the other regions of the discharge. This "positive feedback" can cause the developments of arcs which destroy the glow discharge and, due to their very low resistance, do not absorb more energy from the

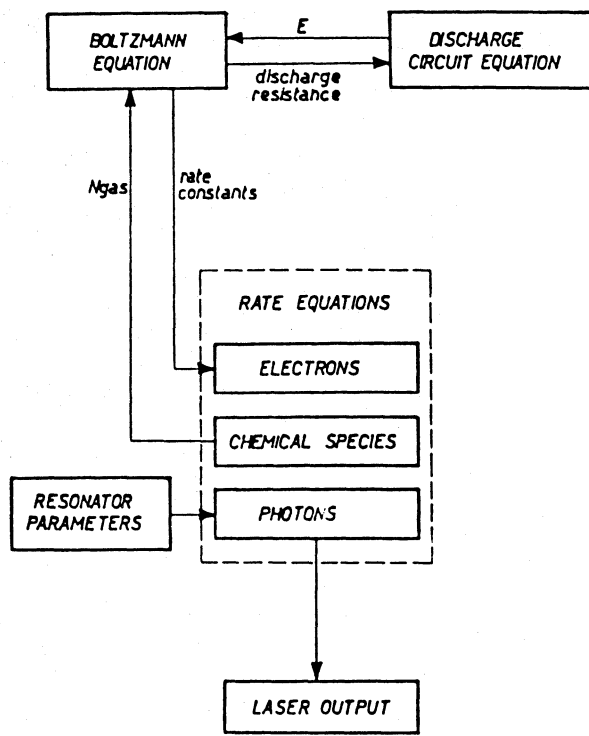


Fig.10. General scheme of a simulation code for discharge pumped RGH lasers. E = electric field.

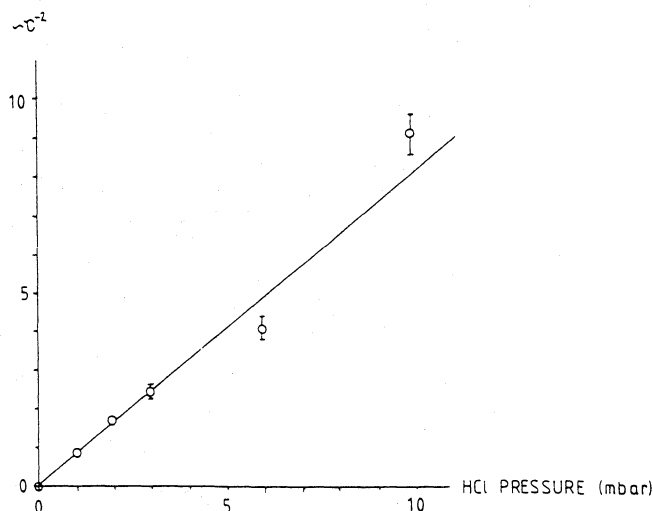


Fig.11. A plot of τ^2 against HCl partial pressure, for 1 bar Ne, 20 mbar Xe mixture [20].

external circuit, producing no more photons. The duration τ of the glow, useful discharge has been put in relation with the initial density of the halogen donor in the case of the XeCl^* laser with HCl_{20} as reported in Fig. 11.

The shape of the electrodes, which must create an electric field as uniform as possible in the discharge region, affects the time length of the diffuse discharge: ideally the electric field would be constant in the discharge region and it would go

to zero outside, in order to avoid flow of current outside the useful region. Many solutions have been investigated^{21,22} which reasonably approximate the required conditions.

In discharge pumped lasers the pumping density is a very important and critical parameter. It is obvious that, increasing the power delivered to the gas, it is possible to reach higher output energies, but on the other hand this can also increase the rate at which instabilities develop in the discharge.^{19b} Moreover, going at higher energies stored in the main discharge bank usually leads to a decrease of the discharge efficiency, because (seen from a macroscopic point of view) the discharge resistance drops and so also the power dissipated on it.

Related to the power density deposited into the gas is an important parameter, the small signal gain coefficient g_0 . From the theory we know that:

$$g_0 = \sigma n_0 \quad (9)$$

where:

σ = stimulated emission cross section

n_0 = initial population inversion.

Depending on the kinetic processes during discharge, the number density of the active molecules formed is roughly proportional to the deposited power density and so g_0 is, from (9):

$$n_0 = \frac{n_f P_d \tau}{h \nu} \quad (10)$$

where:

- n_f = formation efficiency = energy in active molecules/deposited energy

- τ = active molecules lifetime

- P_d = deposited power density.

For typical values in the case of XeCl* laser ($\sigma = 4.5 \times 10^{-16} \text{ cm}^2$, $\tau \approx 2 \text{ ns}$, $h\nu \approx 4 \text{ eV}$, $\eta_f \approx 0.2$):

$$g_0 [\text{cm}^{-1}] \approx 0.3 P_d [\text{MW/cm}^3] \quad (11)$$

It is evident that to obtain a gain coefficient of the order of 10%/cm a very high power density, in the range of MW/cm³, is required.

Usually, when operating with electric discharges, common values of P_d are between 0.1 to 0.5 MW/cm³, giving a gain coefficient up to 10%/cm, which maintains a linear dependence on P_d , as shown in Fig.12a, where experimental data for XeCl* laser are reported; the angular coefficient is ≈ 0.33 , very similar to the estimated one.²³

With the electron-beam pumping technique higher power density deposition can be achieved, up to several MW/cm³, but in this case the behaviour of g_0 vs. P_d is no more linear. This can be explained with: 1) the smaller formation efficiency and 2) the shorter lifetime of the active molecules. In fact with e-beam pumping there is need of a high mean electron energy in order to obtain a uniform excitation of the gas and this can favour some formation channels (e.g. through direct ionization) that are not necessarily the most efficient. Instead with a discharge pumping the electrons are continuously accelerated, from almost zero energy, from the applied electric field, leading to the activation of different channels for the excimer formation so that finally the lost energy is lower. For the same reason, in the case

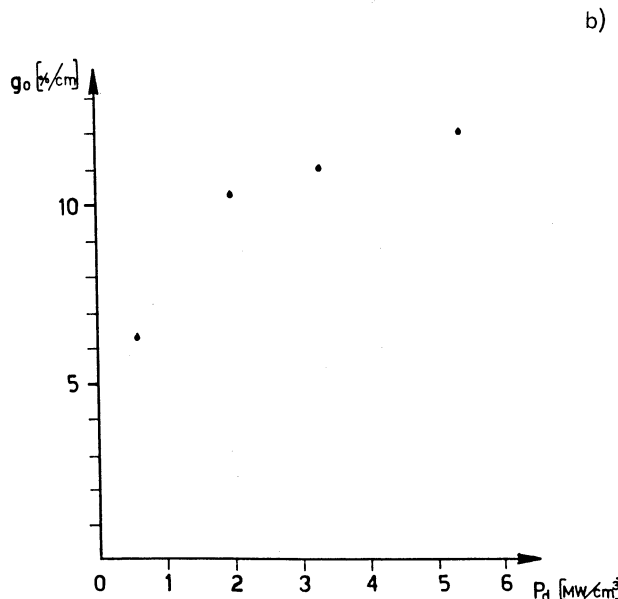
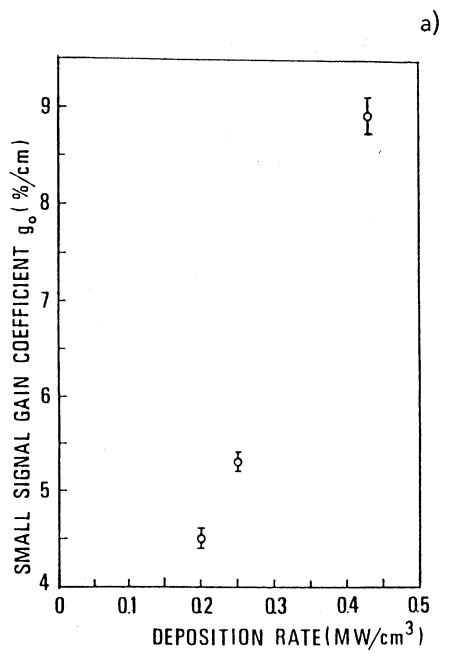


Fig.12. Small signal gain coefficient g_0 vs energy deposition rate in (a) a discharge pumped [23] and (b) an e-beam pumped [8] XeCl active medium.

of e-beam the quenching rate of the active molecules is faster and this results in a shorter lifetime.

An experimental result which shows a saturate behaviour of g_0 vs. P_d is reported in Fig.12b.⁸

5. OSCILLATOR, AMPLIFIER AND EXTRACTION EFFICIENCY

It is possible to understand the importance of g_0 , together with other two parameters, α , non saturable absorption coefficient, and I_s , saturation intensity, examining the equation which controls the propagation of a collimated beam, with initial intensity I_0 and pulse duration much longer than the upper state lifetime, in an inverted medium with homogeneous line broadening, say in x direction:

$$\frac{dI(x)}{dx} = \left[\frac{g_0}{1 + I(x)/I_s} - \alpha \right] I(x) \quad (12)$$

From the equation it is clear that the gain term decreases with increasing intensity and reaches one half of the initial value when the beam intensity is equal to the saturation intensity. At the same time the losses don't change, leading to a constant reduction of the amplification, until, in an infinitely long active medium, the intensity reaches its asymptotic value, that can be obtained equating to zero dI/dx :

$$I(+\infty) = I_{\max} = I_s \left(\frac{g_0}{\alpha} - 1 \right) \quad (13)$$

The amplification of light beams inside laser oscillators has been extensively studied²⁴ to try to optimize the output intensity or the extraction efficiency (defined as the ratio between output energy and energy stored in the active molecule) changing the oscillator length, L, or the output mirror reflectivity, R. In Fig. 13 a plot of the maximum extraction efficiency vs optimum output coupler is reported for different combinations of $g_0L - \alpha L$.^{24b}

These considerations all refer to the case of a flat-flat cavity with a totally reflecting mirror and an output coupler. Indeed this is the configuration that allows to extract the highest energy from the active medium, because involves it completely, but it gives also a poor beam quality, doing no transverse mode

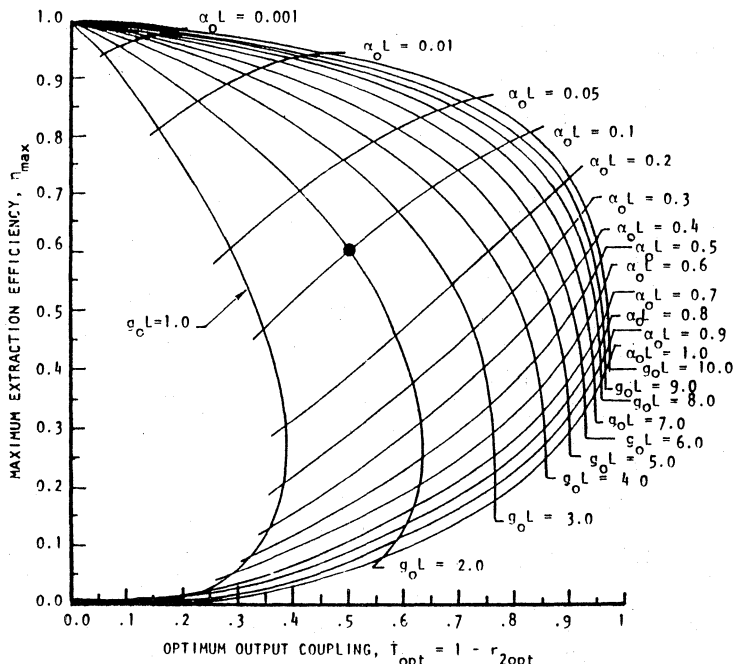


Fig.13. Maximum extraction efficiency vs optimum output coupling for constant αL and constant $g_0 L$ [24b].

selection and so resulting in high divergent beam, typically with divergence value around some milliradians.

So, often low energy, high quality beams generated with special cavities are sent in excimers' active media for amplification. Also for an amplifier an extraction efficiency is defined:

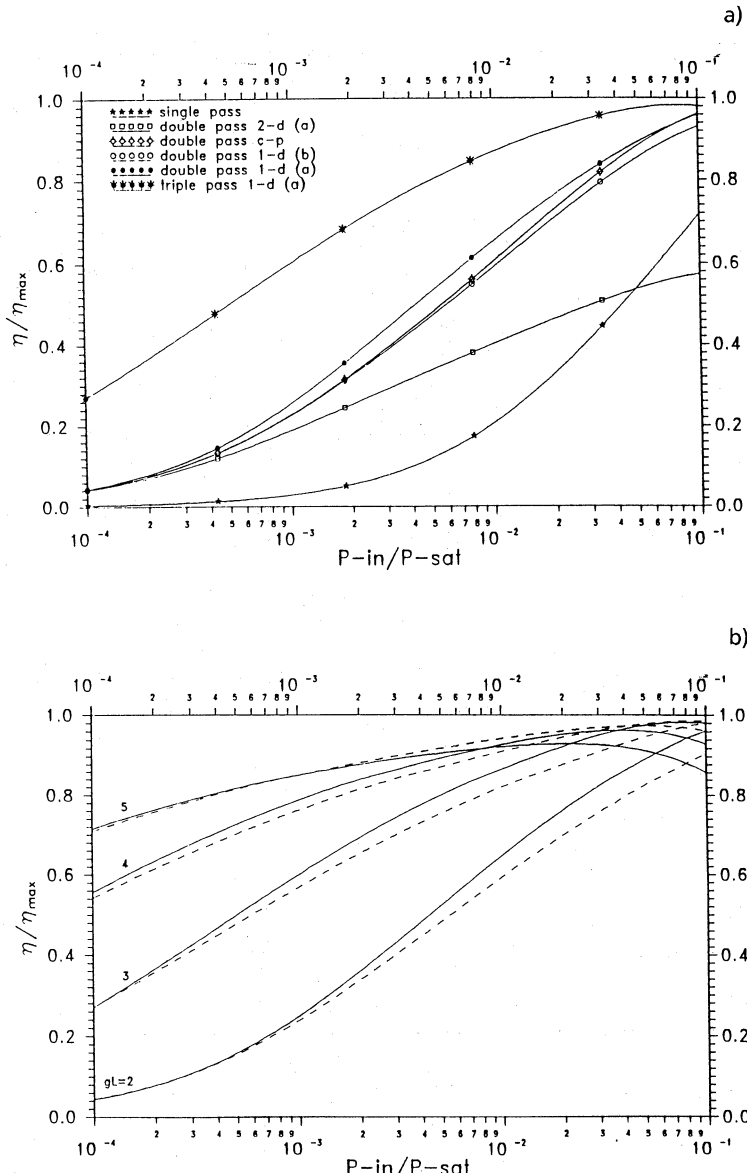


Fig.14. Ratio extraction efficiency/maximum extraction efficiency vs. normalized input power, for: (a) different amplifier configurations (c-p = counter propagating, 1/2-d = expansion in 1/2 dimensions, (a): $h_0/D = 0.05$, (b): $h_0/D = 0.5$, h_0 = input beam diameter, D = amplifier diameter), with $g_0 L = 3$, $g_0/\alpha = 10$; (b) different $g_0 L$ values, $g_0/\alpha = 10$ (solid line) and $g_0/\alpha = 20$ (dashed line), triple passage [25].

$$\eta_{\text{ext}}^{\text{am}} = \frac{P_{\text{out}} - P_{\text{in}}}{P_s} \quad (14)$$

where:

- P_{in} = power at the input of the amplifier
- P_{out} = power at the output of the amplifier
- P_s = saturation power = $(hv_n V/t) = I_{sg0} V$, maximum extractable power
- V = amplifier active volume.

How to maximize the output power, given the input, that is $\eta_{\text{ext}}^{\text{am}}$, exploiting as better as possible the amplifier active medium? Two basic possibilities are: 1) single passage with collimated beam with diameter equal to the amplifier one; 2) single passage with an expanding beam with output diameter equal to the amplifier one. To understand which one of these two configurations can give the best results, it is better to rewrite the propagation equation (12) for the beam power:

$$\frac{dP(x)}{dx} = g_0 \left(\frac{1}{1 + I(x)/I_s} - \frac{a}{g_0} \right) P(x) \quad (15)$$

For a fixed input power, the increase dP/dx will be higher if the intensity is as low as possible: it is more convenient to work with a collimated beam investing all the active medium. In Fig. 14 calculated extraction efficiencies are reported as function of P_{in}/P_s for different amplifier configurations and $g_0 L$ values. For a more exhaustive treatment, we refer you to Ref. 25.

6. MAIN CHARACTERISTICS OF COMMERCIAL EXCIMER LASER SOURCES

In Table 2 some characteristics of commercial systems are reported.

Table 2. Main characteristics of commercial RGH excimer systems

	ArF	KrF	XeCl	XeF
Wavelength [nm]	193	248	308	351
Average power [W]	50	100	150	30
Pulse width [ns]	5-25	2-50	1-300	1-30
Energy/p [J]	.5	2	2	.5
Repetition rate [Hz]	1-1000	1-500	1-500	1-500
Efficiency [%]	1	2	2.5	2
Beam cross section [mm ²]	2 × 4 - 25 × 30			
Beam divergence [mrad]	2	-	6 (< .2)	

7. LASER SOURCES WITH UNCONVENTIONAL CHARACTERISTICS

In some cases, depending on the specific applications, characteristics of the laser beam much different from those available in commercial systems could be required; very advanced systems have been designed in order to have:

- low beam divergence, up to the diffraction limited angle ($\approx .1$ mrad)
- ultrashort pulse, up to the region of femtoseconds
- narrow bandwidth, up to the single longitudinal mode
- long pulse, up to the region of microsecond

- high energy/pulse, up to the region of many kJ/pulse
- high average power, up to the region of many kW.

A quantity which can express the spectral and spatial quality of a laser radiation is the spectral brightness, that is defined as the energy radiated per unit time, frequency interval, surface and solid angle at a given wavelength. Several methods have been developed to obtain a beam with a good brightness from one or more of the possible improvements.

Low Divergence Beams

The solid angle and surface of emission can be reduced selecting only one or few low transverse modes. This can be accomplished by means of unstable cavities and/or spatial filters.²⁶ Near diffraction limited beams have been obtained using a SFUR²⁷ (Self Filtering Unstable Resonator), a confocal, negative branch unstable resonator, with a spatial filter with given aperture in the focus common to the two cavity mirrors, whose schematic diagram is shown in Fig. 15a.^{27b} The extraction efficiency in the involved volume is very high, but the mode volume is very small and so the final output energy is reduced with respect to a flat-flat cavity. Another kind of unstable cavity which gives good results on the transverse mode selection is the PBUR (Positive Branch Unstable Resonator)²⁸, a scheme of which is reported in Fig. 15b.

Narrow Bandwidth Beams

Near or single longitudinal mode lasers have been realized by means of intracavity gratings, prisms and etalons.²⁹ An arrangement of a laser cavity with a line-narrowing element is shown in Fig. 16, together with its effect on the linewidth after several roundtrips. It is evident that the more round trips in the cavity, the more effective the line narrowing becomes.

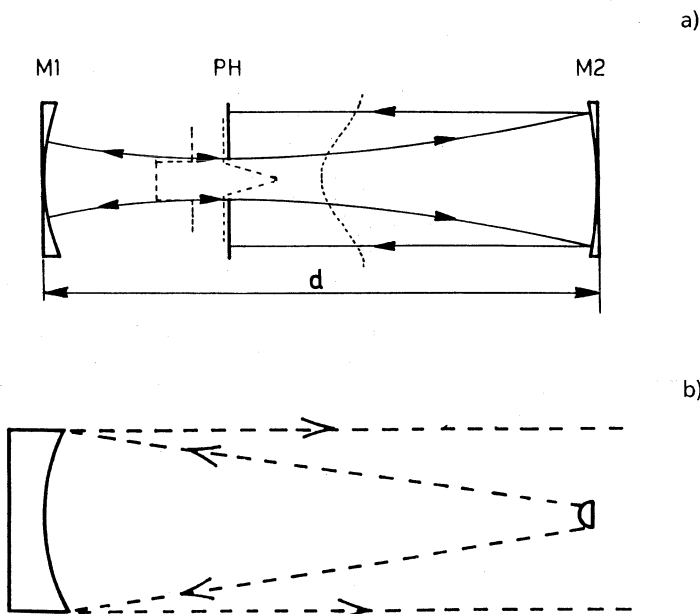


Fig.15. Schematic representation of two kinds of unstable cavities: a) negative branch, SFUR; b) positive branch, PBUR (see text).

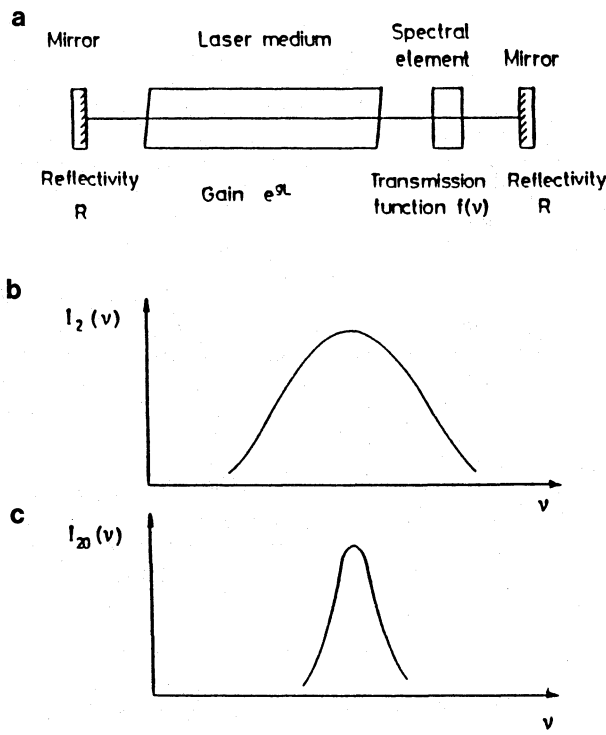


Fig.16. Laser cavity with a line-narrowing element (a) and its effect on linewidth after (b) 2 and (c) 20 roundtrips.

Ultrashort Pulses

To reduce the pulse duration of excimer lasers conventional methods like active and passive modelocking have been employed, obtaining pulses of ≈ 2 ns duration.³⁰ The use of an intracavity fast Pockels cell allowed to reach laser pulses of ≈ 300 ps;³¹ but, to go in the region of pico- or femtoseconds u.v. pulses, at least a double device system is needed, the first device generating the ultrashort pulse, usually with very low energy, in the visible or u.v. region, the second one, the excimer active medium, (after an eventual frequency duplication) acting as amplifier. Usually a CPM (Colliding Pulses Modelocked) dye laser is used as oscillator to generate ultrashort pulses in the visible region; then they are amplified in another dye and frequency doubled before entering the last stage, the excimer amplifying medium. The time width of the amplified pulse has a lower limit set by the limited spectral bandwidth of the excimer media. Anyway, 160 fs pulses have been obtained from a "CPM-dye amplifier-KDP-XeCl* amplifier" chain with 12 mJ final energy;^{32a} 80 fs pulses resulted from two KrF* final amplifiers (with a little different initial configuration), which have a gain bandwidth broader than XeCl*, with a final energy of 15 mJ.^{32b} More recently 1 TW pulses have been obtained from a XeCl* laser, with a longer pulse, 310 fs, but an higher energy, 300 mJ.^{32c}

The most difficult problems to be solved concerning the amplification in excimer media are: the overmentioned temporal lengthening due to the relatively narrow gain bandwidth; the presence of ASE (Amplified Spontaneous Emission), that becomes considerable when the value of $g_0 L$ is high (> 1) and can be contained to few percent of the total extracted energy by means of spatial filters;³² the group velocity dispersion, which causes pulse broadening, because the different spectral components of the pulse propagate with different speeds, and can be compensated introducing systems with negative dispersion;³³ the gain saturation, which is a not completely well understood phenomenon on the femtosecond scale, but surely for

such short pulses the maximum extractable energy is limited by the saturation energy of the active medium:

$$E_{\text{ext}} = h\nu n V = E_s g_0 V \quad (16)$$

where:

$$E_s = \frac{hv}{\sigma}, \text{ saturation energy}$$

In the case of RGH lasers E_s is in the range of 1 mJ/cm^2 , so that with a $g_0 \approx 0.1 \text{ cm}^{-1}$ and an active volume of 11 the maximum extractable energy ($\eta_{\text{ext}}^{\text{am}} = 1$) is $\approx 100 \text{ mJ}$.

Long Pulses

In conventional systems the time length of laser pulses, when the source is operated in the self sustained discharge mode, is shorter than $\approx 200 \text{ ns}$. This is due to the discharge instabilities, which do collapse the diffuse discharge into arcs after few hundreds of nanoseconds, terminating the laser action. On the other hand, some applications would require longer pulses:

- in material processing, when high peak power, with consequent ablative processes, must be avoided;
- when the beam must be transported in fibers (especially for medical applications) because the damage limit of the fibers is associated with peak power, not with average power.

Clearly, these types of applications do not justify the use of e-beam pumping technique which can deliver much longer pulses.

Some techniques have been successfully developed in order to increase the stability of the discharge, and so the timelength of the pulse.

The instability of the discharge can be associated with a halogen donor depletion. Webb et al.²⁰ succeeded in stabilizing the discharge inserting in the circuit external ballast resistors. In this way, microsecond pulse duration, at low efficiency and low energy/pulse, have been achieved.

Quite recently³⁴ the double pulse technique has permitted the achievement of very long pulses at very high efficiency. The double pulse technique was introduced for the first time by Long et al.³⁵ To explain the system, we observe that we can distinguish in the process of the self-sustained discharge, two temporal phases: in the first phase (few nanoseconds) we observe in the gas a strong increase of the electron density, which passes from the initial density of about 10^7-10^8 e/cm^3 to the final density of about $10^{14}-10^{15} \text{ e/cm}^3$. In the second phase, the electron density is essentially stationary, and the flowing current pumps the active medium. The two phases are essentially driven by the applied electric field and its optimized value is different for the two phases. Usually, the charged capacitors, with associated output impedance which is in series with the time varying impedance of the discharge, play the double role of electron density multiplication (high electric field) and pumping discharge (low electric field). The use of the same circuit for the two functions does not permit an optimization of the process. Separation of the two functions in two different circuits (prepulse technique or double pulse technique) permitted an increase of efficiency and stability. The same technique, associated with magnetic switches and pulse forming line, has permitted the operation [34] of a system with pulses $.5 \mu\text{s}$, $.5 \text{ J/p}$, efficiency of 2%.

High Energy Pulses

Scaling of excimer laser systems to very high energy per pulse in self-sustained discharge operation has been done for XeCl resulting in a source delivering 60 J/p, in a 120 nsec pulse.³⁶

Much higher energy can be obtained in e-beam pumped systems. A KrF fusion device (AURORA) developed at Los Alamos will deliver in the future 10 kJ/p, in a pulse 5 ns long. Presently, 2.5 kJ have been achieved.³⁷

High Average Power

Excimer laser sources having average power in the kW range are interesting for material processing (cutting, surface treatments) and for photochemistry applications on industrial scale.

Only combinations on a limited range of energy/pulse and repetition rate are realistic; systems up to now operated or under study consider energy/pulse ranging from a fraction of Joule/pulse to about 10 J/p, with repetition rate ranging from few kHz to 100 Hz. In every case, very severe problems have to be solved: for gas flow, which must have a speed in the discharge region of about 100 m/s; for switches, which would be of the saturable magnetic type, and for damping of shock waves, which modulate the gas density and reduce the quality of the laser beam. Average powers near 500 W for XeCl and KrF systems have been recently achieved.³⁸

8. EXPERIMENTAL MEASUREMENTS

From a more experimental point of view, it is interesting to see how some macroscopic parameters that have been introduced before can be measured.

Gain, absorption and saturation intensity measurements

If a light beam enters in an active medium with intensity much lower than the medium saturation intensity, Eq. (12) can be rewritten as follows:

$$\frac{dI(x)}{dx} = (g_0 - \alpha) I(x) \quad (17)$$

This equation can be easily integrated to give:

$$I(x) = I_{in} e^{(g_0 - \alpha)x} \quad (18)$$

This behaviour is true if $I(x) \ll I_s$, so if at the output of the active medium (say, $x = L$) this condition still holds, the intensity will be grown exponentially all the way long and:

$$\frac{I_{out}}{I_{in}} = e^{(g_0 - \alpha)L} \quad (19)$$

With this simple formula it is possible to mount a setup for the measure of the "net" gain, i.e. $g_0 - \alpha$, injecting a probe beam at the laser wavelength in the excited active medium and carefully controlling the input and output intensities; nevertheless there are still other few considerations to be done.

The first is that it is desirable to distinguish the two parameters, g_0 and α , because also their ratio is important to characterize a laser (see Eqs. (13) (15)); the second is about the spectral and temporal dependance of g_0 and α . As far as the spectral dependance is concerned, it can help to discriminate the two parameters. In fact $g_0(\lambda)$ receives contribution only from the excimer and is sensitively different from zero only around the wavelengths correspondent to the main RGH transitions, following the behaviour of the fluorescence in Fig.3; on the contrary $\alpha(\lambda)$ sums all the contributions of the species which form during the discharge in the active volume and, in the case of XeCl^* from a mixture $\text{Ne}/\text{Xe}/\text{HCl}$, it has been shown that the stronger absorbers (Xe^+ , Cl^- , Ne^{**}) have almost the same absorption at $\lambda_L = 308 \text{ nm}$ (laser wavelength) and at longer λ ($\lambda > 311 \text{ nm}$), where the gain is negligible. In this way it is possible to estimate the value of $\alpha(\lambda_L)$ measuring the absorption coefficient out of the gain spectral region and extrapolating it at the laser wavelength, and then measure the net gain at λ_L , finally deducing $g_0(\lambda_L)$.

As regards the temporal dependance of g_0 and α , due to the pulsed operation of excimer lasers, it is convenient to use a long pulse probe laser, in such a way to follow directly, from the time behaviour of the output probe pulse with respect to the input one, the time behaviour of the gain or absorption.

An experimental setup for small signal gain and absorption coefficient measurements is schematically shown in Fig. 17. The probe beam comes from a dye laser, a visible, tunable source, is frequency doubled and sent into the active medium, being examined both in input and at the output. If the value of the saturation intensity of the excimer medium is not known, it is possible to check that the requirement on the intensity ($I(x) \ll I_s$, $0 < x < L$) is satisfied by simply trying to see if Eq. (19) is true for different values of I_{in} . Results for temporal and spectrally resolved g_0 and α are reported in Figs. 18-19.²³

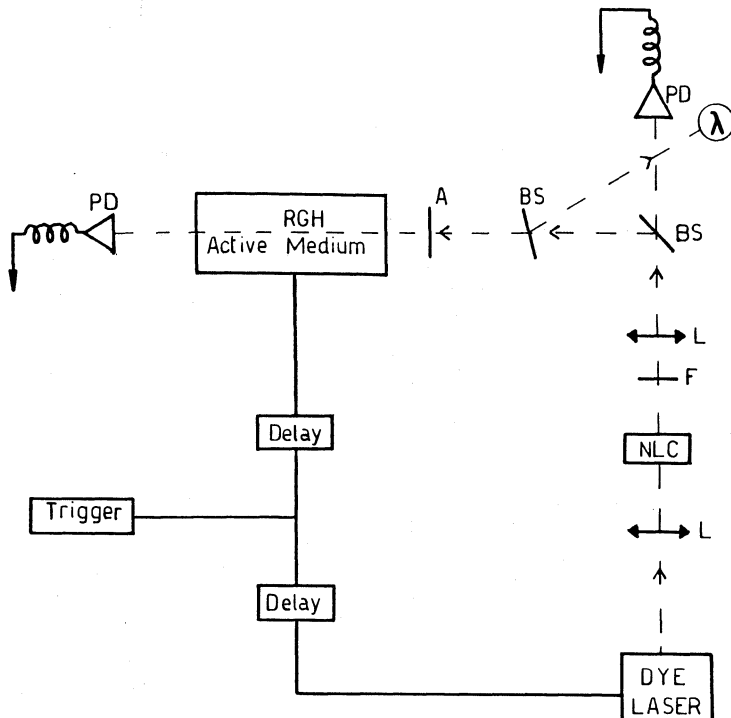
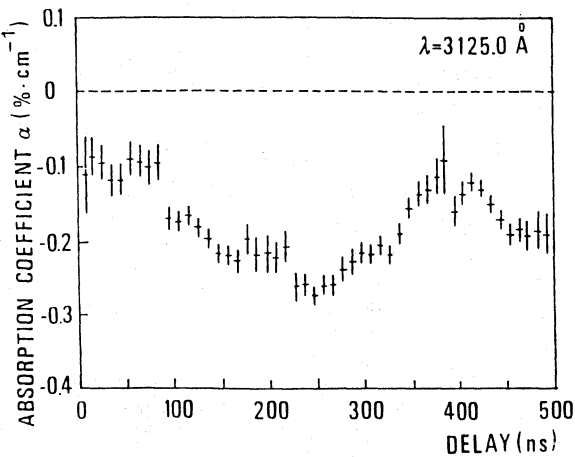


Fig.17. Experimental scheme for g_0 and α measurements.
 L=lens; NLC=non linear crystal; F=u.v. filter;
 BS=beam splitter; A=attenuator; PD=photodiode;
 λ =wavelength measure.

a)



b)

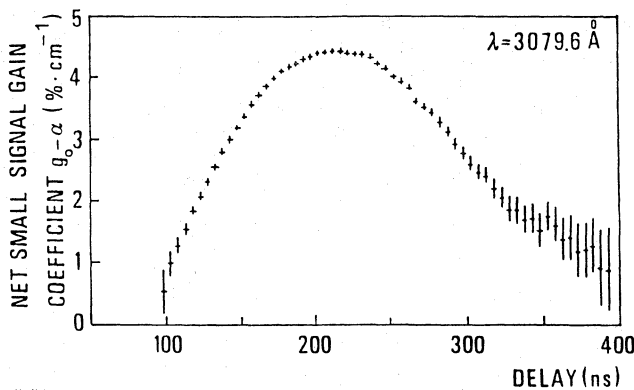


Fig.18. (a) Absorption coefficient α vs time for $\lambda = 3125 \text{ \AA}$; (b) net small signal gain coefficient $g_0\alpha$ vs time for $\lambda = 3079.6 \text{ \AA}$. $T=0$ corresponds to the beginning of the discharge voltage risetime. Both measurements have been done with a pumping power density of 200 kW/cm^2 [23].

The measure of the saturation intensity I_s is little more difficult and usually estimates of this parameter are given with large errors.^{8,39} A more exact evaluation of I_s can be accomplished by using Eq. (12) in a different way. Suppose to send a laser probe beam into an laser oscillating with the same laser wavelength and with the probe beam intensity, I_p , much lower than the intracavity intensity, I_c . The Eq. (12) for I_p propagating in the laser medium is:

$$\frac{dI_p(x)}{dx} = (g - \alpha) I_p \quad (20)$$

where

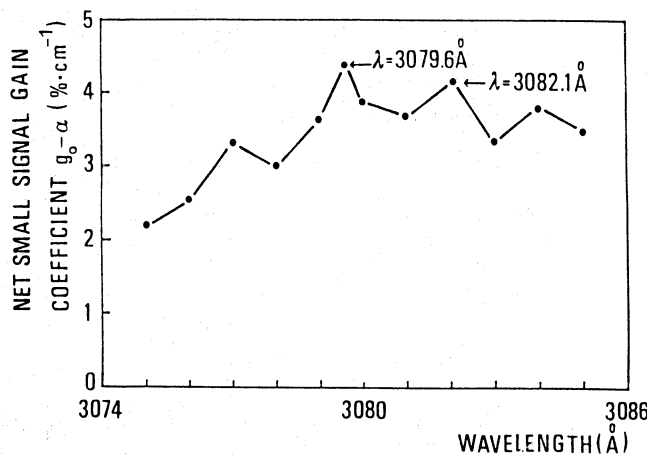


Fig.19. Net small signal gain coefficient $g_0 - \alpha$ vs wavelength λ , for delay time of 230 ns and a pumping power density of 200 kW/cm^3 [23].

$$g = \frac{g_0}{1 + (I_c + I_p)/I_s}$$

As $I_p \ll I_c$ for $0 < x < L$ (L = active medium length), this equation simplifies:

$$\frac{dI_p(x)}{dx} = \left(\frac{g_0}{1 + I_c/I_s} - \alpha \right) I_p \quad (21)$$

If the time width of the probe pulse is rather shorter than the laser oscillation, it is reasonable to think that during its propagation the probe pulse meets a rather constant intracavity intensity, so that the coefficient in front of I_p in (21) is constant and the growth of I_p is exponential.

Measuring $I_p^{\text{out}}/I_p^{\text{in}}$, that is $(g_0/(1+I_c/I_s) - \alpha)$, and knowing I_c , g_0 and α , it is possible to deduce the value of I_s . Several points can be taken, varying I_c , and then g (not g_0), by changing the output coupler reflectivity, to reduce the error on the measure.

From a practical point of view, there is the need to distinguish the probe beam at the output of the oscillator from the laser radiation, seen that $I_p \ll I_c$. This can be accomplished by means of windows sealing the active medium at the Brewster angle, so that the oscillator radiation is p-polarized and a s-polarized probe can be extracted nearly without noise. An experimental setup for this kind of measure is reported in Fig. 20. The relative error on this measure can be $\approx 20\text{-}25\%$, while with standard methods it is as high as 50%.

Electron Density Measurements by Holographic Techniques

This technique⁴⁰ permits the measurement of electron density in a plasma during the discharge with a sensitivity of the order of $N_e L \approx 10^{16}/\text{cm}^2$, if N_e is the electron number density in cm^{-3} and L is the total optical path in the plasma in cm, with time resolution of the order of some nanoseconds. The principle of the method is the following: the refractivity n of a plasma can be expressed as

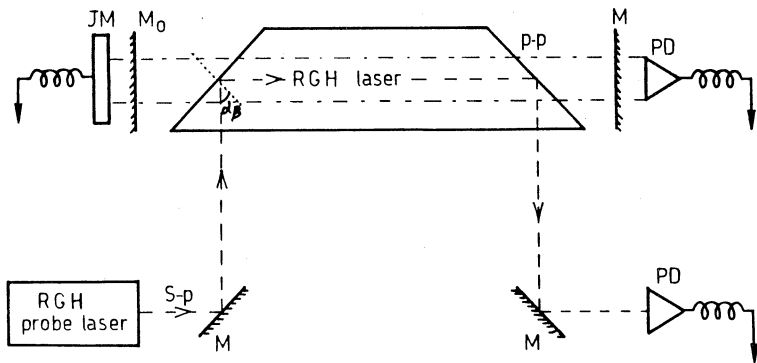


Fig.20. Schematic diagram for an experimental setup for saturation intensity measurement. M = mirror; M_0 = output mirror; JM = joulemeter; PD = photodiode.

$$(n - 1) = (n_e - 1) + \sum_k (n_k - 1) \quad (22)$$

where $(n_e - 1)$ and $(n_k - 1)$ are the components due to the electron density N_e and to the heavy particle density N_k . If the radiation frequency is much higher than the plasma frequency and far enough from the resonance frequencies of the heavy particles, Eq. (22) may be approximated by

$$(n - 1) = \sum_k \left(A_k + \frac{1}{\lambda^2} B_k \right) N_k - 4.47 \times 10^{-14} N_e \lambda^2 \quad (23)$$

where A_k and B_k are characteristic coefficients of the species considered and λ is the radiation wavelength.

In interferometric measurements of the refractivity of a homogeneous plasma layer of thickness L the normalized fringe shift S caused by introducing an optical path difference is related to the refractivity variation $\Delta(n-1)$ by the expression

$$S = \frac{L}{\lambda} \Delta(n - 1) \quad (24)$$

Usually, $(n-1)$ refers to the initial state characterized by $N_e = 0$. From Eqs. (23) and (24) and taking into account that in the visible spectral region the contribution of the heavy particles to the fringe shift is negligible, compared to the electronic contribution, we may write the following expression:

$$S = -4.47 \times 10^{-14} N_e \lambda L \quad (25)$$

for the normalized fringe shift S of radiation with wavelength λ after an optical path L in a plasma which had a variation N_e in electron number density.

The sensitivity limit of the electron density measurement can be evaluated assuming for the smallest detectable fringe shift the realistic value $S = 0.1$, so that it must be

$$(N_e L) \geq 3.2 \times 10^{16} \text{ cm}^{-2} \quad (26)$$

at the wavelength of ruby laser ($\lambda = 694 \text{ nm}$).

Preionization Density Measurements by Collecting Electric Charge

Preionization by X-ray or UV radiation provides an effective method for initiating homogeneous discharges in rare gas halide excimers at high pressure. The measurement of the preionization electron number density is required not only in the computation of the characteristics of discharge lasers, but also in the identification of the preionization electrons formation or loss mechanism. The measurements are often made by determining the gas mixture conductivity or electron drift current between two collecting electrodes subject to a given voltage. However, due to a very strong electro-magnetic interference (typically, in the first few μs) arising from the firing of the preionizer, it is difficult to use the laser discharge electrodes as collecting plates. In order to overcome this problem, the preionization electron density has been measured by collecting the electric charge of the drifting electrons. In this way the measurements can be done with a high signal-to-noise ratio. The measurements require rather long ($> \mu\text{s}$) collecting time, so that they must be done without the electron attaching species in the gas mixture.

An important process which must be taken into account is the ion space charge which develops near the cathode due to the drifting electrons. This space charge field or potential drop can strongly influence the drifting process of the electrons.

A model⁴¹ has been developed to describe the collection of the drifting electrons in presence of space charge.

The main results are: if the ionized region is limited by parallel electrodes of area S , at a distance d , and if n_e is the uniform electron density produced by the preionization, the applied voltage V_0 in order to collect all the electric charge must be

$$V_0 \geq e n_e \frac{d^2}{2 \epsilon_0} = V_{\min} \quad (27)$$

If $V_0 < V_{\min}$, then the collected electron charge Q will be expressed by

$$Q = S \sqrt{2 \epsilon_0 V_0 n_e e} \quad (28)$$

while when $V_0 > V_{\min}$, it will be

$$Q = S d n_e e \quad (29)$$

which is independent of collecting voltage.

REFERENCES

1. N.G.Basov et al., Sov.J.Quantum Electron. **1** (1971), 18.
2. R.Srinivasan and V.Mayne-Bantom, Appl.Phys.Lett. **41** (1982), 576.
3. H.A.Koehler et al., Appl.Phys.Lett. **21** (1972), 198;
P.W.Hoff et al., Opt.Comm. **8** (1973), 128;
G.B.Gerardo, A.W.Johnson, IEEE J.Quantum Electron. **QE-19** (1973), 748;
W.H.Hughes et al., Appl.Phys.Lett. **24** (1974), 488;
W.H.Hughes et al., Appl.Phys.Lett. **25** (1974), 85.

4. J.H.Parks, *Appl.Phys.Lett.* **31** (1977), 192;
 J.H.Parks, *Appl.Phys.Lett.* **31** (1977), 297; W.T.Whitney, *Appl.Phys.Lett.* **32** (1978), 239;
 K.Y.Tang et al., *Appl.Phys.Lett.* **32** (1978), 226.
5. C.K.Rhodes: "Excimer Lasers", II ed., Springer-Verlag, 1984.
6. J.E.Velazco et al., *J.Chem.Phys.* **65** (1976), 3468.
7. V.Boffa et al., SPIE **701**, pg.158, ECOOSA '86.
8. G.C.Tisone et al., *IEEE J.Quantum Electron.* **QE-18** (1982), 1008.
9. J.H.Jacob et al., *J.Appl.Phys.* **50** (1979), 5130.
10. M.Hunter et al., *IEEE J.Quantum Electron.* **QE-22** (1986), 386.
11. C.P.Christensen et al., *Opt.Lett.* **12** (1987),169.
12. L.G.Wiley et al., *Appl.Phys.Lett.* **35** (1979), 239.
13. M.S.Arteev et al., *Sov.J.Quantum Electron.* **16** (1986), 1448.
14. M.A.Prelas et al., *Laser & Particle Beams* **6** (1988), 25.
15. W.H.Long Jr.and M.L.Bhaumik, *J.de Physique* **40** (1979),C7,127.
16. J.I.Levatter, S.C.Lin, *J.Appl.Phys.* **51** (1980), 210.
17. K.Midorikawa et al., *IEEE J.Quantum Electron.* **QE-20** (1984), 198.
18. G.Stielow et al., *Appl.Phys.B* **47** (1988), 333; M.Ohwa, M.Obara, *J.Appl.Phys.* **59** (1986), 32;
 M.Maeda et al., *Jap.J.Appl.Phys.* **21** (1982), 1161; H.Hokazono et al., *J.Appl.Phys.* **56** (1984), 680.
19. a) M.R.Osborne, M.H.R.Hutchinson, *J.Appl.Phys.* **59** (1986),711;
 b) R.S.Taylor, *Appl.Phys.B* **41** (1986),1.
20. J.Coutts,C.E.Webbs, *J.Appl.Phys.* **59** (1986),704.
21. T.Hermsen, *Opt.Comm.* **64** (1987), 59.
22. C.A.Luca and H.N.Rutt, *Opt.& Laser Techn.* **21** (1989),99.
23. T.Letardi et al., ENEA Technical Report, RT/TIB/87/49.
24. a) W.W.Rigrod, *IEEE J.Quantum Electron.*, **QE-14** (1978), 377;
 b) G.M.Schindler, *IEEE J.Quantum Electron.* **QE-16** (1980), 546;
 c) D.Eimerl, *J.Appl.Phys.* **51** (1980),3008.
25. T .Hermsen, to be published on ENEA Technical Report.
26. A.E.Siegman, *Appl.Opt.* **13** (1974), 353.
27. a) P.G.Gobbi, G.C.Reali, *Opt.Comm.* **52** (1984), 195;
 b) V.Boffa et al., *IEEE J.Quantum Electron.* **QE-23** (1987), 1241.
28. P.Di Lazzaro et al., *Appl.Phys.B* **39** (1986),131;
 D.T.J. McKee and G.T. Boyd, *Appl. Opt.* **27** (1988), 1810.
29. a) J.P.Partanen, M.J.Shaw, *Appl.Phys.B* **43** (1987),231;
 b) T.J.Pacala et al., *Appl.Phys.Lett.* **45** (1984), 507.
30. a) Efthimiopoulos et al., *Can.J.Phys.* **57** (1979), 1437;
 b) C.P.Christensen et al., *Appl.Phys.Lett.* **29** (1976), 424.
31. G.Reksten et al., *Appl.Phys.Lett.* **39** (1981), 129.
32. a) J.H.Glownia et al., *J.Opt.Soc.Am.B* **4** (1987), 1061;
 b) S.Szatmari et al., *Opt.Comm.* **63** (1987), 305;
 c) S.Watanabe, *Opt.Lett.* **13** (1988), 580.
33. R.L.Fork et al., *Opt.Lett.* **9** (1984), 150.
34. R.S.Taylor and K.L.Leopold, *J.Appl.Phys.* **65** (1989), 22.
35. W.G.Long et al., *Appl.Phys.Lett.* **62** (1987), 735.
36. L.F.Champagne et al., *J.Appl.Phys.* **62** (1987), 1576.
37. Lasers & Optronics, January 1989, pg.8.
38. Laser Focus, September 1988, pg.8.
39. J.K.Rice et al., *IEEE J.Quantum Electron.* **QE-16** (1980), 1315.
40. A.De Angelis et al., *Appl.Phys.B* **47** (1988), 1.
41. G.Giordano et al., ENEA Technical Report RT/TIB/87/65.

FUNDAMENTAL PROPERTIES OF RF GLOW DISCHARGES:
AN APPROACH BASED ON SELF-CONSISTENT NUMERICAL MODELS

J.P. Boeuf and Ph. Belenguer

Centre de Physique Atomique de Toulouse
CNRS Unité de Recherche Associée 277
Université Paul Sabatier, 118, route de Narbonne
31062 Toulouse, Cedex, France

INTRODUCTION

Non thermal plasmas such as those generated by DC or RF glow discharges are attractive for plasma chemistry due to their ability to achieve high temperature chemistry at low gas temperature. In DC or RF glow discharges, the electrons carry the energy which is necessary to excite, dissociate or ionize the gas molecules and to create reactive species. The resulting plasma can be chemically reactive both in the gas phase and with the surfaces exposed to it. An important application of reactive plasma concerns the microelectronics industry and is related to VLSI (very large scale integration) processing.

Due to the complexity and intricacy of the physico-chemical processes which take place in a plasma reactor, our understanding of plasma processing is far from being complete and its use is still empirical. The aim of this paper is to illustrate the basic physical properties of RF glow discharges in the light of recent results obtained from self-consistent numerical models. During the past three years, the development of self-consistent numerical models of RF and DC glow discharges has contributed to provide a better insight in the basic mechanisms and properties of these discharges. It is now generally acknowledged that the development and extension of such models represent a very promising way of assisting the conception and design of RF reactors used in the processing of semiconductor devices. In the present paper emphasis is put more on the general *physical* properties of RF discharges than on specific processing conditions, and no attempt will be made to describe the plasma chemistry of a particular type of processing reactor.

In a non thermal plasma the central role is played by the electrons which transform the electric power into "chemical power". The energy gained by the electron from the electric field is released in the form of excitation, dissociation, ionization or heating of the gas molecules. The first step toward a realistic description of the plasma chemistry in a reactor is to understand the mechanisms of electron energy gain and deposition in the discharge. In most practical condi-

tions, the electron energy deposition is not uniformly distributed throughout the discharge gap and it is of paramount importance to know where in the gap and at which time of the cycle each particular species is produced. The role of the electric field in the sheath or in the plasma bulk in the electron energy balance must be analyzed.

In this paper, we present an analysis of the electrical properties of RF glow discharges based on numerical self-consistent models, including the description of the space and time variations of electric field, charged particle densities and current densities, power deposition etc... These models consist in the solution of fluid equations to represent electron and ion transport, coupled with Poisson's equation for the field distribution. The parameters which characterize a particular RF discharge regime are: frequency, pressure, power, geometry, nature of the gas (e.g., electropositive vs electronegative gas). Depending on the conditions defined by these parameters, the basic power deposition and discharge sustaining mechanisms can change drastically. This will be illustrated by results from the numerical models for a wide range of discharge conditions: frequency (0 to a few tens of Mhz), pressure (a few tens of mtorr to a few torr), power (up to tens of mW/cm²), electropositive or electronegative gas, and symmetric or asymmetric configuration of electrodes.

PHYSICAL MODELS OF RF GLOW DISCHARGES

A self-consistent electrical model of a RF discharge is based on a description of the charged particle creation and transport processes in the electric field resulting from the voltage applied across the electrodes and from the space charge distribution. Three problems must be faced in the construction of a discharge model; one must:

- 1) choose a realistic way of describing the electron and ion kinetics
- 2) find the basic data which characterize the charged particle creation and transport processes: collision cross-sections, transport coefficients, secondary emission coefficients
- 3) build a numerical method able to solve the strongly coupled and non-linear equations and to deal with extremely large density gradients.

In this section emphasis will be put on the first point. The second point is mentioned here just to define the data used in our calculations, and the problem of the numerical method will be addressed very briefly at the end of this section. The first point is discussed below.

Fluid model vs microscopic model

The ideal way of representing the electron and ion kinetics in a weakly ionized gas is through the Boltzmann equation. The Boltzmann equation is an integro-differential equation in a 7-dimensional space (time plus 6-dimensional phase space: position-velocity) whose solutions yield the particle velocity distribution function $f(\mathbf{r}, \mathbf{v}, t)$. The excitation, dissociation and ionization rates can be deduced from the electron energy distribution function (EEDF).

In a discharge the charged particle motion is coupled with the electric field, and the transport equations must be solved together with Poisson's equation for the electric field. Although numerical methods for solving the Boltzmann equation for a given electric field distribution are available (Boeuf and Marode, 1982, Ségur et al. 1983, Moratz et al. 1987), the coupling between the electron and ion Boltz-

mann equations and Poisson's equation is a formidable numerical problem, especially if one is concerned with steady state situations. Non or "semi" self-consistent simulations of the electron and ion transport by Monte-Carlo techniques in DC (Boeuf and Marode, 1982) or RF (Kushner, 1983, 1986, Kline et al., 1989) discharges and for a given space and time distribution of the electric field have been performed. Such simulations can provide valuable information, but since the electric field distribution is not obtained self-consistently, they do not allow to predict easily how the discharge properties evolve when one of the main parameters (frequency, power, pressure) is changed. Some attempts have been made to develop self-consistent microscopic simulations based on Monte-Carlo (Kitamori and Tagashira, 1988) or particle in cell (Boswell, 1988) techniques. It seems that these methods are very time consuming and not practical to perform parametric studies of the discharge properties. Therefore, it is necessary to simplify the description of the charged particle kinetics and to use fluid models where the particle transport is characterized by mean values (density, drift velocity, mean energy, etc...) appearing in moment equations. These equations are obtained by taking the successive moments of the Boltzmann equation in the velocity space. A finite number of moment equations is not equivalent to the Boltzmann equation (B.E.) and does not form a closed system. In order to close the system, a number of assumptions concerning the particle velocity distribution function must be made. This is discussed below.

Description of the physical models

One of the most important problems in the modeling of a self-sustaining discharge is to find an accurate way of describing the ionization rate and its spatial distribution in the gap. In the moment equations approach the charged particle transport is generally described by three equations (continuity, momentum transfer, energy), the unknown functions being the first three moments of the electron velocity distribution function (EVDF): density n , drift velocity v and mean energy ϵ . However, some of the terms of these equations depend on higher order moments of the B.E., and closing the system of equations means using approximations in order to express these terms as a function of the first three moments of the EVDF or of known quantities. Let us take the example of the electron continuity equation in the one dimensional case (in the following the indexes e, p, n correspond to electrons, positive and negative ions respectively, x is the position from the left electrode, E the electric field):

$$\frac{\partial n_e}{\partial t} + \frac{\partial(n_e v_e)}{\partial x} = n_e v_i$$

$v_i(x,t)$ is the ionization rate. The ionization rate depends on the electron energy distribution function (EEDF) which is unknown. There are several possible ways to express v_i in term of known quantities:

1) One can assume as in Barnes et al. (1987), and Boeuf (1987, 1988) that the EEDF at (x,t) is similar to the EEDF which would exist under uniform conditions (e.g., in a drift tube experiment) for a constant value of the electric field, equal to $E(x,t)$. This is the local equilibrium assumption and leads to: $v_i(x,t) = v_{i,eq}(E(x,t)/N)$ (N is the gas density).

This approximation is valid when the characteristic time or distance of variations in the electric field are much larger than the mean time or distance between collisions.

2) Phenomenological ("memory factor", Ségur et al., 1983) or semi-empirical models (Sato and Tagashira, 1985) can be used.

3) One can assume that the ionization frequency depends on (x,t) only through $\epsilon_e(x,t)$. The functional dependence of v_i on ϵ_e can be obtained by assuming a given shape of the EEDF (e.g., Maxwellian) as in Graves and Jensen (1986), Graves (1987). Another approach is to take the same functional dependence of v_i on ϵ_e as under equilibrium conditions, as done by Richards et al. (1987a).

4) In the context of glow discharges, the above (1 and 3) approximations can fail completely to describe ionization by fast electrons in the glow. Assuming that the ionization rate in the glow is related to the local electric field is not correct because ionization in the glow is due to electrons which have gained their energy in the sheath. On the other hand, field reversals (Chapman, 1980, Graves and Jensen, 1986, Graves 1987, Boeuf and Ségur, 1988, Gottscho et al., 1988), tend to trap electrons in the glow; the electron density is very high in the glow and the mean energy very low (fraction of eV). It is therefore not realistic to assume that the ionization rate in the glow has a functional dependence on the local mean electron energy. It seems more realistic to consider separately electrons emitted by the cathode, accelerated in the sheath to high energies and releasing their energy in the glow, and low energy electrons created in the glow.

The results presented below have been obtained with a two electron group fluid model (described in Boeuf and Ségur, 1988; similar models have been used by Gottscho et al., 1988 and Surendra and Graves, 1988). The kinetic properties of each electron group are defined as follows:

1) the fast electrons (or beam electrons) are emitted by the electrodes under ion bombardment. In the RF case, two beams are considered, one for each electrode. They gain energy in the sheath and release their energy in the glow; they are assumed to form a monoenergetic beam (Phelps et al., 1987) whose velocity is directed toward the anode. Secondary electrons created by ionization by the fast electrons are assumed to belong to the beam if they are created in the sheath; when the ionization takes place in the glow, the secondary electrons join the low energy group which is described below. The transport of the fast electrons is described by a continuity equation and an energy equation (see below). The beam is supposed to release instantaneously its energy in the discharge (the continuity and energy equations for the beam are steady state equations).

2) The low energy electrons (bulk electrons) are created in the glow by ionization due to fast electrons; when the beam energy falls below the ionization threshold, fast electrons join the low energy group. Bulk electrons are supposed to be in equilibrium with the local electric field; they can gain energy from the field and ionize the gas molecules. The kinetics of the low energy group is described by a continuity equation and a momentum transfer equation (see below). The momentum transfer equation for the bulk electrons (as well as for the ions) is simplified by omitting the time derivative term and neglecting the drift energy with respect to the thermal energy, as in Boeuf (1987); this neglect of the inertia terms is reasonable in a collisional regime and leads to the representation of the particle flux by the sum of a drift term and a diffusion term.

The transport equations describing the two electron groups are coupled with continuity and momentum transfer equations for ions (as in Boeuf, 1987) and with Poisson's equation.

The boundary conditions are as follows:

- the gap voltage is given and of the form $V(t) = V_{RF} \cos(\omega t)$
- the density of bulk electrons and ions on the electrodes is zero

- the flux of beam electrons leaving one of the electrodes is proportional to the flux of ions reaching the cathode (coefficient γ)

We expect this model to be realistic in the domain: pressure, $p >$ a few 10 mtorr, frequency, $F <$ a few 10 MHz, gap length on the order of a few cm and electrode diameter \gg gap length. For higher F/p values 1) the inertia term of the momentum transfer equation cannot be neglected, 2) the local equilibrium description of the ionization rate of the bulk electrons is not correct.

Data

In the following sections, results are presented in helium, nitrogen and chlorine. The transport coefficients for the bulk electrons and for ions (drift velocity, ionization coefficient) for He and N₂ are taken from Ward (1962). The electron transport coefficients in chlorine (drift velocity, ionization and attachment coefficients) have been calculated by solving the Boltzmann equation (Ségur and Bordage, 1988, unpublished results), using the set of cross sections of Rogoff et al. (1986). The diffusion coefficients of the bulk electrons have been chosen in such a way that their mean energy is constant and equal to 1 eV. The electron molecule cross sections for the beam model have been taken from Phelps and Pitchford (1985) for nitrogen, and are the same as in Boeuf and Marode (1982) for helium.

Numerical methods

We do not intend to present here a review of the different numerical methods which are currently used. We just give below a few informations concerning the numerical method which has been used to obtain the results described in the present paper:

- the method is based on a finite difference representation of the transport equations and Poisson's equation; the discretization scheme of the electron and ion continuity equations is similar to the Gummel scheme used in the modeling of electron and hole transport in semiconductor devices (Gummel 1964, Scharfetter and Gummel 1969, Selberherr and Ringhofer 1984). This scheme was found to be extremely efficient for our problem (Boeuf, 1987, 1988)
- contrary to Boeuf (1987), the transport equations and Poisson's equations are solved in an implicit way and not successively; the equations are first linearized with respect to the three variables (electron density, ion density, electric potential): this leads to a bloc-tridiagonal system which is easily solved by standard methods. Since larger time steps can be used, this implicit method is much faster than the one described in Boeuf (1987)
- the principles and details of the numerical method can be found in Kurata (1982) (in the context of semiconductor device modeling).

The main problem which remains to be solved is related to the question of the convergence of the solutions. Harmonic steady state can be reached by following a large number of cycle, until the particle densities and field do not change significantly from one cycle to the next. In the results presented below, it has been sometimes necessary to follow the time evolution of the system during more than 1 ms at 1 torr; at 10 MHz, this corresponds to 10^4 cycles and several hours of CPU are necessary on a typical workstation to simulate such a large number of cycles. Methods based on Fourier series expansions of the equations do not seem to be more efficient in term of computation time (Graves and Jensen, 1986). The computation time can probably be improved by coupling time averaged solutions with time dependent solutions (Paranjpe et al., 1988).

In this section we illustrate the basic properties of RF glow discharges with the help of numerical results from the two electron group model described above. These results have been obtained for a parallel plate configuration of electrodes, the applied voltage on the right electrode being of the form $V = V_{RF} \cos(\omega t)$ (left electrode grounded).

Field and charged particle density distributions

Figure 1 shows the spatial variations of the electric field and charged particle densities at four different times of a cycle for a typical RF discharge in helium: $V_{RF} = 300$ V, $F=10$ MHz, $d=5$ cm, $p=1$ torr, $\gamma=0.2$. In this figure and in the following, the plotted field is positive when directed toward the left electrode. At this frequency the ions cannot respond to the instantaneous electric field and are only sensitive to the time averaged field; the ion density profile is time independent. The plasma density (electron or ion density in the center of the discharge) is of the order of $1.5 \cdot 10^{11} \text{ cm}^{-3}$. The electrons are much more mobile, and their motion in the regions close to the electrodes is coupled to the formation of sheath electric fields. As can be inferred from the electric field profile each electrode is alternatively cathode-like and anode-like. The sheaths expand and contract during each cycle. During the sheath contraction the electrons flow to the electrode while during the sheath expansion those which have not reached the electrode in the preceding contraction are swept back into the plasma.

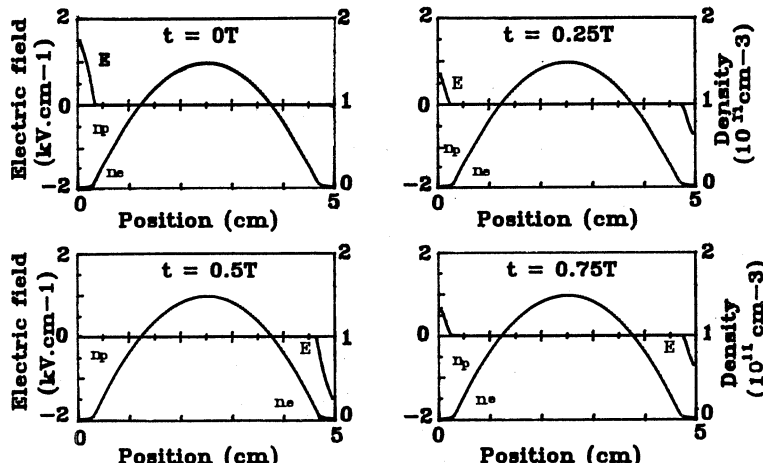


Figure 1. Spatial variations of the electric field and charged particle densities at four different times of a RF cycle; helium, $V_{RF}=300$ V, $F=10$ MHz, $d=5$ cm, $p=1$ torr, $\gamma=0.2$ (the plotted field is opposite in sign to the real field)

The motion of the electrons in the sheaths can be seen clearly in Fig. 2 which shows the space and time variations of the electron and ion density during one cycle of a lower power discharge in helium: $V_{RF}=100$ V, $F=10$ MHz, $d=5$ cm, $p=1$ torr, $\gamma=0.2$. Note that the plasma density

is about two orders of magnitude lower than in the case presented in Fig. 1 (same conditions except $V_{RF}=300V$). This point will be discussed in detail in the next section.

Space and time resolved experimental measurements of the electric field have been performed by Gottscho (Gottscho and Gaebe, 1986, Gottscho, 1987) and by Derouard et al. (1987) using laser induced fluorescence techniques. The sheath oscillations predicted by the model are confirmed by these experimental measurements.

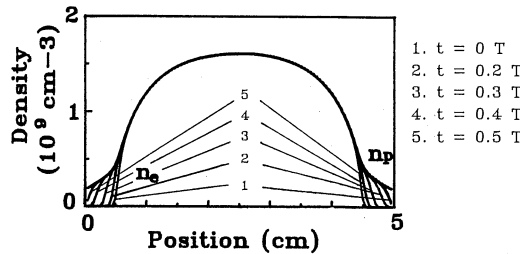


Figure 2. Space and time variations of the electron density: helium, $V_{RF}=100$ V, $F=10$ MHz, $d=5$ cm, $p=1$ torr, $\gamma=0.2$

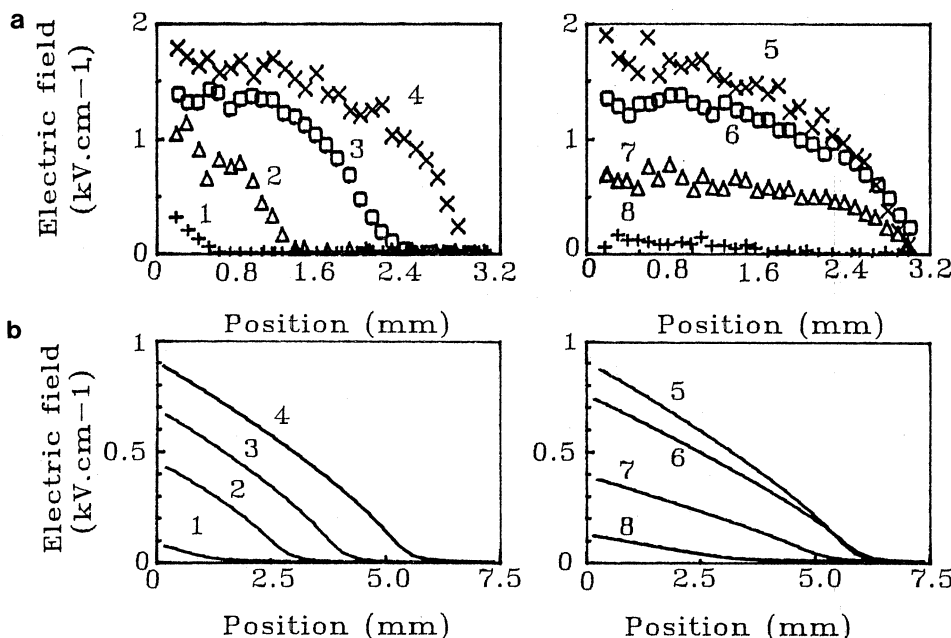


Figure 3. Spatial distribution of the electric field in the sheath region at different times in a low frequency RF discharge
 a) numerical results in helium, $V_{RF}=300$ V, $F=50$ kHz, $d=3$ cm, $p=1$ torr, $\gamma=0.2$, b) experimental measurements of Gottscho (1987) in argon (5% BCl_3), $V_{rms}=508$ V, $F=50$ kHz, $d=1.6$ cm, $p=0.3$ torr; times: (1): 0.75 T, (2): 0.8 T, (3): 0.85 T, (4): 0.95 T, (5): T, (6): 1.1 T, (7): 1.2 T, (8): 1.25 T

Gottsch noticed that for high frequency discharges, the sheath expansion and contraction are symmetric (in agreement with the numerical results corresponding to Fig. 1) and that an asymmetry appears between the expansion and the contraction when the frequency is decreased. This asymmetry at low frequencies is also predicted by the model, as shown in Fig. 3 which presents the space and time variations of the sheath electric field for a low frequency case in helium (the results of Gottsch are also reproduced).

The qualitative agreement between experimental and numerical results is striking. The differences between the low frequency and the high frequency cases can be explained as follows. At 10 MHz, the ions do not respond to the instantaneous electric field but to its time average. The ion density in the sheath stays constant and the motion of the electrons covers and uncovers the ion space charge respectively during the contraction and expansion of the sheath. At 50 kHz, the ions have time to cross the sheath during a cycle, and the ion density is therefore modulated and decreases during the sheath contraction (see the experimental results of Gottsch et al., 1984).

Current densities

The time variations of the total current densities and of its different components (displacement, electron and ion current densities) at two locations in the gap are presented in Figs. 4a and 4b for the

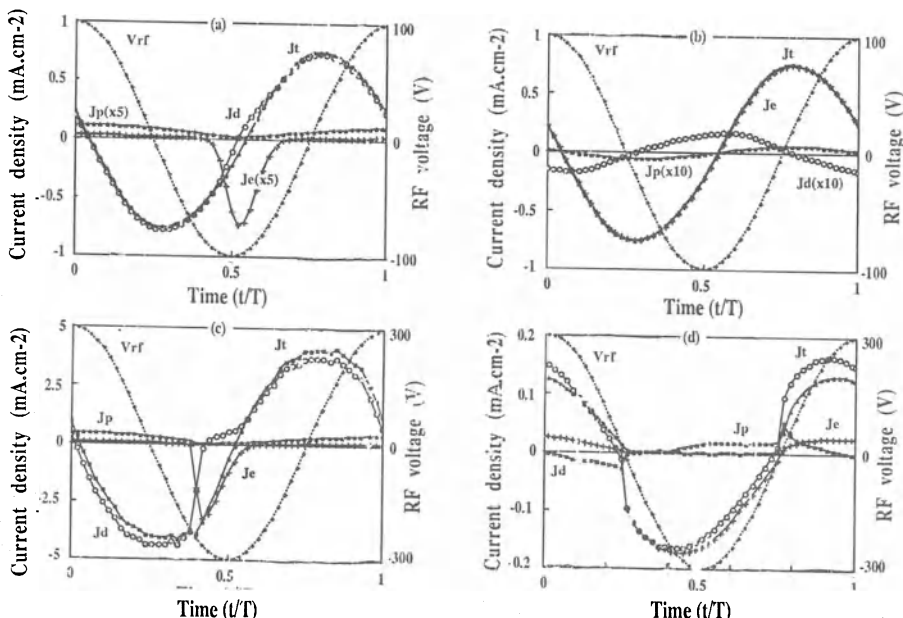


Figure 4. Time variations of the total current density J_t and of its components (displacement J_d , electron J_e , ion J_p); the applied RF voltage is also represented; a) same conditions as Fig. 2 the components of the current on the left electrode are plotted, b) same conditions as Fig. 2 the components of the current in the plasma center are represented, c) same conditions as Fig. 1 (components of the current on the left electrode), d) same conditions as Fig. 3 (components of the current on the left electrode)

high frequency case of Fig. 2. We first note that the phase shift between voltage and current is close to $\pi/2$. As expected at this frequency, the discharge impedance is mainly capacitive. The dominant current on the electrode is the displacement current ($\epsilon_0 \partial E / \partial t$). During the cathodic part of the cycle for the left electrode, the ion and electron current densities have the same sign: this corresponds to the collection of ions by the electrode and to the emission of secondary electrons leaving the electrode. In the anodic part of the cycle a large flow of electrons reaches the electrode during a short time; during this time, the electron conduction current in the sheath becomes larger than the displacement current. The net flow of charges averaged over one cycle on the electrode is zero. In the center of the plasma (Fig. 4b) the dominant current is the electron current. Figure 4c shows the time variations of the current densities on the left electrode in the conditions of Fig. 1 (higher voltage); note that the contribution of the ions to the total current in that case is higher than in Fig. 4a.

The time variations of the current density and its components in the low frequency case are plotted in Fig. 4d. The phase shift between voltage and current is now much smaller and the discharge impedance is mostly resistive, the main component of the current on the electrode being the ion current during the cathodic part of the cycle, and the electron current during the anodic part. Note the important distortion of the current waveform in this case. This distortion is related to the asymmetry between sheath expansion and contraction and to the ion density modulation in the sheaths.

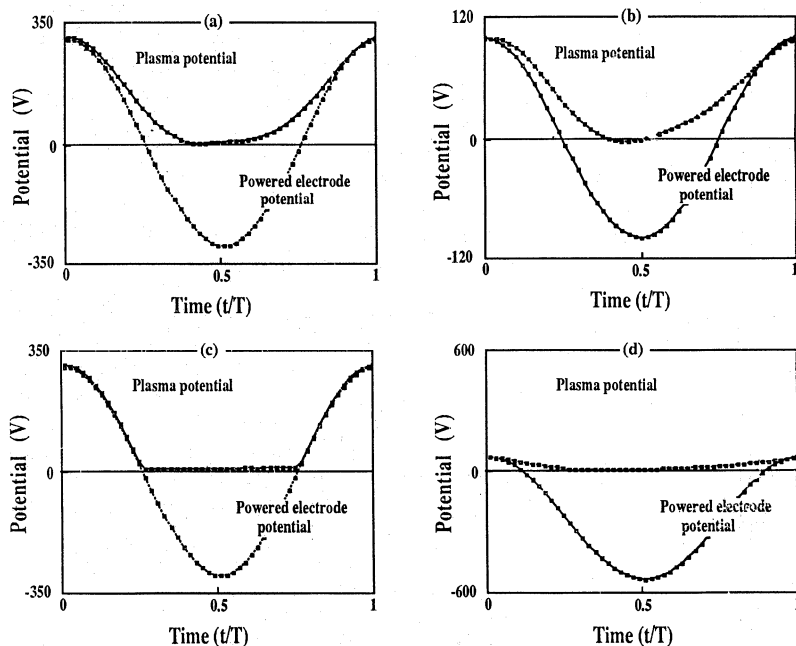


Figure 5. Time variations of the plasma potential; the potential of the powered electrode is also represented; a) same conditions as Fig. 1, b) same cond. as Fig. 2, c) same cond. as Fig. 3, d) asymmetric electrodes, same cond. as Fig. 20

Plasma potential

Figure 5 shows the time variations of the plasma potential (potential in the center of the gap) for the conditions of Figs. 1, 2 and 3 and for the case of asymmetric electrodes (see the section on asymmetric electrodes). The reference potential is the potential of the left electrode and is set to zero. The potential of the right electrode ($V_{RF} \cos(\omega t)$) is also represented. There is an important difference between the high power and the low power cases. In the first case, the plasma potential is always larger than the temporary anode potential while in the second case, the plasma potential is always lower than the temporary anode potential. The physical meaning of this difference is that in the high power case, the electric field on the anode side tends to confine the electrons inside the plasma, the net electron flow to the anode being due to the diffusion component of the current which is dominant in that case; this can be compared to the case of a DC discharge when the anode is located in the negative glow (Chapman, 1980). In the low power case the situation is opposite: the plasma potential can be lower than the anode potential and the electric field on the anode side of the discharge tends to draw the electrons out of the plasma (the drift component and the diffusion component of the electron flux are both directed toward the anode), as in the positive column of a DC glow discharge. The results presented in Fig. 5 are in good agreement with the analytical description of Köhler et al. (1985b).

In the low frequency case, the plasma potential is also always higher than the anode potential. Note that the plasma potential in that case follows very closely the momentary anode potential and is higher by only a few volts. In this conditions the discharge starts to behave like a succession of DC discharges with different voltages (this is however not completely the case since at 50 kHz, the cycle duration is still shorter than the plasma relaxation time).

The differences between the low power and the high power cases are fundamental and correspond, as will be discussed in the next section to very distinctive discharge regimes. The influence of the discharge power, frequency, pressure and gap length on the discharge properties are also discussed below.

ENERGY DEPOSITION AND SELF-SUSTAINING MECHANISMS

Different regimes of RF discharges

RF discharges can be operated in a wide range of conditions. The parameters which characterize the discharge regime are: power, frequency, pressure, nature of the gas, geometry of the reactor and nature of the surfaces.

All the other parameters being kept constant, if one of them, for example the power, is substantially modified the dominant energy deposition or self-sustaining mechanisms of the discharge can change drastically. We can first distinguish between situations where the electron energy gain and deposition processes related to either the plasma bulk or the sheath regions are dominant.

The first case corresponds to a positive column type of plasma. An RF discharge can be operated in a "positive column regime" for example if the pd product (pressure \times gap length) is large enough and if the electron losses are important (ambipolar diffusion to the wall, attachment etc...). These electron losses must be compensated by an increase in the electric field in the plasma which in turn enhances the role of the plasma field in the energy gain and deposition processes.

The sheath regions can also play in particular situations (and in most plasma processing conditions) a key role in the power balance of the discharge, for two distinct reasons which are discussed below:

- the secondary electrons emitted by the electrodes subjected to ion, metastable or photon bombardment are accelerated by the intense sheath field to very high energy (up to the RF voltage amplitude). They release their energy when entering the plasma region. When this mechanism is dominant, the plasma is similar to the negative glow of a DC glow discharge. Experimental evidence of the existence of a regime where these mechanisms are dominant has been obtained by Hebner and Verheyen (1986) and by Hebner et al. (1988). By photographing RF discharges in helium (0.3-1 torr, 1-2.6 MHz) with a high speed framing camera Hebner and Verheyen have shown the existence of ballistic electrons in the body of the glow. Microwave diagnostic techniques have been used by Hebner et al. to measure the electron density and the radiation temperature in RF discharges in helium at 2.5 MHz and 0.5 torr (also in other gases); they deduced from their measurements that the beam electrons were a significant source of ionization in these conditions, that the electron distribution function in the glow is far from being Maxwellian, and that the electric field inferred from their measurements could not agree with a calculation based on positive column theory. The experimental results show also that when the gap length is increased for a constant discharge power, the plasma density passes through a maximum for a given electrode spacing d_{\max} . For gap lengths shorter than d_{\max} , the beam electrons reach the momentary anode before they have released in inelastic collisions all the energy gained in the sheaths; the discharge is obstructed. d_{\max} corresponds to the penetration length of the beam electrons. Calculations performed with the fluid two electron group model described above in conditions similar to those of Hebner et al. are in good agreement with the experimental results and lead to the same conclusions (Boeuf 1988, unpublished results)

- the sheath oscillations which are characteristic of RF discharges can also constitute an important source of energy for the electrons. As well known, a RF discharge can be self-sustained even without secondary emission processes, and the presence of the electrodes inside the discharge vessel is not a prerequisite for the existence of a steady state self-sustained regime, contrary to the case of DC discharges. The role of the sheath oscillation in the electron energy gain and deposition mechanisms can be understood if one consider two extreme conditions:

1) the first one defines a regime which will be termed as "wave-riding" (Kushner, 1986) regime. It corresponds to a situation where the sheath is collisional for the electrons (i.e., the electron mean free path is small with respect to the sheath length). In this regime, the sheath expansion imparts some energy to the plasma bulk electrons in the following way: during the anodic part of the cycle, the electrons are flowing to the electrode and the electron density close to the electrode is large (equal to the ion density in the sheath); the following sheath expansion sweeps the cold electrons back into the plasma. If the sheath expansion is fast enough, these electrons can gain energy from the sheath field. This mechanism has been illustrated by Kushner (1986) with a Monte-Carlo simulation of a RF discharge in a argon-silane mixture. To better understand this phenomenon, let us consider one of these electrons and follow its motion during the sheath expansion. A very simple picture of this motion is the following: once the electron has been reached by the sheath field, it "rides" the expanding sheath, its average position being such that its drift velocity ($v_d = \mu E$) in the field corresponding to that position is equal to the sheath velocity (v_s). The electric field "felt" by this electron ($E = v_s/\mu$) is therefore proportional to the sheath expansion ve-

locity. The efficiency of this energy gain mechanism is therefore higher for larger sheath velocity or larger frequencies. The term "wave riding" illustrates this motion of the electrons on the sheath field "wave". Note that the problem is more complex than this simple picture, and that the sheath expansion which pushes the electrons toward the plasma center is itself the consequence of the electron motion which uncovers the ion space charge.

2) the other extreme condition corresponds to a *non collisional* (low pressure) situation where the electron mean free path is of the order of magnitude of the gap length and will be termed as "electron-sheath collision regime". In this regime the electron has a larger probability to interact with the sheaths than to undergo a collision with a molecule (while in the previous case the electron could undergo a large number of collisions during the sheath expansion). The electron exchanges momentum with the sheath and can be reflected by it (Pennebaker, 1979, Keller and Pennebaker, 1979, Popov and Godyak, 1985, Godyak, 1986, Goedde et al., 1988). Note that resonant conditions may exist where the electrons oscillate in the gap, being reflected by each sheath. Such phenomena could be related to the existence of the so-called plasmoids described in some papers (Taillet, 1968). Although the "electron-sheath collision regime" seems very rich in terms of electron kinetics, it cannot be described in the frame of a fluid model and we shall not consider it in the following. Note finally that the wave riding and the electron-sheath collision mechanisms as described above correspond only to extreme conditions and that practical situations are intermediate. However it seems useful to classify the energy gain processes due to the sheath oscillations in these two categories and this classification helps in defining the validity domain of a model.

Let us summarize the above discussion. We have defined four different regimes corresponding to different dominant mechanisms for electron energy gain. They are listed below:

- positive column regime. The electron gain energy from the plasma field which can generally be supposed to be uniform in space, and time varying.
- secondary emission regime (or γ regime in the terminology of Levistkii, 1958). Most of the electron energy is carried by electrons which are emitted by the electrodes and accelerated in the sheaths. They release their energy into a negative glow type of plasma; in this regime the plasma is similar to the negative glow of a DC discharge.
- wave riding regime (or α regime). Most of the electron energy is provided by the sheath oscillation. During the sheath expansion the electrons "surf" on the sheath field. The regime is collisional and the electron energy gain is locally balanced by the losses.
- electron-sheath collision regime. Electrons gain momentum and energy by being reflected by the expanding sheath. The regime is non collisional.

In the rest of this section, the first three of these regime are illustrated with results from the two electron group self-consistent model described above and from Monte-Carlo simulations. The purpose of this section is to show that the above classification is not academic but can be very useful in characterizing a particular situation.

Transition between wave riding regime and secondary electron regime

As mentioned earlier, when one of the discharge parameters is substantially changed, the other being kept constant, the discharge can switch, some times abruptly from one to the other of the regimes described above. In practical plasma chemistry conditions, since the processing efficiency can be strongly dependent on the discharge

regime (Perrin et al., 1988) it is of paramount importance to be aware of such transitions.

This is illustrated in Fig. 6 where an example of the transition between the wave-riding regime and the secondary emission regime is shown. In the conditions which are considered in this example, the plasma is not a positive column type of plasma in the sense defined above. The energy deposition is not uniform in the plasma and occurs mainly at the plasma-sheath boundary.

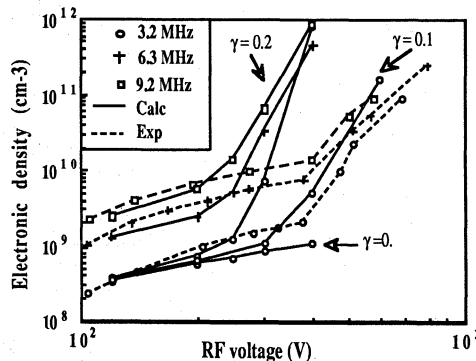


Figure 6. Variations of the plasma density as a function of the applied RF voltage: helium, $d=3$ cm, $p=3$ torr, for three values of the frequency ($\gamma=0$ and $\gamma=0.1$ curves given for 3.2 MHz only). Experimental results are from Godyak and Kanneh, 1986

This figure presents the variations of the plasma density when the amplitude of the RF voltage is increased from 120 V to 400 V in a (3 torr, 3 cm) discharge in helium, for three different values of the field frequency (3.2, 6.3, 9.2 MHz). These conditions correspond to the experimental conditions of Godyak and Kanneh (1986) except for the gap length which was larger in the experiments (7.7 cm). In the calculations, the radial dimension of the discharge is supposed to be large enough so that radial particle losses can be ignored; on the other hand the electron ion recombination has been neglected. The numerical results are plotted in Fig. 6 for a value of 0.2 of the secondary emission coefficient γ and are compared to the experimental results (numerical results for $\gamma=0$ and $\gamma=0.1$ at 3.2 MHz are also plotted). The striking feature of these curves is the sharp increase in the plasma density for a given transition voltage. The numerical model predicts a transition voltage around 220 V for $\gamma=0.2$; a good agreement with the experiment (transition voltage around 400 V) is obtained with a lower value of the secondary emission coefficient ($\gamma=0.1$, see Fig. 6). This transition can be explained as follows: for low RF voltages the multiplication of the electrons emitted by the electrode in the sheath regions is not sufficient to sustain the discharge; roughly speaking, the time averaged sheath voltage is less than the minimum DC glow discharge voltage. A supplementary ionization source is provided by the wave riding electrons which gain energy from the sheath expansion (see above). The ionization provided by these electrons increases with frequency as can be inferred from Fig. 6: in the left hand side of the plotted curves, the plasma density increases with frequency. This part of the curves corresponds to the wave-riding regime described above: most of the electron energy gain occurs at the sheath-plasma boundary

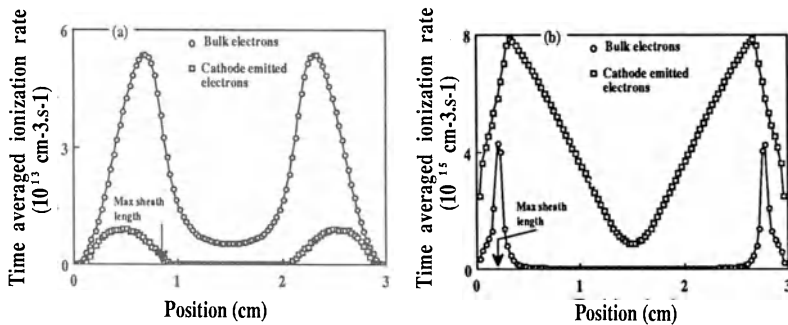


Figure 7. Spatial variations of the time averaged ionization rates; the contributions of the secondary (beam) electrons and of the wave riding electrons are separated; the maximum sheath length is indicated; helium, $F=3.2$ MHz, $d=3$ cm, $p=3$ torr, $\gamma=0.2$; a) : $V_{RF}=120$ V, b) : $V_{RF}=400$ V

and is due to the sheath expansion which imparts some energy to the plasma electrons.

A comparison of the time averaged ionization rates due to the wave-riding electrons and to the electrode-emitted electrons (beam electrons of the fluid model) can be seen in Fig. 7a in the case of a RF voltage amplitude of 120 V. The contribution of wave-riding electrons to the total ionization and therefore to the total electron energy deposition is clearly dominant in these conditions. Note the maximum at the plasma sheath boundary, which corresponds to the well known maximum emission intensity of the discharge at this location. The same curves have been plotted for a RF voltage of 400 V in Fig. 7b: the contribution of the beam electrons is here much larger than the contribution of the wave-riding electrons. Note that in this case, the secondary electrons accelerated in the sheath can penetrate deeply in the (negative glow type) plasma.

A simple way to define clearly the transition between the two regimes is to define the transition voltage as the voltage for which the total averaged ionization rates due to the wave riding electrons

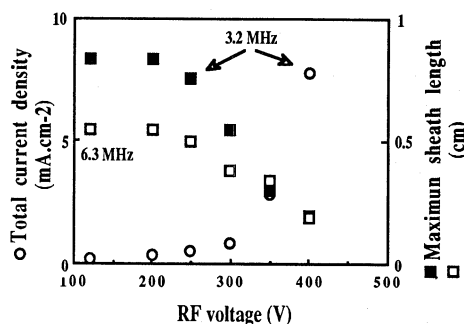


Figure 8. Variations of the maximum sheath lengths and of the total current density as a function of the applied RF voltage in helium, $F=3.2$ MHz, $d=3$ cm, $p=3$ torr, $\gamma=0.2$

and to the beam electrons are equal; this definition yields a transition voltage of 325 V for the $\gamma=0.1$ case of Fig. 6 (3.2MHz).

The transition between the wave riding regime and the secondary electron regime is accompanied by a sharp decrease in the sheath length and a large increase in the current density (Fig. 8).

In the wave riding regime, the sheath length does not change very much with the RF voltage and decreases with increasing frequencies. The variations with the RF voltage of the fractional part of the electric power dissipated by ions in the sheath, wave riding electrons and secondary electrons is shown in Fig. 9. In the case of low power densities, most of the power is dissipated by wave riding electrons; as the RF voltage (and therefore power density) is increased, the contribution of the secondary electrons becomes much larger than that of wave riding electrons but most of the power is dissipated by ions in the sheaths.

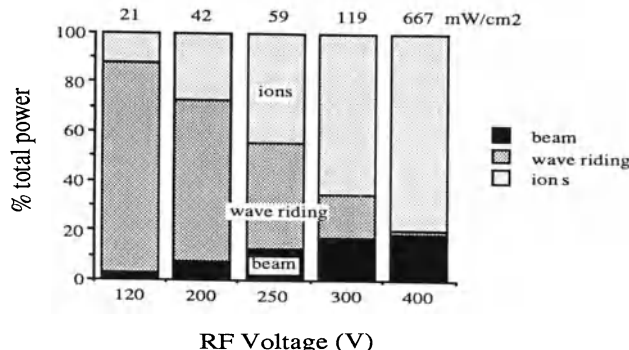


Figure 9. Partial contributions of the ions, wave riding electrons and secondary (beam) electrons to the total power deposition for five values of the RF voltage in helium, $F=9.2$ MHz, $d=3$ cm, $p=3$ torr, $\gamma=0.2$; the total power flux is also indicated

When the secondary electron emission is set to zero in the calculations (the curve corresponding to $\gamma=0$ at 3.2 MHz is also plotted in Fig. 6) there cannot be a transition, and the plasma density increases smoothly with the RF voltage.

Note that in the light of the above discussion, we can conclude that the discharge regimes corresponding to Fig. 1 and Fig. 2 of the previous section correspond respectively to the secondary electron regime and to the wave riding regime. The low frequency case of Fig. 3, corresponds clearly to the secondary electron regime since at this frequency (50 kHz) the sheath expansion is not fast enough to provide energy to the plasma electrons.

Let us mention that since the discharge parameter space is multi-dimensional, there are different ways to observe such transitions. In the above example the transition occurred while increasing the applied RF voltage, all the other parameters being kept constant. It would be possible to observe this transition by increasing the pressure (Perrin et al., 1988) or by decreasing the frequency at constant discharge power. Note finally that at relatively high pressures, the

transition can be discontinuous and present some hysteresis (Vidaud et al., 1988).

Positive column regime

In this regime most of the electric power is dissipated in the body of the plasma. This situation may occur when the charged particle losses are non negligible, e.g., radial ambipolar losses in long discharge gaps or losses due to recombination or attachment. In order to maintain the current continuity, these losses must be compensated by a supplementary ionization in the plasma volume which is made possible by an increase in the plasma field. If this field is high enough or the column long enough, the power dissipated in the column can become much larger than the power dissipated in the sheath regions.

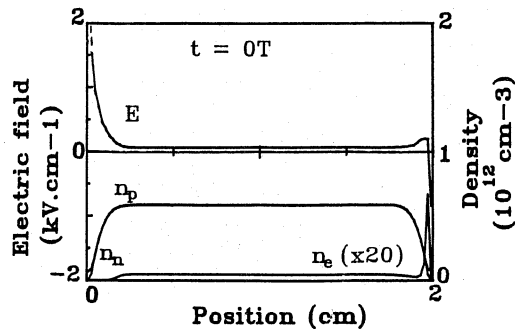


Figure 10. Spatial variations of the electric field and charged particle densities at time $t=0$ of a RF discharge in chlorine, $V_{RF}=280$ V, $F=13$ MHz, $d=2$ cm, $p=1$ torr, $\gamma=0.05$

This situation is illustrated here with the case of a 13 MHz discharge in chlorine at $p=1$ torr, $d=2$ cm and for $\gamma=0.05$. Fig. 10 shows the spatial variations of the electric field and charged particle densities at the beginning of a cycle. As in the previous cases, the sheaths oscillate although the shape of the electric field in the sheath is different than in the case of Fig. 1. The positive (Cl_2^+) and negative (Cl^-) ion densities in the plasma are much higher than the electron density (more than two orders of magnitude) due to the important attachment. The electron density profile will be discussed with more details in the next section. Let us note the relatively high value of the electric field (70 V/cm); the electric field and the ion densities are almost spatially uniform in the plasma, which is similar to a positive column DC plasma with a time varying field.

The time variations of the electric field at different positions in the discharge are shown in Fig. 11a and are in good agreement with the results obtained by Rogoff et al. with a simpler model.

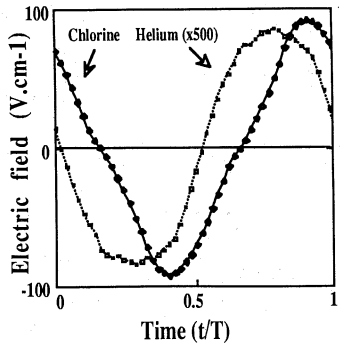


Figure 11. Time variations of the electric field in the plasma center: a) chlorine, same conditions as Fig. 10, b) helium, same conditions as Fig. 1.

The comparison of the electric field in the plasma bulk in this case and in the case of helium (Fig. 11b, same conditions as Fig. 1) illustrates the difference between the positive column regime and the secondary electron regime; in the latter case the plasma field is much smaller and plays no role in the power deposition. On the other hand, we note the different phases of the plasma field in the chlorine and in the helium cases: this indicates that the chlorine discharge is much more resistive (due to the importance of the plasma field) than the helium discharge, in agreement with the experimental results of Flamm and Donnelly (1986). The spatial distributions of the time averaged ionization and attachment rates in the gap are plotted in Fig. 12. It appears clearly in this figure that 1) the energy deposition in the column can be considered to be uniform, 2) the total energy deposition in the column is larger than the energy deposition in the sheath regions (and could be much larger for longer gaps or higher pressure) and, 3) the electric field in the plasma has adjusted in such a way that the electron losses by attachment are compensated by ionization.

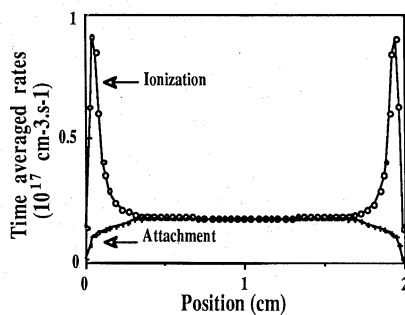


Figure 12. Spatial distribution of the time averaged ionization and attachment rates in chlorine, same conditions as Fig. 10

The atomic chlorine concentration has also been calculated assuming creation by electron impact dissociative excitation and attachment of Cl₂ and destruction by recombination on the electrodes; this concentration was found to be between 5 and 10 % of the molecule concentration, in reasonable agreement with the measurements of Richards et al. (1987b).

To conclude this part let us note that in these conditions (existence of a positive column type of plasma where most of the energy deposition takes place) and only in these conditions the power deposition balance of the discharge can be obtained by solving the Boltzmann equation in a spatially uniform, time varying electric field as has been done in a number of papers (Winkler et al., 1985, Ferreira and Loureiro, 1989, Capitelli et al., 1988). Unfortunately, in a lot of practical conditions of plasma processing the dominant energy deposition processes occur in the sheath regions where the electron kinetics is much more complicated due to strong density gradients and spatially non uniform time varying electric fields. This complexity is illustrated below.

Electron kinetics in the wave-riding regime (Monte-Carlo simulations)

We present here, with a Monte-Carlo simulation, an illustration of the wave riding mechanism.

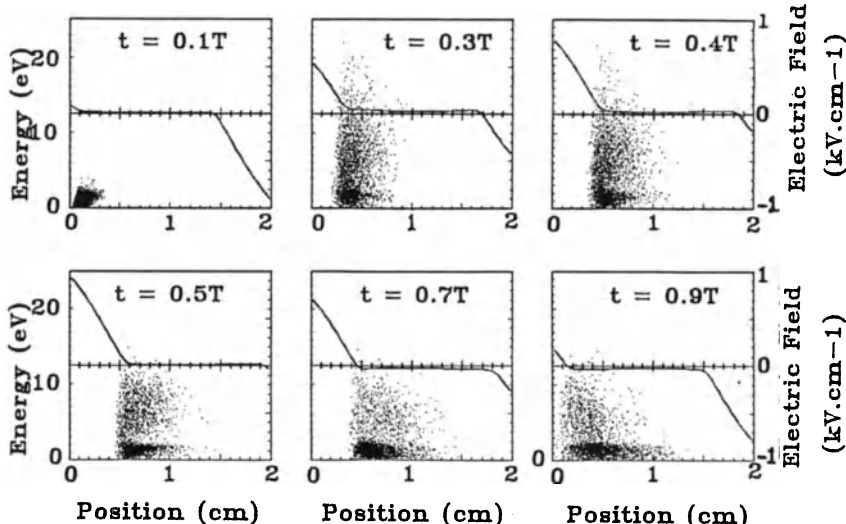


Figure 13. Evolution of the positions in the energy-position space of a sample of electrons during the sheath expansion and contraction in nitrogen, $V_{RF}=300$ V, $F=10$ MHz, $d=2$ cm, $p=1$ torr, $\gamma=0.02$; the electrons are supposed to be located at 1 mm from the cathode and to have a monoenergetic distribution (0.5 eV) at time $t=0$; the electric field distribution at each time is also plotted

Using the self-consistent space and time varying field obtained with the two electron group model in the case of a discharge in nitrogen ($V_{RF}=300$ V, $F=10$ MHz, $d=1$ cm, $p=1$ torr, $\gamma=0.02$), we follow the trajectories of a sample of electrons which are exposed to the sheath expansion. Such simulation can help understanding qualitatively and quantitatively how the plasma electrons gain energy from the expanding sheath. The results are presented in Fig. 13. Let $t=0$ be the time when

the potential of the right electrode is ($-V_{RF}$) with respect to the potential of the left electrode (momentary anode). We consider at time $t=0$, a large number of monoenergetic (0.5 eV) electrons located at 0.1 mm from the left electrode. Their initial energy distribution function (EEDF) is therefore a δ function in space and energy. The maximum sheath length being around 6 mm under the above conditions, these electrons are going to be swept into the plasma by the sheath expansion starting around $t=0$ on left electrode side. Fig. 13 shows this phenomenon.

This figure represents, at 6 different times of the cycle, the positions of the initial electrons and of the electrons created by ionization in the energy-position space; the spatial distribution of the instantaneous electric field is also plotted at the same times. One can see that during the sheath expansion, the electrons are pushed toward the plasma center and that a large number of electrons are accelerated to energies high enough to create substantial ionization and electronic excitation. During the following sheath contraction the electrons release their energy through inelastic collisions while diffusing and drifting toward the electrode. Note on this figure at time $t=0.5$ T, the lack of electrons in the energy range 3-7 eV. This corresponds to a hole in the distribution function in this energy range which is due to the fact that there is no important inelastic energy losses in nitrogen in the domain between the maximum of the vibrational excitation and the first electronic excitations. This hole in the distribution function is characteristic of the energy relaxation of electrons in nitrogen in a post discharge (i.e., in a zero field) as shown for example by Capitelli et al. (1981). The effect of superelastic vibrational collisions which have not been taken into account in the present calculation would be to "fill" this hole in EEDF (ibid.).

Note finally that although the electrons can get enough energy from the sheath expansion to produce substantial ionization, they are not accelerated to very high energy. The situation is different in the case of secondary electrons emitted by the momentary cathode, because these electrons may, at some time of the cycle, "see" the maximum sheath potential. This is never the case for wave riding electrons as seen in Fig. 13. The kinetics of secondary electrons in RF discharge is discussed below.

Electron kinetics in the secondary electron regime (Monte-Carlo simulations)

We consider here a RF discharge in nitrogen for the following conditions which correspond to the secondary electron regime: $V_{RF}=700$ V, $F=2$ MHz, $d=1$ cm, $p=1$ torr, $\gamma=0.02$. For these conditions, the space and time variations of the electric field have been obtained from the self-consistent two group fluid model. Using this electric field distribution, A Monte-Carlo simulation has been performed to analyze the transport of the secondary electrons over one single cycle. The flux of the secondary electrons emitted by the electrode is supposed to be proportional to the flux of ions on the cathode (deduced from the fluid model).

Figure 14 shows, at the time corresponding to the maximum sheath length on the left electrode (momentary cathode), the spatial variations of the electron energy distribution function $f(\epsilon, x)$ (where ϵ is the energy and x the position from the left electrode). In this representation of the EEDF the electron density $n_e(x)$ is proportional to $(\int f(\epsilon, x) \epsilon^{1/2} d\epsilon)$. A Maxwellian distribution would correspond to a

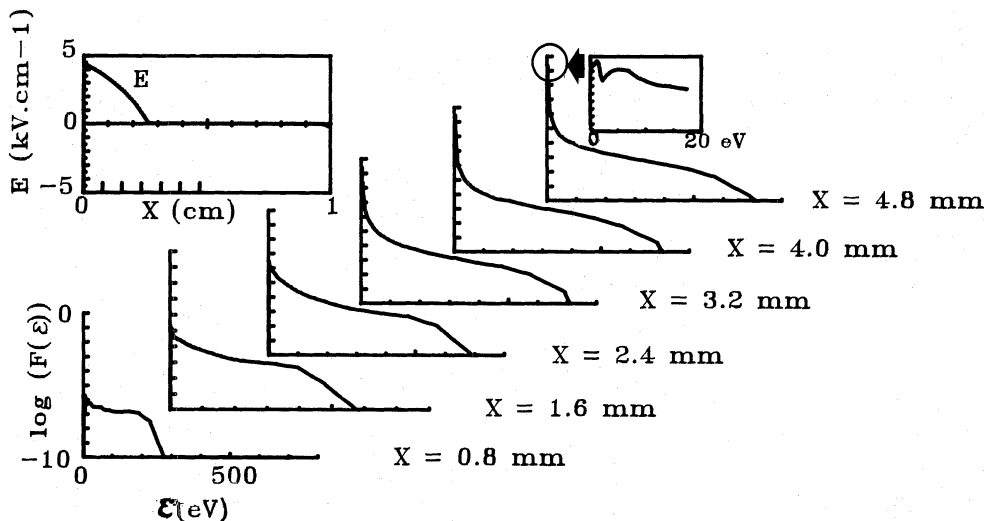


Figure 14. Spatial variations at time $t=T/2$ of the EEDF corresponding to secondary electrons emitted between $t=0$ and $t=T/2$ in a RF discharge in nitrogen, $V_{RF}=700$ V, $F=2$ MHz, $d=1$ cm, $p=1$ torr, $\gamma=0.02$; $t=T/2$ corresponds to the maximum sheath length; the electric field is also represented

straight line in this representation. The spatial distribution of the instantaneous electric field is also represented in this figure.

The striking feature of Fig. 14 is related to the very non Maxwellian shape of the EEDF and to the large number of high energy electrons in the sheath and in the glow. The EEDF at a position x where the electric field is $E(x)$ is also very different from the EEDF which could be calculated for the same value of the electric field but in a uniform steady state situation. This is related to the non equilibrium nature of the transport of the cathode emitted electrons in the sheath region: the energy gained by the electrons in the sheath is not locally balanced by the losses but is released while they penetrate into the zero field region (glow) in the form of inelastic collisions. This appears in Fig. 14 where the density of low energy electrons resulting from the relaxation of high energy electrons coming from the sheath increases abruptly at the sheath-plasma boundary. Note the shape of the EEDF in the 0-10 eV region in the glow which is characteristic of the electron relaxation in nitrogen (see above).

Note finally that one can deduce from Fig. 14 that the representation of the EEDF by a "two temperature Maxwellian" would be a reasonable approximation in a fluid model.

Equivalent electric circuit of a RF discharge

The representation of a RF discharge by an equivalent electric circuit is very appealing and can be useful to help predicting the discharge behavior when parameters such as frequency or power are changed. We do not intend here to present a review (see for example Logan et al., 1977, Pennebaker, 1979, Keller and Pennebaker, 1979, Köhler et al., 1985) of this question but rather to emphasize that a real knowledge and understanding of the energy deposition mechanisms is a prerequisite to the determination of the equivalent circuit. On the other hand, experimental measurements of the discharge impedance and can help determining the dominant energy deposition mechanisms and

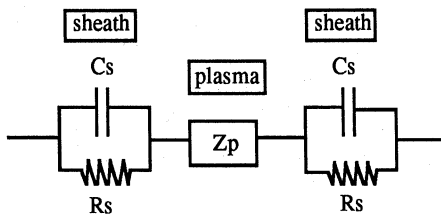


Figure 15. Equivalent circuit of a RF discharge

their change with changes in the discharge parameters (van Roosmalen et al., 1985, Bletzinger and Flemming, 1987).

The classical equivalent circuit of a RF discharge is presented in Fig. 15. The sheaths are represented by a capacitor C_s in parallel with a resistor R_s ; the resistor is related to the ohmic power dissipated by the ions in the sheaths and the capacitor to the displacement current in these regions. The plasma impedance Z_p has a resistive component corresponding to the ohmic power dissipated by electrons (and ions) in the plasma bulk. The plasma impedance can also have an inductive part related to the inertia of the charged particles which induces, at low pressures (i.e., when the angular frequency of the applied voltage is non negligible with respect to the momentum transfer frequency) a phase shift between charged particle velocities and electric field (and therefore between current and voltage) (Popov and Godyak, 1985). Our model cannot describe this inductive part since inertia has been neglected in the momentum transfer equations but could be extended to include this phenomenon (this has been done for ions by Richards et al., 1987a).

This representation is generally satisfactory although it cannot account for the distortion which may exist in the current for a given applied RF voltage. A possible reason of the existence of this distortion can be the sheath oscillation. The oscillation of the sheaths implies that each sheath separately cannot be represented by a constant capacitor but rather by a time varying capacitor (Metze et al., 1986, Bletzinger and Flemming, 1987); however, since at high frequencies the sum of the two sheath lengths can be to the first order considered to be constant over one cycle (Godyak, 1986), the equivalent capacitance of the two sheaths is approximately constant. There is generally no strong distortion at high frequencies (see Fig. 4d) because the current in the sheaths is mainly a displacement current and because the assumption of a constant equivalent capacitance is good as explained above. At low frequencies the dominant current in the sheaths is the ion current (Fig. 4) and the distortion is due to the fact that the ion density is modulated in time.

The determination of the dependence of the components of the equivalent circuit on the discharge parameters (frequency, pressure, power) is very difficult (van Roosmalen et al., 1985) and no satisfactory analytical model able to describe the discharge behavior in a large domain of parameter variations exists. In trying to estimate these components, one must be aware of the different possible energy deposition mechanisms described in this section. For example, if the energy deposition is due mainly to secondary electrons emitted by the momentary cathode, the classical representation of the plasma by a resistor whose conductivity is simply related to the electron density and mobility by $\sigma = qne\mu_e$ fails completely because the electron power balance is not local in the glow (i.e. the energy deposited by the

electrons in the glow is not related to the energy gained in the glow but to the energy gained in the sheath); this representation is also not valid in the case of energy deposition by wave riding electrons.

ROLE OF NEGATIVE IONS

Negative ions can play an important role in RF discharges even in the case of weakly attaching mixtures. At high frequencies (for example at the industrial frequency of 13.56 MHz) the oscillations of the sheaths tend to trap the negative ions into the discharge volume. While, due to their larger mobilities, the electrons can easily reach the momentary anode, the negative ions are not fast enough to reach the electrode during the anodic part of the cycle. The only negative ion loss processes in these conditions are therefore ion-ion recombination, detachment, ambipolar diffusion to the walls. Another aspect of the importance of the presence of negative ions in the plasma which has already been illustrated in the previous section is the higher plasma field which is generally associated with it.

In this section we use the example of a discharge in chlorine to discuss the specific properties of RF discharges in electronegative gases. Results from the fluid models are presented and compared with experimental results in similar conditions.

Field and charged particle density - Double layers

We mentioned above that the negative ions tend to be trapped by the oscillating sheaths at high frequencies. When the frequency is decreased from 13 MHz, we reach a point where the ions become more sensitive to the instantaneous variations of the electric field and the modulation of their density becomes non negligible. This modulation can induce some important space charge effects in the regions close to the electrodes. Such space charge effects have been first detected experimentally by Gottscho and Gaebe (1986), Gottscho (1987) by measuring the space and time variations of the electric field (by laser induced fluorescence) in discharge containing BCl_3 . These measurements showed that for frequencies less than the ion plasma frequency (which is of the order of the inverse of the time necessary for the ions to cross the sheath), the electric space distribution presents a local maximum at the plasma-sheath boundary and during a short part of the cycle. Such local maxima in the electric field profile are necessarily due to the formation of double layers in the charged particle density distribution. The presence of these double layers has been analyzed with the help of fluid models and has been attributed (Boeuf, 1987) to the existence of a maximum in the modulation of the negative ion and positive ion number densities at the plasma-sheath boundary.

This is illustrated, in the case of chlorine, by Fig. 16 which shows the charged particle density and field distribution at four different times of a cycle for the following conditions: $V_{RF}=400$ V, $f=1$ MHz, $d=1$ cm, $p=0.3$ torr, $\gamma=0.05$, which correspond roughly to the experimental conditions of Flamm and Donnelly (1986). The local maximum of the electric field at the plasma-sheath boundary is as large as 400 V/cm and occurs when the applied potential between the electrodes is maximal. Note the large value of the positive and negative ion number densities in the plasma (10^{11}cm^{-3}) compared with the electron number density (2.10^7cm^{-3}).

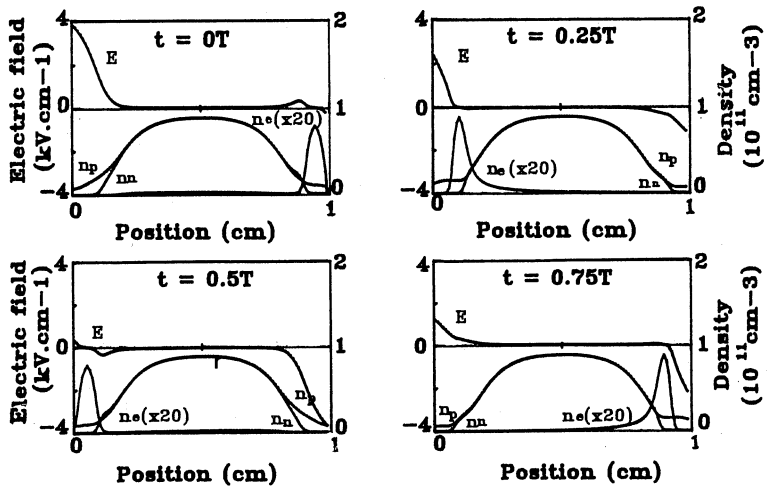


Figure 16. Electric field and charged particle densities profiles at $f_c = 1.6 \text{ GHz}$ and $V_{RF} = 400 \text{ V}$, $F = 1$.

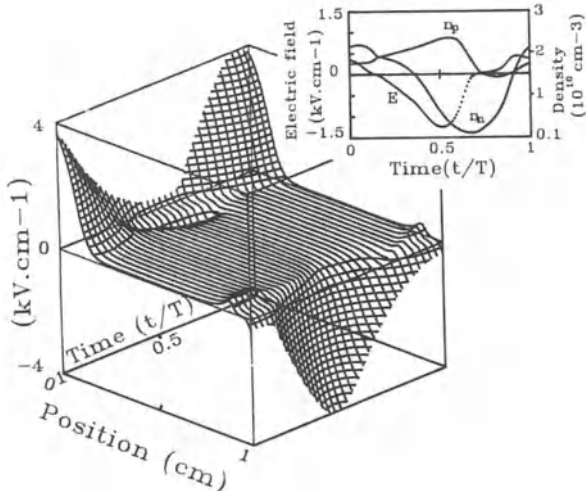


Figure 17. a) space and time variations of the electric field in a 1 MHz discharge in chlorine, same conditions as Fig. 16; b) time variations of the charged particle densities and field over one cycle at the location of the local maximum of the electric field in Fig. 17a

The space and time variations of the electric field and the double layer effect can also be seen in Fig. 17a. In Fig. 17b are shown the time variations over one cycle of the charged particle densities and electric field at the position of the local maximum of the electric field. The large modulation of the ion densities at this location appears clearly in this figure. Since the modulation of the negative and positive ions are opposite in sign, this phenomenon induces a large double layer which is responsible for the field maximum in space.

The qualitative agreement between the experimental results of Gottscho (1987) and the numerical results is striking and shows that such models can be very useful to predict the discharge properties in particular conditions and to analyze the influence of a parameter (frequency, power etc...) on the discharge regime.

Electron kinetics - Excitation rates

As can be seen in Fig. 16, the space and time evolution of the electron density in electronegative gases presents some specific features. The electron density profile at different times in the first half of a RF cycle for a frequency of 13 MHz in chlorine (experimental conditions of Flamm and Donnelly, 1986) are presented in Fig. 18 (the electric field distribution at each time is also represented).

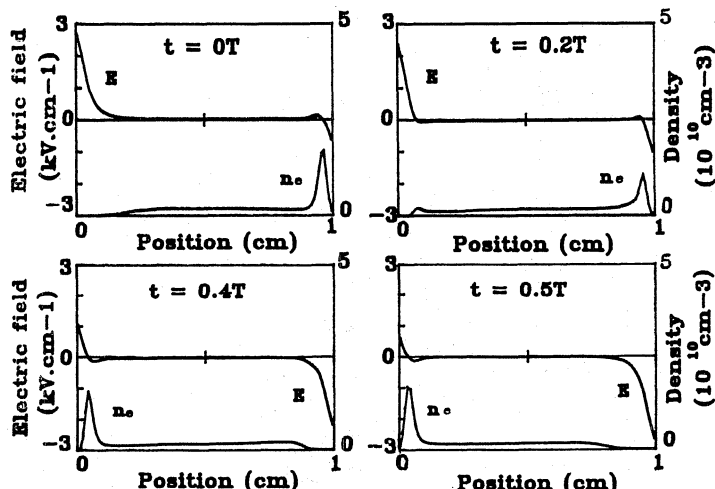


Figure 18. Electron density and electric field distributions at four different times of a RF half cycle in chlorine, $V_{RF}=140$ V, $f=13$ MHz, $d=1$ cm, $p=0.3$ torr, $\gamma=0.05$

The shape of the density is similar to the 1 MHz case of Fig. 16. The maximum in the electron density in the region of the momentary anode can be explained as follows. During the anodic part of the cycle the electric field draws the plasma electrons toward the momentary anode. A field reversal near the anode tends to prevent the electrons from reaching the electrode. Therefore the electrons accumulate in this region (some of them being reflected by the potential barrier) until the diffusion current overcomes the conduction current allowing part of the electrons to reach the anode; the increase of the electron space charge can also induces a decrease in the potential barrier mak-

ing possible the electron flow to the anode. The reflection of the electrons by the potential barrier increases the energy deposition by these electrons in the form of inelastic collisions (this energy would have been otherwise lost in the electrode). It seems that this phenomenon, which has been also predicted by other numerical models (Gogolides et al., 1988, 1989, see also Boeuf, 1987) corresponds to the emission observed by Flamm et Donnelly (1986) (also Gogolides et al., 1989) on the anode side and during the anodic part of the cycle in electronegative gases. The increase in the electron density and energy deposition predicted by the model could be associated with an increase in the excitation rates and therefore in the emission intensity. If confirmed, this explanation of the experimental observations by the model is another striking illustration of the potential of the fluid models.

ASYMMETRIC ELECTRODES

In a number of practical situations, for example in sputtering and ion etching systems (Chapman, 1980) the target area can be much smaller than the wall area. If the electric power is loaded into the discharge through a blocking capacitor, the asymmetry of the electrodes induces the formation of a DC self-bias across the discharge gap which superimposes with the RF voltage. A description of the establishment of this DC bias can be found in Chapman (1980).

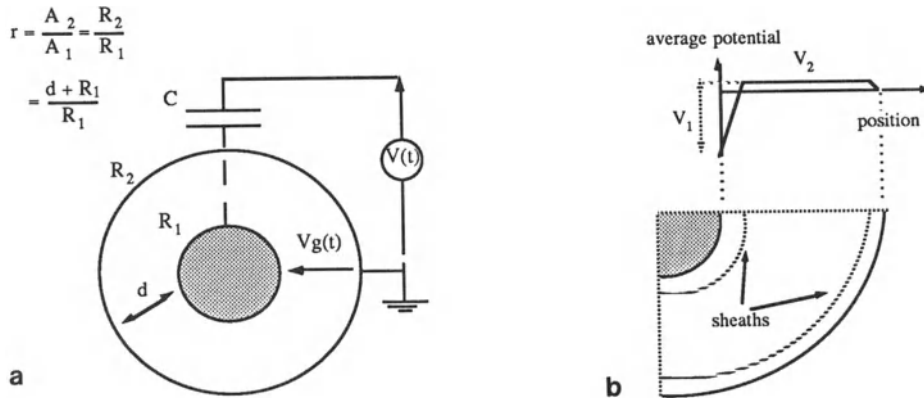


Figure 19. a) scheme of the asymmetric configuration of electrodes used in the numerical model; r is the electrode area ratio
b) definition of the time averaged sheath potentials; the outer electrode being grounded, V_2 is also the plasma potential with respect to this electrode

In this section we show how the numerical models can help understanding the specific properties of RF discharges with asymmetric electrode configurations. The simplest way to include electrode asymmetry in a model is to stay in the frame of a 1D model and to use a cylindrical configuration. Only minor changes in the model described above are necessary to pass from a parallel plate configuration to a cylindrical geometry. The geometry of the discharge which is considered in this section is presented in Fig. 19: the electrodes are two infinite concentric cylinders; the outer cylinder is grounded while the RF voltage is loaded to the inner cylinder through a capacitance. The applied RF voltage is still of the form $V(t)=V_{RF}\cos(\omega t)$ but the resulting voltage $V_g(t)$ across the gap is different due to the charging of the blocking capacitor and is calculated self-consistently. For a constant gap length, the area ratio of the electrodes can be changed by changing the electrode radii.

Field and charged particle density - DC bias

Figure 20 shows the spatial variations of the electric field and charged particle densities at different times of a RF cycle for a discharge in Helium under the conditions: $V_{RF}=300$ V, $F=10$ MHz, $d=4$ cm, $p=1$ torr, $\gamma=0.2$; the area ratio of the electrodes is 0.5. The left electrode corresponds to the inner cylinder. It appears in Fig. 20 that the electrode asymmetry has induced an asymmetry in the sheaths. The sheath corresponding to the smaller electrode area has a larger maximum length and a much larger electric field, in agreement with the experimental observations. The mean sheath voltages are now different, the larger sheath voltage corresponding to the inner electrode (smaller area). This difference in the mean sheath voltages is related to the existence of a DC bias across the gap which can be seen in Fig. 21. In this figure are shown the time variations of the RF voltage applied to the capacitor $V(t)$, and of the resulting voltage across the gap $V_g(t)$. The distortion of V_g is negligible (this would not be the case at lower frequencies), and $V_g(t)$ is the sum of the RF voltage $V(t)$ and a self-bias DC voltage which appears to be 250 V under these conditions. One of the consequences of the electrode asymmetry is therefore the fact that the smaller area electrode behaves like a cathode during most of the cycle while the larger area electrode is anode-like. This property is also illustrated in Fig. 5d which shows the time variations of the plasma potential over one RF cycle.

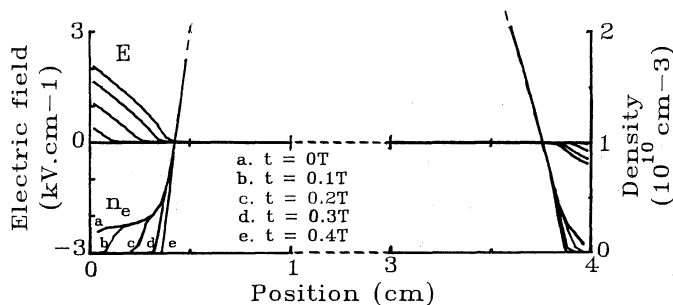


Figure 20. Spatial variations of the electric field and charged particle densities at different times for a discharge in helium, $V_{RF}=300$ V, $F=10$ MHz, $d=4$ cm, $p=1$ torr, $\gamma=0.2$ in an asymmetric configuration of electrodes (area ratio $r=5$)

Note that in such conditions, the inner electrode sheath can operate in a secondary electron regime while the outer electrode sheath operates in a wave riding regime (see above). Therefore, the nature of the interaction of the plasma with the surfaces is different on both electrodes not only because ion energies are different (larger sheath voltage on the smaller electrode) but also because the electron energy deposition mechanisms in the vicinity of each electrode are different. It is therefore important to know accurately how the asymmetry of the sheaths is related to the asymmetry of the electrode configuration. This point is discussed below.

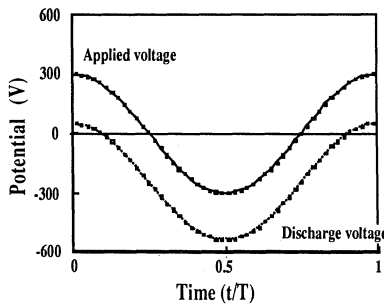


Figure 21. Time variations of the voltage V_g across the discharge in the conditions of Fig. 20; the applied RF voltage is also represented

Relation between mean sheath voltage and area ratios

The "electric" asymmetry can be characterized by the ratio of the time averaged sheath potentials (V_2/V_1) while the geometric asymmetry can be defined by the area ratio (A_2/A_1) of the electrodes (subscript 1 refers to the inner electrode and subscript 2 to the outer cylinder; see Fig. 19b).

Koenig and Maissel (1970) developed a simple analytical theory where it was assumed (see also Chapman, 1980) that 1), the sheath is collisionless for the ions, 2) the ion current density is uniform and equal on both electrodes 3) the sheath capacitance is proportional to the electrode area and inversely proportional to the sheath thickness and 4) the RF voltage is capacitively divided between the two sheaths. These assumptions lead to the relation:

$$\frac{V_1}{V_2} = \left(\frac{A_2}{A_1}\right)^n \quad \text{with } n=4$$

Different assumptions have been used by other authors, leading to similar relations but with a power dependence ranging from 3/2 to 4 (Zarowin, 1983, Suzuki et al., 1986, Pointu, 1986, Riemann, 1989; see also Turban 1988). Experimental results by Coburn and Kay (1972) concerning the effect of asymmetric geometry and the relation between sheath potentials and electrode area ratios have been analyzed by Chapman (1980) and suggest a power dependence between 1 and 1.4 in the case of argon, at 50 mtorr, gap spacing 1.88 cm and for mean sheath voltages less than 700 V.

The agreement between the analytical models and the experiments is therefore not very good, and the use of a self-consistent numerical model can help clarifying this problem. Figure 22 shows the variations of the average potential of the inner electrode V_1 as a function of V_2 in helium ($p=1$ torr, $d=1$ cm, $\gamma=0.2$) for different values of the electrode area ratio (i.e., for different values of the electrode radii).

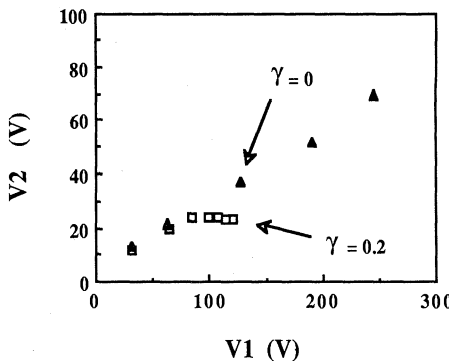


Figure 22. Time averaged sheath potential of the larger area electrode vs time averaged sheath potential of the small area electrode for an area ratio $r=5$, with ($\gamma=0.2$) and without ($\gamma=0$) secondary electron emission

One can deduce from these figure that:

- 1) V_1 changes linearly with V_2 when there is no secondary emission, the slope of the curve depending only on the electrode area ratio
- 2) the power dependence of the sheath voltage ratio on the inverse electrode area ratio is of the order of 1 for $\gamma=0$ (and for $\gamma=0.2$, only in the case of low voltages)
- 3) when the voltage is increased, a transition occurs for $\gamma=0.2$; beyond the transition voltage, the power dependence is much larger than 1
- 4) this phenomenon is related to the transition between the wave riding regime and the secondary electron regime

To summarize this section, we can say that the numerical model predicts a power dependence (of the order of 1) in reasonable agreement with the experimental results of Coburn and Kay (1972) in the case of the wave riding regime and indicates that the power dependence of the sheath voltage on the inverse electrode area ratio increases abruptly during the transition between the wave riding regime and the secondary electron regime.

VALIDITY OF THE FLUID MODEL - COMPARISONS WITH MICROSCOPIC MODELS

As has been illustrated along this paper, the two electron group fluid model seems realistic and can reproduce surprisingly well the experimental results in a lot of situations. It must be kept in mind that such models are more useful to predict the trends in the discharge behavior when one of the discharge parameters is changed than to provide very accurate estimates of some specific characteristic parameters of the discharge. An example of this ability to predict the trend is given in Fig. 23 which shows the variations of the discharge current density with pressure and frequency in argon obtained with the fluid model, compared with the experimental results of Bletzinger and Flemming 1987. The trends predicted by the model are correct but the calculated current are smaller than the experimental ones by a factor between 2 and 3. Knowing the assumptions of the model and the complexity of the problem, the quantitative agreement between experiment and model can be considered to be good.

The ability of the model to reproduce experimental results relies on the accuracy of the description of the electron and ion transport. As discussed above, the fluid model used in this paper should be real-

istic for pressures larger than 100 mtorr and frequency less than a few 10 MHz. It is however difficult to estimate accurately the validity domain of the model. Monte-Carlo simulations can be used to check the validity of the model in a given situation. This is illustrated in Figs 24 and 25.

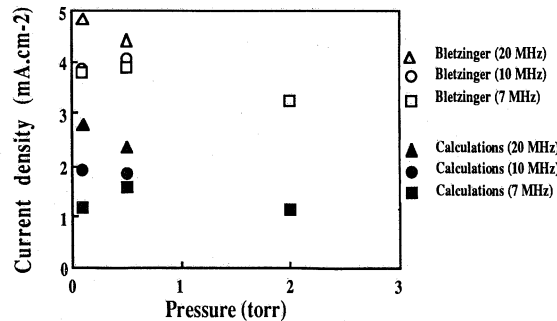


Figure 23. Discharge current density vs pressure for different values of the frequency in argon, $d=3$ cm, $\gamma=0.05$, the RF voltage in each case is taken from the experimental measurements of Bletzinger and Flemming, 1987 (constant total power).

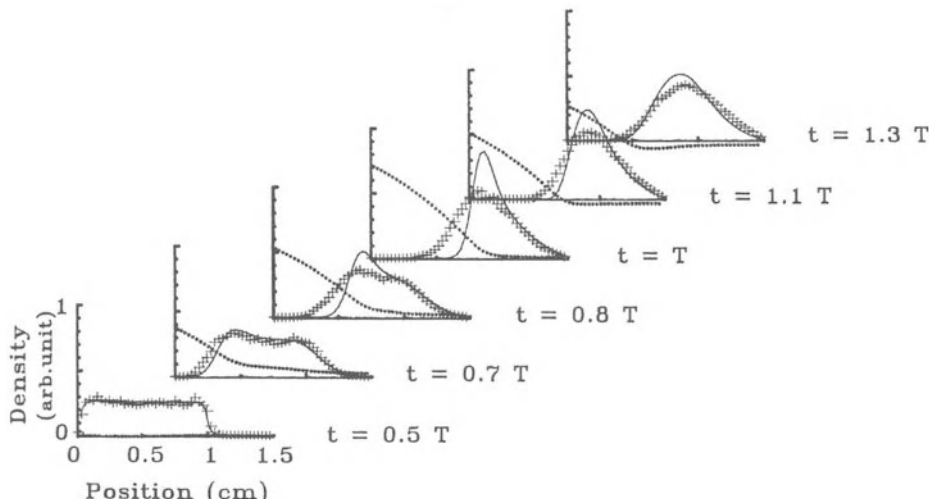


Figure 24. Time evolution of the electron density profile during the sheath expansion and contraction in helium, $V_{RF}=120$ V, $F=3.2$ MHz, $d=3$ cm, $p=3$ torr, $\gamma=0.2$ showing the motion of the wave riding electrons; at $t=0$, electron density is assumed to be uniform for $0 < x <$ maximum sheath length; symbols: Monte-Carlo results, full lines: fluid model, dotted line: electric field (unit=300 V/cm).

Figure 24 corresponds to an RF discharge in helium. The self-consistent electric field is first obtained from the fluid model. Then, the electron kinetics during the sheath expansion and contraction is studied both with the fluid model and the Monte-Carlo simulation, the electron density being supposed to be uniform in the sheath region at time $t=0$ (beginning of the sheath expansion). A comparison of the results obtained with the fluid model and the Monte-Carlo simulation is given in Fig 24 which shows the time evolution of the electron density. The agreement between both methods is very good, as was expected in this collisional regime. Note that this result illustrates the transport of wave riding electrons. When the pressure is decreased below a few 100 mtorr in helium (and for the same sheath length) the fluid model is no longer realistic.

A similar comparison can be performed to study the transport of secondary electrons emitted by the electrode. This is done in Fig. 25.

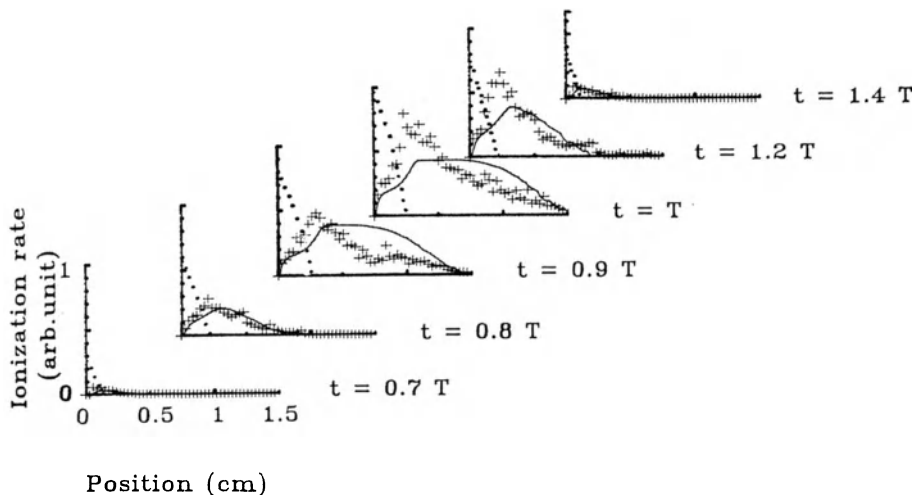


Figure 25. Space and time variations of the ionization rate due to the secondary electrons: helium, $V_{RF}=400$ V, $F=3.2$ MHz, $d=3$ cm, $p=3$ torr, $\gamma=0.2$; symbols: Monte-Carlo results, full lines: fluid model, dotted line: electric field (unit=2500 V/cm)

The space and time variations of the electric field are first obtained from the self-consistent fluid model. The transport of the secondary electrons is then analyzed both with the fluid model and with the Monte-Carlo simulation by assuming a given flux of electrons leaving the cathode over one cycle (this flux is supposed to be proportional to the ion flux on the electrode, deduced from the fluid model). It is possible to calculate with both models the ionization rate of these electrons as a function of space and time. These rates are presented and compared in Fig. 25.

The agreement is good and show that the beam model can provide a realistic description of the transport of cathode emitted electrons. Note that the agreement is not always as good as shown in this figure and that for higher voltages, the beam model tends to exaggerate the penetration depth of high energy electrons in the glow.

CONCLUSION

Fluid models appear to be a very powerful and efficient tool to study plasmas created by RF discharges. A number of points concerning

the sheath oscillations, the power deposition and sustaining mechanisms, the role of negative ions and the influence of asymmetric configurations of electrodes have been elucidated or clarified by such models in conjunction with experimental measurements based on classical electric characteristic measurements as well as powerful laser diagnostic techniques.

Although these models can be useful to help understanding and predicting the discharge properties in a number of practical situations, improvements are still necessary to extend the validity domain of the models to higher frequency and lower pressure which seem to be the trends in plasma processing.

ACKNOWLEDGMENTS

This work has been supported by GRECO 57 (CNRS) and by NATO in the frame of a collaborative program with R.A. Gottscho, J. Derouard and N. Sadeghi.

REFERENCES

- Barnes M.S., Cotler T.J. and Elta M.E., 1987, J. Appl. Phys. 61, 81
Boeuf J.P. and Marode E., 1982, J. Phys. D: Appl. Phys. 15, 2169
Boeuf J.P., 1987, Phys. Rev. A 36, 2782
Boeuf J.P., 1988, J. Appl. Phys. 63, 1342
Boeuf J.P. and Sécur P.S., 1988, in "Interactions Plasma Froids Matériaux", ed. by C. Lejeune, GRECO 57 CNRS, Les Editions de Physique, p. 113.
Bletzinger P. and Flemming M.J., 1987, J. Appl. Phys. 62, 4688
Boswell R.W. and Morey I.J., 1988, J. Appl. Phys. 52, 21
Capitelli M., Gorse C. and Ricard A., 1981, J. Physique 42, 469.
Capitelli M., Gorse C., Winkler R. and Wilhelm J., 1988, Plasma Chem. Plasma Process. 8, 399.
Chapman B., 1980 'Glow Discharge Processes', (John Wiley and Sons: New York)
Coburn J.W. and Kay E., 1972, J. Appl. Phys. 43, 4965
Derouard J., Debontride H. and Sadeghi N., 1987, J. Physique 48, Colloque C7, 725; see also Derouard J., 1989, this volume
Ferreira C.M. and Loureiro J., 1989, J. Phys. D 22, 76
Flamm D.L. and Donnelly V.M., 1986, J. Appl. Phys. 59, 1052
Godyak V.A. and Kanneh A.S., 1986, IEEE Trans. Plasma Sc. PS-14, 112
Godyak V.A., 1986, "Soviet Radio Frequency Discharge Research", (Delphic Asociates)
Goedde C.G., Lichtenberg A.J., Lieberman, 1988, J. Appl. Phys. 64, 4375
Gogolides E., Nicolai J.P. and Sawin H.H., 1988, Proc. of the 41st GEC, Minneapolis, Minnesota, p 141
Gogolides E., Nicolai J.P. and Sawin H.H., to be published, 1989, "Comparisons of experimental measurements and model predictions for RF SF₆ discharges"
Gottscho R.A., Burton R.H., Flamm D.L., Donnelly V.M., and Davis G.P., 1984, J. Appl. Phys. 55, 2707
Gottscho R.A. and Gaebe C.E., 1986, IEEE Trans. Plasma Science PS-14, 92
Gottscho R.A., 1987, Phys. Rev. A 36, 2233
Gottscho R.A., Mitchell A., Scheller G.R., Schryer G.R., Graves D.B. and Boeuf J.P., 1988, Proc. 7th Symp. Plasma Proc. Electrochem. Soc., G.S. Mathad, G.C. Schwartz and D.W. Hess
Graves D.B. and Jensen K.F., 1986, IEEE trans. Plasma Science PS-14 78
Graves D.B. 1987, J. Appl. Phys. 62, 88
Gummel H.K., 1964, IEEE Trans. Electron Devices ED-30, 1097
Hebner G.A. and Verdeyen J.T., 1986, IEEE Trans. Plasma Science PS-14, 132
Hebner G.A., Verdeyen J.T., Kushner M.J., 1988, J. Appl. Phys. 63, 2226

- Keller J.H. et Pennebaker W.B., 1970, IBM J. Res. Dev. 14, 168
- Kitamori K. and Tagashira T., 1988, Proc. of the 9th ESCAMPIG, Lisbon, Portugal, Ed. C.M. Ferreira, (European Physical Society), p 277
- Kline L.E., Partlow W.D. and Bies W.E., 1989, J. Appl. Phys. 65, 70
- Koenig H.R. and Maisel L.I., 1970, IBM J. Res. Develop. 14, 168
- Köhler K., Coburn J.W., Horne D.E., Kay E., 1985a, J. Appl. Phys. 57, 59
- Köhler K., Horne D.E. and Coburn J.W., 1985b, J. Appl. Phys. 58, 3350
- Kurata M., "Numerical Analysis for Semiconductor Devices", D.C. Heath and Company, (Lexington Mass 1982)
- Kushner M.J., 1983, J. Appl. Phys. 54, 4958
- Kushner M.J., 1986, IEEE Trans. Plasma Science PS14, 188
- Levitskii S.M., 1958, Sov. Phys. Tech. Phys. 2, 887
- Logan J.S., Keller J.H., Simmons R.G., 1977, J. Vac. Sci. Technol. 14, 92
- Makabe T., 1988, Proc. of the 9th ESCAMPIG, Lisbon, Portugal, Ed. C.M. Ferreira, (European Physical Society), p 277
- Metze A., Ernie D.W. and Oskam H.J., 1986, J. Appl. Phys. 60, 3081
- Moratz T.J., Pitchford L.C. and Bardsley J.N., 1987, J. Appl. Phys. 61, 2146
- Paranjpe A.P., Mc Vittie J.P. and Self S.A., 1988, Proc. of the 41st GEC, Minneapolis, Minnesota, p 45
- Pennebaker W.B., (1979), IBM J. Res. Dev. 23, 3
- Perrin J., Roca i Cabarrocas P., Allain B. and Friedt J.M., 1988, Jap. J. Appl. Phys. 2041
- Phelps A.V. et Pitchford L.C., (1985) Phys. Rev. A 31, 2932
- Phelps A.V., Jelenkovic B.M. and Pitchford L.C., 1987, Phys. Rev. A 36, 537
- Pointu A.M., 1986, J. Appl. Phys. 60, 12 4113
- Popov O.A. and Godyak V.A., 1985, J. Appl. Phys. 57, 53
- Richards A.D., Thompson B.E. and Sawin H.H., 1987a, Appl. Phys. Lett. 50, 492
- Richards A.D., Thompson B.E., Allen K.D. and Sawin H.H., 1987b, J. Appl. Phys. 62, 792
- Riemann, K.U., 1989, J. Appl. Phys. 65, 999
- Rogoff G.L., Kramer J.M. and Piejak R.B., 1986, IEEE Trans. Plasma Science PS-14, 103
- Sato N. and Tagashira H., 1985, J. Phys. D 18, 2451
- Selberherr S. and Ringhofer C.A., 1984, IEEE Trans. Computer-Aided Design CAD-3, 52
- Séguir P., Yousfi M., Boeuf J.P., Marode E., Davies A.J. et Evans J.G., 1983, in 'Electrical Breakdown and Discharges in Gases', NATO ASI series 89a, Eds E.E.Kunhardt et H.L. Luessen, 331
- Sharfetter D.L., Gummel H.K., 1969, IEEE Trans. Electron. Dev. ED-16, 64
- Surendra M. and Graves D.B. 1988, Proc. of the 41st GEC, Minneapolis, Minnesota, p 45
- Suzuki K., Ninomiya Nishimatsu S., Thomas J.W. and Steinfeld J.I., 1986, Jap. J. Appl. Phys. 25, 1569
- Taillet J., 1968, Am. J. Phys. 37, 423
- Thompson B.E., Allen K.D., Richards A.D. and Sawin H.H., 1985, J. Appl. Phys. 59, 1891
- Turban, in "Interactions Plasma Froids Materiaux", ed. by C. Lejeune, GRECO 57 CNRS, Les Editions de Physique 1988,, p. 79.
- Van Roosmalen A.J., W.G.M. Van den Hoek W.G.M. and Kalter H., 1985, J. Appl. Phys. 58, 653
- Vidaud P. Durrani S.M.A. and Hall D.R., 1988,, J. Phys. D 21, 57
- Ward A.L., 1962, J. Appl. Phys. 33, 2789
- Winkler R., Wilhelm J. et Hess A., (1985) Ann. Phys., Leipzig. 42, 537
- Zarowin C.B., 1983, J. Electrochem. Soc. 130, 1144

THEORY OF HIGH – FREQUENCY DISCHARGES

C. M. Ferreira

Centro de Electrodinâmica da Universidade Técnica de Lisboa (INIC)
Instituto Superior Técnico, 1096 Lisboa Codex, Portugal

1. INTRODUCTION

This work reviews the theory of gas discharges sustained by HF fields with emphasis on the electron kinetics as described by the Boltzmann equation. The analysis is however restricted to discharges controlled by processes occurring in the bulk, so that plasma-electrode interactions which play a major role in some RF discharges are not considered here. It is also assumed that $\omega \gg \tau_e^{-1}$, where ω is the angular frequency of the applied field and τ_e is the characteristic time for electron energy relaxation by collisions with the gas molecules.

In section 2 we analyse the electron Boltzmann equation taking into account both the applied HF field and the space-charge field and we discuss the electron particle balance and the mean energy balance. Section 3 presents an application of the Boltzmann theory to discharges in Ar and in N₂. The effects of the velocity dependence of the electron collision frequency on wave-plasma interactions are considered in Section 4, where it is shown that the plasma relative permittivity can be expressed in terms of an effective collision frequency and an effective electron density which depend on ω . A calculation of these effective parameters is presented for Ar. Finally, in Section 5 the conditions for steady-state discharge operation are investigated by coupling the electron kinetics to the ion particle and momentum balance equations. It is shown that the reduced maintenance field and the average absorbed power per electron at unit gas density can be expressed as a function of the discharge operating parameters under the form of similarity laws.

2. THEORY BASED ON THE BOLTZMANN EQUATION

In this section we review the basis of the Boltzmann equation formalism applied to the case of HF sustained plasmas. The analysis will closely follow the work of Allis, Rose and Brown^{1–4} and their notation will be used. A review on this subject was recently given by Ferreira and Moisan⁵.

2.1 The Boltzmann Equation for Electrons in a HF Field

Let $F(\vec{r}, \vec{v}, t)$ denote the electron distribution function at point \vec{r} in configuration space and at point \vec{r} in velocity space, at time t , the normalization condition being $\int F d^3v = n(\vec{r})$, where n is the electron density. We assume that the total electric field acting on the electrons has the form $\vec{E} = \vec{E}_s + \vec{E}_p \exp(j\omega t)$, where E_s is the DC space-charge field intensity and E_p is the HF electric field intensity in the plasma with angular frequency ω , resulting from the external HF source. The intensity E_s varies with position but E_p will be assumed to be spatially constant.

The distribution F is determined by the Boltzmann equation

$$\frac{\partial F}{\partial t} + \vec{\nabla}_{\vec{r}} \cdot (\vec{v}F) - \vec{\nabla}_{\vec{v}} \cdot \left(\frac{e\vec{E}}{m} F \right) = \left(\frac{\partial F}{\partial t} \right)_c , \quad (1)$$

where \vec{v} is the electron velocity, e and m are the electron absolute charge and mass, respectively, and $(\partial F / \partial t)_c$ denotes the collision operator. This equation is solved by expanding F in spherical harmonics in velocity space and in Fourier series in time,

$$F = \sum_{\ell} \sum_p F_p^{\ell} P_{\ell}(\cos \Theta) \exp(jp\omega t) . \quad (2)$$

Let us assume that: i) the electron-neutral mean free path, λ_e , is much smaller than any relevant dimension of the container, L , i.e., $\lambda_e \ll L$; ii) the energy gained from the electric field per collision by a representative electron is much smaller than the mean thermal energy of the electrons; iii) the oscillation amplitude of the electron motion under the action of the HF field is small as compared to L ; and iv) $\omega \gg \tau_e^{-1}$, where τ_e is the characteristic time for electron energy relaxation by collisions. The latter assumption implies that the electrons do not lose appreciable energy during a cycle of the HF field oscillation. Assumptions i) and ii) ensure that the anisotropies resulting from the spatial gradients and the field are small. Assumption iii) ensures that the HF field does not clear the electrons out of the plasma in each half-cycle. Under these assumptions, it is sufficient to consider only the following terms in expansion (2)

$$F \simeq F_0^0 + (\vec{v}/v) \cdot [\vec{F}_0^1 + \vec{F}_1^1 \exp(j\omega t)] , \quad (3)$$

where F_0^0 , \vec{F}_0^1 , and \vec{F}_1^1 are time-independent, isotropic functions.

Introducing (3) into (1), expressing the collision operator in terms of the electron-neutral collision frequency for momentum transfer, ν_c , and of the inelastic collision frequencies ν_j and ν_i (j and i holding for the excitation of the j -th level and for direct ionization, respectively), and then equating terms of similar time and angle dependence, one obtains one scalar and two vector equations²

$$\begin{aligned} \frac{v}{3} \vec{\nabla}_{\vec{r}} \cdot \vec{F}_0^1 &- \frac{1}{v^2} \frac{\partial}{\partial v} \left\{ \left(\frac{ev^2}{6m} \right) [Re(\vec{E}_p \cdot \vec{F}_1^1) + 2\vec{E}_s \cdot \vec{F}_0^1] + \frac{m}{M} \nu_c v^3 F_0^0 \right\} \\ &= (q - \nu_x - \nu_i) F_0^0 , \end{aligned} \quad (4)$$

$$\nu_c \vec{F}_0^1 = -v \vec{\nabla}_r F_0^0 + \frac{e}{m} \vec{E}_s \frac{\partial F_0^0}{\partial v} , \quad (5)$$

$$(\nu_c + j\omega) \vec{F}_1^1 = \frac{e \vec{E}_p}{m} \frac{\partial F_0^0}{\partial v} . \quad (6)$$

Here, *Re* means the “real part of”, $\nu_x = \sum_j \nu_j$, and q is an operator representing the reintroduction of electrons in the distribution after the inelastic collisions. These processes are treated mathematically as though “fast” electrons disappeared at the rate $(\nu_x + \nu_i) F_0^0$ and “slow” electrons appeared at the rate $q F_0^0$. For the moment, we do not need an explicit expression for $q F_0^0$ but we just note that the following relation is necessarily satisfied

$$\int_0^\infty q F_0^0 4\pi v^2 dv = n (\langle \nu_x \rangle + 2 \langle \nu_i \rangle) , \quad (7)$$

where the brackets $\langle \rangle$ represent the average over the distribution. The factor $2 \langle \nu_i \rangle$ in the r.h.s. of (7) accounts for the new free electron produced in each ionizing collision.

The terms on the l.h.s. of (4) represent the divergence of the electron flux in configuration (1^{st} term) and velocity space. The latter flux is composed of three terms accounting for the fluxes driven by the HF field, the space-charge *DC* field and the recoil collisions, respectively.

2.2 Electron Particle Balance

Integrating (4) over the velocity space and taking (7) into account one obtains

$$\vec{\nabla}_r \cdot \int_0^\infty \vec{F}_0^1 \frac{4\pi v^3}{3} dv = \langle \nu_i \rangle n . \quad (8)$$

The integral on the l.h.s. is just the electron particle flow vector $\vec{\Gamma}$, which can be obtained from (5), yielding

$$\vec{\Gamma} = \int_0^\infty \vec{F}_0^1 \frac{4\pi v^3}{3} dv = -\vec{\nabla}_r (D_e n) - n \mu_e \vec{E}_s , \quad (9)$$

where

$$D_e = \frac{1}{n} \int_0^\infty \frac{v^2}{3\nu_c} F_0^0 4\pi v^2 dv \quad (10)$$

and

$$\mu_e = -\frac{1}{n} \int_0^\infty \frac{ev}{3m\nu_c} \frac{\partial F_0^0}{\partial v} 4\pi v^2 dv \quad (11)$$

are the electron free diffusion coefficient and *DC* mobility, respectively.

Therefore, eq. (8) is simply the electron continuity equation

$$\vec{\nabla}_r \cdot \vec{\Gamma} = <\nu_i> n . \quad (12)$$

2.3 Electron Energy Balance

The electron energy balance is obtained by multiplying eq. (4) by the electron energy, $u = mv^2/2$, and then integrating over the velocity space. The resulting equation can be written as

$$\begin{aligned} \vec{\nabla}_r \cdot \int_0^\infty \frac{1}{2} mv^2 \vec{F}_0^1 \frac{4\pi v^3}{3} dv &= \frac{1}{2} Re(\vec{j}_1 \cdot \vec{E}_p) + \vec{j}_0 \cdot \vec{E}_s - \frac{2m}{M} < u \nu_c > n \\ &- \left(\sum_j e V_j < \nu_j > + e V_i < \nu_i > \right) n , \end{aligned} \quad (13)$$

where V_j and V_i are the excitation potential of the j -th level and the ionization potential, respectively, and \vec{j}_1 and \vec{j}_0 are the *AC* and *DC* electron current densities given by

$$\vec{j}_1 = -e \int_0^\infty \vec{F}_1^1 \frac{4\pi v^3}{3} dv , \quad (14)$$

$$\vec{j}_0 = -e \vec{\Gamma} = -e \int_0^\infty \vec{F}_0^1 \frac{4\pi v^3}{3} dv . \quad (15)$$

The term on the l.h.s. of (13) represents the divergence of an energy flux in configuration space. The various terms on the r.h.s. represent, in order, the power gain from the HF field, the power lost by the electrons in flowing against the space-charge field (note that $\vec{j}_0 \cdot \vec{E}_s$ must be in fact a negative term; this power lost by the electrons is ultimately carried toward the wall by the ions accelerated in the space-charge field), and the power loss due to elastic and inelastic collisions, all per unit volume.

It is convenient, at this point, to introduce the plasma complex conductivity, σ , defined by the relation $\vec{j}_1 = \sigma \vec{E}_p$. From (14) and (6) it follows that σ is given by

$$\sigma = -\frac{e^2}{m} \int_0^\infty \frac{1}{\nu_c + j\omega} \frac{\partial F_0^0}{\partial v} \frac{4\pi v^3}{3} dv \quad (16)$$

The power absorbed from the HF field, then, can also be expressed as $Re(\sigma) E^2$, where E denotes the r. m. s. field, and

$$Re(\sigma) = -\frac{e^2}{m} \int_0^\infty \frac{\nu_c}{\nu_c^2 + \omega^2} \frac{\partial F_0^0}{\partial v} \frac{4\pi v^3}{3} dv . \quad (17)$$

2.4 Homogeneous Boltzmann Equation. Energy Distribution Function

The eqs.(4)–(6) are difficult to solve, even numerically, due to the presence of the space-charge field terms. The difficulties are twofold. First, when we insert in (4) the expressions for \vec{F}_0^1 and \vec{F}_1^1 obtained from (5) and (6), we get crossed space and velocity terms involving \vec{E}_s which makes that exact separable solutions of the form $F_0^0(\vec{r}, v) = n(\vec{r}) f_0(v)$ do not exist. Second, \vec{E}_s cannot be consistently determined without taking into account the ion motion as well, so that eqs. (4)–(6) must be coupled to the ion kinetics. Therefore, we need further approximations.

A reasonable approximation that is useful in practice, for the purposes of discharge modeling consists in neglecting the space-charge field term in eq. (4) (Note, however, that the space-charge field term must be kept in (6), as it nearly balances the diffusion term and makes that the total electron particle flow, Γ , becomes a small quantity). In fact, it seems physically correct to neglect the flux driven in velocity space by \vec{E}_s , as compared to that driven by the external field. In a self-sustained discharge the electrons must be able to produce ionization at a rate that just compensates for the rate of electron loss. To reach the ionization energy level, an electron has to extract much more energy from the HF field than just the ionization energy, since it makes, on the average, several excitations before it ionizes an atom. Additionally, as the electrons try to build up in energy they have to overcome the losses resulting from recoil collisions and from their average motion against \vec{E}_s , towards the wall.

Thus, neglecting the term $2\vec{E}_s \cdot \vec{F}_0^1$ in eq.(4) and taking into account (5) and (6), we obtain the following equation for F_0^0

$$\begin{aligned} -\frac{v^2}{3\nu_c} \nabla_r^2 F_0^0 + \frac{ev}{3m\nu_c} \vec{\nabla}_r \left(\vec{E}_s \frac{\partial F_0^0}{\partial v} \right) - \frac{1}{v^2} \frac{\partial}{\partial v} \left[v^2 \left(\frac{u_c \nu_c}{3m} \frac{\partial F_0^0}{\partial v} + \frac{m}{M} \nu_c v F_0^0 \right) \right] \\ = (q - \nu_x - \nu_i) F_0^0 , \end{aligned} \quad (18)$$

where we have introduced u_c , the average energy gained from the HF field per collision, given by³

$$u_c = \frac{(eE_p)^2}{2m(\nu_c^2 + \omega^2)} . \quad (19)$$

We note that u_c is generally a function of the electron energy through ν_c ; the product $\nu_c u_c$, which represents the power transfer from the field to the electrons of energy u , reaches a maximum when $\nu_c(u) = \omega$. This remark will be important later on, when we will discuss the changes in the distribution induced by the changes in ω .

The first two terms on the l. h. s. of (18) may be each quite large but they nearly cancel each other under discharge conditions, their difference being small as compared to the other terms in the equation. It suffices, therefore, to use an approximation for the small difference between these two terms. Let us assume following Rose and Brown², that \vec{E}_s can be expressed in the form

$$\vec{E}_s = -u_s \frac{\vec{\nabla}_r n}{n} , \quad (20)$$

where u_s is a measure of the potential drop associated with the space-charge field. In this case eq.(18) is satisfied by separable solutions of the form $F_0^0(\vec{r}, v) = n(\vec{r}) f_0(v)$, and we readily obtain, by integration over all velocities

$$-D_s \nabla_r^2 n = < \nu_i > n , \quad (21)$$

where

$$D_s = D_e - u_s \mu_e \quad (22)$$

represents an effective diffusion coefficient

We can also write (21) in the form

$$\nabla_r^2 n = -n/\Lambda_e^2 \quad (23)$$

where the effective diffusion length, $\Lambda_e = (D_s / \langle \nu_i \rangle)^{1/2}$, is found by solving (23) with appropriate boundary conditions for n (we obtain, for example, $\Lambda_e = \Lambda$, the characteristic diffusion length for the container, if we assume that n vanishes at the wall). Taking into account (20) and (23), and renormalizing the distribution $f_0(v)$ so that $\int_0^\infty f_0(v) 4\pi v^2 dv = f(u) \sqrt{u} du$ ($f(u)$ will be termed, hereafter, the electron energy distribution; note that $\int_0^\infty f(u) \sqrt{u} du = 1$), we obtain from (18)

$$\begin{aligned} \frac{2u}{3m\nu_c\Lambda_e^2} \left(f + eu_s \frac{df}{du} \right) - \frac{2}{3\sqrt{u}} \frac{d}{du} \left[u^{\frac{3}{2}} \nu_c \left(u_c \frac{df}{du} + \frac{3m}{M} f \right) \right] \\ = (q - \nu_x - \nu_i) f . \end{aligned} \quad (24)$$

At breakdown, we can neglect the space-charge, and, thus, take $u_s = 0$. We can also assume that $\Lambda_e = \Lambda$. In this case, eq. (24) can, in principle, be solved for a given gas (i.e., for a specific set of electron cross sections). The independent parameters involved in (24) are, as seen by simple inspection, E_p/N , ω/N (from eq. (19) defining u_c), and $N\Lambda$, where N is the gas density. Therefore, the solutions of (24) provide a relationship between these three reduced variables which we can represent, for example, as curves of E_p/N vs. $N\Lambda$ for constant ω/N . These curves are called breakdown characteristics⁴. Note that these characteristics implicitly satisfy the equation $D_e/\Lambda^2 = \langle \nu_i \rangle$, since the latter is exactly obtained by integrating (24), with $u_s = 0$, over all energies.

In a quasineutral, diffusion-controlled discharge at sufficiently high pressures $D_s \approx D_a$ (see Sect. 5), where

$$D_a = \frac{\mu_i D_e + \mu_e D_i}{\mu_e + \mu_i} \quad (25)$$

is the well-known ambipolar diffusion coefficient⁶ (μ_i and D_i are the ion mobility and diffusion coefficient, respectively). In this case, we have from (22) $u_s = (D_e - D_a)/\mu_e$, which we can approximately write in the form (taking into account that $D_a \ll D_e$) $u_s \approx u_k$, where $u_k = D_e/\mu_e$ is the electron characteristic energy expressed in electron-volts. Thus, we can also solve, in principle, eq.(24), with $\Lambda_e = \Lambda$ and $u_s = u_k$, and obtain discharge characteristics for the maintenance field expressed in the form E_p/N vs. $N\Lambda$ for constant ω/N . Note, however, that the solutions are now more difficult to obtain than for breakdown conditions, since u_k is, itself, a functional of $f(u)$. The solutions must also be such that the equation $D_a/\Lambda^2 = \langle \nu_i \rangle$ is implicitly satisfied, since this equation is exactly obtained by integrating (24) over all energies.

In spite of the simplifications already introduced in deriving eq.(24), finding its solutions remains a complex problem requiring a great deal of numerical work. The problem is considerably simplified, however, when one can neglect the diffusion term. This term is in ratio $(N\Lambda_e)^{-2}$ to the remaining terms in eq.(24), hence it actually can be neglected at sufficiently high pressures. In this case eq.(24) reduces to the much simpler form

$$-\frac{2}{3} \frac{d}{du} \left[u^{3/2} \nu_c \left(u_c \frac{df}{du} + \frac{3m}{M} f \right) \right] = (q - \nu_x - \nu_i) f \sqrt{u} \quad (26)$$

which is known as the homogeneous Boltzmann equation. It is a continuity equation for $f(u)$ along the energy axis alone, expressing the fact the change in the total electron upflux (the net flux resulting from the applied field and the elastic recoil losses) in an energy interval du is equal to the difference between the rates for the reintroduction and the removal of electrons by inelastic collisions.

When the diffusion term is neglected as above one must also neglect, for consistency, the new electrons produced by ionization (since the diffusion term exactly compensates for the rate of appearance of these new electrons). In this case, the ionization must be treated like an ordinary excitation process and $\int_0^\infty qf(u)\sqrt{u}du = <\nu_x> + <\nu_i>$. The neglect of diffusion and of the source of new electrons altogether is, therefore, permissible as long as the energy losses associated with ionization are much smaller than those resulting from excitation or elastic recoil. In most active plasmas at not too low pressures $<\nu_x> \gg <\nu_i>$ so that eq.(26) is a good approximation. Note, however, that, for the purposes of discharge modelling, one must take into account the electron continuity equation independently of eq. (26), since the former is no longer implicit in the latter (as it was, for example, in (24) and in (4)).

When eq.(26) can be used the modelling of a discharge can proceed in two independent, successive steps. First, eq. (26) is solved and the electron transport and collisional rate coefficients are calculated from $f(u)$. Second, these data are inserted into the continuity and the momentum transfer equations for the electrons and the latter are solved along with the corresponding equations for the ions, taking into account appropriate boundary conditions. The first step involves two independent variables E_p/N and ω/N (from u_c in (26)). The second step involves the solution of a boundary-value problem from which a relationship between E_p/N , ω/N , and $N\Lambda$ is obtained as an eigenvalue solution. This relationship is the characteristic for the maintenance field. Specific examples will be given later, in Section 5.

For the moment, we return to the general electron energy balance equation (13) in order to discuss useful approximations resulting from eqs.(24) and (26).

2.5 Approximations to the General Electron Energy Balance Equation

The homogeneous Boltzmann equation (26) embodies the following mean energy balance per electron (which is simply obtained by multiplying it by u and integrating over all energies)

$$\Theta \equiv \frac{Re(\sigma)}{n} \frac{E_p^2}{2} = \frac{2m}{M} <u\nu_c> + \sum_j eV_j <\nu_j> + eV_i <\nu_i> . \quad (27)$$

Obviously, this equation is the same as (13) with the energy flux and the space-charge field terms neglected. The power absorbed by the electrons from the HF field is totally spent in collisions with the gas molecules, in this case.

The quantity Θ is the average absorbed power per electron. We note that Θ/N is only a function of E_p/N and ω/N . Since E_p/N is a function of $N\Lambda$ for constant ω/N

(see above), it follows that the average absorbed power per electron at unit gas density also satisfies characteristics of the form Θ/N vs. $N\Lambda$ for constant ω/N .

We can estimate the power losses associated with the electron flux toward the wall and the maintenance of the space-charge field using the analysis of the previous sections.

The former of these losses is given by the divergence term on the l.h.s. of (13). As an order of magnitude estimate, we have using eqs.(8) and (9),

$$\vec{\nabla}_r \cdot \int_0^\infty \frac{1}{2} mv^2 \vec{F}_0^1 \frac{4\pi v^3}{3} dv \simeq \langle u \rangle \vec{\nabla}_r \cdot \vec{\Gamma} = \langle u \rangle \langle \nu_i \rangle n , \quad (28)$$

The average power carried away to the wall per electron is, therefore, of the order of $\langle u \rangle \langle \nu_i \rangle$, which is just the average rate of escape of electrons (obviously, equal to $\langle \nu_i \rangle$) multiplied by the electron mean energy $\langle u \rangle$.

The power lost by the electrons in flowing against the space-charge field is $\vec{j}_0 \cdot \vec{E}_s$, per unit volume, as we have seen in eq.(13). In order to estimate this loss per electron we consider a cylindrical plasma column of radius R and integrate the term $\vec{j}_0 \cdot \vec{E}_s$ over the cylinder cross-section. We must, however, split the integration into two parts, one corresponding to the quasineutral plasma, between the axis ($r = 0$) and the plasma-sheath boundary ($r = R - \Delta$), and the other one corresponding to the sheath near the wall, of thickness $\Delta \ll R$, viz.,

$$\int_0^R \vec{j}_0 \cdot \vec{E}_s 2\pi r dr = -e \int_0^{R-\Delta} \vec{\Gamma} \cdot \vec{E}_s 2\pi r dr - e \int_{R-\Delta}^R \vec{\Gamma} \cdot \vec{E}_s 2\pi r dr . \quad (29)$$

Assuming a collisionless sheath, $r\vec{\Gamma}$ is a constant across the sheath so that the second integral yields $-2\pi R \Gamma_b e\varphi$, where the subscript b denotes values at the plasma-sheath boundary and φ is the potential drop in the sheath. It is well known⁷ that $e\varphi \simeq \langle u \rangle \ln \sqrt{M/m}$. On the other hand, from the continuity equation, we find that $2\pi R \Gamma_b = \pi R^2 \bar{n} \langle \nu_i \rangle$, where \bar{n} is the radially averaged density. Therefore,

$$-e \int_{R-\Delta}^R \vec{\Gamma} \cdot \vec{E}_s 2\pi r dr \simeq -\pi R^2 \bar{n} \langle u \rangle \langle \nu_i \rangle \ln \sqrt{\frac{M}{m}} . \quad (30)$$

The contribution of the integral over the plasma can be estimated using the approximation (20) for \vec{E}_s . This yields

$$\begin{aligned} & -e \int_0^{R-\Delta} \vec{\Gamma} \cdot \vec{E}_s 2\pi r dr \simeq e u_s \int_0^{R-\Delta} \Gamma \frac{d}{dr} (\ln n) 2\pi r dr \\ & = e u_s \left[2\pi R \Gamma_b \ln n_b - \int_0^{R-\Delta} \ln n \frac{1}{r} \frac{d}{dr} (r\Gamma) 2\pi r dr \right] , \end{aligned} \quad (31)$$

where the second equality is obtained by integration by parts. Now, we note that $(1/r)d(r\Gamma)/dr = \langle \nu_i \rangle n$ and take $\ln n \simeq \ln n_0$ in the integrand term, the subscript zero denoting the axial value. We finally get from (31)

$$-e \int_0^{R-\Delta} \vec{\Gamma} \cdot \vec{E}_s 2\pi r dr \simeq -\pi R^2 \bar{n} e u_s \langle \nu_i \rangle \ln \left(\frac{n_0}{n_b} \right) . \quad (32)$$

Collecting the results (30) and (32), we find that the average power loss per electron resulting from their flow against the space-charge field is $\sim <\nu_i><u>(\ln\sqrt{M/m} + \ln(n_0/n_b))$, where we have assumed $eu_s \sim <u>$. Taking into account this result together with (28) the average power balance per electron (obtained by integrating (13) over the tube cross-section and dividing the result by $\pi R^2 \bar{n}$) can be expressed as

$$\frac{Re(\sigma) E_p^2}{n} \frac{2m}{M} <uv_c> + \sum_j eV_j <\nu_j> + eV_i <\nu_i> + <u><\nu_i> \left[1 + \ln\sqrt{\frac{M}{m}} + \ln\frac{n_0}{n_b} \right] . \quad (33)$$

This equation differs from (27), the simplified form obtained from the homogeneous Boltzmann equation, by the last term on the r.h.s. . The numerical factor $[1+\ln\sqrt{M/m} + \ln(n_0/n_b)]$ may be quite large, of the order of ten or even larger, at relatively high pressures, for, then, $n_0 \gg n_b$. However, in this case $<\nu_i>$ is small and the energy losses associated with excitation and recoil are predominant. The approximation (27) fails, however, at low pressures, when $<\nu_i>$ and $<u>$ become quite large. In any case, eq.(33) can be used to test the accuracy of eq.(27) and of the homogeneous Boltzmann equation from which (27) is derived.

2.6 Electron-Electron Collisions

So far, we have neglected electron-electron collisions in the Boltzmann equation but they should be taken into account at high electron densities. In fact, the degree of ionization can be relatively high in HF and microwave discharges so that $f(u)$ can tend toward a Maxwellian due to electron-electron collisions.

One can account for such collisions in the homogeneous Boltzmann equation by simply adding another flux term, G_{ee} , on the l.h.s. of eq (26). This equation can be expressed in the general form

$$\frac{dG}{du} = (q - \nu_x - \nu_i) f \sqrt{u} , \quad (34)$$

where $G = G_E + G_c + G_{ee}$ is the total electron upflux in energy space, viz., the sum of the fluxes driven by the applied field, the elastic collisions, and the electron-electron collisions. The latter flux is obtained from the Fokker-Planck equation and can be expressed as^{3,8}

$$G_{ee} = -2\nu_{ee} u^{3/2} \left[I(u)f(u) + J(u) \frac{df}{du} \right] , \quad (35)$$

where

$$I(u) = \int_0^u f \sqrt{u} du , \quad (36)$$

$$J(u) = \frac{2}{3} \left(\int_0^u f(u) u^{3/2} du + u^{3/2} \int_u^\infty f(u) du \right) , \quad (37)$$

and

$$\nu_{ee} = 4\pi \left(\frac{e^2}{4\pi\epsilon_0 m} \right)^2 \frac{\ln\Lambda_c}{v^3} n , \quad (38)$$

Here, ν_{ee} is the electron-electron collision frequency, ϵ_0 is the permittivity of free space and $\ln\Lambda_c$ is the Coulomb logarithm³, where $\Lambda_c = 12\pi n \lambda_D^3$, λ_D denoting the electron Debye length.

Obviously, $\int_0^\infty u dG_{ee} = - \int_0^\infty G_{ee} du = 0$, as electron-electron collisions do not change the total energy of the electron gas. Therefore, the electron power balance equation obtained from (34) is the same as (27). When the distribution becomes a Maxwellian eq. (27) constitutes a relationship between T_e , E_p/N , and ω/N , where T_e is the electron temperature. In this case, Θ/N , as given by the r.h.s. of (27) divided by N, is a function of T_e alone. Then, as the solutions of the fluid-type equations for the charged particles generally enable one to express T_e as a unique function of $N\Lambda$ (as, for example, in the classical, linear ambipolar diffusion theory for the positive column), Θ/N can also be expressed as a unique function of $N\Lambda$, for any ω/N . The single functional dependence of Θ/N on $N\Lambda$ constitutes, therefore, a fundamental similarity law for the discharge when $f(u)$ is a Maxwellian. These considerations will be made more precise in Section 5 where illustrative numerical examples are presented.

3. ELECTRON KINETICS IN ARGON AND IN NITROGEN

In this section we present an application of the theory to Ar and N₂ which follows from numerical solutions to the homogeneous Boltzmann equation (26) using an appropriate set of electron cross sections for each of these gases. The material presented here has been previously reported by Ferreira and Loureiro⁸⁻¹⁰ and the reader should refer to these publications for further details.

We recall that $f(u)$ as obtained from (26) is a function of the two independent parameters E_p/N and ω/N through $u_c(u)$, the energy gain per collision, defined by (19). It is useful, for the purposes of physical interpretation, to use a dimensionless parameter ω/ν_{ce} , where ν_{ce} is the collision frequency of a representative electron with a given energy, in place of ω/N (note that ω/ν_{ce} is, in fact, proportional to ω/N , since ν_{ce} is proportional to N). The limiting situations of $\omega \ll \nu_{ce}$ and of $\omega \gg \nu_{ce}$ correspond, therefore, to many and to vanishingly few collisions in a cycle of the field oscillation, respectively. It is also useful to introduce an effective field, E_e , defined as

$$E_e = E \frac{\nu_{ce}}{(\omega^2 + \nu_{ce}^2)^{1/2}} , \quad (39)$$

where $E = E_p/\sqrt{2}$ is the r.m.s. field.

This definition is similar to that employed when one assumes that ν_c is independent of the electron energy (in which case $f(u)$ would be a unique function of E_e/N). We see from (39) that $E_e/N \propto E/\omega$ for $\omega \gg \nu_{ce}$ and that $E_e/N \approx E/N$ for $\omega \ll \nu_{ce}$.

3.1 Argon

Figure 1 shows two sets of curves of $f(u)$ in Ar obtained for $\omega \ll \nu_{ce}$ (similar to DC case) and for $\omega/\nu_{ce} = 2$, respectively, and various values of E/N . For argon, we have adopted the value $\nu_{ce}/N = 2 \times 10^{-7} \text{ cm}^3 \text{s}^{-1}$, which corresponds to electrons of $u \sim 8.5 \text{ eV}$, because it just happens, with this value, that the ionization coefficient, $C_i = \langle \nu_i \rangle / N$, nearly becomes a unique function of E_e/N as shown in fig. 2.

The shape of $f(u)$ is quite different in the two sets of curves shown in fig. 1, the distribution becoming much closer to a Maxwellian in the case of $\omega/\nu_{ce} = 2$. The number of electrons in the high-energy tail relative to that in the body is much larger in this case. In absolute value, the distributions for $\omega \ll \nu_{ce}$ have more electrons in the tail but this results from the fact that they correspond to higher power transfers in absolute value, hence, to a higher range of mean electron energies (note, in fact, that the energy gain per collision u_c given by (19), decreases in absolute value as ω/N increases for constant E/N). For this reason it is more convenient to compare distributions with the same mean energy but corresponding to different values of ω/ν_{ce} as shown in fig. 3. In order to obtain identical mean energies as ω increases one has also to increase E/N . From fig. 3 it is clearly seen that the relative number of high-energy electrons increases indeed with ω/N although $\langle u \rangle$ is kept constant. This is a direct consequence of the fact that the power transfer, $\nu_c u_c$, has a maximum, for given ω , when $\nu_c(u) = \omega$. As in argon $\nu_c(u)$ is an increasing function of u above the Ramsauer minimum up to $u \sim 12 \text{ eV}^{11}$, the maximum power transfer occurs for electrons of increasingly higher energies as ω increases, until $\omega \simeq \nu_c(12 \text{ eV})$, which results in a progressive enhancement of the tail. For $u \gtrsim 12 \text{ eV}$ $\nu_c(u)$ nearly saturates, so that a further increase in ω only introduces minor changes in the shape of the distribution.

This discussion illustrates that the changes in the shape of $f(u)$ as ω varies can be qualitatively understood from the behavior of the power transfer function, $\nu_c u_c$, for a given variation law of ν_c vs. u .

The percentage electron energy losses in Ar through elastic collisions, excitation and ionization are represented as a function of Θ/N in fig. 4, for the two limiting cases of $\omega \ll \nu_{ce}$ and $\omega \gg \nu_{ce}$, when electron-electron collisions are ignored, and also for a Maxwellian distribution. As expected, the changes in ω strongly affect the distribution of the power transfer among the various collisional channels, the curves for $\omega \gg \nu_{ce}$ being shifted towards lower Θ/N values as compared to those corresponding to $\omega \ll \nu_{ce}$.

Figure 5 shows the electron characteristic energy, u_k , and the kinetic temperature, $T_e = (2/3) \langle u \rangle$, both expressed in eV, vs. E_e/N for various values of ω/ν_{ce} . We note that T_e and u_k have quite different values, which is indicative of strong departures from a Maxwellian distribution (in which case one would have $T_e = u_k$) in the body of the distribution. For comparison, fig. 5 also shows T_e vs. E_e/N for the case of a Maxwellian distribution and $\omega \gg \nu_{ce}$. It is interesting to note that u_k strongly decreases as ω/ν_{ce} increases, reaching values well below 1 eV. This fact is connected with the behavior of the HF distributions at low energies, namely with the strong peak occurring at the origin.

Figure 6 illustrates the effects of electron-electron collisions on the tail of $f(u)$ in the case of $\omega \gg \nu_{ce}$, for various values of E_e/N and n/N . For the values of E_e/N here considered, which fall in the expected range for a low-pressure discharge, the "Maxwellization" of $f(u)$ is practically achieved for $n/N \gtrsim 10^{-4}$. Degrees of ionization of this order or even higher are often attained in microwave discharges. The assumption of a Maxwellian distribution is, then, well justified.

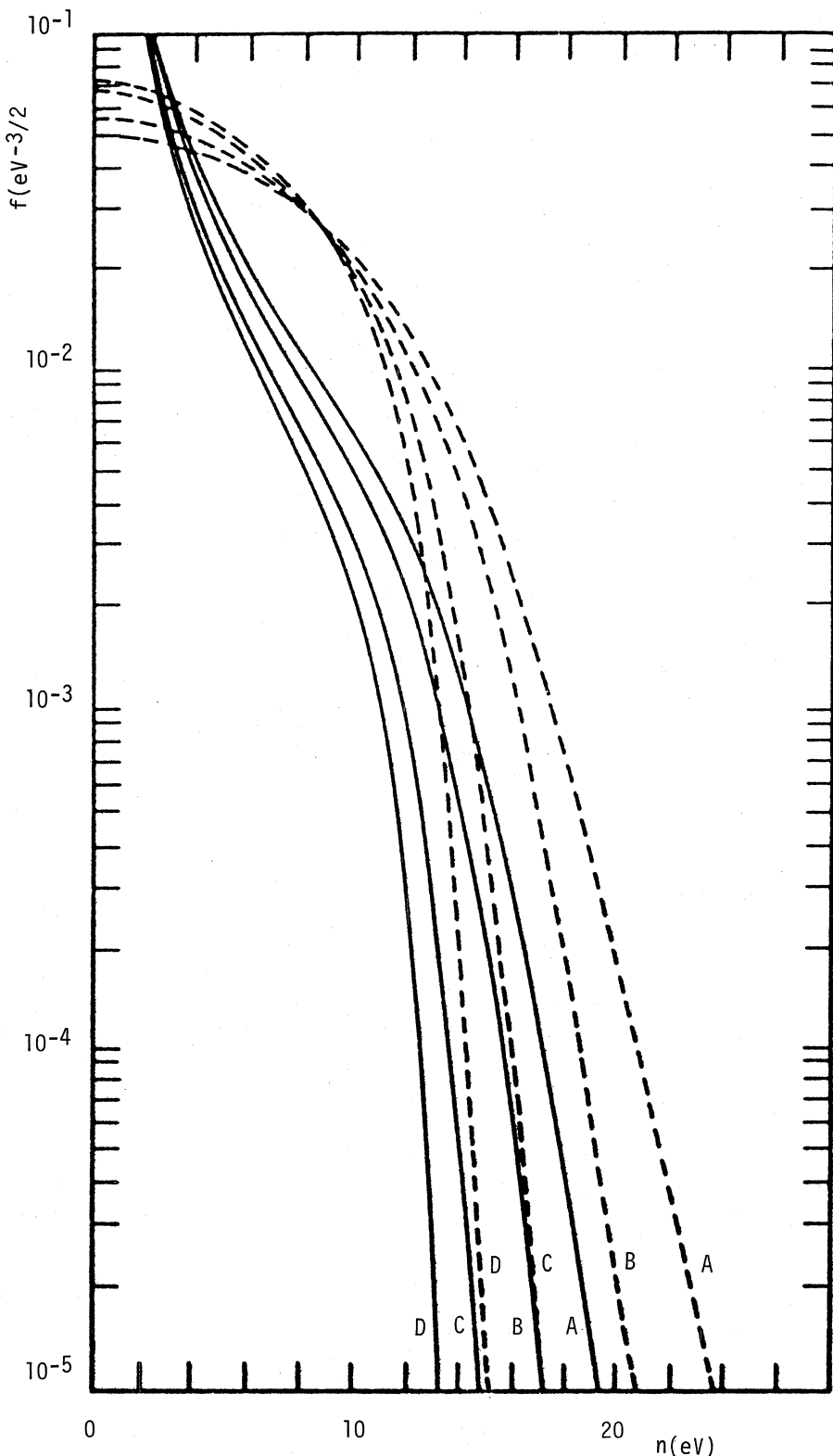


Fig. 1. Electron energy distributions in Ar for $\omega/\nu_{ce} = 2$ (full curves) and $\omega \ll \nu_{ce}$ (broken curves) and for the following values of E/N in $10^{-16} V cm^2$: 10(A); 6.5(B); 3(C); 1.5(D).

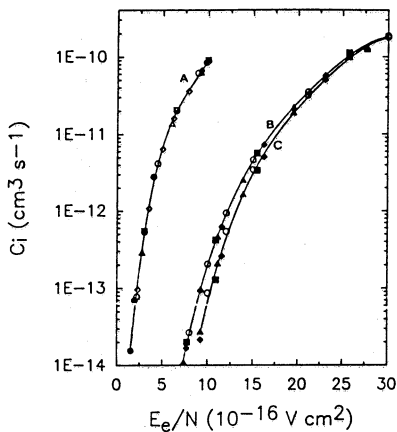


Fig. 2. Ionization rate coefficient vs. E_e/N in Ar (A) and in N₂ for $T_v = 4000\text{K}$ (B) and 400K (C). Data points are calculations for various values of ω/ν_{ce} ranging from 0 to ∞ . The curves are best fits to these points.

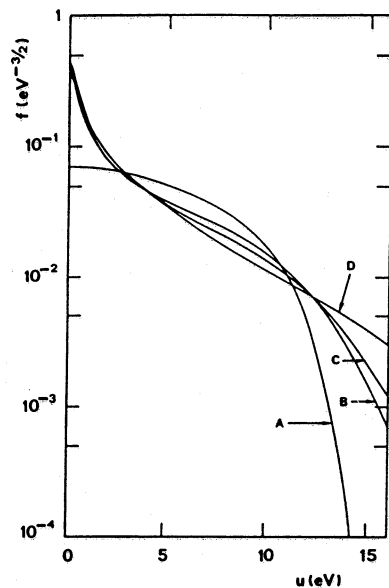


Fig. 3. Electron energy distributions in Ar with the same mean energy of 3.5 eV for the following values of ω/ν_{ce} : 0(A); 0.5(B); 0.8(C); $\gg 1$ (D).

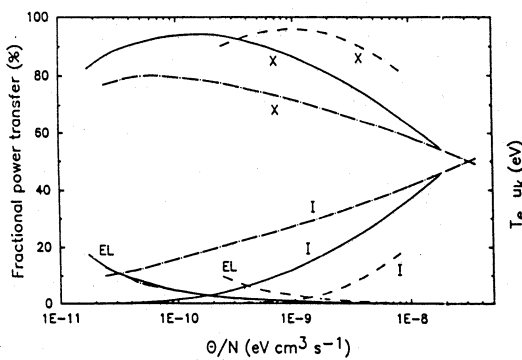


Fig. 4. Percentage electron energy losses in Ar through excitation (X), ionization (I), and elastic recoil (EL) vs. Θ/N in the following cases: no electron-electron interactions, for $\omega \ll \nu_{ce}$ broken curves) and $\omega \gg \nu_{ce}$ (full curves); Maxwellian distribution (chain curves).

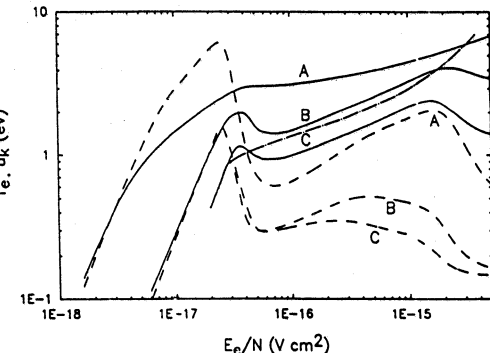


Fig. 5. Electron kinetic temperature (full curves) and characteristic energy (broken curves) in Ar vs. E_e/N , for $\omega/\nu_{ce} = 0.15$ (A); $= 0.8$ (B); $\gg 1$ (C). The chain curve is for a Maxwellian distribution and $\omega \gg \nu_{ce}$.

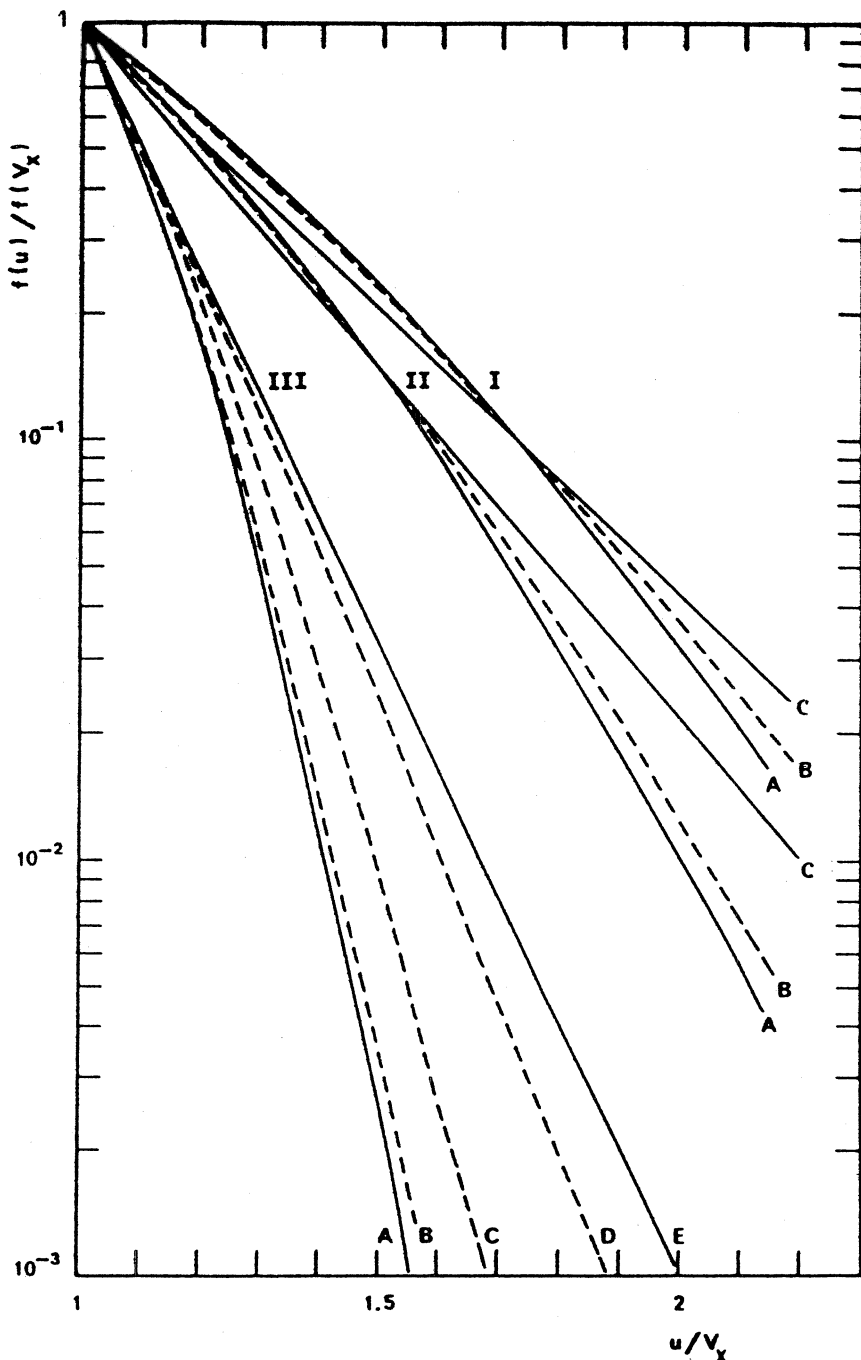


Fig. 6. Calculations of the tail of the electron energy distribution in the case of $\omega \gg \nu_{ce}$ for various ratios of E_e/N in $V\text{cm}^2$ and ionization degrees. Curves I: $E_e/N = 1.70 \times 10^{-15}$ and $n/N = 0(A), = 1.5 \times 10^{-5}(B), \geq 1.5 \times 10^{-4}(C)$. Curves II: $E_e/N = 1.18 \times 10^{-15}$ and $n/N = 0(A), = 8.7 \times 10^{-6}(B), \geq 8.7 \times 10^{-5}(C)$. Curves III: $E_e/N = 2.94 \times 10^{-16}$ and $n/N = 0(A), = 9.6 \times 10^{-7}(B), = 9.6 \times 10^{-6}(C), = 9.6 \times 10^{-5}(D), \geq 5 \times 10^{-4}(E)$.

3.2 Nitrogen

The solution of the homogeneous Boltzmann equation (26) in a molecular gas like N₂ is more complicated, since one has to account for superelastic collisions of the electrons with vibrationally excited molecules¹² in the inelastic collision term on the r.h.s. of (26). Moreover, a flux term accounting for rotational excitation must be included in the total upflux¹³. For consistency, eq.(26) must be solved together with the system of rate balance equations determining the populations in the various vibrational levels of the electronic ground state N₂(X, v). Self-consistent solutions of this type under steady-state discharge conditions have recently been reported in the literature^{10,14}.

The vibrational rate balance equations introduce n/N as a further independent parameter in the theory, even in the absence of electron-electron collisions, in addition to E_e/N and ω/N (or E_e/N and ω/ν_{ce}). For N₂ we have chosen $\nu_{ce}/N = 2.4 \times 10^{-7} \text{ cm}^3 \text{s}^{-1}$, which corresponds to electrons of 2.1 eV or 2.9 eV or even 10.4 eV (due to the particular shape of $\nu_c(u)$ in N₂¹⁵) for the same reasons as in Ar (see fig. 2). In practice, one can use a characteristic vibrational temperature, T_V , measuring the degree of vibrational excitation as an independent parameter in place of n/N , since T_V and n/N are related to each other for given E_e/N and ω/ν_{ce} ¹⁰. Figure 7 shows curves of n/N vs. E_e/N for constant T_V , in the two limiting cases of $\omega \ll \nu_{ce}$ and of $\omega \gg \nu_{ce}$. Producing a given T_V value requires somewhat higher degrees of ionization as ω increases because the rate coefficient for vibrational excitation decreases in this case (fig. 8).

Figure 9 shows $f(u)$ for $E_e/N = 10^{-15} \text{ V cm}^2$, $T_V = 400 \text{ K}$ and $T_V = 4000 \text{ K}$, and two values of ω/ν_{ce} . A higher vibrational temperature results in a higher population in the tail of $f(u)$, which is a consequence of the energy gained by the electrons in superelastic collisions.

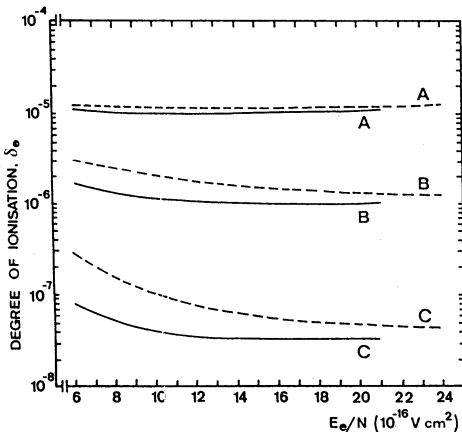


Fig. 7. Curves of the degree of ionization vs. E_e/N in N₂, for $\omega \ll \nu_{ce}$ (full curves) and $\omega \gg \nu_{ce}$ (broken curves) and for the following constant values of T_V in K: 6000(A); 4000(B); 3000(C).

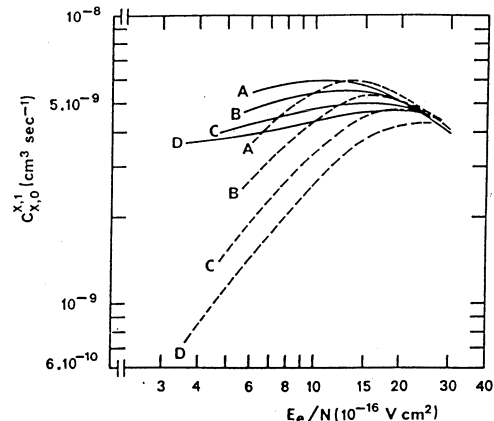


Fig. 8. Electron rate coefficient for vibrational excitation from v=0 to v=1 in N₂ vs. E_e/N , for $T_V = 4000 \text{ K}$ (full curves) and 400 K (broken curves) and for $\omega/\nu_{ce} = 0(\text{A})$; $0.42(\text{B})$; $0.83(\text{C})$; $1.67(\text{D})$.

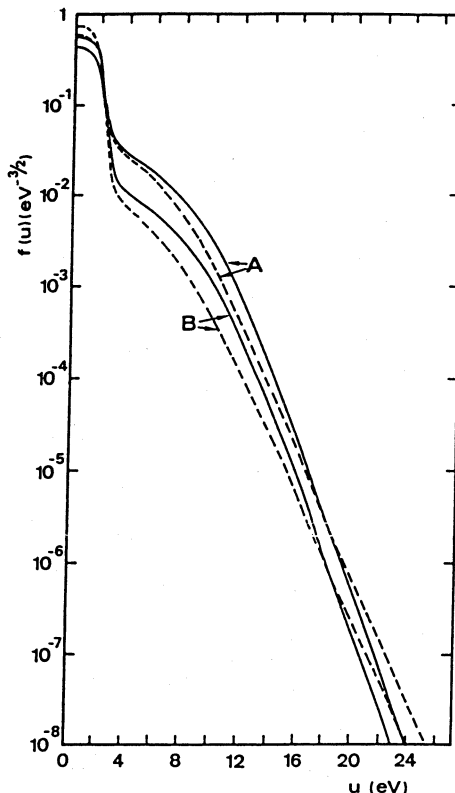


Fig. 9. Electron energy distributions in N_2 for $E_e/N = 10^{-15} V cm^2$, $T_V = 4000K$ (A) and $T_V = 400K$ (B), $\omega/\nu_{ce} = 0.42$ (full curves) and $\omega/\nu_{ce} = 1.67$ (broken curves).

Apparently, the changes in ω modify $f(u)$ to a much lesser extent than in Ar, but the effects are far from negligible. This can be better evaluated from the curves for the percentage energy losses through vibrational excitation (net power loss, i.e., including the gain from superelastic collisions) and electronic excitation represented vs. Θ/N in fig. 10. The power losses through elastic collisions and rotational excitation are much smaller in the range considered and are not shown on the figure. As ω/ν_{ce} increases the fractional power transferred to the vibrational mode decreases whereas the losses into electronic excitation and ionization consequently increase. As in Ar, such a behavior follows from the dependence of $\nu_c u_c$ on u and the fact that this function reaches a maximum for $\nu_c(u) = \omega$. In N_2 , $\nu_c(u)$ peaks at around 2.5 eV and grows monotonically at higher energies, so that the maximum power transfer occurs for electrons with increasingly higher energy as ω increases.

Figures 11 and 12 represent, respectively, $T_e = 2/3 < u >$ and u_k vs. E_e/N for $T_V = 4000K$ and $T_V = 400K$ and various values of ω/ν_{ce} . Both T_e and u_k decrease as ω/ν_{ce} increases for constant E_e/N but, here, the decrease in u_k is much less important than in Ar. This is due to the fact the HF distributions in N_2 do not peak at low energies as one can see from fig. 9.

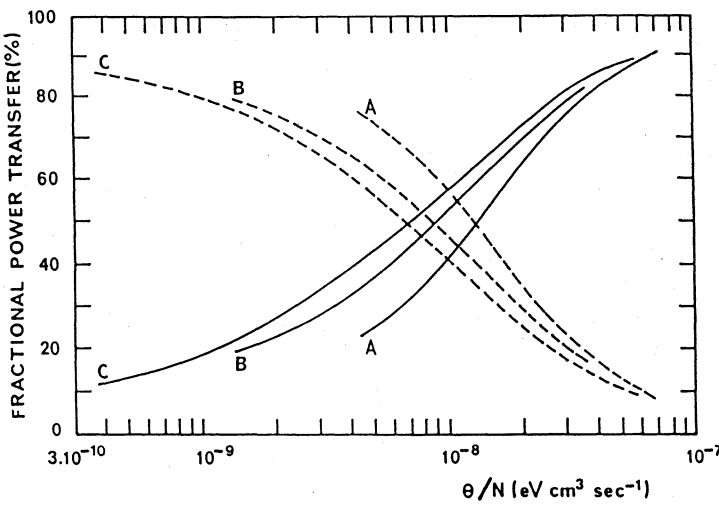


Fig. 10. Percentage electron energy losses in N_2 through vibrational excitation (broken curves) and electronic excitation plus ionization (full curves) as a function of Θ/N , for $\omega/\nu_{ce} = 0(A)$; $= 0.83(B)$; $\gg 1(C)$.

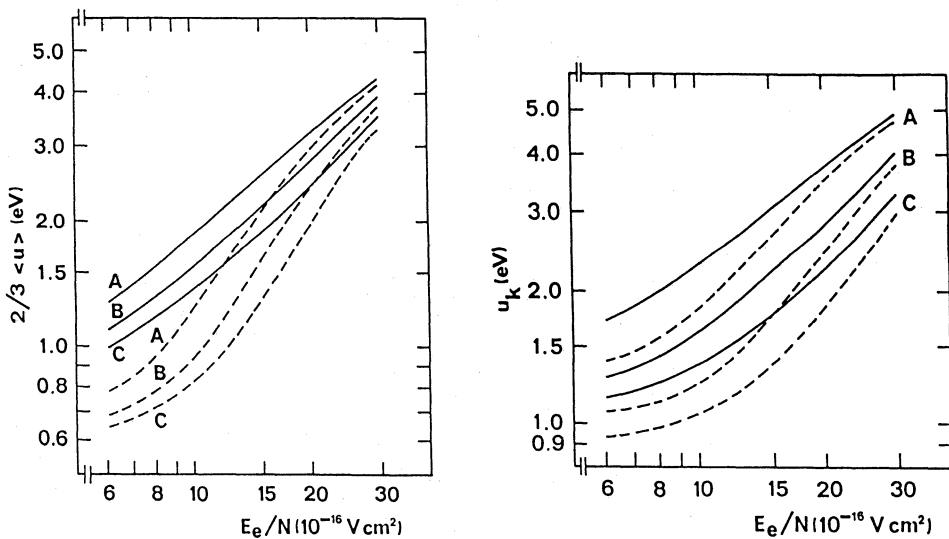


Fig. 11. Electron kinetic temperature in N_2 vs. E_e/N , for $T_V = 4000K$ (full curves) and $400K$ (broken curves), and for $\omega/\nu_{ce} = 0(A)$; $= 0.83(B)$; $\gg 1(C)$.

Fig. 12. As in figure 11 but for the characteristic energy.

4. THE PLASMA RELATIVE PERMITTIVITY: EFFECTIVE ELECTRON DENSITY AND COLLISION FREQUENCY

The characteristics of electromagnetic waves propagating in an ionized gas are usually investigated by considering that this medium can be fully described by two parameters, the electron plasma frequency, $\omega_p = (ne^2/\epsilon_0 m)^{1/2}$, and the effective electron-neutral collision frequency, ν_e . The latter is generally assumed to be independent of the electron energy and to represent, therefore, some proper average value. Experimentally, these parameters are often determined from measured values of the attenuation and the phase characteristics of the wave as it propagates through the plasma.

In fact, as regard to wave propagation the plasma can be described as a dielectric medium with a complex relative permittivity given by

$$\epsilon_p = 1 - j \frac{\sigma}{\omega \epsilon_0} , \quad (40)$$

where σ is the complex conductivity given by eq. (16). This equation is valid whatever the dependence of ν_c on the electron energy. In the particular, but quite ideal case of a constant collision frequency, $\nu_c(u) = \nu_e$, eqs. (16) and (40) reduce to the simple forms

$$\sigma = \frac{e^2 n}{m} \frac{1}{\nu_e + j\omega} = \epsilon_0 \omega_p^2 \frac{1}{\nu_e + j\omega} , \quad (41)$$

$$\epsilon_p = 1 - \frac{\omega_p^2}{\nu_e^2 + \omega^2} \left(1 + j \frac{\nu_e}{\omega} \right) . \quad (42)$$

In the case of an energy dependent ν_c , as first shown by Whitmer and Herrmann¹⁶, it is possible to express σ and ϵ_p in the forms (41) and (42) provided one defines ω -dependent, effective values n_e and ν_e given by the expressions

$$\nu_e = \frac{\int_0^\infty \frac{\nu_c u^{3/2}}{\nu_c^2 + \omega^2} \frac{df}{du} du}{\int_0^\infty \frac{u^{3/2}}{\nu_c^2 + \omega^2} \frac{df}{du} du} , \quad (43)$$

$$\frac{n_e}{n} = \left(-\frac{2}{3} \int_0^\infty \frac{u^{3/2}}{\nu_c^2 + \omega^2} \frac{df}{du} du \right) (\nu_e^2 + \omega^2) . \quad (44)$$

Whitmer and Herrmann have calculated these effective parameters for He, Ne, Ar, and N₂, assuming a Maxwellian distribution. Recently, Boisse-Laporte¹⁷ used a similar analysis in the diagnostic of argon discharges sustained by HF surface waves. Hereafter, we present calculations of these quantities for an argon discharge sustained by a traveling wave of frequency ω using the solutions to the homogeneous Boltzmann equation (26) and we compare these calculations with those for a Maxwellian distribution.

First, we note from (43) and (44) that ν_e/N and n_e/n are functions of E_e/N and ω/ν_{ce} (or, alternatively, of E/N and ω/N) for a non-Maxwellian distribution, and of T_e and ω/ν_{ce} (or ω/N) for a Maxwellian one. For the purposes of comparison, we represent in figs. 13 and 14 ν_e/N and n_e/n , respectively, as a function of the electron kinetic temperature in both cases, by making use of the calculated values of T_e vs. E_e/N and ω/ν_{ce} for a non-Maxwellian distribution (see fig. 5). However, this representation, which is

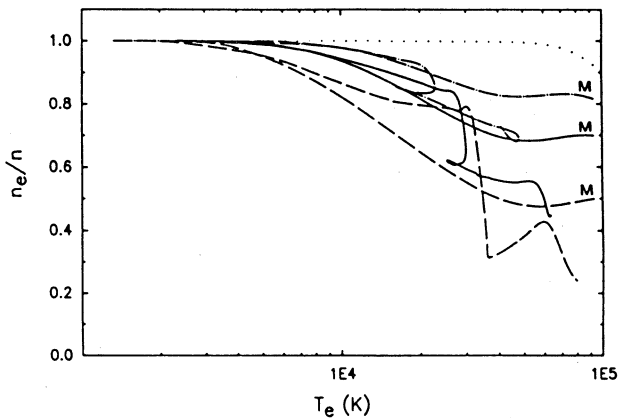


Fig. 13. Ratio of the effective to the real electron density in Ar as a function of the electron kinetic temperature for $\omega/\nu_{ce} = 0.15$ (broken curves); $= 0.4$ (full curves); $= 0.8$ (chain curves); $\gg 1$ (dotted curve), in the absence of electron-electron collisions (unlabelled curves) and for a Maxwellian distribution (M).

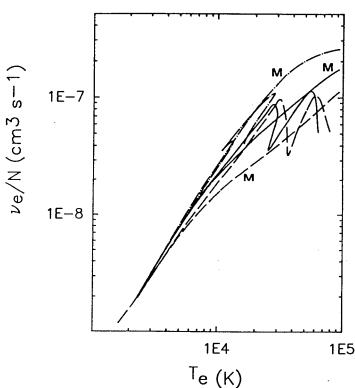


Fig. 14. As in figure 13 but for the effective collision frequency at unit gas density and excepting that the chain curve is now for $\omega \gg \nu_{ce}$.

only useful for comparing the non-Maxwellian results to the Maxwellian ones, introduces some problems, since the curves of T_e vs. E_e/N for a non-Maxwellian distribution go through a maximum for $E_e/N \sim 4 \times 10^{-17} V cm^2$ and $E_e/N \sim 2 \times 10^{-15} V cm^2$. This makes that $E_e/N, \nu_e/N$, and n_e/n become multivalued functions of T_e over a small range of electron temperatures around $1 - 2$ eV (see figs. 13 and 14). This peculiar behavior of the curves of ν_e/N and n_e/n vs. T_e is, therefore, just an artifact associated with this representation. The curves of ν_e/N and n_e/n are, in fact, well-behaved, single-valued functions of E_e/N and ω/ν_{ce} , the actual independent parameters on which the non-Maxwellian distributions depend.

From eqs. (43) and (44), one sees that $n_e \rightarrow n$ for sufficiently large values of ω . In this limit, $\nu_e \rightarrow \bar{\nu}_c$, where $\bar{\nu}_c$ is defined by

$$\bar{\nu}_c = -\frac{2}{3} \int_0^\infty \nu_c(u) u^{3/2} \frac{df}{du} du . \quad (45)$$

For given ω , we also have $n_e \rightarrow n$ and $\nu_e \rightarrow \bar{\nu}_c$ as T_e (or E_e/N) decreases, since one always reaches a situation in which $\nu_c(u) \ll \omega$ for most of the electrons, when T_e decreases sufficiently. Moreover, in this limit of low temperatures, the non-Maxwellian distributions nearly Maxwellize (this occurs when $\omega \gg \nu_c(u)$ for most of the electrons and T_e is sufficiently low so that the elastic losses prevail over the inelastic ones⁹) and the results approach those obtained with a Maxwellian distribution.

The results of figs. 13 and 14 indicate that the effective electron density is substantially smaller than the real one except when ω is much larger than the collision frequency for most of the electrons. The effective collision frequency ν_e also differs substantially from the collision frequency of a representative electron, except for sufficiently large ω in which case $\nu_e \sim \bar{\nu}_c \sim <\nu_c>$. Therefore, consideration for these effective parameters is, in general, essential in the interpretation of experiments involving wave propagation in plasmas.

5. DISCHARGE CHARACTERISTICS AND SIMILARITY LAWS

The momentum transfer equation for the ions can be written in the form

$$(<\vec{v}_i> \cdot \vec{\nabla}_r) <\vec{v}_i> = \frac{e\vec{E}_s}{M} - \frac{eT_i}{M} \frac{\vec{\nabla}_r n_i}{n_i} - (\nu_{in} + <\nu_i>) <\vec{v}_i> , \quad (46)$$

where T_i is the ion temperature in eV, which is assumed spatially constant, and ν_{in} is the collision frequency for ion-neutral momentum transfer. At sufficiently high pressures the nonlinear term on the l.h.s. of (46) can be neglected and we also have $<\nu_i> \ll \nu_{in}$, so that eq.(46) reduces to the simpler form

$$\vec{\Gamma}_i = n_i <\vec{v}_i> = -D_i \vec{\nabla}_r n_i + n_i \mu_i \vec{E}_s , \quad (47)$$

where $\mu_i = e/(M\nu_{in})$ and $D_i = eT_i/(M\nu_{in})$ are the ion mobility and diffusion coefficient, respectively.

In the ambipolar limit, i.e., for $n_i = n$ and $\vec{\Gamma}_i = \vec{\Gamma}$, eq.(46) can be solved together with the continuity equation (12) and the electron particle flow equation (9), with D_e

and u_e assumed spatially constant. The solutions of this system of equations have been given by Self and Ewald¹⁸ for planar and cylindrical geometry and for the complete range of gas pressures from the free-fall limit to the collision-dominated limit. As first noted by Persson¹⁹, the retention of the nonlinear inertia terms in eq.(46) results in a plasma-sheath boundary at the point where the ion drift velocity equals the isothermal sound speed, which in this case is $[e(u_k + T_i)/M]^{1/2}$, with u_k also expressed in eV.

As shown by Ingold²⁰, analytical results similar to those of Self and Ewald can be obtained by making use of the fact that the ion drift velocity is small compared to the isothermal sound speed except near the edge of the column. For example, in cylindrical geometry, eqs.(9), (12), and (46), with D_e and μ_e assumed spatially constant, can be written as

$$\frac{1}{r} \frac{d}{dr}(rn v_d) = <\nu_i> n , \quad (48)$$

$$v_d = -D_e \frac{d}{dr}(\ln n) - \mu_e E_s , \quad (49)$$

$$v_d \frac{dv_d}{dr} = \frac{eE_s}{M} - \frac{eT_i}{M} \frac{d}{dr}(\ln n) - (\nu_{in} + <\nu_i>) v_d , \quad (50)$$

where $\vec{v}_d \equiv <\vec{v}_i> = <\vec{v}>$ is the radial drift velocity. Solving eq.(48) for dv_d/dr , eq.(49) for E_s , and inserting the results into (50) one obtains, neglecting terms in v_d^2 and noting that $\mu_i/\mu_e \ll 1$,

$$\Gamma \equiv nv_d \simeq -D_s \frac{dn}{dr} , \quad (51)$$

where D_s is an effective diffusion coefficient given by

$$D_s = D_a \left(1 + \frac{2 <\nu_i>}{\nu_{in}} \right)^{-1} . \quad (52)$$

Here, $D_a = e(u_k + T_i)/(M\nu_{in}) = \mu_i u_k + D_i$ is the ambipolar diffusion coefficient (25) in the limit $\mu_i/\mu_e \rightarrow 0$.

Taking into account eq.(51) the continuity equation (48) can be expressed as

$$-D_s \nabla_r^2 n = <\nu_i> n , \quad (53)$$

and the space-charge field, as obtained from eqs.(49), is given by

$$E_s = -\frac{D_e - D_s}{\mu_e} \frac{d}{dr}(\ln n) . \quad (54)$$

The above derivation assumes that μ_e and D_e are spatially constant. We can see, however, that this assumption is consistent with the analysis of the Boltzmann equation given in Sect.2.4, since eqs.(53) and (54) precisely have the form required for the existence of separable solutions of that equation. In this case, the transport coefficients D_e and μ_e are indeed spatially constant.

The continuity equation (53) can also be expressed in the form

$$\frac{D_s}{\Lambda_e^2} = \langle \nu_i \rangle , \quad (55)$$

where Λ_e is the effective diffusion length defined by eq.(23).

The solution of eq.(53) (or eq.(23)) is

$$n(r) = n_0 J_0(r/\Lambda_e) , \quad (56)$$

where J_0 is the zero-order Bessel function of the first kind. Using eqs.(56) and (51), the boundary condition $v_d(R) = [e(u_k + T_i)/M]^{1/2}$ can be expressed in the form

$$J_0(R/\Lambda_e)/J_1(R/\Lambda_e) = \left(\frac{\langle \nu_i \rangle}{\nu_{in} + 2 \langle \nu_i \rangle} \right)^{1/2} , \quad (57)$$

an equation that determines the ratio R/Λ_e as a function of the ratio $\langle \nu_i \rangle / \nu_{in}$. The r.h.s. member of eq.(57) ranges from $1/\sqrt{2}$ at low pressures, in which case $\langle \nu_i \rangle \gg \nu_{in}$, to about zero at high pressures, in which case $\langle \nu_i \rangle / \nu_{in} \rightarrow 0$, thus yielding, from eq.(57), $R/\Lambda_e = 1.19\sqrt{2} \simeq 1.68$ and $R/\Lambda_e \simeq 2.405$, in these two limiting cases, respectively. In other words, $\Lambda_e/\Lambda \simeq 2.405/1.19\sqrt{2} \simeq 1.43$ at low pressures and $\Lambda_e \simeq \Lambda$ at high pressures, $\Lambda = R/2.405$ being the characteristic diffusion length for cylindrical geometry. The fact that $\Lambda_e > \Lambda$ at low pressures means that n_b , the plasma density at the plasma-sheath boundary, is not vanishingly small: its value is, in fact, from eq.(56), $n_b = n_0 J_0(1.19\sqrt{2})$, thus $n_b/n_0 \simeq 0.41$. This value is close to that derived from the exact free-fall theory^{21,22}, viz., $n_b/n_0 = 0.315$.

At high pressures $D_s \rightarrow D_a$ and $\Lambda_e \rightarrow \Lambda$, so that eq.(55) is the same as $D_s/\Lambda^2 = \langle \nu_i \rangle$, the well-known result obtained from the classical ambipolar diffusion theory⁶. At low pressures, we have from (52) $D_s \simeq D_a \nu_{in} / (2 \langle \nu_i \rangle)$, which yields, taking into account the expression for $D_a, D_s \simeq e(u_k + T_i) / (2M \langle \nu_i \rangle)$. Therefore, as $\Lambda_e \simeq R/1.19\sqrt{2}$ at low pressures, the particle balance equation (55) can be written in the form

$$\frac{1.19}{R} \left[\frac{e(u_k + T_i)}{M} \right]^{1/2} = \langle \nu_i \rangle . \quad (58)$$

Equation (55) constitutes a fundamental relationship between the product NR and the set of parameters on which the electron energy distribution depends. As seen in Sections 2 and 3 these parameters are E_e/N and ω/ν_{ce} (or E/N and ω/N), and also n/N in molecular gases or when electron-electron interactions are important. The above relationship determines, therefore, the reduced effective field required for the steady-state discharge operation under the form of a similarity law of the type

$$\frac{E_e}{N} = f_E \left(NR, \frac{\omega}{\nu_{ce}}, \frac{n}{N} \right) . \quad (59)$$

Since Θ/N , the reduced average absorbed power per electron, is a unique function of $E_e/N, \omega/\nu_{ce}$, and n/N , eq.(59) also implies the existence of similarity laws for Θ/N expressible in the form

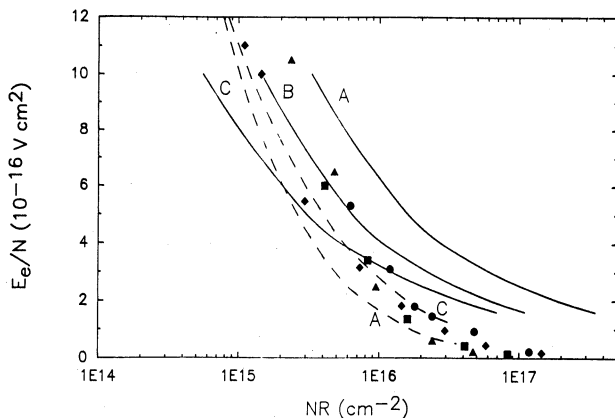


Fig. 15. Reduced maintenance field for Ar discharges as a function of NR for negligible electron-electron interactions (full curves) and for a Maxwellian distribution (broken curves), for $\omega/\nu_{ce} = 0$ (A); = 0.15 (B); $\gg 1$ (C). The data points are from experiments on surface wave discharges (see main text).

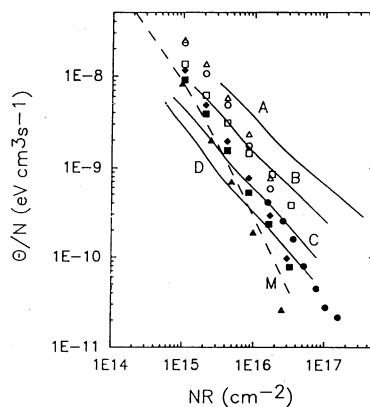


Fig. 16. As in figure 15 but for the reduced average absorbed power per electron, Θ/N , and excepting that curves C and D are for $\omega/\nu_{ce} = 0.8$ and $\omega \gg \nu_{ce}$, respectively. Note that the Maxwellian case (M) yields a unique characteristic for all values of ω/ν_{ce} .

$$\frac{\Theta}{N} = f_{\Theta} \left(NR, \frac{\omega}{\nu_{ce}}, \frac{n}{N} \right) . \quad (60)$$

However, in atomic gases no dependence on n/N is to be expected at sufficiently low electron densities, when electron-electron interactions are negligible. In the opposite limit of high electron densities, as $f(u)$ nearly Maxwellizes, E_e/N becomes a unique function of $N\Lambda$ and ω/ν_{ce} , while Θ/N becomes a unique function of $N\Lambda$ (as indicated by eq.(27) or eq.(33) for a Maxwellian distribution).

Figures 15 and 16 show calculated characteristics of E_e/N and Θ/N for cylindrical argon discharges as a function of NR and ω/ν_{ce} in the case of negligible electron-electron interactions and also in the case of a Maxwellian distribution. The data points on this figures are from experiments on surface wave produced discharges^{23,24} at frequencies ranging from 25.8 MHz up to 2.45 GHz using various tube diameters (from a few millimeters to a few centimeters). The closed points on both figures are for frequencies above 210MHz while the open points on fig. 16 are for the range 25.8-200 MHz. At these lower frequencies the application of the theory is subject to caution since the oscillation of $f(u)$ may be important. We note, however, that the overall agreement between theory and experiment is quite satisfactory since all the points lie in between the predicted limits. It is difficult to confirm from these data the theoretical predictions concerning the role of the parameter ω/ν_{ce} . In fact, electron-electron collisions may play a non-negligible role at frequencies above a few hundred MHz as, then, the degree of ionization becomes relatively high. Therefore, the observed trends in the experimental data as ω varies probably reflect the simultaneous influence of the parameters ω/ν_{ce} and n/N . At frequencies above 1GHz (closed triangles and squares on fig.(16)) $f(u)$ can be expected to be nearly a Maxwellian and, in fact, the Maxwellian calculations yield the best predictions, especially in what concerns the variation of Θ/N vs. NR , as seen from fig. 16.

6. CONCLUDING REMARKS

The combination of the solutions to the electron Boltzmann equation with the charged particle continuity and momentum transfer equations provides a unified picture of HF discharges independently of the particular set-up used as a HF source. This formulation predicts that the sustaining field for steady-state HF discharges cannot be externally imposed and is, on the contrary, determined by the balance between the average creation and loss rates for the charged particles, as in a DC discharge. This balance determines, in fact, specific similarity laws for the reduced maintenance field, E_e/N , and the reduced average absorbed power per electron, Θ/N , as a function of the discharge operating parameters (gas density N , electron density n , angular frequency ω , diffusion length Λ). In the simple case of a diffusion dominated regime, the only case discussed here, the above similarity laws involve only combinations of these parameters in the form $N\Lambda, \omega/\nu_{ce}$ (or ω/N) and n/N (proper variables).

The theory can be extended to higher pressures by including stepwise ionization processes and volume electron-ion recombination but this introduces great complexity in the formulation. Such an extension was discussed by Ferreira et al²⁵.

For the sake of mathematical simplicity we have assumed here a uniform HF field. However, in recent years this theory has been extended to include the effects of the field non-uniformity in the case of surface wave produced discharges^{5,26,27}. These discharges have been extensively studied in recent years not only because of their many applications but also because they are particularly accessible to detailed experimental investigation (see, e.g., the reviews by Moisan et al^{28,29}). Although the modelling of these discharges is far more complex due to the field nonuniformity, the basic conclusions resulting from this modelling remain essentially the same as those derived here for a uniform field, namely, in what concerns the similarity laws for E_e/N and Θ/N .

For this reason, the formulation presented in this work provides physical insight and sufficient numerical accuracy for the purposes of basic discharge modelling.

ACKNOWLEDGEMENTS

The author is indebted to Dr. J. Loureiro and Mrs. A. B. Sá for collaboration and discussions. This work was supported in part by NATO Research Grant 105/87.

REFERENCES

1. W. P. Allis and S. C. Brown, Phys. Rev. 87 : 419 (1952).
2. D. J. Rose and S. C. Brown, Phys. Rev. 98 : 310 (1955).
3. W. P. Allis, Hand. of Physics 21 : 383 (1956).
4. S. C. Brown, Hand. of Physics 22 : 531 (1956).
5. C. M. Ferreira and M. Moisan, Physica Scripta 38 : 382 (1988)
6. W. P. Allis and D. J. Rose, Phys. Rev. 93 : 84 (1954).
7. V. E. Golant, A. P. Zhilinsky and I. E. Sakharov, "Fundamentals of Plasma Physics", John Wiley and Sons, New York, 1980.
8. C. M. Ferreira and J. Loureiro, J. Phys. D : Appl. Phys. 17 : 1175 (1984).
9. C. M. Ferreira and J. Loureiro, J. Phys. D : Appl. Phys. 16 : 2471 (1983).
10. C. M. Ferreira and J. Loureiro, J. Phys. D : Appl. Phys. 22 : 76 (1989).
11. L. S. Frost and A. V. Phelps, Phys. Rev. A 136 : 1538 (1964).
12. M. Capitelli, M. Dilonardo, and C. Gorse, Chem. Phys. 56 : 29 (1981).
13. L. S. Frost and A. V. Phelps, Phys. Rev. 127 : 1621 (1962).
14. J. Loureiro and C. M. Ferreira, J. Phys. D : Appl. Phys. 19 : 17 (1986).
15. A. G. Engelhardt, A.V. Phelps, and C. G. Risk, Phys. Rev. A 135 : 1566 (1964).
16. R. F. Whitmer and G. F. Herrmann, Phys. Fluids 9 : 768 (1966).
17. C. Boisse-Laporte, Thesis, University Paris-Sud, Orsay (1989).
18. S. A. Self and H. N. Ewald, Phys. Fluids 9 : 2486 (1966).
19. K. B. Persson, Phys. Fluids 5 : 1625 (1962).
20. J. H. Ingold, Glow Discharges at DC and Low Frequencies, in "Gaseous Electronics", Vol. I, M. N. Hirsh and H. J. Oskam, eds., Academic Press. New York, 1978.
21. L. Tonks and I. Langmuir, Phys. Rev. 34 : 876 (1929).
22. S. A. Self, J. Appl. Phys. 36 : 456 (1965).

23. C. Boisse-Laporte, A. Granier, E. Dervisevic, P. Leprince, and J. Marec, J. Phys. D : Appl. Phys. 20 : 197 (1987).
24. C. Barbeau, M. Sc. Thesis, University of Montreal, 1988.
25. C. M. Ferreira, J. Loureiro, and A. B. Sá, Proceedings XVIII Int. Conf. Phenom. Ionized Gases (book of Invited Lectures), W. T. Williams, ed., Adam Hilger, Bristol (1987).
26. C. M. Ferreira, J. Phys. D : Appl. Phys. 14 : 1811 (1981).
27. C. M. Ferreira, Plasmas Sustained by Surface Waves at Radio and Microwave Frequencies: Basic Processes and Modeling, in "Radiative Processes in Discharge Plasmas", J. M. Proud and L. H. Luessen, eds., Plenum, New York, 1986.
28. M. Moisan, C. M. Ferreira, Y. Hajlaoui, D. Henry, J. Hubert, R. Pantel, and A. Ricard, Revue Phys. Appl. 17 : 707 (1982).
29. M. Moisan and Z. Zakrzewski, Plasmas Sustained by Surface Waves at Microwave and RF Frequencies : Experimental Investigation and Applications, in "Radiative Processes in Discharge Plasmas", J. M. Proud and L. H. Luessen, eds., Plenum, New York, 1986.

VOLUME PRODUCTION OF HYDROGEN NEGATIVE IONS

M. Bacal

Laboratoire de Physique des Milieux Ionisés
Laboratoire du C.N.R.S.
Ecole Polytechnique
91128 Palaiseau Cedex, France

INTRODUCTION

Negative hydrogen ion beams have numerous applications. They are necessary for producing beams of energetic neutral atoms, which are important in magnetic fusion for heating, fueling, and current drive. Accelerators also need negative ion beams since charge exchange injection and extraction are more efficient than other methods. One approach under investigation for strategic defense is the use of powerful beams of neutral atoms derived from negative hydrogen ions.

The interest in volume H^-/D^- ion sources developed following the measurement by probes and laser photodetachment of high fractions ($\leq 30\%$) of negative ions in electron-beam sustained discharges in H_2/D_2 .^{1,2} The observed H^-/D^- formation rates were several orders of magnitude higher than could be explained by the mechanisms previously investigated. One possibility proposed in 1977 was the enhancement of dissociative electron attachment (DA) due to vibrational excitation of molecules. Dissociative electron attachment to vibrationally cold $H_2(v''=0)$ molecules



is known to have a very small cross section³ ($\sim 10^{-21} \text{ cm}^2$). The idea that the H^- production by dissociative attachment could be considerably enhanced when the hydrogen molecules were vibrationally excited emerged from discussions with W. L. Fite and K. T. Dolder and was formulated in Refs. 1 and 2. In 1979 the experiment of Allan and Wong⁴ and the theoretical calculations by Wadehra and Bardsley⁵ showed that indeed the cross sections for dissociative attachment increase by five orders of magnitude when the hydrogen molecules are vibrationally excited from $v''=0$ to $v''=5$. An important feature discovered is that the cross sections peak at threshold and the threshold energy is smaller at higher v'' .^{4,5} Thus low energy electrons (≤ 1 eV) can be very effective in generating H^- ions by DA to highly vibrationally excited molecules:



The DA to the upper portion of the vibrational spectrum, Eq. (2), was adopted as a working hypothesis for negative hydrogen ion generation,

following the observation that there was no isotope effect for the H/D density². The theoretical values of the DA cross section for the higher portion of the vibrational spectrum in H₂ and D₂ are very close.

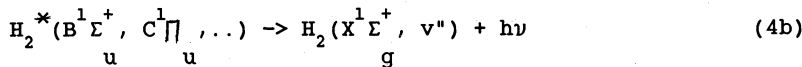
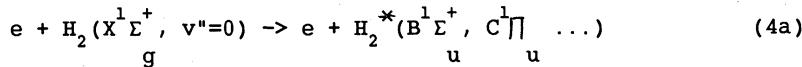
Very recently several groups⁶⁻⁸ have directly measured the populations of vibrationally excited molecules, which appear to be consistent with this hypothesis.

An important question is to define the processes which could generate sufficient density of highly vibrationally excited molecules in the discharge. Vibrational excitation of molecules in collisions with low energy electrons through the H₂⁻ resonance:



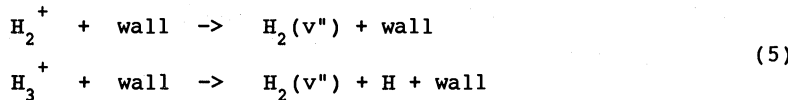
is very effective in changing the vibrational state. We will designate the process described by Eq. (3) as "e-V excitation"; this notation indicates that low energy electrons produce vibrationally excited molecules. By far the most probable change in v'' is $\Delta v'' = +1$, so a high collision rate will be required to significantly populate the H₂(v'') spectrum. Therefore it seemed improbable that e-V excitation could⁹ populate the high vibrational levels in the medium density discharge.

The plausibility of the working hypothesis described by Eq. 2 was greatly supported by the identification in 1980 by Kunkel¹⁰ of an effective source of highly vibrationally excited molecules. Kunkel suggested that the higher vibrational states could be populated by radiative decay from singlet electronic states, excited by collisions of ground state molecules with energetic primary electrons, i.e. the reaction:



We designate the process described by Eq. 4 as "E-V excitation", to indicate that vibrational excitation is produced by high energy electrons. Generally electron excitation collisions populate all the electronic states of the molecule, but only the excited singlet states will lead to the eventual repopulation of the X¹ Σ_g^+ ground state by radiative decay. The triplet states can be ignored because radiative decay towards the singlet ground state is not allowed. The electron excitation cross sections leading from v''=0 ground state through the excited B and C singlet states, to v'' levels of the ground state were calculated by Hiskes¹¹. Later Marx et al.¹² performed similar calculations taking into account all the singlet states and found cross sections 20 to 40% higher than those reported in Ref. 11. The E-V excitation is efficient when the electron energy exceeds ~20 eV. Thus the reason why the electron-beam sustained medium density discharge contains a high density of negative ions became obvious: the high energy electrons (~100 eV) produce the vibrational excitation, while the low temperature plasma electrons ($kT_e \leq 1$ eV) attach to the highly vibrationally excited molecules, producing H⁻ ions through DA (Eq. 2).

Another effective process of vibrational excitation to the higher vibrational states was identified by Hiskes and Karo¹³ and relies on the Auger neutralization on the walls of molecular hydrogen ions, H₂⁺ and H₃⁺, accelerated through the plasma potential sheath which is typically 2 V or more:



Theoretical work is in progress¹⁴ to quantify the contribution to vibrational excitation of the process (5) in the low energy range relevant to volume sources.

The full understanding of a volume negative ion source requires the consideration of the H⁻ destruction processes and of the various processes, which determine the vibrational spectrum, the electron energy distribution (typically non-maxwellian), the plasma density and the degree of gas dissociation. Among the H⁻ destruction processes, most important are mutual neutralization in collisions with positive ions and detachment in collisions with electrons. For a detailed description of the various processes, we refer to earlier reviews.¹⁵⁻¹⁸

VOLUME NEGATIVE ION SOURCES

A further step toward a more efficient H⁻/D⁻ production and extraction was the introduction of the tandem concept where the source was spatially separated into two chambers by a transverse magnetic field which is designated as the magnetic filter. An example of this concept is shown by Figure 1. This has been accomplished in several different configurations.^{15,19-21} Energetic electrons are introduced into the "source" chamber by thermionic emission. Usually the thermionic emitter is a tungsten filament, which is biased to a negative potential of 50-100 V. The emitted electron current is in the range of 10-1000 A. The magnetic filter reflects the energetic electrons and thus confines them in the source chamber. Negative ions are extracted on the other side of the filter from the "extraction" chamber, through one or several extraction orifices. Usually the source is a magnetic multicuspl plasma generator, a device which is magnetic field free in the central region. Permanent magnets applied on the walls shield the walls from energetic electrons and thus enhance the ionization efficiency. This is important since low gas density is required in order to limit the H⁻ destruction in collisions with atoms and molecules;¹⁸ the typical pressures used are in the range 5 to 15 mTorr.

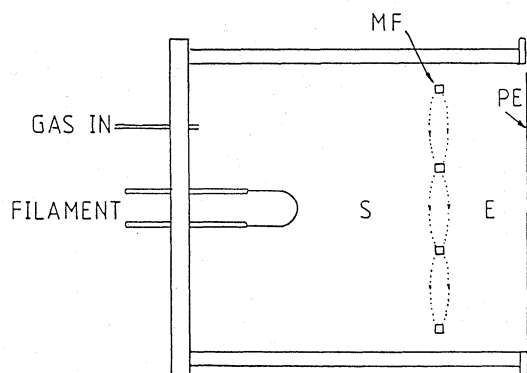


Figure 1. Tandem ion source, with the source chamber S separated from the extraction chamber E by a magnetic filter.

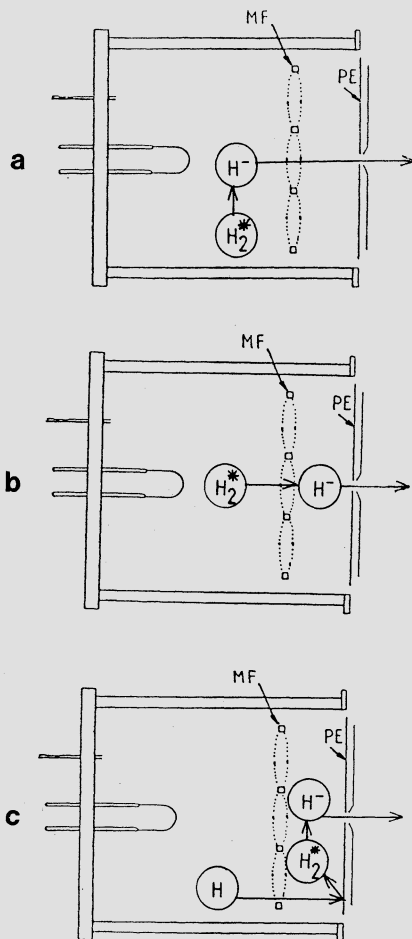


Figure 2. Illustration of various viewpoints on the origin of negative ions in a tandem source:

- (a) H^- is formed in the source chamber.
- (b) H^- is formed in the extraction chamber from $H_2(v'')$ formed in the source chamber.
- (c) Both $H_2(v'')$ and H^- are formed in the extraction chamber. The source chamber is a source of atoms.

There are three viewpoints on the origin of the extracted negative ions in the tandem sources. Figure 2 shows schematically these three viewpoints for production of $H_2(v'')$ and of H^- . According to the first viewpoint²⁰ the extracted negative ions originate from the source chamber (See Fig. 2a), where they are formed by DA, reaction (2); the advantage of the tandem configuration is, according to this viewpoint, a reduced electron density in the extraction chamber, and consequently, a lower electron component extracted in meantime with the negative ions. According to the second viewpoint²² the vibrationally excited molecules formed in the source chamber by reaction (4) travel across the magnetic filter into the extraction chamber to create there negative ions by DA, reaction (2), with cold electrons. (See Figure 2b.) The absence of energetic electrons and the lower electron temperature which characterizes the extraction chamber are favourable for negative ion production by DA and for their survival.

If these two viewpoints assume that the production of vibrationally excited molecules occurs in the source chamber, a third viewpoint²³ suggests that the source chamber is a source of atoms, which produce vibrationally excited molecules by recombinative desorption on the plasma electrode. (See Figure 2c.) Negative ions can then be produced by DA in the extraction chamber. More experiments and simulation are required before deciding about the relevance of these viewpoints to the various operating conditions.

In the tandem source the magnetic filter region is characterized by both a magnetic field and a plasma potential difference. The magnetic field of typical magnetic filters is strong enough to impede the passage of electrons from one chamber to the other, but not strong enough to block most of the ions. Thus the magnetic field principally affects electron transport and the potential principally affects ion transport. A potential difference is naturally associated with the magnetic filter. Due to their different temperatures, the plasmas on each side tend to establish different plasma potentials with respect to the chamber wall. Experiments have shown the utility of altering this natural difference by biasing the plasma electrode (a large magnetically unshielded surface in the extraction region).^{17, 20} The bias can be chosen to equalize the two plasma potentials, thereby allowing ions to pass unhindered across the filter. A stronger bias voltage would trap the negative ions formed in the extraction chamber.

The separate extraction chamber with its distinct conditions provides several advantages. The lower electron temperature is favorable for negative ion production by DA (although the accompanying lower electron density is unfavourable and could offset this advantage). The H^- destruction processes are reduced: mutual neutralization because of the lower positive ion density, and electron detachment because of the absence of energetic electrons and because of the cooler, less dense electrons. The sheath potential and the potential difference across the filter can serve to trap ions created in this more favorable region. The lower electron density is also an advantage during extraction, since fewer electrons are extracted along with the negative ions.

A weak magnetic field near the extraction orifice can further improve negative ion source performance. Experiments have shown that a weak magnetic field of the order of 50 Gauss can raise the ratio of negative ion density to plasma density from 10% in the center of the extraction chamber to 90% at the extraction orifice.²⁴ The result is an important

reduction in the current extracted along with the negative ions, which was the principal benefit sought through the modification. However, it was also found that the magnetic field actually increases the absolute negative ion density near the extractor and the negative ion extracted current, by as much as a factor of three.²⁴ Optimizing the extracted negative ion current involved varying both the strength of the small magnetic field and the potential bias applied to the plasma electrode. This unexpected concentration of negative ions in the magnetic field may be a rather general phenomenon of these plasmas, for it has also been observed in the strong multipole fields which shield the walls. This effect confuses the interpretation of the experimental effort to find the optimum magnetic filter position and configuration, in which this small field may be generated at the orifice.

NEGATIVE ION SATURATION AT HIGH POWER

Increasing the primary electron current (or discharge current) and thus increasing the density of vibrationally excited states would appear to be the most direct way to increase the negative ion production. Experimental work, however, has shown that negative ion production saturates as the discharge current is increased at constant gas pressure.²⁵ (See Figure 3.) The increase in pressure allows enhancement of the maximum extracted current, but the effect of pressure also saturates.

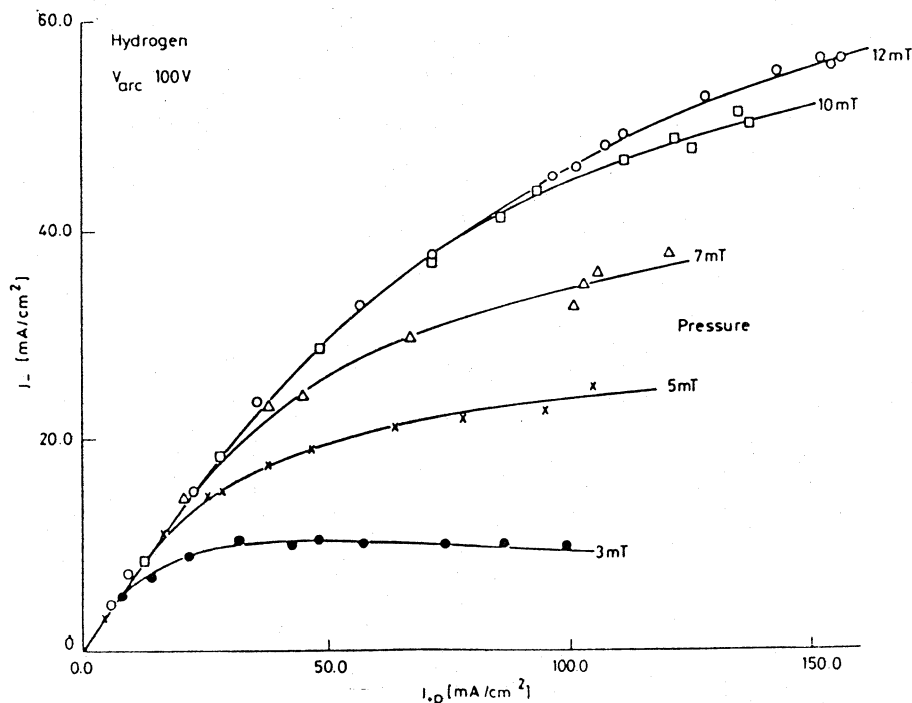


Figure 3. Saturation of extracted H^- current as a function of plasma density and gas pressure. The horizontal scale is a probe current proportional to plasma density. (From Ref. 21)

A French-Italian team has developed a computer code which models negative ion production.^{26,27} This code is appropriate for a homogeneous system, or, for any system smaller than the various mean free paths involved. Therefore, it is appropriate to study the vibrational spectrum in the "source" chamber. The code simultaneously solves the Boltzmann equation for the electron distribution function and the vibrational master equation for the H₂(v") spectrum in a zero-dimensional time-dependent model. Zero-dimensional means that the plasma is assumed homogeneous and isotropic. The code calculates the densities of atoms and molecules, the electron density and the electron energy distribution function, as well as the densities of various ion species (H₊, H₂⁺, H₃⁺, H₄⁺).

The "source" chamber of a large tandem source has recently been simulated.²⁸ This work has been performed as a scaling exercise to elucidate the causes of saturation in negative ion production at high power. The calculated vibrational spectrum is displayed on Figure 4. As power input is increased both the plasma density and the primary electron density increase. Volume reactions generally dominate surface reactions. Due to high dissociation and ionization rates, the atomic hydrogen fraction, n(H)/n(H₂), increases with input power and attains values exceeding 90%. (See Fig. 5). Surface reactions which remain important include the recombination of atomic hydrogen (there is no volume reaction which disposes of atomic hydrogen at these low pressures) and neutralization of positive ions on the walls. At the highest power considered here collisions with electrons dominate other reactions in establishing the molecular vibrational distribution. For vibrational levels up to v"=8, e-V collisions (Eq. 3) with plasma low energy electrons are the most frequent process; although the most probable change in v" is $\Delta v'' = \pm 1$, e-V collisions are very efficient in redistributing the molecules along the vibrational spectrum. Dissociative attachment, reaction (2), is an important depopulating process for v" = 6, 7 and 8. Thus, according to this simulation H formation by DA is important in the source chamber, in support of the first viewpoint mentioned above. The levels v">5 are principally populated by radiative decay from higher singlet electronic states which are created by collisions with high energy electrons (E-V process, Eq. 4). Because of the large atomic density, vibration-translation, V-T, transfer collisions with atoms are also an important loss at high power. According to this simulation²⁸ the dramatic reduction in molecular density is the principal reason why the vibrational population decreases as the current is increased beyond 100 Ampère. Higher discharge current indeed produces a more energetic vibrational distribution, but the drop in total molecular density can defeat this improvement. Maximum negative ion production occurs at some intermediate power.

A second potential reason for saturation is the growing role of thermal electrons in establishing the vibrational distribution. In the case of 100 and 1000 Ampère (Fig. 4) the e-V collisions are the most frequent ones in the range of v" from 0 to 8. The levels v" = 6, 7 and 8 are most important for negative ion production. In this simulation, the vibrational populations characteristically follow a Boltzmann distribution in the range where the e-V process is the most frequent. Under high discharge current, high plasma density conditions, the e-V process promotes molecules up the vibrational ladder as far as v" ~ 6, so it has a generally favorable effect. The e-V process seems therefore to determine a particular vibrational temperature. As can be noted from Fig. 4, in the studied discharge conditions (100 V, 3 mTorr) the vibrational temperature varies in the range 3200 K to 6400 K (or 0.28 eV to 0.55 eV), while the electron temperature is sensibly higher (varies from 1.8 eV to 4.1 eV in the same conditions).

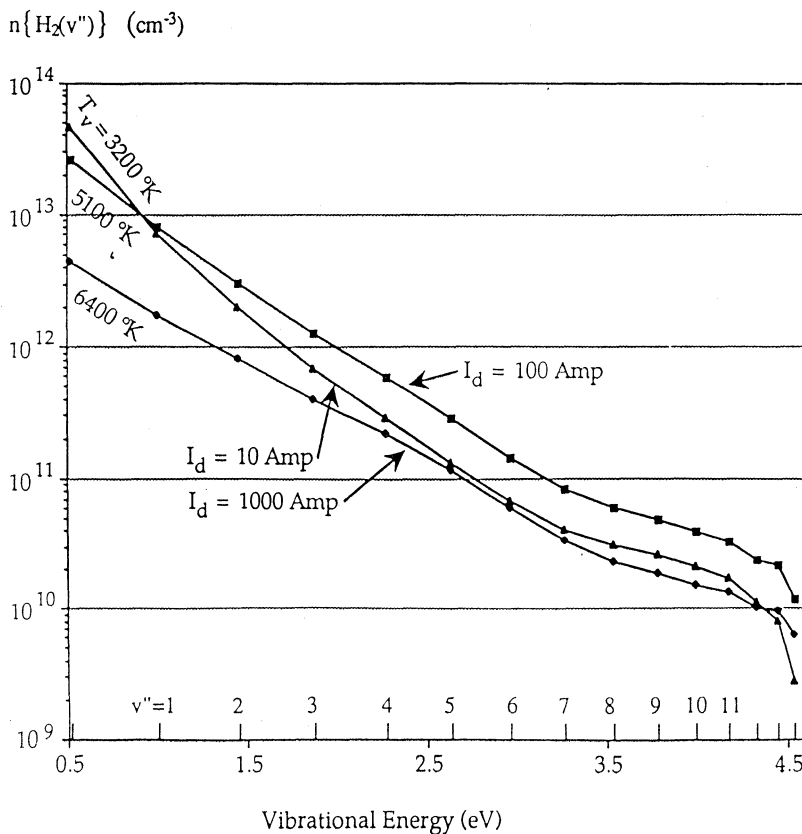


Figure 4. Computed vibrational populations versus vibrational energy for three discharge currents. Discharge voltage: 100 V. Filling pressure: 3 mTorr. (From Ref. 28.)

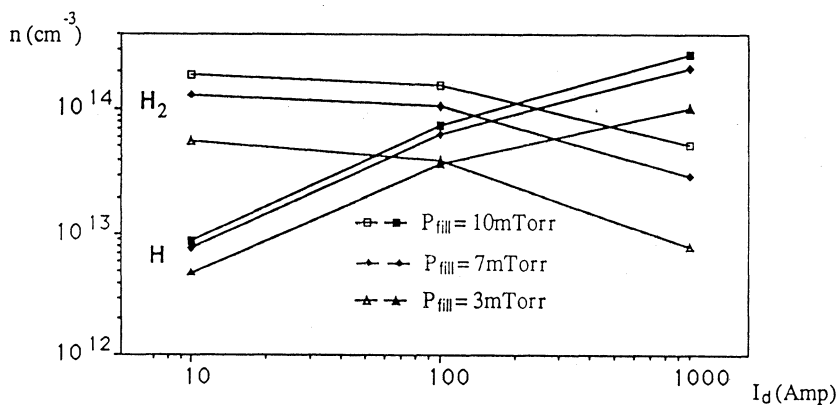


Figure 5. Computed densities of H and H_2 as functions of discharge current and of gas filling pressure. (From Ref. 28.)

Thermal electrons, via the e-V process, Eq. 3, actually have a cooling effect at the upper v'' levels, which are principally pumped by primary electrons through the E-V process (Eq. 4). The vibrational distributions of Fig. 4 have higher local temperature at the upper v'' levels. Even if a way is found to increase E-V pumping (without dissociating too much the gas) the cooling effect may well limit the benefits at vibrational levels of interest.

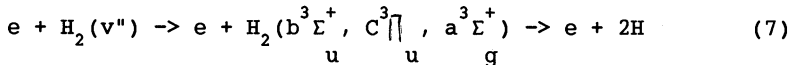
THE ROLE OF ATOMIC HYDROGEN

The atomic hydrogen is a known impediment in the operation of negative ion sources. Through collisions it both directly destroys H/D by associative detachment:

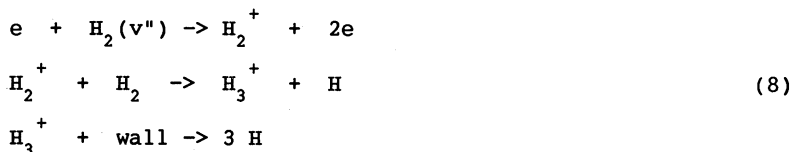


and relaxes the intermediate $H_2(v'')$ distribution (by vibration-translational transfer). Atomic hydrogen is formed through many processes, but it can be eliminated (at the low pressure used in ion sources) only by wall processes, such as recombination on the wall. A large experimental effort has been undertaken^{6-8,29,30} to determine the atomic density and energy distribution.

In the tandem sources, the atomic hydrogen is formed essentially in the "source" chamber, in electron collisions leading to dissociation, ionization and excitation. It is well known that the electron excitation leading to triplet states produces two atoms:



It is perhaps less obvious that the formation of each H_2^+ ion followed by its rapid conversion^{26,27} to H_3^+ produces, after wall neutralization of H_3^+ , a total of four atoms:



Even the E-V excitation process, which is an important source of $H_2(v'')$ (Eq. 4), also leads to dissociation. Hiskes¹¹ has shown that approximately 60% of the original excitations through the B state return to discrete vibrational levels of the ground state. The remaining 40% return to the continuum, i.e. dissociate. The formation of each H^- ion by DA (Eqs. 1 and 2) also produces one additional atom, while the destruction of a negative ion by mutual neutralization with positive ions can produce as many as four atoms.

Figure 5 shows the computed densities of H and H_2 as functions of discharge current and gas filling pressure.

Figure 6 shows, taking the example of a 100 V - 7 mTorr discharge that the atoms are formed by at least three different processes. The relative importance of ionization of $H_2(v'')$ molecules followed by wall recombination increases with the discharge current.

The actual density of atomic hydrogen in the source depends on the recombination probability of atoms on the wall, γ . Several reviews of this subject are available.^{31,32} Wise and Wood³¹ have limited the discussion to the recombination associated with chemisorbed atoms (but not with weakly bound adsorbed species), for which two mechanisms are known. The Eley-Rideal mechanism (E-R) postulates the direct reaction of an atom from the gas phase with a chemisorbed atom. The Langmuir-Hinshelwood mechanism (L-H) involves surface recombination of two chemisorbed atoms. Rosner³² reports the experimental work of G. A. Beitel at a pressure lower than 10^{-6} Torr, when the L-H mechanism is active; γ was found to be close to 1 for tungsten and platinum surfaces, as predicted by theory.³³ However in the pressure range relevant to ion source operation ($10^{-3} - 10^{-1}$ Torr) the observed trends are consistent with the E-R mechanism.

A theoretical model of the E-R mechanism³⁴ predicts a characteristic dependence of γ on the surface temperature, where γ increases as the temperature is raised above room temperature. One might expect that heating of the walls could increase γ in negative ion sources. For the special case of hydrogen, however, the model permits a temperature independent of γ . This is in agreement with the measurements of Wood and Wise³⁵ in which the hydrogen recombination coefficient is independent of temperature for titanium, aluminum, nickel, copper, palladium, and tungsten (listed in order of decreasing γ), but is temperature-dependent for

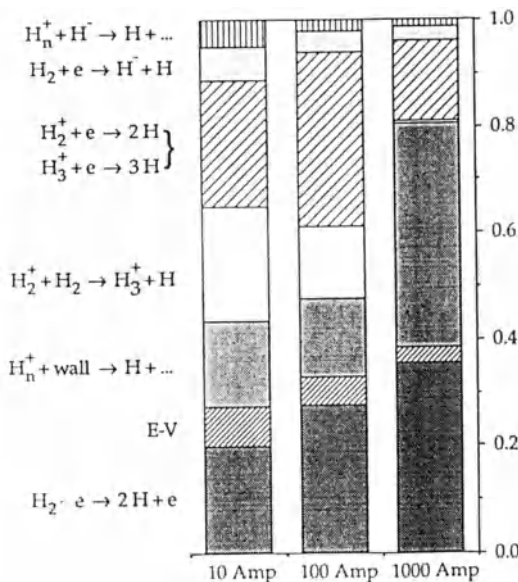


Figure 6. Production rates of atomic hydrogen for three values of the discharge current. The discharge voltage is 100 V, the filling pressure is 7 mTorr. (From Ref. 28.)

gold and platinum. For most metals, then, heating the walls would be an effective way to increase γ in hydrogen sources only if the surface achieved the temperature where adsorbed atoms become mobile enough for the L-H mechanism to become dominant, on the order of 1300 K or greater.³⁵

Wood and Wise^{35,31} showed that their measured values of γ for different metals increase with the Debye characteristic temperature Θ_D , with titanium having the highest γ (~ 0.4) and also the highest Debye temperature (~ 420 K) among the metals studied. The Debye temperature is associated with a cutoff frequency $f_{\max} = \Theta_D(k/h)$ of lattice vibrations in the Debye theory of specific heat capacity, and is related to the lattice force constant and the compressibility. In the non-reactive interaction of a gas with a surface the amount of kinetic energy which can be transferred in a collision with the lattice decreases with increasing lattice force constant.³⁶ Thus an impinging atom is more likely to recombine with one adsorbed on a surface which absorbs less of the energy liberated at recombination. I.e., a surface may exhibit a high recombination coefficient and low energy accommodation. Molecules desorbed from a surface of low energy accommodation may be expected to be in higher vibrational states (as actually found in Ref. 23 and discussed in Ref. 37.)

The γ values for negative ion source walls have been inferred from simulation and comparison of simulation results with experimental data: typical values for γ are in the range from 0.05 to 0.1. This is in agreement with the value $\gamma = 0.06$ reported by Wood and Wise for tungsten.³⁵ The fact that wall properties are determined, after some hours of operation, by an evaporated film of filament material rather by the native wall material has been established through several series of experiments in which different filament and wall materials have been tried.^{23, 38-41} The low value of γ in current sources with conventional tungsten filaments leaves room for improvement, perhaps by development of other filament materials or of low temperature non-evaporative emitters.

The importance of the filament material has also been noted in the recent experiment of Hall et al.²³; similar experiments have been also effected by Eenshuistra et al.⁴² and were extended to higher v'' by Robie et al.⁴³ There the production of vibrationally excited hydrogen molecules (with measurements reported⁴³ up to $v'' = 11$) has been demonstrated even in the absence of a discharge. By a series of experiments it has been established that these vibrationally excited molecules are formed by recombinative desorption from the walls, with atoms derived from molecular dissociation on contact with the heated filament. The measured vibrational spectrum of the desorbed molecules depends on the filament material.²³ The formation of these very highly excited states ($v'' > 5$) is not energetically possible within the E-R mechanism. To explain the existence of these highly vibrationally excited populations, Hall et al.⁴⁴ invoke very weakly bound, physisorbed atomic states, which were observed by Wilsch.⁴⁵

Another indication of the importance of surface conditions in negative ion sources comes from the work of Eenshuistra.⁴⁶ He first operated a negative ion source with tungsten filaments in the conventional way and measured the vibrational spectrum. When he ended the discharge while keeping the filaments heated, ten minutes elapsed before the resumed production of the vibrationally excited molecules via recombinative desorption. Eenshuistra⁴⁶ suggested that this surface production mechanism would not be important in the presence of a discharge because

the necessary weakly bound hydrogen layer would be sputtered away. The delay before this production resumed after the discharge end suggests that surface conditions are changed by the discharge in some fashion which takes ten minutes to be reversed. One possibility is the wall recovery after the ion pumping during the discharge period. During the discharge, the wall is bombarded by atoms and positive ions. It has been observed¹⁹ that during the discharge the walls absorb a large quantity of gas which is then released when the discharge ends, a phenomenon known as ion pumping. Wood and Wise³⁵ have noted that the presence of atomic hydrogen in a gas completely alters the sorption characteristic of metal surfaces, and that a large amount of hydrogen in a material changes its surface properties - enhancing recombination and other catalytic properties. The characteristics of negative ion source walls may thus differ from those of surfaces used for fundamental measurements of γ , and indeed may vary with discharge properties.

If the gas were strongly dissociated, we would expect improved performance for titanium with its higher γ value. However the strong gas absorption by the surface may have dominated the other effects.

In interpreting the results obtained with different wall materials, it is important to know whether the main effect is variation in the de-excitation of vibrationally-excited molecules in wall collisions (low power regime), or different γ (high power regime). The knowledge of the atomic hydrogen density in each experiment is essential. Future studies should cover high plasma density conditions, where it is anticipated that wall de-excitation of vibrationally excited molecules is negligible compared to other loss processes.

ACKNOWLEDGEMENTS

We are grateful to C. Bruno, M. Capitelli, and R. I. Hall for enlightening discussions. We also acknowledge the computational resources granted by the Conseil Scientifique du Centre de Calcul Vectoriel pour la Recherche, France, the support Direction des Recherches, Etudes et Techniques, France, the Oak Ridge National Laboratory, and the European Atomic Energy Community (NET No. 88-174).

REFERENCES

1. M. Bacal, E. Nicolopoulou, and H. J. Doucet, "Proc. of the Intern. Symposium on the Production and Neutralization of Negative Hydrogen Ions and Beams", BNL, Upton, N. Y., Sept. 1977. Report BNL 50727, ed. by K. Prelec, p. 26.
2. M. Bacal and G. W. Hamilton, Phys. Rev. Lett., 42, 1538 (1979).
3. G. J. Schultz, Rev. Modern Phys., 45, 423 (1973).
4. M. Allan and S. F. Wong, Phys. Rev. Lett., 41, 1791 (1978).
5. J. M. Wadehra and J. N. Bardsley, Phys. Rev. Lett., 41, 1795 (1978).
6. M. Péalat, J. P. E. Taran, M. Bacal, and F. Hillion, J. Chem. Phys., (1985).

7. P. J. Eenshuistra, A. W. Kleyn, and J. H. Hopman, Europhys. Lett., 8, 423 (1989).
8. G. C. Stutzin, A. T. Young, A. S. Schlacter, K. N. Leung, and W. B. Kunkel, Chem. Phys. Lett., 155, 475 (1989).
9. J. R. Hiskes, M. Bacal, and G. W. Hamilton, LLL UCID-18031, Lawrence Livermore Laboratory, Livermore, CA (1979).
10. W. B. Kunkel, Private Communication (1980).
11. J. R. Hiskes, J. Appl. Phys., 9, 4592 (1980).
12. J. Marx, A. Lebehot, and R. Campargue, J. Phys. (Paris), 46, 102 (1985).
13. J. R. Hiskes and A. M. Karo, AIP Conf. Proc. 111, 1250 (1984).
14. J. R. Hiskes and A. M. Karo, p. 543 in SPIE Proceedings vol. 1061, "Microwave and Particle Beam Sources and Directed Energy Concepts", H. E. Brandt, ed., Los Angeles, (1989).
15. M. Bacal, Phys. Scripta, 2/2, 467 (1982).
16. J. R. Hiskes, Comments At. Mol. Phys., 19, 59 (1987).
17. M. Bacal, Nucl. Instrum. Methods in Physics Research, B37/38, 28 (1989).
18. M. S. Hug, L. D. Doverspike and R. L. Champion, Phys. Rev. A27, 2831 (1983).
19. M. Bacal, A. M. Bruneteau and M. Nachman, J. Appl. Phys. 55, 15 (1984).
20. K. N. Leung, K. W. Ehlers and M. Bacal, Rev. Sci. Instrum., 54, 56 (1983).
21. A. J. T. Holmes, G. Dammertz and T. S. Green, Rev. Sci. Instrum., 56, 1697 (1985).
22. J. R. Hiskes and A. M. Karo, J. Appl. Phys., 56, 1927 (1984).
23. R. I. Hall, I. Cadez, M. Landau, F. Pichou and C. Schermann, Phys. Rev. Lett., 60, 337 (1988).
24. M. Bacal, J. Bruneteau, and P. Devynck, Rev. Sci. Instrum., 59, 2152 (1988).
25. A. J. T. Holmes, G. Dammertz, and T. S. Green, Rev. Sci. Instrum., 56, 1697 (1985).
26. C. Gorse, M. Capitelli, J. Bretagne, M. Bacal, Chem. Phys., 93, 1 (1985).
27. C. Gorse, M. Capitelli, M. Bacal, J. Bretagne and A. Laganà, Chem. Phys., 117, 177 (1987).
28. M. Bacal, P. Berlemont and D. A. Skinner, in SPIE Proceedings vol. 1061, "Microwave and Particle Beam Sources and Directed Energy Concepts", H. E. Brandt, ed., Los Angeles, (1989).
29. J. H. M. Bonnie, P. J. Eenshuistra and H. J. Hopman, Phys. Rev. A37, 1121 (1988).
30. A. S. Schlacter, A. T. Young, G. C. Stutzin, J. W. Stearns, H. F. Dobele, K. N. Leung, W. B. Kunkel, p. 610 in SPIE Proceedings vol. 1061, "Microwave and Particle Beam Sources and Directed Energy Concepts", H. E. Brandt, ed., Los Angeles, (1989).
31. H. Wise and B. J. Wood, in "Advan. At. Mol. Phys.", 3, 291 (1967), ed. by D. R. Bates and I. Estermann, Academic Press, New York, London.
32. D. E. Rosner, Annual Review of Materials Science, 2, 573 (1972).
33. M. I. Baskes, J. Nucl. Mat., 128/129, 676 (1984).
34. A. Gelb and S. K. Kim, J. Chem. Phys., 55, 4935 (1971).
35. B. J. Wood, H. Wiese, J. Phys. Chem., 65, 1976 (1961).
36. R. W. Zwanzig, J. Chem. Phys., 32, 1173 (1960).
37. B. Halperin and D. E. Rosner, "Heterogeneous Atmospheric Chemistry, Geophysical Monograph Series", 26, 167 (1982).
38. K. N. Leung, K. W. Ehlers and R. V. Pyle, Rev. Sci. Instrum., 47, 227 (1985).

39. O. Fukumasa and S. Saeki, J. Phys. D:Appl. Phys., 20, 237 (1987).
40. T. Inoue, Proc. of the US-Japan Workshop on Negative Ion Beam, Nov. 14-17, 1988, Japan Atomic Energy Research Institute.
41. M. Bacal, T. Inoue, Y. Ohara and Y. Okumura, Report P.M.I. N⁰ 1991, Ecole Polytechnique (1988).
42. P. J. Eenshuistra, J. H. M. Bonnie, J. Los, H. J. Hopman, Phys. Rev. Lett., 60, 341 (1988).
43. D. C. Robie, L. E. Jusinski, W. K. Bischel, in SPIE Proceedings Series vol. 1061, "Microwave and Particle Beam Sources and Directed Energy Concepts", H. E. Brandt, ed., Los Angeles, (1989).
44. R. I. Hall, I. Cadej, M. Landau, F. Pichon, and C. Schermann, "Proc. of International Workshop on Negative Ion Sources", Ecole Polytechnique, Palaiseau (1988).
45. H. Wilsch, private communication.
46. P. J. Eenshuistra, "Vibrational Excitation in a Hydrogen Volume Source", PhD Thesis, University of Amsterdam (1989).

LASER DIAGNOSTICS OF A HYDROGEN DISCHARGE

H.J. Hopman

*FOM Institute for Atomic and Molecular Physics, P.O. Box 41883
NL-1009 DB Amsterdam ,THE NETHERLANDS
and
The NET Team, Max-Planck-Institut für Plasmaphysik
D-8046 Garching, BRD*

INTRODUCTION

When modelling a partially ionized plasma, one is working with a set of rate equations, describing the production and destruction of the particle species occurring in the discharge (Hiskes, 1987; Gorse et al., 1987). Depending on the level of detail of the description, the number of interacting species can increase to a large number. An elementary description of a hydrogen plasma would involve molecules, H₂, metastable molecules, H₂^{*}, atoms, H⁰, one type of ion, H_i⁺, and electrons. When more precision is required, one would have to replace the ion by H⁻, H⁺, H₂⁺ and H₃⁺, and successively add more and more excited states, including both electronic and molecular excitations. The reaction rates occurring in the equations are expressions of the following form:

$$R = \int \int \sigma(|v_1 - v_2|) (|v_1 - v_2|) F^a(v_1) F^b(v_2) d^3v_1 d^3v_2, \quad (1)$$

where, σ , which is a function of the relative velocity $|v_1 - v_2|$, is the cross section describing the interaction between particles of species a and b, and $F^a(v_1)$ and $F^b(v_2)$ are their distribution functions. Equation (1) clarifies that an ideal diagnostic technique measures the complete distribution function of each particle species. Only then, a precise comparison between modelling and experimental results is possible. In the majority of discharges, however, the particles make a sufficient number of collisions for the distribution function to approach a Maxwellian. Then, a measurement of density and temperature would suffice. For two species of the same temperature T, Eq. (1) attains the much simpler form,

$$R = n_a n_b \sqrt{(8kT/\pi\mu)} \int \sigma(E) \exp(-E) E dE, \quad (2)$$

where, n gives the densities of species a and b, respectively, $E = (\mu v^2/2kT)$ is the relative energy of motion with v the relative velocity, and μ is the reduced mass, $\mu = (m_a + m_b)/m_a m_b$.

Diagnostics are required for two reasons. The first one of course is the fundamental need to check any theory against the experiment, the second is the fact that many cross sections have not been measured and the model uses a good guess for the value of the reaction rates. Such guesses can play the role of fitting parameters, and their real value is approximated by adjusting the outcome of the model to that of the experiment.

DIAGNOSTIC TECHNIQUES

Passive spectroscopy is one of the oldest techniques to obtain information as temperature and density about particles. The technique is limited to those excited particles that can radiate their excess energy. However, for non-radiating particles, such as ground-state molecules and atoms or metastable particles, which together form the great majority of all particles in a weakly ionized plasma, more sophisticated diagnostics are required. This also holds for vibrationally excited symmetric molecules, like H₂ or N₂. When in the electronic ground state, these molecules do not have a dipole moment and can not radiate their vibrational energy.

An elementary task of a diagnostic technique is the ability to distinguish between the species involved. This is accomplished by inducing a transition between two quantum states in the same or in a derived particle and detecting the corresponding photon. In the more versatile approach a higher lying state is populated by means of particle or photon beams injected into the discharge, and one detects the photons emitted on the decay of this state. Figure 1 illustrates a typical set up when a photon beam is used. The process is called *Laser-Induced Fluorescence (LIF)*.

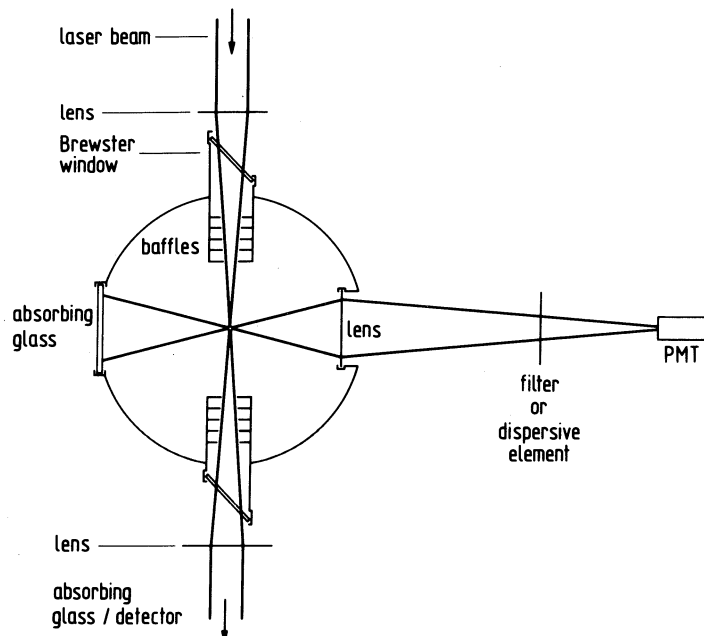


Figure 1. Typical set up used to perform laser-induced fluorescence.

The photon beam excites particles in a state of energy E1 to a state of energy E2, see Fig. 2. The photon frequency ν is tuned to the energy difference between the states, such that $h\nu = E_2 - E_1$. One observes emission corresponding to a transition to the same or to a third level, $h\nu' = E_2 - E_3$. The latter has the advantage of a higher signal to noise ratio, especially when the lower lying state 1 is the ground state, and of the absence of interference from the injected photon beam.

Providing one selects a transition for which the spontaneous plasma radiation is weak, the number of photons observed is essentially proportional to the occupation of level E1. Thus the signal intensity is related to the density of the particles of interest. The width of the emitted line is largely equal to its Doppler width, which is related to the kinetic energy of the emitting particles. If a narrow laser line is used, this can be scanned over the Doppler profile. This way, one can measure the distribution over the velocities parallel to the exciting laser beam. Conversely, if the laser line is broader than the width of the transition, one can measure the profile of the emitted line and obtain the velocity distribution in the direction of the viewing beam. For a Maxwellian distribution, the half width of the line profile dv is related to the temperature according to (Demtröder, 1982),

$$dv/v = \sqrt{(8kT \ln 2 / mc^2)}. \quad (3)$$

In principle, LIF is a technique with which the above formulated ideal can be achieved. An advantage of using strong pulsed laser beams for LIF is the ability to saturate the transition, i.e. to take all the particles from the lower to the higher lying level. Knowledge of the photon excitation cross section is not required in this case. A condition is that the laser pulse duration is just one half Rabi period (Demtröder, 1982) of the levels involved, a so called π pulse. An interesting variation on the LIF technique was recently reported by Den Hartog et al. (1989). They detect the fluorescence from a level E4 that is collisionally coupled to the E2 level, see Fig. 2. When E4 and E2 are closely separated in energy, one obtains information on the density of the low-energy electron fraction in the discharge.

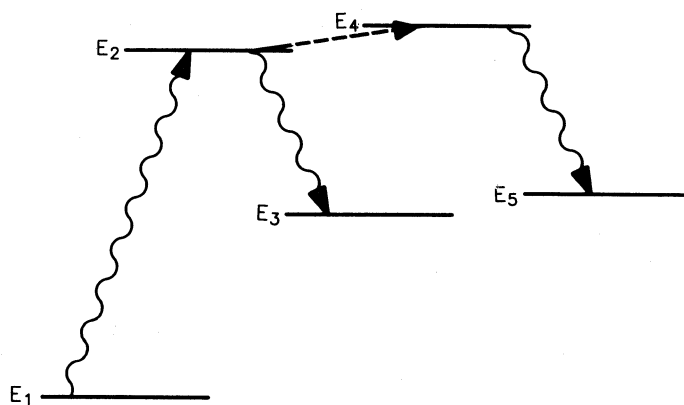
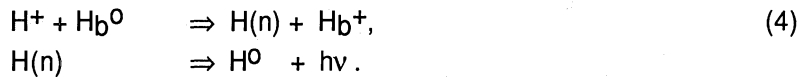


Figure 2. Energy level diagram illustrating the principle of laser-induced fluorescence.

A hydrogen discharge has three types of particles that are singular in the sense that two bound states are not available. They are the H⁻ ion which is lacking a bound excited state, and the H⁺ ion and the electron, which have no bound states et all. In the case of H⁻, E2 lies in the continuum and the extra electron is ejected. Now one could detect the electron, which is usually done by means of probes (Bacal et al., 1979). *Laser detachment* has the property that the transition is no longer resonant, because the ejected electron takes up the difference between photon and detachment energy (0.75 eV for H⁻). This brings with it the problem that electrons may come from H⁻ or from high lying excited states in H₂ that might be ionized non-resonantly. If the density of the latter is sufficiently low compared to the H⁻ density, the photo-electrons can be attributed to H⁻. Otherwise one would have to rely on electron spectroscopy (Kruit and Read, 1983; Bonnie et al., 1986), which can only be done exterior to the plasma chamber. In discharges used in ion sources, no interference from high lying states could be detected (Eenshuistra, 1989).

To detect H⁺ ions one may make use of the charge transfer process, which transforms the ion into an excited atom radiating characteristic lines:



To cause a locally enhanced charge transfer rate, a beam of fast neutral atoms, indicated by the subscript b in Eq. (4), is injected into the discharge. The process is referred to as *charge exchange recombination spectroscopy* and is of great importance in diagnosing fusion plasmas (Boileau et al., 1989).

In the case of electrons, one applies elastic scattering of the photons, the so-called *Thomson scattering* (Sheffield, 1975). Of course, this involves a free-free transition, but because there is no third particle, as in the case of electron detachment of H⁻, the energy of the scattered photon is precisely determined. In accordance with the Doppler effect, the frequency of the scattered photons is shifted with respect to the mean frequency in proportion to the electron velocity. Thus the spectrum and the intensity of the scattered photons give the energy distribution and the density of the electrons, respectively. In principle the technique works for ions too, but in practice the ion feature is hidden in that of the electrons. The Thomson scattering technique is complicated and expensive. If one already has probes available to assist the detection of negative ions, it is natural to use the probes (Hopkins and Graham, 1986) for electrons and positive ions as well.

The advantage of using crossed beams (exciting and viewing beams) of course is the spatial resolution it offers. The signal comes out of the area where both beams overlap. Further, optical techniques are non-intrusive and essentially non-perturbative. However, excited particles generally have larger cross sections. Therefore, the exciting beam may change the plasma collisionality and thus modify the discharge parameters. This effect is used in a positive sene as a diagnostic tool with the *opto galvanic effect* (Demtröder, 1982; Jongerius et al., 1984). It is not a necessity to have the viewing beam different from the exciting beam. Especially for low lying states that are densely populated one could measure the *attenuation* of the exciting beam. One obtains the integral over the density along the photon beam. So, there is the disadvantage that one looses the spatial resolution, but this could be recovered by applying tomographic techniques.

Finally, we mention the *optical tagging* technique (Stern et al., 1983). This is done by choosing for the level E2 a long lived one. It means that one locally creates an over population of metastable (tagged) particles. These then diffuse and/or stream away and create an excess of metastables at other places. With a second laser, crossing the discharge at some distance from the first laser, one excites the tagged particles to a radiating level. By detecting the fluorescence, one is able to determine their density. The intensity pattern of the induced radiation as a function of the distance to the first laser beam contains such information as the diffusion velocities or drift motions of heavy particles in a discharge. The technique has been used to study local ion heating as well as the emergence of chaos (Skiff et al., 1988) in plasmas. For ease of experimentation, the technique has not yet been applied to hydrogen plasmas.

We have indicated that providing suitable photon sources are available it is possible to measure the distribution function of the neutrals, atoms and molecules, in a hydrogen discharge. For the charged particles, Langmuir probes are more convenient.

THE NEED FOR MULTI-PHOTON PROCESSES

The application of LIF to the detection of hydrogenic neutrals is a complicated technique, because of the required vacuum ultra violet light. The necessary VUV photons are obtained via non-linear interaction between light and matter. For instance, it is possible to triple a dye laser beam in a gas cell (Hintz, 1982; Northrup et al., 1984). For LIF on atoms one would need a 365 nm laser beam and on molecules ≤ 330 nm is required. Instead of tripling the photon energy prior to entering the plasma, one can envisage the tripling taking place at the particles under investigation. This is multi-photon absorption, leading to excitation or ionization of the particle. The advantage of ionization is the high efficiency. Charged particles can be collected with a 100% efficiency, whereas of all radiated fluorescence photons only those in a small solid angle (typically a fraction 10^{-3}) are collected. A disadvantage is the loss of spatial resolution, when applying multi-photon ionization to a discharge: one has to stay at the plasma edge, to be able to discriminate the photo ions from the plasma ions. We do not discuss another non-linear approach, the very successful **CARS** (*coherent anti-Stokes Raman scattering*) technique, because it is generally executed using two laser beams (Demtröder, 1982; Pealat et al., 1981, 1985) and it can not be applied to atomic hydrogen. In the following we concentrate on the multi-photon technique.

THE PRINCIPLE OF RESONANT MULTI-PHOTON IONIZATION

In Fig. 3 is presented a potential energy diagram of the hydrogen molecule. Plotted is the energy of some electronic levels as function of the internuclear separation. Also indicated are vibrational levels. These are the horizontal lines in some of the electronic potential energy wells. A minimum of 11 eV (≈ 110 nm) is needed to rise H₂ from the ground state to an excited state. This is conveniently done with two (Marinero et al., 1982), three (Pratt et al., 1983) or more photons. Multi-photon absorption proceeds via so-called virtual states, the dotted lines in Fig. 3. Such states are not eigenfunctions of the molecular Hamiltonian. They are short lived states with a lifetime of $\approx 10^{-15}$ s, given by the Heisenberg uncertainty

relation. Therefore, it is essential to have a sufficiently high photon density that a subsequent photon is absorbed when the molecule is in this virtual state. Around 300 nm this means a laser with a power density of $\sim 10^{14} \text{ Wm}^{-2}$. Once the molecule is excited, it is in a long lived state, life time $\approx 10^{-8} \text{ s}$, and because of the high photon density it has a probability of order 1 to pick up a next photon and become ionized. If a multiple of the photon energy does not precisely match (that is resonates with) the energy of the considered transition, the molecule is again in a short lived virtual state and the probability of picking up the next photon is very much smaller. Thus there is a large difference in ion yield for resonant and non-

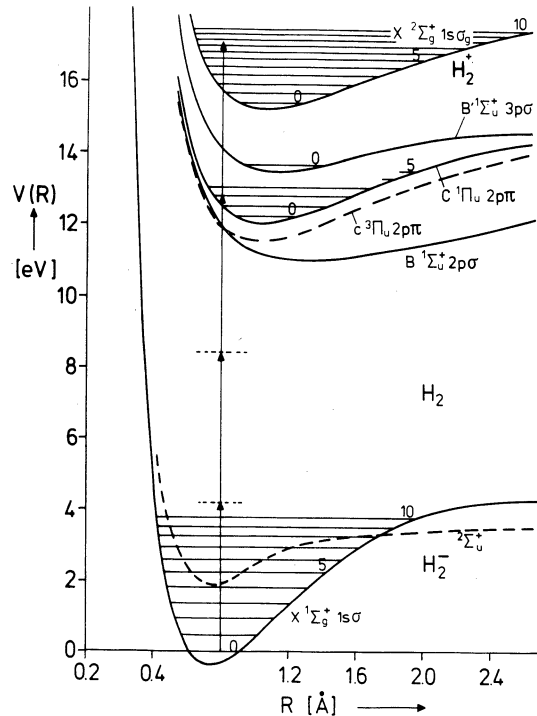


Figure 3. Potential energy diagram of the hydrogen molecule. Indicated is a three-photon transition from the vibrational and electronic ground state to the $v' = 2$ vibrational level of an electronically excited state, proceeding via two short lived virtual states (dotted lines). The absorption of one additional photon leads to ionization of the molecule.

resonant multi-photon ionization with the same number of photons. In addition, with *Resonant Multi-photon Ionization* (**RMI**, or **REMPI** for resonantly enhanced multi-photon ionization) one is able to interrogate a particular state of the particle considered. By scanning the laser frequency and detecting the resulting RMI ions one obtains signals that are proportional to the population of the levels. Though explained for molecular hydrogen, the technique works for atomic hydrogen as well (Bonnie et al., 1988). A discussion of the application of selection rules in multi-photon excitation can be found in the works of Pratt et al., (1983/4).

A MULTI-PHOTON IONIZATION DIAGNOSTIC SYSTEM

Apparatus

A schematic set-up of the RMI experiment (Bonnie et al., 1987) is shown in Fig. 4. A laser beam is focused (1, in Fig. 4) approximately 5 mm in front of an aperture in a discharge chamber (8) from which a gas-plasma mixture effuses. A magnetic field, of ≈ 1 T at the laser focus, prevents charged plasma particles from reaching the detection volume. An electric field $E \approx 1$ MV/m accelerates the laser-produced ions into a lens system (5), which transports them to the detector, a Johnston particle detector (7). The geometry is such that the three axes, formed by the jet, the laser, and the fields, are orthogonal; E is parallel to B .

The electric field is generated with a 4 kV potential difference between the soft iron pole pieces (4, in Fig. 4), that are part of the closed magnetic circuit (2). The laser beam is focused in the middle of the 4 mm wide gap. Thus, the RMI ions are born at a 2 kV potential. This allows the separation, by means of the parallel plate energy analyzer (6), of the RMI ions with 2 keV energy and the ions formed by photon stimulated desorption on nearby surfaces, which have 0 or 4 keV energy. Because the discharge is a copious source of UV radiation this precaution is necessary.

A periodic focusing lens system (5, in Fig. 4) located in a bore of the magnetic circuit transports the particles from the laser focus region with a high field (1 T) to a region of low magnetic field (10^{-3} T). Such low fields are required because of the use of an energy analyzer and a detector. The transport system is a unique feature of the diagnostic system, that allows essentially 100% detection efficiency. It consists of 8 cylindrical lenses, of 1 cm diam., alternatingly carrying potentials of 0 and -5 kV. Trajectories have been computed for ions having an energy of 10 eV, at

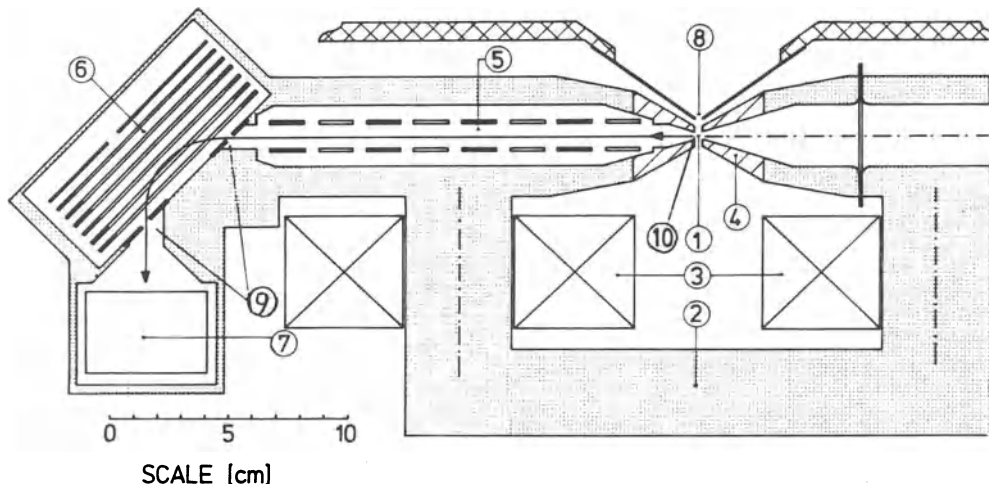


Figure 4. Scale diagram of the RMI diagnostic system. The labeled parts are: 1) position of the laser focus; 2) magnetic circuit; 3) water cooled energizing coils; 4) insulated part of the magnetic circuit that is biased to a potential of 4 kV; 5) periodic focusing transport system; 6) parallel plate energy analyzer; 7) particle detector (multiplier); 8) aperture in the front plate of the discharge chamber. The electric field in the gap between the pole pieces accelerates RMI ions into the transport system (5). A detection efficiency of 100% can be reached. The magnetic field in the gap prevents plasma particles from reaching the laser focus (1).

the moment they are born in the laser focus, but having a variable angle between their velocity and the axis. The 10 eV is thought of being a realistic upper bound on the kinetic energy of particles in a weakly ionized plasma. It was found that the system works well for these energies (Bonnie et al., 1987). In fact the ions stay sufficiently far away from the boundaries that calculations based on the paraxial ray approximation adequately predict the transport properties (Granneman and Van Der Wiel, 1983). Lens potentials are chosen such that the laser focus is imaged on the entrance slit of the analyzer. The 30 cm length of the transport system permits time of flight separation of ions of different mass, like H⁺ and H₂⁺ (Bonnie et al., 1986), created during the short laser pulse. The rather short length of the bore, being nearly magnetic field free, makes the apparatus unfitted as an electron time of flight mass spectrometer. We have observed that all measures taken to prevent the pollution of RMI ions with ions from other sources are necessary indeed. At the pressures we are using, mean free paths are of the order of the discharge dimensions, which are much larger than the separation of focus and discharge. Therefore, our data are characteristic for the discharge.

The discharge chamber is a magnetic multipole bucket source with dimensions of 14×14×19 cm³. It can be operated up to 30 A, 200 V dc at pressures between 0.1 and 5 Pa. Figure 4 only shows the electrically floating front plate of the chamber, which is equipped with a pyramid shaped roof to bring the plasma to the point of analysis. Tunable UV radiation is generated by frequency doubling the output of an excimer pumped dye laser (a Lambda Physik EMG 111 MSC and FL 2002). Around 300 nm the output pulse is typically 2 mJ in 20 ns. The laser beam is focused to a spot of ≈ 20 mm diameter by a lens with a focal length of 8 cm.

Detection limit

The set-up of Fig. 4 has two intrinsic problems. At the laser focus, the density of a species is less than in the discharge chamber due to gas expansion. Further, the discharge produces metastable molecules that are ionized by a single photon. The metastable particle signal may easily eclipse the wanted signals. Most electronically excited particles decay during their passage from the plasma to the laser focus (distance ≈ 5 mm). The density ratio related to the gas expansion was determined by finding the back ground pressure in the experiment (no gas admitted to the source) for which the same signal results as when gas is admitted to the source only. The ratio is ≈ 30 for discharge off conditions, when the perturbation by the metastables is absent. In addition there is the problem that the gas pressure in the source is not known when the discharge is on.

Because of the much smaller ionization threshold, metastables are ionized in a much larger volume than the wanted particles. The best signal to noise ratio is then obtained by adjusting the detector acceptance volume to the laser focus volume. To approach this condition, we use slits in the energy analyzer of 4 × 1 mm² (9 in Fig. 4), and an opening of 0.5 mm diam. in the pole piece, see Fig. 4b. The detector acceptance volume has been determined by scanning the laser focus through this region and measuring the signal due to RMI of ground state hydrogen. The data are presented in Fig. 5. It is seen that the acceptance volume has a length parallel to the electric field of 0.1 mm, and a width of 0.4 mm in both other directions. For this system a detection limit in the laser focus of 8×10^7 state selected particles per cm⁻³ was obtained. Taking into account the expansion, this corresponds to 2×10^9 cm⁻³ state selected particles in the source. This number is accurate within about a factor of two.

The use of a multi-mode laser

The laser used in the experiments of Bonnie and Eenshuistra et al., is a normal commercial laser. It means that no mode selection takes place. As a results, mode interference causes very large variations in the light intensity at the focus within each laser pulse. Owing to the irreproducibility of these statistical fluctuations some kind of averaging is required. Therefore, each measurement is repeated 30 times or

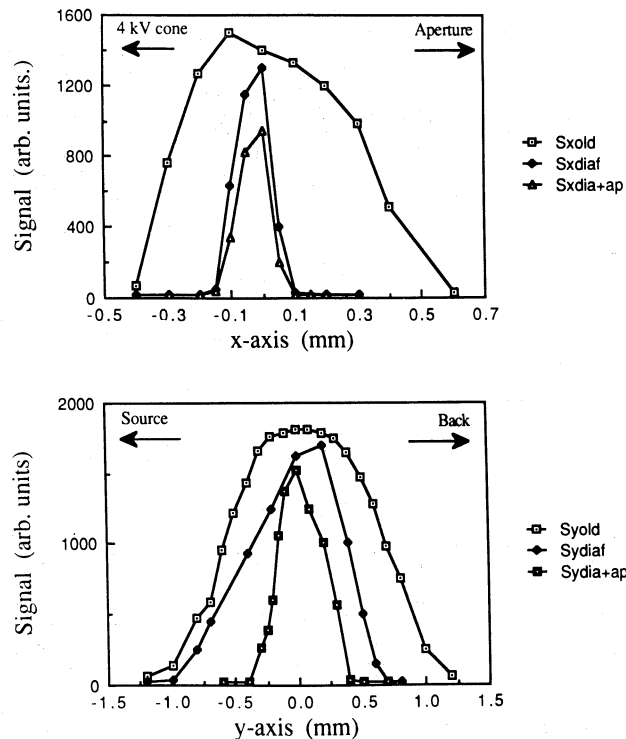


Figure 5. Variation of the RMI signal with the position of the laser focus in the gap (1) in Fig. 4; x-axis parallel to B field; y-axis parallel to gas jet; S_{xold}: aperture in the cone (10 in Fig. 4) is 2.5 mm and no diaphragms in the energy analyser; S_{diaf}: same cone aperture, diaphragms of $1 \times 4 \text{ mm}^2$ in energy analyser; S_{dia+ap}: diaphragms of $1 \times 4 \text{ mm}^2$ and apertures of 0.5 mm in cone. From these data follows a minimum detector acceptance volume of $\approx 10^{-2} \text{ mm}^3$. Detection limit $\approx 8 \times 10^7$ particles per cm^3

more at fixed conditions and laser frequency. Despite of such measures the measured order of linearity of the three-photon excitation process is 4.4 (Van Scheelt, private communication) and not 3 as one would expect. When three photons need to be simultaneously absorbed, the signal should increase with the third power of the laser intensity. Working with single mode lasers, the correct order is obtained (Lompré et al., 1977).

A possible approach to circumvent the construction of a single mode laser, but reduce the disadvantages of mode competition, is the idea to increase the number of modes and that way to reduce the statistical variations in light intensity. There are various suggestions how to achieve this. For instance the use of random phase plates (Burckhardt, 1970), the reflection of the laser beam from an echelon (Lehmberg et al., 1987), or by applying spectral dispersion (Short and Skupsky, 1989). These techniques of *induced incoherence* have proved successful in laser-pellet compression.

RESULTS

With our RMI technique we have investigated the internal energy distribution of molecules effusing from a hydrogen discharge. For the vibrational quantum numbers $v'' = 0, 1$, and 2 of the hydrogen ground state $X^1\Sigma_g$ we were able to measure rotational branches associated with the transition to the $C^1\Pi_u$ and $B' ^1\Sigma_u$ excited state, see Fig. 6. The ions are created in a three-photon excitation, one-photon ionization scheme: (3+1) RMI. The area of the rotational lines in the

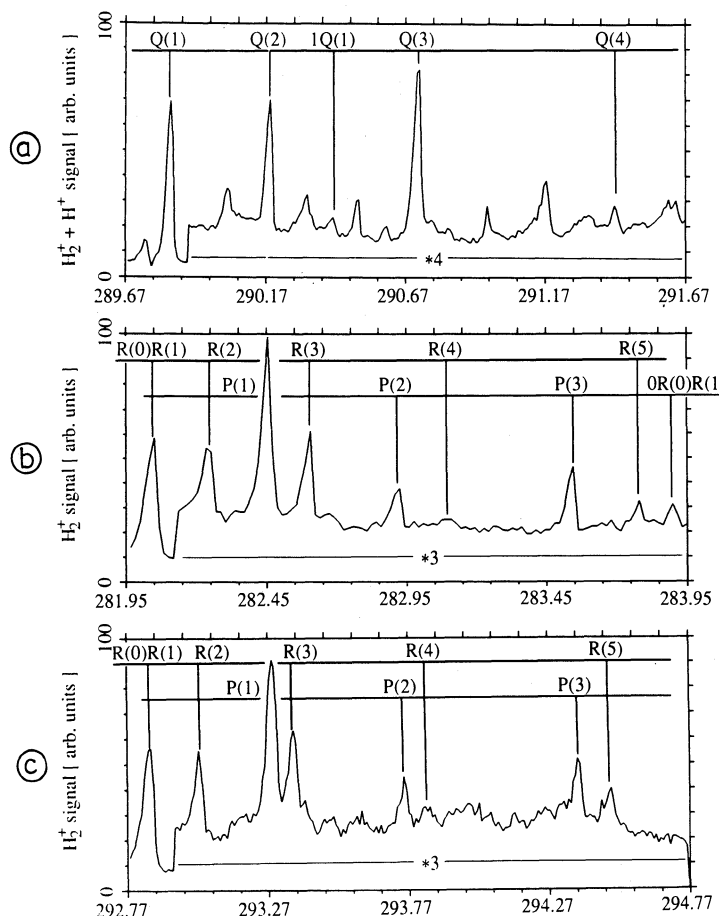


Figure 6. An example of measured RMI spectra of hydrogen molecules, with vibrational quantum number $v'' = 0, 1$ and 2 in (a), (b) and (c), respectively. The Q branch in (a) originates from the $C^1\Pi_u(v'=2) \leftarrow X^1\Sigma_g(v''=0)$ transition. The branches in (b) and (c) result from the $B' ^1\Sigma_u(v'=0) \leftarrow X^1\Sigma_g(v''=1, 2)$ transition. Discharge parameters are: current 10 A, pressure 1.2 Pa and voltage 100 V. The high background is attributed to one-photon ionization of metastable molecules.

spectrum is proportional to the population of the levels. By plotting this area, corrected for the degeneracy of the level and nuclear spin states, against the energy of the rotational level, a so called Boltzmann plot, the rotational temperature can be determined from the slope of the resulting line. For the particular case of Fig. 6, this results in $T_r = 390, 400$ and 410 K for $v'' = 0, 1$ and 2 , respectively (Bonnie et al., 1988), see Fig. 7. The temperatures for $X^1\Sigma_g$ as obtained by Pealat et al. (1985), but using CARS, and Stutzin et al. (1989), but using single photon absorption, are in the same range as ours. An other common observation is the super thermal occupation of higher rotational levels $J > 4$.

More recently, spectra have been obtained for the ground-state vibrational levels with quantum numbers $v'' = 1$ to 5 . Via a fairly complicated procedure, also the densities of these states could be related to each other, so that the low energy part of the vibrational distribution was obtained (Eenshuistra et al., 1989). The result is shown in Fig. 8. Again we observe a tendency to over populate the higher quantum state as is the case with the rotational distribution. Now our data are at variance with those of others. Stutzin et al. (1989) measured the absorption of a VUV beam and inferred from that the density of vibrationally excited molecules up to $v'' = 5$. They do not observe deviations from a Boltzmann distribution.

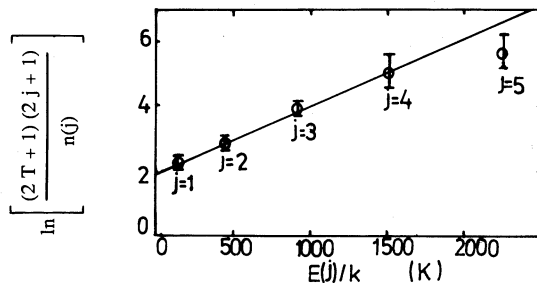


Figure 7. Boltzmann plot of the normalized height of the rotational line intensity versus energy of rotational levels in units of Kelvin. Presented is the R branch of the transition used to obtain Fig. 6 (c). Discharge parameters are, 20 A arc current, 100 V discharge voltage and 1 Pa gas pressure.

DISCUSSION

RMI is a new technique that still has many draw backs. A main complication is the lack of suitable knowledge of multi-photon cross sections. Research, stimulated by the recent discovery of simple sources of vibrationally excited molecules (Eenshuistra et al. 1988, Hall et al., 1988), is just embarking on this problem. An example is the measurement and comparison with theory of the absolute two-photon excitation cross section by Buck et al. (1989). Studied is the $E, F^1\Sigma_g$ ($v' = 6$) $\leftarrow X^1\Sigma_g$ ($v'' = 0$), $Q(1)$ transition in hydrogen with an incoming laser beam at 193 nm.

In multi-photon ionization, it is assumed that the multi-photon excitation step is rate limiting, because the succeeding single-photon ionization step is much faster. This is no longer true for (1+1) RMI, where the two steps are competing with each other. Using this technique, Rottke et al. (1983) found rotational temperatures that were not consistent with experimental conditions. Later experiments by Kung et al. (1988) clarified this point, by using a second more intense UV laser beam (the frequency doubled dye-laser beam with which the experiment is performed) for the ionization step. Therefore, it is an important result that (2+1) or (3+1) RMI yield monotonic rotational distributions and rotational temperatures in agreement with other diagnostics, which shows that we can have confidence in the technique.

Because of the lack of data on multi-photon excitation cross sections, it is reassuring to note that vibrational distributions are currently being investigated by absorption of VUV laser light. However, the RMI and the VUV absorption measurements should be performed under as similar conditions as possible to allow a comparison of the results.

Recently, Robie et al. (1989) started experiments using (2+1) RMI via the E,F state. This way they were able to detect vibrationally excited states as high as the $X^1\Sigma_g$ ($v'' = 11$) state, an achievement similar to that by Hall et al. (1988) applying dissociative attachment. However, these measurements were not performed on a plasma so that interference from other excited states is absent and a much better signal to noise ratio is possible.

Since the first attempts were made to determine the vibrational distribution in a hydrogen discharge by CARS nearly ten years ago, a lot of progress has been made. Available are now scaling laws for vibrationally excited molecules up to $v'' = 5$, as function of discharge parameters (like current, pressure and voltage) relevant for H^- production. The range of observed levels increased and more different techniques were added to the investigation. However, the final goal of determining the complete vibrational distribution of hydrogen molecules under discharge conditions has not yet been reached.

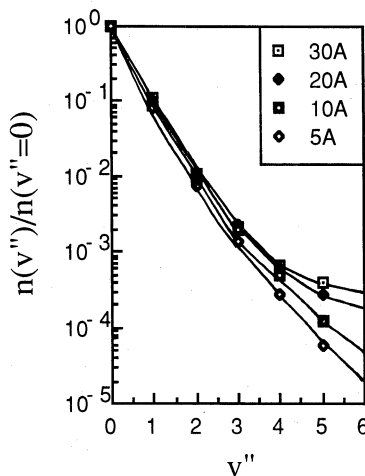


Figure 8. Measured vibrational distribution. Discharge parameters are, 5, 10, 20 and 30 A arc current, 100 V discharge voltage and 1 Pa gas pressure.

ACKNOWLEDGEMENTS: This work is part of the research program of the association agreement EURATOM-FOM, with financial support from NWO and EURATOM.

REFERENCES

- M. Bacal, G.W. Hamilton, A.M. Bruneteau, H.J. Doucet and J. Taillet, 1979, Measurement of H⁻ density in plasma by photodetachment, Rev. Sci. Instr., 50 : 719.
- A. Boileau, M. von Hellermann, W. Mandl, H.P. Summers, H. Weisen and A. Zinoviev, 1989, Observation of motional Stark features in the Balmer spectrum of deuterium in the JET plasma, J. Phys. B 22 : L145.
- J.H.M. Bonnie, P.J. Eenshuistra and H.J. Hopman, 1988, Scaling laws for atomic and molecular hydrogen in a multicusp ion source, Phys. Rev. A 37 : 1121.
- J.H.M. Bonnie, E.H.A. Granneman and H.J. Hopman, 1987, Resonance-enhanced multiphoton ionization for diagnosis of a weakly ionized plasma, Rev. Sci. Instr. 58 : 1353.
- J.H.M. Bonnie, J.W.J. Verschuur, H.J. Hopman and H.B. Van Linden Van Den Heuvel, 1986, Photoelectron spectroscopy on resonantly enhanced multiphoton dissociative ionization of hydrogen molecules, Chem. Phys. Letters 130 : 43.
- J.D. Buck, D.C. Robie, A.P. Hickman, D.J. Bamford and W.K. Bischel, 1989, Two-photon excitation and excited state absorption cross sections for H₂ E,F¹Σ_g (v = 6): measurement and calculation, to be published in Phys. Rev. A.
- C.B. Burckhardt, 1970, Use of a random phase mask for the recording of Fourier transform holograms of data masks, Appl. Opt. 9 : 695.
- W. Demtröder, 1982, "Laser Spectroscopy", Springer Verlag, Berlin.
- E.A. Den Hartog, T.R. O'Brian and J.E. Lawler, 1989, Electron temperature and density diagnostics in a helium glow discharge, Phys. Rev. Letters 62 : 1500.
- P.J. Eenshuistra, J.H.M. Bonnie, J. Los and H.J. Hopman, 1988, Observation of exceptionally high vibrational excitation of hydrogen molecules formed by wall recombination, Phys. Rev. Letters 60 : 341.
- P.J. Eenshuistra, A.W. Kleyn and H.J. Hopman, 1989, Plateau formation in the measured vibrational distribution of hydrogen in a volume source, Europhys. Letters 8 : 423.
- P.J. Eenshuistra, 1989, "Vibrational Excitation in a Hydrogen Volume Source", Thesis, University of Amsterdam.
- C. Gorse, M. Capitelli, M. Bacal, J. Bretagne and A. Lagana, 1987, Progress in the non-equilibrium vibrational kinetics of hydrogen in magnetic multicusp H⁻ ion sources, Chem. Phys. 117 : 177.
- E.H.A. Granneman and M.J. Van Der Wiel, Transport, dispersion and detection of electrons, ions and neutrals, in: "Handbook on Synchrotron Radiation", Vol. I, E.E. Koch, ed., North Holland Publishing Co, Amsterdam (1983).
- R.I. Hall, I. Ćadež, M. Landau, F. Pichou and C. Scherman, 1988, Vibrational excitation of hydrogen via recombinative desorption of atomic hydrogen gas on a metal surface, Phys. Rev. Letters 60 : 337.
- E. Hintz, 1982, Plasma boundary diagnostics by laser induced fluorescence, Physica Scripta T2: 454.

- J.R. Hiskes, 1987, Atomic processes in hydrogen negative ion discharge, *Comments At. Mol. Phys.* 19 : 59.
- M.B. Hopkins and W.G. Graham, 1986, Langmuir probe techniques for plasma parameter measurement in a medium density discharge, *Rev. Sci. Instr.* 57: 2210.
- M.J. Jongerius, A.J. Ras and Q.H. Vrehen, 1984, Optogalvanic detection of acoustic resonances in a high-pressure sodium discharge, *J. Appl. Phys.* 55 : 2685.
- P. Kruit and F.H. Read, 1983, Magnetic field paralleliser for 2π electron-spectrometer and electron-image magnifier, *J. Phys. E* 16 : 313.
- A.H. Kung, T. Trickl, N.A. Gershenfeld and Y.T. Lee, 1988, State-selective detection of H_2 by 1+1 REMPI via the $\text{C}^1\Pi_u$ ($v'=0, J'$) states, *Chem. Phys. Letters* 144 : 427.
- R.H. Lehmberg, A.J. Schmitt and S.E. Bodner, 1987, Theory of induced spatial incoherence, *J. Appl. Phys.* 62 : 2680.
- A.L. Lompré, G. Manfray, C. Manus, J. Thébault, 1977, Multiphoton ionization of rare gases by a tunable-wavelength 30-psec laser pulse at 1.06 μm , *Phys. Rev. A* 15 : 1604.
- E.E. Marinero, C.T. Rettner and R.N. Zare, 1982, Quantum-state-specific detection of molecular hydrogen by three-photon ionization, *Phys. Rev. Letters* 48 : 1323.
- F.J. Northrup, J.C. Polanyi, S.C. Wallace and J.M. Williamson, 1984, VUV laser-induced fluorescence of molecular hydrogen, *Chem. Phys. Letters* 105 : 34.
- M. Pealat, J.P.E. Taran, M. Bacal and F. Hillion, 1985, Rovibrational molecular populations, atoms and negative ions in H_2 and D_2 magnetic multicusp discharges, *J. Chem. Phys.* 82 : 4943; M. Pealat, J.P.E. Taran, J. Taillet, M. Bacal and A.M. Bruneteau, 1981, Measurement of vibrational populations in low-pressure hydrogen plasma by coherent anti-Stokes Raman scattering, *J. Appl. Phys.* 52 : 2687.
- S.T. Pratt, P.M. Dehmer and J.L. Dehmer, 1983, Resonant multiphoton ionization of H_2 via the $\text{B}^1\Sigma_u$, $v=7, J=2$ and 4 levels with photoelectron energy analysis, *J. Chem. Phys.* 78 : 4315; 1984, Photoionization of excited molecular states, $\text{H}_2 \text{C}^1\Pi_u^*$, *Chem. Phys. Letters* 105 : 28.
- D.S. Robie, L.E. Jusinski, W.K. Bischel and W. Huo, 1989, Generation of highly vibrationally excited H_2 and detection by 2+1 resonantly enhanced multiphoton ionization, submitted to *Chem. Phys. Letters*.
- H. Rottke and K.H. Welge, 1983, State-selective resonant excitation-ionization of H_2 with tunable VUV laser light, *Chem. Phys. Letters* 99 : 456.
- J. Sheffield, 1975, "Plasma Scattering of Electromagnetic Radiation", Academic Press, New York.
- D. Short and S. Skupsky, to be published.
- F. Skiff, F. Anderegg, T.N. Good, P.J. Paris, M.Q. Tran, N. Rynn and R.A. Stern, 1988, Conservation laws and transport in Hamiltonian chaos, *Phys. Rev. Letters* 61 : 2034.
- R.A. Stern, D.N. Hill and N. Rynn, 1983, Direct ion-transport measurement by optical tagging, *Phys. Letters A* 93 : 127.
- G.C. Stutzin, A.T. Young, A.S. Schlachter, K.N. Leung and W.B. Kunkel, 1989, In-situ measurement of rovibrational populations of H_2 ground electronic state in a plasma by VUV laser absorption, *Chem. Phys. Letters* 155 : 475.

HYDROGEN-SURFACE INTERACTIONS

H.J. Hopman

*FOM Institute for Atomic and Molecular Physics, P.O.Box
41883, NL-1009 DB Amsterdam ,THE NETHERLANDS.
and
The NET Team, Max-Planck-Institut für Plasmaphysik
Boltzmann str. 2, D-8046 Garching, BRD*

INTRODUCTION

Two types of surface physics experiments performed at the FOM Institute in Amsterdam are particularly relevant for negative hydrogen ion production. The first type is the sputtering of adsorbed hydrogen from low work function surfaces. This effect is applied in "surface-plasma" sources. The second is the formation of vibrationally excited hydrogen molecules by recombination of atoms on tungsten surfaces. These molecules might be among the precursors from which H⁻ is formed by dissociative attachment in "volume" sources.

In a surface-plasma source, an extra electrode, called the converter, is placed in a discharge chamber such that it is in good contact with the plasma. When the converter is given a negative voltage, it is bombarded by the positive plasma ions. In this process, large amounts of plasma ions are implanted into the converter material. When the equilibrium concentration is reached, as many plasma ions are implanted, as there are sputtered. So far the low work function converter materials chosen were mainly tungsten covered by a fractional mono layer of cesium, and barium. If the discharge is struck in hydrogen gas, some of the sputtered hydrogen atoms may pick up an extra electron from the metal substrate and become an H⁻ ion. Typical conditions are a converter voltage of 100 V, and a positive ion current density of $\approx 1 \text{ A/cm}^2$. To handle the power density involved, the converter is water cooled. With a Ba

converter, the yield is up to 80 mA/cm² of negative hydrogen ions (Van Os et al., 1989)

An ion source generally is a well cooled copper box in which a plasma is often created by a hot cathode arc discharge. Cathode materials may be W or Ta filaments. The hot cathode material evaporates and within a short while completely covers the source wall. So surface effects are related to properties of filament material and not to copper. Hydrogen atoms formed in the discharge cross the source, until they collide with a surface and stick. The question is what two atoms do when they meet each other at the surface. There is a chance that a molecule is formed and that it comes free. In this process energy is released partially going into motion and into internal energy of the molecule. Early experiments on surface recombination, done with permeation of hydrogen through thin membranes, showed that a very small fraction of the molecules is in the v" = 1 vibrational state (Kubiak et al., 1985). Therefore, it was a surprise to find much higher vibrational states being populated in molecules resulting from the recombination of hydrogen atoms on walls inside ion sources boxes (Eenshuistra et al., 1988; Hall et al., 1988), under conditions that the cathodes are heated, but the discharge is turned off.

The paper deals with the fundamental aspects of the surface processes indicated above.

CHARGE EXCHANGE COLLISIONS AT SURFACES

Introduction

The electron affinity Ea of hydrogen, i.e. the binding energy of the extra electron in H⁻, is as small as 0.75 eV. The work function, Φ , of all simple materials has a larger value. In an energy diagram, the affinity level of a particle incident on a surface lies above the Fermi level of the substrate, $\Phi - E_a > 0$. It means that population of the affinity level in surface collisions occurs only under non-equilibrium conditions, obtained by giving particles super thermal energies of order of 5 eV. The reaction has a reasonable yield if the energy differences are not too large. Examples of suitable substrates are W covered by a half mono layer of Cs ($\phi = 1.45$ eV, Los et al., 1981), W with thick Cs layer ($\phi = 2.1$ eV, Schneider et al., 1980), Ba ($\Phi = 2.5$ eV, Van Os et al., 1990), and LaB₆ or ThO₂ (Massmann et al., 1979). Then, negative ion fractions $\eta^- \geq 10\%$ are possible, and technical or scientific applications are realistic. Beside surface negative ion sources, we also mention the detection of low energy hydrogen neutrals in plasma experiments (Van Toledo et al., 1986).

At FOM, Amsterdam, data on charge changing collisions have been obtained in an apparatus, in which a well defined beam of protons (10² to 10⁴ eV) is scattered from a rotatable W(110) target, located in the middle of an UHV chamber (Geerlings et al., 1985). The target is cleaned by Ar ion sputtering and annealing. The target surface can be covered by full or fractional mono layers of metals like Cs or Ba. The ratio of negative ions and neutrals in the reflected beam is determined by periodically sweeping the negative ions out of the path to the channeltron detector.

Theory

We assume that the affinity level is the only level interacting with the metal conduction band. We further assume that the incoming proton is neutralized into an excited state in the incoming trajectory followed by Auger de-excitation close to the surface. When a hydrogen atom is brought close to a metal surface the originally sharp affinity level is shifted and broadened into a band of finite width. The shift is caused by the interaction between the atom and its mirror image induced in the metal. The level shift ΔE is given by (Van Os et al., 1990):

$$\Delta E(z) = -\frac{e^2}{4\pi\epsilon_0} \left(\frac{1}{4(z+k_s^{-1})} + \frac{\alpha_H}{8\pi(2(z+k_s^{-1}))^4} \right), \quad (1)$$

where z is the atom-surface distance, k_s^{-1} the electrostatic screening length, and α_H the polarizability of the negatively charged atom. The first term gives the classical image potential. The electrostatic screening of the image charge by the metal electrons causes a shift of the classical image plane with respect to the surface. The second term is needed, because in the case of barium the interaction takes place very close to the surface ($z \approx 2 a_0$, or twice the Bohr length) compared to a cesiated W(110) surface where the interaction region is in the range of 4 to 6 a_0 . A value of $65 a_0^3$ has been reported.

The affinity level can be shifted below the Fermi level at small values for z . As a consequence, it becomes degenerated with the occupied metal states, so that resonant charge transfer can take place. The initially sharp affinity level is broadened due to this interaction. The electrons tunnel between the metal states and the affinity level with a given transition frequency, $w(z)$, which according to Heisenberg's uncertainty principle, results in a broadening of the affinity level with a width $\Delta(z) = (h/2\pi) w(z)$. The transition frequency can be calculated from Fermi's golden rule in first order perturbation theory,

$$w(z) = 2\pi \sum p(E_a(z)) | \langle i | V | k \rangle |^2. \quad (2)$$

The sum has to be taken over all metal states, $|k\rangle$, in the conduction band; $|i\rangle$ is the negative ion state; p is the density of metal states, which varies within the free electron model as $\epsilon_k^{1/2}$, and V is the unperturbed core potential of the atom. Eq. (2) shows that the level width, e.g. the transition frequency, is a function of the density of states in the metal surface. The higher the density of states, the higher the transition frequency.

In Table I, are collected the figures for the work function and the density of states for barium and W(110) covered with 0.6 mono layers of cesium. The work function of barium compared to the cesiated tungsten is more than 1 eV higher, however the density of states is more than two times that of the cesiated tungsten. The high density of states for barium, resulting in a higher transition frequency, may partly compensate for the effect of the higher work function in negative ion formation.

Table I. The work function and Electron density at the Fermi level for barium and cesiated tungsten.

Material	Work function [eV]	Electron density at Fermi level $[a_0^{-3}]$
Barium	2.5	2.44×10^{-3}
0.5 mono layer Cs	1.45	1.03×10^{-3}

From the overlap of the shifted and broadened affinity level and the conduction band, we are able to calculate the equilibrium charge state, $N(z)$, as a function of z . In the case of a moving hydrogen atom the charge state, $P^-(z)$, after reflection from the surface, can be computed by integrating the following rate equation,

$$\frac{dP^-}{dz} = \frac{\Delta(z)}{v_\perp} (N(z) - P^-(z)), \quad (3)$$

where v_\perp denotes the normal velocity of the hydrogen atom. The integration results in an expression for $P^-(\infty)$, the negative ion formation probability at infinity, which can be compared with experimental data.

Results

Based on the theory described above, a strong dependence is expected of the ionization probability on the normal velocity in the

outgoing part of the trajectory. Therefore, the ionization probability was measured as a function of the normal velocity by changing the detection angle, see Fig. 1. The experimental data were fitted with the model discussed above. A least squares fitting procedure is used, with the turning point and the screening length as free parameters. In the region where the model is valid, for grazing angles of reflection, the ion yield increases with increasing energy, as predicted by this model.

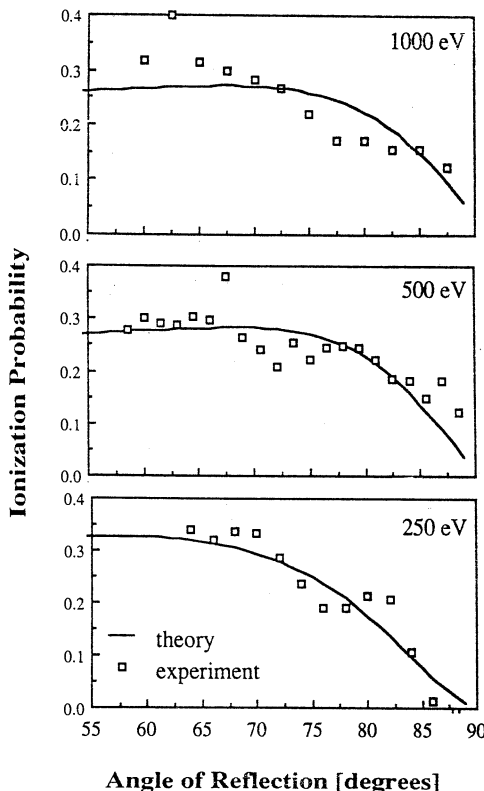


Figure 1. The measured negative ion fraction in the outgoing beam vs scatter angle for three different beam energies, 1000, 500 and 250 eV. The solid line depicts the results from model calculations and the open symbols are the measurements. The ambient pressure is below 10^{-9} Pa and the angle of incidence is 80° .

In a surface conversion source, the converter is heavily "polluted" with hydrogen. It is therefore worthwhile to measure the effect of this contamination on the charge exchange process. For a W(110) surface covered with half a mono layer of cesium, a decrease by almost a factor of two after an exposure to 900 Langmuirs of hydrogen has been measured (Van Amersfoort et al., 1986). However, co-adsorption of hydrogen and barium with a thickness of approximately 0.4 mono layer did not influence the negative ion yield, irrespective of the order of depositing the two elements. Therefore, adsorbed hydrogen on top or underneath the barium layer does not affect the charge exchange process. This is important for

the application of barium in a surface conversion source where the converter is exposed to very large fluxes of positive hydrogen ions and molecular hydrogen.

Summarizing, for incident energies in the range of 250 to 1000 eV negative ion fractions in the reflected beam are as high as 30 percent despite the relatively high work function of barium. This is related to the high density of electron states of the barium metal.

SURFACE RECOMBINATION OF HYDROGEN

Experimental technique

Experiments were carried out in a small bucket ion source. The main aim of the work is the measurement of the vibrational distribution of hydrogen molecules in a hot cathode arc discharge. The detection technique is resonant multi-photon ionization, applied to the plasma/gas mixture effusing through a small orifice out of the source. In this technique (Hopman, 1990, and references there in), atoms or molecules in one particular vibrational and rotational state are ionized with intense laser light and are subsequently detected with nearly 100% efficiency. Scanning the laser frequency, one obtains a spectrum in which the lines correspond to particular molecular states and the line areas with the population of the state. The present apparatus was found to have a detection limit as low as 8×10^7 state selected particles per cm^{-3} , just sufficient to detect hydrogen molecules in vibrational states up to $v'' = 5$ (Eenshuistra et al., 1988). The high sensitivity is one of the attractive features of this otherwise cumbersome technique.

The dimensions of the bucket source are $14 \times 14 \times 19 \text{ cm}^3$. The water cooled walls are made of oxygen free copper and on the outside covered by rows of permanent CoSm magnets, creating on the inside a multi-cusp field of ≈ 700 Gauss. In the back plate 6 tungsten filaments with a diameter of 1.5 mm are mounted on insulated water cooled feed throughs. Due to evaporation of filament material, the walls are covered by a grayish non-transparent layer of W. During experiments, in which the time behaviour of certain molecular states was followed in a pulsed discharge, it was found that vibrational molecules were present before striking the discharge. The mode of operation was such that the filaments were continuously heated, but the arc current was pulsed. The observations led to the hypothesis that the hydrogen molecules dissociated on the hot filament, the only available source of energy, but that the resulting hydrogen atoms recombined on the cold chamber walls. Because of the two step process, measurements were concerned both with the atom density $n(\text{H})$ and with the densities of vibrationally excited molecules. Of the

latter, mainly those of high vibrational excitation, i.e. $n(v'' = 4)$ and $n(v'' = 5)$, were recorded.

Results

The experimentally available degrees of freedom are the filament temperature T_f , and the gas pressure p . Varying the filament current between 40 and 110 A, the temperature was measured to vary from 1700 to 3000 K. The pressure was increased from 0.3 to 2 Pa. The pressure dependence is presented in Fig. 2. We see that all densities are proportional to p . Similarly, it could be shown that the densities are proportional to the number of filaments heated.

Density versus pressure, filament temperature 2800 K

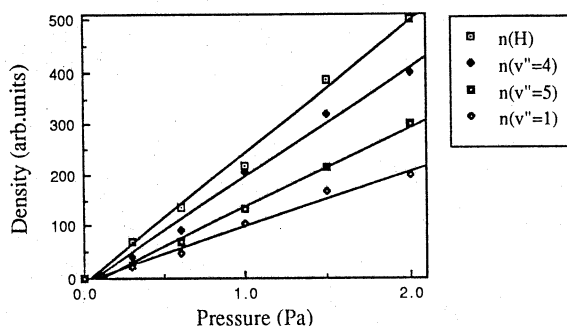


Figure 2. Measurements showing the linear relation between the source pressure and the densities of atomic hydrogen and of molecular hydrogen in the $v'' = 1$, 4, and 5 vibrational state, respectively. Data are obtained by applying RMI to gas flowing out of an ion source in which only the filaments are heated.

At a pressure of 1 Pa, the atom density was monitored as function of T_f , while heating 2 filaments. The shape of the measured curve, having a steep increase of $n(H)$ around 2000 K, and a saturation near 2800 K, agreed with predictions based on dissociation of molecules. The atom flux $\phi(H)$ leaving the hot filament is given by:

$$\phi(H) = 2 s_m \text{ Pa } \phi(H_2), \quad (4)$$

where $\phi(H_2)$ is the flux of molecules towards the filament, s_m is the sticking coefficient, $s_m \approx 0.07$ for clean poly crystalline W, and Pa is the atomization probability for molecules sticking to a surface. An expression for Pa has been given by Brennan and Fletcher (1959). It is the T_f dependence of Pa that is found back in the measured T_f dependence of $n(H)$. At $T_f = 2500$ K, Eq. (a) predicts $\phi(H) = 4 \times 10^{17} \text{ s}^{-1} \text{ cm}^{-2}$. The formula also predicts the observed linear pressure dependence. So, it can be concluded that the observed atoms results from dissociation of molecules on the hot filament.

Just as the filaments are the source of the atoms, they could also be the source of vibrational excitation. In that case, one would expect an increase of the ratio of $n(v'' = 5)$ and $n(v'' = 4)$ with T_f . Figure 3 gives the striking result that the densities of atoms and vibrationally excited molecules are proportional to each other, implying that the atoms form the source for the molecules. Further, the figure implies that the ratio $n(v'' = 5)/n(v'' = 4)$ is essentially independent of T_f . In this figure, the changes in $n(H)$ cover a range of nearly two orders of magnitude. Therefore, vibrational excitation taking place on the filament can be ruled out as being the dominant source of vibrational excitation.

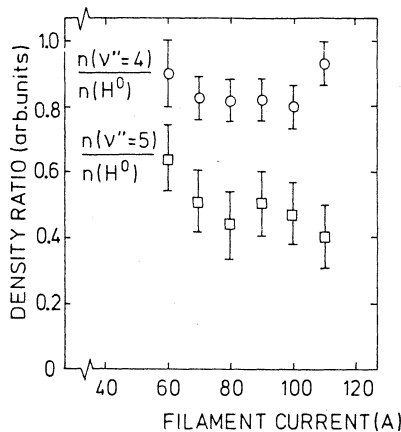


Figure 3. The density ratios of vibrationally excited molecules and atoms approximately remain constant, though the filament current is varied from 60 to 110 A, so that the filament temperature increases from ≈ 2200 to ≈ 3000 K.

Beside excitation on hot parts, vibrational excitation can result from recombination of atoms in the gas phase, or on the walls. The value of the rate coefficient for three-body gas phase recombination leads to a negligibly small production of molecules. Moreover, gas phase recombination of atoms would give a linear increase of the ratio $n(v'' = 4, 5)/n(H)$ with $n(H)$, which is not observed. These findings leave surface recombination as the source of vibrational excitation. The same conclusion was reached by Hall et al. (1988), who provided complementary experimental evidence.

Discussion

At low coverage of the discharge chamber inner walls by hydrogen atoms, freshly formed atoms reaching the surface will mainly arrive at unoccupied sites and stick. While migrating over the surface, atoms may meet, recombine, and use the energy released in the process to escape from the adsorption potential well. In such a case, the energy available for occupation of internal degrees of freedom is the difference of the dissociation energy and twice the energy with which atoms are bound to the surface. For the H-W system this is just sufficient to populate $v'' = 1$. In agreement with this simple model is the observation of molecules in $v'' = 1$ in hydrogen permeation experiments (Comsa and David, 1985; Kubiak et

al., 1985). The model can not explain the observation of much higher vibrational excitation. Moreover, the atomic coverage Θ_a should be proportional to $n(H)$, and therefore, one would expect that the densities $n(v'' = 4, 5)$ are proportional to Θ_a^2 , and thus to $n(H)^2$. Such a behaviour is not observed, see Figs. 2 and 3.

Because the hot filament is an ample source of atoms, we assume a high coverage, $\Theta_a \approx 1$. Then, molecules may be formed by recombination of a surface and a gas phase atom. The available energy is the dissociation energy (4.5 eV) minus one times the binding energy E_b . Values for E_b range between 2 and 2.5 eV. Thus enough energy remains to populate $v'' = 4$ or even $v'' = 5$, in agreement with the data. In addition, this models explains the observed proportionality of the densities of atoms and excited molecules, when varying p and T_f . The recombination of a free and an adsorbed atom is a so called **Eley-Rideal** reaction, of which so far few observations have been reported. The other possible process, the recombination of two adsorbed atoms, which was rejected on basis of the experimental data, is called the **Langmuir-Hinshelwood** mechanism.

We have seen that the L-H mechanism may give rise to $v'' = 1$, but that the E-R mechanism may lead to $v'' = 1$ to 5. For this reason, the measurements concentrated on the higher vibrational states, for which only one mechanism is possible. Implicit in this discussion is the assumption that the atom binds to a bare W surface. If this is the case, the binding energies reported in literature preclude the generation of states with $v'' > 5$, which have been observed by Hall et al. (1988). To overcome the problem, Hall et al. postulated a weakly bound physisorption state. At high coverage of this state, the E-R mechanism would allow the formation of vibrationally highly excited molecules, while preserving the proportionality of densities. An alternate explanation is the recombination of free atoms with those at subsurface sites, which have a smaller binding energy (Comsa and David, 1985). Presently, experiments do not seem to provide an answer, in part because the wall material is restricted to that of the filament. So, other types of discharges that allow experimenting with many different materials might be a possible route.

In the experiments of Hall et al., and Eenshuistra et al., the ratio of the areas of the wall and the orifice through which the molecules escape before being detected, is about 1000 to 1. It means that a vibrationally excited molecule is capable of surviving some 10^3 wall collisions. It is a second unexpected result of these experiments, that definitely is related to the peculiar surface condition in these sources. Until recently, surface de-excitation of vibrationally excitation was expected to be a rapidly process (Hiskes and Karo,

1984). However, there is evidence that a discharge destroys the surface condition (Eenshuistra et al., 1989). So, the results reported here can not directly be transferred from a chamber with heated filaments to one with a hot cathode arc discharge.

ACKNOWLEDGEMENTS: The author is indebted to Dr. Van Os for permission to use his results (Fig. 1, Table I). This work is part of the research program of the association agreement EURATOM-FOM, with financial support from NWO and EURATOM.

REFERENCES

- D. Brennan, and P.C. Fletcher, 1959, Proc. Royal Soc. London A **250** : 389.
G. Comsa, and R. David. 1985, Dynamical parameters of desorbing molecules, Surf. Sci. Rep. **5** : 145.
P.J. Eenshuistra, J.H.M. Bonnie, J. Los, and H.J. Hopman, 1988, Observation of exceptionally high vibrational excitation of hydrogen molecules formed by wall recombination, Phys. Rev. Letters **60** : 341.
P.J. Eenshuistra, R.M.A. Heeren, A.W. Kleyn, and H.J. Hopman, 1989, Dissociation and vibrational excitation of H₂ molecules, and wall influences on the densities in a multi-cusp ion source, Phys. Rev. A **40** : 3613.
J.J.C. Geerlings, P.W. Van Amersfoort, L.F.Tz. Kwakman, E.H.A. Granneman, J. Los, and J.P. Gauyacq, 1985, H⁻ formation in proton-metal collisions, Surf. Sci. **157** : 151.
R.I. Hall, I. Cadez, M. Landau, F. Pichou, and C. Scherman, 1988, Vibrational excitation of hydrogen via recombinative desorption of atomic hydrogen gas on a metal surface, Phys. Rev. Letters **60** : 337.
J.R. Hiskes, and A.M. Karo, 1984, Generation of negative ions in tandem high-density hydrogen discharges, J. Appl. Phys. **56** : 1927.
H.J. Hopman, 1990, Laser diagnostics of a hydrogen discharge, these Proceedings.
G.D. Kubiak, G.O. Sitz, and R.N. Zare, 1985, Recombinative desorption dynamics: molecular hydrogen from Cu(110) and Cu(111), J. Chem. Phys. **83** : 2538.
J. Los, E.A. Overbosch, A.D. Van Wunnik, 1980, Positive and negative ionization by scattering from surfaces, Proc. 2-nd Int. Symp. on Production and Neutralization of Negative Ions and Beams, Brookhaven Natl. Lab. Report BNL 51304, Upton, NY.
P. Massmann, H.J. Hopman, and J. Los, 1979, Negative surface ionization of hydrogen and its application to plasma diagnostics, Nucl. Instr. Methods, **165** : 531.
P.J. Schneider, K.H. Berkner, W.G. Graham, R.V. Pyle, and J.W. Stearns, 1980, H⁻ and D⁻ production by back scattering from alkali targets, Phys. Rev. B **23** : 941.
P.W. Van Amersfoort, J.J.C. Geerlings, R. Rodink, E.H.A. Granneman, and J. Los, (1986), Formation of negative hydrogen ions on a co-adsorbed layer of cesium and hydrogen on W(110), J. Appl. Phys. **59** : 241.
C.F.A. Van Os, C. Leguit, R.M.A. Heeren, J. Los, and A.W. Kleyn, 1989, H⁻ formation via surface conversion at a barium surface in high power dc environment, accepted for publ. in J. Opt. Eng.
C.F.A. Van Os, H.M. Van Pinxteren, A.W. Kleyn, and J. Los, 1990, Negative ion formation during scattering of a proton beam from a barium surface under grazing angles of incidence, submitted to J. Appl. Phys.
W. Van Toledo, H.J. Van Der Meiden, J.J.C. Geerlings, and P.W. Van Amersfoort, 1986, Detection of low-energy hydrogen atoms from a tokamak plasma by means of H⁻ formation on tungsten surfaces, Phys. Letters A **119** : 126.

PLASMA ASSISTED THIN FILM PRODUCTION

WC, a-C:H AND DIAMOND FILMS

H. Ehrhardt

Physikalisches Institut der Universität Kaiserslautern
Erwin-Schrödinger-Str. 46
6750 Kaiserslautern, Federal Republic of Germany

INTRODUCTION

During several decades and for numerous technical purposes thin films on substrates have been deposited by Chemical Vapor Deposition (CVD). The bulk material is heated mostly to about 1000° C in an atmosphere of a gas or a gas mixture (pressures $p \leq 1$ bar) which reacts with the surface and a film of several micrometers thickness is produced. These films have mechanical or chemical properties which are quite different from the bulk material. The films are used for surface hardening, wear resistance, corrosion protection and as diffusion barriers. Many property combinations of the materials of the film and the substrate are possible. Most cutting tools in mechanical engineering are produced by plating of steel by TiN, TiC, WC and other films. For corrosion protection TiC, NbC, Cr-Carbide, Al₂O₃ are used and SiC-films are used against high temperature corrosion in turbines. A severe disadvantage of the CVD-method is that high temperatures are needed for the chemical reactions of the gas with the substrate material and for the mass transport (by diffusion) of the gas molecules into the bulk material in order to produce a film of ca. 10 μm thickness. This high temperature normally changes the exact dimensions of the product.

In recent years Physical Vapor Deposition (PVD) methods have been introduced increasingly and we have now world wide a PVD market of well over $10 \cdot 10^9$ US \$. All the modern PVD methods are connected somehow with dc-, rf- or microwave plasmas and make use of high energy neutrals or ions which are deposited on the substrate. These methods work at much lower temperatures of the substrate material compared to the CVD methods, since

- i) A large fraction of the necessary processes occur already in the plasma, e.g. the formation of unstable species such as radicals, electronically metastable atoms or the formation of vibrationally highly excited molecules, which react more easily with the surface particles than molecules in their ground states.
- ii) The kinetic energies of the impinging neutrals and ions can easily be in the range from a few eV to some hundred eV and therefore they carry the reaction energy to the surface. In addition, the kinetic

energy of the incoming particles is of use for the mixing of the atoms in the region of the interface between the substrate and the film material leading to a large adhesive strength and to a larger density and hardness of the films.

Deposition rates in the order of 10 Å/s to several 100 Å/s are usual. Often high speed sputtering is used with magnetrons, ion beam and plasma beam methods and ion plating. Examples of products treated by these methods are scratch and corrosion resisting watches, fast cutting tools, tribological films made from MoS₂, WSe₂ and carbon, low absorption multilayer laser mirrors, transparent and electrically well conducting films of SnO₂-In₂O₃ for opto-electronic components, TiN-films for medical purposes.

In the lecture we will concentrate on carbon containing films such as tungsten carbide, hydrogenated amorphous carbon a-C:H and diamond films. The collisions involved in the three methods for the particle preparation in the gas phase and the interactions of these particles on the surface are quite different and they are representative in many aspects for nearly all other PVD methods. Of course, we are far away from understanding all the physics concerning the collision induced particle preparation and film formation and hence we know only little about the relations between the mechanical, chemical and optical properties of the films and the collisional parameters.

EXAMPLES OF PVD-METHODS AND ROLES OF COLLISIONS

1. Magnetron sputtering and ion plating: Tungsten carbide films

Sputtering of tungsten carbide (WC) by a magnetron sputter source with a rf-argon discharge (13.6 MHz, 500 W) is used with an additional ion plating unit to produce WC on an iron substrate. Due to the collisions of the argon ions with the solid WC-target mostly neutral particles are sputtered with a broad distribution of kinetic energies. The maximum of this distribution is between 10 and 30 eV with a long tail up to about 100 eV. The percentage of positive and negative charged sputter particles is only about 1 or 2 %. The neutral flux consists of W, C, WC and minor cluster contributions such as W_nC_m with n,m = 0,1,2... The total flux of tungsten atoms compared to the total flux of carbon atoms must be 1:1 since a WC-target is sputtered. Most of the atomic and molecular species will be in their electronic ground states at the time just before hitting the substrate. An investigation concerning the composition of the flux with respect to masses, charge states and kinetic energies is underway. The WC molecules probably will be heavily vibrationally excited. SNMS measurements show that the neutral flux is W/C/WC ≈ 1/1/0.1 and W_nC_m ≤ 5 %. Depth profile measurements of the films yield a chemical (overall) composition of WC as expected.

The energy for chemical reactions on the surface and the surface mobility of W and C atoms originates practically totally from the kinetic energy (and vibration energy) of the impinging particles. The temperature measured at the substrate is only about 200°C and depends on the incoming particle flux. Collision induced electronic excitations of the particles on the surface seem to play only a minor role, since i) only very few photons can be detected and ii) electron impact induced chemical reactions are orders of magnitudes slower than reactions induced by ions with the same kinetic energy. Since electrons cannot transfer momentum to the surface atoms, they could only initiate a chemical reaction by their charge and by electronic excitation.

For the ion plating argon ions from the magnetron discharge are pulled to the substrate with energies from zero to 300 eV. This additional particle flux to the surface has two effects:

- i) More kinetic energy is transferred to the surface particles, which changes the structure of the films from columns to glass-like, the hardness increases up to 6000 VH Kp/mm² and the internal stress also increases to 6 GPa. The adhesion strength of the films to the surfaces is, due to ion induced mixing about equal to the strength of the substrate material (HSS-steel).
- ii) The argon ions give rise to a resputtering from the surface which leads to a change in the chemical composition. Since the carbon atoms are preferentially resputtered due to their mass, the chemical composition ranges between WC and W₂C depending on the energies of the argon ions and the ratio of the fluxes of W, C, ... and Ar⁺.

The use of ion plating does not change the principle role of the kinetic energy of all particles involved for the chemical reactions, but it changes the cristal and film growth and hence the mechanical properties of the films.

2. Inductively coupled rf-discharge: Amorphous hydrogenated carbon films

In recent years, amorphous carbon films have been investigated with increasing emphasis, since properties such as chemical inertness, low friction coefficients and hardness predispose this material for applications such as antireflective coatings, coatings for medical transplants, low friction coatings for tribological systems, protective coatings in fusion reactors and overcoats on thin-film media for magnetic recording.

The chemical, physical and mechanical properties of these films depend strongly on the preparation technique. A review of a-C:H deposition techniques has been given in 1986 by Angus et al /1/. The most frequently applied processes are plasma enhanced CVD using rf-discharge, ion beam deposition and sputtering of carbon to the substrate occasionally combined with subsequent ion plating. Most important parameters are the ion energy and the substrate temperature. The ion energy is freely tunable in ion beam techniques. But this method suffers from rather low deposition rates of ca. 1 Å/s. Typical growth rates in rf-glow discharges are in the order of 20 Å/s, but due to the relative high pressures (ca. 10⁻² mbar) the ion energy distribution is rather broad and the average impact energy is an order of magnitude smaller than the sheath potential due to ion collisions with neutrals. Therefore, in capacitively coupled rf-discharges potentials of more than 1 kV are biased to the substrate in order to obtain hard a-C:H films.

In the present paper an apparatus is described with inductively coupled rf-discharge working in a pressure range from 5 · 10⁻⁴ mbar to about 10⁻¹ mbar. This configuration allows to vary the substrate bias independently from the rf-power. In the low gas pressure region the average ion energy is essentially given by the sum of the plasma potential and an additional bias voltage and can be chosen up to values of several hundred eV. On the other hand, even at low pressures the deposition rate is still rather high, namely 30 Å/s at 6 · 10⁻⁴ mbar and for a rf-power of 100 W.

In Figure 1 the apparatus is shown schematically. A background

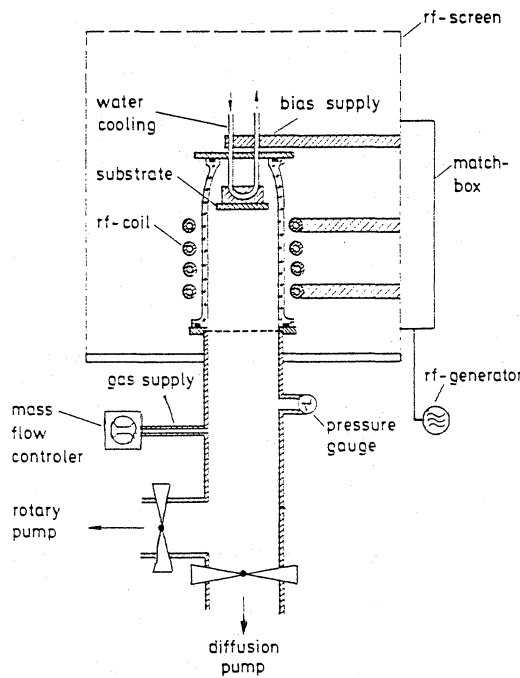


Figure 1. Schematic presentation of the apparatus with inductively coupled rf-discharge. The gas discharge pressure ranges from $3 \cdot 10^{-2}$ to $5 \cdot 10^{-4}$ mbar.

pressure of 10^{-6} mbar is obtained by an oil diffusion pump. The gas supply for the discharge chamber is controlled by 4 mass-flow-meters with an accuracy of 1 %. The rf-discharge is operated in a glass cylinder of 10 cm diameter and 26 cm height. The substrate holder consists of a copper block which can be heated up to 750° or cooled by water of 15° C. The substrates used are silicon single crystals, glass or metal plates depending on the intended analysis of the films. Polymerlike films have been prepared with an inductively coupled 27.12 MHz rf-generator which supplies a symmetric rf-voltage and power of 20 Watt. With this configuration the ion energies are in the range of some eV.

Hard a-C:H films have been made with a 13.56 MHz rf-generator with tunable power between 50 W and 500 W. The rf-power is inductively coupled to the plasma via an impedance matching network and a copper coil around the glass cylinder. The matchbox allows to extract a portion of the radio frequency power and couples it capacitively to the substrate. This additional rf-bias can be varied between 30-70 % of the rf-voltage.

For the preparation of the a-C:H films C_2H_4 and C_2H_2 have been used. The electron temperature and the plasma density have been measured by using heated single and double Langmuir probes /2,3,4/.

The Figures 2(a) and 2(b) show the electron temperature and the plasma density of argon- and C_2H_2 -discharges as functions of the gas pressure. The electron temperatures in hydrocarbon-plasmas are lower than in the Ar-plasma because low energy excitation processes, e.g. ro-, vibrational excitation and dissociation can occur. The C_2H_2 -plasma density is smaller due to the fact that volume recombination is more effective than in rare gas plasmas.

The plasma potential and the additionally applied bias determined the ion energies (Fig. 3). In the present case they have been varied from a few eV up to 300 eV. The ion energy distributions have been measured directly with a retarding field unit behind the substrate. Without additional bias the ion energies vary with the gas pressure, ranging from 84 eV at $7.7 \cdot 10^{-3}$ mbar to 200 eV at $3.5 \cdot 10^{-4}$ mbar. These high plasma potential values cannot be reached by a purely inductive coupling. In this latter case the plasma potentials (corresponding to the measured electron temperatures) should be in the order of 40-60 V. The higher values of the ion energies up to 220 eV can only be explained by a capacitive component of the discharge. The energy widths of the ion distributions are between 40 and 60 eV.

The polymerlike a-C:H films have been prepared at rather high pressures and temperatures. Due to the rf-coupling the potential drop in the plasma sheath is about 40 eV. Collisions of ions with neutrals in the sheath reduce the ion energies to a few eV.

The influence of the substrate temperature T_d on the film properties is quite strong. The electrical conductivity increases strongly with the substrate temperature in the range from 350°C to 550°C by more than 8 orders of magnitude (from 10^{-11} to about $10^{-3} (\Omega\text{cm})^{-1}$). This variation of the conductivity is strongly correlated with the IR-absorption coefficients for the C=C-bond (1580 aromatic, 1600 olefinic) /5/ and the integrated CH_x ($x=1,2,3$) vibrational absorption coefficients in the range from $3300-2850\text{ cm}^{-1}$. Raising of the substrate temperature results also in a reduction of the hydrogen content from 46 at% to 32 at%. Due to the enhanced proportion of sp^2 - to sp^3 -coordinated carbon atoms the optical gap decreases to 0.4 eV. Similarly the H-content decreases and the conductivity increases towards lower pressures if T_d is larger than 350°C . This enhancement of the conductivity again is strongly connected with an increasing percentage of sp^2 -coordinated carbon atoms resulting in a reduction of the optical gap.

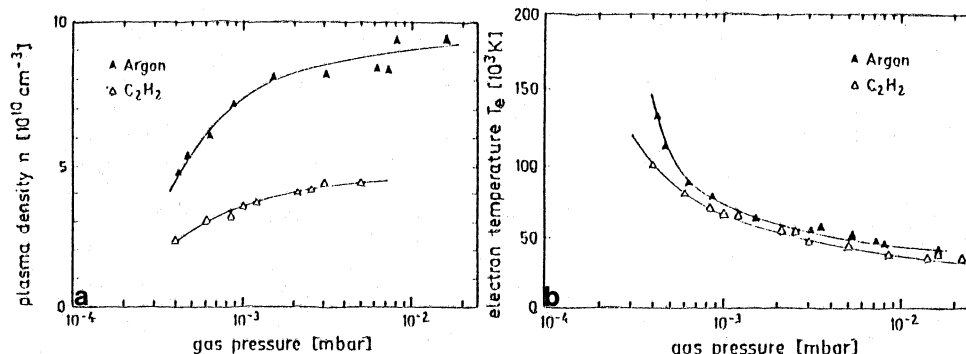


Figure 2. Plasma density (a) and electron temperature (b) of Argon and C_2H_2 rf-discharges as functions of the gas pressure.

Hard a-C:H films are usually produced at low substrate temperatures and rather low gas pressures. The influence of the discharge pressure on some film properties is shown in Figure 4 where the gas pressure of C_2H_2 is varied between $3 \cdot 10^{-4}$ mbar. The influence of the pressure on the film properties may not only be a consequence of the ion energy but also of other parameters like the deposition rate which is simultaneously changed. The rf-power was 50 W. No additional bias was applied and the substrate was water cooled.

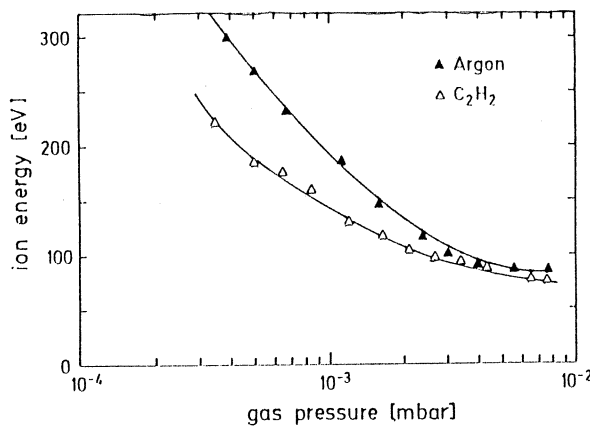


Figure 3. Ion energies measured with a retarding field unit behind the substrate in an Argon and a C_2H_2 discharge versus gas pressure.

In the high pressure range of about 10^{-2} mbar the ion energies are in the order of 80 eV (Figure 3). Due to these rather large impact energies the a-C:H films are quite hard. The density of the films is about 1.5 g/cm^3 with a hydrogen content of ca. 40 at%. The optical gap is 1.7 eV. Hardness measurements show values of 700 kp/mm^2 in this pressure range. The critical load of these films is in the range of 30 N and the internal stress 1 GPa.

With decreasing pressure sp^1 -bonded hydrogen vanishes completely (3300 cm^{-1}). Higher ion energies up to 220 eV in the low pressure range leads to preferential sputtering of hydrogen due to the lower binding energies of the C-H bonds compared to the C-C bonds /1/. At low pressure a hydrogen content of 27 at% was measured. Simultaneously the density increases up to 2.0 g/cm^3 and the optical gap reduces to 1.1 eV. Model calculations of Robertson and O'Reilly /6/ show that the gap is primarily determined by the $sp^2:sp^3$ ratio and the size of the clustered sixfold rings. The hardness of the films reaches values of 2000 kp/mm^2 and the stress is enhanced to 5.7 GPa. A similar behaviour has been found by Couderc and Catherine /7/ who attribute the increased stress to the change of C=C bonds.

3. Radicals producing reactors: Diamond films

1977 Derjaguin and Fedoseev /8/ have proposed theoretically that diamond could be produced from the gas phase. 1982 Matsumoto et al /9/ have proved this prediction experimentally by using a heated filament CVD. Shortly after this several groups, especially in Japan and in USA, entered the field. The large interest results from properties of diamond films which are quite unique: High electrical resistivity but with the possibility to dope and the production of semi-conducting elements with high thermal conductivity, high elasticity, very high hardness, low wear and very good chemical resistivity.

The methods used up to now are quite similar: H- and CH_3 -radicals are formed by a heated filament /9/, by a microwave cavity or by rf-CVD

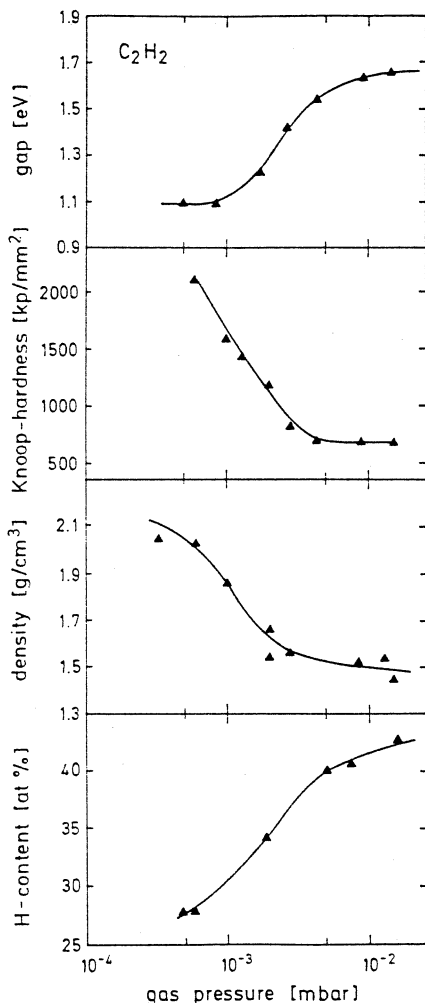


Figure 4. The optical gap, the Knoop-hardness, the density and the hydrogen content (at%) of hard a-C:H films produced from C₂H₂ at room temperature versus the gas pressure in the rf-discharge.

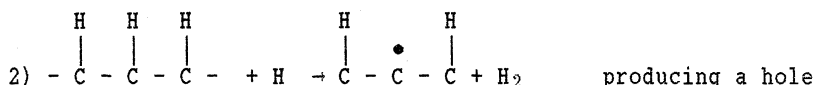
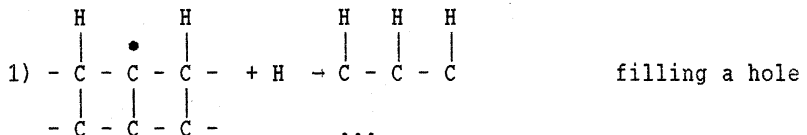
/10,11/, UV-CVD /12/ or electron assisted CVD /13/. The substrates, mostly SiC, WC, molybdenum and silicon, are on high temperatures of ca. 800° C and a gas mixture of ca. 99 % H₂ and 1 or 2 % CH₄ or some other CH₃ containing substance is introduced and passing over the radicals producing element. The deposition rates are 0.1-10 μm/h, i.e. quite high. The diamond crystals or films are identified by Raman-spectroscopy and X-ray diffraction.

As a first approximation the following processes are assumed:

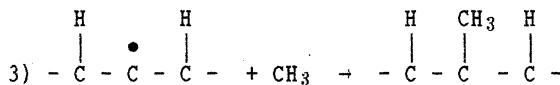
- a) In the gas phase: $H_2 \rightarrow H + H$
 $CH_4 \rightarrow CH_3 + H$
 $H + CH_4 \rightarrow CH_3 + H_2$

The polymerisation of hydrocarbons should be less important

- b) On the surface: We assume that we have already a diamond layer. Because of the high H-radical density this layer is nearly completely covered with H-atoms sticking to the free carbon valences. Occasionally there is a hole in the H-"carpet" which contains a free C-valence of the diamond film below. H-radicals which hit the surface can make two types of processes:



The CH₃-radicals migrate on the surface and can also fill a hole and in this way contribute to the growth of the diamond film:



Arguments for the existing of such a hydrogen-"carpet" are the facts that the adsorption energies of H₂ and CH₄ are much less than those for H- and CH₃-radicals and that the density of H-atoms is a factor 100 larger than the concentration of CH₃-particles. An important role of the H-radicals is to etch C=C double bonds which leads to pure sp³-configurations, i.e. diamond films.

An important parameter for the above mentioned surface processes is the temperature of the substrate (ca. 800° C - 1000° C), which determines the speed of the reactions and the mobility of the radicals on the surface.

We assume that the processes 1), 2) and 3) are most important and assign

n_L the number of holes per cm²

n_H the number of H-atoms per cm² migrating on the H-surface

n_{CH₃} the number of CH₃-radicals per cm² migrating on the H-surface

n_S the number of sites per cm² of the surface

k₁, k₂, k₃ are the velocity constants according to the equations 1 to 3.

Then we have the equations

$$\frac{dn_L}{dt} = -k_1 n_L n_H - k_3 n_L n_{CH_3} + k_2 (n_S - n_L) \cdot n_H$$

$$\frac{dn_{CH_3}}{dt} = -k_3 n_L n_{CH_3} + f_1(CH_3)$$

$$\frac{dn_H}{dt} = -k_1 n_L n_H - k_2 (n_S - n_L) \cdot n_H + f_1(H)$$

$f_1(H)$ resp. $f_1(CH_3)$ are the fluxes of H resp. HC_3 -radicals from the gas phase to 1 cm^2 surface and per second. Since $n_S \gg n_L$ and $f_1(H) \gg f_1(CH_3)$, the equations can be solved.

$$\text{It is } n_L = \frac{k_2}{k_1} \cdot n_S$$

$$n_H = \frac{1}{2k_2} \cdot \frac{f_1(H)}{n_S}$$

$$n_{CH_3} = \frac{k_1}{k_2 k_3} \cdot \frac{f_1(CH_3)}{n_S}$$

It is of course questionable if the k_i can be obtained, but it will be very probable, that the reactions of this model and their importance for the formation of diamond films will be cleared up by particle analysis in the gas phase and on the surface.

In the context of this paper it is interesting to note that for the diamond film preparation quite different and very low energy processes are of importance. High energy processes would introduce dangling bonds in the films and therefore disturb the pure sp^3 -configuration.

REFERENCES

- /1/ J.C. Angus, P. Koidl and S. Domitz, "Carbon Thin Films", In "Plasma Deposited Thin Films", CRC Verlag, ed. J. Mort, F. Jane, Cleveland, Ohio, 1986
- /2/ E. Eser, R.E. Ogilvie and K.A. Taylor, Thin Solid Films, 68 (1980) 381
- /3/ Ch. Wild, J. Wagner and P. Koidl, J. Vac. Sci. Technol. A5 (1987) 2227
- /4/ E.O. Johnson and L. Malter, Phys. Rev., 80 (1950) 58
- /5/ B. Dischler, R.E. Sah, P. Koidl, W. Fluhr and A. Wokaun, Proc. 7th Int. Symp. on Plasma Chemistry, Eindhoven (1985)
- /6/ J. Robertson and E.P. O'Reilly, Phys. Rev., B35 (1987) 2946
- /7/ P. Couderc and Y. Catherine, Thin Solid Films, 146 (1987) 93
- /8/ B.V. Derjaguin, D.V. Fedoseev: Growth of Diamond and Graphite from the Gas Phase, Jzd. Nauka, Moskow, 1977 (in Russian)
- /9/ S. Matsumoto, Y. Sato, M. Kamo, N. Setaka: Jpn. J. Appl. Phys. 21 (1982) L183
- /10/ C.-P. Chang, D.L. Flamm, D.E. Ibbotson and J.A. Mucha: J. Appl. Phys. 63(5) (1987) 1744
- /11/ S. Matsumoto, M. Hino and T. Kobayashi: Appl. Phys. Lett. 51(10) (1987) 737
- /12/ K. Kitahama, K. Hirata, H. Nakamatsu, S. Kawai, N. Fujimori, T. Imai, H. Yoshino, A. Doi, Appl. Phys. Lett. 49 (1986) 634
- /13/ A. Sawabe and T. Inuzuka, Thin Solid Films, 137 (1986) 89

ELECTRIC DISCHARGE LAMPS

L.C. Pitchford

Centre de Physique Atomique de Toulouse
CNRS Laboratoire Associeé URA N°277
31062 Toulouse, Cedex, France

INTRODUCTION

Electric discharge lamps are a common example of an application of phenomena in partially ionized gases. An estimated two billion electric discharge lamps are currently in existence worldwide¹. Although the first discharge lamps were carbon arc lamps used briefly for street lighting near the turn of the century, it was not until the 1940's that discharge lamps in the form of fluorescent lamps came into common usage. This explosive growth of the use of discharge lamps testifies to their efficiency, long life and reliability. This article will briefly describe the major lamp types and their performance. Of these lamp types, it is in particular the fluorescent lamp which exemplifies many of the topics discussed at this meeting.

LAMP FUNDAMENTALS

For purposes of general illumination, the wavelength range of interest is between 380 and 780 nm. Light of these wavelengths is emitted from solids or liquids when they are heated to temperatures above about 1000°K. The thermodynamics of the complex processes leading to this radiation and the spectrum of the radiation are described by Planck's law when the emitting solid or liquid can be considered as a black body. The spectra of radiation from such thermal or blackbody sources are shown in Fig. 1 for three values of the blackbody temperature. A curve illustrating the relative sensitivity of the eye as a function of wavelength is shown for comparison². As the blackbody temperature increases, the peak of the radiation spectrum is shifted to the blue, and the intensity of the radiation increases. The spectrum of solar radiation as seen on the surface of the earth, the standard by which all other light sources are judged, is negligible below about 250 nm. It increases and then becomes essentially flat above about 300 nm and remains flat throughout the visible.

The radiation from the hot filament in incandescent lamps is the result of an electrical current flowing through the thin tungsten filament. The temperature of the filament increases because of joule heating and is around 2500°K, depending on the lamp type³. Tungsten is an especially suitable filament material because of its high melting point (3653°K)⁴, and its low evaporation rate at these high temperatures.

The radiation, however, from a blackbody source at 3000 or even 3500°K is extremely broadband compared to the visible spectrum, and hence, much of the energy in the radiation from incandescent lamps is infrared or ultraviolet rather than 'useful' radiation, although the ultraviolet can be converted to visible with the use of phosphor (fluorescent powder deposited on the inside wall of the discharge).

The blackbody temperature for which the emitted thermal radiation reaches a peak in the visible region of the spectrum is about 5000°K. No solid or liquid exists at these temperatures so it is not possible to simply push incandescent sources to higher temperatures in order to increase their efficiency of conversion of electrical energy to visible radiation or to improve the color of the emitted radiation. It is possible, however, to attain discharge temperatures in excess of 5000°K. This is accomplished by means of a gas discharge in which a current passing through a gas creates a hot discharge, in analogy to the heating of a filament by an electric current. This is the basis of electric discharge lamps.

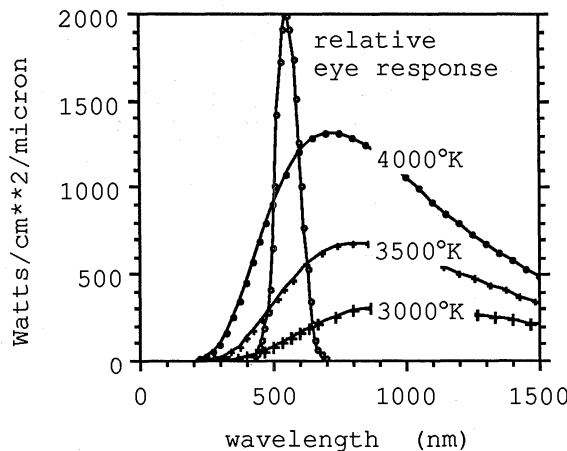


Fig. 1. Blackbody radiation as a function of wavelength for three different temperatures as indicated. A curve representing the relative sensitivity of the eye is shown for comparison.

The radiation emitted by a discharge is characteristic of the atoms and molecules present and it is not generally blackbody radiation because there is no equilibrium between the 'temperature' of the photons and the temperature of the gas. That is, the collisional processes between the electrons and the gas particles determine the electron and the gas temperatures. Thus, the radiation emitted by gas discharges cannot be simply predicted from thermodynamics. This brings up another advantage of gas discharge light sources. By the appropriate choice of gas mixtures and discharge conditions, it is possible to tailor the spectra of discharge lamps to fulfill certain application needs to an extent not possible with hot filament lamps using, for example, various filters or coatings on the lamp envelope.

LOW PRESSURE DISCHARGE LAMPS

Low pressure discharge lamps embody many of the phenomena in non-equilibrium phenomena in partially ionized gases that have been the subject of this meeting. In this section, the importance of non-equilibrium phenomena in determining the geometry and operating conditions of fluorescent lamps will be described.

Low pressure mercury fluorescent lamps are by far the most widely used and most successful of all the electric discharge lamps to date. The low pressure sodium lamp, often used in street lighting because of its extremely high efficacy due to radiation almost exclusively from the sodium D-lines at 589 nm where the eye response is near its maximum, has many similarities to the low pressure mercury lamp. Both of these lamps are electric discharges in a few millitorr of the metal vapor and a few torr of a rare gas, and the radiation in both cases is resonance radiation, radiation from the first excited states to the ground state. In discharge parlance, these are hot cathode glow discharges (gas temperature \ll electron 'temperature') with the positive column being the region which generates the useful radiation. Ambipolar diffusion is the principal charged particle loss mechanism, and multistep ionization dominates ionization by electron impact from the ground state as the charged particle production mechanism. The rare gas buffer at a few torr is needed mainly to control the diffusion rate of the charged particles to the walls.

Under optimized conditions, up to 60% of the electrical energy input to the low pressure mercury/argon discharge can be converted to radiation at 254 nm which results from excitation of the first excited state in mercury⁵. With suitable phosphor coatings on the inside of the discharge tube wall, the 254 nm radiation in turn can be converted to broadband radiation in the visible region of the spectrum with efficiencies near the quantum efficiency; i.e., about 50%. The net result is a 30% efficiency for conversion of electrical energy to visible radiation in a long-lived (7500 hours or more) gas discharge tube. The low pressure sodium lamp is in many respects quite similar to the fluorescent lamp, a main difference being that the sodium resonance radiation is in the visible and no phosphor is needed.

The energy levels of mercury important for this discussion are shown in Fig. 2. As Waymouth has described⁵, this particular configuration of the energy levels has several features which lead to very efficient generation 254 nm photons. The first group of excited states, the 6^3P levels at about half the ionization potential, is well separated in energy from the next excited state, the 6^1P state. A large fraction of the electron energy can therefore be selectively deposited into the 6^3P levels in a mercury/argon discharge if the electron energy distribution function is, for example, a Maxwellian with a temperature on the order of 1 eV. The lowest excited state of argon lies higher in energy than the ground state of the mercury ion, and so electrons only collide elastically with the argon atoms. Of the three levels in the 6^3P manifold, the upper and lower ones are metastable. Atoms excited to these levels have a large probability of being excited or deexcited to the 6^3P_1 level before losing their energy to any other process. The net effect is a very efficient coupling of electrical energy to energy in the 6^3P_1 level for certain values of the electron temperature. The electron energy distribution function can be controlled by the pressure of the buffer gas since the buffer gas pressure determines the loss of electrons due to ambipolar diffusion and, hence, the electron temperature

needed to produce enough new electrons to sustain the discharge. Thus, the efficacy is a maximum for a certain rare gas buffer pressure.

The assumption of a Maxwellian electron energy distribution function has been relaxed in recent models⁶⁻⁹. Vriens et al⁶⁻⁸ have concluded that a two-temperature Maxwellian distribution (one temperature on the low energy side of the 6^3P excitation threshold and another above it) predicts most of the features of more detailed calculations. These models have also confirmed the earlier work¹⁰⁻¹² which assumed that ionization was the result of multistep processes from the metastable 6^3P levels. This latter fact explains the inherent negative voltage-current characteristics in the positive column of these discharge - an increase in the voltage leading to an increase in the electron temperature causes a decrease in the current because less metastables are created at higher electron temperatures.

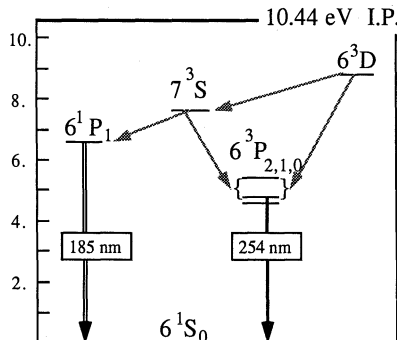


Fig. 2. Partial energy level diagram in mercury showing the levels important in fluorescent lamp operation.

The most characteristic aspect of fluorescent lamps is their long, tubular shape. The length of a fluorescent lamp is due mainly to limited light output per centimeter of positive column in these discharges, and long tubes are needed to produce enough light for many applications. As a function of current and for otherwise constant conditions, the 254 nm radiation output saturates because superelastic collisions start to play an important role in the kinetics of the radiating level. In other words, the decrease in efficiency with increasing current density is due to the approach to LTE (local thermodynamic equilibrium) conditions for which the excited state temperature, defined through the ratio of the excited state to the ground state, cannot exceed the electron temperature. The efficiency of generation of 254 nm photons decreases as a function of current because elastic and other collisional losses continue to increase with increasing current. The decrease in efficiency due to radiation trapping (see below) is enhanced under these conditions¹³. Usually it is the efficiency which has been optimized in determining the operating current.

The lamp bulb diameter and the partial pressure of mercury are determined largely by radiation trapping considerations. The 254 nm radiation output saturates and the efficiency of generation of 254 nm radiation decreases past an optimum of several millitorr mercury vapor because of radiation trapping. The average resonance photon is emitted and reabsorbed on the order of 100 times before exiting the lamp. Because the effective radiative lifetime is thus increased, decay of the 6^3P_1 state by non-radiative processes is enhanced, and the efficiency of uv production is reduced. This tendency can be compensated for to some extent by changing the bulb diameter. However, a reduced bulb diameter leads to an increased electron density for a constant current, and the efficiency for 254 nm photon generation decreases with electron density because of the increasing importance of superelastic collisions as described above. Ingold has recently discussed various suggested ways of reducing radiation trapping and some related experimental results¹³.

A major emphasis now in fluorescent lamp research and development is in the area of compact fluorescent lamps. This emphasis is driven by the desire to penetrate the residential market. A prerequisite for compact fluorescent lamp development was the development of fluorescent powders which can withstand higher fluxes of uv radiation. In order to produce the 600 to 1200 lumens required for domestic applications in a compact geometry, a price has to be paid in terms of efficiency. For roughly 1000 lumens, a discharge tube of 30 to 50 cm with a diameter of about 1 cm seems to be an optimum, and such lamps are currently on the market with about a 30% reduction in efficiency compared to standard fluorescent lamps¹⁴. The ballast and starting circuit requirements must be included in the base of the lamp if it is intended to be used in incandescent lamp fixtures.

The fluorescent lamps in use today are finely tuned devices operating at or near theoretical efficiencies. Attempts to understand the detailed interplay of the various collisional and radiative processes in the discharge have been remarkably successful, and although discrepancies between experiment and theory exist, it is possible to predict with a large degree of confidence the lamp performance.

HIGH PRESSURE OR HIGH INTENSITY DISCHARGE (HID) LAMPS

High intensity discharges lamps are arc discharges in a relatively compact geometry with a much higher power density and total operating pressure than the low pressure discharges described above. Table 1 compares operating conditions for typical fluorescent and high pressure mercury lamps. At the high power levels in HID lamps, the components can be considered to be in LTE with temperatures on the discharge axis of up to 6000°K¹⁶. The wall temperatures are about 1000°K, and there is a significant gas temperature gradient along the few centimeter radius from the axis to the wall. HID lamps are typically operated such that 50% or more of the power dissipation of the plasma column is by radiation, and 10 to 30% goes to heating the arc tube wall. This arc tube heating is essential if the desired radiating species are to be vaporized in the lamp itself. Mercury, a major component of most all HID lamps, is ideally suited to high pressure discharge lamps because its pressure is only high when the lamp has reached operating temperatures, and the lamp discharges are initiated and started in a lower pressure, rare gas environment.

Table 1. Comparison of operating conditions of a 40W fluorescent lamp and a 400W high pressure mercury lamp. (from ref. 15)

Wattage	40	400
Hg pressure	5 mtorr	4 atmos
Rare gas pressure	5 torr	150 torr
Current density	.04 A/cm ²	1.4 A/cm ²
Electron density at axis	5 10 ¹² cm ⁻³	5 10 ¹⁵ cm ⁻³
Axis temperature	320°K	6000°K
Wall temperature	320°K	1000°K
Arc length	100 cm	5 cm
Efficiency for production of visible rad.	25%	17%

High pressure mercury lamps are manufactured for a wide range of conditions, from 250 to 1000 watts or more. Their color and efficacy depend on the vapor pressure within the arc tube, and they are known for their long life (up to 20,000 hours). The effect of mercury vapor pressure can be seen when these lamps are turned on. Initially, when the arc tube walls are cool, the lamp operates as a fluorescent lamp, with a low mercury pressure and a low voltage drop across the nominal 5 cm arc tube. Then, as the lamp temperature rises, more mercury is vaporized, and the discharge is localized along the axis. This has the effect of further heating the gas and increasing the mercury pressure. In full operation, the total pressure is 2 to 10 atmospheres, and the radiation is from transitions between excited states of mercury. These are broadened and there is a continuum component in the spectra, but the overall color is not especially pleasing. The resonance radiation is almost completely trapped. Efforts to improve the color have led to the high pressure sodium and the metal-halide lamp families.

The high pressure sodium lamp (HPS), invented over 25 years ago, is second only to the low pressure sodium lamp in luminous efficiency¹⁷. HPS lamps are discharges in several 10's of torr of a rare gas, typically 500 torr of mercury vapor, and less than 100 torr of sodium vapor. The mercury in HPS lamps fulfills many of the same functions that the argon fulfills in fluorescent lamps. It acts to control the electron temperature through frequent elastic momentum transfer collisions with the electrons, and yet its excitation and ionization levels are too high to play much of a role at the axis temperature of about 4000°K. The radiation from HPS lamps is predominately radiation from the resonance lines and a few of the lines terminating on the 3^2P level which is the resonance level. From 25 to 35% of the energy input to the lamp is returned as visible radiation, while another 20 to 25% is IR radiation. Thermal conduction accounts for most of the non-radiative energy loss. The most characteristic aspect of the HPS spectrum is the self-reversal and extreme broadening of the resonance lines. Models of HPS discharges are highly developed and rather accurate predictions of the spectra are possible^{17,18}.

The newest category of HID lamps is the metal-halide lamp family¹⁹. The spectrum of many metals is especially rich in the visible, and thus, the addition of such metals to mercury lamps can result in vastly im-

proved color properties. Scandium is an example of such a multiline radiator, but the vapor pressure of the pure metal is too low for metal atoms to enter the gas phase at reasonable wall temperatures. However, the vapor pressure of the metal-halide, ScI_3 , at the wall temperature of about 1000°K is several torr²⁰. When included as components in the lamp fill, metal halides evaporate and diffuse to the hotter regions of the arc near the axis where they dissociate, releasing the metal into the gas phase. The desired, multiline spectrum due to the metal is thus produced preferentially in the hot, central regions of the arc. The metals are prevented from condensing on the walls of the arc tube because they recombine with the halides in the cool regions near the wall before they reach the wall. The resulting radiation is of extremely high color quality, and the efficacy (30% of the energy dissipated leads to visible radiation) and lifetimes (5000 to 15000 hours) of these lamps are quite reasonable. The most recent innovations in metal halide lamps are in the area of compact, low wattage light sources for indoor applications where high color quality is important such as in display lighting.

CONCLUDING COMMENTS

Fluorescent lamp discharges are especially good examples of non-equilibrium phenomena in partially ionized gases. In these discharges, the electron temperature is on the order of 1 eV ($12,000^\circ\text{K}$), while the gas temperature may be only about 320°K . The degree of internal excitation in the gas cannot be simply characterized by a temperature, and the effect of the internal excitation in the gas is manifested in the dependence of the generation of uv radiation on the various lamp operating parameters. HID lamps, on the other hand, are usually considered to be in local thermal equilibrium where a one-temperature description of the electron energy and the gas internal and kinetic energies valid. The radiation field, however, is not thermal radiation characteristic of the gas temperature.

The brief discussion of electric discharge lamps here has focussed on the operating conditions and the gas discharge aspects of these lamps. There are many other aspects which taken together with the discharge comprise the lamp system, the electrode and arc tube materials, the electrical behavior of the lamp and ballast system, etc.

REFERENCES

1. J.F. Waymouth, in: "Radiative Processes in Discharge Plasmas", J.M. Proud and L.H. Luessen, eds., Plenum, New York, (1986).
2. Illuminating Engineering Society, Color Rendering Subcommittee, Illum. Eng. 57:471 (1962).
3. G.E. Coxen, in: "Lamps and Lighting", third edition, M.A. Cayless and A.M. Marsden, eds., Edward Arnold, London, (1983).
4. "American Institute of Physics Handbook", third edition, McGraw-Hill, Inc., New York, (1972).
5. J.F. Waymouth, "Electric Discharge Lamps", MIT Press, Cambridge, Mass, (1971).
6. L. Vriens, J. Appl. Phys. 44:3980 (1973).
7. L. Vriens, R.A. Keijser, and F.A.S. Lighart, J. Appl. Phys. 49:3807 (1978).
8. W.L. Morgan and L. Vriens, J. Appl. Phys. 51:5300 (1980).
9. R. Lagushenko and J. Maya, J. Illum. Engs. Soc. 14:306 (1984).
10. C. Kenty, J. Appl. Phys. 21:1309 (1950).
11. J.F. Waymouth and F. Bitter, J. Appl. Phys. 27:122 (1956).

12. M.A. Cayless, Br. J. Appl. Phys. 14:863 (1963) .
13. J.H. Ingold, in: "Radiative Processes in Discharge Plasmas", J.M. Proud and L.H. Luessen, eds., Plenum, New York, (1986) .
14. A.G. Jack, in: "Radiative Processes in Discharge Plasmas", J.M. Proud and L.H. Luessen, eds., Plenum, New York, (1986) .
15. J.A.J.M. vanVliet and J.J. deGroot, IEE Proc. 128:415 (1981) .
16. W. Elenbaas, "The High Pressure Mercury Vapor Discharge", North-Holland Publishing Company, Amsterdam (1951) .
17. J.J. deGroot and J.A.J.M. vanVliet, "The High Pressure Sodium Lamp", Kluwer Technische Boeken, B.V., Deventer, (1986) .
18. D.O. Wharmby, IEE Proc. 127A:165 (1980) .
19. W.M. Keeffe, IEE Proc. 127:181 (1980) .
20. Dale E. Work, Lighting Research and Technology 13:143 (1981) .

INELASTIC SCATTERING OF ELECTRONS FROM H₂ MOLECULE AND FIRST-BORN APPROXIMATION: ROLE OF CORRELATION

G.P. Arrighini*, C. Guidotti* and N. Durante**

*Dipartimento di Chimica, Via Risorgimento 35, 56100 Pisa, Italy

**ICQEM (C.N.R.), Via Risorgimento 35, 56100 Pisa, Italy

SUMMARY

Inelastic scattering of electrons from the ground state of H₂ is investigated in the context of the first Born approximation (plus exchange *à la* Ochkur). The relevant transition properties have been obtained either in terms of a correlated wavefunction arising from a fairly extended CI procedure or in some approximation (TDA, RPA) corresponding to low-order solution of the equation-of-motion formalism put forward by Rowe.

INTRODUCTION

Some years ago M. Inokuti, admittedly a leader in the field of physics of atomic collisions, published a short but incisive comment entitled "The Future of Theoretical Atomic Collision Physics"¹. After an amusing, very critical prologue on the best way for a not too innovative author to efficiently generate papers in atomic-collision theory, Inokuti went on with his comment presenting serious personal views about which problems appear really prominent in Atomic-Collision Physics, thus breaking a lance in defence of a selective scientific production in the field. It is rather difficult to escape from Inokuti's irony, and we do not constitute an exception, considering the surely not extraordinary and innovative character of this paper. Despite such an admission and Inokuti's authority, however, we still presume this contribution can be of some utility, even though we shall only provide an outline in quantum-chemist style of a few approaches to inelastic electron-molecule scattering in the spirit of First Born Approximation (FBA), with the declared intention of putting in evidence for the case of the molecule H₂ how large is the prominence of electron-electron correlation effects.

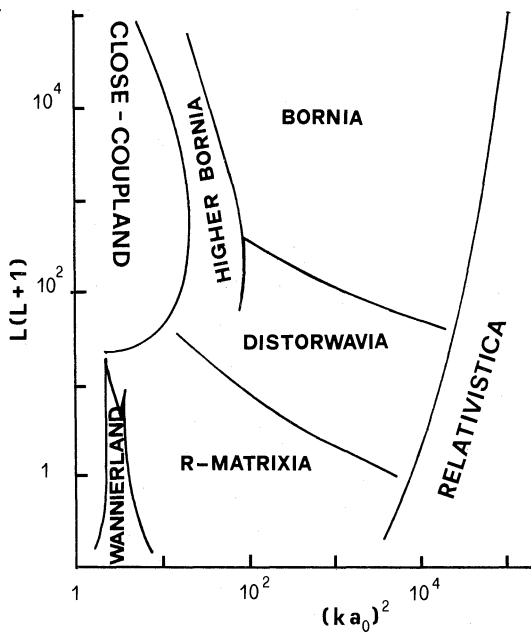


Fig.1 – “Geographic” regions of suitability of different theoretical treatments for the process $e + He (n=1) \rightarrow e + He^* (n=2)$ (according to Inokuti, ref.1).

INELASTIC SCATTERING Á LA BORN: A SHORT REVIEW OF FORMULAE FOR ELECTRON-DIATOMIC MOLECULE COLLISION

FBA is generally presented as an approach valid at high collision energies, but a specification, in terms of appropriate parameters, that allows to clearly establish its validity domain for general collisional processes does not seem to be available. Thus, in the absence of such a useful (and suggestive) map as that drawn by Inokuti for the process $e + He (n=1) \rightarrow e + He^* (n=2)$ ¹ (see Fig. 1), displaying regions of suitability of different theoretical treatments for that collision event, we shall be occasionally induced to apply out of Bornia behaviour rules possibly adequate only in such country, with results that the present authors are honestly unable to vigorously defend.

In the post-interaction representation², the differential cross section for excitation of a particular final state $|f\rangle$ of a molecule by electronic impact (atomic units with $e=\hbar=a_0=1$ are used throughout this paper unless differently stated) is given by

$$(1) \quad \frac{d\sigma_{fi}}{d\Omega} = \frac{1}{4\pi^2} \frac{|\vec{k}_f|}{|\vec{k}_i|} |\langle f; \vec{k}_f | \hat{V} | \psi_i^+ \rangle|^2$$

where \vec{k}_i (\vec{k}_f) is the momentum of the incident (emerging) electron, \hat{V} the interaction potential energy operator, $|f; \vec{k}_f\rangle = |f\rangle |\vec{k}_f\rangle$ the non-interacting final state of the electron-molecule system and $|\psi_i^+\rangle$ the (fully antisymmetrized) scattering state

with outgoing boundary conditions. If we label the incident electron as particle 1, for a diatomic molecule containing N electron with space-spin coordinates $\vec{x}_j = (\vec{r}_j, \vec{s}_j)$ the final state wavefunction will be expressed in the Born–Oppenheimer (B.O.) form

$$(2) \quad \langle \vec{x}_1, \vec{x}_2, \dots, \vec{x}_{N+1} | f; \vec{k}_f \rangle = e^{i\vec{k}_f \cdot \vec{r}_1} \chi(\vec{s}_1) \Phi_n(\vec{x}_2, \dots, \vec{x}_{N+1}; R) \cdot \zeta_v^n(R) Y_{L', M'}(\theta, \phi)$$

n, v', L', M' denote electronic, vibrational and rotational quantum numbers of the final molecular state, with $\Phi_n(\vec{x}_2, \dots, \vec{x}_{N+1}; R)$ fully antisymmetric wavefunction of given electronic state of the molecule, parametrically dependent on the internuclear separation R . Analogously $\zeta_v^n(R)$ and $Y_{L', M'}(\theta, \phi)$ represent respectively vibrational and rotational wavefunctions associated with the n -th electronic state, the polar angles (θ, ϕ) fixing the orientation of the molecular axis with respect to the laboratory frame.

The 1-st Born Approximation (FBA) is essentially a lowest-order perturbation theory approach, that corresponds simply to assume

$$(3) \quad \langle \vec{x}_1, \vec{x}_2, \dots, \vec{x}_{N+1} | \psi_i^+ \rangle \simeq e^{i\vec{k}_i \cdot \vec{r}_1} \chi(\vec{s}_1) \Phi_0(\vec{x}_2, \dots, \vec{x}_{N+1}; R) \cdot \zeta_v^0(R) Y_{L, M}(\theta, \phi)$$

with $\Phi_0(\vec{x}_2, \dots, \vec{x}_{N+1}; R)$ B.O. wavefunction of the ground electronic state of the molecule (more generally, the initial electronic state), while v, L, M label vibrational and rotational states pertaining to the ground electronic state. After simple manipulations, the (direct) excitation collision amplitude is expressible as follows^{3,4}

$$(4) \quad \langle f; \vec{k}_f | \hat{V} | \psi_i^+ \rangle^{Born} = \frac{4\pi}{q^2} \int d\vec{R} \zeta_v^n(R) \zeta_v^0(R) \cdot Y_{L', M'}^*(\theta, \phi) Y_{L, M}(\theta, \phi) \int d\vec{x}_2 \dots d\vec{x}_{N+1} \Phi_n^*(\vec{x}_2, \dots, \vec{x}_{N+1}; R) \cdot \sum_{j=2}^{N+1} e^{i\vec{q} \cdot \vec{r}_j} \Phi_0(\vec{x}_2, \dots, \vec{x}_{N+1}; R)$$

where $\vec{q} = \vec{k}_i - \vec{k}_f$ is the momentum transferred by the electron to the molecular target.

Eq.(4) provides a way for evaluating state-to-state excitation amplitudes induced by electronic collision. If the experimental set-up does not allow to resolve the rotational structure, what is observed is a differential cross section summed over the final rotational quantum numbers and averaged with respect to the initial rotational states. If we neglect the generally slight dependence of the energy on the rotational quantum numbers, we attain to the following expression for the rotationally averaged differential cross section corresponding to the excitation ($nv' \leftarrow ov$) between definite electronic-vibrational states

$$(5) \quad \left\langle \left(\frac{d\sigma}{d\Omega} \right)_{ov}^{nv'} \right\rangle_{rot.av.} = \frac{4}{q^2} \frac{|\vec{k}_f|}{|\vec{k}_i|} \left\langle \left| \int_0^\infty dR R^2 \zeta_v^n(R) \zeta_v^0(R) \Im(S(R, \theta; q)) \right|^2 \right\rangle_{rot.av.}$$

with

$$(6) \quad \Im(\mathbf{R}, \theta; q) \equiv \langle \Phi_n(\mathbf{R}) | \sum_{j=2}^{N+1} \exp\{iq(z_j \cos \theta + x_j \sin \theta)\} | \Phi_o(\mathbf{R}) \rangle$$

Here $\langle (\dots) \rangle_{rot.av} \equiv \frac{1}{4\pi} \int_0^{2\pi} d\phi \int_0^\pi d\theta \sin \theta (\dots)$ and the laboratory z-axis has been chosen along the transferred momentum vector \vec{q} .

The latter result is susceptible of further approximations. If the electronic transition matrix element $\langle \Phi_n(\mathbf{R}) | \sum_{j=2}^{N+1} \exp\{iq(z_j \cos \theta + x_j \sin \theta)\} | \Phi_o(\mathbf{R}) \rangle$ can be assumed a slowly varying function of the internuclear separation R around the ground state equilibrium distance R_e , then³⁻⁶

$$(7) \quad \left\langle \left(\frac{d\sigma}{d\Omega} \right)_{ov}^{nv'} \right\rangle_{rot.av.} = \frac{4}{q^4} \frac{|\vec{k}_f|}{|\vec{k}_i|} I_{ov}^{nv'} \left\langle \left| \Im(\mathbf{R}_e, \theta; q) \right|^2 \right\rangle_{rot.av.}$$

where

$$(8) \quad I_{ov}^{nv'} \equiv \left| \int_0^\infty dR R^2 \zeta_{v'}^n(R) \zeta_v^o(R) \right|^2$$

is known as Franck–Condon overlap factor.

It is also common practice to define so-called generalized oscillator strengths (GOS)

$$(9) \quad F_{no}(q, \theta) \equiv \frac{2E_{no}(R_e)}{q^2} \left| \Im(\mathbf{R}_e, \theta; q) \right|^2$$

and their rotationally averaged values

$$(10) \quad F_{no}(q) \equiv \langle F_{no}(q, \theta) \rangle_{rot.av.}$$

$E_{no}(R_e)$ being the vertical transition energy at $R = R_e$ between excited and ground electronic states. The rotationally averaged differential cross section can therefore be rewritten as

$$(11) \quad \left\langle \left(\frac{d\sigma}{d\Omega} \right)_{ov}^{nv'} \right\rangle_{rot.av.} = \frac{2}{q^2} \frac{|\vec{k}_f|}{|\vec{k}_i|} I_{ov}^{nv'} \frac{F_{no}(q)}{E_{no}(R_e)}$$

Eqs.(5), (7), (11) for the cross sections are often presented in a form that takes approximately into account exchange effects arising from the indistinguishability of the electrons involved in the collision, something ignored in our previous treatment. The final result, frequently referred to as Born–Ochkur (B.Oc.) approximation^{3,4,7}, is simply deducible on replacing the kinematical factor $|\vec{k}_f|/|\vec{k}_i|$ by the new one $[1 - q^2/(2k_i^2)]|\vec{k}_f|/|k_i|$, with k_i momentum of the incident electron. Integral cross section data are then easily obtained from differential cross sections by integration with respect to the scattering angle.

MOLECULAR TRANSITION PROPERTIES: A FAST COMPENDIUM OF QUANTUM CHEMISTRY APPROACHES

The computation of cross sections according to the formalism developed in the preceding section requires that we are in a position of obtaining reasonably accurate molecular excitation energies and electronic transition matrix elements as well. In the more general case, which corresponds to probe rotationally resolved transitions [see eq.(4)] or even in the situation where we are content with rotationally averaged cross sections for excitations involving definite electronic-vibrational states [eq.(5)] the solution of the electronic problem in the spirit of the B.O. approximation constitutes the first step of the required computational effort. After we have got $\mathfrak{S}(R, \theta; q)$, eq.(6), as a parametric function of the internuclear distance R, the next step involves the solution of the vibrational motion for the pairs of electronic states under investigation, so as to dispose of the nuclear wavefunctions $\zeta_v^n(R)$ which enter eq.(5). Clearly, even though FBA allows one to get rid of the remarkable difficulties inherent to the general scattering-theory machinery, the compessity of any molecular problem with respect to the atomic cases is hardly questionable and leads to heavy complications of computational order.

In the following we shall accept basically the assumption underlying eq.(11). As a consequence, for a given pair of electronic states, one of which is the ground state one, all that is needed is to evaluate vertical generalized oscillator strengths and excitation energy at the internuclear equilibrium distance $R = R_e$ of the ground electronic state, provided that independent information about the relevant Franck-Condon overlap factors is available elsewhere.

Quantum chemists have gained very much experience in computational problems involving molecules, as attested by a truly impressive bulk of scientific papers, through the realization of original and powerful computer codes able to carry out calculations at various levels of sophistication, from SCF to configuration interaction (CI), to multiconfiguration SCF, etc., using very extended sets of basis functions of different types (usually, Gaussian or Slater-type orbitals). But all of this is well known or, anyway, we take it for granted⁸.

The largest and most accurate calculations reported in this paper for electronic states connected by the transition of interest have been carried out in terms of a CI procedure involving all singly- and doubly-excited configurations of singlet symmetry arising from a basis set of SCF molecular orbitals, in turn obtained by expansion in a three-center basis set of 37 Slater-type orbitals⁴. Besides basis functions centered at the two hydrogen nuclei, which are clamped at the equilibrium distance $R_e = 1.4$ a.u., we have enriched the expansion basis by including at the midpoint between the nuclei a fairly abundant number of diffuse orbitals, so as to generate molecular orbitals that are considered important for describing molecular excited states belonging to the H₂ Rydberg series $^1\Sigma_u^+$ $1s\sigma$ $n\rho\sigma$ and $^1\Pi_u$ $1s\sigma$ $n\rho\pi$. From the symmetry point of view the 36 virtual molecular orbitals generated by SCF procedure are classified as follows: $\sigma_g(10)$, $\sigma_u(8)$, $\pi_g(4)$, $\pi_u(5)$, $\bar{\pi}_g(4)$, $\bar{\pi}_u(5)$ and give rise in the CI step to secular problems of dimensions (152×152) for Σ_g , (128×128) for Σ_u , (84×84) for Π_g and

(87×87) for Π_u symmetry, respectively. From the diagonalization of the Σ_g secular problem, at $R = 1.4$ a.u. we obtain a CI ground state energy $E_0 = -1.170482$ a.u. to be compared with the exact value $E_{ex} = -1.174474$ a.u., which accounts for more than 90% of the correlation energy of the molecule.

In addition to the full CI calculation, we have explored two other ways of generating excitation energies and electronic transition matrix elements, which are conventionally referred to as Tamm-Danoff Approximation (TDA) and Random Phase Approximation (RPA). Assuming that the reader may be not familiar with these methods, we shall give here a very concise sketch of them, by using an approach based on the equations-of-motion formalism⁹⁻¹⁴.

The search for excited states and energies of the Schrödinger equation (\hat{H} denotes the electronic B.O. Hamiltonian) can be reduced to solve the equivalent equation

$$(12) \quad [\hat{H}, \hat{O}_n^\dagger] |E_0\rangle = \Delta E_n \hat{O}_n^\dagger |E_0\rangle$$

where $\Delta E_n = E_n - E_0$ is the (vertical) electronic excitation energy from the ground state $|E_0\rangle$ and \hat{O}_n^\dagger defines an excitation operator to the state n , according to

$$(13) \quad |E_n\rangle \equiv \hat{O}_n^\dagger |E_0\rangle$$

After simple manipulations eq.(12) can be cast in the following form involving double commutators

$$(14) \quad \langle E_0 | [\delta \hat{O}_n, [\hat{H}, \hat{O}_n^\dagger]] + [[\delta \hat{O}_n, \hat{H}], \hat{O}_n^\dagger] |E_0\rangle = 2\Delta E_n \langle E_0 | [\delta \hat{O}_n, \hat{O}_n^\dagger] |E_0\rangle$$

with $\delta \hat{O}_n$ arbitrary infinitesimal variation of the de-excitation operator \hat{O}_n associated with \hat{O}_n^\dagger (obviously $\hat{O}_n |E_0\rangle = 0$ for any n). As often remarked⁹, the advantage of using double commutators instead of simple products of operators makes itself felt as approximations $|\tilde{E}_0\rangle$ are introduced for the ground state $|E_0\rangle$, because the commutator of two operators is of lower particle rank than the product and, therefore, less sensitive to the correlation details present in $|E_0\rangle$.

TDA and RPA are simply two approximations to the solutions of eq.(14) based on the following assumptions: (i) in both cases $|E_0\rangle \rightarrow |\tilde{E}_0\rangle = |HF\rangle$, $|HF\rangle$ being the H.F. approximation to the ground electronic state; (ii) excited electronic states are generated by excitation operators \hat{O}_n^\dagger respectively of the form

$$(15) \quad \begin{aligned} \text{TDA : } \hat{O}_n^\dagger &\equiv \sum_m^{\text{virt.}} \sum_\gamma^{\text{occ.}} Y_{m\gamma}^{(n)} \hat{a}_m^\dagger \hat{a}_\gamma \\ \text{RPA : } \hat{O}_n^\dagger &\equiv \sum_m^{\text{virt.}} \sum_\gamma^{\text{occ.}} \left[Y_{m\gamma}^{(n)} \hat{a}_m^\dagger \hat{a}_\gamma - Z_{m\gamma}^{(n)} (\hat{a}_m^\dagger \hat{a}_\gamma)^\dagger \right] \end{aligned}$$

$Y^{(n)}$ and $Z^{(n)}$ denote (column) vectors of transition amplitudes $Y_{m\gamma}^{(n)}$ and $Z_{m\gamma}^{(n)}$, while \hat{a}_m^\dagger , \hat{a}_γ are creation and annihilation operators associated with H.F. spinor-bitals m (virtual) and γ (occupied).

From eqs.(14), (15) one obtains in a rather straightforward way the following eigenvalue equations

$$(16) \quad \begin{aligned} \text{TDA : } & \mathbf{A} \mathbf{Y}^{(n)} = \Delta E_n^{\text{TDA}} \mathbf{Y}^{(n)} \\ \text{RPA : } & \begin{pmatrix} \mathbf{A} & \mathbf{B} \\ -\mathbf{B}^* & -\mathbf{A}^* \end{pmatrix} \begin{pmatrix} \mathbf{Y}^{(n)} \\ \mathbf{Z}^{(n)} \end{pmatrix} = \Delta E_n^{\text{RPA}} \begin{pmatrix} \mathbf{Y}^{(n)} \\ \mathbf{Z}^{(n)} \end{pmatrix} \end{aligned}$$

A and **B** are matrices of elements $\mathbf{A}_{m'\gamma',m\gamma} \equiv \langle m', \gamma' | \hat{H} - E_{HF} | m\gamma \rangle$ and $\mathbf{B}_{m'\gamma',m\gamma} \equiv \langle HF | \hat{H} - E_{HF} | \begin{pmatrix} m' \gamma' \\ m\gamma \end{pmatrix} \rangle$ respectively, where $|m\gamma\rangle \equiv \hat{a}_m^\dagger \hat{a}_\gamma |HF\rangle$ is a singly-excited configuration and $\left| \begin{pmatrix} m' \gamma' \\ m\gamma \end{pmatrix} \right\rangle \equiv \left(\hat{a}_{m'}^\dagger \hat{a}_{\gamma'} \right) \left(\hat{a}_m^\dagger \hat{a}_\gamma \right) |HF\rangle$ a double-excited configuration.

As clearly seen, the TDA results are equivalent to those obtained by simply diagonalizing the electronic Hamiltonian \hat{H} in a Hilbert subspace spanned by singly-excited configurations only, so that no correlation effects are included, while the RPA solutions take partially into account correlation effects through the presence of the matrix **B** in the corresponding eigenvalue problem. Just to allow one some appreciation of the quality of the results arising from our full CI calculation as well as the role of more approximate computational schemes, in Table 1 we report excitation energies E_{no} and spectroscopic dipole oscillator strengths $f_{no} \equiv F_{no}(0)$ for several final electronic states, corresponding to transitions all starting from the ground electronic state $X^1\Sigma_g^+$, along with some comparison entries referred to as "exact". Although TDA and RPA are unequivocally simplified procedures for calculating transition properties of atoms and molecules, their use is seen to lead for H₂ to very good results in comparison with the more rigorous (and more exacting) full CI procedure.

Table 1 – Vertical excitation energies E_{no} (eV) and dipole oscillator strengths f_{no} (a.u.) for H₂ ($R=1.4$ a.u.) All excitations are from the $X^1\Sigma_g^+$ ground state.

Final State	$B^1\Sigma_u^+$	$B'^1\Sigma_u^+$	$B''^1\Sigma_u^+$	$E, F^1\Sigma_g^+$	$G^1\Sigma_g^+$	$C^1\Pi_u$	$D^1\Pi_u$	$D'^1\Pi_u$	$I^1\Pi_g$
Full CI ^a	E_{no} 0.2907	12.728 0.0611	14.768 0.0207	15.469 0.0	13.056 0.0	14.816 0.3492	13.203 0.0940	14.928 0.0427	15.555 0.0
RPA ^b	E_{no} 0.2863	12.677 0.0626	14.622 0.0257	15.312 0.0	12.999 0.0	14.662 0.3451	13.107 0.0978	14.779 0.0445	15.397 0.0
TDA ^b	E_{no} 0.3090	12.744 0.0728	14.643 0.0309	15.322 0.0	13.019 0.0	14.662 0.3615	13.121 0.1042	14.784 0.0474	15.400 0.0
Exact ^c	E_{no} 0.300	12.754 0.057	14.85 0.0		13.13 0.0		13.29 0.356	14.996 0.0	15.626 0.0

^a See ref. 4

^b G.P. Arrighini, F. Biondi, C. Guidotti, A. Biagi and F. Marinelli, Chem. Phys. 52, 133 (1980)

^c See ref. 4

e-H₂ INELASTIC SCATTERING: SOME RESULTS

As evident from eq.(11), besides kinematical and Franck-Condon overlap factors the crucial ingredient needed for evaluating the FBA differential cross section for a given electronic transition is the ratio $F_{no}(q)/E_{no}(R_e)$ between (rotationally averaged) generalized oscillator strength (GOS) $F_{no}(q)$ [eqs.(9), (10)] and (vertical) electronic transition energy $E_{no}(R_e)$ at $R=R_e$. GOS in the range of transferred momentum $0 \leq q \leq 1$ a.u., evaluated according to the CI, RPA and TDA procedures are collected in Table 2 for several final states.

Table 2 – (Rotationally averaged) GOS (a.u.) for vertical transitions ($R=1.4$ a.u.) from the ground electronic state to some excited states of H₂.

q (a.u.)		$B^1\Sigma_u^+$	$B'^1\Sigma_u^+$	$E, F^1\Sigma_g^+$	$C^1\Pi_u$	$D^1\Pi_u$	$I^1\Pi_g$
0.1	CI	2.845(-1) ^a	5.945(-2)	2.042(-3)	3.367(-1)	9.049(-2)	2.542(-4)
	RPA	2.801(-1)	6.198(-2)	1.980(-3)	3.319(-1)	9.419(-2)	2.520(-4)
	TDA	3.024(-1)	7.205(-2)	2.082(-3)	3.478(-1)	1.003(-1)	2.528(-4)
0.2	CI	2.665(-1)	5.830(-2)	7.439(-3)	3.124(-1)	8.613(-2)	8.799(-4)
	RPA	2.625(-1)	6.043(-2)	7.179(-3)	3.077(-1)	8.954(-2)	8.731(-4)
	TDA	2.837(-1)	7.006(-2)	7.552(-3)	3.228(-1)	9.536(-2)	8.760(-4)
0.4	CI	2.072(-1)	5.072(-2)	2.200(-2)	2.351(-1)	7.301(-2)	2.116(-3)
	RPA	2.040(-1)	5.275(-2)	2.106(-2)	2.311(-1)	7.559(-2)	2.087(-3)
	TDA	2.214(-1)	6.084(-2)	2.223(-2)	2.433(-1)	8.050(-2)	2.095(-3)
0.6	CI	1.389(-1)	3.821(-2)	3.164(-2)	1.507(-1)	5.144(-2)	2.472(-3)
	RPA	1.370(-1)	3.977(-2)	3.006(-2)	1.478(-1)	5.317(-2)	2.426(-3)
	TDA	1.498(-1)	4.573(-2)	3.192(-2)	1.567(-1)	5.680(-2)	2.439(-3)
0.8	CI	8.238(-2)	2.579(-2)	3.161(-2)	8.046(-2)	3.201(-2)	1.945(-3)
	RPA	8.152(-2)	2.694(-2)	2.981(-2)	8.246(-2)	3.304(-2)	1.886(-3)
	TDA	9.022(-2)	3.097(-2)	3.193(-2)	8.823(-2)	3.549(-2)	1.899(-3)
1.0	CI	4.454(-2)	1.567(-2)	2.486(-2)	4.214(-2)	1.775(-2)	1.129(-3)
	RPA	4.449(-2)	1.647(-2)	2.330(-2)	4.146(-2)	1.834(-2)	1.080(-3)
	TDA	5.004(-2)	1.901(-2)	2.524(-2)	4.498(-2)	1.987(-2)	1.091(-3)

^a $A(-n)=A \cdot 10^{(-n)}$

Their behaviour is seen to be quite regular and similar to that found for atomic systems. For the allowed transitions here considered, one observes that the GOS

decrease monotonically, as q increases, from the largest value at $q=0$ (where they coincide with the dipole oscillator strengths reported in Table 1).

Even though it is difficult to claim that our full CI calculations are unequivocally so well balanced to take into substantial account the electron correlation effects involved in the various states, it seems safe to remark (i) a decrease of the generalized oscillator strength values on passing from TDA to CI estimates (with the only exception of the transition $I^1\Pi_g \leftarrow X^1\Sigma_g^+$); (ii) a slightly more marked role of electron correlation in the case of transition to optically allowed final states (ungerade symmetry).

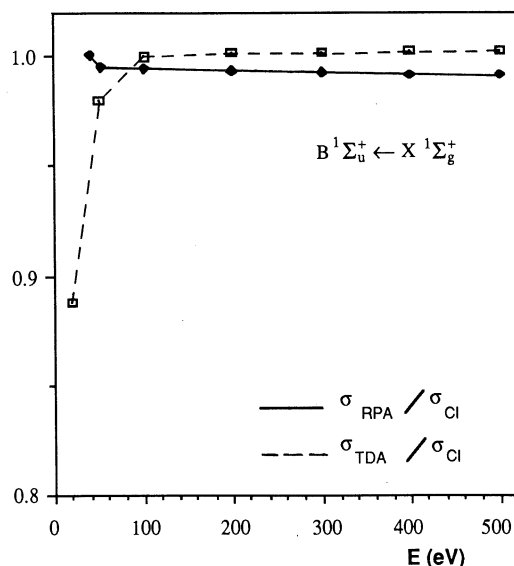


Fig.2 – Comparison between integral cross sections for the transition $B^1\Sigma_u^+ \leftarrow X^1\Sigma_g^+$ of H_2 as evaluated according to full CI, RPA and TDA procedures.

In order to allow some comparisons between results obtained by the different approaches, in Figs. 2 and 3 we have represented as a function of the collisional energy E the ratios σ_{TDA}/σ_{CI} and σ_{RPA}/σ_{CI} for a couple of electronic transitions, σ_{TDA} , σ_{RPA} and σ_{CI} being integral scattering cross sections evaluated according to self-evident procedures. The extent to which the curves drawn deviate from one over the energy range considered is a measure of the electronic correlation effects neglected by the two more approximate treatments RPA and TDA with respect to the full CI calculation. Marked discrepancies between total scattering cross section values evaluated in the presence or in the absence of correlation effects are particularly

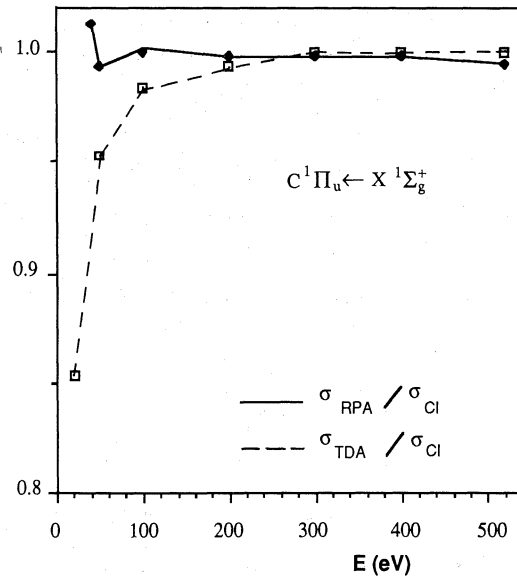


Fig.3 – See the caption of the preceding figure. The only difference is that we are considering here the transition $C^1\Pi_u \leftarrow X^1\Sigma_g^+$.

evident only at rather low collisional energy values, a situation where the Bornia rules are expected to be no hardly acceptable.

Integral cross section data for the transition $B^1\Sigma_u^+ \leftarrow X^1\Sigma_g^+$ are collected in Table 3 at several incident energy values ranging from 15 to 100 eV. The extension of FBA to rather low energies, where the relevance of such approximation is felt to be at the least doubtful, is motivated essentially by the availability of comparison data coming from various theoretical or experimental sources. The entries in the columns labeled B^a and B.Oc.^a correspond to integral cross sections obtained in this paper by using CI ingredients, according to first Born and Born–Ochkur approximation, respectively (one notices how the prominence of exchange effects becomes rapidly negligible as the incident energy is sufficiently high), while in the columns headed B.Oc.^b and C.C.^b we have reported values evaluated by Chung and Lin⁷ according to the Born–Ochkur approximation and the much more refined close-coupling approach, respectively. SMC refers to cross section values evaluated by McKoy and collaborators in terms of a rather sophisticated formulation of the electron–molecule scattering founded on the Schwinger multichannel method¹², while the last three columns collect experimental data from different sources^{13–15}.

Several other evaluated integral cross section data for few additional electronic transitions of H₂ are reported in Table 4. In all cases they were obtained by resorting

Table 3 - Integral cross section values (10^{17} cm 2 units) for the transition
 $B^1\Sigma_u^+ \leftarrow X^1\Sigma_g^+$ of H₂.

Incident	Experiments							
Energy/eV	B ^a	B.Oc. ^a	B.Oc. ^b	C.C. ^b	SMC ^c	d	e	f
15	3.14	2.36			1.41	1.7±0.5		
20	4.67	4.01			2.66	2.5±0.7	2.12	
25	5.09	4.60	5.31	4.31				
30	5.16	4.79			4.0	2.4±0.7	2.44	
40	4.94	4.72				3.04		
50	4.62	4.47	5.14	4.71				
60	4.30	4.20				2.95		
75	3.88	3.81	4.36	4.09				
100	3.34	3.30	3.76	3.58			4.02±0.6	

^a B.Oc. approximation + CI (present authors). See ref. 4

^b See ref. 7

^c See ref. 12

^d See ref. 15

^e See ref. 14

^f See ref. 13

to a full CI procedure in the Born-Ochkur approximation. As already remarked¹³, while one recognizes a rather good agreement with the experimental findings of Ajello et al.¹³ at 100 eV for the transitions $B^1\Sigma_u^+ \leftarrow X^1\Sigma_g^+$, $C^1\Pi_u \leftarrow X^1\Sigma_g^+$, $D^1\Pi_u \leftarrow X^1\Sigma_g^+$, $E, F^1\Sigma_g^+ \leftarrow X^1\Sigma_g^+$, in the case of the transition $B'^1\Sigma_u^+ \leftarrow X^1\Sigma_g^+$ the agreement is not so good. For this latter transition, the comparison with experimental values reported by Khakoo and Trajmar¹⁴ at incident energies between 20 and 60 eV suggests a substantial inadequacy of FBA, particularly at the lowest energies, even

Table 4 – Integral cross section values (10^{17} cm 2 units) for inelastic scattering of electrons off the electronic ground state of H₂.

Incident Energy/eV	$B'^1\Sigma_u^+$ Evlt ^a	Exptl	$C^1\Pi_u$ Evlt ^a	Exptl	$D^1\Pi_u$ Evlt ^a	Exptl	$E, F^1\Sigma_g^+$ Evlt ^a	Exptl
20	0.616		3.587	1.558 ^c	0.714		1.144	
30	0.842		4.636	1.760 ^c	1.078		1.058	
40	0.858		4.703	1.961 ^c	1.131		0.898	
60	0.773		4.296	2.220 ^c	1.049		0.667	
100	0.624	0.76±0.11 ^b	3.441	3.86±0.10 ^b	0.844	0.76±0.11 ^b	0.432	0.43±0.10 ^b
500	0.214		1.240		0.302		0.097	

^a B.Oc. approximation + CI (present authors). See ref. 4

^b See ref. 14

^c See ref. 13

though some discordance between experimental data from different sources is to be pointed out.

As a final remark we limit ourselves to assert that previous conclusions¹⁶ on the rather small role of correlation effects in influencing dipole transition moments for the optically allowed transitions $C, D^1\Pi_u \leftarrow X^1\Sigma_g^+$ and $B^1\Sigma_u^+ \leftarrow X^1\Sigma_g^+$ in H₂ can be extended, in virtue of the present results, to generalized transition moments, such as those involved in inelastic scattering cross sections à la Born.

REFERENCES

1. M. Inokuti, Comm. At. Mol. Phys. 10, 99 (1980)
2. J.R. Taylor, Scattering Theory, J. Wiley & Sons, N.Y. 1972
3. D.C. Cartwright and A. Kuppermann, Phys. Rev. 163, 86 (1967)
4. G.P. Arrighini, F. Biondi and C. Guidotti, Mol. Phys. 41, 1501 (1980)
5. F.H. Read and G.L. Whiterod, Proc. Phys. Soc. 82, 434 (1963)
6. T.N. Rescigno, C.W. McCurdy, V. McKoy and C.F. Bender, Phys. Rev. A13, 216 (1976)
7. S. Chung and C.C. Lin, Phys. Rev. A17, 1874 (1978)
8. For a recent survey of methods of computational quantum chemistry, see for instance G.H.F. Diercksen and S. Wilson (eds.) Methods in Computational Molecular Physics, D. Reidel Pub. Co., 1983
9. D.J. Rowe, Rev. Mod. Phys. 40, 153 (1968)
10. T. Shibuya and V. McKoy, Phys. Rev. A2, 2208 (1970)
11. T. Shibuya, J. Rose and V. McKoy, J. Chem. Phys. 58, 500 (1973)

12. W.G. Gibson, M.A.P. Lima, V. McKoy and W.M. Huo, Phys. Rev. A35, 2473 (1987)
13. J.M. Ajello, D. Shemansky, T.L. Kwok and Y.L. Yung, Phys. Rev. A29, 636 (1984)
14. M.A. Khakoo and S. Trajmar, Phys. Rev. A34, 146 (1986)
15. S.K. Srivastava and S. Jensen, J. Phys. B10, 3341 (1977)
16. S. Rothenberg and E.R. Davidson, J. Molec. Spettrosc., 22, 1 (1967)

ELECTRON - MOLECULE COLLISION CROSS SECTIONS FOR ETCHING GASES

Kurt H. Becker

Department of Physics
City College of The City University of New York
New York, NY 10031 USA

INTRODUCTION

The purpose of this article is twofold. Firstly, we will review the current status of electron - molecule collision cross sections for those etching gases that are most commonly used as the reactive constituents of processing plasmas. This includes a discussion of (1) what are the molecules for which cross section data are needed most urgently and (2) what are the particular cross sections that are needed for the various target molecules. Secondly, we will discuss some specific aspects of dissociative electron collisions with the reactive constituents of processing plasmas, since the dissociation of the feedstock molecules in a discharge mixture induced by electron impact plays a key role in any effort to understand and to model the complex processes in the plasma.

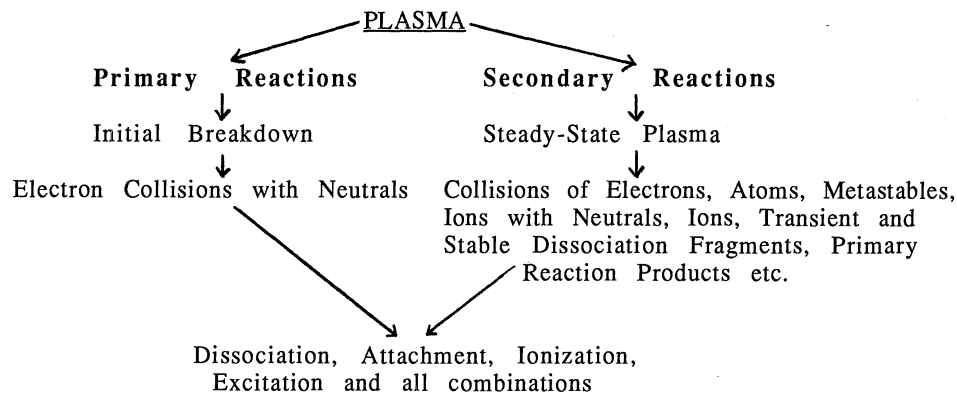
BACKGROUND

Plasma based processes are indispensable for the rapid advancement of key technologies such as the fabrication of very-large-scale-integrated (VLSI) micro-electronic devices ¹⁻⁴. A cold plasma represents a system far from equilibrium which is, on the other hand, exactly the property that makes it attractive for processing purposes. The high ratio of electron to gas temperature produces highly excited species which drive "high temperature" chemistry while keeping the gas temperature quite low thus avoiding the deleterious effects of high temperatures. Up to now the many successful applications of plasma processing have been developed largely empirically utilizing a time-consuming trial-and-error approach. On the other hand, recent developments in the modelling of low-temperature plasmas are encouraging⁵⁻⁷ and suggest that further advances in processing technology will most likely be achieved by combining the empirical approach with the predictive capabilities of reliable ab initio and semi-empirical plasma models. The major limitations of current plasma models arise no longer from mathematical or numerical problems, but much rather from the lack of a microscopic data base for the fundamental processes that determine the ground and excited state densities of the various neutral and ionic plasma species.

Etching and deposition in a typical plasma reactor is accomplished by ions in conjunction with neutrals. Volatile reaction products produced by the complex surface chemistry diffuse back into the bulk of the plasma. The two areas where major research efforts are currently being carried out are the plasma where the

reactive species are produced and the surface where the etching and deposition occurs. The two areas of research are highly correlated. On one side, the surface chemistry is determined by the nature of the species that are produced in the plasma and on the other side, the volatile reaction products that diffuse back into the plasma influence the gas phase processes.

A simplified picture of a plasma distinguishes between primary and secondary processes:



A measure of our understanding of the basic processes and dominant mechanisms in a low-temperature plasma is the ability to predict the characteristics of the plasma given such physical parameters as gas mixture and pressure, power deposition, flow rate and reactor geometry. A plasma model utilizes these input parameters and produces as output data the densities of radicals, ions and other species of interest as a function of time and position. Aside from mathematical and numerical problems there are four issues when a plasma model is constructed:

- (1) Identification of the important plasma reactions
- (2) Creation of a data base for these reactions
- (3) Comparison of the prediction of the model with experimental data
- (4) Evaluation of the sensitivity of the model to a variation of the input data

A working model of a low-temperature plasma must have on the input side a comprehensive set of cross sections and reaction rates for the processes of interest. On the output side one must have experimental data of time and space resolved species densities and other plasma characteristics in order to validate the predictions of the model. Whereas there is a wealth of data on species densities and other plasma characteristics from extensive plasma diagnostics utilizing predominantly optical and mass spectroscopic techniques⁷⁻¹⁰, there is a serious lack of reliable cross section data, i.e. there is an insufficient input data base. While the establishment of a comprehensive microscopic data base requires data from a number of different fields, there are compelling reasons why electron impact cross sections should have the highest priority. Electron collisions are the dominant processes in the initial breakdown of the discharge mixture. The various dissociative and ionizing electron collisions play a particularly important role, since they produce the reactive species that are responsible for the etching and deposition from the comparatively inert feedstock molecules.

TARGET MOLECULES OF INTEREST

A list of target molecules of prime technological importance for plasma processing purposes for which no satisfactory electron impact cross section data base is available was compiled recently^{11,12}. The list includes CF₄, O₂, SiH₄, SF₆,

BCl_3 , CF_3H , Cl_2 , CCl_2F_2 , H_2 and NF_3 . The list comprises primarily the most commonly employed reactive constituents of processing plasmas, but also O_2 and H_2 which together with He and Ar are frequently used to dilute the discharge mixture. The noble gases have been omitted from the above list, since the electron impact cross section situation for these atoms is rather satisfactory.

ELECTRON IMPACT CROSS SECTIONS OF PRINCIPAL INTEREST

Cross sections that are of principal interest for plasma modelling include:

- Q_{tot} , the total (elastic + total inelastic) cross section
- $Q(\text{el})$ and $dQ(\text{el})$, the elastic and angular dependent elastic cross section
- $Q(\text{rot})$ and $Q(\text{vib})$, the rotational and vibrational excitation cross sections
- $Q(\text{bs})$, the total (bound state) excitation cross section
- $Q(\text{ion})$, the total ionization cross section
- $Q(\text{da})$, the total dissociative attachment cross section
- $Q(\text{di})$, the total dissociation cross section
- $Q(\text{din})$, the total dissociation cross section into neutral fragments

In addition, it is desirable for many applications to have detailed information on the formation of a specific product (or class of products) m , i.e. one would also like to know partial cross sections for a particular channel such as $Q(\text{ion},m)$, $Q(\text{da},m)$, $Q(\text{di},m)$, $Q(\text{din},m)$ and finally also $Q(\text{di, rad})$ which is the cross section for dissociation into radiating fragments. Table 1 summarizes the current need for cross section data for the 10 target molecules listed above.

DISSOCIATIVE EXCITATION OF CF_4 , SF_6 , NF_3 , BCl_3 AND CCl_2F_2

A detailed review of the status of dissociative excitation has been given by Compton and Bardsley¹³. We restrict the discussion here to the dissociation of the etching gases SF_6 , CF_4 , NF_3 , BCl_3 and CCl_2F_2 which have been the target of a comprehensive research effort in our laboratory¹⁴⁻¹⁸. Experimental evidence suggests¹⁹ that electronic excitation of these molecules leads almost always to dissociation. Processes that produce radiating fragments are particularly straightforward to study by analyzing the subsequent photon emission. Processes that produce metastable fragments can be studied with a pulsed electron beam and

Table 1. Cross section needs as a function of molecular species. A star system has been employed that ranges from three stars indicating a critical need to no stars indicating that reasonable data already exist or that the cross section in question is not of particular interest for modelling purposes.

Molecule	Q_{tot}	Q_{el}	Q_{vib}	Q_{bs}	Q_{ion}	Q_{da}	Q_{dis}
CF_4		***		**	*	**	***
O_2				*			
SiH_4	**	**	**	*			***
SF_6			**	*	**		***
BCl_3	**	**			***	***	***
CF_3H	**	**			***	***	***
Cl_2				*			***
CCl_2F_2		*	**	*	*	***	***
H_2				*			
NF_3	**	*	*	*	***	*	***

time-of-flight (TOF) techniques often combined with mass spectroscopic techniques. Processes that produce neutral ground-state fragments are difficult to study, since there is no excess energy or charge that can be exploited for their detection and the applicability of laser-induced fluorescence (LIF) techniques is limited. Processes that produce ground-state parent or fragment ions can be studied using the fast neutral beam - electron beam method²⁰.

The Formation of Radiating Dissociation Fragments

The minimum energy to break up a molecule and produce one or more electronically excited fragments in a single step process is typically quite high (10 eV to 50 eV)¹⁴ in comparison with the average energy of plasma electrons which is in the range of one to a few electronvolts. Consequently, the relevance of these processes is restricted to a few very specific areas of application such as (1) rf plasmas under conditions where the energy deposition due to energetic "beam electrons" which are produced at the temporary cathode is an important process^{5,7,21}, (2) the interpretation of plasma-induced emission (PIE) spectroscopic studies of plasmas, and (3) the identification of optical emissions that one can hope to exploit for LIF plasma diagnostics purposes.

We built a crossed electron beam - gas beam apparatus to investigate the formation of radiating fragments by analyzing the optical emissions produced by dissociative electron impact of the above listed five molecules. We measured absolute emission cross sections from the vacuum ultraviolet (VUV) to the near-infrared and determined appearance potentials for the various emission features. The apparatus also includes provisions to pulse the electron beam for a study of the formation of metastable dissociation fragments using TOF techniques.

Mass spectroscopy and PIE spectroscopy are the two most commonly employed plasma diagnostics techniques to probe the concentration of reactive species in the plasma. Optical diagnostic techniques such as PIE and LIF spectroscopy have the additional advantage of being a non-intrusive, *in situ* technique, whereas mass spectroscopy cannot be considered a truly non-intrusive, *in situ* probe. PIE spectroscopic studies often utilize the intensity of the $3p \rightarrow 3s$ emissions of atomic fluorine (FI), in particular of the 7037.5 Å line corresponding to the $3p\ 2P^o \rightarrow 3s\ 2P_{1/2}$ fine structure transition to monitor the fluorine concentration. We measured absolute photoemission cross section and appearance potentials for the most intense $3p \rightarrow 3s$ atomic fluorine lines in the spectral range between 6000 and 8000 Å produced by dissociative excitation of SF₆, CF₄, NF₃ and CCl₂F₂. Absolute emission cross sections are needed to decipher the various processes that can contribute to the emission of a particular spectral feature from a plasma. The results taken from Blanks et al.¹⁴ and Jabbour and Becker¹⁸ are given in table 2. Cross section values range from 0.1 to 6×10^{-19} cm² at 100 eV. The dominant dissociation channel was identified as the total fragmentation of the parent molecule via optically allowed excitation routes.

PIE spectroscopy has its limitations in quantitative measurements because of the myriad of processes that can contribute to the emission of a particular line or band. LIF techniques proved to be a superior diagnostic tool which is highly sensitive and provides inherently high spatial resolution. It is limited, however, to the spectral range which is accessible by currently available tunable dye lasers. Most atomic fragments produced by the break-up of the above listed halogen-containing molecules have resonance lines in the VUV which are not easily accessible with current laser system. Therefore, most of the LIF plasma diagnostic studies so far have focused on transitions in molecular, and in particular in diatomic dissociation fragments such as BCl from BCl₃ and CCl from CCl₄ and CCl₂F₂. We could demonstrate that the continuous emissions in the wavelength range around 3000 Å produced by dissociative electron impact on SF₆

Table 2. Absolute emission cross sections Q_{em} at 100 eV electron energy for various visible FI $3p \rightarrow 3s$ line emissions.

Transition and Line (Å)		$Q_{\text{em}} (100 \text{ eV}) \text{ in } 10^{-19} \text{ cm}^2$			
		NF_3 a)	SF_6 a)	CF_4 a)	CCl_2F_2 b)
$4S^0 - 4P$	6240	1.4	0.6	1.2	0.9
	6349	1.0	0.4	0.8	0.6
	6413	0.8	0.3	0.6	0.4
$4D^0 - 4P$	6774	1.1	0.4	0.8	0.9
	6795	0.2	<0.1	0.2	0.1
	6834	1.6	0.6	1.2	0.9
	6856	6.1	2.5	4.7	3.5
	6870	1.3	0.4	0.9	0.7
	6902	3.8	1.4	2.8	2.0
$2P^0 - 2P$	6910	1.3	0.4	0.9	0.7
	7037	1.5	0.6	1.2	0.9
	7128	0.9	0.3	0.7	0.5
$2S^0 - 2P$	7202	0.5	0.2	0.4	0.3
	7311	4.3	1.4	3.3	2.4
	7332	5.3	2.1	3.9	2.8
$4P^0 - 4P$	7465	0.9	0.3	0.6	0.6
	7552	2.6	1.1	1.9	1.5
	7573	2.6	1.1	1.9	1.5
$2D^0 - 2P$	7607	4.8	2.0	3.5	2.7
	7755	2.7	1.1	2.1	1.6

a)From Blanks et al., J. Chem. Phys. 86, 4871 (1987)

b)From Jabbour and Becker, J. Chem. Phys. 90, 4819 (1989)

and NF_3 have the potential to be utilized for LIF plasma diagnostic purposes of SF_6 and NF_3 containing processing plasmas. Figure 1 shows the emission spectrum produced by 200 eV and 25 eV electrons, respectively, on NF_3 . The 200 eV scan (top diagram) shows three distinct features, a fluorine ion line at 3504 Å and a structured emission with maxima at 2880, 3005 and 3130 Å which is superimposed on a continuous background emission from 2500 to 3500 Å. The fluorine ion line has an onset potential of about 100 eV¹⁵ and is therefore no longer present in the 25 eV scan (bottom diagram). We also found no longer any indication of the continuous background in the low energy scan, whereas the structured emission was easily detectable. Figure 2 shows the emission cross section in the low energy regime recorded at two different wavelengths, at 3130 Å (the position of the most intense peak) and at 3200 Å, which is in a region where the continuous background is the dominant emission. The 3130 Å cross section (full circles) rises from a sharp onset at 8.5 ± 2 eV to a maximum at around 20 eV followed by a plateau and a second onset around 35 eV. The 3200 Å cross section (open circles) reveals a distinct onset around 30 ± 3 eV, but no indication of a low energy contribution was observed. The 30 eV onset agrees rather well with the extrapolated second onset of the 3130 Å cross section. We conclude that the NF_3 emission spectrum in the 2500

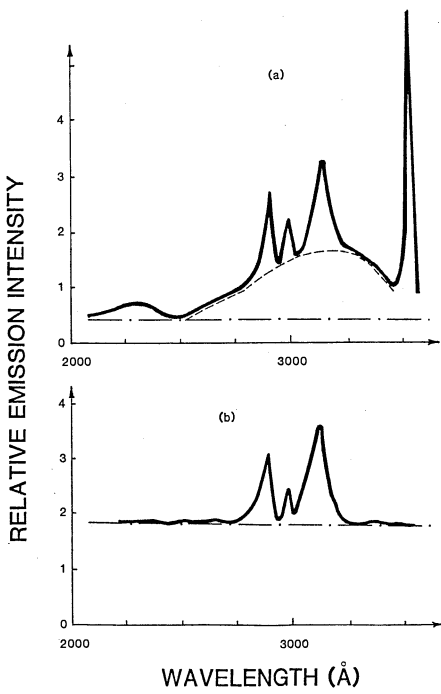


Figure 1 (a) Emission spectrum between 2000 and 3500 Å produced by 200 eV electrons on NF_3 . The broken line indicates the continuous emission, the horizontal line (- · -) represents the noise. (b) Same as (a) for 25 eV electrons.

to 3500 Å region consists of two components, a structured emission with an onset around 8.5 eV and a continuum with an onset around 30 eV. The photon energy corresponding to the emission of the structured feature is 4.2 eV. The low appearance potential of 8.5 eV allowed the unique identification of the underlying process as the partial fragmentation of NF_3 into NF_2 and F which requires a minimum energy of 2.6 eV with the simultaneous excitation of NF_2

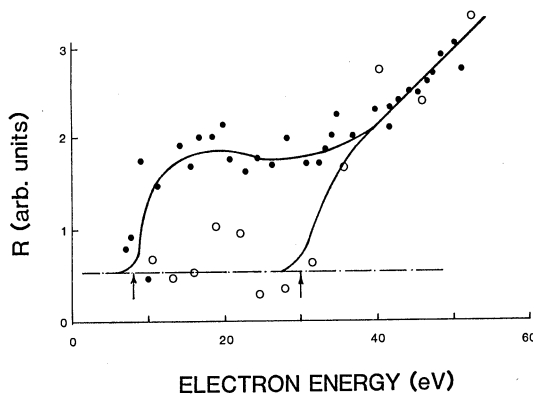
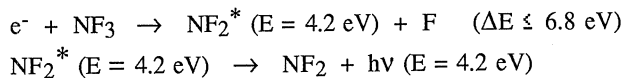
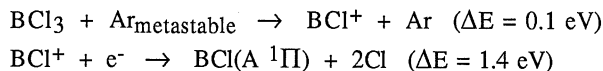


Figure 2. Relative emission cross section R as a function of electron energy at 3130 Å (full circles) and 3200 Å (open circles). The two curves have been normalized at 60 eV. The two onsets at 8.5 eV and 30 eV are marked by arrows.

Although the fragmentation of NF_3 into NF and 2F or F_2 with minimum energies of respectively 5.4 eV and 3.8 eV is also consistent with the measured 8.5 ± 2 eV onset, this possibility can be ruled out, since there are no known NF emissions around 3000 \AA . Since we are not aware of any bound excited states of the NF_3 molecule that could produce an emission around 3000 \AA , we assign the structured emission to a transition of the NF_2 fragment that terminates in the ground state. This emission is in the operating range of currently available tunable dye lasers and can be utilized for LIF diagnostics of NF_3 processing plasmas. Similarly, a weak emission feature in the SF_6 spectrum at 3160 \AA was found to have the potential to be employed in LIF diagnostics of SF_6 plasmas. Very recently, preliminary LIF studies of NF_3 and SF_6 discharges revealed emission features very similar to the emissions that we observed under single collision conditions²².

Gas mixtures of BCl_3 and Ar have been studied in great detail by Gottscho and collaborators⁷ using time and space resolved optical diagnostic techniques. They observed a dramatic increase in the $\text{BCl}(\text{A}^1\Pi)$ excited state density in BCl_3/Ar discharges when the Ar concentration was increased. Several mechanisms were proposed to account for the observed enhancement of the BCl excited state density, e.g. super-elastic collisions of cold electrons with Ar metastables, electronic quenching of Ar metastables followed by radiative heating and Penning ionization of BCl_3 by Ar metastables followed by the dissociative recombination of the BCl^+ ions. Only one mechanism, the Penning ionization followed by dissociative recombination



was consistent with the $\text{BCl A} \rightarrow \text{X}$ emission cross section and appearance potential measured by us¹⁷. The cross section (see figure 3) rises from a first onset at 14 ± 1.5 eV to a first maximum around 25 eV and then rises again sharply around 28 eV to reach its overall maximum just below 40 eV. Based on a comparison of the dissociation limits for various fragmentation processes of the BCl_3 molecule with the measured onset potentials we proposed that $\text{BCl}(\text{A}^1\Pi)$ fragments are produced via two mechanisms: one process in which two ground state chlorine atoms are produced (14 eV onset) and one process in which simultaneously a ground state chlorine atom and a ground state chlorine ion are produced (26 eV onset).

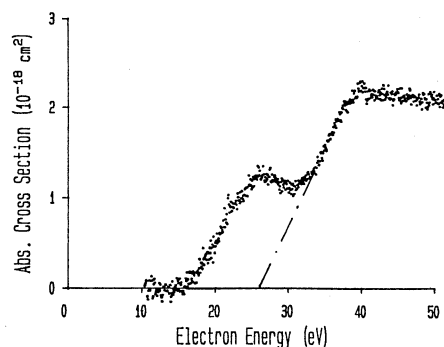


Figure 3. Absolute emission cross section of the $\text{BCl A} \rightarrow \text{X}$ system

The Formation of Metastable and Neutral and Ionic Ground-State Fragments

Work along those lines has been scarce. Projects are currently underway at CCNY to study (1) the formation of neutral ground-state BCl and CCl fragments from BCl₃ and CCl₄/CCl₂F₂ and (2) the formation of singly and multiply charged parent and fragment ions and mass spectral cracking patterns.

ACKNOWLEDGMENTS

I wish to thank my collaborators Anne. E. Tabor, Keith A. Blanks, Zeina J. Jabbour, Kevin E. Martus, Fred Olchowski, Mario Roque and Ralph Siegel for their contributions to the work described in this article. Thanks must go to Professor Ralph J. Jaccodine and Dr. Richard A. Gottscho for many helpful and stimulating discussions. The financial support of the work by the National Science Foundation through Grant Nos. CBT-8614513 (to Lehigh University), CBT-8896249 (to CCNY) and CBT-8902405 (to CCNY) and by a PSC-CUNY grant is gratefully acknowledged.

REFERENCES

1. J.B. Gerado and J.T. Verheyen, "Low-Temperature Plasma Physics: Its Importance and Potential in Technology and Commerce", Sandia National Laboratory Report No. SAND87-1875 (1987)
2. G. Ecker and K.U. Rieman, "The Technological Potential of Plasma Physics", *Experimentelle Technik der Physik* 35, 119 (1987)
3. H.F. Winters, R.P.H. Chang, C.J. Mogab, J. Evans, J.A. Thornton and H. Yasuda, "Coatings and Surface Modifications Using Low-Temperature Non-Equilibrium Plasmas", *Materials Science and Engineering* 70, 53 (1985)
4. G.S. Oehrlein, "Advances in Dry Etching Processes Depend on Understanding Plasma-Surface Interactions", *Physics Today* 39 (10), 26 (1986)
5. J.P. Boeuf and E.E. Kunhardt, in "Swarm Studies and Inelastic Electron-Molecule Collisions", eds: L.C. Pitchfors, V.B. McCoy, A. Chutjian and S. Trajmar (Springer Verlag: New York, 1987), p. 369
6. L.E. Kline and M.J. Kushner, private communication (1987, 1988)
7. G.R. Scheller, R.A. Gottscho, T. Intrator and D.B. Graves, *J. Appl. Phys.* 64, 4384 (1988)
8. C.E. Gaebe and R.A. Gottscho, "Laser and Other Diagnostics of RF Discharges", in "Radiative Processes in Discharge Lamps", editors: J.M. Proud and L.H. Luessen (Plenum Press: New York, 1988)
9. R.A. Gottscho and M.L. Mandich, *J. Vac. Sci. Techn.* A3, 617 (1985)
10. R.A. Gottscho and T.A. Miller, *Pure Appl. Chem.* 56, 189 (1984)
11. R.A. Bonham, private communication (1987, 1988)
12. M. Hayashi, in "Swarm Studies and Inelastic Electron-Molecule Collisions", eds: L.C. Pitchford, V.B. McCoy, A. Chutjian and S. Trajmar (Springer Verlag: New York, 1987), p. 167
13. R.N. Compton and J.N. Bardsley, "Dissociation of Molecules by Slow Electrons", in "Electron-Molecule Collisions", editors: I. Shimamura and K. Takanayama (Plenum Press: New York, 1984), p. 275
14. K.A. Blanks, A.E. Tabor and K. Becker, *J. Chem. Phys.* 86, 4871 (1987)
15. K.A. Blanks and K. Becker, *J. Phys. B* 20, 6157 (1987)
16. Z.J. Jabbour, K. Blanks, K.E. Martus and K. Becker, *J. Chem. Phys.* 88, 4252 (1988)
17. Z.J. Jabbour, K.E. Martus and K. Becker, *Z. Phys. D* 9, 263 (1988)
18. Z.J. Jabbour and K. Becker, *J. Chem. Phys.* 90, 4819 (1989)
19. H.F. Winters and M. Inokuti, *Phys. Rev. A* 25, 1420 (1982)
20. R.C. Wetzel, F.A. Baiocchi, T.R. Hayes and R.S. Freund, *Phys. Rev. A* 35, 559 (1987)
21. G.R. Heßner, J.T. Verheyen and M.J. Kushner, *J. Appl. Phys.* 63, 2226 (1988)
22. P.J. Hargis and K.E. Greenberg, *Bull. Am. Phys. Soc.* 34, 319 and 320 (1989)

ELECTRON COLLISIONS IN GAS SWITCHES*

Loucas G. Christophorou

Atomic, Molecular, and High Voltage Physics Group, Health and Safety Research Division, Oak Ridge National Laboratory and Department of Physics, University of Tennessee

I. INTRODUCTION

Many technologies rely on the conduction/insulation properties¹ of gaseous matter for their successful operation.² Many others (e.g., pulsed power technologies) rely on the rapid change (switching or modulation) of the properties of gaseous matter from an insulator to a conductor and vice versa.² Studies of electron collision processes in gases aided the development of pulsed power gas switches, and in this paper we shall briefly illustrate the kind of knowledge on electron collision processes which is needed to optimize the performance of such switching devices. To this end, we shall refer to three types of gas switches: (i) spark gap closing, (ii) self-sustained diffuse discharge closing, and (iii) externally-sustained diffuse discharge opening. The desirable properties and characteristics of these three types of switches are listed in Table 1, along with the required properties of the gaseous medium.

In efforts to optimize the performance of pulsed power gas switches by appropriate choice of the gaseous medium, knowledge is needed on those basic processes which crucially determine the number densities and energies of free electrons in electrically-stressed gases. Foremost among these are electron attachment, detachment, impact ionization, scattering and recombination. Photon interactions are also important in that they can affect the electron and the anion number densities, through, for example, the processes of photodetachment and photo-ionization and through photoenhanced electron collision processes.

*Research sponsored by the Office of Health and Environmental Research, U.S. Department of Energy, under contract DE-AC05-84OR21400 with Martin Marietta Energy Systems, Inc.

In this paper, we shall restrict ourselves to recent work on electron attachment, electron impact ionization, and electron drift velocities in switching gases. We shall, in particular, discuss recent results on electron attachment cross sections $\sigma_a(\epsilon)$ and coefficients $\eta/N_a(E/N)$, electron impact ionization coefficients $\alpha/N(E/N)$, and electron drift velocities $w(E/N)$ of switching gases/mixtures (ϵ is the electron energy, N_a and N are, respectively, the attaching gas and the total gas number densities and E/N is the density-reduced electric field). We shall also discuss the effect of internal energy of excitation of the switch-gas molecules on electron collision processes. The significance of these quantities and processes and of the effective ionization

TABLE I. DESIRABLE CHARACTERISTICS OF AND GAS PHYSICAL PROPERTIES/ PROCESSES FOR THREE TYPES OF GAS SWITCHES

Type of Switch	Switch Characteristics	Gas Physical Properties/Processes
A. Spark Gap Closing	<ul style="list-style-type: none"> • High Power <ul style="list-style-type: none"> - Efficiency - Repetition Rate • Fast Recovery <ul style="list-style-type: none"> - Closing/Opening • Control of Closing/Opening Time 	<ul style="list-style-type: none"> • Good insulator in hold-off stage and good conductor in closing stage [large $(E/N)_{lim}$; low $(E/N)_{conduction}$] • Short formative time lag • Large $k_a(\epsilon)$ which decreases with T (gas is strongly electron attaching when cold ($\sim 300K$) and weakly attaching or nonattaching when warm) • Steep increase of $\bar{\alpha}/N$ with E/N around $(E/N)_{lim}$
B. Diffuse Discharge Closing (Self-Sustained)	<ul style="list-style-type: none"> • Optical Modification of Conduction/Insulation Properties • Good Discharge Stability (to ~100 ns) for B 	<ul style="list-style-type: none"> • Good insulator in hold-off stage and good conductor in closing stage [large $(E/N)_{lim}$; low $(E/N)_{conduction}$] • Long diffuse discharge conduction time • $k_a(\epsilon)$ (large; high-energy onset; decreases with T) • Slow-varying $\bar{\alpha}/N$ (E/N) near $(E/N)_{lim}$ • Delicate dependencies of α/N and η/N on E/N
C. Diffuse Discharge Opening (Externally-Sustained)		<ul style="list-style-type: none"> • Good conductor in closing stage (low E/N) and good insulator in opening stage (high E/N) • $k_a(E/N)$ small at low E/N and large at high E/N • w large for $(E/N)_{conduction}$ and low at high E/N (negative differential conductivity) • Optical modification of conduction/insulation • High efficiency of electron production by external means

coefficient $\bar{\alpha}/N(E/N) = \alpha/N(E/N) - \eta/N_a(E/N)$ in optimizing the properties of gas switches, as well as of the optical modification of electron attachment in developing new techniques to actively control the switch opening and closing time will be elaborated upon. Examples of new switching concepts based on recent knowledge of electron collision processes in gases will be outlined.

II. ELECTRON COLLISIONS IN SWITCHING GASES

A. Electron Attachment

Dissociative and nondissociative electron attachment reactions depend strongly on the electron energy, the position of the negative ion state via which attachment occurs, and the internal energy of the electron attaching molecule.^{3,4} With regard to the internal energy of the molecule, we can distinguish electron attachment to (i) ground state, (ii) vibrationally/rotationally-excited ("hot"), and (iii) electronically-excited molecules. Knowledge on such processes is indispensable for understanding the insulating/switching properties of gaseous matter. Examples of recent knowledge--mostly from the author's Laboratory--on (i)-(iii) for gases of direct interest to gas switches are given in this section.

(i) Electron attachment to ground-state molecules

Recently, detailed studies have been performed on electron attachment in a number of gases/mixtures of interest to gas switches over wide ranges of E/N , N , and buffer gases (e.g., see Refs. 2-5). In Fig. 1 are shown our recent measurements on the electron attachment rate constant k_a^{5d} for SF_6^- in the buffer gases N_2 , Ar, and Xe over a wide range of E/N values. In Fig. 2, the same data are plotted as a function of the mean electron energy $\langle\epsilon\rangle$ in the respective buffer gases determined from the corresponding electron energy distribution functions $f(\epsilon, E/N)$. The $k_a(E/N)$ in Fig. 1 for SF_6^- in the three buffer gases have been used along with electron transport and electron scattering cross section data (see Ref. 5d) in a numerical two-term, spherical harmonic Boltzmann equation analysis, and the electron attachment cross sections $\sigma_a(\epsilon)$ shown in Fig. 3 have been obtained. In these calculations a nondissociative attachment cross section for SF_6^- formation, a dissociative attachment cross section for SF_6^- formation, and a composite dissociative attachment cross section for F^- , F_2^- , and SF_4^- formation were used; the cross section set of Klein et al.⁶--modified in accordance with recent cross-section shape measurements⁷--was used as the initial attachment cross section input.

Total electron attachment rate constants $k_a(\langle\epsilon\rangle)$ and cross sections $\sigma_a(\epsilon)$ for a most interesting for switching purposes group of molecules--the perfluoroalkanes $n-C_{N}F_{2N+2}$ ($N = 1$ to 6)--are shown in Fig. 4. As the size of these molecules increases, the magnitude of $k_a(\langle\epsilon\rangle)$ and $\sigma_a(\epsilon)$ increases and the function $k_a(\langle\epsilon\rangle)$ and $\sigma_a(\epsilon)$ shifts progressively to lower energies. While for CF_4 and C_2F_6 electron attachment is entirely due to dissociative processes, as the molecular size increases beyond C_2F_6 , increasingly a larger fraction of the measured $k_a(\langle\epsilon\rangle)$ is

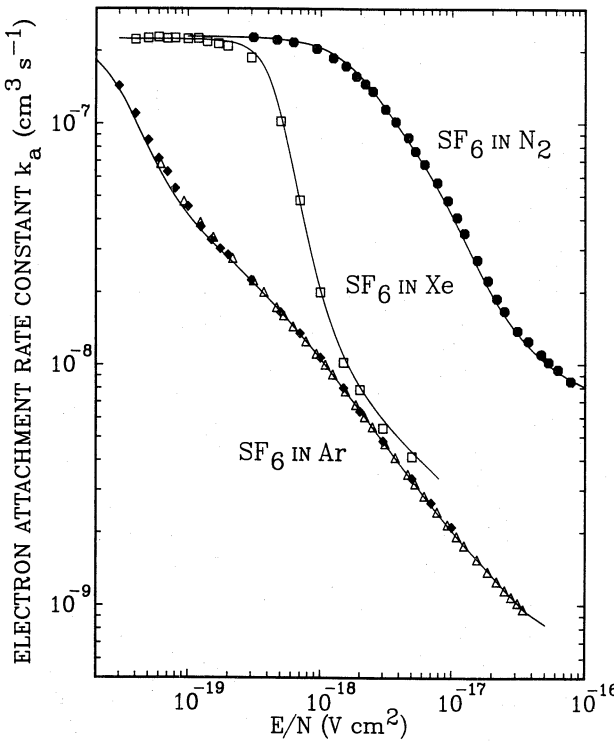


Fig. 1. Experimental (data points) and calculated (solid lines) electron attachment rate constants $k_a(E/N)$ for SF₆ in the buffer gases N₂, Ar, and Xe [From Ref. 5d].

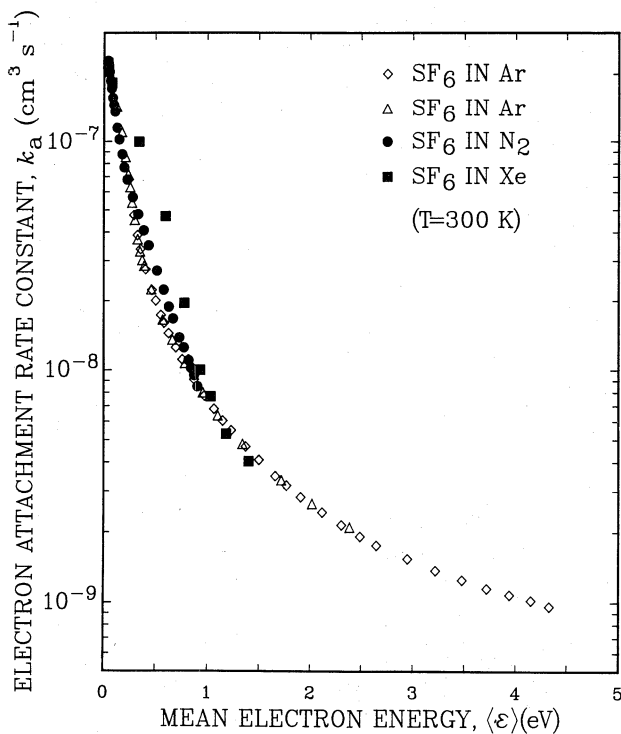


Fig. 2. k_a vs $\langle \epsilon \rangle$ for SF₆
measured^{5d} in mixtures with
N₂, Ar, and Xe.

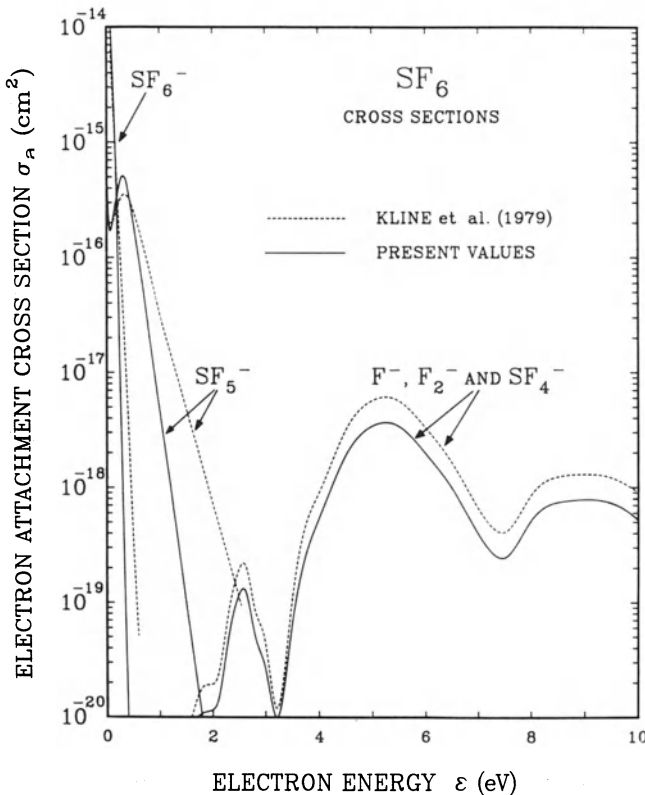


Fig. 3. $\sigma_a(\varepsilon)$ for SF₆⁻, SF₅⁻, and F⁻ + F₂⁻ + SF₄⁻ (see the text and Ref. 5d).

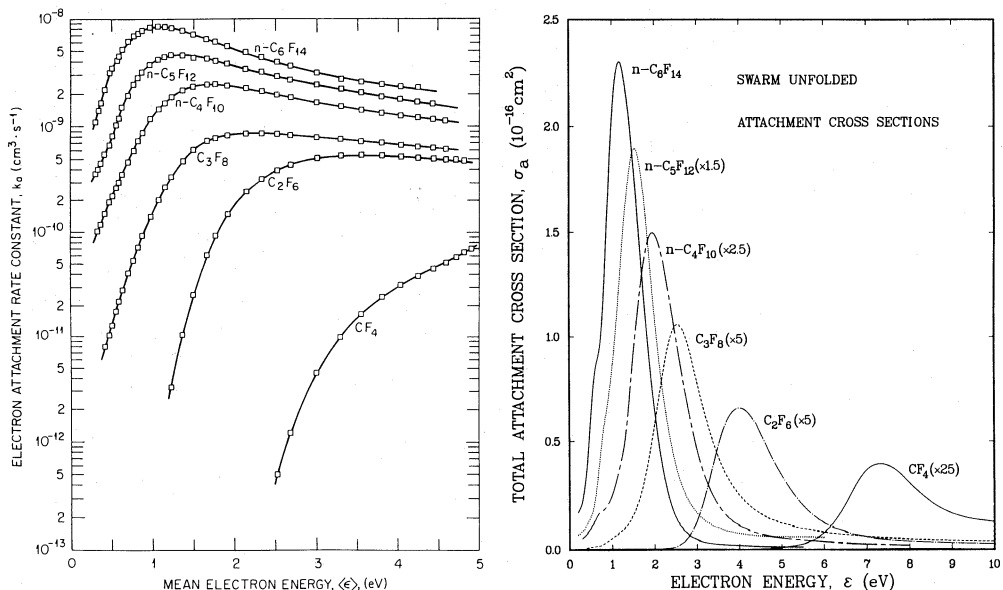


Fig. 4. $k_a(\langle \varepsilon \rangle)$ and $\sigma_a(\varepsilon)$ for the perfluoroalkane molecules n-C_NF_{2N+2} (N = 1 to 6) (From Ref. 5b).

due to parent anions, whose rate of formation delicately depends on N and temperature T (Fig. 5; see Ref. 5c and later this section). The small values of k_a at low $\langle\epsilon\rangle$ (low E/N) and the large values of k_a at high $\langle\epsilon\rangle$ (high E/N) make this group of molecules serious candidates as constituents in gas mixtures for diffuse discharge switches.⁸

(ii) Electron attachment to vibrationally/rotationally-excited ("hot") molecules

Low energy ($\lesssim 2$ eV) electron attachment processes can be extremely sensitive to gas temperature. As the internal energy of a gas molecule increases, delicate and often profound changes occur in its electron attaching properties which crucially depend on the molecule itself and the mode (dissociative or nondissociative) of electron attachment.^{4,5c,9-11}

For dissociative electron attachment, the rate constant/cross section generally increases with increasing internal energy of the molecule, i.e., with increasing T. From the view point of gas switches, of particular interest is the reported^{4,5c,9-11} sensitivity to T of the low-energy dissociative electron attachment processes in freons and halocarbons. In Fig. 6, are shown recent measurements¹⁰ of $\sigma_a(\epsilon, T)$ for the production of Cl^- from $\text{C}_2\text{H}_3\text{Cl}$. Especially interesting for switching purposes are molecules possessing very low-lying dissociative attachment resonances with a vertical onset behavior,⁴ since these are expected to show a profound increase of the dissociative attachment cross section with small increases in T above ambient temperature. This is clearly shown by our¹¹ preliminary measurements of $k_a(\langle\epsilon\rangle, T)$ for CH_3Cl (Fig. 7) (See also Ref. 12). Such a type of behavior would make such gases (or their mixtures with appropriate buffer gases) poorly electron attaching when cold ($\lesssim 300\text{K}$) and strongly electron attaching when "warm". The profound changes with T for molecules such as those in Figs. 6 and 7 indicate possible infrared laser photoenhanced attachment for these species.

For nondissociative electron attachment, the $k_a(\langle\epsilon\rangle, T)$ generally decreases with increasing internal energy of the molecule, i.e., with increasing T.⁹ Figure 8 shows examples of this type of behavior for c-C₄F₆ and c-C₄F₈ which are of interest as electronegative additives in gas switching mixtures.² The decrease in $k_a(\langle\epsilon\rangle, T)$ with increasing T can be due to a decrease in the cross section for formation and/or an increase in the autodetachment rate of the transient anions of these molecules. The precipitous decrease of electron attachment with increasing T affects (decreases) the dielectric strength of such gases and is potentially useful for pulsed power switching (see Refs. 2, 9g, and Section III).

When dissociative and nondissociative electron attachment processes occur concomitantly, over a common energy range, then $k_a(\langle\epsilon\rangle, T)$ and $\sigma_a(\epsilon, T)$ can increase or decrease with increasing T depending on the relative significance of the two processes.^{4,9} An example of this type of behavior is shown in Fig. 5c,d. The total attachment cross section deduced from these measurements are shown in Fig. 9a; they decrease with increasing T due to the depletion of the parent anions. If, however, the dissociative component of the measured rate constant is separated^{5c} from

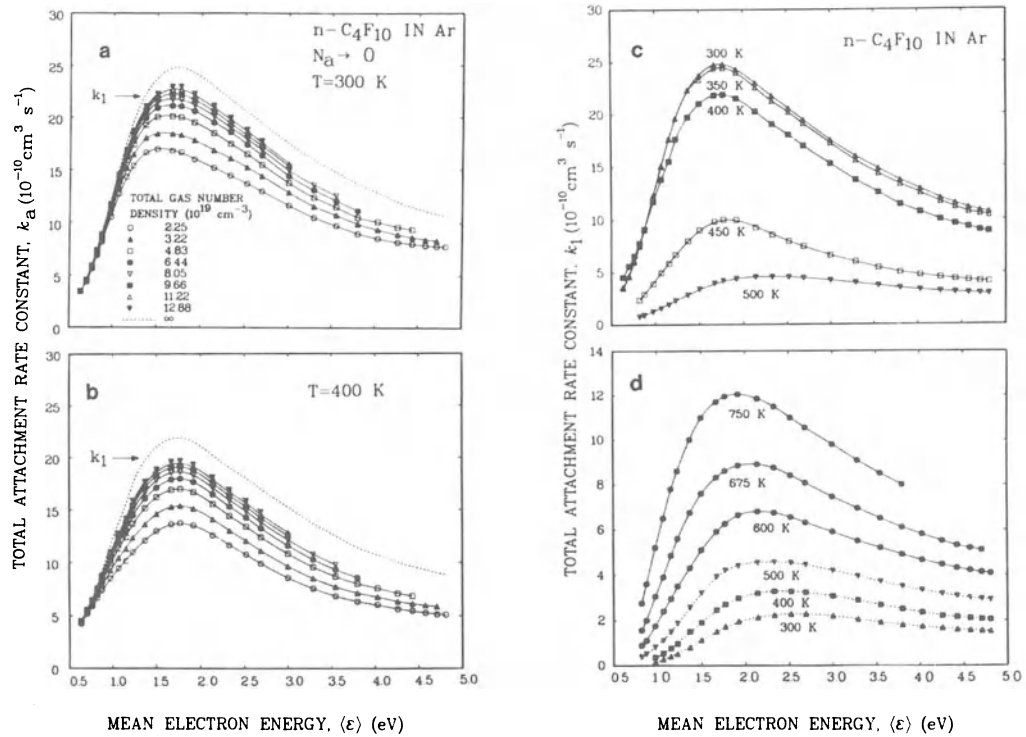


Fig. 5. Total electron attachment rate constant, k_a (for $N_a \rightarrow 0$), for $n\text{-C}_4\text{F}_{10}$ in Ar buffer gas versus mean electron energy, $\langle \epsilon \rangle$, at the indicated total gas number densities, N_t , for $T = 300\text{K}$ (Fig. 5a) and $T = 400\text{K}$ (Fig. 5b). The broken curves are the rate constants, k_1 , for $N_t \rightarrow \infty$. The $k_1(\langle \epsilon \rangle)$ at 300, 350, 400, 450, and 500K, are shown in Fig. 5c, and the $k_1(\langle \epsilon \rangle)$ for 600, 675, and 750K in Fig. 5d. The 300, 400, and 500K curves in Fig. 5d are the dissociative attachment components of the total rate constant k_1 at these temperatures [From Ref. 5c].

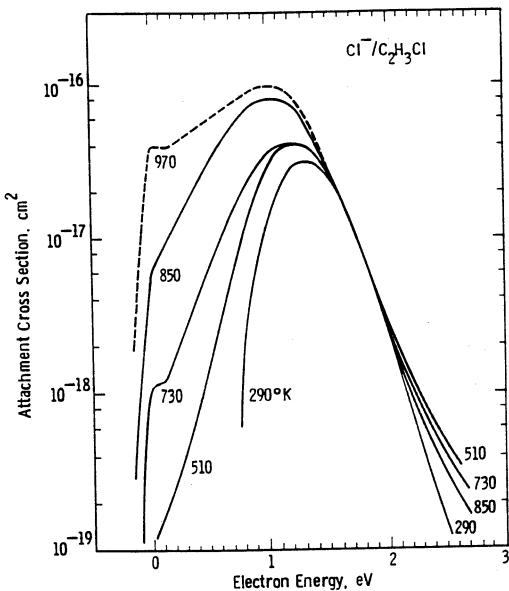


Fig. 6. $\sigma_a(\epsilon, T)$ for $\text{C}_2\text{H}_3\text{Cl}$. The data at 970K are uncertain due to thermal dissociation of the molecule [From Ref. 10].

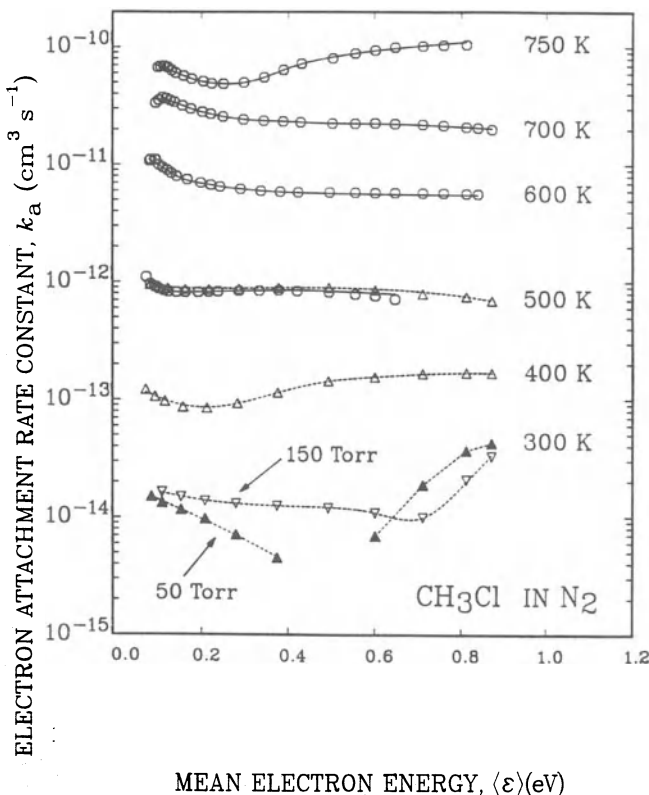


Fig. 7. $k_a(\langle\epsilon\rangle, T)$ for CH_3Cl [Ref. 11].

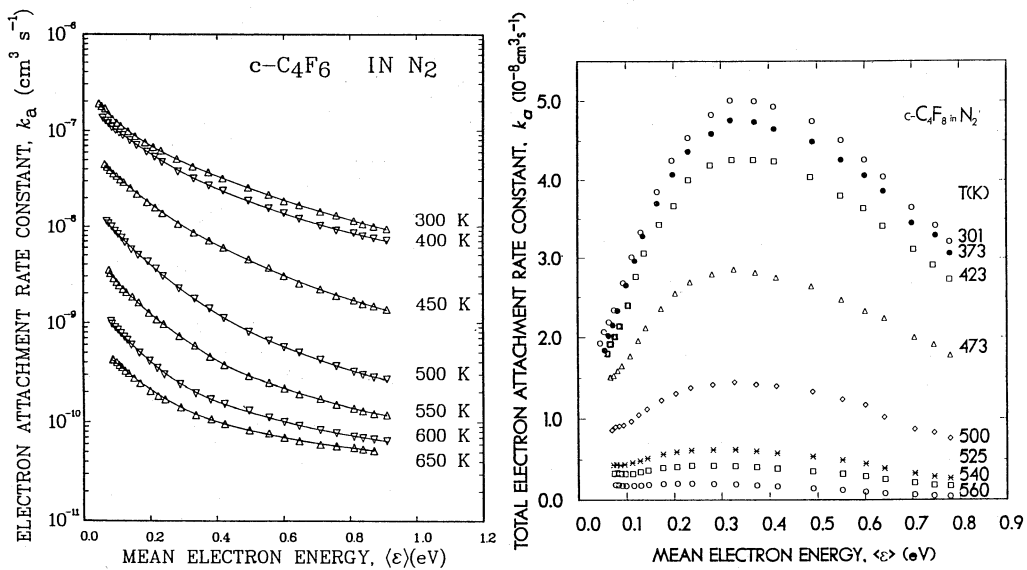


Fig. 8. $k_a(\langle\epsilon\rangle, T)$ for $c\text{-C}_4\text{F}_6$ [Ref. 9h] and $c\text{-C}_4\text{F}_8$ [Ref. 9c].

the nondissociative component, and the resultant rate constant due to dissociative attachment is used to unfold the dissociative attachment cross section as a function of T, $\sigma_{da}(\epsilon, T)$, these increase monotonically - as expected - with increasing T (Fig. 9b).

In the aforementioned examples the internal excitation of the molecules is nonselective. Direct or indirect laser-induced selective vibrational excitation of parent or fragment species leading to (optically) enhanced electron attachment has been observed in a number of cases (e.g., Ref. 13) and is useful in gas switching schemes.

(iii) Electron Attachment to Electronically-Excited Molecules

Electron capture in the field of an excited electronic state for very short times ($\lesssim 10^{-14}$ s) has long been known to occur as resonances in electron scattering and in dissociative electron attachment reactions.⁴ It has, also, been reported¹⁴ that long-lived (auto-detachment lifetimes $> 10^{-5}$ s) anions of the p-benzoquinone molecule can be formed in collisions with slow ($\sim 2\text{-}3$ eV) electrons whereby the initial kinetic energy of the colliding electron is almost entirely expended in exciting the molecule to its lowest excited (triplet) state with the resultant thermal electron being concomitantly captured by the so-produced electronically-excited molecule. The first example of dissociative electron attachment to pre-prepared electronically-excited molecules is that for O_2^* ($a^1\Delta_g$) produced in a microwave discharge.¹⁵

Electron attachment to electronically-excited molecules produced indirectly by laser irradiation has also been reported recently.¹⁶ In Fig. 10 are shown the observed large enhancements in the electron attachment coefficient η/N_a for thiophenol (C_6H_5SH) effected by UV excimer laser irradiation.^{16a} Curves 1 and 2 are the η/N_a for dissociative attachment to ground state molecules and curve 3 is the η/N_a for dissociative attachment to thiophenol molecules excited to their lowest triplet state populated indirectly by internal conversion from higher excited singlet states originally reached by laser light absorption. Curves 4 - 7 show the measured η/N_a for a double laser pulse experiment where the gas was excited by a laser pulse and electron attachment was measured 12 ms later when the attaching electrons were produced by a second similar laser pulse. This "delayed" photoenhanced electron attachment process occurred at times $> 100 \mu s$ after the first laser pulse and is much stronger than that for a single pulse.¹⁶ The single pulse attachment is due to dissociative electron attachment to thiophenol molecules in their lowest triplet state and occurs within a few μs of laser irradiation, while the "delayed" photoenhanced attachment is believed^{16b} to be due to electron attachment to diphenyl disulfide ($C_6H_5SSC_6H_5$) produced by the interaction of thiophenoxy radicals ($C_6H_5S^\cdot$) formed directly or indirectly via laser irradiation.

The limited knowledge to date in this area clearly shows that the cross sections for electron scattering by and electron attachment to electronically excited molecules far exceed those of the corresponding ground state molecules. The importance of such processes in pulsed power gas switches can not be overstated. Optical enhancement of electron attachment can, for example, form the basis for fast switching (or modulation) of the impedance (electronic conduction/insulation) properties of gaseous matter in the μs to the ns range.^{2,16} In this

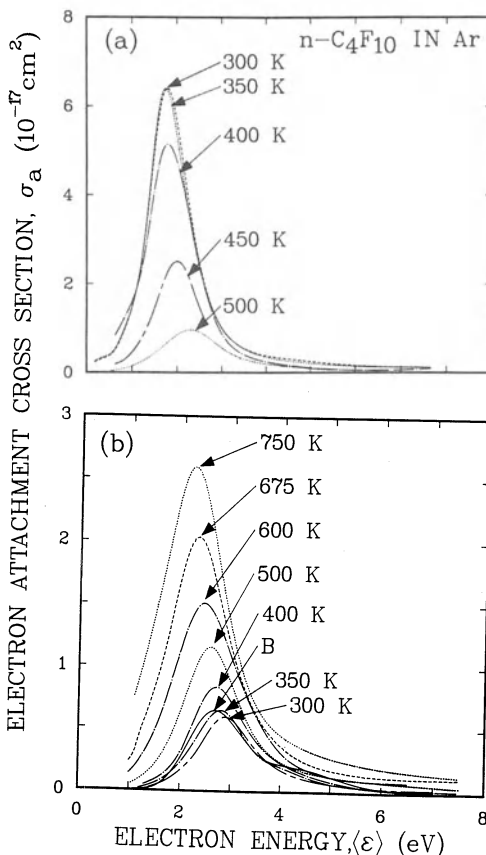


Fig. 9. The swarm unfolded total electron attachment cross sections $\sigma_a(\epsilon, T)$ for $n\text{-C}_4\text{F}_{10}$ at (a) 300, 350, 400, 450, and 500 K and (b) 600, 675, and 750 K. The 300, 350, 400, and 500 K curves (b) are the dissociative attachment cross sections at these temperatures [From Ref. 5c].

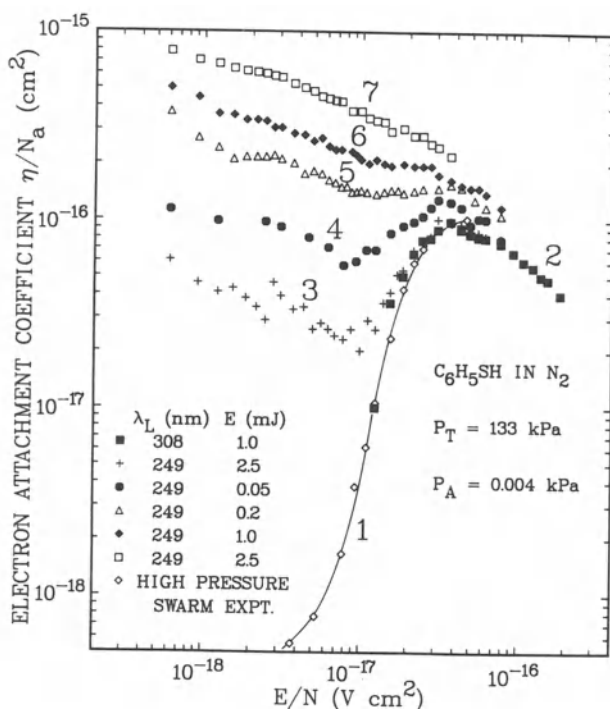


Fig. 10. Electron attachment coefficient, η/N_a vs E/N for C_6H_5SH in N_2 for the ground-state (curves 1 and 2) and the electronically excited (curves 3-7; curve 3 is for a single laser pulse, and curves 4-7 are for the double laser pulses) C_6H_5SH molecules. The values of the photoenhanced attachment are at least 100 times larger than shown since the number of excited attaching gas molecules is < 1% of those in the ground state, N_a [From Ref. 16a].

connection, the observation of photoenhanced electron attachment to short-lived electronic species (e.g., TMAE and TEA)^{16c} is most significant.

B. Electron Impact Ionization

The understanding and modeling of the gas discharge processes in gas switches requires knowledge not just on the electron loss, but also on the electron gain processes occurring in the discharge. In this regard, the physical quantities most commonly measured are the density-normalized electron impact ionization α/N and effective ionization $\bar{\alpha}/N = \alpha/N - \eta/N_a$ coefficients, measured as a function of E/N . In general, α/N does not depend strongly on either N or T, and the variation of $\bar{\alpha}/N$ with N and T normally reflects the variation of η/N_a with N and T (e.g., see Fig. 11).

Both α/N and $\bar{\alpha}/N$, however, depend rather strongly and delicately on E/N and knowledge of the magnitude and E/N dependence of these coefficients aid the tailoring of gaseous media for the various types of gas switches (Table 1) (e.g., see Refs. 2 and 8).

Two recent examples of α/N (E/N) and η/N (E/N) measurements^{17,18} are shown in Fig. 12 for BF_3 and SiF_4 . These two molecules possess dissociative electron attachment processes which have high energy onsets ($\gtrsim 10.0$ eV)¹⁷ and also relatively low $(E/N)_{lim}$ values (123×10^{-17} V cm² for BF_3 and 121×10^{-17} V cm² for SiF_4); the latter can be further lowered by small concentrations of low ionization onset (IO) additives (e.g., triethylamine, TEA; IO ≈ 7.5 eV) (see Fig. 12). Such gases and gas mixtures possessing low $(E/N)_{lim}$ values and $\bar{\alpha}/N$ which varies slowly with E/N near $(E/N)_{lim}$ (i.e., mixtures in which the rate of change of electron production and loss is minimal during small perturbations in E beyond $(E/N)_{lim}$) are ideal for use in new self-sustained diffuse discharge closing switching concepts^{2,18} since they can enhance the efficiency and the stability of the discharge.

C. Electron Drift Velocities/Scattering

The speed with which free electrons drift in a gas under an applied electric field affects the gas conductivity and the rates of electron gain and loss. The size of the electron drift velocity w is determined by the elastic and inelastic electron scattering properties of the gas and varies with E/N , T, and N (e.g., see Refs. 3a, 4a, 8, 17, and 19-21). Many investigations studied the dependencies of w on E/N , T, and N over broad ranges of values for a number of switch gases/mixtures.^{2,4,8} For the gas pressures (a few atmospheres or less) normally employed in gas switches, the collision mean free path ℓ is much larger than the electron de Broglie wavelength λ and hence the well-known^{4a,19} effects of N on w which occur--especially at low E/N --when $\ell \lesssim \lambda$ do not manifest themselves. However, w can vary with N at low N when electron gain and loss processes are significant. Such changes have been reported^{21b} for C_3F_8 and n-C₄F₁₀ for E/N regions where η/N becomes density dependent due to the formation of parent--along with fragment--negative ions in these gases.

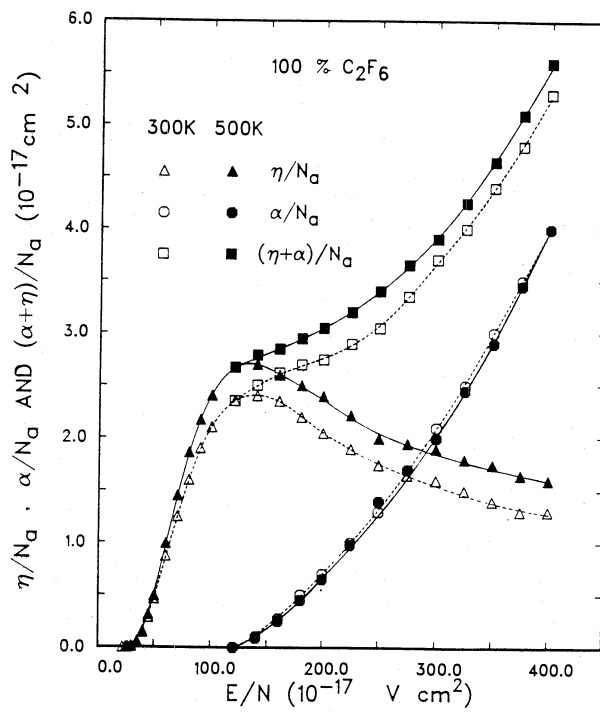


Fig. 11. Electron attachment coefficient η/N_a , electron impact ionization coefficient α/N_a and total ion production coefficient $(\eta+\alpha)/N_a$ of pure C_2F_6 at 300 and 500K as a function of E/N .

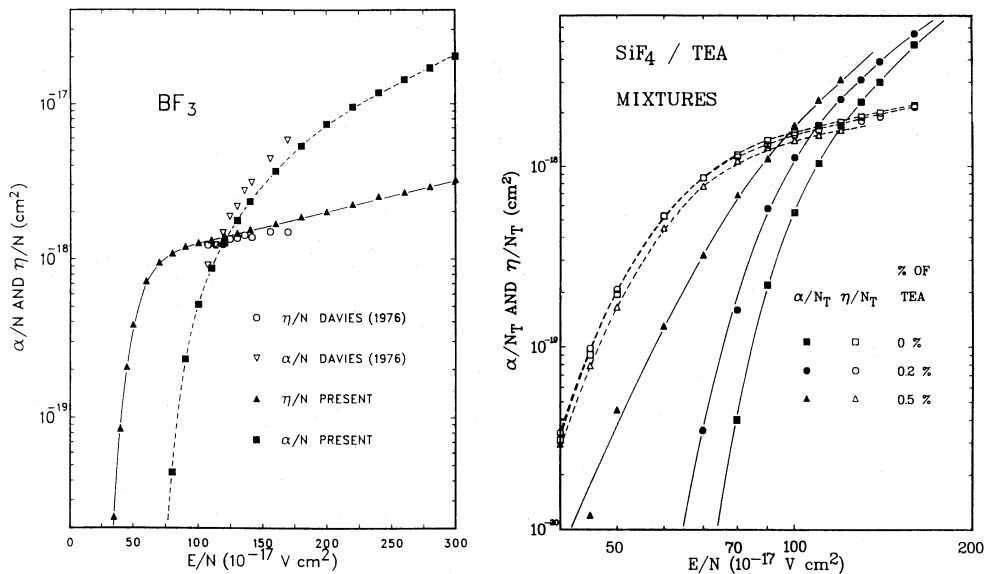


Fig. 12. $\alpha/N(E/N)$ and $\eta/N(E/N)$ for BF_3 [Ref. 17] and SiF_4 and SiF_4/TEA mixtures [Ref. 18].

From the point of view of gas switches, knowledge and control of the magnitude and E/N dependence of w are most significant. For example, in the case of externally-sustained diffuse discharge opening switches an electron drift velocity is required which maximizes at the (E/N)_{conduction} and which then falls off for higher E/N values. Studies

of electron motion in gases have shown^{2,4,8,21} that knowledge of the cross sections for elastic and inelastic processes in gases can be employed to identify gaseous media with enhanced drift velocities and/or specific w (E/N) dependencies. For example, it has been shown that for a number of molecular gases¹⁷ and gas mixtures^{8,21a} (e.g., Ar-CF₄, Ar-C₂F₆, Ar-C₃F₈, CH₄-CF₄), w can be enhanced and a rapidly increasing w with increasing E/N at relatively low E/N can be followed by a region of higher E/N values where w actually decreases with increasing E/N. The latter phenomenon--where w decreases with increasing E/N ($\partial w / \partial (E/N) < 0$)--has been termed negative differential conductivity (NDC) and roughly occurs when²²

$$\frac{\partial w}{\partial (E/N)} = \frac{A \epsilon_i}{2m w} \frac{\langle v_i \rangle}{\langle v_m \rangle} \left[\frac{1}{\langle v_i \rangle} \frac{\partial \langle v_i \rangle}{\partial (E/N)} - \frac{1}{\langle v_m \rangle} \frac{\partial \langle v_m \rangle}{\partial (E/N)} \right]$$

Here, v_i is the inelastic and $v_m(v) (= Nv\sigma_m(v))$ the momentum transfer collision frequency, ϵ_i is the energy loss for the inelastic process, and A is a slowly varying constant as a function of E/N with a value near unity. From the above approximate expression it is seen that an NDC effect will be observed when $\langle v_m \rangle$ rapidly increases and $\langle v_i \rangle$ rapidly decreases with increasing E/N.

In Fig. 13a, are shown examples of gases with distinct maxima in $w(E/N)$, very high values of w , and an NDC effect,^{8,21} and in Fig. 13b are shown mixtures of C₂F₆ in Ar exhibiting similar behavior. The latter measurements (see, also, Refs. 2 and 8) show that the maximum in $w(E/N)$ can be moved along the E/N axis by changing the concentration of the additive in Ar thus allowing flexibility in the tailoring of switching gas mixtures. The molecules CH₄, CF₄, and C₂F₆ are known to possess--as does Ar--Ramsauer-Townsend-type minima in their total electron scattering cross sections along with large vibrational excitation cross sections at electron energies of a few tenths of an eV.²³ The SiF₄ and BF₃ molecules may exhibit a similar cross section behavior¹⁷ in view of the $w(E/N)$ data in Fig. 13a.

III. EXAMPLES OF NEW GAS SWITCHING CONCEPTS BASED ON RECENT KNOWLEDGE OF ELECTRON COLLISIONS IN GASES

The specific, delicate, and frequently strong dependencies of η/N , α/N , and w on E/N, and of electron attachment on the internal energy content of switch gas molecules has recently led to a number of promising new switching concepts. Thus, the dependencies of k_a and w on E/N of a number of gases/mixtures which have the desirable properties listed in Table 1 for C (Column 3) has led to the identification of excellent gaseous media for externally-sustained diffuse discharge opening switches (Table 2, Column 3, Refs. 2 and 8). Similarly, since optically-enhanced

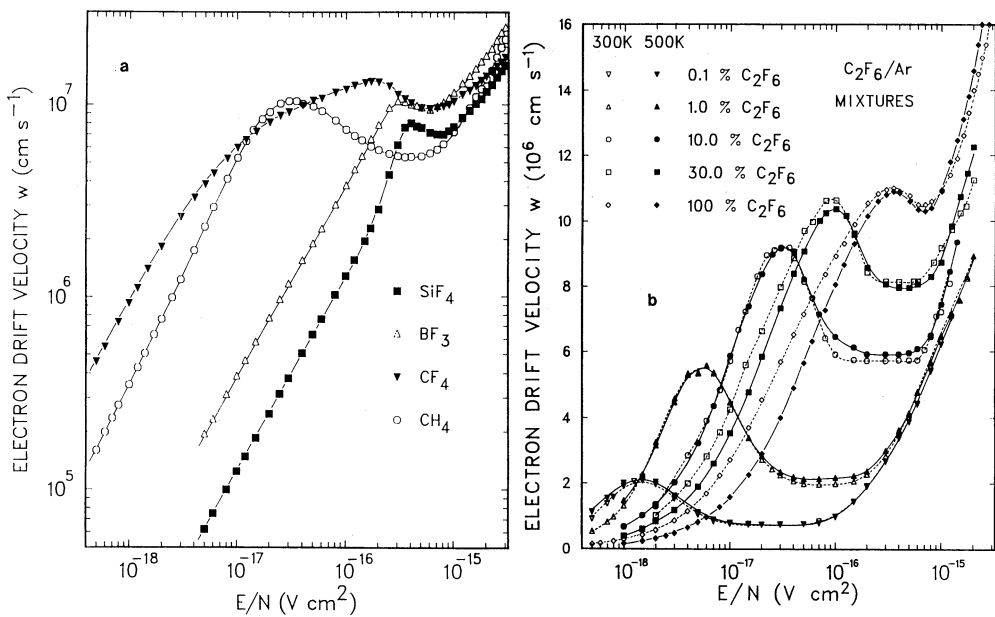


Fig. 13. (a) $w(E/N)$ for SiF_4 , BF_3 , CF_4 , and CH_4 ($T \approx 300\text{K}$; Ref. 17). (b) $w(E/N)$ for C_2F_6 and $\text{C}_2\text{F}_6/\text{Ar}$ mixtures at 300 and 500K.

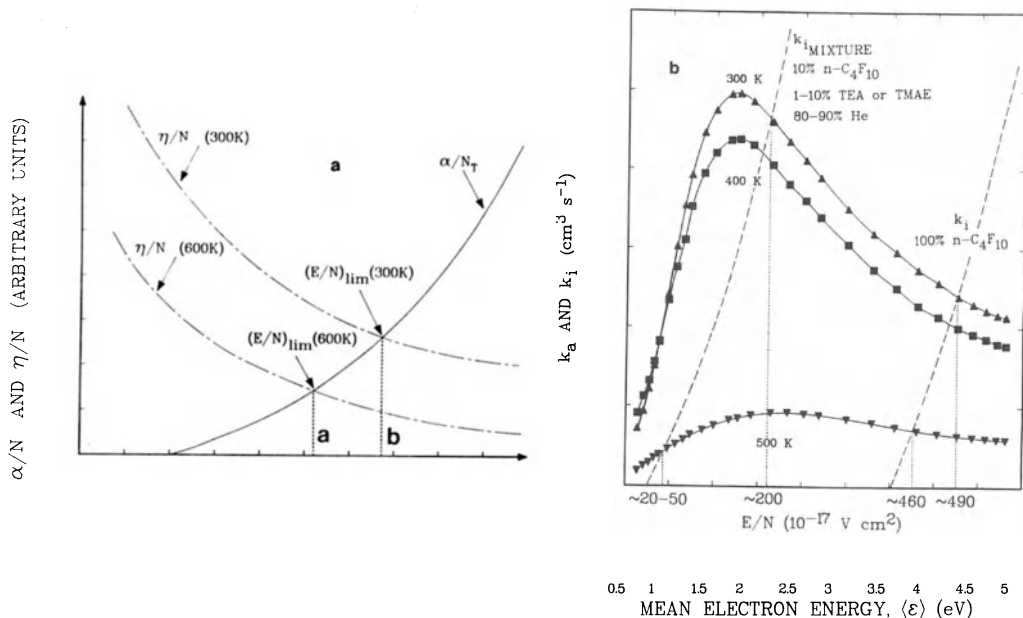


Fig. 14. (a) Schematic of the desirable η/N (E/N) and α/N (E/N) characteristics at 300 and 600K. The desirable $(E/N)_{lim}$ values at these temperatures are also indicated. (b) The approximate dependence of the rate constant k_a for attachment and k_i for ionization on $\langle\varepsilon\rangle$ and E/N in pure $n\text{-C}_4\text{F}_{10}$ and in a gas mixture composed of $\sim 10\%$ $n\text{-C}_4\text{F}_{10}$, 1-10% TEA or TMAE and the balance He [9h, 18].

electron attachment processes can allow a gas which is a conductor when it is not irradiated by a laser become an insulator when it is irradiated by a laser, and, conversely, since photodetachment of pre-formed negative ions can allow a gas which is an insulator when it is not irradiated by a laser to become a conductor when it is irradiated by a laser, the possibility exists of developing an optical switch whereby the electrical insulation/conduction properties of the gas are switched optically at ns times. While, in principle, these two mechanisms--optically-enhanced attachment and photodetachment--can be employed as discharge control mechanisms, more basic studies are required before an optical switch is realized.^{2,16,18,24}

Dielectric gases/mixtures (see Table 2, first column) which are excellent insulators when cold ($\sim 300K$) due largely to their large k_a at these T, and which become poorly electron attaching when warm (e.g., see Fig. 8) can be used to improve the efficiency of spark gap closing switches.^{9g} The efficiency of such devices is increased when the ratio V_c/V_s of the voltage V_c between the switch electrodes during the conducting stage and V_s during the insulating stage is reduced. The gases $c\text{-C}_4\text{F}_8$ and $c\text{-C}_4\text{F}_{10}$ are especially good additives in binary and ternary mixtures because at room temperature their V_s is high and because their $k_a(\langle\epsilon\rangle)$ are small at low E/N and high T.

The recent knowledge on $k_a(\langle\epsilon\rangle, T, E/N)$, $\eta/N_a(T, E/N)$, and $\alpha/N(E/N)$ on a number of gases/mixtures can possibly be used^{2,18} to increase the efficiency of self-sustained diffuse discharge closing switches (i.e., lower the voltage drop across the switch) and the stability of the discharge (i.e., increase the conduction time of the discharge to ~ 100 ns) during switch conduction. Two ways through which this can be done are depicted in Fig. 14a,b. The example in Fig. 14a refers to a gaseous medium (e.g., $c\text{-C}_4\text{F}_6$ in He) whose $k_a(\langle\epsilon\rangle)$ or $\eta/N_a(E/N)$ peaks at thermal energies ($T \approx 300K$) and decreases with increasing T above ambient. During the opening stage of the switch the gas is cold ($\approx 300K$) and the $(E/N)_{lim}$ is high (represented by b in Fig. 14a). During the conducting stage of the switch the energy dissipated in the gas can increase the internal energy of the attaching gas molecules, i.e., warm up the gas. This will decrease η/N_a , but it will not affect α/N and consequently the self-sustaining electric field of the discharge will decrease (dropping, say, to a value a as shown in Fig. 14a). Hence, the impedance of the discharge will be lowered and the switch efficiency increased.

Figure 14b depicts the principle of a second concept whereby a three-component system is employed: a rare gas buffer (e.g., He), a low-ionization onset ($\lesssim 8$ eV) additive (e.g., TEA or TMAE), and an electronegative gas (e.g., $n\text{-C}_4\text{F}_{10}$) whose k_a at room temperature peaks at $\epsilon \gtrsim 1$ eV, decreases considerably with increasing T, and its peak shifts to lower E/N as T increases. In Fig. 14b the k_a for $n\text{-C}_4\text{F}_{10}$ is plotted versus E/N (and $\langle\epsilon\rangle$; see also Fig. 5) along with the expected¹⁸ electron impact ionization rate constant $k_i(E/N)$ for $n\text{-C}_4\text{F}_{10}$. Addition of TEA or TMAE to a mixture of $n\text{-C}_4\text{F}_{10}$ in He will cause the $k_i(E/N)$ curve for the

Table 2. Examples of Candidate Gases for Three Types of Gas Switches
(See the text and cited literature.)

Spark Gap Closing	Diffuse Discharge Closing (Self-Sustained)	Diffuse Discharge Opening (Externally-Sustained)
c-C ₄ F ₈ or n-C ₄ F ₁₀ or C ₃ F ₈ in Ar or He or N ₂ or Ar + C ₂ H ₂ [†] or He + C ₂ H ₂ [†]	c-C ₄ F ₆ + He n-C ₄ F ₁₀ + He + TEA [†] SiF ₄ or BF ₃ in He or Ne or Ar or He, Ne, Ar, + TMAE [†]	C ₂ F ₆ or C ₃ F ₈ in Ar or CH ₄ or Ar + C ₂ H ₂ [†] or Ar + c-C ₄ H ₈ [†]

[†]Or other low ionization onset additive.

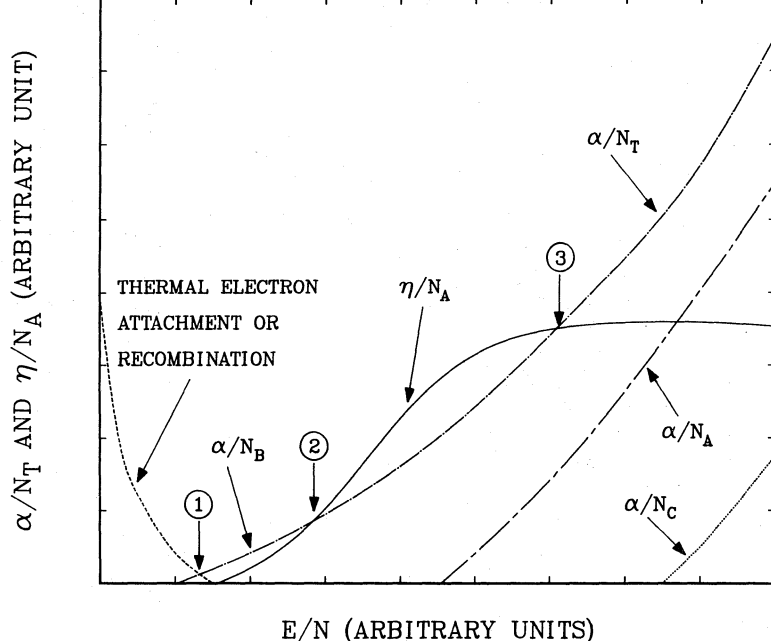


Fig. 15. The desirable η/N_A and α/N_T (N_T = total gas number density) characteristics of gas mixtures for efficient self-sustained diffuse discharge closing switches: α/N_A , α/N_B , and α/N_C , refer respectively to the ionization coefficient of the electron attaching, low IO additive and high IO buffer gases. Between regions 1 and 2 the total ionization coefficient α/N_T is larger than the attachment coefficient η/N_A while

between regions 2 and 3 η/N_A is larger than α/N_T . $\bar{\alpha}/N_T = 0$ at E/N values denoted by 1, 2, and 3 [From Ref. 18].

ternary mixture to move to lower E/N until for the appropriate concentrations of the components shown in Fig. 14b, the $k_i(E/N)$ for the mixture resembles that shown in the figure. The $(E/N)_{lim}$ for this mixture (Fig. 14b) is reduced from $\sim 200 \times 10^{-17} \text{ V cm}^2$ at $T \approx 300\text{K}$ to $\sim 20 \times 10^{-17} \text{ V cm}^2$ at $T = 500\text{K}$. If such an increase in T is manifested during the operation of the gas discharge, the switch efficiency would be enhanced.

Finally, specific E/N dependencies of α/N and η/N_a can be employed^{2,18}--in several ways--to improve the efficiency and stability of high current self-sustained diffuse gas discharges. Thus, the use of electronegative gases in which the $\bar{\alpha}/N$ near the $(E/N)_{lim}$ of the gas is minimal will enhance the stability of the discharge while the addition of a rare gas to the mixture will lower $(E/N)_{lim}$ and thus increase the switch efficiency. Also, it may be possible to tailor the $\alpha/N(E/N)$ and $\eta/N_a(E/N)$ of a gas mixture such that the gas is ionized and conducts at low E/N and is an insulator at higher E/N (see Fig. 15 and Refs. 2 and 18).

IV. CONCLUSION

Significant basic new knowledge on electron-molecule--especially on electron-excited molecule--collisions in switch gases has been methodically acquired recently, and is being successfully used to modify, control and/or modulate the insulation/conduction properties of gaseous matter and the development of pulsed power gas switches.

V. REFERENCES

1. Crudely speaking, a gas is a good conductor when the free electrons present in it remain free and have large drift velocities w, and it is a good insulator when w is small and virtually all the electrons present are attached forming negative ions. Thus, switching or modulating the conduction/insulation properties of gaseous matter largely involves switching or modulating the relative numbers of free and attached electrons.
2. See, for example, articles in: (a) L. G. Christophorou and M. O. Pace (Eds), Gaseous Dielectrics IV, Pergamon (New York, 1984), Chapter 5; (b) L. G. Christophorou and D. W. Bouldin (Eds), Gaseous Dielectrics V, Pergamon (New York, 1987), Chapter 7; (c) A. Guenther, M. Kristiansen, and T. Martin (Eds), Opening Switches, Plenum (New York, 1987); (d) P. J. Turchi and B. H. Bernstein (Eds), Proceedings of the 6th IEEE Pulsed Power Conference, Arlington, Virginia, IEEE Catalog Number 87CH2522-1, (1988).

3. See, for example, (a) L. G. Christophorou, Atomic and Molecular Radiation Physics, Wiley-Interscience, New York, 1971; (b) H. S. W. Massey, Negative Ions, Cambridge University Press, London, 1976; (c) B. M. Smirnov, Negative Ions, McGraw-Hill, New York, 1982.
4. (a) L. G. Christophorou (Ed), Electron-Molecule Interactions and Their Applications, Academic Press, New York, 1984, Volumes 1 and 2; (b) L. G. Christophorou, Plasma Physics 27, 237 (1987).
5. (a) S. M. Spyrou, I. Sauers, and L. G. Christophorou, J. Chem. Phys. 78, 7200 (1983); (b) S. R. Hunter and L. G. Christophorou, J. Chem. Phys. 80, 6150 (1984); (c) P. G. Datskos and L. G. Christophorou, J. Chem. Phys. 86, 1982 (1987); (d) S. R. Hunter, J. G. Carter, and L. G. Christophorou, J. Chem. Phys. 90, 4879 (1989).
6. L. E. Kline, D. K. Davies, C. L. Chen, and P. J. Chantry, J. Appl. Phys. 50, 6789 (1979).
7. A. Chutjian and S. H. Alajajian, Phys. Rev. A 31, 2885 (1985).
8. L. G. Christophorou, S. R. Hunter, J. G. Carter, and R. A. Mathis, Appl. Phys. Lett. 41, 147 (1982); S. R. Hunter, J. G. Carter, and L. G. Christophorou, J. Appl. Phys. 58, 3001 (1985).
9. (a) Ref. 4; (b) S. M. Spyrou, and L. G. Christophorou, J. Chem. Phys. 82, 1048 (1985); (c) A. A. Christodoulides, L. G. Christophorou, and D. L. McCorkle, Chem. Phys. Lett. 139, 350 (1987); (d) P. G. Datskos and L. G. Christophorou, J. Chem. Phys. 90, 2626 (1989); (e) S. M. Spyrou and L. G. Christophorou, J. Chem. Phys. 82, 2620 (1985); (f) S. M. Spyrou and L. G. Christophorou, J. Chem. Phys. 83, 2829 (1985); (g) L. G. Christophorou, R. A. Mathis, S. R. Hunter, and J. G. Carter, J. Appl. Phys. 63, 52 (1988); (h) L. G. Christophorou, S. R. Hunter, L. A. Pinnaduwage, P. G. Datskos, and J. G. Carter, Proc. IXth Intern. Conf. Gas Discharges and Their Applications, Venice, 19-23 Sept. 1988, p. 657.
10. P. J. Chantry and C. L. Chen, J. Chem. Phys. 90, 2585 (1989).
11. P. G. Datskos, L. G. Christophorou, and J. G. Carter (unpublished).
12. Z. Lj. Petrovic, W. C. Wang, and L. C. Lee, J. Chem. Phys. 90, 3145 (1989).
13. C. L. Chen and P. J. Chantry, J. Chem. Phys. 71, 3897 (1979); I. M. Beterov and N. V. Fateyev, J. Phys. (Paris) Colloq. C7-447 (1983); M. W. McGeorch and R. E. Schlier, Phys. Rev. A 33, 1708 (1986); M. J. Rossi, H. Helm, and D. C. Lorents, Appl. Phys. Lett. 47, 576 (1985).
14. L. G. Christophorou, J. G. Carter, and A. A. Christodoulides, Chem. Phys. Lett. 3, 237 (1969); 4, 646 (1970).
15. P. D. Burrow, J. Chem. Phys. 59, 4922 (1973).
16. (a) L. G. Christophorou, S. R. Hunter, L. A. Pinnaduwage, J. G. Carter, A. A. Christodoulides, and S. M. Spyrou, Phys. Rev. Lett. 58, 1316 (1987); (b) L. A. Pinnaduwage, L. G. Christophorou, and S. R. Hunter, J. Chem. Phys. 90, 6275 (1989); (c) Ref. 2d, p. 81.
17. S. R. Hunter, J. G. Carter, and L. G. Christophorou, J. Appl. Phys. 65, 1858 (1989).

18. S. R. Hunter, L. G. Christophorou, J. G. Carter, and P. G. Datskos, in Ref. 2d, pp. 1-8.
19. L. G. Christophorou, in The Liquid State and Its Electrical Properties, E. E. Kunhardt, L. G. Christophorou, and L. H. Luessen (Eds), Plenum Press, New York, 1988, p. 283.
20. S. R. Hunter, J. G. Carter, and L. G. Christophorou, *J. Chem. Phys.* 86, 693 (1987).
21. (a) L. G. Christophorou, D. L. McCorkle, D. V. Maxey, and J. G. Carter, *Nucl. Instr. Meth.* 163, 141 (1979); (b) S. R. Hunter, J. G. Carter, and L. G. Christophorou, *Phys. Rev. A* 38, 58 (1988).
22. Z. Lj. Petrovic, R. W. Crompton, and G. N. Haddad, *Austr. J. Phys.* 37, 23 (1984).
23. G. N. Haddad, *Austr. J. Phys.* 38, 677 (1985); M. Hayashi and A. Niwa in 2b, p. 27.
24. G. Schaefer and K. H. Schoenbach, *IEEE Trans. Plasma Sci.* PS-14, 561 (1986).

THEORY OF e^- - DIATOM SCATTERING AT LOW ENERGIES

E. Ficocelli Varracchio and U.T. Lamanna

Department of Chemistry
University of Bari
70100 Bari - Italy

I. INTRODUCTION

In this Lecture we want to consider e^- - diatom collisions, in the low energy regime, e.g. essentially vibrorotational excitation processes, taking place in the ground electronic state of the diatom. As pointed out in recent reviews on the subject¹⁻³, such a problem is of remarkable theoretical and technological relevance. Here we shall essentially be concerned with the theoretical aspects of such processes and, in particular, we shall mostly concentrate on a consideration of their "ab initio" treatment, along the lines explored in our research group, during the last few years.

The theoretical difficulties encountered in a quantum mechanical treatment of low energy e^- - diatom scattering are, essentially, of a twofold nature. These partly arise from the enforcement, as is common practice in the literature, of the Adiabatic (or Fixed Nuclei (FN)) approximation. This last one certainly represents a very convenient scheme, within which to perform computations, for the vibrorotational energy transfers of interest. Unfortunately, recent investigations have pointed out the breakdown of such approximation, even at impact energies several times the threshold of the process³. The second source of difficulty arises from the lack of any, well established, functional form for the "effective" potential, presiding over the full dynamical process. In particular, this should take into consideration the "response" of the target, to the external perturbing projectile, making full allowance for the possibility of exchange of this, with the target electrons. The full quantity of interest, is usually referred to, in the literature, as the "dynamical polarization" of the target¹⁻³.

In the following, we shall then briefly summarize the theoretical developments, recently proposed in our research group, in order to overcome the two types of limitations, mentioned above. In the first place, we shall

point out that an "off-shell" generalization of the FN approximation, is able to increase the range of validity of the corresponding dynamical scheme. This aspect will be analyzed in Section II. In Section III we shall outline, instead, the possibility of utilizing the many-body Green's function formalism, for the purpose of building up the required "dynamical polarization" potential. All relevant theoretical aspects will be illustrated, numerically, by explicit applications to the basic $e - H_2$ system. In Section IV we shall finally conclude with a consideration of some, yet unanswered, questions and an outline of possible future developments, of the formalism.

II. OFF-SHELL GENERALIZATION OF THE FIXED-NUCLEI APPROXIMATION

The FN approximation represents the generalization of the Born-Oppenheimer (BO) adiabatic criterion, to scattering situations. It was first suggested by Chase⁴, in nuclear physics, and later transferred to the area of e^- molecule processes. Details of all the relevant aspects of the formulation are readily available in recent reviews¹⁻³, on the subject, and will not be considered here. For our present purposes, we simply wish to stress that the FN scheme can be enforced to two different levels of approximation. These correspond to an adiabatic "freezing" of the rotational motion only, or of the full vibrorotational motion, respectively. In the following we shall consider the second situation, corresponding to a formulation of the e^- diatom, vibrorotational energy exchange process, according to

$$T_{k_f \alpha_f; k_i \alpha_i} \approx \langle \xi_{\alpha_f} | T_{k'_i; k_i}^e (\varepsilon_i; R) | \xi_{\alpha_i} \rangle \quad (1)$$

In eq. (1) the key quantity is represented by the T^e amplitude, on the right hand side (rhs). This pictures "elastic" scattering of the impinging electron, off a diatom, frozen in space at position R . Besides, $\varepsilon_i = k_i^2/2$ (in atomic units) represents the energy of the incident electron, and $|k'_i| = |k_i|$, with k'_i and k_f pointing in the same direction. Finally, the $|\xi_\alpha\rangle$ states stand for the vibrorotational functions of the target, with the "i" and "f" indices referring to the entrance and exit channels, respectively.

Equation (1) suffers from severe shortcomings, chief among which is the fact that it leads to cross sections that do not decrease to zero, as the scattering energy approaches the threshold of the process considered. For the purpose of remedying such a limitation of the FN picture and, more generally, in order to find higher order corrections to Chase's formulation, we have suggested, some time ago^{5,6}, the following generalization of eq. (1)

$$T_{k_f \alpha_f; k_i \alpha_i} \approx \langle \xi_{\alpha_f} | \exp(\hat{G}) T_{k_f; k_i}^e (\varepsilon_f, \varepsilon_i; R) | \xi_{\alpha_i} \rangle \quad (2)$$

We refer to the original papers, for a formal justification of (2). Here we simply point out that such a relationship follows, in an "ab initio" fashion, from a rearrangement of the resolvent operator, presiding over the e^- diatom scattering process. It will be noticed that (1) and (2)

have, essentially, the same formal structure, implying that the evaluation of either of them will involve, roughly, the same amount of numerical work. In spite of this, the two expressions are quite dissimilar. The first difference, between them, follows from the fact that the T^e , electronically elastic scattering amplitude, appears "off-the-energy-shell", in (2), (as shown by its dependance on both the ε_i and ε_f , initial and final channel energies, respectively). The second new aspect of (2) is due to the appearance of the " $\exp(\hat{C})$ " operator that, as pointed out in the original derivation of the theory, introduces "nuclear relaxation effects". The " \hat{C} " operator is defined, in detail, by

$$\hat{C} = - \left[\hat{P}_N^2/2\mu - (\omega_{\alpha_i} - E_i) \right] \frac{d}{d\varepsilon_i} \quad (3)$$

with \hat{P}_N the nuclear kinetic energy term, ω_{α_i} the initial vibrorotational target energy and E_i the (target) BO electronic energy. For the purpose of performing numerical applications, the exponential operator, in (2), must be expanded. A convenient grouping of terms, then leads to

$$\begin{aligned} T_{K_f \alpha_f; K_i \alpha_i} &\simeq \langle \xi_{\alpha_f} | T_{K_f; K_i}^e(\varepsilon_f, \varepsilon_i; R) | \xi_{\alpha_i} \rangle + \\ &+ \langle \xi_{\alpha_f} | \left[\hat{C} + \frac{\hat{C}^2}{2} + \dots \right] T_{K_f; K_i}^e(\varepsilon_f, \varepsilon_i; R) | \xi_{\alpha_i} \rangle = \\ &= T_{K_f \alpha_f; K_i \alpha_i}^{FN}(\varepsilon_f, \varepsilon_i) + T_{K_f \alpha_f; K_i \alpha_i}^{res}(\varepsilon_f, \varepsilon_i) \end{aligned} \quad (4)$$

with T^{FN} (first term of the second equality, in (4)) representing the off-shell generalization of Chase's theory and T^{res} containing the full effect of the \hat{C} (nuclear relaxation) operator. It should be stressed, at this point, that, actually, the $T_7^{FN}(\varepsilon_f, \varepsilon_i)$ approximation had already been suggested by Shugard and Hazi, prior to the development of the more general expression (4). As for the T^{res} term (rightmost contribution in (4)), it has been argued (see Ref. 6) that this should contribute, mostly, to vibrational processes, taking place through a resonant mechanism. More at this regard will be said in Section IV.

Up to the time of writing, only the T^{FN} term, of (4), has been enforced, for e- diatom scattering calculations (see, however, Ref. 8, for an analysis of the contribution of T^{res} , in the case of heavy-particle collisions). We shall then present selected numerical results, relative to both rotational and vibrational processes, with the purpose of testing the reliability of the T^{FN} , off-shell approximation. It is important to stress that the problem of a correct representation of the "dynamical response" of the target (mentioned in the Introduction), has been set aside, for the time being. In the remaining portion of the present Section, we shall then only concentrate on a comparison of FN results, with "exact" Close Coupling (CC) values. In this spirit we consider, in Fig. 1, theoretical results, for the $0 \rightarrow 2$ rotational excitation cross section, for the e- H_2 system.

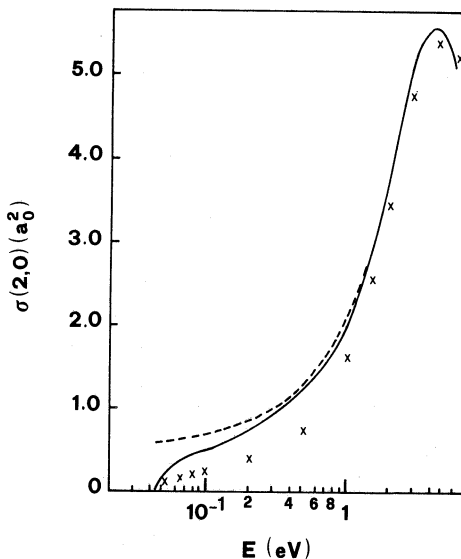


Fig. 1 Total cross sections for the $0 \rightarrow 2$ rotational excitation process: —, off-shell results of the present theory; - - -, on-shell results; x, CC values of Morrison et al. (Ref. 10)

The FN, on- and off-shell values (dashed and full curves, respectively), in the Figure, have been obtained using a Static-Exchange approximation, augmented by a semiempirical polarization potential⁹. The CC results (crosses, in the Figure), have been calculated, independently, by Morrison and coworkers¹⁰. In particular, these authors have used a similar form of the interaction potential, but they have approximated exchange, in the spirit of the free-electron-gas model. The first interesting point, brought out by the results, of Fig. 1, corresponds to the fact that the off-shell cross section correctly goes to zero, as the threshold for the process (at about 0.044 eV) is approached. Besides, the two curves, in the Figure, clearly point out that the two types of adiabatic calculations (on- and off-shell), actually start merging only above 1 eV, e.g. at energies more than 20 times the threshold of the process. In order to make the comparison with CC more quantitative, we have next tried to "scale" our off-shell values, so as to account for differences in the interaction potentials, characteristic of the two calculations. The scale factor (a different one for each energy) has been obtained by taking the ratio of the FN on-shell results of Morrison, onto the corresponding values obtained by us (see Ref. 9, for details). The FN off-shell results (full curve in the Figure) can then be multiplied by such scale factors, leading to the numerical values of Table 1. The very good agreement, of the two sets of cross sections, is then a clear indication of the fact that the FN off-shell scheme can reliably be applied, to rotational excitation processes. This is further confirmed by more extensive computations, for both total and differential rotational excitation cross sections, performed on the $e^- - H_2$ system⁹ and by more detailed analysis, on different diatomic targets, performed by Morrison³.

Table 1. Total cross sections for the $0 \rightarrow 2$ rotational process:
 the close coupling (CC) results have been obtained by
 Morrison et al. (Ref. 10). Off-shell are the present
 results, properly scaled (see text), in order to account
 for the different interaction potentials of the two
 computations.

E(eV)	CC	Off-shell
0.047	0.058	0.088
0.050	0.082	0.117
0.065	0.151	0.184
0.080	0.192	0.217
0.1	0.234	0.248
0.2	0.378	0.355
0.5	0.714	0.793
1.0	1.619	1.629
1.5	2.557	2.564
3.0	4.742	4.727

It is interesting to investigate, at this stage, what is the basic mechanism through which the off-shell constraint is able to lead the FN approximation, towards a correct dynamical picture, of the rotational process. In order to clarify this aspect, we have to consider, in more detail, the angular momentum transfers, in the system. This can conveniently be analyzed, by rewriting the total (rotational) cross section, in terms of its single partial wave components, according to

$$G_{j_f j_i} = (4\pi/\kappa_i^2) \sum_{\ell \ell'} (-)^{\ell - \ell'} G_{j_f j_i}(\ell', \ell) \quad (5)$$

The amplitudes, on the rhs of (5), depict the single contributions, deriving from angular momenta "1" and "1'", in the entrance and exit channels, respectively. For the $0 \rightarrow 2$ rotational excitation process, the most important terms are found to be the $G(0,2)$ and $G(1,1)$ quantities, that are plotted in Fig. 2, for both the on-shell and off-shell approximations. It can then be noticed that, while in the conventional, on-shell, approach the p-wave ($l=1 \rightarrow l'=1$) represents the dominant effect, over the whole energy range, in the more sophisticated off-shell theory the d \rightarrow s transition is, by far, the leading term, in the threshold region. On the other hand, CC computations confirm that, for a small residual energy of the scattered electron, only s-waves should be allowed in the outgoing channel^{10,11}. This then shows that a FN, off-shell, formalism is able to account for the finer details, of more sophisticated coupled theories.

We would finally like to spend a few words on the application of the off-shell formalism, in eq. (4), to vibrational excitation processes. We would expect, in such a situation, that the T^{res} amplitude (rightmost term

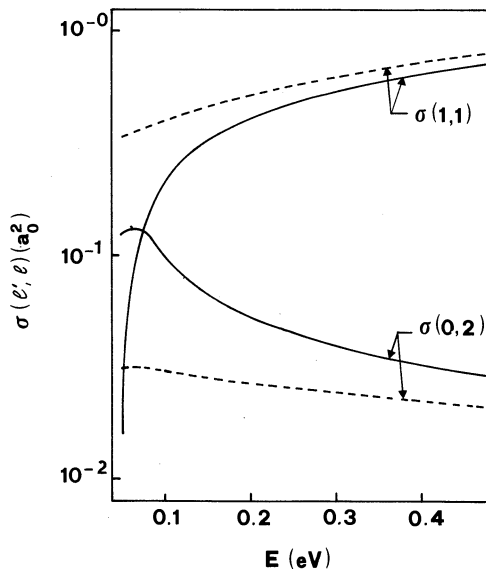


Fig. 2 Partial wave contributions to the total cross section for the $0 \rightarrow 2$ rotational excitation process: — off-shell FN approximation; - - - on-shell FN approximation.

in (4)), should make a non negligible contribution to the vibrational nuclear dynamics⁶. Unfortunately, this term has not yet been included in explicit numerical calculations, so that the only numerical applications are based on the T_{FN}^{12} , off-shell, amplitude, as in the case of rotational processes. Computations for vibrational processes have been performed by Morrison and coworkers¹², again for the $e - H_2$ system (the relevant formulation has been called "First-Order Non-Degenerate Adiabatic" theory, or FONDA, by such authors). The results obtained show a quantitative agreement of the off-shell formulation, with the full CC calculations. We believe that such a lucky situation will not hold for all diatomic targets and that, in general, the contribution of the T_{res} term, in eq. (4), will have to be considered, for vibrational processes. We shall spend a few more words, at this regard, in Section IV. Here we would like to summarize the situation by saying that, on the basis of the numerical results so far obtained, the off-shell formalism, (4), definitely seems to contain all the correct physical ingredients, necessary for performing accurate calculations, for $e -$ diatom systems. A similar formulation has also been applied to heavy-particle collisions, for both the subreactive^{13,14} and rearrangement regimes¹⁵, leading, in all cases considered, to good agreement with the results of more sophisticated theoretical calculations.

III. AB INITIO "DYNAMICAL RESPONSE" OF THE TARGET

In the previous Section we have shown that the FN off-shell scheme

represents a correct kinematical "picture", within which to formulate e⁻- diatom energy transfer processes. The determination of the correct "effective potential", presiding over the full dynamical process, is still an open problem, that we shall address in the present Section.

Target polarization effects, in e⁻- diatom scattering, represent a very important contribution to the full interaction potential. The first few phenomenological approaches, to this quantity, were based on the well known asymptotic form of the polarization potential, modulated by a (parameter dependant) cut-off function¹. Such a crude approximation was soon shown to be inadequate for realistic calculations, so that much work has been undertaken¹⁶⁻²¹ in order to obtain an "ab initio" representation of this interaction²². On the other hand, from a formal point of view, it is well known, since the pioneering paper of Bell and Squires²², that the full answer to such a problem is offered by the, so called, "self-energy operator", Σ ²³, characteristic of the many-body Green's function formalism²³. From a physical point of view, Σ contains full information on all possible energy exchange mechanisms, that finally leave the target into its initial (usually the ground) electronic state. The Σ "optical potential"^e is, then, just the basic quantity required for a determination of the T^e (off-shell) electronically elastic amplitude, of the previous Section. Once Σ has been determined, the T^e amplitude can most conveniently be evaluated by solving the conventional Lippmann-Schwinger equation

$$T^e = \Sigma + \Sigma G_0 T^e \quad (6)$$

The problem of evaluating the dynamical response of the diatomic target can then be reduced to a determination of some (possibly non perturbative) approximation scheme to Σ . The first move in this direction, for collisional problems involving diatomic targets, was taken by Klonover and Kaldor¹⁶, who used a perturbative representation of Σ , up to second order terms. On the other hand, similar scattering calculations, involving atomic targets, had clearly pointed out that a much more sensible approximation to Σ could be obtained, by means of a non perturbative representation, based on a solution of "two-particle" (Bethe-Salpeter) equations²⁴. In the language of Feynman diagrams, this corresponds to a full summation of the Random Phase Approximation (RPA) series of "bubble" diagrams²³. The calculations of Klonover and Kaldor, mentioned above, were just based on a consideration of the first diagram, in such a series. The RPA formulation seemed, therefore, a likely candidate for a useful representation of the dynamical polarization effects. At the same time, before proceeding to numerical applications, two "drawbacks" of the formalism (as it had been proposed, in the literature) had to be overcome. The first of these is relevant to the fact that Bethe-Salpeter type of equations are not very common, in more conventional scattering formulations. It would be very convenient, therefore, to try to reformulate the RPA scheme, in terms of (much easier to solve) single-particle equations. The second aspect follows from the fact that, in the RPA atomic calculation, mentioned above²⁴, only "singlet" excited states of the target, contributed to a representation of the optical potential. This would be, obviously, a severe limitation, in the

case of diatomic targets, since it is well known that "triplet" excited states play a central role, in the low energy electronic spectroscopy, of such systems²⁷. We have examined such limitations of the many-body formalism and we have found that both aspects, mentioned above, can actually be overcome^{25-26,28}. While we refer to the original literature for details at this regard, here we would simply like to summarize the corresponding final working equation, for the optical potential, in the RPA approximation

$$\begin{aligned} \Sigma^{\text{RPA}}(\varepsilon_i) = & V_N + \sum_{\alpha \leq F} \langle \Psi_{\alpha}^{\text{HF}} | \Gamma_o | \Psi_{\alpha}^{\text{HF}} \rangle + \\ & + \frac{1}{2} \sum_{\alpha \leq F} \sum_{j > F} \sum_{\ell} \frac{\langle \Psi_{\alpha(j)}^{\text{RPA}} | \Gamma_o | \Psi_{j(\alpha)}^{\text{RPA}} ; \Psi_{\ell}^{\text{HF}} \rangle \langle \Psi_{\ell}^{\text{HF}} ; \Psi_{j(\alpha)}^{\text{RPA}} | \Gamma_o | \Psi_{\alpha(j)}^{\text{RPA}} \rangle}{\varepsilon_i - (\varepsilon_{j(\alpha)}^{\text{RPA}} - \varepsilon_{\alpha(j)}^{\text{RPA}} - i\eta) [\Theta(\ell-F) - \Theta(F-\ell)] - \varepsilon_{\ell}^{\text{HF}}} \quad (7) \end{aligned}$$

In (7), F refers to the Fermi level of the target, while HF (Hartree-Fock) and RPA superscripts denote the approximation to the corresponding single-particle orbitals, whose energies appear at denominator of the same expression. Besides, V_N represents the nuclear interaction term, while Γ_o is the "antisymmetrized" e⁻ e⁻ Coulomb interaction, given in detail by

$$\Gamma_o(z_1 z_2, z_3 z_4) = V(z_1, z_2) [\delta(z_1 - z_3) \delta(z_2 - z_4) - \delta(z_1 - z_4) \delta(z_2 - z_3)] \quad (8)$$

By using (8) in (7), the RPA potential (rightmost term in (7)), generates four contributions, which are pictured in Fig. 3. In particular, a more detailed spin analysis would readily show that the contribution of triplet excited states is associated with the diagram in Fig. 3(c). Besides, if the RPA, single-particle orbitals, in (7), are replaced by the corresponding HF, unperturbed functions, the second order potential of Klonover and Kaldor is immediately obtained.

The Σ^{RPA} optical potential, (7), has been used in (6) and total elastic cross sections have correspondingly been evaluated^{26,28}. The results obtained are illustrated in Fig. 4, showing that the theory is certainly able to lead, once the contribution of vibrational excitation will be included, to quantitative agreement with experiment.

In summary, we would like to say that the build up of the Σ^{RPA} approximation can be performed, for more complex diatomic targets, with a computational effort comparable to that involved in the case of the H₂ system. Equation (7) then represents the required "ab initio" functional form of the dynamical polarization potential, characteristic of e⁻ diatom processes.

IV. FUTURE DEVELOPMENTS OF THE THEORY

We would like to conclude this Lecture by pointing out some aspects,

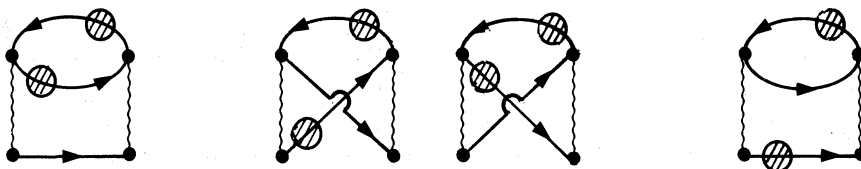


Fig. 3 Diagrammatic representation of the four terms contributing to "dynamical polarization" (see eq. (7)). The full curves, with and without a hatched circle, picture RPA and HF orbitals, respectively. Wavy lines represent the Coulomb potential V . The interpretation of the diagrams is as follows: (a) "direct" contribution to polarization effects; (b) "single" exchange mechanism; (c) "double" exchange mechanism.

of the present formalism, that, in our opinion, still need further clarification. The first of these is relative to the role played by the T^{res} term, in (4). Apparently, the contribution of this amplitude was not needed, for the H_2 target. On the other hand, it is well known that vibrational excitation, for H_2 , takes place through a \sum_u^{2+} compound state, characterized by a very short lifetime. As this increases (as for example in the case of the N_2 and O_2 targets), we should expect that T^{res} will make a non negligible contribution (see Ref. 6 for an interpretation of T^{res} in terms of the lifetime of the compound intermediate state). The question then remains if the series expansion defining T^{res} (see (4)) is convergent, at all, or whether useful numerical techniques can be found (e.g. Padé approximants, Borel summations,...) in order to extract some physical information, from it. Should this be the case, then the FN off-shell formalism will be completely applicable, to low energy e^- - diatom processes, in both the resonant and non resonant regimes.

We would next like to draw the attention on some recent, rather peculiar, experimental results, that the present formalism may possibly contribute to clarify. These correspond to the huge peaks, observed at threshold of vibrational excitation processes, for polar systems^{29,30}. An explanation of these, through a resonant mechanism, would require a centrifugal barrier ($l > 0$), in the effective potential, for the resonant symmetry. Contrary to such expectations, the differential cross sections are found to be isotropic, implying s-wave scattering. More details, at this regard, can be found in a recent review by Morrison³. On the other hand, we have seen, in Section II, that the off-shell constraint contains dynamical features, characteristic of Coupled theories. It is then likely that such an aspect of the present formalism, together with a sophisticated, Σ^{RPA} , treatment of the interaction potential, may contribute towards an understanding of such interesting features, in the cross sections.

To conclude, we finally mention that the Ψ^{RPA} single-particle states and ε^{RPA} , corresponding energies, involved in the construction of Σ^{RPA} , can be readily used to extract information on the target's electronic excited states³¹. This then immediately opens up the possibility of extending the formalism, to perform theoretical studies of the electronic excitation (by e^- impact) of diatomic targets, which is still a rather unexplored area.

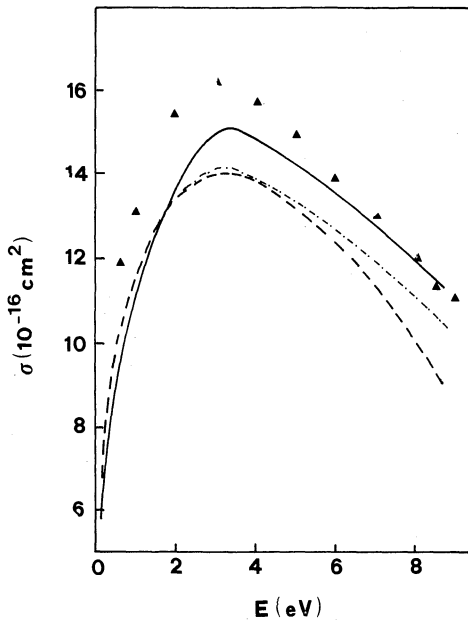


Fig. 4 Total elastic cross sections for the $e - H_2$ system:
 — Σ_{RPA} optical potential (eq. (7)), including
 both singlet and triplet target excited states;
 - - - Σ_{RPA} optical potential, including singlet
 excited states only; - - - perturbative (second order)
 values of Klonover and Kaldor (Ref. 16); ▲, expe-
 rimental results of Jones (Ref. 32).

REFERENCES

1. N.F. Lane, Rev. Mod. Phys. 52:29 (1980).
2. Gy. Csanak, D.C. Cartwright, S.K. Srivastava and S. Trajamar, in "Electron-Molecule Interactions and Their Applications", L.G. Christophorou ed., (Academic Press, N.Y.), 1:2 (1984).
3. M.A. Morrison, Adv. At. Mol. Phys. 24:51 (1988).
4. D.M. Chase, Phys. Rev. 104:838 (1956).
5. E. Ficocelli Varracchio, Lett. Nuovo Cim. 30:133 (1981).
6. E. Ficocelli Varracchio, J. Phys. B 14:L511 (1981).
7. M. Shugard and A.U. Hazi, Phys. Rev. A12:1895 (1975).
8. E. Ficocelli Varracchio and R. Celiberto, Chem. Phys. 68:303 (1982).
9. E. Ficocelli Varracchio and U.T. Lamanna, J. Phys. B17:4395 (1984).
10. M.A. Morrison, A.N. Feldt and D. Austin, Phys. Rev. A29:2518 (1984).
11. N.F. Lane and S. Geltman, Phys. Rev. 160:53 (1967).
12. M. Abdolsalami and M.A. Morrison, Phys. Rev. A36:5474 (1987).
13. E. Ficocelli Varracchio, Chem. Phys. Lett. 83:324 (1981).
14. E. Ficocelli Varracchio, Chem. Phys. Lett. 117:609 (1985).
15. E. Ficocelli Varracchio, Chem. Phys. 74:153 (1983).
16. A. Klonover and U. Kaldor, J. Phys. B11:1623 (1978).
17. B.I. Schneider and L.A. Collins, J. Phys. B15:L335 (1982).
18. C.J. Noble, P.G. Burke and S. Salvini, J. Phys. B15:3779 (1982).
19. K. Onda and A. Temkin, Phys. Rev. A28:621 (1983).
20. T.L. Gibson and M.A. Morrison, Phys. Rev. A29:2497 (1984).
21. T.L. Gibson, M.A. Lima, K. Takatsuka and V. McKoy, Phys. Rev. A30:3005 (1984).
22. J.S. Bell and E.J. Squires, Phys. Rev. Lett. 3:96 (1959).
23. A.L. Fetter and J.D. Walecka, "Quantum Theory of Many-Particle Systems" McGraw-Hill Book Co., New York (1971).
24. B.S. Yarlagadda, Gy. Csanak, H.S. Taylor, B. Schneider and R. Yaris, Phys. Rev. A7:146 (1973).
25. E. Ficocelli Varracchio, J. Phys. B17:L611 (1984).
26. E. Ficocelli Varracchio and U.T. Lamanna, J. Phys. B19:3145 (1986).
27. G.J. Schulz, rev. Mod. Phys. 45:423 (1973).
28. E. Ficocelli Varracchio, U.T. Lamanna and G. Petrella, J. Phys. B20:L765 (1987).
29. K. Rohr and F. Linder, J. Phys. B8:L200 (1975).
30. K. Rohr, in "Symposium on Electron-Molecule Collisions", I. Shimamura and M. Matsuzawa eds., University of Tokyo, Tokyo (1979).
31. E. Ficocelli Varracchio, in "Atomic Physics with Positrons", J.W. Humberston and E.A.G. Armour eds., NATO ASI Series, B169, Plenum, New York (1987).
32. R.K. Jones, Phys. Rev. A31:2898 (1985).

A PARAMETER-FREE THEORETICAL MODEL FOR LOW-ENERGY ELECTRON SCATTERING FROM
POLYATOMIC MOLECULES

F.A. Gianturco and S. Scialla

Department of Chemistry
The University of Rome
Città Universitaria, 00185 Rome, Italy

INTRODUCTION

In the last fifteen years or so an enormous amount of work has been carried out in the field of low-energy electron-molecule collision theory and the increase of experimental activity has not lagged behind the dramatic expansion of theoretical treatments.

The reasons for the success of this particular field of molecular physics (or of chemical physics) are related to the vast number of collision processes which can take place when an electron collides with a molecule and therefore to the rather wide audience, within the scientific community, that can be interested in them.

We know, for instance, that rearrangement processes like dissociative attachment, ionization and dielectronic recombination are likely to occur during collisions and that their treatment requires handling of both the structure of the target and the dynamics of the scattering event. We also know that direct (non-rearrangement) events can take place and that they involve elastic collisions as well as the excitation of electronic and/or nuclear states of the molecular partner. Such direct processes are often the only ones which are open at low collision energies (less than about 10 eV) and are also occurring under fully quantal conditions as far as the collision process is concerned. Hence the theoretical problems one encounters in this field are of interest from the fundamental point of view of quantum mechanics and of its representation of molecular processes.

One of the main complications of this area is to have to combine the quantal treatment of multichannel scattering theory with the many-body behaviour and properties of the molecular target. As a consequence of this fact, the need for large and powerful computers in the calculation of cross sections for all the processes involved becomes here dominant, thus producing one of the reasons why this field is not as advanced as, say, the theory of low-energy electron-atom scattering [1] and also explains how only in recent years considerable advances have been made in our qualitative

and quantitative understanding of electron-molecule scattering processes.

2. OUTLINE OF THE GENERAL THEORY

We start with an overview of the general theoretical formulation of the quantum problem to be solved, giving due attention to physical features peculiar to electron-molecule systems and to the difficulties these features cause.

One starts usually by neglecting all magnetic interactions, such as spin-orbit coupling, by simply assuming that they are weaker than the Coulomb term in the standard electrostatic, non-relativistic Hamiltonian:

$$H = T + V \quad (1)$$

where T and V are operators for the kinetic and potential energies of all particles in the system (nuclei, bound electrons and scattering electron).

The above operator can conveniently be written as the sum of the Hamiltonian of the isolated molecule, H_m , the k.e. operator for the scattering electron, T_e , and the electron-molecule interaction potential V_{int} , i.e.:

$$H = H_m + T_e + V_{int} \quad (2)$$

The H_m operator deals with the bound state structure of the many-nuclei and the many-electron systems which make up the target molecule. The last term in (2) arises from the electrostatic forces between the scattering electron and the constituent nuclei and electrons of the target, i.e.:

$$V_{int} = V_{eN} + V_{ee} \quad (3)$$

the above potential therefore provides a mechanism by which the quantum-mechanical 'motion' of the scattering electron influences and is influenced by that of the molecular constituents. This essentially dynamical effect, once coupled with the structural features of the target, gives rise to all the serious complications in the theoretical modelling, and to all the variety of processes, as listed before, that are typical of electron-molecule scattering.

Once we are able to write down the Hamiltonian (2), then one can, in principle, obtain the stationary state wavefunctions for each total system energy E by solving the corresponding time-independent Schrödinger equation, where E is now the sum of the asymptotic kinetic energy of the scattered electron and the energy of the target molecule. Preeminent among the constraints which need to be applied to solve the usual Schrödinger equation are the scattering boundary conditions: as the continuum electron moves into the asymptotic region (where detector and experimentalist are located) the system wavefunction must reduce to the sum of an undistorted incident wave and a scattered wave. The latter term, which is altered by the effect of the interaction potential, contains the scattering information. Letting Σ denote the coordinate of the scattered electron and Σ_m collectively represent all the coordinates (nuclear and electronic) of the target molecule, we can write these boundary conditions as:

$$\Psi_E(\Sigma, \Sigma_m) \underset{r \rightarrow \infty}{\sim} \exp(k_r \cdot \Sigma) \Phi_i(\Sigma_m) + \\ + \sum_f \frac{\exp(k_f \cdot \Sigma)}{r} \Phi_f(\Sigma_m) f_{i \rightarrow f}(\hat{r}) \quad (4)$$

The incident wave term in eq. (4) is the product of a plane wave, representing the scattering electron with initial wavevector k , and the initial state molecular wavefunction $\Phi_i(\Sigma_m)$. The scattered term in eq (4) are more interesting for elucidating the basic physics of the process each of them represents an energetically accessible final state of the molecule, $\Phi_f(\Sigma_m)$, and is given as a product of a final-state molecular wavefunction, an outgoing spherical wave with wavenumber k_f corresponding to that of the electron after the collision and the scattering amplitude for the transition $f_{i \rightarrow f}(\hat{r})$. This amplitude is the fundamental quantity that the theory seeks: given it, one can then compute any desired cross section.

Stated as above, the theory of e^- -molecule collisions may look like a rather standard application of quantum mechanics to continuum systems. However, the fact that we have electrons and molecules poses special difficulties to its solution.

First, the scattering electron is indistinguishable from the molecular electrons. Hence the wavefunction must obey the Pauli principle for Fermions, i.e. Ψ_E must be antisymmetric under exchange of any two electrons. This requirement gives rise to exchange effects which are demonstrably important in the calculation of cross sections for low energy collisions. Second, because the scattering electron is a charged particle, it will distort the target charge cloud. This distortion gives rise, in turn, to

polarisation effects, which are also important in low-energy scattering.

Another set of difficulties in the theoretical development arises because the target is a molecule and therefore the presence of several nuclei gives rise to the question; in what coordinate system do we formulate the collision process. In the spherical coordinate system of an atomic target, the troubles related to the nuclear singularity are placed at the origin of the reference frame, where they can do minimal damage, whereas in the general case of polyatomic molecules one is forced to contend with one or more Coulomb singularities located away from the coordinate origin. They are especially worrisome in eigenfunction-expansion methods that entail partial-wave expansions such as those appearing in the close coupling (cc) equations which will be discussed below. They force, in fact, the inclusion of a large number of partial waves that help to describe the strong off-centre singularities but, for most of them, do not actually contribute to the asymptotic cross sections.

A further source of troubles is a consequence of the molecular nature of the target and derives from the V operator of eq. (3). This dynamical interaction is responsible for the non-separability of the Schrödinger equation and makes rather difficult its numerical solution. In the more familiar case of bound stationary-state wavefunctions, $\Psi_f(\mathcal{Z}_m)$, the interaction of the motion of the nuclei and molecular electrons is usually dealt with by invoking the Born-Oppenheimer approximation, which is an approximate separation of the two motions. Such a separation can be applied to the e^- -molecule continuum problem only under certain, rather imprecisely defined, circumstances. The result is the use of an approximation which is usually called the adiabatic nuclei approximation (ANA) which will be discussed more in detail below. Alternatively, one can let the continuum electron and the nuclei interact dynamically; this strategy leads then to close-coupling (cc) methods which force us to incorporate into the theory a large number of rotational and vibrational nuclear states. These states define a corresponding big number of scattering channels which greatly complicate the implementation of cc calculations even on large computers. Moreover, the method suggests the use of a laboratory frame of reference as the natural choice for performing the calculations. Earlier on, the ANA method provided instead an approximate way of solving the dynamics first in a reference frame rigidly connected with the target molecule. The two different representations therefore constitute the two major pathway when dealing with computational procedures in electron-scattering problems.

3. THE COMPUTATIONAL MODEL

In order to calculate accurate cross sections at low electron impact energies, it is necessary to accurately include the effect of the direct, of the exchange and of the correlation (or polarisation) potentials. Even at

collision energies of only 1 Ryd, using only the static interaction (corresponding to the inclusion of only terms of the direct potential of eq. (3) that couples to the ground electronic state) leads to errors of over 30%. The situation is improved by including electron exchange with respect to the ground state target. However, such static-exchange (SE) calculations are often inadequate to reproduce low-energy resonances [3]. These features are only obtained, in fact, only by including polarization-correlation effects through virtual excitations to the closed electronic channels [4].

3.1 Local exchange potentials

One of the most successful and widely used methods of obtaining a local exchange potential is the Hara free-electron gas exchange (HFEGE) [2] model. In this approach the total wave function is assumed to be composed of plane waves which are antisymmetrised in accordance with the Pauli exclusion principle and the exchange energy obtained by summing all states up to the Fermi level. The resultant form of the potential is

$$V^{\text{HFEGE}}(r) = -\frac{2}{\pi} k_F(r) \left[\frac{1-\gamma^2}{4\gamma} \ln \left| \frac{1+\gamma}{1-\gamma} \right| \right] \quad (4)$$

where

$$k_F(r) = (3\pi^2 \rho(r))^{1/2}, \quad \gamma(r) = (k^2 + 2I + k_F^2(r))^{1/2} / k_F(r) \quad (5)$$

I is the ionisation potential of the molecule and $\rho(r)$ is the molecular charge distribution. It can be seen that as r goes to ∞ the numerator of γ should be k and not $(k^2 + 2I)^{1/2}$ as in eq. (5). This has led to the introduction of the asymptotically adjusted form of the HFEGE potential where

$$\gamma(r) = (k^2 + k_F^2(r))^{1/2} / k_F \quad (6)$$

This is usually called the AAFEGE model. Alternatively, I can be made an adjustable parameter in the model.

Another approach for defining a local exchange potential is the semiclassical exchange (SEC) approximation. If one performs a Taylor expansion about r , the point in space where the exchange integral is computed, one finds that [3,6]:

$$I = \int \phi^*(r_1) |r - r_1|^{-1} G(r_1) dr_1 = \\ = \int |r'|^{-1} \exp[(\nabla_{\phi} + \nabla_G) \cdot r'] \phi^*(r) G(r) dr' \quad (7)$$

where $r' = r_1 - r$ and the ∇ operators act on either the bound electron wave function ϕ or on the continuum function G depending on their subscripts. Using spherical polar coordinates we can solve the integral giving

$$I = - \frac{4\pi}{|\nabla_{\phi} + \nabla_G|^2} \phi^*(r) G(r) \quad (8)$$

For high energy collisions, the bound functions are slowly varying compared with the continuum functions and hence we can disregard the ∇_{ϕ} operator compared with the ∇_G operator. We then find the following expansion for the semiclassical exchange (SCE) potential

$$V_{ex}^{SCE}(r) = 1/2(2k^2 - V_{st}(r)) - 1/2[(2k^2 - V_{st}(r))^2 + 4\pi \rho(r)]^{1/2} \quad (9)$$

where we have summed over all the bound orbitals. Hence the SCE potential is energy dependent and depends on the molecular charge distribution (r) . The extension of this potential to lower collision energies can be carried out starting from eq. (9) and including the effect of the bound electron momenta on the scattered electron. This has been discussed recently [3,6] and the SCE potential has been used for a number of studies of diatomic molecules as well as recently being employed for e^- -polyatomic scattering [7].

3.2 Polarisation potentials

In many early low-energy electron-molecule collision calculations, the polarisation potential was represented by its asymptotic form for some $r \gg a$ and was cut-off at shorter distances by an empirical function. Thus we could write then:

$$V_{pol}(r, R) = -(\frac{\alpha_1}{2r} + \frac{\alpha_2}{2r} P_2(\cos \vartheta)) f_C(r, r_C) \quad (10)$$

Several forms of the cut-off function f_C have been considered [8] one of the most frequently used being

$$f_C(r, r_C) = 1 - \exp[-(r/r_C)^6] \quad (11)$$

were the cut-off parameter r_C is usually determined by fitting some "landmark" feature in the cross section such as the position of a resonance. For example in e^-N_2 scattering the position of the $^2\pi g$ resonance at 2.3 eV has been used in the fit. This approach may be seriously called into question since frequently the cut-off function will be reflecting an attempt to compensate for important non-adiabatic or dynamical effects which have been neglected and which will be different in different symmetry states of the electron-molecule system. Further, it is found in many cases that the collision cross sections at low energies and in the vicinity of resonances can depend sensitively on the value of the parameter r_C again throwing doubt on the validity of this approach.

Another parameter-free polarisation potential has recently been introduced for atoms by O'Connell and Lane [9] and applied to diatomic molecules by Padial and Norcross [10] and to polyatomic molecules by Gianturco et al. [4] with rather good results. The method is based on the free-electron-gas (FEG) model, whereby the correlation energy can be expressed in terms of the molecular charge density in the high and low density limits. However the correlation energy defined in this way does not have the correct asymptotic behaviour. Consequently the rather ad-hoc procedure is adopted of joining the asymptotic form of the potential to the short range FEG form where they cross on the boundary of the atom or molecule. It is found that this crossing radius is only weakly dependent on the target molecule giving further credence to the method [10].

4. RESULTS OF CALCULATIONS

As mentioned earlier, the present computational model contains no adjustable parameters and starts out from the molecular densities obtained from SCF calculations of near Hartree-Fock quality and generated via a single centre expansion around the heavy-atom of the polyatomic target.

The present model has been tested rather extensively on diatomic targets [11], on polyatomic nonpolar systems like CH_4 and SiH_4 [3,4,2] and for collisions with polar polyatomic targets like H_2O [13] and NH_3 [14]. It is interesting to note that the exchange potential computed here via the

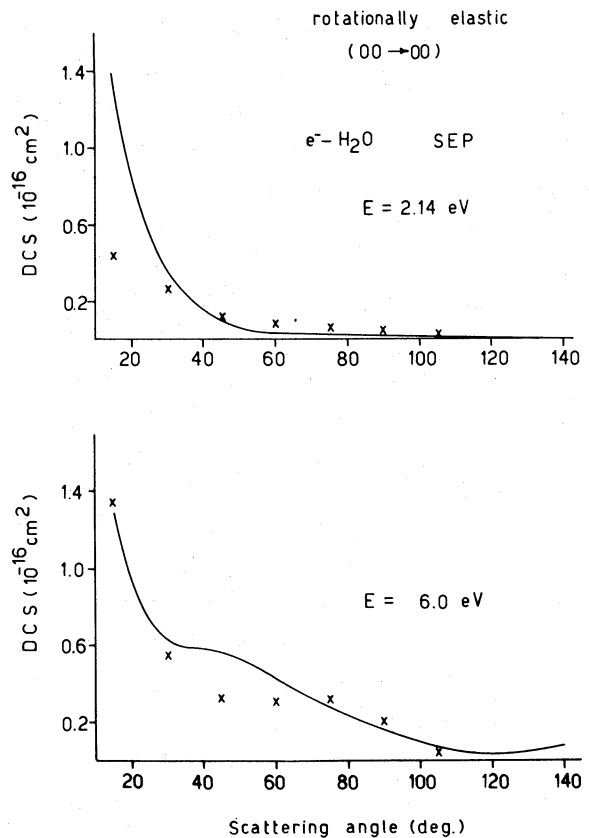


Fig. 1 - Differential, state-to-state cross sections for the H_2O system computed at two different collision energies and using the full (SEP) interaction discussed in the main text. The crosses are the experimental data from ref. 16

semiclassical model turns out to be practically coincident with the correct one computed later with the same target wavefunction [15].

Further examples of the predictive quality of the present approach are shown in Figures 1 and 2 for the H_2O molecule. State-to-state differential cross sections (DCS) are shown there for the rotationally elastic (Fig. 1) and rotationally inelastic (Fig. 2) scattering processes. The experimental points are from Jung et al. [16]. One clearly sees there that the general qualitative behaviour is well reproduced by our calculations and the size of cross sections is also in fairly good accord with experiments. Discrepancies in the small-angle region, on the other hand, could be attributed both to our use of a two-stage hybrid S-matrix theory [17] and to experimental difficulties in

subtracting correctly the contribution from unscattered projectiles [16].

In conclusion, we have shown that the treatment of low-energy electron collisions off simple polyatomic targets can be carried out fairly successfully via the present model calculations which do not contain any parameter and employ the full coupled equation approach within a simplified derivation of the interaction forces. This implies that, at least for the very popular polyatomic systems discussed here (e.g. H_2O , CH_4 , SiH_4 , NH_3 , H_2S etc.), the present approach could allow us to carry out more extensive computations of total, integral cross sections, of differential cross

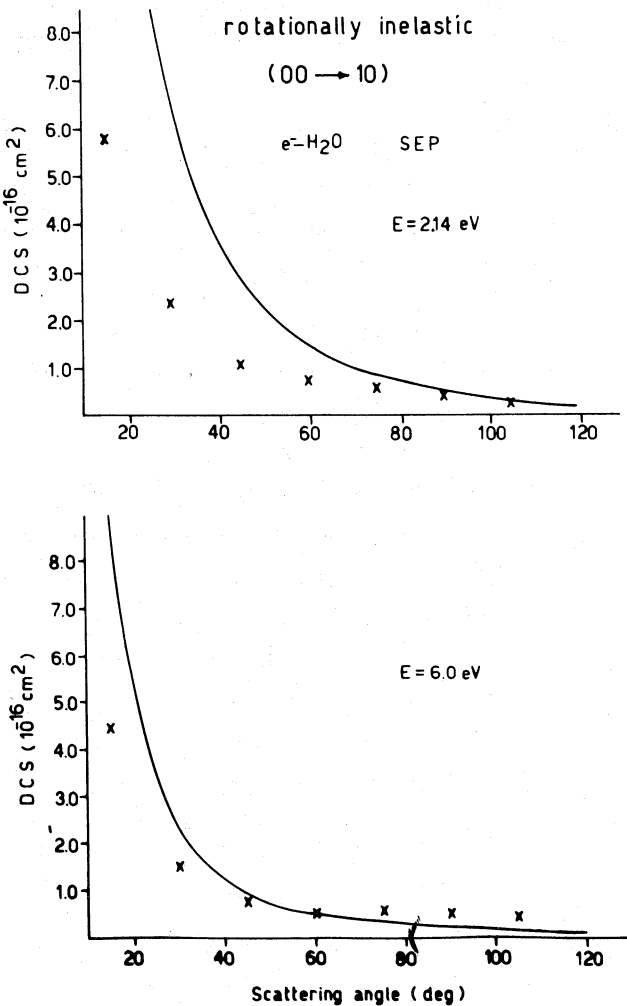


Fig. 2 - State-to-state rotationally inelastic differential cross sections computed for the H_2O system at two different collision energies. The crosses are the experiments from ref. 16.

sections and of individual state-to-state cross sections with a contained amount of computational effort and an acceptable confidence level on the produced outcomes.

REFERENCES

1. e.g. see: Nesbet, R.K., Adv. Quant. Chem. 9, 215 (1975).
2. e.g. see: Gianturco, F.A. and Jain, A., Phys. Rep., 143, 347 (1973).
3. Gianturco, F.A. and Scialla, S., J. Phys. B., 20, 3171 (1987).
4. Gianturco, F.A., Jain, A. and Pantano, L.C., J. Phys. B., 19, 571 (1986).
5. Hara, S., J. Phys. Soc. Japan, 22, 710 (1967).
6. Furness, J.B. and McCarthy, I.E., J. Phys. B, 6, 2280 (1973).
7. Gianturco, F.A. and Scialla, S., Electron molecule scattering and photoionisation, P.G. Burke and J.B. West Ed.s, Plenum Press, New York, 1989, pg. 169.
8. Gianturco, F.A. and Thompson, D.G., J. Phys. B, 9, L383 (1976).
9. O'Connell, J.K. and Lane, N.F., Phys. Rev., A27, 1893 (1983).
10. Padial, N.T. and Norcross, D.W., Phys. Rev., A29, 1742 (1984).
11. Gianturco, F.A., Palma, A. and Pantano, L.C., Nuovo Cim. 7D, 339 (1986).
12. Gianturco, F.A., Pantano, L.C. and Scialla, S., Phys. Rev. A36, 557 (1987).
13. Gianturco, F.A. and Scialla, S., J. Chem. Phys. 87, 6468 (1987).
14. Gianturco, F.A. and Scialla, S., in preparation.
15. McNaughton, P. and Thompson, D.G., J. Phys. B21, L703 (1988).
16. Jung, K., Antoni, Th., Müller, R., Kochem, K.H. and Ehrhardt, H., J. Phys. B15, 3535 (1982).
17. Jain, A. and Thompson, D.G., J. Phys. B., 16, 3077 (1983).

ELECTRON COLLISION CROSS-SECTIONS DETERMINED
FROM BEAM AND SWARM DATA BY BOLTZMANN ANALYSIS

Makoto Hayashi

Nagoya Institute of Technology
Gokiso-cho, Showa-ku, Nagoya, 466
Japan

INTRODUCTION

Whenever free electrons collide with atoms and molecules, a wide variety of kinetic processes may take place. Electron collision cross-sections, of interest in plasma processing of VLSI production, carbonization of surfaces and so on, modeling of gas lasers, physics of gaseous dielectrics, analysis of high current discharge switches, applications for space science and radiation physics and chemistry, have been determined from available electron beam and electron swarm data utilizing the Boltzmann analysis. The goal of electron collision studies is to provide absolute values of cross-sections for all processes involved, from elastic to inelastic scattering, as a function of incident electron energy and scattering angle. In spite of many experimental and theoretical studies, electron impact cross-sections for atoms and molecules have not been systematically quantified.

Recently some good reviews on electron collision cross-sections have been published by Trajmar et al. (1983), Takayanagi et al. (1984), Christophorou et al. (1984) and Pitchford et al. (1987). I have also reported the concrete values of cross-sections for some atoms and molecules at Lake Tahoe Seminar (1987) and recent report (1989b). I fell deeply in love with cross-sections. The method of the determination of cross-section set are discussed in the first report (Hayashi, 1987a). The beam data of cross-sections are given highest priority. Simultaneously, we have used the exact values of electron swarm data, such as electron drift velocity, characteristic energy, ionization and attachment coefficients.

CROSS-SECTION SETS

The gases for which the authour with my coworkers have determined sets of cross-sections are shown in table 1.

Itikawa, et al. (1986, 1989) have presented the recommended values of cross-section sets for N₂ and O₂. I (1989a) have discussed the same set for H₂O which have revised recently, and I (1988, 1989c) have reviewed the sets for plasma processing gases, such as SiH₄, CF₄ and SF₆. In the Proceeding of Lake Tahoe Seminar, I (1987a) have shown the cross-section sets for CF₄, HCl, H₂O, SO₂, CH₄, C₂H₆, SiH₄, Si₂H₆, CC₁₂F₂ and CC₁₄. Cross-section sets for N₂O and C₂F₆ are given in our report of the Symposium on Gaseous Dielectrics (Hayashi, et al., 1987b).

In 1988, we have determined the revised cross-section set for Ne, including seven electronic excitation cross-sections. The total excitation cross-sections for Ne are shown in figures 1 and 2.

Then we have shown the other cross-section set for some molecules here, Hg, NO, CO₂, NH₃, C₂H₂, C₂H₄, which we have determined during these a few years, in the figures from 3 to 8.

Recently, Tanaka et al. (1987, 1988, 1989) have measured and measuring the absolute values of elastic, vibrational excitation and electronic excitation cross-sections for SiH₄ and Si₂H₆ for the first time. Kurachi and Nakamura(1988) have measured the electron drift velocities for SiH₄ and Ar mixtures, and then determined the values of vibrational excitation cross-sections as a function of electron energy. These two values are almost coincide with each other, that is, vibrational excitation cross-sections have a second peaks at about 2.5 eV of electron energy.

Table 1. The gases for which the authour's group has determined set of cross-sections.

He	Ne	Ar	Kr	Xe	H	O	F	Cu	Cd	Hg
H ₂	N ₂	O ₂	F ₂	CO	NO	HCl				
H ₂ O	SO ₂	N ₂ O	CO ₂	C ₂ H ₂	NH ₃	BF ₃				
CH ₄	SiH ₄	CF ₄	CCl ₂ F ₂	CCl ₄						
C ₂ H ₄	SF ₆	C ₂ H ₆	Si ₂ H ₆	C ₂ F ₆	C ₃ H ₈					

Integrated values of elastic total and momentum transfer cross-sections q_t and q_m are shown in figures 9 and 10, togher with our old estimated q_m values and also some theoretical values as shown in the figure caption. We have also theoretical values of Gianturco (1987) and experimental data of Tronc et al. (1989) which was reported very recently.

CONCLUSIONS

We have determined a set of electron collision cross-sections of about 36 atoms and molecules for the electron energies from 0 to 10^3 eV. We would like to improve these cross-section values and also to increse the number of molecular species, using new exact data of beam and swarm experiments, in the near future.

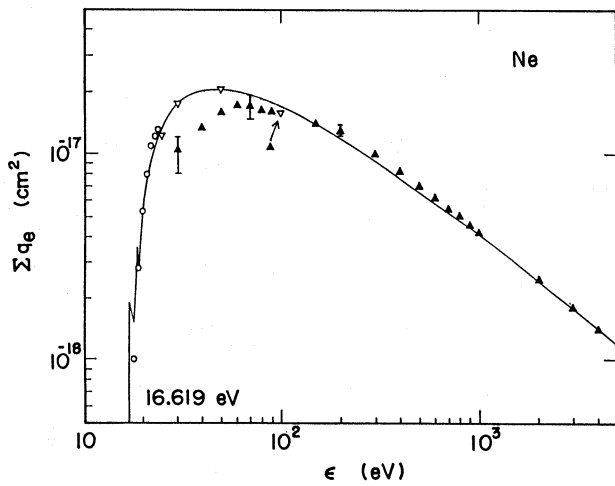


Fig. 1. Total excitation cross-section for Ne. Solid line is our recommended values. \circ : Maier-Leibniz, \blacktriangle : de Heer, ∇ : Register.

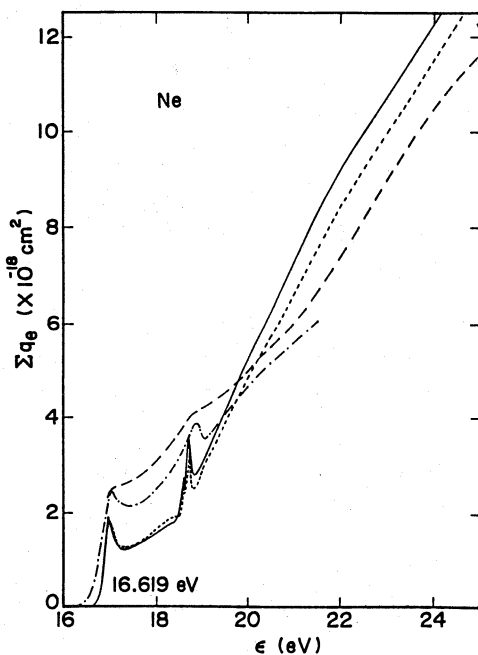


Fig. 2. Total excitation cross-section for Ne at threshold region. Solid line is our values. Chain line is Schaper, small dot one is Tachibana and long dot is Thomas.

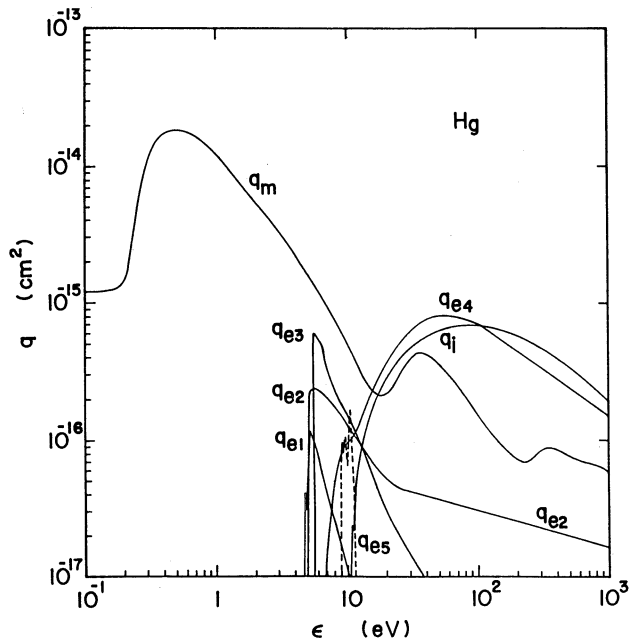


Fig. 3. Cross-section set for Hg (1987).

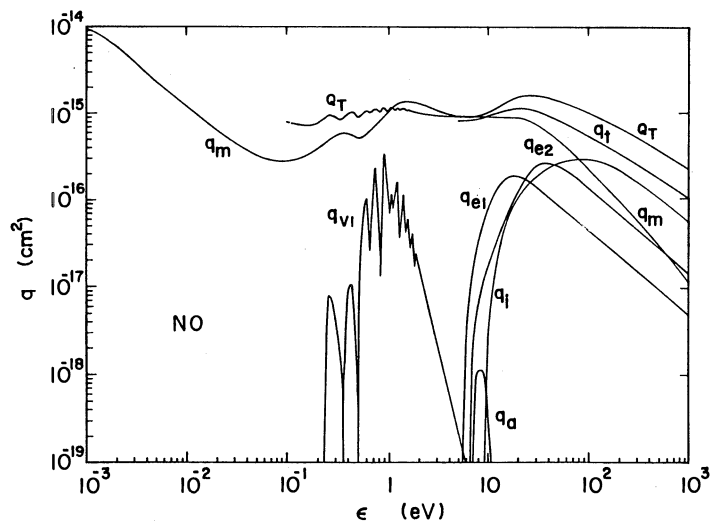


Fig. 4. Cross-section set for NO (1986).

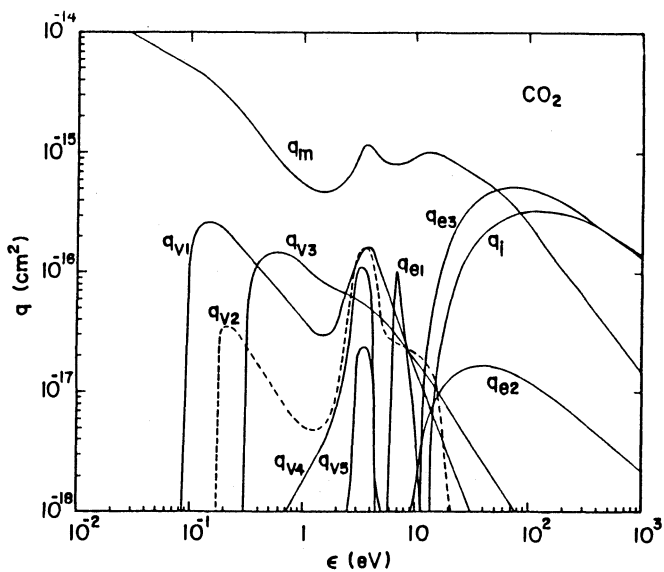


Fig. 5. Electron collision cross-section set for CO_2 (1987).

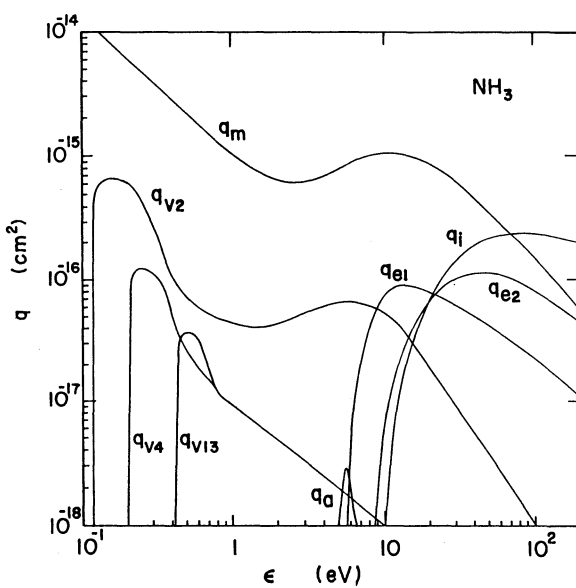


Fig. 6. Electron collision cross-section set for NH_3 (1986).

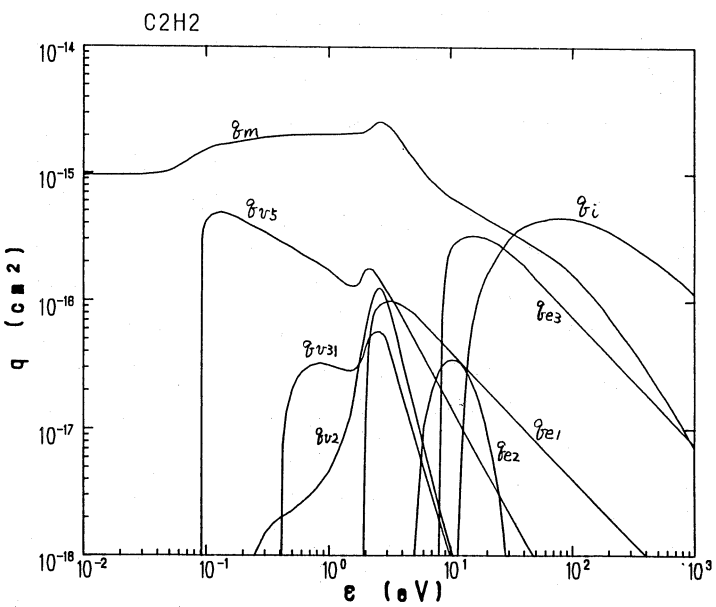


Fig. 7. Electron collision cross-section set for C₂H₂ (1987).

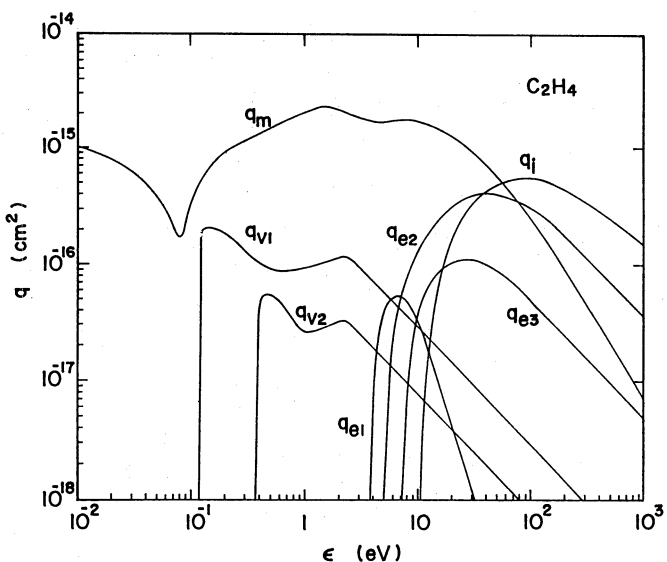


Fig. 8. Electron collision cross-section set for C₂H₄ (1987).

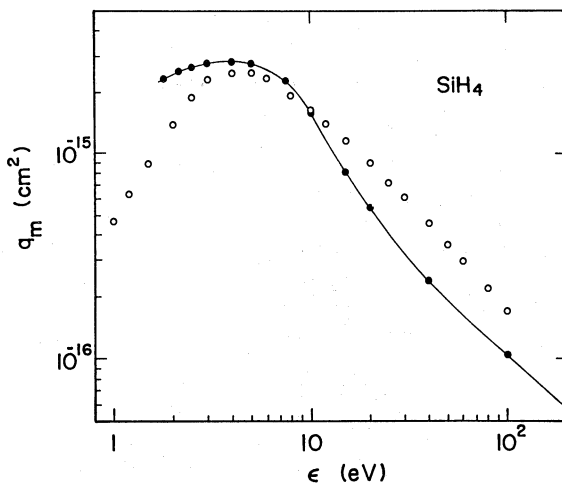


Fig. 9. Momentum transfer cross-sections q_m for SiH_4 . Black circles are beam data measured by Tanaka (1988) for the first time. White circles are Hayashi's old values (1984).

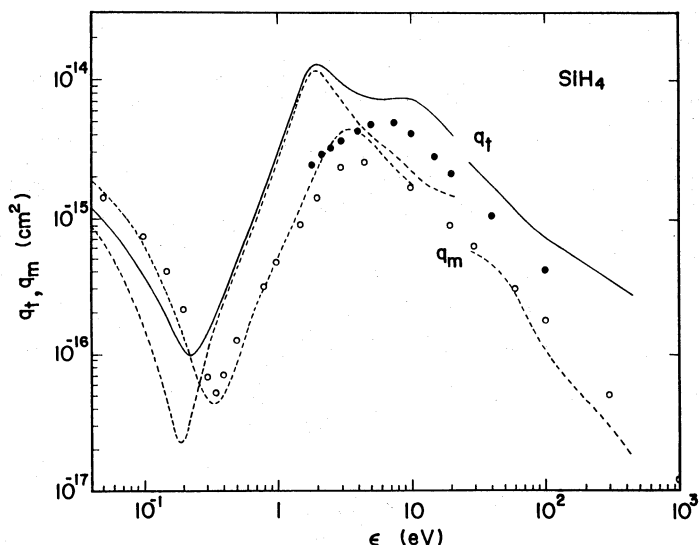


Fig. 10. Elastic q_t and q_m for SiH_4 . ● : q_t measured by Tanaka ('88). Solid line : theoret. values of q_t by Yang ('87, left) & Jain ('87, right). ○ : q_m estimated by Hayashi ('84). Dotted line : theoretical values of q_m by Yang ('87), Jain ('85) and Jain ('87) from left to right.

REFERENCES

- Christophorou, L. G. ed., 1984, "Electron-Molecules Interactions and Their Applications, Vol. I and II", Academic Press, Orlando.
- Gianturco, F. A., Pantano, L. C. and Scialla, S., 1987, Phys. Rev. A36:557.
- Hayashi, M., 1987a, "Swarm Studies and Electron-Molecules Collisions", Springer-Verlag, New York, P. 167.
- Hayashi, M., and Niwa, A., 1987b, "Gaseous Dielectrics V", ed. by Christophorou, L. G. and Bouldin, D. W., Pergamon Press, New York, P. 27.
- Hayashi, M., 1988, Abstracts of Papers, Japan-Australia Workshop on Gaseous Electronics and Its Applications, Sydney, P. 72.
- Hayashi, M., 1989a, IAEA Advisory Group Meeting on Atomic and Molecular Data for Radiotherapy, Vienna, to be published.
- Hayashi, M., 1989b, Oyo-Buturi (Japan society of Applied Physics) 58:2 (in Japanese).
- Hayashi, M., 1989c, Abstract of 44th Annual Meeting of the Physical Society of Japan, Vol. 4, P. 101 (in Japanese).
- Itikawa, Y., Hayashi, M., Ichimura, A., Onda, K., Sakimoto, K., Takayanagi, K., Nakamura, M., and Takayanagi, T., 1986, J. Phys. Chem. Ref. Data, 15:985.
- Itikawa, Y., Ichimura, A., Onda, K., Sakimoto, K., Takayanagi, K., Hatano, Y., Hayashi, M., Nishimura, H., and Tsurubuchi, S., 1989, J. Phys. Chem. Ref. Data, 18:23.
- Jain, A., 1985, Private communication.
- Jain, A., 1987, J. Chem. Phys. 86:1289.
- Jain, A., and Thompson, D. G., 1987, J. Phys. B20:2861.
- Jain, A. K., Tripathi, A. N. and Jain, A., 1987, J. Phys. B20:L389.
- Kurachi, M., and Nakamura, Y., 1988, J. Phys. D21:602.
- Pitchford, L. C., McKoy, B. V., Chutjian, A., and Trajmar, S., ed., 1987, "Swarm Studies and Inelastic Electron-Molecule Collisions", Springer-Verlag, New York.
- Takayanagi, K., and Shimamura, I., ed., 1984, "Electron Molecule Collisions", Plenum Press, New York.
- Tanaka, H., and Boesten, L., 1987, Abstract of 42nd Annual Meeting of the Physical Society of Japan, Vol. 4, P. 33 (in Japanese).
- Tanaka, H., 1987, 1988, 1989, Private communications.
- Tanaka, H., Boesten, L., Sato, H., Kimura, M., Dillon, M. A., and Spence, D., 1989, J. Phys. B, to be published.
- Trajmar, S., Register, D. F., and Chutjian, A., 1983, Phys. Rep. 97:219.
- Tronc, M., Hitchcock, A., and Edard, F., 1989, J. Phys. B22:L207.
- Yang, X., and Gou, Q., 1987, J. of Atomic and Molec. Phys. 4:395 (in Chinese).

ELECTRON COLLISION CROSS SECTIONS INVOLVING EXCITED STATES

Winifred M. Huo

NASA Ames Research Center
Moffett Field, California 94035, USA

INTRODUCTION

It has long been recognized that atoms and molecules in the flow field around a hypersonic space vehicle, upon its entry into the planetary atmosphere, undergo a variety of chemical reactions. These include dissociation, ionization, charge transfer, and exchange reactions, along with rotational, vibrational, and electronic excitations. At low altitudes, where the air density is high, these chemical phenomena tend to reach thermodynamical equilibrium and the flow fields can be described using equilibrium relationships. At high altitudes where the air density is low, equilibrium may not be reached. The problem of nonequilibrium is much more severe for the next generation of space vehicles. In the current conceptual design of the Aeroassisted Space Transfer Vehicle (ASTV),^{1,2} it will return into the earth's atmosphere from a high earth orbit and, using aerodynamic drag, change into a low earth orbit. This aerobraking has the advantage of reducing the amount of fuel required for an orbital transfer. The aerobrake consists of a blunt body with a large nose-radius. Because of its large size, the shock layer over the aerobrake will be thick and the flow field in the shock layer will most likely be in a chemical and thermodynamical nonequilibrium.

Park³ showed that the nonequilibrium flow field should be described at least by a three-temperature model where the vibrational, electronic, and rotational-translational temperatures are distinct. The rotational-translational temperature is expected to be very high, reaching up to 50,000 K, whereas the vibrational and electron temperatures are lower, \approx 10,000 K. To model such nonequilibrium phenomena and the associated radiative heating requires an extensive data base of reaction rates, excitation cross sections, emission probabilities, and transport properties. Electron collision cross sections constitute a part of this data base. While the number densities of ionic species in the shock layer depend on the vehicle speed and altitude, varying from 1% to 30%, the frequency of electron-atom, molecule collisions in the low-density atmosphere makes such processes effective in transferring energy, which leads to the eventual equilibration in the flow field. Electron impact excitation is also an important mechanism in creating radiative species and radiation from the shock layer can be an important factor in designing the thermal protection for the vehicle. Due to the sparsity of available data, the collisions of electrons with excited atoms and molecules are of particular interest. This paper presents our results on electron - excited N₂ collisions. We investigated the vibrational

excitation/de-excitation of vibrationally and rotationally hot N₂ by electron impact.⁴ It is well known that the ²Π_g shape resonance around 2.3 eV in e-N₂ collisions significantly enhances the vibrational excitation cross sections. While the average electron temperature in the flow field lies below the resonance energy, the Boltzmann distribution still gives significant number of electrons with energy in the resonance region. We also found that the resonance position shifts to a lower energy when N₂ is rotationally hot. Electron impact excitations between electronic excited states of N₂ have also been investigated using a multichannel treatment. Experimental data on these transitions are nonexistent. Current nonequilibrium flow field calculations³ assume that the excited - excited cross sections to be the same as the ground - excited cross sections resulting in the same final state. Our calculations show this assumption to be invalid and provide a more reliable set of data on N₂.

METHODOLOGY

The calculations were done in two steps. First, electron collision cross sections were determined in the fixed nuclei approximation using the Schwinger variational principle. For electronic excitations, these calculations⁵⁻⁷ were done at the equilibrium internuclear distance, R_e , of the ground state and at electron energies from threshold to 20 eV. For vibrational excitations,^{4,8} the calculations included six internuclear distances and up to 8.16 eV. Second, nuclear dynamics calculations of vibrational excitation cross sections were carried out using the Feshbach projection operator formalism,⁹ where the width function is deduced from the electronic calculations.

The fixed nuclei, multichannel calculations of electron collisions uses the combined Lippmann-Schwinger and Schrödinger equations of Takatsuka and McKoy;¹⁰

$$A^{(+)}\Psi_n^{(+)} = VS_n, \quad (1)$$

with

$$A^{(+)} = \frac{1}{2}(PV + VP) - VG_P^{(+)}V + \frac{1}{N+1}\hat{H} - \frac{1}{2}(P\hat{H} + \hat{H}P), \quad (2)$$

where $\hat{H} = E - H$, N the number of target electrons, V the interaction potential between the incident electron and the target, S_n is an eigenfunction of the interaction-free Hamiltonian. The projection operator P defines the open-channel space in terms of the eigenfunctions of the target Hamiltonian, and $G_P^{(+)}$ is the projected, interaction-free Green's function. Based on Eq. (1) and the fractional form of the Schwinger variational principle, the collision amplitude for a transition from the target state n to m , is expressed as,

$$f_{mn} = -\frac{1}{2\pi} \frac{\langle S_m | V | \Psi_n^{(+)} \rangle \langle \Psi_m^{(-)} | V | S_n \rangle}{\langle \Psi_m^{(-)} | A^{(+)} | \Psi_n^{(+)} \rangle} \quad (3)$$

The above quantity is calculated in the molecular frame using the fixed-nuclei approximation. Transformation to the laboratory frame is achieved via partial wave decompositions.

For resonant enhanced vibrational excitations, our treatment^{4,8} is similar to the work of Berman et al.⁹ By partitioning the electronic states into discrete (resonant) and continuum parts using the Feshbach projection operators, an effective Hamiltonian for

the nuclear motion of the temporary negative ion, H_{eff} , is defined in terms of the optical potential V_{opt} ,

$$H_{eff} = T_{vib} + V_{opt}. \quad (4)$$

Here T_{vib} is the nuclear kinetic energy operator. V_{opt} contains the adiabatic potential of the negative ion as well the shift and width functions. The latter are deduced by analytically fitting the fixed-nuclei, electronically elastic, partial amplitudes of the resonant channel determined in a quadrature of internuclear distances and electron energies. Similarly, the coupling potential U_{dE} between the negative ion and the target vibrational states is also deduced from electronic width functions. The rotationally elastic, vibrational excitation cross section is given by

$$\sigma_{if} = \frac{(2\pi)^3 d_g}{E} |\langle v_f, J | U_{E_f d}(E - H_{eff})^{-1} U_{dE} | v_i, J \rangle|^2. \quad (5)$$

Eq. (5) assumes one single partial wave to be dominant in the resonance, a case applicable to N_2 . The initial and final vibrational levels of the target are labeled by v_i and v_f , J the rotational quantum number, E and E_f the energies of the incoming and outgoing electron, and d_g is the spatial degeneracy factor of the resonant state.

All electron collision calculations used the AMES SMC code. The code for vibrational excitations cross sections was also developed at NASA Ames.

VIBRATIONAL EXCITATION OF N_2 BY LOW-ENERGY ELECTRON IMPACT

The electronic calculations of low-energy e- N_2 elastic scattering using a correlated treatment have been described elsewhere.^{8,11} The resonant widths in the $^2\Pi_g$ channel were deduced from the $l = 2, m = 1$ K-matrix elements determined in a grid of internuclear distances and electron energies. In total 129 grid points were used. Our nuclear dynamics calculations differ from the work of Berman et al.⁹ in the use of the RKR

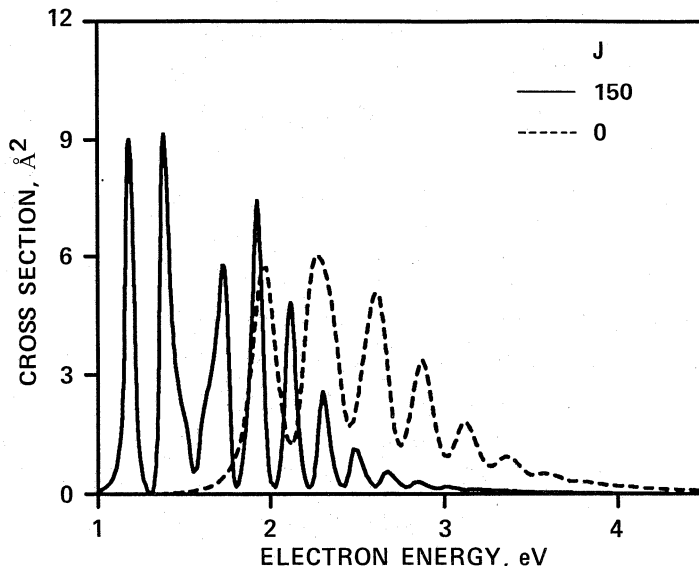


Fig. 1. e - N_2 $v = 0 - 1$ excitation cross section for $J = 0$ and 150, from Ref. 4.

potential instead of the Morse potential for the target vibration. This is important for high vibrational levels. For the resonant state we used the semiempirical potential of Berman et al.⁹ Since our study is limited to rotationally elastic transitions, the rotational effect is introduced through the centrifugal potential, $J(J+1)/2\mu R^2$, in the vibrational Hamiltonian. The present calculations also neglect nonresonant contributions. They are negligibly small so that, outside the resonant region, vibrational excitation/de-excitation of N₂ by electron impact is much less effective than by heavy particle collisions.

The calculated vibrational excitation cross sections from $v_i = 0$ to $v_f = 1 - 17$ at $J = 0$ have been compared⁸ with the recent measurements of Allan¹². Good agreements are found in both resonant positions and cross sections. Comparison^{4,8} with other theoretical treatments and experimental data also indicate the validity of the present approach.

Fig. 1 shows the effect of high rotational quantum number in the $v = 0 - 1$ transition of N₂. Two distinct features are evident when we compare the cross sections at $J = 0$ and 150. At high J , the position of the first resonance peak is shifted to a lower energy. For $J = 150$ the first resonant peak occurs at 1.18 eV versus 1.96 eV for $J = 0$. Also, the resonant structures for $J = 150$ are significantly narrower than the $J = 0$ result, even though the same electronic width was used in the calculations. Both features can be attributed to the centrifugal potential. The introduction of a centrifugal potential raises the ro-vibrational energy of the target as well as the resonant state. But the energy increase of the resonant state is less than that of the target state because the minimum of the resonant state potential occurs at a larger internuclear distance and the rotational

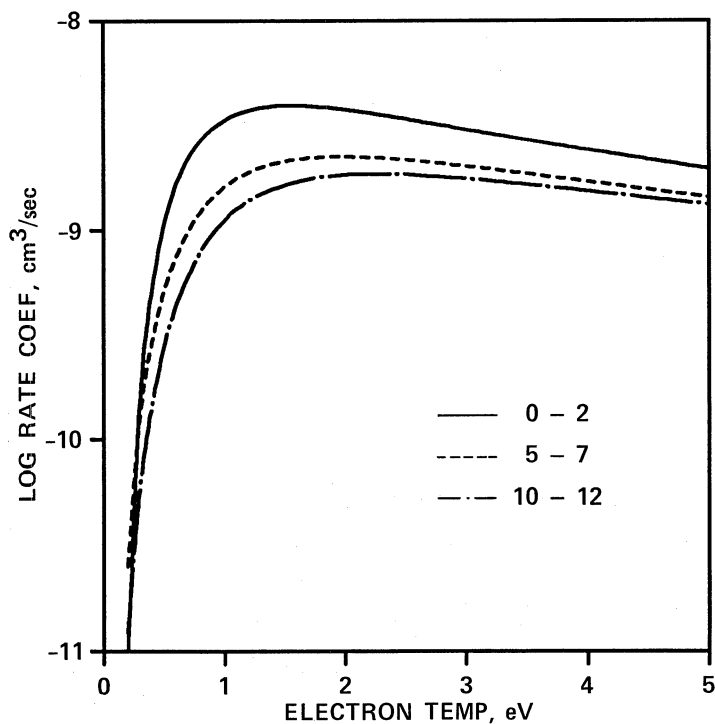


Fig. 2. e - N₂ $v = 0 - 2$, 5 - 7, and 10 - 12 vibrational excitation rate coefficients.

energy is proportional to $\langle 1/R^2 \rangle$. Consequently, the energy difference between the target and resonant states, i.e. the resonant energy, decreases with increasing J . Also, for a given $v_i - v_f$ transition, the position of the resonant peaks are related to the vibrational levels of the resonant state. Increasing J not only increases the rovibrational energies, but also decreases the energy gap between levels. As the energy levels of the resonant state become closer, destructive interference between neighboring resonances causes the resonant peaks to become narrower.

The rate coefficients of the vibrational excitations/de-excitation of N₂ by electron impact have been determined with the assumption of a Maxwellian electron velocity distribution. Fig. 2 presents the rate coefficients for the $v = 0 - 2$, $5 - 7$, and $10 - 12$ transitions, calculated at $J = 50$, as a function of electron temperature. All three rates coefficients are strongly temperature dependent. The sharp increase at the low temperature end indicates the onset of the resonance. The slow decrease at the high temperature end reflects the fact that an increasing portion of the Maxwellian electrons have energies above the resonance. The maximum rate is reached at a temperature between 1.5 and 2 eV. The position of this maximum is dependent on v and J , relating to the v, J -dependence of the resonance. Also, the rate coefficients decrease with increasing v_i , its maximum value decreased by a factor of 2 as v_i increases from 0 to 10.

For a given v_i , the rate coefficients for de-excitation are larger than the corresponding excitation rate coefficients. But their ratio is usually less than 2. Tabulations of the excitation/de-excitation rate coefficients for $v_i = 0 - 12$ and $\Delta v = \pm 1 - 5$ have been given elsewhere.⁴

ELECTRONIC TRANSITIONS BETWEEN EXCITED STATES BY ELECTRON IMPACT

In a multichannel treatment, excited to excited transitions are determined at the same time as ground to excited transitions. A major problem in multichannel electron-atom, molecule collisions is the limitation in the number of open channels that can be handled even when state-of-the-art computer codes are used. For most atoms and molecules, the number of open channels increases very rapidly as the electron energy becomes larger than the first excitation threshold. Thus, it is important to choose a set of strongly coupled channels. In the present study of N₂, the open channels consist of the ground state and the set of low-lying valence excited states arising from the excitation of the three/four highest valence orbitals to the lowest antibonding orbitals. Based on chemical arguments, we expect the excitation of these valence states to be strongly coupled. Test calculations mixing Rydberg and valence states confirmed this conjecture. We also found the coupling between singlet and triplet states to be significantly weaker than the coupling among themselves. Thus, in most calculations those states were coupled separately. In total four sets of calculations were carried out. The open channels in the first set include the X¹ Σ_g^+ , B³ Π_g , A³ Σ_u^+ , W³ Δ_u , and B³ Σ_u^- states. The second set includes the X¹ Σ_g^+ , a¹ Π_g , a'¹ Σ_u^- , and w¹ Δ_u states. At an electron energy where the C³ Π_u state becomes energetically accessible, a third set of triplet calculations were done including the C³ Π_u state in the open channel space. Finally, we also ran a set of calculations mixing the singlet states with the B³ Π_g state to deduce the excitation of the B³ Π_g state to the singlets. In all the calculations, the threshold energy of the excited state corresponds to the experimental excitation energy from the lowest vibrational level

of the ground state to a vibrational level of the excited state with maximum overlap, i.e., \approx vertical excitation energy.

The details of the calculations will be given elsewhere.⁵⁻⁷ Strong resonance effects are found near threshold. These resonances are observable in both the elastic and inelastic channels. Because of the resonance effects, the results of two-state calculations differ significantly from the multichannel results. It is also important to use a large basis set for a proper description of the shape of the resonances. The integral and differential cross sections of the ground to excited transitions determined from the present calculations compare well with the experimental data of Cartwright et al.,¹³ indicating the validity of the present multichannel treatment.

Fig. 3a presents the excitation cross section of the $A^3\Sigma_u^+ - B^3\Pi_g$ transition as a function of the scattered electron energy. For comparison, the $X^1\Sigma_g^+ - B^3\Pi_g$ excitation cross sections from the present calculation, and the experimental data of Cartwright et al.¹³ on the same transition, are also included. For the ground - excited transition, theory and experiment are in agreement. The theoretical curve also shows two peaks. They appeared to be weaker than actual, because of the scale used in plotting. Both peaks are due to resonances.^{5,6} The position of the first resonance agree well with the observations of Schulz¹⁴ and Mazeau et al.¹⁵ Our calculated cross section of the $X^1\Sigma_g^+ - A^3\Sigma_u^+$ transition, not shown here, also has a low-energy resonance near 9 eV, in agreement with the results of Mazeau et al.¹⁵ and Huetz et al.¹⁶ Detailed description of these resonances in the ground - excited cross sections and comparison with experiment are given elsewhere.⁵⁻⁷ These resonance peaks become strongly amplified in the A - B cross section. The correlation between the peak positions of these two curves indicates that these structures most likely are due to the same transient ion formation. Also notice

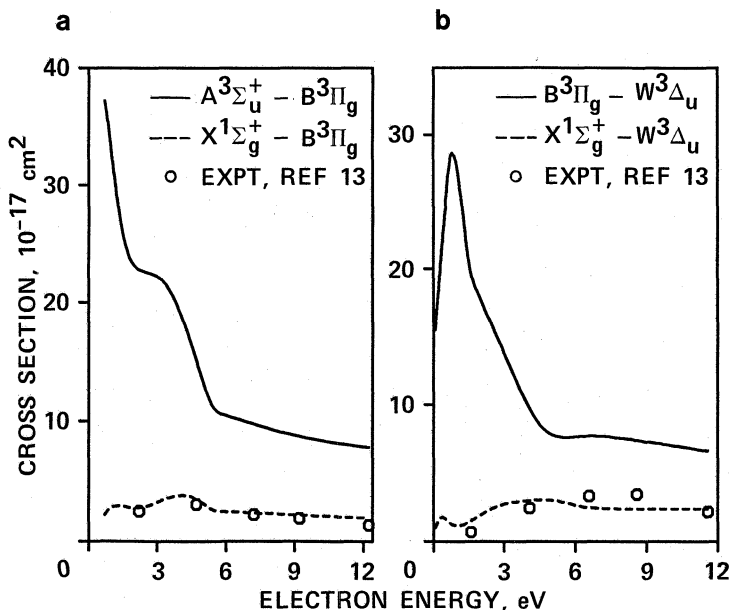


Fig. 3. (a) Left figure, $N_2 A^3\Sigma_u^+ - B^3\Pi_g$ and $X^1\Sigma_g^+ - B^3\Pi_g$ excitation cross sections. The experimental data of the $X^1\Sigma_g^+ - B^3\Pi_g$ transition are from Ref. 13. (b) right figure, $N_2 B^3\Pi_g - W^3\Delta_u$ and $X^1\Sigma_g^+ - W^3\Delta_u$ excitation cross sections. The experimental data of the $X^1\Sigma_g^+ - W^3\Delta_u$ transition are from Ref. 13.

that the excited - excited cross sections are significantly larger than the ground - excited cross sections, especially near the threshold where they differ by an order of magnitude.

The $B^3\Pi_g - W^3\Delta_u$ excitation cross sections are presented in Fig. 3b, together with the $X^1\Sigma_g^+ - W^3\Delta_u$ cross sections. The experimental data of the Cartwright et al.¹³ for the latter transition are also included. The general feature of this transition is similar to $A^3\Sigma_u^+ - B^3\Pi_g$. The low-energy resonance in the $X^1\Sigma_g^+ - W^3\Delta_u$ transition is apparent in the theoretical curve. This resonance has the same origin as those observed in the ground - $A^3\Sigma_u^+$, $B^3\Pi_g$ transitions. Again the resonance structures observed in the ground - excited transition are evident in the excited - excited transitions.

Figs. 4a and 4b present the cross sections for the transitions from the $a^1\Pi_g - a'^1\Sigma_u^-$ and $w^1\Delta_u$. While the adiabatic excitation energy of the $a'^1\Sigma_u^-$ state is smaller than $a^1\Pi_g$, its vertical excitation energy is higher. Also presented are our calculated cross sections for transitions from the ground state to the same final excited states, and the data of Cartwright et al.¹³ Analogous to the case of triplets, structures are also found in these singlets transitions. The first peak in the excited - excited curves corresponds to a resonance structure in the $X^1\Sigma_g^+ - a^1\Pi_g$ transition, which is not evident in the $X^1\Sigma_g^+ - a'^1\Sigma_u^-$ and $w^1\Delta_u$ transitions.

One significant result from the present set of calculations is the magnitude of the excited - excited cross sections. They are much larger than the ground - excited cross sections, particularly near the threshold. Our calculations indicate that the assumption of excited - excited and ground - excited cross sections to be comparable must be invalid. Since these excited states are energetically close, the large threshold cross sections mean that electronic energy can be transferred very efficiently between one excited state to another. Because of the large energy gap between the ground and first excited state, the

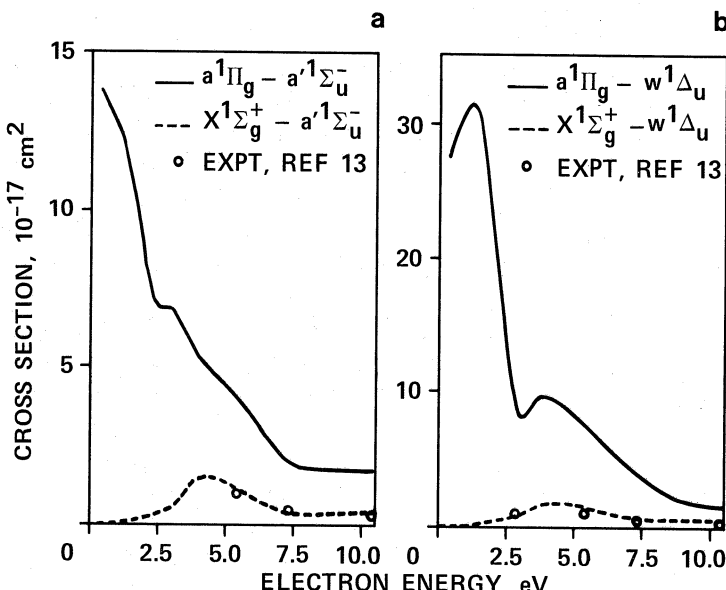


Fig. 4. (a) left figure, $N_2 a^1\Pi_g - a'^1\Sigma_u^-$ and $X^1\Sigma_g^+ - a'^1\Sigma_u^-$ cross sections; (b) right figure, $N_2 a^1\Pi_g - w^1\Delta_u$ and $X^1\Sigma_g^+ - w^1\Delta_u$ cross sections. Both sets of experimental data are from Ref. 13.

percentage of electrons with sufficient energy for electronic excitations is small. However, once the molecule is in the first excited state, it will rapidly equilibrate with other valence excited states. Thus we anticipate the set of valence excited states may be in a quasi-steady state among themselves, but still out of equilibrium with the ground state. This feature may have important consequences in modeling the concentration of radiative species.

While the present set of cross sections was determined for applications in entry physics, it should also be applicable to other modeling problems involving ionized gases.

REFERENCES

1. J. T. Howe, *J. Spacecraft and Rockets*, 22, 19 (1985).
2. C. Park, AIAA Paper No. 87-0514 (1987).
3. C. Park, "Thermal Design of Aeroassisted Orbital Transfer Vehicles," edited by H. F. Nelson, *Progress in Astronautics and Aeronautics* Vol. 96, (American Institute of Aeronautics and Astronautics, New York, 1985) p. 395.
4. W. M. Huo, V. McKoy, M. A. P. Lima, and T. L. Gibson, "Thermophysical Aspects of Re-Entry Flows," edited by J. N. Moss and C. D. Scott, *Progress in Astronautics and Aeronautics* Vol. 103, (American Institute of Aeronautics and Astronautics, New York, 1986) p. 152.
5. W. M. Huo, *Phys. Rev. A* (submitted for publication).
6. W. M. Huo, *Phys. Rev. A* (to be submitted).
7. W. M. Huo and T. L. Gibson, *Phys. Rev. A* (to be submitted).
8. W. M. Huo, T. L. Gibson, M. A. P. Lima, and V. McKoy, *Phys. Rev. A*36, 1632 (1987).
9. M. Berman, H. Estrada, L. S. Cederbaum, and W. Domcke, *Phys. Rev. A*28, 1363 (1983).
10. K. Takatsuka and V. McKoy, *Phys. Rev. A*24, 2473 (1981); *ibid.*, A30, 1734 (1984).
11. W. M. Huo, M. A. P. Lima, T. L. Gibson, and V. McKoy, *Phys. Rev. A*36, 1642 (1987).
12. M. Allan, *J. Phys. B*18, 4511 (1985).
13. D. C. Cartwright, S. Trajmar, A. Chutjian, and W. Williams, *Phys. Rev. A*16, 1041 (1977). See also S. Trajmar, D. F. Register, and A. Chutjian, *Phys. Rep.*, 97, 219 (1983) for renormalized data.
14. G. J. Schulz, *Rev. Mod. Phys.* 45, 423 (1973).
15. J. Mazeau, F. Gresteau, R. I. Hall, G. Joyez, and J. Reinhardt, *J. Phys. B*6, 862 (1973).
16. A. Huetz, C. Cadez, F. Gresteau, R. I. Hall, D. Vichon, and J. Mazeau, *Phys. Rev. A*21, 622 (1980).

ELECTRON COLLISION CROSS SECTIONS INVOLVING EXCITED STATES

E. J. Mansky

School of Physics
Georgia Institute of Technology
Atlanta, Georgia 30332-0430 U.S.A.

Knowledge of the integral cross sections for the electron-impact excitation of atoms initially in a metastable state is of fundamental importance not only in determining the number densities of atoms in various excited states, but also in understanding the overall collision dynamics of energy transfer and excited-state diagnostics in partially ionized gases. Recently, the study of transitions between metastable states of He has been revitalized by experimental measurements at Kaiserslautern (Muller-Fiedler et al. 1984) of the differential cross sections, and at Madison (Rall et al. 1989) of the integral cross sections for the $2^3S \rightarrow 3^3L$ electronic excitations in helium. This signals a new era in experiments involving metastable states in that much more detailed information can now be obtained by modern measurements than was possible in the pioneering work of Phelps (1955). This has also marked a resurgence in theoretical activity in this area as well with recent distorted wave calculations (Mathur et al., 1987) and optical potential calculations (Vučić et al. 1987). In this note we will briefly summarize the original multichannel eikonal theory of Flannery and McCann (1974a,b,c, 1975a,b), together with the correction needed to account for the influence that distant trajectories have on the scattering amplitude for states dipole-coupled via an optically-allowed transition to the initial state (Mansky and Flannery 1989a). In particular, attention will be focused on the results for the $2^3S \rightarrow 3^3L$ transitions in He due to the recent experimental data which has become available.

The basic expression in the multichannel eikonal theory (MET) for the complex scattering amplitude for the transition $i \rightarrow n$ is (Flannery and McCann 1975a,c)

$$f_{ni}(\theta) = -(i)^{\Delta+1} \int_0^\infty J_\Delta(q'p) [I_1(\rho, \gamma(\theta)) - i I_2(\rho, \gamma(\theta))\rho] d\rho \quad (1)$$

where the integrals I_1 and I_2 are defined,

$$I_1(\rho, \gamma(\theta)) = \int_{-\infty}^{\infty} dz \kappa_n(\rho, z) \frac{\partial C_n(\rho, z)}{\partial z} \exp[i\gamma(\theta)z] \quad (2a)$$

$$I_2(\rho, \gamma(\theta)) = \int_{-\infty}^{\infty} dz [\kappa_n(\kappa_n - k_n) + \frac{\mu}{\hbar^2} V_{nn}] C_n(\rho, z) \exp[i\gamma(\theta)z] \quad (2b)$$

The other terms in equations (1) and (2) are: $q' = k_n \sin\theta$; $\gamma(\theta) = k_n(1-\cos\theta)$; $\Delta = m_i - m_n$, where $m_i (m_n)$ is the magnetic quantum number of state $i(n)$; J_Δ is an ordinary Bessel function of order Δ ; $k_n^2 = k_n^2 - \frac{2\mu}{\hbar^2} V_{nn}$. The complex amplitude functions $C_n(\rho, z)$ in equation (2) are solutions of the following set of coupled first-order partial differential equations,

$$i \frac{\hbar^2}{\mu} \kappa_n \frac{\partial C_n(\rho, z)}{\partial z} + [\frac{\hbar^2}{\mu} \kappa_n(\kappa_n - k_n) + V_{nn}] C_n(\rho, z) = \sum_{j=1}^N V_{nj} C_j \exp[i(k_j - k_n)z] \quad (3)$$

which are solved subject to the asymptotic boundary condition condition, $C_n(\rho, z \rightarrow \infty) = \delta_{ni}$ for the N states in the basis set ($n = 1, 2, \dots, N$). For definitions of the remaining terms in equations (1-3) and a complete derivation of these equations see the original MET papers of Flannery and McCann (1974a,b,c, 1975a,b).

The main assumptions made in the derivation of (3) is that the trajectory for the relative motion of the electron in channel n is accurately characterized by a straight-line, and that the contribution of exchange to the inelastic integral cross section for channel n is negligible. The assumption of a straight-line trajectory for the relative motion of the projectile electron in $e^- + A^*$ collisions should be reliable due to the dominant nature of the long range part of the projectile-target electrostatic interaction in these collisions. However, in heavy particle collisions account must be taken of the curvature of the trajectory in order for accurate inelastic integral cross sections to be obtained. This has been done within the MET for applications in heavy particle collisions by McCann and Flannery (1975, 1978).

Similarly, in electron-metastable atom collisions the neglect of electron exchange effects should not introduce a great deal of error (Vučić et al. 1987). This is due to the increased size of the target atom when the incident state is an excited state. Recall that for hydrogen (Bethe and Salpeter 1977), the mean value of r , the electron-nucleus distance, scales with n as, $\langle r \rangle = [3n^2 - \ell(\ell+1)]/2Z$. This increase results in a concomitant decrease in the electronic charge density $\rho(r)$ of the target atom, which results in a lowering of the probability of overlap of the projectile electron's wavefunction with that of the bound electron, thereby decreasing the importance of electron exchange when compared to the case of scattering from ground state targets (i.e., target atoms initially in the ground state).

In actual calculations the coupled PDE's (3) are solved over a finite 2-dimensional grid: $0 \leq \rho \leq \rho_{\max}$, $-z_{\max} \leq z \leq z_{\max}$. The subsequent ρ -integration in (1) is then from $\rho = 0$ to $\rho = \rho_{\max}$. Typical values of

z_{\max} for ground state targets is $100-120 a_0$, while for metastable targets (i.e., target atoms initially in a metastable state) z_{\max} ranges from $250-300 a_0$. The typical values of ρ_{\max} range from 11 to $35 a_0$ for ground state targets, while for metastable targets the corresponding range is from 48 to $207 a_0$. These ranges on z_{\max} and ρ_{\max} refer to 10-channel eikonal theory results for hydrogen and helium (Mansky and Flannery 1989a,b). While the above values of z_{\max} and ρ_{\max} for ground state targets is sufficient to insure convergence of the inelastic integral cross section to the corresponding Born value at high energy, in the case of metastable targets this is not the case. The contribution that trajectories, with impact parameters ρ in the range $\rho_{\max} \leq \rho < \infty$, make to the scattering

amplitude for metastable transitions (e.g., $2^3S \rightarrow 3^3L$, $L = S, P, D$) is not negligible at high energies. This is particularly true of metastable states dipole-coupled to the initial state via an optically-allowed transition. The correction to the scattering amplitude needed to account for these distant trajectories is given by (Mansky and Flannery 1989a),

$$f_{ni}^{(DMET)}(\theta) = \Gamma \int_0^{\rho_{\max}} J_{\Delta}(q' \rho) [I_1(\rho, \gamma) - i I_2(\rho, \gamma)] \rho d\rho + f_{ni}^{(dipole)}(\theta)$$

$$= f_{ni}^{(MET)}(\theta) + f_{ni}^{(dipole)}(\theta), \text{ dipole-coupled transitions} \quad (4a)$$

$$= f_{ni}^{(MET)}(\theta) \quad , \text{ all other transitions} \quad (4b)$$

where,

$$f_{ni}^{(dipole)}(\theta) = \Gamma(i)^{\Delta+1} \frac{2\mu d'_{ni}}{t^2} \frac{\alpha'}{q'^2 + \alpha'^2} [x_1 J_{\Delta+1}(x_1) K_{\Delta}(x_1) - x_2 J_{\Delta}(x_2) K_{\Delta+1}(x_2)] \quad (5)$$

and $\Gamma \equiv -(i)^{\Delta+1}$, $\alpha' = \gamma(\theta) - \alpha$, $\alpha = 2\mu(\epsilon_n - \epsilon_i)/\hbar^2(k_i + k_n)$, $d'_{ni} = \sqrt{3/4\pi} d_{ni}$, with d_{ni} denoting the dipole moment for the transition $i \rightarrow n$, and $x_1 \equiv q' \rho_{\max}$, $x_2 \equiv \alpha' \rho_{\max}$. The eigenenergies of the target atom are denoted ϵ_n , while $K_m(x)$ is a modified Bessel function of order m .

In this note the dipole correction (5) has been applied only to the $2^3S \rightarrow 2^3P_{o,\pm 1}$ and $2^3S \rightarrow 3^3P_{o,\pm 1}$ ($\Delta = 0, 1$) transitions within a 9-channel basis (2^3S , $2^3P_{o,\pm 1}$, 3^3S , $3^3P_{o,\pm 1}$ and $3^3D_{o,\pm 1, \pm 2}$). The present multi-channel eikonal theory results for these transitions are hereafter denoted DMET. However, to avoid confusion with Flannery and McCann's (1975) original MET results, the present results for the remaining triplet transitions will also be denoted DMET (with equations (4a) and (4b) in mind this should cause little confusion).

In figure 1 the present DMET results for the differential cross sections for the $2^3S \rightarrow 2^3P$ and $2^3S \rightarrow 3^3L$ ($L = S, P, D$) transitions at $E = 20$ eV

are compared with the experimental data of Müller-Fiedler et al. (1984), the original MET results of Flannery and McCann (1975b) and (where available) the distorted-wave (DW) results of Mathur et al. (1987). The present DMET results for the $2^3S \rightarrow 3^3S$ and $2^3S \rightarrow 3^3D$ optically-forbidden transitions are clearly in excellent agreement with the experimental data. In particular, the agreement of the DMET results with experiment for the former transition is a direct result of the improved numerical solution of (3) used in the present results compared to that used in the original MET results. For the optically allowed $2^3S \rightarrow 2^3P$ and $2^3S \rightarrow 3^3P$ transitions, the present DMET results are seen to be underestimating the experimental data of Müller-Fiedler et al. This is also the case with the original MET results and the DW results. Interestingly however, all three theoretical results predict the existence of a deep diffractive minimum at about 12° in the $2^3S \rightarrow 3^3P$ DCS. No such behavior is seen however in the experimental data, leading one to question the theoretical results. While the DW results of Mathur et al. (1987) includes electron exchange within the primary, $2^3S \rightarrow 3^3P$, transition (with no couplings to other states), both the original MET results and the present DMET results neglect exchange but include couplings up to the 3^3D state. These points, taken together with the DCS experimental data for the n=4 triplet states (cf. Table 1), seem to indicate that the major physical mechanism missing from the theoretical results shown in figure 1 is coupling to the n=4 triplet states of helium. At least both dipole ($2^3S \rightarrow 4^3P$) and quadrupole ($2^3S \rightarrow 4^3S$, 4^3D) couplings should be included in a theoretical calculation in light of the relative magnitudes observed in the Kaiserslautern experiment between the DCS for the 3^3P state and the n=4 triplet states.

TABLE 1. Experimental Differential Cross Sections for $e^- + He(2^3S \rightarrow n^3L)$
 $(\pi a_0^2 / \text{str.})$ (Müller-Fiedler et al. 1984).

θ	2^3P	3^3S	3^3P	3^3D	$4^3S+4^3P+4^3D+4^3F$
10	300	4.9	5	25	10
15	85	1.4	1.9	10	6
20	26	.99	2.1	4	1.8
25	7.5	.60	.78	1.7	.78
30	2.8	.38	.58	.37	.50
35	1.6				
40	.82				

The DMET integral cross sections for the 2^3P and 3^3L ($L=S,P,D$) states are compared in figure 2 with the Born results of Flannery et al. (1975), the original MET results of Flannery and McCann (1975b) and (where available) the distorted-wave results of Mathur et al. (1987). Also, for the 2^3P and 3^3S states, the 5-state R-matrix results of Fon et al. (1981) and the Glauber theory results of Khayrallah et al. (1978) are shown, respectively. The above theoretical results are compared in figure 2 with the recent experimental data of Rall et al. (1989) for the 3^3S , 3^3P and 3^3D states. In the case of the 3^3S and the 3^3D states the experimental results are absolute apparent cross sections, so a direct comparison with theory will require the subtraction of the cascade contribution from the apparent measurements. Only the 3^3P results of Rall et al. (1989) are direct measurements. These were determined from the optical cross sections for

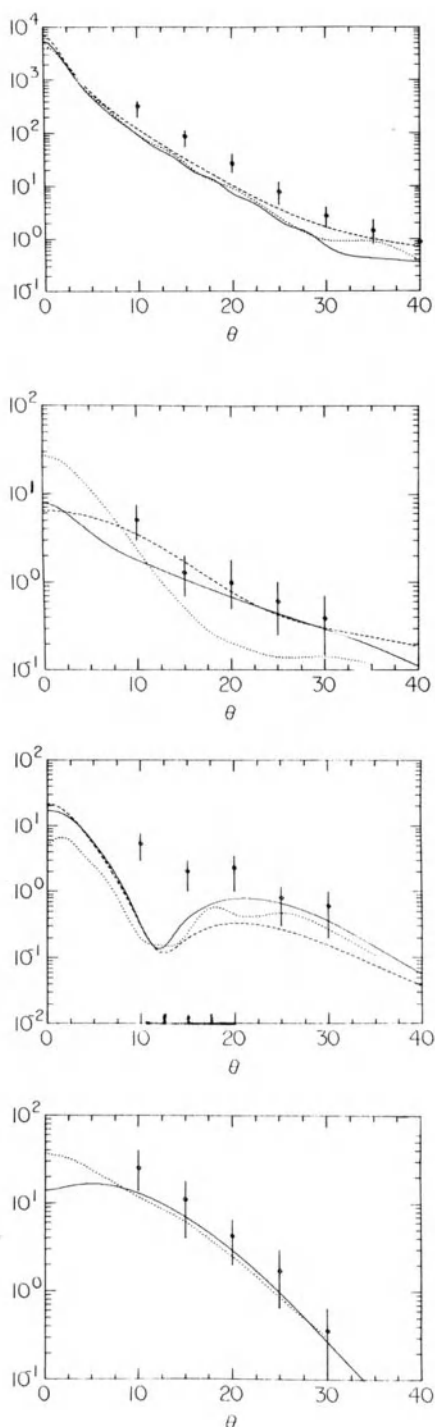


Figure 1. $e^- + He(2^3S \rightarrow n^3L)$ differential cross sections ($\pi a_0^2/\text{str.}$) at $E = 20 \text{ eV}$; —, present DMET results; -----, DW results (Mathur et al. 1987);, original MET results (Flannery and McCann, 1975b); o, experimental data (Müller-Fiedler et al. 1984).

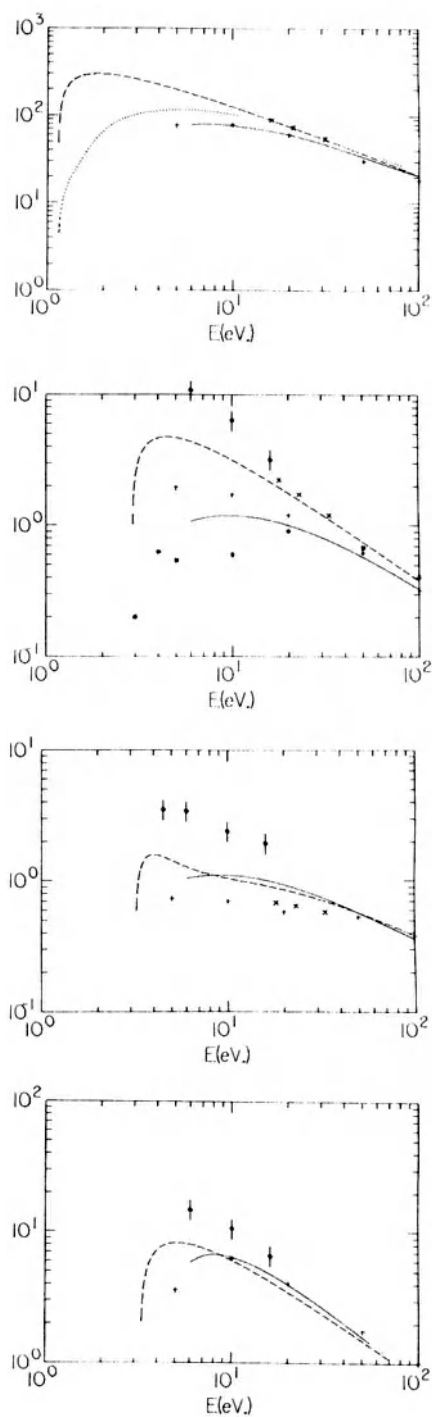


Figure 2. $e^- + He(2^3S \rightarrow n^3L)$ integral cross sections (πa_0^2). ---, Born results (Flannery et al. 1975); —, present DMET results; +, original MET results (Flannery and McCann 1975b); \times , DW results (Mathur et al. 1987); $*$, Glauber results (Khayrallah et al. 1978);, R-matrix results (Fon et al. 1981); \circ , experimental data (Rall et al. 1989).

the 2^3P and 3^3P and Einstein A coefficients (see Rall et al. (1989) for details). Clearly, further theoretical work will be required in order to convert the remaining apparent cross section measurements of Rall et al. to direct cross sections. However, the measurements of Rall et al. do confirm the basic trend, seen in both the MET and DMET, of the optically-forbidden $2^3S \rightarrow 3^3D$ cross section being larger than the optically-allowed $2^3S \rightarrow 3^3P$ cross section in the intermediate energy region.

ACKNOWLEDGEMENTS

This research is supported by AFOSR Grant No. 84-0233. Additional support from NATO and the Georgia Tech Research Corporation is also gratefully acknowledged.

REFERENCES

- Bethe, H. A. and Salpeter E. E., 1977, Quantum Mechanics of One- and Two-Electron Atoms, Plenum Press (N.Y.)
- Flannery, M. R. and McCann, K. J., 1974a, J. Phys. B: At. Mol. Phys. 7, L223-7
- 1974b, J. Phys. B: At. Mol. Phys. 7, 2518-32
- 1974c, J. Phys. B: At. Mol. Phys. 7, L522-7
- 1975a, J. Phys. B: At. Mol. Phys. 8, 1716-33
- 1975b, Phys. Rev. A 12, 846-55
- Flannery, M. R., Morrison, W. F. and Richmond, B. L., 1975, J. Appl. Phys. 46, 1186-90
- Fon, W. C., Berrington, K. A., Burke, P. G. and Kingston, A. E., 1981, J. Phys. B: At. Mol. Phys. 14, 2921-34
- Khayrallah, G. A., Chen, S. T. and Rumble, J. R., 1978, Phys. Rev. A 17, 513-22
- Mansky, E. J. and Flannery, M. R., 1989a, "The Multichannel Eikonal Theory of Electron-Hydrogen Collisions I. Excitation of H(1s)", to be submitted
- 1989b, "The Multichannel Eikonal Theory of Electron-Heilium Collisions I. Excitation of He(1^1S)", to be submitted
- Mathur, K. C., McEachran, R. P., Parcell, L. A. and Stauffer, A. D., 1987, J. Phys. B: At. Mol. Phys. 20, 1599-1608
- McCann, K. J. and Flannery, M. R., 1975, J. Chem. Phys. 63, 4695-4707
- 1978, J. Chem. Phys. 69, 5275-87
- Müller-Fiedler, R., Schlemmer, P., Jung, K., Hotop, H. and Ehrhardt, H., 1984, J. Phys. B: At. Mol. Phys. 17, 259-68
- Phelps, A. V., 1955, Phys. Rev. 99, 1307-13
- Rall, D. L. A., Sharpton, F. A., Schulman, M. B., Anderson, L. W., Lawler, J. E. and Lin, C. C., 1989, Phys. Rev. Lett. 62, 2253-6
- Vučić, S., Potvliege, R. M. and Joachain, C. J., 1987, J. Phys. B: At. Mol. Phys. 20, 3157-70

NEW THEORETICAL APPROACHES FOR STUDYING ELECTRON COLLISIONS WITH SMALL MOLECULES*

T. N. Rescigno

Lawrence Livermore National Laboratory
P. O. Box 808
Livermore, California 94550, USA

I. INTRODUCTION

There has been a recent resurgence of interest in the use of algebraic variational methods for studying a variety of collision problems. Much of this interest stems from the discovery that spurious singularities, which plagued the traditional methods, can be eliminated when the variational principle is formulated with outgoing-wave boundary conditions.^{1,2} Another reason for the recent activity is the obvious suitability of these methods to present-day supercomputers. My purpose here is to describe an implementation of the complex Kohn method³, an algebraic variational technique, for studying electron collisions with small molecules, both linear and non-linear. Unlike variational principles based on the integral form of the Schrödinger equation (Lippmann-Schwinger equation), the method only requires Hamiltonian matrix elements. I will also show how the formalism allows one to develop a variational principle for computing first-order properties, such as bound-free dipole transition amplitudes. I will show results for the electron-impact dissociation of hydrogen as a function of initial vibrational quantum number. I will also illustrate the method for polyatomic molecules with results for elastic scattering of electrons by formaldehyde.

II. THEORY

A. Trial Wave Function

To describe the scattering of low energy electrons, incident in a channel denoted by the label Γ^1 , by an N -electron target molecule, we formulate the problem in body-frame coordinates within the framework of the fixed-nuclei approximation using an antisymmetrized trial wave function of the form,

$$\Psi_{\Gamma^1} = \sum_{\Gamma} A(\chi_{\Gamma} F_{\Gamma\Gamma^1}) + \sum_{\mu} d_{\mu}^{\Gamma^1} \oplus_{\mu} . \quad (1)$$

where the first sum runs over the energetically open N -electron target states, denoted by the normalized functions χ , and the operator A antisymmetrizes the orbital functions F into the functions χ . The \oplus are an

orthonormal set of antisymmetric, square-integrable ($N+1$)-electron functions used to represent polarization and correlation effects not included in the first summation. The symbol Γ is being used to label all the quantum numbers needed to represent a physical state of the composite system, ie. the internal state of the target molecule as well as the energy and orbital angular momentum of the scattered electron.

To calculate physical differential cross sections, it is necessary to express the scattering amplitude in the laboratory frame⁴. Since this is easily accomplished by projecting the T-matrix onto a set of angular functions, the channel continuum functions, F , are further expanded as:

$$rF_{\Gamma\Gamma^1}(\vec{r}) = \sum_{\ell m} [f_\ell^\Gamma(r) \delta_{\ell\ell^1} \delta_{mm^1} \delta_{\Gamma\Gamma^1} + T_{\ell m \ell^1 m^1} g_\ell^\Gamma(r)] Y_{\ell m}(\hat{r}) + \sum_k c_k^{\Gamma\Gamma^1} \varphi_k^\Gamma(\vec{r}) \quad (2)$$

where $Y_{\ell m}$ is a normalized spherical harmonic, the φ_k are a set of square-integrable functions, and the functions {f} and {g} are linearly independent continuum orbitals which are *regular* at the origin and, in the case of neutral targets, behave asymptotically as regular and *outgoing* Riccati-Bessel functions, respectively,

$$\begin{aligned} f_\ell^\Gamma(r) &= \sin(k_\Gamma r - \ell\pi/2)/\sqrt{k_\Gamma}; \\ g_\ell^\Gamma(r) &= \exp(i(k_\Gamma r - \ell\pi/2))/\sqrt{k_\Gamma}. \end{aligned} \quad (3)$$

The channel momenta are determined by energy conservation,

$$k_\Gamma^2/2 = E - E_T, \quad (4)$$

where E is the total energy and E_T is the energy of target state χ_Γ . The functions {f} and {g} may be modified to Coulomb form to treat ionic targets. The coefficients [T] are elements of the T-matrix and are the fundamental dynamical quantities that determine scattering amplitudes and cross sections.

If the target molecule has symmetry, we can use it to restrict the sum over angular quantum numbers that appear in Eq. (2). For example, in linear molecules, m is a good quantum number and the sum over m collapses to the single term with $m=m^1$. Moreover, the sum over ℓ -values can be restricted to the number of "asymptotic ℓ 's" needed to represent the channel wave function at large distances and to provide converged cross sections at a particular energy.

Electron scattering cross sections can be expressed solely in terms of the T-matrix. In such cases, all we need is the open-channel part of the wave function and the correlation functions Θ can be formally incorporated into an effective optical potential. This is accomplished using Feshbach partitioning with operators P and Q that project onto the open- and closed-channel subspaces, respectively. However, there are cases where we need the full wave function. For example, if we wish to calculate properties such as dipole transition matrix elements, we will need both $P\Psi$ and $Q\Psi$. In such cases, it may be simpler to work with Eq. (1) directly.

B. Variational Principles

The Kohn principle⁵ can be used to characterize the T-matrix as the stationary value of the functional:

$$T_{\text{stat}}^{\Gamma\Gamma^1} = T^{\Gamma\Gamma^1} - 2 \int \Psi_{\Gamma} (\mathbf{H} - \mathbf{E}) \Psi_{\Gamma^1} . \quad (5)$$

Trial values for the coefficients \mathbf{T} , \mathbf{c} and \mathbf{d} , which define the "Kohn trial wave function", are determined from the linear equations obtained by requiring that the derivatives of elements of $T_{\text{stat}}^{\Gamma\Gamma^1}$ with respect to these parameters vanish. These coefficients, when substituted back into Eq. (5), give a stationary expression for the T-matrix. In a condensed matrix notation, in which open-channel indices are suppressed, the result is³

$$[T_{\text{stat}}] = -2 \left(M_{oo} - M_{qo} M_{qq}^{-1} M_{qo} \right) \quad (6)$$

where o refers to $A(\chi_{\Gamma} f_{\ell}^{\Gamma} Y_{\ell m})$ and q to $A(\chi_{\Gamma} g_{\ell}^{\Gamma} Y_{\ell m})$, $A(\chi_{\Gamma} \varphi_k^{\Gamma})$ and Φ_{μ} . For example, the elements of M_{qo} are defined as

$$(M_{qo})_k^{\Gamma\Gamma^1} = \int A(\chi_{\Gamma} \varphi_k^{\Gamma}) (\mathbf{H} - \mathbf{E}) A(\chi_{\Gamma^1} f_{\ell^1}^{\Gamma^1} Y_{\ell^1 m^1}) . \quad (7)$$

Because of the outgoing-wave behavior of the functions $\{g\}$, the matrix M_{qq} will be complex-symmetric and thus its inverse will be non-singular for real energies^{1,2}. Thus with complex, outgoing-wave boundary conditions, the Kohn method leads to an anomaly-free expression for the T-matrix.

The Kohn trial wave function, when substituted into Eq. (5), gives a stationary expression for the T-matrix. Less obvious, but nonetheless true, is that this same wave function, when used to compute any first-order property, will also give a value accurate through second-order. Suppose we wish to calculate the amplitude,

$$B \equiv \langle W | \Psi_{\Gamma^1} \rangle \quad (8)$$

where W is some known function. For example, if $|W\rangle = \mu |\Psi_0\rangle$, where μ is the dipole operator and Ψ_0 is the initial state of the target, then B is simply the bound-free dipole transition amplitude for photoabsorption. We start with a stationary principle for B given by Gerjouy, Rau and Spruch⁶:

$$B' \equiv \langle W | \Psi_{\Gamma^1} \rangle + \langle h' | M | \Psi_{\Gamma^1} \rangle \quad (9)$$

where $M = H - E$ and h' is some auxillary function. The second term in Eq. (9) obviously vanishes when Ψ_{Γ^1} is exact. The auxillary function is required to satisfy the equation:

$$M|h'\rangle + |W\rangle = 0 \quad (10)$$

along with the boundary condition

$$\langle h' | M | \delta\Psi_{\Gamma^1} \rangle - \langle \delta\Psi_{\Gamma^1} | M | h' \rangle = 0 , \quad (11)$$

where

$$\delta\Psi_{\Gamma^1} = \Psi_{\Gamma^1}^{\text{exact}} - \Psi_{\Gamma^1} . \quad (12)$$

Because of the asymptotic boundary conditions specified by Eqs. (2) and (3), Eq. (11) will be satisfied if h' is chosen to be regular at the origin and to behave as a purely outgoing scattered wave asymptotically. Thus we take, in analogy with Eqs. (1)-(3),

$$h' = \sum_{\Gamma} A(\chi_{\Gamma} G_{\Gamma\Gamma^1}) + \sum_{\mu} e_{\mu}^{\Gamma^1} \oplus_{\mu} . \quad (13)$$

with

$$rG_{\Gamma\Gamma^1}(\vec{r}) = \sum_{\ell} [U_{\ell m \ell^1 m^1}^{\Gamma \Gamma^1} g_{\ell}^{\Gamma}(r)] Y_{\ell m}(\hat{r}) + \sum_{\mathbf{k}} i_k^{\Gamma\Gamma^1} \varphi_{\mathbf{k}}^{\Gamma}(\vec{r}) \quad (14)$$

The derivation proceeds as before. We substitute Eqs. (1), (2), (13) and (14) into Eq. (9) and set the derivatives of B' with respect to the trial coefficients in both h' and Ψ_{Γ^1} equal to zero. The result, when substituted back into Eq. (9), gives:

$$B' = \langle W | A(\chi_{\Gamma^1} f_{\ell^1}^{\Gamma^1} Y_{\ell^1 m^1}) \rangle - V_q M^{-1}_{qq} M_{q0} \quad (15)$$

where M is as in Eq. (6) and V is a vector whose elements are:

$$V_q = \langle W | q \rangle \quad (16)$$

where q again refers to the space spanned by $A(\chi_{\Gamma} g_{\ell}^{\Gamma} Y_{\ell m})$, $A(\chi_{\Gamma} \varphi_{\mathbf{k}}^{\Gamma})$ and \oplus_{μ} . But Eq. (15), which we have now shown to be a stationary expression, is simply the result one would have obtained by using the Kohn trial wave function in Eq. (8).

C. Orthogonality and Separable Expansions

The essence of the entire calculation can be reduced to the evaluation of the matrix elements of one- and two-body operators over bound and continuum basis functions. The first practical step is to reformulate the entire procedure in terms of mutually orthogonal bound and continuum functions. This can be done quite rigorously and follows from a property of the Kohn principle called *transfer invariance* which has been described elsewhere^{7,8}. The matrix elements involving only bound functions can be evaluated using the standard techniques of bound-state molecular electronic structure theory. The matrix elements involving continuum (Bessel or Coulomb) functions are more problematic, and the principal difficulty of any molecular scattering calculation is their evaluation. There are two critical steps in making this problem tractable for molecules. The first is the rigorous relegation of exchange forces to matrix elements over the square-integrable part of the basis. That reformulation is accomplished by constructing a separable representation of all exchange operators and by orthogonalizing the continuum basis functions to the square-integrable basis used in the representation of exchange. If an optical potential is

used, it too is treated in separable form. I will give no further details of that step here because it has been discussed in detail elsewhere^{3,8}. The only remaining matrix elements involving continuum functions are "direct". Thus the second step in rendering the molecular problem tractable is to devise an efficient numerical scheme for evaluating these intergals.

D. Adaptive Quadratures

All direct "bound-free" and "free-free" matrix elements can be reduced to single three-dimensional integrals. For diatomic targets, single-center expansions can be used to further reduce these to sums of radial integrals, which can be quadratured numerically, times known angular factors. For polyatomic targets, single-center expansions can converge quite slowly so we evaluate the three-dimensional integrals directly using novel quadrature schemes.

The key to making this quadrature practical is to make it adaptive so that points are clustered with nearly spherical symmetry around each nucleus while the points at large distances from the molecule are arranged with spherical symmetry around its center⁹. We begin by defining a new variable:

$$\vec{r}(\vec{q}) = \vec{q} - \sum_{\text{nuc}} (\vec{q} - \vec{R}_{\text{nuc}}) S_{\text{nuc}}(\vec{q}) \quad (17)$$

where $S_{\text{nuc}}(\vec{q})$ is a strength function depending on the distance of a point from the nuclear position R_{nuc} . The function S_{nuc} may be chosen in any number of ways, but it must have the property that

$$S_{\text{nuc}}(\vec{q}) \xrightarrow[q \rightarrow \infty]{} 0 \quad (18)$$

so that the transformation in Eq.(17) will reduce to the identity, and r will be the same as q at large distances from the molecule. With this change of variable, a typical integral we wish to evaluate becomes

$$I = \int F(\vec{r}(\vec{q})) |\partial \vec{r}/\partial \vec{q}| d^3q \quad (19)$$

Now we choose a quadrature in \vec{q} consisting of shells of points around the center of the molecule which we can construct from standard Gauss quadrature points and weights. Applying that quadrature to Eq.(19) transforms the points under the new mapping so that they are distributed adaptively while the Jacobian, $|\partial \vec{r}/\partial \vec{q}|$, provides the correct weights. Further details and an evaluation of the accuracy of such quadratures are given elsewhere⁹.

III. EXAMPLES

A. Electron Impact Dissociation of Hydrogen

At low energies, electron-impact dissociation of molecular hydrogen proceeds mainly through excitation of the lowest triplet electronic state, which dissociates to neutral ground-state hydrogen atoms. Cross sections for this process, and particularly their dependence on initial vibrational

quantum number, are required for accurate modelling of hydrogen plasmas. We previously calculated these cross sections¹⁰ in a two-state close-coupling approximation using the complex Kohn method. The complex Kohn equations were solved by using Cartesian Gaussian basis sets in each of four symmetries, $\sigma_g, \sigma_u, \tau_g$, and τ_u , along with regular and outgoing-wave Bessel functions up to $\ell=12$. The details of these computations, including basis set information, target state description and assumptions about the nuclear dynamics, have all been given previously and will not be repeated here. I have since extended these calculations to lower energies than were originally reported and these new results are shown here. Figure 1 gives the energy dependence of the excitation(dissociation) cross sections for hydrogen starting in each of the first ten vibrational levels.

B. Low Energy Electron-Formaldehyde Scattering

A low energy shape resonance, corresponding to a ${}^2\text{B}_1$ state of CH_2O^- , has been observed in elastic electron-formaldehyde collisions as well as in vibrational excitation^{11,12}. Target distortion effects are critical in determining the positions and widths of such resonances. In our calculations on formaldehyde¹³ we included these effects through the use of a Feshbach optical potential constructed using the techniques of *ab initio* electronic structure theory. This formalism allows the description of the elastic scattering problem in terms of an effective, energy-dependent, nonlocal Hamiltonian. In our case P projects on the space appropriate to the static-exchange approximation while the physics included by the optical potential is determined by the choice of configurations which span the Q -space. In these calculations we chose configurations representing the dominant effect of correlation in a shape resonance, which is the relaxation of the occupied target orbitals in the presence of the scattered electron. The ground state of formaldehyde was represented by a closed-shell Hartree-Fock wave function. The configurations in the Q -space

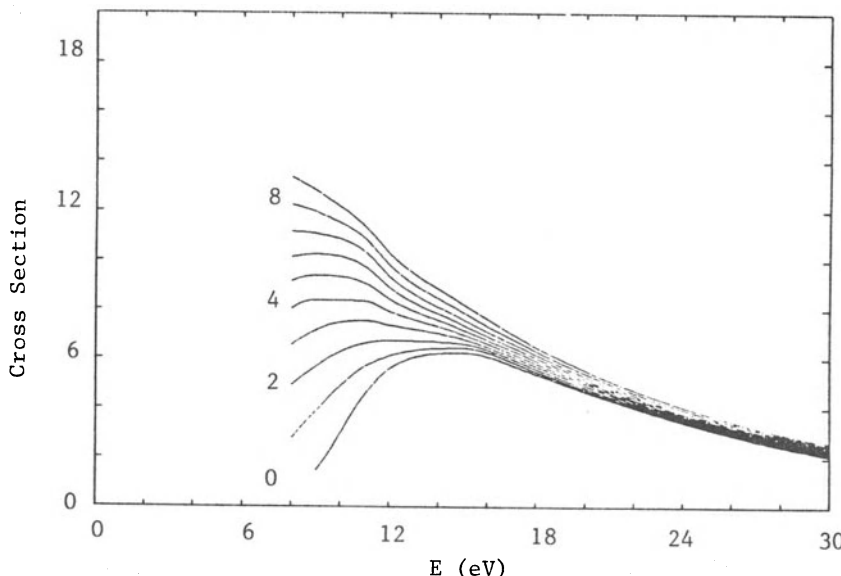


Figure 1. Total cross sections (a_0^2) for excitation of the $b^3\Sigma^+$ state of H_2 from various vibrational levels of the ground state.

all consisted of antisymmetrized products of a basis orbital and target configurations which are singlet-coupled, single excitations from the occupied Hartree-Fock orbitals to virtual orbitals of the same symmetry. We used 624 such Q-space configurations to effectively allow the target orbitals to relax in the presence of a scattered electron at the resonance energy. The *ab initio* optical potential has the correct energy dependence to represent the enhancement of target orbital relaxation near the resonance energy and its reduction elsewhere, while preserving the correct asymptotic dipole behavior of the interaction.

Except in b_1 symmetry, where there is a shape resonance, electron scattering from CH_2O at low energies can be expected to be dominated by its permanent dipole potential. This presents us with an additional physical problem, because the partial wave expansion of the total cross section in terms of the body-frame T-matrix elements fails to converge, as does the differential cross section in the forward direction. A simple remedy for this problem was proposed by Norcross and Padial¹⁴. It is summarized by the expression for the laboratory frame differential cross section for the rotational transition $j-j'$, where j denotes all relevant rotational quantum numbers,

$$\left[\frac{d\sigma}{d\Omega} \right]_{j \rightarrow j'} = \left[\frac{d\sigma}{d\Omega} \right]_{j \rightarrow j'}^{\text{Born}} + \Delta \left[\frac{d\sigma}{d\Omega} \right]_{j \rightarrow j'}; \quad (20)$$

In Eq. (20) the first term is the Born approximation to the cross section for a rotating point dipole (whose magnitude is that of the molecule's permanent dipole) and the second term denotes the difference between the contribution due the computed T-matrix elements and that due to their counterparts in the Born approximation for the point dipole. The latter is evaluated in the fixed-nuclei approximation. This treatment is called the

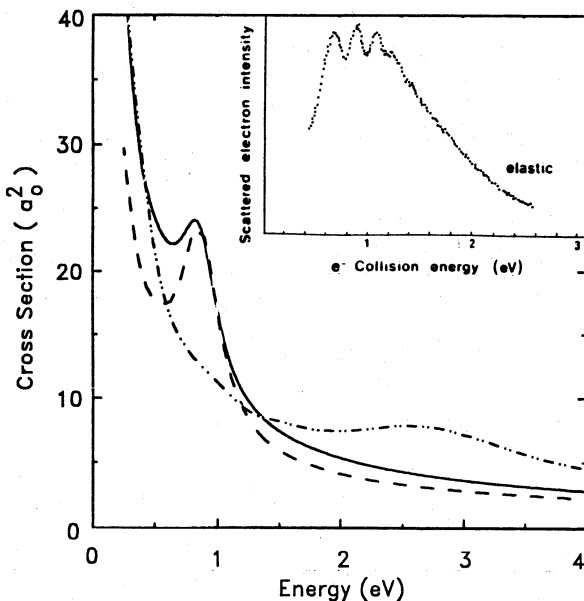


Figure 2. Elastic differential cross section for $e^- - \text{CH}_2\text{O}$. Solid curve: optical potential results at 90° ; dashed curve: optical potential results at 120° ; dashed-dot curve: static-exchange result at 90° . Insert shows experimental results of Benoit and Abouaf (ref. 12).

multipole extracted adiabatic nuclei (MEAN) method^{1,4} because it is the result of adding and subtracting the Born cross section in two different representations: the analytic expression for the laboratory cross section and its body-frame partial wave expansion. Additional details of the transformation of the partial wave amplitudes from the body-fixed to laboratory-fixed frames are given by Lane⁴.

Our results^{1,3} are summarized in Figure 2. In the static-exchange approximation the resonance appears at an energy nearly two eV above the correct position and with a far broader width than both the optical potential results and experiment^{1,2}. The results of the optical potential calculation place the resonance essentially exactly at the experimentally observed position. Our calculations at the molecule's equilibrium geometry produce a width which is somewhat narrower than the experimentally observed resonance peak in elastic scattering. Also shown in Figure 2 is the cross section from the optical potential calculation at a scattering angle of 120°. The resonance peak is increasingly visible at higher angles and is essentially invisible near the forward direction where scattering from the dipole potential dominates.

The experimental elastic scattering measurements shown in Figure 2 display vibrational structure due to the vibrational states of the metastable formaldehyde anion. A complete comparison between theory and experiment must wait for theoretical calculations which have been performed over a range of nuclear positions so that vibrational motion can be included.

IV. REFERENCES

1. W.H. Miller and B. Jansen op de Haar, *J. Chem. Phys.* **86**, 6213 (1987).
2. C.W. McCurdy, T.N. Rescigno, and B.I. Schneider, *Phys. Rev. A* **36**, 2061 (1987).
3. B.I. Schneider and T.N. Rescigno, *Phys. Rev. A* **37**, 3749 (1988).
4. N.F. Lane, *Rev. Mod. Phys.* **52**, 29 (1980).
5. W. Kohn, *Phys. Rev.* **74**, 1763 (1948).
6. E. Gerjouy, A.R.P. Rau and L. Spruch, *J. Math. Phys.* **13**, 1797 (1972).
7. R.K. Nesbet, *Variational Methods in Electron-Atom Scattering Theory*, (Plenum, New York, 1980).
8. T.N. Rescigno and B.I. Schneider, *Phys. Rev. A* **37**, 1044 (1988).
9. C. W. McCurdy and T. N. Rescigno, *Phys. Rev. A* **39**, 4487 (1989).
10. T.N. Rescigno and B.I. Schneider, *J. Phys. B* **21**, L691 (1988).
11. P.D. Burrow and J.A. Michejda, *Chem. Phys. Letts.* **42**, 223 (1976).
12. C. Benoit and R. Abouaf, *Chem. Phys. Letts.* **123**, 134 (1986).
13. T. Rescigno, C.W. McCurdy and B.I. Schneider, *Phys. Rev. Letts.* (submitted for publication).
14. D.W. Norcross and N.T. Padial, *Phys. Rev. A* **25**, 226 (1982).

* This work was performed under the auspices of the U.S. Department of Energy by the Lawrence Livermore Laboratory under contract No. W-7405-ENG-48.

ION-NEUTRAL REACTIONS

Rainer Johnsen

University of Pittsburgh
Pittsburgh, PA U.S.A.

INTRODUCTION

Experimental studies of ion-neutral reactions are often carried out with specific applications in mind, for instance atmospheric or laser plasmas. Well-developed experimental methods are available in the form of flow tubes, ion-cyclotron resonance methods, ion drift tubes, and ion beam techniques, all of which have been employed extensively.

My talk at this meeting is essentially a progress report on ongoing drift-tube experiments in our laboratory. I will cover several subjects, beginning with ion-molecule reactions with organophosphates. These studies were conducted in support of research to assess the feasibility of using discharges to destroy harmful organic substances. A second topic deals with reactions of doubly-charged molecular oxygen ions and the effect of vibrational excitation of the parent ion.

Thirdly, I will present some new data on the three-body association of protons and deuterons to helium and will describe a simple theoretical model which may be useful to estimate three-body association rates of ions in atomic gases.

EXPERIMENTAL METHODS

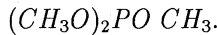
I will keep my remarks on experimental methods rather brief since these have been adequately described in published papers [1,2]. An ion drift tube, in the form presently used by us, employs two mass spectrometers. Parent ions are produced in an electron impact ion source (other sources may be substituted), they are mass selected by a quadrupole mass spectrometer and injected into the drift/reaction region which is filled with typically 1 Torr of buffergas (usually helium) and small additions of the reactant. The residence time of the ions in the drift tube may be varied by programmed electric drift fields (additional residence time technique [2]). A second mass spectrometer mass analyzes the ions effusing from the drift tube through a small sampling orifice. Rate coefficients and product-ion branching ratios are inferred from the observed loss rates of parent ions and product-ion signal intensities.

The technique allows determinations of rate coefficients in the ion energy range from thermal to about 1 eV (center of mass of the ion-reactant system). Extensive

use is made of the product- and parent-ion arrival time spectra which contain useful information on ion mobilities, and sometimes permit separating ions in different electronic states.

REACTIONS OF ATMOSPHERIC IONS WITH DIMETHYL-METHYPHOSPHONATE (DMMP)

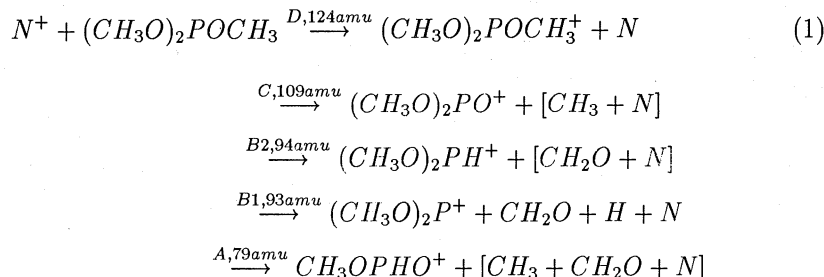
The study of reactions with DMMP was undertaken to gain some insight into the ion chemistry of this substance in support of model calculations of air/DMMP discharges. I will not have the time or space to present all data here, but will give a brief overview of the results. The chemical formula of DMMP is



DMMP is liquid at room temperature. In our experiments DMMP vapor was admitted to the drift tube from a dry-ice cooled sample at vapor pressures near 10^{-5} Torr. The experiments consisted of measuring the total rate coefficients, the product ion yields, and their variation with ion energy in the energy range from 0.04 to about 1 eV (center of mass).

REACTIONS OF O⁺, O₂⁺, N⁺, N₂⁺ WITH DMMP

The product ion yields and total rate coefficients for those ions reacting with DMMP are rather similar. Typically the rate coefficients are on the order of 10^{-9} cm³/s and vary little with ion energy, as one would expect for fast ion-molecule reactions. For instance, the products of the reaction of atomic nitrogen ions



arise from charge transfer (D), dissociative charge transfer (C), or rearrangement (A,B1,B2). In channels A, B1, and B2 there is an ambiguity in deriving the chemical composition of the ions from the observed product-ion masses. For instance, CH₃PO₃⁺ and PO₃⁺ have the same masses as the ions listed in branches A and B2 (79 and 94 amu). High mass-resolution, electron-impact ionization studies of DMMP by Bafus et al [3a], however, suggest that fragmentation into the ions listed is more likely than these alternatives.

Similar product-ion patterns occur for the reactions of molecular nitrogen, atomic, and molecular oxygen ions, but the relative abundance of branches A, B1, B2, C, D depends strongly on the ionization potential of the parent ion and the ion energy. An example is shown in Fig. 1, where the product ion yields for both atomic and molecular oxygen ions are shown as a function of ion energy. The energy scale for the atomic oxygen ion is shifted by 1.55 eV (difference of ionization potentials of the

Table I. Measured total rate coefficients and product yields of ion-molecule reactions with dimethyl-methylphosphonate (DMMP). The energy ranges given refer to the measurements of total rate coefficients. Product yields are at thermal energy unless otherwise indicated. The abbreviations A, B1, B2, C, D denote the product-ion branches defined in the text.

Ion	$k (10^{-9} \text{ cm}^3 / \text{s})$	Product Yield (%)			
O^+	1.4 (0.04 to 0.7 eV)	A	60		
		B1+B2	30 (B1<20% of B1 + B2)		
		C	10		
		D	0		
O_2^+	0.8 (0.04 to 0.9 eV)	A	18		
		B	40		
		C	8		
		D	34		
N^+	1.3 (0.04 to 0.9 eV)	A	25		
		B1+B2	45 (B1<30% of B1 + B2)		
		C	13		
		D	17		
N_2^+	1.1 (0.04 to 1.0 eV)	A	45		
		B1	18		
		C	27		
		D	10		
$\text{NO}^+ (\text{X}^1\Sigma^+)$	1.1 (0.04 eV)	NO ⁺	(DMMP) 100		
$\text{NO}^+ (\text{a}^3\Sigma^+)$	≈ 1	A	≈ 40 (at 0.2 eV)		
		B	≈ 25 (at 0.2 eV)		
		C	≈ 20 (at 0.2 eV)		
		D	≈ 15 (at 0.2 eV)		
H_2O^+	≈ 1	A	≈ 0		
		B	≈ 66		
		C	≈ 0		
		D	≈ 33		
H_3O^+	≈ 1	DMMP H ⁺	100		

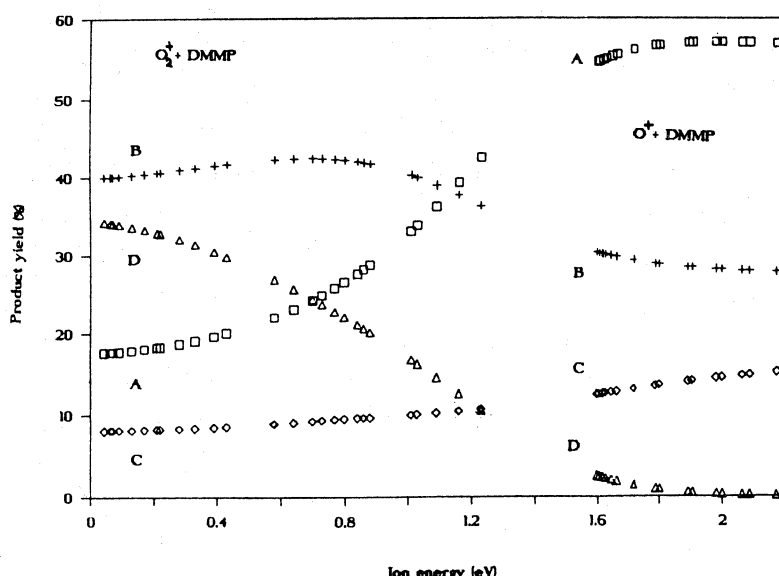
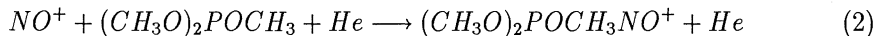


Figure 1. Product yields of reactions of molecular and atomic oxygen ions as function of ion energy. Scale for the atomic oxygen reaction shifted by 1.55 eV.

two ions) to show that in this case it is essentially the total (electronic plus kinetic) energy that determines the product yield.

REACTIONS OF NO⁺ WITH DMMP

The results of the reaction study of NO⁺ with DMMP were somewhat confusing at first until it was realized that the NO⁺ ions were a mixture of ions in the electronic ground state and the metastable $^3\Sigma$ state. The metastable ion fraction was found to behave very much like the dissociative charge transfer reactions discussed above. The ground-state fraction reacted by three-body association to DMMP



with helium (the buffergas) acting as third body. Although a third body is required to stabilize the cluster ion, we did not observe a dependence of the association rate coefficient on helium density (the effective, binary rate coefficient was near the Langevin limit). It seems likely that the lifetime of the unstable complex formed in a collision with such a complicated molecule is sufficiently long that third-body stabilization occurs with near unit probability, even at low gas densities. The reaction may be an example of a "saturated" three-body reaction.

The observation that ground-state nitric oxide ions do not charge transfer with DMMP suggests that the ionization potential of DMMP is larger than that of NO (9.25 eV), in agreement with the DMMP ionization potential of 10.5 eV given by Bafus et al, [3a].

REACTIONS OF H₂O⁺ and H₃O⁺ with DMMP

H₂O⁺ ions reacted fast with DMMP in dissociative charge transfer reactions. Branches B and D were observed.

The reaction of hydronium ions is the more interesting of the two. The only reaction channel observed is proton transfer to DMMP. This finding indicates that the proton affinity of DMMP is quite large, larger than that of water (7.4 eV). This value is compatible with independent determinations (9.7 eV) [3b].

SECONDARY REACTIONS OF THE PRIMARY PRODUCT IONS WITH DMMP

The product ions listed above (branches A-D) were found to undergo secondary reactions with DMMP. Although we have not been able to unravel the fairly complicated secondary reaction scheme, the mass spectra obtained indicate that the secondary reactions eventually produce ions containing DMMP. It may be premature to speculate on the feasibility of using ion-chemistry to destroy molecules similar to DMMP, but there appears to be a propensity to reform the molecules which one seeks to destroy.

The results of this work are compiled in Table I. A full account of this work will be given elsewhere[4].

REACTIONS OF DOUBLY-CHARGED MOLECULAR OXYGEN IONS WITH ATMOSPHERIC MOLECULES AND NEON

Only very few reactions of doubly-charged molecular ions have been studied ex-

perimentally. In earlier work on reactions of metastable oxygen ions we noticed that O_2^{++} ions are produced copiously in electron impact ion sources and that their ionic mobility in helium is somewhat smaller than that of singly charged atomic oxygen ions of the same charge-to-mass ratio [5]. This makes it possible to study reactions of O_2^{++} ions in the presence of a much larger abundance of O^+ ions. It appeared interesting to examine some reactions of O_2^{++} with molecules more closely.

We find that single charge transfer

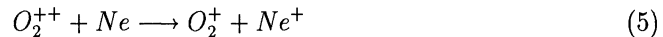


is the dominant reaction mechanism for the reactants $R = O_2, N_2, CO_2$. The rate coefficients are on the order of $2 \times 10^{-9} \text{ cm}^3/\text{s}$ at thermal energy 0.04 eV and vary little with ion energy in the near-thermal energy range. The magnitude of the rate coefficient for the reaction with nitrogen agrees with a flow tube result of Glosik et al. [6]. The reaction with nitric oxide



proceeds with essentially the same rate coefficient but it is the only example of a reaction in which an atom is transferred rather than an electron.

The potential energy curves of O_2^{++} calculated by Hurley [7] and the threshold for electron impact ionization of molecular oxygen observed by Märk [9] indicate that vertical ionization of oxygen should produce the doubly-charged ion in vibrational states of $v=5$ and $v=6$. To investigate the vibrational state of the O_2^{++} ions in our experiments, we studied the reaction



For ions in the vibrational ground state, the exoergicity of the reaction is about 1 eV, for ions in $v=5$ and $v=6$ the exoergicity would be about 2 eV. Past experiments on charge transfer between atomic species [9] have indicated that the charge transfer probability (defined as the charge transfer rate divided by the Langevin collision rate) is about 10^{-3} for exoergicities near 2 eV, but negligibly small for 1 eV. The measured rate coefficient for this reaction was 1.6×10^{-3} , close to that expected for vibrationally excited ions. We conclude that the O_2^{++} ions in our experiments were vibrationally excited to $v=5$ or 6 and that consequently the rate coefficients for the reaction discussed earlier also refer to vibrationally excited ions. This also implies that quenching of vibrational excitation in collision with the helium buffergas atoms must be very slow. The results of this work have been submitted for publication [10].

ION-ATOM ASSOCIATION

It is not an easy task to account theoretically for the observed rates of three-body association reactions of atomic ions in atomic gases, i.e. processes of the kind



where A, B, and M are atomic species. Earlier theoretical treatments [11,12,13] generally failed to reproduce the observed dependences of the rate coefficients on gas temperature, which provides a more sensitive test of a proposed theory than merely accounting for the magnitude of the rates. A very elaborate treatment by

Russell [14], however, succeeded in quantitatively reproducing experimental data on the three-body association of helium ions in helium. The motivation for Russell's very extensive effort, in part, was to test ideas on the rate of formation of muonic helium, a subject of considerable current interest.

We have derived a simple formula which, although it is based on very crude assumptions, reproduces experimental data fairly well. The basic idea is that ion-atom association is essentially an energy loss process. As a result of the attractive induced-dipole interaction, the kinetic energy of an ion during a collision is increased. Dissipation of this excess energy in collision with a third atom then leads to a bound molecular ion.

The potential energy of an ion of charge Ze at distance r from a polarizable atom is given by

$$U(r) = -(Ze)^2 \alpha / 8\pi\epsilon_0 r^4 \quad (7)$$

where α is the atom's polarizability and ϵ_0 is the permittivity of the vacuum. In the presence of N atoms/unit volume, randomly distributed, the average potential energy is given by

$$\langle U \rangle = \int_{r_c}^{\infty} N U(r) 4\pi r^2 dr = -N(Ze)^2 \alpha / 2\epsilon_0 r_c \quad (8)$$

where r_c is a cutoff radius to be defined later. We assume that the center of mass of the ion-atom system, on average, is at rest in the laboratory frame and then take the average excess kinetic energy of the ion during a collision to be

$$\langle \epsilon \rangle = \langle U \rangle m/m_i \quad (9)$$

where m is the reduced mass of the ion (m_i) and the atom (M). In the next step, we make the crude assumption that the rate at which the energy $\langle \epsilon \rangle$ is lost can be estimated from the collisional energy loss rate of an ion drifting in an electric field through a gas with mobility μ . It is shown easily, using Wannier's formula for the average field energy of drifting ions, that the collisional energy loss rate is given by

$$d \langle \epsilon \rangle / dt = 2 \langle \epsilon \rangle e / \mu(m + M) \quad (10)$$

By combining equations and choosing r_c to be the radius at which $\langle \epsilon \rangle = 3kT/2$ we obtain an expression for the energy loss rate. The three-body rate coefficient, which describes the conversion from atomic to molecular ions, should be given by

$$k_3 = (3kT/2)^{-1} N^{-2} d \langle \epsilon \rangle / dt \quad (11)$$

The result is

$$k = (64\pi)^{1/4} (Ze)^{5/2} (\alpha m/Tm_i)^{3/4} (3\epsilon_0 k)^{-3/4} / N_L \mu_0 (m + M) \quad (12)$$

where N_L (Loschmidt's number) enters when we introduce the reduced mobility (μ_0). In customary units,

$$k(cm^6/s) = 3.27 \times 10^{-27} Z^{5/2} (\alpha m/Tm_i)^{3/4} / \mu_0 (m_i + M) \quad (13)$$

with α in units of 10^{-24} cm^3 , T in Kelvin, all masses in atomic units, and the mobility in cm^2/Vs . Obviously, this derivation is crude and may amount to little more than dimensional analysis. It is astonishing, though, that the formula reproduces experimental data quite well.

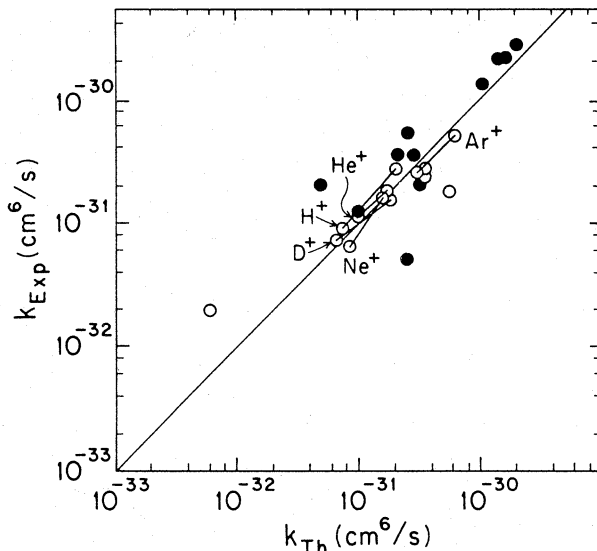


Fig. 2

Fig. 2 shows a comparison between measured data on three-body association rate coefficients (open circles). The data points connected by short lines refer to association reactions measured at two different temperatures (77K and 300K). Several of the experimental data points (solid circles) refer to association into excited states of the molecular ion since the ionization potential of the ion is higher than that of the atom (see [9]). The excited state then decays by radiation to the ground state, i.e., the overall process is radiative charge transfer, enhanced by three-body stabilization [see 1,9]. Space limitations do not allow to list all sources of experimental data; a fuller description will be published [15].

The association rate coefficient of protons and deuterons to helium at 300K and at 77K has recently been measured in our laboratory [15]. The data points at both temperatures have been entered in Fig. 3. Too much should not be made of this "theory", but it may be useful to obtain reasonable estimates for rate coefficients if one knows ionic mobilities from measurements or theory.

Acknowledgments: This work was, in part, supported by the NASA Planetary Atmospheres Program under Grant NGL 39-0110137, by the U.S. Army Research Office under Grant DAAL 0387K0048, and the U.S. Air Force/AFWL under Contract F 33615-87-2745.

REFERENCES

1. R. Johnsen, Phys. Rev. A 22, 933 (1983).
2. J. Heimerl, M. A. Biondi, and R. Johnsen, J. Chem. Phys. 51, 5041 (1969).
- 3a. D. A. Bafus, E. J. Gallegos, and R. W. Kiser, J. Phys. Chem. 70, 2614 (1966).

- 3b. R. V. Hodges, T. J. McDonnel, and J. L. Beauchamp, *J. Am. Chem. Soc.* 102, 1327 (1980).
4. B. K. Chatterjee, R. Tosh, and R. Johnsen, to be published.
5. R. Johnsen, M. A. Biondi, and M. Hayashi, *J. Chem. Phys.* 77, 2545 (1982).
6. J. Glosik, A. B. Rakshit, N. D. Twiddy, N. G. Adams, and D. Smith, *J. Phys. B* 11, 3365 (1978).
7. A. C. Hurley, *J. Molec. Spectroscopy* 9, 18 (1962).
8. T. D. Märk, *J. Chem. Phys.* 63, 3731 (1975).
9. R. Johnsen and M. A. Biondi, *Phys. Rev. A* 20, 87 (1979) and *Phys. Rev. A* 18, 989 (1978).
10. B. K. Chatterjee and R. Johnsen, *J. Chem. Phys.* (1989), accepted for publication.
11. F. E. Niles and W. W. Robertson, *J. Chem. Phys.* 40, 3568 (1964).
12. B. H. Mahan, *J. Chem. Phys.* 43, 3080 (1965).
13. A. S. Dickinson, R. E. Roberts, and R. B. Bernstein, *J. Phys. B* 5, 355 (1972).
14. J. E. Russel, *J. Chem. Phys.* 83, 3363 (1985).
15. B. K. Chatterjee and R. Johnsen, to be published.

ENERGY POOLING COLLISIONS:

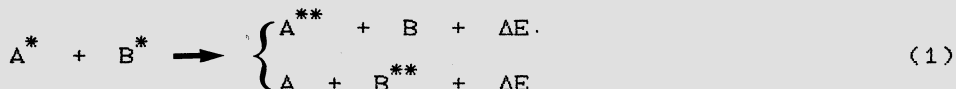
A STEP TOWARDS IONIZATION

S. Gozzini, C. Gabbanini and L. Moi

Istituto di Fisica Atomica e Molecolare del C.N.R.
Via del Giardino, 7
56100 Pisa Italy

INTRODUCTION

Different collisional processes may contribute to the evolution of a gas under resonant laser excitation¹⁾. The aim of this paper is to put in evidence the role of the collisional process called "energy pooling" (EPC) with respect to a possible complete ionization of the vapor under relatively low laser power densities. EPC is described by the reactions:



where A^*, B^* are the resonantly laser excited atoms, A^{**}, B^{**} are the atoms in a highly excited level and ΔE is the energy defect. Being thermal collisions, the reaction is effective when ΔE is of the order of KT . Alkali atoms satisfy this condition and are, up to now, the more studied atoms for this process²⁾.

Dealing with alkali atoms, another important process can take place, that is the associative ionization (AI) described by:



where $\Delta E \approx KT$ and AB^+ is the molecular ion.

The associative ionization supports the seeding electrons which, in presence of a high density of excited atoms, may undergo superelastic collisions and, eventually, trigger an avalanche process. Therefore, the combination of energy

pooling collisions, which provide a reservoir of atoms with a low ionization energy, and AI collisions, which provide a reservoir of cold electrons, may bring the vapor to a complete ionization, even with low power laser density.

This has been demonstrated for the first time by Lucatorto and McIlrath³⁾ which excited a sodium vapor at a density of the order of 10^{16} atoms/cm³ by a laser with power density $W_L \cong 1\text{MW}/\text{cm}^2$ and a pulse width $\tau \cong 1\mu\text{s}$, tuned to the 3S-3P transition. While W_L was not sufficiently high to produce an appreciable three-photon ionization of the sodium vapor, they observed an almost complete evolution to a plasma. The interpretation of such result lies, as already discussed, in the high atomic density and in the long laser pulse width which exceeds the atomic excited state lifetime even in presence of radiation trapping. That allows a multistep process where AI produces the first cold electrons which are heated by superelastic collisions with the 3P atoms. These electrons can ionize the levels pumped by EPC that have a reduced ionization threshold. Finally, if the atomic density is high enough, the secondary emitted electrons can produce an avalanche process. This explanation was supported by a contemporary experiment⁴⁾ where, working with c.w. laser excitation and a low atomic density (10^{12} atoms/cm³), the EPC populated levels of sodium were seen for the first time. A computer model describing this laser ionization scheme has been developed by Measures and Cardinal⁵⁾.

The complete understanding of these processes requires, therefore, the measurement of EPC and AI cross sections in order to compare them with other possible channels along which the gas can evolve. We focus our attention to the EPC process which gives also informations on the long range interaction potentials between excited atoms. The EPC cross section measurements require the solution of many problems. Here measurement methods will be reported with a particular attention to our last experiment on EPC between two different alkali species.

The theoretical approach has well defined procedures which may give relatively good results. The calculations, which are very heavy, have been performed only for few cases while a lot of work must be still done. At this stage the experimental results, part of which we will present in the following, are more complete and precise.

EPC RATE EQUATIONS AND MEASUREMENT METHODS

The EPC processes described by (1) have been extensively studied for alkali atoms even if recent experiments have been done on Sr⁶⁾. In the case of alkali atoms both homonuclear systems²⁾ and heteronuclear systems^{7,8)} have been investigated. The interest in such collisions relates not only with the above mentioned possibility of creating a ionization of the gas with low power laser density, but also with the chance of testing theoretical intermolecular potentials. Recently these processes assumed an important role also for atom cooling experiments because they can limit the densities achievable in optical molasses⁹⁾. Therefore a new interesting branch of atomic collision physics is born where the processes can be highly non-classical and

long-range potentials can become dominating¹⁰.

If the experimental conditions are such to have a population of the upper levels due only to EPC, one can write the rate equations for these states as:

$$N_{nl} = \frac{1}{2} N_{mp}^2 \langle \alpha_{nl} v \rangle - N_{nl} \sum_{n'l'} A_{nl-n'l'} \quad (3)$$

where $A_{nl-n'l'}$ is the spontaneous transition probability for $nl-n'l'$ with the sum extending to all levels allowed by dipole transition rules. Looking to the steady state regime it results:

$$K_{nl} = \langle \alpha_{nl} v \rangle = \frac{\frac{2}{N_{nl}}}{\frac{2}{N_{mp}^2} \sum_{n'l'} A_{nl-n'l'}} = \frac{N_{nl} A_{nl-mp}}{N_{mp}^2 (1 + \gamma_{nl-mp})} \quad (4)$$

where γ_{nl-mp} represents the inverse of the branching ratio of the transition. Introducing the fluorescence intensities, one can write:

$$K_{nl} = 2 \alpha_{nl-mp} \gamma_{nl-mp} \frac{\omega_{mp-ms}}{\omega_{nl-mp}} \frac{I_{nl-mp}}{I_{mp-ms}} \frac{1}{N_{mp} \tau_{eff}} \quad (5)$$

where α_{nl-mp} indicates the efficiency of the experimental apparatus and τ_{eff} is the lifetime of the mp level in presence of radiation trapping. The experimental troubles come from the measurement of the excited state density N_{mp} and from the lifetime τ_{eff} that strongly depend upon the effective experimental conditions; the radiation trapping also causes a variation of the excitation volume. A wrong evaluation of these parameters have carried to measurement errors in the cross section values of some orders of magnitude. The first reliable values have been reported in two experiments^{11,12} (on 4D and 5S levels in sodium) that agree between them and also with ab initio theoretical calculations¹³. In the experiment of ref.11, the excitation volume was kept constant and the radiation trapping was minimized by the use of a capillary cell and of a very narrow transverse slit. The cell was uniformly illuminated by a low power c.w. dye laser and the density was kept to low levels (10^{12} atoms/cm³). The apparatus was absolutely calibrated by saturating the 3P-3S transition at very low temperature while

τ_{eff} was evaluated by radiation trapping calculations.

In the experiment of ref.12 a stainless-steel cross cell with sapphire rods, which reduce the optical depth, was used. The vapor was excited by a pulsed laser while a very low power c.w. dye laser, detuned to the wings of the resonance, was used as a probe of N_{3p} .

The authors obtained cross section values that overlap, into the reported indetermination, with those of ref.11.

Other methods have been correctly applied to EPC cross section measurements as that used by Cheret et al.¹⁴⁾ to determine σ_{5d} of rubidium. While the experimental conditions

were similar to the experiment of ref.11 (low power c.w. laser excitation, low atomic density), the excited state densities N_{5p} and N_{5d} have been measured by counting the ions obtained photoionizing the sample with different lines of an Ar⁺ laser; the apparatus was absolutely calibrated for current and the volume was determined by the overlap of the two laser shifting the Ar⁺ beam on a vertical plane. This direct photoionization method is that commonly used for AI cross section measurements.

A different approach has been used by Le Gouet et al.¹⁵⁾ and recently by another group¹⁶⁾. A low power c.w. laser was sent to a sodium atomic beam, and the detection was done on the electrons emerging from the excitation zone by a cylindrical mirror analyzer. The energy spectrum of the emitted electrons shows peaks at energies corresponding to the process:



Other peaks result from AI ; all peaks repeat with a period corresponding to the 3P energy, showing the importance of the superelastic collisions. The cross section values for 4D and 5S levels were only estimated from the electron peaks and resulted of the right order of magnitude.

All the measured cross sections are in the range 10^{-13} - 10^{-16} cm² that means of the order or even larger than the geometrical cross sections. This supports the ionization pathway described before.

RECENT DEVELOPMENTS : HETERONUCLEAR ALKALI SYSTEMS

The study of heteronuclear alkali systems is still far to be complete. Until now the spectroscopy of all heteronuclear molecules is not performed and few informations are available for the interaction potentials.

The measured EPC cross sections for homonuclear alkali samples are few just because the process requires a quasi-resonance between the sum of the energy of the first excited state and an upper level. Such condition is met in a single alkali vapor only for few levels. That is not longer true in heteronuclear alkali systems, in which the resonance condition includes many levels. In fig.1 we report the level scheme for the mixtures Na-Rb, Na-K and K-Rb that we have investigated up to now; as one can see, the number of levels within three KT from the EPC resonance is relatively high¹⁷⁾.

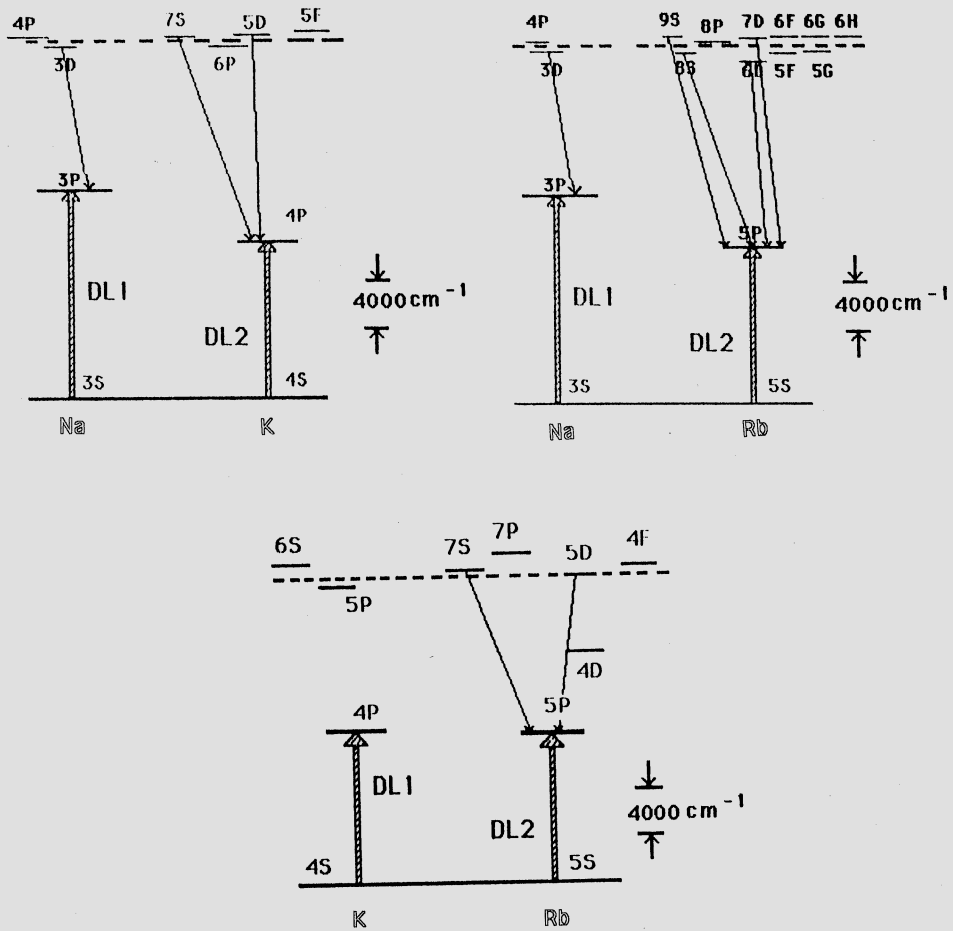


Fig.1. Energy level schemes for Na-K, Na-Rb and K-Rb mixtures. Arrows represent laser excitations (thick arrows) and transitions used for cross section determination (thin arrows). Dashed lines indicate the energy sum of the laser excitations.

The study of an heteronuclear mixture gives some new troubles. Infact there is a contemporary contribution to the population of the EPC pumped levels from both homonuclear and heteronuclear processes that has to be discriminated. Moreover the atomic densities of the two species must be of the same order of magnitude: the different alkalis have infact considerably different vapor pressures. This last problem was solved by adopting mixtures with different percentages of the two alkali metals following the empirical Raoult's law; for instance a 99% of sodium and a 1% of rubidium should carry to similar atomic densities for the two species in a Na-Rb mixture.

To solve the problem of discriminating heteronuclear and homonuclear collisions, we adopted a particular experimental scheme that is shown in fig.2. Two c.w. dye lasers excite the fundamental transitions of the alkali species which are contained in an heated capillary cell as in ref.7. The two laser beams are modulated by a mechanical chopper at two different frequencies ω_1 and ω_2 and the fluorescence is phase detected at the sum frequency $\omega_3 = \omega_1 + \omega_2$; in this way only the processes due to both laser excited levels (the heteronuclear ones) are detected. The fluorescence is analyzed in a large range of the spectrum (.3-2.5 μm) detecting it by a photomultiplier and by a cooled PbS detector.

The necessity of an absolute calibration of the apparatus was overcome by measuring the heteronuclear cross sections relatively to a known homonuclear one; in particular σ_{5s} of sodium of refs.11,12 was used for the Na-K mixture while σ_{5d} of rubidium of ref.14 was used for Na-Rb and K-Rb mixtures. The possibility of such procedure becomes clear if one looks to the rate equations for heteronuclear EPC to the j level:

$$\frac{dN_j}{dt} = - N_j \sum_{l \neq j} A_{jl} + K_j (N^e_A)_{\omega_1} (N^e_B)_{\omega_2} \quad (7)$$

where $N^e_{A,B}$ are the laser excited state populations of the two species, and K_j is the rate constant to be determined ($K_j = \langle \sigma, v \rangle$). If the laser exciting the B-kind atoms is substituted with another exciting the A-kind atoms, always at a frequency ω_2 , one can write:

$$\frac{dN_i}{dt} = - N_i \sum_{k \neq i} A_{ik} + K_i (N^e_A)_{\omega_1} (N^e_A)_{\omega_2} \quad (8)$$

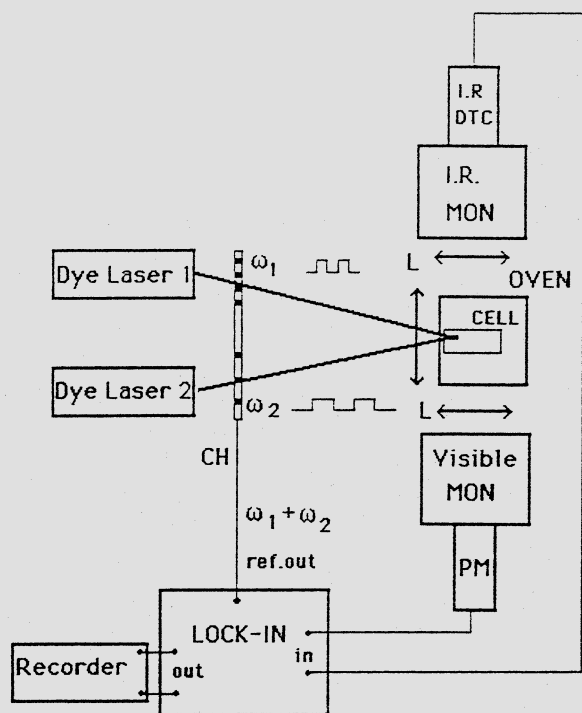


Fig. 2. Sketch of the experimental apparatus:
 Mon= monochromator, PM= photomultiplier, DTC= detector,
 CH= chopper.

where K_i is a known homonuclear rate constant used as a reference. Introducing the fluorescence line intensities, one obtains from eq. 7,8:

$$\frac{\alpha_{ik}\gamma_{ik}}{K_j} \frac{\nu_{ik}\tau_A}{\alpha_B\nu_B} \frac{I_{jl}I_A}{\alpha_{jl}\gamma_{jl}} = \frac{\alpha_{jl}\gamma_{jl}}{\alpha_A\nu_A} \frac{\nu_{jl}\tau_B}{I_{ik}I_B} \quad (9)$$

where I_A , τ_A and I_B , τ_B are the line intensities and the effective lifetimes of the two laser excited levels, and the other parameters were defined for eq.5. This is valid if the beam modulated at ω_1 is the same in the two measurement and if the volume excited doesn't change. This is assured by the geometry of the apparatus; the two measurements were done by using for the ω_2 modulated beam, firstly the laser resonant with the B-kind atoms and then the laser resonant with the A-kind atoms that was already splitted to be sure that the ω_1 beam remains the same in the two cases. To complete the measurement it was necessary to determine the effective lifetimes τ_A and τ_B ; that was done exciting the two alkali's resonances one at a time by a pulsed dye laser nitrogen pumped, with a pulse width much narrower than the effective atomic lifetimes, and measuring the decay times of the D lines. In this way up to 10 heteronuclear EPC cross sections, (besides the homonuclear σ_{7s} of rubidium) were measured. That constitutes the first consistent set on which it is possible to make considerations on the dependence of the EPC cross sections on different parameters. We found that the stronger dependence comes from the energy defect of the reaction ΔE ; in table I the heteronuclear cross sections together with the reference homonuclear cross sections are reported as a function of $\Delta E/KT$. The dependence on the energy defect seems to be similar for all the heteronuclear systems and is stronger than in other atomic systems like Sr⁶. Work is in progress on a Na-Cs mixture where the heteronuclear levels that are involved in the EPC process are further more^[17].

CONCLUSIONS

We have shown that the EPC cross section can be relatively large, ranging from 10^{-17} to 10^{-14} cm², and are one or two

order of magnitude larger than AI cross sections. Therefore EPC, being for a considerable range of laser power densities some orders of magnitude larger than any other process like multiphoton ionization, can be the dominant process in the evolution of a vapor under resonant excitation.

Table I

Mixture	level	$\Delta E/KT$	$\sigma (10^{-15} \text{ cm}^2)$	Ref.
Na - K	3D (Na)	+ 2.3	2.8 ± 1.4	7
	5D (K)	- 0.5	3.8 ± 1.9	
	7S (K)	- 0.8	1.8 ± 0.9	
Na - Rb	3D (Na)	+ 1.1	31 ± 16	8
	8S (Rb)	+ 1.5	17 ± 9	
	7D (Rb)	- 1.5	9.4 ± 4.7	
	6D (Rb)	+ 2.6	8.5 ± 4.3	
	9S (Rb)	- 2.2	6.0 ± 3.0	
K - Rb	5D (Rb)	+ 0.5	58 ± 29	8
	7S (Rb)	- 1.4	6.4 ± 3.2	
* Na - Na	5S	+ 2.2	3.6 ± 1.3	11, 12
Rb - Rb	5D	- 0.2	64 ± 26	14

* Homonuclear EPC reference cross sections

REFERENCES

- 1) L. Moi Acta Physica Polonica A 69 (1986) 641
- 2) M. Allegrini, C. Gabbanini and L. Moi Journal de Phys. 46 (1985) c1-61
- 3) T.B. Lucatorto and T.J. McIlrath Phys. Rev. Lett. 37,(1976) 428
- 4) M. Allegrini, G. Alzetta, A. Kopystynska, L. Moi and G. Orriols Opt. Comm. 19 (1976) 96
- 5) B.M. Measures and P.G. Cardinal Phys. Rev. A 23 (1981) 804
- 6) J.F. Kelly, M. Harris and A. Gallagher Phys. Rev. A 38 (1988) 1225
- 7) S. Gozzini, S.A. Abdullah, M. Allegrini, A. Cremoncini and L. Moi Opt. Comm. 63 (1987) 97
- 8) C. Gabbanini, S. Gozzini, G. Squadrito, M. Allegrini and L. Moi Phys. Rev. A, in press
- 9) P. L. Gould, P.P. Lett, P.S. Julienne, W.D. Phillips, W.R. Thorsheim and J. Weiner Phys. Rev. Lett. 60 (1988) 788
- 10) M.X. Wang, J. Keller, J. Boulmer and J. Weiner Phys. Rev. A 34 (1986) 4497
- 11) M. Allegrini, P. Bicchi and L. Moi Phys. Rev. A 28 (1983) 1338
- 12) J. Huennekens and A. Gallagher Phys. Rev. A 27 (1983) 771

- 13) M. Allegrini, C. Gabbanini and L. Moi Phys. Rev. A 32 (1985) 2068
- 14) L. Barbier and M. Cheret J. Phys. B: At. Mol. Phys. 16 (1983) 3213
- 15) J.L. Le Gouet, J.L. Pique', F. Willeumier, J.M. Bizeau, P. Dhez , P. Koch and D.L. Ederer Phys. Rev. Lett. 48 (1982) 600
- 16) M.W. Muller, H.A.J. Meijer, T. Kraft, M.W. Ruf and H. Hotop III ECAMP Conf. Abs. (1989) p. 500
- 17) S. Gozzini, S.A. Abdullah, M. Allegrini, A. Cremoncini and L. Moi Proc. International Conference on Lasers '85, Las Vegas, ed. by C.P. Wang (STS Press, 1986) p. 98

POTENTIAL ENERGY CURVES OF OPEN SHELL SYSTEMS (EXCIMERS) FROM
MOLECULAR BEAM SCATTERING

V.Aquilanti, R.Candori, D.Cappelletti, and
F.Pirani

Dipartimento di Chimica dell'Università, 06100
Perugia, Italy

ABSTRACT

Ground state and lower lying excited state potential energy curves for the interaction of fluorine atoms with He, Ne, Ar, Kr, Xe, H₂ and CH₄ have been obtained from measurements of integral scattering cross sections at thermal energies. The results are of interest for the modelling of excimer laser mechanisms.

INTRODUCTION

The interactions between halogen atoms and rare gases are characterized by the presence of an internal structure of the halogen atoms which are in a ²P state. This makes anisotropic these interactions which can be described by a manifold of three adiabatic potential energy curves. These curves are very important for understanding the radiative decay of rare gas-halogen excimer molecules [1], because they represent the interaction between the two atomic partners in the final ground state.

In this laboratory the interactions between halogen atoms and rare gas atoms are studied measuring the integral scattering cross sections as a function of the collision velocity and selecting the halogen m_j state during the collision. Limited information from differential cross sections [2] is available. Spectroscopic results have been reported [3] only for a few systems (XeF and XeCl), since the

Franck-Condon transition from excimers to the ground state often leads to dissociation and therefore to diffuse bands [4].

EXPERIMENTAL APPARATUS

The apparatus used for absolute integral cross section measurements is formed by a source of the open-shell atomic beam (the atoms are produced by a microwave discharge in a proper gas mixture), by a velocity selector, by a scattering chamber where the target gas is confined, and by a quadrupole mass filter as detector [5]. The characterization of the atomic beam is performed using a Stern-Gerlach magnetic selector, in Rabi configuration, inserted along the beam path and measuring the beam transmittance as a function of the applied magnetic field strength [6]. In general the paramagnetic open shell species, interacting with the inhomogeneous magnetic field, undergo a deflection which depends on features of the magnet and on the mass, the velocity and the effective magnetic moment of the particles [6]. The last property is characteristic of the electronic state of the atom and in particular depends on the considered magnetic sublevel.

As described elsewhere, the transmittance of oxygen atom beam has been measured at different magnetic field strengths and at various beam velocities [7]. The magnetic analysis of oxygen atom beam confirms that under our experimental conditions atoms are essentially produced in the electronic ground state. In fact the calculated transmittance, using the ground state magnetic moments, adequately reproduces the experimental behaviour [7].

For halogen atoms the evaluation of the effective magnetic moments, which are fundamental properties for the state selection, is more complicated because these atoms exhibit a nuclear spin quantum number i different from zero. Two different limiting behaviors are possible: on one limit f (defined as $f = j + i$, where j is the total electronic angular momentum) is the good quantum number, in the opposite case j decoupled from i is the good quantum number [8]. Obviously two different sets of effective magnetic moments are associated with the two limiting cases. Therefore it is necessary to use the exact decoupling schemes of the angular momenta to correctly define the good atomic quantum number,

and the associated magnetic moments, at the experimental magnetic fields [8].

The measured transmittance of the fluorine atom beam is shown in Fig.1. At high magnetic fields experimental data and calculations (dashed line) disagree if f is used as good quantum number. A better agreement, but not completely satisfactory at high magnetic fields (dotted line), is obtained using f as the good quantum number for $j=1/2$ state and j as a good quantum number for $j=3/2$ state [6] (this assumption is suggested by the different hyperfine constants for the two atomic states). The experimental behavior is

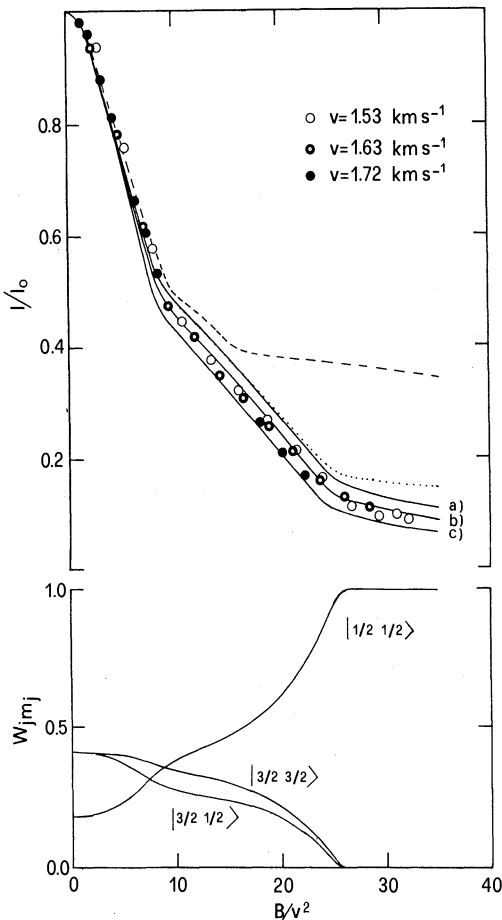


Fig.1 - Transmittance I/I_0 of the fluorine atom beam as a function of the reduced parameter B/v^2 , where B is the magnetic field strength and v is the velocity of the beam. The abscissa units are in $10^2 \text{ G Km}^{-2} \text{ s}^2$. The dashed line is calculated assuming f as a good quantum number; dotted line is calculated assuming j as a good quantum number for $j=3/2$ state and f for $j=1/2$ state; the full line are calculated using the exact decoupling scheme of the angular momenta. The curves a), b), c) are obtained assuming

slightly different relative populations (at zero field) of the excited $j=1/2$ state (22% for a), 18% for b), 14% for c)). In the lower panel the relative weights W_{jmj} of the $|j mj\rangle$ states of the $F(^2P_j)$ are shown.

adequately described at all values of the field if the exact decoupling schemes of the angular momenta are used (continuous curves).

In this way it is possible also to deduce information on the fluorine atom magnetic sublevel weights: i) at zero field, i.e. for completely transmitted beam, curves labelled as a), b) and c) correspond to three different populations of the excited $j=1/2$ state; ii) in the attenuated beam at the various magnetic field strengths. For the latter case it is important to note that since the magnetic field direction is orthogonal to the atom beam direction, it is necessary to perform a rotation by $\pi/2$ of the reference axis, using suitable rotation matrix elements [9], to obtain the appropriate weights in the collision frame (quantization axis along the beam velocity) [6]. The weights so obtained are shown in the lower panel of fig.1 as a function of the applied magnetic field.

THEORETICAL FRAMEWORK

Having characterized the atomic beam, we have measured the integral cross section for scattering of fluorine atoms by rare gases and by simple molecules. For the analysis of the present experimental data, in terms of the adiabatic decoupling scheme [10], it is convenient to define three effective adiabatic potential energy curves $v_{|j \Omega\rangle}$ correlating with the different $|j m_j\rangle$ states of F atom ($\Omega = |m_j|$) as follows [11]:

$$v_{|3/2 1/2\rangle} = v_o + \frac{1}{10} v_2 + \frac{1}{2} \Delta - \frac{1}{2} \left(\frac{9}{25} v_2^2 + \Delta - \frac{2}{5} v_2 \Delta \right)^{1/2}$$

$$v_{|3/2 3/2\rangle} = v_o - \frac{1}{5} v_2$$

$$v_{|1/2 1/2\rangle} = v_o + \frac{1}{10} v_2 + \frac{1}{2} \Delta + \frac{1}{2} \left(\frac{9}{25} v_2^2 + \Delta - \frac{2}{5} v_2 \Delta \right)^{1/2}$$

(where Δ is the spin-orbit constant, 50.1 meV for fluorine). The $v_o(R)$, spherical component, and $v_2(R)$, anisotropic component, are related to the more familiar V_Σ and V_Π electrostatic interactions by [10]

$$v_0 = 1/3 (v_{\Sigma} + 2v_{\Pi}) \quad v_2 = 5/3 (v_{\Sigma} - v_{\Pi})$$

Σ and Π stand for $\Lambda=0$ and $\Lambda=1$, respectively, where the quantum number Λ is the projection of the electronic angular momentum L on the interatomic axis. Within this adiabatic decoupling schemes it is possible also to derive the nonadiabatic coupling matrix element $P(R)$ [7] between the $\Omega=1/2$ curves, which assume this form

$$P(R) = \frac{10/\sqrt{2}}{9\beta^2 - 10\beta + 25} \frac{d\beta}{dR}, \text{ where } \beta = \frac{v_2}{\Delta}$$

When the contribution from this element can be neglected, as under present low energy conditions, the integral cross sections will be given by a weighted sum of the cross sections $Q_{j\Omega}(v)$ for scattering by the potentials $v_{|j\Omega\rangle}$:

$$Q(v) = \sum_{j\Omega} w_{j\Omega} Q_{j\Omega}(v)$$

In the present experiments the weights $w_{j\Omega}$ are determined, as described before, by the magnetic analysis, while $Q_{j\Omega}(v)$ are obtained by the quantum mechanical theory for potential scattering.

RESULTS AND DISCUSSION

The adiabatic curves for F-rare gas systems obtained from this work are reported in Fig.2, while in table I some characteristic parameters for all interactions are presented. From the table and figure it can be seen that while the v_0 parameters vary along the series $F-He \rightarrow F-Xe$ in agreement with the trend which can be predicted from considerations of the polarizabilities of rare gas atoms [12], the anisotropy increases regularly in the same series (see Fig.2 and the differences between the well depths of the v_{Π} and v_{Σ} interactions in Tab.I). This trend can be attributed to an increasing ionic contribution to the interaction due to a lower ionization potential in going from He to Xe. An interesting feature obtained from this analysis is given by the nonadiabatic coupling terms, reported in the lower panels

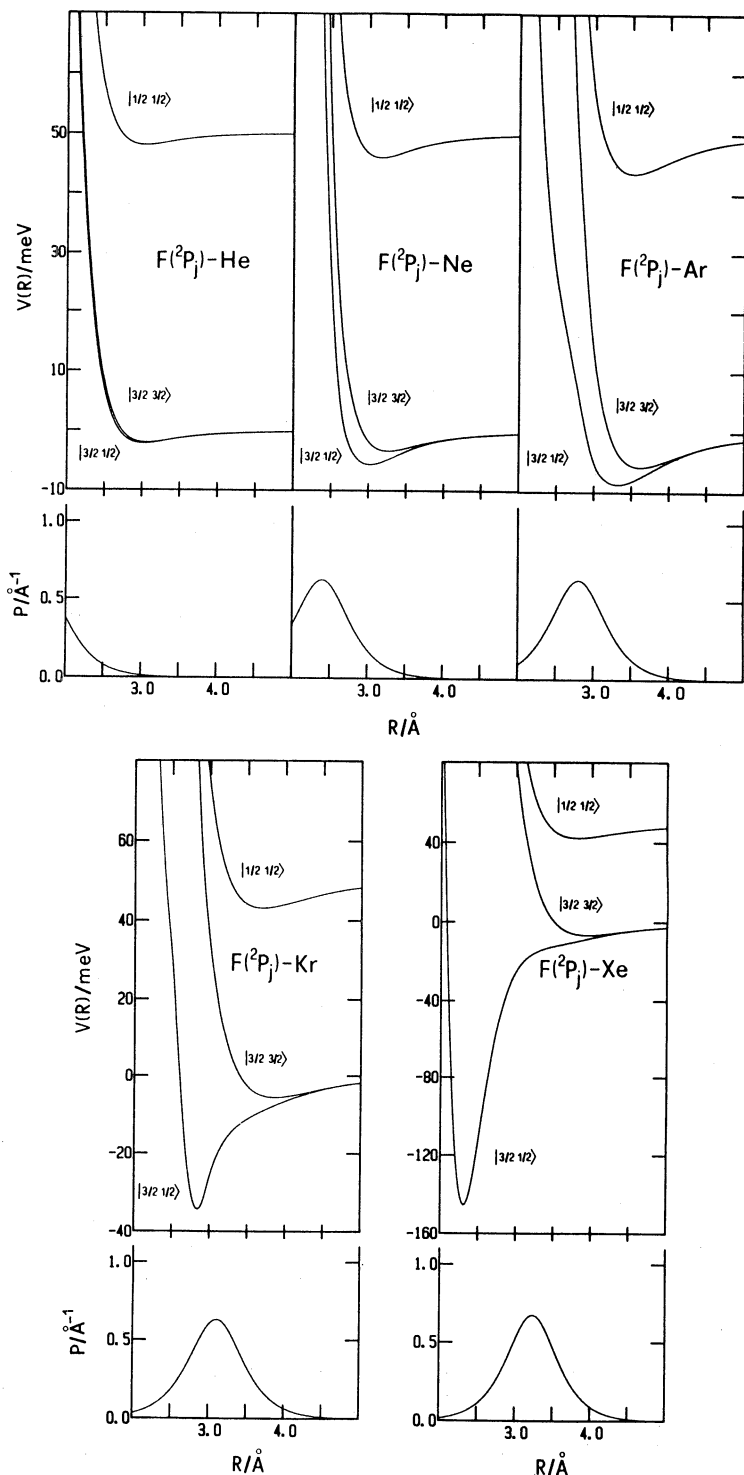


Fig.2 - Adiabatic potential energy curves $V_{|j\Omega\rangle}$ for $F-He$, Ne , Ar , Kr and Xe systems. Also shown in the figure is the nonadiabatic coupling matrix elements P between the $|3/2\ 1/2\rangle$ and $|1/2\ 1/2\rangle$ states.

of Fig.2: they mark the transition between an atomic coupling scheme (Hund's case(c)) at long range and a molecular coupling scheme (Hund's case (a)) at short range [10,11].

From the position of the $P(R)$ maximum in Fig.2 it is possible to deduce that while the well depths for the ground state of F-He,Ne,Ar systems are completely described by Hund's case (c), the well depths of the same state for F-Kr and F-Xe have a more prominent molecular character, being confined partially or totally in the Hund's case (a) at the distances around the minimum.

We have also studied, using the same technique, the $F(^2P)-D_2$ and $F(^2P)-CH_4$ systems which are of interest for reactive scattering. This integral cross sections at thermal energies are mostly dominated by large impact parameters, and

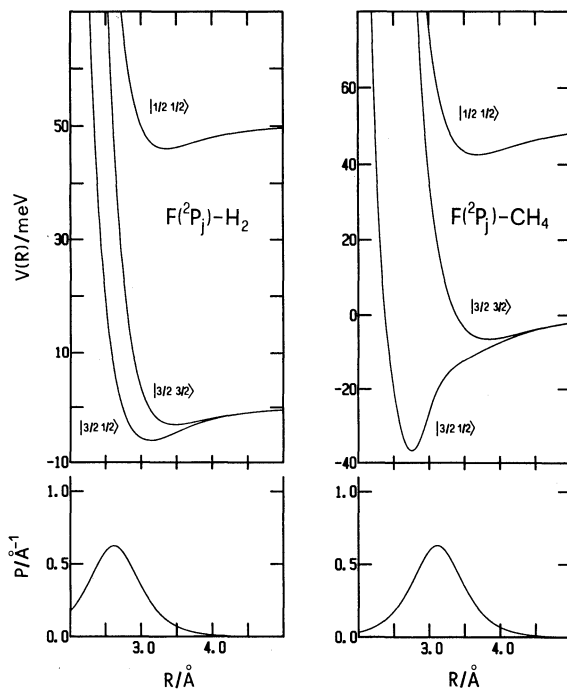


Fig.3 - Adiabatic potential energy curves $V_{|j\Omega\rangle}$ for $F-H_2$ and $F-CH_4$ systems. Also shown in the figure is the nonadiabatic coupling matrix elements P between the $|3/2\ 1/2\rangle$ and $|1/2\ 1/2\rangle$ states.

the experimental data are not affected by reactive collisions. Considering in addition that these molecules have low interaction anisotropy at long range and are at a sufficiently high rotational temperature, the present experimental data are not influenced by molecular anisotropy [13]: any anisotropic effect is therefore attributed to the open shell atom and from this analysis it is possible to obtain the spin orbit effect on the long range behavior of the reactive potential energy surface (see Fig.3 and Tab.I). In particular, it is noted that only the ground state adiabatically correlates, at thermal energies, with reactive channels [14]. In the near future these studies will be extended also to the interaction between chlorine atoms and rare gas atoms, which are related to the rare gas chloride excimer lasers.

Table I - Some characteristic features of the F-rare gases interaction(*)

	F-He	F-Ne	F-Ar	F-Kr	F-Xe	F-D ₂	F-CH ₄	
V _O	{ε R _m σ	2.12 3.04 2.71	4.21 3.16 2.81	6.80 3.50 3.08	7.20 3.65 3.17	8.10 3.78 3.34	4.12 3.34 2.97	7.80 3.64 3.17
V ₂	{ε R _m σ	0.06 3.84 3.40	0.04 4.72 4.25	0.11 4.88 4.41	0.11 5.21 4.72	0.24 5.02 4.56	0.04 5.00 4.53	0.11 5.00 4.70
V _Σ	{ε R _m σ	2.28 3.00 2.67	7.64 2.90 2.61	12.00 3.12 2.73	47.30 2.83 2.55	161.80 2.31 2.07	9.36 2.94 2.58	50.70 2.74 2.32
V _Π	{ε R _m σ	2.05 3.04 2.72	3.33 3.26 2.91	5.80 3.61 3.20	5.70 3.85 3.39	6.80 3.93 3.50	3.17 3.48 3.11	6.17 3.84 3.38
V	{ε R _m 3/2 1/2>	2.19 3.02 2.69	5.65 3.02 2.68	8.70 3.31 2.89	34.40 2.84 2.60	145.40 2.31 2.08	6.05 3.12 2.74	36.74 2.74 2.38
V	{ε R _m 1/2 1/2>	2.12 3.04 2.71	4.17 3.16 2.83	6.70 3.51 3.11	7.10 3.69 3.25	8.00 3.80 3.39	4.06 3.36 3.00	7.61 3.68 3.25

(*) The parameters for V_{|3/2 3/2>} are the same as for V_Π. Well depths ε, their position R_m and zeros of the potential σ are in meV and Å respectively. Estimated uncertainties are about 10% for ε and 2% for R_m and σ.

ACKNOWLEDGMENTS

This research is supported by ENEA, the EEC Science program and the CNR bilateral agreements.

REFERENCES

- [1] See, e.g., S. Bollanti and T. Letardi, this book. Also J.H.Kolts, D.W.Setser, *J.Phys.Chem.* 82, 1767(1978); Y.C.Yu, D.W.Setser, and H.Horlguchi, *J.Phys.Chem.* 87, 2199 (1983) and references therein; H.Helm, L.E.Jusinski, D.C.Lorentz, and D.L.Huestis, *J.Chem.Phys.* 80, 1796 (1984).
- [2] C.H.Becker, P.Casavecchia, and Y.T.Lee, *J.Chem.Phys.* 69, 2377 (1978); C.H.Becker, P.Casavecchia, and Y.T.Lee, *J.Chem.Phys.* 70, 2986 (1979); P.Casavecchia, G.He, R.K.Sparks, and Y.T.Lee, *J.Chem.Phys.* 77, 1878 (1982) and references therein.
- [3] J.Tellinghuisen, J.M.Hoffman, G.C.Tisone, and A.Hays, *J.Chem.Phys.* 64, 2484 (1976); J.Tellinghuisen, P.C.Tellinghuisen, G.C.Tisone, J.M.Hoffman, and A.K.Hays, *J.Chem.Phys.* 68, 5177 (1978); P.C.Tellinghuisen, J.Tellinghuisen, J.A.Coxon, J.E.Velazco, and D.W.Setser, *J.Chem.Phys.* 68, 5187 (1978); A.Sur, A.K.Hui, and J.Tellinghuisen, *J.Mol.Spectr.* 74, 465 (1979)
- [4] J.Tellinghuisen, A.K.Hays, J.M.Hoffman, and G.C.Tisone, *J.Chem.Phys.* 65, 4473 (1976);
- [5] V.Aquilanti, F.Pirani, E.Luzzatti, and G.G.Volpi, *Gazz.Chim.Ital.* 110, 57 (1980);
- [6] More details are in V.Aquilanti, E.Luzzatti, F.Pirani, and G.G.Volpi, *J.Chem.Phys.* 89, 6165 (1988)
- [7] V.Aquilanti, R.Candori, and F.Pirani, *J.Chem.Phys.*, 89, 6157 (1988)
- [8] N.F.Ramsey: Molecular Beams (Clarendon Press, Oxford, 1956)
- [9] A.R.Edmonds: Angular Momentum in Quantum Mechanics (Princeton University, Princeton-New Jersey, 1960).
- [10] V.Aquilanti and G.Grossi, *J.Chem.Phys.* 73, 1165 (1980); V.Aquilanti, P.Casavecchia, G.Grossi, and A.Laganà, *J.Chem.Phys.* 73, 1173 (1980).
- [11] V.Aquilanti, G.Liuti, F.Pirani, and F.Vecchiocattivi, *J.Chem.Soc.Faraday Trans. 2*, 85 (1989) in press.
- [12] G.Liuti and F.Pirani, *Chem.Phys.Lett.* 122, 245 (1985)
- [13] V.Aquilanti, R.Candori, L.Mariani, F.Pirani, and G.Liuti, *J.Phys.Chem.* 93, 130 (1989)
- [14] For the F-H₂ system see for example J.C.Tully, *J.Chem.Phys.* 59, 5122 (1973); J.B.Anderson, *Adv.Chem.Phys.* 41, 229 (1980)

MOLECULAR BEAM MEASUREMENTS OF IONIZATION CROSS SECTIONS
RELEVANT TO THERMAL PLASMAS AND EXCIMER LASER SYSTEMS

Sebastiano Bianco, Brunetto Brunetti,
Miguel González, and Franco Vecchiocattivi

Dipartimento di Chimica, Università di Perugia
06100 Perugia, Italy

INTRODUCTION

Rare gas atoms in their lowest excited levels often exhibit interesting properties mainly due to their high electronic energy and long lifetime. The electronic energy ranges from 19.82 eV for the He atom in the 2^3S state to 8.32 eV of the Xe atom in the 3P_2 state, while the lifetime ranges from 4.2×10^3 s for the former atom to 149.5 s for the latter.

When a metastable rare gas atom collides with another particle the "quasi-molecule" which is formed during the collision may have very short lifetime and, if energetically accessible, the autoionization of this "quasi-molecule" is one of the most probable processes. In particular, when the metastable atoms are He^* or Ne^* generally the ionization is the most important de-excitation process [1]. Therefore, the quenching of these metastable atoms can involve the formation of Penning ions, associate ions or ionic fragments (if the target is a molecule). In some cases, however, electronic energy transfer or chemical reactions leading to the formation of an excimer molecule significantly occur [2].

Because their importance in several applications such as thermal plasmas, electrical discharges or laser systems, these processes have been extensively studied both in bulk and under single collision conditions. The long lifetime of

rare gas metastable atoms makes possible the study of collisional processes of excited rare gas atoms by the molecular beam technique [3,4].

In this paper we report some recent experimental results about the ionization processes occurring in collisions between metastable rare gases and some atomic and molecular targets. The experiments have been carried out in a crossed beam apparatus which allows to measure the absolute cross sections, for each ionization channel, as a function of the collision energy in the thermal range.

THE CROSSED BEAM APPARATUS

The crossed beam experimental set up, schematically shown in Fig.1, has been described in detail elsewhere [3,5]. Only a general description is given here.

The metastable rare gas atom beam is produced by electron bombardment of an effusive rare gas beam. The ions and the high Rydberg state rare gas atoms, which also are produced in the electron impact excitation region, are removed from the beam by an electric field of about 2.0 kV/cm. The target beam is produced by a microcapillary array beam source and crosses the metastable atom beam at 90°. The temperature of both beam sources can be adjusted from room temperature up to about 900 K. The metastable atom beam is monitored by a channel electron multiplier which can be moved into the beam crossing center. The product ions are extracted from the scattering volume by an electric field, focused by an electrostatic lens system, mass analyzed by a quadrupole filter and finally detected by another channel electron multiplier.

The absolute value of the ionization cross sections is obtained by a calibration method. A beam monitor, which consists of a total ionization detector, is located in a box with a slit placed along the direction of the target beam. The signal provided by this instrument, when corrected for the relative sensitivity to the specific target gas used, is proportional to the beam intensity. Therefore, the value of an ionization cross section is obtained by measuring the

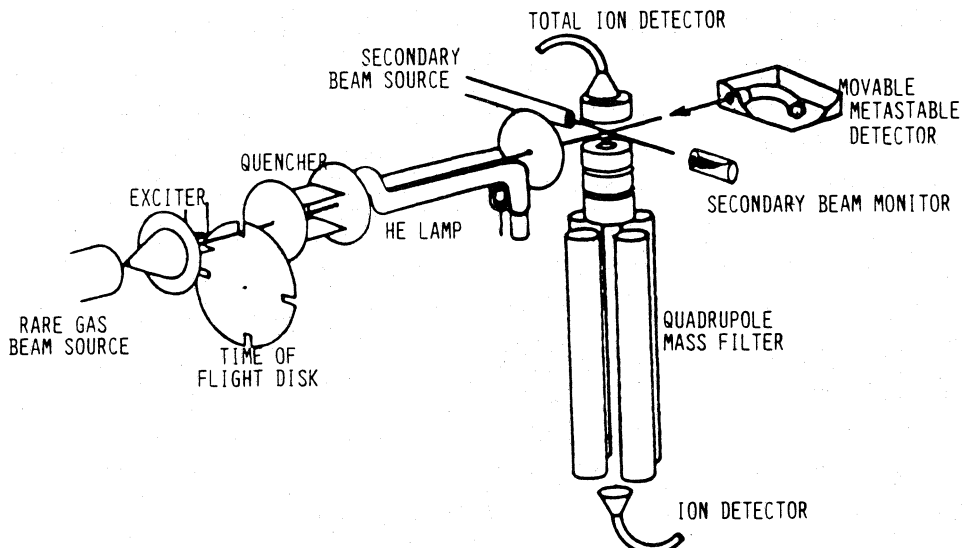


Fig.1 - The experimental set up.

intensity of the product ions formed with the gas under study and with a reference target whose cross section value is known. In our experiments we have used the Ne^* -Ar total ionization cross section, measured by West et al. [6], as reference value.

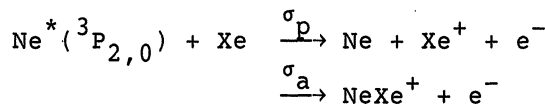
The velocity selection is accomplished by a time of flight technique. The metastable atom beam is pulsed by a rotating slotted disk and the pulses from the metastable atoms or from the product ions are counted as a function of the delay time, with respect to the slit opening. The time of flight spectra are obtained by sending the pulses to a computer controlled CAMAC unit data acquisition system based on a high-speed multichannel scaler and a PDP 11/23 unit. The time of flight spectra for the product ions are then corrected for the ion flight time and the transmission throughout the mass filter. From the time spectra and by means of a numerical procedure, the velocity dependence of the ionization cross sections can be obtained.

IONIZATION CROSS SECTION RESULTS

Some examples of the studies we are currently carrying out in our laboratory are reported in this section, in order

to present some interesting aspects of these processes.

An example is the study of the ionization of heavier rare gas atoms by metastable neon atoms. From these studies a good insight on the ionization dynamics has been obtained, and some conclusions on the role played by the anisotropy of the interaction have been achieved [3,7]. Beyond the fundamental interest of the understanding of the ionization dynamics, the study of the ionization of xenon by neon metastable atoms appears to be very interesting, because this reaction plays an important role in some laser sources, e.g. in the XeCl laser, where the excimer molecule is produced in a discharge of a Xe/HCl mixture in a bath of neon [8]. In this case two ionization channels are possible:



In our experiment, we have found $\sigma_p = 7.4 \cdot 10^{-16} \text{ cm}^2$ and $\sigma_a = 2.8 \cdot 10^{-16} \text{ cm}^2$ at a collision energy around 50 meV. In Table I, the cross sections for the total ionization, $(\sigma_p + \sigma_a)$, at such a collision energy, are reported together with the rate constant for the total quenching of Ne^* by Xe obtained in other laboratories with different techniques. An essential agreement exists between all available results, therefore we can consider the value of this cross section, or the related rate constant, as well assessed and suitable for a realistic description of those systems where these processes are involved.

Recent results have been also obtained for the ionization of simple molecules such as N_2 , O_2 , NO , CO , Cl_2 , and CH_3Cl with metastable neon atoms. For these systems all the possible ionization channels have been studied [12,13].

In Fig.2 is shown, as an example, the energy dependence of the total ionization cross section for the $\text{Ne}^*(^3P_{2,0})-\text{CH}_3\text{Cl}$ system.

For the $\text{Ne}^*-\text{CH}_3\text{Cl}$ system, the study of the branching ratios on ionic fragmentation can allow the determination of the relative yield of formation of ionic excited states compared to that of the ground state. For this system, an

TABLE I

experimental technique	$\sigma(50 \text{ meV})$ 10^{-16} cm^2	$k(300 \text{ K})$ $10^{-11} \text{ cm}^3 \text{s}^{-1}$	Reference
crossed beams	10.2 ± 1.5	7.1 ± 1.0^a	this work
crossed beams	14.9 ± 3.0	—	[6]
flowing afterglow	12^b	7.4	[9] ^c
laser absorption	—	7.5 ± 1.0	[10] ^c
merging beams	14.0 ± 5.2	9.8 ± 3.6^a	[11]

a) Estimated from the experimental cross section.

b) Estimated from the experimental rate constant.

c) In this case $\text{Ne}^*(^3\text{P}_2)$ has been used.

increase of the relative population of excited ionic states on increasing collision energies has been observed [13].

The behaviour of all the molecules studied shows analogies and differences which can be attributed to the autoionization resonance width and/or to the possibility of formation of an ionic intermediate, for molecules with positive electron affinity, which strongly modifies the interaction between the collisional partners [12,14].

For the investigated systems, the absolute value and the collision energy dependence of the total ionization cross section allow a good characterization of the autoionization resonance width. Therefore, when these experimental data are analyzed together with other scattering properties, such as differential and/or integral elastic cross sections, detailed information on the complex optical potential which describes the interaction between the collisional partners can be obtained [15].

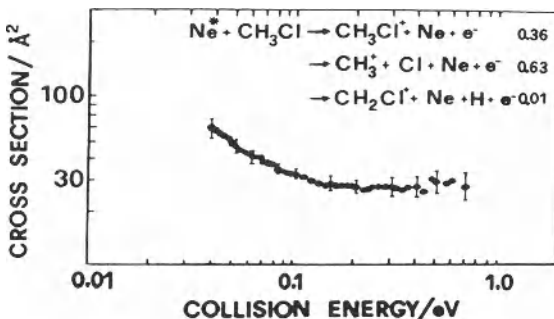


Fig. 2 - Energy dependence of the total ionization cross section for the collisions between Ne^* (${}^3\text{P}_{2,0}$) atoms and CH_3Cl molecules. The relative yields for the observed ionic channels, at around 0.050 eV, are also indicated.

ACKNOWLEDGEMENTS

This research is supported by ENEA, the EEC Science program and the CNR bilateral agreements. One of the authors (M.G.) is grateful to the "Ministerio de Educación y Ciencia" of Spain for a postdoctoral fellowship.

REFERENCES

- 1 - M.T.Jones, T.D.Dreiling, D.W.Setser, and N.McDonald, *J.Phys.Chem.* 89, 4501 (1985).
- 2 - J.Balamuta, M.F.Golde, and A.M.Moyle, *J.Chem.Phys.* 82, 3169 (1985) and references therein.
- 3 - A.Aguilar, B.Brunetti, S.Rosi, F.Vecchiocattivi and G.G.Volpi, *J.Chem.Phys.* 82, 773 (1985).
- 4 - T.Bregel, W.Bussert, J.Ganz, H.Hotop, and M.-W.Ruf, in "Electronic and Atomic Collisions", D.C.Lorentz *et al.* editors, North Holland, Amsterdam 1986, p.577.
- 5 - L.Appolloni, B.Brunetti, J.Hermanussen, F.Vecchiocattivi, and G.G.Volpi, *J.Chem.Phys.* 87, 3804 (1987).
- 6 - W.P.West, T.B.Cook, F.B.Dunning, R.D.Rundel, and R.F.Stebbins, *J.Chem.Phys.* 63, 1237 (1975).
- 7 - B.Brunetti, F.Vecchiocattivi and G.G.Volpi, *J.Chem.Phys.* 84, 536 (1986).
- 8 - See for example: S.Bollanti and T.Letardi, this book.

- 9 - J.M.Brom, J.H.Kolts, and D.W.Setser, *Chem.Phys.Lett.* 55, 44 (1978).
- 10 - D.L.Huestis, R.M.Hill, H.H.Nakano, and D.C.Lorentz, *J.Chem.Phys.* 69, 5133 (1978).
- 11 - R.H.Neynaber and S.Y.Tang, *J.Chem.Phys.* 70, 4272 (1979).
- 12 - L.Appolloni, B.Brunetti, F.Vecchiocattivi and G.G.Volpi, *J.Phys.Chem.* 92, 918 (1988).
- 13 - B.Brunetti, M.González, and F.Vecchiocattivi, to be published.
- 14 - B.Brunetti and F.Vecchiocattivi, in "Electronic and Atomic Collisions", H.B.Gilbody et al. editors, North Holland, Amsterdam 1988, p.495.
- 15 - J.Baudon, P.Feron, C.Miniatura, F.Perales, J.Reinhardt, J.Robert, H.Haberland, B.Brunetti, and F.Vecchiocattivi, XII International Symposium on Molecular Beams, Perugia 1989, Book of Abstracts, p.386.

THE SILENT DISCHARGE AND ITS APPLICATION TO OZONE AND EXCIMER FORMATION

B. Eliasson and U. Kogelschatz

Asea Brown Boveri Corporate Research
5405 Baden, Switzerland

INTRODUCTION

In this chapter a short review will be presented of the silent discharge and its applications. The silent discharge, or dielectric barrier discharge as it is sometimes called, has been known since the 1850's when von Siemens used it for generating ozone. Because of this it is sometimes referred to in the literature as the "ozonizer discharge". It is a non-equilibrium, high pressure discharge. It is one of the most important discharge types used in industrial plasma chemistry. In spite of the widespread applications of such discharges there were until recently few investigations of the structure of such discharges being done. During the last 10 years considerable progress has been achieved in understanding both the physics of the discharge process itself as well as the ensuing chemistry¹⁻³.

A silent discharge forms when an AC voltage is applied between two electrodes at least one of which is covered by a dielectric (Fig. 1).

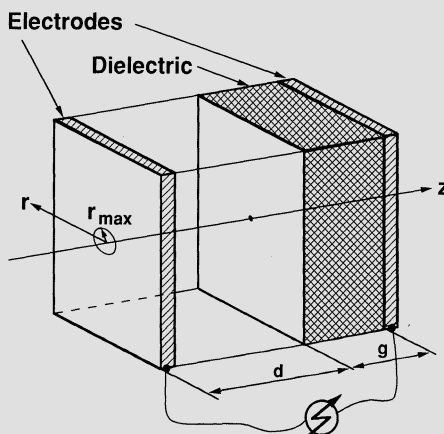


Fig. 1. A silent discharge electrode configuration

The voltage in the gap must exceed the breakdown voltage (Paschen) of the gas. The discharge current is carried across the gap in a multitude of microdischarges which are randomly distributed in space and time. These microdischarges are of very short duration due to charge build-up on the dielectric which leads to choking of the electric field within the microdischarge. In the microdischarges energetic electrons and excited species are generated. Otherwise the neutral gas in between the microdischarges is left untouched by that particular discharge and the neutral gas remains essentially at the ambient temperature.

The silent discharge is predestined for applications in volume plasma chemistry. It has inherent advantages over discharges like the low pressure glow discharge or the inhomogeneous corona discharge. The main advantages of silent discharges are:

- **high pressure discharge**, i.e. it generates high electron densities and high densities of excited species
- **non-equilibrium discharge**, i.e. almost all of the energy goes initially into the generation of energetic electrons
- the energetic electrons have a short lifetime and can transfer almost all of their energy to excited species
- the electron energy can be influenced by changing the pressure and the gap width
- such discharge configurations can be connected in parallel and one can thus reach power levels in the range of MW's.

The silent discharge is very simple to run. In the simplest case it can be run from the mains with a step-up transformer. One practical problem is to get as much power as possible into the gap. Due to the capacitive nature of the coupling this is most easily accomplished by using a large area discharge, a small dielectric thickness g , a high dielectric constant or higher frequencies.

Two specific applications of the silent discharge will be treated, viz. the generation of ozone in a mixture of oxygen and nitrogen and as a second new application the generation of excimers. Excimers are short-lived molecules which can only exist in an excited state. Once the excimer falls back to the ground state it emits a UV photon. In this way a silent discharge arrangement can be transformed into an efficient source of UV radiation ⁴.

PHYSICS OF SILENT DISCHARGES

A discharge is a source of electrons and ions. In case of the silent discharge the electrons have high energy (< 20 eV) and excite the atoms and molecules present. These excited species can, in turn, initiate chemical reactions (e.g. dissociation and/or synthesis of new molecules). It is helpful as a gedanken experiment to differentiate between the discharge itself, i.e. the physical process of bridging the discharge gap by a current pulse and the ensuing chemical reactions. Due to the short current pulses occurring in a silent discharge this separation of physics and chemistry comes almost naturally. Each chemical process one wants to maintain calls for a specific optimization of the physical process of the discharge itself. In reality, of course, the phenomena of physics and chemistry are indelibly intertwined.

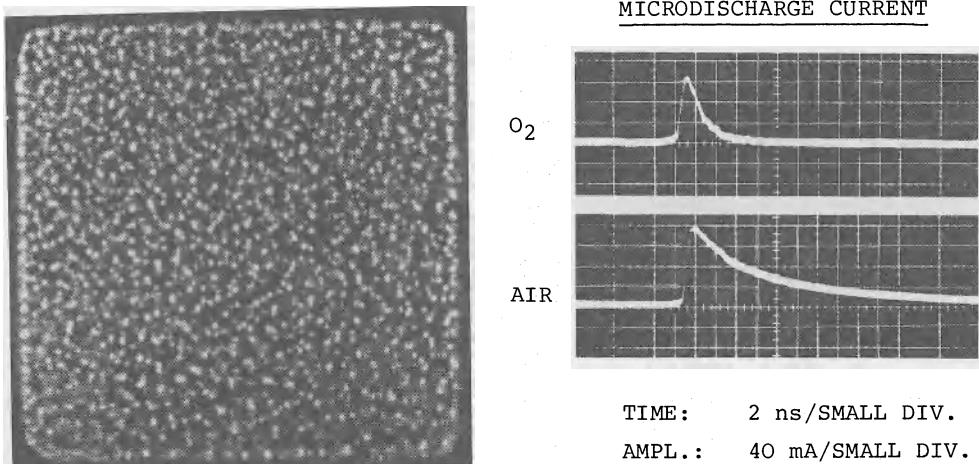


Fig. 2. A photograph of microdischarges in air (exposure time: 20 ms) (left). Measured current pulses in air and oxygen for single microdischarges (right).

As mentioned above, as one applies an increasing sinusoidal voltage to the discharge gap (Fig. 1) the gap breaks down creating a number of microdischarges randomly distributed in time and space (Fig. 2)

Each microdischarge leads to a very short current pulse of width τ_1 , where τ_1 is given by

$$\tau_1 = \left(\frac{8}{\alpha \cdot n \cdot d(E/n)/dt} \right)^{1/2} \Big|_{j=j_{\max}} \quad (1)$$

where α is the derivative of the difference of the ionization and attachment rate coefficients with respect to the reduced field E/n . Because of the parameter α , electronegative gases as e.g. O₂ have shorter pulses than e.g. the rare gases or N₂.

One distinguishes between two kinds of breakdown in a discharge gap. If the product of gas density n and the gap width d is small a Townsend discharge occurs. It is started by a succession of avalanches which interact with the electrodes through charged particles and photons. If the product nd is large a streamer breakdown is initiated ⁵. The streamer breakdown is a single-pass breakdown. Due to a high build-up of eigenfield, i.e. build-up of space charge, the initial breakdown is very much localized in the gap. The effective reduced breakdown field is considerably higher than in the case of the classical Townsend breakdown. The electrons are accelerated to high energies and the breakdown itself self-propagates (streamers) towards both electrodes. It leaves behind a fairly homogeneous conducting channel of low electric field and excited particles. Streamer breakdown depends less on the state of the electrodes as rather on the characteristics of the bulk gas itself. Typical parameters of microdischarges in pure oxygen are shown in Table I.

Table I
Characteristic Parameters of Microdischarges in Oxygen

Duration	:	1 - 10 ns
Current density	:	1 kA/cm ²
Diameter	:	200 μm
Electron energy	:	1 - 20 eV
Electron density	:	10 ¹⁴ - 10 ¹⁵ cm ⁻³
Reduced field	:	E/n ≈ (1-2) E/n Paschen
Gas temperature	:	300 K

The energy of the electrons is determined by two parameters: a) the total reduced electric field they are subjected to. It consists of the applied field and the usually much higher eigenfield. b) the interaction with other particles, i.e. their cross sections. By solving the Boltzmann equation one gets the distribution of electron energies once the above parameters are known. In silent discharges the electrons are in equilibrium with the electric field at each instant. At 1 bar they reach equilibrium at <10⁻¹¹s which is much faster than all the variations due to the discharge phenomena like ionization and attachment. In Fig. 3 we show calculated current densities and electron and ion densities as a function of time after a reduced field pulse of the form shown in Fig. 3 (a) has been applied.

At each instant the Boltzmann equation was solved. The excited species created within a microdischarge diffuse within some ms into the volume between the discharges (Fig. 4). In a discharge in oxygen the time for the formation of the O₃ (τ_2) is much longer than the time for the formation of atomic oxygen, i.e. the width of the discharge pulse τ_1 . But both are much shorter than the diffusion time τ_3 .

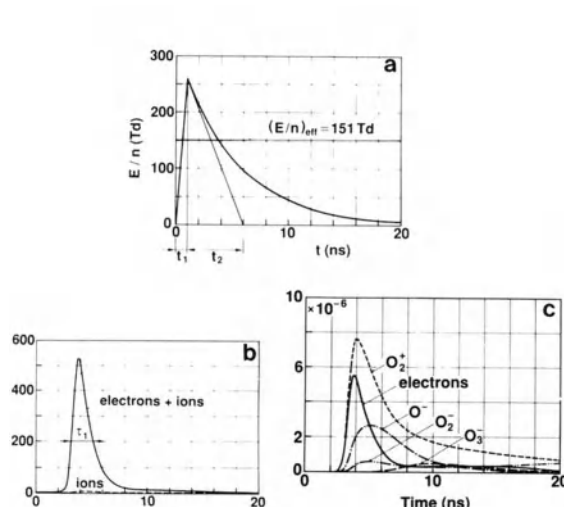


Fig. 3. Reduced field (a), current densities (b), electron and ion densities in oxygen (c)

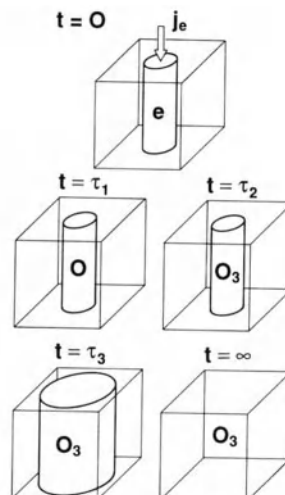


Fig. 4. Diffusion of ozone formed in a microdischarge channel

DIELECTRIC-BARRIER DISCHARGE
(OXYGEN)

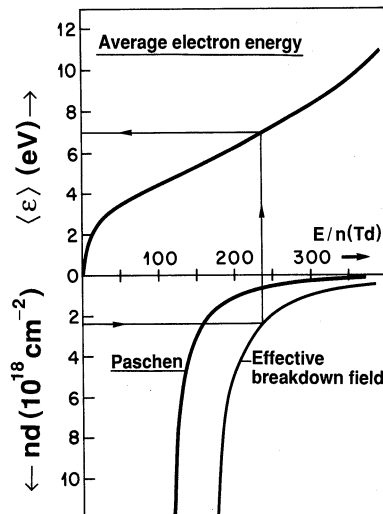


Fig. 5. The dependence of the reduced field E/n and average electron energy on the product nd . Effective breakdown field: $1.5 * \text{Paschen field}$.

One can influence the average electron energy $\langle \varepsilon \rangle$ by changing the product of the total gas density and the gap distance (Fig. 5). One can also influence the energy and other parameters of the microdischarge by applying a very fast voltage pulse to the discharge gap.

As we have seen the silent discharge is not only instationary but also a very inhomogeneous supply of electrons. The spatial inhomogeneity of the silent discharge is due to the fact that the microdischarges are single transit discharges. They start where the conditions are favourable (i.e. rough surface, high local field). In the end they are self-propagating, i.e. they propagate under the influence of their own eigenfield, and more or less independent of what is going on around them. Such a propagation is inhomogeneous by its very nature.

Over long time periods the microdischarges, which are randomly distributed by the way they are initiated, will tend to fill the volume available evenly. Thus the inhomogeneity of the silent discharge does not lead to a disadvantage. To the contrary, this way the produced species in the microdischarge filaments have leeway to diffuse into the charged-particle free regions between the filaments before the next discharge strikes at the same location. This separation of electron producing regions and the bulk gas can, no doubt, be very beneficial in certain cases.

Due to their very intricate nature, the modelling of silent discharges is a complex task. E.g. the local electron temperature within a microdischarge changes with the local field. The electrons, which are always in equilibrium with the electric field, react immediately to any field change. This very fact makes it mandatory to solve the Boltzmann equation for the electron energy distribution function for every change in field. But there is a major difference to the approach for e.g. glow discharges. The silent discharge is a local volume phenomenon, it is enough to understand one microdischarge and one has understood the whole discharge process. Due to the high pressure wall phenomena are only of a minor importance for the modelling of silent discharge.

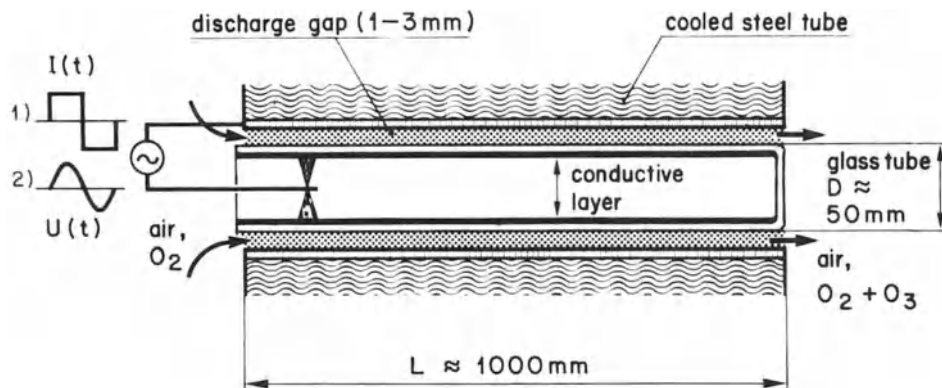


Fig. 6. Schematic diagram of an ozone discharge tube

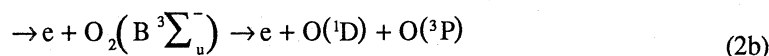
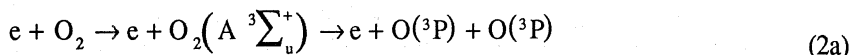
OZONE PROPERTIES AND OZONE GENERATORS

The most important industrial application of silent discharges is the generation of ozone from dried air or pure oxygen⁶. Large installations reach power levels of a few megawatts and produce several tons of ozone per day. Ozone is mainly used for the purification of potable water and the treatment of waste water. Due to its high oxidizing power, its superior germicidal and bleaching properties ozone has also found a number of additional applications. The main incentive to replace other oxidants such as chlorine or chlorine compounds by ozone is its better environmental compatibility as far as transport, storage and decay products are concerned.

In most technical ozone generators the dielectric is a cylindrical glass tube which is mounted coaxially in a stainless steel tube. The discharge burns in the annular gap between the outer steel tube and the glass tube (Fig. 6). The electrodes are provided by an internal metallic coating inside the glass tube and by the steel tube which is normally grounded and water cooled. Since large electrode areas are required for mass production several hundred of these discharge tubes are mounted in large technical ozone generators. Traditionally, ozone generators were run at power line frequencies with a sinusoidal feeding voltage of about 20 kV peak value. Modern ozonizers operate at 500-3000 Hz supplied by thyristor controlled frequency converters that impress a square-wave current. This technique allows much higher power densities and consequently results in more compact ozone installations. During the past decade the size of ozone generators has been reduced by a factor of ten while, at the same time, the specific power consumption of large installations has been cut by a factor of two.

OPTIMIZING OZONE GENERATION IN OXYGEN

The plasma conditions in the individual microdischarges can be optimized for the ozone formation process. In oxygen the main reactions are:



where M is a third collision partner (O_2 , O, O_3 , in air also N_2 , N) and O_3^* is a transient excited ozone molecule which is the initial product of the three-body reaction (3). The 1) Maximize the fraction of the discharge energy that is furnished to the electrons (i.e. minimize energy losses due to ions)

- 2) Optimize the electron energy for the dissociation process (2a) and (2b)
- 3) Optimize the conditions (pressure, temperature, atom concentration) for the ozone formation process (3) and suppress side and back reactions.

The first condition requires a minimum electron and ion density in the microdischarges to speed up ion recombination. The dissociation proceeds via excitation of electronic levels with threshold energies of 6 eV and 8.4 eV respectively. In oxygen this range of electron energies will be established when the effective reduced field is in the range of 150-350Td. The main influence we can exert on the reduced field is to adjust the product nd and, to a lesser degree, the surface properties. The third requirement is the suppression of undesired side reactions that consume oxygen atoms which are then no longer available for ozone formation, or that even destroy already formed ozone molecules.



This requirement puts an upper limit on the desired atom concentration in the microdischarge channel. Since the number of atoms depends on the charge that has been transported by the microdischarge we have to limit the charge density. The main quantities of influence are the dielectric properties (thickness and dielectric constant) and the gap spacing.

Fairly extensive reaction schemes treating about 70 reactions between 15 different neutral and charged atomic and molecular species are used for this optimization process ³. Fig.7 (left) shows the evolution of decay of different particle species due to a single microdischarge.

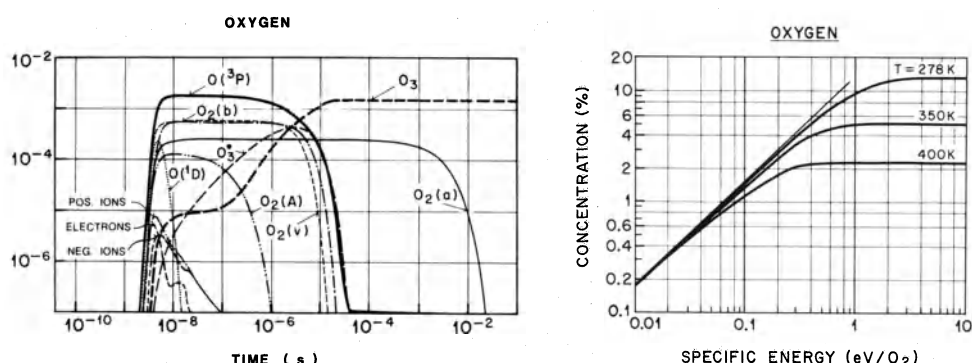
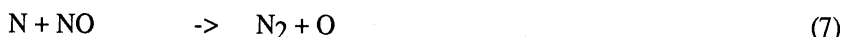


Fig. 7. Numerical simulation of ozone formation in a single microdischarge (left) and the concentration build-up due to the action of many microdischarges (right)

Higher ozone concentrations have to be built up by a series of microdischarges. A volume element traveling through an ozone discharge tube typically is subjected to the action of several hundred microdischarges. Fig. 7 (right) shows a numerical simulation of the concentration build-up. Two aspects are important. After a certain number of microdischarges, or a certain amount of energy deposited in the feed gas, a saturation concentration is reached. From now on each additional microdischarge will destroy as much ozone as it creates. Secondly, the average gas temperature in the discharge has a strong effect on the ozone concentration. For this reason all ozonizers rely on efficient cooling circuits to remove excessive heat.

OZONE GENERATION IN AIR

For economic reasons only the largest ozone installations are operated on oxygen. Smaller ozone generators use dehumidified air as a working gas. As a matter of fact, the nitrogen molecules present do not merely act as a passive buffer gas. The presence of additional species such as N, N_2^+ , N^+ , N_2^* and different nitrogen oxides have a profound influence on the reaction kinetics. Interestingly enough some reactions involving nitrogen atoms or excited nitrogen molecules lead to the formation of oxygen atoms that eventually react to form ozone⁷



These reactions explain the experimental fact that in air discharges the abundance of oxygen atoms and also the ozone generating efficiency is about twice as high as one would expect from the oxygen content of air.

EXCIMER FORMATION IN SILENT DISCHARGES

The plasma conditions in the individual microdischarges can also be optimized for excimer formation. Typical examples of such excimers are Xe_2^* , ArF^* , $XeCl^*$. The scientific and technical importance of these excimers results from the fact that they decay within nanoseconds and give off their binding energy in the form of narrow-band UV or vacuum UV radiation. Most information about different excimers has been gained from pumping different gas mixtures with high energy electron beams^{8,9}. Commercial excimer lasers use transversely pulsed gas discharges with complicated preionization schemes.

The simple silent discharge configuration is ideally suited for the generation of incoherent excimer radiation. Since the discharge volume can be completely sealed in quartz and the electrodes can be kept outside no problems with electrode erosion have to be expected. As an example the vacuum UV radiation from the Xe_2^* excimer shall be described. Xe_2^* can be formed either directly in a three-body reaction involving excited xenon atoms or indirectly starting from a xenon ion. Model calculations indicate that high efficiencies can be obtained if mainly the direct excitation path is favoured⁴.

XENON EXCIMER XENON ATOM

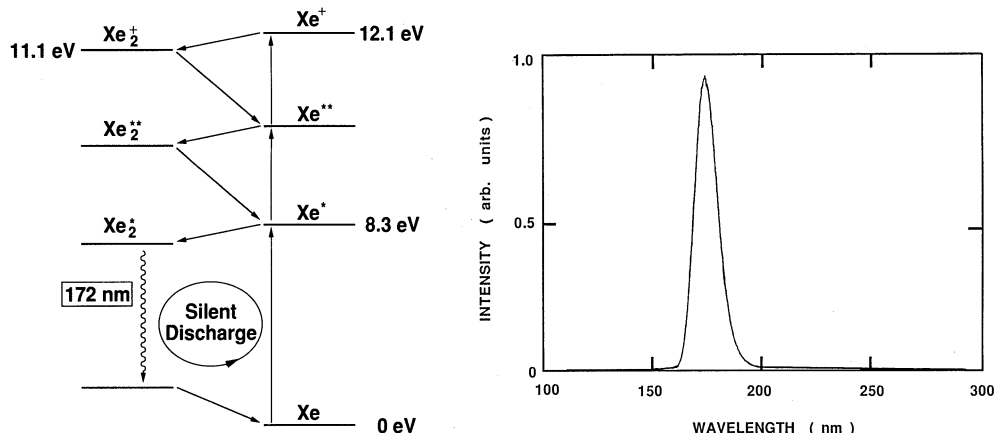


Fig. 8. Schematic reaction scheme and measured spectrum of Xe_2^* excimer radiation from a silent discharge

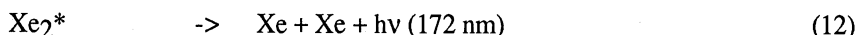


Fig. 8 shows a schematic presentation of the pumping mechanism and an obtained spectrum showing clearly the second continuum of Xe_2^* . Surprisingly enough, practically no other radiation comes from this discharge in the whole spectral range 100 - 800 nm. The half width of the emission band is about 12 nm and the UV efficiency is estimated to reach 5-10%.

We also obtained the excimer spectra of Ar_2^* and Kr_2^* peaking at 128 nm and 148 nm respectively. Silent discharges in mixtures of rare gases plus halogens or halogen compounds lead to the emission of rare gas/halogen excimer spectra. Again one obtains almost monochromatic UV radiation with a half-width of a few nm. In these discharges the recombination of ions is the most likely reaction path leading to excimer formation. For example:



In the same way the radiation of ArCl^* and KrCl^* was obtained, peaking at 175 nm and 222 nm respectively.

PRACTICAL CONSIDERATIONS

The silent discharge configuration is a fairly simple device that can be operated over a wide frequency range. Efficient power supplies are available from ozone technology. Since the excimer formation process is a three-body reaction higher pressures favour excimer formation. Under these conditions streamer breakdown will occur and result in short-lived localized microdischarges. Consequently, these excimer UV sources will emit bursts of light pulses of high peak intensity. Due to the absence of a stable ground state no self-absorption of the

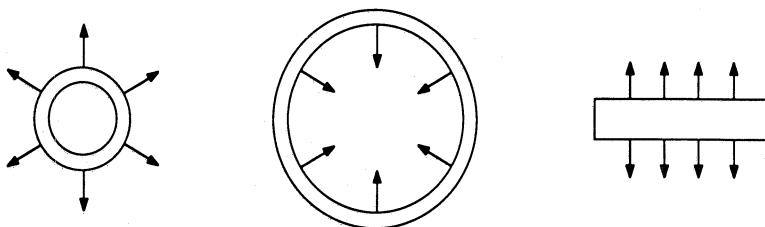


Fig. 9. Different configurations for excimer UV sources

radiation in the discharge volume is likely to occur. The narrow discharge gaps normally used in silent discharges allow a number of different geometrical configurations for these new UV sources which are ideal for the irradiation of surfaces or volumes (Fig. 9). Thus the flexibility with respect to wavelength and geometry make these silent discharge excimer sources promising candidates for a number of UV initiated biological, physical and chemical processes.

REFERENCES

1. S. Yagi and M. Tanaka, Mechanism of ozone generation in air-fed ozonizers, J. Phys. D: Appl. Phys. 12: 1509 (1979).
2. V. I. Gibalov, V. G. Samoilovich and Yu. V. Philippov, Physical chemistry of electrosynthesis of ozone. The results of numerical experiments. Russ. J. Phys. Chem. 55: 471 (1981).
3. B. Eliasson, M. Hirth and U. Kogelschatz, Ozone synthesis from oxygen in dielectric-barrier discharges, J. Phys. D: Appl. Phys. 20: 1421 (1987).
4. B. Eliasson and U. Kogelschatz, UV excimer radiation from dielectric-barrier discharges, Appl. Phys. B 46: 299 (1988).
5. E. E. Kunhardt and W. W. Byszewski, Development of overvoltage breakdown at high gas pressure, Phys. Rev. 21: 2069 (1980).
6. U. Kogelschatz, Advanced ozone generation, in "Process Technologies for Water Treatment", S. Stucki, ed., Plenum, New York (1988).
7. B. Eliasson, U. Kogelschatz and P. Baessler, Dissociation of O₂ in N₂/O₂ mixtures, J. Phys. B: At. Mol. Phys. 17: L797 (1984).
8. Ch. K. Rhodes, "Excimer Lasers", Topics in Applied Physics, Vol. 30, Springer, Berlin (1984).
9. D. J. Eckstrom, H. H. Nakano, D. C. Lorents, T. Rothen, J. A. Betts, M. E. Lainhart, D. A. Dakin and J. E. Maenchen, Characteristics of electron-beam-excited Xe₂* at low pressures as a vacuum ultraviolet source, J. Appl. Phys. 64: 1679 (1988).

NON EQUILIBRIUM EXCIMER LASER KINETICS

C. Gorse

Centro di Studio per la Chimica dei Plasmi del CNR
Dipartimento di Chimica, Università di Bari
Trav. 200 Re David, 4 70126 Bari, Italy

Excimer lasers with wavelengths in the visible and UV regions have been extensively studied in these last years¹⁻⁸ for their importance in many technological applications. Those lasers are mostly formed by a combination between a rare gas and an halogen containing molecule. We report here the description of a self-consistent model which describes the temporal evolution of an excimer laser mixture under the action of the voltage applied to the electrodes of the laser cell and provided by an electrical external circuit. The laser mixture we considered Ne-Xe-HCl (0.95-0.044-0.006) is used in the experimental device, (10 liter volume,⁹ X Ray preionization) setted at the ENEA Laboratories of Frascati.

Self-consistent model

In the excimer laser mixture the deposited energy is carried by the electrons, stocked in the three initial species (Ne, Xe, HCl) and then redistributed via chemical processes to all species like the lasing one XeCl*. Laser photons ($\lambda=308\text{nm}$) are formed in spontaneous and stimulated emission processes and lost in the optical path or captured by some absorbers (Xe_2^+ , Ne_2^+ , ...). Thus the model we have to build must give informations about the energy deposited in the laser cell, the energy distribution of electrons and the concentrations of the different heavy species.

The voltage applied to the electrodes of the laser cell is provided by an electrical circuit shown in figure 1. All the elements of this circuit but the resistance R_L have fixed values which are those given by the constructor or are experimentally measured¹⁰. The charging voltage V_0 can be varied. The laser cell resistance

$$R_L(t) = \frac{d}{\mu_e(t) n_e(t) A e} \quad 1)$$

(d:distance between the electrodes (10cm), A:transversal section of the discharge (1000cm^2), e:electron charge)

is time dependent as are the electron mobility (μ_e) and density (n_e). The electron mobility can be obtained solving the Boltzmann equation (BE) which gives us, in particular, the electron energy distribution function (eedf). To solve the BE it is necessary to know both the reduced electric field (E/N) and the concentrations of the heavy particles which enter in the terms simulating the effects of inelastic and superelastic processes. The kinetics of heavy particles calls up among other things the electronic rate coefficients which depend on the eedf. The electron number density obtained solving the kinetics is utilized, in the electrical circuit, to calculate a new value of R_L . As we can see we need a self-consistent model as the one schematically represented on figure 2.

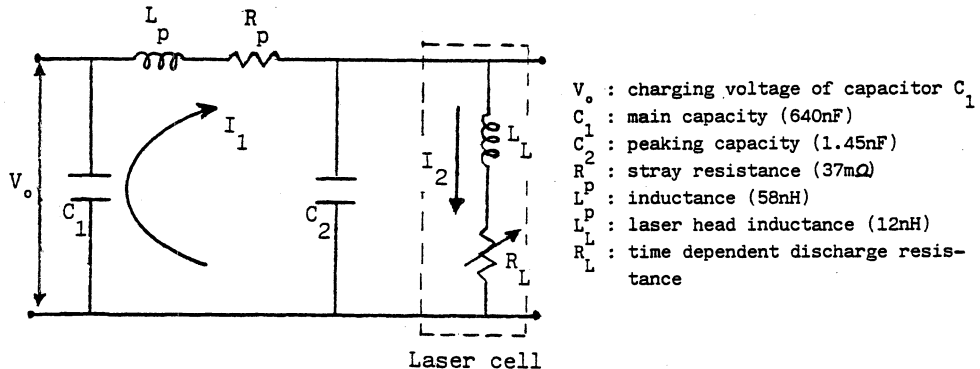


Fig. 1 External electrical circuit scheme

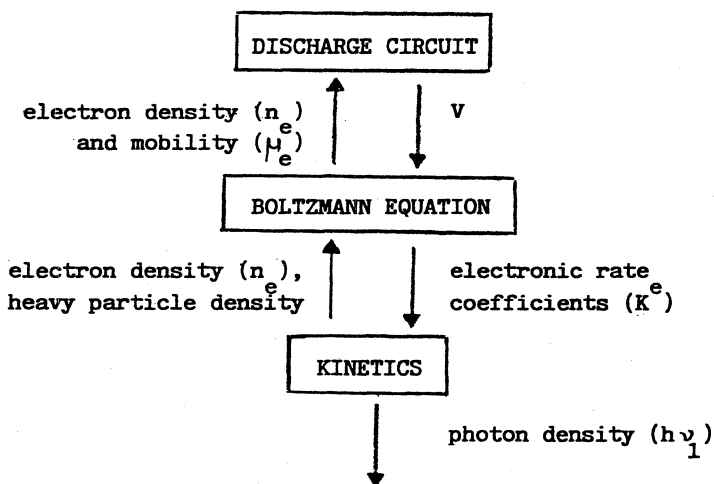


Fig. 2 Self-consistent model

In this theoretical modeling one of the most important steps is the characterization of the electron energy distribution function. In fact, ionization and electronic excitation processes are controlling both the number density of electrons and the whole heavy particle kinetics. It is worth noting that our zero-dimensional code solves the time dependent

Boltzmann equation in the two terms approximation including both the superelastic (vibrational and electronic) and electron-electron (e-e) collisions. The solution of the BE is obtained using the Rockwood's method¹¹ (see also ref.12)

$$\frac{\partial n(\epsilon, t)}{\partial t} = - \frac{\partial J_f}{\partial \epsilon} - \left(\frac{\partial J_{el}}{\partial \epsilon} \right)_{e-M} - \left(\frac{\partial J_{el}}{\partial \epsilon} \right)_{e-e} + In + Sup + Rot \quad 2)$$

where $n(\epsilon, t)$ represents the electron number density with energy in the range between ϵ and $\epsilon + d\epsilon$, and the different terms on the right hand side represent respectively the flux of electrons along the energy axis driven by the electric field, the elastic electron-heavy particle and electron-electron collisions, by inelastic, vibrational and electronic superelastic and rotational collisions.¹³

The continuous approximation has been used to develop the rotational term (Rot). The momentum transfer cross sections for HCl, Ne and Xe, reported in refs. 14-16, have been considered in this work, while table 1 lists the inelastic cross sections. Use has been made of detailed balance principle to calculate the superelastic ones.

Table 1. List of the inelastic electronic cross sections

<u>inelastic process</u>		<u>threshold (eV)</u>	<u>Ref.</u>
a) e + HCl(v=0)	--->	e + HCl(v=1,2)	0.36, 0.70
b) e + HCl	--->	e + HCl*(A, B+C)	5.5, 9.3
c) e + HCl	--->	2e + HCl ⁺	12.7
d) e + HCl(v=0,1,2)	--->	H ⁻ + Cl ⁻	0.84, 0.4, 0.12
e) e + HCl(v=0)	--->	H ⁻ + Cl	5.6
f) e + Ne	--->	e + Ne*	16.7
g) e + Ne	--->	e + Ne**	16.8
h) e + Xe	--->	e + Xe*	8.5
i) e + Xe	--->	e + Xe**	8.9
j) e + Ne	--->	2e + Ne ⁺	21.5
k) e + Xe	--->	2e + Xe ⁺	12.1
l) e + Ne*	--->	2e + Ne ⁺	4.9
m) e + Xe*	--->	2e + Xe ⁺	3.2

For the kinetics of heavy particles we considered 76 chemical reactions (table 2) involving 26 chemical species (Ne, Ne*, Ne⁺, Ne²⁺, Ne³⁺, Xe, Xe*, Xe⁺, Xe²⁺, Xe³⁺, HCl(v=0,1,2), H, Cl, Cl⁻, Cl⁺, Cl₂, Cl₂^{*}, XeCl*, Xe₂Cl*, NeXe², NeCl², e, h₁ (laser), h₂). To solve the coupled system of the 26 differential equations we used the method reported by Trigiani¹⁷.

Table 2. List of chemical reactions

<u>electron processes</u>		<u>Rate coefficient</u>	<u>Ref.</u>
e + Ne	↔	e + Ne*	BE
e + Xe	↔	e + Xe*	BE
e + Ne	--->	2e + Ne ⁺	BE
e + Xe	--->	2e + Xe ⁺	BE
e + Ne*	--->	2e + Ne ⁺	BE
e + Xe*	--->	2e + Xe ⁺	BE

(cont.)

Table 2. (cont.)

$e + HCl(v=0)$	\rightleftharpoons	$e + HCl(v=1)$	BE
$e + HCl(v=0)$	\rightleftharpoons	$e + HCl(v=2)$	BE
$e + HCl(v=0,1,2)$	\longrightarrow	$H + Cl^-$	BE
electron quenching			
$e + Cl_2$	\longrightarrow	$Cl + Cl^-$	$1.0(-10)cm^3/s$
$e + Cl_2^*$	\longrightarrow	$e + Cl^-$	$3.0(-7)$
$e + NeCl^*$	\longrightarrow	$e + Ne + Cl^-$	$3.0(-7)$
$e + XeCl^*$	\longrightarrow	$e + Xe + Cl^-$	$1.0(-7)$
$e + Xe_2^*$	\longrightarrow	$e + Xe + Xe$	$1.0(-9)$
$e + Ne_2^*$	\longrightarrow	$e + Ne + Ne$	$1.0(-9)$
HCl(v) quenching			
$HCl(v=1) + Ne$	\longrightarrow	$HCl(v=0) + Ne$	$6.2(-17)cm^3/s$
$HCl(v=1) + HCl(v=0)$	\longrightarrow	$HCl(v=0) + HCl(v=0)$	$2.7(-14)$
neutral reaction			
$Xe^* + Xe + Xe$	\longrightarrow	$Xe_2^* + Xe$	$8.0(-32)cm^6/s$
$Xe^* + Xe + Ne$	\longrightarrow	$Xe_2^* + Ne$	$1.6(-32)$
$Ne^* + Ne + Ne$	\longrightarrow	$Ne_2^* + Ne$	$4.1(-34)$
$Xe^* + HCl(v=0)$	\longrightarrow	$Xe + H + Cl^-$	$5.6(-10)$
$Xe^* + HCl(v=1)$	\longrightarrow	$Xe + H + Cl^-$	$5.6(-10)$
$Xe^* + HCl(v=1)$	\longrightarrow	$XeCl^* + H$	$2.0(-10)$
$Xe^* + HCl(v=2)$	\longrightarrow	$XeCl^* + H$	$2.0(-10)$
penning ionization			
$Xe^* + Xe^*$	\longrightarrow	$Xe^+ + Xe + e$	$5.0(-10)cm^3/s$
$Xe_2^* + Xe^*$	\longrightarrow	$Xe_2^+ + Xe + Xe + e$	$3.5(-10)$
$Ne^* + Xe_2$	\longrightarrow	$Ne + Xe^+ + e$	$7.5(-11)$
$Ne^* + Xe$	\longrightarrow	$NeXe^+ + e$	$1.8(-11)$
charge transfer			
$Xe^+ + Xe + Xe$	\longrightarrow	$Xe_2^+ + Xe$	$3.6(-31)cm^6/s$
$Xe^+ + Ne + Ne$	\longrightarrow	$NeXe^+ + Ne$	$1.0(-31)$
$Xe^+ + Xe + Ne$	\longrightarrow	$Ne + Xe_2^+$	$1.0(-31)$
$Ne_2^+ + Xe + Ne$	\longrightarrow	$Xe^+ + 3Ne$	$4.0(-30)$
$Xe^+ + Ne + Ne$	\longrightarrow	$NeXe^+ + Ne$	$1.0(-31)$
$Ne^+ + Ne + Ne$	\longrightarrow	$Ne_2^+ + Ne$	$4.4(-32)$
$Ne^+ + Xe$	\longrightarrow	$NeXe^+ + Ne$	$1.0(-14)cm^3/s$
$Ne_2^+ + Xe$	\longrightarrow	$NeXe^+ + Ne$	$1.0(-13)$
$NeXe^+ + Xe$	\longrightarrow	$Xe^+ + Ne + Xe$	$5.0(-10)$
$NeXe^+ + Xe$	\longrightarrow	$Xe_2^+ + Ne$	$5.0(-12)$
ion-electron recombination			
$Xe^+ + e$	\longrightarrow	$Xe^* + Xe$	$2.2(-7)Te^{-0.5}cm^3/s$
$NeXe^+ + e$	\longrightarrow	$Xe^* + Ne$	$2.0(-7)Te^{-0.5}$
$Ne_2^+ + e$	\longrightarrow	$Ne^* + Ne$	$3.7(-8)Te^{-0.43}$
ion-ion recombination			
$Ne^+ + Cl^-$	\longrightarrow	$NeCl^*$	$3.0(-6)cm^3/s$
$Ne_2^+ + Cl^-$	\longrightarrow	$NeCl^* + Ne$	$2.5(-6)$
$NeXe^+ + Cl^-$	\longrightarrow	$XeCl^* + Ne$	$1.8(-6)$
$Cl^- + Xe^+$	\longrightarrow	$XeCl^*$	$2.0(-6)$
$Cl^+ + Cl^-$	\longrightarrow	Cl_2^*	$2.0(-6)$
$Xe_2^+ + Cl^-$	\longrightarrow	$XeCl^* + Xe$	$1.8(-6)$
radiation			
Xe_2^*	\longrightarrow	$2Xe + h\nu_2$	$6.0(7)s^{-1}$
Ne_2^*	\longrightarrow	$2Ne + h\nu_2$	$3.6(8)$
Cl_2^*	\longrightarrow	$Cl_2 + h\nu_2$	$5.0(7)$
$XeCl^*$	\longrightarrow	$Xe + Cl + h\nu_1$	$2.5(7)$
Xe_2Cl^*	\longrightarrow	$2Xe + Cl + h\nu_2$	$7.4(6)$
$XeCl^* + h\nu_1$	\longrightarrow	$Xe + Cl + h\nu_1 + h\nu_2$	$1.25(-16)cm^2$
predisociation			
$NeCl^*$	\longrightarrow	$Ne + Cl^+ + e$	$1.0(10)s^{-1}$

XeCl* quenching

$\text{XeCl}^* + \text{Ne}$	\rightarrow	$\text{Xe} + \text{Cl} + \text{Ne}$	$1.0(-12) \text{ cm}^3/\text{s}$	45
$\text{XeCl}^* + \text{Xe}$	\rightarrow	$\text{Xe} + \text{Xe} + \text{Cl}$	$3.2(-11)$	45
$\text{XeCl}^* + \text{HCl}(v=0)$	\rightarrow	$\text{Xe} + \text{Cl} + \text{HCl}(v=0)$	$1.7(-9)$	25
$\text{XeCl}^* + \text{HCl}(v=1)$	\rightarrow	$\text{Xe} + \text{Cl} + \text{HCl}(v=0)$	$7.7(-10)$	7
$\text{XeCl}^* + \text{Xe} + \text{Xe}$	\rightarrow	$\text{Xe}_2\text{Cl}^* + \text{Xe}$	$1.5(-31) \text{ cm}^6/\text{s}$	46
$\text{XeCl}^* + \text{Xe} + \text{Ne}$	\rightarrow	$\text{Xe}_2\text{Cl}^* + \text{Ne}$	$1.5(-31)$	8
$\text{XeCl}^* + \text{Ne} + \text{Ne}$	\rightarrow	$\text{Xe} + \text{Cl} + \text{Ne} + \text{Ne}$	$1.0(-33)$	45

Xe₂Cl* quenching

$\text{Xe}_2\text{Cl}^* + \text{Cl}_2$	\rightarrow	$2\text{Xe} + \text{Cl}_2 + \text{Cl}$	$2.6(-10) \text{ cm}^3/\text{s}$	46
$\text{Xe}_2\text{Cl}^* + \text{Xe}$	\rightarrow	$3\text{Xe} + \text{Cl}$	$6.0(-15)$	46
absorption				
$\text{h}\nu_1 + \text{Xe}_2$	\rightarrow	$\text{Xe}_2^+ + \text{Xe}$	$2.6(-17)$	47
$\text{Ne}_2^+ + \text{h}\nu_1$	\rightarrow	$\text{Ne}^+ + \text{Ne}$	$1.3(-17) \text{ cm}^2$	47
$\text{NeXe}^+ + \text{h}\nu_1$	\rightarrow	$\text{Ne} + \text{Xe}^+$	$1.0(-19)$	7
$\text{Xe}_2^* + \text{h}\nu_1$	\rightarrow	$e^- + \text{Xe}_2^+$	$1.4(-17)$	48
$\text{Xe}^* + \text{h}\nu_1$	\rightarrow	$\text{Xe}^+ + e^-$	$6.0(-20)$	49
$\text{Cl}^- + \text{h}\nu_1$	\rightarrow	$\text{Cl}^- + e^-$	$2.0(-17)$	50
$\text{Xe}_2\text{Cl}^* + \text{h}\nu_1$	\rightarrow	$\text{Xe} + \text{Cl} + \text{Xe}^+ + e^-$	$2.6(-17)$	8

Results

We applied the self-consistent model previously described to the modeling of an excimer laser mixture at a total pressure of 3 atm and under a charging voltage $V_o = 40\text{ KV}$. Figure 3 reports the temporal evolution of the reduced electric field (E/N). After about 40ns the electric field applied to the electrodes of the laser cell, reaches a maximum ($\sim 10\text{ Td}$).

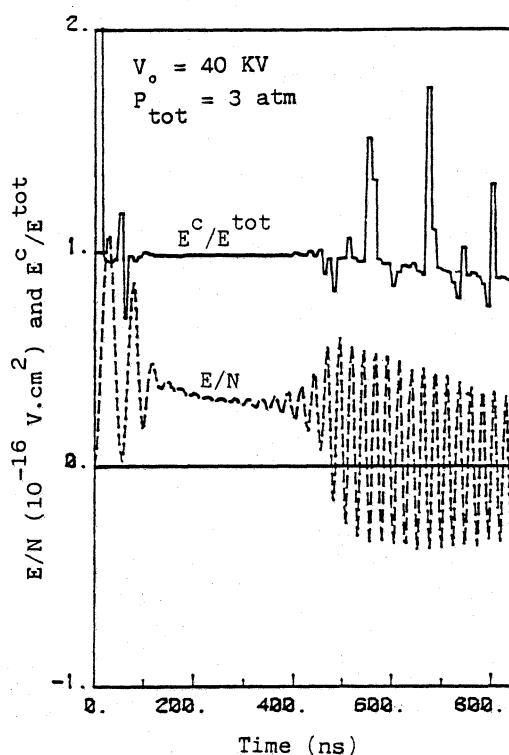


Fig. 3 Reduced electric field (E/N) and ratio E^c/E^{tot} as a function of time

This high field value is necessary to assure the increase, by means of the ionization processes ($Xe + e \rightarrow Xe^+ + 2e$), of the number of the electrons introduced after the end of the preionization stage ($n_e = 10^{10} \text{ cm}^{-3}$). This first peak is followed by an other one lower and then over about 250 ns a plateau ($E/N \sim 3 \text{ Td}$) spreads out. For longer residence times we notice an oscillating decay of the value of E/N . The experimental measurements on the voltage applied to the laser cell show a similar behaviour but in this case the plateau is followed by a smooth decay. Discrepancies between theoretical and experimental results could come from the fact that in the experimental device, instead of a peaking capacity (C_p), the voltage is applied through a pulse forming line. The power deposited in the gas mixture is about 1100 MW for this 10 liters cell (fig. 4) at the end of the plateau found in the temporal evolution of E/N .

The electron mobility (μ_e) is more or less constant during the discharge (fig. 5). We should expect that the temporal value of the discharge resistance R_L will depend mostly on the evolution of the electron density (see eq. 1). We report the value of R_L as a function of time on figure 5. At the begining of the discharge, this resistance strongly decreases by several orders of magnitude, then the decrease slows down until a residence time of about 400ns and starts up again. To understand this behaviour we will now investigate the temporal evolution of the electron energy distribution function shown on figure 6. The main modifications in this evolution happen on the tail of the eedf and cannot be connected to an effect of the varying electric field (the eedf are

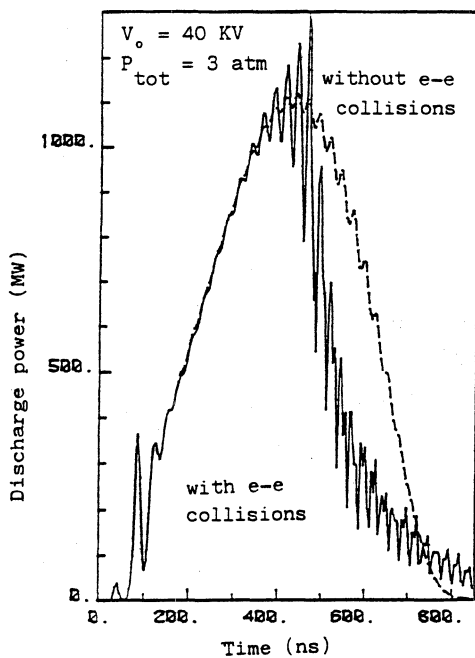


Fig. 4 Power ($P=VI_2$) deposited in the laser gas by the discharge as a function of time

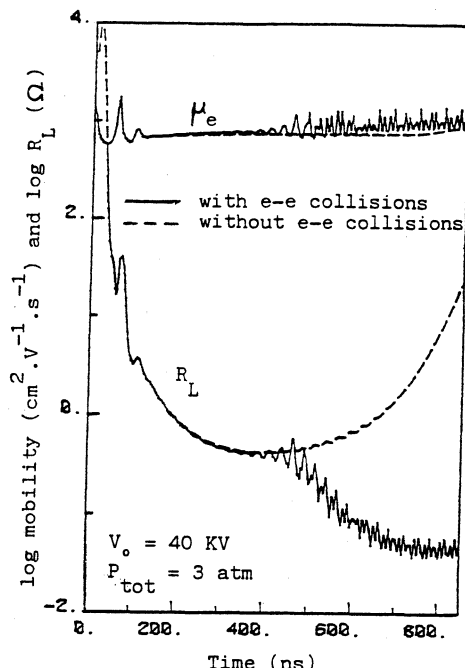


Fig. 5 Electron mobility (μ_e) and discharge resistance R_L as a function of time

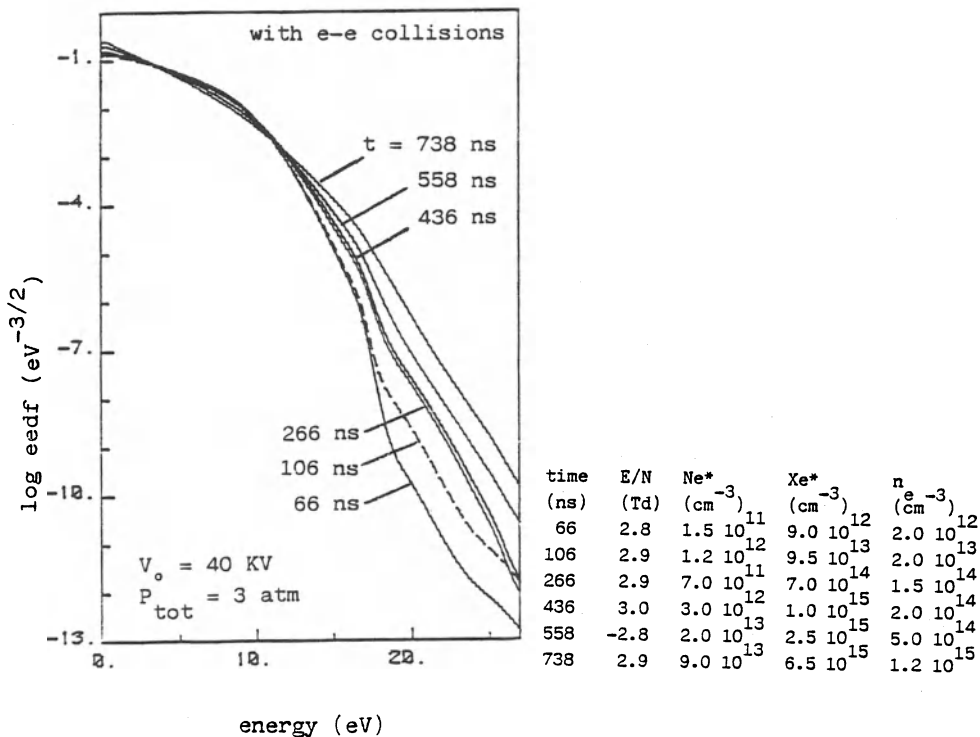


Fig. 6 Temporal evolution of the eedf

pictured at an almost constant value of E/N (~ 3 Td)). Between 66 and 106 ns the increase of the eedf's tail takes place at about 17eV as a result of the action of superelastic collisions $e+Ne^* \rightarrow e+Ne$ which heat low energy electrons. The difference between curves at 106 and 266ns happening at energies higher than 10eV is mainly a result of the heating of the electrons by the superelastic process $e+Xe^* \rightarrow e+Xe$. After a residence time of about 450ns, the density of the electrons in the mixture is high enough to promote a change in the shape of the eedf's which are more and more Maxwellian under the effect of the electron-electron interactions. This temporal behaviour of the eedf's is reflected on the temporal evolution of the rate coefficients for inelastic electronic processes (figs. 7-8). Processes with low energy thresholds (for instance the dissociative attachment) depend only on the value of E/N . For a fixed value of E/N (on figures 7-8 points represent the values of the rate coefficient at the same residence times where we represented the eedf's on figure 6) we have no variation of those coefficients (fig. 7). But rate coefficients for inelastic processes with high energy thresholds (fig. 8) will depend both on the variations of E/N and of the eedf (difference by 2 orders of magnitude for the Ne ionization at 3 Td between early and long stage in the discharge).

Figure 9 reports the temporal evolution of some species created in the laser cell. The electron concentration increases strongly at the beginning of the discharge when the electric field is relatively high. The second impulse happens as soon as the electron-electron collisions become effective since the enhancement of the eedf's tail promotes the excitation of Xe favouring the stepwise ionization ($Xe^* + e \rightarrow Xe + 2e$). The

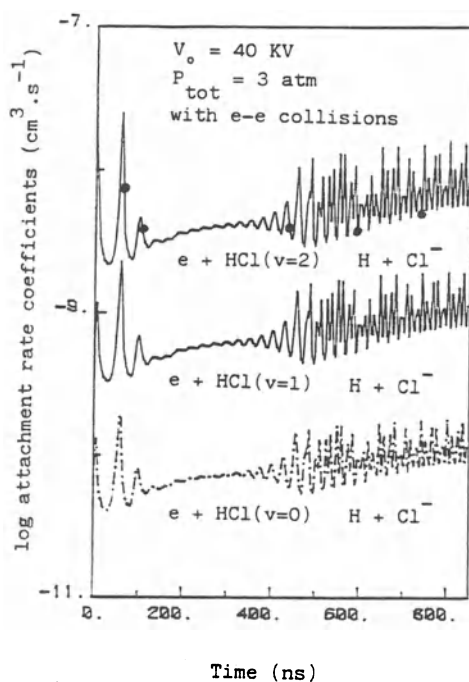


Fig. 7 Temporal evolution of dissociative attachment rate coefficient

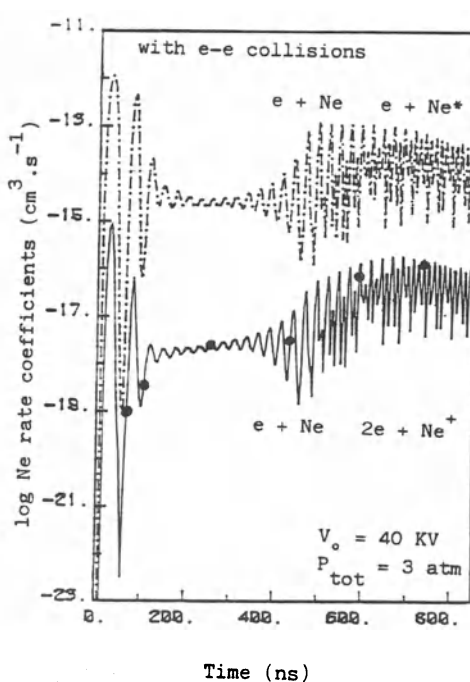


Fig. 8 Temporal evolution of Ne electronic rate coefficients

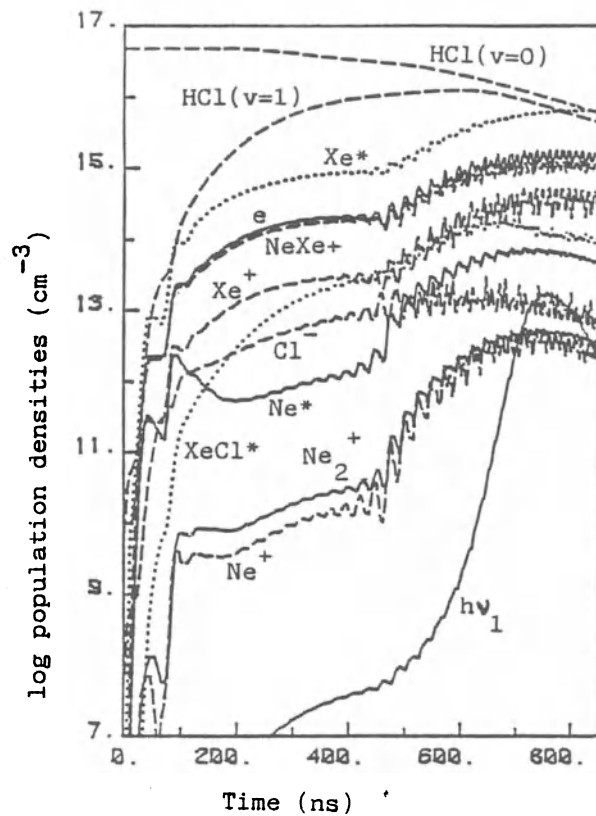


Fig. 9 Temporal evolution of some species ($V=40\text{KV}$, $P_{\text{tot}}=3\text{atm}$, with electron-electron collisions)

most part of the new species in the laser mixture follows the temporal evolution of the electron density. Photons ($h\nu$) originate first in XeCl^* spontaneous emission, but as XeCl^* concentration increases the stimulated emission becomes the main process for this production. In this particular case ($P_{\text{tot}} = 3 \text{ atm}$, $V_0 = 40 \text{ KV}$) the laser pulse extinguishes because of the photons losses in optical path and in absorption by XeCl^* species, but also because of the quenching of the lasing species XeCl^2 .

Discussion

We would like now to show up some important points in the modeling used here. We have shown previously that electron density can be strongly affected by electron-electron collisions. So we did again the same calculation disregarding this process. The first thing to note is that the temporal evolution of the reduced electric field E/N (fig. 10) does not present, after the plateau region, the oscillating behaviour reported in the first case. Looking at figure 5 we note that without e-e collisions the laser cell resistance R_L after a strong decay remains constant for a long while and then increases at the end of the discharge. So this resistance never reaches the very small values ($R_L < 5 \cdot 10^{-1} \Omega$) we found in the first case. The discharge circuit simulation provides oscillatory behaviour of the tension applied to the laser cell electrodes only when the resistance R_L assumes low values. Figure 11 reports the temporal evolution of eedf, we note that after the increase due to superelastic collisions the eedf's tails do not change any more. So after

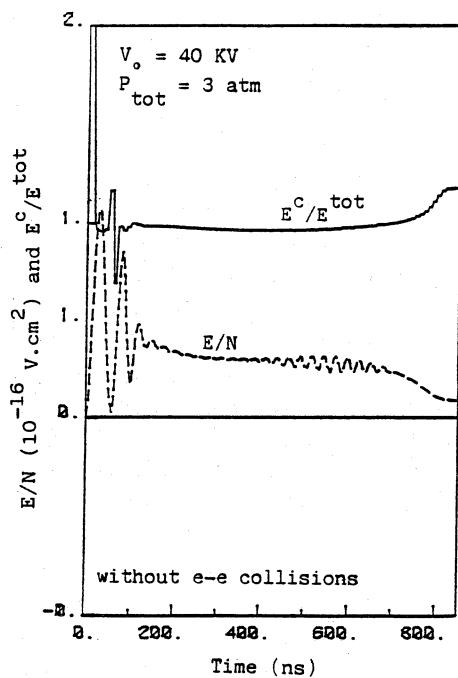


Fig. 10 Reduced electric field (E/N) and ratio E^c/E^{tot} as a function of time

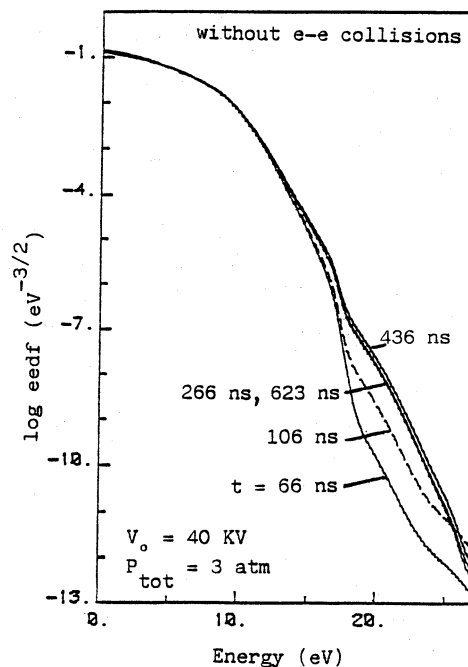


Fig. 11 Temporal evolution of eedf

a first enhancement the electron density stays more or less constant for a long period and then decreases as a result of the recombination with NeXe^+ ions (fig. 12). It is worth noting that under those conditions the XeCl^* concentration never reached a value high enough to start the stimulated emission.

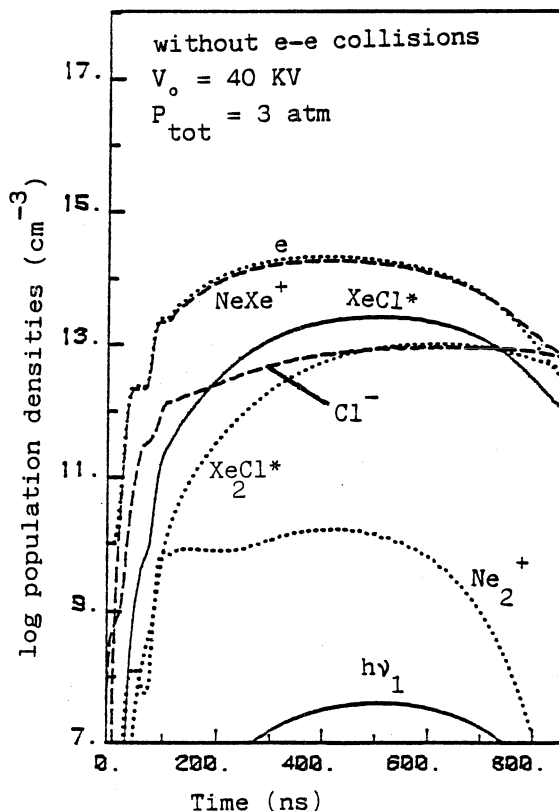


Fig. 12 Temporal evolution of some species

An other aspect of this modeling to be underlined is the use of a time dependent Boltzmann equation. When the eedf is stationary the energy gained by electrons (E_{tot}^c) both from the applied electric field and superelastic collisions must be exactly compensated by the energy (E^c) they loose in inelastic collisions. Figures 3 and 10 show unambiguously that at low values of E/N the ratio E^c/E_{tot}^c is no longer equal to one. So in the early and late stage in the discharge use of a stationary solution of the Boltzmann equation could be open to question (see also ref.51).

Figure 13 shows the laser radiated energy at a total pressure of 3 atm and for different values of the charging voltage V_o . The strong decrease of those theoretical values for $V_o > 45 \text{ KV}$ comes from a shrinking of the laser pulse width accountable to a high density of electrons efficient in quenching the lasing species XeCl^* . We have reported on figure 14 the theoretical evolution of the photon densities for different pressures under a charging voltage $V_o = 45 \text{ KV}$. We see on this figure that the photon densities are increasing with the total pressure in the studied range.

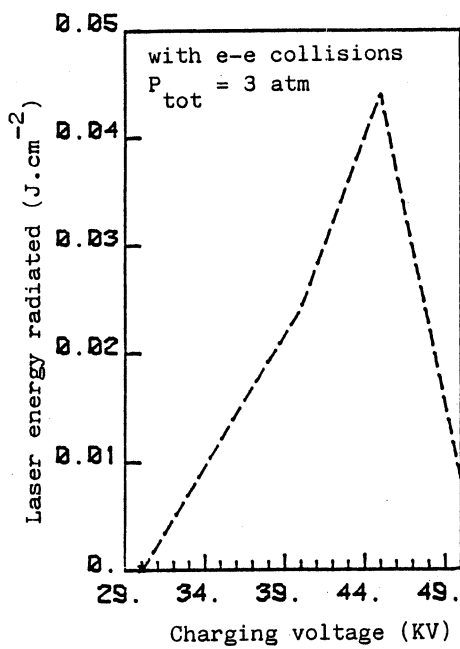


Fig. 13 Laser energy radiated as a function of charging voltage

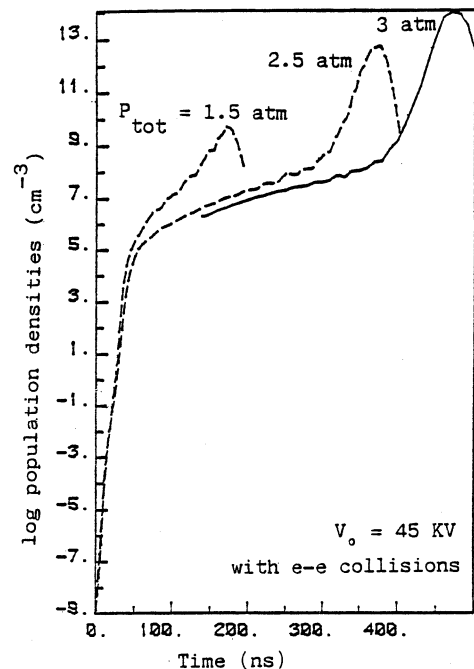


Fig. 14 Temporal evolution of $(h\nu_1)$ photon densities at different pressures

In all cases reported, the initial electron number density we chose is $n_e = 10^{10} \text{ cm}^{-3}$, which is by at least 2 orders of magnitude higher than the experimental one at the end of the preionization stage. However the only change we found starting up the calculations with a lower density of the electrons, is a translation of the previous reported results towards longer residence times.

Conclusions

The self-consistent model used in this work has shown the importance of electronic superelastic and electron-electron collisions in enhancing the tail of the eedf's and thus promoting processes like electronic excitation and ionization. Inclusion of those collisions can completely change the heavy particle kinetics (compare for instance figures 9 and 12). The second point well evidenced is that at low values of the reduced electric field applied to the laser cell the more appropriate Boltzmann equation is the time-dependent one. But it is worth noting that both the inclusion of electron-electron collisions and the use of a time-dependent Boltzmann equation are highly time consuming.

An other important point to evidence is that our model is a zero-dimensional one. Future improvements will be devoted to the building of more realistic multidimensional codes. The other improvements to carry out, in our model, interest the input data. In fact, we need a more accurate and extended set of cross sections for both HCl and Xe. It could be also important to consider, in the chemical kinetics, new species like

NeXe* to decrease the Xe* species, and slow down the electrons increase in the late discharge region. We have seen that a high production of electrons in this region will correspond to a low value of the discharge resistance and promote additional oscillations on the voltage applied to the electrodes of the laser cell.

Acknowledgments

The author wishes to gratefully acknowledge Mario Capitelli for many insightful discussions. This work was partially supported by ENEA.

References

- 1 S. Bollanti, T. Letardi, this volume
- 2 M.J. Kushner, this volume
- 3 T. Letardi, S. Bollanti, P. DI Lazzaro, F. Flora, G. Giordano, T. HermSEN, C. Zheng, "Excimer Lasers and Applications" ECO 1, Ed. D. Basting, Hamburg, 21-23 Sept. 1988
- 4 G. Stievlow, T. Hammer, W. Bötticher, Appl. Phys. B 47:333 (1988)
- 5 C. Gorse, M. Capitelli, Proc. IX ESCAMPIG, Lisbon, Ed. C.M. Ferreira, p 193 (1988), C. Gorse, R. Caporusso, M. Capitelli, "New Laser Technologies and Applications", Olympia, eds. A.A. Carabelas and T. Letardi, Societa Italiana di Fisica p 439 (1988)
- 6 M. Maeda, A. Takahashi, T. Mizunami, Y. Miyazoe, J. Appl. Phys. 21:1161 (1982)
- 7 L.A. Levin, S.E. Moody, E.L. Klosterman, R.E. Center, J.J. Ewing, IEEE J. Quantum Electron. QE-17:2282 (1981)
- 8 H. Hokazono, K. Midorikawa, M. Obara, T. Fujioka, J. Appl. Phys. 56:680 (1984)
- 9 S. Bollanti, P. Di Lazzaro, F. Flora, G. Giordano, T. Letardi, T. HermSEN, C.E. Zheng, ENEA (Frascati) Report RT/TIB/88/43 (1988)
- 10 S. Bollanti, Thesis University of Rome (1986)
- 11 S.D. Rockwood, Phys. Rev. A 8:2348 (1973)
- 12 C.J. Elliott, A.E. Greene, J. Appl. Phys. 47:2946 (1976)
- 13 R.D. Hake, A.V. Phelps, Phys. Rev. 158:70 (1967)
- 14 D.K. Davies, Westinghouse report AFWAL-TR+82 :2083 (1982)
- 15 A.G. Robertson, J. Phys. B 5:648 (1972)
- 16 L.S. Frost, A.V. Phelps, Phys. Rev. A 136:1538 (1964)
- 17 D. Trigiante, Computing 18:117 (1977)
- 18 N.J. Mason, W.R. Newell, J. Phys. B : At. Mol. Phys. 20:1357 (1987)
- 19 P.S. Ganas, Molec. Phys. 38:1127 (1979)
- 20 D. Rapp, P. Englander-Golden, J. Chem. Phys. 43:1464 (1965)
- 21 H.V. Boening, "Plasma Science and Technology Cornell Univ. Press", Ithaca (1982)
- 22 D. Ton-That, M.R. Flannery, Phys. Rev. A 15:517 (1977)
- 23 M. Rokni, J. Jacob, J.A. Mangano, Appl. Phys. Lett. 34:187 (1979)
- 24 J. Jacob, J.C. Hsia, J.A. Mangano, M. Rokni, J. Appl. Phys. 50:5130 (1979)
- 25 G.C. Tisone, J.M. Hoffman, IEEE J. Quantum Electron. QE-18:1008 (1982)
- 26 F. Kannari, A. Suda, M. Obara, T. Fujioka, IEEE J. Quantum Electron. QE-19:1587 (1983)

- 27 R.W.F. Gross, J.F. Bott, "Handbook Chemical Laser", Interscience, New-York (1976)
- 28 P. Millet, A. Birot, H. Brunet, J. Galy, B. Pons-Germain, J.L. Teyssier, J. Chem. Phys. 69:92 (1978)
- 29 D.C. Huestis, R.M. Hill, H.H. Nakano, D.C. Lorentz, J. Chem. Phys. 69:5133 (1978)
- 30 J.H. Kolts, J.E. Velazco, D.E. Setser, J. Chem. Phys. 71:1247 (1979)
- 31 R.S.F. Chang, J. Chem. Phys. 76:2943 (1982)
- 32 D.C. Lorentz, D.J. Eckstrom, D. Huestis, "Excimer formation and decay processes in rare gases" (AD-778-326) Stanford Research Inst. Rep. MP 73-2, Sept. 1973
- 33 E. Zamir C.W. Werner, W.P. Lapatovich, E.V. George, Appl. Phys. Lett. 27:56 (1975)
- 34 R.H. Neynaber, S.Y. Tang, J. Chem. Phys. 70:4272 (1979)
- 35 D. Smith, A.G. Deam, J. Phys. B 5:2134 (1972)
- 36 C.B. Collins, F.W. Lee, J. Chem. Phys., 72:538 (1980)
- 37 T.G. Finn, L.J. Palumbo, L.F. Champagne, Appl. Phys. Lett. 33:148 (1978)
- 38 A.P. Vitols, H.J. Oskam, Phys. Rev. A 5:2618 (1972)
- 39 R.J. Johnson, J. Chem. Phys. 68:2991 (1978)
- 40 H.J. Oskam, V.R. Mittelstad, Phys. Rev. 32:1445 (1963)
- 41 J. N. Bardsley, Adv. At. Mol. Phys. 6:2 (1970)
- 42 J.M. Hoffman, J.B. Moreno, Sandia Nat. Lab. Rep. SAND80-1486, Albuquerque (1980)
- 43 B. Schneider, J. Chem. Phys. 61:3240 (1974)
- 44 G.P. Glass, F.K. Tittel, W.L. Wilson, M.S. Smayling, Chem. Phys. Lett., 83:585 (1981)
- 45 T.G. Finn, R.S.F. Chang, L.T. Palumbo, L.F. Champagne, Appl. Phys. Lett., 36:789 (1980)
- 46 H.P. Grieneisen, H. Xue-Jing, K.L. Kompa, Chem. Phys. Lett., 82:421 (1981)
- 47 W.R. Wadt, J. Chem. Phys. 73:3915 (1980)
- 48 N. Basov et al., Sov. Tech. Phys. Lett. 5:183 (1979)
- 49 C. Duzy, H.A. Hyman, Phys. Rev. A 22:1878 (1980)
- 50 D.E. Rothe, Phys. Rev. 177:93 (1969)
- 51 C. Gorse, M. Capitelli, A. Dipace, J. Appl. Phys. (1990) in press.

STUDY OF A PHOTOSWITCHED DISCHARGE FOR EXCIMER LASER

V. Puech*, S. Mizzi* and B. Lacour[§]

[§] Laboratoires de Marcoussis, (C.G.E.)

Route de Nozay, 91460 Marcoussis, France

* Laboratoire de Physique des Gaz et des Plasmas*

Université Paris-Sud, 91405 Orsay Cédex, France

INTRODUCTION

Since their discovery (Searles and Hart, 1975, Ewing and Brau, 1975), the rare-gas halide lasers have been developed rapidly. In discharge-pumped systems, many improvements in preionization (Lin and Levatter, 1979), laser mixture (Sze, 1979), impedance matching between the driving circuit and the discharge (Sarjeant et al., 1978, Long et al., 1983) and high repetition rates (Christensen, 1978) have led to systems delivering multi-joules pulses with an efficiency of a few percent, usable as industrial tools in such fields as microelectronics, photochemistry or material processing. For the most part of excimer lasers, first the high pressure mixture is preionized, and then a high voltage pulse is applied across the electrodes. In such classical schemes, good performances require to switch a large amount of current in a very short time. As a result, the limited lifetime of the switching component, usually a thyratron, induces an important problem of reliability.

A novel discharge concept was advocated (de Witte et al., 1982) in which the difficulties connected to the fast electric switch were solved by the complete removal of this component. In this new scheme, the electrodes are directly connected to the storage line and the discharge is simply fired by the preionization itself. With devices working in such a way, laser energy greater than 1 Joule have been obtained (Lacour and Vannier, 1987) while high efficiency (4%) and high pulse repetition rates (600 Hertz) were also achieved (Beaupère et al., 1988). Excimer lasers working along this switchless concept are now commercially available (Sopra SEL 500 series).

In this paper, we report on X-rays photoswitched XeCl lasers, with an emphasis on the physical processes which determine the behaviour of these new discharges.

BACKGROUND

A schematic timing of the self-sustained discharges for excimer laser is shown in Figure 1. In the classical devices, Figure 1a, a preionization pulse is first applied while the laser electrodes are connected to the high voltage only after a time delay which can be as high as 1 μ s. The duration of the preionization as well as the time delay before the switching of the main discharge circuit are important parameters in order to obtain stable homogeneous discharge. Their values depend on the gaseous mixture, the gap and the shape of the electrodes. However, the main discharge parameters are the rise time and the value of the applied voltage. To initiate a uniform gas breakdown, the rise time of the voltage must be very short, about 10 ns, while the voltage must be higher than 5

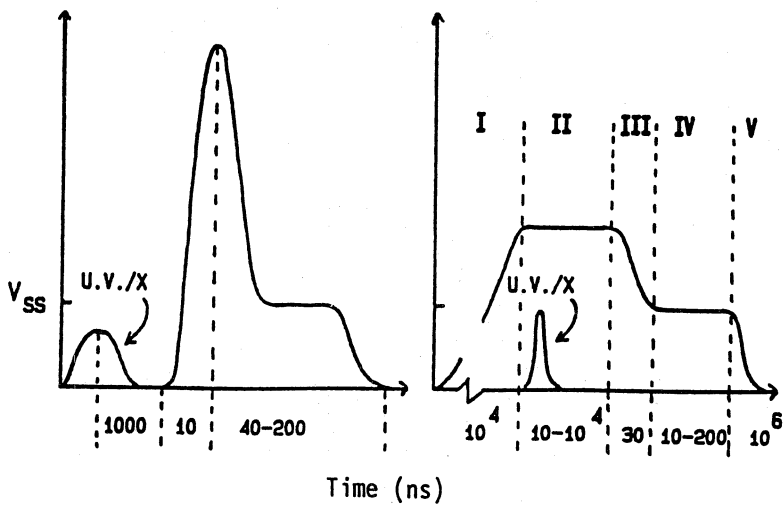


Figure 1. Schematic voltage evolution versus time for self-sustained excimer discharges.
a): classical device b): photoswitched device.

times the steady state voltage. These requirements lead to an impedance mismatch between the storage circuit and the discharge while the condition for an efficient energy transfer requires to apply on the storage line a voltage about twice the steady state voltage. As a result, in the most advanced devices, one often uses two separated discharge circuits: a spiker one to breakdown the gas mixture and to obtain a uniform glow discharge into which the energy is deposited by the main electric circuit, impedance matched with the laser head.

On the other hand, the Figure 1b shows how works the photoswitched discharge. In a first phase (phase I), the storage line directly connected

to the laser head is charged, with a long rise time, to a value twice the steady state voltage. As a result, the impedance matching is easily obtained without any severe constraints on a fast switch. When the voltage across the electrodes reaches the satisfactory value, the preionization circuit is fired. X-rays beams as well as U.V. photons produced either by spark gap, corona discharge, or laser illumination can be used. For the present purpose, the advantages of the X-ray beams are the same than in classical devices: the mean penetration depth is larger than that of UV radiation, so a large volume of high pressure mixture can be homogeneously preionized without gas contamination due to an auxiliary discharge. Moreover, for research studies, the X-rays photoswitching allows to study the influence of the initial electron density, which can be easily measured. On the other hand, from a technical point of view, the UV photoswitching is more simple to handle, particularly for lasers working at high repetition rates. The phase II of the photoswitched device operating mode lasts from the injection of the UV or X-ray photons up to the discharge breakdown. During this phase, the only processes which take place are the multiplication of the initial electrons through ionizing collisions. The voltage across the electrodes remains constant, and no current goes through the laser head up to the time at which the impedance of the medium is sufficiently low to allow the discharge breakdown. At this time (phase III), the voltage drops across the electrodes, the current rapidly increases, and the stored energy is deposited in the laser mixture. It produces a large amount of molecular excitation, and finally laser action during phase IV. In order to have an homogeneous energy deposition during phase III, a minimum initial electron density must have been created during phase II. During this phase, the electronic density increases from typically 10^7 up to 10^{15} cm $^{-3}$, with a e-folding time of about 10 ns; as a result, to be useful, the duration of the UV or X-rays pulse must be shorter than that. The breakdown delay time (i.e. the duration of phase II) is one of the important parameters of the photoswitched devices. Finally during phase V, the laser action and all the electrical parameters are relaxed, but the medium remains subjected to important aerothermic processes, which determine for a large part the possibilities to work at high repetition rates. However, the analysis of these processes will not be attempted here.

EXPERIMENTAL SET UP

In Figure 2, we show a cross sectional view of the laser head. The discharge chamber is made of aluminium, and designed for a maximum filling pressure of 5 bars. The electrodes, 50 cm long, have a gap of 1 cm and a flat profile over the same distance. The X-rays diode consists of a cold carbon felt cathode and a tantalum target anode. It is directly powered by a low inductance Marx generator producing a voltage pulse of up to 200 kV. The resulting X-rays pulse is monitored with a scintillator/photomultiplier detector, while the current in the diode is followed by a Rogowski coil. Taking into account the time response of the

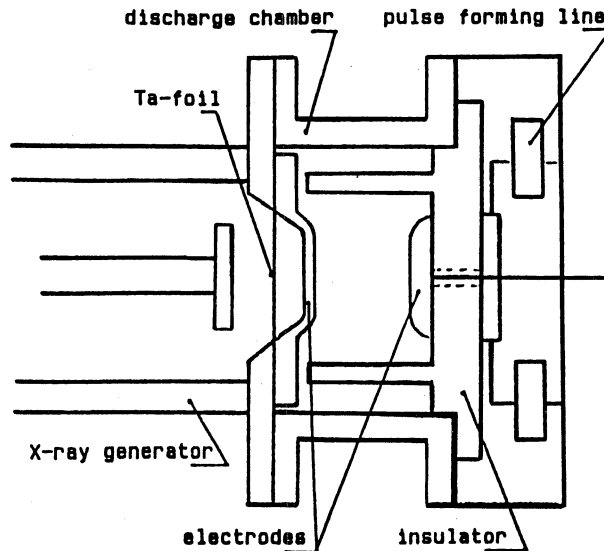


Figure 2 . Cross-sectional drawing of the laser head.

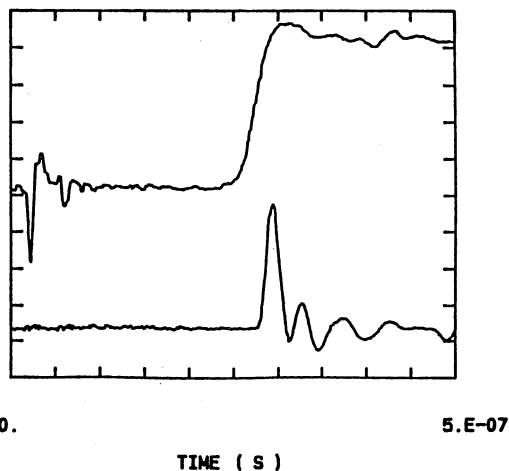


Figure 3. Temporal evolution of the discharge current (lower trace) and discharge voltage (upper trace) on which the X-rays pulse has been superimposed.

X-rays detector, the two signals show an identical temporal behaviour: a rise time of 2 ns and a duration of 4 ns (FWHM). The main discharge circuit is made of two rows of 18 ceramic capacitors, each 4 nF capacitance, closely connected to the discharge chamber to minimize the circuit inductance. The discharge current and the voltage are respectively

measured with a Rogowski coil and a resistive divider. Typical electric parameters recorded by two synchronized transient digitizers (Tektronix 7912 AD) are shown in Figure 3. To evaluate the importance of the preionization on the performances of the photoswitched device, it is of importance to investigate the initial electron density produced by the X-rays pulse. For that purpose, the laser head is used as an ionization chamber. The pulse forming line is disconnected from the electrode, which is now continuously polarized and connected to a storage capacitor. The electrons generated by the X-rays drift towards the anode and the terminal voltage on the capacitor varies proportionally to the total number of collected electrons.

RESULTS AND DISCUSSION

The breakdown delay time, which plays a central role in the discharge stability, has been carefully investigated as well in pure rare gases as in laser mixtures. This delay time corresponds to the duration of the phase II (Figure 1), and is defined as the time elapsed between the X-rays pulse injection and the half of the voltage drop across the electrodes. Owing to the very short duration of our X-rays beam, this time can be measured with a good accuracy (figure 3). The evolution of the breakdown delay time versus the reduced electric field is shown in Figure 4 which points out a

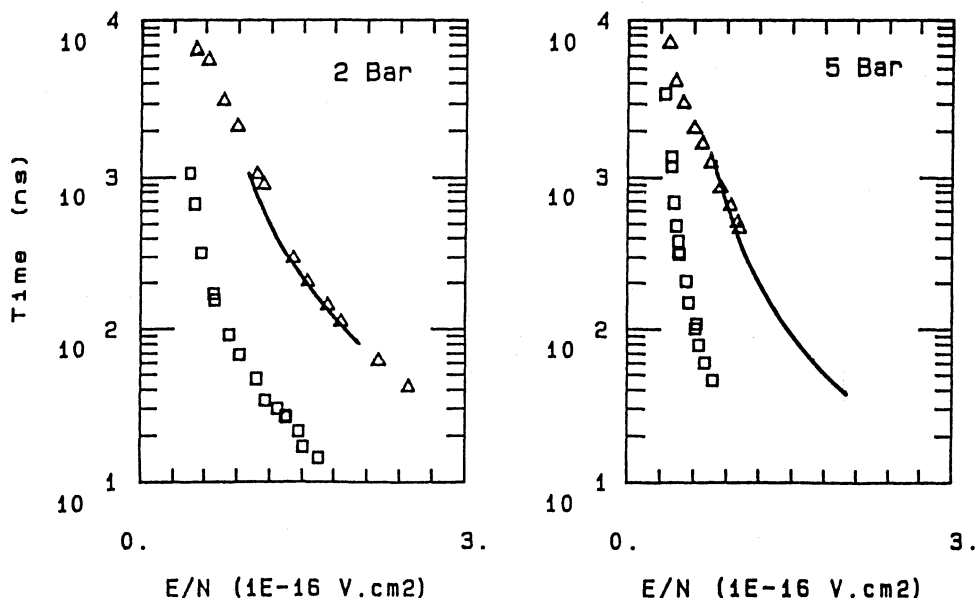


Figure 4 . Evolution of the breakdown delay time versus the reduced electric field. Δ :pure Neon experiments, —:pure Neon calculations, \square :laser mixture

very sharp decrease of the delay time as E/N increases. As a result, the reduced electric field is the leading parameter in the behaviour of the phase II while the variations of the other electric parameters (capacitance and inductance of the circuit, initial ionization density) induce only small variations of the breakdown delay time. Compared to the pure Neon data, Figure 4 shows a dramatic decrease in the delay time when a laser mixture is introduced in the discharge, whereas the partial pressures of Xenon and HCl remain low (respectively 5100 and 1600 ppm). As a matter of fact, the addition of only 20 ppm of Xenon in pure Neon reduces the delay time by a factor of 5. For pure Neon, Figure 4 also shows a good agreement between the experimental and theoretical delay times. The calculations (Brunet 1989) take into account the driving electric circuit, the heavy particle kinetics and the Boltzmann equation for the electrons, solved in the classical two-terms approximation (Brunet and Vincent 1979). The electron kinetics includes the direct ionization, the ionization of the 3s and 3p levels, the direct excitation of 19 states as well as their deexcitations through superelastic collisions. In such calculations, the reliability of the collision cross sections used as inputs in the Boltzmann equation, is of fundamental importance. For Neon the calculations used the validated set of cross sections recently reported (Torchin et al 1987) while for Xe and HCl such sets are not available at the present time. Their elaboration is in progress and the detailed modeling of photoswitched discharges in laser mixtures will be possible in the near future.

The specific XeCl laser energy is plotted in Figure 5 versus the initial electron density, n_{e0} . For each pressure, a minimum value of n_{e0} is required to obtain a laser action. Above this threshold value, the laser output increases logarithmically up to a critical value above which it remains constant. Qualitatively, such a behaviour can be understood as an increase in the homogeneity of the preionized volume up to a value above which the individual streamers overlap during the discharge breakdown; however, the quantitative analysis of the requirements is still far from complete. Whereas all the authors (Palmer, 1974, Levatter and Lin, 1980, Herziger et al, 1981) consider as crucial the need for the heads of the initial streamers to overlap before the space charge field becomes too important, the value as well as the pressure dependence of n_{e0} is not firmly established. Our experimental results seem to be in agreement with the Levatter and Lin model giving a pressure dependence as $p^{3/2}$.

For various pressures, we have shown in Figure 6 the dependence of the laser efficiency on the specific stored energy. The highest efficiency is obtained for a pressure of 5 Bar which is the highest allowed pressure in our discharge cell. For each pressure, the maximum efficiency is rapidly reached above the threshold value; then it slowly decreases as the stored energy increases, and the output laser energy raises about linearly. As a result, a high specific energy, 5 J/l, is obtained with a good efficiency, 2 %, at the maximum stored energy. For given initial electron density and

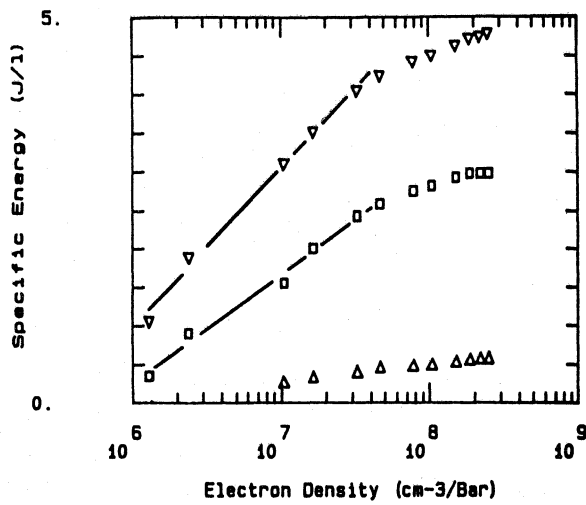


Figure 5. Specific XeCl laser energy as a function of the reduced initial electron density for three pressures:
 ▽ : P=5 Bar; □ : P=3 Bar; △ : P=1.6 Bar

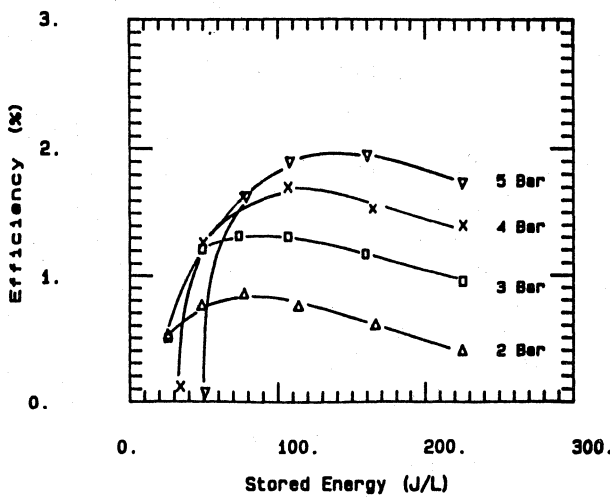


Figure 6. XeCl laser efficiency versus the energy stored in the pulse forming line.

stored energy, the same output energy has been obtained with various combinations of storage capacitance and applied voltage. This result seems to show that, once the discharge breakdown is reached, the reduced electric field is not the leading parameter of the discharge. But, recent results obtained with the same laser head and electric circuit but with an U.V. photoswitching produced by a corona discharge lead to an opposite conclusion. More works remain to do to clarify this point .

ACKNOWLEDGMENTS

This work is supported by the Eureka Eurolaser EU 205 program. The authors wish to thank Dr H. Brunet from the Laboratoires de Marcoussis for unpublished calculations and fruitful discussions. They acknowledge the experimental supports of M. Legentil, S. Pasquier.

REFERENCES

- Beaupère, D., Lacour, B., Gagnol, C. and Pinson, P., 1988,
Conference on Lasers and Electro Optics, Anaheim CA, paper TUH6
Brunet, H. and Vincent, P., 1979, J. Appl. Phys., 50, 4700
Brunet, H., 1989, private communication
Christensen, C.P., 1978, in High Power Lasers and Applications,
K.L. Kompa and H. Walter eds., Springer-Verlag, Berlin
Ewing, J.J. and Brau, C.A., 1975, Appl. Phys. Lett., 27, 350
Herziger, G., Wollermann-Windgasse, R. and Banse, K.H., 1981,
Appl. Phys., 24, 267
Lacour, B. and Vannier, C., 1986, J. Appl. Phys., 62, 754
Levatter, J.I. and Lin, S.C., 1980, J. Appl. Phys., 51, 210
Lin, S.C. and Levatter, J.I., 1979, Appl. Phys. Lett., 34, 505
Long, W.H., Plummer, M.J. and Stappaerts, E.A., 1983,
Appl. Phys. Lett., 43, 735
Midorikawa, K., Obara, M. and Fujioka, T., IEEE J. Quantum Electron., QE 20, 198
Palmer, A.J., 1974, Appl. Phys. Lett., 25, 138
Sarjeant, W.J., Alcock, A.J. and Leopold, K.E., 1978,
IEEE J. Quantum Electron., QE 14, 177
Sze, R.C., 1979, J. Appl. Phys., 50, 4596
Torchin L., Mizzi S. and Puech V., 1987, 40° Gaseous Electronics
Conference, Atlanta GA, paper HA6
de Witte, O., Lacour, B. and Vannier, C., 1982, Conference on Lasers
and Electro-Optics, Phoenix AZ, paper WD6

A SELF-CONSISTENT MONTE CARLO MODELING OF RF NON-EQUILIBRIUM PLASMA

A. Date, K. Kitamori* and H. Tagashira

Department of Electrical Engineering
Hokkaido University, Sapporo 060

*Department of Industrial Engineering
Hokkaido Institute of Technology, Sapporo 006

INTRODUCTION

To develop a technique which can quantitatively simulate rf glow discharges is very important because these discharges are used for a wide variety of thin film fabrication processes and etching processes. For example, rf glow discharges in SiH₄ are used for plasma CVD of amorphous silicon for solar cells. However, the properties of glow discharges have not yet been well understood.

As the title shows, the present paper uses a Monte Carlo method. Kushner(1988) investigated the discharge kinetics in SiH₄/H₂ and Ar mixtures including plasma chemistry by using rate equations, and the rate constants for electron impact are obtained from the electron energy distribution calculated by a Monte Carlo simulation. However, it appears that the electric field in the discharge is assumed by a linear function of position (Kushner 1986), and the behaviour of ion does not seem to have been treated explicitly.

In a previous paper (Kitamori et al. 1988), we have developed a simulation technique based on a Monte Carlo method, which can self-consistently predict the structure of rf glow discharges(Kitamori et al. 1989). In the present paper, the Monte Carlo technique is applied to an rf glow discharge in SiH₄ gas, and the kinetics of electrons, positive ions and negative ions have been simulated. We have also calculated the time/space variations of the generation rate of radical which are produced by electron impact dissociation, and the results are presented.

SIMULATION MODEL

In the present model, we consider an rf glow discharge between symmetrical parallel plate electrodes with large area in comparison with separation so that discharge parameters

may be obtained from calculating one-dimensional problem in space. The calculation in velocity space is performed here by a three dimensional model. The space between the electrodes is divided into n slabs parallel to the electrode surface. In each slab, discharge parameters such as the electron mean energy or the electric field, are obtained. Furthermore, the simulation time unit Δt_s is defined in order to take account of temporal variations of these parameters. The simulation progresses by repeating the Δt_s step-calculation.

Calculation of the behaviour of charged particles

In the present model, we calculates the behaviour of electrons, positive ions and negative ions by a Monte Carlo method. In calculating the behaviour of ions, we use an approximate and simple method (Okada et al. 1978). The flight time between the collisions are defined by means of null-collision method. The scattering after collisions is assumed to be isotropic

Velocity distributions

In the present model, velocity space is assumed to be axially three dimensional. The velocity space has an energy range for each of the x-direction(taken in the inverse field direction, perpendicular to the electrodes) and r-direction(parallel to the electrodes), and the space for each direction is divided into k and m equal cells, respectively. Therefore, the velocity space consists of $k \times m$ velocity cells. Velocity space of the same structure is allocated to each slab.

After simulation for electrons and ions are carried out in Δt_s , the velocities of all electrons and ions in the discharge are stored in the velocity cells in the slab corresponding to their position. Therefore, the electron or ion number distribution in the velocity cells represents the electron or ion velocity distribution in the slab, and particles in the same slab have the same velocity distribution function.

At the begining of a simulation step, the initial velocity of particles is obtained from the velocity distribution in each slab.

Scaling Technique

Since, in real discharges, the number of electrons or ions increases because of ionisation, it is impossible to simulate all electrons or ions. In the present model, a scaling technique is used in order to deduce the true particle number in a slab from the behaviour of sample particles.

In each slab, the initial electron number is set to N_s . After the simulation unit Δt_s , if the electron number and velocity distribution change respectively to N_j and $F_j(v)$, a new velocity distribution $F_s(v)$ and weight factor W are calculated as follows.

$$F_s(v) / N_s = F_j(v) / N_j$$

$$W = N_j / N_s$$

Therefore, $F_s(v)/N_s$ and $F_j(v)/N_j$ have the same normalized velocity distribution. If the initial electron velocity is taken out from $F_s(v)$, we have only to simulate N_s electrons. The real number and real velocity distribution of electrons in each slab, N_j and F_j , are obtained from N_s , $F_s(v)$ and W .

$$\begin{aligned}N_j &= N_s \times W \\F_j(v) &= F_s(v) \times W\end{aligned}$$

By means of the scaling technique, the simulation is continued in almost the same computing time even when electrons increase extremely because of ionisation. Furthermore, the swarm parameters and energy distributions of electrons are correctly calculated. The same technique is used for ions.

Electron/Ion density and the Electric field

The electron and ion densities can be obtained by summing the particle number in all the velocity cells in a slab. Since each of the electrons and ions has its own weight factor, the densities are calculated by summing the weight of all particles in one slab.

The electric field in the gap has two components, E_{in} which is the component due to space charge and E_{ex} which represents the applied voltage component. E_{in} is obtained from space charge $\rho(x)$ by solving one-dimensional Poisson's equation.

$$\begin{aligned}\rho(x) &= n_+(x) - n_-(x) - n_e(x) \\n_+(x), n_-(x) &: \text{positive and negative ion density} \\n_e(x) &: \text{electron density}\end{aligned}$$

$$E_{in}(x) = \frac{1}{\epsilon_0} \int_x^d \rho(x) dx - \frac{1}{\epsilon_0 d} \int_0^d x \rho(x) dx$$

d : gap length

E_{ex} is defined as $E_{ex} = V_g/d$ where V_g is the applied voltage and d is the gap length.

Energy distribution

The electron energy distribution in each slab is determined by counting weight factors W_j of electrons which fall in the velocity cells in the slab in every Δt_s . The electron mean energy in a slab is determined as below.

$$\bar{\epsilon} = \sum v_e^2 * F_e(v) / n_e$$

The energy distribution in a slab $F(\epsilon)$ is given by

$$F(\epsilon) = \Delta n_e / n_e$$

where n_e is the number of electrons which fall in an energy range $[\epsilon, \epsilon + \Delta \epsilon]$, and $\Delta \epsilon$ is a constant for sampling. The ion mean energy and ion energy distribution are calculated in a similar manner.

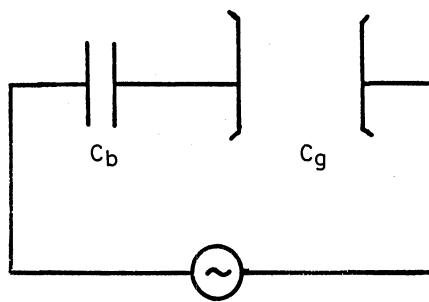


Fig. 1. External circuit

Discharge current and gap voltage

The total discharge current consists of the conductive current i_g caused by the motion of charged particles in the discharge, and the displacement current i_d caused by the gap capacity. The conductive current i_g is calculated as follows.

$$i_g = \frac{1}{d} \int_0^d (n_+ \cdot w_+ - n_- \cdot w_- - n_e \cdot w_e) dx$$

w_+ , w_- : positive/negative ion mean velocity
 w_e : electron mean velocity

In the present model, we consider an external circuit shown in Fig.1. It represents a most simple external circuit for capacitively-coupled discharges. Under these condition, the gap voltage V_g is determined as

$$V_g = \frac{C_b}{C_g + C_b} \cdot V_s + \frac{1}{C_g + C_b} \int_0^t i_g dt'$$

V_s : rf source voltage

The displacement current i_g is obtained from

$$i_d = \frac{C_b * C_g}{C_g + C_b} \cdot \frac{dV_s}{dt} + \frac{C_g}{C_g + C_b} \cdot i_g$$

CROSS SECTIONS

For electron-gas molecule collisions, we use a set of cross sections by Ohmori et al.(1986). The main difference between these cross sections and those used by Kushner (1988) is the shape of the vibrational excitation cross sections. For ion-gas molecule collisions, the momentum transfer and charge exchange processes are considered for positive and negative ions, and the values of the collision frequencies are quoted from Kushner(1988). The momentum transfer cross section is assumed to be 10^{-15} A^2 , and the total collision frequency is deduced from rate constants and defined as follows.

$$\nu_t = 6.43 \times 10^7 + 7.87 \times \sqrt{\epsilon} \times 10^6 \text{ s}^{-1} \quad (\epsilon \leq 50 \text{ eV})$$

$$\nu_t = 1.20 \times 10^8 \text{ s}^{-1} \quad (\epsilon > 50 \text{ eV})$$

RESULTS AND DISCUSSION

Simulation condition and parameters

In the present simulation, we consider an rf glow discharge between symmetrical parallel-plate electrodes and the space between the electrodes are divided into 25 slabs. The discharge parameters are calculated in each slab and recorded 50 times per one rf cycle.

The gas pressure and the rf frequency of the source voltage are respectively set to 300 mTorr (20°C) and 13.56MHz. The applied voltage is 450 V (peak) and the gap length is chosen equal to 1.71 cm. The gap capacity C_g and the blocking capacitance C_b in series to the gap electrodes are respectively set to 10 pF and 8 pF. Secondary electron emission by positive ion bombardment was included in the present simulation, and secondary electrons are emitted from both electrodes at a rate of 0.15 per positive ion with the velocity corresponding to 0.05 eV. The electrodes are assumed to be perfectly absorbing surface for both electrons and ions.

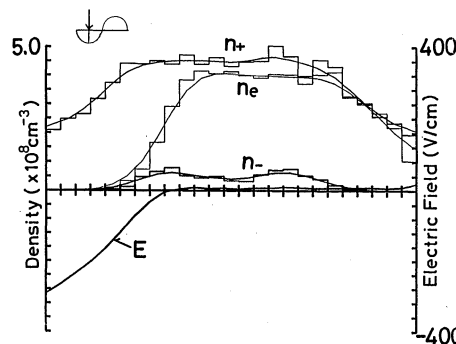


Fig. 2. The densities of electrons, positive ions and negative ions between the electrodes (at $t=T/4$ in an rf cycle)

Results and discussion

Fig.2 is the profile of electron, positive ion and negative ion densities and the electric field as a function of position between the electrodes when the largest negative bias voltage is applied to the left-hand-side electrode. Both ion densities show symmetrical profile. At the neighbourhood of the electrodes, the positive ion density becomes much larger than the electron density. Therefore,a positive ion sheath is formed here. In this region, the electric field is large and it shows a more or less linear profile. The sheath

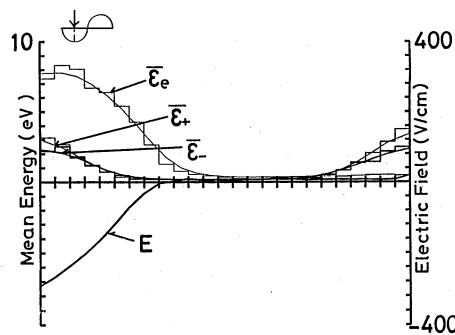


Fig. 3. The mean energies of electrons, positive ions and negative ions between the electrodes (at $t=T/4$ in an rf cycle)

width is about 5.6 mm, and this width is found vary from about 1.0 mm to 6.0 mm with time during an rf cycle. In the bulk region, the positive ion density is also larger than the electron density, but negative ions exist mainly in this region, so that the value of the positive charge density is almost equal to that of the negative charge and the electric field becomes very small here.

In Fig.3 is shown the profile of the electron, positive ion and negative ion mean energies as a function of position between the electrodes at the same instant as in Fig.2. In the bulk, the mean energies of both electrons and ions are very small because of low electric fields. In the sheath, the mean energies become larger because of the high electric field. In the neighborhood of the electrodes, the electron mean energy becomes lower despite that the intensity of the electric field increases because the secondary electrons with low energy are emitted from the electrodes. When the electric field intensity becomes smallest, the electron mean energy shows a very small value. This is because SiH₄ has a large vibrational excitation cross section at low electron energies, so that the electron energy decreases immediately after the field intensity becomes small. The ion mean energy has little time variation, therefore the ion energy does not become so small even when the electric field is small.

The temporal variation of the electron and ion densities at a position between the gap is shown in Fig.4. At the boundary of the bulk and the sheath, the electron density becomes larger than positive ion density at instants during an rf cycle, and the profile of the electric field is distorted. This is because the electron diffusion flux towards the electrodes grows larger than the electron drift flux when the electric field become small, so that electrons flow suddenly into the sheath region against the electric field.

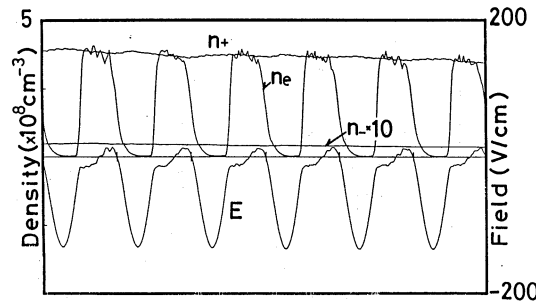


Fig. 4. The time variations of the electron, the positive ion, and the negative ion densities

This phenomenon can be also explained from the electron drift velocity. Fig.5 shows the electron mean velocity obtained by the present simulation (\bar{v}_e), the drift velocity calculated from the local field and electron mobility (v_d) and the diffusion flux calculated from the gradient of the electron density and diffusion coefficient (v_{diff}). Mobility and diffusion coefficient of electrons in SiH₄ gas are quoted from the swarm data given by Ohmori et al.(1986). When the electric field becomes small, a sharp peak of diffusion flux appears, and while the electric field is relatively high, \bar{v}_e is almost equal to the sum of v_d and v_{diff} .

In the present simulation, generation of radicals which are produced by electron impact dissociation is also calculated. Fig.6 shows the time variation of the generation rate of radicals in the gap for two rf cycles. The threshold

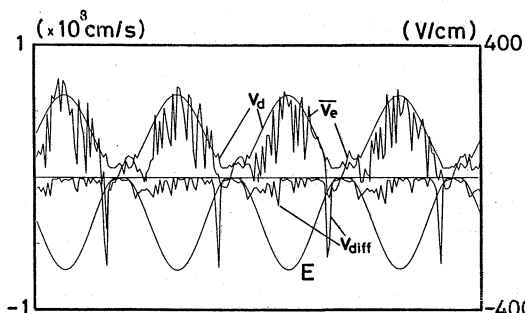


Fig. 5. The time variations of the electron mean velocity obtained by the present simulation (\bar{v}_e), the electron drift velocity (v_d) and the diffusion flux (v_{diff}).

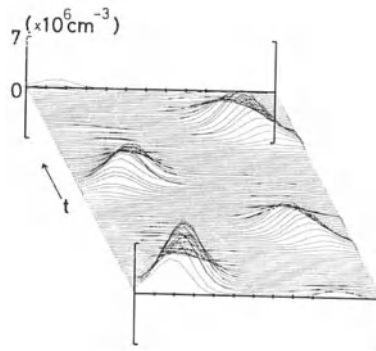


Fig. 6. The time variation of generation of radicals producing by the electron impact dissociation in the gap.

energy of electron impact dissociation is 8.4 eV. Therefore, dissociation collisions will occur frequently in the region in which the electron energy is high. However, in the sheath, the generation rate is not large because the electron density is very small. Consequently, the radicals are mainly produced at the boundary between the sheath and the bulk where many high-energy electrons exist. The peak of the generation rate moves with the motion of sheath boundary.

CONCLUSIONS

An rf glow discharge in SiH₄ gas is simulated by a Monte Carlo method. In the present work, simulation has been done for electrons, and positive ions and negative ions. The spatial distribution of positive ions and negative ions are practically symmetrical between the electrodes. Particularly, negative ions tend to accumulate in the bulk, and the positive charge balances with negative charge here. Radicals are mainly produced at the boundary between the sheath and the bulk. In a near future, we will simulate the motion and reaction of radicals and apply this method to other gases and mixtures.

REFERENCES

- Kushner, M.J., 1988, J.Appl.Phys., 63 : 2532-2551
- Kushner, M.J., 1986, IEEE Trans. Plasma Sci., PS-14 : 188-196
- Kitamori, K., Yokozawa, A., Sakai, Y. and Tagashira, H., 1989, Conf. Plasma Processing, Vol.6 : No.5-6
- Ohmori, Y., Shimozuma, M., and Tagashira, H., 1986, J.Phys.D, 16 : 1029
- Okada, I., Sakai, Y., Tagashira, H. and Sakamoto, S., 1978, J. Phys. D, 11 : 1108

CHARGED PARTICLES DYNAMICS IN ELECTROPOSITIVE GLOW DISCHARGES
PROBED BY OPTICAL DIAGNOSTICS

J. Derouard, H. Debontride, M.P. Alberta and N. Sadeghi

Laboratoire de Spectrométrie Physique (CNRS UA 08)
Université Joseph Fourier Grenoble I
BP 87 38402 Saint Martin d'Hères, France

INTRODUCTION

In glow discharges the electric field $\vec{E}(\vec{r})$ can be considered as the key parameter which determines the motion of charged particles and the ionization processes. In addition, using Poisson's equation, one can calculate the net charge density from the $E(r)$ distribution and also obtain insight into the charged particle dynamics.

The determination of the electric field is thus of primary importance for a better understanding of the glow discharge mechanisms and the carrying out of realistic numerical models (See Boeuf and Belenguer, 1989, these proceedings).

Because of the lack of sensitive, local, non intrusive and fast diagnostics, little is known about the electric field distribution in glow discharges. The situation is now changing, however, with the recent development of optical laser spectroscopic techniques, which have many interesting features. Beside Rydberg atom laser Stark spectroscopy (Den Hartog et al, 1988; Shoemaker et al, 1988), molecular laser Stark spectroscopy has been recently successfully used to probe the electric field in R.F. discharges of electronegative gases (Moore et al, 1984; Gottscho, 1987). Here we have applied the latter method to probe discharges in mixtures of rare gases and potassium vapor using the NaK molecule (present as traces in these mixtures) as a spectroscopic probe of the electric field (Derouard and Sadeghi, 1986).

After a presentation of the method, where its physical limits will be discussed, we shall give some examples of applications. They include investigations of either steady-state and R.F discharges, and transient phenomena related to photoelectron initiated avalanches.

MEASURING THE ELECTRIC FIELD

Our method is based on the dependence of the laser induced fluorescence spectrum of NaK to the electric field (See Fig.1). Briefly, the laser tuned to a $^1\Sigma^+, J'' - ^1\Pi, J$ molecular transition excites and prepares the molecule in either e or f Λ -doublet

substates (Moore et al, 1984; Derouard and Sadeghi, 1986), depending whether $J-J''=+1$ or 0, respectively. In the presence of an electric field, the e and f substates are coupled by the Stark interaction $V(J,M)$:

$$V(J,M) = \langle J,M;e|V|J,M';f\rangle = \delta_{M,M'} \mu E M / (J(J+1)) \quad (1)$$

where E is the magnitude of the electric field, μ the vibrationally averaged dipole moment of the molecule, and the M 's are the projection of the angular momentum J along the direction of the electric field. As a consequence, this electric field induced mixing induces the appearance of new "forbidden" lines in the fluorescence spectrum, (See Fig.1) whose intensity is borrowed from the intensity of the "allowed" lines. From simple two level quantum mechanics we see that this mixing, and therefore the forbidden to allowed line intensity ratio "Q/R", is an increasing function of the ratio T :

$$T = |V(J,M) / (E_e - E_f)| \quad (2)$$

where $E_e - E_f$ is the zero-field energy splitting between e and f molecular substates.

For $V(J,M) \gg E_e - E_f$ the eigenstates are a complete 50%-50% mixture of e and f states, and the Q/R ratio saturates. The ratio T strongly depends on J, M , and of course on E , as shown previously both experimentally (Mandich et al, 1985; Derouard and Sadeghi, 1986; Derouard et al, 1989) and theoretically (Derouard and Alexander, 1986). Enough experimental data are now known to allow the calculation of the Q/R ratio vs E for a variety of experimental conditions. From these calculations one gets calibration curves which can be subsequently used for the determination of the local electric field with NaK as the spectroscopic probe.

Fig.1 shows that fields as small as a few V/cm can in principle be detected using this method, while 50 V/cm is easy to measure. In practice we choose the J level according to the magnitude of the electric field we want to measure. This is similar to the Rydberg atom spectroscopic method, the n quantum number is properly adjusted.

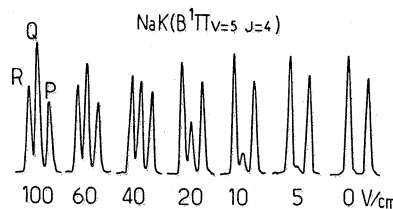


Fig. 1. Fluorescence spectrum of laser excited NaK($B; V=5, J=4$) for different values of the applied electric field. The laser is tuned to a P line which excites the e component of the Λ -doublet, whose fluorescence spectrum is composed of P and R lines. The electric field induces the mixing with the f which fluoresces according to the Q transition.

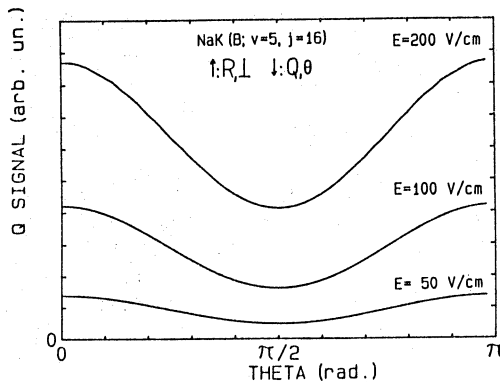


Fig. 2. Polarisation of the "forbidden" (electric field induced) Q fluorescence of laser excited molecules with respect to the direction of the electric field. Calculated intensity of the Q line transmitted through an analyzer whose axis makes an angle θ with respect to the E-field. Excitation is assumed to occur via an R transition with laser polarization perpendicular to E.

It is very interesting that the Stark mixing depends on M (See Eq.1), the projection of the angular momentum onto the E-field direction. It implies that, conversely, the Stark induced "forbidden" fluorescence lines are polarized along a direction which is related to (and, in some cases, can be) that of the E-field vector (See Fig.2). This demonstrates the capability of the method for determining the electric field vector. Such has been already demonstrated using Rydberg atom spectroscopy (Ganguly and Garscadden, 1985). The measurements using this latter method are averaged over the path of the laser beam, however, due to the optogalvanic detection. (This limitation could be in principle overcome using two photon-two colors excitation (Doughty et al, 1984)). Our fluorescence method does not suffer from this limitation since the observation region is determined by the crossing between the line of sight of the optical detection and the laser beam.

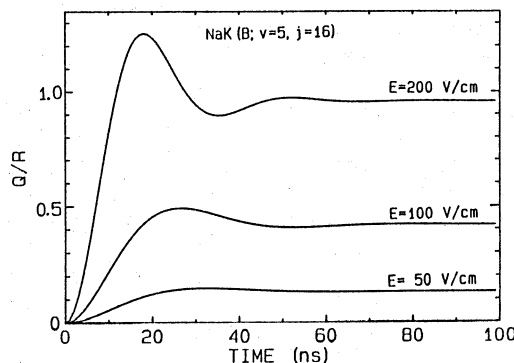


Fig.3. Time response of the NaK LIF spectrum to an applied electric field. Calculated Q/R ratio vs time following the application of steps of electric field of various magnitudes at $t=0$. Polarization of the laser is assumed perpendicular to the E-field, and the fluorescence is analyzed with polarization parallel to the E-field.

Another interesting feature of the molecular Stark mixing method is its application for doing time resolved measurements. The smallest time scale which can be probed is determined by the time response of the molecule to variations of the electric field. This is mostly determined by the Bohr frequencies between the Stark-shifted eigenlevels (which reduce to $E_e - E_f$ in zero field). Fig.3 shows examples of theoretical simulations of the Q/R ratio following steps of electric field of various amplitudes applied at $t=0$. It shows that the typical time response is smaller than 15 ns. It can be further reduced at the expense of reduced sensitivity by choosing rotational levels with larger $E_e - E_f$.

ELECTRIC FIELD VECTOR MAP IN 2-D GLOW DISCHARGES

In many respects radial effects associated with the finite size of the electrodes and/or the vessel can be important in the physics of the discharges.

For instance, in the "normal regime" of D.C. discharges, the glow does not cover the whole cathode. When the current is decreased the discharge area decreases, keeping the current density constant. This has been known for a long time, but is still not very well understood (Von Engel, 1965; Emeleus, 1981; Boeuf, 1988).

It is also important to characterize and understand the boundary potentials, the effects of electrode geometry which are related to the self polarization of R.F. plasmas (Boeuf and Belenguer, 1989), and also the edge effects which can be responsible for non uniformity in plasma processing.

Here we present some results concerning the determination of the electric field lines and magnitude in D.C.glow discharges established in a mixture of Ar(98%)+K(2%), $p=0.4$ Torr at 210°C . The cell is a cylindrical pyrex cell, 60mm diameter, with two stainless steel circular plane electrodes. The anode diameter is 30mm, the cathode diameter is 15mm. A laser directed along a diameter of the cathode excites the fluorescence of NaK whose spectrum is analysed perpendicular to it. The laser beam is sent with polarization parallel to the cathode so that it is by symmetry perpendicular to the E-field. In these conditions, as shown above (Fig.2), the Stark induced fluorescence is preferentially polarized parallel to the direction of the E-vector, which can thus be determined.

Fig.4 shows the results. Fig.4a corresponds to conditions close to the normal regime, while Fig.4c corresponds to a current density ten times larger. In this latter case the magnitude of the field has also been determined and is indicated by the length of the vectors. For low currents it is clearly apparent that many field lines emanating from the edge of the cathode are lost toward the wall of the cell. By contrast, for higher current we see that every field lines starting from the cathode ends in the negative glow. A careful inspection of the field magnitude on the axis shows also that it does not decrease linearly with the distance from the cathode: through the Poisson equation this suggests an increase of the charge density (=ion density in the cathodic sheath) as one approaches the negative glow. Such a behavior has been already seen experimentally (Warren, 1955; Gottsho, 1987) and theoretically (Boeuf and Segur, 1988). It is related to the existence throughout the sheath and the negative glow of a beam component in the electron distribution function which ensures the ionization of the gas.

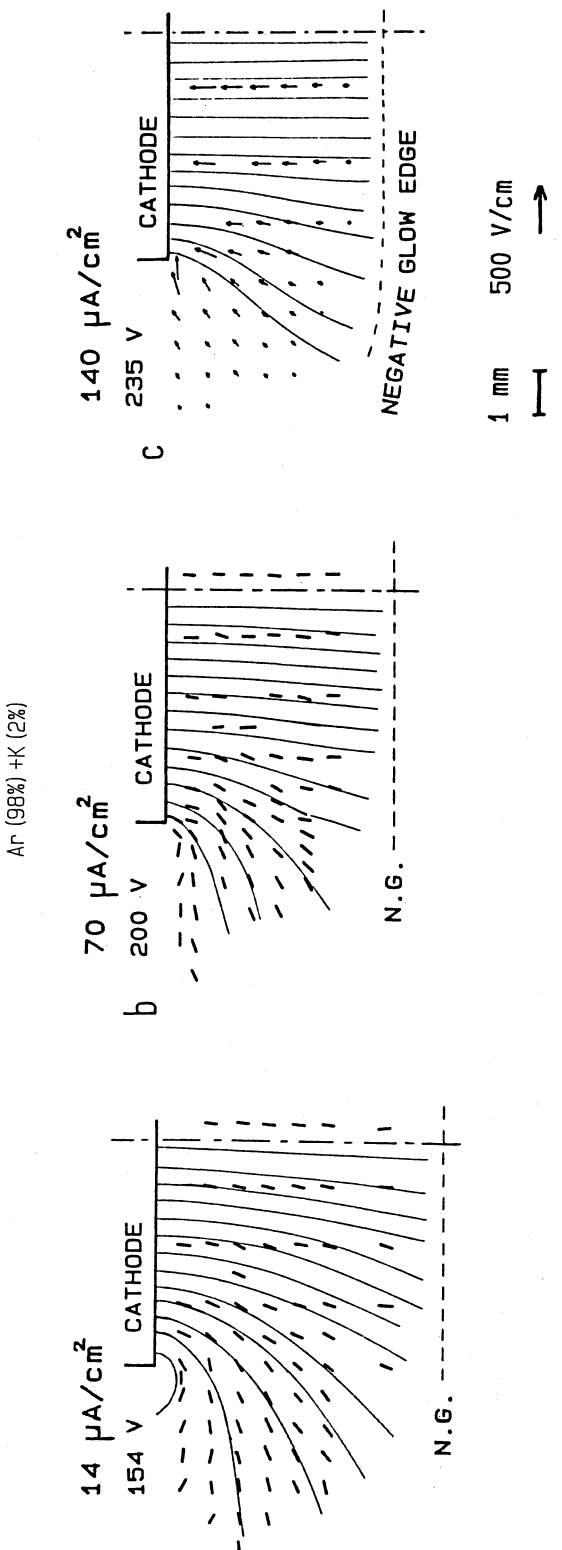


Fig. 4.Two dimensional electric field maps in D.C. discharges through a Ar(98%)-K(2%) mixture heated at $T=210^\circ\text{C}$, $p=0.4$ Torr.

The direction of the E-field is determined from the polarization of the "forbidden" Q line of the LIF spectrum of NaK, its magnitude from the Q/R ratio.

In Fig. 4a the current density is close to the normal regime conditions, while it is ten time larger in Fig. 4c.

Time resolved sheath electric field profiles in R.F. discharges have been investigated recently by Gottscho et al (Moore et al, 1984; Gottscho, 1987) using the molecular laser Stark spectroscopy of BC₁ (present in BC₁₃ discharges). In this case the laser was pulsed and fired synchronously with the R.F. cycle. In our case we use a C.W. laser to excite the NaK molecules and time resolution has been simply achieved by time recording the NaK fluorescence by means of a transient multichannel analyzer. Using this method we have studied R.F. discharges, again established in a mixture of Ar and K, as above.

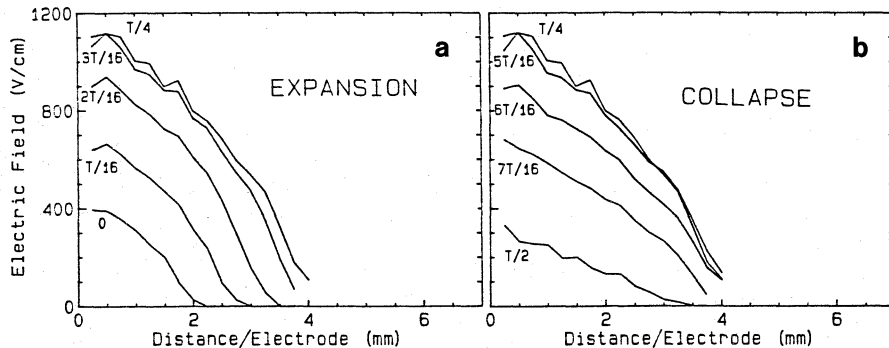


Fig. 5. Sheath electric field profiles for different times during (a) the first quarter and (b) the second quarter of cathodic half cycle of a 35kHz discharge through the same Ar-K mixture as Fig.4. The amplitude of the applied voltage between the electrodes is 700 V.

Fig.5 shows an example of results obtained when applying a symmetrical (with respect to ground) voltage, $V=V_0\sin(\omega t)$, between two identical electrodes (30mm diameter) spaced by 35mm. The frequency is 35kHz. (We were able to investigate R.F. discharges at frequencies up to 6MHz as well). We observe the "breathing motion" of the sheath: Starting from $V=0$, the sheath expands as the voltage applied onto the electrode grows more negative. After $V=-V_0$ the sheath begins to collapse, and eventually vanishes during most (but not all) the anodic part ($V>0$) of the R.F. cycle. We note, in agreement with previous observations by Gottscho (1987) that the sheath does not collapse as it expands: during the expansion motion the plasma-sheath boundary moves away from the electrode; by contrast, during the second quarter of the cathodic half cycle the sheath keeps the same length, which indicates (Poisson equation) a uniform decrease of the ion density throughout the whole sheath. This type of behavior has been reproduced theoretically (Boeuf and Belenguer, 1989) within the self consistent "beam model". It is related to the fact that there exists a large number of ions produced beyond the sheath edge by fast electrons accelerated through the sheath.

When a pulsed laser beam is sent onto the cathode of a D.C. discharge there is a sudden release of a bunch of photoelectrons (provided of course that the photon energy exceeds the work function of the cathode). These photoelectrons are accelerated and initiate an avalanche in the gas, which is accompanied by a considerable increase of the discharge current (See Fig.6). This latter constitutes what has been called the "Photoemission Opto-Galvanic Signal"(POGS) by Downey et al(1988) and has been demonstrated to be a potentially interesting phenomenon for the in-situ diagnostic of surfaces in plasma reactors.(Downey et al ,1988; Selwyn et al,1988) Beside this, the understanding of this phenomenon is strongly related to that of R.F. and other non steady-state discharges: In some respect it gives us the opportunity to study the response of a discharge to an almost instantaneous perturbation, and its observation yields directly the relevant time scales.(Mitchell et al,1989; Debontride et al, 1989).

Fig.6 shows the transient current which follows the photoelectron emission in a D.C. discharge (established in the same Ar-K mixture as above) induced by the impact of a short laser pulse (Copper vapor laser, FWHM=30ns, $3\mu\text{J}/\text{pulse.cm}^{-2}$) on the cathode. Note the considerable increase of the current. After the fast electron avalanche which results from the photoemission the plasma is left with strongly perturbed ion and electron densities. It then relaxes back to its steady state regime, which takes about 100 to 150 μs in our conditions.

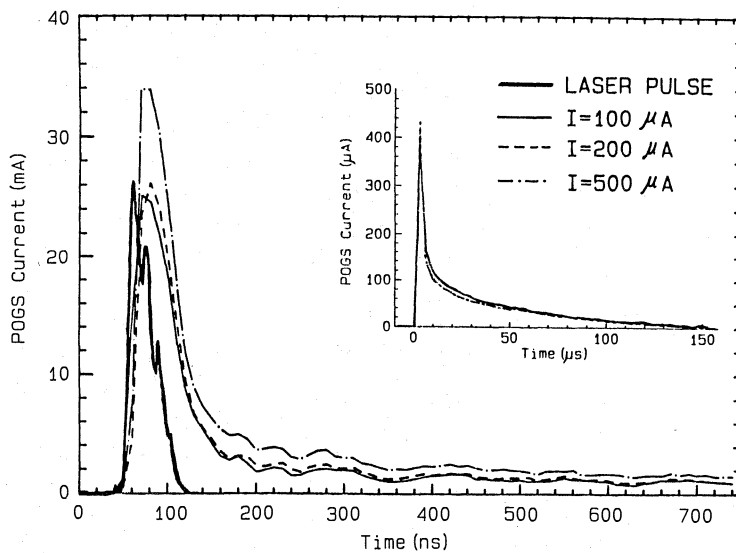


Fig. 6.Optogalvanic signals as a function of time following the emission of a bunch of photoelectrons at $t=0$ induced by the impact of a short laser pulse onto the cathode of a D.C. discharge. Same gas as Figs.3 and 4. The integrating gate width is 10ns, and 3 μs in the inset.The steady-state current has been subtracted off, and is indicated.Cathode diameter is 30mm.

Again spectroscopy allows us to have insights about what is happening in the volume of the gas, as shown on Fig.7 where we have represented the time resolved electric field and emission profiles. Just before the arrival of the photoemission pulse (time labelled "0⁻") the shape of the electric field closely reproduces the steady-state case. (Derouard et al, 1987). But just after the photoemission one sees the dramatic shortening of the sheath and the subsequent increase of the field at the cathode (the voltage is maintained constant so that one expects the area under the field profile to remain constant)

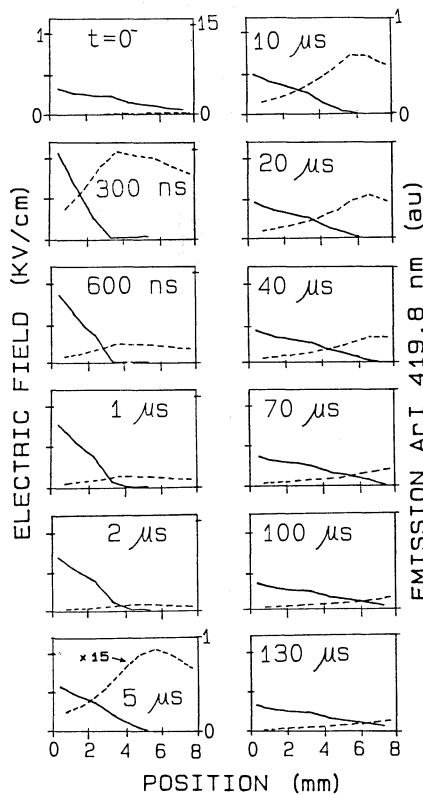


Fig. 7. Electric field (continuous line) and Ar emission (dashed line) profiles as a function of time following the photo-emission induced avalanche at $t=0$. Conditions corresponding to $100\mu\text{A}$ (or $14\mu\text{A}/\text{cm}^2$) in Fig. 6, 154 V

Correlatively note the considerably enhanced optical emission, and the shift of its maximum, which follows the sheath edge (Von Engel, 1965). Afterwards one observes the motion of the sheath which eventually recovers its initial shape after 100 to 150 μs , like the discharge current (Fig. 6).

All these results are in excellent qualitative agreement with self consistent beam model simulations (Debontride et al, 1989).

CONCLUDING REMARKS

The experiments reported in this paper demonstrate that one can use NaK as a spectroscopic probe of the electric field in glow discharges. Indeed this spectroscopic probe has many exceptional features such as sensitivity and fast time response. Although NaK could not be introduced in most application devices, some of their features could be hopefully experimentally "simulated" and studied by observing similar NaK containing discharges. For instance, our observations restricted to discharges in Ar-K mixtures have enabled us to assess the validity of the "beam-model" (Boeuf and Belenguer, 1989) and to describe the properties of glow discharges in general.

ACKNOWLEDGEMENTS

This work has been supported by DRET, contracts 85-071 and 88-108 and by CNET

REFERENCES

- Boeuf J.P., 1988, *J. Appl. Phys.*, 63:1342
Boeuf J.P. and Ségur P., 1988, in "Intéractions Plasmas Froids Matériaux", ed. by C. Lejeune, Les Editions de Physique, Paris, p. 113
Boeuf J.P. and Belenguer Ph., 1989, these proceedings
Debontride H., Derouard J., Edel P., Romestain R., Sadeghi N. and Boeuf J.P., 1989, *Phys. Rev.A*, submitted
Den Hartog E.A., Doughty D.A. and Lawler J.E., 1988, *Phys. Rev. A*38:2471
Derouard J. and Sadeghi N., 1986, *Opt. Comm.*, 57:239
Derouard J. and Alexander M.H., 1986, *J. Chem. Phys.*, 85:134
Derouard J., Debontride H. and Sadeghi N., 1987, *J. Physique*, 48:Colloque C7:725
Derouard J., Debontride H., Nguyen T.D. and Sadeghi N., 1989, *J. Chem. Phys.*, 90:5936
Doughty D.K., Salih S., Lawler J.E., 1984, *Phys. Lett.*, 103A:41
Downey S.W., Mitchell A., Gottscho R.A., 1988, *J. Appl. Phys.*, 63:5280
Emeleus K.G., 1981, *Int. J. Electronics*, 51:269
Ganguly B.N. and Garscadden A., 1985, *Phys. Rev.*, A32:2544
Gottsch R.A., 1987, *Phys. Rev.*, A36:2233
Mandich M.L., Gaebe C.E., Gottsch R.A., 1985, *J. Chem. Phys.*, 83:3349
Mitchell A., Scheller G.R., Gottsch R.A. and Graves D.B., 1989, *Phys. Rev.A*, submitted
Moore C.A., Davis G.P., Gottsch R.A., 1984, *Phys. Rev. Lett.*, 52:538
Selwyn G.S., Ai B.D. and Singh J., 1988, *Appl. Phys. Lett.*, 52:1953
Shoemaker J.R., Ganguly B.N. and Garscadden A., 1988, *Appl. Phys. Lett.*, 52:2019
Von Engel A., 1965, "Ionized Gases", Oxford University Press, London
Warren R., 1955, *Phys. Rev.*, 98:1650

PROBLEMS IN THE EXPERIMENTAL DETERMINATION OF ELECTRON ENERGY

DISTRIBUTION FUNCTION IN RF DISCHARGES

G. Dilecce, M. Capitelli, S. De Benedictis and C. Gorse

Centro di Studio per la Chimica dei Plasmi

Dipartimento di Chimica, Università di Bari

Trav 200 Re David, 4, 70126, Bari, Italy

INTRODUCTION

The measurement of electron energy distribution function (EEDF) in RF discharges is a topic of great interest for understanding the processes taking place in a kind of discharge where sheath processes and inelastic and superelastic collisions are thought to play a fundamental role in shaping the EEDF, giving to it a pronounced non-maxwellian character as well as a noticeable spatial dependence /1/.

The technique employed to this aim is the second derivative analysis of a Langmuir probe characteristic which, for a correct execution and interpretation of the measurements, requires one to face the problems of the RF oscillations of the plasma potential and of electron emission and reflection from the probe surface.

The present paper contains a brief review of the main concepts about these problems and their solution or interpretation, together with an application of these ideas to a number of measurements the correctness of which is discussed in such a framework.

The measurements have been carried out in a parallel plate stainless steel discharge chamber diffusion pumped down to 10^{-6} torr with a leak rate of about 10^{-6} torr l sec⁻¹. The electrodes have a 10 cm diameter and are separated by a distance of 3 cm, and the discharge is driven by a 27 MHz power generator. The probe is a 0.127 mm thick and 8 mm long molybdenum wire, while the measuring apparatus is a computer controlled data acquisition system which, after collecting the current data, carries out a numerical double differentiation together with an analysis of the electron and ion saturation regions. The scheme is analogous to that described in ref. /2/, except for some differences in the hardware; further details on the technique can be found in /3/.

Results of EEDF measurements in He, N₂ and He-N₂ mixture, at a pressure of 0.1 torr and at a power of 10-20 W delivered to the discharge are presented. The EEDFs show the presence of space dependent high energy tails as well as inelastic collisions participation in determining its structure.

The effects of RF oscillations of plasma potential (V_p) on probes i-V characteristics have been widely analyzed and discussed in a number of papers /4/,/5/,/6/,/7/, and a detailed discussion of them is far beyond the scope of this report. It is nevertheless useful to point out here the features which can be thought of as the fingerprints of this phenomenon, and which can give us a mean of interpreting the results of measurements. The most apparent effect is a shift of the entire characteristic towards more negative potentials. The floating potential (V_f) changes accordingly, and this effect is used to establish a criterion of best RF rejection corresponding to the maximum value of V_f achievable. The effect of V_p oscillations on the second derivative of the probe current is depicted in fig. 1(a-b), where results of a simulation of averaging an i-V characteristic over one period of the signal $A(.8\sin(\omega t)+.2\sin(2\omega t))$ plus gaussian noise are shown at different A/kT_e values, and assuming a Maxwellian EEDF for electrons and OML collection for accelerated particles. The maximum and minimum of the second derivative are almost antisymmetric around the plasma potential, and their distance amounts to $2A$. This fact generates another criterion of best RF rejection, but cannot safely be used to estimate A owing to the contribution of surface

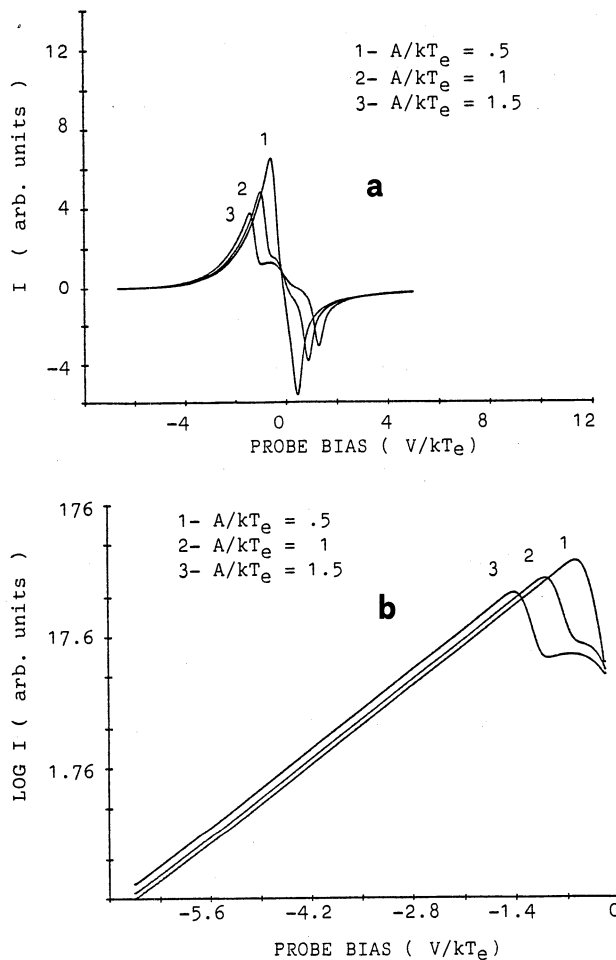


Fig.1a-b

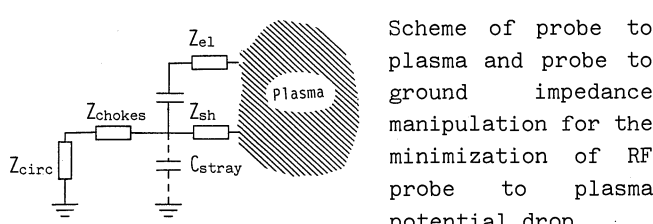
Effect of RF averaging on the second derivative of probe current. Results are plotted in linear (a) and logarithmic (b) scale. This latter plot is restricted to the electron retarding region. Calculations have been performed by the method of ref./6/. Note that the second derivative always crosses zero at the plasma potential.

effects to the smoothing of the transition at the plasma potential. The exponential behaviour of the second derivative in the electron retarding region is, instead, preserved, although with a loss of information on the EEDF at low energies. This allows the measurement of T_e , but the region of the characteristic suitable for such calculation is, in practical cases, strongly reduced as A is increased. In view of this one can state that RF averaging is not capable of producing artificially a non-exponential behaviour of the second derivative starting from an exponential one (except, of course, in the vicinity of V_p).

There are essentially two ways of reducing RF oscillations of the probe-to-plasma potential:

- by driving the probe by an RF voltage adjusted in phase and amplitude until a criterion of best RF rejection is satisfied /8, /9/. This technique provides an easy way of looking at the minimum of the undesired oscillations but cannot compensate higher harmonics of the V_p oscillations. This turns out to be not a great disadvantage unless the harmonics have a big amplitude;
- by lowering as much as possible the ratio between the probe sheath impedance (Z_{sh}) and the probe-to-ground impedance due to the measuring circuitry (Z_{circ}) and to stray capacitances, according to the scheme of fig.2, so that only a small part of V_p oscillations drops on the probe sheath /10/. Z_{sh} can be lowered by virtue of a large electrode or an heated probe /11/ (Z_{el}) capacitively or inductively coupled to the probe, while Z_{circ} is enhanced by the insertion of small RF chokes tuned to the first and second harmonics of the RF discharge generator. This method has been adopted for the measurements reported here, in which the large electrode has the shape of a ring lying at the boundary of a parallel plate RF discharge in a plane parallel to the electrodes. Further details together with a discussion on the validity of such configuration are given in ref. /3/.

It is worth mentioning here a third technique /12/ in which the RF problem is circumvented by time resolving the current measurements. It has successfully been applied to low frequency discharges (up to 100 kHz) in which the V_p oscillations have the form of approximately an half wave rectified sinusoid, with a large part of the period in which V_p is



Scheme of probe to plasma and probe to ground impedance manipulation for the minimization of RF probe to plasma potential drop

almost constant. The current measurements taken at the end of this part of the period (after ions have had sufficient time to form a stable sheath: this determines the maximum frequency which can be investigated) give the i-V characteristic in the absence of RF oscillations.

Theories on charged particle collection assume that the probe is capable of absorbing all the particles striking it. When this turns out to be not true, the quantities extracted from probe measurements can be different to some extent from the real ones. Recognizing the traces of surface effects on the measurements can then give useful informations on the reliability of the parameters inferred from probe characteristics. These effects are, essentially, electron reflection and secondary emission from the probe surface. The following discussion cannot be more than qualitative, as the lack of knowledge of the surface conditions makes it impossible to quantify the phenomena we are going to describe.

The reflection coefficient for different metals has been measured to be of the order of 0.2 for ultra clean metals and of 0.7 for non outgassed or "dirty" (i.e. covered by some other materials) metals /13/. The latter value is a somewhat dramatic one and must be avoided in order to obtain reliable EEDF measurements (for the effects on EEDF measurements of electron reflection and secondary emission see ref. /14/). In our measurements the probe was kept under continuous ion bombardement except in the period of data acquisition (5 sec), even if the gases investigated were only He and N₂, because of the observation of the slow formation on the surfaces of the vacuum chamber of deposits mainly composed of steel (from the sputtering of the RF driven electrode) and of oxygen (from the leak of the vacuum chamber). Further precautions must be taken in the presence of reactive gases (see, for ex., ref. /15/).

The energy dependence of the reflection coefficient shows important features in the low energies range, with a sharp rise in the curve below 1 eV /13/ and then, after a minimum, a smooth increase towards high energies of the incident electrons. As a consequence very low energy electrons are more reflected than the others, and this implies that, on trespassing V_p of about 1 V in the electron accelerating region, an increase of the current should be observed owing to the lower amount of reflected electrons. Furthermore, according to the energy distribution of reflected electrons given in /16/, only a fraction of them is reflected with an energy only slightly less than the incident one, which means that at a fixed electron attracting potential not all the reflected electrons are capable to escape out of the sheath. This argument assigns more reliability, then, to the plasma density inferred from the electron saturation region.

Secondary emission is caused by incident ions, photons and, if present in a large amount, by metastables. A discussion of these phenomena has been given in /17/, /18/, but, essentially, they lead to a possible increase of ion current (secondary emission yields are of about 0.2-0.3 for ions and metastables /19/) and to an increase of the electron current just after V_p in the electron accelerating region in a way depending on the energy distribution of emitted electrons.

As a whole, all these effects should act on the second derivative of the probe current so as to raise the minimum (refer to fig 1a) and eventually to give birth to a second maximum emerging from the primary minimum (this effect has been described in /17/). The second derivatives shown in fig.3, which are representative of all the measurements reported in this paper, exhibit all the effects just described, indicating the

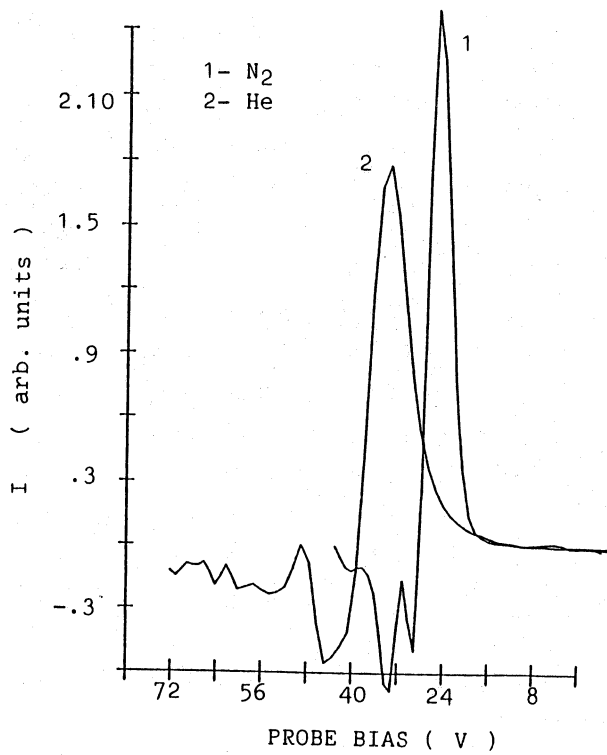


Fig.3

Second derivative measurements in the plasma potential region. Curve 1: 10 W, 0.1 torr He discharge. Curve 2: 20 W 0.1 torr N₂ discharge.

presence of one or more of the discussed phenomena. In particular the presence of the secondary maximum substantiates the choice of V_p as the zero crossing point of the second derivative, while it is to be expected that the plasma densities measured from the electron and ion saturation regions may be, respectively underestimated and overestimated.

RESULTS AND DISCUSSION

Results of EEDF measurements in He, N₂ and He-N₂ mixtures are shown in Fig. 4 a, b, c respectively. In the spirit of the preceding discussion, the plasma potential has been chosen to be the zero crossing point of the second derivative. He and N₂ EEDFs have been studied varying the position of the probe in the discharge (fig. 4 a-b), while in the mixture case the composition is varied, the position in the discharge remaining fixed: both space and mixture markedly affect the EEDF. A strong non-maxwellian character is anyway evident in all the measurements, mainly dictated by the presence of highly populated high energy tails.

The general spatial behaviour is a reduction of the high energy tails accompanied by an increase in the population of the low energy levels,

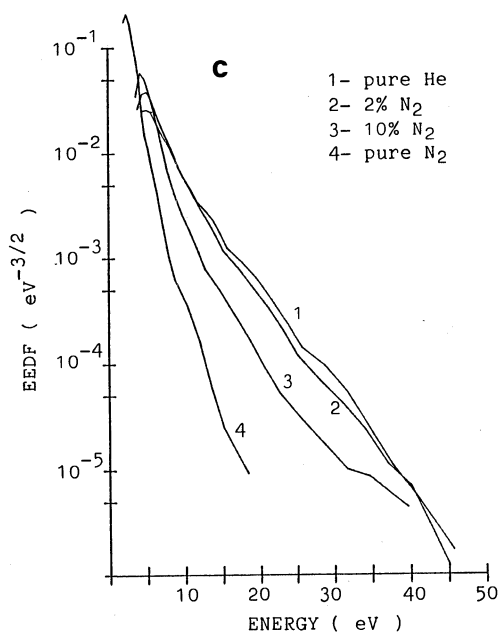
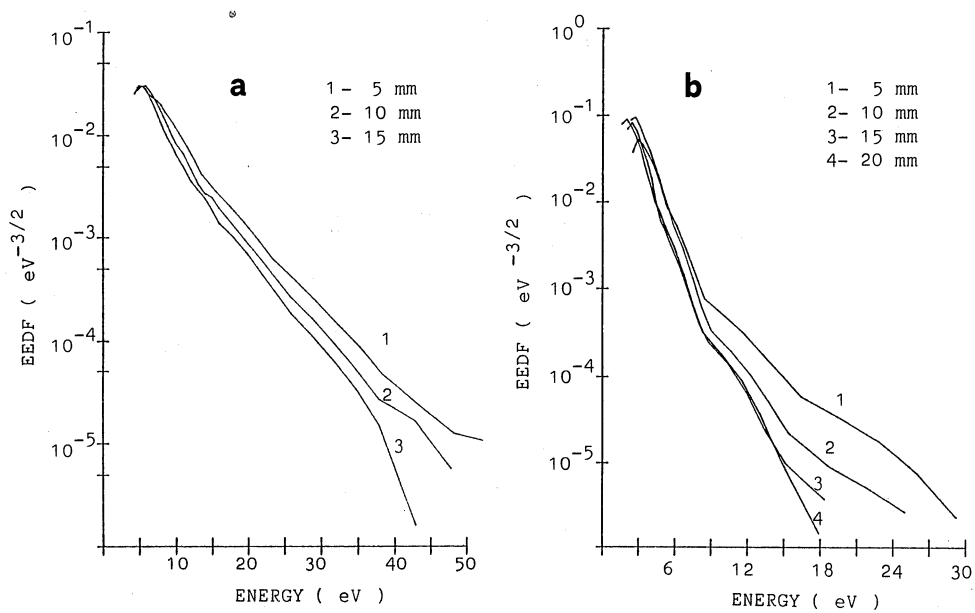


Fig. 4 (a-b-c)
 EEDF measurements
 (error bars are not
 displayed for the
 sake of clarity)
 showing:
 a) space dependence
 of EEDF in a 0.1
 torr 10 W He
 discharge; b) space
 dependence of EEDF
 in a 0.1 torr 20 W
 N_2 discharge (the
 distance from the
 powered electrode is
 indicated); c) EEDF
 variations with
 He- N_2 ratio in a 0.1
 torr total pressure,
 20 W discharge, at
 15 mm from the
 powered electrode.

with a corresponding lowering of the average energy and of the bulk electron temperature (how much it makes sense to speak of a bulk electron temperature will be discussed later). The spatial dependence, especially of the mentioned tails, is stronger in the nitrogen case, in which inelastic energy losses possess take the field. Adding N_2 to He has the analogous effect of depopulating the high energy region for the benefit of the low energy one in a fashion increasing with N_2 percentage increase.

More words have to be spent now about the problems of the low energy region of the EEDF and of the plasma density. As said before, owing to noise and residual RF captation the low energy part of the EEDF is lost in the so called "rounding of the knee" near V_p , and this is evident in all the figures. Measurements in He and in $^p_{He-N_2}$ at 2% of nitrogen display a low energy region which, in logarithmic scale is a straight line. Extrapolating this Maxwellian behaviour towards lower energies until the integral of the EEDF over the whole energy range equals the plasma density inferred from the electron saturation region gives a value of V_p which agrees fairly well with the one obtained from the zero crossing point of the second derivative. Such Maxwellian extrapolation seems then to be reasonable. The situation is different in the case of pure nitrogen and 10% N_2 mixture. Apart from the difficulty of identifying a well defined Maxwellian character at low energies, any attempt of doing the above mentioned extrapolation gives lower values of the plasma potential. Assuming then that the zero crossing point marks the correct position of V_p one can infer that the EEDF in these cases is deprived of low energy electrons, and this can be attributed to inelastic vibrational collisions the cross section of which is important in the energy range 1-4 eV /20/.

The plasma density has been calculated from the electron saturation region, by an i^2 vs V_p plot, in the frame of OML theory /21/, as the value of the ratio r_p / D (probe radius to Debye length) is about 0.3-0.4 in all the measurements. Performing the same analysis of the ion saturation region gives a value more than two times higher than the previous one. This is due to the fact that, as discussed in /22/, /23/, the plasma is not entirely collision free and that the ion motion is essentially radial. The ABR theory /24/, as developed by Chen /25/ for the cylindrical probe, is more suitable for the analysis of the ion current /26/. In our case, application of the Chen/ABR theory leads to a value of the plasma density slightly lower than the electron saturation one, which means, in the frame of the preceding discussion on surface effects, that the radial motion assumption, although better than the OML one, is not reached limit in our conditions. We have chosen the i^2 vs V_p plot technique, instead of deducing the plasma density from the value of the current at plasma potential, because of the incertitude of the V_p value which, although small, falls in a region of fast variation of the current, and because of surface effects which are most effective around the plasma potential. On the other hand the method employed suffers from the fact that in gases with low ionization threshold the region suitable for such analysis is limited by the onset of secondary ionization after sufficient polarization is delivered to the probe, being already limited by the fact that the polarization must have a value much higher than kT_e for the beginning of the square root behaviour.

ACKNOWLEDGMENTS

We are grateful to V. Sacchetti and G. Cosmai for having built the vacuum chamber, and to M.B. Hopkins for many useful discussions.

REFERENCES

1. M.J. Kushner, IEEE Trans. on Plasma Sci., PS-14 n 2 (1986) 188
2. M.B. Hopkins, W.C. Graham T.J. Griffin, Rev. Sci. Instrum., 58 (1987) 475
3. G. Dilecce, S. De Benedictis, M. Capitelli and C. Gorse, Contr. Papers ICPIG-19, Belgrade 1989; Contr. Papers ISPC-9, Pugnochiuso 1989
4. A. Garscadden, K.G. Emeleus, Proc. Phys.Soc.(London), 78 (1962) 535
5. A. Boschi, F. Magistrelli, Nuovo Cimento, 29 (1963) 487
6. K. Matsumoto, M. Sato, Contr. Papers ICPIC-15, Minsk, 1981 p 1001
7. S. Klagge, M. Maas, Beitr. Plasmaphys., 23 (1983) 355
8. H. Sabadil, S. Klagge, Contr. Papers ICPIG-17, Budapest, 1985 p 322
9. N.St.J. Braithwaite, N.M.P. Benjamin, J.E. Allen, J. Phys. E: Sci. Instr., 20 (1987) 1046
10. R.R.J. Gagné, A. Cantin, J. Appl. Phys., 43 (1972) 2639
11. V.A. Godyak, O.A. Popov, Sov. Phys. Tech. Phys., 22 (1977) 461
12. M.B. Hopkins, C.A. Anderson, W.G. Graham, Europhys. Lett., 8 (1989) 141
13. N.L.S. Martin, A. von Engel, J. Phys. D, 10 (1977) 868
14. K.G. Emeleus, Int. J. Electronics, 47 (1979) 97
15. E.P. Szuszczewicz, J.C. Holmes, J. Appl. Phys., 46 (1975) 5134
16. H.E. Farnsworth, Phys. Rev., 25 (1925) 41
17. K. Wiesemann, Z. Physik, 219 (1969) 462
18. R. Mewe, Physica, 46 (1970) 626
19. H.D. Hagstrum, Phys. Rev. 89 (1953) 244; 91 (1953) 543; 96 (1954) 325; 104 (1956) 672
20. W. Domcke, L.S. Cedermann, Phys. Rev. A, 16 (1977) 1465
21. J.G. Laframboise, L.W. Parker, Phys. Fluids 16 (1973) 629
22. S.D. Hester, A.A. Sonin, Phys. Fluids, 13 (1970) 1265
23. P.M. Chung, L. Talbot, K.J. Touryan, Electric Probes in Stationary and Flowing Plasmas, Springer-Verlag 1975, p. 27
24. J.E. Allen, R.L.F. Boyd, P. Reynolds, Proc. Phys. Soc. B, 70 (1957) 297
25. F. Chen, J. Nucl. Ener. Part C, 7 (1965) 47
26. M.W. Allen, B.M. Annaratone, J.E. Allen, Contr. Papers Gas Discharges and their Applications, Venezia 1988

SPECTROSCOPIC DIAGNOSTICS IN THE CATHODE FALL AND NEGATIVE GLOW OF A NITROGEN GLOW DISCHARGE

Jacques Jolly

Laboratoire de Physique des Gaz et des Plasmas
Bât. 212, Université de Paris-Sud
91405 Orsay Cedex, France

INTRODUCTION

The development of plasma techniques in industrial processes is arousing many studies on glow discharges, and more particularly on the ionized gas interfacing with a surface. The fundamental mechanisms can be understood only if the characteristics of the plasma in the vicinity of the material are well known; numerical models can then be developed in order to optimize and control the processes in any other than the trial-and-error approach, that most often prevails, when there are no experimental data or numerical models to go by.

In the plasma-material interface region, where the presence of electrical sheaths produces very high gradients for most of the characteristic quantities of the plasma, the diagnostics must be made "in situ" by non-intrusive methods that offer good space and time resolution. Spatially and spectrally resolved spectroscopic diagnostics such as plasma-induced emission, laser-induced fluorescence and laser optogalvanic spectroscopy can be used to generate diagnostics satisfying the above criteria.¹⁻³

In this paper, we present the results of diagnostics made in the cathode fall and the negative glow of a glow discharge in nitrogen, used to study fundamental processes in nitridation of steels. The measurements concern the spatial distributions of the excited states $N_2(C)$ and $N_2^+(B)$, the determination of the concentration of ground state ions and the axial variation of the rotational temperatures of the different species.

EXPERIMENTAL SETUP

The experimental setup and the diagnostic systems used in this study have been described previously.^{2,3} The plasma is created in a discharge of diode structure-type having 29 mm diameter iron electrodes. The inter-electrode spacing can be adjusted by moving the cathode. The cathode is encased in a ceramic insulator, so as to define the emissive surface of the electrode. The discharge operates in a flow of nitrogen (~0.2 l/min.) and the pressure, measured with a capacitive gauge, may be fixed between 0.5 and 2 Torr.

The spectroscopic systems include a high-resolution monochromator ($\lambda/\Delta\lambda \leq 150000$) providing a good spectral definition in the emission and induced

fluorescence modes, a dye laser emitting in the range 380-392 nm, and a low-resolution monochromator ($\lambda/\Delta\lambda \leq 1000$) to observe the plasma globally in order to monitor and normalize the laser excitation. The light signals are detected by photomultipliers coupled with a digitizer or samplerboxcar averager offering a good time resolution (2 ns).

SPECTROSCOPIC DIAGNOSTICS

Plasma Induced Emission (PIE) plays an important role in plasma diagnostics although it concerns only short livetime levels. In this study we observed the space-resolved emission of two excited levels of nitrogen: the $N_2(C)$ state on the (0-0, $\lambda = 337$ nm) transition and the $N_2^+(B)$ state on the (0-0, $\lambda = 391$ nm) or (0-1, $\lambda = 428$ nm) transition. The light emitted by the plasma is collimated and then focussed onto the monochromator inlet slit by a set of moving lenses and mirrors. The spatial resolution is defined by the height and width of the monochromator slit and by the geometrical aperture of the optical beam. The plasma is studied locally, by moving the mirrors. The lens and mirrors are motor-driven to record the spatial profiles continuously.

Laser-induced fluorescence (LIF) has the undeniable advantage over PIE since it gives informations directly on the population of the ground and metastable states of the active species. The intensity of the induced fluorescence, emitted by a level n' populated by the laser from a level n , is expressed as a function of the population $[n]$, of a factor depending on the oscillator strengths of the transitions used for the laser and the fluorescence detection, and of the number of photons available at the energy corresponding to the laser transition^{4,5} (when no saturation or optical pumping effects occur). Then, for a given transition and species, the fluorescence signal is proportional to the concentration of the species in the starting level, and is independent of the experimental conditions of the plasma provided that the deactivation of the upper level is principally control by radiations. In this study, LIF was used to determine, locally, the ion concentrations. Molecular ions in the ($X, v''=0, N''$) level are photo-excited to the ($B, v'=0, N'$) state by the tunable dye laser (N' and N'' are the upper and lower rotational levels respectively). The laser allows us to populate a given rotational level. The fluorescence is observed perpendicular to the discharge axis and laser beam, through a monochromator, on the ($B, v'=0$) \rightarrow ($X, v''=1$) transition. Local measurements are made by moving the laser beam between the electrodes or by moving the discharge in the crossed fields of the laser and optical detection system.

The resonant optogalvanic effect is defined as the modification of the plasma impedance by absorption of photons at a wavelength corresponding to an atomic or molecular transition of the gas. For nitrogen ions, the optogalvanic effect resulting from the absorption of photons corresponding to the ($X, v''=0$) \rightarrow ($B, v'=0$) transition is due to the difference of mobility between the two species of ions.⁶ In the cathode sheath region, the mobility of the ions in the ground level is mainly limited by symmetrical charge exchange collisions in which the ions give up their energy to the neutral molecules. The corresponding cross section is $\sim 50 \text{ \AA}^2$ at an energy of 10 eV.⁷ For 1 Torr of nitrogen the mean free path is 0.1 mm, thus very much less than the thickness of the cathode sheath (3 mm). Some thirty charge exchange collisions will occur as a ground state ion passes through the cathode sheath. To our knowledge there is no bibliographical data reported for the corresponding cross section of the $N_2^+(B)$ ion. But it is clear that the symmetrical charge transfer corresponds to a much more "complicated" collision as it would involve the transfer not only of a valence electron but also of electronic excitation. An asymmetrical charge transfer would be possible,

but there again, an energy conversion would be necessary. The result is that the charge transfer of the $N_2^+(B)$ ions is much less probable, and therefore its mean free path will be much greater than the one of the ground level ions. We will adopt the hypothesis that the $N_2^+(B)$ ions undergo no charge transfer collisions during their transit through the cathode sheath; however, the mean free path is limited by their radiative lifetime (60 ns). The $N_2^+(B)$ ions created by the laser are then accelerated in the cathode fall. They reach the cathode with a much higher velocity than the ground state ions, slowed down by the charge transfer collisions. The excitation of the ions by the laser will thus result in a temporary increase in the discharge current constituting the laser optogalvanic effect (LOG). The LOG effect on the nitrogen ions, which depends on the difference between the drift velocity of the ions, exists only in that part of the discharge in which the electric field is large, i.e. in the cathode fall. In this region, the LOG effect is a good substitute for the LIF as a means of ion diagnostics, since LIF is less sensitive because of the low concentration and the drift velocity of the ions.

EXPERIMENTAL RESULTS AND INTERPRETATION

All of the experiments reported in this study were carried out for an inter-electrode spacing of 10 mm, a nitrogen pressure of 1 Torr and a discharge current ranging from 5 to 15 mA. The voltage across the discharge at 10 mA is 550 V and the thickness of the cathode fall is of the order of 3 mm which corresponds to a field of 3200 V/cm on the cathode by assuming an electric field varying linearly through the cathode sheath.⁸ We first present the spatial profiles of the excited states of nitrogen and then the one in the ground state ions.

Spatial Profile of the Excited States of Nitrogen

The profiles of the excited states $N_2(C)$ and $N_2^+(B)$ observed in emission on the axis of the discharge are shown in figure 1. The spatial resolution is about 0.2 mm. One observes, for neutral molecules, a dark space starting at the cathode and corresponding to the cathode sheath, then a sharp increase of the light intensity followed by a slower decrease in the negative glow. For the ions, the increase of the light emitted at the border of the cathode fall is less abrupt, but the decrease in the negative glow is very similar for the ions and neutrals. Note that, except at low current (~5 mA), the negative glow is obstructed in a 10 mm discharge. The shape of these profiles can be explained by considering the energy dependence of the electronic excitation cross sections of these levels⁹ and their radiative lifetimes.¹⁰

The shape of the electronic excitation cross section of $N_2(C)$ is very sharp. It has a threshold at 11 eV, a maximum at 15 eV and decreases rapidly by a factor of thirty at 50 eV.⁹ The electrons emitted by the cathode reach and very quickly exceed the energy corresponding to the maximum of this cross section. The secondary electrons created, also quickly exceed the energy of the maximum of the cross section and it is only at the edge of the cathode sheath, where the electrons are large in number and the electric field weaker, that the excitation efficiency becomes large. In the negative glow, the electrons no longer gain energy as the electric field is nearly zero, and so they gradually lose their energy and then the possibility to excite the molecules. This explains the decrease of emitted light. Considering the low velocity of the particles and the short lifetime of the $N_2(C)$ level, the molecules relax at the point where they are created. Thus the profile of emitted light represents the axial excitation function.

There are two distinct reasons for which the emission profiles of the

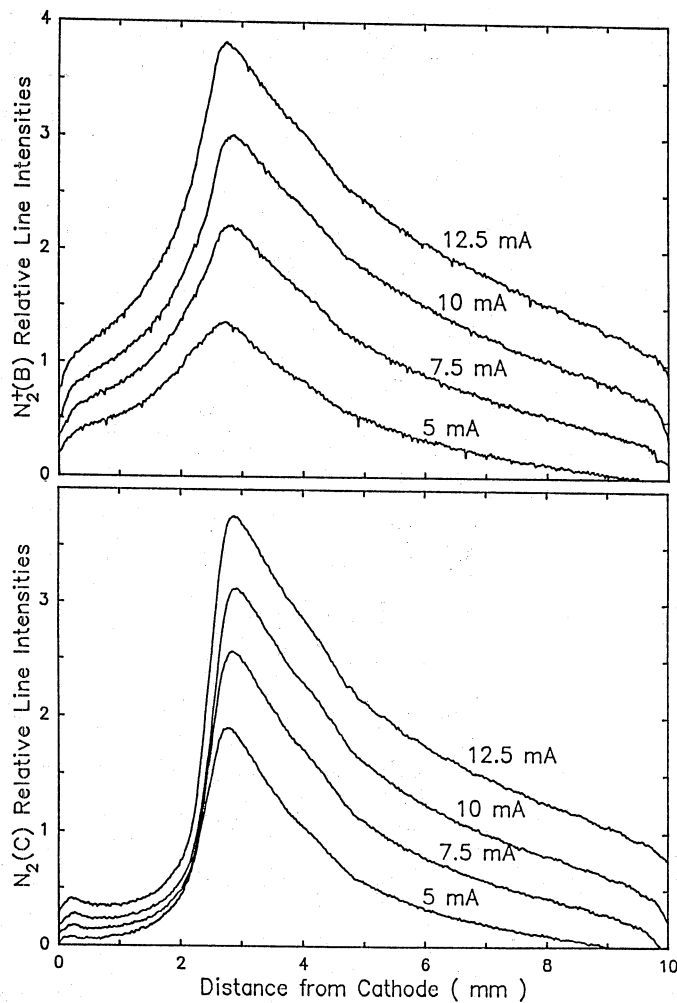


Fig. 1. Emission profiles of the $N_2^+(B)$ and $N_2(C)$ levels for different values of the discharge current.

$N_2^+(B)$ ions are different in the cathode fall. Firstly, the form of the cross section for direct electron excitation is very different than that of the neutral molecule. It has a maximum at 100 eV and decreases slowly by a factor of 3 at 500 eV.⁹ The cross section is large for the high-energy electrons. So it is expected to find relatively more excited ions than excited molecules in the cathode sheath. Secondly, the ions are accelerated toward the cathode in the cathode fall. Their emission profile is therefore not directly representative of the place where they are created. The $N_2^+(B)$ ions relax at a distance that is, on the average, equal to the space travelled through during their radiative lifetime. This is true within the limit of the above hypothesis where we assume no charge exchange collisions, for the excited ions, in the cathode sheath. Then it is possible to calculate, from the emission profile, the $N_2^+(B)$ ion creation profile in the cathode sheath (fig. 4 in ref. 3). The excited ion creation function should be very close to the ionization profile since the electronic collision cross sections for the creation of $N_2^+(X)$ and $N_2^+(B)$ have similar energy dependences.

Spatial Distribution of the Nitrogen Ions

Using LIF technique, we determined the axial ion concentration profile.

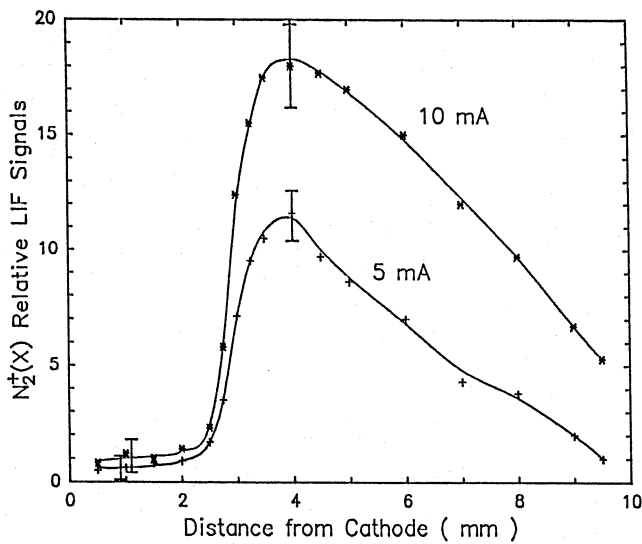


Fig. 2. Spatially resolved LIF signal for two different values of the discharge current.

Spatial resolution is obtained by moving the laser beam (0.5×2 mm cross section) from one electrode to the other and detecting the corresponding induced fluorescence. The profiles of the fluorescence signal are given in figure 2. The spatial resolution is defined by the 0.5 mm width of the laser since the fluorescence is observed nonlocally on the centerline of the discharge. In the negative glow, the fluorescence signal is directly proportional to the local concentration of the ions. On the other hand, in the cathode fall, where the ions are accelerated toward the cathode, the fluorescence photon is detected only if the excited ion has enough time to emit before reaching the cathode. This is all the more important since the excited ions created by the laser have a greater mobility than those at the ground level. We have calculated the correction to be applied to the fluorescence signal as a function of the point where the ion is excited in the cathode sheath. If $t_c(x)$ is the time the ion created at distance x takes to reach the cathode, then the factor $1 - \exp(-t_c(x)/\tau)$ is the correction to be applied to the observed profile, τ being the lifetime of the excited ion.

The fluorescence profile is different from that of the emitted light. In the negative glow, the maximum density of the (fundamental) ions is located at a greater distance from the cathode than that of the light emitted by the $N_2^+(B)$ state, while they have similar excitation functions (as stated above). This is due to the large difference in lifetime between the excited ions (60 ns) and the ions in the ground state ($\sim 40 \mu s^{-1}$). So the ground state ions have the time to diffuse in the negative glow where the electric field is near zero.

The absolute values of the ion density may be determined from the ion current, computed at the cathode by assuming that the discharge current i_d in this region is entirely ionic. We get

$$i_d / S = j_i(x=0) = e n_i(x=0) v_i(E(x=0))$$

where $E(x=0)$ is the electric field on the cathode and v_i the mean velocity the ions gained in their last mean free path before reaching the cathode. The lack of precision, due to the very low intensity of the fluorescence signal in the cathode sheath, brings in a major uncertainty (about 50 %) in the absolute value of the ion concentration.

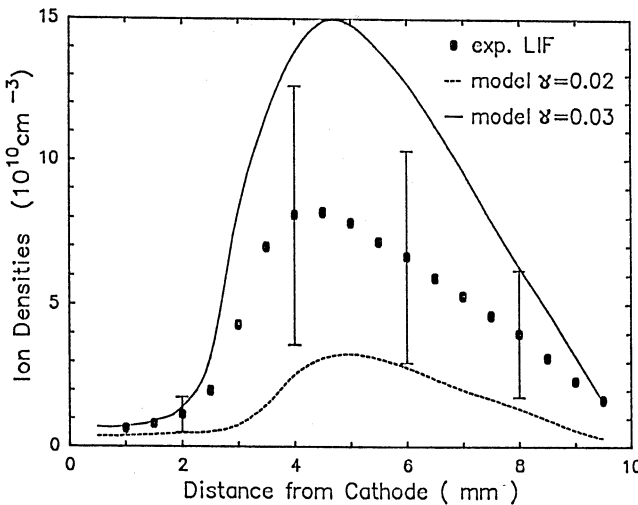


Fig. 3. Absolute ion concentrations (1 Torr, 10 mA) deduced from LIF measurements and calculated with a self-consistent numerical simulation.^{13, 14}

Despite the low precision in the absolute values of the ion densities it is interesting to compare the experimental ion profile with the results of a self-consistent numerical simulation, developed by Boeuf et al.^{13, 14} The model provided the spatial variations of the electric field and charged particle densities in the different regions of the discharge for a given applied potential. Results are presented in Fig. 3. The calculations were performed for a given discharge voltage V and for two different values of the secondary emission coefficient by ion impact at the cathode γ . As observed in Fig. 3, it turns out that a value of $\gamma = 0.03$ yields a sheath length equal to the one experimentally found. The large error bars corresponding to the experimental points are induced by the normalization of the fluorescence signal in the cathode sheath. Despite the factor of two existing between the experiment and the model it is interesting to note that spatial variations of the ion concentrations are quite well duplicated by the numerical simulation.

Axial Profile of the Rotational Temperatures

The temperature of the gas in the various regions of the discharge plays an important role, since it determines the gas concentration and then the population of molecular levels. We measured the rotational temperatures, resolved spatially, for the excited states $N_2(C)$ and $N_2(B)$ using PIE and for the ground state ions using either LIF in the negative glow or LOG spectroscopy in the cathode fall. The experimental techniques are identical to those described before, with the dye laser wavelength scanning the rotational structure of the transition. The rotational temperatures are computed from the relative intensities of the rotational R-branch lines.¹² The results are presented in figure 4. In the negative glow, all the measured temperatures are identical, within the experimental uncertainties; they show a weak dependence on the distance from the cathode. The rotational temperatures of the various states are in equilibrium with the translational temperature of the gas. In the cathode sheath, the rotational temperature of the $N_2(C)$ level increases slowly. The neutrals acquire energy by charge exchange collisions. This energy of translation is redistributed by collisions within

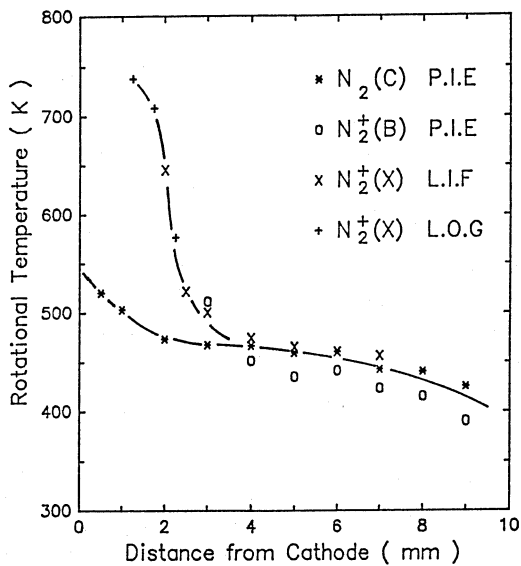


Fig. 4. Rotational temperatures of $\text{N}_2(\text{C})$, $\text{N}_2^+(\text{B})$ and $\text{N}_2^+(\text{X})$ along the axis of the discharge.
Experimental conditions : 1 Torr, 10 mA.

the gas. Moreover, at the surface of the cathode, the gas is in thermal equilibrium with the electrode.^{15,16} This heating of the gas decreases the concentration of the molecules in the cathode sheath. For the ions, the increase of the rotational temperature is much more sudden because they rapidly gain energy in the electric field. A part of this energy is transferred to the rotations by the collisions with the gas. The rotational temperature is no longer representative of the translational temperature of the gas but of the amount of rotational energy that the ions acquire in the electric field.

CONCLUSION

The spectroscopic diagnostics discussed here can be used to characterize the plasma-material interface, with a good spatial resolution. Optical emission is used mainly to characterize the energy distribution of the electrons along the centerline of the discharge and to find from this the excitation and ionization functions. It also makes possible to determine the rotational temperature of the excited states of the molecule which, in the case where thermal equilibrium exists, provides information concerning the temperature of the gas. Laser-induced fluorescence is used to measure, locally, the concentrations of non emitting species, such as the ions in the ground state, and to obtain rotational temperatures for the same species. The laser optogalvanic effect complements the measurements made by laser-induced fluorescence, in the discharge regions such as the sheaths, where the induced fluorescence is not very sensitive.

The experimental data, such as the emission profiles of the excited states of nitrogen and more particularly the population profile of the ions determined using laser-induced fluorescence, are very useful as tests for the development of numerical models, as measurements can be compared with the predictions from existing theoretical models. Then, by analyzing any discrepancies there may be between the computed and experimental data, it may help a better understanding of the basic mechanisms occurring in the cathode region of glow discharges.

Acknowledgments. This research was conducted with the support of the GRECO 57, C.N.R.S. and the D.R.E.T. under contract no. 87/049.

REFERENCES

1. R.A. Gottscho and T.A. Miller, Pure & Appl. Chem. 56:189 (1984).
2. J. Jolly, Diagnostics du plasma par spectroscopie laser, in "Interactions Plasmas Froids Matériaux", Edited by GRECO 57, Les éditions de physique, (1988).
3. A. Margulis and J. Jolly, Revue Phys. Appl. 24:323 (1989).
4. J.L. Kinsey, Ann. Rev. Phys. Chem. 28:349 (1977).
5. T.A. Miller and V.E. Bondybey, J. Chem. Phys. 77:695 (1980).
6. R. Walkup, R.W. Dreyfus and Ph. Avouris, Phys. Rev. Lett. 50:1846 (1983).
7. N. Kobayashi, J. Phys. Soc. Jpn. 38:519 (1975).
8. D.K. Doughty and J.E. Lawler, Appl. Phys. Lett. 45:611 (1984).
D.K. Doughty, S. Salih and J.E. Lawler, Phys. Lett. 103A:41 (1984).
9. P. Laborie, J-M. Rocard et J.A. Rees, "Tables de sections efficaces électroniques et coefficients macroscopiques". Tome 2: Vapeurs métalliques et gaz moléculaires. Dunod Paris (1971)
10. A. Lofthus and P.H. Krupenie, J. Phys. Chem. Ref. Data. 6:113 (1977)
11. H. Böhringer and F. Arnold, J. Chem. Phys. 77:5534 (1982).
R.A. Gottscho, R.H. Burton, D.L. Flamm, V.M. Donnelly and G.P. Davis, J. Appl. Phys. 55:2707 (1984).
12. G. Herzberg, "Molecular Spectra and Molecular Structure". Vol.I: Spectra of Diatomic Molecules. Van Nostrand Reinhold Company, New-York (1950).
13. J.-P. Boeuf and P. Segur, Modélisation des décharges basse pression, in "Interactions Plasmas Froids Matériaux", edited by GRECO 57, Les éditions de physique, (1988).
14. R. A. Gottscho, A. Mitchell, G. R. Scheller, N. L. Schryer, D. B. Graves and J.-P. Boeuf, Proc. 7th Symp. Plasma Proc. Electrochem. Soc. G. S. Mathad, G. C. Schwartz and D. W. Hess ed., 88-22:1 (1988).
15. M. Lefebvre, M. Péalat, B. Massabieaux, A. Pilorget et A. Ricard, I.S.P.C. Tokyo (1987) 483.
16. G.P. Davis and R.A. Gottscho, J. Appl. Phys. 54:3080 (1983).

ELECTRON KINETICS IN RF DISCHARGES

Toshiaki Makabe

Department of Electrical Engineering
Faculty of Science and Technology
Keio University
Yokohama, Japan

INTRODUCTION

The energy breathing of electrons is a remarkable feature in an RF glow discharge.^{6,7,12,15} This has an influence on the sheath oscillation and the time modulation in the plasma emission. In an RF discharge, the parameterization of the electron transport by the local and instantaneous reduced-field, $E(z,t)/N$ will be generally perturbed by the non-hydrodynamic effect, that the electron keeps memory of its initial conditions. We look at the electron kinetics in an RF glow discharge by the Boltzmann equation connecting the microscopic collision cross section and the macroscopic electron transport. As has been well known, the conventional transport theory is described by the physical conservative laws for energy and momentum. Then, the velocity distribution of electrons is expressed by the isotropic and the directional components, $g_0(v,t)$ and $g_1(v,t)$ by the two-term expression of the Boltzmann equation as¹

$$\partial g_0(v,t)/\partial t + \xi[E,\omega,g_1] = - g_0(v,t)/\tau_e(v), \quad (1)$$

$$\partial g_1(v,t)/\partial t + \zeta[E,\omega,g_0] = - g_1(v,t)/\tau_m(v), \quad (2)$$

where, $\tau_e(v)^{-1} \sim (2m/M)v_m(v) + \varepsilon_v d\nu_v(v)/d\varepsilon + v_{ex}(v) + v_i(v) + v_a(v)$,
(3)

$$\tau_m(v)^{-1} \sim v_m(v) + \sum v_j(v) + v_i(v) + v_a(v). \quad (4)$$

Expressions (1) and (2) have the form of relaxation equations for energy and momentum, and $\tau_e(v)$ and $\tau_m(v)$ are called collisional energy relaxation time and momentum relaxation time (See figure 1). The appearance of interesting time characteristics in the electron kinetics will be attributed to the great difference of the magnitude between $\tau_e(v)$ and $\tau_m(v)$ in comparison with the period of the driving RF source.

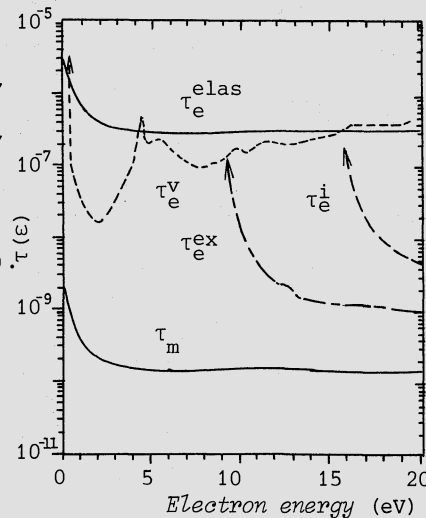


Fig. 1. Collisional relaxation times of electrons in H_2 .

Time-dependent Electron Energy Distribution

We deal with the electron swarm transport under a spatially uniform and a temporally varying electric field with the angular frequency ω ,

$$E(t) = E_0 + E_1 \exp(i\omega t), \quad (5)$$

where E_0 and E_1 are real constant. We consider the swarm including the birth and death processes due to the ionization and the attachment collisions, in addition to the elastic and the excitation collisions from the Boltzmann equation

$$\partial G(\mathbf{v}, t) / \partial t + eE(t)/m \cdot \partial G(\mathbf{v}, t) / \partial \mathbf{v} = J(G) \quad (6)$$

where e and m are the electron charge and mass, v the electron velocity. θ is the angle between $-E$ and \mathbf{v} expressed as $\theta = \cos^{-1}[-(\mathbf{v}, \mathbf{E})/vE]$. The velocity distribution function $G(\mathbf{v}, t)$ will be written, considering the time variation of the electron number density $n(t)$ in the electron non-conservative case, by the expansion in spherical harmonics in velocity space and in Fourier series in time

$$G(\mathbf{v}, t) = n(t) \sum_k \sum_s g_s^k(v) P_s(\cos\theta) \exp(ikwt). \quad (7)$$

The energy gain described by the isotropic velocity component is proportional to $E(t)^2$, and the drift flux expressed by the directional component is a function of $E(t)$. Therefore, $g_s^k(v)$ and $g_s^k(v)$ have the time harmonics with $k \geq 0$. When each component of the energy distribution is defined by

$$f_s^k(\varepsilon) = (4\pi/m) v g_s^k(v); \quad \varepsilon = m v^2 / 2, \quad (8)$$

$f_s^k(\varepsilon)$ satisfies the differential equation derived from the Boltzmann equation.

$$\begin{aligned} & ik\omega \left(\frac{m}{2\varepsilon} \right)^{1/2} f_s^k(\varepsilon) \\ & + eE_0 \left\{ \frac{d}{d\varepsilon} \left[\frac{s}{2s-1} f_{s-1}^k(\varepsilon) + \frac{s+1}{2s+3} f_{s+1}^k(\varepsilon) \right] + \frac{1}{\varepsilon} \left[\frac{-s^2}{2(2s-1)} f_{s-1}^k(\varepsilon) + \frac{(s+1)^2}{2(2s+3)} f_{s+1}^k(\varepsilon) \right] \right\} \\ & + \frac{eE_1}{2} \left\{ \frac{s}{2s-1} \frac{d}{d\varepsilon} [\lambda f_{s-1}^{k-1}(\varepsilon) + f_{s-1}^{k+1}(\varepsilon)] + \frac{s+1}{2s+3} \frac{d}{d\varepsilon} [\lambda f_{s+1}^{k-1}(\varepsilon) + f_{s+1}^{k+1}(\varepsilon)] \right\} \\ & + \frac{eE_1}{2} \frac{1}{\varepsilon} \left\{ \frac{-s^2}{2(2s-1)} [\lambda f_{s-1}^{k-1}(\varepsilon) + f_{s-1}^{k+1}(\varepsilon)] + \frac{(s+1)^2}{2(2s+3)} [\lambda f_{s+1}^{k-1}(\varepsilon) + f_{s+1}^{k+1}(\varepsilon)] \right\} \\ & = R_T + \left\{ \begin{array}{ll} -N [Q_m(\varepsilon) + \sum_j Q_j(\varepsilon) + Q_i(\varepsilon) + Q_a(\varepsilon)] f_s^k(\varepsilon), & (s \neq 0) \\ J(f_s^k(\varepsilon), T_g), & (s = 0). \end{array} \right. \quad (9) \end{aligned}$$

$$\begin{aligned} \text{Here, } J(f_0^k(\varepsilon), T_g) &= \varepsilon^{1/2} \frac{2m}{M} \frac{d}{d\varepsilon} \left\{ NQ_m(\varepsilon) \varepsilon^{3/2} f_0^k(\varepsilon) + kT_g NQ_m(\varepsilon) \varepsilon^2 \frac{d}{d\varepsilon} [\varepsilon^{1/2} f_0^k(\varepsilon)] \right\} \\ &+ \varepsilon^{1/2} \sum_j \frac{d}{d\varepsilon} \left[\frac{\varepsilon + \varepsilon_j}{\varepsilon} NQ_j(\varepsilon) \sqrt{\varepsilon} f_0^k(\varepsilon) \right] d\varepsilon + \varepsilon^{1/2} \int_\varepsilon^0 NQ_a(\varepsilon) \sqrt{\varepsilon} f_0^k(\varepsilon) d\varepsilon \\ &+ \varepsilon^{1/2} \frac{d}{d\varepsilon} \left\{ \int_\varepsilon^{\varepsilon/\Delta + \varepsilon_i} + \int_0^{\varepsilon/(1-\Delta) + \varepsilon_i} \right\} NQ_i(\varepsilon) \sqrt{\varepsilon} f_0^k(\varepsilon) d\varepsilon. \quad (10) \end{aligned}$$

where λ is equal to 1 for $k \neq 1$, except for $\lambda=2$ at $k=1$. N and T are the gas number density and temperature. R_T is the net electron production rate by ionization and attachment. In equation (9), $f_s^k(\epsilon)$ for $k>0$ is a complex function to represent the time delay as against the temporal behavior of the applied field, while $f_s^0(\epsilon)$ is a real function. The normalization condition appropriate to $f_s^k(\epsilon)$ is

$$\int f_s^0(\epsilon) d\epsilon = 1. \quad (11)$$

In particular, it will be noted that, under a pure sinusoidal field, the isotropic part of the distribution $f_s^k(\epsilon)$ has only even harmonics, whereas the directional part, $f_s^k(\epsilon)$, has odd ones.² In the following argument, we study the electron transport in a pure sinusoidal field, $E(t) = \sqrt{2}E_R \exp(i\omega t)$.⁴ Then, physically acceptable truncation of $f_s^k(\epsilon)$ is given by $k+s = 2\beta$, $\beta=1, 2, \dots$ in order to keep the order both in Legendre and Fourier expansions. Figure 2(a) shows the energy dependence of each component of the distribution obtained for $\beta=2$ at $E_R/N = 5 \times 10^{-16} \text{ Vcm}^2$ and $\omega/N = 10^6 N_0^{-1} \text{ cm}^3 \text{s}^{-1}$ in CH_4 , as a typical example of the fully modulated energy distribution in time for a low frequency field. The corresponding instantaneous distribution, $f_0(\epsilon, t)$ is described in figure 2(b) as a parameter of ωt during the first half period of the field. $f_0(\epsilon, t)$ in $\pi < \omega t < 2\pi$ is the same as that in $0 < \omega t < \pi$. The appearance of the finite magnitude of $f_0^2(\epsilon)$ and $f_0^4(\epsilon)$ exhibits the non-linear energy breathing in $f_0(\epsilon, t)$ according to the temporal change of the field in the form of first harmonic. This is due to the great difference of the energy relaxation times respective to the elastic, vibrational and electronic excitation collisions. It is found that $f_0(\epsilon, t)$ is temporarily modulated describing a hysteresis loop with a period of π . That is, the distribution during a decreasing part of the field shifts towards the higher-energy side as compared with the function for the corresponding field strength during an increasing part, since $\tau_e(\epsilon)$ generally becomes shorter with the increase of

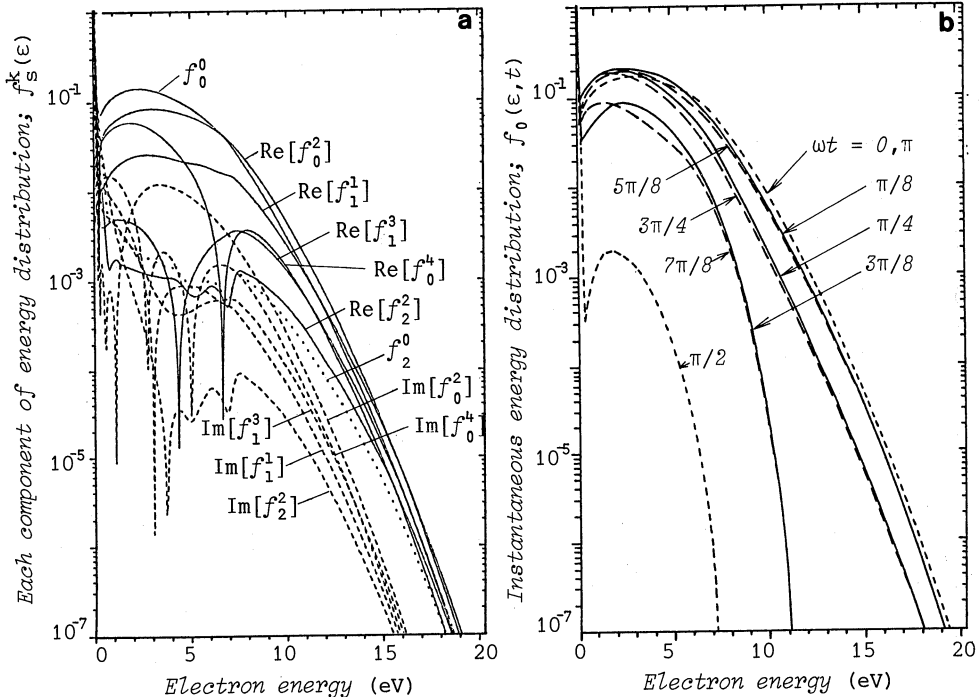


Fig. 2. (a) Each component of the electron energy distribution $f(\epsilon, t)$ at $E_R = 5 \times 10^{-16} \text{ Vcm}^2$ and $\omega/N = 10^6 N_0^{-1} \text{ cm}^3 \text{s}^{-1}$ in an RF field in CH_4 . (b) Instantaneous energy distribution $f_0(\epsilon, t)$ for different values of ωt at the same condition as (a).

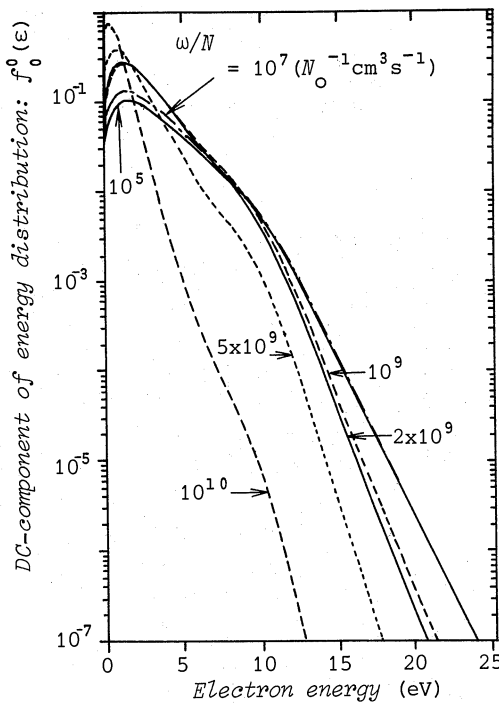


Fig. 3. DC component of the energy distribution for different values of ω/N at $E_R/N = 5 \times 10^{-16}$ Vcm² in an RF field in H₂.

energy. As ω/N decreases, $f_0(\varepsilon, t)$ comes to have the same profile both at ωt and $(\pi - \omega t)$. On the other hand, according as ω/N increases, the collisions with $\tau_e(\varepsilon)$ comparable to ω^{-1} are limited to the electronic excitation and the ionization. Then, $f_0(\varepsilon, t)$ is locally modulated over a restricted range of energy above the threshold energy ε_{ex} . At very high frequency field, $\omega > \tau_m^{-1}$, the distribution begins to exhibit a stationary form with the apparent DC field, $E_{app} = E_R [1 + (\omega / \Sigma v(\varepsilon))^2]^{1/2}$, over a cycle as

$$f_0^0(\varepsilon) = A\sqrt{\varepsilon} \exp\left\{-\int \frac{\frac{NQ_V(\varepsilon)}{NQ_m(\varepsilon)} \frac{\varepsilon_V}{\varepsilon} \frac{M}{2m}}{kT_g + \frac{6\frac{m}{M}N(Q_m + Q_v)NQ_m\varepsilon\{1 + [\frac{\omega}{\sqrt{2\varepsilon/mN(Q_m + Q_v)}}]^2\}}{(eE_R)^2}} d\varepsilon\right\}, \quad (12)$$

and the distribution shifts towards low energy, since the apparent field decreases in accordance with the increase of ω/N , and the collision between the electron and the molecule is limited to the elastic scattering and the vibrational excitation at low energy $\varepsilon < \varepsilon_{ex}$. If we deal with the atomic gas ($Q_v=0$), $f_0^0(\varepsilon)$ approaches a Maxwellian distribution² at an effective gas temperature,

$$T_{g_{eff}} = T_g \left\{ 1 + \frac{M}{6kT_g} \left[\frac{\sqrt{2eE_R}}{m\omega} \right]^2 \right\} \quad (13)$$

The appearance of the spike-like component at very low energy $\varepsilon < \varepsilon_v$ in low frequency field in $f_0^0(\varepsilon)$ in CH₄ is a remarkable difference in comparison with the DC $f_0^0(\varepsilon)$ for the same apparent field E_{app} . Figure 3 shows the change of the time averaged isotropic distribution, $f_0^0(\varepsilon)$ with ω/N at $E_R/N = 5 \times 10^{-16}$ Vcm² in H₂.

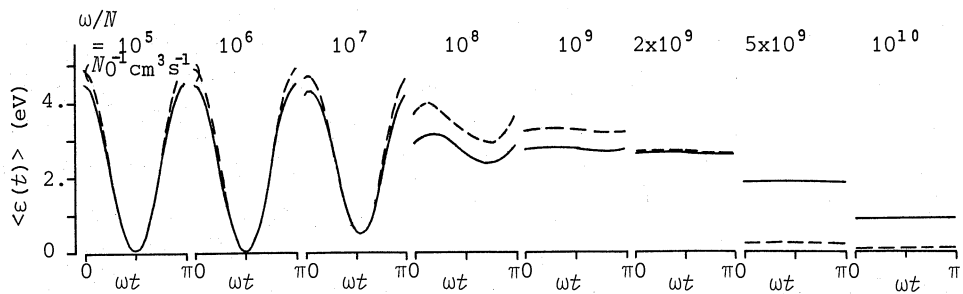


Fig. 4. The time behaviour of the ensemble average of electron energy $\langle \varepsilon(t) \rangle$ in an RF field in CH_4 and H_2 for different values of ω/N at $E_R/N = 5 \times 10^{-16} \text{ V cm}^2$.

Electron Swarm Parameters

The time modulation of the electron energy distribution in a pure sinusoidal field has an influence on the macroscopic swarm behaviour. The ensemble average of the energy, the excitation rate and the drift velocity, $\langle \varepsilon(t) \rangle$, $R_j(t)$ and $v_d(t)$ are written as

$$\begin{aligned}\langle \varepsilon(t) \rangle &= \text{Re} \left[\int (mv^2/2)g(v,t)dv \right] \\ &= \text{Re} \left[\sum_p \int \varepsilon f_0^{2p}(\varepsilon) \exp(i2p\omega t) \right],\end{aligned}\quad (14)$$

$$\begin{aligned}R_j(t) &= \text{Re} \left[\int v N Q_j(v) g(v,t) dv \right] \\ &= \text{Re} \left[\sum_p \sqrt{2/m} (\sqrt{\varepsilon} N Q_j(\varepsilon)) f_0^{2p}(\varepsilon) \exp(i2p\omega t) \right],\end{aligned}\quad (15)$$

$$v_d(t) = \text{Re} \left[\int v g(v,t) dv \right] = \text{Re} \left[\sum_p \{ \sqrt{2/m} / 3 \} \sqrt{\varepsilon} f_1^{2p+1}(\varepsilon) \exp(i(2p+1)\omega t) \right]. \quad (16)$$

It is noted again that the swarm parameters related to the isotropic part of the distribution have only even time-harmonics, whereas the parameter on the directional part has odd ones. Finite time delay to the applied field

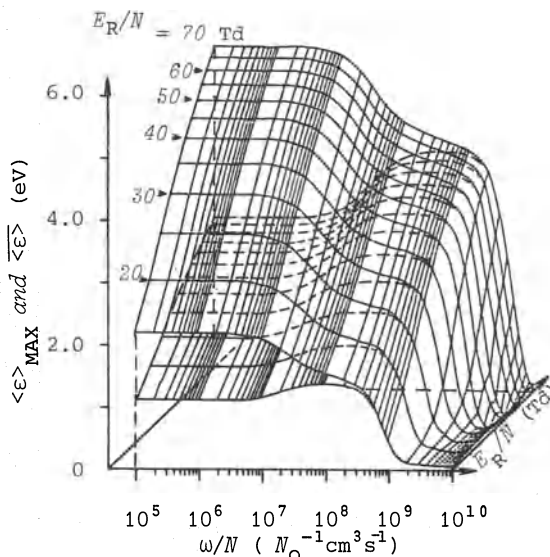


Fig. 5. Maximum and time-average of the ensemble average of the electron energy, $\langle \varepsilon \rangle_{\text{MAX}}$ and $\langle \varepsilon \rangle$ as the functions of both E_R/N and ω/N in CH_4 . $\langle \varepsilon(t) \rangle$ has the time variation with the amplitude, $\langle \varepsilon \rangle_{\text{MAX}} - \langle \varepsilon \rangle$.

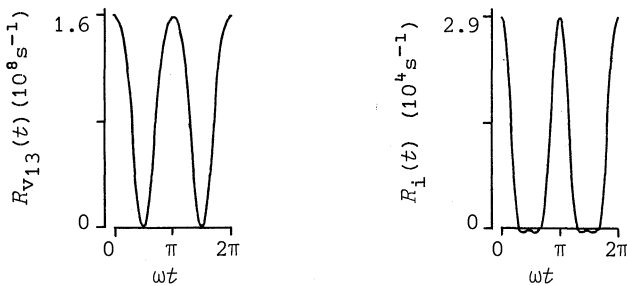


Fig. 6. Comparison between the time behaviour in $R_v(t)$ and $R_i(t)$ at $E_R/N = 5 \times 10^{-16} \text{ Vcm}^2$ and $\omega/N = 10^5 N_O^{-1} \text{ cm}^3 \text{s}^{-1}$ in CH_4 .

waveform will appear in the swarm parameters by the degree of the collisional relaxation. Figure 4 shows the ensemble average of the energy $\langle \varepsilon(t) \rangle$ in CH_4 and H_2 at $E_R/N = 5 \times 10^{-16} \text{ Vcm}^2$ over the wide range $10^5 \leq \omega/N \leq 10^{10} N_O^{-1} \text{ cm}^3 \text{s}^{-1}$. The time behaviour of $\langle \varepsilon(t) \rangle$ changes from the full modulation at low ω/N to the time independence at high ω/N due to the relative magnitude between ω and τ_e^{-1} . At low frequency, all the electron is always fully relaxed to the instantaneous field during a period because of $\tau_e(\varepsilon) \ll \omega^{-1}$. As ω/N increases, $f_0(\varepsilon, t)$ gradually ceases energy relaxation from the low energy part, since the collisional relaxation time $\tau_e(\varepsilon)$ at low energy has a long time subject to the elastic scattering, while $\tau_e(\varepsilon)$ controlled by the inelastic collision at $\varepsilon > \varepsilon_j$ is much shorter. This is the reason the peak value of $\langle \varepsilon(t) \rangle$ is kept constant, while the minimum value rises up with increasing ω/N . As the results, the time-average of $\langle \varepsilon(t) \rangle$ has a maximum at $\omega/N \sim 10^8 N_O^{-1} \text{ cm}^3 \text{s}^{-1}$. The successive rapid decrease of the time-average is caused by the decline of the energy gain from the field with the occurrence of the phase delay in $v_d(t)$. This coincides with the beginning of electron trapping at $\omega > \tau_m^{-1}$. These circumstances in CH_4 are shown in figure 5 as the functions both of E_R/N and ω/N . In this situation, it will be understood that the electron transport is controllable by changing both the reduced field strength E_R/N and the reduced angular frequency ω/N . There is a remarkable difference from the swarm parameters in a DC field. The influence of the non-linear energy breathing in $f_0(\varepsilon, t)$ will be clearly found in the comparison between the time behaviour in the ionization rate and that in the vibrational excitation rate, $R_i(t)$, and $R_v(t)$, at $E_R/N = 5 \times 10^{-16} \text{ Vcm}^2$ and $\omega/N = 10^5 N_O^{-1} \text{ cm}^3 \text{s}^{-1}$ in CH_4 in figure 6. $R_v(t)$ has nearly the symmetric profile as against the time averaged value, while $R_i(t)$ shows the asymmetry owing to the rapid attenuation of $f_0(\varepsilon, t)$ at $\varepsilon > \varepsilon_i$.

ELECTRONIC PROPERTY IN AN RF DISCHARGE

We have studied in the preceding section that the temporal change in the electron transport is an intrinsic character in an RF field.^{3,4,5} In this section, we will make a survey of the influence of the time varying electron transport on the structure in a glow discharge driven by the RF field.

Description of the Relaxation Continuum Model⁶

We consider an RF glow discharge in a parallel plate geometry, maintained by the applied voltage with the angular frequency ω ,

$$V(t) = V_0 \cos(\omega t). \quad (17)$$

The discharge has the structure formed of the ion-sheaths in front of the electrodes and the bulk-plasma. The system is described in one dimension by

the relaxation continuum model by considering the charged particle transport including the collisional relaxation kinetics. That is, the continuity equation of the electron and the ion is written by the zeroth-order moment of the Boltzmann equation as

$$\partial n_j(z,t)/\partial t + \partial\{n_j(z,t)v_j(z,t)\}/\partial z = R_i(z,t)n_e(z,t), \quad (18)$$

where $n_e(z,t)$ is the electron number density, $v_j(z,t)$ is the mean speed of the electron or the ion, given by the sum of the drift and the diffusion velocities $v_{dj}(z,t) + v_{Dj}(z,t)$. The momentum transfer equation will be described as the form of the relaxation equation by the first moment.

$$\partial\{m_jv_j(z,t)\}/\partial t = eE(z,t) - m_jv_j(z,t)/\langle\tau_m\rangle - m_jv_j(z,t)\partial v_j(z,t)/\partial z, \quad (19)$$

where $\langle\tau_m\rangle$ is given by $m_jv_j(z,t)/eE$ by using the DC value of the mean speed as a function of E/N . The second moment of the Boltzmann equation yields the conservation of energy, and the mean electron energy $\epsilon_{me}(z,t)$ is written by

$$\begin{aligned} \partial\{\epsilon_{me}(z,t)n_e(z,t)\}/\partial t &= eE(z,t)n_e(z,t)v_{de}(z,t) \\ &- \{(2m/M)R_m\epsilon_{me}(z,t) + \sum R_j\epsilon_j + R_i\epsilon_i\}n_e(z,t) \\ &- \{n_e(z,t)v_e(z,t)\epsilon_{me}(z,t)\}/\partial z. \end{aligned} \quad (20)$$

Here, we define the effective field for $\epsilon_{me}(z,t)$ by $E_{eff}^2 = \epsilon_{me}/e\mu\langle\tau_e\rangle$. Then, the relaxation equation for E_{eff}^2 is derived as

$$\begin{aligned} \partial\{E_{eff}(z,t)^2n_e(z,t)\}/\partial t &= -\{E_{eff}(z,t)^2 - E(z,t)^2\}n_e(z,t)/\langle\tau_e\rangle \\ &- \partial\{v_e(z,t)E_{eff}(z,t)^2n_e(z,t)\}/\partial z, \end{aligned} \quad (21)$$

where $\langle\tau_e\rangle$ is the energy relaxation time for the mean electron energy. Then, $\epsilon_{me}(z,t)$ at position z and time t is given as a function of $E_{eff}(z,t)/N$ from the values obtained under a uniform and constant reduced field. The ionization and excitation rates $R_i(z,t)$ and $R_j(z,t)$ are also given in a manner similar to equation (21) by the concept of the effective field. The system equations of the electron and the ion are numerically solved with Poisson's equation.

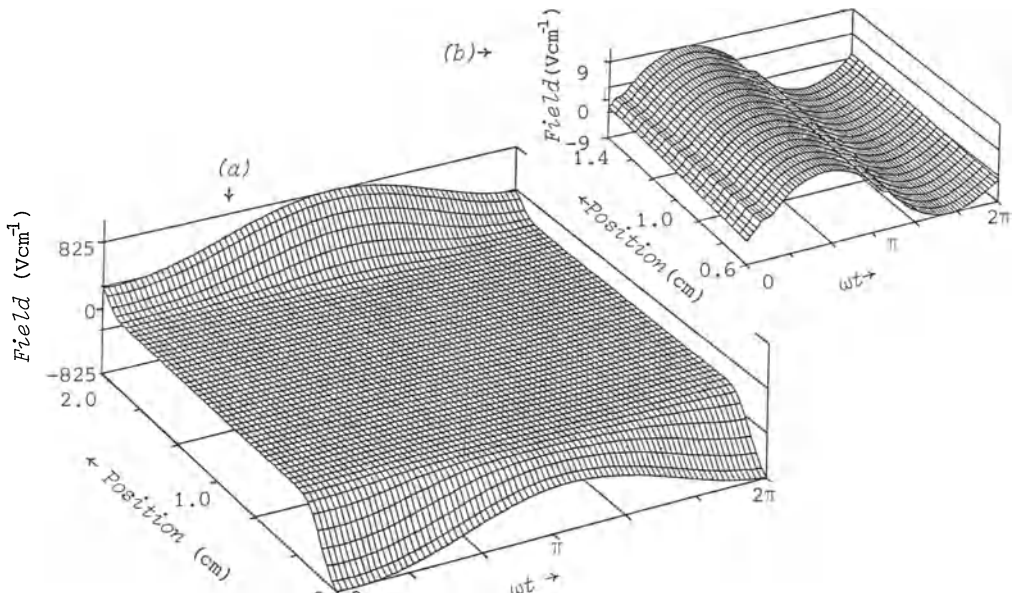


Fig. 7. Electric field distribution in the RF glow discharge in Ar at 13.56MHz and 1 Torr.

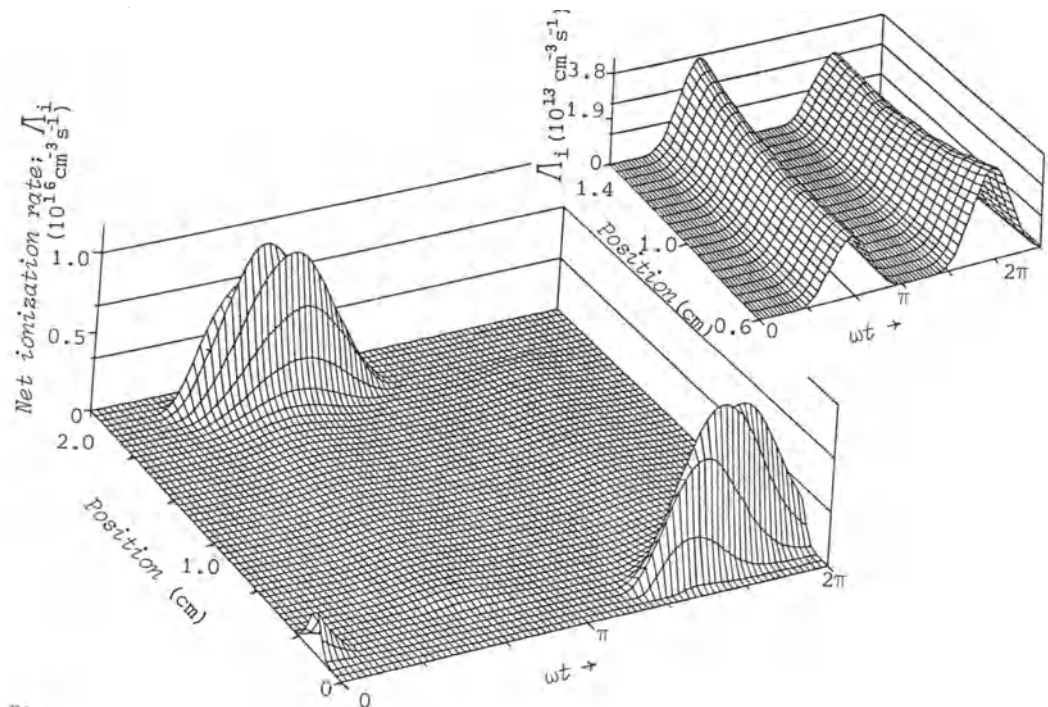


Fig. 8. Net-ionization-rate distribution in the RF glow discharge in Ar.
External condition is the same as that in figure 7.

The boundary conditions are written as $n_e = n_i = 0$ and $E_{eff} = 0$ at the ground ($z=0$) and at the RF ($z=d$) electrodes, when the perfectly absorbing metallic electrodes are postulated. The secondary electron currents by the ion impact are given by $j_e = \gamma j_i$ at both electrodes. j_e and j_i are the electron and ion currents in front of the electrodes.

Electronic Property in an RF Discharge

Figure 7(a) shows the field distribution during a period in the RF glow discharge in Ar, sustained between both electrodes $d=2$ cm by $V_0=100$ V, 13.56 MHz, 1 Torr, $\gamma=0.01$ and $T_g=300$ K.⁷ In this external discharge condition, the drift motion of the ion is trapped in space, since $\int_0^d v_{di}^{-1} dz \gg \omega^{-1}$ is satisfied, or the ion plasma frequency fulfills the relation $\omega_{pi} < \omega$. The RF glow discharge is characterized by the high-field oscillating sheaths in front of both electrodes. The spatial distribution at $wt = 0$ has the same profile as that in a DC discharge with the cathode at $d = 0$. Figure 7(b) exhibits the weak penetration of the driving RF force with the frequency ω into the bulk-plasma. The phase delay in the bulk-field arises from the requirement of the spatial conservation of total current. Figure 8 shows the net ionization rate, given by $\bar{I}_i = R_i(z, t)n_e(z, t)$, in Ar corresponding to the field distribution in figure 7. The bulk-property is enlarged in order to investigate the electron kinetics in the bulk-plasma. It is evident that the generation of electrons is nearly zero at $wt = \pi/10$ and $11\pi/10$, when the sheath width is near the maximum and the highest sheath field is constructed in front of the electrodes. This means the lack of the secondary electron emission on the electrodes with coefficient $\gamma = 0.01$ by the ion impact, since most of the ion is spatially trapped by the applied RF frequency. Two symmetric peaks, both with the magnitude of $10^{16} \text{ cm}^3 \text{s}^{-1}$ appears in $\bar{I}_i(z, t)$,

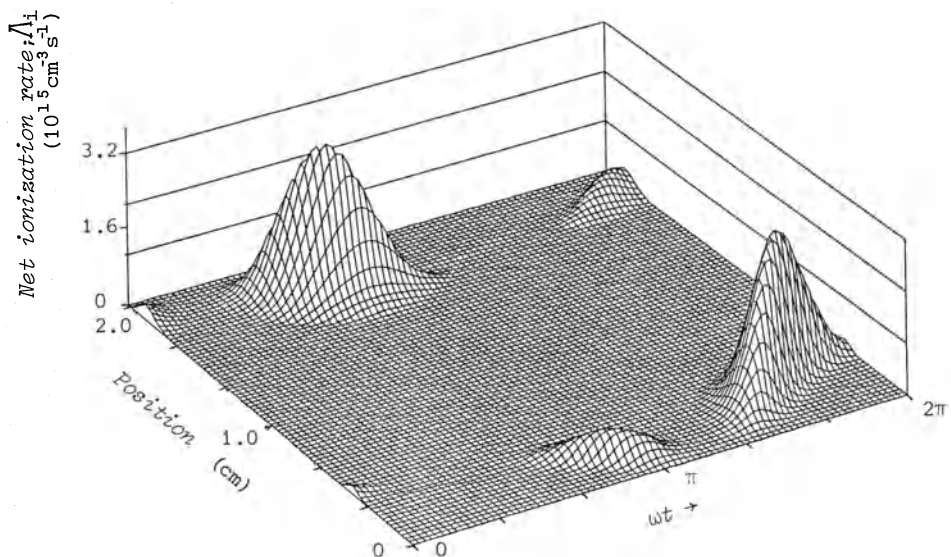


Fig. 9. Net-ionization-rate distribution in the RF glow discharge in CH_4 at 13.56 MHz, 1 Torr.

when the maximum arises with a slight delay of 10° with respect to the current peak. As the results, the discharge is maintained through the volume ionization in the sheath due to the reflected electrons in front of the electrodes. The sheath expansion speed is estimated from the spatio-time behaviour of $\Lambda_i(z,t)$ as $2 \times 10^6 \text{ cms}^{-1}$. In the bulk-plasma, the electron transported by the influence of the small RF field in figure 7 causes the time varying ionization. This is due to the non-linear energy breathing in $f_0(\varepsilon, t)$ as discussed in the previous section, since the bulk density of electrons is temporarily constant. The net ionization rate in CH_4 has the remarkable characteristics in comparison with that in Ar. Figure 9 is the results in CH_4 at $V_0 = 150\text{V}$, 13.56 MHz, 1 Torr, $\gamma = 0.001$ and $T_g = 300\text{ K}$. Two small peaks in front of the anodic parts occur in $\Lambda_i(z,t)$, in addition to the two large symmetric peaks as in Ar. The anomalous spatial distribution seems to be the results of the negative differential conductivity (NDC) of the electron in CH_4 at $4 < E/N(\text{DC}) < 40 \text{ Td}$. That is, methane is known as one of the gases, which have the drift-characteristics, $dv_{de}/d(E/N) < 0$, in a DC field.^{8, 9, 10} As a result, when the local instantaneous field increasingly changes across the NDC-region, the electron accumulation more than the ion density begins in the pre-sheath at the anodic part, where the electron drift flux has the outer direction towards the electrode as the diffusion. The local negative net density moves gradually towards the electrode. Then, the small depression in the field distribution appears in front of the anodic part, and the finite magnitudes of the ionization occurs as shown in figure 9. The net excitation rate shows, of course, the same spatio-temporal characteristics in CH_4 . The experimental evidence of the additional two-peaks is given from the time- and space-resolved optical emission spectroscopy in $\text{CH}_4(10\%) / \text{H}_2$ at 13.56 MHz.¹¹

Figure 10 shows the applied voltage, total current and dissipated power characteristics during one period under the same external discharge condition as that in figure 7 in Ar. The current form with the sinusoidal waveform leads the applied voltage by 72.2° . The power density, calculated by the current-voltage waveforms, has the positive values except the ranges, $0.1\pi < wt < \pi/2$ and $1.1\pi < wt < 3\pi/2$. The time averaged power density of 33 mWcm^{-2} is dissipated in the discharge. The appearance of the sinusoidal nature in total current depends on the percentage of the displacement current

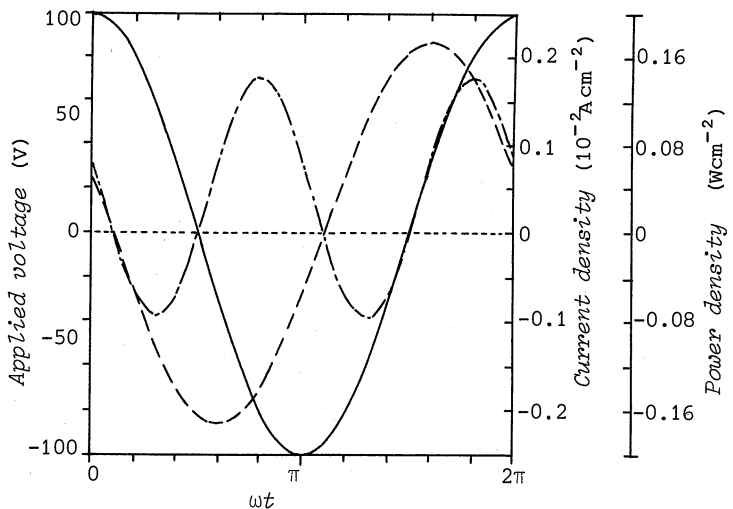


Fig. 10. Applied voltage $V(t)$, total current $I(t)$ and power $W(t)$ characteristics in Ar at 13.56 MHz and 1 Torr. Other condition is the same as that in figure 7.

at the sheath. The displacement current density is expressed in term of the charged-particle density as

$$J_D(z, t) = e \frac{\partial}{\partial z} \int_z^{z+dz} \{n_i(z, t) - n_e(z, t)\} dz / \partial t. \quad (22)$$

Under the condition of $\omega_{pi} < \omega$, if the time derivative of $n_e(z, t)$ has the sinusoidal waveform, the displacement current will show the sinewave. Also equation (22) indicates that the sheath width strongly depends on the magnitude of the drift velocity, as shown in comparison of figure 8 in Ar and figure 9 in CH₄.

ACKNOWLEDGMENT

The author wish to thank Mr. N. Goto and M. Nishimura for their helpful work. This work has been supported in part by the grant-in-aid for scientific research in priority areas.

REFERENCES

1. V. E. Golant, A. P. Zhilinsky and I. E. Sakharov, "Fundamentals of Plasma Physics," John Wiley & Sons, New York (1980).
2. H. Margenau and L. M. Hartman, *Theory of high frequency gas discharges. II. Harmonic components of the distribution function*, Phys. Rev. 73:309 (1948).
3. R. Winkler, H. Deutsch, J. Wilhelm and Ch. Wilke, *Electron kinetics of weakly ionized HF plasmas*, Beitr. Plasmaphys. 24:285(1984).
4. T. Makabe and N. Goto, *The time behaviour of electron transport in RF fields in gases*, J. Phys. D 21:887 (1988).
5. M. Capitelli, R. Celiberto, C. Gorse, R. Winkler and J. Wilhelm, *Electron energy distribution functions in radio-frequency collision dominated nitrogen discharges*, J. Phys. D 21:691 (1988).
6. K. Okazaki, T. Makabe and Y. Yamaguchi, *Modeling of a rf glow discharge plasma*, Appl. Phys. Lett. 54:1742 (1989).
7. T. Makabe, M. Nishimura and Y. Yamaguchi, *Relaxation continuum modeling of RF glow discharges in argon at 13.56 MHz*, to be published.

8. Z. Lj. Petrovic, R. W. Crompton and G. N. Haddad, *Modeling calculations of negative differential conductivity in gases*, Aust. J. Phys. 37:23 (1984).
9. R. E. Robson, *Generalized Einstein relation and negative differential conductivity in gases*, Aust. J. Phys. 37:35 (1984).
10. R. Hunter, J. G. Carter and L. G. Christophorou, *Electron transport measurements in methane using an improved pulsed Townsend technique*, J. Appl. Phys. 60:24 (1986).
11. T. Kokubo, F. Tochikubo and T. Makabe, *Diagnostics of high-frequency processing plasma in CH_4/H_2 by time- and space-resolved optical emission spectroscopy*, ICPIG XIX, Belgrade (1989).
12. D. B. Graves, *Fluid model simulations of a 13.56-MHz rf discharge: Time and space dependence of rates of electron impact excitation*, J. Appl. Phys. 62:88 (1987).
13. A. D. Richards, B. E. Thompson and H. H. Sawin, *Continuum modeling of argon radio frequency glow discharges*, Appl. Phys. Lett. 50: 492 (1987).
14. J. P. Boeuf, *Numerical model of rf glow discharges*, Phys. Rev. A 36:2782.
15. M. J. Kushner, *A model for the discharge kinetics and plasma chemistry during plasma enhanced chemical vapour deposition of amorphous silicon*, J. Appl. Phys. 63:2532 (1988).

A RADIOFREQUENCY TRAP FOR TESTS ON PRODUCTION
AND EXCITATION OF IONS

G. Brautti, A. Boggia, A. Rainò and V. Stagno
Dept. of Physics, Bari University and INFN

V. Variale and V. Valentino
INFN, Bari, Italy

Most of the reaction vessels which are used as ion sources, ion lasers and to study reactions of ionized species use a confinement of the ionizing electrons with magnetic fields, while no attempt is made to contain the most interesting species to be studied, i.e. the ions. While magnetic fields are quite inefficient in low energy ion containment, RF multipole fields(Paul) are extremely effective. Ion containment seems to be particularly interesting for volume ion sources. Indeed, if the ions have to reach the extraction slit by diffusion, the depth of the source cannot be extended, in order not to loose most of them on the side walls. Increasing the source depth, with reduction of the wall losses, can bring several benefits:

- a) increased probability of ion production.
- b) easier separation of regions of different population(e.g. hot and cold electrons).
- c) possibility of filtering according to the $|q/M|$ ratio.
- d) elimination of sputtering, reducing poisoning of the gas and wall corrosion.
- e) possibility of "sweeping" the source with a potential well, to produce intense pulsed beams.

The same benefits are to be expected for ion and recombination lasers. For these reasons we have built a vessel which presently contains an RF octupole, with a containment region about 80 cm. long and 11 cm in diameter. We start with a cold(hollow) cathode, and no magnetic containment of the electrons. Later the addition of a multicusp magnetic field and warm cathodes are foreseen. In a preliminary experiment with a 20 cm long source, with no cathode

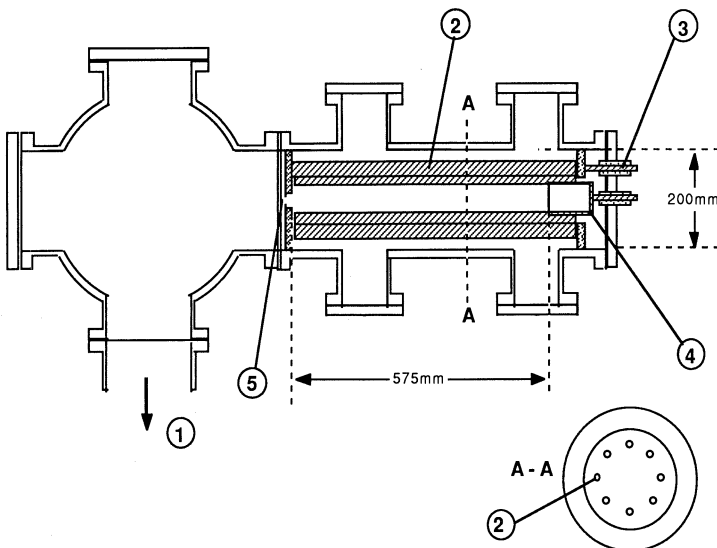


Fig 1. Overall view of the multipole reactor. A-A is a cross section.

1)To pump manifold.2)Multipole electrode.3) Radiofrequency input.4)Hollow cathode. 5)Extraction slit.

at all, we were able to contain stable discharges in nitrogen and argon, while the excitation energy was supplied only by the containing RF.

A drawing of the source is shown in fig.1.

RF containment

When we have a particle of charge q in a rapidly oscillating electric field $\mathbf{E}(\mathbf{r}, t) = \mathbf{E}_0(\mathbf{r}) \cos \omega t$, and its motion is "slow", i.e.

$$v |\text{grad } \mathbf{E}_0(\mathbf{r})| \ll \omega |\mathbf{E}_0(\mathbf{r})| \quad (1)$$

the effect of the field is equivalent[1] to a time-independent pseudopotential

$$V(\mathbf{r}) = q^2 E_0^2(\mathbf{r}) / 4 \omega^2 M \quad (2)$$

A (two-dimensional) multipole field can be produced by $2N$ bar electrodes alternatively connected to the poles of a RadioFrequency(RF) voltage source. The pseudopotential is azimuthally symmetrical, and it has a radial dependence of the type

$$V(r) \propto r^N \quad (3)$$

If the electrode geometry is sufficiently symmetrical, a single

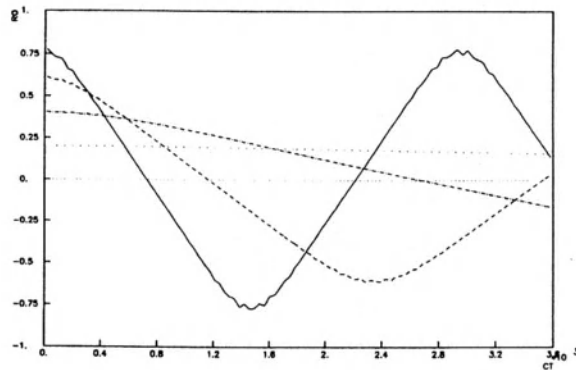
multipole field will be present, determined by the number of electrodes. To obtain a pure multipole field, the profile of the electrodes should be hyperbolic. We expect fields of higher multipolarity to be present, because we chose as electrodes cylindrical bars for ease of fabrication, but the effect of higher multipoles is negligible for low radii, where ions will be contained. In our present geometry we have built an octupole, because with the same RF voltage it produces a much deeper potential well than a quadrupole. However we foresee the possibility of replacing the electrode assembly with a different multipole. In some cases the quadrupole may prove particularly advantageous, because it provides an harmonic potential which allows mass-spectrometric selective containment.

Since $V(r)$ is quadratic in the charge, it contains equally well positive and negative ions. It can be shown also that one can obtain stable ion containment at the endcaps. A special extractor must be provided to extract the ion beam.

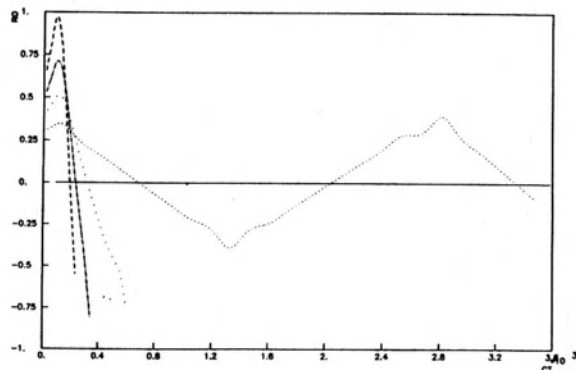
The potential well of the octupole is αr^4 , so the condition (1) cannot be fulfilled within all the trap volume. To study the stability regions, the equations of motion of the ions were integrated by a Runge-Kutta method. For the moment we have only single-particle trajectories, but later we can also attack space-charge and collective motion problems. A sample of the radial motion vs. time is shown in fig. 2, for single hydrogen ions starting at rest, and for several initial values of the radius, and for different frequencies of operation. It can be seen that ions at lower radii have smooth, well contained trajectories, while ripples start at higher radii, until the trajectories become unstable. Raising the frequency of operation increases the stability region.

RF circuit

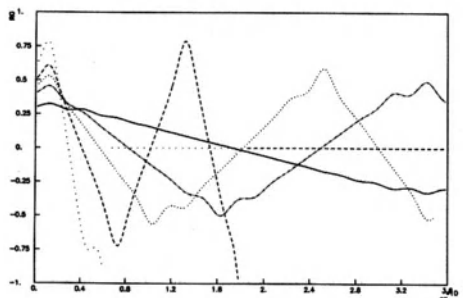
One polarity of the multipole assembly is connected to ground as is the vacuum vessel. The other polarity is connected by an alumina-insulated feedthrough to a tuning-matching external circuit (fig. 3). The choice of the working frequency is a compromise which we plan to optimise by experiment. As shown by (2) the confining forces are proportional to the inverse squared of the frequency. However care must be taken not to exceed the limit (1). We had previous experience with trapping nitrogen and argon ions at the fixed frequency of 4.5 MHz.



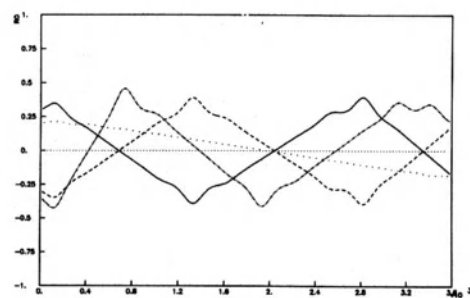
a



b



c



d

Fig 2. Radial motion of hydrogen ions in the octupole trap, for several values of the initial radius. Horizontal scale in ct units. Vertical scale:ratio of the radial position to the trap dimension. a) RF 5 MHz, $V=100$ volts. b) and d) RF 1 MHz, $V=200$ volts .c) RF 1 MHz, $V=100$ volts.

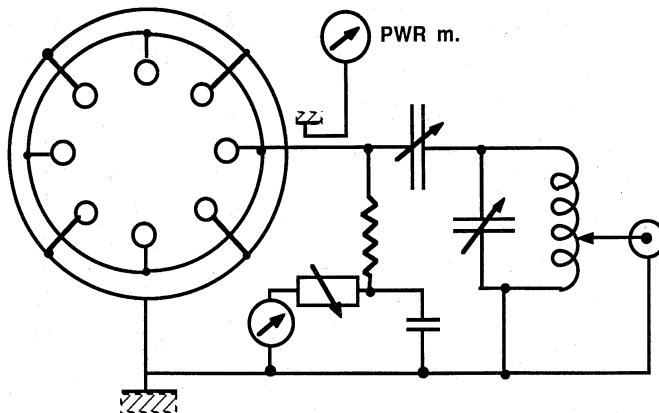


Fig 3.The circuit of the RF multipole.Variable capacitors are used for tuning and matching. It is possible to add a DC bias to one set of poles, and to measure the collected current.

As shown by the circuit scheme, we have the possibility of DC biasing of one half of the electrodes of the multipole, and to measure the average current collected by the same electrodes. RF power is delivered by a synthesized RF generator followed by a 200 watts wideband(1-200 MHz) amplifier.

Electron dynamics

We start the operation of the reactor using only a cold hollow cathode, which can sustain the discharge at fairly low pressures, owing to the large discharge volume. We plan to confine the electrons with a multicusp system, having the same multipolarity of the RF electrodes, but with the magnetic poles set azimuthally centered with the gap of the electric ones.In this way the electrons which tend to drift away from the central region, following the lines of force of the magnetic field, reach a point where there is cyclotron resonance with the RF field, where they are accelerated and where they produce further ionization and molecular excitation. We rely on this mechanism to maintain a good density of high energy electrons in an annular region, separated from the region where we intend to confine the ions.

Diagnostic methods

Our reactor shows an increased complexity if compared, for

example, to multicusp sources, where the population parameters can be considered spatially homogeneous in most of their volume. The foreseen diagnostic methods are the following:

- a) Ion beam extraction, with mass analysis.
- b) Langmuir probe, which can be moved radially.
- c) Laser photodetachement.
- d) Excitation of longitudinal plasma waves.
- e) Pulsed operation of the cathode.
- f) Amplitude modulated operation of RF.
- g) Frequency sweeping of RF.

Reference

[1] L.Landau and E.Lifchitz, Theoretical Physics, Vol.I-Mechanics.

GAS-PHASE AND GAS-SURFACE INTERACTIONS OF VIBRATIONALLY EXCITED HYDROGEN MOLECULES

M.Cacciatore

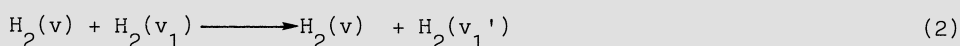
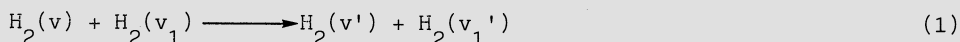
CNR-Centro Studi per la Chimica dei Plasmi
Dipartimento di Chimica, Università di Bari
Via Amendola 173, 70126 Bari (Italy)

INTRODUCTION

The storage of energy in highly vibrationally excited H₂ molecules can lead to the activation of a variety of physical and chemical processes of great interest in various areas of research which fall in the field of non-equilibrium kinetics¹. Dissociative electron attachment², electron excitation to dissociative electronic states³, reaction of neutral and charged molecules at surfaces⁴, are few examples where a particular process in H₂ may be significantly enhanced when the excited vibrational states are sufficiently populated.

It turns out that one of the most problematic points in the vibrational kinetics is the knowledge of a large number of state-to-state rate constants of collisional processes responsible for the building up and redistribution of vibrational quanta in the molecules.

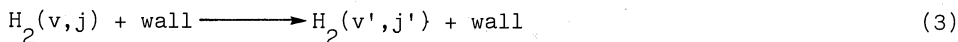
As far as the collisional processes in the gas-phase are concerned, in absence of strong external perturbations, vibrational energy redistribution takes place primarily through (1) vibration-to-vibration (V-V) and (2) vibration-to-translation/rotation (V-T) collisional exchanges:



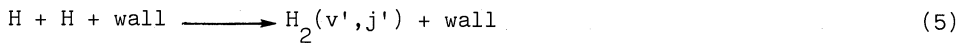
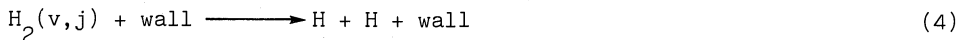
It is known that the rate constants K(v,v'|v₁,v₁') for these processes depend critically on the vibrational quantum numbers v and v₁. However, due to known difficulties, there is little information on the relaxation of high vibrational states in diatomics⁵. For H₂ the experimental data are even more rare due to the difficulty of pumping and probing molecules without permanent dipole moment. There are, however few known exceptions^{6,7}. From the theoretical point of view, when rotations are properly treated, exact quantum mechanical calculations are generally not feasible for generating large sets of state selected

rate constants^{8,9}. On the other hand, we have shown that approximated methods (SSH, Sharma-Brau, IOSA, etc) as well as simple analytical scaling relations, can easily fail (up to orders of magnitude) in reproducing both the existing experimental data and the correct vibrational quantum number dependence of the rate constants¹⁰.

The interaction of H₂ with metallic surfaces can affect the vibrational kinetics in the gas phase as well. In fact, an important channel in creating non-equilibrium vibrational distribution in H₂ could be the vibrational relaxation in wall collisions:



Dissociative chemisorption (4) and atom recombination at surface (5) can also be very effective channels for creation/annihilation of vibrational quanta:



Although a great deal of theoretical¹¹⁻¹⁴ and experimental¹⁵⁻¹⁷ works has been done in the last few years on the interpretation of molecule-surface collisions, a number of fundamental questions are still open. Moreover, detailed dynamical informations on the energy relaxation processes (3), (4) are almost absent¹⁸. On the other hand, the importance of inelastic and reactive processes in the wall region has emerged in several works on the vibrational kinetics of H₂^{19,20}.

It is evident from such brief considerations that the search for complete set of accurate state-selected rate constants of bulk and surface processes is still far from being solved.

The purpose of this paper to present some of the results obtained in our study²¹⁻²⁴ on the dynamics of processes (1)-(4). Refined semiclassical models have been developed in order to describe the dynamics of processes under consideration. This, together with the use of the best available interaction potentials, allowed us to obtain detailed state selected informations on the vibrational relaxation in H₂.

VIBRATIONAL ENERGY EXCHANGES IN H₂(v)-H₂(v') GAS-PHASE COLLISIONS

In a series of papers which have been appeared in the last few years^{10,25}, we have shown that, when a realist interaction potential is known, a semiclassical coupled state model²⁶ can be applied for the generation of accurate (within 20-30%) rate constants.

According to this method, the translational and rotational motion of the colliding molecules are treated classically by solving the Hamilton equations of motion for a rigid rotor moving in an effective potential. The 18 classical equations are solved together with the time dependent Schrodinger equation for the vibrational quantum degree of freedom. The equations for the quantum amplitudes are obtained by expanding the total wave function in the rotationally distorted Morse oscillators:

$$\Psi_n(r_i, t) = \Psi_n^o(r_i) + \sum_{m \neq n} (E_n^o - E_m^o)^{-1} H_{n,m}(i) \Psi_m^o \quad (6)$$

$$H_{n,m}(i) = -j_i^2(t) (\bar{r}_i^3)^{-1} \langle \Psi_m^o | (r_i - \bar{r}_i) | \Psi_n^o \rangle \quad (7)$$

where Ψ^o is the Morse wave function, m_i is the mass of the i -th oscillator, \bar{r}_i the equilibrium H-H distance and $j_i(t)$ is the time dependent rotational angular momentum. E_n^o is the vibrational energy of the unperturbed Morse oscillators. Therefore, the centrifugal stretching term is explicitly included in this calculation and for molecules with small moment of inertia as in H_2 it is an important coupling term. The rate constant at a given temperature for a given transition $(n, n') = (v, v' | v_1, v_1')$ is defined by:

$$K_{n,n'}(T) = \left(\frac{8kT}{\pi\mu}\right)^{1/2} \left(\frac{T_0}{T}\right)^3 \int d(\beta U) \exp(-\beta U) \sigma_{n,n'}(\bar{U}, T_0) \quad (8)$$

where U is the total semiclassical energy, μ is the reduced collision mass. \bar{U} is the symmetrized total energy σ is the cross-section obtained by averaging the quantum amplitudes over a Boltzmann distribution of rotational states. The amplitudes for the transition (n, n') are obtained by averaging over a convergent number of trajectories defined by randomly selecting the initial action-angles for the two rotators. $\beta = 1/kT$.

The interaction potential for the H_2 - H_2 system is expressed as :

$$V(R, r_1, r_2, \theta_1, \theta_2, \gamma_1, \gamma_2) = V_{sr} + V_{qq} + V_{disp} \quad (9)$$

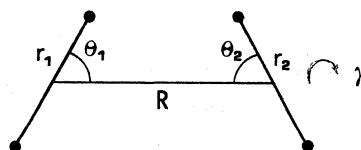


Figure 1. A schematic representation of diatom-diatom collision.

In expression (9) V_{sr} is the short-range potential, V_{qq} is the quadrupole-quadrupole interaction and V_{disp} is the dispersion term. The angles are shown in Figure 1. This potential has been previously fitted by Billing to ab initio values. It turns out that this potential together with the harmonic approximation used in Ref. 26 gives the rate constant $K(0,1|2,1)$ much larger when compared to recently reported experimental value. Here we use a slightly modified potential which gives good agreement with recent experimental beam measurements of the isotropic part of the potential. The rate constants obtained within the coupled state method and the new potential are in much closer agreement with the experimental results. In Fig. 2 it is reported the $V-T$ rate out of the first excited level as a function of the translational temperature. The existing experimental results have also been reported.

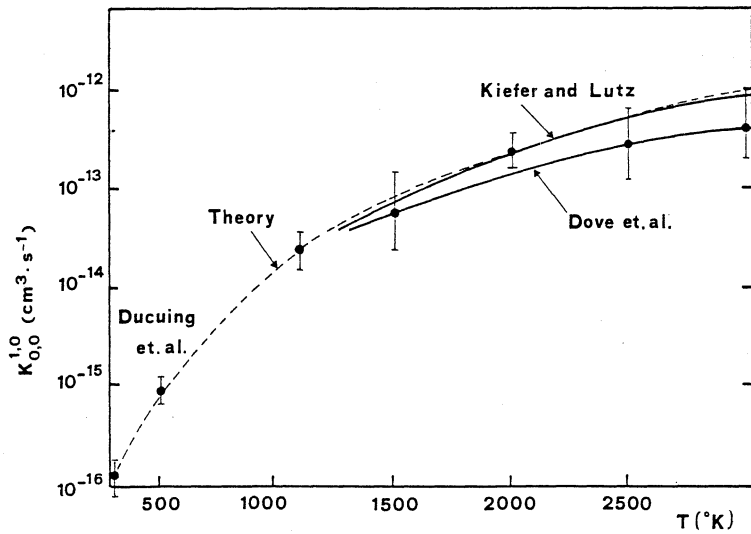


Figure 2. V-T $K(0,0|1,0)$ rate constant as a function of temperature. Comparison between theory (this work) and experiments is shown.

Of special interest is the agreement between the semiclassical value and the determination reported by Ducuing at 300K. In the low temperature regime the coupling between molecular rotations and vibrations becomes efficient so that the energy transfer in the vibrational motion can be enhanced when this term is properly introduced in the collisional model.

In Figure 3 we have reported the V-V rate constant $K(0,1|2,1)$ for the relaxation of the $v=2$ state in $H_2^{6,7}$. Two experimental determinations have also been reported.

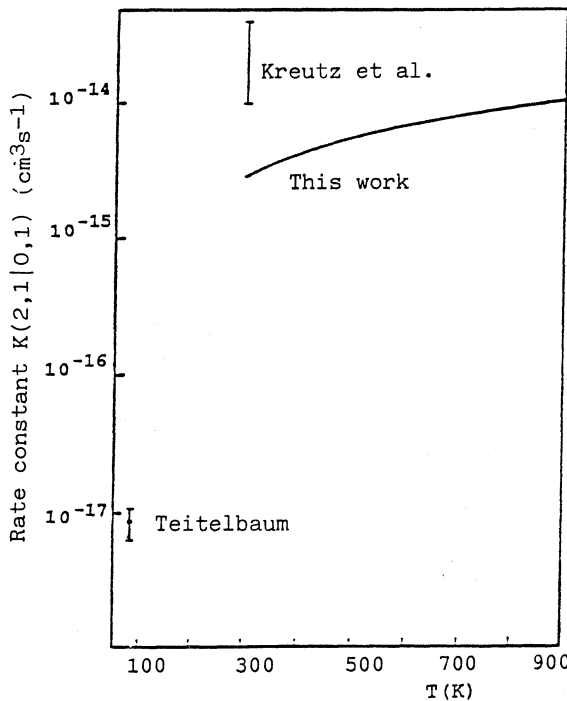
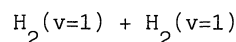
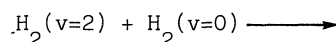


Figure 3. Theoretical (full curve) V-V rate constant for the process:



The experimental values by Kreutz et al. and by Teitelbaum have been reported

The semiclassical rate constant $K(0,1|2,1)$ at 300K is a factor of $\sqrt{6}$ two smaller than the experimental value reported by Kreutz et al.. We found a much better agreement for the V-T rate $K(0,0|2,1)$, as shown in Fig.4. It is generally not easy to get accurate V-V rate constants. In fact, due to the dependence upon the second derivative of the potential with respect to the internal coordinate r_i , the V-V cross-sections are very sensitive to the shape of the interaction potential. Therefore an r_i dependence of the potential better than that obtained in this work is needed.

In Figure 4 it is reported the V-T rate constant out of the v state for the processes:

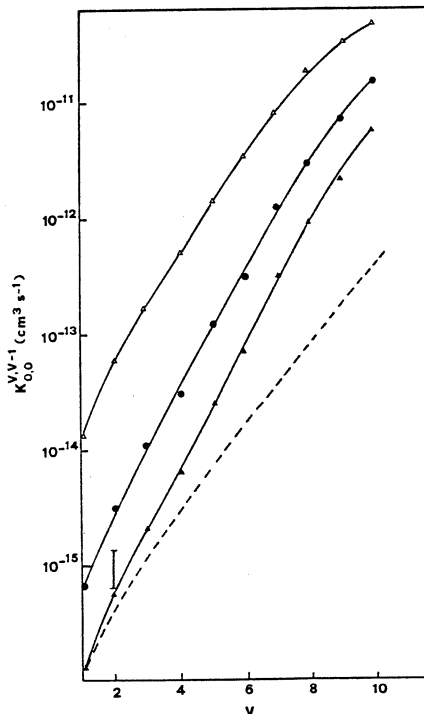
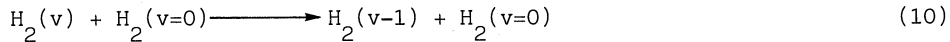
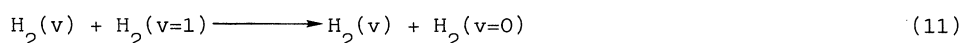


Figure 4. Semiclassical deactivation rate constant $K(0,0|v,v-1)$ for process (10) as a function of v and the temperature $T=300k(\Delta), 500K(\bullet)$ and $1000K(\triangle)$. The vertical bar shows the experimental value at 297K. The dashed curve shows the SSH v-scaling.

The semiempirical SSH scaling approximation does not reproduce the semiclassical trend in the full range of v. At high v the SSH predicts rate constants which are one order of magnitude smaller compared to the semiclassical results. The large dispersion of experimental values reported in Ref.6 indicates the difficulty in determining accurate rates for the relaxation of excited states, even in such refined experiments.

Figure 5 shows the V-T deactivation rate of the v=1 state in collisions with vibrationally excited H_2 :



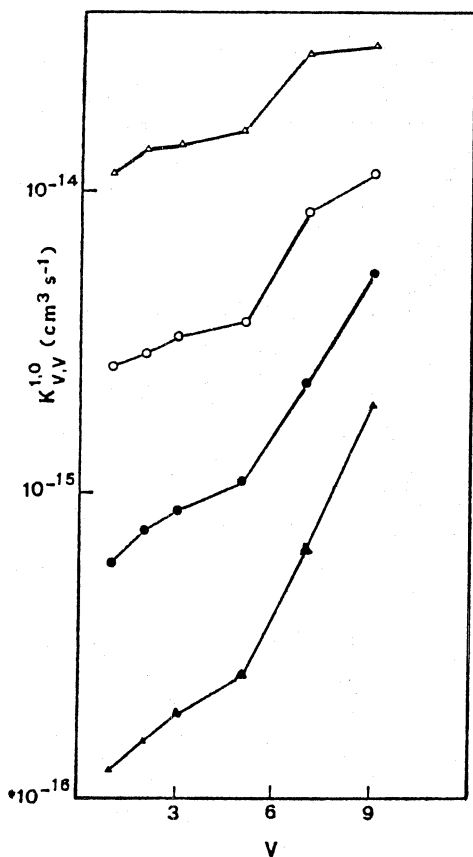
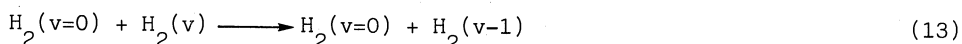
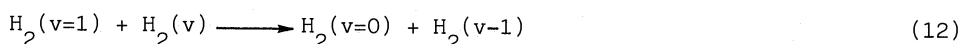


Fig.5. Semiclassical rate constants for vibrational deactivation of $H_2(v=1)$ colliding with vibrationally excited $H_2(v)$ as a function of temperature $T(K)=300(\blacktriangle), 500(\bullet), 700(\circ), 1000(\triangle)$.

The energy mismatch for processes (11) does not depend on the v-state, nevertheless these results show that the rate constants have such a dependence. This result has an explanation²¹ and it is one of the most interesting behaviour of the vibrational energy transfer in H_2 .

Figure 6 shows the V-V $K(1,0|v,v-1)$ and V-T $K(0,0|v,v-1)$ rate constants for the processes:



The rate constants are reported as a function of v at $T=300K$. The resonant V-V rate is not the highest V-V rate, instead there is a broad maximum around $v=5$. It is worth noting that the V-V energy exchanges dominate in the region of the medium-lying vibrational states, while the V-T relaxation is predominant in the region of highly excited states.

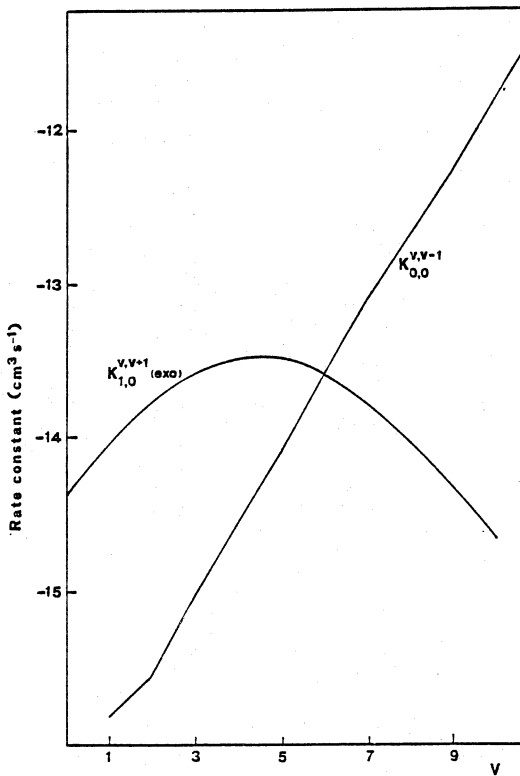


Figure 6. Exothermic V-V and V-T rate constants for processes (12) and (13) as a function of v . The translational temperature is $T=300K$.

In Ref. 22 we have also reported V-V rate constants for double quantum transitions involving high vibrationally excited levels. At $T=300K$ the rate constant for the two-quantum transitions $(9,7|0,1)$ is one order of magnitude higher than the corresponding single quantum rate $K(9,8|0,1)$. This is quite a general behaviour: in the region of high vibrational levels the multiquantum transitions can be of the same importance as the single quantum transitions.

VIBRATIONAL RELAXATION AND DISSOCIATION IN $H_2(v,j)-Cu$ INTERACTIONS

When the dynamical probabilities for collisional processes (3),(4) are to be computed, then the first step is the search for an accurate potential energy surface (PES). An analytical PES has been fitted²⁴ to the ab initio points reported in a cluster SCF-CI calculation³¹. The phonon forcing needed in the semiclassical calculations is then obtained by expressing the potential as a sum of pair-wise H-Cu interactions. It turns out that the derived PES is very site dependent (see Fig.7), which explains the difficulty in interpreting the H_2-Cu interactions in terms of a one dimensional activation barrier.

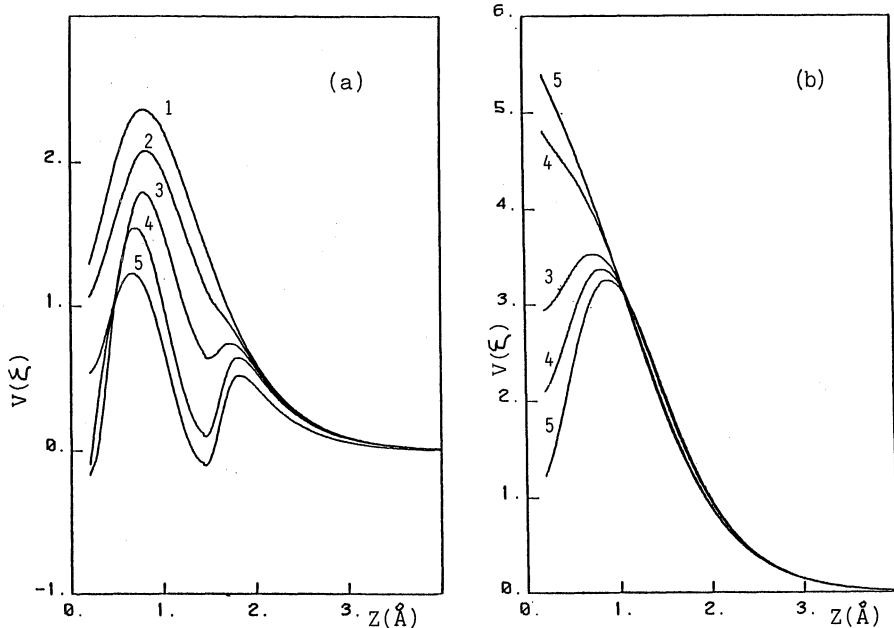


Figure 7a,b. $\text{H}_2\text{-Cu}$ potential interaction in unit of ξ with H_2 interacting perpendicular (a) and parallel (b) at the bridge site as a function of molecule-surface distance z and H-H bond distance.

(a): $R_{\text{HH}}(\text{\AA})=0.8, 0.9, 1.0, 1.2, 1.4$ curve 1 to 5. (b): $R_{\text{HH}}(\text{\AA})=0.7, 0.9, 1.1, 1.7, 2.1$, curve 1 to 5. $1\xi=100\text{Kcal/mol}$.

The barrier heights in the PES also show a remarkable dependence on the r bond distance in H_2 : as r increases the barrier height usually decreases. The barrier of H_2 in the vibrational ground state is high in most configurations, but in some configurations it may be as low as 1.0eV. Anyway, the barriers are in accord with the ab initio ³¹¹.5eV value, the 0.9eV found for $\text{H}_2\text{-}(\text{Cu})$ ¹³ and the 0.9eV jellum model adjusted¹². It is in agreement with the experimental value recently reported¹⁷, but appreciably higher than the 0.2-0.5 activation energies claimed in early investigations^{11,15}. A light molecule like H_2 will have a large probability to tunnel through the physisorption and chemisorption potential barriers, entering into a bound state and dissociates. In Ref.23 it has been computed the dissociation probability $P(v, E)$ due to tunneling as a function of the vibrational state v and the impact energy E .

$$P(v, E) = \int_{R_-}^{R_+} dR \Psi_v^2(R_{\text{H-H}}) T_R(R_{\text{H-H}}, E) \quad (14)$$

Ψ is the vibrational wave function, R_- and R_+ are the inner and outer turning points respectively. T_R is the transmission coefficient through the first two barriers. In Figure 8 it is shown $P(v, E)$ for $\text{H}_2(v, j=0)$ placed perpendicular at the fourfold site of $\text{Cu}(001)$. We note that, due to the strong dependence of the barrier heights to the H-H distance, the chemisorption probability due to tunnelling increases rapidly with the

Figure 8. Chemisorption probability $P(v, E)$ due to tunnelling through the first two energy barriers as a function of v and the impact energy E . H_2 is placed perpendicularly in the four-fold site.

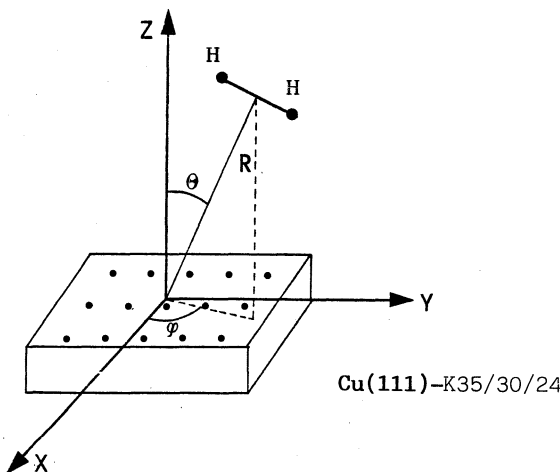
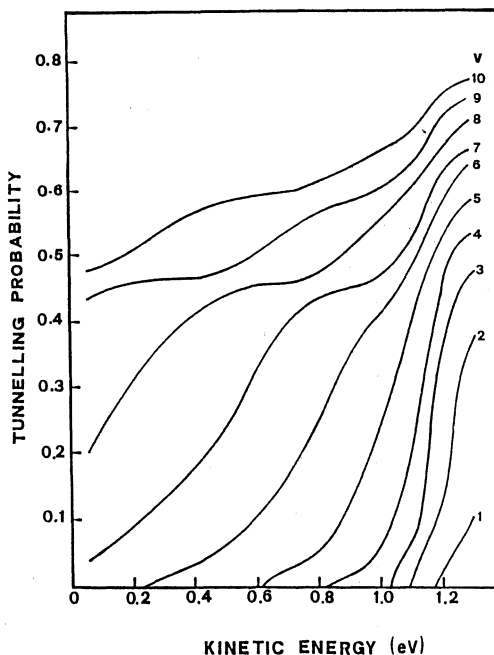


Figure 9. A schematic 3D representation of H_2 colliding with a solid surface.

vibrational quantum number v . Furthermore, tunnelling contributes substantially in lowering the energy barrier to dissociation. It appears as the dissociation of H_2 occurs mainly through tunnelling.

In the remaining part of this work we discuss the results obtained by classical trajectory calculations for H_2 propagating in the gas-phase or in the surface interface.

In the trajectory calculations²⁴, the translational and internal motions of H_2 are treated classically, by defining an 'effective' dynamical Hamiltonian. The phonon modes of the lattice atoms are quantized and treated within the harmonic approximation^{20,32}. The effective additional hamiltonian which couples the dynamics of the molecular motions to the dynamics of the phonons is derived and expressed as:

$$V_{\text{add}} = \sum_k \eta_k(t) V_k^{(1)} \quad V_k^{(1)} = \left. \frac{\partial V_0}{\partial Q_k} \right|$$
(15)

This dynamical potential depends upon time and surface temperature. $V_k^{(1)}$ is the first derivative of the potential with respect to the k -th normal coordinate, η_k is the phonon excitation strength of the k -mode.

In Ref.20 an additional term is included in V_{add} which accounts for the electron-hole pair excitation mechanism in the metal. It comes out that, although both mechanism should be in principle retained in the dynamics, dissociation is mainly due to the phonon excitation in Cu.

The dynamical probabilities for the inelastic and dissociative collisions have been computed as a function of the incident angles (Θ, φ) shown in Figure 9, the impact kinetic energy and the initial internal state (v, j). The surface temperature is kept to 300K.

In Table 1 we have reported the dissociation probability for H_2 in a given initial roto-vibrational state (v, j) as a function of the impact energy E_{kin} for two values of the incident angle.

Table 1. Dissociative chemisorption probability P_{diss} as function of the kinetic energy E_{kin} and the initial internal state (v, j). Eint is the average energy transferred to the phonons, (v', j') are the final actions (in unit of \hbar) for the reflected molecules

$\theta = 0^\circ$

v	j	E_{kin}/eV	P_{diss}	v'	j'	E_{int}/eV
0	0	1.55	0.00	0	1.1	0.124
2	0	1.55	0.30	1.3	7.4	6.78(-2)
5	0	1.00	0.44	4.3	4.0	3.99(-2)
5	5	1.00	0.90	2.7	10.0	3.91(-2)
6	0	0.20	0.00	5.9	0.8	6.46(-3)
6	5	0.20	0.00	5.7	5.5	6.96(-3)
.....						

$\theta = 45^\circ$

v	j	E_{kin}/eV	P_{diss}	v'	j'	E_{int}/eV
2	0	1.55	0.00	2.0	1.2	2.54(-2)
5	0	1.00	0.00	4.9	0.9	1.60(-2)
5	5	1.00	0.17	4.4	5.4	1.84(-2)
6	0	0.20	0.00	5.8	0.6	2.40(-3)
6	5	0.20	0.00	5.7	5.5	1.78(-2)
6	0	0.50	0.00	6.0	0.7	7.71(-3)

$\star 6.78(-2) = 6.78 \times 10^{-2}$

Inspection of Table 1 shows that the dissociation probability has a strong dependence on the angle. P_{diss} increases with decreasing the incident angle, and this is in agreement with the experimental findings.¹⁵ For H_2 in the ground vibrational state, the molecule does not dissociate in the energy range explored here. This is in contrast with the results reported in Ref.15, where $\text{H}_2(v=0)$ apparently dissociates at much lower energy(0.2eV), but in agreement with the most recent results of Ref.17. The energy transferred to the surface phonons appears to be small, due to the large mass difference between the H-atom and the lattice atoms.

Table 1 also shows that, at small kinetic energy the vibrational quenching remains negligible, though it increases with decreasing the incident angle. Nonetheless a complex excitation-deexcitation mechanism is acting when the molecule comes closer to the surface, as it is shown in Figure 10,11.

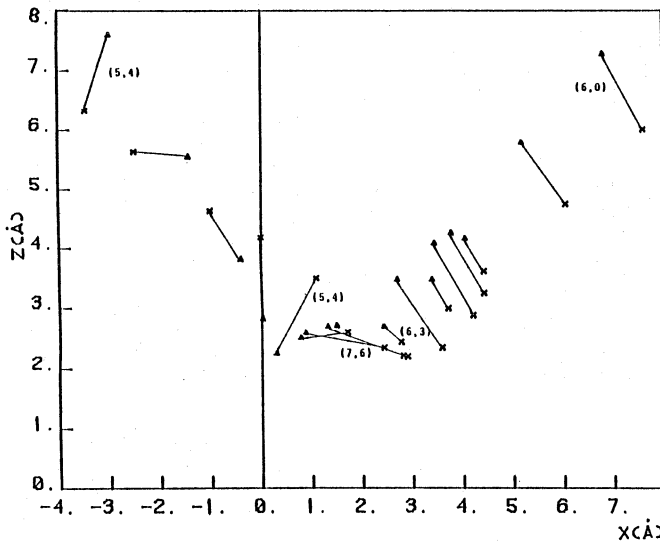


Figure 10. A collision trajectory where H_2 in the initial state $(v,j)=(6,0)$ is quenched to $v=5$ and rotationally excited to $j=4$. The approach angle is $\theta=45^\circ$, the initial kinetic energy is 0.2eV. Numbers in parenthesis are the instantaneous v and j values

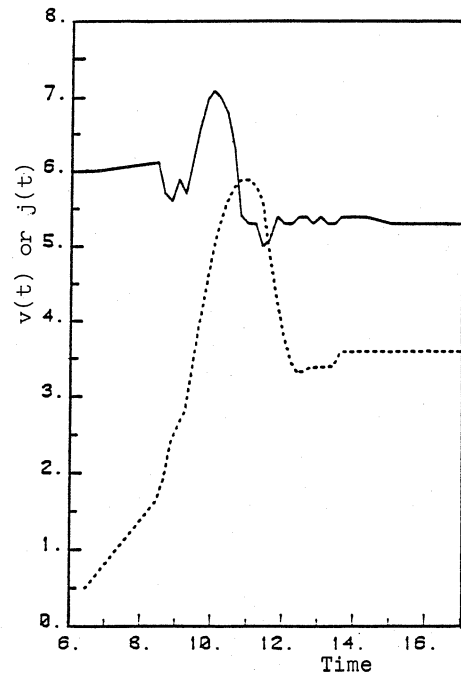


Figure 11. Rotational $j(t)$ and vibrational $v(t)$ action in unit of \hbar as a function of time (in unit of 10^{-16} s) for the trajectory plotted in Fig.10.

On the basis of the trajectory analysis the general conclusion we can draw is that the Cu surface is quite inert toward dissociation and vibrational quenching of H₂. This is in agreement with recent experimental results^{33,34}. H₂ has a low dissociation probability, unless it is produced in the gas-phase in hot vibrational and translational states. This is due to the high energy barriers to dissociation exhibited by the PES: from 1.0eV up to 3.0eV depending on the absorption site and the H-H bond distance.

Moreover, the dissociation mechanism is direct: the molecule dissociates in the gas phase before a precursor absorbed state is formed. Atom recombination at the surface has not been considered in this work. However, since the Hamilton equations of motion are invariant under time reversal operation, qualitative considerations can be drawn by considering the recombination process (5) as reverse dissociative trajectories. Therefore, very likely, direct atom recombination will produce vibrationally excited molecules. Due to the insignificant vibrational quenching, the so formed molecules leaves the interfacial layer in the unperturbed vibrationally excited state. Indeed, this is what is experimentally found³³. A detailed analysis on the dynamics of atom reaction at surface, although related to a different chemical system, can be found in Ref.³⁵.

ACKNOWLEDGMENTS

I wish to thank Gert Billing and Mario Capitelli for usefull discussions on the content of this paper. This work was partially supported by the 'Progetto Finalizzato Chimica Fine II' of the italian CNR.

REFERENCES

1. M.Cacciato,M.Capitelli,S.DeBenedictis,M.Dilonardo and C.Gorse
Topics in Current Physics 139,5(1986).Ed.M.Capitelli(Springer 1986)
2. J.N.Bardsley and J.M.Wadehra Phys.Rev.A20,1298(1979)
J.M.Wadehra Phys.Rev. A29,1061(1984)
3. M.Cacciato and M.Capitelli Chem.Phys. 55,67(1981)
R.Celiberto,M.Cacciato and M.Capitelli Chem.Phys. 133,369(1989)
J.R.Hiskes Comments At.Mol.Phys. 19,59(1984)
4. J.R.Hiskes and A.M.Karo J.Appl.Phys. 56,1927(1984)
J.R.Hiskes: this volume
5. T.A.Brunner and D.Pritchard Advan.Chem.Phys.50,589(1982) in
'Dynamics of Excited Staes',Ed.K.P.Lawley(Wiley,N.Y.1982)
6. T.G.Kreutz,J.Gelfand,R.B.Miles and H.Rabitz Chem.Phys. 124,359(1988)
7. H.Teitelbaum Chem.Phys.Lett. 106,69(1984)
8. R.B.Bernstein .'Atom-molecule collision theory. A guide for the experimentalists.',(Plenum,N.Y.,1979)
9. D.C.Clary J.Phys.Chem. 91,1718(1987)
10. M.Cacciato and G.D.Billing Chem.Phys.58,395(1981)
M.Cacciato,M.Capitelli and G.D.Billing Chem.Phys. 82,1(1983);
ibid 89,17(1984)
11. A.Gelb and Cardillo Surf.Sci. 59,128(1976)
12. A.De Pristo,C.Y.Lee and J.M.Hutson Surf.Sci. 169,451(1986)

13. J.Harris and S.Andersson Phys.Rev.Lett. 55,1583(1985)
14. M.Ha  d and S.Holloway Surf.Sci. 211,940(1989)
15. M.Balooch,M.J.Cardillo,D.R.Miller and R.E.Stickeney Surf.Sci. 46,358(1974)
16. G.Anger,A.Winkler,R.D.Rendulic Surf.Sci. 220,1(1989)
17. B.E.Hayden and C.L.A.Lamont Phys.Rev.Lett. 63,1823(1989)
18. K.Christman Surf.Sci.Report, vol.9(1988)
19. C.Gorse,M.Capitelli,M.Bacal,J.Bretagne and A.Lagan   Chem.Phys.117,177 (1987)
20. M.Bacal: this volume
21. M.Cacciatore,M.Capitelli G.D.Billing Chem.Phys.Lett. 157,305,1989)
22. M.Cacciatore,G.D.Billing:'Semiclassical Theoretical Study on the Vibrational Energy Transfer by H₂(v)-H₂(v') Collisions':to be published
23. M.Cacciatore,M.Capitelli,G.D.Billing Surf.Sci. 217,L391(1989)
24. M.Cacciatore and G.D.Billing: 'Dynamical Relaxation of H₂(v,j) on a Cu Surface': submitted for publication.
25. G.D.Billing in 'Non-equilibrium Vibrational Kinetics'.Ed.M.Capitelli Topics in Current Physics.39,85(1986),(Springer 1986)
26. G.D.Billing Chem.Phys.Lett. 97,188(1983)
G.D.Billing and M.Cacciatore Chem.Phys.Lett. 86,20(1982)
27. G.D.Billing Chem.Phys. 20,35(1977)
28. M.J.Norman,R.O.Watts and U.Buck J.Chem.Phys. 81,3500(1984)
29. M.M.Audibert,R.Vilaseca,J.Lakasik and D.J.Ducuing Chem.Phys.Lett. 31,232(1975)
J.E.Dove,D.G.Jones,H.Teitelbaum IV Symposium on Combustion,University Park, Pennsylvania 1972 (Pittsburg 1973)
J.H.Kiefer J.Chem.Phys. 48,2332(1968)
30. M.Cacciatore and G.D.Billing Chem.Phys.Lett. 94,218(1983)
Ph.Brechignac Chem.Phys. 34,119(1978)
31. P.Madhavan and J.L.Whitten J.Chem.Phys. 77,2673(1982)
32. G.D.Billing Chem.Phys. 74,143(1983)
33. R.I.Hall,I.Cadez,M.Landau,F.Pichou and I.Sherman Phys.Rev.Lett. 60,337(1988)
34. P.J.Eenshuista,J.H.M.Bonnie,J.Los and H.J.Hopman Phys.Rev.Lett. 40,341(1988)
35. G.D.Billing and M.Cacciatore Chem.Phys.Lett. 113,23(1985)

TRANSLATIONAL ENERGY DISTRIBUTION FUNCTIONS OF H AND H⁺ IN H₂

VOLUME DISCHARGES

M. Capitelli, R. Celiberto and M. Cacciatore

Dipartimento di Chimica Università di Bari
Centro di Studio per la Chimica dei Plasmi del
CNR-Bari (Italy)

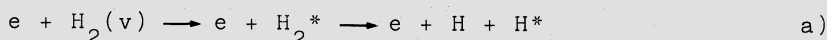
INTRODUCTION

In these last years large attention has been devoted to the nonequilibrium plasma kinetics of H₂ in multicusp magnetic plasmas, due to their wide use for the production of negative ions (H₂, D⁻)¹⁻³. The accepted mechanism for H⁻ production is dissociative attachment from vibrationally excited H₂ molecules (H₂(v)). Therefore the theoretical effort has been addressed to the understanding of numerous microscopic processes affecting the vibrational distribution of H₂(N_v). One of the open problems concerns the translational energy distribution function (TEDF) of atomic hydrogen and of protons, which can affect N_v. Usually it is assumed that the translational temperature of H and H⁺ are much higher than the corresponding one for H₂.

In this paper we present a calculation of TEDF of H and H⁺ coming from direct electron impact dissociation processes, emphasizing in particular the role of non equilibrium vibrational distributions of H₂ in affecting TEDF.

METHOD OF CALCULATION

Let us suppose that a beam of monoenergetic electrons impinges on a hydrogen plasma, the vibrational distribution of which is denoted by N_v. The electron beam can dissociate H₂(v) through direct dissociation mechanisms as well as through dissociative ionization, i.e. by processes:



Denoting by $\sigma_{\text{exc}}^i(\varepsilon)$ and $\sigma_{\text{ion}}^i(\varepsilon)$ the cross sections for dissociation and dissociative ionization linking the v th vibrational level of H_2 to the i th potential curve of H_2^* and H_2^+ , the nascent distribution can be written as :

$$F_{\text{H}}(E, \varepsilon) \propto \sum_i \sum_v N_v / N_{\text{tot}} \left[\sigma_{\text{exc}}^i(\varepsilon) (\text{FC})_v + \sigma_{\text{ion}}^i(\varepsilon) (\text{FC})_v \right]$$

$$F_{\text{H}^+}(E, \varepsilon) \propto \sum_i \sum_v N_v / N_{\text{tot}} \left[\sigma_{\text{ion}}^i(\varepsilon) (\text{FC})_v \right]$$

where $(\text{FC})_v$ denotes the Franck-Condon density, depending on E and ε and describing the overlapping of the v th vibrational wavefunction of the H_2 ground electronic state with the continuum wavefunction of the i th excited state. $(\text{FC})_v$ is calculated according to the δ function approximation. E and ε are the translational energy of heavy particles (H, H^+) and of electrons. N_v / N_{tot} is the fraction of molecules in v th vibrational level.

Cross sections for processes a,b have been discussed in refs. 4-6, where one can also find the different potential curves utilized in the calculations.

RESULTS

3a. TEDF for $\text{H}_2^*(n = 3, 4)$

Figure 1 shows the non equilibrium vibrational distribution of H_2 utilized for calculating F_{H}^2 and F_{H^+} .

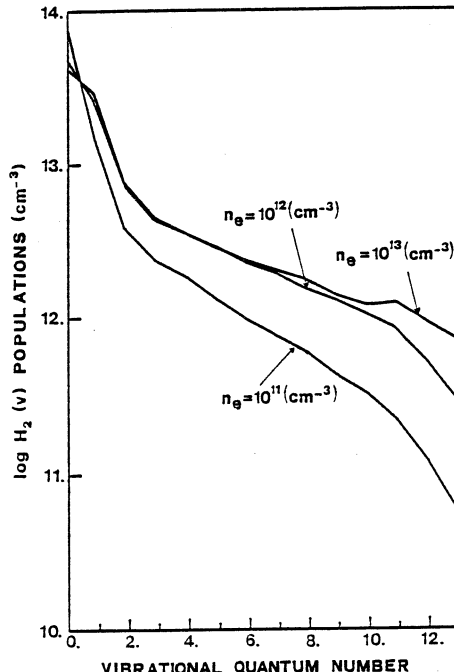


Fig.1 Non equilibrium vibrational distributions versus vibrational quantum number for different electron densities.

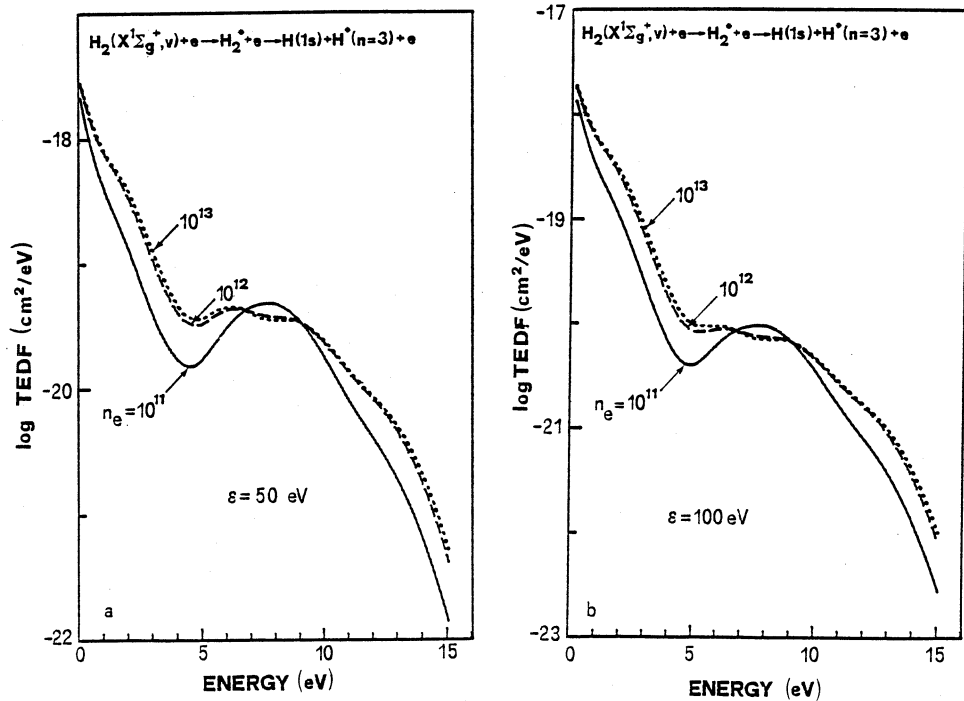


Fig.2a-b Translational energy distribution function of excited atomic hydrogen (principal quantum number $n = 3$) versus the translational energy of atoms at two electron energies (a: $\epsilon = 50$ eV; b: $\epsilon = 100$ eV).

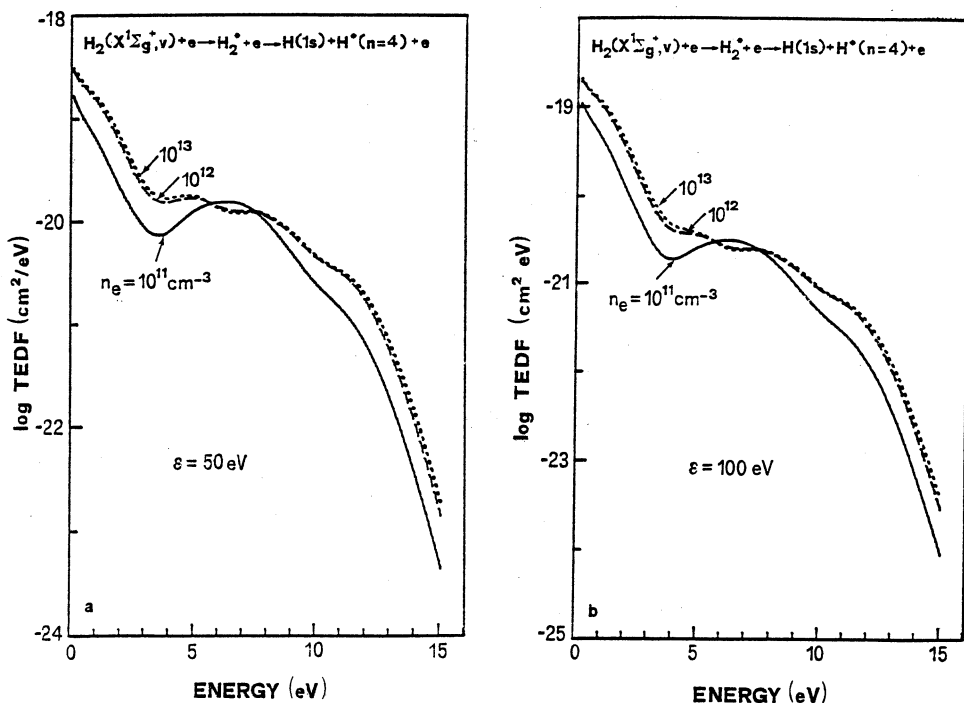


Fig. 3a-b Same as 2a-b for $H^*(n = 4)$.

Figures 2,3 a-b report calculated TEDF for $H^*(n = 3,4)$ for two electron impact energies ($\mathcal{E} = 50, 100$ eV). We note that in both cases TEDF presents two typical groups of atoms, cold and hot ones. Cold atoms come from dissociative processes over the repulsive part of bound electronic states, hot atoms coming from completely repulsive states. It is worth noting that the presence of vibrationally excited H_2 molecules, the concentration of which increases with increasing the electron density in the discharge (see fig.1) tends to fill the gap between cold and hot atoms in agreement with the results reported in ref. 4. In this reference one can find TEDF for $H^*(n = 1,5)$ obtained by considering different N_v .

3b. TEDF for H^+

Figure 4a,b reports the translational energy distribution function of protons as a function of the translational energy of H^-H^+ pair. Once again we note the appearance of cold and hot protons, coming respectively from $^2\Sigma_g^+$ and $^2\Sigma_u^+$ potential curves. Vibrational excited states affect TEDF of H^+ as in the case of H atoms i.e. they tend to fill the gap between cold and hot protons.

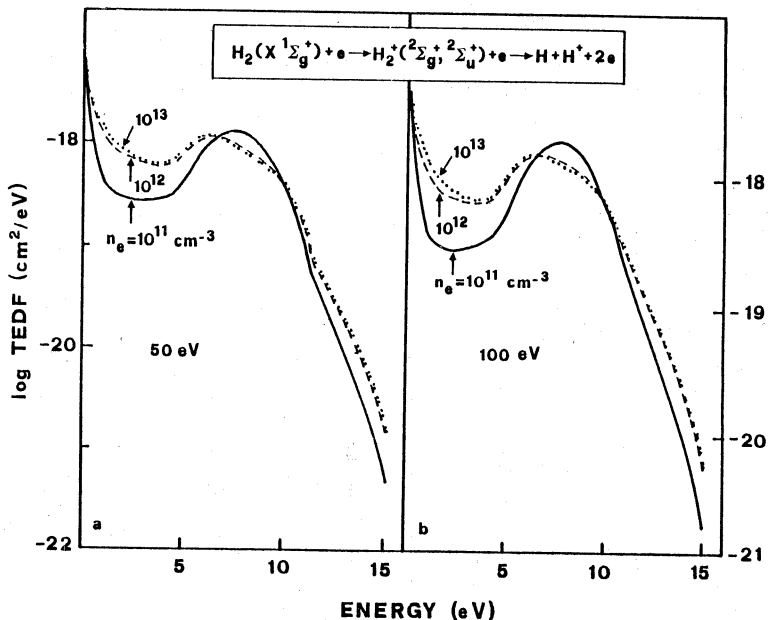


Fig.4a-b Translational energy distribution function of protons versus the traslational energy of H^-H^+ pair at two electron energies (a: $\mathcal{E} = 50$ eV; b: $\mathcal{E} = 100$ eV).

COMMENTS

The results presented in the different figures as well as those presented in ref. 4 show that highly non Maxwell translational energy distributions of H^* and H^+ are produced in H_2 discharge. These distributions will tend to be

thermalized even though experiments⁷ support the idea of these kinds of distributions after thermalization.

As for the accuracy of TEDF reported in figures 2,4a-b it depends 1) on the accuracy of the used cross sections, 2) on the neglection of indirect processes leading to H and H⁺.

The accuracy of cross sections has been discussed in ref. 5-6, where we have shown that our cross sections for H* production (n = 3) are accurate within a factor 2, while those leading to H*(n = 4) are accurate within a factor 5. A better accuracy can be predicted for dissociative ionization cross sections. More important is point 1) in deciding the reliability of calculated TEDF. Many authors in fact have

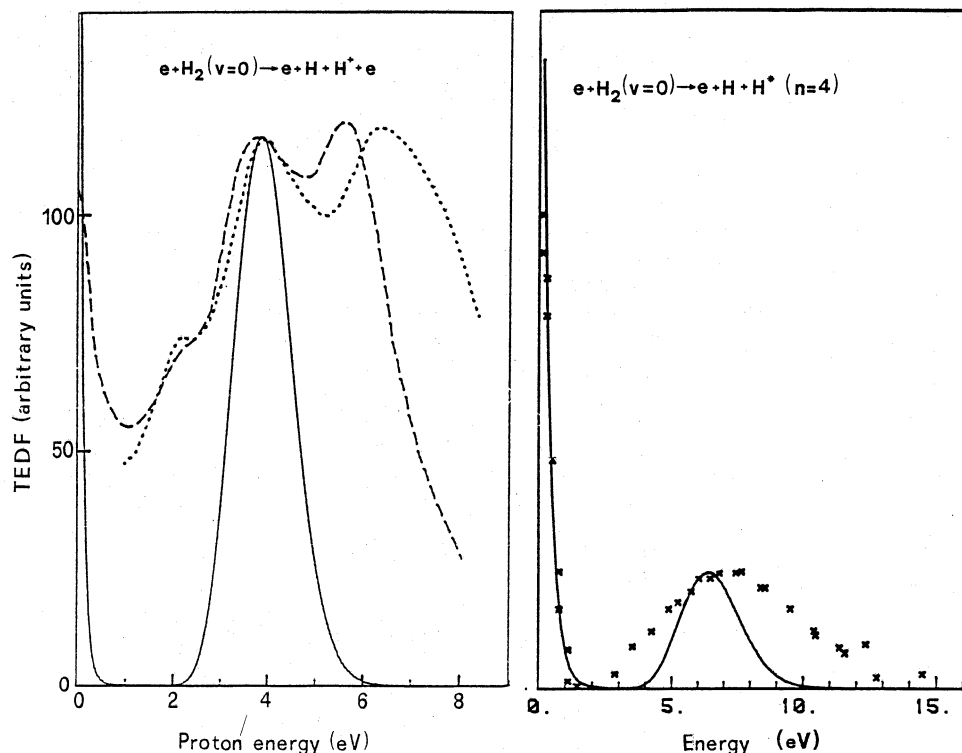


Fig.5 A comparison between theoretical (solid lines) and experimental (---ref.8;...ref.9) translational energy distribution functions for H⁺ ($\Sigma = 75$ eV). The data have been normalized to the experimental maximum at $E_{H^+} \approx 4$ eV.

Fig.6 A comparison between theoretical (solid lines) and experimental (x) translational energy distribution functions for H*(n=4). The data have been normalized to the experimental maximum.

emphasized the importance of indirect processes in affecting TEDF of H⁺ and H. This point is particularly true for H⁺ as can be appreciated by comparing our theoretical values with the corresponding ones of refs. 8-9. We see (fig. 5) that our calculated TEDF reproduce only two portions of experimental TEDF, the last being strongly structured by indirect processes

(in particular excitation of double excited states followed by autoionization). The situation appears better for TEDF of $H^*(n = 4)$ atoms, as can be seen in fig. 6 where we compare theoretical and experimental¹⁰ TEDF. In this case we can note that direct dissociation mechanisms account for a large portion of experimental translational energy distribution function. Note that the results reported in figs. 5-6 refer to transitions from $H_2^2(v = 0)$ and that the theoretical values have been normalized to the experimental ones.

As a conclusion we can say that the present TEDF could modify the rates involving H and H^+ colliding with $H_2(v)$. It has been infact shown¹¹ that $H - H_2(v)$ rates strongly depend on the translational temperature of atomic hydrogen. These rates have been calculated under the assumption of a Maxwell distribution function of atomic hydrogen. Use of the present TEDF could therefore modify $H - H_2(v)$ rates having important consequences on the modeling of H_2 discharges.

REFERENCES

- 1) C. Gorse, M. Capitelli, M. Bacal, J. Bretagne and A. Laganà: Chem. Phys., 117, 177 (1987).
- 2) J.R. Hiskes and A.M. Karo, J. Appl. Phys., 56, 1827 (1984); J. R. Hiskes and A. F. Lietzke, Proceedings of IAEA TMC Meeting, Culham 1987.
- 3) M. Bacal, this volume.
- 4) R. Celiberto, M. Cacciato, and M. Capitelli, Chem. Phys., 133, 369 (1989).
- 5) R. Celiberto, M. Cacciato, M. Capitelli and C. Gorse, Chem. Phys., 133, 355 (1989).
- 6) R. Celiberto, M. Cacciato, M. Capitelli and C. Gorse, Proceedings XIX ICPIG (International Conference on Phenomena in Ionized Gases) Belgrade (1989); Chem. Phys. (1990), in press.
- 7) M. Pealat, J. P. Taran, M. Bacal and F. Hillion, J. Chem. Phys., 82, 4943 (1985).
- 8) M. Landau, R. I. Hall and F. Pichou, J. Phys. B: Atom. molec. Phys., 14, 1509 (1981);
- 9) J. P. Johnson and J. C. Franklin, Int. J. Mass. Spectrom. Ion. Phys., 70, 393 (1980).
- 10) T. Ogawa and M. Higo, Chem. Phys., 52, 55 (1980).
- 11) A. Laganà, this volume.

NUMERICAL SIMULATION ON TANDEM NEGATIVE ION SOURCE

Osamu Fukumasa and Setsuya Ohashi

Department of Electrical Engineering
Yamaguchi University, Ube 755, Japan

INTRODUCTION

It is commonly accepted that in a hydrogen volume source the negative hydrogen ions H^- are formed by dissociative attachment of slow plasma electrons e to vibrationally excited molecules $H_2^*(v'')$, where v'' is the vibrational quantum number.^{1,2} The vibrational excitation is attributed to electron impact excitation of hydrogen molecules H_2 by the fast primary electrons e_f in the discharge.³ To clarify the mechanism of H^- production and to show the dependence of H^- ions on plasma parameters concretely, we have proposed a set of particle balance equations for a steady-state hydrogen plasma in a single chamber system.^{4,5} According to our recent simulation results,⁶⁻⁸ most H^- ions are produced by the two-step process mentioned above, i.e. $H_2 + e_f \rightarrow H_2^*(v'') + e_f ; H_2^*(v'') + e \rightarrow H^- + H$. Besides, the presence of e_f with energies E_{fe} in excess of 40 eV is reasonable for $H_2^*(v'')$ production while plasma electrons e with electron temperature $T_e \approx 1$ eV are optimum for H^- formation.

In order to improve H^- yield, therefore, it is efficient to divide the entire source chamber into two parts, i.e. an arc discharge with e_f and an extraction region with low T_e . To this end, a water-cooled permanent magnetic filter is installed,⁹ and it divides the source chamber into two parts, i.e. a tandem two-chamber system.

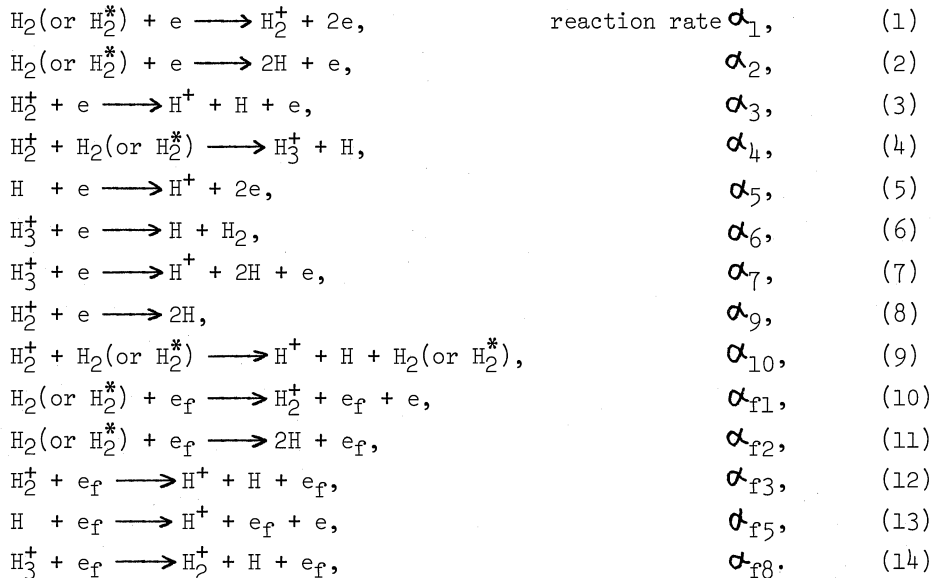
Optimization of the tandem system has been discussed theoretically by several authors.^{1,10,11} Hiskes et al.¹⁰ discussed the feasibility of the tandem system, and showed the optimum size of the source changing the densities of molecules, atoms and plasma as parameters. So far as we know, however, superiority of the tandem system to the single chamber system or the role of the magnetic filter is not clarified well although enhancement of extracted H^- current has been observed experimentally in a multicusp source with the magnetic filter.^{9,12}

In this paper, we calculate the dependences of H^- and $H_2^*(v'')$ productions on some key parameters(including the role of the magnetic filter), and discuss the effectiveness of the tandem system compared with the single chamber system. Furthermore, application of the extended multi-chamber model to the real ion sources is attempted to study H^- production further.

Figure 1 shows the tandem two-chamber model. In order to study H^- production in the tandem system, we divide the single chamber of volume $L \times L \times L$ into two parts. Two chambers of volume $L \times L \times L_1$ (the first) and $L \times L \times L_2$ (the second) contact each other through the region of the magnetic filter, where $L_1 + L_2 = L$. In both regions, there are 4 ion species (H^- , H^+ , H_2^+ and H_3^+), 2 electron species (e and e_f) and 3 species of neutral particles (H , H_2 and H_2^*). For simplicity, we assume that only one species of $H_2^*(v''=7)$ is present because we have confirmed that optimum level of v'' for H^- production ranges from 7 to 9.^{6,8} However, this simplified model is sufficient to discuss the parameter dependence of H^- production and the effectiveness of the tandem system.

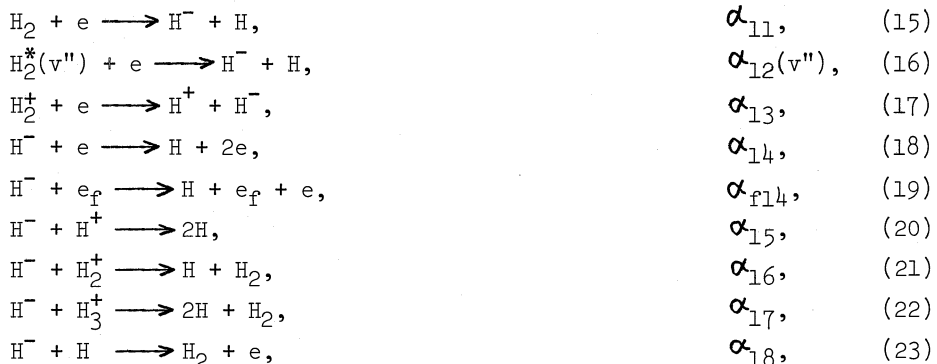
Reaction Processes

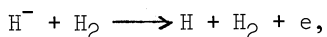
The model considers 27 important collision processes for the production of H^- , positive ions, H and H_2^* . First of all, the reaction processes concerning production of positive ions are presented.



For loss processes in the balance equation of H_2^* , we take into account dissociation, ionization, etc.. As is shown above, however, we use the same values of reaction rates as those for H_2 .

In the next place, the reaction processes concerning H^- production are as follows:





α_{19} . (24)

In the previous reports,⁴⁻⁸ we used the rate coefficient α_{15} ($= 5 \times 10^{-7} \text{ cm}^3/\text{s}$) which was five times as large as the coefficients α_{16} and α_{17} . According to the results by Fussen and Kubach,¹³ in the present simulation, we use the reduced α_{15} by a factor five, i.e. the same value as α_{16} and α_{17} .

Finally, the reaction processes for $H_2^*(v'')$ formation are as follows:



H_2^* production due to neutralization probabilities p_2 and p_3 ,
of molecular ions H_2^+ and H_3^+ ,



Basic Equations

We assume that e_f is present only in the first chamber because the role of the magnetic filter is to impede e_f to come into the second chamber. Particles except e_f are assumed to move freely between two chambers without being influenced by the filter. Amount of particles passing through the filter is treated in the form of flux nv , where n and v are the particle density and average velocity, respectively.

The six rate equations for H , H_2^* , H^- , H^+ , H_2^+ and H_3^+ are derived by taking into account the reaction processes and the above mentioned interaction between two chambers. Besides these, there are two boundary conditions, i.e. the charge neutrality and the particle number conservation. Then, for the tandem two-chamber system, a set of 16 equations are solved numerically as a function of plasma parameters. They are the electron densities of the two chambers $n_e(1)$ and $n_e(2)$, electron density ratio $n_e(2)/n_e(1)$, fast primary electron density $n_{fe}(1)$, electron temperatures of the two chambers $T_e(1)$ and $T_e(2)$, and filter position($L_1:L_2$).

NUMERICAL RESULTS AND DISCUSSION

First of all, in Fig.2, we show a concrete example of the dependences of H^- and H_2^* productions on n_e for the tandem system case. This result is obtained by varying $n_e(1)$, the electron density of the first chamber, on the assumption that other numerical conditions are kept constant, i.e. $L_1:L_2 = 15:15 \text{ cm}$, $n_e(2)/n_e(1) = 1.0$, hydrogen gas pressure $p = 5 \times 10^{-3} \text{ Torr}$, $E_{fe} = 40 \text{ eV}$, $n_{fe}(1)/n_e(1) = 0.1$, $T_e(1) = 5 \text{ eV}$, $T_e(2) = 1 \text{ eV}$, and e_f is absent in the second chamber. From the view point of the development of negative ion source, it is important to enhance $H^-(2)$ density. The magnetic filter can change and control plasma parameters in the second chamber, i.e. $n_e(2)/n_e(1)$, $T_e(2)$ and $T_e(2)/T_e(1)$. Namely, filter position and filter strength affect $H^-(2)$ density. Relationships between $H^-(2)$ and some key plasma parameters are discussed in the followings.

Dependences of H^- and H_2^* on Some Key Parameters

Figure 3 shows the effect of filter position on $H^-(2)$. With decreasing L_2 , $H_2^*(2)$ increases in its density, and then $H^-(2)$ also increases. As e_f is absent in the second chamber, collisional excitation of H_2^* caused by e_f is neglected in this region. The source of $H_2^*(2)$ is mainly the incoming flux from the first chamber across the filter. In the rate equation for $H_2^*(2)$, this source term is given by $n^*(1)v^*(1)S_f/V_2 = n^*(1)v^*(1)/L_2$, where S_f is filter area, V_2 volume of the second chamber, $n^*(1)$ density of $H_2^*(1)$, and $v^*(1)$ mean velocity of $H_2^*(1)$. With decreasing L_2 , effect of this source term becomes large. Then, $H_2^*(2)$ and also $H^-(2)$ increase. It is observed

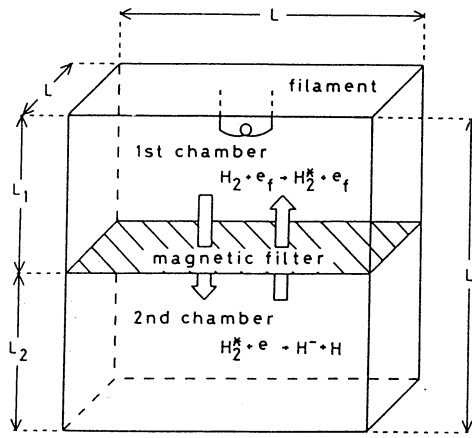


Fig.1. Simulation model for the tandem two-chamber system.

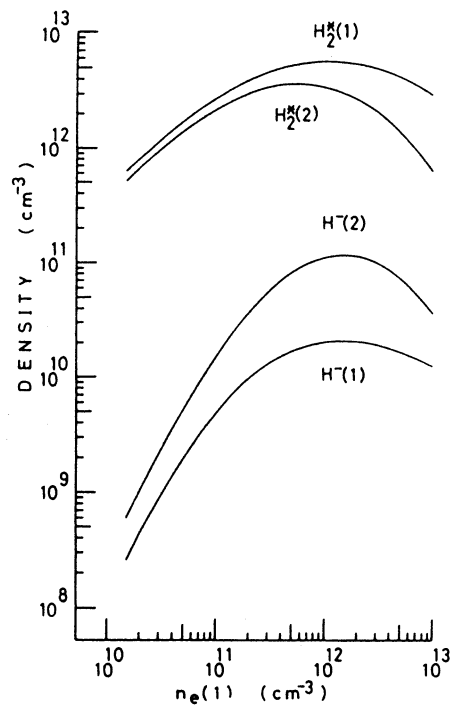


Fig.2. Numerical result of the tandem system: n_e dependence of $H^-(1)$, $H^-(2)$, $H_2^*(1)$ and $H_2^*(2)$.

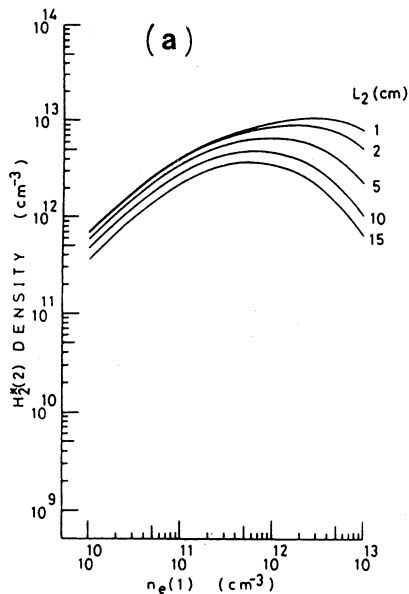
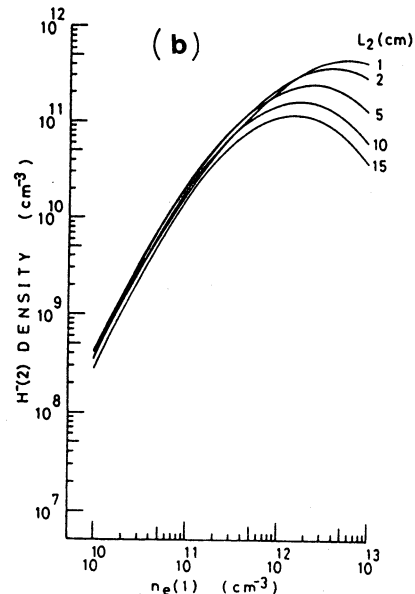


Fig.3. Effect of filter position on $H^-(2)$ production: (a) H_2^* and (b) H^- . Numerical conditions are the same as those in Fig.2.



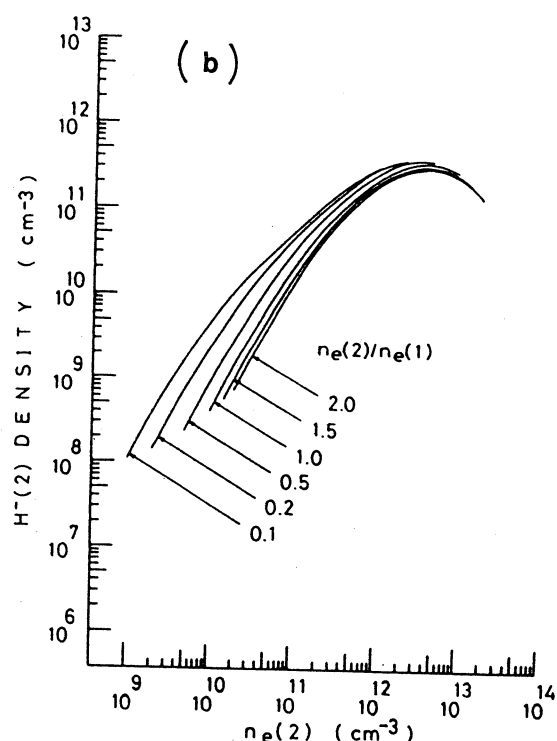
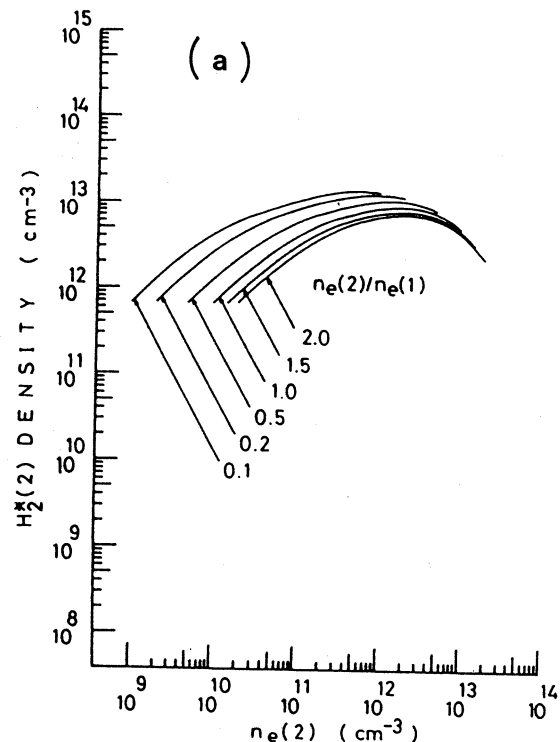


Fig.4. Effect of density ratio $n_e(2)/n_e(1)$ on $H^- (2)$ production: (a) H_2^* and (b) H^- . $L_1:L_2=28:2 \text{ cm}$. Other conditions are the same as those in Fig.2.

that the extracted H^- current increases steadily as the filter is moved toward the extraction electrode.^{12,14,15}

Figure 4 shows the effect of electron density ratio $n_e(2)/n_e(1)$ on $H^-(2)$ production. $H_2^*(2)$ and $H^-(2)$ densities are plotted as a function of $n_e(2)$. In real ion sources, $n_e(2)$ is much lower compared to $n_e(1)$. It is realizable that $n_e(2)/n_e(1) = 0.1-0.2$. As is shown previously for the single chamber case,⁴ there is a certain optimum value in n_e , i.e. $n_e(2) \approx 2 \times 10^{12} \text{ cm}^{-3}$.

Figure 5 shows the dependence of $H^-(2)$ production on $T_e(2)$, where $T_e(1)$ is kept constant at 5 eV. With increasing $T_e(2)$, $H^-(2)$ density reaches maximum at $T_e \geq 1 \text{ eV}$, and then decreases monotonically. This tendency is quite similar to that of the single chamber system.^{7,8} The reaction rate of the process (16) has a maximum value at $T_e = 0.5-1.0 \text{ eV}$ and then decreases with T_e while the rate of the process (18) increases abruptly with T_e . Therefore H^- density decreases with T_e above 1 eV.

Figure 6 shows the effect of e_f on $H^-(2)$ production. With increasing $n_{fe}(1)/n_e(1)$ up to 40 %, both $H_2^*(2)$ and $H^-(2)$ increase monotonically. This feature is one of the merits of the tandem system. In the single chamber case,⁶⁻⁸ H^- density reaches a maximum at some optimum value, i.e. $n_{fe}/n_e = 0.1-0.2$. At larger n_{fe}/n_e , e_f destroys H^- ions through the process (19) with high reaction rate.

So far, we do parametric study on H^- and H_2^* productions in the tandem system. However, the approach to modeling H^- volume sources is based on several simplifying assumptions :

1. The fast primary electrons are considered as monoenergetic.
2. The kinetics of H_2^* is studied neglecting two important processes, i.e. quenching in collisions with atomic hydrogen and excitation in collisions with plasma electrons.

In order to discuss this point, we have now finished improving the present model. According to the preliminary results, inclusion of effects of $H-H_2^*$ de-excitation collisions, $e-H_2$ excitation collisions and flat distribution of fast electrons couldn't change remarkably the dependences of $H^-(2)$ production on plasma parameters. Details will be reported elsewhere in the future.

Lastly, to discuss effectiveness of the tandem system, H^- density in the second chamber(i.e. the extraction chamber) is compared with H^- density in the single chamber system. In the single chamber case,^{7,8} optimum conditions for H^- yield are $T_e \geq 1 \text{ eV}$, $E_{fe} = 40 \text{ eV}$ and $n_{fe}/n_e \geq 0.1$.

Figure 7 shows the density ratio $H^-(2)/H^-(S)$ as a function of $n_e(1)$ for two cases, i.e. $n_e(2)/n_e(1) = 0.2$ and 1.0. Parameter is T_e in the single chamber case. If $H^-(2)/H^-(S)$ is larger than unity, H^- yield in the tandem system is more efficient than one in the single chamber system. Experimentally, it is difficult for the single chamber system to produce source plasma with low $T_e (\geq 1 \text{ eV})$ and with high $n_{fe}/n_e (\geq 0.1)$. By taking into account that T_e in the source plasma of the tandem system is from 3 to 5 eV,¹⁶ we assume that $T_e(S)$ should be from 3 to 5 eV. In this case, $H^-(2)$ is much higher than $H^-(S)$ in a high density region.

Application of the Present Model to the Real Ion Sources

In the previous section, we have assumed that plasma parameters(i.e. n_e , T_e etc.) in both first and second chambers are kept constant at certain values throughout the respective regions. However, in order to discuss or explain the experimental results of H^- production in detail, we must take into account spatial distributions of n_e and T_e . To this end, we have attempted to extend the present model, i.e. an idea of a multi-chamber model.¹⁶ As a concrete example, we apply the multi-chamber model to the JAERI Bucket

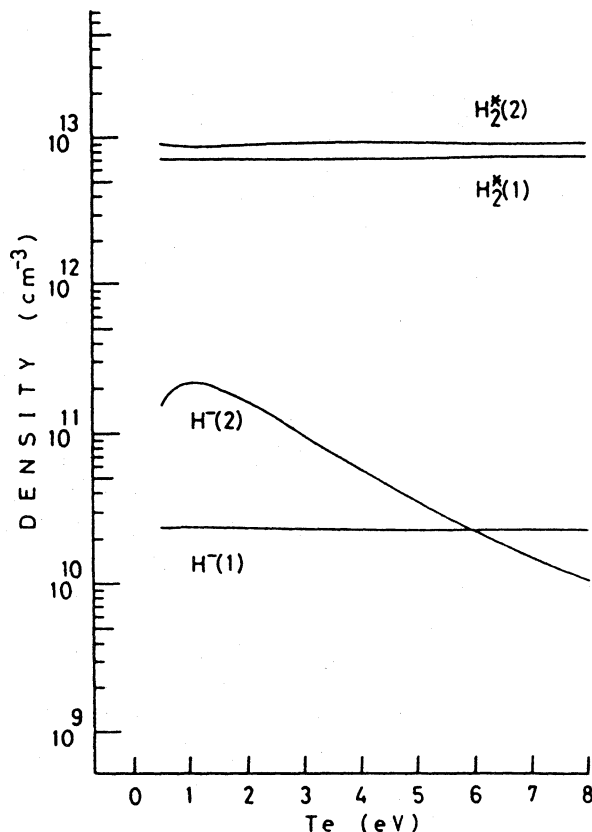


Fig.5. $T_e(2)$ dependence of $H^-(2)$ production. $L_1:L_2=28:2$ cm and $n_e(2)/n_e(1)=1.0$. Other conditions are the same as those in Fig.2.

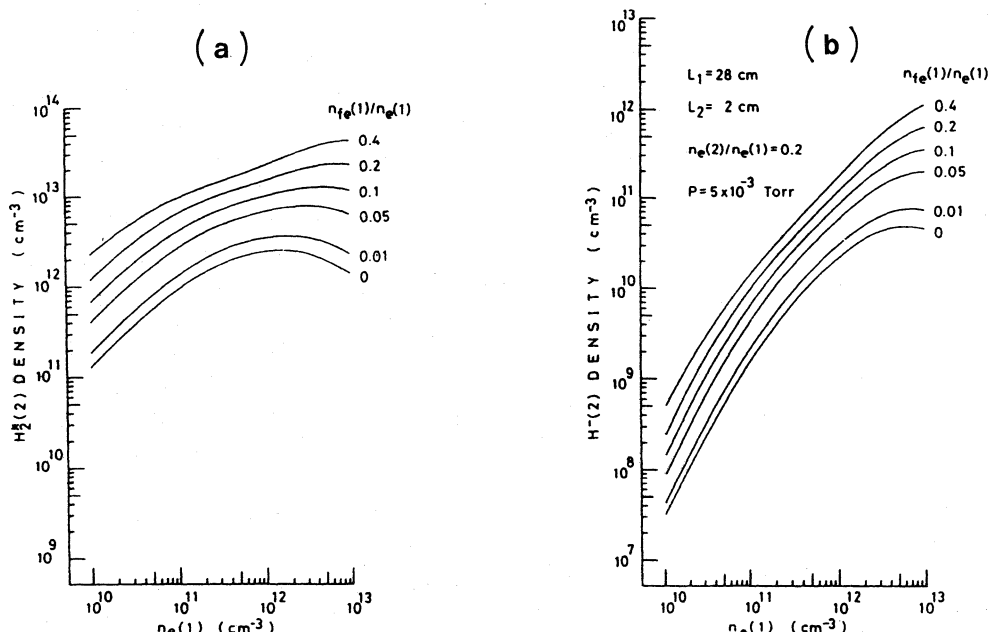


Fig.6. Effect of primary electrons on H_2^* and H^- productions: (a) H_2^* and (b) H^- .

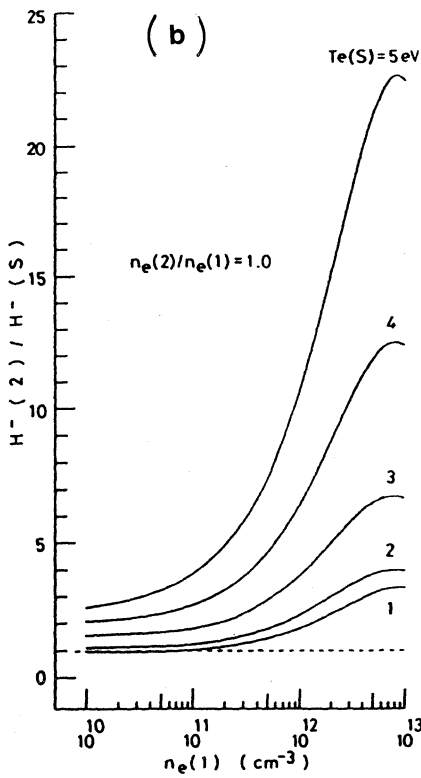
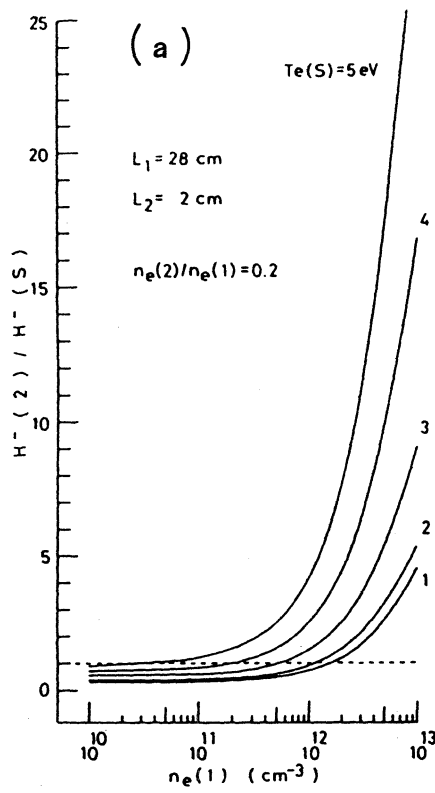


Fig.7. Illustration of effectiveness of the tandem system: Density ratio $H^-(2)/H^-(S)$ versus n_e .

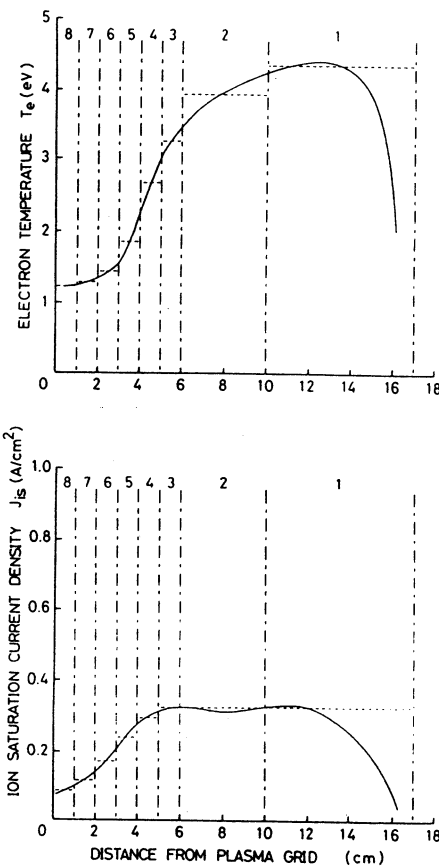


Fig.8. Plasma parameters of the JAERI Bucket Source.

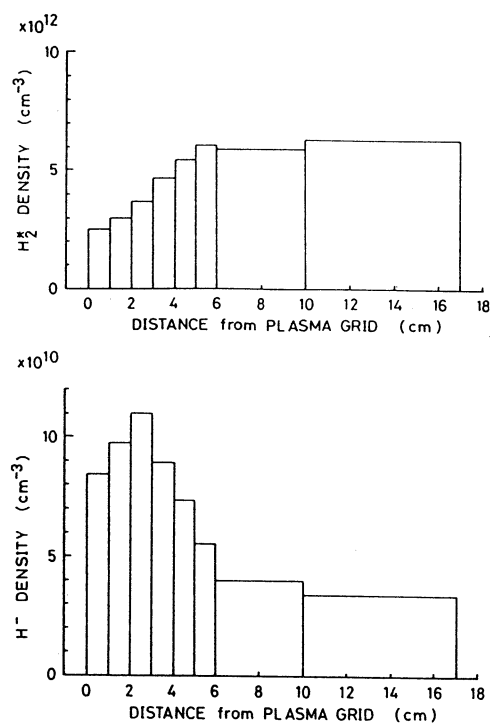


Fig.9. Numerical results corresponding to Fig.8.

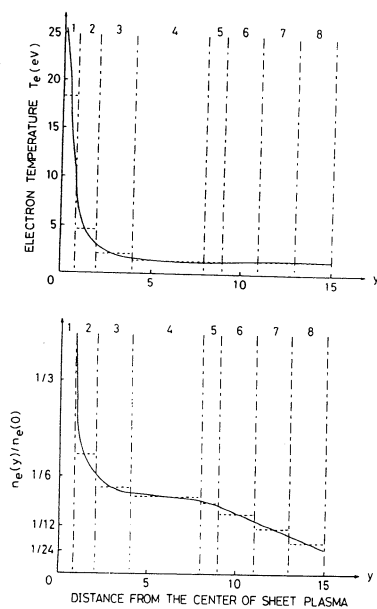


Fig.10. Plasma parameters of the Sheet Plasma Source of IIP Nagoya University.

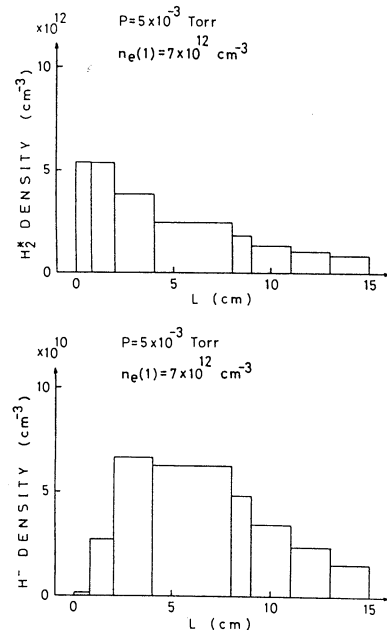


Fig.11. Numerical results corresponding to Fig.10.

Source¹⁷ and the Sheet Plasma Source of IPP Nagoya.¹⁸ In the followings, we show only the calculation procedure and the numerical results.

Figure 8 shows a typical example of plasma density and T_e distributions for the JAERI Bucket Source. Magnetic filter is located at 3 cm apart from the plasma grid. To apply the multi-chamber model, the source is divided into 8 regions(i.e. the first chamber is from 1 to 5, and the second chamber is from 6 to 8). In each region, n_e and T_e have constant values as shown in the figure, and a set of 8 equations is derived.

Figure 9 shows the numerical results of H_2^* and H^- densities corresponding to the distributions of n_e and T_e in Fig.8. Here, we assume that $n_{fe}/n_e = 0.1$ in the first chamber, and that e_f is absent in the second chamber. The optimum H^- density along the second chamber is obtained at an axial position near the magnetic filter.

Another example of distributed plasma parameters(i.e. the Sheet Plasma Source¹⁸) is shown in Fig.10. Numerical results corresponding to Fig.10 are also shown in Fig.11, where $n_{fe}/n_e = 0.1$ in the region 1(center of sheet plasma), and in other regions(diffused plasma) e_f is absent. The optimum H^- density towards the extraction grid is obtained also at some medium point.

SUMMARY

Dependences of volume produced H^- ions on some key plasma parameters have been calculated by using a set of particle balance equations in the tandem two-chamber system. Effectiveness of the tandem system for the H^- ion source is clarified concretely by comparing the relative H^- yields for the single-chamber and the tandem systems. Application feasibility of the extended multi-chamber model to the real ion sources is also reported. Concerning this point, detailed discussion will be reported elsewhere.

REFERENCES

1. J.R. Hiskes and A.M. Karo, J.Appl.Phys. 56:1927(1984).
2. C. Gorse, M. Capitelli, J. Bretagne and M. Bacal, Chem.Phys. 93:1(1985).
3. J.R. Hiskes, Comments At.Mol.Phys. 19:59(1987).
4. O. Fukumasa and S. Saeki, J.Phys.D:Appl.Phys. 18:L21(1985).
5. O. Fukumasa and S. Saeki, Kakuyugo Kenkyu(Nuclear Fusion Research) 55:189(1986); ibid. 56:409(1986). (in Japanese)
6. O. Fukumasa, S. Saeki and S. Shiratake, "Optimization of Volume Produced H^- Ions in a Low-Pressure Hydrogen Plasma", Research Report IPPJ-853 Nov. (1987) Institute of Plasma Physics, Nagoya University, Nagoya, Japan.
7. O. Fukumasa, Kakuyugo Kenkyu 60:419(1988).
8. O. Fukumasa, J.Phys.D:Appl.Phys.(accepted for publication).
9. K.N. Leung, K.W. Ehlers and M. Bacal, Rev.Sci.Instrum. 54:56(1983).
10. J.R. Hiskes, A.K. Karo and P.A. Willmann, J.Appl.Phys. 58:1759(1985).
11. M. Ohmatsu, K. Shimura and M. Ogasawara, "Role of Filter in the Tandem Type Negative Ion Source", Proc. 11th Symp. on Ion Sources and Ion-Assisted Technology 183(1987).
12. K.N. Leung, K.W. Ehlers and R.V. Pyle, Rev.Sci.Instrum. 56:364(1985).
13. D. Fussen and C. Kubach, J.Phys.B:At.Mol.Phys. 19:L31(1986).
14. T. Inoue, M. Araki, M. Hanada, T. Kurashima, S. Matsuda, Y. Matsuda, Y. Ohara, Y. Okumura, S. Tanaka and K. Watanabe, Nucl.Instrum.&Methods in Phys. Research B37/38:111(1989).
15. N. Shigeyama, O. Fukumasa and H. Mizuno, "Control of Plasma Parameters in a Magnetically Filtered Multicusp Plasma Source", Annual Meeting of Physical Society of Japan, 29a-A2(1989).
16. O. Fukumasa, "Numerical Simulation on Negative Ion Source", US-JAPAN Workshop on Negative Ion Beam, JAERI, Japan Nov.(1988).

17. Y. Okumura, private communication.
18. J. Uramoto, "Volume Produced H⁻, D⁻ Ion Source for Proton Accelerator and Thermo-Nuclear Fusion Research by Sheet Plasma(I)", Research Report IPPJ-760 Jan.(1986) Institute of Plasma Physics, Nagoya University, Nagoya, Japan.

ATOMIC AND MOLECULAR SURFACE AND VOLUME PROCESSES IN THE ANALYSIS OF NEGATIVE HYDROGEN DISCHARGES

J.R. Hiskes and A.M. Karo

Lawrence Livermore National Laboratory, University of California
Livermore, California, U.S.A. 94550

Abstract

The generation of hydrogen negative ions in hydrogen discharges is due to a combination of electronic excitation and wall relaxation processes. Principal processes are energetic electron excitation to form $H_2(\nu'')$, followed by low-energy electron dissociative attachment to form $H^- + H$. Wall recombination of H_2^+ , H_3^+ ions are also a source of $H_2(\nu'')$.

We consider the formation of $H_2(\nu'')$ and H^- by H_2^+ and H_3^+ ions incident upon metal surfaces.¹ A four-step model for incident $H_2^+(\nu)$ recombination and dissociation proceeds via: (1) Electric dissociation of high ν ions in the image field ultimately producing atomic dissociation fragments; (2) resonant capture to form $H_2(b^3\Sigma_u)$ and $H_2(X^1\Sigma_g, \nu'')$, with b dominant over X in ratio 69:31; (3) Auger relaxation of b to X to contribute to the $H_2(X^1\Sigma_g, \nu'')$, yield; (4) $H_2(\nu'')$ drift to surface to experience "hard" nuclear collision and form final population distribution, $H_2(\nu'')$, and final dissociation products.¹ Experimental H_2/H yields are consistent with four-step ratio, not consistent with single-step singlet-model ratio, and imply rapid Auger relaxation following b -state capture. Final vibrational distributions reported here differ markedly from earlier calculated distributions. Level shifts due to image effects cause H_2 n = 2-parentage capture to be marginally accessible for barium surfaces ($\phi = 2.7$ eV) but quite possible for cesium ($\phi = 2.14$ eV) and Cs/Mo ($\phi \approx 1.6$ eV) surfaces. Predissociation of $H_2(c^3\Pi_u)$ competes with Auger relaxation but predissociation times are too long to allow significant H_2 dissociation.

Opposing image shifts of $H_2^-(2\Sigma_u)$, $H_2(X^1\Sigma_g)$ allow direct H^- formation from $H_2(\nu'')$ by rebounds from Ba, Cs, Cs/Mo surfaces. H^- yields are evaluated explicitly for Ba surfaces.

For H_3^+ incident: (1) Small (2%) electric dissociation to $H^+ + H_2$; (2) resonant capture to $2p^2E' \rightarrow ^2A_1, ^2B_2$ states; (3) drifting $H_3(\nu'')$ in 2A_1 ground electronic state dissociates into $H_2 + H$ to provide $H_2(\nu'')$ distribution; (4) hard collision of drifting $H_2(\nu'')$ produces final distribution $H_2(\nu'')$. Final vibrational distributions from H_2^+ and H_3^+ are compared. Low work function surfaces allow capture into $H_3(2s\ ^2A'_1)$ and $H_3(2p\ ^2A''_2)$ states. Vibrational and rotational couplings, respectively, couple

these states to $2p\ ^2A_1$ to allow predissociation to yield $H_2(\bar{\nu}'') + H$. The lowest vibrational level of $2s\ ^2A'_1$ is too long-lived (1.8×10^{-13} sec.) to compete favorably with Auger relaxation to $2p\ ^2E'$, but predissociation lifetimes may shorten for higher vibrational levels, analogous to $H_2(c\ ^3\Pi_u)$, to provide a final $H_2(\nu'')$ distribution, that is distinct from that obtained from $H_3(2p\ ^2E')$ resonant capture.² The lifetime of $2p\ ^2A''_2$ against predissociation appears to be too long, $10^{-11} - 10^{-13}$ sec, to be competitive with Auger relaxation. $H_3(n = 3)$ states can be accessed only with very low work function surfaces, $\phi < 1.5$ eV. But predissociation times appear to be excessively long compared with Auger relaxation to allow one to access the broad H_2 vibrational distributions observed³ in the predissociation of the $3s\ ^2A'_1$, and $3d\ ^2E''$ states.

I. Introduction

The principal source of negative ion generation in hydrogen discharges is now recognized to be low-energy electron attachment to $H_2(\nu'')$ molecules excited to the middle portion of the vibrational spectrum.⁴ Electron excitation processes are generally taken to be the principal source of $H_2(\nu'')$ generation,⁵ with high-energy excitations through the singlet spectrum being the principal excitation process populating the active portion of the vibrational spectrum. A description of the collisional re-excitation from level $\underline{\nu}''$, to level ν'' , requires a 15×15 matrix of cross sections linking all initial and final levels. These cross sections have been evaluated and incorporated into the modelling code.⁶

An additional source of vibrational excitation may be derived from recombination of H_2^+ and H_3^+ ions on the surfaces of the discharge. In this case the molecular ions will impinge with kinetic energies given by the plasma potential, 1–10 eV. In this paper we report the evaluation of the $H_2(\nu'')$ resulting from the surface recombination process.

The use of low-work-function materials for the discharge surfaces makes possible two additional source of negative ions: the direct formation of negative ions by hydrogen atoms rebounding from the surface, and the dissociation of H_2^- ions formed in the surface selvage. In a recent paper van Os et al.⁷ have demonstrated the efficacy of Ba surfaces as an active medium for H^- formation. Here we shall extend our discussion to H_2^+ , H_3^+ collisions on Ba surfaces and inventory the generation of H , $H_2(\nu'')$, and H^- rebounding from these surfaces.

II. Surface Recombination and Dissociation of H_2^+ and H_3^+ ions

The surface recombination of H_2^+ and H_3^+ proceeds through a four-step model outlined earlier.¹ We shall summarize briefly the H_2^+ problem: (1) the initial populations, $p(\nu)$, of the $H_2^+(\nu)$ vibrational level $\nu = 18, 17, 16, \dots$, are successively quenched as the image field electrically dissociates the incoming H_2^+ ion. (2) Resonant electron capture from the surface forms $H_2(b^3\Sigma_\mu)$ halting any further electric dissociation. (3) Almost immediately, i.e. with a rate comparable to the resonant capture rate, Auger relaxation relaxes the repulsive b state to form the ground electronic state, $H_2(X'\Sigma_q)$. With some lesser probability resonant capture occurs directly to the singlet ground state.⁸ The final vibrational distributions for the ground state formed by transitions through each of these channels is illustrated in Ref. 10.

In the fourth step (4) molecules in these distributions strike the surface and undergo a "hard" nuclear collision,⁹ rebounding to form the final distribution, $H_2(\nu'')$. This distribution, for 10 eV incident $H_2(\nu')$ molecules and taken from a forthcoming paper,¹⁰ is shown in Fig. 1.

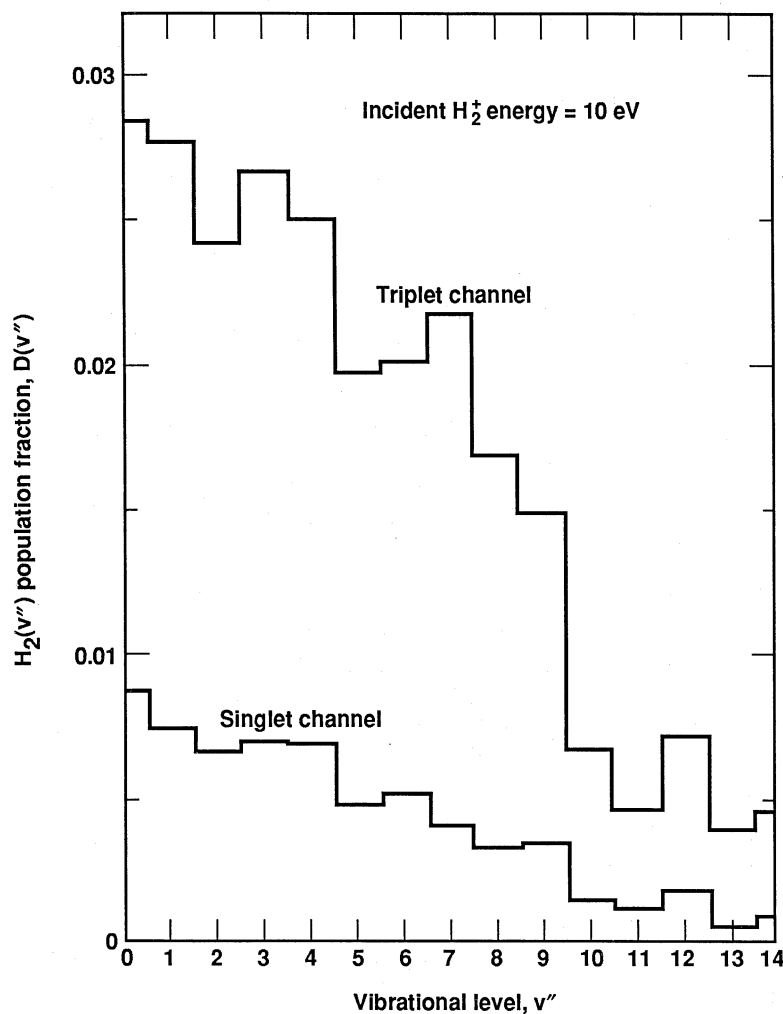


Figure 1. Final population distribution, $H_2(\nu'')$, per incident 10 eV H_2^+ ion.

The $H_3^+(\nu''')$ recombination for conventional metals with work functions $\phi > 4.5$ eV proceeds through the $2p\ ^2E' \rightarrow 2p\ ^2A_1$ state to yield $H_2(\nu'') + H$. The $H_2(\nu'')$ distribution is obtained by projecting the initial population of ν''' on the H_3^+ potential surface¹¹ onto the H_3 surface,¹² followed by a projection onto the $H_2(\nu'')$ plane.¹⁰ This $H_2(\nu'')$ in turn undergoes a "hard" collision to provide the final $H_2(\nu'')$ distribution shown in Fig. 2.

Inspection of the distribution here for $\nu'' > 5$ and comparing with final H_2^+ distributions¹⁰ shows that the H_3^+ ion is a more useful ion for negative ion generation than is H_2^+ .

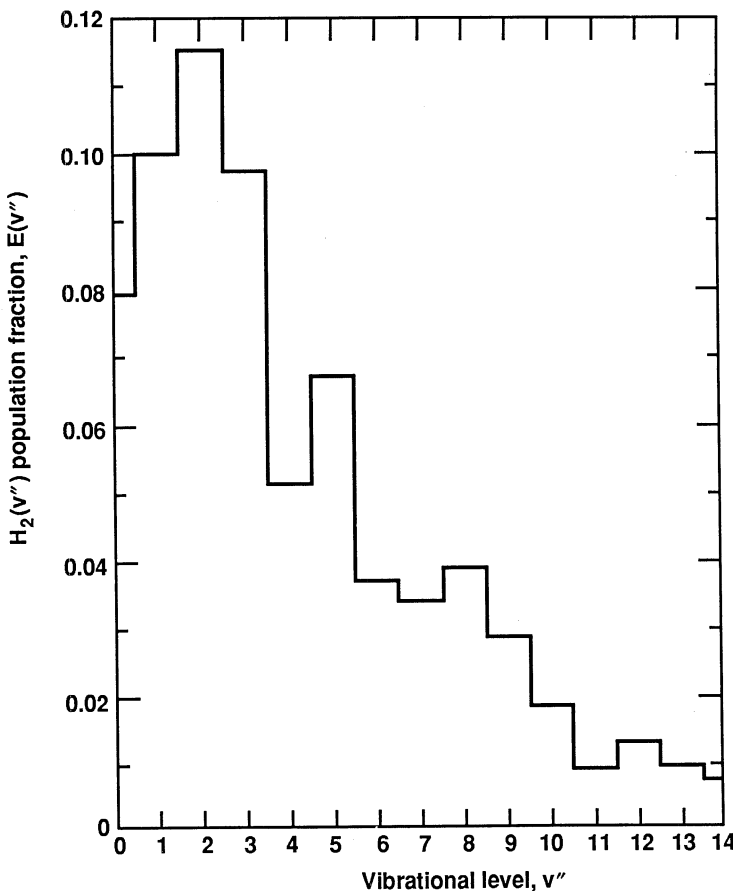


Figure 2. Final population distribution, $H_2(v'')$, per incident 6 eV H_3^+ ion.

III. Molecular Ion Collisions with Low Work-Function Surfaces

Molecular ion collisions with low work-function surfaces will allow for resonant captures into higher electronic states. These captures in turn will be Auger relaxed to provide an additional contribution to the ground state vibrational distribution. Low work-function collisions also allow for two additional mechanism for negative ion generation: Direct H^- production by electron capture to H atoms backscattering from the surface, and H^- production by dissociation of H_2^- ions formed from rebounding $H_2(v'')$ moving outward through the surface selvage.

The generation of H^- ions by H^+ , H incident upon barium surfaces has been characterized experimentally by van Os et al.⁷ In Fig. 3 their data is re-plotted for comparison with the product function

$$N(-) = a(H)[1 - \exp -\nu_{\perp}/\nu_{\perp}^o], \quad (1)$$

plotted against the outgoing perpendicular velocity component, ν_{\perp} .

From this figure the asymptotic dependence on ν_{\perp} indicates a formation probability, $a(H)$, equal to 0.3; the survival probability, given by the bracketed factor, remains as large as 0.33 for perpendicular energy components as low as 2.0 eV.

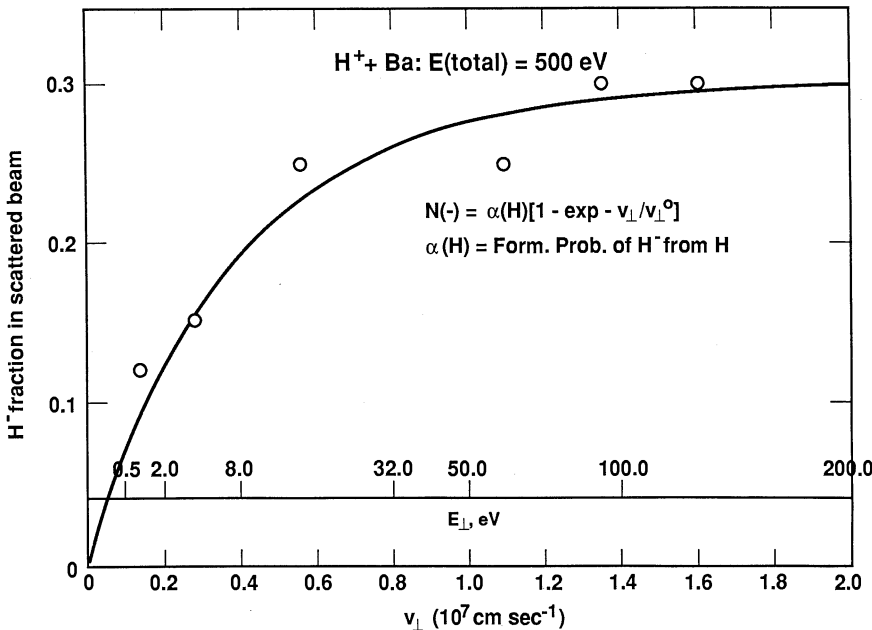


Figure 3. H^- generation vs outgoing normal velocity or energy, Eq. 1.

In general one expects the energy level of a neutral atomic or molecular system to be raised as it experiences an increasing image field. Bruch and Ruijgrok¹³ have shown however, that there is an insignificant level shift for image-plane separations $z - z_o > 3a_o$, the range where resonant electron capture would be expected to occur. For the downward shift of the negative ion level we use the expansion,

$$\Delta E = -\frac{1}{4} \frac{1}{z - z_o} - \frac{1}{2!} \alpha \frac{1}{16(z - z_o)^4} - \frac{1}{4!} \beta \frac{1}{256(z - z_o)^8} + \dots . \quad (2)$$

The dipole and quadrupole polarizabilities, α, β for H^- are 215.5 and 7765.0, respectively.^{14,15} No information is available for the polarizability of the H_2^- ion, but in a first approximation the H_2^- configuration is an $H^- + H$ configuration from the level crossing outward, and for this discussion we shall approximate the H_2^- level shift by Eq. (2) and using the H^- polarizabilities.

The energetics of the barium $-H_2^-, H_2(\nu'')$ system is illustrated isometrically in Fig. 4 where is shown the energy variations as a function of image-plane separation and internuclear separation. The relative positions of the $H_2^-, H_2(\nu'')$ potentials are shown in the right hand plane for infinite surface-molecule separation. At this separation the H_2^- level lies too high to allow resonant capture from the barium ($\phi = 2.7$ eV) to $H_2(\nu'')$ to form H_2^- .

At an image-plane molecule separation of $3.2 a_o$ the H_2^- configuration has shifted downward with respect to $H_2(\nu'')$ such that the asymptotic H_2^- potential lies as low as the $H_2(\nu'' = 0)$ level. At this separation resonant electron capture can occur from the barium to levels $\nu'' = 0, 1, 2$, and 3 of H_2 , resulting in H_2^- dissociation into $H^- + H$.

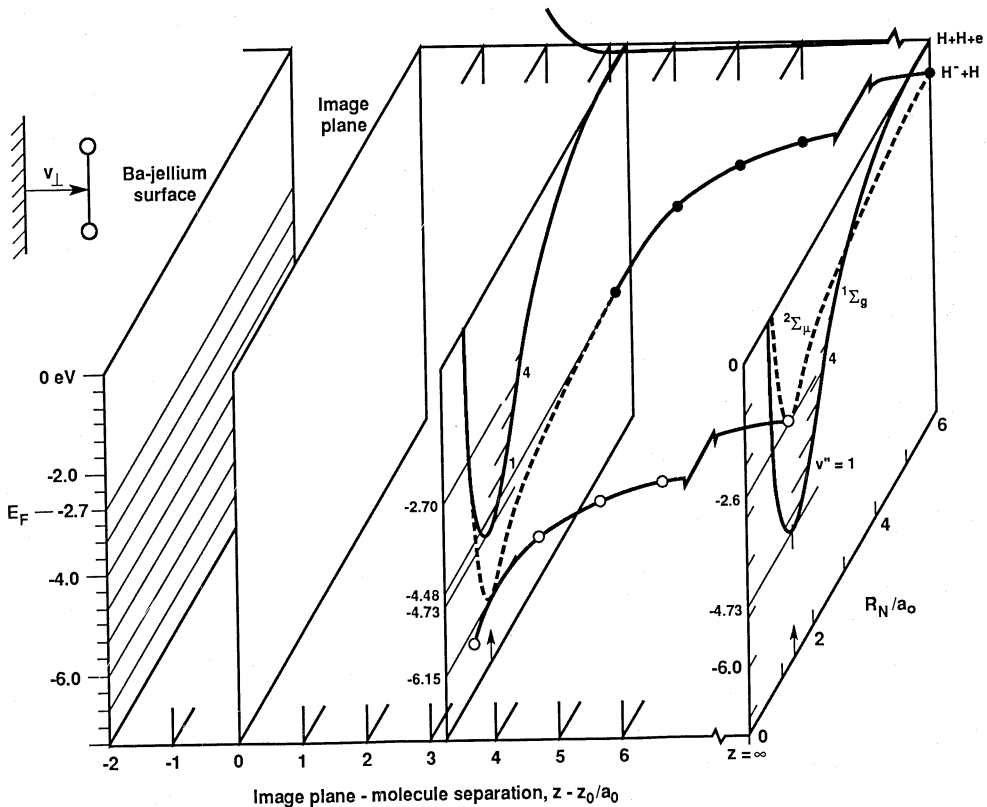


Figure 4. Energetics of the barium H_2^- , $H_2(\nu'')$ system.

We can now summarize the resonant capture possibilities for a 6 eV incident H_3^+ ion rebounding as 4 eV $H_2(\nu'')$ and 2 eV H fragments. In the initial recombination process 20% of the H_3^+ leads to $3H$ dissociation 80% and to $H + H_2$ to give a yield¹⁶ of $1.4H/H_3^+$. From the van Os data of Fig. 3 we conclude that 10% of these atoms will appear as H^- ions to give $0.14H^-/H_3^+$.

From Ref. 10 we have that 32% of the rebounding $H_2(\nu'')$ are in levels $\nu'' = 0, 1, 2$, and 3, and these molecules are subject to H_2^- formation and dissociation in their flight from $z - z_o = 2$ to $3.2 a_o$. From Fig. 3 we find that 0.33 of these H^- survive to give an additional $0.10 H^-/H_3^+$. The remaining flux is then $0.54 H^-/H_3^+$. For those $H_2(\nu'' > 3)$, representing a fraction $0.48 H_2/H_3^+$, no resonant capture to form H_2^- can occur.

One can now take inventory of the subsequent capture and dissociation processes for 6.0 eV incident H_3^+ on barium. The relative ratios $H : H_2 : H^-$ per incident H_3^+ ion are found to be 1.80:0.48:0.24. The new contribution offered by the low work-function barium surface is the $0.24 H^-/H_3^+$. The H_2^- intermediary state has effectively converted the low-lying $H_2(\nu'')$ population into an additional source of H^- and H .

Acknowledgment

Work performed under the auspices of the U.S. Department of Energy by the Lawrence Livermore National Laboratory under contract number W-7405-ENG-48 and AFOSR-ISSA-89-0039.

References

- ¹J.R. Hiskes and A.M. Karo, *Dissociative Recombination: Theory, Experiment, and Applications*, J.B.A. Mitchell and S. Guberman, Eds., World Scientific, p. 204, Teaneck, NJ (1989).
- ²A.E. Orel and K.C. Kulander, "Wave Packet Studies...", Abstracts of the XVI ICPEAC, NY 1989.
- ³P.C. Cosby and H. Helm, Phys. Rev. Lett. **61**, 298 (1988).
- ⁴J.R. Hiskes, AIP Conf. Ser. 158, p. 2 (1987).
- ⁵J.R. Hiskes and A.M. Karo, "Interpretation and Analyses of the H_2 Vibrational Distribution In a Hydrogen Discharge," this NATO volume.
- ⁶J.R. Hiskes, XV Int. Conf. on the Physics of Electronic and Atomic Collisions Abstracts, p. 122, Brighton, U.K., July (1987).
- ⁷C.F.A. van Os, H.M. van Pinxteren, and J. Los, Proc. III European Workshop on the Production and Application of Light Negative Ions, Feb. 17-19, p. 266, Amersfoort, Netherlands (1988).
- ⁸U. Imke, K.J. Snowdon, and W. Heiland, Phys. Rev. B**34**, 41 (1986).
- ⁹A.M. Karo, J.R. Hiskes, and R.J. Hardy, J. Vac. Soc. Technol. A**3**, (3) 1222 (1985).
- ¹⁰J.R. Hiskes and A.M. Karo, (submitted to J. Appl. Physics).
- ¹¹K.C. Kulander and E.J. Heller, J. Chem. Phys. **69** 2439 (1978).
- ¹²R.N. Porter, R.M. Stevens, and M. Karplus, J. Chem. Phys. **49**, 5163 (1968).
- ¹³L.W. Bruch and Th.W. Ruijgrok, Surf. Sci. **79**, 509 (1979).
- ¹⁴S.A. Adelman, Phys. Rev. A**5**, 508 (1972).
- ¹⁵K.T. Chung and R.P. Hurst, Phys. Rev. **152**, 35 (1966).
- ¹⁶B. Willerding, K. Snowdon, and W. Heiland, Z. Phys. B**59**, 435 (1985).

INTERPRETATION AND ANALYSIS OF THE H₂ VIBRATIONAL DISTRIBUTION IN A HYDROGEN DISCHARGE

J. R. Hiskes and A. M. Karo

Lawrence Livermore National Laboratory
Livermore, California 94550

We have used a model employing standard collisional processes to analyze the H₂(v") vibrational distribution experimentally observed in a medium-density hydrogen discharge. No adjustable parameters are used in describing these processes. We find the calculated distribution to be a sensitive function of the wall-relaxation process. Our analysis of a warm-gas-temperature discharge shows substantially more rapid H₂(v") wall relaxation than is inferred from experimental observations on cold-gas systems. By using limiting assumptions that range from complete wall quenching to the absence of wall relaxation we are able to obtain solutions that essentially span conflicting experimental data. We present a hypothesis that resolves the experimental situation.

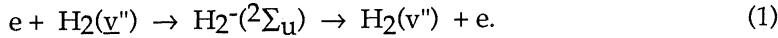
It is well-known that in a hydrogen discharge vibrationally excited H₂ molecules enhance the formation of negative ions by dissociative attachment, and it is also recognized that the production of a large concentration of negative ions requires a significant population of H₂ molecules in vibrational states lying above v" = 5. Recently, Stutzin et al.¹⁻³ have measured the distribution of excited molecules up through v" = 5 and thus have reached the threshold of the active vibrational states required for H⁻ formation. In the present paper we have used known formation and destruction processes to calculate H₂(v") distributions and have compared our results with their observations.

A number of model calculations have been carried out in recent years that have attempted to identify the underlying mechanisms which determine the equilibrium vibrational distribution.⁴⁻⁶ Coherent anti-Stokes resonance scattering (CARS) measurements^{7,8} through the v" = 2,3 levels provide the experimental base for these models, which have employed a hypothetical H₂(v") wall-relaxation coefficient as an adjustable parameter correlating the experimental and model-determined H⁻ concentrations.

Work performed by LLNL for USDOE under Contract W-7405-ENG-48 and AFOSR-ISSA 88-0002.

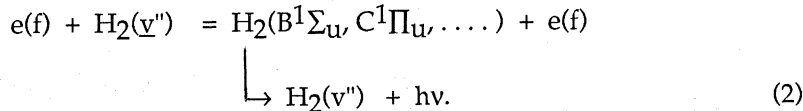
However, the importance of specifying the $H_2(v'')$ distribution independently of the H^- yield has been emphasized recently by several groups. This has prompted experiments from which one can directly infer the $H_2(v'')$ population.^{9,10} In addition, over the past few years we have carefully examined the wall relaxation process using computer molecular dynamics.^{11,12} Results of this analysis can be incorporated directly into the modelling studies, thus providing a parameter-free description of these distributions.¹³

The vibrational spectrum is populated by two-fold electron excitation processes whereby the lower portion of the vibrational spectrum is populated principally by electron excitations proceeding via the H_2^- resonance,



Mundel et al.¹⁴ have analysed this excitation process using a full non-local potential. They found the $\underline{v}'' = 0 \rightarrow v'' = 0, 1, 2$ cross sections to be in satisfactory agreement with the experimental values of Ehrhardt et al.¹⁵ but to exceed the experimental values by a factor of 2.3 for the higher v'' final states.¹⁶

We have evaluated the Maxwellian rates $\bar{\sigma} \bar{v} (\underline{v}'', v'')$ for an electron temperature of 2.7 eV, corresponding to the discharge of ref. 1, and have normalized them to the experimental values for $v'' \geq 3$. Above the first several vibrational levels the excitation is dominated by high-energy electron excitations ($E > 20$ eV) that proceed via the higher singlet states of the H_2 spectrum,¹⁷



The reaction rates for these high energy electrons were evaluated using the electron distribution function for slowing electrons,¹³ and cross sections were referenced to the excitation cross sections of Gibson et al.,¹⁸ Hazi,¹⁹ and Lee et al.²⁰

We note that the mean-free-path for the excited molecules in the discharge of ref. 1 is a two- to four-fold multiple of the chamber dimensions, and we have found the principal $H_2(v'')$ vibrational relaxation mechanism to be molecule-wall collisions. We have shown from our molecular trajectory model¹¹⁻¹³ that over several wall collisions the decay of a level \underline{v}'' can be approximated by an exponential factor,

$$H_2(\underline{v}'') = H_2^O(\underline{v}'') \exp [-C/b(v'')],$$

where C is the wall collision number. The $b(v'')$ have been evaluated for a gas and wall temperature near 500K and are given in Table I.

TABLE I. Parameter values for wall relaxation.

v''	1	2	3	4	5	6	7	8	9	10	11	12	13	14
$b(v'')$	2.5	2.0	1.9	1.8	1.6	1.5	1.5	1.4	1.4	1.3	1.2	1.1	1.0	1.0

Thus we see that the relaxation of a level v'' repopulates lower levels $v'' < v''$ with a repopulation probability, $w(v'', v'')$ as illustrated in Fig. 1. The values shown will change slowly with increasing temperature.

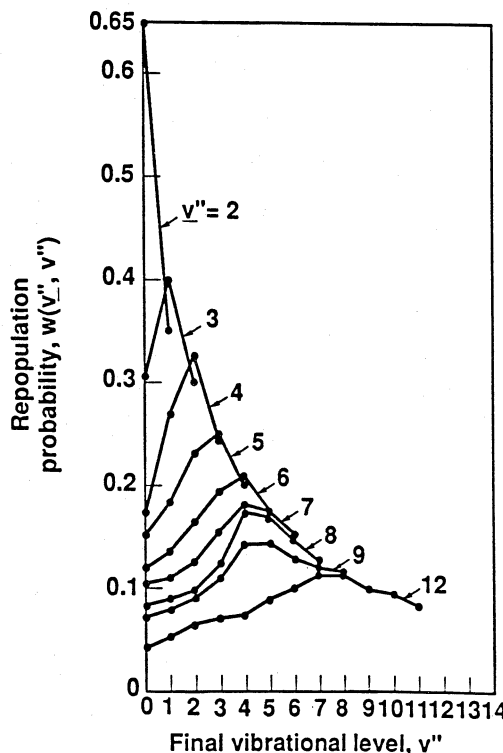


FIG. 1. Repopulation probability $w(v'', v'')$ for repopulating levels $v'' < v''$ following a wall collision of a molecule initially in level v'' .

As we have discussed previously,¹¹⁻¹³ a feature of the relaxation model is the redistribution of the initial vibrational excitation energy into the vibrational, rotational, and translational degrees of freedom of the molecule, tending to statistical equipartition after several wall collisions, while retaining a broad energy distribution in all three of these modes. In Fig. 1 of ref. 1 the rotational spectrum observed at $v'' = 1$ shows a rotational temperature of 470K for the low J values, but exhibits an excess rotational energy for $J = 4-8$. If we attribute this excess to initial levels $v'' > 1$ that have relaxed their vibrational energy equipartitionally toward rotation and translation, and if we take the initial population of the $v'' > 1$ levels to be proportional to the rates (1) and (2), the observed excess is reproduced to within a factor of two. Furthermore, Stutzin et al. comment that low J states tend to have lower translational

energies and vice-versa. This tendency is qualitatively consistent with a thermal gas distribution and a superimposed energetic distribution relaxing toward equipartition.

Stutzin et al.² have observed the relative atom/molecule concentration in the discharge to be approximately 7%. When compared with wall relaxation, the remaining atom-molecule and molecule-molecule collision processes, which are included in the total relaxation process,¹³ play a minor role. The evolution of the $H_2(v'')$ system of fourteen excited levels v'' tends toward a steady-state distribution described by a set of fourteen linear algebraic equations. The solutions of these equations are shown in Fig. 2 and are compared with the experimental observations reported by Stutzin et al.¹

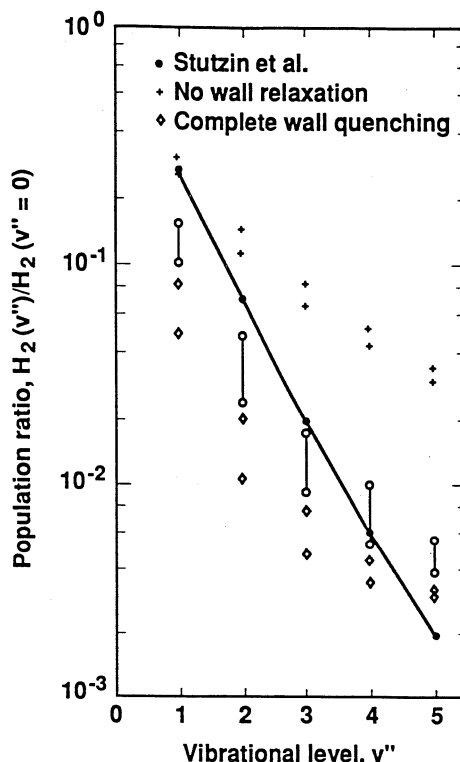


FIG. 2. Population ratio $H_2(v'')$ as a function of vibrational level v'' . (Closed circles) experimental data of Ref. 1. (Open circles) distributions calculated here for two electron densities $n = 8 \times 10^{11}$ and $4 \times 10^{11} \text{ el. cm}^{-3}$. (Crosses) calculated distributions for no wall relaxation, $b \rightarrow \infty$, $w(\underline{v}'', v'') = 0$. (Diamonds) calculated distributions with complete wall quenching, $b = 1$, $w(\underline{v}'', v'') = 0$.

The measured distribution¹ is shown in the figure by closed circles joined by the sloping line. The calculated distributions are given by open circles. These are shown in double entry and are joined by light vertical lines. The upper open circles are for a thermal electron density of 8×10^{11} electrons/cm³ which is

an upper limit taken from the probe measurements.¹ The lower circles are solutions for half this density, a value taken somewhat arbitrarily as a lower limit. For both cases the figure shows the calculated distribution to be a factor of two or three lower than the observed distribution near $v'' = 1$, and a factor two to four higher at $v'' = 5$ (experimental error quoted at $\pm 15\%$), giving an overall distribution more shallow than the experimental curve.

To display the sensitivity of the calculated distributions to the wall relaxation process we have looked at two limiting cases. In the first, shown by crosses, no wall relaxation is assumed; here $b(v'') \rightarrow \infty$ and all $w(\underline{v}'', v'') = 0$. The calculated and observed populations at $v'' = 1$ now agree to within the experimental uncertainty, but at $v'' = 5$ the calculated ratio is now twenty times larger than the observed.

Hall et al.⁹ have reported that desorption of atomic hydrogen on the walls of a gas cell populates vibrational levels up to $v'' = 9$ and that the vibrational distribution does not relax during a time sufficient for more than a hundred wall collisions. Our calculations show that the $b \rightarrow \infty$ result shown in Fig. 2 is already closely approximated by $b = 100$. A distinguishing aspect of the experiments of Hall et al. and Stutzin et al. are the gas and wall temperatures. In the former experiment the walls are water-cooled to near room temperature with no discharge present to heat the gas. The low temperature is confirmed by the observation of no appreciable rotational excitation above room temperature. In the latter experiment the gas and the wall are heated by the discharge to higher temperatures, in excess of 470K.

The dispersion of our solutions away from the experimental distribution for the situation where there is no wall relaxation, shown by crosses in Fig. 2, leads to a new hypothesis for the wall relaxation: whereas no appreciable wall relaxation occurs at low gas/wall temperatures, as in the experiment of ref. 9, an onset of relaxation occurs for increasing temperature and vibrational excitation. The large dispersion in the distributions as they tend toward higher v'' values suggests an onset mechanism that is dependent both on the degree of vibrational excitation and the system temperature.

Thus we show in Fig. 2 solutions (diamonds) for the limiting case of complete wall quenching, i.e., all $b(v'')$'s set equal to unity and $w(\underline{v}'', v'') = 0$. The calculated distributions now lie well below the experimental distribution except at $v'' = 5$ where the population ratio remains above the range of the experimental uncertainty. Our calculations may overestimate the fast electron density entering into (2) if the magnetic multipole does not confine the injected electrons until they have slowed to join the thermal distribution. In this event the contributions (2) will be less and the higher v'' ratios will be reduced. But for the most part the two limiting assumptions concerning wall relaxation give results that span the observed population distribution and emphasize the importance of properly characterizing the wall relaxation for this particular discharge-parameter regime.

Finally, we note that over most of the range of v'' there is a constant tendency for the calculated distribution to fall below the experimental values. This might be accounted for by an additional source of $H_2(v'')$ over and above that of (1) and (2). Not included in the present discussion are the effects of

molecular-ion recombination occurring at the walls and serving as an additional source of $H_2(v'')$. No information is available at present as to the molecular ion species mix in the discharge, but if these ionic components were large compared to the total positive ion concentration they would contribute an amount comparable to the observed discrepancy.²¹

To summarize, in this paper we have shown that parameter-free model calculations, taking into account standard processes, provide a fair agreement with the vibrational distribution observed in the medium density discharge. The calculated $H_2(v'')$ distribution is quite sensitive to wall relaxation phenomena. Limiting assumptions ranging from complete wall quenching to no wall-relaxation provide solutions that essentially span the experimental data. The apparent lack of wall relaxation observed in ref. 9 for a cold system when taken into account in our calculations leads to a large disparity when compared with the observations of ref. 1. To account for this discrepancy, a hypothesis has been proposed whereby the onset of wall relaxation for warm systems is a dispersive function of increasing temperature and vibrational excitation. The role of molecular ion surface-recombination as it affects the vibrational distribution remains to be clarified.²²

ACKNOWLEDGMENTS

The authors are indebted to G. C. Stutzin and co-workers for discussions pertaining to their discharge operation.

REFERENCES

1. G.C. Stutzin, A.T. Young, A.S. Schlachter, and W.B. Kunkel, *Chem. Phys. Letters* 155, 475 (1989)
2. G.C. Stutzin, A.T. Young, A.S. Schlachter, J.W. Stearns, K.N. Leung, W.B. Kunkel, G.T. Worth, and R.R. Stevens, *Rev. Sci. Instr. Conf. Series* (1988).
3. G.C. Stutzin, A.T. Young, A.S. Schlachter, J.W. Stearns, K.N. Leung, W.B. Kunkel, G.T. Worth, and R.R. Stevens, *Rev. Sci. Instr.* 59 (8), 1363 (1988).
4. J.R. Hiskes, *Notas de Fisica* 5, 348 (1982).
5. J.R. Hiskes, A.M. Karo, M. Bacal, A.M. Bruneteau, and W.G. Graham, *J. Appl. Phys.* 53 (5), 3469 (1982).
6. C. Gorse, M. Capitelli, J. Bretagne, and M. Bacal, *Chem. Phys.* 93, 1 (1985).
7. M. Pealat, J.P.E. Taran, J. Taillet, M. Bacal, and A.M. Bruneteau, *J. Appl. Phys.* 52, 2687 (1981).
8. M. Pealat, J.P.E. Taran, M. Bacal, and F. Hillion, *J. Chem. Phys.* 82 (11), 4943 (1985).

9. R.I. Hall, I. Cadez, M. Landau, F. Pichou, and C. Schermann, Phys. Rev. Lettr. 60 (4) 337 (1988).
10. P.J. Eenshuistra, J.H.M. Bonnie, J. Los, and H.J. Hopman, Phys. Rev. Lettr. 60 (4) 341 (1988).
11. A.M. Karo, Notas de Fisica 5 (1), 305 (1982).
12. A.M. Karo, J.R. Hiskes, and R.J. Hardy, J. Vac. Sci. Technl. A3, (3) 1222 (1985).
13. J.R. Hiskes and A.M. Karo, J. Appl. Phys. 56 (7), 1927 (1984).
14. C. Mundel, M. Berman, and W. Domcke, Phys. Rev. A 32, 181 (1985).
15. H. Ehrhardt, D.L. Langhans, F. Linder, and H.S. Taylor, Phys. Rev. 173, 222 (1968).
16. M. Allan, J. Phys. B 18, L451 (1985).
17. J.R. Hiskes, XV Int. Conf. on the Physics of Electr. and At. Collisions Abstracts, p. 122, Brighton, U.K., July (1987).
18. T.L. Gibson, M.A.P. Lima, V. McKoy, and W.M. Huo, Phys. Rev. A 35, 2473 (1987).
19. A.N. Hazi, Phys. Rev. A 23, 2232 (1981).
20. M.T. Lee, R.R. Lucchese, and V. McKoy, Phys. Rev. A 26, 3240 (1982).
21. J.R. Hiskes and A.M. Karo, "Dissociative Recombination: Theory, Experiment, and Applications," J.B.A. Mitchell and S. Guberman, Eds. p. 204, World Scientific, Teaneck, NJ (1989).
22. J.R. Hiskes and A.M. Karo, Appl. Phys. Lett. 54(6), 508 (1989).

ELECTRON ENERGY DISTRIBUTION FUNCTIONS
IN MAGNETIC MULTIPOLE PLASMAS

M. B. Hopkins

Department of Physics
Dublin City University
Glasnevin, Dublin 9, Ireland

INTRODUCTION

Low pressure hot cathode discharges have been used for many years as plasma generators for fundamental and applied research. The most simple form of hot cathode, the hot filament has a series of wire filaments heated directly to electron emission temperatures. The hot filaments are biased 50-100V negative with respect to the chamber wall; primary electrons are emitted from the filaments and accelerated across the cathode-plasma sheath. In travelling to the wall the primary electrons have sufficient energy to ionize the background gas. For efficient operation the mean free path of the primary electrons must be comparable with characteristic length of the source, otherwise a substantial portion of the input energy is lost to walls. This limits the minimum pressure at which a hot cathode plasma source will operate.

In an important paper¹ Limpeacher and Mackenzie (1973) describe a magnetic multipole containment device. This multipole device produced a vast improvement in plasma generation efficiency, quiescence and uniformity. The Multipole has now established itself as important plasma production device, particularly suited to low pressure plasma generation. Examples of its use are in basic plasma experiments for which it was originally designed¹, positive and negative ion sources^{2,3}, plasma etching⁴, thin film deposition⁵, high temperature treatment of materials⁶ and ion implantation⁷. This list is by no means exhaustive but illustrates the technological interest in multipole devices. The multipole is no longer confined to hot cathode discharges but also is used with micro-wave and rf produced plasmas, again trapping of fast electrons must offer the most plausible explanation of its efficient operation.

This paper concentrates on the results taken in low pressure H₂ multipole plasmas being investigated as volume sources of² H₂ ions for neutral beam injection systems⁸. There are several basic configuration of multipole H₂ ion

being studied at present, using either a checkerboard or line cusp symmetry. H formation is believed to be a two step process involving the attachment of low energy electrons to highly vibrationally excited H₂. H production requires a low temperature electron group to optimize the attachment process, simultaneous with a high temperature electron group to produce the dense plasma and vibrationally excite the H molecules. This dual temperature requirement has lead to the development of the Tandem multipole concept⁹. A practical Tandem device is produced by magnetically shielding the primary injection region, or driver, from the extraction region. The magnetic shielding field, called a filter field, prevents primary electrons entering the extraction region and has been shown to support a substantial electron temperature difference.

EXPERIMENTAL SET-UP

The results presented here refer to two types of source the Tandem source¹⁰ and the Hybrid Source¹¹. The Tandem Source consists of a stainless steel box 190 × 190 × 240 mm. Samarium-Cobalt permanent magnets are spaced 45 mm apart on the outside in a normal line cusp symmetry. This symmetry is broken on opposing walls near the extraction end of the source allowing a one-dimensional filter field to cross the source and dividing it to two regions. The discharge is produced by electrons emitted from two tantalum filaments heated by a DC current. The filaments are biased negatively with respect to the vessel wall which forms the anode. The Hybrid source consists of a cylindrical stainless steel vessel 254 mm in diameter and 236 mm high. The source has 10 columns of SmCo magnets on the outside wall forming a line cusp symmetry. Unlike the Tandem source there are no magnets on the end plates of the cylindrical chamber in the Hybrid case, this results in a large area of the wall, which acts as the anode, being unmagnetized. Ten tungsten hairpin filaments are arranged on a circle of 192 mm diameter, the center of each filament is located in the magnetic field between two neighboring magnetic columns.

Measurement of the Electron Energy Distribution Function

The EEDF is obtained from the numerical second derivative of a Langmuir probe characteristic¹². Langmuir probes are particularly useful in multipole plasmas where the confining magnetic fields ensure an isotropic velocity distribution, even for high energy electrons. A further advantage of the Langmuir probe is that it is movable and can be used to obtain spatial information without greatly perturbing the plasma. The time response of a Langmuir probe is of the order of several μ s making it ideally suited to measuring transient phenomenon in pulsed and rf plasmas.

The major problems associated with the Druyvestyn method of obtaining the EEDF are first, in achieving an adequate signal to noise ratio in the measured probe characteristic and secondly in being able to establish the contribution of ion current, due to sheath expansion, to the second derivative. The necessary high signal to noise ratio is normally obtained by using the harmonic analysis method. In this method an ac

voltage ($\sim 50\text{mV}$) is superimposed on the probe bias and the modulated current component at the second harmonic is detected which is proportional to the second derivative. The method is subject to systematic errors due to circuit nonlinearities, stray capacitive effects and the possibility of waves being launched by the probe. The perturbing potential, δv , must be kept very low to keep perturbation of the probe sheath to a minimum; this is a severe limit on this technique as the resolution obtainable in the second derivative goes as $(\delta v)^2$. In general, it is not possible to obtain absolute measurements of the eedf with the ac modulation method because of the large systematic errors present, neither is it possible to correct for the presence of an ion current component in the second derivative.

A major improvement is achieved in the work described here by using a numerical differentiation of the digitally stored current voltage characteristic. By integrating the current-voltage measurements over long periods a great reduction in noise is obtained. The integration is performed numerically and each measurement of current and voltage is made simultaneously, the resulting voltage-current correlation greatly improves the signal/noise ratio. The most significant improvement in the resolution of the EEDF is achieved by the fact that the energy step used in obtaining the derivative, δv , is no longer limited to $\sim 50\text{mV}$ as is the case with the modulation method. The energy resolution, δv can be increased to several volts which results in several orders of magnitude improvement in resolution. As the second derivative of the probe characteristic is obtained numerical from the current-voltage characteristic and not via sensitive electronics, absolute measurements of the eedf are possible and the ion current contribution to the second derivative may be substantially removed, improving the ultimate resolution of the Druyvestyn method by about an order of magnitude.

THEORETICAL MODEL

A theoretical model of a multipole plasma will only succeed if it is possible to determine the shape of the eedf and its dependence on discharge parameters, and position. Any model assuming a Maxwellian eedf is not valid especially when considering energetic electron induced processes. While the eedf has been obtained by detailed numerical solution of the Boltzmann equation¹³ with results which are in reasonable agreement with experiment, showing a highly non-maxwellian eedf, they are volume averaged and give no information on the spatial variation of the eedf.

The spatial variation of the eedf can be estimated quite well by a model¹⁴ which follows the trajectories of the primary electrons starting at the filament location with an initial velocity of magnitude, $v_e = (2eV_d/m_e)^{1/2}$, and random direction. The spatial variation of the magnetic field is calculated by treating the field as originating at discontinuities in the magnetization vector at the surface of the magnets. The resultant magnetic field at any point in the source is obtained by integrating over the contribution from each magnetic surface element on the

outside wall or indeed any magnet in the vicinity of the source.

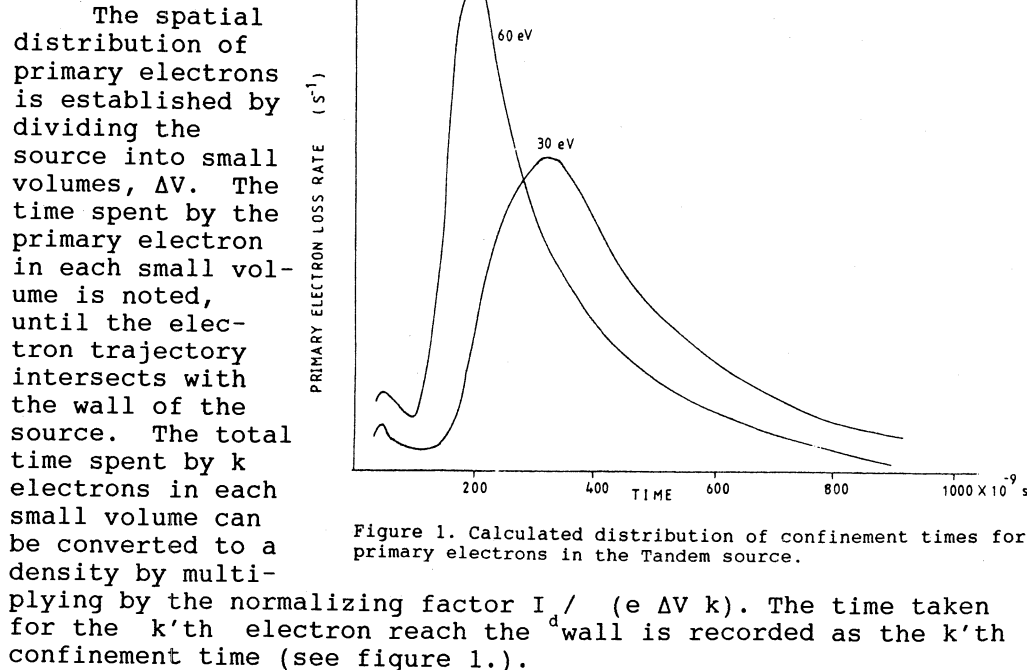


Figure 1. Calculated distribution of confinement times for primary electrons in the Tandem source.

The model predicts well the spatial distribution of primary electrons as well as the average confinement time, τ_w , provided the wall confinement time τ_w is small compared to the mean time for inelastic collision of primary electrons with the background gas, τ_g . The mean time for inelastic collisions can be approximated $\tau_g = \{1/(\sigma_i + \sigma_e) V_p \times n_o\}$, where σ_i is the ionisation cross section, σ_e is the cross section for electronic excitation of the H₂ molecule and n_o is the H₂ density in m⁻³, for 60 eV primaries $\tau_g \approx n_o^{-1} \times 1 \times 10^{13}$ s. From figure 1, $\tau_w = 3.7 \times 10^{-7}$ s for 60 eV primaries; the condition $\tau_w \ll \tau_g$ holds for gas densities $n_o \ll 2.7 \times 10^{19}$ m⁻³. This represents a source pressure of about 0.1 Pa, as the this pressure is approached primary electrons will begin to undergo inelastic collisions before they reach the wall. These primary electrons reappear at lower energies as degraded primaries. At pressure above 0.1 Pa, in the case of the Tandem, it is necessary to include inelastic collisions in the model¹⁴.

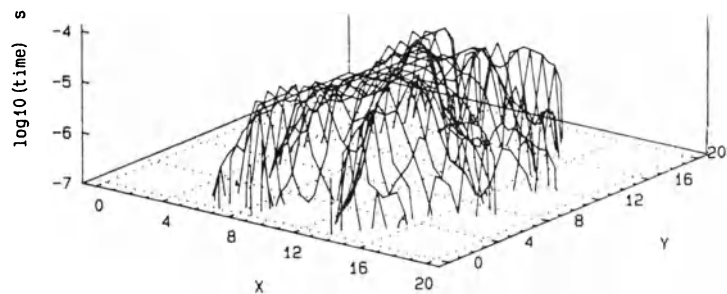


Figure 2. Theoretical time spent by 1×10^3 electrons ($c = 60$ eV) in each part of the Tandem source. The Beam forming electrode is at $X = 0$ cm, and the filter field is at $X = 6$ cm. Filaments are at $X = 14$ cm, $Y = 7$ cm, and $X = 14$ cm, $Y = 12$ cm.

Figure 2 shows the theoretical spatial distribution of 60eV primary electrons in the Tandem source. The x direction is 0 at the Beam Forming Electrode¹², with the filter at $x \sim 6$ cm. The Y axis is parallel to the Beam Forming Electrode. It is seen that the primary electrons are confined away from the walls by the magnetic fields. It can be further seen that the weak magnetic field which cross the source due to the presence of the filter field¹⁴ is sufficient to prevent primaries from entering the extraction region.

In the Hybrid source the filaments are not located in the central region¹¹ but are placed in the cusp fields near the wall. In order to investigate what happens in this situation the model is run with the filaments located at 3cm from the wall between cusp fields ($Y = 3$ and 16).

As can be seen from

figure 3 in this case the primaries are confined in localized driver regions near each filament (there are two filaments in this model). The Hybrid source will be a less efficient plasma producing device because of the smaller confinement volume. The model does not have a large unmagnetized area as is the case in the Hybrid source but this is not expected to have a significant effect on the primary confinement except at the edges of the plate where primary electrons may leak out leading to a lower average primary confinement time.

EXPERIMENTAL RESULTS

Figure 4 shows a typical EEDF measured in the centre of the Tandem source showing a degraded group of fast electrons. Also shown in figure 4 is a typical EEDF taken under similar conditions near the filaments in the Hybrid source. Note the electrons are not as degraded in the case of the Hybrid source due to the shorter confinement times. The degradation of the primaries disappears as the pressure of the source is reduced. Low pressures measurements of the EEDF show the energy spread, due to the fact that there is a voltage drop of ~ 8 V across each filament, of electrons emitted from the filaments. Figure 6 shows the EEDF in the fast electron energy region in the center of the Tandem source. The filaments were operated in series with the center of the filaments biased 60V negative with respect to the anode. The measured EEDF in the high energy

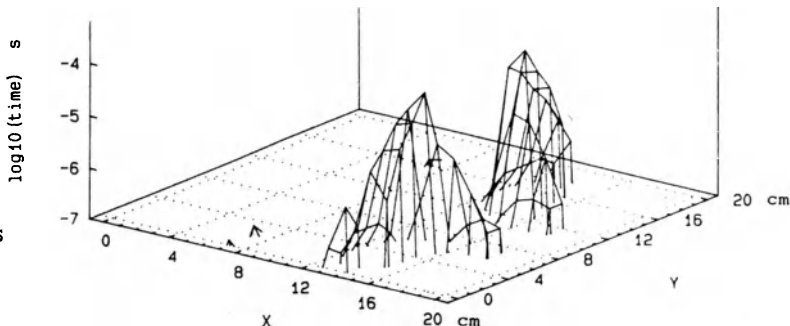


Figure 3. As figure 2 but with the filaments at $X = 14$ cm, $Y = 3$ cm and $X = 14$ cm, $Y = 16$ cm.

region appears as two distinct groups of primaries, one from each filament, as is confirmed by operating with alternative filaments turned off. It is noted that one filament was emitting more electrons than the other, this was confirmed by comparing the discharge currents from each filament.

Spatial Variation of the EEDF

A detailed study of the spatial variation of the EEDF in the Tandem source can be found in ref 12. Figure 3 from ref 12 shows the spatial variation of the EEDF from the extraction region into the hot driver region (along the X direction).

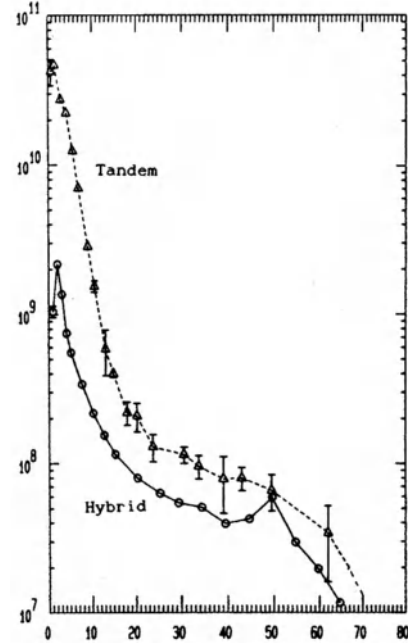


Figure 4. EEDF measured in the centre of the Tandem source and near the filaments of the Hybrid source.
 $I_d = 5A$, $p = 2$ mTorr.

This again confirms the effect of the filter field in confining fast electrons. In a similar manner figure 5 shows the spatial variation of the EEDF from the center of the Hybrid source to the wall. It is clearly seen that the fast electrons are confined in the region close to the filament as predicted by the model. Bulk plasma densities are also about an order of magnitude less in the case of the Hybrid due to the smaller driver volume and reduced τ_w .

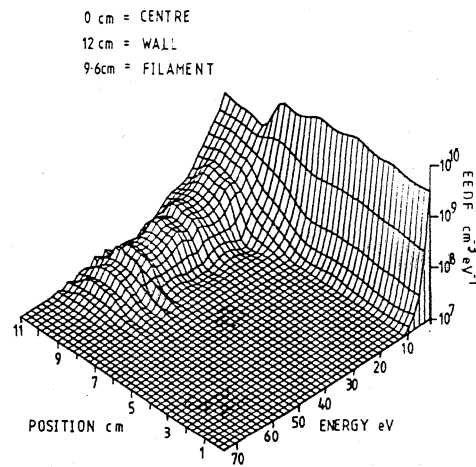


Figure 5. Spatial variation of the EEDF from the centre of the Hybrid source to the wall. $I_d = 5A$, $p = 2$ mTorr.

Calculation of Reaction Rates

It is found experimentally¹⁵ that the Lyman α light intensity increases in proportion to $I_d^{1.2}$ in the driver region of the Tandem source. On the assumption that fast electrons density scales linearly with I_d , it was generally thought that the Lyman α production must include a component other than direct fast electron excitation to explain the non-linear dependence. The problem can be resolved by using the measured EEDF's to establish the production rate or pumping rate, p of any process.

$$p = \int_0^{\infty} n f(\varepsilon) \sigma(\varepsilon) v(\varepsilon) \delta\varepsilon$$

Figure 7 shows the measured Lyman α light intensity as a function of discharge with the Lyman α pumping rate calculated using the measured EEDF's. The Lyman α intensity does indeed scale with the fast electron pumping rate as expected.

To further illustrate the usefulness of the eedf measurements Figure 8 shows the pumping rates derived from the measured

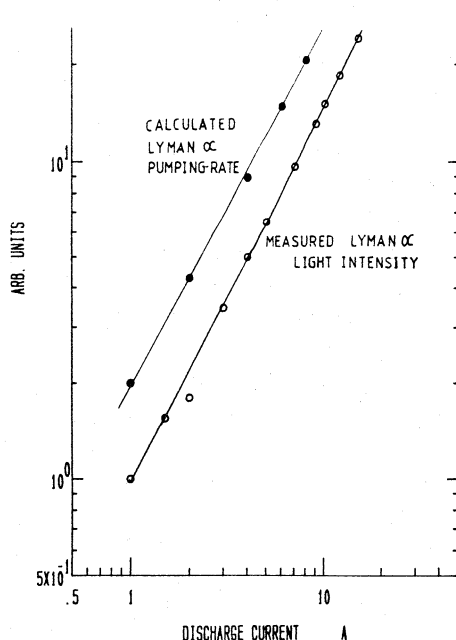


Figure 7. Comparison of the measured Lyman α light intensity calculated pumping rate derived from the measured EEDF's. pressure = 5mTorr.

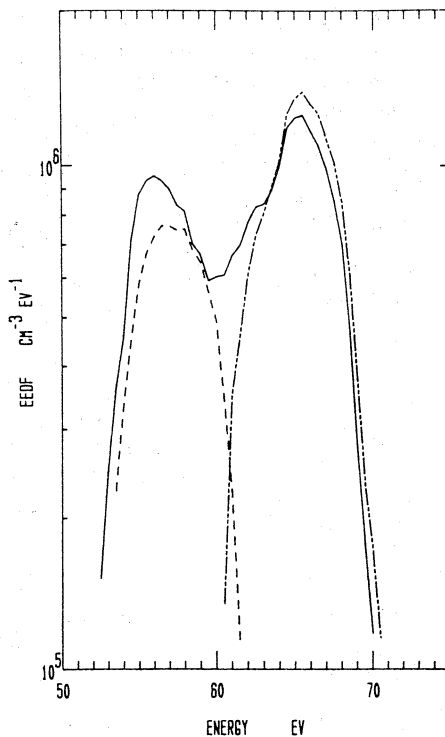


Figure 6. High Energy portion of the EEDF in the Tandem source at low pressures. Dashed lines indicate EEDF's measured with one filament operation.
 $I_d = 10\text{mA}$, $p = 0.07\text{mT}$

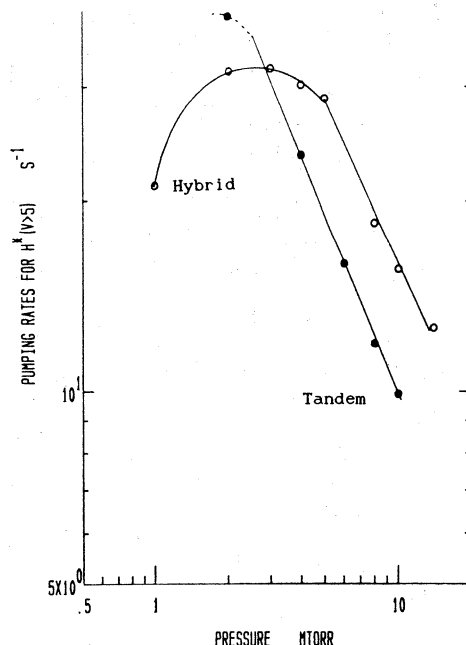


Figure 8. Pumping rates for $H_2(v>5)$ via fast electron collisions in the driver of the Tandem and Hybrid sources

EEDF's, for H₂(v>5) in the tandem and Hybrid source. It is seen that p decreases linearly with pressure showing that the fast electron density is inversely proportional to the pressure. However, in the case of the Hybrid the rapid change in the shape of the EEDF in the region of 1 - 3 mTorr as the primary distribution becomes degraded leads to a maximum in the pumping rate at ~ 3 mTorr. This maximum coincides with a maximum in the H⁻ density at the same pressure¹¹. No maximum in H⁻ density is reported in the case of the Tandem source. It is likely that the maximum in the H⁻ density in the Hybrid is linked to the primary confinement time.

CONCLUSIONS

It has been shown that the Langmuir probe is a useful method for establishing the EEDF in multipole plasmas. The new technique of obtaining the EEDF outlined here offers a substantial improvement in measurement resolution over previous methods. The technique has been further exploited to make time resolved measurements of the EEDF in repetitive pulsed and RF plasmas, with temporal resolutions of several μ s. This offers many exciting new applications for the Langmuir probe.

ACKNOWLEDGEMENTS

The experimental work described in this paper was carried out in collaboration with Dr. W.G. Graham, Queens Univ., Belfast and Dr. M Bacal, Ecole Polytechnique, Paris.

REFERENCES

1. Limpaecher R, and MacKennzie, (1973) Rev. Sci. Instrum. 44(6)
2. Pincosy P.A., Ehlers K.W., and Lietzke A.F. (1986) Rev. Sci Instrum. 57(10) p.2387
3. Proc. Second Int. Symp. Production and Neutralization of Negative Ions and Beams. Brookhaven Oct. 1980, BNL Report 51304.
4. Wicker T.E., and Mantei T.D., (1985) J. Appl. Phys. 57(5) p.1638
5. Drevillon M.J., Huc J.,Lloret A., Perrin J. deRosny G., and Scmitt J.P. (1980) Appl. Phys. Lett. 37(7) p.646
6. Pelletier J., and Arnl Y. (1984) Rev. Sci. Instrum. 55(10) p.1636
7. Conrad J.R., Castagna T. (1986) Bull. Am. Phys. Soc. 31 p.1479
8. Bacal M. Physica Scripta (1982) T2/2 p.467
9. Hiskes J.R.,and Karo A.M. (1984) J Appl. Phys. 56, p.1927
10. Hopkins M.B., and Graham W.G. Rev. Sci. Instrum. (1986) 57(9) p.2210
11. Bacal M., Bruneteau A.M., and Nachman M., (1984) J. Appl. Phys. p.15
12. Hopkins M.B., and Graham W.G.,(1987) J.Phys. D:Appl. Phys. 20 p.838
13. Bretagne J., Delouya G.,Capitelli M.,Gorse C.,and Bacal M., (1986) J.Phys. D:Appl. Phys. 18 p.811
14. Hopkins M.B. Proc. III'rd Euro. Workshop Production and Application of Light Negative Ions, Amersfoort,The Netherlands, Feb 17-19,1988, p.106
15. Graham W.G. and Hopkins M.B. (1986) AIP Conf. Proc. No. 158 p.145

EFFECTS DUE TO NEGATIVE IONS AND PARTICLES IN PLASMAS

Alan Garscadden

Wright Research and Development Center
Wright-Patterson AFB, OH 45433-6563

This paper considers some of the varied effects that may occur in electronegative plasmas, plasmas containing particles, and the effects of the negative ions and particles on the plasma properties and plasma chemistry. Important work relating to the topics has been given recently by Mandich and Reents (1989) on the reactions of silicon clusters with SiD₄; by Emeleus and Breslin (1970) on the influence of dust in discharge positive columns, and by Gibson (1966) on ionization phenomena in gas-particle plasmas. The chemistry and atom-atom recombination promoted by the presence of particles has been considered by Gould and Salpeter (1963) and by Herbst and Klemperer (1973) with relevance to the formation and depletion of molecules in interstellar space. Ferreira et al (1988) have analyzed quasi-neutral columns in electronegative gases.

For convenience we consider the silane discharge as a representative plasma that is an example of a reasonably complex system. The occurrence of particulates in deposition and etching plasmas is of technical concern in semiconductor processing. Previous studies of electron kinetics in silane have treated ionization, excitation and dissociation in reasonable detail however silane has not been regarded as an electronegative gas and there have been only a few reports mentioning negative ions in silane. At first sight this would appear to be appropriate. Hayashi's recommended cross section set (1986) for silane shows that the cross section for all negative ion forming channels is a relatively narrow resonance about 8eV with a peak magnitude of approximately $2 \times 10^{-18} \text{ cm}^2$. Many of the other cross sections have magnitudes in the range of $3 \times 10^{-16} \text{ cm}^2$. The momentum transfer cross section Q_{mt} is especially large. It does display a Ramsauer minimum around 0.35eV, although in Hayashi's cross section the value of Q_{mt} at the minimum is still quite large. We performed experiments by adding 1% silane to a dc positive column operating in argon. The impedance of the discharge increased and the electron density decreased markedly. The electron density was measured using a resonant cavity and it decreased by at least an order of magnitude on addition of silane (12mm id tube, 5 mA slow flow).

Fledderman et al (1985) also found in studies of pulsed discharges that a silane plasma demonstrated strong attachment which was discharge power dependent. The interpretation was that the effects were due to dissociated products. Si(1.39), SiH(1.3), SiH₂(1.1) and SiH₃(1.44) all have fairly large electron affinities. Perrin et al discuss reaction schemes of positive and negative ion clusters in silane and disilane (1984). The hydrogen depletion of large oligomeric negative ions is attributed to increasing electron affinities of Si₂H_x species as hydrogen is removed. These results were followed up by Srivastava (1987) who made direct scattering measurements of the dissociative attachment cross section of silane (with mass-spectrometric identification of the products). The new data and those of previous investigators are summarized in Table 1. The scattering measurements of the different experimenters, while they do not agree, all give low values for the cross sections. However there is evidence from mass-spectrometric experiments of Drevillon et al (1981), that negative ions are present in significant numbers in a magnetic multiple discharge. These investigators found clustering of both positive and negative ions even at pressures below 10 millitorr. The silicon to hydrogen ratios also increased, markedly so for the negative ions.

Srivastava (1989) has recently measured dissociative attachment from SiH₄ and SiH₆. Using the silane data as a summed cross section, we have calculated from a two-term solution of the Boltzmann equation, the attachment rates, ionization rates and the detachment rates of several silane-argon mixtures. The detachment cross section has been estimated from the analogous data for H⁻, from experiments by Peart and Dolder (1973) and from theory by Bely and Schwartz (1969). The cross section is very large (3x10⁻¹⁵ cm²) and in many cases, detachment would appear to be the dominant loss process for the negative ions. Some of the results of these calculations are shown in figure 1.

It is necessary to consider why the small DA cross section actually gives an attachment rate comparable to, or exceeding the ionization rate over a wide range of E/N. It occurs because there is a large excitation (dissociative) cross section between the attachment cross section and the ionization threshold. The electron energy distribution function (EEDF) falls off rapidly in this region at low E/N and the result is that k_a (attachment rate coefficient) is larger than k_i (ionization rate coefficient). As long as the gas is only weakly ionized it is expected that significant concentration of negative ions can still develop. The relative concentrations of negative ions is estimated in steady state from

$$\frac{dn_-}{dt} = k_a n_e [SiH_4] - k_d n_e n_- - \alpha n_- n_i$$

$$n_i = n_e + n_- : \text{plasma neutrality}$$

$$j = \sum_k n_k w_k q : \text{total current}$$

Table 1. Cross sections for the production of negative ions by dissociative electron attachment to silane. Cross sections are given in the units of 10^{-19} cm^2 .

<u>Ion</u>	<u>Ebinghaus et al</u>	<u>Potzinger & Lampe</u>	<u>Srivastava</u>
SiH_3^-	20	1.76	6.0
SiH_2^-	10	0.67	2.3
SiH^-	7	0.48	1.9
Si^-	2	0.10	0.12
H^-	-	-	2.2

Table 2. Estimated plasma parameters 0.3 torr, 10% silane in argon.

	<u>RF</u>	<u>DC</u>	
$[\text{SiH}_4]$	10^{15}	10^{15}	cm^{-3}
T_e	0.5	3	eV
a	10^{-7}	10^{-8}	$\text{cm}^3 \text{s}^{-1}$
k_a	10^{-13}	10^{-11}	$\text{cm}^3 \text{s}^{-1}$
k_d	10^{-9}	10^{-8}	$\text{cm}^3 \text{s}^{-1}$

$$n_- = \frac{n_e k_a}{(n_e k_d + \alpha n_i)} [\text{SiH}_4]$$

The negative ion concentration can be bounded by the conditions of no recombination and of no detachment

$$n_- = \frac{k_a}{k_d} N_0 ; \quad n_- = \frac{n_e k_a}{\alpha n_i} N_0$$

Note that diffusion of negative ions has been neglected. This is permissible because as long as some electrons are present, there will be an ambipolar field confining the negative ions. Significant differences are expected between low frequency RF discharges and positive column discharges as illustrated in Table 2. In the former the EEDF is bimodal and does not intercept the DA cross section efficiently as compared to the EEDF of the positive column discharge. The latter situation gives a good overlap and a large rate constant. This results in relatively large negative ion concentrations in the positive column discharge. The positive column discharge also showed sharp striations similar to those described by Emeleus et al (1968) in an iodine discharge and it was also quite unstable. The stability of electronegative plasmas has been analyzed by Haas (1973). The stability depends on the ratio of the derivatives of the attachment and ionization rate constants. The calculated stability onset for 5% silane in argon is illustrated in figure 2.

The efficiency of plasma enhanced chemical reactors is strongly influenced by contamination and particle formation. The particles can be conducting or insulating. The particles can be introduced by several mechanisms. These include flaking from the substrate or walls, clustering (neutral-or ion-induced), or polymerization of the gas and/or its decomposition products, sputtered material or ablation from the substrate gas contamination and aerosols in the gas introduced in the reactor. The sizes of the cluster or particle can range a few atoms to 10^{-2} cm. The aerosol size distribution will often be log-normal (Reist, (1984)). The neutral or ion clustering is observed to occur more rapidly in silane mixtures at higher power loadings and at higher pressures. (Roth(1986)) The initial clustering steps are the most important and the most difficult to explain. Mandich and Reents (1989) have shown that silicon cluster positive ions undergo exothermic sequential clustering reactions with deuterated silane (and presumably silane). There is a series of three stepwise additions of SiD_2 accompanied by loss of D_2 . The sequence then terminates and further cluster growth occurs only by absorption of SiD_4 . These authors report that the positive ions $\text{Si}^+, 4, 6, 7$ and all of the negatively charged silicon clusters (up to $n=7$) do not react exothermically with SiD_4 . (In many species it is expected that the growing cluster will reach an unstable geometry or that in a high density plasma recombination energy will cause it to heat up to temperatures that cause evaporation of the cluster or in

the case of some metals, thermionic emission). Silane compounds may cluster more easily because of the elimination of hydrogen from a growing cluster. The propensity of clustering to be observed in many electronegative gases at low pressures (Selwyn et al. (1989)) and the long residence time of negative ions in the plasma, suggests that other negative ion channels leading to clustering may occur.

These channels include ion-ion recombination, which usually proceeds at a very fast chemical rate and, at larger cluster masses, may be diffusion limited at quite low pressures, and ion-radical clustering. At high power densities ablation and supersonic cooling, possibly produce clustering. If the particle is macroscopic (liquid or solid), it is expected that in the plasma usually it will charge up negative, acting like a floating Langmuir probe, in both senses. If the excitation is at high frequency and at relatively high pressure, the particle will acquire a potential negative wrt plasma potential of a few kT_e/e . At low excitation frequencies and low pressures the particle will intercept the fast beam electrons and, in order to maintain charge equilibrium on the particle, a corresponding high negative potential will be acquired. The potential will be higher, the closer it is to the electrode (but outside the sheath). In both situations the particles act as efficient recombination sinks for the electrons and ions. Other effects on neutral chemistry can occur depending on the nature and surface properties of the particles and from the self-consistent fields of the reactor. Figure 4 illustrates the principal effects introduced by the presence of the particle in the plasma. We extend the study of Emeleus and Breslin (1970) (E&B) to the rf reactor. The ambipolar fields of the plasma in a particle contamination situation will tend to concentrate the particles on axis, given sufficient time, for the particles to drift to the center of the discharge (assumed symmetric excitation). If the line density is such that there is sheath interaction between the particles, or if the recombination loss is large on these particles, than these effects form a new boundary condition for the plasma. Since the dimension of the perturbation is actually determined by the Debye length and not by the dimensions of the particles, relatively few particles are required to exact a new boundary condition. It is noted that the surface area of 1 milligram of silica of particles of 0.1 microns in diameter equals approximately 230 cm^2 . Once formed, even if they are not negatively charged, such particles will have low diffusion coefficients (e.g. a 10^{-4} cm sphere will have a diffusion coefficient of approximately $3 \times 10^{-4} \text{ cm}^2/\text{sec}$ at 1 torr) relative to the electrons and ions.

Following E & B, the ionization balance equation for the plasma with homogeneous particle losses and possible beam intercept is now

$$D_a \frac{d^2 n}{dx^2} + (B - b) - C_1 n N = 0$$

where n is the averaged electron concentration, D_a is the ambipolar diffusion coefficient, B is now the total ionization frequency in the absence of particles, b is introduced as an

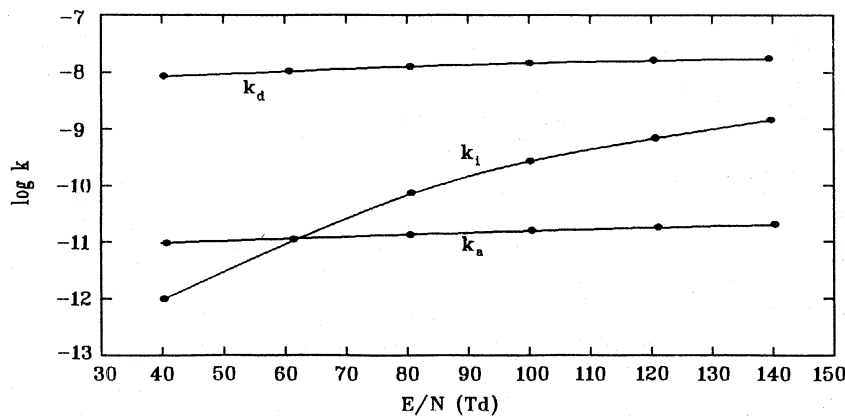


Figure 1. Ionization attachment and detachment coefficients for 10% silane and 90% argon.

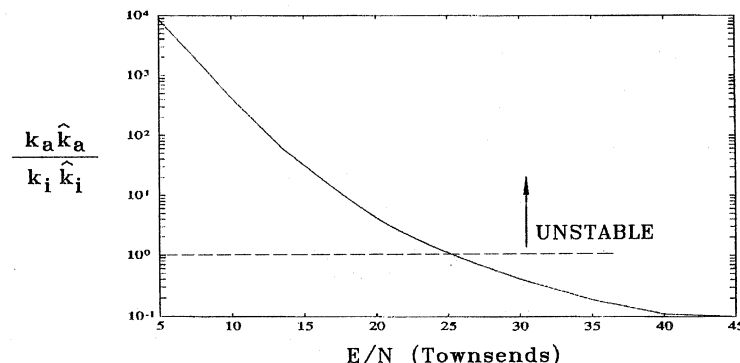


Figure 2. Ionization wave stability for 5% silane in argon.

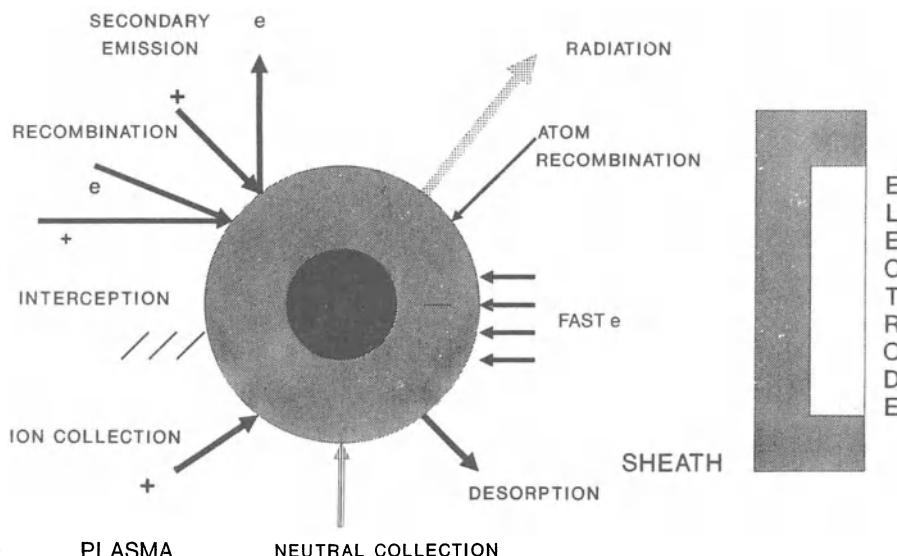


Figure 3. Particle - plasma interactions near an electrode.

interception factor for fast electrons, C_1 is a coefficient of volume loss of electrons, and N is the density of the particles

$$C_1 = \frac{1}{4} \left(1 - \frac{\pi}{6} \alpha^3 N C_2 \right)^{-1} \frac{v_e}{\pi} \alpha^2 \exp(-|V_p|)$$

C_2 is a factor depending on the ratio of the Debye length to particle diameter a , by which the volume denied to ionization is determined.

Then the net effect of increasing b or C_1 is to increase the required ionization frequency for a requested current or electron density. E & B have made calculations for ideal positive column conditions. If the particles are distributed non-uniformly, say near Gaussian, then one derives the relevant balance equation as

$$\frac{d^2 n}{dx^2} + (k_1 - k_2 f(x)) n = 0$$

where

$$X = \frac{x}{L} \quad k_1 = \frac{L^2 (B - b)}{D_a} \quad k_2 = \frac{LC_1}{D_a}$$

where $f(x)$ is the spatial distribution of the particles.

In the rf plasma the term $k_2 f(x)$ will be greater than k_1 over part of the oscillation cycle. Under these circumstances the electron concentration profile will develop an off-axis maximum if the time constants for the losses are fast enough. If the particles form an internal line sink then the discharge approximates a coaxial plasma for radial geometry with an off-axis maximum in density even for very small dimensions of the sink.

The actual particle position is given by a balance between the electrostatic and gravitational forces. The charge on the particle is determined by the requirement of equal fluxes of positive and negative species to its surface. If $a=10^{-4}$ cm and the floating potential is -3 volts then the number of electronic charges required is approximately 2000; at specific density of 4, the weight of the particle is 2×10^{-12} gms; thus equilibrium is reached in a field of approximately 0.6 volts cm^{-1} , a relatively low field. Selwyn et al (1989) from results of LIF and light scattering experiments on an asymmetric reactor, suggest that particles and negative ions are co-localized near the potential maximum, in this case near the sheath boundary. The equilibrium scales as $V_p E \propto a^2$, so that larger particles will move to appropriately higher fields. In a rf reactor this may cause the particles to intercept higher energy electrons and to acquire a higher surface charge. One therefore expects a larger spatial distribution of particles as compared to the negative ions, which corresponds to Selwyn's observations. There are limits on the magnitude of charge that a particle can acquire (Reist,

l.c.). If the particle is a spherical solid the maximum number of charges is $n(\text{max}) = E_s a^2 / 4e$ where E_s is the surface field intensity at which emission of ions or electrons occurs. For ions this is approximately 2×10^8 volts cm^{-1} , and for electrons it is 10^7 volts cm^{-1} . For 1 micron particles these values correspond to 3.5×10^6 and 1.7×10^5 electronic charges per particle respectively. If the particle is actually in liquid form then a much lower charge limit exists, known as the Rayleigh limit. It occurs when the electrostatic repulsive force exceeds the surface tension of the droplet, and is

$$n(\text{Rayleigh}) = \frac{(2\pi\gamma a^3)^{1/2}}{e} \cong 5 \times 10^3 \gamma^{1/2}$$

where γ is the surface tension of the liquid for a 1 micron droplet. Therefore the above estimates indicate that such a droplet can easily attain the required charge for a few volts floating potential. Very high potentials can be reached if the particle is a solid.

The energy balance equation for the particle (assumed spherical) is

$$\frac{\pi a^3}{6} \rho_s \frac{dT}{dt} = \pi a^2 (H_1 - H_2 - H_3 + H_4)$$

H_1 , H_2 , H_3 and H_4 are thermal energy transfer rates for e-ion recombination (including ion bombardment energy), radiation cooling, gas cooling and the net of atom/radical recombination and desorption respectively. Letting p equal the ratio of the ion current on the particle surface to the random ion current density, then

$$H_1 = \frac{1}{4} nq \langle v_+ \rangle \frac{(V_i + V_f)p}{4.18}$$

The radiation loss is assumed to be given by the Stefan-Boltzmann law

$$H_2 = \sigma (T_p^4 - T_g^4)$$

where T_p , T_g are the particle and gas temperatures. H_3 is a gas cooling term dependent on the collision frequency, surface accomodation and gas species. E & B discuss the gas cooling at both low pressures (Knudsen) and at high pressures (continuum). In low pressures plasma reactors, Knudsen-type cooling is operative. An additional term in reactive plasmas is H_4 which is caused by atom-atom or radical recombination on the surface of the particle. There may also be cooling due to desorption. While the net results will be only of the order of eV per reaction, the density of radicals is likely to be order of magnitude larger than the electron density. The sum of the ion heating is approximated to be the order of the ionization energy

per recombination (Gibson) so that a rough approximation is that the ion and radical heating terms are equal. Then one obtains $H_1 + H_4$ as approximately $10^{-12} n_e \text{ cal cm}^{-2} \text{ s}^{-1}$. At electron densities of 10^{11} , 10^{12} and 10^{13} the equilibrium particle temperatures (at low pressure, neglecting gas cooling) for an emissivity of 0.6 are 595, 1050 and 1850 K respectively. Heating times are in the range of millisecs for 10^{12} electron density. Thus under normal circumstances thermionic emission from the particles in an rf reactor is not anticipated. In a constricted dc discharge sufficient heating of the particle to cause electron emission might occur and the particle then becomes positively charged.

The electron emission that can occur from low work function particles is of interest in combustion and to magnetohydrodynamic generators. As the particle loses negative charge to the gas through thermionic emission, its effective work function increases by the amount $2.88 \times 10^{-7} n_r/a$ electron volts if a (diameter) is measured in cm, and n_r is the number of residual positive charges (Lawton and Weinberg, 1969). Space limitations do not permit discussion of the influences of particles on combustion plasmas or on electrical breakdown (Laghari and Qureshi, 1981).

REFERENCES

- Bely, O., and Schwartz, S.B., 1969, J. Phys., B2, 159.
- Drevillon, B., Huc, J., Lloret, A., Perrin, J., de Rosny G., and Schmitt, J.P.M., 1981, "Positive and Negative Ions in Silane Plasmas", 634-637, Proceedings of the 5th International Symposium on Plasma Chemistry, eds Waldie, B., and Farnell, G.A.
- Emeleus, K.G., and Breslin A.C., 1970, Int. J. Electronics, 29, 1.
- Emeleus, K.G., Gray, E.W., Coulter, J.R.M., and Woolsey, G.A., 1968, Int. J. Electronics, 25, 367.
- Ferreira, C.M., Gousset, G., and Touzeau, M., 1988, J. Phys. D., Appl. Phys., 21, 1403.
- Fledderman, C.B., Beberman, J.H., and J.T. Verdheyen, 1985, J. Appl. Phys., 58, 1344.
- Gibson, E.G., 1966, PhD Thesis, California Institute of Technology.
- Gould, R.J., and Salpeter, E.E., 1963, Astrophys. J., 138, 393
- Haas, R., 1973, Phys. Rev., A8, 1017.
- Hayashi, M., 1987, in "Swarm Studies and Inelastic Electron-Molecule Collisions" eds L.C. Pitchford, B.V. McKoy, A. Chutjian and S. Trajmar, Springer Verlag, New York.
- Herbst, E., and Klemperer, W., 1973 Astrophys. J., 185, 505.
- Lawton, J., and Weinberg, F.J., 1969, "Electrical Aspects of Combustion", Clarendon Press, Oxford.

Mandich, M.L., and Reents, W.D., 1989, J. Chem Phys., 90, 3121.

Peart, B., and Dolder, K.T., 1973, J. Phys., B6, 1497.

Perrin, J., Lloret, A., de Rosny, G., and Schmitt, J.P.M., 1984, Intl J. of Mass Spec. and Ion Physics, 57, 249.

Reist, P.C., 1984, "Introduction to Aerosol Science", Macmillan, New York.

Roth, R.M., Spears, K.G., Stein, G.D., and Wong, G., 1986, Appl. Phys. Lett., 46, 253.

Selwyn, G.S., Singh, J., and Bennett, R.S., 1989, J. Vac. Sci. Tech., to be published.

Srivastava, S.K., and de A Souza, A.C., to be published.

ELECTRON AND VIBRATIONAL KINETICS IN MOLECULAR DISCHARGES

J. Loureiro

Centro de Electrodinâmica da Universidade Técnica de Lisboa (INIC)
Instituto Superior Técnico, 1096 Lisboa Codex, Portugal

INTRODUCTION

Great attention has recently been devoted to the study of the coupling between the electron energy distribution function (EEDF) and the vibrational distribution function (VDF) of molecules in the electronic ground-state in discharges in molecular gases, such as N_2 [1-4] and H_2 [5-6]. This coupling, which is principally caused by the superelastic collisions of the electrons with vibrationally excited molecules, has been shown to increase the high-energy tail of the EEDF, thereby affecting the whole discharge kinetics.

The theoretical study of this subject is, therefore, of great interest in such important applications as gas lasers, plasma chemistry, and plasma processing. Gas mixtures with N_2 are usually employed for surface treatments such as metal nitriding and coating. In surface nitriding, for example, the plasma is a glow discharge in a $N_2 - H_2$ mixture [7].

Self-consistent analyses of this problem have been developed mostly for time-dependent conditions by Capitelli and co-workers [4,6]. So far, self-consistent analyses for steady-state conditions have been performed only for N_2 discharges by Rohlrena and Mašek [3] and for N_2 and H_2 discharges by the present author [1,2,5].

This paper reviews the electron and vibrational kinetics in stationary glow discharges in pure N_2 , pure H_2 , and in $N_2 - H_2$ mixtures. For this purpose, we present, both for discharges in pure N_2 [1,2] and in pure H_2 [5], self-consistent calculations of the steady-state, homogeneous, electron Boltzmann equation and of a system of steady-state rate balance equations for the vibrational levels of the electronic ground-state, including $e - V$, $V - V$, and $V - T$ energy exchange processes. For the case of $N_2 - H_2$ mixtures, self-consistent calculations are not yet available. We present only Boltzmann calculations of the EEDF taking into account the effects of $e - V$ superelastic collisions assuming given vibrational distributions for both types of molecules [8].

A comparative analysis of the behaviour and main features of the EEDF is carried out for N_2 , H_2 , and $N_2 - H_2$ discharges, as well as a comparison between the calculated VDF in pure N_2 and pure H_2 .

Finally, this paper also presents other relevant calculated data, such as, e.g., the rate coefficients for excitation by electron impact.

THEORETICAL FORMULATION

Discharges in Pure N_2 and Pure H_2

For the case of pure N_2 and pure H_2 discharges, we have used and solved simultaneously the steady-state, homogeneous, electron Boltzmann equation, as derived from the usual two-term expansion in spherical harmonics [9], and the system of steady-state rate balance equations for the vibrational levels of $N_2(X^1\Sigma_g^+)$ and $H_2(X^1\Sigma_g^+)$ including $e - V$, $V - V$, and $V - T$ energy exchange processes. The superelastic $e - V$ collisions were taken into account both in the Boltzmann and in the rate balance equations, owing to the large populations N_v in $v > 0$ levels usually present in a discharge. On the contrary, superelastic collisions of the electrons with electronically excited molecules were neglected.

The excitation of electronic states and the direct ionisation were treated as single-energy loss processes ($X - Y$ transitions, where Y denotes an electronic excited state or the ground-state of N_2^+ and H_2^+). In the case of N_2 , we have also extended our model by properly taking into account the effect of the $X, v - Y, v'$ transitions in the solutions to the Boltzmann equation. The simplest approach was, however, proved to be accurate enough in the case of N_2 [2]. Moreover, the secondary electrons produced by ionisation were neglected which is justified for the range of the ratio of the electric field to the gas density, E/N , $\lesssim 2.5 \times 10^{-15} V cm^2$ of interest here [10,11].

Under these assumptions the Boltzmann equation can be written as [9]

$$\frac{d}{du} \left[\frac{1}{3} \left(\frac{E}{N} \right)^2 \frac{u}{\sigma_c} \frac{df}{du} + \frac{2m}{M} \sigma_c u^2 \left(f + \frac{kT_g}{e} \frac{df}{du} \right) + 4 B_0 \sigma_0 u f \right] = J_e(f) + J_v(f). \quad (1)$$

Here, $f(u)$ is the EEDF with the normalisation $\int_0^\infty f \sqrt{u} du = 1$, u is the electron energy in eV , e is the absolute value of the electron charge, m and M are the electron and the molecular mass, respectively, T_g is the gas temperature, k is the Boltzmann constant, σ_c is the momentum transfer cross section, B_0 is the rotational constant, and σ_0 is a constant electron cross section which takes into account the excitation of rotations in the continuous approximation [9]. $J_e(f)$ and $J_v(f)$ account for the excitation of the electronic states plus ionisation and for the inelastic and superelastic $e - V$ energy exchanges, respectively, and may be written as follows:

$$J_e(f) = \sum_Y [uf(u)\sigma_X^Y(u) - (u + V_X^Y)f(u + V_X^Y)\sigma_X^Y(u + V_X^Y)]; \quad (2)$$

$$\begin{aligned} J_v(f) = & \sum_{v,w} [\delta_v [uf(u)\sigma_v^w(u) - (u + V_v^w)f(u + V_v^w)\sigma_v^w(u + V_v^w)] \\ & + \sum_{w,v} \delta_w [uf(u)\sigma_w^v(u) - (u - V_v^w)f(u - V_v^w)\sigma_w^v(u - V_v^w)]]. \end{aligned} \quad (3)$$

The term $J_e(f)$ is written in the form expressed by (2) only when the excitation of electronic states and the ionisation are treated as single-energy loss processes. Otherwise, equation (2) should be replaced by another expression taking into account the $X, v - Y, v'$ transitions [2]. In equations (2) and (3), σ_X^Y and V_X^Y denote the cross

section and the energy threshold for the excitation of the electronic state Y from X, respectively, σ_v^w and σ_v^v denote the inelastic and the superelastic cross sections for $e - V$ energy exchanges (V_v^w is the corresponding energy threshold), and $\delta_v = N_v/N$ is the fractional population in the $v - th$ level.

In each of these gases, equation (1) is coupled through the fractional vibrational populations δ_v to a system of steady-state rate balance equations for these populations. These equations are of the type

$$\left(\frac{dN_v}{dt} \right)_{e-V} + \left(\frac{dN_v}{dt} \right)_{V-V} + \left(\frac{dN_v}{dt} \right)_{V-T} + R_v = 0 , \quad (4)$$

where the dN_v/dt terms, whose explicit form may be found in [1], account for $e - V$, $V - V$, and $V - T$ processes and atomic recombination, respectively. In the case of H_2 discharges the $V - T$ terms include also reactions involving H atoms, as non-negligible atom concentrations were experimentally detected [12]. These reactions include both a direct process and a reactive one in which atomic exchange occurs between two collision partners, H and H_2 [12].

The system (4) takes into account dissociation by $V - V$ and $V - T$ processes which is modelled here, following Capitelli and co-workers [4,6], as a transition to a pseudolevel $v = n^* = n + 1$ above the last bound vibrational level $v = n$ ($n = 45$ in N_2 and $n = 14$ in H_2). The total rate of dissociation by these processes, which is given by

$$v_{\text{diss}}^V = N_n \left(N P_{n,n^*} + \sum_{v=1}^n N_v P_{n,n^*}^{v,v-1} \right) , \quad (5)$$

where the coefficients P denote the rate coefficients for the $V - T$ and $V - V$ processes leading to dissociation, must be exactly balanced in (4), under steady-state conditions, by a set of source terms R_v such that $\sum_{v=0}^n R_v = v_{\text{diss}}^V/N^2$. Mathematically, this condition insures that the $n + 1$ equations (4) ($v = 0$ up to $v = n$) are linearly dependent and thus have a unique solution satisfying the normalisation condition $\sum_{v=0}^n \delta_v = 1$.

The term R_v represents the rate of atomic recombination into the $v - th$ level which is unknown, making it necessary to work out several models in order to test the effects of the recombination. It should be noted, however, that the sum $\sum_{v=0}^n R_v$ does not represent the total recombination rate but only that part of it that compensates for the dissociation rate by $V - V$ and $V - T$ processes given by (5).

When all the collisional data are inserted in (1) - (5) these equations can be solved to yield the EEDF, $f(u)$, and the VDF, δ_v , as a function of the independent parameters E/N , $\delta_e = n_e/N$ (degree of ionisation), and $\delta_a = N_a/N$ (degree of dissociation in the case of H_2 ; N_a is the density of H atoms). Such result constitutes, therefore, a similarity law for the steady-state problem as formulated here. Finally, we note that a self-consistent determination of δ_a is out of the scope of this work as it would require a detailed analysis of the dissociation-atomic recombination balance. Therefore, δ_a is treated here as an independent parameter.

A self-consistent determination of the EEDF and the VDF was not attempted in this case. Here, we present only Boltzmann calculations taking into account the effects of $e - V$ superelastic collisions assuming given vibrational distributions with the form of modified Treanor distributions [13] for both types of molecules.

RESULTS AND DISCUSSION

EEDF, VDF, and Relationships Between Proper Variables

The calculated VDF can be characterised by a vibrational temperature T_V measuring the degree of vibrational excitation, which is defined as the characteristic vibrational temperature of the Treanor-like distribution [13] that best fits to the calculated VDF for $0 \leq v \leq 3$. Therefore, T_V is a function of the independent parameters E/N , $\delta_e = n_e/N$, and $\delta_a = N_a/N$. This function can be inverted making it permissible to use T_V as an independent parameter in place of δ_e . The effects of $V - T$ collisions involving atoms will be considered only for H atoms.

Figs. 1(a) and (b) show the calculated EEDF and VDF in pure N_2 for $E/N = 10^{-15} V cm^2$ and various values of T_V . As T_V increases a plateau appears in the VDF at intermediate v -levels as a result of non-resonant $V - V$ energy exchanges, but, for higher v , it appears a steeply decreasing region principally caused by the effects of dissociation by $V - V$ and $V - T$ processes. The results in fig. 1 were obtained assuming that atomic recombination populates the level $v=0$ only. Fig. 2 shows the changes caused on the VDF by considering different models of recombination. The changes are negligibly small at low v -levels but would become significant at the upper levels if recombination preferentially populated the high vibrational levels. In this work, excepting in fig. 2, all the results were obtained assuming that recombination populates only the level $v = 0$, that is, $R_0 = v_{\text{diss}}^V / N^2$ and $R_v = 0$ for $v > 0$ in equation (4).

Fig. 3 shows, for three different values of E/N , the EEDF consistent with the VDF for $T_V = 4000 K$ and $T_V = T_g = 400 K$. These results illustrate the effects of the $e - V$ superelastic collisions on the high-energy tail of the distribution, which cause a strong enhancement of the tail for the lower E/N values. Finally and still for pure N_2 , fig. 4 presents curves of δ_e vs. E/N for various constant values of T_V . These data represent, therefore, the values of the degree of ionisation necessary to produce a given T_V as a function of E/N .

Figs. 5-8 are for pure H_2 . Fig. 5 represents the relationship $T_V(\delta_e, E/N)$ in H_2 for $\delta_a = 0$. From the comparison with fig. 4 we can conclude that the value of δ_e necessary to produce a VDF with the same value of T_V is significantly higher in H_2 than in N_2 . Figs. 6(a) and (b) show the calculated EEDF and VDF for $\delta_a = 0$, $E/N = 3 \times 10^{-16} V cm^2$ and various values of T_V . The comparison between figs. 3 and 6(a) indicates that the effects of the $e - V$ superelastic collisions are larger in N_2 than in H_2 . On the other hand, the shape of the VDF in fig. 6(b) is rather similar to that for N_2 , but in H_2 the fall-off at high v -levels is entirely caused by $V - T$ deactivation.

The effects of $V - T$ processes with H atoms are illustrated in figs. 7 and 8. These effects are extremely important for the VDF (fig. 7), even for atom concentrations as small as 10^{-2} , originating a rapid depopulation at high v -levels. Nevertheless, the relationship shown in fig. 5 is relatively insensitive to $V - T$ deactivation by H atoms as long as $\delta_a < 10^{-2}$ (see fig. 8).

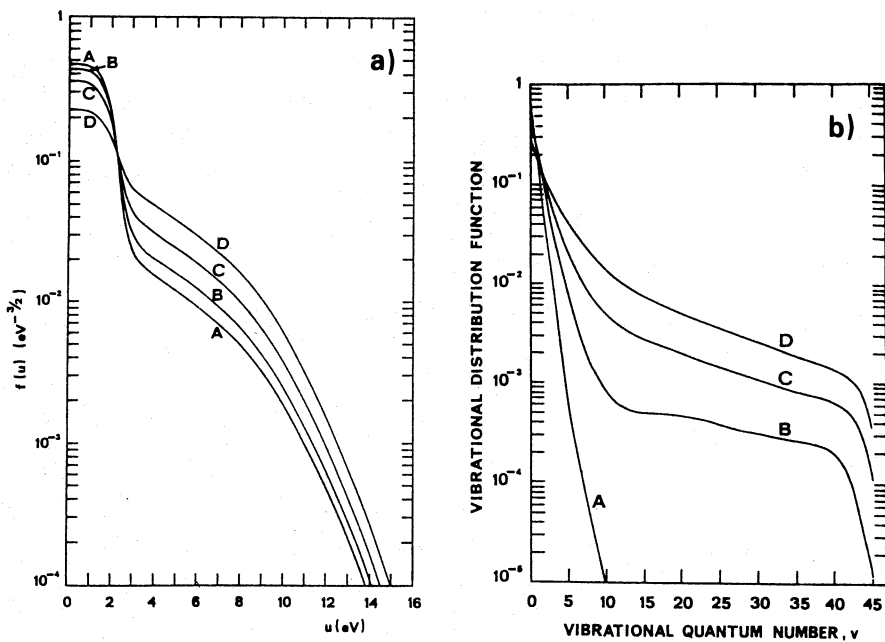


Fig. 1 - (a) EEDF in N_2 for $E/N = 10^{-15} \text{ V cm}^2$ and the following values of T_V in K : (A)2000; (B)3000; (C)4000; (D)6000. (b) VDF for the same conditions as in fig. 1(a) (from [1]).

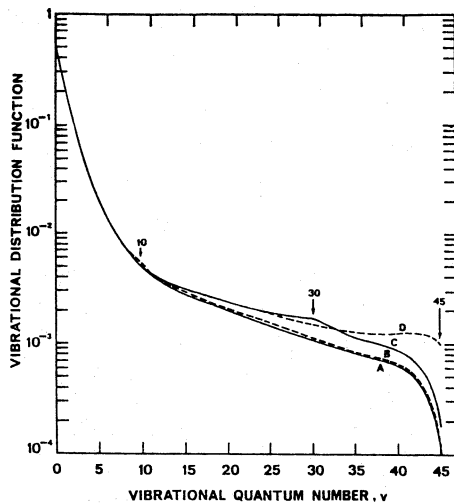


Fig. 2 - Calculated VDF in N_2 for $E/N = 10^{-15} \text{ V cm}^2$ and $T_V = 4000K$ assuming that atomic recombination populates only the following v -level : (A) $v = 0$; (B) $v = 10$; (C) $v = 30$; (D) $v = 45$ (from[1]).

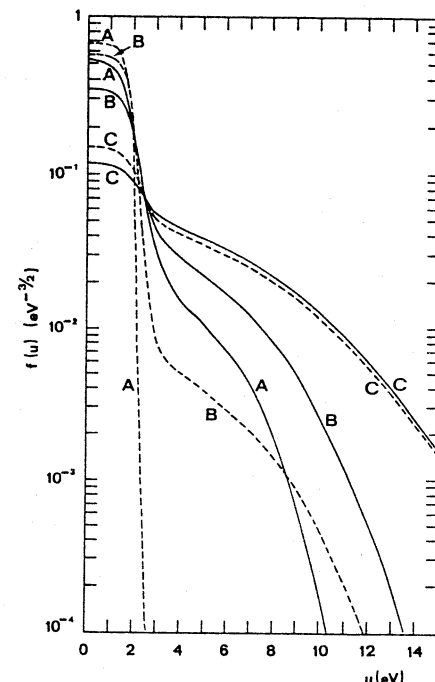


Fig. 3 - EEDF in N_2 for $T_V = 4000K$ (full curves) and $T_V = 400K$ (broken curves) and the following values of E/N in 10^{-16} V cm^2 : (A)3; (B)8; (C)21.1 (from[1]).

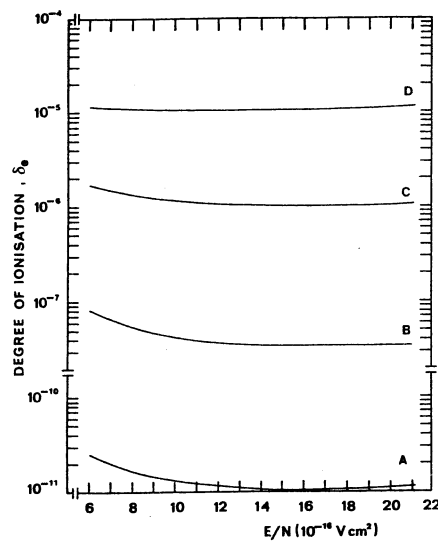


Fig. 4 - Curves of δ_e vs. E/N in N_2 for the following constant values of T_V in K : (A) 2000; (B) 3000; (C) 4000; (D) 6000 (from [1]).

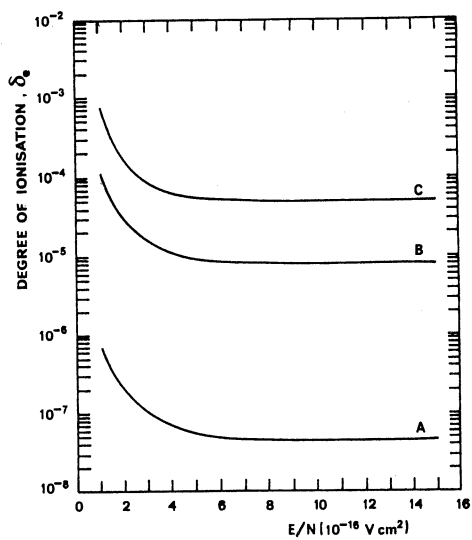


Fig. 5 - Curves of δ_e vs. E/N in H_2 for $\delta_a = 0$ and the following constant values of T_V in K : (A) 2000; (B) 3000; (C) 4000 (from [5]).

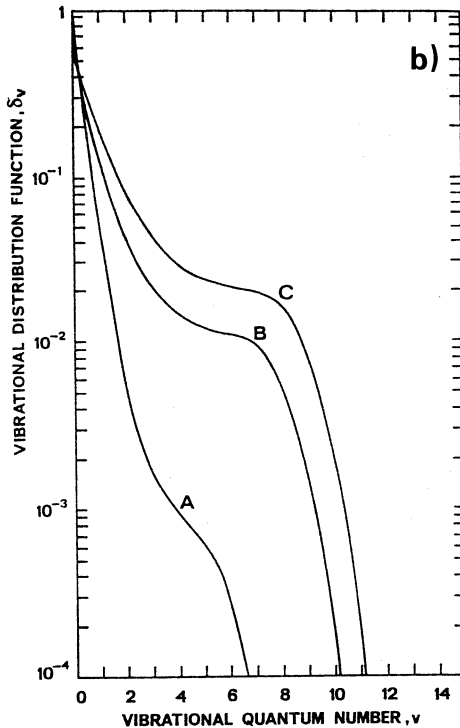
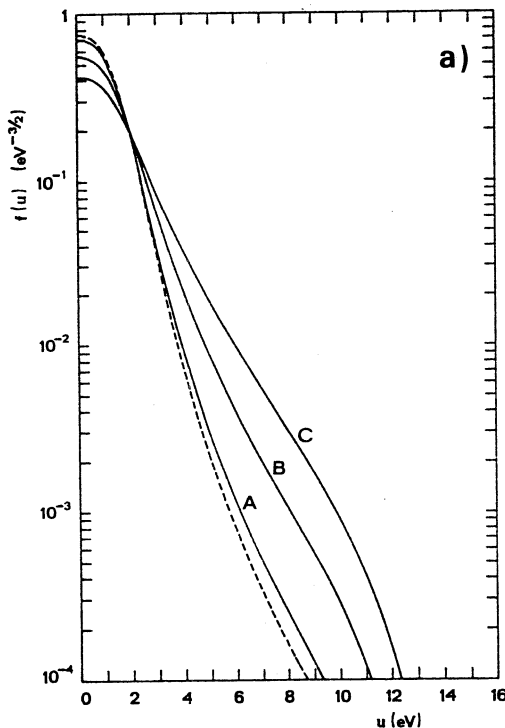


Fig. 6 - (a) EEDF in H_2 for $E/N = 3 \times 10^{-16} \text{ V cm}^2$, $\delta_a = 0$ and the following values of T_V in K : (A) 2000; (B) 3000; (C) 4000. (b) VDF for the same conditions as in fig. 6(a). The broken curve on fig. 6(a) is the EEDF for $T_V = T_g = 400K$ (from [5]).

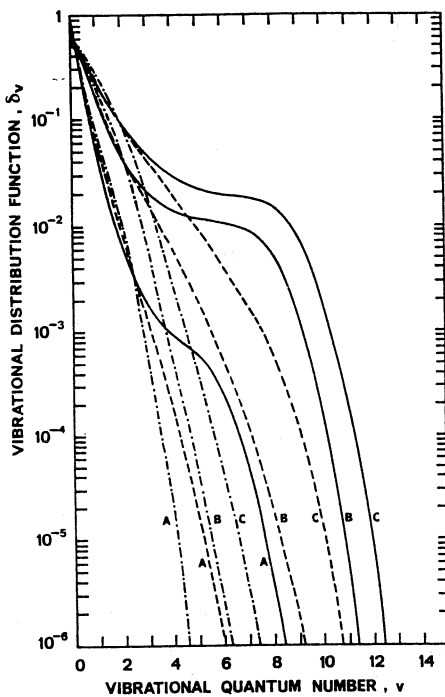


Fig. 7 - VDF in H_2 for $E/N = 3 \times 10^{-16} V cm^2$, the same values of T_V as in fig. 6 (b), and the following values of δ_a : 0 (full curves); 10^{-2} (broken curves); 10^{-1} (chain curves) (from [5]).

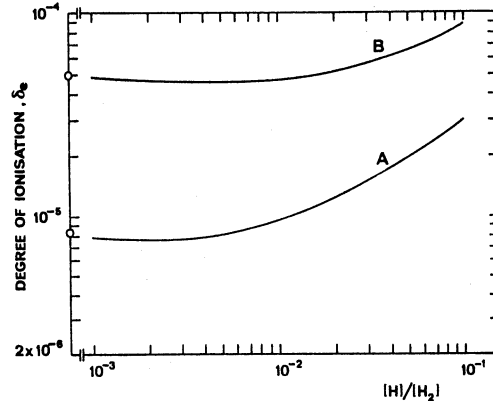


Fig. 8 - Curves of δ_e vs. δ_a for $E/N = 10^{-15} V cm^2$ and the following values of T_V in K : (A) 3000; (B) 4000. The symbols 0 represent the values of δ_e for $\delta_a = 0$ (from [5]).

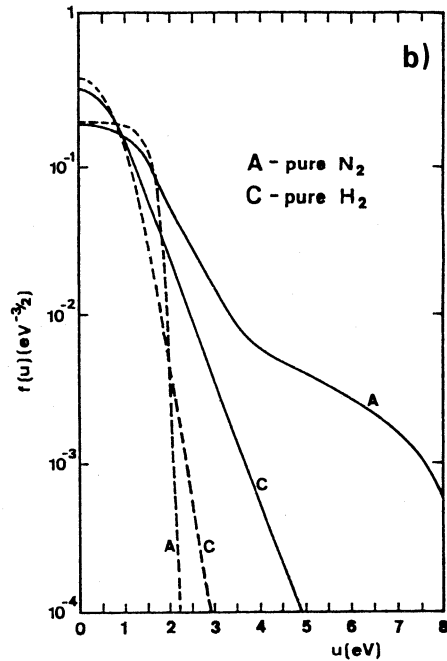
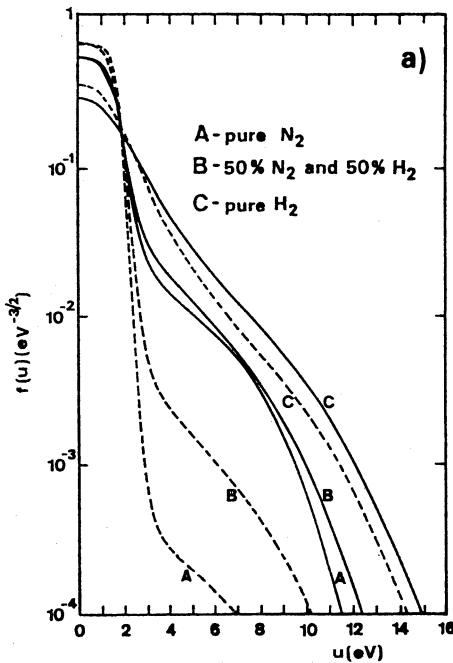


Fig. 9 - EEDF in a $N_2 - H_2$ mixture for $E/N = 5 \times 10^{-16} V cm^2$ (fig. 9a) and $10^{-16} V cm^2$ (fig. 9b). Both figures represent calculated EEDF for the following values of T_V in K : full curves - $T_V(N_2) = 4000$ and $T_V(H_2) = 3000$; broken curves - $T_V(N_2) = T_V(H_2) = 400$.

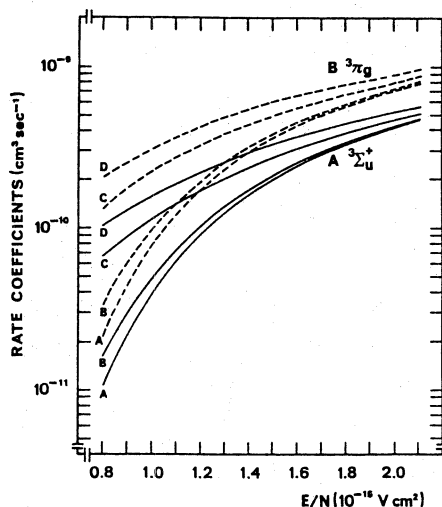


Fig. 10 - Electron rate coefficients for the excitation of the states $N_2(A\ ^3\Sigma_u^+)$ (full curves) and $N_2(B\ ^3\Pi_g)$ (broken curves) vs. E/N and for the following values of T_V in K : (A)400; (B)2000; (C)4000; (D)6000 (from[1]).

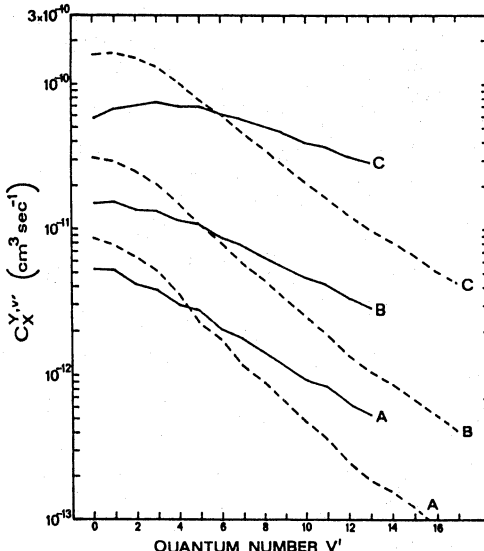


Fig. 11 - Rate coefficients for the excitation of the states $N_2(A\ ^3\Sigma_u^+, v')$ (full curves) and $N_2(B\ ^3\Pi_g, v')$ (broken curves) from the entire $N_2(X)$ state as a function of v' , for $T_V = 4000K$ and the following values of E/N in $10^{-15}V\text{cm}^2$: (A)0.6; (B)1; (C) 2.5 (from[2]).

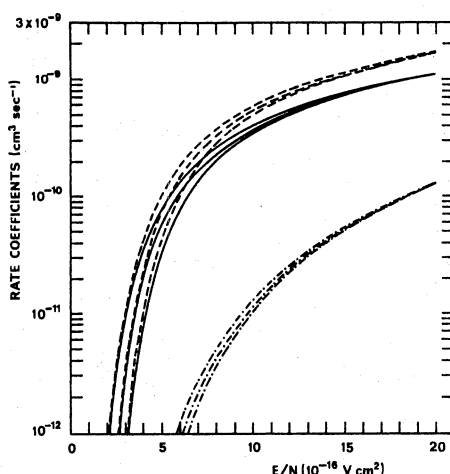


Fig. 12 - Rate coefficients, vs. E/N and for $\delta_a = 0$, for excitation of the state $H_2(b)$ (full curves), dissociation into $H(1s) + H(1s)$ (broken curves), and dissociation into $H(1s) + H(n = 2)$ (chain curves). In each case, the lower, intermediate, and upper curves correspond to the values of $T_V = 400, 3000$, and $4000K$, respectively (from[5]).

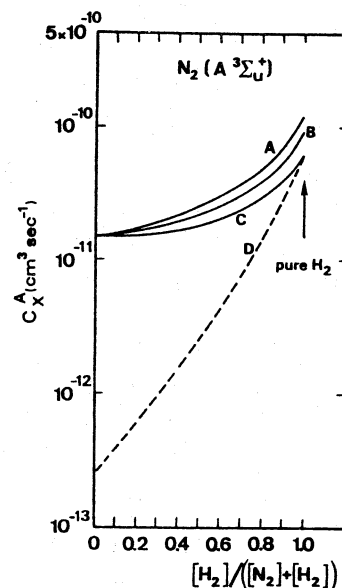


Fig. 13 - Rate coefficients for the excitation of the state $N_2(A)$ in a $N_2 - H_2$ mixture, as a function of the fractional $[H_2]$ concentration, for $E/N = 5 \times 10^{-16}V\text{cm}^2$, $T_V(N_2) = 4000K$ (full curves), and for the following $T_V(H_2)$ values in K : (A)4000; (B)3000; (C)400. The broken curve (D) is for $T_V(N_2) = T_V(H_2) = 400K$.

Finally, figs. 9(a) and (b) show, for comparison, the calculated EEDF for pure N_2 and pure H_2 and for $E/N = 5 \times 10^{-15} V cm^2$ (fig. 9a) and $10^{-16} V cm^2$ (fig. 9b). Both figures represent EEDF for $T_V(N_2) = 4000 K$ and $T_V(H_2) = 3000 K$ and for $T_V(N_2) = T_V(H_2) = 400 K$. On fig. 9(a) we have also represented the EEDF for a mixture of 50% N_2 and 50% H_2 . The results obtained demonstrate that an increase in the concentration of H_2 , in a $N_2 - H_2$ glow discharge, enhances the tail of the EEDF and, therefore, produces an increase in the electron rate coefficients for the excitation of the electronic states, except for the lower E/N and, simultaneously, higher T_V values.

Electron Rate Coefficients

Fig. 10 shows the electron rate coefficients for the excitation of the N_2 triplet states $A^3\Sigma_u^+$ and $B^3\Pi_g$, as a function of E/N and for various values of T_V . An increase in T_V increases all the rates, especially at the lower E/N values, as a result of the enhancement of the high-energy tail of the EEDF. In fig. 11 are presented results obtained when we consider the manifold of vibrational transitions $X, v - Y, v'$ in the Boltzmann equation. Fig. 11 shows the electron rate coefficients $C_X^{Y, v'}$ for excitation of the N_2 states $Y, v' = A^3\Sigma_u^+, v'$ and $= B^3\Pi_g, v'$, from the entire $N_2(X^1\Sigma_g^+)$ state, as a function of v' , for $T_V = 4000 K$ and various values of E/N . These coefficients constitute basic data for the interpretation of measured vibrational populations in excited electronic states.

Fig. 12 shows excitation rates in H_2 . We present the excitation rates of the triplet state $b^3\Sigma_u^+$ and of the group of triplet states $b^3\Sigma_u^+, c^3\Pi_u, a^3\Sigma_g^+$, and $e^3\Sigma_u^+$ which dissociate to yield two $H(1s)$ atoms, as well as the rate coefficient for dissociation leading to $H(1s) + H(n = 2)$.

Finally, fig. 13 shows the rate coefficients for the excitation of the N_2 triplet state $A^3\Sigma_u^+$ in a $N_2 - H_2$ glow discharge, as a function of the fractional concentration of H_2 molecules, for $E/N = 5 \times 10^{-16} V cm^2$, a vibrational temperature of N_2 molecules equal to $4000 K$, and for various values of T_V for the H_2 molecules. On this figure we have also represented the case $T_V(N_2) = T_V(H_2) = 400 K$. This figure shows that for E/N values of this order of magnitude (or higher) the electron rate coefficients increase with the $[H_2]$ concentration. On the other hand, this figure also demonstrates that the effects of the $e - V$ superelastic collisions are larger in N_2 than in H_2 .

Calculations of other relevant quantities were also carried out and may be found in [1,2,5].

REFERENCES

- [1] J. Loureiro and C. M. Ferreira, J. Phys. D: Appl. Phys. 19:17 (1986).
- [2] J. Loureiro and C. M. Ferreira, J. Phys. D: Appl. Phys. 22:67 (1989).
- [3] K. Rohlena and K. Mašek, Proc. 7th Int. Symp. on Plasma Chem. (Eindhoven, The Netherlands), p.1377 (1985); Acta Phys. Slov. 35:141 (1985).
- [4] M. Capitelli, M. Dillonardo, and C. Gorse, Chem. Phys. 56:29 (1981); M. Cacciatore, M. Capitelli, and C. Gorse, Chem. Phys. 66:141 (1982).
- [5] J. Loureiro and C. M. Ferreira, (submitted to J. Phys. D: Appl. Phys.) (1989).

- [6] M. Cacciatore, M. Capitelli, and M. Dilonardo, Chem. Phys. 34:193 (1978); M. Capitelli and M. Dilonardo, Z. Naturforsch 34a:585 (1979); C. Gorse, M. Capitelli, J. Bretagne, and M. Bacal, Chem. Phys. 93:1 (1985).
- [7] A. Ricard, Proc. 17 th Int. Conf. on Phenomena in Ionized Gases (Budapest, Hungary), p. 320 (1985); A. Ricard, G. Henrion, H. Michel, and M. Gantois, Proc. 8 th Int. Symp. on Plasma Chem. (Tokyo, Japan), p. 1055 (1987).
- [8] J. Loureiro and C. M. Ferreira, Proc. 9 th Europ. Sect. Conf. on Atom. and Mol. Phys. of Ionised Gases (Lisbon, Portugal), p. 147 (1988).
- [9] L. S. Frost and A. V. Phelps, Phys. Rev. 127:1621 (1962).
- [10] S. Yoshida, A. V. Phelps, and L. C. Pitchford, Phys. Rev. A 27:2858 (1983).
- [11] S. J. Buckman and A. V. Phelps, J. Chem. Phys. 82:4999 (1985).
- [12] C. Gorse, M. Capitelli, M. Bacal, J. Bretagne, and A. Laganà, Chem. Phys. 117:177 (1987).
- [13] C.E. Treanor, J.W. Rich, and R.G. Rehm, J. Chem. Phys. 48:1798 (1968).

LASER DIAGNOSTIC OF RADIO-FREQUENCY OXYGEN PLASMA

A. Sasso, M. Inguscio and G.M. Tino

Dipartimento di Scienze Fisiche, Università di Napoli
Mostra d'Oltremare Pad.20, 80125 Napoli, Italy

L.R. Zink

Laboratorio Europeo di Spettroscopia Nonlineare (LENS)
Largo E.Fermi 2, 50125 Firenze, Italy

I. INTRODUCTION

We started the investigation of radio-frequency discharges of oxygen-noble mixtures because they are known to be efficient "generators" of atomic oxygen. In addition the discharge, in absence of chemical reactions at the electrodes, is particularly clean to allow high resolution laser spectroscopy investigations [1],[2],[3] which were our main purpose. However, on the way of carrying out spectroscopic investigations, we encountered a number of interesting and somewhat unexpected phenomena related to the production of the atom and its detection. As a consequence the experiment turned out to be a source of information on the collisional processes in the plasma and, in general, provided a diagnostic of the plasma itself.

While part of the problems have been understood still questions remain open, for instance on the possible production of enormously "warm" atoms, not in thermal equilibrium with the remaining plasma.

The purpose of the present work is to summarize the different experimental observations, trying to explain some of the behaviours, and possibly stimulating further speculation and suggestions for a deeper and more complete understanding of the physical processes.

II. EXPERIMENT

As we said the O-atom is produced in a radio-frequency (r.f.) discharge. In particular, the sample cell was a Pyrex tube containing an oxygen-noble gas mixture, placed inside two sets of coils of the same diameter as the cell. The internal diameter of the cell was varied between 5 and 20 mm to optimize the atomic oxygen production. The discharge tube of all the measurements here described is 7 mm internal diameter and 30 cm long.

A scheme of the experimental apparatus is shown in Fig.1. The r.f. of moderate power (50W at 60 MHz) is maintained by an oscillator fed by a current-stabilized power supply. Electrodeless discharge is preferred to d.c. discharge to avoid the introduction of impurities in the cell produced for ion bombardment sputtering of the cathode surface. Moreover, r.f. discharge can be run at a wider pressure range. For high-resolution spectroscopy tunable radiation is provided by an actively stabilized single-mode ($\Delta\nu_L = 1MHz$) ring dye laser (Coherent 699-21) while a multi-

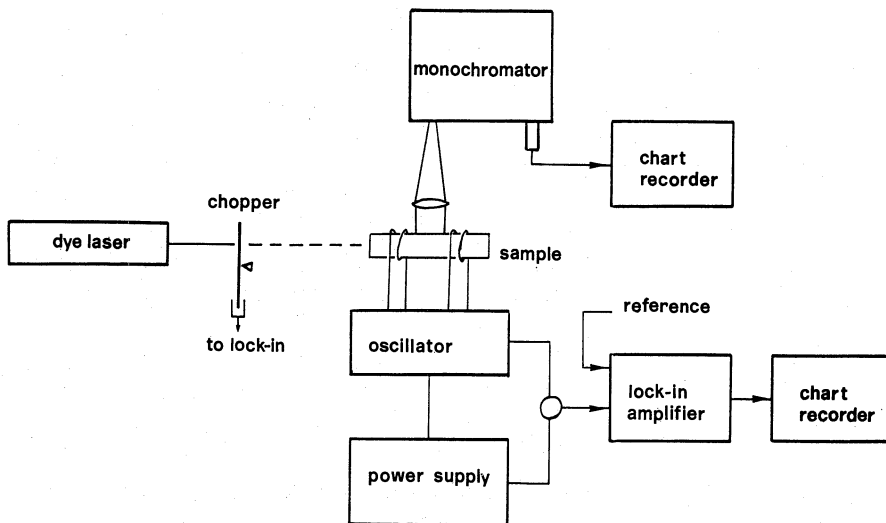


Fig.1 Schematic of the experimental apparatus. The atomic oxygen sample is produced in a O₂-noble gas radio-frequency discharge. Spectroscopic diagnosis is performed either detecting fluorescence or monitoring the optogalvanic effect.

mode ($\Delta\nu_L = 60\text{GHz}$) dye laser (Coherent 599-03) is used for quick and broad scans to detect various atomic species and transitions present in the discharge.

The spectral range of our investigation, 580-650 nm, is covered by using R6G and DCM as laser dye. When the laser radiation is resonant with the optical transition of a species in the discharge region the resulting absorption is not detectable due to the low density of the excited species to be investigated ($n = 10^{10} - 10^{12}\text{at/cm}^3$ in our experimental conditions). Much more sensitivity is provided by optogalvanic (OG) detection scheme. In this case absorbed photons induce changes in the impedance of the discharge. These variations reflect on the feed-back loop between the oscillator and the current stabilized power supply. Signals can be detected with high sensitivity by chopping the laser beam and using phase sensitive detection. More details can be found in ref. [4].

The laser wavelength is determined by recording the absorption spectra from a I₂ cell, and the frequency scan is calibrated by means of the markers from a 300 MHz and a 75 MHz free spectral range confocal Fabry-Perot interferometers.

Light from the discharge is dispersed by a Littrow mounted grating monochromator with 1Å resolution and the light was detected by a photomultiplier tube.

High-purity (> 99.9%) gases (O₂, He, Ne, Kr, Ar) are introduced into the cell through precision micrometering valves and the gas pressure is measured by a capacitance manometer.

III. DISSOCIATION MECHANISMS OF O₂ BY METASTABLE NOBLE GAS COLLISIONS

The dissociation of molecular oxygen by electron impact is an important channel for the production of atomic oxygen in pure O₂ glow discharge [5]. Nevertheless we have observed that oxygen-atoms production is largely enhanced in presence of noble gases. Metastable levels of noble gas atoms are efficiently populated by means of electron-impact excitation and represent a reservoir of energy in the discharge sample. Thermal collisions of a rare gas metastable atom X* with an oxygen molecule O₂ can give place to the following principal processes:



The process (1) is called Penning ionization while the reaction (2) gives place to formation of a quasi-molecule. Direct dissociation of O_2 molecules can occur as alternative to reaction (2).

Several authors [6],[7] have shown that process (1) dominates in presence of $He^*(2^1S, 2^3S)$ and $Ne^*(^3P_{0,2})$ while for Ar^* , Kr^* , and Xe^* Penning ionization is ineffective. As a consequence different mechanisms are expected to contribute to oxygen-atom formation depending on the specific metastable noble gas atom involved into the dissociative collision. We have used helium, krypton, neon and argon as buffer gas. Systematic investigations have been performed only with the last two gases, which also seem to act in different ways in the formation of the oxygen atoms. The different behaviours can be motivated by the different position of the metastable levels relative to the O_2 molecule, and can be understood with the help of Fig.2.

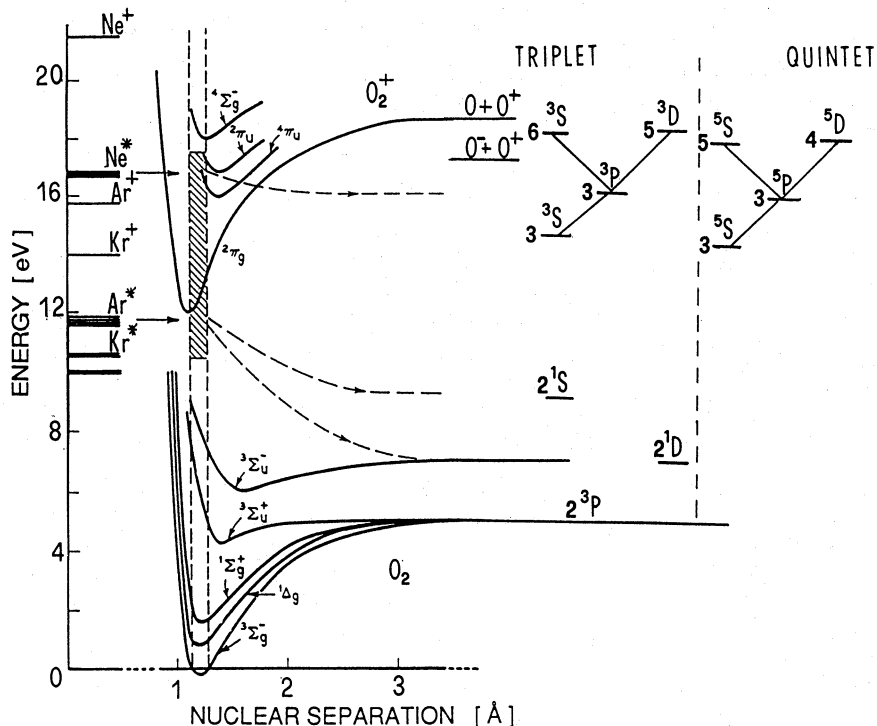
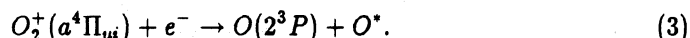


Fig.2 Excited O-atoms are produced by means of collisions involving O_2 , O_2^+ , and a noble gas in metastable state. The internal energy levels of the colliding partners are shown together with the schematic illustration of the O transitions investigated.

III.a Neon-Oxygen mixtures

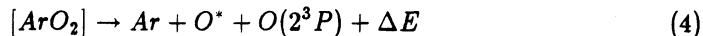
The production of molecular ions O_2^+ in the excited metastable $a^4\Pi_{u,i}$ state is quenched by fast dissociative recombination



O_2^+ ions production in the $4\Pi_{u,i}$ states has been proved in ref.[8] where the $O_2^+(a^4\Pi_{u,i} v'' = 3 \rightarrow b^4\Sigma^+ v' = 4)$ transition at 551 nm has been observed by means of OG detection. Excited atomic oxygen in reaction (3) are produced in both highly excited 3^5P and 3^3P levels while lower-lying metastable 2^1S_0 and 2^1D_2 levels are populated by electron-impact from ground-state $O(2^3P)$ atoms.

III.b Argon-Oxygen mixtures

In $Ar - O_2$ discharge the production of O-atoms seems to take place prevalently through the dissociation of the quasi-molecules indicated in Eq.(2):



where O^* represent now O-atoms in 2^1S_0 and 2^1D_2 metastable levels. The energy defect ΔE , of several eV, is released to the produced oxygen atoms as kinetic energy. As a result, both metastable and ground-state O-atoms exhibit a velocity spread considerably wider than that of the discharge-temperature gas. In some way, such kinetic energy distribution can be transferred to higher excited oxygen atoms through electron impact excitation.

On the other side both metastable and ground state O-atoms are undergoing thermalizing collisions. Such collisions have different consequence for the two group of oxygen atoms. Indeed, metastable $O(2^1S, 2^1D)$ are quenched toward the ground-state and the collision-free atoms conserve a non-thermal distribution of velocities. In contrast, almost all ground-state oxygen atoms reach a velocity distribution in equilibrium with the discharge temperature.

IV. LASER DIAGNOSTIC OF OXYGEN PLASMA

We produce atomic oxygen by dissociation of O_2 molecules present at trace levels in a noble-gas r.f. discharge. Typical O_2 pressure is varied in the range 0.05-0.3 Torr while noble gas pressure is changed between 0.8 and 10 Torr. The diagnostic of the oxygen-atom formation is performed by monitoring the population of several excited atomic levels by means of OG and/or fluorescence detection. In the $Ne - O_2$ discharge the $1s_5 - 2p_6(\lambda = 614.3\text{nm})$ and $1s_3 - 2p_2(\lambda = 616.3\text{nm})$ neon transitions were detected in the immediate neighbourhood of the oxygen multiplet $3^5P_{1,2,3} - 4^5D_j$ at 615 nm.

In Fig. 3a a fluorescence spectra around this region is shown while in Fig.3b the same spectral region was recorded by OG detection by using a broadband dye laser ($P_L = 300mW$). Also if the higher resolution offered by laser excitation allow to resolve the fine structure of the lower ${}^5P_{3,2,1}$ level the lineshapes are instrumental.

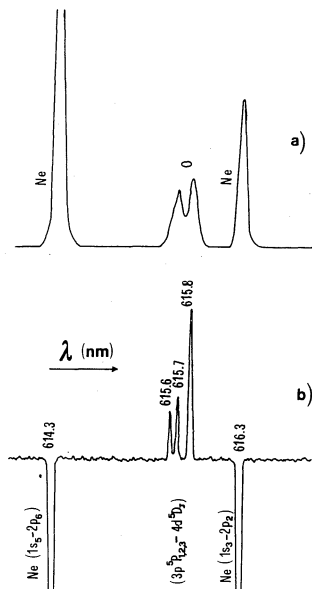


Fig.3 The presence of the excited atoms in O_2 -Ne discharge is evidenced by recording the fluorescence spectra (a) ($p_{O_2} = 0.2$ Torr, $p_{Ne} = 10$ Torr). The same spectral region is investigated in b) by means of radio-frequency optogalvanic detection. In spite of the broad band operation of the laser, the partial fine structure of oxygen transition is better resolved than in a). Note the sign inversion of the neon transitions starting from metastable levels as explained in the text.

It is interesting to note that the two neon transitions originating from metastable levels exhibit negative OG signals with respect to the oxygen multiplet starting from a radiative level, denoting the different mechanisms leading to the OG signal for the two cases [9]. The OG behaviours of the above cited oxygen and neon transitions are reported in Fig.4 as a function of O_2 pressure. It is evident how critical the production of atomic oxygen is to the oxygen-neon pressure. Indeed in the state of equilibrium distribution of the O-atoms there is a balance between two opposing processes, i.e. dissociation of the O_2 molecules according to the reactions (1) and (3), and the recombination of the O-atoms to re-form the O_2 molecules. The two main recombination processes by which the O-atoms can recombine are recombination by two-body collisions (radiative recombination)



and three-body collisions



where M is the third body which takes away the excess of energy and momentum and that, in our case, is represented by O_2 molecules or noble gas atoms.

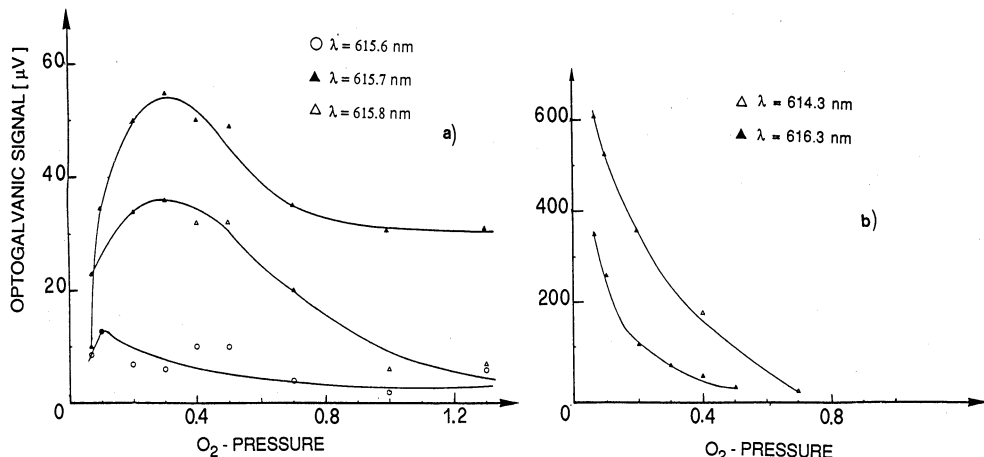


Fig.4 The noble gas (neon) metastable level energy is released in the collision to produce oxygen atoms. This can be evidenced by keeping the Ne pressure constant ($p=10$ Torr) and adding small percentages of O_2 amounts. Correspondingly to the increase in the OG signal a strong decrease of signal from Ne atoms (b) is detected.

On the other hand, the strong decreasing of the OG signals for neon transitions (Fig.4b) is evidence of the reduction of metastable neon atoms due to resonant collisions with O_2 molecules (reaction (1)). Similar behaviours were observed analyzing the fluorescence emission. This phenomenon is also easily observed by looking at the discharge color. In fact the characteristic red glow of a pure neon discharge reduces by adding molecular oxygen.

Another mechanism that could be responsible of the reduction of metastable neon density is due to the modulation of electron energy distribution in presence of molecular species. In particular in molecular r.f. discharges very similar to ours, it has been proven [10] that the electron energy distribution function is depleted at higher energy value. This effect reduces the noble gas excitation while low energy electrons are more efficient for the O_2 dissociation.

Same behaviours as in Fig.4 were observed analyzing the fluorescence emission of the

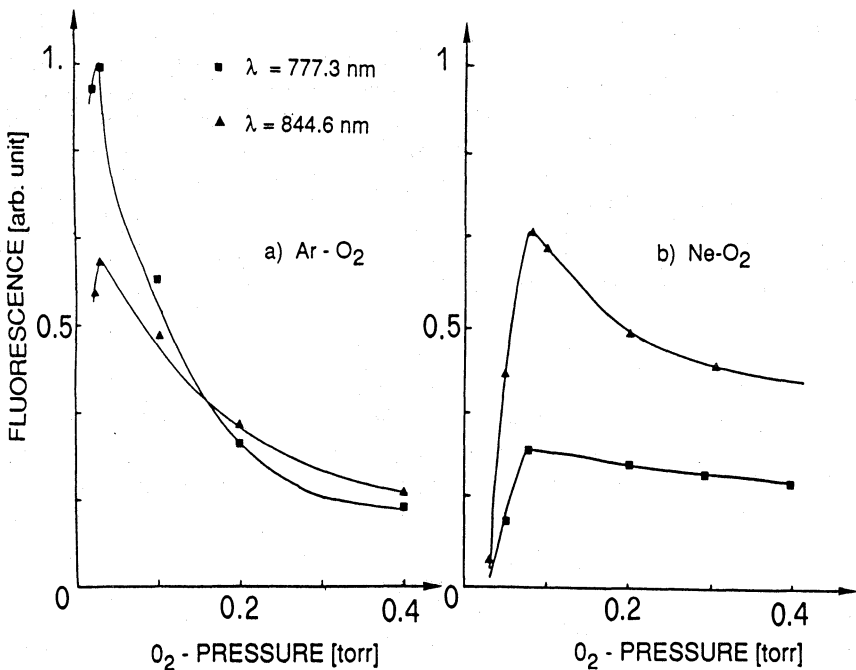


Fig.5 When the oxygen production is investigated by means of fluorescence, the population of the upper level of the transition can be studied. The population of the oxygen 3^5P (777.3 nm) and 3^3P (844.6 nm) atoms is investigated as a function of O₂ pressure for Ar and Ne collisional partner ($p_{Ar} = p_{Ne} = 10 \text{ Torr}$).

transitions under investigation. The diagnostic of O-atoms was also monitored through the fluorescence of the $3^3P - 3^3S$ and $3^5P - 3^5S$ transitions at 844.6 and 777.3 nm respectively (Fig.5) in Ne-O₂ and Ar-O₂ mixtures. The $3^3P - 3^3S$ transition is strongly allowed and the radiative lifetimes of both upper and lower levels are suitable for obtaining laser action as proved in ref. [11] and [12]. On the contrary the 3^5S level is metastable and no population inversion respect to the upper 3^5P level can be reached.

V. LINESHAPES ANALYSIS OF ATOMIC OXYGEN TRANSITIONS

Optical transitions of atomic oxygen predominantly Doppler broadened. In our experimental conditions homogeneous broadening is due to collisions and is smaller than Doppler broadening.

Measurements of the Doppler width provide the value of the temperature associated with the gas in the discharge and, hence, give information on the average kinetic energy of the atoms. We have investigated lineshapes of several optical transitions of oxygen involving both triplet and quintet levels by varying the type of buffer gas in the discharge. For example, in Fig. 6 are shown typical Doppler-limited lineshapes for quintet $3^5P_3 - 5s^5S_2$ transition in Ne-O₂ and Ar-O₂ mixtures. Doppler width for both cases is 2GHz correspondent to a temperature of 570 K.

In Fig.7 is shown the entire multiplet $3p^3P_{1,2,0} - 6s^3S_1$ around 604 nm recorded in different mixtures with He, Ne, Ar, and Kr. By using He, Kr, or Ne as buffer gas (Fig.7 a,b,c) each component of the triplet is resolved and well fitted by Gaussians whose FWHM are of about 2 GHz. A result at first surprising is given by the observation of an extremely large Doppler effect when argon (Fig.7d) is used to sustain the discharge. The large width prevents the observation of three separated components in spite of fine structure splittings in the $^3P_{1,2,0}$ level of 4.7 (0-2) and 16.8 (2-1) GHz respectively. Different from the other noble gases here considered, the lineshapes are not accurately fitted by Gaussian curves or more generally by Voigt profiles.

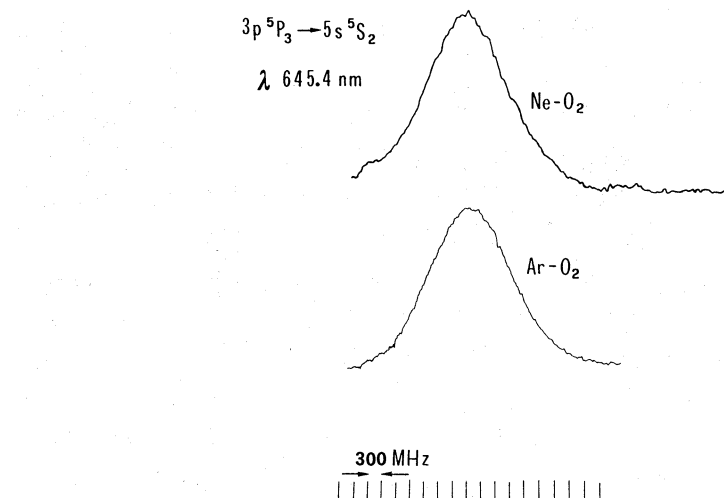


Fig.6 Recording of the Doppler broadened lineshape allows a determination of the kinetic energy of the atoms. In case of transitions between quintet levels this is nearly the same for Ar and Ne buffer gas ($\Delta\nu_D \approx 2$ GHz, $T \approx 570$ K in the figure)

The isolated fine structure component $^3P_1 - ^3S_1$ is analyzed in more detail by fitting the experimental line profile with the superposition of two Gaussian curves of different amplitude and width (Fig.8). As can be noted in Fig.8, the lineshape is asymmetric and this has lead to an unexplainable shift of about 300 MHz between the two Gaussians. The width of the smaller Gaussian is of the same order of magnitude of those obtained with other buffer gases or for quintet transitions, i.e. $\Delta\nu_D = 2$ GHz, while for the larger Gaussian we obtain a Doppler width of 5.7 GHz corresponding to a temperature of about 4500 K, i.e. nearly one order of magnitude larger than that "usually" observed.

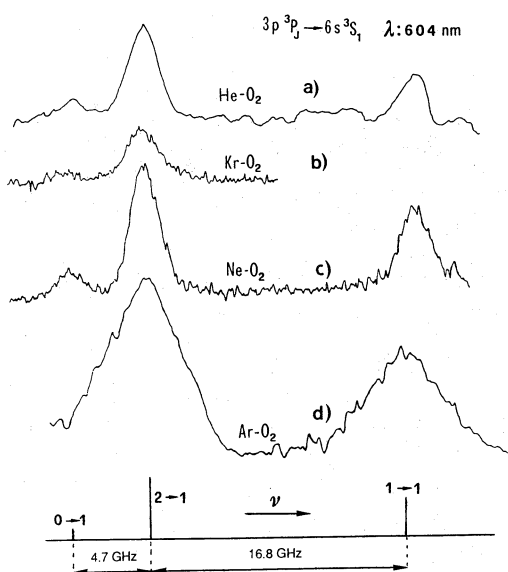


Fig.7 In case of O transitions between triplet states the "temperature behaviour" is anomalous in case of argon used as buffer gas. The recordings in figure evidence for Ar a Doppler width of about 3 times larger than for He, Ne, Kr.

Similar results were found investigating the triplet $3p^3P_{1,2,0} - 5d^3D_{3,2,1}$ transition at 595.9 nm.

To check if the discussed anomalous broadening is caused by reduction of the lifetime of the involved oxygen levels we have analyzed the homogeneous lineshape. For this purpose we have developed a high resolution laser spectroscopy technique which allows us to remove the Doppler broadening. In particular by using polarization spectroscopy, described in detail in ref.[13], we obtain a homogeneous linewidth of 160 MHz (Fig.9) ascribed to the pressure and saturation broadening. The anomalous behaviour with the temperature could be understood according to the model discussed in Sec. III.b and firstly suggested by Feld et al. [11] to explain the peculiar effects observed in the O laser emission at 844 .6 nm sharing the 3^3P excited level with the transition at 604.6 nm (see Fig.2). In that model only metastable O($2^1S, 2^1D$)-atoms

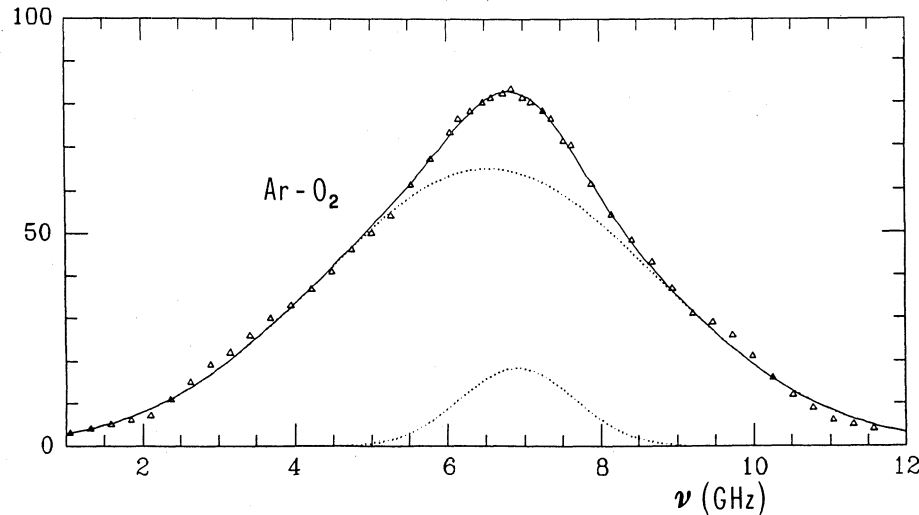


Fig.8 The "enormously" broad lineshape in case of Ar can be fitted to the sum of two Gaussian profiles. The narrower corresponds to the same 570 K temperature observed for other noble gases or quintet transitions. The wider Gaussian corresponds to a temperature of about 4500 K. All the recordings have been obtained using the same experimental conditions (partial pressure, discharge current, etc.).

have a wider velocity distribution ("warm" atoms) while ground-state atoms are essentially in thermal equilibrium ("cold" atoms). The electron-impact excitation of higher excited quintet and triplet state are regulated by selection rules similar to those for optical excitation. In particular, triplet state can be populated through electron collisions with ground- state ($\Delta s = 0$) and metastable singlet state ($\Delta s = \pm 1$). As a result the velocity distribution of such atoms and, hence, the Doppler profiles of the relative transitions, are given by the superposition of a broad ("warm" excitation channel) and narrow ("cold" excitation channel) contribution. In contrast, quintet atoms are produced essentially by excitation of "cold" ground-state atoms, and, as a consequence, for optical transitions involving such levels a normal Doppler width is found.

While some aspects of the phenomenon has been, at least phenomenologically, understood still questions remain not clearly explained.

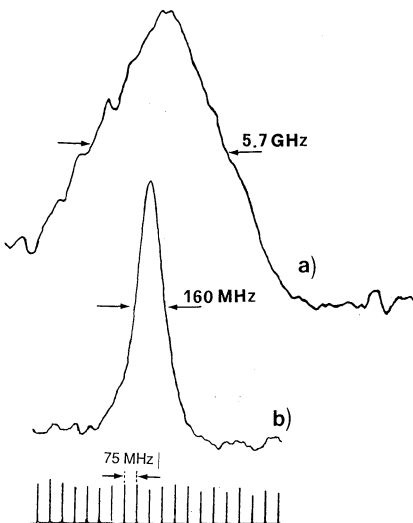


Fig.9 The kinetic origin of the large broadening is demonstrated evidencing the inhomogeneous origin of the lineshape. The homogeneous (sub-Doppler) width is recorded by means of polarization spectroscopy and result to be the same as for "regular" transitions (in figure different x-scale has been used for Doppler (a) and sub-Doppler (b)).

One of these concerns the collisional mechanisms leading to O-atoms formation for $Kr - O_2$ system that should be very similar to that involving argon. On the contrary, the experimental results (Fig.7b) do not show anomalous broadening.

A more complete and deeper knowledge of the basic mechanisms governing the production of oxygen atoms in non thermal equilibrium with the discharge sample requires further investigations which are in progress in our laboratory.

REFERENCES

1. M.Inguscio, P.Minutolo, A.Sasso, and G.M.Tino: Phys.Rev. A 37, 4056 (1988).
2. A.Sasso, P.Minutolo, M.I.Schisano, G.M.Tino, and M.Inguscio: J. Opt. Soc. Am. B 5, 2417 (1988).
3. K.Ernst, P.Minutolo, A.Sasso, G.M.Tino, and M.Inguscio: Opt. Lett., in press.
4. A.Sasso, G.M.Tino, M.Inguscio, N.Beverini, and M.Francesconi: Nuovo Cim. D 10, 941 (1988).
5. M.Touzeau, G.Gousset, J.Jolly, D.Pagnon, M.Vialle, C.M.Ferreira, J. Loureiro, M.Pinheiro, and P.A.Sá, this volume.
6. L.Apolloni, B.Brunetti, F.Vecchiocattivi, and G.G.Volpi: J. Phys. Chem. 92, 918 (1988).
7. W.P. West, T.B.Cook, F.B.Dunning, R.D.Rundel, and R.F.Stebbins: J. Chem.Phys 63, 1237 (1975).
8. N.S.Nogar and G.L.Keaton: Chem. Phys. Lett.120, 327 (1985).
9. A.Sasso, M.Ciocca and E.Arimondo: J.Opt. Soc. Am. B5, 1484 (1988).
10. M.Capitelli, T.Celiberto, C.Gorse, R.Winkler, and J.Wilhelm: J.Phys.D; Appl.Phys. 21, 691 (1988).
11. W.R.Bennet, Jr., W.L.Faust, R.A.Mc Farlane, and C.K.N.Patel: Phys. Rev Lett. 8, 470 (1962).
12. M.S.Feld, B.J.Feldman, and A.Javan: Phys. Rev. A 7, 257 (1973).
13. C.Wieman and T.W.Hansch: Phys. Rev. Lett. 36, 1170 (1976).

SPECTROSCOPY AND KINETICS OF AN OXYGEN GLOW DISCHARGE

M. Touzeau, G. Gousset, J. Jolly, D. Pagnon and M. Vialle

L.P.G.P Université Paris-Sud Orsay, France

C.M. Ferreira, J. Loureiro, M. Pinheiro, and P.A. Sà

Instituto Superior Technico, Lisbon, Portugal

INTRODUCTION

For several years, low pressure oxygen discharges have been extensively used for various applications such as surface treatment, oxidation, polymer etching, etc. The investigation of such plasma is difficult as it is a complex medium composed of electrons, positive and negative ions, excited molecules and atoms. This work deals with the kinetics of these species in the positive column of a low pressure glow discharge. This type of discharge is particularly well suited for kinetic studies as it is a homogeneous medium where the electric field, the gas temperature and the concentration of all the species are uniform along the plasma column. Different diagnostic techniques have been used to determine the concentrations of the active species. They have been reviewed by Wayne¹. Different models have also been proposed including the calculation of the electron energy distribution function, and the resolution of the kinetic equations governing the concentrations of the active species³⁻⁸. However it is difficult to compare the experimental results and the model predictions because the experimental conditions are different from those used in the model. The interaction between the walls and the oxygen atoms^{2,9,10} and gas purity are of particular importance. For this reason, we found it necessary to measure the plasma parameters: electric field E, electron density n_e and the concentrations of the main excited species: singlet molecules $O_2(a^1\Delta)$, $O_2(b^1\Sigma)$, atoms in the ground state $O(^3P)$ and in the negative ions O^- in the same apparatus. The data are compared with the values of a kinetic model valid in the following experimental conditions: reduced electric field $E/N = 30-80$ Td, gas pressure $p = 0.1 - 5$ Torr, discharge current $I_d = 1-80$ mA and gas flowrate up to 3 sccm.

EXPERIMENTAL

Different techniques have been used to determine the main species concentrations: vacuum ultraviolet (VUV) absorption spectroscopy was extensively utilized to measure the concentrations of ground state molecules $O_2(X^3\Sigma)$, metastable singlet molecules $O_2(a^1\Delta)$, ground state atoms $O(^3P)$, excited metastable atoms $O(^1S)$ and $O(^1D)$, ozone molecules O_3 ^{11,12}. Emission

spectroscopy was employed to detect the population of the $O_2(b^1\Sigma)$ singlet molecules and the atomic excited states. The optogalvanic photodetachment technique has allowed the measurement of O^- negative ion concentrations.

The apparatus for VUV measurements has been described elsewhere¹¹. It consists of a Pyrex tube 50cm long and 16mm in diameter. Four electrodes inserted into the tube allow the creation of positive column discharges of different lengths. Two MgF_2 or LiF windows are put on both ends of the tube. The discharge lamp, designed in our laboratory, consists of a microwave, 120 Watt, 2.45 GHz, "surfatron" discharge¹³ in flowing oxygen or hydrogen at low pressure in a capillary quartz tube. The detection system is composed of a 50 cm focal length VUV spectrometer with a 0.17 nm resolution, a sodium salicylate scintillator and a photomultiplier.

Ground state $O_2(X^3\Sigma^-)$ molecules

The neutral concentration of the ground state molecules $O_2(X^3\Sigma^-)$ is deduced from measuring the ratio of the transmitted intensity I_t and the intensity without absorption I_0 using the relation:

$$\ln(I_t/I_0) = -[O_2]\sigma_x\ell \quad (1)$$

where ℓ is the absorption length and σ_x the absorption cross-section. The measurements were performed at 135 nm where $\sigma_x = 2.4 \times 10^{-18} \text{ cm}^2$.

Metastable $O_2(a^1\Delta)$ singlet molecules

In the VUV region between 120 and 170nm, metastable $O_2(a^1\Delta)$ molecules contribute to the light absorption. The absorption cross-sections between 125 and 135 nm, are given by Ogawa and Ogawa¹⁴. The concentration of singlet molecules $O_2(a^1\Delta)$, is deduced by the relation:

$$\ln(I_t/I_0) = -[O_2]\sigma_x\ell - [O_2(a^1\Delta)]\sigma_a\ell \quad (2)$$

where σ_a is the absorption cross-section of $O_2(a^1\Delta)$. The measurements are performed at 128.5nm, where $\sigma_x = 4 \times 10^{-19} \text{ cm}^2$ and $\sigma_a = 165 \times 10^{-19} \text{ cm}^2$.

Ground state $O(^3P)$ atoms

The concentration of ground state $O(^3P)$ atoms: $[O]$ was obtained by measuring the absorption of the triplet line ($3s^3S - 2p^4 ^3P$), at 130.22, 130.49 and 130.6nm. This resonant line is strongly absorbed by the plasma. $[O]$ is related to the absorption $A = 1 - I_t/I_0$ by:

$$A(\lambda_0) = \frac{\int I_0(\lambda) (1 \exp - k(\lambda) \ell) F_a(\lambda_0 - \lambda) d\lambda}{\int I_0(\lambda) F_a(\lambda_0 - \lambda) d\lambda} \quad (3)$$

The spectral profile of each component of the triplet line $I_0(\lambda)$ was measured with a high resolution VUV spectrometer ($\delta\lambda = 8 \times 10^{-4} \text{ nm}$) at Meudon observatory. $k(\lambda)$ is the absorption coefficient corresponding to the Voigt profile, a convolution of the natural broadening (Lorentzian width $\delta\lambda_N = 5 \times 10^{-6} \text{ nm}$) and the Doppler broadening ($\delta\lambda_D = 4 \times 10^{-4} \sqrt{\frac{T}{300}} \text{ nm}$). $F_a(\lambda)$ is the apparatus function of the VUV spectrometer deduced from the line shape of singlet atomic line at 115.2nm. Detailed calculations are given by Gousset et al.¹¹.

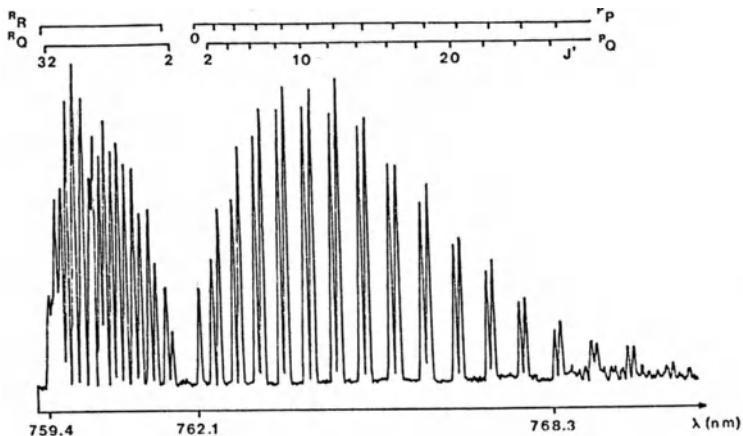


Fig.1. (0-0) A-band of the atmospheric system ($b^1\Sigma^+ - X^3\Sigma^-$) of O_2 . This band has 4 branches R_R , R_Q , P_Q and P_P , where P, Q and R correspond to $\Delta J = -1, 0, +1$, respectively and where the superscripts P and R correspond to $\Delta K = -1$ and $\Delta K = +1$ respectively. $I_d = 50\text{mA}$; $p = 0.7 \text{ Torr}$; $T = 440\text{K}$.

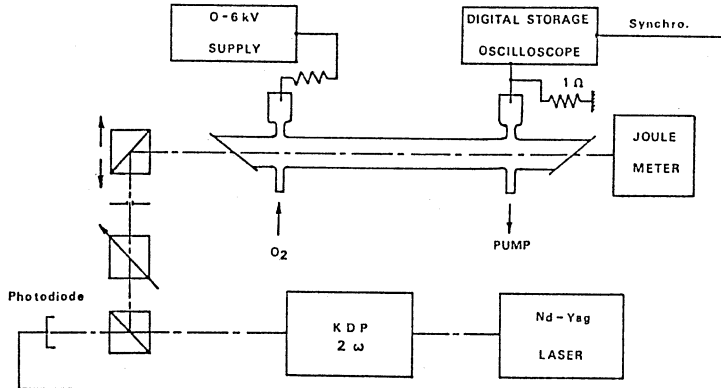


Fig.2. Schematic of the laser photodetachment experiment.

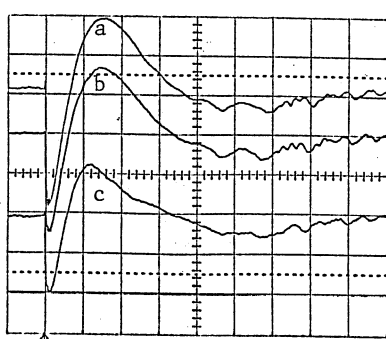


Fig.3. Optogalvanic pulse.
X scale: $2\mu\text{s}/\text{div}$. Y scale: $1\text{mA}/\text{div}$.
 $I_d = 20\text{mA}$. $p = 0.4 \text{ Torr}$.
Laser energy: a) 110mJ ; b) 40mJ ;
c) 13mJ .

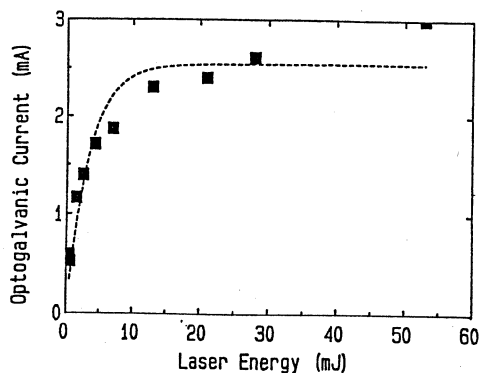


Fig.4. Variation of the optogalvanic current versus laser energy.
 $I_d = 20\text{mA}$; $p = 0.4 \text{ Torr}$.

Metastable O(¹D) and O(¹S) atoms

The metastable O(¹D) and O(¹S) atoms at 1,96 eV and 4,17eV of the ground level are efficiently excited by the electrons whose mean energy ranges 2.2 to 3.5eV, for E/N = 30 - 100 Td. These concentrations are determined by measuring the absorption of the O ($3s^1 1P^0 - 2p^4 1S$), 121.7nm and O ($3s^1 1D^0 - 2p^4 1D$), 115.2 nm lines . The metastable atom concentrations are calculated numerically using the relations $[O(^1S)] = f(A(122 \text{ nm}), T)$ and $[O(^1D)] = f[A(115 \text{ nm}), T]$, introducing the experimental profiles of the line source in the relation (3) ¹².

Ozone

The ozone concentration is deduced from the measurement of the absorption at 253.7nm, obtaind by replacing the microwave source by a standard Hg lamp. This wavelength corresponds to the center of the Hartley absorption band. The concentration of ozone $[O_3]$ is determined by

$$\ln I_t / I_0 = - [O_3] \sigma_3 \ell \quad (4)$$

where $\sigma_3 = 1.13 \times 10^{-17} \text{ cm}^2$ at 300K and $\sigma_3 = 9.23 \times 10^{-17} \text{ cm}^2$ at 720K.¹⁶

$O_2(b^1\Sigma)$ singlet molecules and gas temperature

In the visible region (300-900nm), the emission of the positive column of O_2 is due primarily to the atomic excited transitions and to the first and second negative systems of O_2^+ .The forbidden transitions of the atmospheric system $b^1\Sigma_g^+ - X^3\Sigma_g^-$ are also emitted with a lower intensity. However, using a photon counting system, the rotational distribution of the A-band 762nm $v' = 0 \rightarrow v'' = 0$ is observed. A typical spectrum is represented in figure 1.The rotational temperature can be deduced from the distribution of the PP and PQ branches :

$$I_{j'j''} \simeq S_{j'j''} \exp(-E_{j'} / kT) \quad (5)$$

where $I_{j'j''}$ is the intensity of the rotational transition, $S_{j'j''}$ the Hön-London factor ¹⁷ and E_j the energy term ¹⁸. Due to the long lifetime of the transition, this rotational temperature is assumed to be in equilibrium with the gas temperature.

Negative ions

It has been shown²⁰ that in a low pressure positive column, the negative ions are confined by the charge space field and cannot reach the wall. In our experimental conditions, the dominant population consists of O^- ions, created by the dissociative attachment reaction $O_2 + e \rightarrow O^- + O$.This population of negative ions has been detected by a laser photodetachment technique. The experimental arrangment is shownschematically in Figure 2. The positive column is irradiated by the second-harmonic (532nm) beam of a Nd-YAG laser (10ns, energy up to 200mJ). Electron detachment is observed according to the reaction $O^- + h\nu \rightarrow O + e + 0.87 \text{ eV}$. A typical optogalvanic signal is represented in figure 3. The optogalvanic current is related to the increase of the electronic concentration by

$$\Delta I / S = \Delta n_e e v_D \quad (6)$$

where S is the area of the discharge probed by the laser and v_D the electron drift velocity. Assuming that v_D does not change significantly during the laser pulse, the relative current variation is written as

$$\Delta I / I = (\Delta n_e / n_e) (S / \pi R^2) \quad (7)$$

As observed in figure 4, the optogalvanic signal increases with the laser energy up to a saturation value ΔI_s , for which all the negative ions in the volume irradiated by the laser are detached. According to the theory³³

$$\Delta I = \Delta I_s (1 - \exp(-E \sigma / S h\nu)) \quad (8)$$

where $\sigma = 6.3 \times 10^{-17} \text{ cm}^2$ is the photodetachment cross-section¹⁹ of O^- at 532nm. In such conditions the concentration of negative ions is related to the saturation current by the relation²¹

$$\frac{\Delta I}{I} = \frac{[O^-]_p}{n_e} \times \frac{S}{\pi R^2} \quad (9)$$

where $[O^-]$ is the concentration of negative ions in the region probed by the laser beam.

Electrons

The electron density has been measured by a resonant cavity tuned on the TM_{020} mode (3.7 GHz) assuming a Bessel radial density profile. These results are in good agreement¹¹ with those obtained by using the current continuity equation: $j = n_e v_D e$

Electric field

In the positive column, the axial electric field can be easily measured by the potential difference between two electrostatic probes. The reduced electric field E/N can therefore be precisely determined from E and N , where the total number density $N = [O_2(X^3\Sigma)] + [O_2(a^1\Delta)] + [O]$ is measured by VUV absorption.

MODEL

A simple kinetic model predicting the concentration of oxygen atoms, metastable singlet molecules $O_2(a^1\Delta)$ and negative ions O^- in the positive column of a discharge was previously developed²². In this model the electron density was calculated from the continuity equation and the rate coefficients for the electron impact processes were taken from the literature²³ as a function of the reduced electric field E/N . This model has been improved to take into account the effect of superelastic collisions of electrons with metastable and vibrationally excited molecules, and the presence of an important relative concentration of atoms. Thus a Boltzmann code²⁴ taking into account such effects has been coupled to the kinetic model. The processes included in the Boltzmann calculation and the related reference data are presented in Table I. The kinetic model has been completed to take into account the creation and destruction processes of $O_2(b^1\Sigma)$ and ozone. The reactions included in the kinetic model are listed in Table II. The electron energy distribution function and therefore the electron rates coefficients, depend on three quantities: E/N , reduced electric field,

$$\delta_a = \frac{[O_2(a^1\Delta)]}{[O_2(a^1\Delta)] + [O_2(X^3\Sigma)]} \quad \text{and} \quad \delta_o = [O] / N. \quad \text{The vibrational temperature}$$

is maintained at 2000 K. This low value can be justified by the fact that the large concentration of atoms leads to a deactivation of the first vibrational states of O_2 ⁵.

The concentration of $O_2(X^3\Sigma)$, O , $O_2(a^1\Delta)$, $O_2(b^1\Sigma)$, O_3 , O^- are computed as a function of the gas pressure P , the gas temperature T_g , the discharge current I_d and the electric field E . It is to be noted that the parameter E/N is not fixed because N is calculated by the model. The initial concentration of ground state molecules is computed from $P = NkT$, and all the others

Table I
Processes included in the Boltzmann code.

PROCESSES	REFERENCES
molecular oxygen	
1) $e + O_2(X, V) \rightleftharpoons e + O_2(X, W)$	(Phelps 1985) ²⁵
2) $e + O_2(X, V = 0) \rightleftharpoons e + O_2(a^1\Delta_g)$	"
3) $e + O_2(X, V = 0) \rightarrow e + O_2(b^1\Sigma_g^+)$	"
4) $e + O_2(X, V = 0) \rightarrow e + O_2(4.5\text{eV})$	"
5) $e + O_2(X, V = 0) \rightarrow e + O_2(6.0\text{eV})$	"
6) $e + O_2(X, V = 0) \rightarrow e + O_2(8.4\text{eV})$	"
7) $e + O_2(X, V = 0) \rightarrow e + O_2(9.97\text{eV})$	"
8) $e + O_2(X, V = 0) \rightarrow e + O_2^+ + e$	"
9) $e + O_2(X, V = 0) \rightarrow e + O_2(14.7 \text{ eV})$	"
atomic oxygen	
10) $e + O(^3P) \rightarrow e + O(^1D)$	(Henry 1969) ³⁰
11) $e + O(^3P) \rightarrow e + O(^1S)$	"
12) $e + O(^3P) \rightarrow e + O(^3S)$	(Stone 1971) ³¹
13) $e + O(^3P) \rightarrow e + O^+ + e$	(Fite 1959) ³²

Table II
Reactions included in the kinetic model.

REACTION N°	REACTION	RATE	reference
1	$O_2(X^3\Sigma) + e \rightarrow O^- + O$	$K_1 = f(E/N)$	a
2	$O_2(a^1\Delta) + e \rightarrow O^- + O$	$K_2 = f(E/N)$	b
3	$O^- + O \rightarrow O_2(X^3\Sigma)$	$k_3 = 1.4 \times 10^{-10} \text{ cm}^3 \text{ s}^{-1}$	23
4	$O^- + O_2(a^1\Delta) \rightarrow O_3$	$k_4 = 3 \times 10^{-10} \text{ cm}^3 \text{ s}^{-1}$	23
5	$O_2(X^3\Sigma) + e \rightarrow O + O + e$	$K_5 = f(E/N)$	a
6	$O_2(a^1\Delta) + e \rightarrow O + O + e$	$K_6 = f(E/N)$	b
7	$O + \text{wall} \rightarrow \frac{1}{2} O_2(X^3\Sigma)$	$K_7 = 200 \text{ s}^{-1}$	22
8	$O_2(X^3\Sigma) + e \rightarrow O_2(a^1\Delta) + e$	$K_8 = f(E/N)$	a
9	$O_2(a^1\Delta) + e \rightarrow O_2(X^3\Sigma) + e$	$K_9 = f(E/N)$	b
10	$O_2(a^1\Delta) + e \rightarrow O_2(b^1\Sigma) + e$	$K_{10} = f(E/N)$	b
11	$O_2(b^1\Sigma) + e \rightarrow O_2(a^1\Delta) + e$	$K_{11} = f(E/N)$	b
12	$O_2(a^1\Delta) + \text{wall} \rightarrow O_2(X^3\Sigma)$	$k_{12} = 0.4 \text{ s}^{-1}$	1
13	$O_2(X^3\Sigma) + e \rightarrow O_2(b^1\Sigma) + e$	$k_{13} = f(E/N)$	a
14	$O_2(b^1\Sigma) + e \rightarrow O_2(X^3\Sigma) + e$	$k_{14} = f(E/N)$	a
15	$O_2(b^1\Sigma) + \text{wall} \rightarrow O_2(X^3\Sigma)$	$k_{15} = 400 \text{ s}^{-1}$	1
16	$O + O + O_2(X^3\Sigma) \rightarrow O_3 + O$	$k_{16} = 2.1 \times 10^{-34} e^{345/T} \text{ cm}^6 \text{ s}^{-1}$	23
17	$O + O_2(X^3\Sigma) + O_2(X^3\Sigma) \rightarrow O_3 + O_2(X^3\Sigma)$	$k_{17} = 6.4 \times 10^{-35} e^{63/T} \text{ cm}^6 \text{ s}^{-1}$	23
18	$O_3 + O \rightarrow O_2(a^1\Delta) + O_2(X^3\Sigma)$	$k_{18} = 1 \times 10^{-11} e^{-2300/T} \text{ cm}^6 \text{ s}^{-1}$	23
19	$O_3 + O \rightarrow 2 O_2(X^3\Sigma)$	$k_{19} = 1.8 \times 10^{-11} e^{-2300/T} \text{ cm}^6 \text{ s}^{-1}$	23
20	$O_2(b^1\Sigma) + O_3 \rightarrow 2 O_2(X^3\Sigma) + O$	$K_{20} = 1.5 \times 10^{-11} \text{ cm}^3 \text{ s}^{-1}$	23
21	$2O_2(a^1\Delta) + O_2 \rightarrow 2 O_3$	$K_{21} = 10^{-31} \text{ cm}^6 \text{ s}^{-1}$	23
22	$O_2(a^1\Delta) + O_3 \rightarrow 2 O_2 + O$	$K_{22} = 5.2 \times 10^{-11} e^{-2840/T} \text{ cm}^3 \text{ s}^{-1}$	23
23	$O_3 + e \rightarrow O + O_2 + e$	$K_{23} = 5 k_5 \text{ cm}^3 \text{ s}^{-1}$	23

The reaction rates are calculated using the cross-sections recommended by Phelps²⁵ (a) or Fournier³ (b).

initial concentrations are set equal to zero. An iterative method of calculation is performed to deduce the concentrations of the species. The initial values of E/N , δ_a and δ_o are introduced in the Boltzmann code in order to calculate the electron rate coefficients, the drift velocity and therefore the electron density. These quantities are then introduced in the balance equations. The steady state solution of the system of differential equations is obtained using the subroutine D02ebf of NAG Fortran library routine. The concentrations of the species are computed and a new set of the three parameters of the calculations: E/N , δ_a , δ_o , is deduced which is reintroduced into the Boltzmann code. The iterative process is stopped when the E/N value converges.

RESULTS AND DISCUSSION

This kinetic model describes the interactions between the species assuming mean values for their concentrations. The concentrations of atoms and singlet molecules $O_2(a^1\Delta)$ are uniform across the tube, but the diffusion has to be taken into account, in order to describe the kinetics of charged particles. A quasi-neutral theory of positive column in electro-negative gases based on fluid type momentum equation has therefore been developed. The positive ions are assumed to be created by collisions with neutral molecules. The negative ions are assumed to be formed by electron dissociative attachment. In oxygen discharges they are lost by detachment with atoms or singlet $O_2(a^1\Delta)$ molecules. This theory, who gives the radial profiles of O_2^+ , O^- , n_e , the ratio of the negative ion density to the electron density and the maintenance reduced electric field E/N , is detailed by Ferreira et al.²⁰ and will not be discussed here.

The results of the kinetic model described above are compared to the experimental data for pressures $P = 0.1 - 5$ Torr and discharge currents up to 80mA. Figure 5 gives an example of the calculated and measured concentrations of the species versus the current ($I_d = 3-80$ mA) for a pressure $P = 0.38$ Torr. As expected, a large concentration of singlet $O_2(a^1\Delta)$ molecules and atoms is observed, even for low discharge currents. The dissociation degree $[O] / [O_2]$ increases almost linearly with the electron density in the range $n_e = 2 \cdot 10^9 - 4 \cdot 10^{10} \text{ cm}^{-3}$. This can be explained by the fact that the concentration of atoms is mainly determined by the equilibrium between creation by electronic dissociation impact (Reactions R5 and R6) and k_7 recombination on the wall (Reaction R7). The k_7 recombination coefficient of oxygen atoms strongly depends on the surface characteristics of the tube wall and is adjusted to fit the experimental data. It should be noted that the main dissociation rate used in this model is calculated from the cross-sections recommended by Phelps²⁵. The calculation of the dissociation rate includes the processes labeled as the 6 and 8.4 eV energy losses in Phelps's report. The 8.4 eV corresponds to the dissociation process $e + O_2 \rightarrow e + O_2(B^3\Sigma_u^-) \rightarrow e + O(^3P) + O(^1D)$, whereas the 6eV energy loss includes the excitation to the $C(^3\Delta_u)$ and $C(^1\Sigma_u^-)$ metastable states in addition to the dissociation process:
 $e + O_2 \rightarrow e + O_2(A^3\Sigma_u^-) \rightarrow e + O(^3P) + O(^3P)$. The excited states $C^3\Delta_u$ and $C^1\Sigma_u^-$ might be quenched without leading to dissociation of the O_2 molecule. The addition of this process is somewhat controversial.^{26,27}

The concentration of singlet $O_2(a^1\Delta)$ molecules calculated using the model is in good agreement with the experimental data for the large discharge currents ($I_d > 50$ mA) corresponding to an electron density $n_e > 10^{10} \text{ cm}^{-3}$. For these conditions, a saturation of $[O_2(a^1\Delta)] / [O_2(X^3\Sigma)] \sim 0.12$ is observed when the electron density increases. These values results from the equilibrium between the electronic excitation process $k_{ce} \sim k_8$ and electronic destruction processes $k_{de} = k_2 + k_6 + k_9 + k_9$ $[O_2(a^1\Delta)] / [O_2(X^3\Sigma)] \sim k_{ce} / k_{de}$. As shown above, because of the space charge field in the positive column of

the oxygen discharge, negative ions cannot reach the wall and are confined in the center of the tube where they are lost by detachment with the atoms (Reaction R3) and the singlet $O_2(a^1\Delta)$ molecules (Reaction R4). Therefore, the ratio of the negative ion concentration to the electron density is:

$$\frac{[O^-]}{n_e} = \frac{\nu_a}{\nu_d}, \text{ where } \nu_a = k_1 [O_2(X^3\Sigma)] + k_2 [O_2(a^1\Delta)] \text{ is the attachment frequency}$$

and $\nu_d = k_3 [O] + k_4 [O_2(a^1\Delta)]$ is the detachment frequency. In our experimental conditions, the concentration of negative ions is of the same order of magnitude as the electron density.

The reactions governing the kinetics of the metastable $O(^1D)$ and $O(^1S)$ atoms have not yet been included in the model. The populations of these states are coupled to the population of the molecular excited states: this can be done by the efficient quenching reaction of $O(^1S)$ by the singlet molecules $O_2(a^1\Delta)$ ($k = 1.7 \cdot 10^{-10} \text{ cm}^3 \cdot \text{s}^{-1}$)²⁸ for instance. This work is in progress.

CONCLUSION

The diagnostics and kinetic model developed for the positive column of a d.c. glow discharge can be used to describe other types of discharges. The concentrations of atoms and singlet molecules $O_2(a^1\Delta)$ have already been measured in a low pressure oxygen discharge created by a surface wave.²⁹ A model similar to the one presented in this paper is used to evaluate the fractional power transferred through electronic dissociation or excitation of singlet $O_2(a^1\Delta)$ molecules. This study will permit further modeling of the surface wave discharge and further comparison with the positive column of the d.c. glow discharge. This work should help to improve plasma reactors using oxygen rich mixtures.

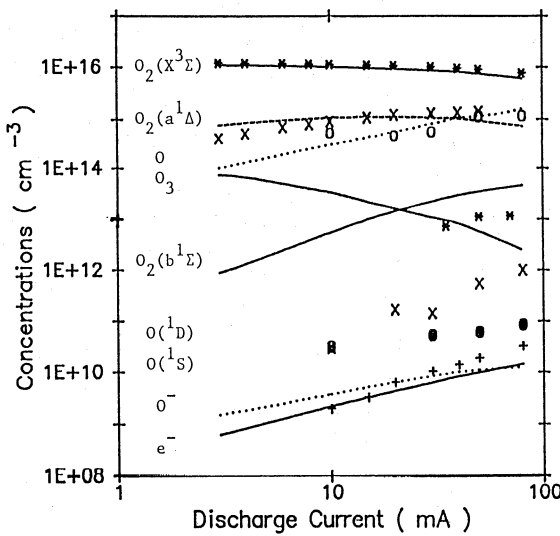


Fig.5. Concentrations of active species in the positive column of a d.c. glow discharge $\Phi=16\text{mm}, p=0.38 \text{ Torr}$ versus discharge current.
 symbols: experimental values.
 lines : computed values.

REFERENCES

1. R. P. Wayne, Reaction of singlet molecular Oxygen in the gas phase, in Singlet O₂, CRC Press, Boca Raton, Florida(1985).
2. H. Sabadil and S. Pfau, Plasma Chem. Plasma Process. **5**:67(1985).
3. G. Fournier, Cinétique de l'Oxygène en milieu Plasma dans Réactivité dans les plasmas, Editions de Physique (1984).
4. K. Masek, L. Laska and T. Ruzicka, Czech. J. Phys B **28**: 1321 (1978).
5. M. Capitelli and M. Dillonardo, Chem. Phys. **30**: 95 (1978).
6. J. W. Dettmer, Ph. D. Thesis, Air Force Institute of Technology, Wright Paterson Air Force, Dayton (1978).
7. L. Laska, K. Masek, and T. Ruzicka, Czech. J. Phys B **29**: 498 (1979).
8. K. Masek and L. Laska, Czech. J. Phys B **30**, 805 (1980).
9. L. Elias, E. A. Ogryzlo, and H. I. Schiff, Can J. Chem **37**:1680(1959).
10. J. W. Linnet, F. R. S, and D. G. H. Marsden, Proc. R. Soc London A **234**:489(1956).
11. G. Gousset, P. Panafieu, M. Touzeau and M. Vialle, Plasma Chem. Plasma Process. **7**, 293(1987).
12. M. Vialle, G. Cernogora, G. Gousset and M. Touzeau, International Conference on Phenomena in Ionized Gases, Belgrade, 1989
13. M. Moisan, C. Beaudry, and P. Leprince, IEEE Trans. Plasma. Sci. **PS3**:55(1975); C. Boisse-Laporte. A; Granier, E. Bloyet, P. Leprince, and J. Marec Appl. Phys. **61**:1970(1987).
14. S. Ogawa and M. Ogawa, Can. J. Phys. **53**:1845(1975).
15. M. A. A. Clyne and L. G. Piper, J. Chem. Soc. Faraday Trans. **72**:2178(1976).
16. Shardanand, Phys. Rev. **186**:5(1969).
17. H. D. Bobcock and L. Herzberg, Astrophys. J. **108**:167(1948).
18. J. H. Miller, R. N. Boese and L. P. Giver, J. Quant. Spectrosc. Radiat. Transfer, **9**:1507(1969).
19. L. C. Lee and G. P Smith, J. Chem. Phys. **70**: 1727(1978).
20. C. M. Ferreira, G. Gousset and M. Touzeau J. Phys. D: Appl. Phys. **21**:1403(1988).
21. G. Gousset, J. Jolly, D.Pagnon and M. Touzeau, IX European Sectional Conference on the Atomic and Molecular Physics of Ionised Gases, Lisbon (1988).
22. G. Gousset, M. Touzeau, M. Vialle and C. M. Ferreira, Plasma Chem. Plasma Process. **9**.189(1989).
23. B. Eliasson, Brown Boveri Report KRL83-40c, Electrical Discharge in Oxygen, CH-5405 Baden, Switzerland(1983).
24. M. Pinhero, P. A. Sà, C.M. Ferreira and J. Loureiro, Report Centro de Electrodinamica, Instituto Superior Tecnico, Lisboa (1988).
25. A. V. Phelps, Joint Institute for Laboratory Astrophysics, Report No. 28, University of Colorado, Boulder (1985).
26. S. A. Lawton, and A. V. Phelps, J. Chem. Phys. **69**:1055(1978); C. Yamabe and A. V. Phelps. J. Chem. Phys. **78**:2983(1983), K. Tachiban and A. V. Phelps. J. Chem. Phys. **75**:3315(1981).
27. U. Kogelschatz, XVI: International Conference on Phenomena in Ionized Gases, Dusseldorf, Invited Papers (1983), p. 240.
28. T. O. Slanger and G. Black Geophys. Res. Lett. **8**:535 (1981).
29. A. Granier, S. Pasquier, C. Boisse-Laporte, R. Darchicourt, P. Leprince, J. Marec. To be published in J. Appl. Phys (1989).
30. R. J. W. Henry, P. G. Burke and A. L. Sinfailam Phys. Rev. **178**:218(1969).
31. K. J. W. Stone and E. C. Zipf, Phys. Rev. A **4**:610(1971).
32. W. L. Fite and R. T Brackmann, Phys. Rev. **113**:815(1959).
33. M. Bacal, G. W. Hamilton, A. M. Bruneteau, H. J. Doucet and J. Taillet, Rev. Sci. Instrum. **50**:719(1979).

SIMULATION WORK IN NOBLE GAS

RADIATION DETECTORS

C.A.N. Conde and Teresa H.V.T. Dias

Physics Department
University of Coimbra
3000 Coimbra
Portugal

ABSTRACT

We present a review of the work on Monte-Carlo simulation of electron transport in noble gases at low reduced electric fields (E/N in the 1.5 to 15 Td range), with interest for nuclear radiation detectors working below or close to the avalanche threshold. Ionization chambers and gas proportional scintillation counters filled with argon, krypton or xenon, are the detectors envisaged and their physics mechanisms discussed. Drift velocities and electroluminescence yields have been calculated as a function of the reduced electric field intensity and compared with experimental results. Other data like total and partial excitation efficiencies, drift time fluctuations, electroluminescence layers, etc., have been calculated using either unidimensional or tridimensional scattering models. Full anisotropy of the differential elastic scattering cross-sections and variation of the electron energy along the path between collisions have been taken into account.

INTRODUCTION

The continued interest in gas based ionizing radiation detectors for fields ranging from astrophysics to high energy physics instrumentation, has led to a continued effort in the detailed understanding of the physical processes involved in these detectors.

Two main types of gas radiation detectors can be considered: ionization based detectors (like ionization chambers and proportional counters) and luminescence based detectors (like scintillation and proportional scintillation counters). In ionization based detectors a charge pulse is formed while the charge carriers (electrons) drift towards the electrodes. In luminescence based detectors light is produced either during the absorption of the incident radiation (scintillation counters) or during the drift of the electrons

under and electric field (gas proportional scintillation counters); this light is detected with photon detectors, like photomultipliers.

In both types of detectors the pulse amplitude obtained is usually proportional to the energy dissipated in the gas. Detectors of those types can also be designed that give information about the coordinates of the interaction point, the so-called position sensitive detectors. Besides information about energy and position of the incident radiation, detectors can also give timing information, i.e., information about the instant when the radiation was detected.

The accuracy of the information obtained about energy, position and time depends not only on the ionization and excitation processes that take place during the absorption of the radiation, but also on the subsequent phenomena that occur during the drift of the electrons in the gas. These phenomena are generally non-equilibrium processes, and provided an accurate set of electron scattering cross-section is used together with a model that describes faithfully the physical processes involved, they can be, in principle, simulated with good accuracy by Monte Carlo methods.

In the present work we describe results obtained previously with Monte Carlo simulation and point out areas open for future research. But before we carry out such a description we will present a brief description of the working principles of two types of detectors: the ionization chamber and the gas proportional scintillation counter.

IONIZATION CHAMBERS AND GAS PROPORTIONAL SCINTILLATION COUNTERS

The simpler Ionization Chamber consists of a two parallel plate electrode chamber filled with a gas and having a radiation entrance window (Fig. 1-a). Electrons produced in the gas by the radiation induce a negative charge pulse in the anode while drifting towards it. The rise time of this pulse depends on the drifting time which is of the order of a microsecond. As positive ions are much slower, their contribution to the induced pulse has a rise time of the order of a millisecond. Therefore, if even moderate counting rates are required, the positive ions contribution to the total induced pulse has to be differentiated with a RC circuit with a time constant of the order of the tens of the microsecond. However, such a pulse (with contributions only from the electron induced charge) has an amplitude that depends on the location of the radiation track, which is a nuisance. To avoid this the anode is shielded with a grid (Fig. 1-b), the Frisch grid. Only when the electrons reach the region between this grid and the anode they start inducing a charge pulse. Therefore the pulse amplitude does not depend on the location of the radiation track, as long as this track does not enter the region between the Frisch grid and the anode.

An alternative solution is to use a cylindrical geometry (Fig. 1-c). Only near the central anode does the voltage change appreciably for the drifting electrons to induce a significant electric charge.

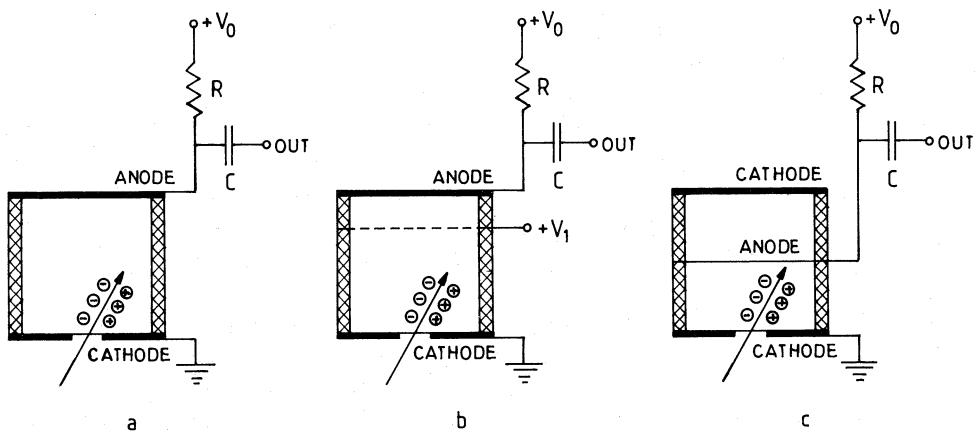


Fig. 1. Ionization Chambers:

- a) Parallel field geometry;
- b) Parallel field geometry with Frisch grid;
- c) Cylindrical geometry.

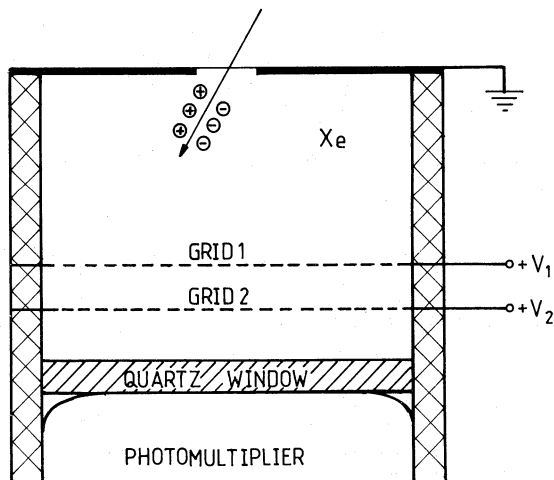


Fig. 2. The Gas Proportional Scintillation Counter.

Ionization chambers have the inconvenience of producing pulses with small amplitudes, which for X-rays may not rise significantly above the noise. A standard technique to increase the pulse amplitude is to raise the anode voltage, V_o (Fig. 1-c), in order to have charge multiplication near the anode; such a detector is called a Proportional Counter.

Another solution for the signal to noise problem is a detector called Gas Proportional Scintillation Counter (Fig. 2). This detector has usually a geometry similar to the Frish grid ionization chamber but its working principle is based in the production of electroluminescence in noble gases, usually xenon. Primary electrons produced by the incident radiation drift towards grid 1. As the voltage of grid 1, V_1 , is low (a few hundred Volts) the electric field in the region between the entrance window and grid 1 is weak (below $1 \text{ V cm}^{-1} \text{ Torr}^{-1}$ i.e. about 3 Td) so the drifting electrons cannot excite, even less ionize, the xenon atoms. However, as V_2 is of the order of 5 to 10 kV, once the electrons reach the region between grids 1 and 2 they meet an electric field ($\approx 5 \text{ V cm}^{-1} \text{ Torr}^{-1}$ i.e. 15.5 Td) strong enough to excite, but not to ionize, the noble gas atoms. The VUV light produced in the deexcitation process (the so called secondary scintillation or electroluminescence) reaches the photomultiplier through a VUV window. In this process one single electron can produce a few hundred VUV photons; thus the pulse amplitude is large and well above the noise. The energy resolution of such a detector is no longer noise limited and it is given by¹

$$\frac{\Delta E}{E} = 2.35 \sqrt{\frac{Fw}{E} + \frac{1}{N}}$$

where F is the Fano factor for the gas (in the 0.13 to 0.17 range for Xe), w the mean energy to produce an electron-ion pair (in the 21.6 to 22.3 eV range for Xe), E the incident radiation energy and N the mean number of effective photoelectrons in the photon detector. The energy resolution obtainable is typically 8% for 5.9 keV X-rays; this is better than the one for standard proportional counters by a factor of ≈ 2 . Experimentally it has been observed that the gas proportional scintillation counters are very sensitive to gas purity and that the intensity of electroluminescence increases almost linearly² from threshold (≈ 3 Td) to 15 Td. Above that, the increase is faster than linear, as charge multiplication starts to occur.

MONTE CARLO SIMULATION

In the Monte Carlo simulation work for electron transport in noble gas radiation detectors it is assumed that electrons lose energy only through two body elastic and inelastic collisions (leading to excitation and ionization of the noble gas atoms); neutral bremsstrahlung is neglected. The set of integral and differential cross sections was obtained from analytical expressions reproducing electron-noble gas atom elastic scattering phase shifts. Fittings to the integral cross sections (elastic and inelastic) with cubic splines were then derived³.

A simple, unidimensional method ⁴ was used at first to obtain faster results and to test the physical models assumed. In this method the variation of the electron energy between collisions was taken into account as well as the anisotropy of the scattering process, through backward and forward scattering probabilities calculated by averaging the differential cross sections over the forward and backward hemispheres. The energy after a collision was obtained from the expression

$$\ln R = -(Nm/\mu eE) \int_{\varepsilon_0}^{\varepsilon_1} \sigma_t(\varepsilon) d\varepsilon$$

where R is a random number from a uniform distribution between 0 and 1, N is the number density of the gas atoms, e and m the electron charge and mass, E the electric field strength, ε the energy of the electron, μ the reduced mass of the electron gas atom system, $\sigma_t(\varepsilon)$ the total cross section, and ε_0 and ε_1 the initial and final energy of the electron.

A detailed tridimensional Monte Carlo method was also used with almost no approximations using the same set of cross sections as for the unidimensional method ³. The thermal motion of the gas and the neutral bremsstrahlung were however neglected.

RESULTS

A variety of Monte Carlo calculations were carried out for Argon, Krypton and Xenon at a pressure of 760 Torr and a temperature of 300 K ^{4,5}. A resume of part of the results obtained is given in Table I.

The calculated values both for the drift velocities and electroluminescence yields agree quite well with the experimental data.

It was found that electrons increase gradually their energy along the electric field direction until they reach sufficient energy for excitation of the noble gas atoms. Soon after they lose almost all the energy in excitation and start drifting again with a low initial energy. The average distance between two successive inelastic collisions (excitations) has a small fluctuation, which implies that the VUV light produced in the three body deexcitation mechanism is localized in narrow zones or layers. Unlike the excitation, the fluctuation in the time between successive inelastic collisions is large.

As the energy lost in elastic scattering recoils is small, the major mechanism for energy loss between 5 and 15 Td is excitation. This leads to a high efficiency for conversion of the energy taken from the electric field for excitation and VUV light.

As the mechanism of ionization chambers and gas proportional scintillation counters is now reasonably well understood new areas for further research can be envisaged like the study of gaseous mixtures with interest for neutron detection,

Table I. Results for the Monte Carlo Simulation

Noble gas	E_p (V/cm/Torr)	E/N (Td)	Unidimensional Monte Carlo Method			Average values between successive inelastic collisions				Tridimensional Monte Carlo Method		
			Excitation efficiency (%)	Scintillation efficiency (%)		Number of elastic collisions ($\times 10^3$)	Drift distance (μm)	Drift time (ns)	Number of elastic collisions ($\times 10^3$)	Drift distance parallel to E (μm)	Drift time (ns)	
Krypton	1.50	4.66	51.9	43.3	156 ± 32	172 ± 69	52 ± 46	1500 ± 1100	964 ± 634	348 ± 280	—	—
	2.50	7.77	79.0	65.0	41 ± 34	67 ± 13	13 ± 12	158 ± 124	108 ± 43	27 ± 23	—	—
	3.50	10.87	88.3	72.8	20 ± 17	43 ± 6	6 ± 5	53 ± 41	51 ± 11	8.6 ± 7.1	—	—
Xenon	1.50	4.66	55.0	46.9	242 ± 172	136 ± 44	53 ± 43	—	—	—	—	—
	2.50	7.77	80.2	67.8	65 ± 54	55 ± 10	13 ± 12	—	—	—	—	—
	3.50	10.87	88.5	74.3	35 ± 29	36 ± 6	7 ± 7	—	—	—	—	—
Argon	1.50	4.66	25.4	21.5	232 ± 216	412 ± 284	107 ± 103	—	—	—	—	—
	2.50	7.77	63.7	53.5	41 ± 36	97 ± 31	17 ± 16	—	—	—	—	—
	3.50	10.87	80.2	66.8	17 ± 14	55 ± 10	6 ± 6	—	—	—	—	—

effects in non uniform electric field regions of the detectors like those near the grids, loss of electrons near the window for low X-ray photon energies, calculation of Fano factors, etc.

ACKNOWLEDGMENTS

Financial support given by Instituto Nacional de Investigação Científica (INIC - Portugal) is acknowledged.

REFERENCES

1. D. G. Simons, P. A. J. de Korte, A. Peacock, and J. A. M. Bleeker. "Energy resolution limitations in a gas scintillation proportional counter", S.P.I.E. vol. 597 "X-Ray Instrumentation in Astronomy" 190 (1985).
2. C. A. N. Conde, L. Requicha Ferreira, and M. Fátima A. Ferreira, "The Secondary Scintillation Output of Xenon in a Uniform Field Gas Proportional Scintillation Counter", IEEE Trans. Nucl. Sci., NS-24:221 (1977).
3. A. D. Stauffer, T. H. V. T. Dias, and C. A. N. Conde, "Analytical Expressions for Phase Shifts and Cross Sections for Low Energy Electron-Atom Scattering in Noble Gases", Nucl. Instr. Meth. in Phys. Res., A242:327 (1986), and Errata Ibd. A256:406(1987) and A261:610 (1987).
4. Teresa H. V. T. Dias, A. D. Stauffer, and C. A. N. Conde, "A Unidimensional Monte Carlo Simulation of Electron Drift Velocities and Electroluminescence in Argon, Krypton and Xenon", J. Phys. D: Appl. Phys., 19:527 (1986).
5. T. H. V. T. Dias, A. D. Stauffer, and C. A. N. Conde "Tridimensional Monte Carlo Simulation of Electrons Drifting in Krypton Under Low Reduced Electric Fields", Published in the Proceedings of 5th International Swarm Seminar, Birmingham, 29-31 July, ed. Birmingham University, pp. 23-27. (1987)

A DESCRIPTION OF THE NON-EQUILIBRIUM BEHAVIOR OF ELECTRONS IN MATTER: MACRO-KINETICS

E. E. Kunhardt

Weber Research Institute
Polytechnic University
Route 110
Farmingdale, NY 11735

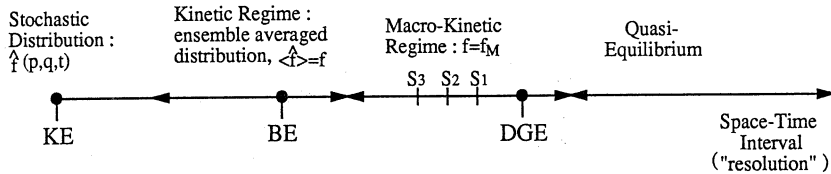
INTRODUCTION

Consider an assembly of non-relativistic, free (or excess) electrons in a background medium (gas or condensed matter) under the influence of an external space-time varying field. The electron density is assumed to be sufficiently low that their mutual interaction and the effect of Fermi-Dirac statistics can be neglected in the description of their behavior; furthermore, the background medium is assumed to be in equilibrium with a thermal bath at temperature, T, and that this equilibrium is unaffected by the passage of the electrons. Then every electron may be treated independently of all others and the behavior of the assembly may be ascertained from the dynamics of a single electron.

The variables that are used to represent the state of the assembly and the corresponding equations of evolution take different forms depending on the space-time "resolution" necessary (or desired) for a particular situation.^{1,2} The various representations that can be obtained for backgrounds corresponding to a dilute gas (classical system) and to a crystal (quantum system) are shown in Fig. 1, arranged according to their space-time resolution. A corresponding diagram can also be developed for the case of interacting electrons. However, when assumed to occur via an average macroscopic (space-charge) field, it is possible to incorporate this interaction into the formulations shown in Fig. 1.

This paper focuses on the behavior of an assembly of electrons in a quantum system, with specific emphasis on the semiclassical regime. The formulation of quantum dynamics in terms of a distribution function in phase-space is briefly review in the next section. In the semiclassical regime, the equation of evolution for the distribution function is a kinetic equation that is formally equal to that encountered in classical systems.¹⁻⁴ Starting from this equation, the macro-kinetic description is derived in the subsequent section and used to simulate the response of an assembly of electrons in gallium arsenide (GaAs) to a step change in an externally applied electric field.

Classical



Quantum

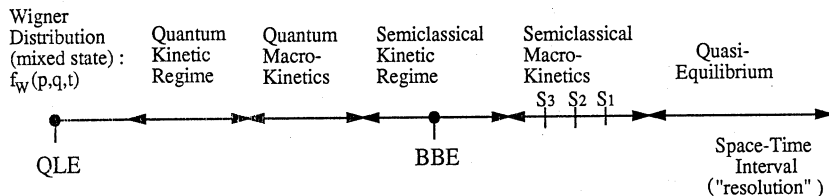


Fig. 1 The various levels of description of an assembly of electrons arranged according to space-time "resolution". The acronyms correspond to: KE - Klimontovich Equation,¹ BE - Classical Boltzmann Equation,^{2,3} DGE - Density Gradient Expansion,^{3,4} QLE - Quantum Liouville Equation,^{1,2} BBE - Boltzmann Bloch Equation,⁵ and S_1 , S_2 , S_3 are the macro-kinetic descriptions discussed in the paper.

QUANTUM DYNAMICS IN PHASE-SPACE

The motion of an electron in a quantum system (such as a semiconductor) under the influence of a generic potential, V_G , is described by a wavefunction, $\Psi(\underline{r},t)$, which satisfies the Schrodinger equation with a Hamiltonian given by^{1,2,5}

$$H = \frac{\mathbf{p}^2}{2m} + V_G \quad (1)$$

The various contribution to the generic potential may be identified as follows:

$$V_G = V_o + V_p = V_o + V_F + V_{e-p} + V_{e-i} + V_B \quad (2)$$

where V_o is the periodic lattice potential, V_F is the external potential field, V_{e-p} and V_{e-i} are stochastic potentials that account for the interactions with phonons and impurities, respectively, and V_B is the potential arising from spatial lattice inhomogeneities (such as barriers).

In this paper the effect of V_o will be taken into account via a renormalization of the electron mass, m .⁵ That is, the effect of V_p (Eq. (2)) is to be treated perturbatively. Thus, in the effective mass approximation, Eq. (1) becomes

$$H = \frac{\mathbf{p}^2}{2m^*} + V_p \quad (3)$$

where m^* is the renormalized (effective mass) and $\mathbf{p} = \hbar\boldsymbol{\kappa}$, with $\boldsymbol{\kappa}$ being the Bloch wavenumber.⁵ Alternative to the Schrodinger equation for Ψ , there exists an equivalent description in terms of a phase-space distribution, $F(p,q)$.⁶⁻¹⁰ Its basic feature is to permit one to calculate expectation values of quantum mechanical observables in the classical manner rather than through the operator formalism of quantum mechanics. For any function A of the operators P and Q corresponding to momentum and position, respectively,

$$\langle \Psi(t) | A(P, Q) | \Psi(t) \rangle = \iint F(p, q) A(p, q) dP dq \quad (4)$$

Due to the ambiguity in the correspondence between functions of operators and functions of commuting variables, p and q , a number of distributions can be defined.⁷⁻¹⁰ An extensive literature exists on this formulation.⁶⁻¹³ Adopting the Weyl ordering for the operators, the Wigner function, $f_w(p, q)$, is obtained for $F(p, q)$. This function is analogous to the classical distribution function (although it has the peculiar property in that it can be negative, thus the name quasi-probability function).⁸ It can provide an insightful view of wavepacket dynamics and to investigate quantum corrections to classical transport.

The equation of evolution for $f_w(p, q, t)$ is found to be⁹

$$\partial_t f_w = -\frac{p}{m^*} \partial_q f_w + \frac{2}{\pi\hbar^2} \left[V_p(q + \frac{i\hbar}{2} \partial_p) - V_p(q - \frac{i\hbar}{2} \partial_p) \right] f_w \quad (5)$$

Consider the situation for which V_F and V_B are slowly varying in the scale of the electron wavelength, and the phonon/impurity densities are sufficiently low that multiple-scattering can be neglected. A description with less resolution than that of Eq. (5) can be obtained in this case by ensemble averaging Eq. (5) (see Fig. 1). This results in the semiclassical Boltzmann-Bloch equation,¹⁴ which for $q \equiv \underline{r}$ and $p \equiv \hbar \underline{\kappa}$ and for a single valley band⁵ has the form

$$\partial_t f + \underline{v} \cdot \nabla_{\underline{r}} f + (e/\hbar) \underline{E} \cdot \nabla_{\underline{\kappa}} f = I(f) \quad (6)$$

where \underline{v} is the electron velocity in the crystal defined as the κ -space gradient of the energy ($\underline{v} = \hbar^{-1} \nabla_{\kappa} \epsilon(\kappa)$), $E = E(r, t)$ is the electric field (either externally applied or arising from space-change), and $I(f)$ is the linear scattering operator arising from V_{e-p} and V_{e-i} . Eq. (6) is formally equivalent to the kinetic equation that arises in the study of classical systems.¹⁻⁴

Coarser descriptions than that provided by Eq. (6) can be obtained by taking appropriate averages of Eq. (6).³ Since their space-time resolution corresponds to that of macroscopic variables, the resulting distributions are collectively referred to as macro-kinetic distributions. In the next section, the macro-kinetic description is developed by making use of moments of the distribution function to specify the space-time resolution.

ELECTRON MACRO-KINETICS

As in the classical regime, moment equations follow on taking moments of Eq. (6).^{10,15-17} It is significant to note that these equations are independent of assumptions regarding local equilibrium. The problem in using them lies in the fact that the calculation of the parameters that appear in these equations requires knowledge of the distribution function, i.e., the solution to Eq. (6). If these parameters are known, a finite set of ordered (according to characteristic scales of variation) moment equations could be used to describe the dynamics of the system with a space-time resolution (scale) that is characteristic to the particular set of equations chosen. Dynamics faster than these characteristic scales would not be properly taken into account. The finite set of equations define an equivalent averaged (over the faster scales) system. To this averaged system corresponds a distribution function, f_M , that likewise is an averaged distribution over the faster scales.¹⁸ The equation for f_M (a priori assumed to be easier to solve than Eq. (6)) and a finite set of moment equations form the closed set of equations that constitute the macro-kinetic description. To each finite set of moment

equations corresponds a space-time dynamics (slower than that of Eq. (6)) and an averaged distribution function, f_M . In this approach to obtaining a coarser description than that of Eq. (6), the moments of f are used to define the space-time resolution of the desired distribution function.¹⁸ A number of techniques can then be used to obtain the equation for f_M . Essentially, Eq. (6) needs to be projected onto the slower dynamics of the finite set of moment equations. The functional technique of Bogoliubov is used in this paper to effect this projection.¹⁸

Since $\tau > \tau_\epsilon > \tau_m$ for electrons in matter,^{3,18} where τ , τ_ϵ and τ_m are the electron density, energy and moment relaxation times, respectively, the moment equations can be ordered and a finite set selected depending on the level of description or degree of space-time coarseness desired in the model.¹⁸ The first three moment equations for a single valley band structure⁵ are:

$$\partial_t n + \nabla \cdot (n \underline{u}) = \frac{n}{\tau} \quad (7a)$$

$$\partial_t (n \bar{\epsilon}) + \nabla \cdot \langle \epsilon \underline{v} \rangle - q n \underline{E} \cdot \underline{u} = - \frac{n(\bar{\epsilon} - \epsilon_0)}{\tau_\epsilon} \quad (7b)$$

$$\partial_t (n \bar{p}) + \nabla \cdot \langle p \cdot \underline{v} \rangle - q \underline{E} = - \frac{n \bar{p}}{\tau_m} \quad (7c)$$

where the bracket represents an average over the distribution, n is the carrier density, \underline{u} is the average velocity, $\bar{\epsilon}$ is the mean energy, \bar{p} is the average momentum, and ϵ_0 is the thermal energy. The carrier density, energy, and momentum relaxation times are defined by

$$\frac{n}{\tau} = \int \left(\frac{\partial f}{\partial t} \right)_c d\underline{k} \quad (8a)$$

$$-\frac{n(\bar{\epsilon} - \epsilon_0)}{\tau_\epsilon} = \int \epsilon \left(\frac{\partial f}{\partial t} \right)_c d\underline{k} \quad (8b)$$

$$-\frac{n \bar{p}}{\tau_m} = \int p \left(\frac{\partial f}{\partial t} \right)_c d\underline{k} \quad (8c)$$

Subsequently, the various levels of macro-kinetic description that can be obtained using Eqs. (7) are discussed.¹⁸

1. The S_1 description, valid for time scale $\geq \tau$

In this time scale, the resolution of the description is determined by the density and the dynamics of the assembly is described by Eq. (7a). Consequently, the corresponding macro-kinetic distribution (MKD) is taken to have the same space-time dependence as the electron density; that is,

$$f(\underline{k}, \underline{r}, t) = f_M^{(1)} [\underline{k}, n(\underline{r}, t)] \quad (9)$$

Using Eqs. (7a) and (9) in Eq. (6), the equation for $f_M^{(1)}$ is obtained. Solving for $f_M^{(1)}$ and using it to evaluate \underline{u} and τ in Eq. (7a), leads to the well-known drift-diffusion equation for $n(\underline{r}, t)$.^{3,4,18} That is,

$$n \underline{u} = n \mu \underline{E} - D \nabla n \quad (10)$$

where μ is the mobility and D is the diffusion coefficient and are obtained in terms of the known function $f_M^{(1)}$.¹⁸

2. The S_2 description, valid for time scale $\geq \tau_e$

In this case, the description of the assembly is in terms of a MKD that depends on the electron density and mean energy,

$$f(\underline{k}, \underline{r}, t) = f_M^{(2)} [\underline{k}, n(\underline{r}, t), \bar{\epsilon}(\underline{r}, t)], \quad (11)$$

and the corresponding first two moment equations [Eqs. (7a) and (7b)]. The equation for $f_M^{(2)}$ has been shown¹⁸ to be, for uniform conditions and in lowest order,

$$q E_{eq} \partial_{k_z} f_M^{(2)} = \left(\frac{\partial f_M^{(2)}}{\partial t} \right)_c \quad (12a)$$

where

$$q E_{eq} = \frac{\bar{\epsilon}(t) - \epsilon_0}{u_s \tau_e} \quad (12b)$$

with

$$nu_s = \int f_M^{(2)} (\underline{k}, n, \bar{\epsilon}) \underline{v} d\underline{k} \quad (12c)$$

Eq. (12a) represents a system that obeys a steady-state Boltzmann-Bloch equation with an equivalent field, E_{eq} , as the driving force. u_s is the "steady-state" average velocity that is seen to depend on the time-varying mean energy. Eq. (12c) implies that in this description the mean momentum of carriers responds instantaneously to an equivalent field, E_{eq} .

The unknown rates in Eqs. (7a) and (7b) can be obtained in terms of the mean energy by evaluating the integrals in Eq. (8a) and (8b) using the MKD obtained from Eq. (12a). The S_2 MKD can be obtained, for example, from MC simulations and the rates tabulated as functions of the mean energy or equivalent field. For a given problem, it is then only necessary to solve Eqs. (7a) and (7b). Other averaged properties of the assembly may be obtained from $f_M^{(2)}$.

3. The S_3 description, valid for time scale $\geq \tau_m$

The system of equations that describe the system in this time scale consist of first three moment equations [Eqs. (7a)-(7c)] and the corresponding MKD, which is taken to depend on electron density, mean energy, and average momentum:

$$f(\underline{k}, \underline{r}, t) = f_M^{(3)} [\underline{k}, n(\underline{r}, t), \bar{\epsilon}(\underline{r}, t), \bar{k}(\underline{r}, t)] \quad (13)$$

In a previous paper,¹⁸ a relaxation process has been used to model the evolution of the smaller time scale distribution ($f_M^{(3)}$) into the larger time scale distribution ($f_M^{(2)}$). An alternative is to approximate $f_M^{(3)}$ with $f_M^{(2)}$ in the evaluation of the averaged rates [Eqs. (8a)-(8c)]. This simple approach is valid when the momentum relaxation time is relatively small compared to the energy relaxation time. This is in general true for GaAs and Si, unless the behavior is desired at relatively low fields.²⁰ Similarly to the S_1 and S_2 descriptions, the unknown coefficients in Eqs. (7a)-(7c) can be evaluated using $f_M^{(3)}$.

ILLUSTRATION: THE RESPONSE OF A HOMOGENEOUS CONCENTRATION OF ELECTRONS TO A STEP CHANGE IN ELECTRIC FIELD

In this section, the response of a homogeneous concentration of electrons in GaAs to a step change in electric field is investigated using the theory developed in the previous section. For the sake of simplicity, it is assumed that there is no particle gain; that is, $n(r,t) = \text{const}$. Again, a single-valley model has been used for the band structure.⁵ The objective of this example is to illustrate the application of the theory presented in the previous section with a "model" calculation. The evolution of the electrons is discussed in the context of the S_3 description. This is dictated by the time scale of the applied field. For this example, Eqs. (7a)-(7c) reduce to

$$\partial_t \bar{\varepsilon} = -v_\varepsilon (\bar{\varepsilon} - \bar{\varepsilon}_0) + q u E, \quad (14a)$$

$$\partial_t \bar{p} = -v_m \bar{p} + q E \quad (14b)$$

where $\bar{\varepsilon}_0$ is the mean energy corresponding to the lattice temperature and v_i , $i = \varepsilon, m$, are obtained from Eqs. (8b) and (8c) with $f = f_M^2$. This distribution is obtained from Eq. (12). The electron scattering processes are given in Reference 18.

These equations have been solved numerically using finite difference techniques.²¹ At the j th time step, the mean energy $\bar{\varepsilon}(j)$ and average momentum $\bar{p}(j)$ are obtained from the discrete equations, given their values and the rates at the previous time step $j-1$.

The evolution of the mean energy and average velocity of the electrons in GaAs subjected to a step change in electric field is shown in Figs. 2 and 3. These correspond to the time dependence of the electric field shown in Fig. 4. The initial field is kept constant for a time such that the electrons have attained equilibrium with the field by the time the field begins to change. Also shown in Figs. 2 and 3 are the results obtained using: (a) Monte Carlo methods, with a three-valley model,²² and (b) the S_1 approximation.

The differences between the results obtained with the S_3 description and the Monte Carlo simulation in Fig. 3 arise primarily from the fact that the S_3 description uses a single-valley representation. For such high fields [see Fig. 4] intervalley scattering dominates the scattering process of electrons in GaAs. It causes the slower approach of the average velocity (relative to the S_3 description) to the equilibrium state. The evolution of the system from the initial equilibrium state (I) to the final equilibrium state (F) is displayed in $(\bar{\varepsilon}, u)$ space in Fig. 5. The fast transient (nonequilibrium) behavior obtained with the S_3 approximation is clearly contrasted with those obtained from the S_1 approximation (which in essence yields an evolution through a series of

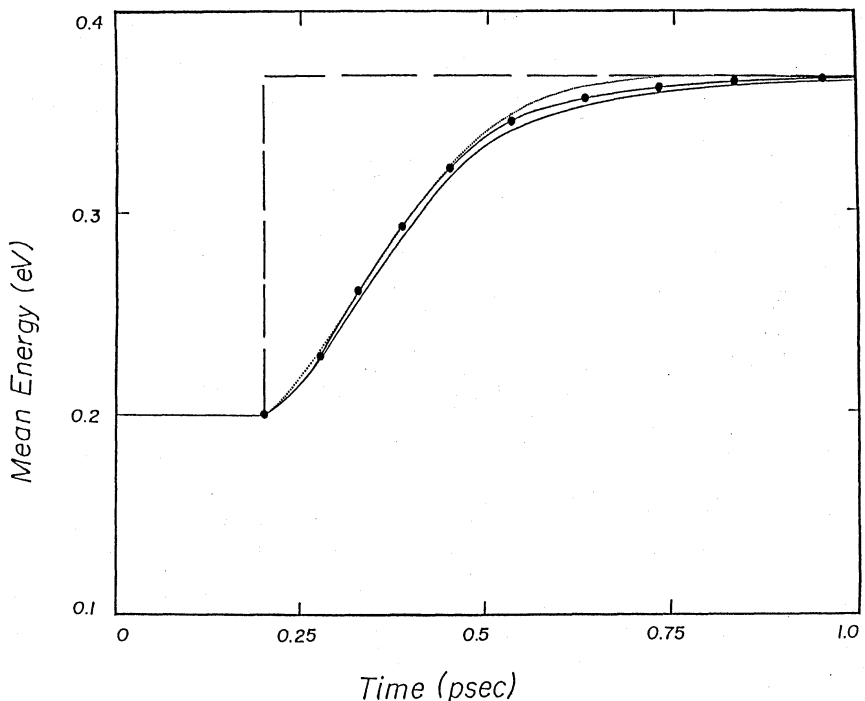


Fig. 2 Evolution of the electron mean energy as a consequence of a step change in the applied field (see Fig. 4). On the figure, the solid, long dash, and small dot lines correspond to the response obtained with the S_3 , S_1 descriptions and Monte Carlo simulation, respectively.

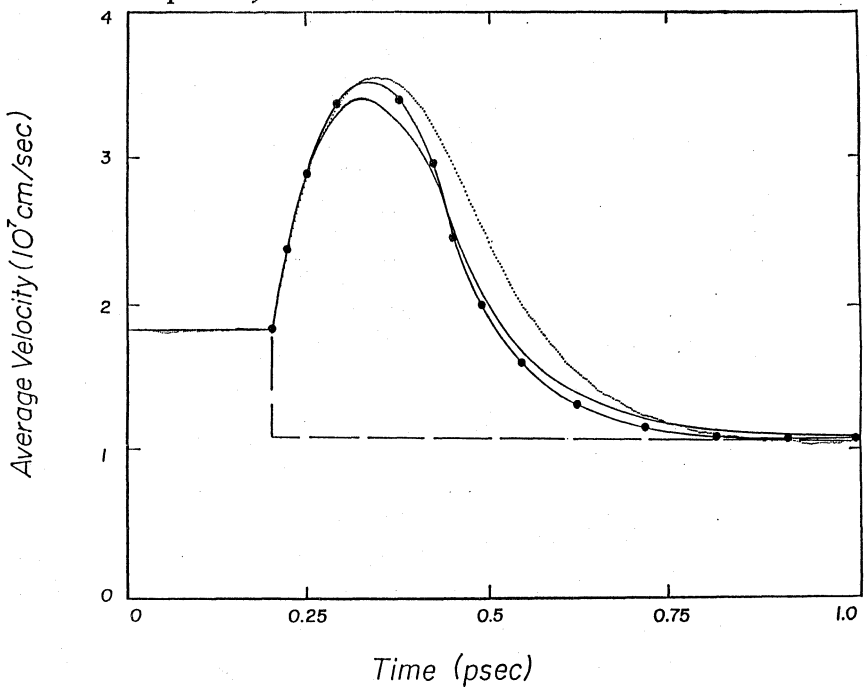


Fig. 3 Evolution of the average velocity of the electrons as a consequence of a step change in the applied field (see Fig. 4). The line symbols correspond to those used in Fig. 2.

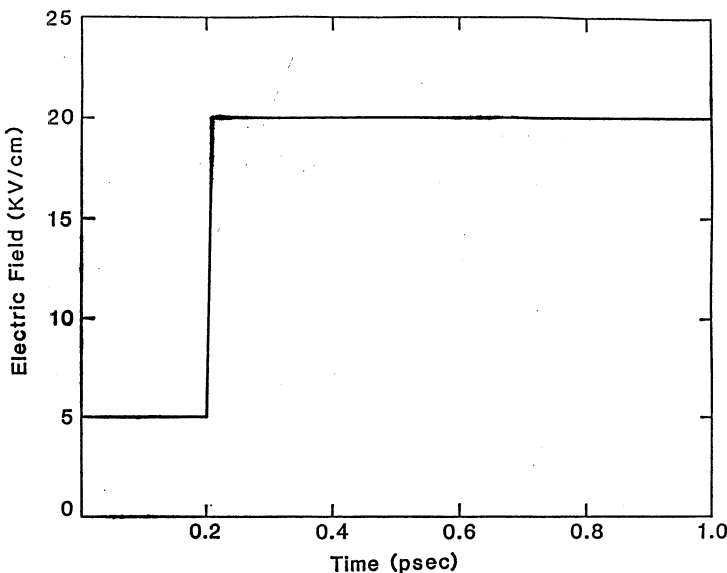


Fig. 4 Time dependence of the applied field corresponding to the results shown in Figs. 2 and 3.

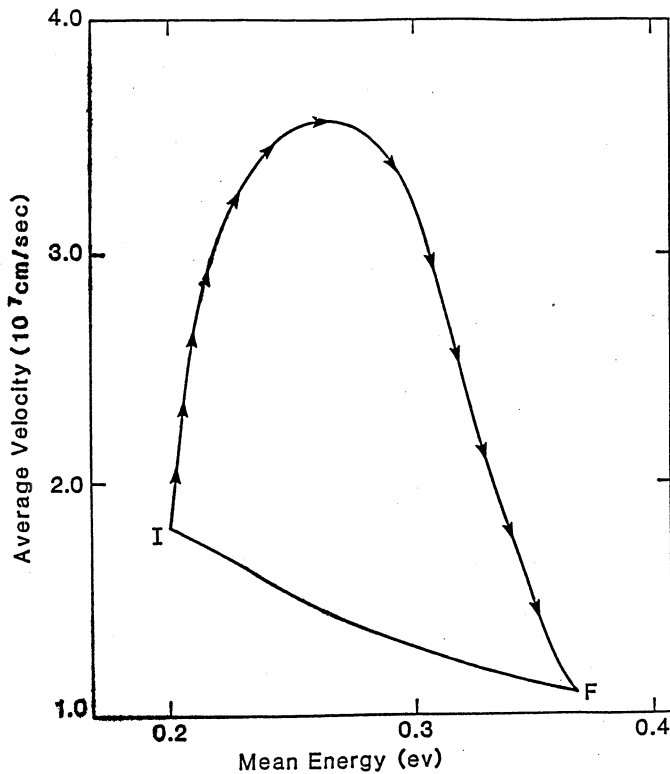


Fig. 5 Phase-space plot of the evolution of the electron assembly. The letters I and F correspond to the initial and final states. The arrows indicate the direction of evolution. The solid line with arrow corresponds to the response in the S₃ description; the line without arrows corresponds to the S₁ description.

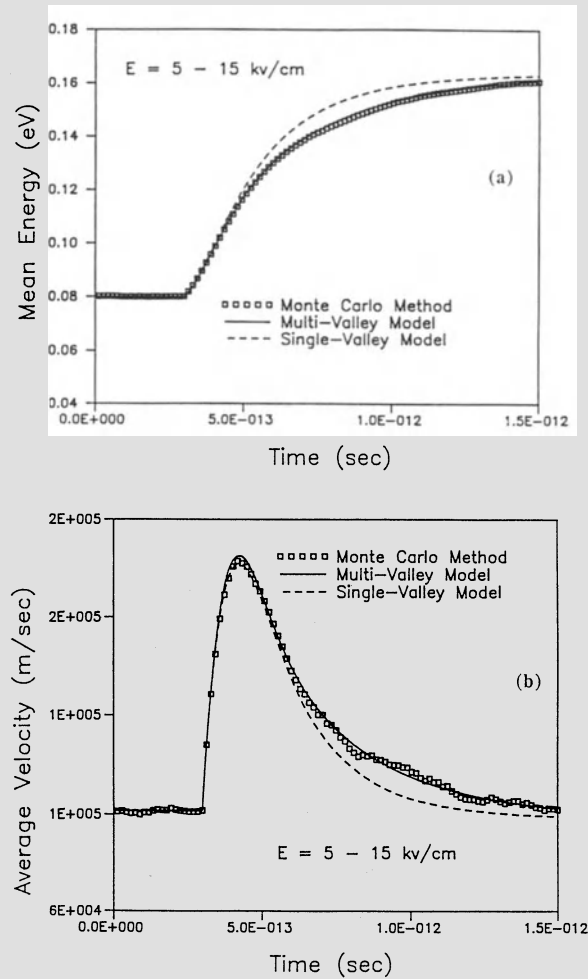


Fig. 6 Evolution of total mean energy and average velocity for the multivalley test model of Reference 22 as a consequence of a step change in applied field from 5 KV/cm to 15 KV/cm. (a) Mean energy, (b) average velocity.

equilibrium states). As expected, for fields changing in time scales $<\nu_e^{-1}$, a description in terms of S_1 is not satisfactory.

The macro-kinetic description can similarly be implemented for a multi-valley band structure.²³ In this case, very good agreement is obtained between Monte Carlo and the MK description. This is shown in Fig. 6 for a two valley band structure and a field change from 5-15 kV/cm. The band properties and the scattering rates used in this calculation correspond to a model semiconductor (see Ref. 23 for details).

CONCLUDING REMARKS

Nonequilibrium descriptions of the dynamics of electrons in matter under the influence of space-time varying fields have been presented. These descriptions are valid in different space-time scales; in particular, the macro-kinetic description is valid for macroscopic space-time scales which are determined from the characteristic scales of the moment equations. The results that have been presented in this paper correspond to the lowest-order solutions of these descriptions. In the fastest scale (S_3), these lowest-order results have been shown to be in reasonable agreement with those obtained from a kinetic description. A number of issues remain to be addressed. Among these issues are (a) the (more) quantitative description of the S_3 state, (b) the relative importance of higher-order terms in the expansions of f_M and of faster times scales (S_4 or higher), and (c) the relationship between a description in terms of S_1 and a modal decomposition of the distribution function.

ACKNOWLEDGMENT

This work is supported by the Office of Naval Research and the Air Force Office of Scientific Research.

REFERENCES

1. Y. L. Klimontovich, *Statistical Physics*, (Hardwood Academic, London, 1986).
2. R. Balescu, *Equilibrium and Non-equilibrium Statistical Mechanics*, (Wiley, New York, 1975).
3. E. E. Kunhardt, C. Wu, and B. Penetrante, Phys. Rev. A37, 1654 (1988).
4. K. Kumar, H. R. Skulander, and R. E. Robson, Aust. J. Phys. 33, 343 (1980).
5. J. M. Ziman, *Principles of the Theory of Solids*, 2nd edition, (Cambridge University Press, Cambridge, 1979).
6. E. Wigner, Phys. Rev. 40, 749 (1932).
7. M. Hillery, R. F. O'Connell, M. O. Scully and E. P. Wigner, Phys. Rev. 106, 121 (1984).
8. L. Cohen, J. Math. Phys. 7, 781 (1966).
9. V. I. Tatarskii, Sov. Phys. Usp. 26, 311 (1983).
10. P. Carruthers and F. Zachariasen, Rev. Mod. Phys. 55, 245 (1983).
11. J. R. Barker, in *Handbook on Semiconductors*, T. S. Moss, editor (North-Holland, London, 1982), p. 617.
12. W. E. Brittin and W. R. Chappell, Rev. Mod. Phys. 34, 620 (1962).

13. J. P. Dahl, Physica 114A 439 (1982).
14. W. Kohn and J. M. Luttinger, Phys. Rev. 108, 590 (1957).
15. G. J. Iafrate in *Gallium Arsenide Technology*, edited by D. K. Ferry (H. W. Sames & Co., 1982), Chap. 12.
16. D. K. Ferry and J. R. Barker, Solid State Comm. 30, 301 (1979).
17. G. J. Iafrate, H. L. Grubin, and D. K. Ferry, J. de Phys. C7, 307 (1981).
18. E. E. Kunhardt, M. Cheng, C. Wu, J. Appl. Phys. 64, 1220 (1988).
19. N. N. Bogoliubov, in *Studies in Statistical Mechanics*, edited by J. deBoer and G. G. Uhlenbeck (Interscience, New York, 1962).
20. N. Goldsman and Jeffrey, IEEE Trans. Elect. Dev. ED-35, 1524 (1988).
21. C. W. Gear, *Numerical Initial Value Problems in Ordinary Differential Equations* (Prentice Hall, New York, 1971).
22. M. Cheng and E. E. Kunhardt, J. Appl. Phys. 63, 2322 (1988).
23. M. Cheng and E. E. Kunhardt, Report No. POLY-WRI-1562-89, Weber Research Institute, Polytechnic University.

THERMALIZATION AND TRANSPORT OF SPUTTERED PARTICLES IN GLOW DISCHARGES

K.T. Waldecker¹, H. M. Urbassek¹,
A. Gras-Marti² and J. A. Vallés-Abarca²

¹ Institut für Theoretische Physik, TU
PO Box 3329, D-3300 Braunschweig, FRG

² Departament de Fisica, Universitat d'Alacant, Apt. 99
E-03080 Alacant, Spain

I. INTRODUCTION

A typical and important problem of nonequilibrium gas dynamics is the fate of the high energy particles sputtered from the cathode in a gas discharge. Sputtered particles leave the cathode with energies of the order of 10 eV which is 2 orders of magnitudes higher than the thermal energy of an atom in the gas discharge. Due to collisions with gas atoms they lose energy and may *thermalize* in the gas discharge. The properties of sputtered particles are of fundamental interest for the technology of thin film deposition by glow discharge sputtering [1].

With each collision a sputtered particle energizes a thermal gas atom which in its turn shares its energy with other gas atoms, etc.: Thus a *collision cascade* is set up. As long as the number of energetic atoms is small enough such that collisions only with thermal atoms occur, we obviously have a linear problem at hand which has been studied thoroughly in the recent past: Energy distribution of sputtered particles in front of the cathode [2, 3] and thermalisation profiles [4, 5] have been determined.

For high sputtering currents, however, - these are routinely realized in magnetron systems operating at 1 A or more - the high amount of energy and momentum put into the gas discharge by the sputtered particles heats up the

gas discharge in the vicinity of the cathode. This may lead to an observable gas flow in the gas discharge which has been termed *sputtering wind* [6] and to a *reduction of gas density* in the front of the cathode [7]. Both phenomena have a profound effect on the transport properties of the sputtered particles and are therefore important for an understanding of thin film deposition in magnetrons.

This feed back between the heating of the gas discharge by the sputtered particles, and its backreaction on the transport of these energetic particles, asks for a genuinely *nonlinear analysis*. We wish to present in this note preliminary results of such an analysis by means of a direct Monte Carlo computer simulation.

II. A MODEL PROBLEM

Consider an Ar glow discharge in a box of 30 cm length and a square of $10 \times 10 \text{ cm}^2$ cross section. The Argon gas is assumed to be initially at 300 K and 10 mTorr. A current of 5 A induces sputtering of the Cu cathode. An effective yield of 1 sputtered atom per bombarding particle is assumed. The flux j of sputtered atoms obeys at the cathode the law [8, 9]

$$j(E, \theta) \propto \frac{E}{(E + U)^3} \cdot |\cos \theta| , \quad (1)$$

where E is the energy of the sputtered atom and θ its polar angle with respect to the surface normal. A surface binding energy of $U = 3.5 \text{ eV}$ corresponding to a Cu cathode has been chosen. Furthermore, a high energy cut-off at 100 eV was introduced.

Only elastic collisions between neutral atoms are taken into account; charge exchange and electron impact collisions are neglected. A pseudo-Maxwellian scattering cross section

$$d\sigma(g, \chi) = \frac{C}{g} d\cos \chi \quad (2)$$

has been adopted, where g is the relative velocity between two collision partners and χ the scattering angle in the center of mass system. C is a constant which was chosen such that the stopping cross section $S(E) = E \int \sin^2(\chi/2) d\sigma(E, \chi)$ at $E = 1.75 \text{ eV}$ is equal to $22.4 \text{ eV}\text{\AA}^2$. This is a realistic value determined from the so called KrC interaction potential [10]. The value of $U/2 = 1.75 \text{ eV}$ denotes the most probable energy of a sputtered particle. The interaction of any particle with the volume walls was assumed to be specularly reflecting.

The cross section (2) corresponds to a scattering rate which is independent of the relative velocity of the colliding particles. For our problem the mean time that passes between the collision events of any particle is

$$\tau = \frac{1}{2nC} = 4.18 \mu\text{s} , \quad (3)$$

where n is the gas density.

III. THE METHOD

The problem of the interaction between the sputtered flux and the glow discharge gas is attacked via a direct Monte Carlo simulation. A variety of such codes have been established which are well described in the literature [11, 12]. Their basic principle of operation is the following. The volume is divided up into cells which are filled with a representative number of particles. At times which are randomly distributed according to the scattering rate (3), the particles in a cell may collide. After a certain time the particles are allowed to stream freely according to their newly acquired velocities, and may move out into the neighbouring cells. This process is repeated up to the time when a measurement of the gas properties - e.g. density, temperature, flow velocity - is undertaken.

For the present simulation we chose the so called BY-scheme [13]. It has the advantage that it operates with relatively few particles per cell which becomes important if we wish to extend the simulation to truly threedimensional problems. A number of 41 cells in the extension between the electrodes and of 15×15 cells in the cross sectional area was chosen. Each cell was initially filled with 4 atoms.

IV. RESULTS

In fig. 1 to 3 the evolution of some of the gas properties is displayed. Since our model problem is strictly one-dimensional we plot all quantities versus the distance z normal to the cathode.

In fig. 1 we plot the gas density at a time of 4τ and 32τ after the start of the sputtering process. It is observed how the initially constant density of around $3 \cdot 10^{14} \text{ cm}^{-3}$ shows a reduction close to the cathode.

In fig. 2 the gas temperature is displayed. Initially at 300 K, the temperature increases considerably throughout the volume due to the energy dissipated by the sputtered flux. Even more dramatically, a drastic temperature enhancement close to the cathode is observed.

Fig. 3 finally shows how the momentum of the sputtered particles and the large pressure gradient in the vicinity of the cathode lead to a considerable gas flow away from the cathode.

The statistics of the plots is poor, particularly in the graph showing the temperature. This is due to the fact that in each slab corresponding to one entry in the histograms in figs. 1 - 3 there are initially only 900 particles in the simulation with a total energy of around 23 eV. Thus one particular sputtered particle may easily have a comparable energy; hence the large spatial fluctuations.

V. CONCLUSIONS

We showed that it is possible to treat the nonequilibrium problem of the thermalization and transport of sputtered particles in a glow discharge via a di-

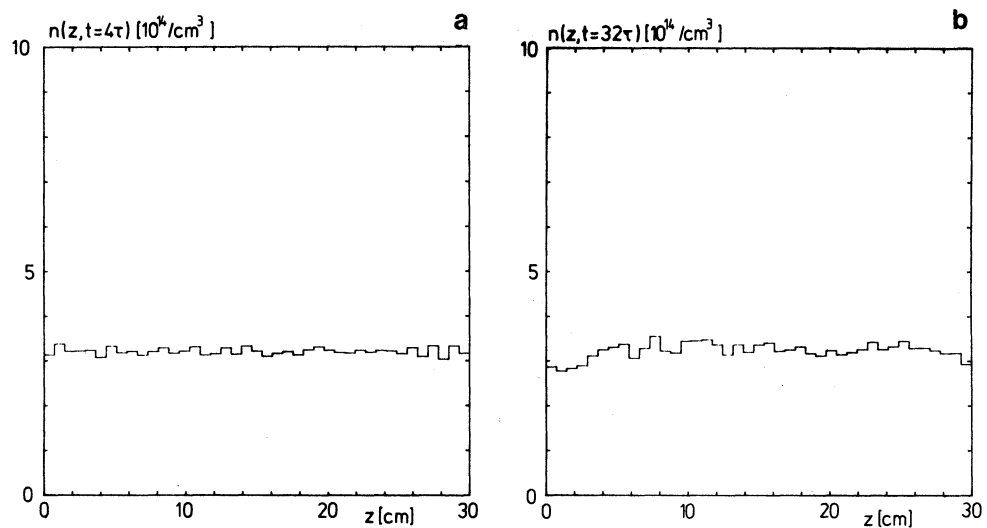


Figure 1. Gas density n vs. distance z from the cathode at time $t = 4\tau$ (a) and $t = 32\tau$ (b).

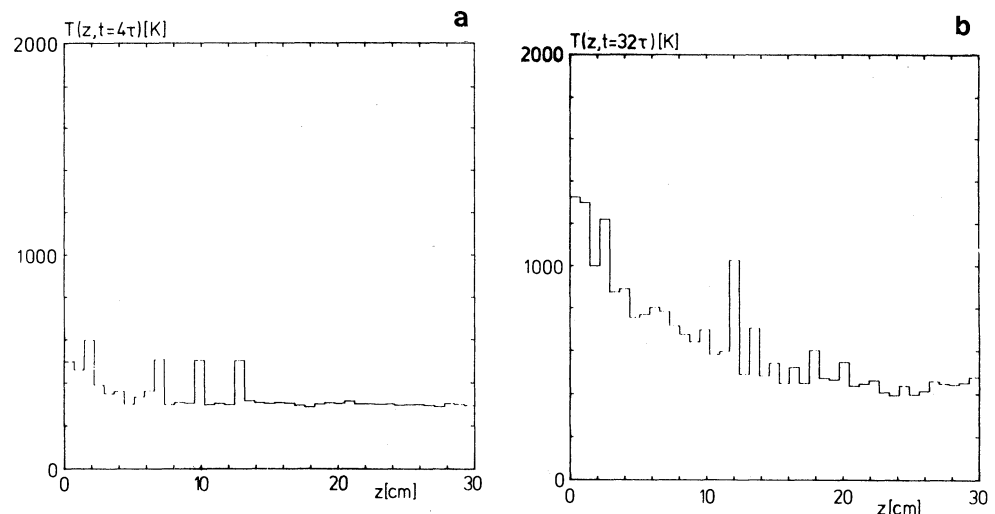


Figure 2. Temperature T vs. distance z from the cathode at time $t = 4\tau$ (a) and $t = 32\tau$ (b).

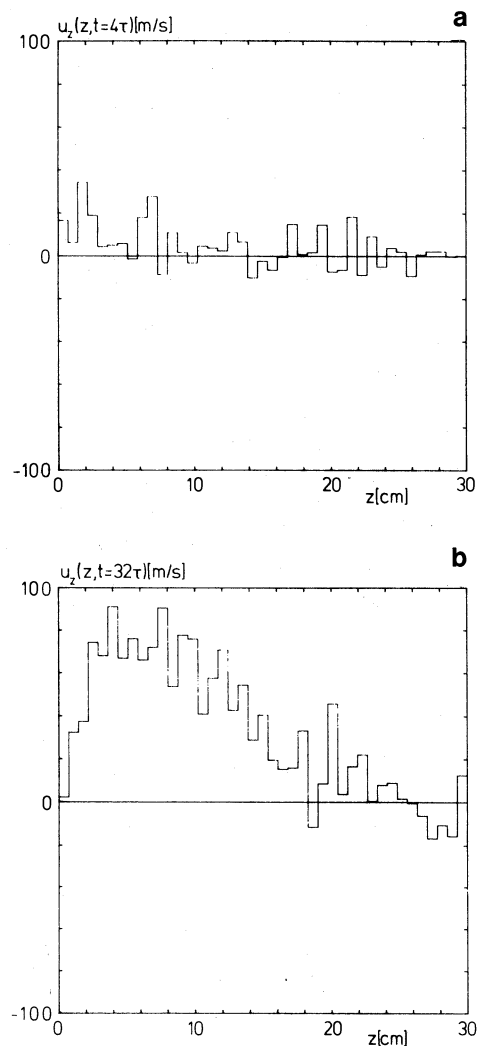


Figure 3. Mean velocity u_z vs. distance z from the cathode at time $t = 4\tau$ (a) and $t = 32\tau$ (b).

rect Monte Carlo computer simulation. Even the simulation of time dependent and threedimensional problems appears feasible. The poor statistics displayed in the figures may be easily improved by increasing the number of runs performed.

The phenomena of a drastic temperature increase and a corresponding gas density reduction in front of the cathode, and of a *sputtering wind* which have been reported in magnetron experiments [6, 7] are clearly observed in the simulation.

The Monte Carlo simulation technique presented here may prove useful in studying a number of other transport problems of nonequilibrium species (e.g. metastables) in glow discharges. The inclusion of inelastic collision events which then becomes necessary appears feasible.

REFERENCES

1. B. Chapman, *Glow Discharge Processes* (John Wiley, New York, 1980).
2. K. Meyer, I. K. Schuller, and C. M. Falco, *J. Appl. Phys.* **52**, 5803 (1981).
3. A. Gras-Marti and J. A. Valles-Abarca, *J. Appl. Phys.* **54**, 1071 (1983).
4. J. A. Valles-Abarca and A. Gras-Marti, *J. Appl. Phys.* **55**, 1370 (1984).
5. I. Abril, A. Gras-Marti, and J. A. Valles-Abarca, *J. Vac. Sci. Technol.* **A4**, 1773 (1986).
6. D. W. Hoffman, *J. Vac. Sci. Technol.* **A3**, 561 (1985).
7. S. M. Rossnagel, *J. Vac. Sci. Technol.* **A6**, 19 (1988).
8. M. W. Thompson, *Philos. Mag.* **18**, 377 (1968).
9. P. Sigmund, in *Sputtering by Particle Bombardment I*, edited by R. Behrisch (Springer, Berlin, 1981), p. 9.
10. W. D. Wilson, L. G. Haggmark, and J. P. Biersack, *Phys. Rev. B* **15**, 2458 (1977).
11. G. A. Bird, *Molecular Gas Dynamics* (Clarendon Press, Oxford, 1976).
12. K. Nanbu, *J. Phys. Soc. Japan* **52**, 3382 (1983).
13. O. M. Belotserkovskiy and V. Y. Yanitskiy, *Fluid Mechanics Soviet Research* **7**, 42 (1978).

THE FREE ELECTRON LASER: A SIMPLE QUANTUM PICTURE

R. Caloi, G. Dattoli, M. Richetta and A. Torre

ENEA, Dip. TIB, U.S. Fisica Applicata, CRE Frascati
C.P. 65 - 00044 - Frascati, Rome, Italy

ABSTRACT

The basic FEL properties are reviewed within the framework of an elementary quantum mechanical analysis.

1. INTRODUCTION

Powerful coherent light may be generated by either the stimulated emission of an inverted atomic or molecular medium or by free electrons moving in a wave-guide or in an undulator magnet. The first mechanism is that of conventional lasers the second is that of travelling wave tubes (TWT). The Free Electron Laser (FEL) is essentially a TWT which can operate on a wider range of frequencies (in principle from VUV up to microwaves).¹ In the field of coherent generation with an electron beam the FEL brought the possibility of overcoming all the problems connected with the miniaturization of the microwave tubes needed to operate at a shorter wave-length. The basic ingredients of an FEL are (see Fig. 1)

- 1) The accelerator which provides a high energy and high quality e-beam.
- 2) The undulator, namely a series of N-S magnetic poles, arranged as in Fig. 1.
- 3) The optical cavity, needed if the system operates in the oscillator configuration.

The interaction takes place in the undulator magnet (UM), which transforms the longitudinal non-radiating electron motion into the transverse motion which allows the coupling to and the amplification of a copropagating TE wave. Infact, as already remarked, the basic principle of an FEL is that of a TWT and can be therefore summarized as follows. Inside the undulator, owing to the Lorentz force, the electrons acquire a transverse velocity, a copropagating TE wave can therefore couple to the e-beam and produce an energy modulation. This energy modulation transforms into a density modulation and a coherent amplification of the input wave occurs when the e-beam has been longitudinally modulated on a scale corresponding to the wave length of the TE wave. We can in general distinguish two processes for the FEL oscillator. The electrons are injected in the UM and emit bremsstrahlung radiation, which is stored in an optical cavity (spontaneous emission). The radiation is then amplified by the above discussed mechanism (stimulated emission) and if the gain is larger than the cavity losses the system may work as an oscillator. We have used classical concepts to describe the FEL and infact the theoretical understanding of this type of laser does not require quantum mechanics, which on the other side may provide a microscopic picture of the

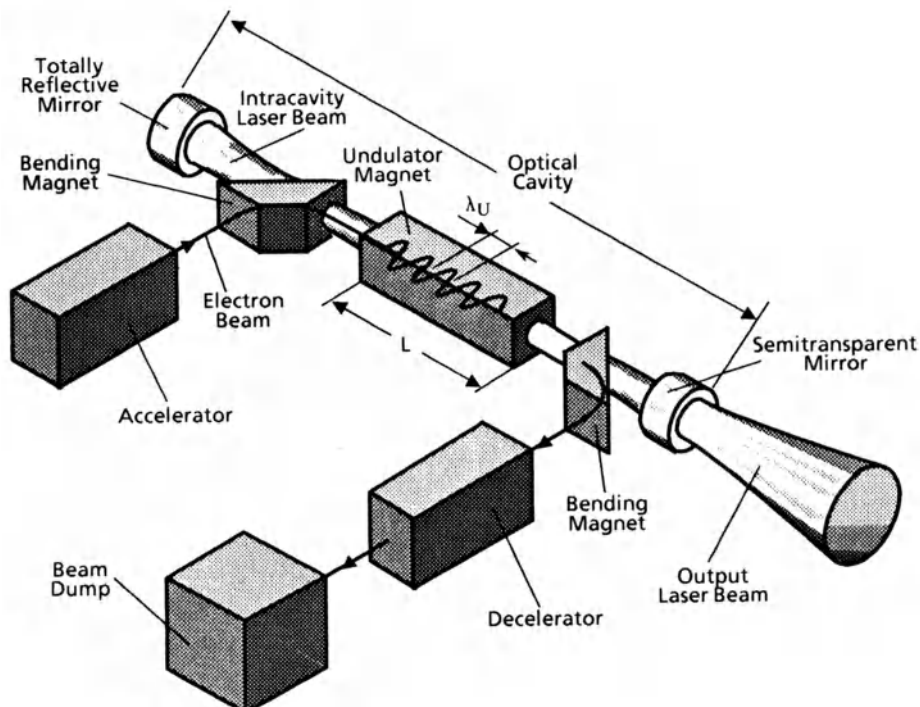


Fig. 1. FEL with electron beam recovery. The electrons, after the interaction with radiation and UM fields, are decelerated in a special item (radio-frequency linac or electrostatic decelerating section) in order to recover part of their energy and charge (the "decelerator" can be the accelerator itself where the electrons are injected, e.g. for a radio-frequency linac, with a decelerating phase).

process perhaps more physically insightful than that based on a full classical description. In the following we discuss frequency selection mechanism, spontaneous emission, stimulated emission and gain using quantum mechanics and point out the link with other processes like e.g. multiphoton dynamics.

However before concluding these introductory remarks and in order to better frame the FEL within the laser devices, a few words of comment on the concept of laser are perhaps in order. Regardless the underlying mechanism of spontaneous emission and gain, the laser is a device that sustains steady state oscillations with a well defined frequency. This concept is rather old and in electrical engineering it is well known as self-sustained amplifier with a frequency dependent feedback. The gain must be present to overcome the losses (unavoidable in any physical system) and the frequency selectivity fixes the oscillation frequency within the working band of the amplifier. A scheme for this idealized amplifier is that given in Fig. 2. (see Ref. [2]). We assume that the output Y depends on the input X through the non linear function

$$Y = A(X) \quad (1.1)$$

and the feedback signal is assumed to be

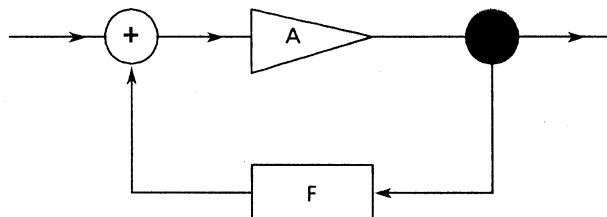


Fig. 2. Loop diagram of a feedback amplifier

$$X_{fb} = F Y \quad (1.2)$$

which is linear but depends on the frequency of the signal. When the feedback is connected, all the system satisfies the equation

$$Y = A(X + FY) \quad (1.3)$$

In some conditions it is possible that this equation gives $Y \neq 0$ even for a vanishing input signal. The loop of Fig. 2 and the Eqs. (1.1-3) contain the essential features of a self-sustained oscillator determining its own amplitude self-consistently. In the following we will see that this is indeed the case of FEL.

2. THE FREQUENCY SELECTION

As already remarked the undulator provides an intense periodic magnetic field which induces the necessary transverse momentum allowing the coupling of the e-beam to a copropagating TE wave. We will not discuss the technological aspects of the UM and only recall that the magnet period λ_u is of the order of few centimeters, the on axis field B_0 is few kG and the length of the undulator $L_u = N\lambda_u$ (where N is the number of periods) is of the order of meters. For ultrarelativistic electrons the undulator can be treated as a radiation field with a wavelength twice the undulator period and with a photon density

$$\bar{n}_u = \frac{a}{4} \frac{K^2}{\lambda_u r_0^2} \quad (2.1)$$

where a and r_0 are the fine structure constant and the electron classical radius respectively furthermore^(*)

$$K = \frac{e B_0 \lambda_u}{2\pi m_0 c^2} \quad (2.2)$$

is the undulator parameter. For typical parameters ($K=1$, $\lambda_u=5$ cm) the photon density associated to the undulator is 10^{52} photons/cm³. Within this context the process of radiation emission by electrons moving in an UM can be viewed as a Compton Scattering. The wave-length of the radiation emitted in the forward direction is therefore given by

(*) In practical units we have

$$K \approx \frac{B_0 [\text{kG}] \lambda_u [\text{cm}]}{10.7}$$

$$\lambda = \frac{\lambda_u}{2\gamma^2} (1+K^2) \quad (2.3)$$

where γ is the electron relativistic factor and $(1+K^2)$ is the intensity dependent shift predicted by Brown and Kibble.³ The interesting aspect of Eq. (2.3) is that the emission wave-length can be tuned over a wide range just varying the electron energy. This is the frequency selection of FEL and we have discussed the mechanism underlying the spontaneous emission process. As we already pointed out in the introduction the amplification process takes place when together with the electrons an e.m. field with a wave-length nearly resonant with (2.3) is copropagating. The analysis of the amplification process can be advantageously carried out in a frame of reference where the e.m. field and the undulator field are seen by the electrons as counterpropagating waves with the same frequency. The velocity v^* of this frame can be chosen according to the above definition

$$2\lambda_L \gamma^* = \frac{\lambda_u}{\gamma^*}, \quad v^* = c \left(1 - \frac{2\lambda_L}{\lambda_u} \right)^{1/2} \quad (2.4)$$

where $\lambda_L \approx (\lambda_u/2\gamma^2)(1+K^2)$ is the wave-length of the field copropagating with the electrons. We assume that both L and u fields are quantized and helically polarized. The FEL process can be therefore reduced to the non relativistic dynamics of an electron moving in the field generated by two counterpropagating e.m. waves.

3. THE GAIN PROCESS

The possibility of treating the undulator magnetic field as a radiation field allows one to visualize the FEL process, when laser field is copropagating with the electron through the undulator, as a stimulated Compton Scattering. The analogy is further supported by the form of the interaction term in the Hamiltonian, as reported below.

As already remarked the FEL interaction is conveniently treated in a frame where the electron is moving non-relativistically, thus greatly simplifying the mathematical details of the analysis. Furthermore, the equivalence of all the frames connected with a Galilean transformation allows to choose a reference frame, where the laser and undulator fields appear as oppositely travelling waves with the same frequency. It is worth stressing that such a choice is only a matter of convenience and may be easily relaxed as for instance in the case of the multimode analysis.¹ Within the context of a quantum-mechanical approach to the problem, the Hamiltonian relevant to the coupled electron-fields system can be immediately written down as

$$\hat{H} = \frac{1}{2m} \left(\mathbf{p} - \frac{e}{c} \mathbf{A} \right)^2 + \hbar\omega \left(\hat{a}_L^\dagger \hat{a}_L + \frac{1}{2} \right) + \hbar\omega \left(\hat{a}_u^\dagger \hat{a}_u + \frac{1}{2} \right) \quad (3.1)$$

The first term in the above expression accounts for the kinetic energy of the electron and for the electron-fields interaction, $(\mathbf{p} - e/c \mathbf{A})$ being the generalized momentum of the electron in the presence of the vector potential $\mathbf{A} = \mathbf{A}_L + \mathbf{A}_u$, due to the laser and undulator fields, identified with the labels L and U respectively. The other two terms represent the free-field energy, \hat{a} and \hat{a}^\dagger being the annihilation and creation operators with the well-known commutation rules:

$$[\hat{a}_\alpha, \hat{a}_\beta^\dagger] = \delta_{\alpha\beta} \quad [\hat{a}_\alpha, \hat{a}_\beta] = [\hat{a}_\alpha^\dagger, \hat{a}_\beta^\dagger] = 0 \quad \alpha, \beta = L, 0 \quad (3.2)$$

Furthermore, according to the previous discussion, the laser and undulator fields are assumed to have the same frequency ($\omega = kc$) and opposite wave vectors ($\mathbf{k}_L = -\mathbf{k}_U$).

Taking the explicit expression of the vector potentials A_L and A_U in the Lorentz gauge and in the assumption of circularly polarized fields, the Hamiltonian (3.1) specializes into^{1*}

$$\hat{H} = \frac{p^2}{2m} + \hbar\omega\left(\hat{a}_u^\dagger \hat{a}_u + \frac{1}{2}\right) + \hbar\omega\left(\hat{a}_L^\dagger \hat{a}_L + \frac{1}{2}\right) + \hbar\Omega\left(\hat{a}_L^\dagger \hat{a}_L e^{-2ikz} + \hat{a}_u^\dagger \hat{a}_L e^{-2ikz}\right) \quad (3.3)$$

where the coupling constant Ω is given by

$$\Omega = \frac{2\pi r_0 c^2}{\omega V} \quad (V = \text{interaction volume}). \quad (3.4)$$

The first three terms in the Hamiltonian (3.3) represent the energy of the electron-fields system in the absence of interaction, the last one describes the dynamics of the interaction, which according to the present model of the FEL process as a stimulated scattering, gives rise to a forward and backward scattering corresponding to the creation of a laser photon, the destruction of a undulator photon with the consequent loss of $2\hbar k$ of electron momentum, and to the destruction of a laser photon, the creation of a undulator photon with the consequent gain of $2\hbar k$ of electron momentum.

The evolution of the system is then governed by the Schrödinger equation for the wave function $\psi(t)$, or equivalent by the Heisenberg equation for the electron and fields operators, appropriately defined. From the Hamiltonian (3.3) two rules of conservation can be derived namely

$$\begin{aligned} n_L + n_u &= \text{const} \\ p + \hbar k(n_L - n_u) &= \text{const} \end{aligned} \quad (3.5)$$

The first of Eqs. (3.5) states the conservation of the total number of photons (laser+undulator) the second establishes that also the total linear momentum (electron+fields) is a constant of motion. The FEL process is therefore vividly understood: the *undulator photons* are transferred to the laser mode and the necessary momentum is provided by the electron. The above rules of conservation allow a further simplification, infact the quantum states on which the Hamiltonian (3.3) acts can be characterized by a single integer specifying the number of photons exchanged during the interaction, namely

$$|\psi\rangle = \exp[i\phi(t)] \sum_{\ell=-n_L}^{n_u} C_\ell(t) |\ell\rangle \quad (3.6)$$

where n_L° , n_u° are the initial number of photons in the laser and undulator modes respectively, $C_\ell(t)$ are the amplitude probability that in the process ℓ photons can be exchanged and ϕ is an unessential phase. The Schrödinger equation yields for C_ℓ the following differential finite difference equation

* Let us notice that the term $p \cdot A$ in (3.1) vanishes, since A is transverse and p is assumed to be directed along the z -axis

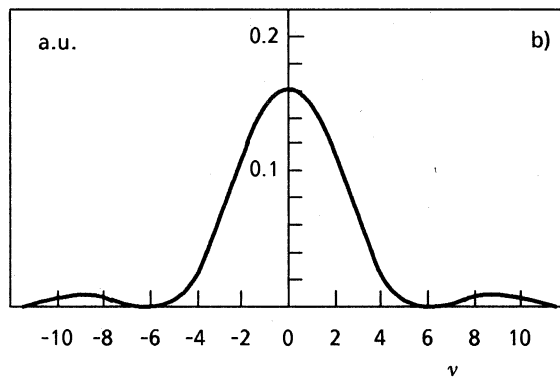
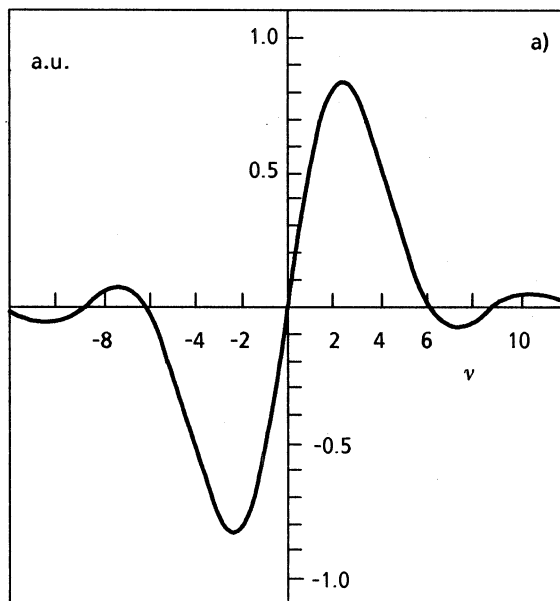


Fig. 3. a) Small-signal gain. b) Spontaneous spectrum

$$i \dot{C}_\ell = -(\nu - \varepsilon \ell) \ell C_\ell + \rho \left(\sqrt{n_L^\circ + \ell + 1} C_{\ell+1} + \sqrt{n_\ell^\circ + \ell} C_{\ell-1} \right) \quad (3.7)$$

where the prime means derivation with respect to the dimensionless time $\tau = t/\Delta t$ (Δt being the interaction time) and

$$\nu = 2\omega\Delta t \frac{P_0}{m c}, \quad \varepsilon = \frac{2\hbar k^2 \Delta t}{m}, \quad \rho = g \sqrt{n_u^\circ} \Delta t \quad (3.8)$$

in deriving (3.7) we have assumed $n_u^\circ \gg \ell$. The equation governing the evolution of the C_ℓ is strongly reminiscent of the equation defining the amplitude probability for a n-level molecular system coupled by a laser field.² The parameter ν plays the role of the detuning and ε (in this case linked to the electron recoil) plays the role of the anharmonic term. Methods have been developed to deal with an entire class of Eqs. of the type (3.7)⁴ (named Raman-Nath type equations after the work of these authors on the light scattering by ultrasounds).⁵ In this note we restrict ourselves to the solution in a very limiting but interesting case, namely the so called small signal regime i.e. when

$$\rho \sqrt{n_L^0} \ll 1 \quad (3.9)$$

The above quantity represents, within the framework of our analogy with multiphoton transitions, the Rabi frequency so that the condition (3.9) is a kind of weak coupling limit, which allows to treat Eq. (3.7) perturbatively, i.e.

$$C_\ell \sim C_\ell^0 + \rho C_\ell^1 \quad (3.10)$$

$$C_\ell^0(0) = \delta_{\ell,0}, \quad C_\ell^1(0) = 0$$

Inserting (3.10) in (3.7) we get

$$C_0^0(t) = 1$$

$$C_1^1(v) = \rho \sqrt{n_L^0 + 1} \frac{1 - \exp(i(v-\varepsilon)t)}{v-\varepsilon} \quad (3.11)$$

$$C_{-1}^1(v) = -\rho \sqrt{n_L^0} \frac{1 - \exp(i(v+\varepsilon)t)}{v+\varepsilon}$$

It is worth stressing that the condition (3.9) allows that in the process only one photon is emitted or absorbed.

Furthermore it is also evident from (3.11) that the electron losses or gains an amount of energy ($\hbar\varepsilon/\Delta t$) according to whether the photon is absorbed or emitted. The average number of emitted photons is therefore given by

$$\Delta n_L = |C_1^1|^2 - |C_{-1}^1|^2 = -\rho^2 \left[-n_L^0 \left(\frac{\sin(v+\varepsilon/2)}{(v+\varepsilon/2)} \right)^2 + (n_L^0 + 1) \left(\frac{\sin(v-\varepsilon/2)}{(v-\varepsilon/2)} \right)^2 \right] \quad (3.12)$$

Expanding up to the lowest order in ε we finally get

$$\Delta n_L \sim \rho^2 \left(\frac{\sin v/2}{v/2} \right)^2 - \rho^2 (2n_L^0 + 1) \varepsilon \frac{\partial}{\partial v} \left(\frac{\sin(v/2)}{v/2} \right)^2 \quad (3.13)$$

We can now understand Eq. (3.13) in terms of the conceptual scheme of the introductory remarks. The output signal Δn_L is a function of the input signal n_L^0 and even when $n_L^0 = 0$ we have still an output

$$\Delta n_L = \rho^2 \left(\frac{\sin v/2}{v/2} \right)^2 - \rho^2 \varepsilon \frac{\partial}{\partial v} \left(\frac{\sin(v/2)}{v/2} \right)^2 \quad (3.14)$$

The first term is the classical spontaneous emission the second term is the quantum spontaneous emission or better the gain due to the vacuum field fluctuations. The part containing n_L^0 will be referred as stimulated emission or gain term as in conventional lasers. The feedback mechanism can be easily introduced just iterating our procedure. We assume that the process occurs in an optical cavity and therefore after each round trip the number of emitted photons depends on those emitted at the previous passage of the e-beam in the undulator, namely (n_c being the number of round trips)

$$n_L(v, n_c) - n_L(v, n_c) = N_e \rho^2 \left[\left(\frac{\sin v/2}{v/2} \right)^2 - \varepsilon \frac{\partial}{\partial v} \left(\frac{\sin (v/2)}{v/2} \right)^2 - 2\varepsilon n_L(v, n_c) \frac{\partial}{\partial v} \left(\frac{\sin (v/2)}{v/2} \right)^2 \right] \quad (3.15)$$

where N_e is the number of electrons in the beam. The feedback depends on the detuning v and we will see below that this automatically fixes the lasing frequency. In Fig. 3 we report the classical spontaneous emission function and the gain function vs v , and it is evident that the positive gain bandwidth is $\Delta v \sim 2n$. Equation (3.15) can be transformed into a differential equation

$$\frac{d}{dT_c} n_L(v, n_c) = N_e \{ F_{SP}(v) - n_L(v, n_c) G(v) \} \quad (3.16)$$

$$F_{SP}^{(v)} = \rho^2 \left(\frac{\sin (v/2)}{v/2} \right)^2 - \rho^2 \varepsilon \frac{\partial}{\partial v} \left(\frac{\sin (v/2)}{v/2} \right)^2$$

$$G(v) = -2\varepsilon \rho^2 \left(\frac{\sin (v/2)}{v/2} \right)^2$$

and its solution can be immediately obtained*

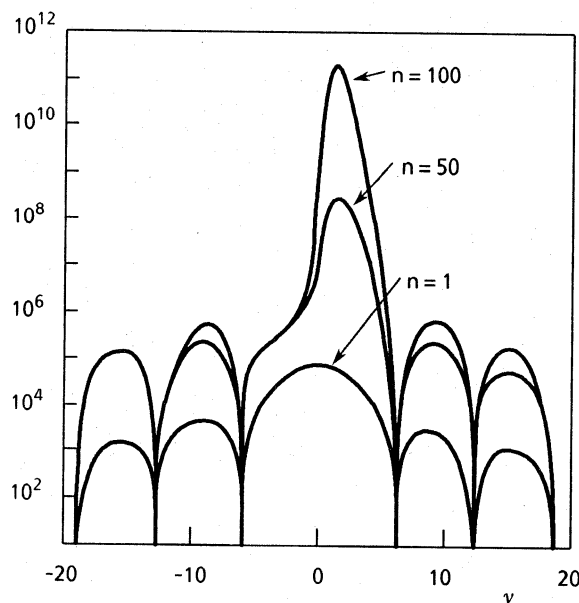


Fig. 4. Laser spectrum vs v ($\lambda_u = 3$ cm; $k = 0.3$; $N_e/V = 10^{11}$ cm $^{-3}$, $N = 50$; $\gamma = 50$)

* In deriving (3.17) we have neglected the term $\varepsilon (\partial/\partial v) [(\sin v/2)/(v/2)]^2$ which is always very small.

$$n_L(v, n_c) = \langle n_L \rangle_{\text{th.}} \frac{\left(\frac{\sin(v/2)}{v/2}\right)^2}{\frac{\partial}{\partial v} \left(\frac{\sin(v/2)}{v/2}\right)^2} \left\{ 1 - e^{-2n_c N_e \epsilon \rho^2 \frac{\partial}{\partial v} \left(\frac{\sin(v/2)}{v/2}\right)^2} \right\} \quad (3.17)$$

where $\langle n_L \rangle_{\text{th.}} = 1/2\epsilon$ represents the threshold value of emitted photons for which the stimulated part of the emission becomes larger than the spontaneous part. The emitted spectrum vs v is shown in Fig. 4. With increasing n_c we see that the peak shifts from $v=0$ up to $v=2.6$ where the maximum of the stimulated emission is located.

The feedback therefore contributes to the frequency selection within the gain bandwidth and to the self determination of the output signal amplitude. We have not mentioned intrinsic saturation mechanisms which cannot be present in the linear analysis so far discussed. We notice that with increasing $\rho \sqrt{n_L}$ the number of emitted photons increases too. For large ℓ the anharmonic term affects more and more the detuning thus "pulling" the region of operation outside the positive gain bandwidth. The condition for the saturation threshold is therefore

$$\ell_s \approx \frac{2n}{\epsilon} \quad (3.18)$$

from which we can get a very interesting conclusion. Using the explicit definition of ϵ we find that the saturation energy ($I_s' = \hbar \ell_s \omega$) is given by

$$I_s' \approx m c^2 \frac{\lambda'}{L_u} \quad (3.19)$$

where λ' and L_u' are the laser wavelength and undulator length in the moving frame. The above equation does not contain \hbar and therefore the saturation process is purely classical. Going back to the laboratory frame we find

$$I_s \approx m \gamma c^2 \frac{1}{2N} \quad (3.20)$$

i.e. a fraction $1/2N$ of the total electron energy is transformed in laser energy. This fraction is the FEL efficiency.

The simple picture of the FEL we have developed has the merit of giving a rather immediate an insightful view to the process. The treatment is very simplified and important effects like those due to the structure of the electron beam have not been considered. The interested reader is addressed to Ref. 1 for a more complete analysis.

REFERENCES

1. G. Dattoli and A. Renieri, FEL Handbook, Vol. IV, Ed. by M.L. Stich and M.S. Bass (North Holland, Amsterdam) p. 1 (1985).
2. S. Stenholm, "Foundations of Laser Spectroscopy", Wiley, New York (1984).
3. L.S. Brown and T.W. Kibble, Phys. Rev. 133A (1964) 705.
4. G. Dattoli, J.C. Gallardo and A. Torre, J. Math. Phys., 27 (1986), 772.
5. C.W. Raman and N.S. Nath, Proc. Ind. Acad. Sci. 2 (1936), 406.

ELECTRON AND PHOTON COLLISIONS IN STRONG LASER FIELDS

R. Daniele*, G. Messina[^], F. Morales[§] and G. Ferrante[#]

* Istituto di Fisica, Palermo

[^] Facolta' di Ingegneria, Istituto del Biennio, Reggio Calabria

[§] Dipartimento di Energetica e Applicazioni di Fisica, Palermo

[#] Dipartimento di Fisica Teorica, Messina

1. Introduction

In application to gas and plasma physics, the characteristics of the involved elementary processes (transition rates, cross sections and so on) are frequently calculated within the simplest possible methods. It because of the complexity of the many-particle character of any gas and plasma physics problem. It applies as well to elementary processes of radiation-matter interaction such, for instance, as photoionization or stimulated bremsstrahlung, of interest in problems like gas breakdown or plasma heating.

In particular, to describe multiphoton ionization frequently lowest-order perturbation theory (LOPT) treatments are used, which yield cross-sections proportional to I^n , with I the field intensity and n the number of absorbed photons. Additionally, as a rule, to describe the laser field the ideal model of a single-mode (SM), purely coherent field is assumed. Loosely speaking, it amounts to say that the field fills all the space, and that its parameters have well-fixed values. Instead, it is now becoming well known that strong real lasers are noiser than they should be, and that for them the purely coherent field model is a rather poor representation.

Recent experiments on different elementary processes involving the interaction with strong laser fields^[1-3] have produced evidence of a highly nonperturbative character of the radiation-matter interaction, which is likely to affect significantly the occurrence of the related plasma processes (see Figs. 1 and 2).

Below we report on examples, worked out theoretically, showing that in strong field contexts the use of the LOPT treatments and/or SM models is generally not allowed. To this end, a theoretical approach is outlined, based on transitions between states embedded in the radiation field, which reproduces satisfactorily many of the perturbative features exhibited by the experiments. The approach is applied to: (a) study the modifications induced in the ordinary bremsstrahlung process by the presence of a strong laser field; (b) study the energy absorption rate by a classical plasma irradiated by a strong laser field. Both problems are studied using: (a) the fundamental model of a purely coherent field; and (b) the more realistic model of a multimode field with uncorrelated modes.

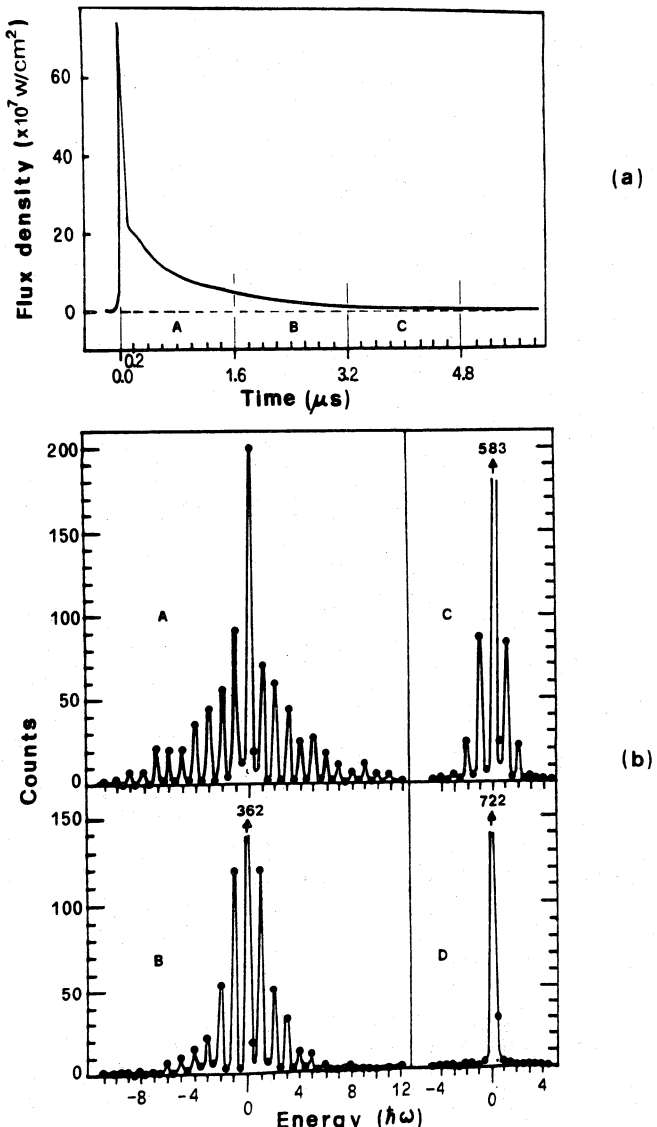


Fig. 1 - Multiphoton free-free transitions in e-Ar elastic scattering in the presence of a CO_2 laser ($\hbar\omega=0.117 \text{ eV}$).

a) Temporal shape of the pulse of the CO_2 laser used in the experiments.
 b) Energy gain-loss spectra (counts for 500 1.6 μs pulses plotted against energy in units of laser photons). Incident electron energy $\xi_i=9.923 \text{ eV}$; scattering angle $\theta=155^\circ$. Polarization vector \hat{e}_L parallel to the scattering plane.
 The spectra A, B and C show the number of scattered electrons (in 500 laser shots) as a function of decreasing flux density corresponding to the time interval A, B and C of the laser pulse shown in the upper part of the figure. Spectrum D shows the energy distribution without the laser. Dots are experimental points; full curves trace out the multiphoton processes approximately (from ref.1).

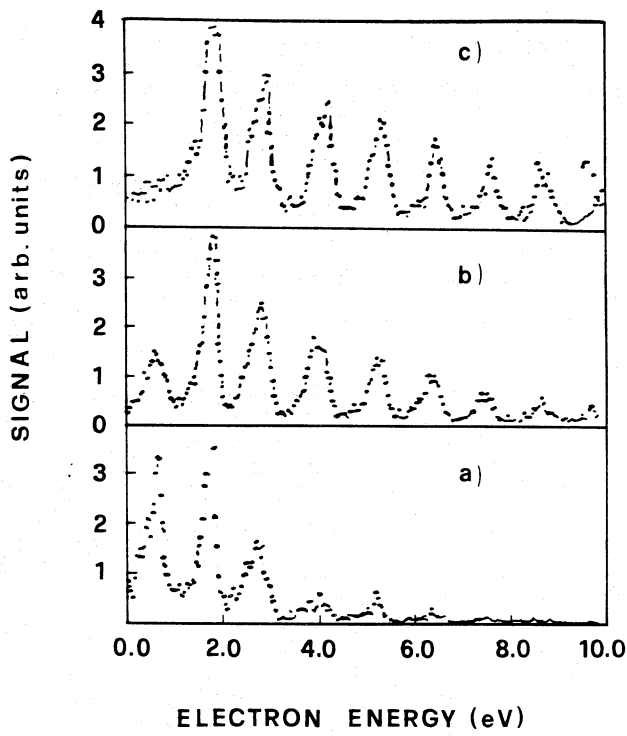


Fig. 2 - Typical electron spectra from multiphoton ionization. A linearly polarized Nd:Yag laser at 1064 nm with different pulse energies ϵ_0 ionises Xenon atoms at different pressures p . Spectrum a): $\epsilon_0 = 12 \text{ mJ}$; $p = 40 \text{ Pa}$. Spectrum b): $\epsilon_0 = 17 \text{ mJ}$; $p = 2.8 \text{ Pa}$. Spectrum c): $\epsilon_0 = 22 \text{ mJ}$; $p = 0.16 \text{ Pa}$. The estimated intensity is $\epsilon_0 (\text{mJ}) \times 2 \times 10^{12} \text{ W/cm}^2$ (From ref.3).

For the plasma heating problem, additionally, we consider the cases of a Maxwellian distribution for the electrons and of a directed, monoenergetic electron beam.

The reported results strongly depart from the predictions based on LOPT calculations.

2. Theory

a. Multiphoton Direct and Inverse Bremsstrahlung

The idea of using states embedded in the radiation field as unperturbed states is best illustrated for the fundamental case of charged particle scattering by a static potential in the presence of a strong laser. In the distant past and future the free particles are assumed to be in the radiation field; the static potential is taken as the perturbation responsible for the transition. During a single scattering act the particles may absorb or emit simultaneously an arbitrary number of laser photons (obviously, compatibly with conservation of energy)^[4]. Let

$$(1/2m)[(h/i)\nabla - (e/c)\mathbf{A}(t)]^2 \Psi(\mathbf{r},t) + V(r) \Psi(\mathbf{r},t) = i\hbar \dot{\Psi}(\mathbf{r},t) \quad (2.1)$$

be the Schrödinger equation for an electron in the presence of a radiation field, described by the vector potential $\mathbf{A}(t)$, and of a scattering, static potential $V(r)$. The radiation field is taken in the dipole approximation, which is sufficiently accurate for the kind of processes we will consider below. In Eq.(2.1) $V(r)$ is treated as a perturbation; thus we need to solve Eq.(2.1) with $V(r)=0$. The equation

$$(1/2m)[(h/i)\nabla - (e/c)\mathbf{A}(t)]^2 X(\mathbf{r},t) = i\hbar \dot{X}(\mathbf{r},t) \quad (2.2)$$

yields

$$X_{\mathbf{k}}(\mathbf{r},t) = \exp \left\{ ik \cdot \mathbf{r} - (ih/2m) \int^t [k^2 - (2e/hc) \mathbf{k} \cdot \mathbf{A}(\tau)] d\tau \right\} \times \\ \times \exp \left\{ -(i/h) \int^t (e^2/2mc^2) A^2(\tau) d\tau \right\}, \quad (2.3)$$

which are plane waves modulated by the field, and are known as Volkov waves. The waves $X_{\mathbf{k}}(\mathbf{r},t)$ enter the theory as unperturbed initial, intermediate and final states. An explicit expression of $X_{\mathbf{k}}$ is readily obtained taking the field linearly polarized within the single-mode model:

$$\mathbf{A}(t) = A_0 \cos(\omega t) \quad (2.4)$$

b. Scattering Theory Formalism

To derive the cross sections for the potential scattering in the presence of a laser field of a charged particle from the initial state \mathbf{k}_i to \mathbf{k}_f , our starting point is the exact S matrix

$$S_{fi} = (-i/\hbar)(X_f, V \Psi_i^\dagger) \quad (2.5)$$

where X_f is the final state Volkov wavefunction, Ψ_i is the exact wavefunction satisfying the complete Schrödinger equation (2.1) with causal boundary conditions, and the round brackets indicate both space and time integrations. Formally, we can write

$$\Psi_i^\dagger = X_i + G_V^\dagger V X_i, \quad (2.6)$$

where G^\dagger is the retarded full Green function (in the presence of both the static potential and the radiation field). G^\dagger is now expanded in powers of the scattering potential

$$G^\dagger = G_o^\dagger + G_o^\dagger V G_o^\dagger + G_o^\dagger V G_o^\dagger V G_o^\dagger + \dots \quad (2.7)$$

with

$$G_o^\dagger = G_o^\dagger(\mathbf{r},t; \mathbf{r}',t'; E_0) = (-i/\hbar) \Theta(t-t') \sum_m X_m(\mathbf{r},t) X_m^*(\mathbf{r}',t') \quad (2.8)$$

the retarded Green function in the presence of the radiation field only and $E_0 = \omega A_0/c$. Using (2.6)-(2.8) in (2.5) one has

$$S_{fi} = (-i/\hbar)[(X_f, V X_i) + (X_f, V G_o^\dagger V X_i) + \dots] = \sum_{\nu=1}^{\infty} S_{fi}^{(\nu)} \quad (2.9)$$

where

$$S_{fi}^{(1)} = (-i/\hbar)(X_f, V X_i) = (-i/\hbar) \int_{-\infty}^{\infty} dt \int d^3r X_f^*(\mathbf{r},t) V(r) X_i(\mathbf{r},t); \quad (2.10)$$

$$S_{fi}^{(2)} = (-i/\hbar)^2 \int_{-\infty}^{\infty} dt_1 \int_{-\infty}^{t_1} dt_2 \sum_m \int d^3r_1 \chi_f^*(\mathbf{r}_1, t_1) V(\mathbf{r}_1) \chi_m(\mathbf{r}_1, t_1) \times \\ \times \int d^3r_2 \chi_m^*(\mathbf{r}_2, t_2) V(\mathbf{r}_2) \chi_i(\mathbf{r}_2, t_2) \quad (2.11)$$

and so on. χ_a 's appearing in (2.9)-(2.11) are Volkov wavefunctions, and it is the new feature as compared with the conventional S matrix series of potential scattering. Expanding in series of Bessel functions the exponentials containing the periodic functions, the time integration required in (2.9) are easily carried out to give the S matrix expressed now as

$$S_{fi} = \sum_n^{\infty} \langle f | S_n | i \rangle \quad (2.12)$$

with

$$\langle f | S_n | i \rangle = (-2\pi i) \langle f | T_n | i \rangle \delta(\epsilon_f - \epsilon_i - n\hbar\omega) \quad (2.13)$$

the brackets $\langle \dots \rangle$ indicating now space integration only and $|a\rangle = \exp(i\mathbf{k}_a \cdot \mathbf{r})$. $\langle f | T_n | i \rangle$ may be considered the generalization of the T matrix to include the presence of the radiation field (however, in general, it is off the energy shell) and it is given by

$$\begin{aligned} \langle f | T_n | i \rangle = & \langle f | V(n) | i \rangle + \sum_m \sum_{n_1} \langle f | V(n-n_1) | m \rangle \langle m | V(n_1) | i \rangle \times \\ & \times [(\epsilon_i - \epsilon_m + n_1 \hbar\omega + i\eta)]^{-1} + \sum_{m,j} \sum_{n_1, n_2} \langle f | V(n-n_1-n_2) | j \rangle \times \\ & \times \langle j | V(n_2) | m \rangle [(\epsilon_i - \epsilon_j + (n_1 + n_2) \hbar\omega + i\eta)]^{-1} \times \\ & \times [\langle m | V(n_1) | i \rangle [(\epsilon_i - \epsilon_m + n_1 \hbar\omega + i\eta)]^{-1} + \dots] \end{aligned} \quad (2.14)$$

In the T matrix (2.14) the basic ingredient is the "compound" matrix element

$$\langle \beta | V(\mu) | \gamma \rangle = J_\mu(\lambda_{\beta\gamma}) \langle \beta | V | \gamma \rangle \quad (2.15)$$

formed: (i) by the Bessel function J_μ with argument

$$\lambda_{\beta\gamma} = \lambda_\beta - \lambda_\gamma = (e/m\omega^2) \mathbf{E}_\beta \cdot \mathbf{Q}_{\beta\gamma}; \quad (2.16)$$

$$\hbar\mathbf{Q}_{\beta\gamma} = \hbar(\mathbf{k}_\beta - \mathbf{k}_\gamma) \quad (2.17)$$

being the transferred momentum in going from state γ to state β ; and (ii) by

$$\langle \beta | V | \gamma \rangle = \int d^3r \exp(-i\mathbf{Q}_{\beta\gamma} \cdot \mathbf{r}) V(r) \quad (2.18)$$

the Fourier transform of the scattering potential.

From the S and T matrices the Fermi Golden Rule and the cross sections are obtained proceeding in the usual way. Without additional assumptions, however simple and manageable expressions are obtained only at the first order in the scattering potential. (Note, however, that the radiation field, through the Volkov waves, is included to all orders). For the First Born Approximation (FBA) one has the Fermi Golden Rule

$$P_{fi}^{FBA} = (2\pi/\hbar) \sum_n^{\infty} J_n^2 (\lambda_{fi}) |\langle f | V | i \rangle|^2 \rho[\epsilon_f(n)] \quad (2.19)$$

with

$$\rho[\epsilon_f(n)] = m(2\pi\hbar)^{-3} \frac{1}{2} k_f(n) d\Omega \quad (2.20)$$

the density of final scattering states;

$$\epsilon_f(n) = \epsilon_i + n\hbar\omega = \frac{1}{2} k_f^2(n)/2m \quad (2.21)$$

the final energy fixed by the energy conserving delta function; accordingly, the final state wavenumber is given by

$$k_f(n) = (1/\hbar)[2m(\epsilon_i + n\hbar\omega)]^{1/2} \quad (2.22)$$

For the FBA differential cross section we get

$$(d\sigma/d\Omega)_F^{\text{FBA}} = \sum_n J_n^2(\lambda_{fi}) [k_f(n)/k_i] (d\sigma(n)/d\Omega)^{\text{FBA}} \quad (2.23)$$

with

$$(d\sigma(n)/d\Omega)^{\text{FBA}} = (m/2\pi\hbar)^2 | \langle f | V | i \rangle |_n^2 \quad (2.24)$$

the field-free FBA differential cross section, but evaluated at the shifted energy $\epsilon_f(n)$ and momentum $\frac{1}{2}k_f(n)$, and because of it dependent on n . Recent experiments[1] have lent unambiguous support to cross sections having the structure of Eq.(2.23), (see Fig.s 1 and ref.5). Fig. 3 shows total cross sections calculated on the basis of Eq.(2.23), exhibiting an highly nonlinear behaviour, departing, for $n>1$, from LOPT calculations at relatively moderate intensities[6].

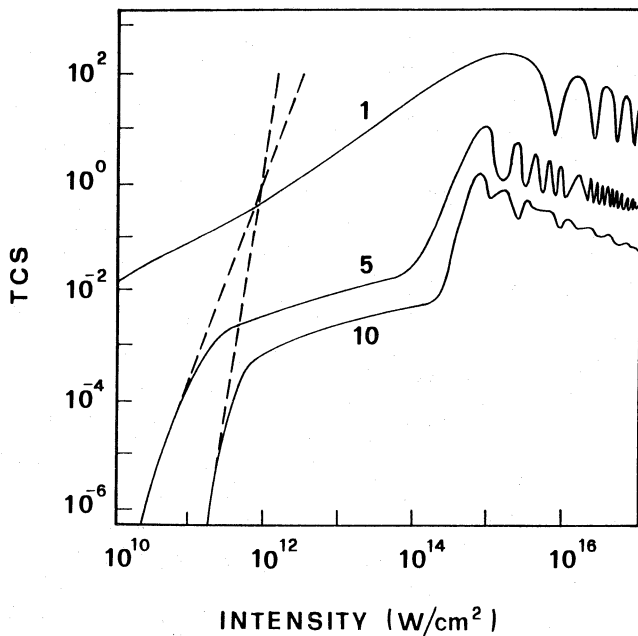


Fig. 3 - Total cross sections (TCS) (in πa_0^2 units) vs the field intensity (in W/cm^2) for one, five and then photons absorbed. The incident particle energy is 100 eV, the field polarization is parallel to the incoming particle momentum, and the scattering potential is Yukawa type, with unitary charge and screening radius $r_0=50 a_0$ (a_0 being the Bohr radius). Energy of the field photon $\hbar\omega_1=1.17$ eV. Dashed lines - LOPT limit (From ref.6).

c. Multichannel Multiphoton Ionization

In the last few years a lot of experiments have been performed of ionization of atoms by very strong lasers^[2]. One of the most peculiar features of the observations is that the atomic electrons go to the continuum absorbing from the laser different numbers of photons above the minimum number to be ionized, and that the photoelectron final energy distribution bears some similarity with the final energy distribution of electrons which have undergone multiphoton inverse bremsstrahlung (see, for instance, Fig.s 1 and 2). This feature should be not surprising, because, as schematically shown in Fig.4, in the scattering in the presence of lasers and in multiphoton ionization the second halves of the two processes are physically largely the same.

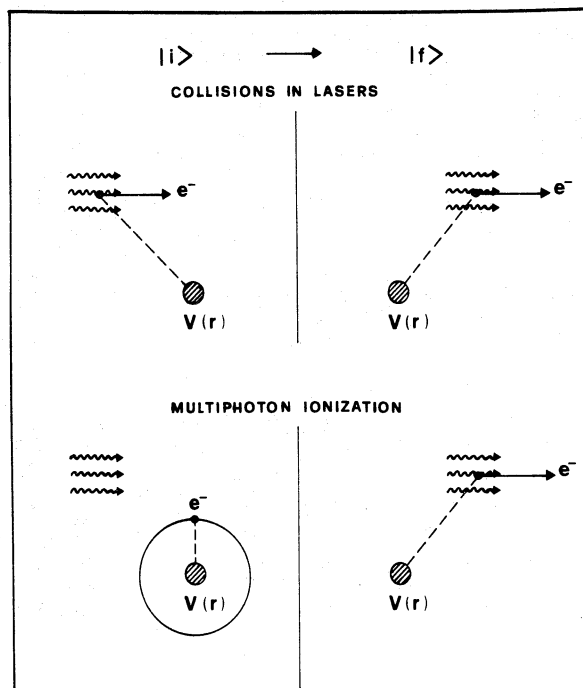


Fig. 4 - Picture suggesting differences and similarities between multiphoton free-free transitions and multiphoton bound-free transitions.

The remarked similarity suggests to try to construct for the multiphoton ionization theoretical treatments using, for the electrons in the continuum, states embedded in the radiation field. However, the frequently encountered physical circumstance that the electrons are ejected with low energies makes immediately necessary to include in the final state also the influence of the coulomb interaction with the residual ion. With it in mind, we write the exact S-matrix element of ionization of an hydrogen atom by a laser as

$$S_{fi} = (-i/\hbar) (\Psi_k^-, eE \cdot r \Phi_i^-) \quad (2.25)$$

where Ψ_k^- is the full interacting final state obeying the Schrödinger equation

$$[(p^2/2m) - (e^2/r) + eE(t) \cdot r] \Psi(r,t) = i\hbar \dot{\Psi}; \quad (2.26)$$

$E(t)$ is the electric field and Φ_i the initial state obeying the same Schrödinger equation as above without the $eE \cdot r$ term (we note that in the case of bound-free transitions, provided that the dipole approximation is used, is physically more transparent to use the gauge of the electric field, as we have done in Eq.s (2.25) and (2.26)). As no exact solution to Eq.(2.26) is known we use the ansatz[7]

$$\Psi = \Psi_k^- = \exp\{ie/\hbar c A(t) \cdot r\} \exp\left\{(-i/\hbar)[\epsilon_k + \int_0^t d\tau \lambda_k(\tau) + (e^2/2mc^2) \int_0^t d\tau A^2(\tau)]\right\} \Phi_k(r,t), \quad (2.27)$$

$$E(t) = (-1/c) \partial A(t) / \partial t \quad (2.27a)$$

in which $\lambda_k(\tau)$ and $\Phi_k(r,t)$ may be determined to different degrees of accuracy according to appropriate procedures.

When $\lambda_k = \lambda_k^V = (e/mc) A(t) \cdot k$; and $\Phi_k(r,t) = \exp\{ik \cdot r\}$, Eq. (2.27) goes over the Volkov wave seen above. In the present case instead the $\Phi_k(r,t)$ is demanded to asymptotically behave as the incoming Coulomb wavefunction in the absence of the radiation field $\Phi_k^-(r)$. Writing $\Phi_k(r,t)$ and λ_k as

$$\Phi_k(r,t) = \Phi_k^-(r) + \sum_{m=\pm 1} \phi_k^{(m)}(r) \exp\{imwt\} + \text{plus similar terms}$$

with $|m| > 1$ (2.28)

and

$$\lambda_k(t) = \lambda_k^V(t) + \lambda_k^{(1)} + \lambda_k^{(2)} + \dots \quad (2.29)$$

a systematic procedure may be devised[7] to calculate the corrections $\phi_k^{(m)}$ and $\lambda_k^{(m)}$ to Φ_k^- and λ_k^V . Here, however, we confine to the "minimal" wavefunction in which $\Phi_k(r,t) \approx \Phi_k^-(r)$ and $\lambda_k(t) \approx \lambda_k^V(t)$. It amounts to use in Eq.(2.24) a wavefunction formed by a coulomb wave times a field modulation factor identical to that appearing in the Volkov solution. Although not exact, such Volkov-Coulomb wavefunction represents a state in which both the radiation field and the coulomb interaction are included nonperturbatively, and it has been found to perform well in a number of cases[7].

3. A Model of a Multimode Laser Field

Now we try to improve the description of the laser field; such an improvement is especially required in the domain of very high intensities. Below it is done by means of a model of a multimode field with uncorrelated modes. There are good reasons to improve the laser description, and some of them may be stated as follows. First of all, in some cases the experiments have been performed with lasers operated in a multimode configuration. Secondly, averaging mechanisms are always present in any real experiment, due to the laser statistics, focussing, pulse-shape and -duration effects. As a consequence, during the elementary process different particles and/or atoms in the different points of the scattering or ionization volume and in different instants of time experience different values of the field intensity. Thus what is measured is a signal averaged over the many realizations of the field. To mimick to some extent the real physical situations some effective average should be included in any theoretical treatment. Below it is done through an average over the intensity fluctuations, which naturally arises in the multimode model to be described soon. It is to be remarked that the average over the intensity fluctuations is very effective and

may be considered to account to some extent for other averaging mechanisms as well.

The N-mode classical laser field is written as

$$\mathbf{A}(t) = \hat{\epsilon} \sum_{i=1}^N (cE_i/\omega_0) \cos(\omega_0 t + \phi_i) \quad (3.1)$$

where for simplicity we have assumed that all the frequencies of the N modes are approximately equal to ω_0 . Equation (3.1) is then rewritten as

$$\mathbf{A}(t) = \hat{\epsilon} (cE/\omega_0) \cos(\omega_0 t + \phi) \quad (3.2)$$

with

$$E_o^2 = \sum_{i=1}^N E_i^2 + 2 \sum_{i>j} E_i E_j \cos(\phi_i - \phi_j) \quad (3.2a)$$

and

$$\tan \phi = \left[\sum_{i=1}^N E_i \sin(\phi_i) \right] \left[\sum_{i=1}^N E_i \cos \phi_i \right]^{-1} \quad (3.2b)$$

Now the derivation, say, of the differential cross sections of scattering or ionization may be carried out as for the single-mode case. The differential cross sections will depend on the field amplitudes and phases E_i and ϕ_i through E_o , Eq.(3.2a):

$$d\sigma(E_o)/d\Omega = d\sigma(E_i, \phi_i)/d\Omega \quad (3.3)$$

and the appropriate average over the realizations of E_i and ϕ_i is required. To this end, we adopt the following assumptions: (1) the total power of the laser is constrained to be fixed from pulse to pulse, that is

$$\epsilon_o^2 = \sum_{i=1}^N E_i^2$$

(2) the phases are statistically independent and have a random distribution within the interval $[-\pi, \pi]$; (3) the amplitudes E_i have a Gaussian distribution with dispersion $a^{-1/2}$. Accordingly, the following average is required

$$\begin{aligned} \langle d\sigma(E_o)/d\Omega \rangle &= C_N \int \dots \int E_1 \dots E_N dE_1 \dots dE_N d\phi_1 \dots d\phi_N \times \\ &\times \delta\left(\sum_{i=1}^N E_i^2 - \epsilon_o^2\right) \exp\left\{-a \sum_{i=1}^N E_i^2\right\} [d\sigma(E_o)/d\Omega] \end{aligned} \quad (3.4)$$

which is rewritten as an average over a distribution function of the field intensity

$$\langle d\sigma/d\Omega \rangle = \int_0^\infty d\xi [d\sigma(\sqrt{\xi})/d\Omega] P_N(\xi) \quad (3.5)$$

where

$$d\sigma(E_o)/d\Omega = \int_0^\infty d\xi \delta(\xi - E_o^2) [d\sigma(\sqrt{\xi})/d\Omega] \quad (3.6)$$

and

$$\begin{aligned} P_N(\xi) &= C_N \delta(\xi - E_o^2) \int \dots \int E_1 \dots E_N dE_1 \dots dE_N d\phi_1 \dots d\phi_N \times \\ &\times \delta\left(\sum_{i=1}^N E_i^2 - \epsilon_o^2\right) \exp\left\{-a \sum_{i=1}^N E_i^2\right\}. \end{aligned} \quad (3.7)$$

The distribution function $P_N(\xi)$ must fulfil the normalization condition

$$\int_0^\infty d\xi \quad P_N(\xi) = 1,$$

which allows the determination of the constant C_N . Evaluation of $P_N(\xi)$ [8-9] gives

$$P_N(\xi) = (1/\epsilon_0^2)(N-1/N) [1-\xi/N\epsilon_0^2]^{N-2} \Theta(1-\xi/N\epsilon_0^2) \quad (3.8)$$

where $\Theta(x)=1$ if $x>0$ and $\Theta(x)=0$ if $x<0$.

When the number of modes is allowed to become very large, the so-called chaotic field limit is approached and the intensity distribution function becomes

$$\lim_{N \rightarrow \infty} P_N(\xi) = \epsilon_0^{-2} \exp\{-\xi/\epsilon_0^2\} \quad (3.9)$$

Below, as a rule, this limiting case will be used in conjunction with Eq.(3.5). In Fig.s 5 and 6 are reported calculations based on the use of eq.(3.9) and (3.5). In Fig. 5 is shown the total cross section vs intensity for a scattering event in which $n=4$ photons are absorbed, while in Fig. 6 are shown the total ionization rates of the hydrogen atom for the first 5 ionization channels. The calculations of the rates are based on the theory of Section 2c and on the use of the Volkov-Coulomb wavefunctions [10].

Fig. 7 showing instead experimental rates [11], is meant as a qualitative comparison, emphasizing the nonlinear behaviour and the saturation (and eventually the slow decrease) occurring at high intensities, as predicted

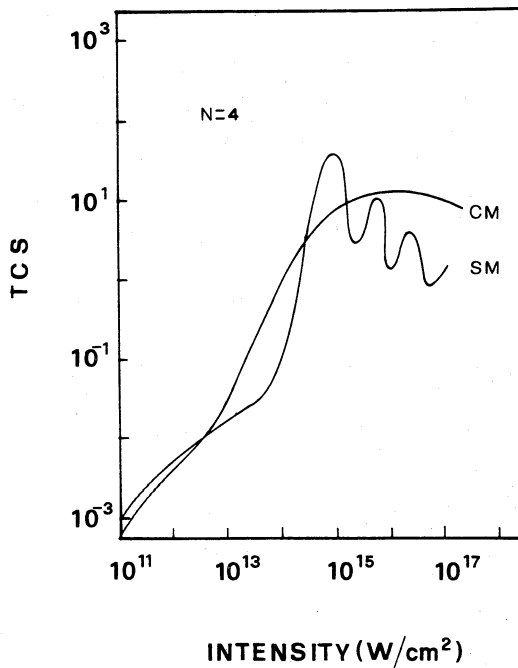


Fig. 5 - Total cross sections (TCS) (in πa_0^2 units) vs the field intensity (in W/cm^2) for 4 photon absorbed. SM-curve: single-mode field; CM-curve: chaotic field. Caption as to Fig.3.

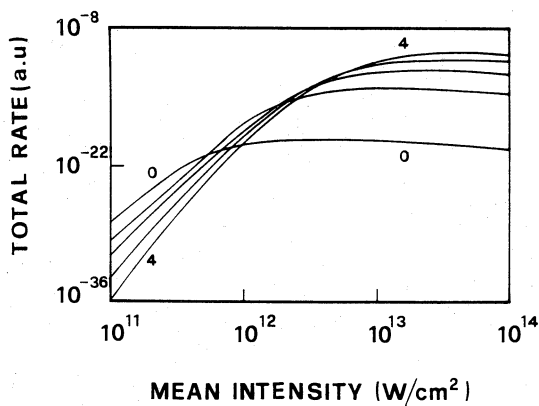


Fig. 6 - Total ionization rates (in atomic units) for the first 5 channels of ground state hydrogen atoms vs the mean intensity of a chaotic field (in W/cm^2). The numbers on the curves denote the photons in excess to the minimum required to ionize the atom. Field polarization: linear. Field wavelength $\lambda=1064 \text{ nm}$ (From ref.10)

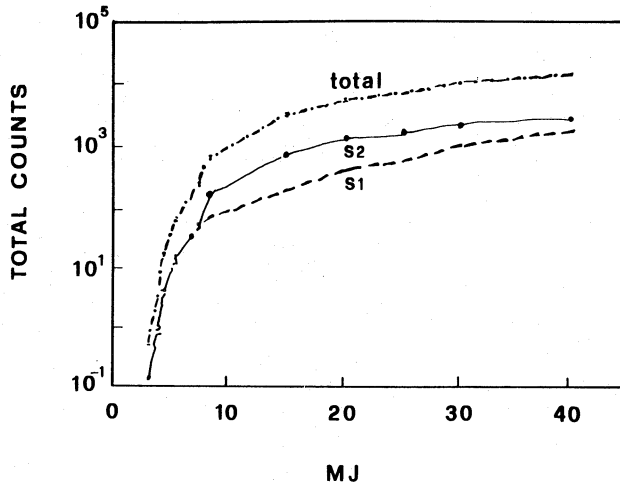


Fig. 7 - Electron signal vs 1064 nm laser energy in the peaks of the two first Xenon ionization channels S1 and S2 and total electron signal. At low energies the electron signal scales as $\sim I^{1.3}$, and the saturation intensity is $\sim 10^{13} \text{ W}/\text{cm}^2$. Field polarization: linear. (From ref.11).

by the theory. We observe that: i) the reported behaviour of cross sections and rates vs intensities is well out of reach of any LOPT calculations; ii) this behaviour for realistic laser models is rather smooth and could be profitably fitted to be included in more realistic modelling of many-particle processes.

4. Bremsstrahlung at ω_1 Stimulated by a Strong Laser Field at ω_2

a. Basic Cross Sections

Now we present a nonrelativistic treatment of emission of a bremsstrahlung photon of energy $\hbar\omega_1$ in the presence of a strong laser field of frequency ω_2 . The treatment is first-order in the scattering potential $V(r)$ (Fig. 8).

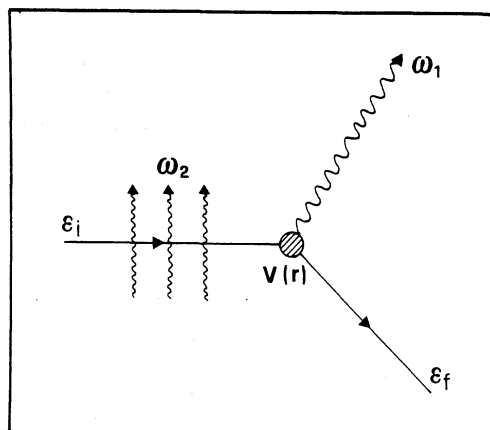


Fig. 8 - Bremsstrahlung at ω_1 stimulated by a strong laser field at ω_2

First we consider a more general problem; namely we consider the case of an electron being scattered by the potential $V(r)$ in the presence of two strong radiation fields. As in Section 2, as unperturbed initial and final states we take Volkov waves embedded in two radiation fields

$$A(t) = A_1(t) + A_2(t) = A_1 \cos(\omega_1 t + \phi_1) + A_2 \cos(\omega_2 t + \phi_2) \quad (4.1)$$

Following the procedure of Section 2, the differential cross section, averaged over the unobservable phases ϕ_1 and ϕ_2 is given by [12]

$$(d\sigma/d\Omega) = (m/2\pi\hbar)^2 \sum_{n,j} J_j^2(\lambda_1) J_n^2(\lambda_2) [k_f/k_i] |\langle f | V | i \rangle|_j^2 \quad (4.2)$$

where the electron final energy is

$$\epsilon_f(n,j) = \epsilon_i + j\hbar\omega_1 + n\hbar\omega_2 \quad (4.3)$$

the matrix element $\langle f | V | i \rangle$ has the structure of Eq. (2.18) and $\lambda_{1,2}$ are

defined by Eq.(2.16) for the ω_1 - and ω_2 -field respectively. The pertinent cross section of stimulated bremsstrahlung is now obtained from Eq.(4.2) assuming that the ω_1 -field is weak: we need to retain only the $j=\pm 1$ terms in the sum over j ; additionally of the left Bessel functions $J_{\pm 1}(\lambda_1)$ we take the first term of the small-argument expansion

$$J_j(\lambda_1) \approx (\lambda_1/2)^{|j|} \{1/\Gamma(|j|+1)\} \quad (j=\pm 1) \quad (4.4)$$

In conclusion, the differential cross section of emission or absorption of $\hbar\omega_1$ photon of a weak field in the presence of a single mode ω_2 -strong field is found as

$$(d\sigma/d\Omega)^{\pm 1} = \sum_n (d\sigma/d\Omega)_n^{\pm 1} = (m/2\pi\hbar^2)^2 \sum_n [k_f/k_i] (e^2 E_1^2 / 4m^2 \omega_1^4) \times \\ \times (\hat{e}_1 \cdot Q_{fi})^2 J_n^2(\lambda_2) | \langle f | V | i \rangle |^2 \quad (4.5)$$

If the strong spectator field is operated in a multimode configuration, then Eq.(4.5) must be averaged over P_N as given by Eq.s (3.8) or (3.9).

b. Two Limiting Cases

It is of interest to show that our cross section reduces, in the due limits, to: i) single-photon spontaneous bremsstrahlung cross section, calculated within second order perturbative treatments[13] ; and ii) double atomic-field bremsstrahlung, calculated within third-order perturbative treatments[14]. For the first case, we need to remove any information concerning the strong field, putting $\lambda_2=0$, and account for the density of final ω_1 -photon states. This is done in our treatment with the identification

$$E_1^2/8\pi = (\hbar\omega_1) dN^F = (\hbar\omega_1^3/8\pi^3 c^3) \int \int d\omega_1 d\Omega_1 \quad (4.6)$$

For the Coulomb potential $V(r)=Ze^2/r$

$$\langle f | V | i \rangle = 4\pi Ze^2 / Q_{fi}^2 \quad (4.7)$$

Using (4.6), (4.7), $\lambda_2=0$ and $j=-1$, Eq.(4.5) yields

$$(d^3\sigma/d\omega_1 d\Omega_1 d\Omega) = [(\alpha Z)^2 \alpha/(\pi^2 \omega_1)] (k_f/k_i) [(\hat{e}_1 \cdot Q_{fi})^2 / Q_{fi}^4] \quad (4.8)$$

with $\epsilon_f = \epsilon_i - \hbar\omega_1$ and α the fine structure constant $\alpha=(e^2/\hbar c)$. Eq. (4.8) is exactly the expression quoted in ref. 13.

For the second limiting case, we must treat $J_j^2(\lambda_1)$ and $J_n^2(\lambda_2)$ in the same way, taking the weak field limit of $J_{-1}^2(\lambda_1)$ and $J_{-1}^2(\lambda_2)$ and multiplying Eq.(4.6) by the density of final states of the photon $\hbar\omega_2$. As a result we obtain

$$(d^5\sigma/d\omega_1 d\omega_2 d\Omega_1 d\Omega_2 d\Omega) = (Za^3 a_0 / 2\pi^2)^2 (k_f/k_i) (1/\omega_1 \omega_2 Q_{fi}^4) \times \\ \times (\hat{e}_1 \cdot Q_{fi})^2 (\hat{e}_2 \cdot Q_{fi})^2 \quad (4.9)$$

a_0 being the Bohr radius. Eq. (4.9) corresponds to eq.(4) of ref. 14 written in Z-scaled atomic units.

c. Calculations

Using Eq.s (4.5), (3.9) and (3.5) calculations have been performed

of several quantities of interest[12,15] and a sample of them is reported in Fig.s 9 and 10. Due to the rather large number of independent physical parameters, as a rule, the calculations are restricted to a "collinear" geometry in which the linear polarizations of the two fields are parallel to the incoming wavevector: $\hat{e}_1 \parallel \hat{e}_2 \parallel k_1$. Besides being in a completely nonlinear behaviour regime, the most peculiar features exhibited by the calculations may be summarized as follows.

i) The spectator strong laser field makes practically equal the processes of emission and absorption of a weak field photon $\hbar\omega_1$, which otherwise would have been rather different; ii) Emission or absorption of a weak field photon $\hbar\omega_1$, is generally enhanced increasing the intensity up to some intensity domain, in which the two processes becomes equal and start to decrease. In the latter case, an intensity domain is entered in which the electrons acquire high oscillatory velocities with an ensuing decrease of the interaction with the scattering potential; when the scattering potential is practically switched off, the physical processes we are interested in becomes highly improbable, as show by Fig. 10.

5. Heating of a Plasma Via Multiphoton Bremsstrahlung

a. Preliminary considerations

It is well known that one of the methods used in heating a plasma to high temperatures is the application of electromagnetic radiation. In particular, in the first stage of this process, when collective instabilities have not yet developed, the main mechanism of heating is inverse bremsstrahlung, where electrons absorb energy from the e.m. field when they collide with ions. The physical quantity of interest is the energy absorption rate $d\varepsilon/dt$, i.e. the energy absorbed per unit volume and unit time, and it may be calculated either by classical or quantum mechanical methods. In the classical method the Vlasov equation is used to calculate the induced current and then the resulting absorbed energy. The electrons are generally taken to have a Maxwellian velocity distribution, while the ions are assumed to be at rest and randomly distributed. In the quantum mechanical method, usually one first calculates the transition probability for the elementary process of electron-ion collision in the presence of a radiation field allowing for photon exchanges, and then takes an appropriate statistical average over all the electron momenta. This kind of problems has originally much contributed to start research activity in field assisted particle-atom collisions, which afterwards has developed in its own right. Below, we present a treatment to calculate energy absorption rate within the quantum method. In particular, working in the occupation number formalism, the two steps (calculations of the transition probability and statistical average) are unified, and a more rigorous and elegant treatment results. For low field intensities the energy absorption rate has been calculated by several authors; the main process is one-photon absorption, and the result is given by a simple analytical formula. The treatment outlined below is for a field of arbitrary intensity (within, however, the dipole approximation and nonrelativistic velocities). The available literature on this topic may be traced through refs 16-21.

b. Formalism

Let

$$\hat{H}(t) = \hat{H}_o(t) + \hat{H}_i(t) \quad (5.1)$$

be the total Hamiltonian of a quantized Schrödinger free-electron field

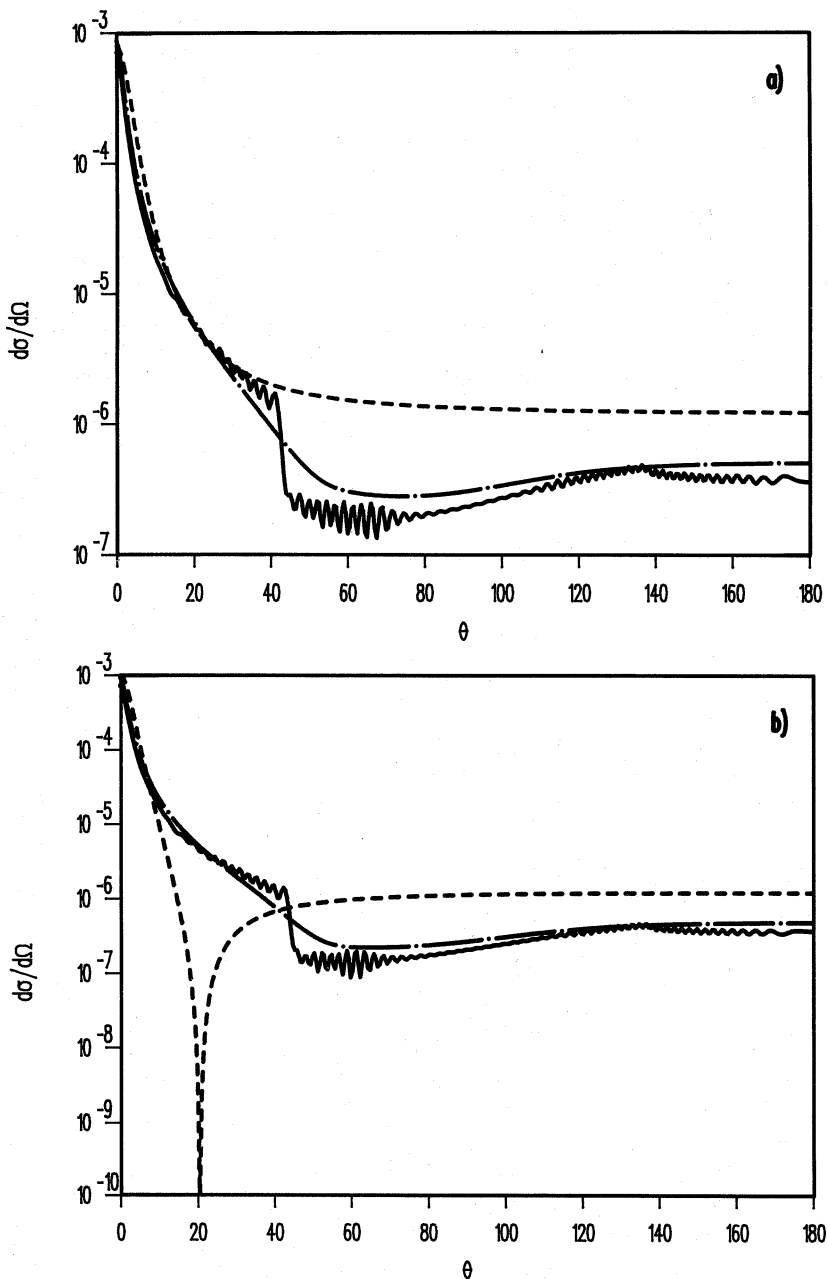


Fig. 9 - Differential cross sections (DCS) (in units of $\pi a_0^2 \text{ ster}^{-1}$) of stimulated bremsstrahlung vs the scattering angle θ (in degrees). a) refers to the emission of a weak-field photon $\hbar\omega_1=3.6 \text{ eV}$; b) to the absorption of a photon of the same energy. Strong-field photon energy $\hbar\omega_2=1.8 \text{ eV}$. Initial particle energy $\epsilon_i=25.5 \text{ eV}$. Scattering potential as in Fig. 3. Strong field intensity $I_2=3 \times 10^{15} \text{ W/cm}^2$. The two linearly polarized fields are parallel to each other and to the direction of the incoming particle beam. Dashed curves - DCS in the absence of the strong ω_2 field; continuous curves - DCS in the presence of a single-mode field at ω_2 ; dot-dashed curves - DCS in the presence of a multimode field at ω_2 (From ref.s 10 and 15).

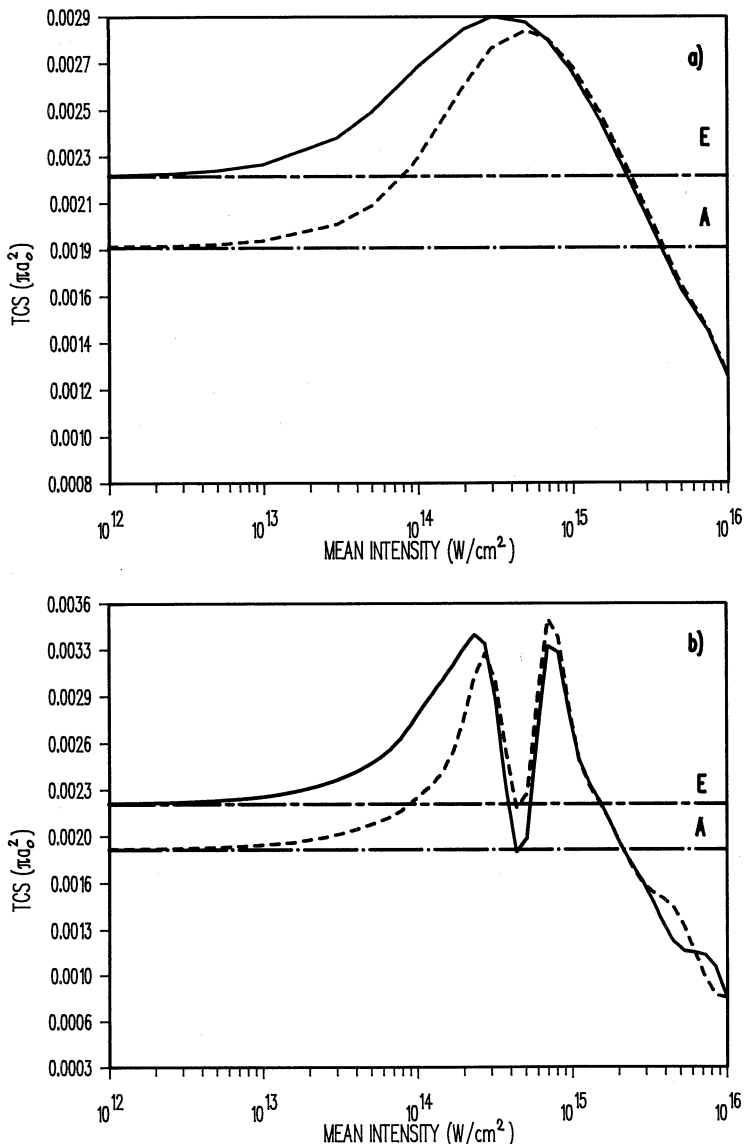


Fig. 10 - Total cross sections (TCS), in units of πa_0^2 , vs the strong-field intensity I_2 , in units of W/cm^2 , of stimulated bremsstrahlung in which a weak-field photon is emitted or absorbed with energy $\hbar\omega_1=0.9$ eV. a) refers to the case when the strong field is a multimode field with a large number of modes. b) refers to the case of a single-mode field.
 Continuous curves - TCS of emission of a weak field photon $\hbar\omega_1$
 Dashed curves - TCS of absorption of $\hbar\omega_1$.
 E - straight lines - TCS of emission of $\hbar\omega_1$ without a spectator field. A - straight lines - TCS of absorption of $\hbar\omega_1$ without a spectator field. Others parameters as in Fig. 9. For the multimode field case as intensity the mean intensity must be understood. (From ref.s 10 and 15).

perturbed by a potential $U(r)$ in the presence of a laser with vector potential $A(t)$.

$$\hat{H}_0(t) = \int d^3r \Psi^\dagger(r,t) [(\hbar/i)\nabla - (e/c)A(t)]^2 \Psi(r,t) \quad (5.2)$$

is the unperturbed Hamiltonian; and

$$\hat{H}_i(t) = \int d^3r \Psi^\dagger(r,t) U(r) \Psi(r,t) \quad (5.3)$$

is the interaction Hamiltonian;

$$U(r) = \sum_i^{N_i} V_i(r_i) = \sum_i^{N_i} V_i(|r-R_i|) \quad (5.4)$$

with R_i the vector position of i -th ion (only one sort of ions), and N_i the ion density. $\Psi^\dagger(r,t)$ and $\Psi(r,t)$ are the free-electron field operators, constructed as a coherent sum of fermion creation and annihilation operators C_p^+ and C_p :

$$\Psi(r,t) = \sum_p C_p X_p(r,t); \quad \Psi^\dagger(r,t) = \sum_p C_p^+ X_p^*(r,t); \quad (5.5)$$

where $\{X_p(r,t)\}$ is a complete set of Volkov plane waves and C_p^+ and C_p obey the usual anticommutation relations

$$\{C_p^+, C_{p'}\} = C_p^+ C_{p'} + C_{p'}^+ C_p = \delta_{p,p'}$$

and so on. Spin variables are omitted as in this process no spin flip is expected to occur, but the Fermi-Dirac statistics is fully taken in account. In this section we find more convenient to label the continuum states with the momentum instead of the wave vector.

Using the expansion (5.5), the interaction Hamiltonian is obtained as:

$$\hat{H}_i(t) = \sum_{p,p'} M(p,p';t) C_p^+ C_{p'}; \quad (5.6)$$

$$M(p,p';t) = \langle p' | U | p \rangle \exp\{(i/\hbar)(\epsilon_{p'} - \epsilon_p)t - i\lambda_{p',p} \sin \omega t\} \quad (5.7)$$

$$\langle p' | U | p \rangle = \int d^3r \exp\{i/\hbar[p' - p] \cdot r\} U(r); \quad (5.8)$$

$$\epsilon_p = p^2/2m \quad (5.9)$$

and $\lambda_{p',p}$ is the same as eq.(2.16). Eq.(5.7) corresponds to the choice of a linearly polarized field. The initial and final states of the quantized field in the occupation number representation are

$$|i\rangle = |..., N(p_i), ..., N(p_f)-1, ... \rangle \quad (5.10)$$

$$|f\rangle = |..., N(p_i)-1, ..., N(p_f), ... \rangle \quad (5.11)$$

where $N(p)$ specifies the number of particles with momentum p (for fermions $N(p)=0,1$). The matrix element between the initial state $|i\rangle$, where an electron with momentum p_i is destroyed, and the final state $|f\rangle$, where an electron with momentum p_f is created is now obtained as

$$\langle 2 | H_i | 1 \rangle = \{N(p_1)[1-N(p_2)]\}^{1/2} M(p_2, p_1, t) (-1)^{\nu_2 + \nu_1} \quad (5.12)$$

In (5.12) to simplify notations we have introduced the following changes

$$\begin{aligned} p_i &= p_1; & p_f &= p_2; & |p_i\rangle &= |1\rangle; & |p_f\rangle &= |2\rangle \\ \nu_{p_f} &= \nu_2; & \nu_{p_i} &= \nu_1 \end{aligned} \quad (5.13)$$

Further, i):

$$\nu_a = \sum_{k=1}^{p_a-1} N(p_k) \quad (5.14)$$

is the sum of the occupation numbers of the states preceding the state p_a ; ii) use has been made of the relations

$$C_p |...,N(p),...> = (N(p))^{1/2} (-1)^{\nu_p} |...,N(p)-1,...>; \quad (5.15)$$

$$C_p^+ |...,N(p),...> = (1-N(p))^{1/2} (-1)^{\nu_p} |...,N(p)+1,...>; \quad (5.15')$$

$$\langle...,N(p_1),...,N(p_2),...|...,N(p_1),...,N(p_2),...> = 1; \quad (5.16)$$

and iii) of the fact that the action of C_p and C_p^+ on the state $|...,N(p'),...>$ gives zero unless $p'=p$.

Using (5.12) the first order amplitude is given by

$$A_{12} = (-i/\hbar) \int_{-T/2}^{T/2} \langle 2 | H_i | 1 \rangle dt \quad (5.17)$$

and for large times the transition probability per unit time is obtained as

$$P_{12} = \lim_{T \rightarrow \infty} |A_{12}|^2 / T = N_i (2\pi/\hbar) \sum_n J_n^2(\lambda_{21}) [N(p_1)(1-N(p_2))] \times \langle 2 | V | 1 \rangle^2 \delta(\epsilon_2 - \epsilon_1 - n\hbar\omega) \quad (5.18)$$

where we have also assumed the target ions to be uncorrelated

$$| \langle 2 | U | 1 \rangle |^2 = N_i | \langle 2 | V | 1 \rangle |^2$$

If we take for the potential created by a single ion of net charge Ze a pure Coulomb potential, then $| \langle 2 | V | 1 \rangle |$ is given by Eq.(4.7) via Eq.(2.18). Now we form the equation giving the change of $N(p_2)$ with time. Four terms enter the equation, which correspond to the process represented in Fig. 11. In Fig. 11 (a) and (b) represent processes in which an electron initially with momentum p_1 is transferred in the state with momentum p_2 and $n\hbar\omega$ photons are absorbed or emitted.

Mathematically (a) and (b) are given by

$$dN(p_2)/dt|_{a+b} = \sum_{n=1}^{\infty} \sum_{p_1} N(p_1) [1-N(p_2)] [\tilde{P}(n, p_1 - p_2) + \tilde{P}(-n, p_1 - p_2)] \quad (5.19)$$

$$\tilde{P}(n, p_1 - p_2) = N_i (2\pi/\hbar) J_n^2(\lambda_{21}) | \langle 2 | V | 1 \rangle |^2 \delta(\epsilon_2 - \epsilon_1 - n\hbar\omega) \quad (5.20)$$

In Fig. 11, (c) and (d) represent the inverse processes in which an electron with momentum p_2 is transferred back to the state with momentum p_1 , and $n\hbar\omega$ photons are absorbed or emitted. Mathematically

$$dN(p_2)/dt|_{c+d} = \sum_{n=1}^{\infty} \sum_{p_1} N(p_2) [1-N(p_1)] [\tilde{P}(n, p_2 - p_1) + \tilde{P}(-n, p_2 - p_1)] \quad (5.21)$$

The net time rate of change of $N(p_2)$ is obtained by subtracting (5.21) from (5.19),

$$dN(p_2)/dt = dN(p_2)/dt|_{a+b} - dN(p_2)/dt|_{c+d} \quad (5.22)$$

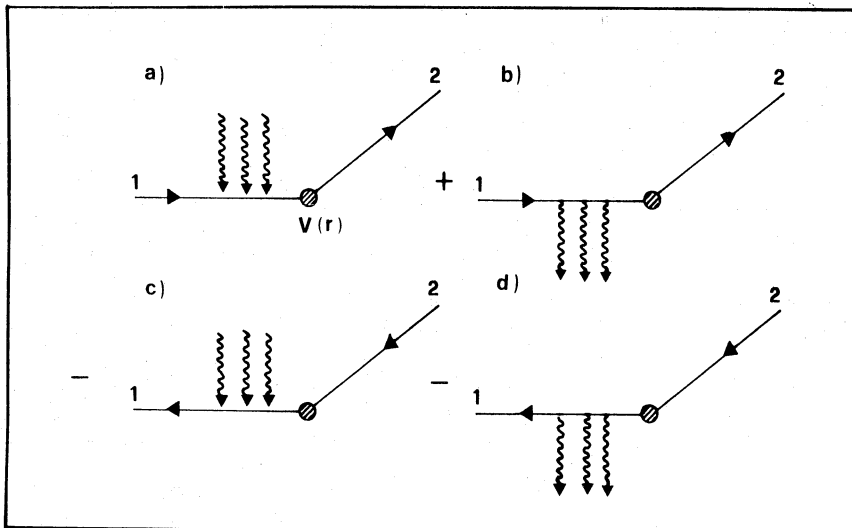


Fig. 11 - Representation of the processes giving the balance of the change of population in the state $| p_2 \rangle = | 2 \rangle$

Considering that the first-order matrix element of potential scattering and the argument of the Bessel function depend on p_1 and p_2 only through their difference, we have that

$$\tilde{P}(n, p_1 - p_2) = \tilde{P}(-n, p_2 - p_1) \quad (5.23)$$

which for $dN(p_2)/dt$ gives

$$dN(p_2)/dt = \sum_{-\infty}^{\infty} \sum_{p_1} [N(p_1) - N(p_2)] \tilde{P}(n, p_1 - p_2) \quad (n \neq 0) \quad (5.24)$$

Equivalently, one could have derived an equation for $N(p_1)$. The change in the average energy of electrons is given by

$$\begin{aligned} d\epsilon/dt &= \sum_{p_2} \epsilon_2 [dN(p_2)/dt] = \sum_{p_1, p_2} \sum_{-\infty}^{\infty} [N(p_1) - N(p_2)] \times \\ &\times (p_2^2/2m) \tilde{P}(n, p_1 - p_2), \quad (n \neq 0) \end{aligned} \quad (5.25)$$

In strong field situations a symmetrized expression may be better suited for actual calculations. Then we write

$$d\epsilon/dt = (1/2) \sum_{-\infty}^{\infty} \sum_{p_1, p_2} [N(p_1) - N(p_2)] (p_2^2/2m - p_1^2/2m) \tilde{P}(n, p_1 - p_2), \quad (5.26)$$

and the restriction $n \neq 0$ in the summation needs not be imposed as it is automatically satisfied.

c. Case of a Nondegenerate Plasma

Now i) we assume that the electrons are far from degeneracy so that $N(p) \ll 1$, and that a classical distribution function may be used: $N(p) \rightarrow f(p)$. Next, ii) we let the volume of the quantization box to become

infinite so that the sum over p_1 in $dN(p_2)/dt$ may be converted into an integral according to the prescription

$$\sum_p \rightarrow (2\pi)^{-3} \int d^3 p$$

(i) and (ii) give

$$df(p_2)/dt = (2\pi)^{-3} \sum_{n \neq 0} \int d^3 p_1 [f(p_1) - f(p_2)] \tilde{P}(n, p_1 - p_2) \quad (5.27)$$

where $f(p)$ is an appropriately normalized distribution function.

Similarly

$$d\epsilon/dt = (2\pi)^{-6} \int d^3 p_2 \int d^3 p_1 \sum_{n \neq 0} (p_2^2/2m)[f(p_1) - f(p_2)] \times \tilde{P}(n, p_1 - p_2) \quad (5.28)$$

$$d\epsilon/dt = (1/2)(2\pi)^{-6} \sum_{n \neq 0} \int d^3 p_2 \int d^3 p_1 [f(p_1) - f(p_2)] \times (p_2^2/2m - p_1^2/2m) \tilde{P}(n, p_1 - p_2) \quad (5.29)$$

The formula (5.29) has been calculated for the case of a single-mode, linearly polarized field, and subsequently averaged over the distribution function $P_N(\xi)$, Eq.(3.9), to account for the case when the laser is operated in a multimode configuration[22]. For both cases, two electron velocity distributions have been considered. Namely,

i) a Maxwellian distribution

$$f(p) = N_e (2\pi m_e kT)^{-3/2} \exp \{-p^2/2mkT\}, \quad (5.30)$$

and ii) a delta-type distribution

$$f(p) = N_e \delta(p - p_0) \quad (5.31)$$

meant to represent a directed, monoenergetic electron beam.

A sample of calculations is reported in Fig. 12, where four $(d\epsilon/dt)$ curves are plotted as functions of the ratio

$$R = v_{osc}/v_T \quad (5.32)$$

$v_{osc} = (eE_0/m_e\omega)$ being the amplitude of the electron oscillatory velocity imparted by the field, and $v_T = (kT/m_e)^{1/2}$ the thermal velocity. Concerning the results of Fig. 12 a number of comments are in order. i) The values of the parameter R control the behaviour of the energy absorption rates, especially for small and moderate intensities, when saturation is not yet reached. ii) For $R \leq 1$ in the case of a mono-energetic beam the Marcuse effect is still present (although less pronounced) also in chaotic field. iii) For a Maxwellian plasma (curves 3 and 4), the statistics of the radiation field does not effect significantly the energy absorption rate, at least up to $R=10$. iv) For higher intensities, corresponding to $R > 10$, the reverse becomes true: the absorption rate becomes insensitive to the particle statistics, and the surviving differences in the four curves depend in practice only on the radiation field statistics. For $R \geq 15$ the four curves of Fig. 12 tend to degenerate into two, the higher belonging to the case of the chaotic field. These results may be understood, considering that at very high intensities, all the plasma electrons have the same high oscillatory

velocity imparted by the field, and the Maxwellian distribution becomes a sort of an unimportant background. While this result appears interesting and plausible, it poses the problem of the actual evolution of a particle energy distribution in the presence of a very strong radiation field (see, for instance, ref. 23).

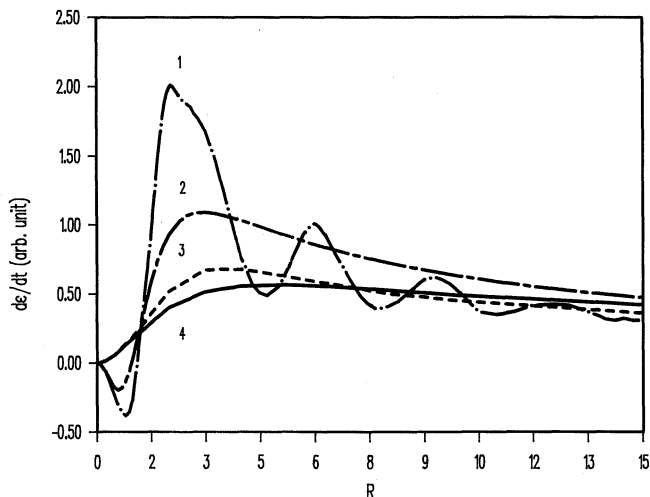


Fig. 12 - Energy absorption rate (in arbitrary units) vs the ratio $R=v_{\text{osc}}/v_T$, where $v_{\text{osc}}=eE_0/m_e\omega$, and $v_T=(kT/m)^{1/2}$. Field polarization: linear and parallel to the initial state electron momentum. Photon energy $\hbar\omega=1.17$ eV. Electron temperature $T=10^5$ °K. Intensity range: $10^7 \div 10^{16}$ W/cm². Scattering potential: coulombic with $Z=1$. Curve 1 is for a monoenergetic directed beam and a single-mode field. Curve 2 is for a monoenergetic directed beam and a multimode field (chaotic limit). Note that for small R , both curves exhibit negative absorption (the so-called Marcuse effect). Curve 3 is for a Maxwellian plasma and a single-mode field. Curve 4 is for a Maxwellian plasma and a chaotic field (from ref. 22). Note that for the chaotic field, E_0 is to be understood as the average field resulting from intensity fluctuations.

6. Concluding Remarks

In the previous sections we have seen that the occurrence of elementary processes in very strong radiation fields can not be described by perturbation theory. Both experiments and nonperturbative treatments predict highly nonlinear behaviours. At relatively high values of the field intensity, the probability of occurrence of an elementary process

in a radiation field shows as a rule a large saturation domain, followed by a decreasing. This last part is due to the large oscillatory velocities imparted by the field, which contribute to make effectively weaker the role of the "third body" necessary to the process occurrence. In the case of a completely ionized, classical plasma an interesting interplay has been found between the radiation field statistics and the particle statistics, leading in the same cases to the irrelevance of the field statistics or to that of the electrons. Finally, the relevant physical quantities as functions of field intensity exhibit in realistic cases, as a rule, a rather smooth behaviour, which could be easily fitted to be incorporated in more realistic modelling of many-particle processes.

Acknowledgements

The authors express their thanks to the University of Palermo Computation Centre for the computer time generously provided to them. This work was supported by the Italian Ministry of Education, the National Group of Structure of Matter and the Sicilian Regional Committee for Nuclear and Structure of Matter Research.

References

1. For collision in the presence of lasers, see, for instance:
B.Wallbank, J.k. Holmes and A. Weingartshofer, J. Phys. B: At. Mol. Phys. 20, 6121 (1987); A. Weingartshofer, J.K. Holmes, J. Sabbagh and S.L. Chin, J. Phys. B: At. Mol. Phys. 16, 1805 (1983).
2. For multiphoton ionization, a considerable amount of information may be found in the special issue 4B of J. Opt. Soc. Am. of 1987.
3. P. Kruit, J. Kimman, H.G. Muller and M.J. van der Wiel, Phys. Rev. A28, 248 (1983).
4. For a more detailed information on particle-atom collisions in strong laser fields and the related literature see, for instance, G. Ferrante in : **Fundamental Processes in Atomic Collision Physics**, Ed. H. Kleinpoppen, J.S. Briggs and H.O. Lutz, pp. 343-395, (New York: Plenum Press, 1985).
5. S. Bivona, R. Burlon, R. Zangara and G. Ferrante, J. Phys. B: At. Mol. Phys. 18, 3149 (1985).
6. R. Daniele, F. Trombetta, G. Ferrante, P. Cavalieri and F. Morales, Phys. Rev. A36, 1156 (1987).
7. a)C. Leone, R. Burlon, F. Trombetta, S. Basile and G. Ferrante, Nuovo Cimento 9D, 609 (1987); b) S. Basile, F.Trombetta, G. Ferrante, R. Burlon and C. Leone, Phys. Rev. A37, 1050 (1988); c) S. Basile, G. Ferrante and F. Trombetta, J. Phys. B: At. Mol. Phys. 21, L377 (1988); d) F. Trombetta, G. Ferrante and S. Basile, J. Phys. B: At. Mol. Phys. 21, L539 (1988); e) F. Ciralli, S. Basile, G. Ferrante and F. Trombetta, J. Phys. B: At. Mol. Phys. 21, L651 (1988); f) S. Basile, G. Ferrante and F. Trombetta, Phys. Rev. Lett. 61, 2435 (1988); g) C. Leone, S. Bivona, R. Burlon and G. Ferrante, Phys. Rev. A38, 5642 (1988); h) S. Bivona, R. Burlon, C. Leone and G. Ferrante, J. Mod. Opt. 36, 000 (1989); i) S. Basile, G. Ferrante and F. Trombetta, J. Opt. Soc. Am. B6, 000 (1989).
8. J. Gersten and M.H. Mittlemann in : **Electron and Photon Interaction with Atoms**, Ed. H. Kleinpoppen and M.R.C. McDowell, pp.553-8, (New York: Plenum Press, 1976).
9. V.A. Kowarskii, N.F. Perel'man, I.Sh. Averbukh, S.A. Baranov and S.S. Todirashku, **Neadiabaticheskiye Perekhody v Sil'nom Elektromagnitnom Pole** (in English : Non-adiabatic Transitions in Strong Electromagnetic Fields) p.129 (Kishinev: Shtiintsa, 1980).
10. S. Basile, G. Ferrante and F. Trombetta, Nuovo Cimento D (1989), in press.

11. a) P.H. Bucksbaum, R.R. Freeman, T.J. McIlrath, M. Bashkansky in: **Multiphoton Ionization of Atoms in Strong Fields** (Proceedings of International Conference held in Orsay (France), 28-29 April 1986);
b) T.J. McIlrath, P.H. Bucksbaum, R.R. Freeman, and M. Bashkansky, Phys. Rev **A35**, 4611 (1987).
12. F. Morales, P. Cavaliere, R. Daniele and G. Ferrante, Nuovo Cimento **10D**, 571 (1988), and references quoted therein.
13. V.M. Galitzkii, B.M. Karnakov and B.I. Kogan: **Solved Problems of Quantum Mechanics** (Nauka: Moscow 1981), chapt. 14, №23.
14. V. Veniard, M. Gavrila and A. Maquet, Phys. Rev. **A35**, 448 (1987), and references quoted therein.
15. R. Daniele, F. Morales and G. Ferrante, "Stimulated Bremsstrahlung in the Presence of a Strong Multimode Laser Field" (in preparation).
16. Y. Shima and H. Yatom, Phys. Rev. **A12**, 2106 (1975).
17. L. Schlessinger and J. Wright, Phys. Rev. **A20**, 1934 (1979).
18. a) S. Bivona, G. Ferrante, S. Nuzzo and M. Zarcone, J. Phys. B: At. Mol. Phys. **15**, 169 (1982); b) S. Bivona, R. Daniele and G. Ferrante, J. Phys. B: At. Mol. Phys. **15**, 1585 (1982).
19. V.P. Silin and S.A. Uriupin, Sov. Phys. JETP **54**, 485 (1982).
20. V.P. Silin, Sov. Phys. Usp. **28**, 136 (1985).
21. S. Rashid, Phys. Rev. **A38**, 2525 (1988).
22. R. Daniele, G. Messina and G. Ferrante, "Plasma Heating by a Strong Multimode Laser Field" (in preparation).

RESONANT PHOTOPUMPING OF LITHIUMLIKE IONS IN LASER-PRODUCED PLASMAS

Yim T. Lee

Lawrence Livermore National Laboratory
Livermore, CA, U.S.A.

I INTRODUCTION

Several demonstrations of lasing in the extreme-ultraviolet (XUV) wavelength region have been successfully achieved using either collisional excitation¹⁻⁶ or recombination pumping⁷⁻¹¹. The first successful demonstration was reported for the 3p-3s transitions in Ne-like selenium ions.¹⁻² Laser transitions at shorter wavelengths have also been achieved by using the 4d-4p transitions in Ni-like ions⁴⁻⁶. These schemes are based on collisional excitation of the upper laser levels, while the other successful schemes⁷⁻¹¹ are based on three-body recombination into highly excited states followed by cascade down to the upper laser levels.

However, lasing using resonant photopumping in the XUV wavelength region has not yet been demonstrated. In resonant photopumping, a photon emitted from one ion is used to excite a transition in an ion of a different element. A successful resonance scheme requires a close match between the wavelengths of these transitions. This concept for achieving population inversions of ions in plasmas was first proposed by Vinogradov et al.¹² and by Norton and Peacock¹³. Although several schemes based on using resonant photopumping to achieve laser amplification at wavelengths less than 100 Å have been proposed¹⁴⁻¹⁹, the shortest wavelength at which significant gain has been measured is 2163 Å²⁰.

In this paper, we describe laser schemes which lase on several 5-4 transitions in lithiumlike ions as a result of resonant pumping of the n=5 levels in these ions. The pumping radiations are 2-1 resonance lines of hydrogenlike or heliumlike ions. We find that the 2-5 transitions in lithiumlike sodium, iron and selenium match the resonance lines of hydrogenlike boron, aluminum, and chlorine. Lasers which lase on the 5-4 transitions in lithiumlike sodium, iron, and selenium have wavelengths of 500 Å, 70 Å, and 39 Å, respectively. A 70 Å laser which lases on the 5-4 transitions in lithiumlike iron has been proposed recently²¹. A similar laser which lases on the 5-4 transitions in lithiumlike selenium is of particularly interesting because it has a wavelength of approximately 39 Å which is ideal for use in laser holography of biological samples²².

In next section, we present calculations for the energy levels of lithiumlike ions and the line matches for x-ray laser pumping. Section III discusses plasma conditions of a laser medium in which these line matches are used to achieve population inversion and hence gain. We also

Table I. Line matches for resonant photopumping.

Pump Ions	Transition	Wavelength (Å)	Lasing Ion	Transition	Wavelength (Å)	$\Delta\lambda/\lambda$ (x 10 ⁻⁴)
B ⁴⁺	2p _{3/2} -1s _{1/2}	48.5835	Na ⁸⁺	2s _{1/2} -5p _{1/2,3/2}	48.578, 48.574	1.13, 2.0
O ⁷⁺	2p _{1/2} -1s _{1/2}	18.9667	C ₂ ¹⁴⁺	2p _{3/2} -5d _{3/2,5/2}	18.957, 18.956	5.14, 5.64
A ₂ ¹¹⁺	2p ³ P ₁ -1s ²	7.8061	Mn ²²⁺	2s _{1/2} -5p _{1/2,3/2}	7.801, 7.797	6.53, 11.6
A ₂ ¹²⁺	2p _{3/2} -1s _{1/2}	7.1709	Fe ²³⁺	2s _{1/2} -5p _{1/2,3/2}	7.170, 7.165	1.3, 8.2
C ₂ ¹⁵⁺	2p ³ P ₁ -1s ²	4.4678	As ³⁰⁺	2p _{3/2} -5d _{3/2,5/2}	4.464, 4.463	8.5, 10.7
C ₂ ¹⁶⁺	2p _{1/2} -1s _{1/2}	4.1908	Se ³¹⁺	2p _{3/2} -5d _{3/2,5/2}	4.190, 4.188	1.9, 6.7

Table IIa. Laser transitions in lithium-like iron.

Transitions	Wavelength (Å)	Oscillator strength	Gain (cm ⁻¹) for N _{hv}	
			0.0025	0.005
5g _{9/2} - 4f _{7/2}	70.25	1.306	2.06	3.85
5g _{7/2} - 4f _{5/2}	70.17	1.342	1.48	2.76
5f _{7/2} - 4d _{5/2}	70.12	0.837	0.90	1.65
5f _{5/2} - 4d _{3/2}	69.94	0.876	0.61	1.13
5d _{5/2} - 4p _{3/2}	69.15	0.498	0.41	0.77
5d _{3/2} - 4p _{1/2}	68.51	0.539	0.22	0.41
5p _{3/2} - 4d _{5/2}	70.77	0.031	0.08	0.15
5p _{1/2} - 4d _{1/2}	67.21	0.156	0.12	0.23

Table IIb. Laser transitions in lithium-like selenium.

Transitions	Wavelength (Å)	Oscillator strength	Gain (cm ⁻¹) for N _{hv}	
			0.0025	0.005
5g _{9/2} - 4f _{7/2}	39.50	1.30	4.80	9.90
5g _{7/2} - 4f _{5/2}	39.41	1.34	1.30	2.70
5f _{7/2} - 4d _{5/2}	39.39	0.83	3.55	7.10
5f _{5/2} - 4d _{3/2}	39.21	0.87	0.84	1.67
5d _{5/2} - 4p _{3/2}	38.87	0.48	2.22	4.48
5d _{3/2} - 4p _{1/2}	38.23	0.51	0.28	0.60
5p _{3/2} - 4d _{5/2}	39.78	0.03	0.15	0.30
5p _{1/2} - 4s _{1/2}	37.89	0.16	0.06	0.15

comment on application of high-power optical lasers to irradiate thin foil targets to produce plasmas which are used as laser media. In section IV, we consider optical laser heated massive slab target as an intense source of resonance line radiation. Section V describes calculation of gains in steady-state plasmas and in thin foil targets irradiated by high-power optical lasers.

II RESONANT PHOTOPUMPING OF LITHIUMLIKE IONS

To find line matches for x-ray laser pumping, we have calculated the energy levels of lithiumlike ions with nuclear charges from 10 to 35. In the calculation, we use the Multi-Configuration Dirac-Fock (MCDF)²³⁻²⁴ code which includes QED correction to the energy levels. A possible source of errors is in the calculation of the screening effect on the self-energy. Using the calculated self-energy of hydrogenic ions²⁵, we estimate the error in the energy of the 2s-5p and 2p-5d transitions to be 0.01 eV and 0.001 eV, respectively. These values are very small in comparison to the acceptable wavelength difference of a line match. Another possible source of errors is the correlation energy contribution which is neglected in MCDF. Using a recent calculation for the correlation energy of hydrogenic ions²⁶, we estimate the error in the energy for the 2s-5p and 2p-5d transitions to be 0.3 eV and 0.1 eV, respectively. These uncertainties in the transition energies are within the wavelength mismatches given later. The results apply to both lithiumlike iron and selenium.

The wavelengths for the 2-1 resonance lines of hydrogenlike and heliumlike ions have been calculated very accurately. For example, the wavelength for the $1s_{1/2}-2p_{3/2}$ transition in hydrogenlike aluminum has been calculated to be $7.1709171 \pm 0.0000003 \text{ \AA}^{27}$. Using the published wavelengths for resonance lines, we have found only six promising line matches among the lithiumlike ions with nuclear charges from 10-35. The wavelengths of these lines together with their oscillator strengths are presented in Table I. Also shown in the table are values for the ratio $\Delta\lambda/\lambda$, where $\Delta\lambda$ is the wavelength mismatch of the pumped and pumping transitions and λ is the wavelength of the pumping transition. The transitions in the following pairs of ions, (B^{4+}, Na^{8+}), (Al^{12+}, Fe^{23+}), and (Cl^{16+}, Se^{31+}) match better than a few parts in 10^4 . In the rest of this paper, we are mainly concerned with achieving lasing on the 5-4 transitions in lithiumlike iron and selenium because of their short wavelengths.

III PLASMA CONDITION FOR THE LASER MEDIUM

The plasma condition of a laser medium is determined by the temperature and density where lithiumlike ions are produced. To estimate these conditions, we have calculated lithiumlike ion populations in steady-state equilibrium using a collisional-radiative model²⁸⁻²⁹. Results for iron and selenium are given in Figures 1a and 1b. Between 20-40% of lithiumlike iron ions is produced at temperatures from 800-1200 eV. The same fractions of lithiumlike selenium ions are produced at higher temperatures from 2000-3200 eV. The results presented in the figures also suggest that lithiumlike ion populations are relatively insensitive to the electron densities from $10^{20} - 10^{21} \text{ cm}^{-3}$.

The electron temperatures and densities needed to strip iron and selenium to lithiumlike ionization state can be obtained in a laser heated foil target. The foil which has a thickness of several thousand Å is irradiated and subsequently exploded by two opposite optical laser beams at line focus to produce an elongated uniform plasma. Such a plasma was used as a laser amplifier in the successful experiment which

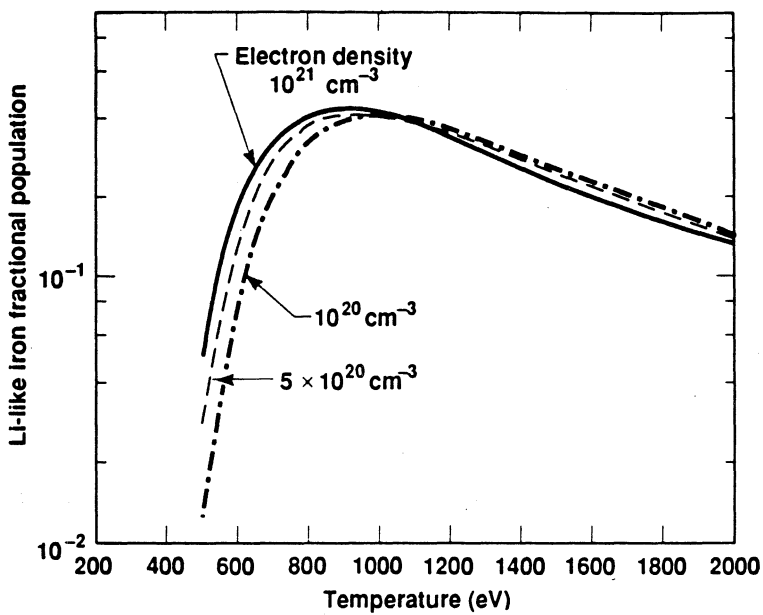


Fig. 1a. Lithiumlike iron fractional population in steady-state equilibrium vs. electron temperature

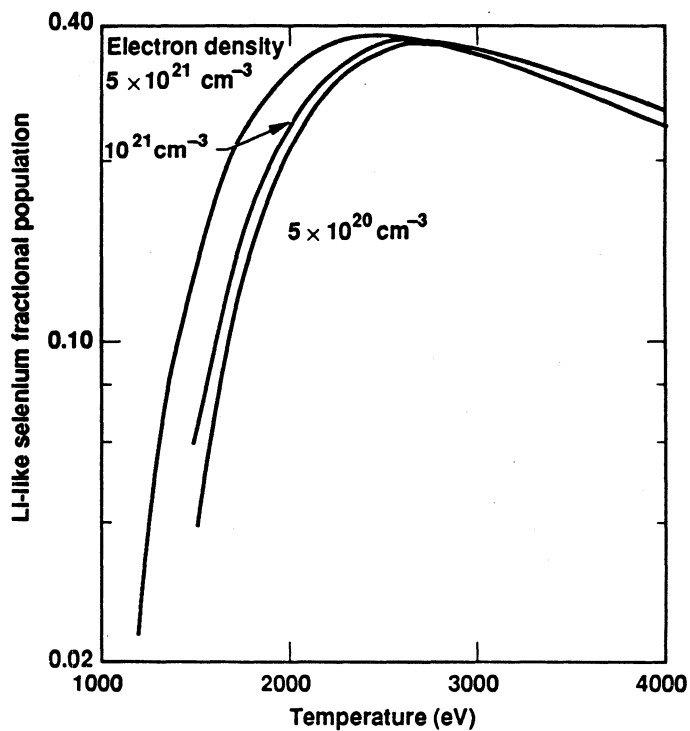


Fig. 1b. Lithiumlike selenium fractional population in steady-state equilibrium vs. electron temperature

first demonstrated gains in neonlike selenium. Calculation of optical laser heated iron foils is presented in details in reference 21. In the calculation, we assume that two 0.35 μm laser beams each in a gaussian pulse of 450 ps FWHM are used to irradiate a foil from both sides. According to the calculations which have been done using the hydrodynamics code LASNEX³⁰, the temperature at the center of a 1000 Å iron foil reaches 800-1700 eV for the total laser intensity of 6×10^{13} - 6×10^{14} W/cm². For selenium, we find that a 6000 Å foil can be heated to a temperature of 2500 eV by using a similar laser pulse at a total intensity of 2.4×10^{14} W/cm². The reason for using a thicker foil is to produce a higher density plasma, thereby absorbing more laser energy. The increase in laser absorption will result in a higher electron temperature which is needed to ionize selenium to lithiumlike.

These calculations suggest that thin foil targets can be heated to produce plasmas which have significant fractional populations of lithiumlike iron or selenium. Calculation of gains for the 5-4 transitions in these ions will be given in section V.

IV PUMPING RADIATION SOURCE

An intense source of resonance line radiation is needed for pumping of lithiumlike ions to achieve population inversions and hence gains. Here, we consider such a source to be a massive slab target irradiated by optical lasers. These targets have been used in many laser-plasma interaction experiments which measure x-ray conversion efficiency³¹ and laser generated shockwave³². Intense K-shell line radiations have also been measured from slab targets³³. To investigate the brightness of 2-1 resonance lines emitted from a slab target, we have used LASNEX²⁹ to calculate the heating of an aluminum slab under irradiation of a high-power optical laser beam. The temperature and density calculated are input into the kinetics code XRASER¹⁷ to compute line radiations emitted from the slab. The transfer of these radiations from the sources inside a slab is calculated using a numerical method³⁵. In the calculations which have been done for a 10 μm aluminum slab, we find that resonance line radiation with brightnesses of 0.002 to 0.005 photons/mode can be produced using a 0.35 μm laser beam in a gaussian pulse of 450 ps. FWHM at intensities from 3×10^{14} to 2×10^{15} W/cm². These line radiations emitted from the slab also have widths of 2 to 4 eV. Pump lines with these widths make it possible to use the line matches in Table I for x-ray laser pumping. Since fine-structure splitting of the 5p and 5d levels in both lithiumlike iron and selenium are about 1 eV, lines with widths of 2-4 eV can effectively pump all of the fine-structure levels. As an example, the 5p_{3/2} level in lithiumlike iron is photoexcited in addition to the 5p_{1/2} level. This is of especially important in pumping of lithiumlike selenium because the oscillator strength for the 2p_{3/2}-5d_{5/2} transition is a factor of five larger than that of the 2p_{3/2}-5d_{3/2} transition.

The intensity in an unit of W/(cm²-eV) can be calculated from the photons/mode N(h ν), as

$$I_{h\nu} = (8\pi h\nu^3/c^2)N(h\nu)$$

$$\approx 6.332 \times 10^4 (h\nu)^3 N(h\nu) W/(cm^2 \cdot eV)$$

where h ν is the photon energy in electron-volt. As an example, a resonance line with a brightness of 0.005 photons/mode and a width of 1 eV is equivalent to an intensity of approximately 10^{12} W/cm² for a photon energy of 1729 eV. Such an intensity will pump the 5p_{1/2} level in lithiumlike iron at approximately 10^{10} sec⁻¹.

V LASER GAIN CALCULATION

The following section describes calculations of small signal gains for the 5-4 transitions in lithiumlike iron and selenium ions which are pumped by resonance line radiations. The plasmas where these ions are produced are assumed to be either at steady-state equilibrium or time-dependent as in an optical laser heated foil. In the steady-state calculation, the electron temperature, ion density and pumping radiation intensity together with an atomic model are input into the kinetics code DCA²⁹ to calculate the level populations and gains. In the laser heated foil calculation, the heating and subsequently exploding of the foil are calculated using LASNEX and the population kinetics are modelled with DCA.

In both of these calculations, a detailed atomic model is used to describe the ions. The atomic models for iron and selenium contain data for the ionization stages from hydrogenlike to neonlike. Each ionization stages have levels with principal quantum number up to 10. Energy levels in the ionization stages from hydrogenlike to boronlike with principal quantum numbers up to 4, 5, 6, 5, and 2, respectively, are calculated using MCDF. The rest of the levels in these ionization stages in the model are Rydberg levels. The energy levels of the other ionization stages in the model are calculated using a hydrogenic approximation. The radiative rates for the dipole, quadrupole, and magnetic dipole transitions between detailed levels are also calculated using MCDF. Photoionization cross sections for the detailed levels are calculated using a relativistic Hartree-Slater model³⁴. The collisional excitation and ionization rate coefficients are either calculated using a classical path method¹⁷ or estimated from simple formulas.

Tables IIa-IIb present the gains for some 5-4 transitions in lithiumlike iron and selenium ions at steady-state equilibrium. In these calculations, we assume the ions are pumped by resonance line radiations with brightnesses of 0.0025 and 0.005 photons/mode and the lines are broadened enough to pump both the $5p_{1/2}$ and $5p_{3/2}$ levels in lithiumlike iron and both the $5d_{3/2}$ and $5d_{5/2}$ levels in lithiumlike selenium. The electron temperature and ion density for iron are 800 eV and $4 \times 10^{19} \text{ cm}^{-3}$ and for selenium are 2400 eV and 10^{20} cm^{-3} . The $5g_{9/2}-4f_{7/2}$ transitions in both of these ions have the largest gains. This results from strong photo-excitation of the $5p_{3/2}$ level in lithiumlike iron and of the $5d_{5/2}$ level in lithiumlike selenium. The $5g_{9/2}$ levels in both ions are populated as a result of strong collisional mixing among the n=5 levels. Since these levels are separated in energy by only few electron-volts, the collisional excitation rates between them are very large, comparing to the photopumping and radiative decay rates.

One of the advantages of lasing on the $5g_{9/2}-4f_{7/2}$ transition is that it has one of the largest oscillator strengths among the 5-4 transitions. The other advantage is that the lower laser level $4f_{7/2}$ does not radiatively decay to any level in the ground state configurations, $1s^2 2s$ and $1s^2 2p$. Therefore, there is no trapping of resonance lines to spoil the population inversion, thereby resulting in a lower or no gain.

Figures 2a-2b show how the gains depend on ion density at steady-state equilibrium. The lasing ions are assumed to be pumped by resonance lines with brightness of 0.005 photons/mode. The gain for iron peaks at an ion density of approximately $6 \times 10^{19} \text{ cm}^{-3}$, while the gain for selenium peaks at a higher ion density of $3.5 \times 10^{20} \text{ cm}^{-3}$.

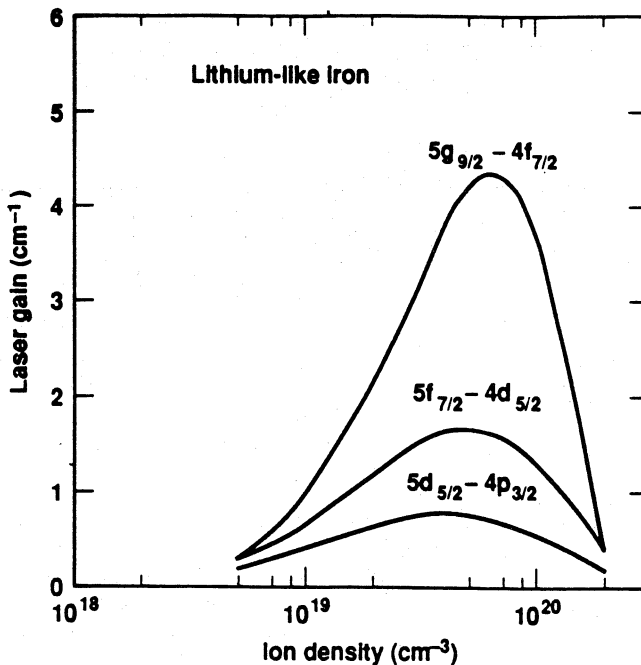


Fig. 2a. Gain in steady-state equilibrium vs. ion density at the electron temperature of 800 eV. The lasing ions are pumped by a line with brightness of 0.005 photons/mode.

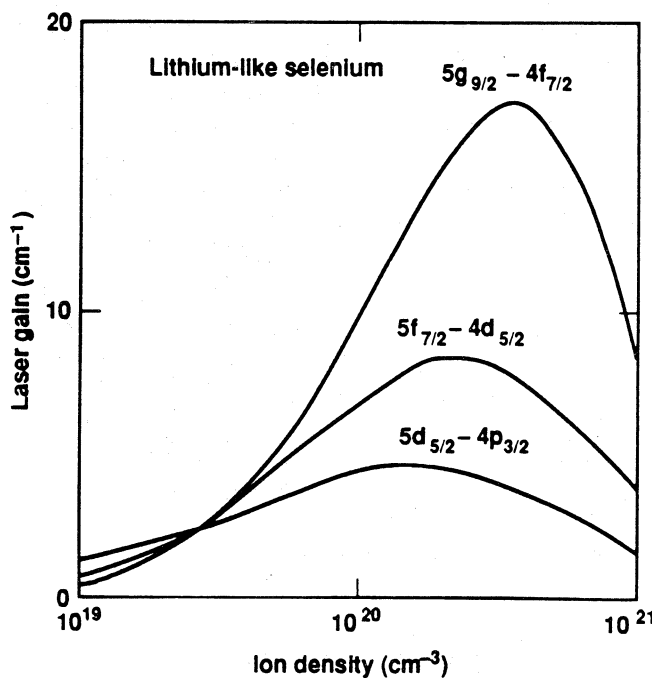


Fig. 2b. Gain in steady-state equilibrium vs. ion density at the electron temperature of 2400 eV. The lasing ions are pumped by a line with brightness of 0.005 photons/mode.

The decrease in the gain with density is due to collisional processes, coupling the n=5 and n=4 levels. The gain starts to decrease at the density where the electron collisional de-excitation rates for the 5-4 transitions begin to compete with the radiative decay rates. Since the radiative rates increase strongly with ionization state Z^* as $(Z^*)^4$, while the collisional de-excitation rates decrease with Z^* , the density where the gain peaks should be higher for selenium than for iron. Assuming the average ionization state is lithiumlike, we find that Figures 2a - 2b give the electron densities where the gains peak to be $1.4 \times 10^{21} \text{ cm}^{-3}$ and $9.3 \times 10^{21} \text{ cm}^{-3}$ for iron and selenium, respectively. These densities can be obtained in foil targets irradiated by a $0.35\mu\text{m}$ laser beam which has a critical density of $9.1 \times 10^{21} \text{ cm}^{-3}$.

Figures 3a-3b present time-dependent gains at the center of a laser heated foil target. In the calculation, the foil is assumed to be irradiated by two $0.35 \mu\text{m}$ laser beams each in a gaussian pulse of 450 ps FWHM. The peak intensities at the iron and selenium foil targets are $6 \times 10^{13} \text{ W/cm}^2$ and $2.4 \times 10^{14} \text{ W/cm}^2$, respectively. The iron and selenium foils also have thicknesses of 1000 Å and 6000 Å, respectively. A pump line in a pulse of the form, $0.005 \times \exp(-[(t-t_0)/\tau_0]^2)$ photons/mode, with $t_0 = 700 \text{ ps}$ and $\tau_0 = 300 \text{ ps}$ is assumed. Such temporal dependence of a pump line is chosen according to the calculations which have been done for an aluminum slab. Using such pumping radiation, we find that the gains are maximum at a time near the peak of the optical laser pulse and last about 300 ps. As in the steady-state calculation, the $5g_{9/2}-4f_{7/2}$ transition has the largest gain. However, comparing to the values for the steady-state gains in Figures 2a-2b, we find that the gains in the iron foil are about 40% lower, but the gains in the selenium foil are a factor of three lower. These results can be understood in terms of the low ion densities produced at the centers of these foils. For example, at a time near the peak of the laser pulse, the ion density at the center of the iron foil is $3 \times 10^{19} \text{ cm}^{-3}$ and the corresponding density in the selenium foil is only $7 \times 10^{19} \text{ cm}^{-3}$. To achieve high gain in a laser which lases on the 5-4 transitions in lithiumlike selenium, we need to design a higher density plasma used as a laser amplifier. Details of these design calculations which are beyond the scope of this paper will be published elsewhere.

VI SUMMARY

We present laser schemes which lase on the 5-4 transitions in lithiumlike ions as a result of resonant photopumping of either the 5p or 5d levels. The 5-4 transitions in lithiumlike iron and selenium have wavelengths of 70 Å and 39 Å, respectively. The calculations show that the temperature and density needed to produce these ions can be achieved in a laser heated foil target. Such a foil which has a thickness of one to several thousands Å is irradiated by two opposite laser beams each in a gaussian pulse of 450 ps FWHM with a total intensity of $6 \times 10^{13} - 2 \times 10^{14} \text{ W/cm}^{-2}$. The $5g_{9/2}-4f_{7/2}$ transition has the largest gain in both lithiumlike iron and selenium. We estimate the peak gain for this transition to be approximately 3 cm^{-1} in an iron foil target and to be 5 cm^{-1} in a selenium foil target. Comparing these values for the gains to the steady-state results, we expect that the gain in lithiumlike selenium would be much larger if lasing can be achieved at a density higher than in a 6000 Å foil presented here.

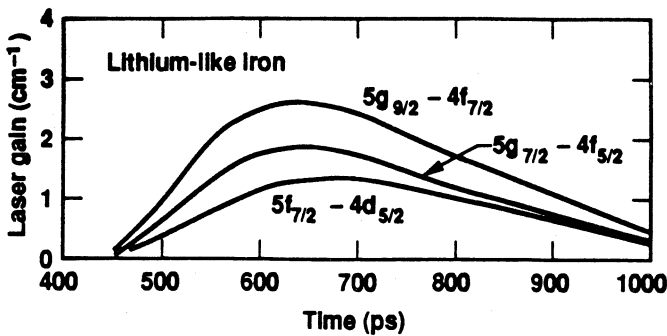


Fig. 3a. Time-dependent gain at the center of a 1000Å laser-heated iron foil. Laser parameters are: wavelength = $0.35\text{ }\mu\text{m}$, gaussian pulse width = 450 ps. FWHM, peak intensity = $6 \times 10^{13}\text{ W/cm}^2$.

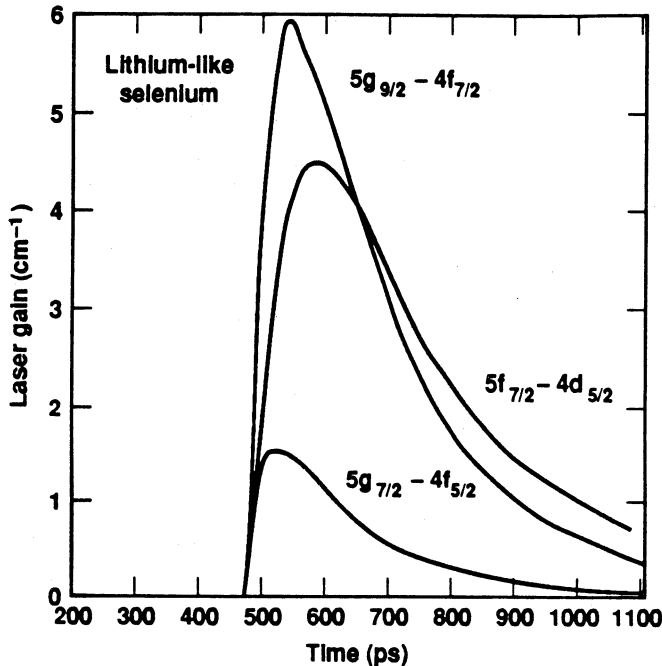


Fig. 3b. Time-dependent gain at the center of a 6000Å laser-heated selenium foil. Laser parameter are: wavelength = $0.35\text{ }\mu\text{m}$, gaussian pulse width = 450 ps. FWHM, peak intensity = $2.4 \times 10^{14}\text{ W/cm}^2$.

Acknowledgements

We are grateful to the following colleagues for many helpful discussions on several aspects of the work presented here: M. Chen, M. Howard, M. Gee, and J. Nash.

This work was performed under the auspices of the U. S. Department of Energy by the Lawrence Livermore National Laboratory under Contract W-7405-Eng-48.

REFERENCE

1. D. L. Matthews, et al., Phys. Rev. Lett. 54, 110 (1985).
2. M. D. Rosen, et al., Phys. Rev. Lett. 54, 106 (1985).
3. T. N. Lee, et al., Phys. Rev. Lett. 59, 1185 (1987).
4. B. J. MacGowan, et al., Phys. Rev. Lett. 59, 2157 (1987).
5. B. J. MacGowan, et al., Lawrence Livermore Natl. Lab. Rept., UCRL-97822 (1987).
6. S. Maxon, et al., Phys. Rev. A 37, 2227 (1988).
7. S. Suckwer, et al., Phys. Rev. Lett. 55, 1753 (1985).
8. J. F. Seely, et al., Opt. Commun. 54, 289 (1985).
9. G. Jamelot, et al., J. Phys. B 18, 4647 (1985).
11. C. C. Popovics, et al., Phys. Rev. Lett. 59, 2161 (1988).
12. C. L. S. Lewis, et al., Plasma Phys. Cont. Fusion 30, 35 (1988).
13. B. A. Norton and N. J. Peacock, J. Phys. B8, 989 (1975).
14. V. A. Bhagavatula, IEEE J. Quan. Elec. 16, 603 (1980).
15. J. P. Apruzese, J. Appl. Phys. 53, 4020 (1982).
16. W. E. Alley, et al., J.Q.S.R.T. 27, 257 (1982).
17. P. L. Hagelstein, Ph. D. thesis, Massachusetts Institute of Technology, 1981 and "Resonantly pumped soft x-ray laser using ICF drivers," Laser Interaction and Related Plasma Phenomena, Vol. 6, H. Hora and G. H. Miley, ed., Plenum Publishing (1984).
18. J. P. Apruzese and J. Davis, Phys. Rev. A 31, 1976 (1985)
19. R. C. Elton, et al., Phys. Rev. A 33, 2817 (1986).
20. N. Qi and M. Krishnan, Phys. Rev. Lett. 59, 2051 (1987).
21. Y. T. Lee, et al., Lawrence Livermore Natl. Lab. Rept., UCRL-99227 (1988).
22. R. A. London, et al., Lawrence Livermore Natl. Lab. Rept., UCRL-100176 (1989).
23. I. P. Grant, et al., Comput. Phys. Commun. 21, 207 (1980).
24. M. H. Chen, Phys. Rev. A31, 1449 (1985).
25. P. J. Mohr, Phys. Rev. A26, 2338 (1982).
26. W. R. Johnson, et al., Phys. Rev. A 37, 2764 (1988).
27. G. W. Erickson, J. Phys. Chem. Ref. Data, 6, 861 (1977).
28. Y. T. Lee, J.Q.S.R.T. 38, 131 (1987).
29. Y. T. Lee, et al., "A time-dependent ionization balance model for non-LTE plasmas," Proceeding of the Third International Conference/Workshop on the Radiative Properties of Hot Dense Matter, B. Rozsnyai et al., ed. World Scientific (1986).
30. G. B. Zimmerman and W. L. Kruer, Comments Plasma Phys. Controlled Fusion 11, 51 (1975)
31. For example, P. Alaterre, et al., Phys. Rev. A 34, 4184 (1986).
32. For example, A. Ng, et al., Phys. Rev. Lett. 24, 2604 (1985).
33. For example, D. L. Matthews, et al., J. Appl. Phys. 54, 4260 (1983).
34. J. H. Scofield, Lawrence Livermore Natl. Lab. Rept., UCRL-51326 (1973).
36. Y. T. Lee, R. A. London, G. B. Zimmerman, and P. L. Hagelstein, in preparation.

IONIZATION AND DEIONIZATION OF ELECTRON BEAM

DISTURBED AIR

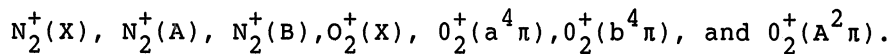
A. W. Ali

Naval Research Laboratory
Washington, DC 203750-5000

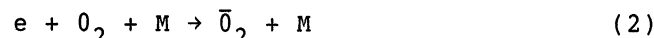
INTRODUCTION

An air plasma generated by the passage of a pulsed electron beam is a discharge which is not in equilibrium. Where the electron T_e , the vibrational T_v , and the gas T_g temperatures are not equal. The interaction of the beam electrons with the air molecules generates a conductivity and a density channel which exemplifies the disturbed air phenomena. The formation of these channels and their relaxation depend on^{1,2} a host of atomic and molecular processes which ensue in air, during and after the passage of the beam. These processes, stated briefly, proceed as follows. The beam and secondary electrons ionize, dissociate, excite the internal modes of N_2 and O_2 , and produce the bulk of the plasma electrons during the passage of the beam. The beam also heats the channel through direct atomic processes and by ohmic heating of the plasma electrons which in turn heat the ions and neutrals by elastic collisions. The evolution of the conductivity and the density channel proceed, after the passage of the beam, by dissociative recombination, charge exchange, quenching of electronic states, clustering, ion-ion recombination, neutral atomic recombination, vibrational-translation energy exchange and channel expansion. The ionization and deionization of the disturbed air, stated above, are delineated and quantified in this paper. Discussions are limited to beams with electrons of one MeV energy, where the energy deposition is mainly collisional³ and ohmic. Furthermore, approaches to the characterization of such channels are provided. Results are presented using a useful approach for beams with several kiloamps and pulse durations of tens of nanosecond, interacting with one atmosphere of air.

The primary and secondary electrons with sufficient energy ionize the molecules producing



They also produce N^+ and O^+ through dissociative ionization. For electron energies of $E \geq 100$ eV, the dissociative ionization constitutes⁴ ~ 20 - 22% of the total ionization in N_2 and ~ 30 - 32% in O_2 . The fractions⁵ of the molecular ions are 0.29, 0.37 and 0.12 for X, A, and B ionization continua in N_2 , respectively, and 0.16, 0.31, 0.12 and 0.08 for X, a, b and A ionization continua in O_2 , respectively. Electron impact collisions also dissociate N_2 and O_2 producing N , $\text{N}(^2\text{D})$, $\text{O}(^3\text{P})$ and $\text{O}(^1\text{D})$. There are several electronic states of the molecules which are excited by electron collisions. Among these are: the triplet states of N_2 and singlets, such as $\text{a}^1\pi$ and $\text{b}^1\pi$. Higher singlets are mainly predissociated⁶ and constitute nearly 60% of the total dissociation of N_2 . For O_2 , $\text{a}^1\Delta$ and $\text{b}^1\Sigma$ are of interest and the excitations of the triplets A and B are considered to lead to the dissociation of O_2 . Low energy electrons, mainly plasma electrons excite the vibrational and rotational states of the molecules. Two negative ions are also produced via the following processes, where M is a third body (N_2 , O_2).



The deionization processes in a partially ionized air proceed by the dissociative recombination of the molecular ions with electrons and by electron attachments which generate negative ions. The positive and negative ions undergo a series of charge exchange, ion-atom interchange, clustering etc, as they neutralize each other. These processes are delineated in Figs 1 and 2. The reactions and their rate coefficients for the deionization processes are given in Table I, where T_e and T_g are in eV. It should be noted that many of these coefficients are based on room temperature data and few have been measured over a limited temperature range. For details see Ref. 1.

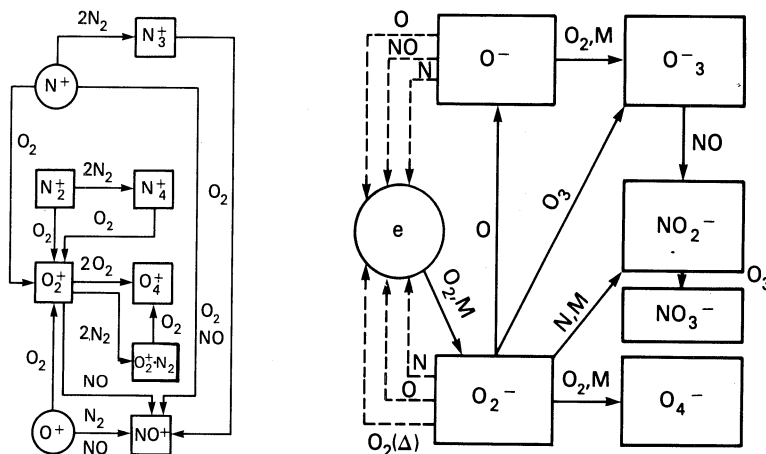


Fig. 1 Positive
Charge Flow Chart

Fig. 2 Negative
Charge Flow Chart

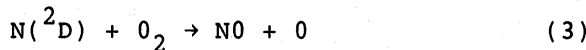
TABLE I. REACTIONS AND THEIR COEFFICIENTS

$N_2^+ + e \rightarrow N+N$	$4.3 \times 10^{-8} (T_e)^{-0.39}$
$O_2^+ + e \rightarrow O+O$	$1.5 \times 10^{-8} (T_e)^{-0.7}, T_e < 0.1$
	$2.1 \times 10^{-8} (T_e)^{-0.56}, T_e > 0.1$
$N_0^+ + e \rightarrow N+O$	$2 \times 10^{-8} (T_e)^{-0.83}$
$N_4^+ + e \rightarrow N_2+N_2$	$3.4 \times 10^{-8} (T_e)^{-1.1}$
$N_3^+ + e \rightarrow N_2+N_2$	$1.75 \times 10^{-8} (T_e)^{-1}$
$O_4^+ + e \rightarrow O_2^+ + O_2$	$1.8 \times 10^{-6}, T_e = 0.015, 3.4 \times 10^{-8} (T_e)^{-1.0}$
$N^+ + 2N_2 \rightarrow N_3^+ + N_2$	$1.25 \times 10^{-32} (T_g)^{-2.0}, T_g = 0.01-0.4$
$N_2^+ + 2N_2 \rightarrow N_4^+ + N_2$	$1.5 \times 10^{-32} (T_g)^{-2.2}, T_g = 0.01-0.4$
$O_2^+ + 2O_2 \rightarrow O_4^+ + O_2$	$1.94 \times 10^{-35} (T_g)^{-3.2}$
$N^+ + O_2 \rightarrow O_2^+ + N$	3.4×10^{-10}
$N^+ + O_2 \rightarrow NO^+ + O$	3.1×10^{-10}
$N^+ + O_2 \rightarrow O_2^+ + NO$	6.7×10^{-11}
$N_2^+ + O_2 \rightarrow O_2^+ + N_2$	5.0×10^{-11}
$N_3^+ + O_2 \rightarrow NO^+ + N_2 + O$	$3.3 \times 10^{-11} \rightarrow NO_2^+ + N_2 \quad 4.4 \times 10^{-11}$
$N_4^+ + O_2 \rightarrow O_2^+ + 2N_2$	4.0×10^{-10}
$O^+ + O_2 \rightarrow O_2^+ + O$	2.0×10^{-11}
$O^+ + N_2 \rightarrow NO^+ + N$	$7.5 \times 10^{-13}, 3.2 \times 10^{-11} (T_g)^{1.38}, T_g > 0.1$
$e + O_2 + \bar{O}_2 \rightarrow O_2^+ + O_2$	$3.6 \times 10^{-31} (T_e)^{-1.0} \text{Exp } -0.052/T_e$
$e + O_2 + N_2 \rightarrow \bar{O}_2 + N_2$	1.0×10^{-31}
$e + O_2 \rightarrow \bar{O} + O$	$1.5 (T_e)^{-1.0} \times 10^{-10} \text{Exp } [-5.0/T_e]$

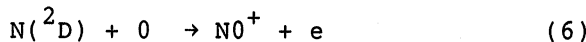
For additional reactions, not included in Table I, see Ref.1.

In addition to the positive and negative ion chemistry the neutral particle chemistry plays a role in both the deionization and heating of the channel. Details of these reactions and their coefficients which include thermal dissociation, ionization, recombination and rearrangement

collisions will not be given here. They can be found in Ref. 7. However few reactions which generate NO will be noted to illustrate the point.



Finally one must consider the associative ionization (see Eq. 6.) which becomes operative in channels with high temperature.



CALCULATIONAL APPROACHES

The interaction of an electron beam with air species, the ensuing chemistry and the channel development can be described by several means. The most detailed approach is to solve the Boltzmann equation for the electron velocity distribution, its generation and recombination. Solve Maxwell's Equation for the beam electric field. Couple these in a self consistent manner with a set of rate equations for all relevant species, excited electronic, and vibrational states of the molecules. The electron velocity distribution and the appropriate cross sections can be utilized to obtain all relevant dissociation, excitation, ionization, recombination rate coefficients, and collision frequencies needed in the rate equations. Electron and vibrational temperatures can be characterized. One needs, in addition, an equation for the heavy particle temperature. This procedure describes the channel completely except for its motion. Another approach, somewhat less cumbersome, is to describe the conductivity and density channels by three temperatures, T_e , T_v and T_g , all Maxwellian, yet different. Solve a set of time dependent rate equations for the relevant species and temperatures. Where the rate coefficients are obtained from a Maxwellian electron velocity distribution for all relevant processes. The source terms to these equations due to the beam, however, is obtained from a Boltzmann Code⁸ which solves for the electron velocity distribution and the production efficiencies of various interaction products. As an example, relevant production rates are given in Table II. Based on these results, one can show that the plasma electrons are born with an energy of 7.5 eV.

Table II. Species Production Per Electron-Ion Pair

$+ N_2$	$+ N$	N	$N_2(A)$	$N_2(B)$	$N_2(C)$	$+ O_2$	$+ O$	$O_2(\Delta)$	O
0.68	0.16	1.3	0.28	0.13	0.06	0.15	0.06	0.36	0.24

The ohmic heating of the plasma electrons is obtained by solving a circuit equation for the axial electric field, i.e., $E_z = - L (dI/dt)$. Where I is the net current given by $I = I_b + \pi R^2 \sigma E_z$. Here, I_b is the beam current, σ the

conductivity and R the beam radius. The beam inductance L is often approximated⁹ by $L = 2[0.25 + \ln(d/r)]$ where $d \gg R$, a point where the conductivity falls to $C/4\pi d$.

The Electron Temperature

The plasma electron temperature is obtained by solving a time dependent equation which includes all heating and cooling terms. The source term due to the beam energy deposition is $7.5 W^{-1} 6.25 \times 10^{18} (dE/dx)j$ where W is the mean energy per ion pair ~ 34 eV., dE/dx the energy loss per unit distance and j the beam current density. The ohmic heating term is σE_z^2 . Super elastic collisions from excited states, also heat the electrons. The cooling terms include inelastic collisions which include ionization, dissociation and excitation of electronic, vibrational and rotational states. The rate coefficients for these processes are obtained using a Maxwellian electron velocity distribution¹⁰. The deexcitation rates are obtained by detailed balance. The elastic losses per electron to neutrals and ions are given by $1.5 f(T_e - T_g) v_{en}$ and $1.5 F(T_e - T_g) v_{ei}$ respectively. F is the fraction of energy loss and v_{en} and v_{in} are electron-neutral and electron-ion collision frequencies^{10,11} respectively. We consider the neutrals and ions to have the same temperature. The energy loss to rotational¹² states of N_2 and O_2 are given by $3.1 \times 10^{-12} M(T_e - T_g)(T_e)^{-0.5}$, where M is total number of molecules. An important energy loss by the plasma electrons is to the vibrational levels of N_2 , which is given below

$$\frac{d}{dt} (3/2 N_e T_e) = -0.3 N_e N_2 \sum_v v x_v [1 - \text{Exp}(-0.3/T_v)] [1 - \text{Exp}(0.3 V T_v^{-1} T_e^{-1} (T_v - T_e))] \quad (7)$$

This term is developed¹³ under the assumption that the vibrational levels are in equilibrium with a temperature T_v and that the levels are approximated by a harmonic oscillator.

The Vibrational Temperature

The vibrational temperature is obtained by solving an equation for the vibrational energy E_v , based on Eq. (7) as a source term due to electron collisions plus other sources. The sink term is given by $K[E_v - E_{vo}]$. Where E_{vo} is energy of a harmonic oscillator with $T_v = T_g$. K the vibrational-translational relaxation rate^{14,15}. Other sources contributing to the vibrational energy are quenching of the triplet states, atom-atom recombination, rearrangements, and the dissociative recombinations of N_3^+ and N_4^+ . The contributions of these processes require educated guesses as to how much vibrational quanta are added to the vibrational reservoir. It should be noted that certain atoms and molecules relax the vibrational energy faster than N_2 and O_2 . Oxygen atom is such an example¹⁶.

The Gas Temperature

The gas temperature denotes the temperature of the heavy particles (atoms, ions, molecules) and is determined by a

rate equation which accounts for all gain and loss processes. The heating of the gas occurs as a result of the direct beam and secondary electron dissociation and dissociative ionization of N_2 and O_2 . The products N^+ , O^+ are observed^{17,18} experimentally to have an average energy of ~ 3 eV. The pure dissociation produces¹⁹ atomic nitrogen with energy of ~ 0.8 eV. The dissociation of O_2 , however, depends on the excitation of the A state or the B state of O_2 . The former yields, atoms with energy of ~ 0.4 eV. While the latter will give atoms with energy of ~ 1.4 eV. Indirect processes such as the dissociative recombination of N_2^+ , O_2^+ and NO^+ produce nitrogen and oxygen atoms with energies of 1.7 and 1.74 eV, and 1.3 eV respectively. Electron elastic collisions with neutrals and ions as well as the rotational excitations of the molecules result in the heating of the gas. Additional heating sources are vibrational-vibrational and vibrational-translational relaxations. Furthermore, certain charge exchange processes also contribute to the gas heating. For example $N^+ + O_2$ gives an excess energy of ~ 3.5 eV which may end up in vibrational as well as transitional energies of the products. The atom-atom recombination and other rearrangement processes also contribute to heating. Finally the cooling of the channel occurs by expansion which can be described by pressure equilibrium and adiabatic expansion.

RESULTS

Some results are shown for a beam with 1.0 nsec risetime, a 0.2 cm radius and a current of 10 kA in one atmosphere of air. Figures 3 - 6 show species time histories. The dependence of the electric field on the beam radius is shown in Figure 7. However, the nature of the non-equilibrium plasma is shown in Figure 8 where the time histories of T_e , T_v and T_g are indicated.

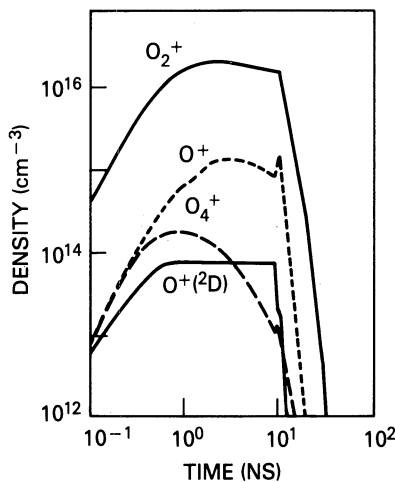


Figure 3

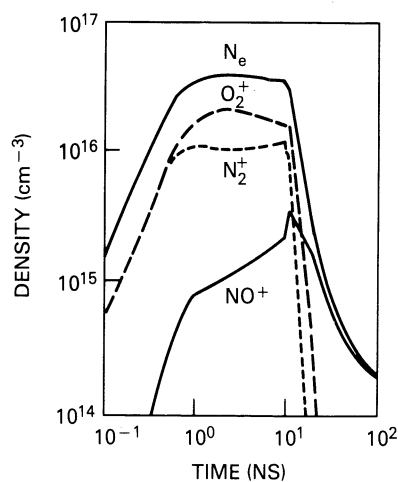


Figure 4

Acknowledgement: This work is supported by DARPA. The collaboration of my colleagues Drs. D. Strickland and S. Slinker is appreciated.

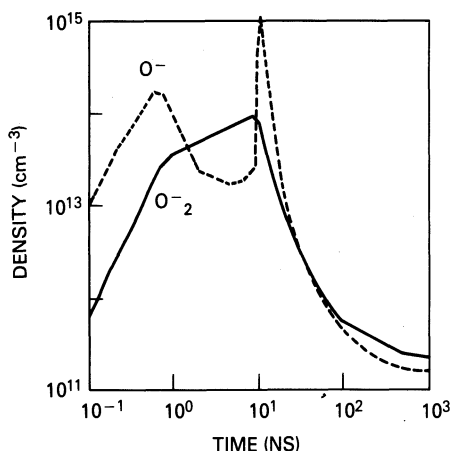


Figure 5

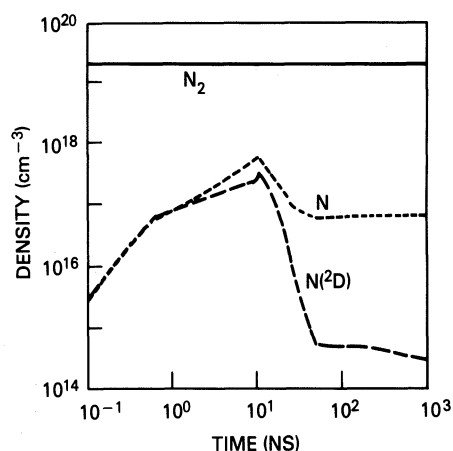


Figure 6

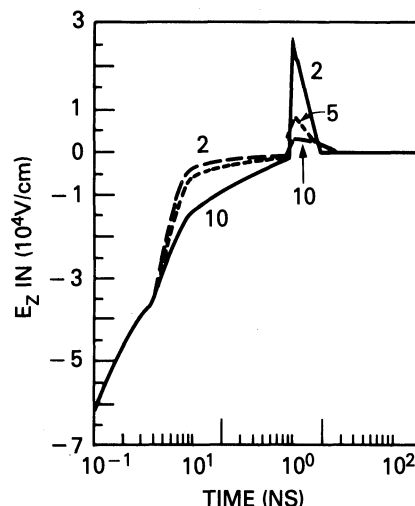


Figure 7

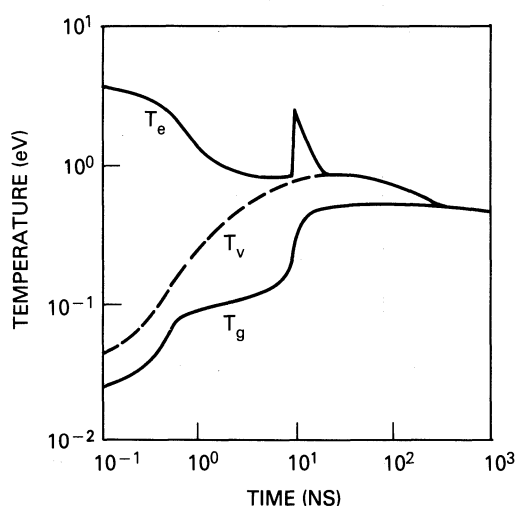


Figure 8

REFERENCES

1. A. W. Ali, On Electron Beam Ionization of Air and Chemical Reactions for Disturbed Air Deionization. Naval Research Laboratory Memo Report 4619, Washington, DC (1981)
2. A. W. Ali and S. Slinker, Electron-Beam-Generated Conductivity in N₂ and Air in Proceeding Fifth International Conference on High-Power Particle Beams, Briggs and Toepfer Eds., Beam 83, San Francisco, CA (1983)

3. L. Pages, E. Bertel, H. Joffre and L. Sklavenitis, Energy Loss, Range and Bremsstrahlung Yield for 10 KeV, to 100 Mev Electrons in Various Elements and Chemical Compounds, Atom Data 4:1 (1972)
4. D. Rapp, P. Englander-Golden and D. D. Briglia, Cross Sections for Dissociative Ionization of Molecules by Electron Impact, J. Chem. Phys., 42:4081 (1965)
5. A. W. Ali, Excitation and Ionization Cross Sections for Electron Beam and Microwave Energy Deposition in Air, Naval Research Laboratory Memorandum Report 4598, Washington, DC (1981)
6. E. C. Zipf and R. W. McLaughlin, On the Dissociation of Nitrogen by electron Impact and by E.U.V. photoabsorption, Planet. Space Sci. 26:449 (1978)
7. R. F. Fernsler, A. W. Ali, J. R. Greig and I. M. Vitkovitsky, The NRL CHMAIR Code: A Disturbed Sea Level Air Chemistry Code, Naval Research Laboratory Memorandum Report 4110, Washington, DC (1979)
8. D. K. Strickland and A. W. Ali, A code for the Secondary Electron Energy Distribution in Air and Some Applications, Naval Research Laboratory, Memorandum Report 4956, Washington, D.C. (1982)
9. F. W. Chambers, Current Multiplication During Relativistic Electron-Beam Propagation in Plasma, Physics Fluids 22: 483 (1979)
10. S. L. Slinker and A. W. Ali, Electron Excitation and Ionization Rate Coefficients for N₂, O₂, NO, N and O., Naval Research Laboratory Memorandum Report 4756, Washington, DC (1982)
11. C. L. Chen, Electron Collisions in Neon Plasma, Phys. Rev. 135:A627 (1964)
12. M. H. Mentzoni and R. V. Row, Rotational Excitation and Electron Relaxation in Nitrogen, Phys. Rev., 130:2313 (1963)
13. A. W. Ali, The Physics and the Chemistry of Two NRL Codes for the Disturbed E and F Regions, Naval Research Laboratory Report 7578, Washington, DC (1973)
14. R. D. Millikan and D. R. White, Systematics of Vibrational Relaxation, J. Chem. Phys. 39:3209 (1963)
15. A. W. Ali, The Harmonic and Anharmonic Models for Vibrational Relaxation and Dissociation of the Nitrogen Molecule, Naval Research Laboratory, Washington, DC (1986)
16. R. J. McNeal, M. E. Whitson, Jr. and G. R. Cook, Temperature Dependence of the quenching of vibrationally Excited Nitrogen by Atomic Oxygen, J. Geophy. Res., 79:1527 (1974)
17. J. A. D. Stockdale and L. Deleanu, Dissociative Ionization of O₂ and N₂ by Electron Impact - N⁺ and O⁺ Kinetic Energies and Angular Distributions, Chem. Phys. Letters, 22:204(1973)
18. R. J. Van Brunt and L. J. Kieffor, Angular Distribution of N⁺ from Dissociative Ionization of N₂ Near Threshold, J. Chem. Phys. 63:3216 (1975)
19. W. C. Wells, W. L. Borst and E. C. Zipf, Translational Spectroscopy of Metastable Fragments Produced by Dissociative Excitation of Atmospheric Gases by Electron Impact I. Nitrogen, Phys. Rev. A, 14:695 (1976)

RE-ENTRY PROBLEMS

C.Bruno¹ and L.Guarino²

¹Dip. di Meccanica, Universita di Roma
Via Eudossiana 18, 00184 Roma, Italy

²Dip. di Aeronautica, Politecnico di Milano
Via Golgi 40, 20133 Milano, Italy

INTRODUCTION

The purpose of this paper is to discuss traditional modeling of gas-gas and gas-surface interaction during re-entry, and how its shortcomings could benefit by new approaches involving classical and QM ab initio calculations.

During re-entry, an orbiting craft dissipates its kinetic energy through viscous drag. The heat generated partly flows past the body, and partly is deposited by convection and diffusion on the surface. The surface temperature, T_w , will increase, and consequently (because of radiation) thermal load will decrease. Ideally, the craft T_w should be high enough to radiate back all heat reaching its surface. Typical initial re-entry speeds are 7.6 Km/s for low orbit (=LEO), 11.2 Km/s for Earth planetary re-entry. Acceptable maximum T_w are in the 1200 - 1500 K range, with sustained hypersonic flight vehicles (such as NASP or HOTOL) requiring probably higher T_w and, likely, some form of active cooling. In essence, thermal protection systems (TPS) must have very low conductivity and high emissivity.

A craft flying at Mach numbers, M, greater than, say, 5-7, creates a bow shock capable of dissociating air into a weakly ionized plasma composed of O₂, N₂, N, O, NO, NO⁺, e⁻ for LEO re-entry, and many more ionized species for larger M in denser air layers (see, for instance, the AOTV environment in Huon's paper in this book). The first problem, in describing hypersonic flows (i.e. flows at M > 5-7) is to accurately predict air composition and species excitation past the bow shock (Park, 1985; Park and Yoon, 1989; Candler, 1989). This paper will not address this problem.

The reactive plasma past the shock is convected and diffuses toward the cooler craft surface; energy is transported toward the surface by molecular conduction, by species diffusion, and also deposited as recombination energy, since the surface acts as a catalyst for reactions such as O and N recombination and possibly for N + O → NO formation. While O, N, NO diffuse and are

convected toward and along the surface, they also react in the gas phase, due to the changing pressure and temperature fields. Both gas phase and heterogeneous reactions are energetically dominated by exothermic recombination. While dissociation is relatively well understood (Park, 1985) exothermic reactions, such as the type $O + O + M \rightarrow O_2 + M$, form molecules in a highly excited state. Similarly, surface recombination produces species that desorb while still excited. This is especially significant at lower T_w where the Eley-Rideal mechanism for atom recombination dominates (see the article by Bacal in this volume). The net energy flux entering the surface is called thermal load.

THERMAL LOAD

In the continuum regime, the net heat flux, q_w , entering the craft surface may be written (Bruno, 1989)

$$q_w = K\partial T/\partial n - \rho \sum_i^N h_i Y_i \vec{V}_i \cdot \vec{n} + q_r - \epsilon_w \sigma T_w^4 \quad (1)$$

where K is the thermal conductivity, \vec{n} is the normal to the surface, h_i, Y_i , \vec{V}_i are the total enthalpy (including formation enthalpy), mass fraction and diffusional velocity of the i -th species; q_r is the heat flux normal to the surface from the radiating gas, ϵ_w the surface emissivity.

Surface reactions influence the \vec{V}_i , since the BC for species i at the surface is

$$\rho Y_i (\vec{V}_i + \vec{V}) \cdot \vec{n} = [\rho Y_i (\vec{V}_i + \vec{V}) \cdot \vec{n}]_s + \omega_i \quad (2)$$

If the wall is macroscopically impermeable, the term inside square brackets is zero, and (2) imposes mass transported by diffusion to equate surface consumption ω_i . In essence, thermal load depends on the entire T, Y_i fields, that need to be solved using Navier-Stokes equations.

AIR CHEMISTRY

For LEO re-entry, q_r may be neglected, and the Bortner's kinetics scheme (Blottner, 1969)



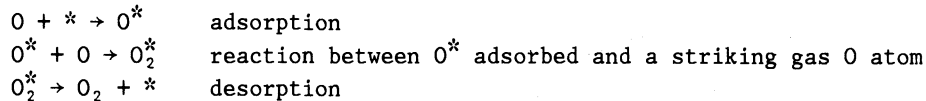
is adequate. Arrhenius kinetics is sufficient to model endothermic reactions. Exothermic reactions yield N_2, O_2 vibrationally excited. Conventional vibrational relaxation models (i.e., Landau-Teller) yields grossly inaccurate predictions (Candler, 1989). Two-temperature, or multi-temperature models have been used to simulate the [unknown] vibrational relaxation process. However, VV, VT transfer processes for N_2 ,

O_2 are still not established to the extent that appropriate modelling can be introduced in conventional Arrhenius kinetics.

From this viewpoint, classical ab initio calculations may be the beginning of a different way to approach this problem. The articles by Lagana and Billing in this volume point to the feasibility of such an approach, with full ab initio QM calculations not yet possible but becoming so a few years from now. The point is that even classical calculations have not been done yet, and would contribute greatly to progress in this area.

SURFACE CHEMISTRY

Current modelling is based on the Eley-Rideal mechanism; for O atoms this is



where adsorption is the controlling step. Accordingly, the rate ω_i in (2) is modeled via 1st order kinetics:

$$\omega_i = k_{wi} \rho Y_i \quad [k_{wi} = \text{"cataliticity"}]$$

with $k_{wi} = (\gamma_i/2 - \gamma_i)(2\pi W_i/RT_w)^{-\frac{1}{2}}$, and γ_i , the recombination probability, given by $\gamma_i = J_i, \text{rec}/J_i$, the ratio of recombining to impinging i atom fluxes.

Empirical Arrhenius fits of experimental arcjet data exist for O and N recombining separately (Scott, 1980); for instance, for O ,

$$Y_O = 16 \exp(-10271/T_w).$$

No attempt was ever made to evaluate simultaneous O and N recombination, which may yield NO (Scott, 1989).

First-principles mechanisms for recombination have never been investigated in the same sense, say, of the CO oxidation mechanism on Pt by Billing and Caciatoore and quoted in the articles by Billing and Caciatoore in this book.

A second aspect of gas-surface interaction is desorption of excited species. Halpern and Rosner (1978) built a phenomenological model for N recombination on W . This qualitatively predicts the shift from Eley-Rideal (ER) to Langmuir-Hinshelwood (LH) kinetics with increasing T_w . This shift has enormous practical importance for TPS: LH kinetics leads to desorption of molecules in thermal equilibrium with the surface, thus depositing all recombination energy and maximizing thermal load. Said otherwise, the LH accommodation factor is, typically, very close to unity. ER kinetics, instead, leads typically to $\beta < 1$, implying reduced thermal load. To-date, Halpern and Rosner's model is the only model predicting β , and applies to metal surfaces,

with clearly defined potential surfaces for the Me-O or Me-N bonds. Current and future TPS will use glassy or ceramic materials based on Si, such as SiO_2 or Si_3N_4 . The structure consists of Si-O or Si-N groups 'sticking out' and possibly reacting with O, and N (Seward, 1985; Newman, 1987). These materials definitely do not behave as metals do.

The point is that accurate thermal load prediction needs both accurate γ and β , for all species involved, and these are not available at all. In principle, there are no impediments to ab initio calculations similar to those of Billing and Cacciatore, even for SiO_2 surfaces, provided the potential surfaces are known (Billing, 1989).

EXAMPLE: FLAT PLATE IN HYPERSONIC FLOW

As an example of what conventional treatment of kinetics can do at the moment, and its shortcomings, consider the hot flow generated by a shock wave and passing over a plate 50 cm long.(Fig.1)

Air conditions at infinity correspond to re-entry conditions at ≈ 70 Km and $M = 12$. These conditions have been chosen so that vibrational nonequilibrium effects are small, and VV, VT exchanges fast, and Arrhenius kinetics data for scheme (3) may be used. The wall has been assumed catalytic not only for O, N recombinations but also for the $O + N^* \rightarrow NO$ reaction, also possible and energetically interesting (the $O^* + N \rightarrow NO$ is also included in this new scheme of gas/surface interaction, but gas N concentration is too low to yield significant NO rates). The ratio $Z = k_{w5,o}/k_{w1}$ between catalyticities of the $N^* + O \rightarrow NO$ and the $O^* + O \rightarrow O_2$ surface reactions is a

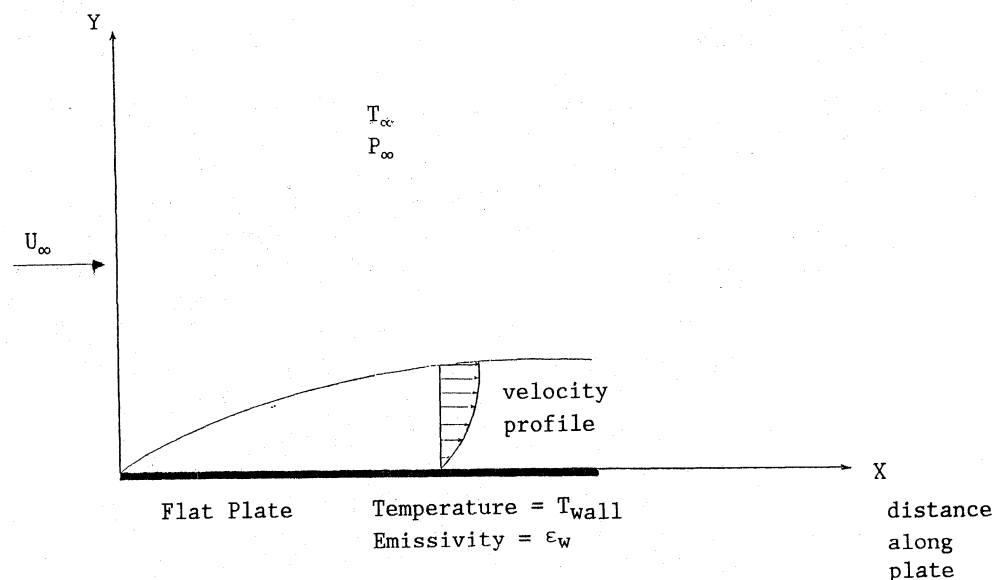


Fig. 1

GEOMETRY AND PARAMETERS OF PROBLEM

parameter defining the relative importance of the two (O-competitive) kinetics.

Fig. 2a and 2b show wall profiles at a fixed x for O and NO species for $Z=0$ (no heterogeneous NO formation) and $Z=1$ (same catalyticicity for O_2 and NO formation). The effect on O, NO mass fractions at the wall is significant: $Z=1$ creates a thin sublayer where NO grows steeply from the lower values in the gas due to the Zel'dovich mechanism (reactions 3-ii to 3-iii).

Fig. 3 shows how $Y(O, Z=1)/Y(O, Z=0)$ changes along the plate and with T_w . The effect of Z is stronger at higher T_w due to the faster NO formation that further depletes the surface of O atoms.

The effect of kinetics on thermal load is illustrated in Fig. 4-7, for the portion of the heat flux of interest for this work, i.e., that due to diffusional transport. Fig. 4 illustrates the total power reaching the plate vs the $k_{ws,o}$ catalyticicity. The nearly linear behaviour implies macroscopically important changes of heat flux varying with NO catalyticicity.

Fig. 5 reports total power transported vs T_w for $Z=1$. and $Z=0$. The expected increase with T_w due to faster diffusion. (proportional, roughly to the 1.7 power of T) and kinetics is magnified by assuming NO heterogeneous formation. Likewise, Fig. 6 shows the % increase in power transported as a function of Z . The effect of $Z \neq 0$ is larger at lower T_w .

Finally, the effect of the accomodation factor $\beta = \beta_O = \beta_{NO}$ on diffusional heat flux along the plate is indicated in Fig. 7. Lower β , accordingly,

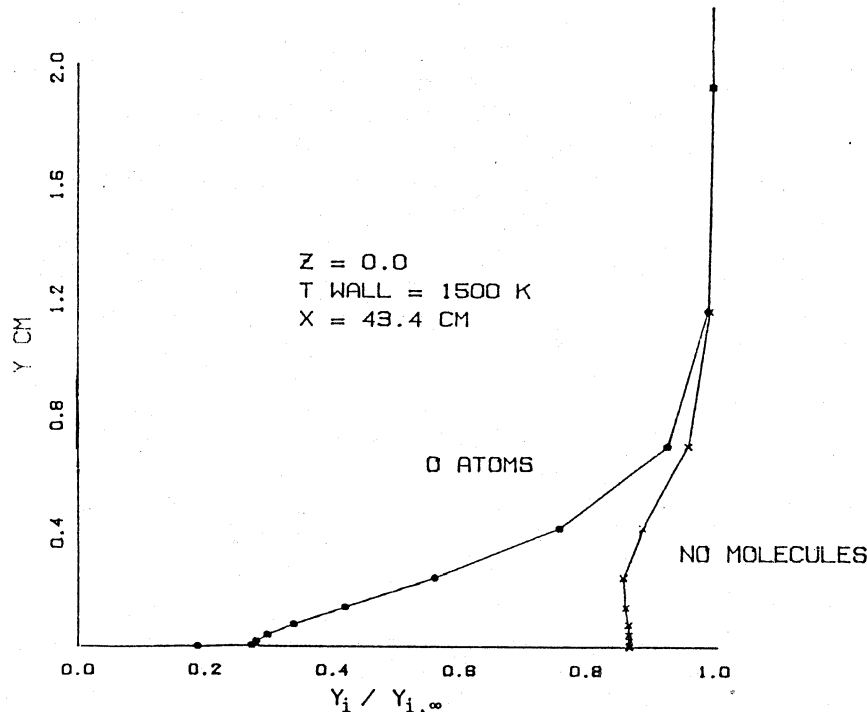


Fig. 2a

RELATIVE MASS FRACTION $Y_i/Y_{i,∞}$ VS Y , DISTANCE FROM WALL

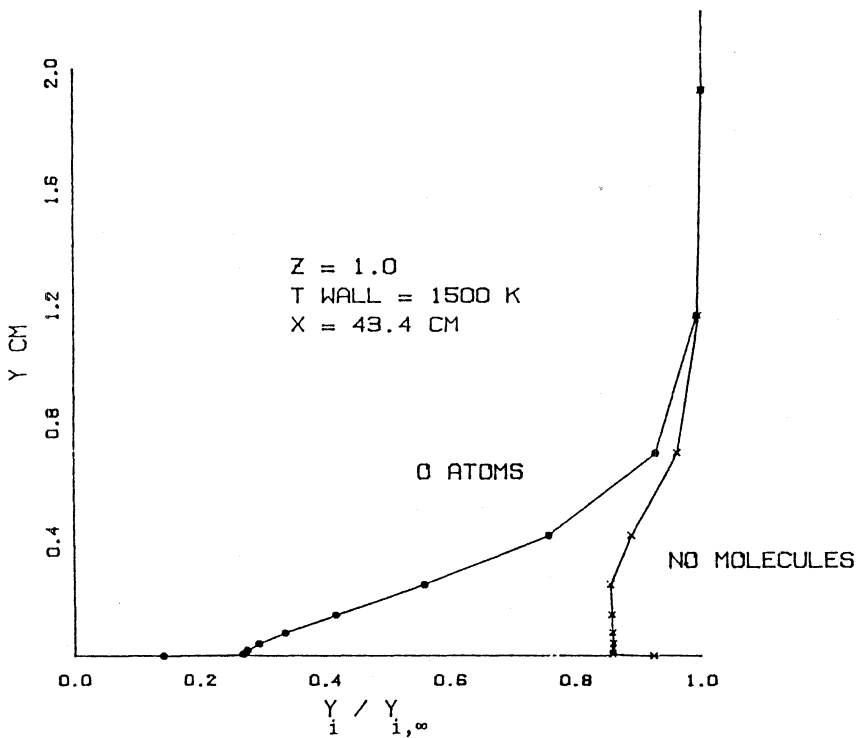


Fig. 2b

RELATIVE MASS FRACTION $Y_i/Y_{i,\infty}$ VS Y , DISTANCE FROM WALL

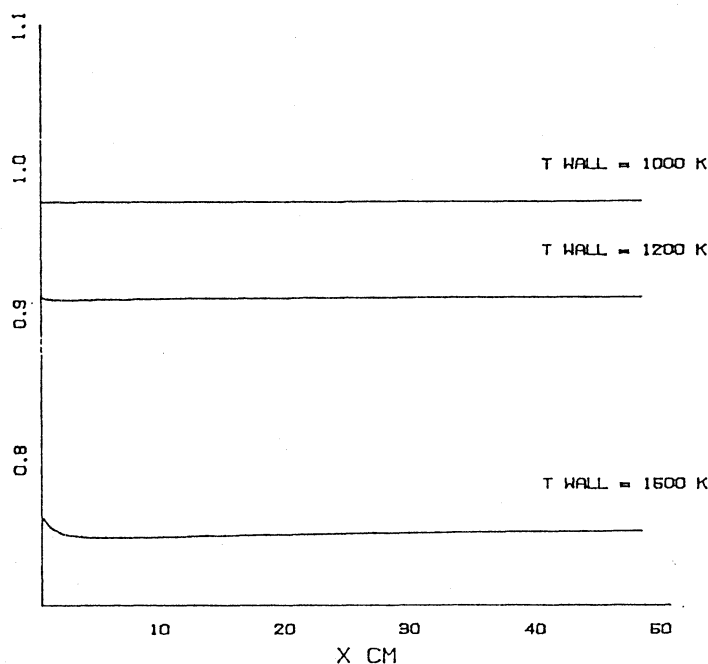


Fig. 3

O MASS FRACTION ($Z=1.0$) AT THE WALL RELATIVE
TO O MASS FRACTION ($Z=0.0$) AT THE WALL

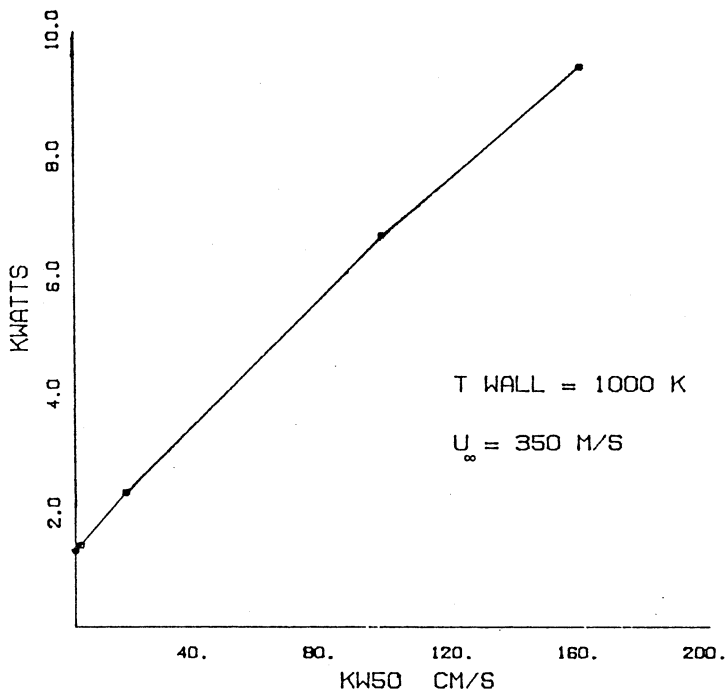


Fig. 4
HEAT BY DIFFUSION

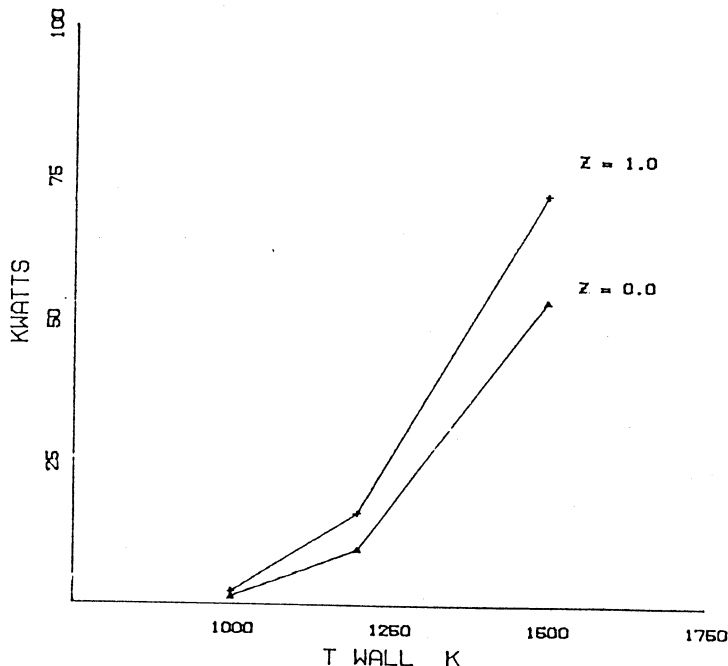


Fig. 5
HEAT BY DIFFUSION

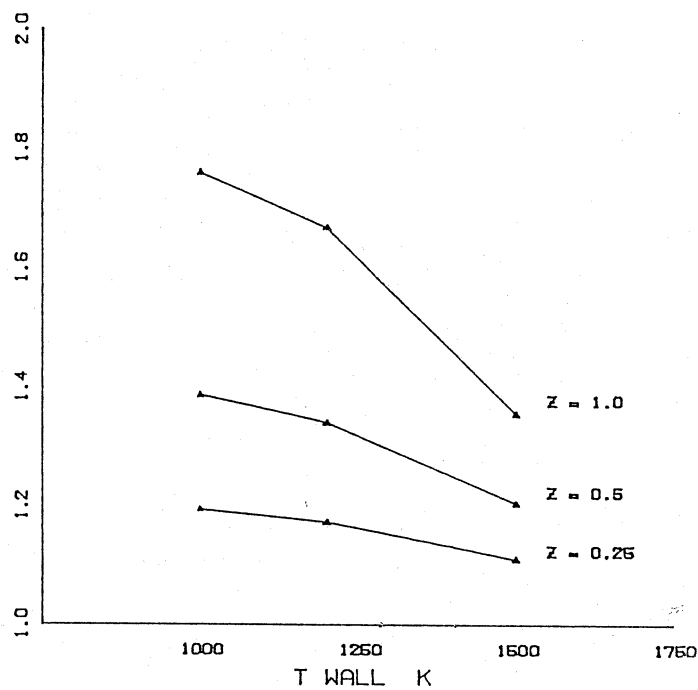


Fig. 6

HEAT BY DIFFUSION ($Z=0.0$) RELATIVE TO HEAT BY DIFFUSION ($Z=0.0$)

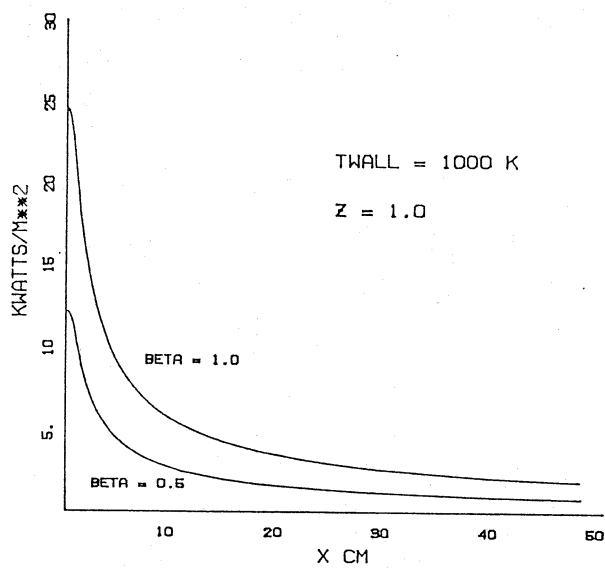


Fig. 7

HEAT FLUX BY DIFFUSION

give rise to lower fluxes. The assumption has been made of relaxation times for excited O₂, NO, N₂ long compared to residence time over the plate, of order L(=50 cm)/U_∞.

CONCLUSIONS

The impact of choosing values for k_w (or γ), Z and β in the 2-D Navier Stokes calculations reported and in the resulting thermal loads is large for re-entry applications, where a 20% change in thermal load estimates may lead to complete redesign, or alternatively, failure, of the structure. Unfortunately, for lack of better physical information, these quantities must be treated at present as unknown parameters.

Thus, besides the need for VV, VT processes description in the gas phase, substantial progress in understanding realistic re-entry flows (and especially the thermally crucial gas-surface interaction) would result from first principles modeling using ab initio calculations. It is hoped that closer interaction between specialists in this area and in that of traditional gas-dynamics will do much toward this goal.

ACKNOWLEDGEMENTS

Acknowledgement is given to CNR-CNPM laboratories, which provided computational facilities and to Bernadine Ooi who kindly typed the manuscript.

REFERENCES

- Billing, G., 1989, personal communication.
- Blottner, F.G., 1969, "Viscous Shock Layer at the Stagnation Point with Nonequilibrium Air Chemistry", AIAA J., vol.8, no.2, p.193.
- Bruno, C., 1989, "Modeling Catalytic Recombination Heating at Hypersonic Speeds", by C. Bruno, Invited Paper 89-0309, presented at the AIAA 27th Aerospace Sciences Meeting, Reno, Nevada, Jan. 8-12, 1989.
- Candler, G., 1989, "On the Computation of Shock Shapes in Nonequilibrium Hypersonic Flows", AIAA Paper 89-0312.
- Halpern, B., and Rosner, D.E., 1978, "Chemical Energy Accommodation at Catalyst Surfaces", J. Chem. Soc., Faraday Trans. I. Vol. 74, p. 1883.
- Newman, M., 1987, "A Model for Nitrogen Atom Recombination on a Silicon Dioxide Surface", Thesis, AFIT/DS/AA/85-1. School of Engineering, Air Force Institute of Technology (AU), Wright-Patterson AFB, Ohio.

Park, C., 1985, "Problems of Rate Chemistry in the Flight Regimes of Aeroassisted Orbital Transfer Vehicles", in: Thermal Design of Aeroassisted Orbital Transfer Vehicles, ed. by H.F.Nelson, AIAA Progress in Astr. and Aeron. Series, Vol. 96, AIAA, New York, p. 538.

Park, C., and Yoon, S., 1989, "Calculation of Real-Gas Effects on Blunt-Body Trim Angles", AIAA Paper 89-0685.

Scott, C.D., "Catalytic Recombination of Nitrogen and Oxygen on High-Temperature Reusable Surface Insulation", AIAA Paper 80-1477.

Scott, C.D., 1989, personal communication.

Seward, W.A., 1985, "A Model for Oxygen Recombination on a Silicon Dioxide Surface". Dissertation, AFIT/DS/AA/85-1. School of Engineering, Air-Force Institute of Technology (AU), Wright-Patterson AFB, Ohio.

DIAGNOSTICS OF ATOMIC SPECIES NEAR THE ELECTRODES OF A FLUORESCENT LAMP

A. K. Bhattacharya

GE Lighting, Nela Park, Cleveland, Ohio 44112

INTRODUCTION

Our knowledge of fluorescent lamps has been considerably enhanced by the application of novel diagnostics to Ar-Hg positive columns.¹⁻⁶ Unfortunately, our understanding of the arc column's interaction with the electrode surface is meager. Electrodes in a fluorescent lamp are tungsten coils coated with a mixture of Ba-Sr-Ca oxides containing small amounts ($\sim 2\text{-}4\%$) of Zr or ZrO_2 . Under normal operating conditions, the temperature of the electrode is fairly high ($\sim 1350\text{-}1450\text{ }^\circ\text{K}$),⁷ which results in the loss of emission material by thermal evaporation and sputtering under ion bombardment. The loss of the emission mix increases the work function for electron emission from $\sim 2.2\text{ eV}$ for such oxide coated electrodes to 4.5 eV for W. Consequently, when all the oxide coating disappears from the electrode surface the lamp fails to start, and defines end of life.

OPTICAL EMISSION

Some of the elements coming off the hot electrode surface undergo excitation and ionization by collision with the electron cloud near the electrode. In the past, several attempts have been made to relate the intensities of atomic radiation — 553.5 nm (BaI), 455.4 nm (BaII) and 460.1 nm (SrI) — emanating from the vicinity of electrodes of an operating lamp to the number densities of the radiating species, and hence to the consumption rate of the emission mix from electrodes.⁸⁻¹⁰ The intensity of 553.5 nm of neutral barium (BaI) measured at a distance of 2 mm in front of an electrode as a function of the lamp current phase angle is shown in Fig. 1. As discussed later, the conclusion drawn from such a measurement gives the erroneous result that the population of various species released from the electrode is higher when the electrode is a cathode. As a matter of fact, the loss of emission mix from electrodes of a lamp operating on 50/60 Hz power line occurs predominantly during the time the electrode acts as an anode. The major disadvantages of this method are its reliance upon the excitation of the species in the electrode fall region of an operating lamp, and the strong dependence of the spectral emission intensity on electrode polarity.

ATOMIC ABSORPTION

A simple evaporation-diffusion model, in conjunction with the atomic absorption technique, may be used to estimate the evaporation rates of different species from the electrode.¹¹ The density, $n(r)$, of Ba atoms at a distance r evaporating from an infinitely long cylindrical electrode coated with an Ba-Sr-Ca oxide is given by the equation,

$$\frac{1}{r} \frac{d}{dr} \left(r \frac{dn}{dr} \right) = 0. \quad (1)$$

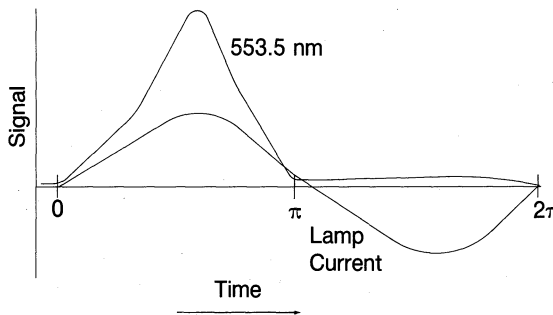


Figure 1. Optical emission at 553.5 nm (BaI) and lamp current.

The solution to Eq. (1) has to satisfy the following boundary conditions: (1) The number density of Ba atoms must be zero at the wall, i.e., $n(r) = 0$ at $r = R_+$, and (2) the net flux of atoms leaving the surface of the cylindrical filament must be determined by the difference in particle flow due to evaporation and back diffusion onto the surface, i.e., at $r = a$,

$$\Gamma_{r=a} = -D \frac{dn}{dr} = \left[4.39 \times 10^{21} G - \frac{v}{4} n(r) \right] \quad (2)$$

where D is the diffusion constant of Ba in the fill gas, G ($\text{gm}/\text{cm}^2/\text{sec}$) is the rate of evaporation of Ba from the electrode surface in vacuum determined by its vapor pressure, and v (cm/sec) is the average thermal velocity of Ba atoms near the cathode surface. The first term on the RHS of Eq. (2) represents the number of atoms leaving the surface by evaporation, and the second term accounts for the atoms returning back onto the electrode surface. The value of the diffusion constant for Ba in Ar at 2.4 Torr may be calculated by the Chapman-Enskog method, and it has a value of $D = 236 \text{ cm}^2/\text{s}$ at 1050°K .²²

The solution of Eq. (1) obtained by integrating twice and applying the two boundary conditions at $r = R$ and $r = a$ is,

$$n(r) = \frac{4.39 \times 10^{21} G}{\left[\frac{D}{a} + \frac{v}{4} \ln(r/a) \right]} \ln\left(\frac{R}{r}\right). \quad (3)$$

The number density of Ba atoms near a hot electrode may be determined by measuring the absorption of its resonance radiation 553.5 nm.

The absorber number density is obtained by measuring the absorption, k_0 , of the resonance radiation at the line center. The measured absorption depends upon the overlap of the source emission profile and the absorption line shape of the absorber. A knowledge of the absorber to source line width ratio is essential for determining the absolute number density. The absorption, A , of the resonance radiation 553.5 nm, passing through an atmosphere of Ba vapor is defined as,

$$A_\alpha = 1 - \frac{\text{Transmitted Radiation}}{\text{Incident Radiation}} = \frac{\int I_\nu (1 - e^{-k_\nu \ell}) d\nu}{\int I_\nu d\nu}, \quad (4)$$

where I_ν is the frequency distribution of the incident radiation from the source, k_ν is the absorption coefficient of the absorbing gas of thickness ℓ . The measured value of the absorption,

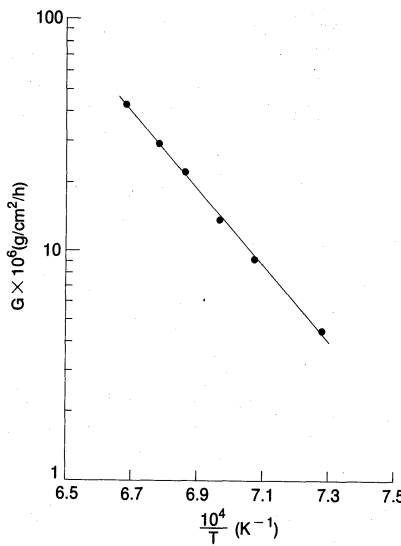


Figure 2. Ba evaporation rate as a function of electrode temperature

A_α is given by ¹³

$$A_\alpha = \sum_1^n (-1)^{n-1} \frac{(k_0 \ell)^n}{n! \sqrt{1+n\alpha^2}}, \quad (5)$$

where $\alpha = (\text{Emission line width})/\text{Absorption line width}$. For a Doppler broadened absorption line of width $\Delta\nu_d$, the maximum absorption coefficient k_0 is given by the relation,¹³

$$k_0 \Delta\nu_d = \sqrt{\frac{\ln 2}{\pi}} \frac{\lambda_0^2}{4\pi} \frac{g_2}{g_1} A^* n, \quad (6)$$

where, $\lambda_0 \Delta\nu = 2\sqrt{2R\ln 2}(T_g/M)^{1/2}$, A^* is the transition probability for radiation from the excited state, n is the number density of Ba, and g_1 and g_2 are the statistical weights of the ground and the excited state atoms, respectively. The number density near a hot electrode is determined by measuring the absorbance A for the resonance radiation, and computing a value of k_0 (for a predetermined value of α), and calculating n using Eq. (6). The average gas temperature T_g may be assumed to be equal to 0.75 times the electrode temperature T . The atomic parameters are obtained from reference (15). The evaporation rate G can be determined as a function of temperature by measuring the Ba number density near the hot electrode and using relation (3).^{11,15}

The measured variation of G for Ba from a Ba-Sr-Ca oxide (with ZrO_2 additive) coated electrode as a function of electrode temperature is shown in Fig. 2. It follows a relation of the form

$$\log G = -\frac{16530}{T} + 6.66. \quad (7)$$

Barium number density near a 40W lamp electrode was determined from the absorption of a collimated beam of 553.5 nm radiation passing through a clear window in the lamp in a plane parallel to the electrode. The electrode was heated by passing a current through it, and the average electrode temperature was determined from the hot-to-cold resistance ratio of tungsten.¹⁶ The electrode temperature determined the evaporation rate of Ba, and hence the Ba number density, near the electrode. The number densities of Ba at $r = 2$ mm from the electrode were measured as a function of the electrode temperature. The evaporation rates G was calculated assuming values for $\alpha = 1$, $R = 1.9$ cm, $T_g = T$, and $a = 0.031$ cm and Eqs. (3) and (6).

LASER INDUCED FLUORESCENCE

A complete mathematical analysis of the laser induced fluorescence scheme, including all the radiative and collisional processes, for an atomic system such as Ba is very complicated. The theory for the LIF technique and the energy level diagrams for neutral and ionized Ba atoms are presented in references (17) and (18). The energy levels for both neutral and ionized barium atoms may be approximated by an atomic system of three levels. It is assumed that the levels are coupled radiatively only, and the laser induced transitions and radiative decay processes are much faster than the collisional excitation/de-excitation rates in low pressure arcs. A radiation source pumps atoms from ground level 1 (BaI: 6^1S_0 and BaII: $6^2S_{\frac{1}{2}}$) → level 2 (BaI: 5^1P_1 and BaII: $6^2P_{\frac{3}{2}}$), which undergoes radiative decay to the ground level 1 and to level 3 (BaI: 5^1D_2 and BaII: $5^2D_{\frac{3}{2}, \frac{5}{2}}$).^{18,19} The lower level 3 is assumed to have an infinitely long life time compared to the duration of the laser pulse. The laser wavelength is tuned to the transition $1 \rightarrow 2$, and the fluorescence signal due to the transition $2 \rightarrow 3$ is detected. A 5–10 ns wide laser signal from a YAG pumped dye laser was used as an excitation source, and a box-car integrator was used for measuring the LIF signal (BaI: 582.6 nm, and BaII: 614.2 nm). The temporal behavior of the laser radiation is treated as a step function, and the laser intensity is assumed to be constant over the beam diameter.

The population of the various states under the laser excitation are obtained from a set of two coupled rate equations.¹⁷ The temporal intensity profile for the laser pulse is approximated by a step function, $\rho(\nu_0, t) = \rho_0$ for $t \geq 0$, and $\rho(\nu_0, t) = 0$ for $t \leq 0$. The LIF signal V_f (recorded by the box-car system) for transition $2 \rightarrow 3$ is given by the expression,

$$V_f = G V \Omega \frac{\hbar\nu}{\pi} \left(\frac{g}{g+1} \right) A N I, \quad (8)$$

where G , V , and Ω are, respectively the electrical gain of the detector, the focal volume, and the solid angle defined by the collection optics and the laser beam. The values for A are respectively $0.97 \times 10^8 \text{ sec}^{-1}$ for $5^1P_1 \rightarrow 5^1D_2$ transition in BaI and $0.37 \times 10^8 \text{ sec}^{-1}$ for $6^2P_{\frac{3}{2}} \rightarrow 5^2D_{\frac{5}{2}}$ transition in BaII.^{14,20} The value for constant I is evaluated for the width of the detector gate, T_b , from the expression,

$$I = \int_0^{T_b} n_2(t) dt. \quad (9)$$

The population, n_2 , of upper level 2 after cessation of the laser pulse, duration T , is given by the relation,

$$n_2(t) = n_2(T) e^{-t/\tau_3}, \quad (10)$$

where

$$n_2(T) = \left(\frac{g}{g+1} \right) N \left\{ 1 - e^{-T/\tau_1} \right\} e^{-T/\tau_2}, \quad (11)$$

$1/\tau_1 = (g+1)B\rho_0 + A_{21} + A_{23}$, $1/\tau_2 = gB\rho_0 A_{23}/[(g+1)B\rho_0 + A_{21} + A_{23}]$, $1/\tau_3 = (A_{21} + A_{23})$, and Einstein's coefficient $B = (A_{21}\lambda^3/8\pi h)$ For high excitation intensities and low atomic densities, the measured fluorescence intensity is directly proportional to total Ba number density, and is independent of the source intensity.

The LIF signals for neutral (582.6 nm) and ionized (614.2 nm) Ba atoms in the vicinity of a 40W lamp electrode operating on a commercial ballast are shown in Fig. 4. The positive polarity of the lamp current represents the direction of the current flow. The experimental arrangements for LIF measurements for neutral and ionized Ba atoms are discussed in detail in references (21) and (22), respectively. A YAG-pumped dye laser was used as the excitation source and LIF signals were recorded by a box-car integrator. Electrodes of the lamp (1.5 in diam. filled with 2.5 Torr of argon and approx. 60 mTorr of Hg) were coated with a mixture

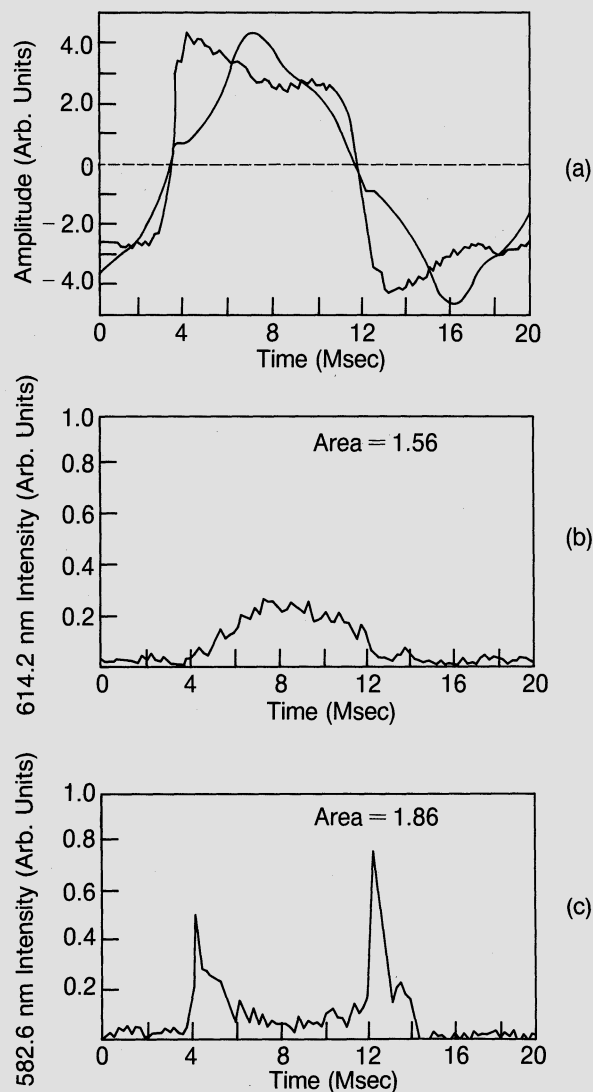


Figure 3. Time dependence of (a) lamp current and voltage, (b) Ba ion signal (614.2 nm), and (c) Ba neutral signal (582.6 nm) for a 40W lamp.

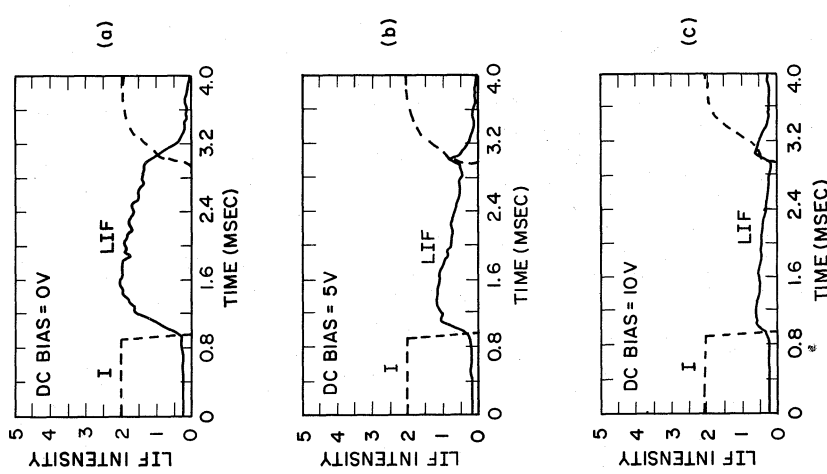


Figure 5. Barium ion measured near cathode during current off period for bias potentials of (a) 0 V, (b) 5 V, and (c) 10 V.

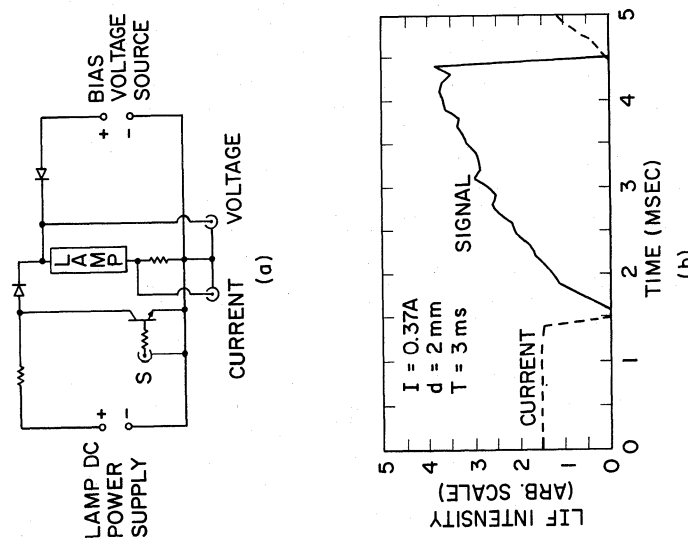


Figure 4. (a) Schematic diagram for dc current interrupt circuit, and (b) Neutral Ba measured near cathode during current off time.

of Ba-Sr-Ca oxides. The heating of the lamp electrode is caused by the auxiliary "cathode" voltage (3.6 V) and the lamp current. Calculation and pyrometric measurements show that the temperature of the electrode hot spot does not vary with the ac-cycle due to its the large thermal mass.⁷ Therefore, emission mix is liberated from the electrode at a constant rate over the entire ac-cycle. The observed variation of LIF signals during the ac-cycle are due to the varying degree of ionization of Ba by the lamp current in the electrode fall (cathode and anode) region. There are significantly more neutral and ionized Ba atoms present near the electrode when it is acting as an anode (positive polarity) than when it is a cathode (negative polarity). A relatively large fraction of atoms near the electrode are ionized in the cathode half cycle due to high electrode fall (15 – 20 V),² and a very low neutral population is detected. However, the majority of ions are then pulled back onto the cathode surface (negative potential), and therefore, very few ions are present to be detected by the laser beam. On the other hand, the electrode fall near an anode is fairly low and therefore, a relatively small fraction of neutrals are ionized, and a significantly larger population of neutral Ba is detected in the anode half-cycle. Also, since the neighboring electrode is now at a positive potential, no sweeping of ions occurs, and also a larger number of ions are detected by the laser beam. The temporal behavior of the Ba ion signal follows the shape of the lamp current wave form in the anode half-cycle very closely. This indicates that the production rate of Ba ions is determined by the discharge current. The relative number densities for Ba I and Ba II estimated from the areas under the LIF vs. time curves indicate that the population of neutrals is about 40% that of ionized Ba.

The application of the LIF technique to Sr atoms near the electrode by exciting the $5^1S_0 \rightarrow 5^1P_1$ transition with 460.7 nm radiation shows a temporal behavior for Sr signal with the current phase angle very similar to that observed for Ba. The number densities of neutral Ba and Sr as well as the ionized Ba atoms in the vicinity of the electrode increase with the arc current because of the increased thermal evaporation from the electrode.^{17,18} Optical pyrometric measurements show that the electrode temperature also increases with the lamp current.

The action of the cathode fall potential on the ionization rate of Ba and the "sweeping" action on Ba ions are clearly observed by operating a lamp on dc and using a current interrupt circuit shown schematically in Fig. 4(a). An application of a positive pulse (0 - 4 ms duration) to the transistor switch S shorts the dc power source and interrupts the current through the lamp, and impresses a dc bias across the lamp.²¹ As in the case of ac operation no measurable amount of either neutral or ionized Ba are detected near the cathode. However, as shown in Figs. 4(b), and 5(a), when the lamp current is interrupted for a short time, large LIF signals are detected. The signal goes down to zero immediately after the current clamp is removed and the lamp current is established. This clearly shows that the majority of Ba atoms near the cathode are ionized in cathode fall and the negative glow regions, and therefore are not detected. The effect of current interruption and the bias voltage on Ba ion density is clearly seen in Fig. 5. The interruption of the lamp current causes the removal of the negative potential on the electrode, and Ba ion population increases during the period when the potential across the lamp is removed. The initial increase in the ionized Ba atom density is due to the removal of the negative potential from the electrode, and the subsequent decrease in the signal is caused by the lowering of the ion density due to diffusion loss. The application of negative potentials to the neighboring electrode and the sweeping action on the ions is apparent from the steady decrease in the signal intensity with increasing negative potential (0 – 10 V).

CONCLUSIONS

The laser induced fluorescence (LIF) technique is an ideal non-intrusive tool for investigating the dynamics of species in the vicinity of discharge lamp electrodes. The main advantages of the LIF technique are: (1) the evaporation of materials from a heated electrode can be measured without the arc on, (2) the removal rates can be determined independent of the electrode's polarity, and (3) the population of the various species can be determined as a phase of the discharge current by using appropriate signal averaging schemes. A calibration of the LIF signal against the absorption measurement will allow determination of the atomic number densities of the various species near the electrode of an operating lamp.

ACKNOWLEDGEMENTS

Much of the work described above was done over the last few years in collaboration with several of my colleagues, especially, Al Awadallah. The active support for this work by the management of GE Lighting is gratefully acknowledged.

REFERENCES

1. W. Elenbaas, "Light Sources," Crane, Russak & Co, New York, NY (1972).
2. J.F. Waymouth, "Electric Discharge Lamps," The MIT Press, Cambridge, MA (1971).
3. P.E. Moskowitz, Novel laser diagnostics for rare gas low pressure discharges, Appl. Phys. Lett. 50:891 (1987).
4. L. Bigio, Density measurements of $Hg(6^3P_{0,1,2})$ in a discharge using saturated laser absorption and hook method, J. Appl. Phys. 63:5259 (1988).
5. L. Bigio and J.T. Dakin, Wall induced inhomogeneties in the low-pressure Hg-Ar positive column, J. Appl. Phys. 63:5270 (1989).
6. L. Bigio and J.T. Dakin, Radial variations of $Hg(6^3P_J)$ in a narrow-diameter low pressure Hg-Ar discharge, J. Appl. Phys. 65:375 (1989).
7. T.F. Soules, et al., Thermal model of the fluorescent lamp electrode, To be published in IES (1989).
8. B. Kuhl, Über das verhalten von oxydkathoden in der niederdruckentladung, in Tech.-Wiss. Abh. Osram-Ges, Ed. W. Meyer, 7:84 (1958).
9. Von E. Krautz, Spektroskopische untersuchungen des verhaltens von oxydkathoden in gasentladungen, Z. Naturforsch 6A:16 (1951).
10. G Lakatos and J. Bito, Evaporation rate of oxide coated cathode, Br. J. Appl. Phys. 15:189 (1964).
11. A.K. Bhattacharya and A. Awadallah, Barium density measurement in the vicinity of oxide coated electrodes, Bull. Am. Phys. Soc. 33:138 (1988).
12. R.B. Bird, W.E. Stewart, and E.N. Lightfoot "Transport Phenomenon", John Wiley & Sons, Inc. New York (1960).
13. A.C.G. Mitchell and M.W. Zemansky, "Resonance Radiation and Excited Atoms", University Press, Cambridge, London (1961).
14. B.M. Miles and W.L. Weise, Critical evaluation of transition probabilities for BaI and BaII, Atomic Data 1:1 (1969).
15. A.K. Bhattacharya, et. al. To be published.
16. A.K. Bhattacharya, Measurement of barium loss from a fluorescent lamp electrode by laser induced fluorescence, To be published in J. Appl. Phys. 65: (1989).
17. A.K. Bhattacharya, Measurement of barium ion density in the vicinity of fluorescent lamp electrodes, To be published in J. Appl. Phys. 65: (1989).
18. A.K. Bhattacharya, Measurement of barium loss rate from oxide coated electrodes by laser induced fluorescence. XVII Int. Conf. on Phenomenon. in Ioniz. Gases, Budapest, HO-7, pp.I-473 (1985).
19. P.G. Hlahol and A.K. Bhattacharya, Measurement of barium ion density in the vicinity of fluorescent lamp electrodes by laser induced fluorescence, Bull. Am. Phys. Soc. 32:114 (1987).
20. L. Jahreiss and M. C. E. Huber, Ba oscillator strengths from a laser-excited vapor, Phys. Rev. A31:692 (1985).
21. J.M. Anderson, Measurement of zero-field electron thermal emission into a low-pressure arc, Bull. Am. Phys. Soc., 29:149 (1984).

EXCITED STATE DIAGNOSTICS IN HIGH PRESSURE ARC LAMPS

Dimitrios Karabourniotis

Department of Physics
University of Crete
Iraklion, Crete, Greece

INTRODUCTION

Information on the population of excited states in an arc discharge can be obtained from spectral line emission. A line may be optically thin (optical depth much less than unity) or optically thick (optical depth much higher than unity). In a plasma where inhomogeneity and strong reabsorption of radiation are present an optically thick line undergoes self-reversal. Commonly one uses optically thin lines to determine the density of the upper state of the line producing transitions. Then, assuming local thermodynamic equilibrium (LTE), the distribution of population among energy levels can be deduced, if the ground state population is known. Validity of LTE is equivalent to the existence of a local thermodynamic temperature.

When conventional spectroscopic methods based on optically thin lines are impractical, self-reversed emission lines can be used for plasma diagnostics. The shape of spectral lines with consideration of self-absorption and plasma inhomogeneity emitted by an axisymmetric arc (Fig. 1) can be found by solving the integral form of the equation of radiative transport in an absorbing medium

$$I(v) = \int_{-R}^{+R} \epsilon(v, r) \exp \left[- \int_r^{+R} \kappa(v, r') dr' \right] dr, \quad (1)$$

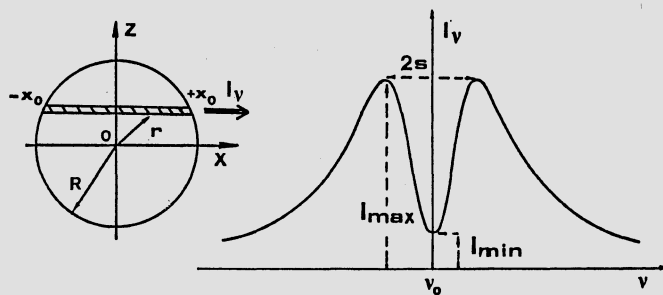


Fig. 1 Coordinate system and key parameters for a self-reversed line.

where $I(v)$ is the radiated line intensity, $\epsilon(v,r)$ the emission coefficient and $\kappa(v,r)$ is the absorption coefficient. In Eq.(1) the absorption decreases with the frequency distance to the line center; consequently the plasma from optically thick around the line center becomes optically thin in the far wings.

The only practical way of line-shape calculation is to approximate the complex plasma state by simplified models. Many phenomenological models for the line self-absorption in inhomogeneous plasmas have been proposed.¹⁻⁷ A detailed discussion of the Bartels and the Cowan-Dieke models has been given by Karabourniotis.⁸ These two models have found applications in the diagnostics of optically thick plasmas.^{9,10} In particular, an approach evolved from the Cowan-Dieke model has been used in the determination of the plasma temperature¹¹, the partial pressure of emitting species¹², and more recently, in the study of deviations from excitation equilibrium.¹³⁻¹⁷

We report here results concerning the deviations from Boltzmann equilibrium of the low-lying Hg 6^3P levels in mercury arcs used as light sources. The method used for the analysis of a self-reversed line and the determination of the required line and plasma parameters will be described.

ANALYSIS OF SELF-REVERSED LINES

According to Cowan and Dieke for a position-independent line profile the shape of a self-reversed line e^2a ($a < e$) depends on i) the line profile $P(v)$, ii) the optical depth p at the line center (absorption parameter), given by

$$p = (hv/c)B N_a P(v_0), \quad (2)$$

and iii) the excitation function $E(y)$, defined by

$$E(y) = \bar{n}_e(r)/\bar{n}_a(r), \quad (3)$$

with $y = \int_r^R \bar{n}_a(r') dr'$, $\bar{n}_a(r) = n_a(r)/N_a$, $\bar{n}_e(r) = n_e(r)/N_e$, $2N_a = \int_{-R}^R n_a(r) dr$, $N_e = \int_{-R}^R n_e(r) dr$,

where $n_j(r)$, $j=e,a$ is the population density of the j excited state, and B the transition probability for absorption. Thus, Eq.(1) may be written in the form

$$I(u) = S_v(0) \cdot K_\mu, \quad (4)$$

where

$$S_v(0) = (2hv^3/c^2) (g_a/g_e) [n_e(0)/n_a(0)], \quad (5)$$

is the "source function" at the arc axis,

$$K_\mu = \mu \int_0^2 \frac{E(y)}{E(1)} \exp(-\mu y) dy, \quad (6)$$

and

$$\mu = p[P(u)/P(o)], \quad u=v-v_o. \quad (7)$$

The optical depth q at the line maxima I_{\max} (Fig.1) can be deduced from the condition for reversal

$$\int_0^2 (1-qy)E(y)\exp(-qy) = 0. \quad (8)$$

The optical depth p at the line minimum I_{\min} (Fig.1) can be deduced from

$$(I_{\max}/I_{\min}) = (q/p) (K_q/K_p). \quad (9)$$

According to Cowan-Dieke, $E(y)$ may be approximated by

$$E(y) = \frac{n}{2} \times \begin{cases} y^{n-1} & 0 \leq y \leq 1 \\ (2-y)^{n-1} & 1 \leq y \leq 2 \end{cases}, \quad (10)$$

with $E(1) = n/2$. Therefore, the so-called inhomogeneity parameter n is given by

$$n = 2[\bar{n}_e(o)/\bar{n}_a(o)]. \quad (11)$$

Assuming further a dispersion line profile, one obtains

$$q/p = (s_o^2 + 1)^{-1}, \quad (12)$$

with $s_o = s/\delta$, where $\pm s$ is the frequency distance to the line center, where reversal occurs, and δ is the HWHM of $P(u)$. The calculated dependence of $\log(I_{\max}/I_{\min})$ vs $\log(2s_o)$ for a given value of n is almost linear.¹¹ Experimental data determining the ratio I_{\max}/I_{\min} and the wavelength separation $2s$ between the line maxima can be obtained by recording the lines emitted at different distances to the arc axis. The slope of $\log(I_{\max}/I_{\min})$ vs $\log(2s)$ plot for these data (Fig.2) can be used to determine the inhomogeneity parameter n . From Eqs.(8) and (10) the value of q is then calculated, while the value of p can be deduced from the value of I_{\max}/I_{\min} for a diametral scan according to Eq.(9). For the same scan the measurement of the wavelength distance $2s$ can be used to determine the value of δ from Eq.(12).

EXCITED STATE DIAGNOSTICS

Degree of deviation from equilibrium

For a dispersion line profile, rearranging of Eq.(2) gives

$$N_a = (c\pi/h\nu)B^{-1} p\delta. \quad (13)$$

We introduce the degree of deviation from excitation equilibrium averaged

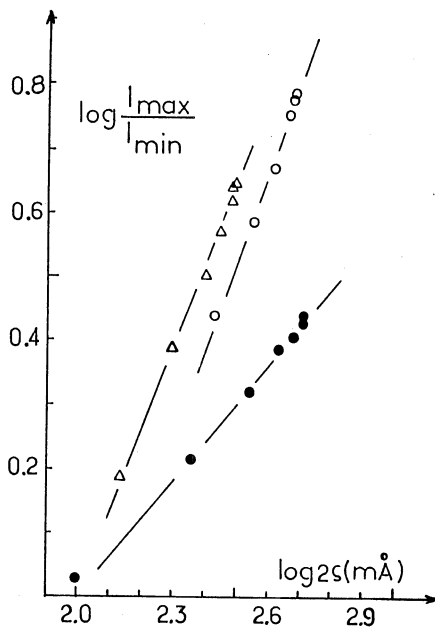


Fig. 2. Experimental dependence of $\log(I_{\max}/I_{\min})$ upon $\log(2s)$ for a dc Hg arc (2 bar, 100 W/cm, $R=1\text{cm}$). ●, 546.1 nm; ○, 435.8 nm; Δ, 404.7 nm. Each consecutive point is displaced 1 μm from the arc axis or the previous point. From Ref. 13.

along an arc radius $B_a = N_a/N_a^{\text{eq}}$, and the degree of deviation from excitation equilibrium in the arc axis $b_a = n_a(o)/n_a^{\text{eq}(o)}$. The superscript (eq) denotes the values under LTE conditions. The equilibrium values can be calculated from the equilibrium temperature profile $T^{\text{eq}}(r)$, obtained from optically thin lines, and Boltzmann's law. B_a and b_a are related by

$$b_a = (n^{\text{eq}}/n)B_a \quad (14)$$

Thus, B_a , b_a , N_a and $n_a(o)$ can be determined from the measurement of $p\delta$, n and T^{eq} .

Experimental Results

In the following we present results concerning the metastable (6^3P_2 and 6^3P_0) and resonance (6^3P_1) mercury levels in high-pressure mercury arcs operating on 50 Hz ($\sim 100 \text{ W/cm}$). The self-reversed Hg 546.1-, 435.8-, and 404.7-nm lines were used. The equilibrium values were obtained from Abel inversion of the optically thin Hg 577-nm line. Figure 3 shows the determined values of B_a and b_a in terms of the arc pressure at 0.5 ms and 5 ms after the voltage zero crossing of the ac cycle. The time modulation of the temperature $T_a(0)$ for the 6^3P_1 level, determined by the formal equation

$$\frac{n_a}{n_a^{\text{eq}}} = \exp \left(-\frac{E_a}{kT_a} \right) / \exp \left(-\frac{E_a}{kT^{\text{eq}}} \right) \quad (15)$$

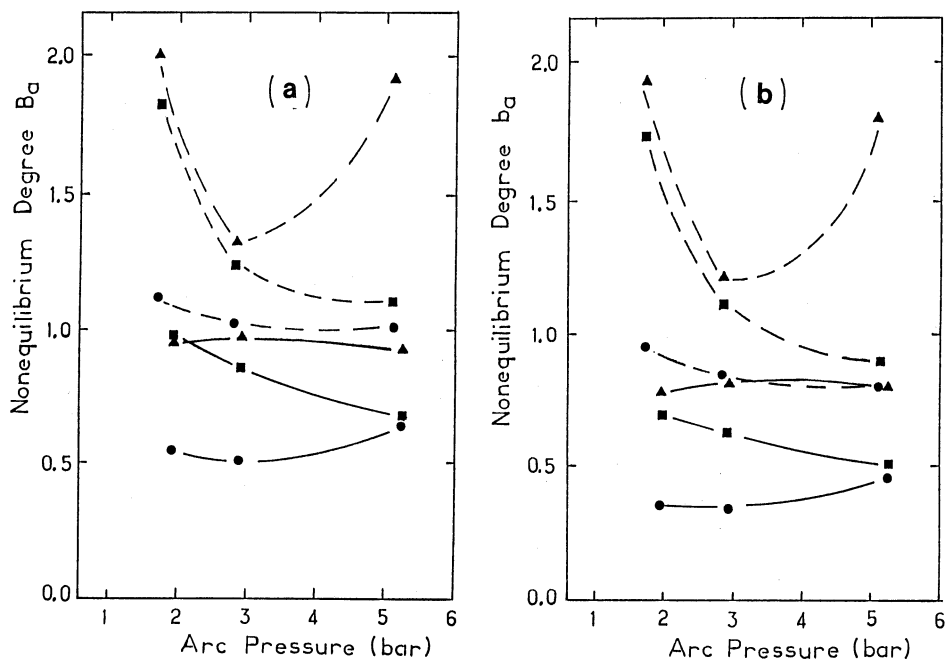


Fig. 3. Experimental dependence of the degrees of excitation nonequilibrium on the arc pressure at 0.5 ms (dashed lines) and 5 ms (solid lines). ▲, 6^3P_2 ; ●, 6^3P_1 ; ■, 6^3P_0 . From Ref. 17.

is given in Fig. 4 along with the modulation of $T_{eq}(0)$. The estimated experimental errors are $\Delta B_a/B_a = 8\%$, $\Delta b_a/b_a = 12\%$ at 5 ms, and $\Delta B_a/B_a = 12\%$, $\Delta b_a/b_a = 16\%$ at 0.5 ms.

DISCUSSION AND CONCLUSIONS

In an ac Hg arc it has been found by an interferometric technique^{18,19} that atom kinetic temperature T_g does not undergo a modulation over the current period and its value is lower about 1000–1500 K than the value of T_{eq} at the moment of maximum current phase.

On the other hand, using an expression for the electron energy distribution function (EEDF)²⁰ which takes into account depletion of the distribution tail due to inelastic electron collisions²¹, the deviations from excitation equilibrium of the Hg 6^3P levels (considered as one level) have been calculated²² without consideration of the radiation emission. It has been found that for $T_{el} > T_g$, then $b_a < 1$, where T_{el} is the electron temperature with $T_{el} = T_{eq}$, this result is in qualitative accordance with the results obtained (Fig. 3 and 4).

Furthermore, the emission of the radiation reduces the density of the excited states in comparison with their equilibrium values. Therefore, the population of the 6^3P level should be affected by the emission of the resonance line 253.7 nm ($6^3P_1 \rightarrow 6^1S_0$) and it explains why the relative population of the metastable levels (6^3P_2 and 6^3P_0) is higher than that of the resonance level. The resonance radiation emitted from the arc core is partially absorbed in the peripheral regions and causes an overpopulation of the 6^3P_1 at the arc periphery, so that $B(6^3P_1) > b(6^3P_1)$. The ensuring high population of the 6^3P_1 is rapidly transferred to the metastable levels by inelastic collisions. It results that $B(6^3P_{2,0}) > b(6^3P_{2,0})$. The overpopulation of the 6^3P_1 level in the periphery has also been confirmed experimentally²³ by determining the temperature from the maximum intensity of the resonance line.

As the pressure increases the electron-atom collision frequency increases too, so that $b_a, B_a \rightarrow 1$, as is the case for the $6^3P_{1,2}$ levels at 5 ms, and $6^3P_{1,0}$ levels at 0.5 ms (Fig. 3). The energy gap between 6^3P_1 and 6^3P_0 is 0.22 eV, and the atomic density two to three orders of magnitude greater than the electronic density. Therefore, the contribution of the atom-atom collision to the $6^3P_0 \rightarrow 6^3P_1$ transition should be considerable. This effect may explain the decrease of the 6^3P_0 population increasing the pressure.

The maximum of the 6^3P_1 population occurs at ~ 2 ms, i.e., at the maximum of the electric field (Fig. 4). From experimental observations it has been concluded¹⁴ that the population of the 6^3D_2 level (upper level of the 577 nm line) and, consequently, T_{eq} is modulated in phase with the electron density, while the modulation of the 6^3P_1 level should be sensitive to the variation of the electronic temperature. This conclusion can be also deduced from calculation of the time modulation of the T_{el}/T_g ratio²⁴. It has been shown that the T_{el}/T_g ratio is modulated in phase with the electric field and, at the moment where the maximum of the electric field occurs, the electron density lags behind the equilibrium values²⁴. Therefore, if we assume that T_g is constant during the current period, the $T_{el}-T_g$ difference attains its maximum value at the moment of the maximum of the electric field.

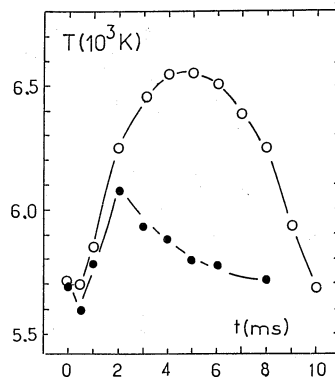


Fig. 4. Modulation of the equilibrium temperature (○) T_{eq} and of the population temperature (●) T_a of the 6^3P_1 level at the axis of an ac, 3 bar H_g arc. From Ref. 14.

The error in the determination of N_a introduced by the particular form of the excitation function [Eq. (10)] used in our model, was recently determined²⁵. This has been done by solving Eq. (1) numerically on the basis of a simulated experiment. It has been found that for the case of a LTE H_g arc with parabolic or cubic temperature profile the model used gives N_a values that fall within 10% of the exact values.

In conclusion we note that our experimental results are in qualitative accordance with calculations. We must however emphasize that the accuracy of the self-reversed line method for excited state diagnostics depends on the choice of the E(y) and P(u) functions.

REFERENCES

1. R.D. Cowan, and G.H. Dieke, **Rev. Mod. Phys.** 20 : 418 (1948).
2. H. Bartels, **Z. Phys.** 127 : 243 (1950).
3. H. Bartels, **Z. Phys.** 128 : 546 (1950).
4. T. Tako, **J. Phys. Soc. Japan**, 16 : 2016.
5. N.G. Preobrazhensky, **Opt. Spectrosc.** 17 : 4 (1964).
6. N.G. Preobrazhensky, **Opt. Spectrosc.** 22 : 95 (1967).
7. N.G. Preobrazhensky, "Spectroscopy of an Optically Thick Plasma" Nauka, Novosibirsk (1971).
8. D. Karabourniotis, in "Radiative Processes in Discharge Plasmas", J.M. Proud and L.H. Luessen, eds., Plenum, NY (1986).
9. W.J. van den Hoek, **Philips J. Res.** 38 : 188 (1983).
10. I.S. Fishman, G.G. Illin, and M.Kh. Salakhov, **J. Phys. D : Appl. Phys.** 20 : 728 (1987).
11. D. Karabourniotis, **J. Phys. D : Appl. Phys.** 16 : 1267 (1983).
12. D. Karabourniotis, S. Couris, J.J. Damelincourt, and M. Aubes, **IEEE Trans. Plasma Sci.** PS14 : 325 (1986).
13. D. Karabourniotis, **Optics Comm.** 61 : 38 (1987).
14. D. Karabourniotis, and S. Couris, **Optics Comm.** 65 : 22 (1988).
15. D. Karabourniotis, and S. Couris, **Optics Comm.** 67 : 214 (1988).
16. D. Karabourniotis, **Optics Comm.** 67 : 218 (1988).
17. D. Karabourniotis, S. Couris, E. Drakakis, and J. J. Damelincourt, **J. Appl. Phys.** (in press).
18. V. G. Vdovin, A. A. Pustoshkin, N. A. Vdovina, and A. A. Pritkov, Proc. 3rd Intern. Symp. Sci. Techn. Light Sources, D. Blanc, ed., Toulouse (1984).
19. V. I. Borodin, L. A. Luizova, and A. D. Khakhaev, **Sov. Phys. - Plasma Phys.** 12 : 511 (1986).
20. R. Lagushenko, and J. Maya, **Journal of IES** 14 : 306 (1984).
21. J. Van der Mulllen, Thesis, Techn. University, Eindhoven (1986).
22. S. Couris, G. Zissis, M. Aubes, and J. J. Damelincourt, Proc. XIXth Inter. Conf. Phen. Ion. Gases, Belgrade (1989).
23. E. Drakakis, Thesis No 275, Univ. P. Sabatier, Toulouse (1988).
24. S. Couris, G. Zissis, and J. J. Damelincourt, Proc. XIXth Intern. Conf. Ion. Gases, Belgrade (1989).
25. P. A. Vicharelli, and D. Karabourniotis, Proc. 5th Intern. Symp. Sci. Tech. Light Sources, York (1989).

PARTICIPANTS

Country : BELGIUM

DESOPPERE ERIC STATE UNIVERSITY OF GENT-ROZIER 44
8-9000 GENT. BELGIUM

Country : DENMARK

BILLING GERT DUE CHEMISTRY LAB. III-ORSTED INSTITUTE
2100 COPENHAGEN, DENMARK

Country : FRANCE

BACAL MARTHE LABORATOIRE PMI-ECOLE POLYTECHNIQUE
91128 PALAISEAU CEDEX, FRANCE

BELENGUER PHILIPPE CENTRE DE PHYS. ATOM.-118 ROUTE DE NARBONNE
31062 TOULOUSE, FRANCE

BERLEMONT PIERRE LABORATOIRE PMI-ECOLE POLYTECHNIQUE
91128 PALAISEAU CEDEX, FRANCE

BOEUF JEAN PIERRE CENTRE DE PHYS. ATOM.-118 ROUTE DE NARBONNE
31062 TOULOUSE, FRANCE

DEROUARD J. LAB. SPECTROMETRIE PHYSIQUE-B.P. 87
38402 SAINT MARTIN D'HERES CEDEX, FRANCE

JOLLY JACQUES L.P.G.P., BAT. 212-UNIVERSITE PARIS-SUD
91405 ORSAY CEDEX, FRANCE

LEROY RENAN LABORATOIRE PMI-ECOLE POLYTECHNIQUE
91128 PALAISEAU CEDEX, FRANCE

PASQUIERS STEPHANE L.P.G.P., BAT. 212-UNIVERSITE PARIS-SUD
91405 ORSAY CEDEX, FRANCE

PITCHFORD LEANNE CENTRE DE PHYS. ATOM.-118 ROUTE DE NARBONNE
31062 TOULOUSE, FRANCE

PUECH VINCENT L.P.G.P., BAT. 212-UNIVERSITE PARIS-SUD
91405 ORSAY CEDEX, FRANCE

TOUZEAU MICHEL L.P.G.P., BAT. 212-UNIVERSITE PARIS-SUD
91405 ORSAY CEDEX, FRANCE

Country : GREECE

COURIS STELIOS	CENTRE DE PHYS. ATOM-U.P.S., 148 ROUTE DE NARBONNE 31053 TOULOUSE, FRANCE
GERASSIMOU DIMITRA	INST. CHEM.ENG. HIGH TEMP. P.-P.O.BOX 1239 GR-261 10 PATRAS, GREECE
KARABOURNIOUTIS D.	PHYSICS DEPT. 71409 IRAKLION, CRETA - GREECE
MATARAS DIMITRI	INST. CHEM.ENG. HIGH TEMP. P.-P.O.BOX 1239 GR-261 10 PATRAS, GREECE
PALLADAS ANNABELLE	PHYSICS DEPT. 71409 IRAKLION, CRETA - GREECE
ZISSIS GEORGES	CENTRE DE PHYS. ATOM.-148 ROUTE DE NARBONNE 31053 TOULOUSE, FRANCE

Country : ITALY

AQUILANTI VINCENZO	DIP. DI CHIMICA-UNIV. DI PERUGIA-VIA ELCE DI SOTTO 06100 PERUGIA, ITALY
ARRIGHINI GIAN PAOLO	DIP. DI CHIMICA-UNIV. DI PISA-VIA RISORGIMENTO PISA, ITALY
BARBAROSSA VINCENZO	ENI RICERCA S.P.A.-VIA E. RAMARINI 00015 MONTEROTONDO (ROME), ITALY
BOLLANTI SARAH	ENEA - TIB-FIS, P.O.BOX 65 00044 FRASCATI (ROME), ITALY
BRAUTTI GIULIO	DEPT. OF PHYSICS - VIA AMENDOLA 173 70126 BARI, ITALY
BRUNO CLAUDIO	DIP. MECC. E AERON.-UNIV. OF ROME-VIA EUODSSIANA 00184 ROMA, ITALY
CACCIATORE MARIO	CENTRO STUDIO CHIM. PLASMI,CNR -VIA AMENDOLA 173 70126 BARI, ITALY
CAPITELLI MARIO	DEPT. OF CHEMISTRY-UNIV. OF BARI -VIA AMENDOLA 173 70126 BARI, ITALY
CAPORUSSO ROSA ANNA	ENI RICERCA S.P.A.-VIA E. RAMARINI 00015 MONTEROTONDO (ROME), ITALY
CAPRIATI GENNARO	DEPT. OF CHEMISTRY-UNIV. OF BARI -VIA AMENDOLA 173 70126 BARI, ITALY
CELIBERTO ROBERTO	DEPT. OF CHEMISTRY-UNIV. OF BARI -VIA AMENDOLA 173 70126 BARI, ITALY
CIVES PATRICIA	DEPT. OF CHEMISTRY-UNIV. OF BARI -VIA AMENDOLA 173 70126 BARI, ITALY
DATTOLI GIUSEPPE	ENEA - TIB-FIS, P.O.BOX 65 00044 FRASCATI (ROME), ITALY

DE BENEDICTIS S.	CENTRO STUDIO CHIM. PLASMI,CNR -VIA AMENDOLA 173 70126 BARI, ITALY
DILECCE GIORGIO	CENTRO STUDIO CHIM. PLASMI,CNR -VIA AMENDOLA 173 70126 BARI, ITALY
FERRANTE GAETANO	DEPT. OF PHYSICS - UNIV. OF MESSINA MESSINA, ITALY
FICOCELLI EDGARDO	DEPT. OF CHEMISTRY-UNIV. OF BARI -VIA AMENDOLA 173 70126 BARI, ITALY
GABBANINI CARLO	ISTITUTO FISICA ATOM. E MOLEC.-VIA DEL GIARDINO 7 56100 PISA, ITALY
GIANTURCO FRANCO A.	DIPARTIMENTO DI CHIMICA-CITTÀ UNIVERSITARIA 00185 ROMA, ITALY
GORSE CLAUDINE	DEPT. OF CHEMISTRY-UNIV. OF BARI -VIA AMENDOLA 173 70126 BARI, ITALY
LAGANA' ANTONIO	DIP. DI CHIMICA-UNIV. DI PERUGIA-VIA ELCE DI SOTTO 06100 PERUGIA, ITALY
LETARDI TOMMASO	ENEA - TIB-FIS. P.O.BOX 65 00044 FRASCATI (ROME), ITALY
LONGO SAVINO	DEPT. OF CHEMISTRY-UNIV. OF BARI -VIA AMENDOLA 173 70126 BARI, ITALY
OGGIONI STAFANIA	DIPARTIMENTO DI INGEGNERIA-UNIV. DI BOLOGNA 40125 BOLOGNA, ITALY
SASSO ANTONIO	DIPT. SCIENZE FISICHE-MOSTRA D'OLTREMARE, PAD. 20 80125 NAPOLI, ITALY
VECCHIOCATTIVI F.	DIP. DI CHIMICA-UNIV. DI PERUGIA-VIA ELCE DI SOTTO 06100 PERUGIA, ITALY

Country : NETHERLANDS

HEEREN R.M.A.	FOM-INST. FOR ATOM. AND MOLEC. PHYS.-KRUISLAAN 407 NL-1098 AMSTERDAM, NETHERLANDS
HOPMAN H.J.	FOM-INST. FOR ATOM. AND MOLEC. PHYS.-KRUISLAAN 407 NL-1098 AMSTERDAM, NETHERLANDS
VAN SLOOTEN U.	FOM-INST. FOR ATOM. AND MOLEC. PHYS.-KRUISLAAN 407 NL-1098 AMSTERDAM, NETHERLANDS

Country : PORTUGAL

ALVES LUIS LEMOS	CENTRO DE ELECTRODINAMICA-INST. SUPERIOR TECNICO P-1096 LISBOA CODEX, PORTUGAL
CONDE CARLOS A.N.	PHYSICS DEPARTMENT-UNIVERSITY OF COIMBRA P-3000 COIMBRA, PORTUGAL
DIAS F. MARQUES	CENTRO DE ELECTRODINAMICA-INST. SUPERIOR TECNICO P-1096 LISBOA CODEX, PORTUGAL

FERREIRA C. MATOS CENTRO DE ELECTRODINAMICA-INST. SUPERIOR TECNICO
P-1096 LISBOA CODEX, PORTUGAL

LOUREIRO JORGE CENTRO DE ELECTRODINAMICA-INST. SUPERIOR TECNICO
P-1096 LISBOA CODEX, PORTUGAL

PERES ALONSO MANUEL AZINHAGA DOS LAMEIROS A-ESTR. DO PACO DO LUMIAR
P-1699 LISBOA CODEX, PORTUGAL

SA' ANA BELA CENTRO DE ELECTRODINAMICA-INST. SUPERIOR TECNICO
P-1096 LISBOA CODEX, PORTUGAL

Country : SPAIN

BAUTISTA J. COTRINO DPTO FISICA APPLICADA-FAC. CIENCIAS SAN ALBERTO M.
S/N 14071 CORDOBA, SPAIN

Country : TURKEY

GOKMEN ALI DEPT. OF CHEMISTRY-MIDDLE EAST TECHNICAL UNIV.
ANKARA 06131, TURKEY

Country : UNITED KINGDOM

GLOSIK J. DEPT. OF PHYSICS-U.C.S. WALES
ALBERYSTWYTH SY23 3BZ, UNITED KINGDOM

JAVAHERY REZA DEPT. OF PHYSICS-U.C.S. WALES
ALBERYSTWYTH SY23 3BZ, UNITED KINGDOM

KAUFMAN Y. BLACKETT LAB.-PLASMA PHYS.-IMP. COL. SCIENCE & TECH.
PRINCE CONSORT RD.-LONDON SW7 2BZ, UNITED KINGDOM

TWIDDY N.D. DEPT. OF PHYSICS-U.C.S. WALES
ALBERYSTWYTH SY23 3BZ, UNITED KINGDOM

Country : USA

ALI A.W. CODE 4700.1-NAVAL RESEARCH LABORATORY
WASHINGTON D.C. 20375, USA

BARDSLEY J. NORMAN LAWRENCE LIVERMORE NATIONAL LABS. P.O.BOX 808
LIVERMORE, CA 94550, USA

BECKER KURT H. DEPT. OF PHYSICS-CCNY COVENT AVE. AT 138TH STREET
NEW YORK, NY 10031, USA

BHATTACHARYA A.K. GENERAL LIGHTING-MS #5433, NELA PARK
CLEVELAND OH 44112, USA

CHRISTOPHOROU L.G. DAK RIDGE NAT. LAB.-P.O.BOX 2008 DAK RIDGE
TN 37831-6122, USA

CLARK STEVEN WEBER RESEARCH INSTITUTE-POLYTECHNIC UNIV.
FARMINGDALE, NY 11735, USA

GALLAGHER ALLAN JILA-JILA UNIVERSITY OF COLORADO
BOULDER, CO 80309, USA

GARSCADDEN ALAN	AIR FORCE WRIGHT AER. LABS.-WRIGHT PATTERSON AFB DAYTON, OH 45433, USA
HISKES JOHN R.	LAWRENCE LIVERMORE NATIONAL LABS.-P.O.BOX 808 LIVERMORE, CA 94550, USA
HUO WINIFRED M.	NASA AMES RESEARCH CENTER-MAIL STOP 230-3 MOFFET FIELD, CA 94035, USA
JOHNSEN RAINER	DEPT. OF PHYSICS AND ASTRONOMY-UNIV. OF PITTSBURGH PITTSBURGH, PA 15260, USA
KUNHARDT ERICH	WEBER RESEARCH INSTITUTE-POLYTECHNIC UNIV. FARMINGDALE, NY 11735, USA
KUSHNER MARK	UNIVERSITY OF ILLINOIS-607 EAST HEALEY CHAMPAIGN, ILLINOIS 61820, USA
LEE YIM T.	LAWRENCE LIVERMORE NATIONAL LABS.-P.O.BOX 808 LIVERMORE, CA 94550, USA
MANSKY II E.J.	SCHOOL OF PHYSICS-GEORGIA INST. OF TECHNOLOGY ATLANTA, GA 30332-0430, USA
MARTUS KEVIN E.	DEPT. OF PHYSICS-CCNY COVENT AVE. AT 138TH STREET NEW YORK, NY 10031, USA
MC CAUGHEY MICHAEL	UNIVERSITY OF ILLINOIS-607 EAST HEALEY CHAMPAIGN, ILLINOIS 61820, USA
PAK HOYOUNG	UNIVERSITY OF ILLINOIS-607 EAST HEALEY CHAMPAIGN, ILLINOIS 61820, USA
PETERKIN FRANCK E.	DEPT. OF ELECTRICAL ENGINEERING-209N WSEC LINCOLN, NEBRASKA 68588-0511, USA
RESCIGNO THOMAS N.	LAWRENCE LIVERMORE NATIONAL LABS.-P.O.BOX 808 LIVERMORE, CA 94550, USA
SKINNER DARREL A.	LABORATOIRE PMI-ECOLE POLYTECHNIQUE 91128 PALAISEAU CEDEX, FRANCE
SOMMERER TIMOTHY J.	DEPT. OF PHYSICS-1150 UNIVERSITY AVENUE MADISON, WISCONSIN 53706, USA

Country : WEST GERMANY

EHRHARDT H.	FACHBEREICH PHYSIK DER UNIV.-E. SCHRODINGER STR. 46 6750 KASERSLAUTERN, WEST GERMANY
STORR HELMUT	INST. FUR PLASMAPHYSIK-UNIV. HANNOVER-CALLIGSTR.38 D-300 HANNOVER 1, WEST GERMANY
WALDEER THOMAS	INST. FUR THEORETISCHE PHYSIK-TECHNISCHE UNIV. MENDELSSOHNSTR. 3, 3300 BRAUNSCHWEIG, WEST GERMANY

NON NATO COUNTRIES

Country : CHINA

SHU F.S.

ENEA - TIB-FIS, P.O.BOX 65
00044 FRASCATI (ROME), ITALY

Country : INDIA

NAGPAL RAJESH

CHEMISTRY DEPARTMENT-INDIAN INST. OF TECH. KAMPUR
KAMPUR 208016, INDIA

Country : IRELAND

HOPKINS MIKE

PHYSICS DEPT.-NIHE, GLASNEVIN
DUBLIN 9, IRELAND

MOLLOY J.

PHYSICS DEPT.-NIHE, GLASNEVIN
DUBLIN 9, IRELAND

Country : JAPAN

FUKUMASA OSAMU

DEPT. ELECTRICAL ENGINEERING-UNIV. UBE
UBE, JAPAN

HAYASHI MAKOTO

NAGOYA INST. OF TECHNOLOGY/GOKISO-CHO,SHOWA-KU
NAGOYA 466, JAPAN

MAKABE TOSHIAKI

DEPT. ELECTRICAL ENGINEERING/HIYOSHI-CHO,KONOKU-KU
KEIO UNIV., YOKOHAMA 223, JAPAN

TAGASHIRA HIROAKI

DEPT. ELECTRICAL ENGINEERING-HOKKAIDO UNIV.
SAPPORO 060, JAPAN

Country : JUGOSLAVIA

POPOVIC D.

INSTITUTE OF PHYSICS
BEOGRAD, JUGOSLAVY

Country : SWITZERLAND

ELIASSON B.

CORPORATE RESEARCH-SEGELHOLF
CH-5405 BADEN, SWITZERLAND

FAVRE MYRIAM

INSTITUT OF MICROTECHNIQUE-BREGET 2
2000 CH NEUCHATEL,SWITZERLAND

HOWLING ALAN

CENTRE RECH. PHYS. PLASMAS-ECOLE POLYT. FEDER.-21
AVE DES BAINS,CH-1007 LAUSANNE,SWITZERLAND

ZIEGLER YVAN

INSTITUT OF MICROTECHNIQUE-BREGET 2
2000 CH NEUCHATEL,SWITZERLAND

OBSERVERS

COLONNA GIAMPIERO

DEPT. OF PHYSICS - VIA AMENDOLA 173
70126 BARI, ITALY

FAVIA PIETRO	DEPT. OF CHEMISTRY-UNIV. OF BARI -VIA AMENDOLA 173 70126 BARI, ITALY
HAMILTON JOHN	LABORATOIRE PMI-ECOLE POLYTECHNIQUE 91128 PALAISEAU CEDEX, FRANCE
MANODORO PIETRO	DEPT. OF CHEMISTRY-UNIV. OF BARI -VIA AMENDOLA 173 70126 BARI, ITALY
PERUGINO VITO	DEPT. OF PHYSICS - VIA AMENDOLA 173 70126 BARI, ITALY
PISCHE VALTER	DEPT. OF CHEMISTRY-UNIV. OF BARI -VIA AMENDOLA 173 70126 BARI, ITALY
RAINO' ANTONIO	DEPT. OF PHYSICS - VIA AMENDOLA 173 70126 BARI, ITALY
TORRE AMALIA	ENEA - TIB-FIS. P.O.BOX 65 00044 FRASCATI (ROME), ITALY

INDEX

- Air chemistry, 652-654, 66
Atom diatom reactive scattering
 D-D₂ rates, 121
 H-ClH rates, 124
 H-HCl rates, 123
 H-H₂ rates, 121
 quantum approach, 109-111
 quasi-classical treatment, 107-109
Boltzmann equation, 35-37, 87-88, 187-189
Carbon films
 amorphous, 253
 diamondlike, 256
Cathode fall, 459
Cross sections from Boltzmann analysis
 C₂H₄, 338
 C₂H₂, 338
 CO₂, 337
 Hg, 336
 Ne, 335
 NH₃, 337
 NO, 336
 SiH₄, 339
Discharge lamps
 excited state diagnostics, 672, 677
 high pressure, 265
 low pressure, 263
Dissociative attachment, 7, 11, 14, 213
Electron-electron collisions, 195, 417
Electron energy distribution function
 Ar high frequency discharges, 197-200
 CH₄ RF discharges, 469
Electron energy distribution function (continued)
 He-N₂ RF discharges, 455-457
 H₂ discharges, 556
 H₂ RF discharges, 470
 H₂ tandem source, 538
 Ne-Xe-HCl RF discharge, 58-59
 N₂ discharges, 48, 555
 N₂-H₂ discharges, 557
 N₂ high frequency discharges, 201-203
 N₂ post-discharges, 49
 N₂ RF discharges, 56-57
Electron impact electronic excitation
 excited He, 352-354
 excited N₂, 345-348
 H₂, 280
 vibrationally excited H₂, 54, 361
Electron impact ionization, 30
Electron impact vibrational excitation
 H₂, 13
 N₂, 343-344
Electron macrokinetics, 591
Electron molecule scattering experiments
 dissociative excitation, 285-289
 electron attachment, 293-301
 electronic excitation, 29
 rotational excitation, 23-26
 vibrational excitation, 26-29
Electron molecule scattering theory
 Born approximation, 270-272
 close coupling method, 326
 Kohn method, 5, 357-361
 Gryzinsky method, 5, 54
 multichannel eikonal theory, 349-351

- Electron molecule scattering
 theory (continued)
 off shell generalization,
 312-317
 resonant scattering theory,
 6
 R-matrix, 4
 Schwinger variational
 principle, 5, 347
 Electron-ion scattering, 15
 Energy pooling collisions,
 373-381
 Energy transfer
 Atom-diatom collisions, 93
 diatom-diatom collisions, 94
 H₂ V-T rates, 489-491
 H₂ V-V rates, 488-491
 V-T processes, 98
 V-V processes, 96-97
 Electron velocity distribution
 function, 34
 Excimer lasers
 Discharge circuit, 66, 134,
 412
 KrF, 65-69
 local field approximation, 70
 photoswitched discharge, 425
 preionization, 65, 153, 429
 pumping schemes, 132-138
 selfconsistent model, 411-415
 streamers, 85-87, 137
 XeCl, 131, 141, 421, 431

 Free electron laser, 607-615

 Gas-switches, 291, 303

 H₂-Cu interaction, 494-495
 H₂ vibrational distribution,
 52, 237-239, 519-520, 528
 H⁻ sources, 50-55, 213-224,
 505-514

 Ion containment, 479
 Ion neutral reactions, 365-371
 Ionization cross sections, 396-
 398

 Laser diagnostics
 Barium lamps, 672
 H₂ discharge, 227-239
 N₂ discharge, 463
 RF oxygen plasmas, 564-566
 Laser gain, 148-151, 610, 646

 Molecular beam, 383, 393
 Molecule surface scattering,
 101, 249
 Monte-Carlo simulation, 37-39,

 Monte-Carlo simulation
 (continued)
 433-440, 584-585, 594,
 602-603
 Multimode laser field, 624

 Multiphoton Bremsstrahlung,
 630
 Multiphoton ionization, 611

 Negative glow, 459
 Nuclear radiation detector,
 581

 Oxygen plasmas
 diagnostics, 571-575
 kinetics, 575-578

 Plasma kinetics, 45
 Potential energy curves
 F-Ar, F-CH₄, F-D₂, F-He,
 F-Kr, F-Ne, 390
 H₂-Cu, 492
 KrF, 66
 O₂, 563
 XeCl, 130

 Resonant photopumping, 643
 RF discharges
 electric field profiles,
 160-161, 446-448
 electron kinetics, 178,
 468-471
 fundamental properties,
 155-186
 modulation, 57
 Monte-Carlo modeling, 433-440
 relaxation continuum model,
 472-476
 secondary electron regime,
 166, 173
 wave riding, 165, 172

 Si-H₄ discharges, 541-550
 Silent discharges
 excimer formation, 408-409
 ozone formation, 406-408
 physics, 402-404
 Superelastic collisions
 electronic, 45-46, 49, 417
 vibrational, 46, 201, 554
 Surface chemistry, 661
 Surface recombination, 518

 Tandem ion source, 215-217,
 505, 536
 Translational energy
 distribution functions
 excited H, 500-501

Translational energy
distribution functions
(continued)
protons, 502

Velocity moments, 39-40
Vibrational kinetics, 46, 551